

1.1 Introduction to Electroanalytical Techniques and Instrumentation

Patrick R. Unwin
University of Warwick, Coventry,
United Kingdom

1.1.1 Context

Many advances in understanding electrochemical processes, described throughout this *Encyclopedia*, have come about as a result of continued developments in techniques and instrumentation for studying electrode reactions and interfaces. This volume is concerned with some of the most important general electrochemical methods, and also highlights some of the more specialized techniques that are of wide applicability in chemistry and its borders with other fields.

Simple electroanalytical techniques fall into three groups: potentiometry, conductivity, and voltammetric/amperometric techniques. This volume is mostly concerned with the third type of method, often referred to under the general heading *dynamic electrochemistry*. Given the importance of potentiometric methods of analysis, these will be introduced and discussed in this chapter. As mentioned in Sect. 1.1.3, there is renewed

interest in potentiometric ion-selective electrodes (ISEs) following the massive breakthrough in detection limits to the pM level [1, 2]. Moreover, potentiometric methods are used in some scanning electrochemical microscopy (SECM) experiments, discussed in Chapter 3.3 and some biosensor formats (Chapter 2.11), and so it is useful to provide a brief summary of the basic principles here.

Conductivity measurements are much less chemically specific and so are not considered in detail in this volume, although Chapter 2.11 describes some biosensors that operate on conductimetric principles. It is also important to note, in passing, the use of conductimetric methods in analysis [3], particularly for capillary electrophoresis [4, 5] and in ion chromatography [6].

Our understanding of electrochemical methods has also been greatly enhanced by the introduction of spectroscopic, structural and other probes of electrochemical surfaces and systems [7]. This continues to be a developing area and consequently there is little scope within a single volume to review all of the techniques available, rather the focus is on some of the most commonly encountered structural and chemical probes of interfaces and solutions.

As discussed in more detail in Sect. 1.1.5, this volume of the *Encyclopedia* is divided into three broad sections. The first section, of which this chapter is an element, is concerned with introducing some of the basic concepts of electroanalytical chemistry, instrumentation – particularly electronic circuits for control and measurements with electrochemical cells – and an overview of numerical methods. Computational techniques are of considerable importance in treating electrochemical systems quantitatively, so that experimental data can be analyzed appropriately under realistic conditions [8]. Although analytical solutions are available for many common electrochemical techniques and processes, extensions to more complex chemical systems and experimental configurations requires the availability of computational methods to treat coupled reaction-mass transport problems.

The second section of this volume is concerned with electroanalytical techniques, starting with the principles of standard voltammetric and amperometric methods, then progressing to more specialized, but equally important, experimental approaches that can provide major insights into electrochemical processes. Finally, the last section of this volume focuses on spectroelectrochemistry and surface microscopy techniques.

1.1.2

Basic Concepts and Terminology

In order to set the scene for some of the chapters that follow, it is useful to provide a brief overview of some of the terminology and basic concepts needed to understand electroanalytical techniques. Electrochemistry is a broad field, encompassing those processes that involve the passage of charge across the interface between two

phases. Electron transfer from a metal electrode to a redox active species in an electrolyte solution, and the transfer of an ion from an aqueous phase to an immiscible organic phase are examples of electrochemical processes. The first case is the most common class of electrochemical process and will be discussed in detail in most of the chapters in this volume. Ion transfer processes are, however, of significant interest in many areas, for example in bioenergetic and cellular processes [9], and in the switching behavior of polymer modified electrodes [10], to name but two. These areas are visited in Volumes 9 and 10 of the *Encyclopedia* and some aspects are highlighted in the treatments of scanning electrochemical microscopy (SECM) and the electrochemical quartz crystal microbalance (EQCM), in Chapters 3.3 and 2.7 of this volume.

Although the interest in an electrochemical system is generally on a single interface, it is important to recognize that an individual interface cannot be studied experimentally. It is necessary to investigate *electrochemical cells* that involve several types of interface coupled together in series. In the simplest form, electrochemical cells involve two electrodes in a single electrolyte phase. The difference in electrical potential between the two electrodes in such a cell can readily be measured, usually with a high impedance voltmeter, to ensure that no current is drawn when the measurement is made. The cell potential is a measure of the energy inherent in the system to transfer charge between the two electrodes via an external circuit. The overall cell potential comprises the individual changes in potential that occur when crossing each of the interfaces in the cell. It is important to recognize that the change in electric potential when moving a test charge from one conducting phase

to an adjacent conducting phase usually occurs over a short length scale so that huge electric fields may predominate at the interfaces in electrochemical cells. There are consequently significant effects on the structure of solvents in the interfacial region and the ion distribution, as discussed further in several of the chapters in Sect. 2 of Volume 1 of the *Encyclopedia*. More generally, the magnitude of the potential difference at an interface controls both the direction and kinetics of electron transfer. It follows that the control and measurement of cell potential is an important aspect of dynamic electrochemistry experiments and methods for achieving this through the appropriate design and operation of

electronic instrumentation are explained in detail in Chapter 1.2 of this volume.

For a two-electrode cell, the *net reaction* comprises two *half-reactions*, involving the processes at the two electrodes. As already mentioned, usually only one of these processes is of interest, and this occurs at the *working electrode* in dynamic electrochemistry experiments or *indicator electrode* in equilibrium (potentiometric) experiments. The other electrode is made up such that it maintains a constant composition throughout the measurement, thus providing a *reference potential*. The most common reference for aqueous solution is the saturated calomel electrode (SCE), depicted in Fig. 1, and this provides

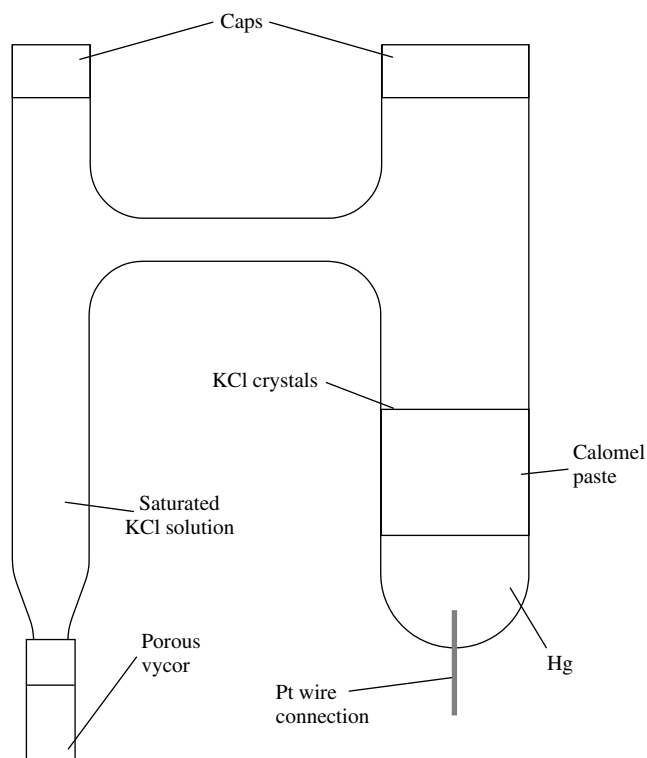
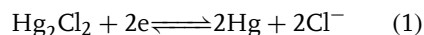


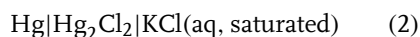
Fig. 1 Schematic of a saturated calomel electrode (SCE). Contact between this reference electrode and the solution is made via the porous vycor.

a useful example with which to introduce some electrochemical notation, terminology, and convention. The half-cell reaction for this electrode is



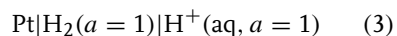
The use of saturated (and solid) KCl in this electrode ensures that the Cl^- concentration is maintained at a constant level. Any reduction of Hg_2Cl_2 (driving Eq. (1) from left to right) produces Cl^- , but this cannot exceed the saturated value. A shift in Eq. (1) from right to left (oxidation of Hg and formation of Hg_2Cl_2) will tend to deplete Cl^- , but this is replenished via the dissolution of solid KCl. Note that both Hg_2Cl_2 and Hg, as solid and pure liquid, respectively, have an activity of unity.

It is convenient to develop a notation for electrochemical cells and half-cells. In the case of Eq. (1), the half-cell would be represented as



Here, a vertical line signifies a boundary between two phases. If a phase contains two or more components, a comma is used to separate them, while a double vertical line denotes a phase boundary in which the interfacial potential drop is negligible, as usually occurs in the case of a salt bridge.

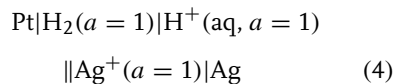
It should be noted that the international standard reference electrode is the *standard hydrogen electrode* (SHE), sometimes referred to as *normal hydrogen electrode* (NHE), in which all the components have unit activity ($a = 1$):



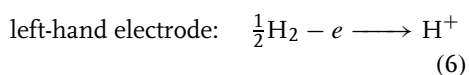
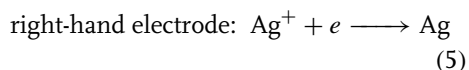
This electrode is not easy to use practically, but the potential of the NHE electrode is assigned the value zero and, strictly, all other electrode potentials are compared

with this. For comparative purposes, tables of electrode (or half-cell) potentials have been constructed, with the half-cell reactions at unit activity. Following convention, they are written as reductions. Such indexes [11, 12] are essentially a measure of the free energy of redox couples, as highlighted below, so allowing one to predict whether a redox reaction of interest will occur spontaneously. Moreover, these tables provide valuable data to permit the calculation of equilibrium constants and complexation constants.

When constructing a cell, by the combination of two half-cells, the convention adopted is that the right-hand electrode is always considered as a *reduction (cathodic) process* and the left-hand electrode is an *oxidation (anodic) process*. This formalism can be illustrated by considering the following cell:



for which the half-cell reactions are



In this case, the cell potential is +0.799 V at 298 K and the silver electrode is positive. This means that the standard potential of the Ag^+/Ag couple has this value, in other words the standard potential for the reduction of Ag^+ to Ag is +0.799 V versus SHE. On the other hand, if the cell had been written with the Ag electrode on the left-hand side, the cell would have a potential of −0.799 V, implying that the Ag electrode is negative and the oxidation potential of Ag to Ag^+ is −0.799 V versus SHE. Strictly then, the potential of any cell,

E_{cell} , is

$$E_{\text{cell}} = E_{\text{RHE}} - E_{\text{LHE}} \quad (7)$$

where E_{RHE} and E_{LHE} represent the potentials of the right- and left-hand electrodes, respectively, written as reduction processes in the particular schematic of a cell.

The terminology adopted to describe electrochemical cells implies that a *spontaneous process* has a *positive electrode potential*. E_{cell} defines the maximum work (free energy), ΔG , that a cell can provide:

$$\Delta G = -nFE_{\text{cell}} \quad (8)$$

where n is the number of electrons in the redox process and F is Faraday's constant (96485 C mol^{-1}). Under standard conditions, with all substances at unit activity:

$$\Delta G^0 = -nFE_{\text{cell}}^0 \quad (9)$$

where E_{cell}^0 is the standard cell potential. A detailed treatment of electrode potentials is given in Chapter 1 of Volume 1 of the *Encyclopedia*.

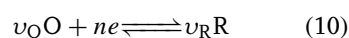
In contrast with potentiometry, where an electrode potential is measured (with no current flowing), in most dynamic electrochemistry experiments, the potential of the working electrode is controlled with respect to a reference electrode and the resulting current is measured. There are exceptions to the latter class of measurements, notably chronopotentiometry [13] in which a constant current is generated and the potential of the working electrode is measured, but for the purposes of this introduction it is appropriate to consider simple potential control of the working electrode. Chronopotentiometry is discussed later in Chapter 2.2 of this volume (Sect. 2.2.5). Since the reference electrode potential is fixed, changing the potential applied to the working electrode

alters the energy of the *Fermi level* in the electrode compared with the energy levels of the chemical moieties in the electrolyte (or immobilized on the electrode surface). For example, taking the electrode to negative potentials increases the energy of electrons and ultimately a level will be attained where the electrons flow from the electrode to vacant states on the chemical species, as shown in Fig. 2(a). This causes a reduction current to flow. Conversely, if the electrode is taken toward positive potentials, a situation will be achieved where electrons will transfer from chemical species in solution to the electrode, causing an oxidation current to flow, as illustrated in Fig. 2(b). The electrode potentials at which these processes occur will clearly be related to the standard potential of the redox process of interest, while the current flow is governed by the kinetics of the reaction. These aspects of dynamic electrochemistry are considered further in Sect. 1.1.4. In the next section, we first consider the analytical applications of electrochemical cells and potential measurements at equilibrium.

1.1.3

Potentiometry

In contrast with amperometric electrodes, potentiometric electrodes are passive in that they do not convert the analyte. The main use of potentiometry is to measure the concentration (strictly activity) of a target analyte and so it is useful to revisit the Nernst equation, relating the cell potential to activity. For this purpose, consider a simple redox reaction at the right-hand electrode of a cell, with SHE as the left-hand electrode. The process at the right-hand electrode is



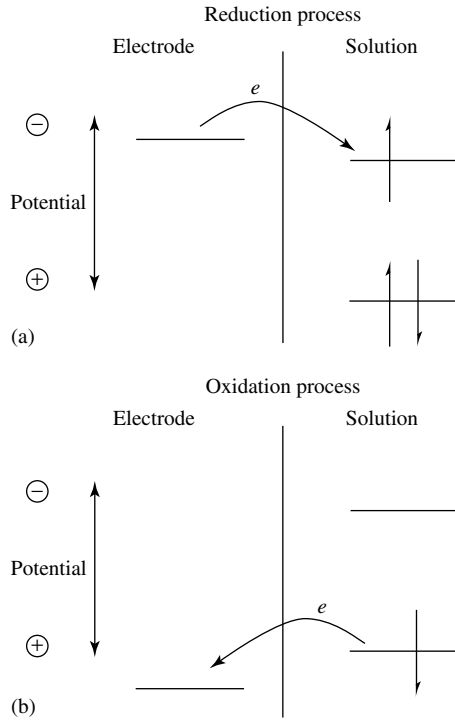


Fig. 2 Schematic of heterogeneous electron transfer for (a) reduction processes and (b) oxidation processes.

of concentrations:

$$E = E^0 - \frac{RT}{nF} \ln \frac{\gamma_R^{v_R}}{\gamma_O^{v_O}} - \frac{RT}{nF} \ln \frac{[R]^{v_R}}{[O]^{v_O}} \quad (14)$$

where γ_i ($i = O$ or R) denotes the activity coefficient. Under conditions in which the activities are effectively constant (for example in systems with a large excess of supporting electrolyte), we may introduce the formal potential, $E^{0'}$, of the O/R couple:

$$E^{0'} = E^0 - \frac{RT}{nF} \ln \frac{\gamma_R^{v_R}}{\gamma_O^{v_O}} \quad (15)$$

allowing us to simplify the Nernst relation:

$$E = E^{0'} - \frac{RT}{nF} \ln \frac{[R]^{v_R}}{[O]^{v_O}} \quad (16)$$

It is convenient to express Eq. (16) on a \log_{10} scale so that

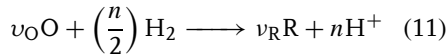
$$E = E^{0'} - \frac{2.303RT}{nF} \log_{10} \frac{[R]^{v_R}}{[O]^{v_O}} \quad (17)$$

Evaluating the prelogarithmic term, this shows that the potential of the cell changes by $\pm 59/n$ mV (at 298 K) for a decade change in concentration of either the O or R species (for $v_O = v_R = 1$), which is the basis of analytical potentiometry.

A practical example of an O/R couple would be $\text{Fe}^{3+}/\text{Fe}^{2+}$ in aqueous solution. To record the potential of such a system, one would typically use an inert metal, such as Pt, as the indicator electrode.

There are many other examples of potentiometric electrodes, including a metal in contact with a solution containing the corresponding metal ions, as in the case of the $\text{Ag}|\text{Ag}^+$ electrode. This electrode, which comes under the classical

Here, v_i ($i = O$ or R) represents the stoichiometric coefficients. The overall cell reaction for the case defined is



The free energy of the process is [14]

$$\Delta G = \Delta G^0 + RT \ln \frac{a_R^{v_R} a_{\text{H}^+}^n}{a_O^{v_O} a_{\text{H}_2}^{n/2}} \quad (12)$$

Since the activities of H^+ and H_2 in the SHE are unity, it follows from Eqs. (8 and 9) that

$$E = E^0 - \frac{RT}{nF} \ln \frac{a_R^{v_R}}{a_O^{v_O}} \quad (13)$$

This is the *Nernst equation*, describing the potential of the O/R couple as a function of the activities of O and R. We may also write the Nernst equation in terms

term *electrode of the first kind*, responds to the concentration of Ag^+ ions in solution. An *electrode of the second kind* involves a metal coated in a sparingly soluble salt of the metal, which responds to the concentration of the anion of the salt in solution. The most well-known example is $\text{Ag}|\text{AgCl}|\text{Cl}^-$, which provides a simple, but effective method for chloride ion analysis in aqueous solution. The SCE, already mentioned, is another example of this type of electrode.

The pH electrode is perhaps the best known ISE [15, 16], in which a thin glass membrane (50 μm dimension) separates an internal solution of fixed pH from an external test solution in which the pH is to be determined [17]. The potential across the glass-barrier membrane is measured with reference electrodes in each phase. The functioning of the glass electrode is complicated, with the majority of the glass membrane in a dry state and a layer about 50 nm into each side of the membrane involved in an exchange process of protons for Na^+ , K^+ and Li^+ [18, 19]. It follows that these ions are the major interferents for pH measurements with this type of electrode, but the effect of each ion depends on the type of glass used. Conduction through the resistive membrane is thought to occur via the movement of mobile cations in the silicate glass network.

The selective membrane may also be a single crystal, as in the F^- ISE [20, 21], which utilizes LaF_3 doped with EuF_2 to create fluoride vacancies that facilitate ionic conduction via F^- . This electrode shows excellent selectivity with μM detection limits, governed by the sparingly soluble nature of LaF_3 in aqueous solution. The only interferent to consider is OH^- ion.

The most versatile class of potentiometric ISEs employ liquid and polymer

membranes, tailored to respond selectively to a specific primary ion [22–28]. Polymeric membranes are frequently based on plasticized polyvinyl chloride or silicone rubber. As with the other membrane-based electrodes described, these act to separate an internal solution containing the ion of interest at a fixed concentration from an external solution containing the target ion at an unknown concentration, which is to be determined. Membrane materials have been developed that have appropriate properties so that they interact selectively with the ion of interest. The response of these electrodes is governed by two-phase host (ionophore)–guest (ion) binding processes and the associated kinetics and thermodynamics of the binding process [25–28]. The membrane-active recognition component of the membrane can either be an ion exchanger or a neutral carrier, such as a macrocyclic compound. A difference in activity across the membrane produces a free energy difference and hence potential difference:

$$E_m = \frac{RT}{z_i F} \ln \frac{a_i^{\text{ext}}}{a_i^{\text{int}}} \quad (18)$$

where a_i^{ext} and a_i^{int} are the activities of the ion, i , of interest (charge z_i) external and internal to the membrane. The ion-recognition event generates an interfacial potential at each side of the membrane and it is the difference in these potentials, E_m , that is measured with two reference electrodes, one on either side of the membrane, as shown schematically in Fig. 3.

In practice, the activity of the target ion in the filling solution of an ISE is constant, so the potentiometric response of a cell comprising an ISE and reference electrode should obey the relation

$$E_{\text{cell}} = \text{constant} + \frac{RT}{z_i F} \ln a_i^{\text{ext}} \quad (19)$$

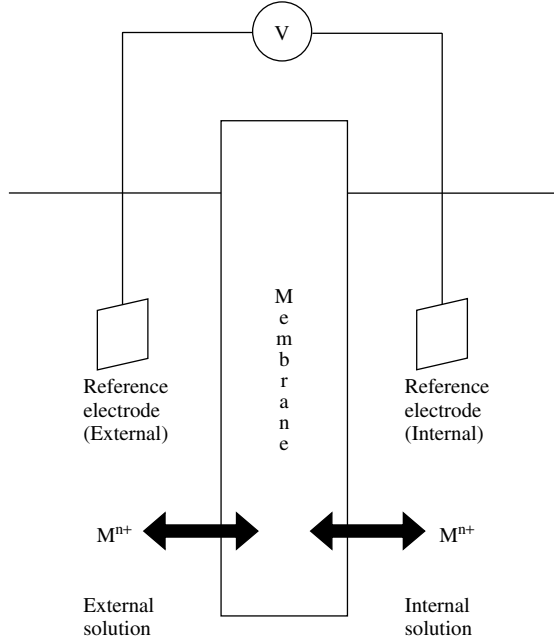


Fig. 3 Principles of membrane-based ISEs. The potential difference between reference electrodes in the solutions on each side of the membrane is determined. In the case shown, the ion of interest is a cation that interacts selectively with the membrane.

The constant in Eq. (19) includes all of the contributions to the cell potential that are invariant and the value is unique to a particular cell. Equation (19) represents the ideal situation in which the ISE responds selectively to only one type of ion, i . In reality, interfering ions, j (charge z_j) may have an effect on the potential. Assuming a linear concentration gradient within the membrane, the *Nicol-sky–Eisenman equation* [29, 30] is obtained for the potential difference:

$$E_{\text{cell}} = \text{constant} + \frac{RT}{z_i F} \times \ln \left(a_i^{\text{ext}} + \sum_j K_{ij} a_j^{z_i/z_j} \right) \quad (20)$$

where K_{ij} is the potentiometric selectivity coefficient. Figure 4 shows how an interfering ion changes the relation between the cell potential and the activity of the ion

of interest, a_i , in the case of one interfering ion type, $z_i = z_j$. Clearly, as the product $K_{ij}a_j$ increases, there is a deviation from Nernstian behavior at higher a_i and the detection limit of the ISE method suffers increasingly.

The selectivity coefficient of an ISE can be measured in several ways [28], the most popular of which are as follows:

1. *The fixed interference method:* The cell potential is determined using solutions in which the primary ion activity is varied, with a constant level of interferent ion present, until a Nernstian response to the primary ion is seen. The corresponding linear response in this region is extrapolated to the potential for the background interferent alone and Eq. (20), in rearranged form, is used to determine K_{ij} .
2. *The separate solution method:* The cell potential is measured for two solutions,

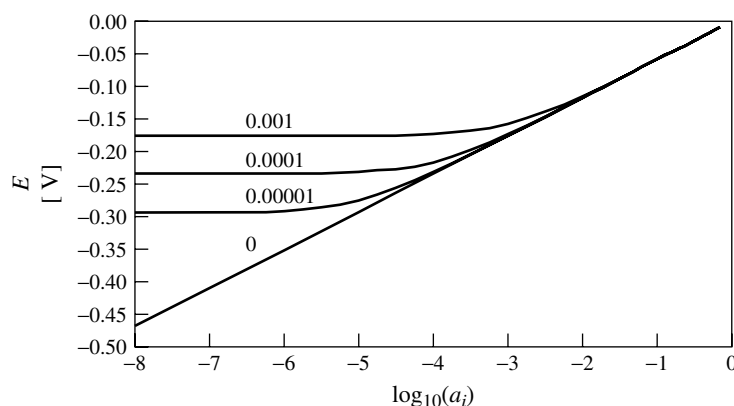


Fig. 4 Effect of an interferent ion, activity, a_j , on the response of an ISE to an ion of interest, activity, a_i . The charges on the two ions are the same (unity), for this example, and the curves are labeled with values of the product, $K_{ij}a_j$. The cell potential is assumed to have a value of zero for unit activity of the ion of interest.

one containing the primary ion only at a known activity and one with the interferent only at the same activity. As with the fixed interference method, the responses obtained are analyzed using Eq. (20).

Given the reliance of these methods on Eq. (20), it is important to note that deviations from this equation have been reported, particularly for mixtures of ions of different charge [31]. Moreover, it has been pointed out that many biased values have been reported using these methods [28]. This has led to a resurgence of interest in the matched potential method [32], which provides a measure of the selectivity of an ISE. Details of the relative merits of each of these methods have been summarized in an excellent review [28].

For analytical purposes, concentration rather than activity is usually of interest. This can readily be obtained through the use of calibration plots. Given the logarithmic dependence of cell potential on activity, calibration plots are in

semilogarithmic form. Moreover, if the ionic strength of solutions is maintained at a fixed level, the Nernst equation can be written in terms of concentrations, as already outlined in the case of cell potentials, in Eqs. (16 and 17). The logarithmic response of ISEs means that the stability and reproducibility of the cell potential are of critical importance. Small uncertainties in cell potential can have a significant impact on concentration measurements, even for an ideally responsive electrode. It follows from Eq. (19) that a small uncertainty, dE_{cell} , in a cell potential results in a corresponding error in the measured activity (or concentration):

$$dE_{\text{cell}} = \frac{RT}{z_i F} \frac{da}{a} \quad (21)$$

In other words, there is a relative error ($\Delta a/a$) in the determination of activity that depends on the error in the cell potential ΔE_{cell} :

$$\left(\frac{\Delta a}{a} \right) = \frac{z_i F \Delta E_{\text{cell}}}{RT} \quad (22)$$

Thus, an error, $\Delta E_{\text{cell}} = \pm 1$ mV results in an error of $\pm 4\%$ in activity for a monovalent ion and $\pm 8\%$ for a divalent ion.

Conventional ISEs typically exhibit a Nernstian response over the concentration range 10^{-1} – 10^{-5} M, with deviation from linearity occurring at lower concentrations, usually in the range 10^{-5} – 10^{-6} M. A significant breakthrough in detection limits by up to six orders of magnitude has been achieved by recognizing that a major factor affecting detection limits is the diffusion of ions from the inner filling solution, across the membrane into the external analyte solution [1, 2]. Internal filling solutions have typically been of concentration about 1–10 mM to ensure that a constant concentration is maintained in the body of the ISE. However, with a much lower concentration external to the membrane, there is a large driving force for diffusion from the electrode filling solution into the analyte solution. Such leakage appears to cause μM levels of primary

ions at the external membrane surface, thereby preventing the detection of sub- μM concentrations. By simply lowering the concentration of the inner electrolyte solution, it has been shown that detection limits may be extended to the 10 nM level [2].

To achieve pM detection, the leaching process was further minimized by using an ion exchange (buffering) process in the filling solution, involving the primary ion and a second ion [1], thereby lowering the concentration of the primary ion in the ISE. This created a flux of primary ion toward the inner solution, but the ion buffering process ensured that the concentration of primary ion within the filling solution remained constant. To establish that the response of the ISE was not biased in the opposite direction, it was important that the flux in the inward direction was not too high, requiring careful experimental design. Figure 5 shows typical potentiometric data for a Pb^{2+} selective electrode of

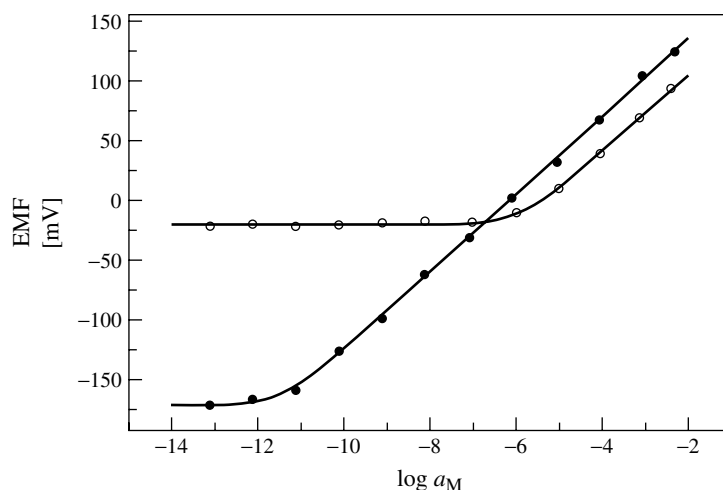


Fig. 5 Response of a Pb^{2+} ISE of conventional design (open symbols) and with an ion buffer as the filling solution (solid symbols); see text for details. (Data are taken from Ref. [1], with permission from the American Chemical Society.)

conventional composition (1:1 mixture of 10^{-3} M PbCl_2 and 0.1 M MgCl_2) compared to the response for the same membrane, but with an ion buffer filling solution comprising 1 cm^3 of 0.1 M $\text{Pb}(\text{NO}_3)_2$ in 100 cm^3 of 0.05 M EDTA-Na_2 (pH 4.34). The calculated activity of Pb^{2+} in the latter solution was 10^{-12} M and this clearly extends the detection limits of the electrode toward the pM regime, compared to the μM limits of a conventional ISE. Several excellent reviews covering developments in this area are available [25–27]. The use of potentiometry in biosensors is considered further in Chapter 2.11 of this volume.

1.1.4

Dynamic Electrochemistry

As already introduced in Sect. 1.1.2, dynamic electrochemistry involves the application of a potential to a working electrode, with respect to a reference electrode, to promote electron transfer at the electrode–solution interface. We also note, in passing, that a variant on this theme is the use of an interface between two immiscible electrolyte solutions as a working electrode to promote either a redox reaction or an ion transfer current [33, 34]. Investigations of liquid–liquid interfaces have extended the range of species that are detectable with dynamic electrochemistry, but will not be discussed further as charge transfer at liquid–liquid interfaces is considered in detail in Chapter 4.2 in Volume 2 of the *Encyclopedia*. Further information on the structure and nature of liquid–liquid interfaces can also be found in Chapter 2.3 in Volume 1. The use of SECM to investigate liquid–liquid interfaces is highlighted in Sect. 3.3.4.2 of Chapter 3.3 in this volume. There are also excellent texts available that cover theoretical and practical aspects of liquid–liquid interfaces [35, 36].

A basic question when introducing dynamic electrochemistry is: what does the current, i , that flows represent? By definition

$$i = \frac{dq}{dt} \quad (23)$$

where q is the charge passed in unit time, t . Charge is simply related to the number of moles of reagent converted by electrolysis, N , via *Faraday's law*:

$$N = \frac{q}{nF} \quad (24)$$

It follows that the rate of reaction is therefore directly related to the current:

$$\frac{dN}{dt} = \frac{1}{nF} \frac{dq}{dt} = \frac{i}{nF} \quad (25)$$

Since the electrochemical process occurs at an electrode of area, A , it is appropriate to express the rate as a surface flux, j_0 ($\text{mol m}^{-2} \text{s}^{-1}$):

$$j_0 = \frac{1}{A} \frac{dN}{dt} = \frac{\bar{i}}{nF} \quad (26)$$

In this last equation, the current density is $\bar{i} = i/A$.

It follows that in dynamic electrochemistry the applied potential represents the driving force for charge transfer (usually electron transfer) and the current that flows is a measure of the rate of the reaction. Electrochemical experiments of this type are classified as voltammetry or amperometry, and several of the most important techniques are considered in subsequent chapters of this volume. These techniques differ in the form of the potential signal applied to the working electrode, the type of mass transport regime employed and the current response measured. For example, cyclic voltammetry, discussed in Chapter 2.1, utilizes a triangular potential waveform with

respect to time and the signal is the current as a function of applied potential. Step and pulse techniques, considered in Chapter 2.2, involve sudden jumps in the potential. For large potential perturbations, the resulting current is usually measured as a function of time, but for small potential perturbations superimposed on a potential ramp, as in differential and normal pulse voltammetry, the signal is current versus potential. With the advent of digital instrumentation (Chapter 1.2), the type of waveform applied to the working electrode is essentially unlimited and there are consequently a huge number of possible dynamic electrochemistry techniques.

In the simplest situation, a voltammetric circuit involves a measurement cell such as that shown in Fig. 6. A potential is applied to the working electrode, with respect to a reference electrode, and the current is measured. Further details on the instrumentation for this type of measurement are given in the following chapter (Sect. 1.2.1). The applied potential, E_{app} , falls sharply across the various phase boundaries in the cell and we

may write

$$E_{\text{app}} = (\phi_{\text{WE}} - \phi_{\text{sol}}) + (\phi_{\text{sol}} - \phi_{\text{ref}}) + iR_{\text{sol}} \quad (27)$$

$$E_{\text{app}} = (\phi_{\text{WE}} - \phi_{\text{ref}}) + iR_{\text{sol}} \quad (28)$$

where ϕ_{WE} , ϕ_{sol} and ϕ_{ref} are, respectively, the potentials of the working electrode, solution and reference electrode. The product, iR_{sol} , is an *ohmic term* associated with the passage of current through the finite resistance of the solution.

The type of set up shown in Fig. 6 is only used for situations where low currents are measured (100 nA and smaller for typical electrolyte solutions), notably for experiments with microelectrodes (or ultramicroelectrodes), discussed in detail in Chapter 2.5. The requirement of a small current is both to make the ohmic term negligible and to ensure that there are minimal changes to the reference electrode composition that would, otherwise, lead to an unstable reference electrode potential. The ohmic term may, of course, also be minimized by making R_{sol} as small as possible, for example, by working with added supporting electrolyte to increase

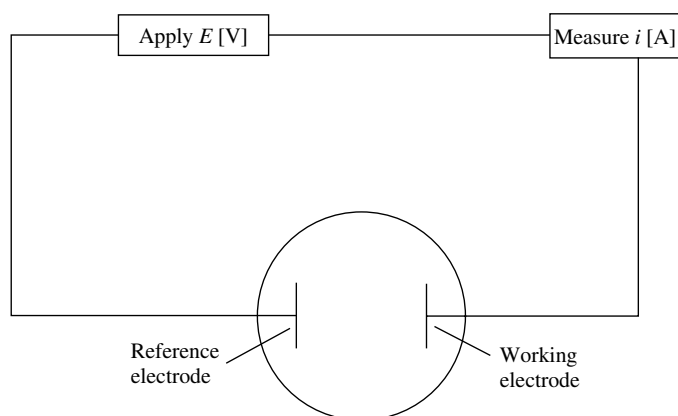


Fig. 6 Simple two-electrode arrangement for dynamic electrochemistry experiments.

the conductivity of the solution. This also ensures that migration of any charged analytes of interest is negligible, and that the full potential drop at the working electrode/solution boundary ($\phi_{WE} - \phi_{sol}$) occurs over sufficiently short distances commensurate with electron tunneling (10 Å).

For experiments in which the current is larger, for example, when larger electrodes are used, it is necessary to use a three-electrode mode (Fig. 7) and make use of a potentiostat. A wide range of potentiostats is available commercially [37]. In addition to the working and reference electrodes, the set up utilizes an auxiliary electrode. The control potential is applied between the working and reference electrodes, but no current flows through the reference, rather this is the role of the auxiliary electrode, which provides the current required by the working electrode without in any way limiting the response. The associated process at the auxiliary (counter) electrode is usually electrolysis of the supporting

electrolyte or solvent, so that current flows without the need for a large overpotential. A consequence is that the auxiliary electrode should have a much larger area than the working electrode. Gauze materials, with high surface area, have proved to be particularly popular as auxiliary electrode materials.

To minimize errors in the applied potential due to uncompensated solution resistance, the reference electrode can be connected to the solution via a tapered glass Luggin probe that may be placed close to the working electrode surface [38]. The optimal position is about twice the diameter of the probe, which decreases the potential drop due to uncompensated resistance seen between the working and reference electrodes [39]. Although moving the probe closer still would decrease this term further, there are detrimental consequences in terms of shielding the current path and perturbing the current distribution. It is also important that the Luggin probe does not perturb mass transport,

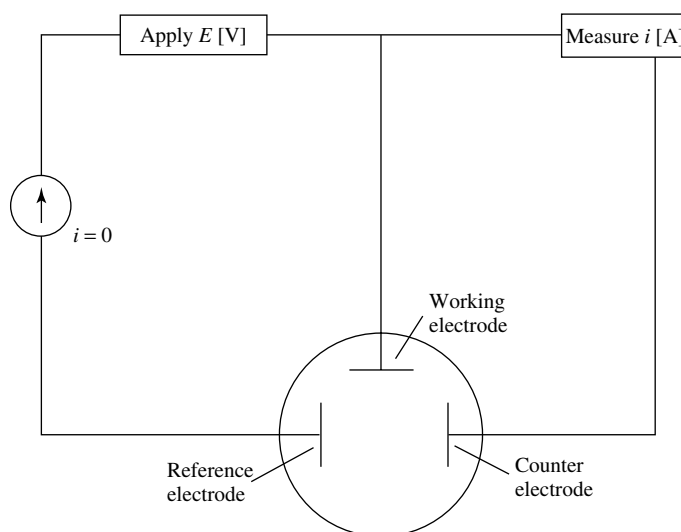


Fig. 7 Three-electrode arrangement for dynamic electrochemistry experiments.

particularly when convective transport is used to deliver material to the surface of the working electrode. Even with these precautions, it is important to note that the ohmic term, due to uncompensated resistance, may not be completely negligible, especially when the solution comprises resistive nonaqueous media. In this case, there are several instrumental methods that can be used to compensate, some of which are discussed in the next chapter (Sect. 1.2.6). Further details on cell and electrode design are available [40] and discussed in many of the chapters in this volume.

We saw from Eq. (26) that the current in a dynamic electrochemistry experiment is a measure of the rate of the electrode process and to complete this section a brief overview is given of the factors that can limit the rate of such reactions. The textbook view [41] of some of the steps that might be involved in an electrode reaction is given in Fig. 8. The steps involved are

1. Mass transfer of species between bulk solution and the electrode surface.
2. Heterogeneous electron transfer at the electrode/solution interface.

3. Chemical reactions, either preceding or following electron transfer.
4. Surface reactions such as adsorption, desorption and electrodeposition–dissolution.

The simplest electrode processes involve only Steps 1 and 2, for example, in the case of the redox reaction of the $\text{Ru}(\text{NH}_3)_6^{2+/3+}$ couple. As already alluded to in Sect. 1.1.2, electron transfer rates are strongly potential dependent and this topic is discussed in several chapters in Volume 2 (Chapters 1.1, 1.2 and 1.3). Mass transfer may occur by diffusion, migration and convection. As discussed above, most dynamic electrochemistry experiments are carried out with a large excess of supporting electrolyte so that if the reactants and products are charged, migration of these species can be neglected [42]. Diffusion is the key transport step because concentration gradients are always involved in electrochemical processes. This is the mass transfer mode assumed for the treatments of cyclic voltammetry in Chapter 2.1 and step and pulse techniques in Chapter 2.2. An overview of transport by diffusion and

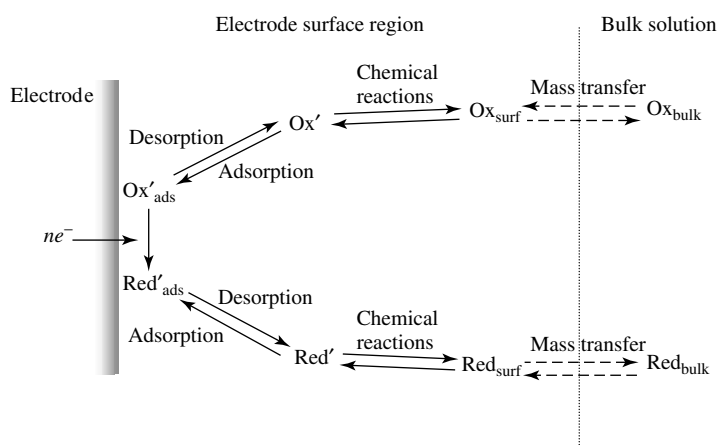


Fig. 8 Typical steps involved in an electrode reaction.

migration is given in Chapter 2.1 in Volume 2. Convection may occur naturally on long timescales and under conditions in which there are significant density and temperature gradients, but such effects are usually undesirable because mass transport is difficult to treat quantitatively under such conditions. On the other hand, well-characterized forced convection can considerably enhance mass transport to electrode surfaces, as in hydrodynamic electrodes [43], discussed in Chapter 2.4. Such electrodes are beneficial in the study of fast heterogeneous electron transfer processes or coupled chemical reactions because the slowest process in the scheme of Fig. 8 limits the rate of the electrode reaction and the associated current flow. When mass transport (or diffusion) limits the rate of the reaction, the electrode process is said to be *transport* (or *diffusion*) *limited*. Conversely, if heterogeneous electron transfer is the sluggish step in the process, one may term the reaction to be in a *surface-limited* regime. Microelectrodes (Chapter 2.5) and SECM (Chapter 3.3) have found application in the characterization of rapid heterogeneous and homogeneous kinetics due to the very high mass transfer rates available, which has expanded the timescale of dynamic measurements before transport effects dominate.

Electrode reactions are often complicated by additional chemical reactions (step 3), which may occur either homogeneously in solution or on the electrode surface. In addition to the techniques mentioned, the use of cyclic voltammetry to investigate such processes is considered in Chapter 2.1 (Sect. 2.1.2.4) in this volume together with several examples of these reactions (Sect. 2.1.5). Adsorption and deposition processes (step 4) are considered extensively in Sects. 3 and 4, respectively, of Volume 1. The EQCM,

scanning tunneling microscopy (STM) and atomic force microscopy (AFM) have also become important tools for investigating these processes, as discussed later in this volume (Chapters 2.7, 3.1 and 3.2).

1.1.5

Outline of This Volume

Modern electroanalytical chemistry is a diverse subject covering instrumentation, technique development, modeling, surface and interfacial science, sensor design, spectroscopy and microscopy, among other topics. Consequently, the chapters and themes selected for this volume reflect the broad scope of electroanalytical chemistry. The scene is set in the first section, which covers some of the core aspects of electroanalytical chemistry. Following this chapter is a treatment of analog and digital instrumentation by Wipf (Chapter 1.2), describing the basic principles of control/measurement protocols in electrochemical systems, including potentiostatic and galvanostatic circuits. Signal transduction, ohmic drop compensation and data acquisition are among the topics that receive particular attention. Chapter 1.3 by Britz considers the application of digital simulation to solve coupled mass transport-reaction problems in electroanalytical chemistry. This chapter covers the basics of digital simulation, by example, and introduces a flavor for some of the more advanced simulation techniques that are becoming increasingly popular. An overview of packages available commercially and from academic groups is also provided.

Section 2 of this volume is concerned with electroanalytical methods, predominantly connected to dynamic electrochemistry. The most widely used techniques in electrochemistry are linear sweep and

cyclic voltammetry (LSV and CV), and consequently Chapter 2.1, by Speiser, covers the basics of these techniques. After an introduction to voltammetric terminology, this chapter presents the theoretical background to LSV and CV, covering mass transport, heterogeneous electron transfer, coupled chemical reactions in solution and surface-bound redox systems. The effects of nonlinear and restricted diffusion, compared to planar diffusion, are also highlighted. Practical considerations, including electrodes, cells, supporting electrolyte and solvents, are discussed along with some of the more common pitfalls that might be encountered when making voltammetric measurements. Advances in LSV and CV, including the use of microelectrodes (or ultramicroelectrodes), are given special attention. This treatment complements Chapter 2.5 on microelectrodes, summarized below. Applications of LSV and CV are described, including both classical examples and more recent developments.

Closely related to LSV and CV are step and pulse techniques, described in Chapter 2.2 by Brett and Oliveira Brett. These techniques are widely used in electroanalytical chemistry and a treatment is provided of discrete step techniques, such as single and double potential step chronoamperometry, staircase voltammetry and pulse techniques such as normal pulse voltammetry, differential pulse voltammetry and square wave voltammetry. Current steps are also considered, including applications in potentiometric stripping analysis, which serves as a link to Chapter 2.3 on stripping methods by Wang. Although more specialized than the other voltammetric techniques discussed above, stripping analysis is an extremely sensitive method for trace-level detection. This is achieved by using a

potential waveform in which there is a preconcentration step, prior to voltammetric analysis (usually by LSV). The preconcentration step needs to be carried out under conditions of well-defined and efficient mass transport, such as the use of hydrodynamic control (the subject of Chapter 2.4) or microelectrodes (Chapter 2.5). Chapter 2.3 covers the main stripping techniques, that is, anodic stripping voltammetry, which is predominantly used for the detection of heavy metals, stripping potentiometry (introduced in Chapter 2.2, Sect. 2.2.5) and adsorptive stripping voltammetry. The latter method allows the detection of a wide range of species, including metals and organic compounds that cannot be readily deposited (preconcentrated) by electrolysis. Practical considerations when using stripping methods are highlighted, including electrode materials, cells and instrumentation.

Many of the methods discussed so far rely on diffusion as the mode of mass transport. The addition of mechanical convection, as well as diffusion, through the forced movement of the solution or electrode can be beneficial for enhancing the reproducibility of mass transport and delivering a steady state regime. Chapter 2.4 by Mount is concerned with hydrodynamic electrodes, which make particular use of forced convection. The focus is on solid electrodes such that the dropping mercury electrode (and polarography), which is of historical interest in the development of electroanalytical chemistry as a subject, is not considered. The interested reader should consult Refs. [44, 45], while Ref. [46] provides an excellent historical overview of the development of electroanalytical chemistry, including the key role of polarography. After an introduction to the basic principles, Chapter 2.4 reviews the main hydrodynamic methods,

including the rotating disc electrode (RDE) and its ring-disc and optical versions. In the RDE and related devices, solution flow to the electrode surface occurs because of the rotating motion of a disc-shaped electrode, which establishes a well-defined and calculable flow pattern in the solution. Alternatively, the solution can be flowed past a stationary electrode, as in the wall-tube, wall-jet and channel (or tube) electrodes, which are also reviewed. A recent trend has been the development of microhydrodynamic systems, which are highlighted briefly. A detailed review of such systems is also available [47].

As already mentioned several times in this chapter, and elsewhere in this volume, microelectrodes (ultramicroelectrodes) have, in many ways, revolutionized the practice of voltammetry. In Chapter 2.5, Forster describes how microelectrodes are pushing the boundaries of electrochemistry in many ways, including basic electroanalysis, in applications in biological systems, in artificial noses and array devices, and for investigations in low conductivity media and the solid state. The exploitation of microelectrodes in the study of ultrafast processes, under both steady state conditions and with fast scan/transient methods, is given particular attention. The earlier parts of this chapter set the scene by reviewing the properties of microelectrodes, including mass transport effects, while the concluding part of the chapter speculates on where the field might develop further.

Impedance spectroscopy differs from many of the voltammetric techniques discussed above, such as linear sweep and potential step methods, in that only a small perturbation (usually of sinusoidal form) is applied to the electrochemical cell. In Chapter 2.6, Krause discusses impedance methods, introducing the basic

principles and theory together with some of the applications. The instrumentation for impedance is described and experimental details are discussed thoroughly. The main impedance techniques make measurements averaged over a macroscopic sample, but it is also possible to make spatially resolved measurements, which are discussed in this chapter.

Several aspects of impedance spectroscopy interface well with the EQCM described in the following chapter by Hillman (Chapter 2.7). The EQCM is a powerful technique for investigating the formation and properties of thin films on electrode surfaces. For thin, rigid films, the EQCM serves as a gravimetric sensor of surface processes. For thicker films, the associated viscoelastic properties can be investigated under electrochemical control. Chapter 2.7 provides a detailed status report on EQCM, covering the history of the technique, the principles and experimental details, including the integration of EQCM with complementary techniques. The diverse range of applications of EQCM are organized by system and discussed in detail.

An aim of this volume is to highlight rapidly developing areas of electroanalytical chemistry and electrochemistry. In this context, the application of ultrasound on electrochemical processes is a topic of particular interest. In a series of three chapters, Compton and coworkers provide a treatment of the underlying physical aspects connected with the coupling of ultrasound to electrochemical systems (Chapter 2.8) and applications in electroanalysis (Chapter 2.9). The first of these chapters considers the effect of ultrasound on mass transport, on the electrode surface and on chemical reactions in solution, while the second chapter looks at the use of sonoelectrochemical methods in

analysis, notably stripping voltammetries, developing some of the ideas in Wang's earlier chapter. The investigation of biphasic systems also receives attention. Traditionally, one of the major interests in sonochemistry has been the possibility of changing the course of chemical reactions and synthetic pathways. For completeness, Chapter 2.10 therefore considers the impact of ultrasound on electrosynthesis, with a discussion of cell design, and a range of examples of sonoelectrosynthetic reactions, which mainly originate from the organic chemistry arena. Further information on organic electrochemistry is provided in Volume 8 of the *Encyclopedia*, while Volume 7 is concerned with inorganic systems.

Perhaps the area of analysis in which electrochemistry has had the biggest impact on society is in biosensors, notably the glucose biosensor [48]. Although Volume 9 is concerned with bioelectrochemistry, it is important that this area of electroanalytical chemistry is represented appropriately in Volume 3. Consequently, Schuhmann and Bensen provide an overview of the physical principles and applications of biosensors in Chapter 2.11. A comprehensive overview is given of amperometric, potentiometric, conductimetric and impedimetric formats for biosensors, and the relative merits of each are fully assessed. Potential new directions are highlighted, particularly connected to miniaturization and multisensor array detection strategies.

The final section of this volume is entitled *In situ structural and spectroscopic probes of electrochemical systems*. The six chapters in this section describe some of the most important microscopy and spectroscopy techniques that have found application in the study of electrode surfaces and systems. It should be noted,

in passing, that a great deal of ex situ work has been carried out on electrode surfaces, but these studies are beyond the scope of this volume. Many of these techniques are based on ultrahigh vacuum electron and ion spectroscopies [49], and consequently the electrode must be transferred from the electrochemical environment to an evacuated chamber prior to analysis. Although special apparatus has been designed to minimize the exposure of the electrode to the atmosphere [50], there are the questions of possible artefacts due to the transfer process [51] and how realistically the conditions of the solid surface in contact with the liquid are maintained after transfer.

The advent of STM has had a significant impact on surface electrochemistry, providing unprecedented information on the structure and dynamics of electrode surfaces. STM is a natural technique for electrochemical surface science, since it allows the electron density of metal and semiconductor surfaces to be imaged with subatomic resolution, while also allowing surface processes to be imaged in a wide variety of environments, including the solid–liquid interface. Chapter 3.1 by Moffat focuses on the use of in situ STM as a probe of electrode surfaces. This includes the principles of the STM technique, experimental details and a glimpse of some of the many applications, ranging from imaging to surface modification.

The related technique of AFM uses the force between a probe and a surface to investigate either structure on the nanometer scale or interfacial forces. As with STM, AFM is much more than a technique for electrochemistry, but it has found considerable application in this area, given that so many electrochemical processes and electroanalytical methods require an understanding of interfacial

structure and properties at high resolution. In Chapter 3.2, Macpherson introduces the principles of AFM and its application to electrified interfaces, covering both measurements of surface structure and interfacial forces. A recent direction has been the integration of microscopic and nanoscopic electrodes into AFM tips, so allowing simultaneous topographical (force) and electrochemical imaging of surfaces, with high spatial resolution [52]. Developments in this area of combined SECM-AFM are highlighted.

The last section of Chapter 3.2 leads neatly into Chapter 3.3 by Horrocks, which is concerned with SECM. This chapter provides a comprehensive overview of the principles and applications of this technique, which continues to attract considerable interest from the electrochemistry community and beyond. The main SECM techniques are described along with the theoretical methods that can be used to treat the SECM response. Selected applications cover solid–liquid, liquid–liquid and liquid–gas interfaces, with examples spanning the life sciences and materials science.

Traditionally, UV-visible spectroscopy has been the main spectroscopic probe of electrochemical systems, covered in Chapter 3.4 by Crayston. This chapter describes the main techniques, theory and applications in the study of solution species (inorganic and organic), thin films and modified electrodes, along with other topics. A wide variety of cells have been described, to allow the use of UV-visible spectroscopy in electrochemistry, and consequently these are described in some detail.

In the past two decades, infrared spectroscopy has become a powerful tool for the investigation of electrochemical systems, as described by Christensen

in Chapter 3.5. This chapter provides a detailed insight into how in situ infrared spectroscopy may be implemented and used most effectively to investigate electrode surfaces. The wide-ranging applications of the various infrared techniques are highlighted through a series of selected examples.

Raman spectroscopy is attracting increasing interest from electrochemists interested in areas as diverse as electrocatalysis, corrosion, electrodeposition, battery technology, and sensor development. In Chapter 3.6, Tian and Ren lay the foundations of Raman spectroscopy and describe how it may be used effectively to investigate electrode surfaces in situ. This chapter covers the basic principles and theory at a readily accessible level and describes the various experimental configurations that can be used for both macroscopic and microscopic investigations. A wide range of applications from several areas of electrochemistry, and some of the current developments and future prospects for the technique are highlighted.

Acknowledgment

The author thanks Mr. I. D. Macklam for preparing the illustrations for this chapter.

References

1. T. Sokalski, A. Ceresa, T. Zwickl, E. Pretsch, *J. Am. Chem. Soc.* **1997**, 119, 11 347.
2. S. Mathison, E. Bakker, *Anal. Chem.* **1998**, 70, 303.
3. F. J. Holler, C. G. Enke in *Laboratory Techniques in Electroanalytical Chemistry* (Eds.: P. T. Kissinger, W. R. Heinemann), 2nd ed., Marcel Dekker, New York, 1996, pp. 237–265, Chap. 8.

4. K. Mayrhoﬀ, A. J. Zemmann, E. Schnell, G. K. Bonn, *Anal. Chem.* **1999**, 71, 3828.
5. T. Kappes, P. C. Hauser, *Electroanalysis* **2000**, 12, 165.
6. J. Weiss in *Ion Chromatography* (Eds.: C. Dyllick, B. Böck), Wiley-VCH, Weinheim, Germany, 1995.
7. G. Jerkiewicz, M. P. Soriaga, K. Uosaki et al., (Eds.), *Solid-Liquid Electrochemical Interfaces*, ACS Symposium Series, ACS, Washington, DC, 1996, Vol. 656.
8. D. Britz, *Digital Simulation in Electrochemistry*, 2nd ed., Springer, Berlin, Germany 1988.
9. R. B. Gennis, *Biomembranes: Molecular Structure and Function*, Springer, New York, 1989.
10. R. W. Murray, (Ed.), *Molecular Design of Electrode Surfaces in Techniques in Chemistry Founding* (Ed.: A. Weissberger), Wiley-Interscience, New York, 1992, Vol. XXII.
11. A. J. Bard, J. Jordan, R. Parsons, (Eds.), *Standard Potentials in Aqueous Solutions*, Marcel Dekker, New York, 1985.
12. G. Milazzo, S. Caroli, *Tables of Standard Electrode Potentials*, Wiley-Interscience, New York, 1977.
13. A. J. Bard, L. R. Faulkner, *Electrochemical Methods*, 2nd ed., Wiley, New York, 2001, pp. 305–330, Chap. 8.
14. E. B. Smith, *Basic Chemical Thermodynamics*, 4th ed., Oxford University Press, Oxford, 1991.
15. A. Evans, *Potentiometry and Ion Selective Electrodes*, Wiley, New York, 1987.
16. D. Amman, *Ion Selective Microelectrodes: Principles, Design and Application*, Springer, Berlin, Germany, 1986.
17. R. G. Bates, *Determination of pH*, 2nd ed., Wiley-Interscience, New York, 1973.
18. F. G. K. Baucke, *Ber. Bunsen-Ges. Phys. Chem.* **1996**, 100, 1466.
19. F. G. K. Baucke, *J. Phys. Chem. B* **1998**, 102, 4835.
20. M. S. Frant, J. W. Ross Jr., *Science (Washington, DC)* **1966**, 154, 1553.
21. J. J. Lingane, *Anal. Chem.* **1967**, 39, 881.
22. A. Guindilis, P. Atanasov, E. Wilkins, *Electroanalysis* **1997**, 9, 661.
23. C. Henry, *Anal. Chem.* **1998**, 70, 594A.
24. W. E. Morf, *The Principles of Ion-Selective Membranes and of Membrane Transport*, Elsevier, New York, 1981.
25. E. Bakker, P. Bühlmann, E. Pretsch, *Chem. Rev.* **1997**, 97, 3083.
26. P. Bühlmann, E. Pretsch, E. Bakker, *Chem. Rev.* **1998**, 98, 1593.
27. E. Bakker, P. Bühlmann, E. Pretsch, *Electroanalysis* **1999**, 11, 915.
28. E. Bakker, E. Pretsch, P. Bühlmann, *Anal. Chem.* **2000**, 72, 1127.
29. B. P. Nicolsky, *Zh. Fiz. Khim.* **1937**, 10, 495.
30. J. W. Ross Jr., *Science (Washington DC)* **1967**, 156, 1378.
31. E. Bakker, R. K. Meruva, E. Pretsch et al., *Anal. Chem.* **1994**, 66, 3021.
32. V. P. Y. Gadzekpo, G. D. Christian, *Anal. Chim. Acta* **1984**, 164, 279.
33. D. J. Fermin, R. Lahtinen in *Liquid Interfaces in Chemical, Biological and Pharmaceutical Applications* (Ed.: A. G. Volkov), Marcel Dekker, New York, 2001, pp. 179–227, Chap. 8.
34. H. H. Girault, D. J. Schiffrin in *Electroanalytical Chemistry* (Ed.: A. J. Bard), Marcel Dekker, New York, 1988, pp. 1–141, Vol. 15.
35. A. G. Volkov, D. W. Deamer, (Eds.), *Liquid-Liquid Interfaces: Theory and Methods*, CRC Press, Boca Raton, Fla., 1996.
36. A. G. Volkov, D. W. Deamer, D. L. Tanelian et al., *Liquid Interfaces in Chemistry and Biology*, John Wiley, New York, 1998.
37. J. Smith, V. Hinson-Smith, *Anal. Chem.* **2002**, 74, 593A.
38. A. J. Bard, L. R. Faulkner, *Electrochemical Methods*, 2nd ed., Wiley, New York, 2001, p. 27.
39. J. Wang, *Analytical Electrochemistry*, 2nd ed., Wiley-VCH, New York, 2000, p. 105.
40. F. M. Hawkridge in *Laboratory Techniques in Electroanalytical Chemistry* (Eds.: P. T. Kissinger, W. R. Heinemann), 2nd ed., Marcel Dekker, New York, 1996, pp. 267–291, Chap. 9.
41. A. J. Bard, L. R. Faulkner, *Electrochemical Methods*, 2nd ed., Wiley, New York, 2001, p. 23.
42. A. J. Bard, L. R. Faulkner, *Electrochemical Methods*, 2nd ed., Wiley, New York, 2001, pp. 137–155, Chap. 4.
43. C. M. A. Brett, A. M. C. F. Oliveira Brett, *Comp. Chem. Kinet.* **1986**, 26, 355.
44. J. J. Lingane, *Electroanalytical Chemistry*, 2nd ed., Wiley-Interscience, New York, 1958.
45. A. M. Bond, *Modern Polarographic Methods in Analytical Chemistry*, Marcel Dekker, New York, 1980.

46. A. J. Bard, C. G. Zoski, *Anal. Chem.* **2000**, 72, 346A.
47. J. V. Macpherson, N. Simjee, P. R. Unwin, *Electrochim. Acta* **2001**, 47, 29.
48. A. E. G. Cass, G. Davis, G. D. Francis et al., *J. Am. Chem. Soc.* **1984**, 56, 667.
49. D. P. Woodruff, T. A. Delchar, *Modern Techniques of Surface Science*, 2nd ed., Cambridge University Press, Cambridge, 1994.
50. J. Lipkowski, P. N. Ross, (Eds.), *Structure of Electrified Interfaces*, Wiley-VCH, Weinheim, Germany, 1993.
51. A. J. Bard, L. R. Faulkner, *Electrochemical Methods*, 2nd ed., Wiley, New York, 2001, p. 709.
52. C. E. Gardener, J. V. Macpherson, *Anal. Chem.* **2002**, 74, 576A.

1.2 Analog and Digital Instrumentation

David Wipf
Mississippi State University, Starkville,
Mississippi, U.S.A.

1.2.1 Electrical Control

Controlling the flow of electricity in an electrochemical cell is fundamental to faradaic electrochemistry. Experiments are arranged to control the potential (voltage) applied across an electrochemical cell or to regulate current flow through a cell. A DC voltage source can be used to apply a voltage between the counterelectrode (CE) and the working electrode (WE) as illustrated in Fig. 1(a). This, and any other DC voltage source, is considered to consist of an ideal internal voltage source (V_{in}) and an internal series resistor (R_{in}). Current (I) passing through the cell alters the voltage applied to the cell

$$V_{cell} = V_{in} - (I \times R_{in}) \quad (1)$$

R_{in} in battery voltage sources varies from about 35 Ω in a 9-V zinc–carbon battery to less than 6 m Ω in a lead-acid cell. Electronically controlled sources produce very low R_{in} , an important point to which we will return.

IR drop generated by the R_{in} of a voltage source compromises accurate potential control, particularly for high cell currents. This point led many early investigators to prefer controlled current methods. A real current source can be considered to consist of an ideal current source in parallel with an internal resistance (Fig. 1b). Current passing through the parallel resistance

reduces current flowing through the cell.

$$I_{cell} = I - I_{in} \quad (2)$$

Making R_{in} much larger than the resistance in the electrochemical cell allows the source to produce nearly the desired current. Adequate current sources can be constructed from high-voltage batteries and a large series resistor. In Fig. 2(a), a 10- μ A current source is made from a 100-V battery and a 10-M Ω series resistor. The rated current is available when the load, R_L , is a short circuit. This circuit can be drawn in an equivalent way (Fig. 2b), with a 10- μ A current source in parallel with a 10-M Ω parallel resistor. These two representations illustrate the presence of a *compliance voltage*, that is, the maximum voltage available for forcing current through a load. The current is only approximately constant for this source and R_L must be 100 times smaller than R_P to maintain a 1% accuracy on supplied current.

The limitations of these voltage and current sources have led to the use of electronic circuitry that allows more efficient and accurate electrical control. A brief discussion of the relevant electronic circuits is required to understand basic electrochemical instrumentation.

1.2.2 Electronic Principles

An essential component of modern electrochemical instrumentation is the operational amplifier (OA or op amp) [1]. An OA is a high-gain differential amplifier with an output voltage (V_o) proportional to the difference between *noninverting* (V_+) and *inverting* (V_-) inputs

$$V_o = A(V_+ - V_-) \quad (3)$$

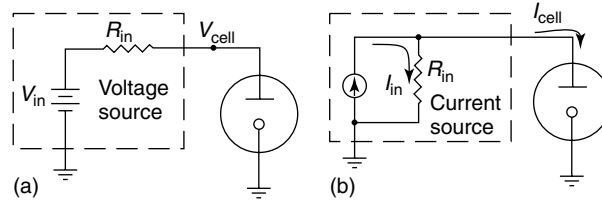
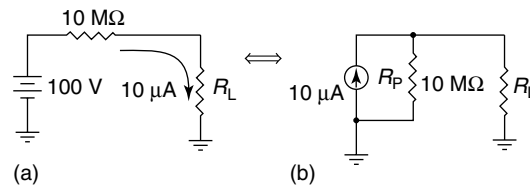


Fig. 1 (a) Voltage and (b) current sources connected to a two-electrode electrochemical cell.

Fig. 2 Current sources applied to a load resistance. (a) Source constructed from a battery and resistor and (b) an equivalent representation of an ideal current source and a parallel source resistance.



where A is the open-loop DC voltage gain. Typically, an OA has an open-loop DC voltage gain greater than 100 000 and input impedances of 10^{11} to $10^{14} \Omega$. OAs are represented schematically as a three-terminal device with two inputs and one output (Fig. 3a). OAs require a power source; however, power connections are often omitted for clarity. The very high open-loop gain of the OA is useful in *negative feedback* (closed-loop) configurations. In fact, OAs are rarely operated in an “open-loop” configuration since A varies significantly with signal frequency and temperature. The voltage-follower configuration (Fig. 3b) is a typical OA circuit. Connecting the output to the inverting input forces the output to match the noninverting input. This is understood by considering the consequence of an unequal input and output voltage. The high differential gain greatly amplifies the voltage difference between the

inverting and noninverting inputs. This produces a restoring voltage that forces the inverting input voltage to approach the value of the noninverting input, eventually stabilizing at equal input and output voltages. In contrast, if the feedback path is reversed, so that the output is connected to the noninverting input, unstable positive feedback forces the output away from the input.

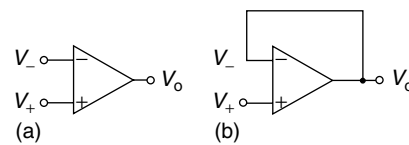
Under negative feedback, a portion, β , of the output is subtracted from V_{in} (i.e. $V_+ - V_-$). Thus, the output is $V_o = A(V_{in} - \beta V_o)$ and the closed-loop voltage gain, $G = V_o/V_{in}$ is

$$G = \frac{A}{1 + A\beta} \quad (4)$$

For the voltage follower of Fig. 3(b), β is 1, so the voltage gain is

$$G = \frac{A}{1 + A} \quad (5)$$

Fig. 3 (a) An operational amplifier (OA) symbol. (b) An OA connected as a voltage-follower amplifier.



The high open-loop gain of the OA increases gain stability. As long as A is much larger than unity, it can vary considerably with little change in G .

Negative feedback also causes the output resistance (R'_o) to be reduced

$$R'_o = \frac{R_o}{1 + A\beta} \quad (6)$$

where R_o is the open-loop output resistance. Figure 4 illustrates this important consequence of negative feedback. A simple model of an OA is made with an internal voltage gain block having internal input and output resistances, R_{in} and R_o . In an open-loop configuration, a voltage divider is formed by R_o and the load resistance, R_L . The voltage divider reduces the output by the ratio $R_L/(R_o + R_L)$. In closed-loop configuration, the negative feedback loop compensates the voltage drop caused by current flowing at the output. Essentially, the voltage difference between inputs, V_d , is adjusted to make V_o equal to V_{in} , within the limits of the open-loop gain. The net effect is to reduce

the output resistance (or impedance) by the factor $1/(1 + A\beta)$.

Voltage followers are used to “buffer” the output of voltage sources. An unbuffered voltage source is “loaded” when a load causes current to flow from the source. In Fig. 5(a), a battery and a potentiometer are used to construct a variable voltage source. In the presence of a load resistance, the load parallels a portion of the potentiometer, changing the parallel portion of the potentiometer resistance to $R_p = R_b R_L / (R_b + R_L)$. This causes the output voltage to depend on the load, that is, $V_o = V_{in}(R_p / (R_p + R_a))$ when R_b is not smaller than R_L . Incorporating a voltage follower improves the situation (Fig. 5b). The follower has a high-input resistance and thus does not significantly load the potentiometer. The low-output impedance of the follower permits small R_L values (i.e. heavy load currents). Thus, the voltage follower is an amplifier. Allowing a very small input current to generate a large current through a load produces a net power gain.

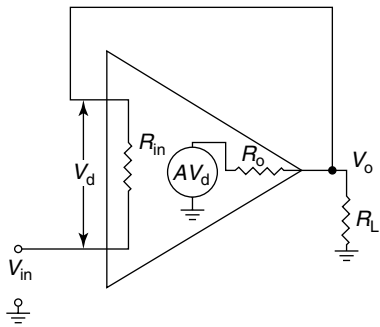


Fig. 4 A simplified model of an OA-based voltage-follower amplifier showing input and output resistance and internal gain.

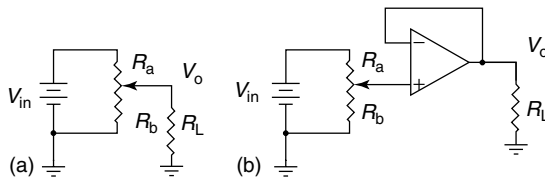


Fig. 5 (a) A variable voltage source constructed with a battery and potentiometer. (b) An improved variable voltage source that employs a voltage-follower buffer to minimize loading by the load resistance.

Three simplifying assumptions often suffice to analyze most OA circuits. These are: (1) the open-loop gain is infinite; (2) the input impedance of the OA is infinite; and (3) the output impedance of the OA is zero. These assumptions are unrealistic but do provide good results for low-frequency applications. An implication of these assumptions is that, under negative feedback, the output voltage will swing to precisely the value required to make the inverting and noninverting inputs equal.

Applying these assumptions to the voltage follower predicts that $V_o = V_{in}$, the input impedance is infinite, and the output impedance is zero. With large A values, these predictions are very close to the analysis above. A simple variation of the voltage-follower circuit produces the *voltage-follower-with-gain* circuit of Fig. 6(a). R_1 and R_2 produce a voltage divider that sets $V_- = V_o R_1 / (R_1 + R_2)$. With the noninverting and inverting inputs equal, $V_o = V_{in}(R_1 + R_2)/R_1$. Thus, the follower-with-gain circuit has a voltage gain, G , equal to $1 + R_2/R_1$ and an input impedance equal to the input impedance of the noninverting input (i.e. “infinite”).

The circuit in Fig. 6(b) is an *inverting amplifier* and has an overall gain of $V_o/V_{in} = -R_{in}/R_f$. This circuit is analyzed by assuming that negative feedback maintains the inputs at the same potential. With the noninverting input connected to circuit common, the inverting input potential is also maintained at circuit common. Since the inverting input is maintained at the common potential but is not connected to common, the inverting input is at *virtual common* (or *virtual ground*). Circuit common (the inverted triangular symbol), rather than earth ground, is used because earth ground is not always necessary or desirable. For example, there is no direct ground connection in a floating or isolated circuit. Circuit common is the designated voltage reference point and is the ultimate sink or source of current of the circuit.

Tracking the current flow at the inverting input simplifies analysis of the inverting amplifier. A voltage applied to R_{in} is dropped across virtual ground, producing an input current $I_{in} = V_{in}/R_{in}$. Since no current is allowed to enter the inverting input, an equal and opposite current, $I_f = V_o/R_f$, must flow from the output to the virtual ground of the inverting input.

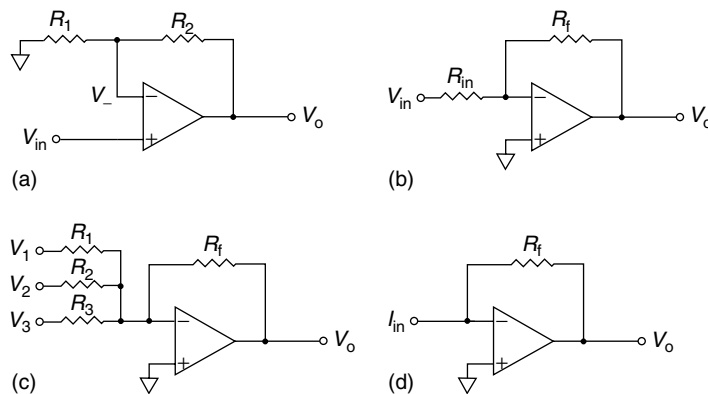


Fig. 6 Various OA amplifier circuits: (a) follower-with-gain; (b) inverting; (c) summing (adding); and (d) current follower.

With $I_{\text{in}} = -I_f$, $V_o/V_{\text{in}} = -R_{\text{in}}/R_f$. The inverting amplifier has a linear gain, easily adjusted by R_f , and can deamplify or amplify input signals. The output inversion is rarely a problem because a second inverting amplifier can restore the signal polarity. The main difficulty with the inverting circuit is that the input impedance is equal to R_{in} , which may cause loading of some signals.

The presence of a virtual ground in the inverting amplifier configuration permits a number of other useful amplifier circuits. The *adder circuit* of Fig. 6(c) allows a scaled summation of a number of voltage sources with $V_o = -(V_1 R_1 + V_2 R_2 + V_3 R_3 + \dots)/R_f$. Analysis of this circuit follows that of the inverting amplifier; each input produces a current flow to virtual ground. A current flowing from the output to virtual ground cancels the net input current. The *current follower* of Fig. 6(d) produces $V_o = -I_{\text{in}}/R_f$, where I_{in} is from a current source (such as an electrochemical cell). Note that the multiple current sources can be connected to the inverting input to produce the equivalent of the adder circuit, where $V_o = -(I_1 + I_2 + I_3 + \dots)/R_f$.

The simple analysis described above breaks down in the absence of negative feedback. For example, exceeding the electrical specifications of the OA prevents negative feedback. A common problem is exceeding the OAs current or voltage capabilities. Most OAs are low-power devices capable of supplying no more than about 20 mA. In addition, the maximum output voltage is usually limited to values somewhat less than the supply voltages (typically ± 15 V). Low signal levels also challenge the analysis. Offset or bias voltages at the OA inputs range from several millivolts to tens of microvolts. This produces output errors that are particularly

apparent with low-level inputs or high-gain circuits. OAs also do not have infinite input impedances, resulting in nanoampere to femtoampere currents flowing in or out of the inputs. These currents produce voltage drops across input resistors or offset the input current in a current follower. In most cases, circuits can be designed to minimize the effects of voltage and current offsets but these methods will not be discussed here. The most serious deviation from the simplifying assumptions made above occurs when OAs are applied to high-frequency signals. Most OAs are designed for low-frequency operation and their use with signals above 100 kHz requires care and careful component selection. The effect of frequency on OA response will be discussed in more detail below.

1.2.3

Electronic Electrical Control

Using OAs allows construction of potential and current control circuitry that operates more ideally than the simple voltage and current sources of Fig. 1 [2]. In voltage control applications, the use of an OA buffer between a voltage source and the cell replaces the internal resistance of the voltage source with the low-output impedance of the OA. However, a simple extension of the OA buffer permits elimination of a large fraction of the solution resistance of the electrochemical cell. This OA circuit is called a *potentiostat* or *voltage clamp*.

1.2.3.1 Potentiostat Circuits

A simple model of an electrochemical cell is made with an electrical resistor, connecting the *counter* and *working* electrodes, representing the electrolyte solution. Flow of current between these electrodes produces an ohmic voltage ($I \times R$), opposing

the applied voltage. As described in Eq. (6) above, introducing a negative feedback connection between the amplifier output to its inverting input reduces the output resistance of an OA. Extending the negative feedback loop further, to include a portion of the solution resistance, reduces ohmic drop. A model of this process is illustrated in Fig. 7, where the solution resistance, R_s , is modeled as two components: the compensated, R_c , and the uncompensated resistance, R_u . A probe, reference electrode (RE), placed between the CE, and the WE, completes a negative feedback loop between RE and the inverting OA input. This connection reduces R_c by the following amount:

$$R'_c = \frac{R_c}{1 + A} \quad (7)$$

where R'_c is the new compensated resistance and A is the open-loop OA gain. For example, if R_c is 1 k Ω , R'_c is 0.010 Ω , with $A = 10^5$. As R'_c becomes negligible, R_s is reduced to R_u . The potential at point RE is now equal to E_{in} (inverting and noninverting inputs have equal potentials under negative feedback) and thus the potential applied across R_u is E_{in} . Drawing this same circuit connected to an electrochemical cell illustrates a simple potentiostat circuit (Fig. 8). The potentiostat maintains

a potential difference (equal to E_c) between RE and WE.

A potentiostat is a significant improvement over the simple voltage source of Fig. 1(a). A reference electrode diminishes the total resistance between counter and working electrodes by sensing (and thus correcting) the voltage near the working electrode. This lowers the IR drop in the cell. Another advantage is that the voltage controlling the cell potential, E_c , is not required to be a low-impedance source, allowing a number of different controlling sources to be used without regard to their ability to drive the necessary current through the cell.

The potentiostat requires a third electrode, RE, to act as a sensing electrode. Although the use of a third electrode may seem to be a disadvantage, in fact, the third electrode is important beyond its role in reducing the cell resistance. A two-electrode voltage source requires that the CE serve both as an RE and as a source or sink of the electrical current flowing at the WE. In order to supply the current without unduly perturbing their equilibrium half-cell potential, CEs must be physically large. In a three-electrode cell, controlled by a potentiostat, the CE function is split between two electrodes: a large surface

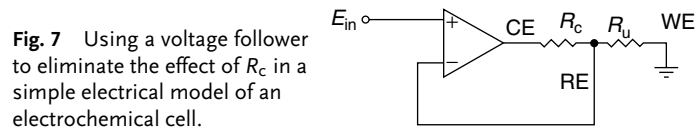


Fig. 7 Using a voltage follower to eliminate the effect of R_c in a simple electrical model of an electrochemical cell.

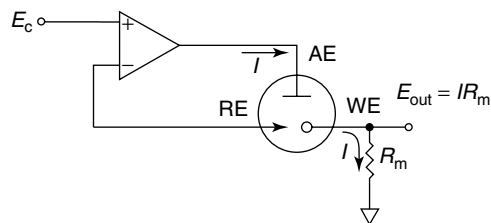


Fig. 8 A potentiostat based on a voltage-follower circuit.

area *auxiliary electrode*, AE, which supplies the cell current, and a *reference electrode*, RE, which maintains a cell potential reference. The RE is not required to supply any significant current to the high-impedance input of the OA. In consequence, the RE is smaller, conserving space and cost. Thus, three-electrode potentiostatic cell control is advantageous even when ohmic drop is not an issue.

However, potentiostatic circuits are not always necessary. A common situation is found in the use of ultramicroelectrodes, UMEs, in which the cell current is in nanoamperes and smaller due to the small size of the WE [3]. With such small currents, even small reference electrodes are used as counterelectrodes without fear of significant perturbation of their half-cell potential. The potentiostat of Fig. 8 can accommodate this case by connecting both the AE and RE leads together. Note that this converts the potentiostat into a simple voltage follower. UMEs are considered further in Chapter 2.5 and Sect. 2.1.4.1 of Chapter 2.1.

A different type of potentiostat circuit is constructed by an adder-type OA circuit (Fig. 9) rather than the follower type of Fig. 8. The adder (or summing) OA input allows multiple control inputs; for example, an offset potential may be added to a separate voltage ramp. Since the adder inputs are not high impedance, a voltage follower buffers the output of the reference electrode. Also, note that inverted control

inputs are required when compared with the follower potentiostat. As in the follower potentiostat, negative feedback is used to reduce cell resistance and the buffered RE voltage again allows small reference electrodes to be used.

Using either the follower or adder potentiostats does permit a very serious fault condition to exist. Negative feedback is only present when AE and RE are in electrolyte solution. Removing either of the electrodes from solution or disconnecting them from the potentiostat prevents the stabilizing effect of negative feedback. An electrocution hazard exists when the AE connection is not present. The lack of negative feedback will force the potentiostat into saturation and voltages from ten to several hundred volts will appear on the AE lead (depending on the power output capability of the potentiostat). In addition, the absence of potential control allows significant current flow between RE and WE. RE can thus be greatly perturbed from equilibrium perhaps ruining the reference electrode. Alternately, disconnecting or removing the RE from solution, produces large potentials between AE and WE as the potentiostat goes into saturation. At the least, this can ruin an experiment or damage the WE. To avoid this, most potentiostats are equipped with a switch to turn the cell potential control off between experiments or during setup. However, securely fastening cell leads and electrodes is a safe practice, as well as disconnecting

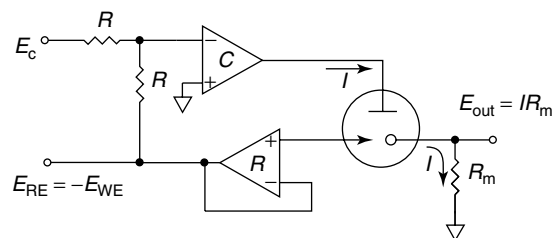


Fig. 9 A potentiostat based on a summing amplifier circuit.

and connecting the WE first and last, respectively, in any experiment.

1.2.3.2 Galvanostatic Circuits

Galvanostats are instruments that provide a controlled current through an electrochemical cell. As in the potentiostatic circuits, negative feedback produces superior current control. A galvanostat constructed from an OA is illustrated in Fig. 10. The current flowing through the cell, I_{cell} , is

$$I_{\text{cell}} = -I_{\text{in}} = -\frac{E_{\text{in}}}{R_{\text{in}}} \quad (8)$$

Conveniently, the input voltage programs the magnitude and polarity of the current. Changing the value of R_{in} scales the current range. Analyzing the operation of the circuit is straightforward. Negative feedback holds the inverting input at virtual ground by matching the current flow across the load to the opposite current produced by dropping E_{in} across R_{in} . As long as negative feedback conditions can be maintained, the current will be maintained at a value programmed by E_{in} and R_{in} . Physical limitations of the OA prevent certain current flows through the load. An open-circuit condition cannot support a current flow and the OA itself can only supply a limited amount of current (about 10–20 mA for typical devices). The voltage required to produce the current (the compliance voltage) is limited to values near

the supply voltages (about 13–15 V for the typical ± 15 V supplies). The voltage output of the OA is $I_{\text{cell}} \times R_{\text{Load}}$ and this can be used to verify correct operation of the galvanostat; outputs near the compliance voltage indicate impending loss of negative feedback control. R_{Load} is not necessarily “ideal”. Such is often the case when the generalized load is replaced with an electrochemical cell, which presents a load that varies nonlinearly with potential and time. The load terminals are the working and auxiliary electrodes. By connecting the WE to the inverting input (virtual ground), the WE potential can be monitored by measuring the potential of RE versus ground. The reference electrode is not necessary for operation of the galvanostat but, since the potential of the working electrode is often desired in constant-current experiments, is often included. Controlled current experiments are not affected by IR drop (as long as the galvanostat has sufficient compliance voltage to overcome the IR drop) but the measurement of WE voltage will include an IR_{u} drop component. Proper placement of the reference electrode will minimize this but an advantage of galvanostatic operation is that the measured potential is corrected by simply subtracting the IR_{u} voltage.

A difficulty with the galvanostatic circuit of Fig. 10 is that the programming voltage E_{in} must supply the identical magnitude

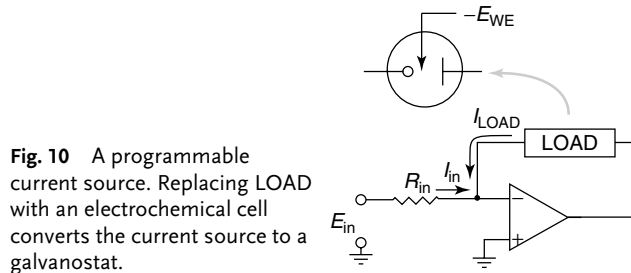


Fig. 10 A programmable current source. Replacing LOAD with an electrochemical cell converts the current source to a galvanostat.

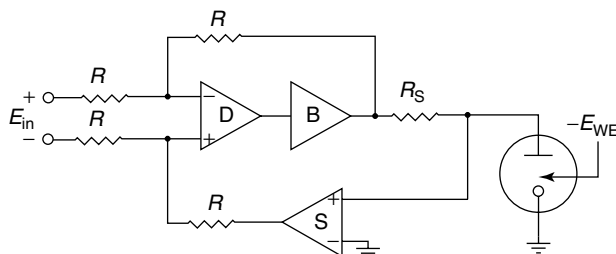


Fig. 11 An improved galvanostat circuit.

of current flowing through the load (cell). This can be a problem for heavy current applications. The galvanostatic circuit in Fig. 11 avoids this problem. The output current is programmed by E_{in} and a “sense” resistor R_s in which

$$I_{cell} = \frac{E_{in}}{R_s} \quad (9)$$

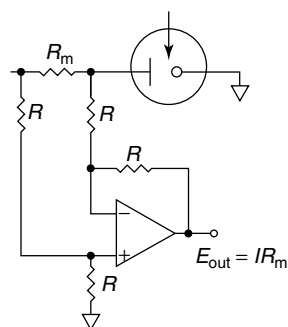
In operation, the current flow through the cell (or load) produces a voltage drop across R_s , which is buffered by the sense amplifier (S). The output of S is applied to the inputs of the differential amplifier (D). A “buffer” amplifier placed in the negative feedback loop provides greater current capacity. Buffer amplifiers, of the type used here, can produce high-output currents, as much as several amperes. Since negative feedback is operating in the differential amplifier feedback loop, the inverting and noninverting inputs are equal, and the output of the buffer amplifier is precisely that required to maintain the programmed current through R_s and, thus, through the cell. For good results, the voltage drop across R_s should be small compared to the compliance voltage of the galvanostat. By using different values of the sense resistor, currents of nanoamperes to amperes can be controlled and programmed by E_{in} .

1.2.4

Signal Transduction

A potentiostat’s function is to maintain a constant potential between the WE and the RE. In most cases, a potentiostat includes, as a separate function, a means to convert the current flowing through the cell into a signal measurable by an external recorder. The current is transduced into a voltage and often further amplified and filtered before presentation at the output terminal. A classical transduction method is to simply measure the voltage developed across a resistor. A measuring resistor, R_m , inserted between WE and common (cf. Figs. 8 and 9) generates a voltage according to Ohm’s law, $V_o = IR_m$. Note that R_m is in series with the solution resistance and the total ohmic drop in the circuit is $I \times (R_u + R_m)$. Thus, a disadvantage of this circuit is that R_m must be carefully matched to the expected cell current to avoid excessive ohmic drop. An alternative procedure is to insert R_m in the CE as illustrated in Fig. 12. R_m is in series with the cell solution resistance but, in this case, R_m is included in the compensated part of the solution resistance and does not contribute to the overall cell ohmic drop. In this method, neither terminal of R_m is connected to circuit common (i.e. it is “floating”). A differential OA is used in this situation to measure

Fig. 12 Current measurement by use of a differential amplifier to measure the voltage drop across R_m connected to the auxiliary electrode. Other control circuitry is not shown.



a potential difference across a floating source. However, a differential OA is not suitable when the resistor terminals are at several tens of volts, or higher, above circuit common (as can occur in high-power potentiostats). In such cases, measuring the small differential voltage across the resistor in the presence of a much larger “common-mode” voltage requires use of an *instrumentation amplifier*. Instrumentation amplifiers are designed to accurately extract the differential voltage while rejecting common-mode voltages five orders of magnitude larger. The figure of merit is the *common-mode rejection ratio* (CMRR), often specified as decibels (i.e. 100 dB is a 10^5 rejection). Although most instrumentation amplifiers do not allow the common-mode voltage to be higher than the amplifier supply voltage, several allow common-mode voltages of up to 200 V, permitting use on high-power potentiostats.

The current-follower OA configuration (Fig. 6d) is often used as a current transducer in potentiostat circuits (Fig. 13). The output voltage is proportional to the feedback resistor, R_f , making amplification of the current signal straightforward. In this

configuration, the WE potential is maintained at “virtual ground”. A disadvantage of this circuit is that loss of negative feedback and potential control occurs when the amplifier’s electrical capacity is exceeded. This is especially a problem for heavy cell currents, where the OA must supply an equal current to maintain virtual ground. The addition of a buffer amplifier will allow operation with cell currents larger than the OA capabilities. Potential control is also lost when the combination of cell current and R_f would require an output voltage greater than the power supply voltage of the OA. In addition, virtual ground is lost at high frequency because of the inadequate high-frequency gain of OAs. High-gain circuits can lose control at frequencies as low as 100 Hz. A more detailed discussion of the frequency response of potentiostatic circuitry is presented in Sect. 1.2.7.

1.2.5

Alternate Control Circuits

In some experiments, such as a rotating ring-disk electrode (see Section 2.4.2.2 of Chapter 2.4) or liquid chromatography

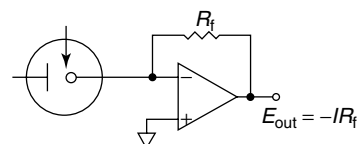


Fig. 13 Current measurement using a current-follower circuit.

detection, it is desirable to control two or more working electrodes in the same electrochemical cell. Although separate potentiostats can be used to control the working electrodes, several problems occur. The control and measurement functions of the potentiostats must be electrically isolated. This requires isolated power supplies (e.g. batteries), control signals, and outputs. In addition, each working electrode requires a separate auxiliary and reference electrode. An alternate strategy is to use a bipotentiostat; a potentiostatic circuit designed to allow simultaneous potential control of two working electrodes. A simplified schematic of a bipotentiostat circuit is illustrated in Fig. 14. The circuit is based on the adder-type potentiostat (Fig. 9). The addition of amplifiers OA4–OA7 provides control of the second working electrode. The bipotentiostat maintains working electrode 1 (WE1) at circuit common, while WE2 is lifted off circuit common by an amount equal to the potential difference between the two working electrodes (i.e. $E_{W2} - E_{W1}$). OA6 is the differential

amplifier that generates this potential difference, which, when applied to the noninverting input of current-transducer amplifier OA4, shifts the potential of WE2 to a value equal to $E_{W2} - E_{W1}$. Amplifier OA4 transduces the WE2 current. Since the voltage output of OA4 is not referenced to circuit common, differential amplifier OA7 is used to restore the output to a circuit common reference. In the bipotentiostat, the auxiliary electrode supplies the total current required at WE1 and WE2; however, OA2 and OA1 act to maintain the potential difference between the first working and RE at E_{W1} . If desired, additional working electrodes can be added to this circuit by duplicating the circuits of OA4–OA7 as many times as necessary.

An alternate method for construction of multipotentiostats is to use a *grounded reference* configuration (Fig. 15). Here the RE is maintained at virtual ground and the potential of the working electrode is changed at the noninverting input of the current transducer. Since the output of the current transducer floats above circuit common by

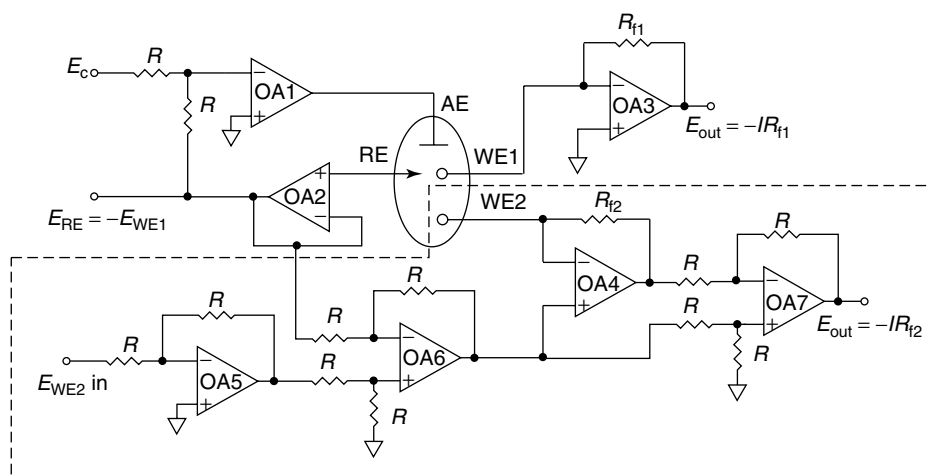


Fig. 14 A bipotentiostat circuit. Circuitry enclosed by the dashed line is that added to support a second working electrode.

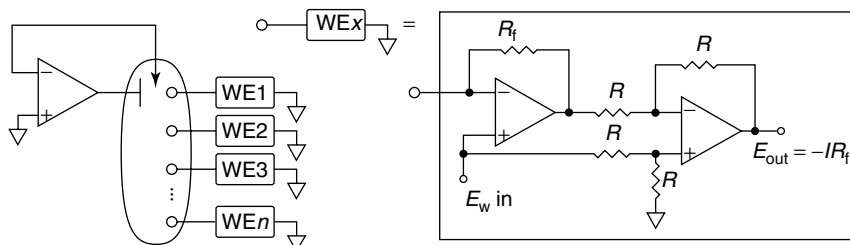


Fig. 15 A multipotentiostat circuit based on a grounded reference configuration. The dashed line surrounds the circuitry required for each working electrode.

E_{in} , the output is referenced to common by a differential amplifier. Additional working electrodes are added by replicating the current-transducer/differential amplifier combination. All working electrodes share the auxiliary and reference electrodes in this configuration.

In bipotentiostats employing shared reference and auxiliary electrodes, the degree to which the solution resistance can be eliminated by RE placement is limited. In such cases, the RE should be located nearest the WE with the heaviest current flow. Obviously, the operation of these bi- or multipotentiostats will be compromised under conditions in which ohmic drop is large. Experimental artifacts are introduced when the loop does not instantaneously respond to changes in current at the working electrode. In particular, potential steps at either working electrode will introduce spurious current transients at the other electrode due to the finite response time of the feedback loop. The transients not only obscure the current signal but also indicate a brief loss of potential control. Using dual potentiostats is not necessarily a solution to this problem, since large currents flowing from either of the two auxiliary electrodes to closely spaced working electrodes will cause a similar loss of potential control.

1.2.6

Ohmic Drop Compensation

In galvanostatic or amperometric experiments, the solution, electrode, and connection resistance produce an ohmic voltage in proportion to the cell current. In galvanostatic measurements, ohmic drop distorts the measured cell voltage. However, a more serious effect occurs in voltammetry in which the ohmic drop opposes the applied potential. Voltage sweeps become nonlinear and potential steps have prolonged rise times producing a distorted voltammetric response. There are many reports of methods to alleviate ohmic drop in the literature [4, 5]. The use of a potentiostat provides a partial solution by employing a negative feedback loop to eliminate a fraction of the solution resistance. Numerous methods to minimize the remaining “uncompensated” resistance (R_u) have been proposed [6–9], but the two most commonly used compensation procedures are *positive feedback* and *current-interruption* compensation.

1.2.6.1 Current Interruption

In the current-interruption method, the flow of current through the cell is periodically stopped. During this time, there is no ohmic drop in the cell ($IR = 0$); therefore, the true potential of the working electrode

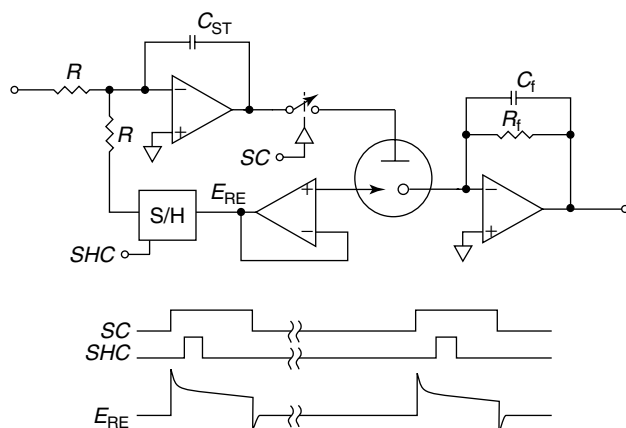


Fig. 16 A simplified schematic and timing diagram of a current-interruption potentiostat used for IR drop elimination. The FET switch is closed and the S/H is in sample mode when digital control signals SC and SHC are high.

can be measured [10]. Figure 16 illustrates the basic instrument. An electronic switch [typically a field-effect transistor (FET) switch] at the auxiliary electrode is disconnected for several microseconds at a frequency of 10 to 50 kHz. At the moment of disconnection, the ohmic potential rapidly drops to zero (the drop is not instantaneous because of the cell inductance and the finite response time of the amplifiers). After a delay to allow the ohmic drop potential to collapse, a pulse signal is sent to a sample-and-hold (S/H) circuit, which monitors the RE potential. The double-layer capacitance maintains the working electrode potential until it eventually decays through faradaic reactions. An S/H circuit collects a sample of the potential using a set of switches to charge a low-leakage capacitor during a sampling pulse. At the pulse end, the capacitor value is output through a buffer amplifier to “hold” the sample potential until another sample pulse occurs. The S/H output is applied to the inverting input of the potentiostat OA. As in the follower potentiostat, the negative

feedback loop maintains the potential between the WE and reference at the control potential (E_c). Unlike the simple follower potentiostat, however, the potential is controlled without ohmic drop distortion. It should be noted that implementation of a properly performing current-interruption potentiostat is significantly more complex than that suggested by the illustration in Fig. 16 [11–13]. Since the potential is not controlled continuously, the potentiostat feedback loop must operate more slowly than otherwise. By adding a compensation capacitor (C_{ST}) in the feedback loop, the frequency response is reduced to a value lower than the pulse frequency. Without this, the interruption pulses will destabilize the feedback loop. In addition, the current follower filters the cell current by the combination of C_f and R_f , which eliminates transients caused by the current switch. Although a higher pulse frequency is desirable, increasing the pulse frequency beyond 100 kHz is practically difficult. This limits this technique to relatively slow measurements. The current-interruption

technique is well suited for corrosion, battery, and electrosynthesis applications that often do not require rapid measurements and in which heavy current flows introduce unacceptable ohmic drop in even highly conducting electrolytes.

1.2.6.2 Positive Feedback

This method introduces a positive feedback path into the potential control circuit. Normally, positive feedback is not desirable but is used here in conjunction with negative feedback such that the overall amount of feedback remains negative. An illustration of an adder-type potentiostat incorporating positive feedback is shown in Fig. 17. A fraction, f , of the voltage output (created by the potentiometer) is summed with the RE potential. (Note that the potentiometer resistance should be much less than the resistance, R , at the inputs of the control amplifier to avoid loading the potentiometer output. Alternatively, a voltage follower can be inserted after the potentiometer.) Because of the inverted current-follower output, the signal is fed back as positive feedback. Positive feedback reduces the uncompensated resistance since the amount of ohmic drop is proportional to the cell current. Thus, adding a voltage proportional to the cell current to the auxiliary electrode potential

offsets the ohmic drop. It is important to realize that the correction occurs continuously. A one-time correction will not suffice since the current flowing is that observed with ohmic drop present. For full correction, the current used for correction must have no ohmic drop. A continuous correction is able to *approach* this ideal but, out of necessity, the correction signal will always lag the cell current, preventing complete correction. For this reason, any delay in the correction loop reduces the amount of correction possible and, as discussed below, can destabilize potential control.

The compensation fraction amount is given by $f \times R_f/R_u$. Although complete compensation is not possible for the reasons given above, the amount of compensation actually achieved in practice is surprisingly low – 80% compensation is typical. Delays introduced in the current transduction and in measuring the RE potential are the main reason for incomplete compensation. Positive feedback also requires knowledge of R_u . Although, R_u can be determined before an experiment in many cases, some experiments, notably corrosion, present situations in which the solution or electrode resistance varies with time. A number of authors have presented methods to automatically measure R_u during an experiment [6,

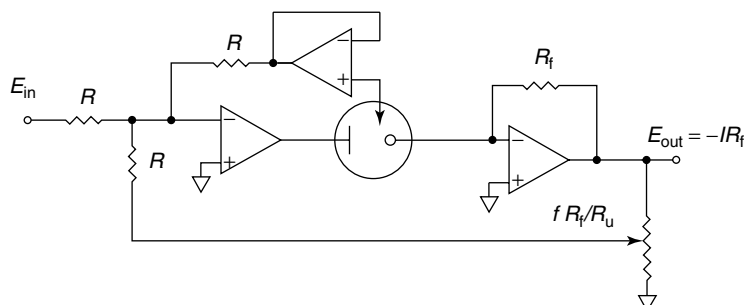


Fig. 17 Potentiostat circuit with positive feedback IR drop correction.

7, 9]. Because of the relatively simple implementation, positive feedback is a popular method for reducing ohmic drop. Positive feedback can also operate more rapidly than current-interruption methods and so is useful in analytical or physical measurements.

1.2.7

Control Loop Frequency Response

The behavior of the control loop was previously considered at low frequencies; however, the ability to control the potential or current at higher frequencies is important in many electrochemical methods, including ac impedance and short-timescale voltammetry. Although the behavior of a potentiostat or galvanostat at all frequencies can be determined through experiment or calculation for a well-defined system (such as when connected to a dummy cell) [14–16], in practice real electrochemical cells are not only electrically complex but also extremely variable. Determining the behavior of a general-purpose instrument is impractical over the wide range of conditions that might occur under normal operation. However, it is possible to determine with some confidence what conditions might cause loss of

potential or current control. To illustrate this, a test circuit (Fig. 18) was modeled using a SPICE-based electronic simulator [17].

Initially, the simulation uses the circuit components noted in the figure and this will serve as a comparison point. A triangle wave generator produces a cyclic voltammetry (CV) wave at 2000 V s^{-1} as the input for the potentiostat. OA1 is a common low-cost LF356 (National Semiconductor) device and stabilizing capacitor C_{ST} is 10 pF. The electrochemical cell is simulated as a dummy cell with 1200Ω of solution resistance, a double-layer capacitance, C_{dl} , of $0.2 \mu\text{F}$, and faradaic impedance, Z_F , of $10^6 \Omega$. The reference electrode is situated to provide $R_c = 1000 \Omega$ and an uncompensated resistance, R_u of 200Ω . R_{RE} and C_{RE} are included to simulate the behavior of a reference electrode. A Luggin–Haber capillary, used to provide for close RE–WE spacing, often exhibits high resistance and capacitance. Initially, R_{RE} and C_{RE} are set to $10 \text{ k}\Omega$ and 1 pF , respectively. OA2 is simulated as an ideal OA. The current follower, OA3, is an LT1007 (Linear Technology) OA, a higher performance OA than the LF356 OA. At 2000 V s^{-1} , the maximum double-layer charging current is $400 \mu\text{A}$ and the 200Ω R_f value produces

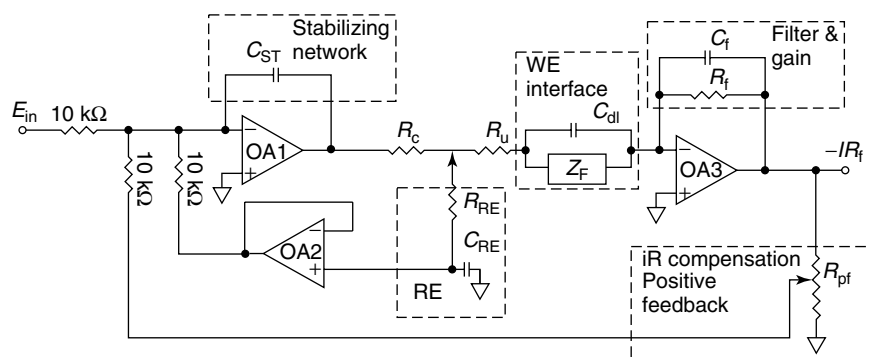


Fig. 18 Model potentiostat and electrochemical cell circuit used in stability calculations.

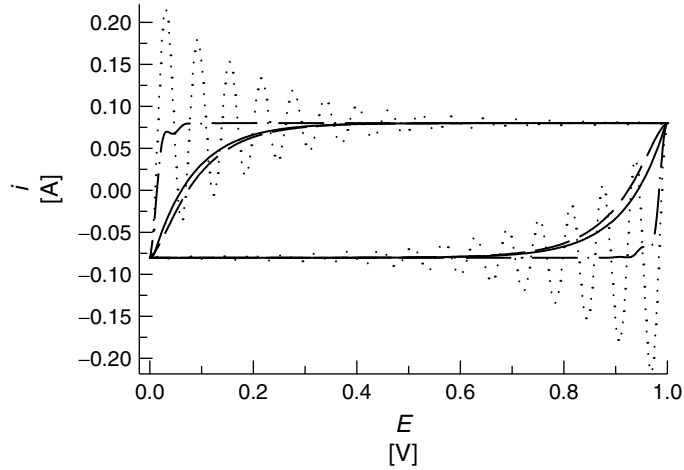


Fig. 19 Calculated CV curves with a 2000 V s^{-1} scan rate applied to the model potentiostat of Fig. 18. (—) $R_c = 1000 \Omega$, $R_u = 200 \Omega$, $C_{ST} = 10 \text{ pF}$, $C_{dl} = 0.2 \mu\text{F}$, $R_{RE} = 10 \text{ k}\Omega$, $C_{RE} = 1 \text{ pF}$, $R_f = 200 \Omega$, $C_f = 1 \text{ nF}$; (\cdots) $R_c = 1198 \Omega$, $R_u = 2 \Omega$, $C_{ST} = 10 \text{ pF}$; ($-\cdot-\cdot-$) $R_c = 1198 \Omega$, $R_u = 2 \Omega$, $C_{ST} = 1000 \text{ pF}$; ($- - -$) $R_c = 1000 \Omega$, $R_u = 200 \Omega$, $C_{ST} = 1000 \text{ pF}$.

an output voltage of 80 mV. A connection for positive feedback ohmic compensation is included. Initially, the potentiometer, R_{pf} , is set to give zero positive feedback.

1.2.7.1 Effect of Reference Position

For R_u of 200Ω , the CV current in Fig. 19 shows that the charging current does not level off to the expected $400 \mu\text{A}$ until about $200 \mu\text{s}$ into the wave. This slow rise is caused by the ohmic drop or, more precisely, the $R_u C_{dl}$ time constant of $40 \mu\text{s}$. Moving the reference electrode closer to the working electrode decreases R_u . A simulation with $R_u = 2 \Omega$ ($R_c = 1198 \Omega$) might be expected to show a 100-fold speed-up in the rise time. In fact, a set of damped oscillations (ringing) is observed on the rising and falling edge of the charging current. The oscillations are evidence of destabilization of the potential control by decreasing R_u . The control loop is unable to maintain the desired potential

because OA1 is unable to supply sufficient current to charge C_{dl} at the rate demanded by the negative feedback loop. Since the OA is unable to supply current at the required rate, there is a delay introduced into the control loop. The bode and phase shift plots of Fig. 20(a, b) plot the behavior of a series of sine waves applied to the input of the circuit. The result is a log-log plot of loop gain and phase shift versus frequency for this circuit. The amount of phase shift, with respect to the low-frequency behavior, is a measure of delay in the feedback loop. At low frequencies, the Bode plot indicates that the magnitude of the gain is 1 (0 dB). At higher frequencies, the voltage gain drops to about 70% (-3 dB) of its DC value for $R_u = 200 \Omega$ at a frequency of 270 kHz . This drop is mainly due to the inherent frequency response of the OA. For clarity, only the phase shift in excess of the 180° shift produced by negative feedback is plotted in Fig. 20(b). For $R_u = 200 \Omega$, the

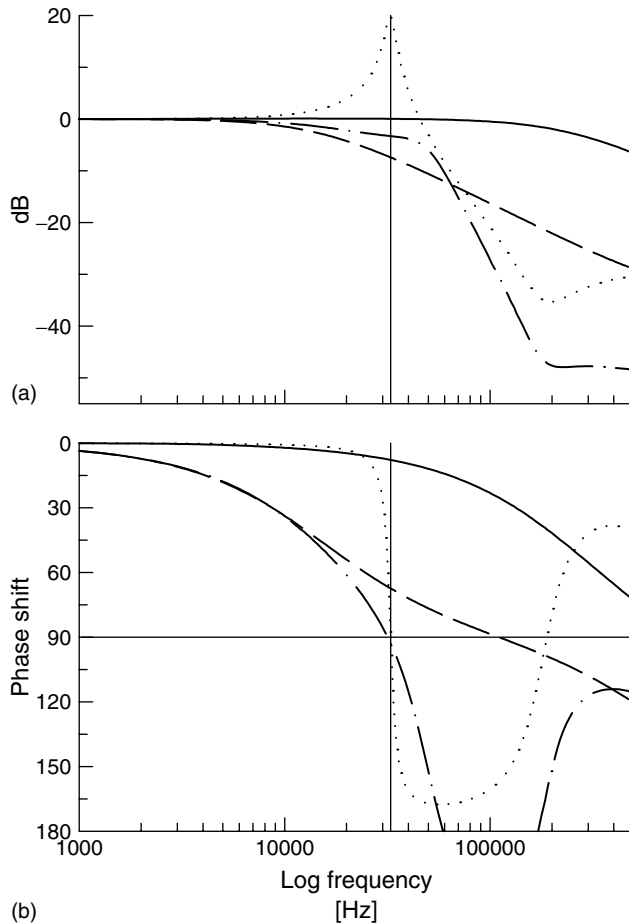


Fig. 20 Calculated (a) bode and (b) phase shift curves for the circuit of Fig. 18. Conditions are given in Fig. 19.

phase shift only becomes appreciable in the region in which the loop gain is already decreasing. However, in the case in which R_u is $2\ \Omega$, the phase shift rapidly grows to 90° near a frequency of 32 kHz. The Bode plot also shows a *peak* in the gain at the same frequency. The nature of the ringing in the CV in Fig. 19 is now clearer: at the frequency at which the phase shift increases to 90° and the gain is larger than unity, oscillations (at 32 kHz) caused by positive feedback are possible. Further

decreases in R_u cause increased ringing duration and amplitude.

Stabilizing the control loop to avoid oscillation is possible in several ways. A recommended procedure to increasing the stability of amplifiers driving capacitive loads is the introduction of a small resistance in series with the load. The benefit of this is clear from the figures above: a too-small R_u value destabilizes the loop. Some amplifiers are specified to drive larger capacitive loads and would

be preferred here. An alternate method is to reduce the loop gain below unity at the oscillation frequency. Changing C_{ST} to 1000 pF stabilizes the potentiostat with $R_u = 2 \Omega$. Ringing is reduced in the CV (Fig. 19). The Bode and phase shift plots (Fig. 20) show that a C_{ST} of 1000 pF reduces the gain below unity for frequencies at which the phase shift is greater than 90° . Note that this reduces the overall frequency response of the potentiostat to below 16 kHz. This is clearer in the CV and bode plots in which R_u is 200 Ω and $C_{ST} = 1000$ pF; the CV response is clearly affected by the slower rise time of the potentiostat circuitry.

The RE itself can also destabilize the control loop. Figure 21 shows the CV acquired under the initial conditions but with $R_{RE} = 50$ k Ω , $C_{RE} = 300$ pF. These values are reasonable for a long, thin Luggin–Haber capillary. The effect is to reduce the frequency response of the RE connection, that is R_{RE} and C_{RE} for a

low-pass filter. This adds an additional delay in the loop, producing oscillations at 50 kHz, as indicated by the peak in the Bode plot at the 90° phase shift (Fig. 22).

1.2.7.2 Positive Feedback Stability

Addition of positive feedback for IR_u compensation produces a control situation similar, but not identical, to condition in which R_u is reduced by moving the RE closer to the WE. The bode plot and CV curve of Fig. 23(a, b) illustrate the potentiostat response when $R_u = 200 \Omega$ ($R_c = 1000 \Omega$) and the compensation fraction is set to 0, 90, and 99%, that is, an effective R_u value of 200, 20, and 2 Ω , respectively. Compare these curves to Figs. 19 and 20, which have actual values of R_u of 200, 20, and 2 Ω . In addition, the effect of a 1000 pF stabilizing capacitor (C_{ST}) is plotted for an effective R_u of 2 Ω . Except for one exception, the CV curves of Figs. 23(b) and

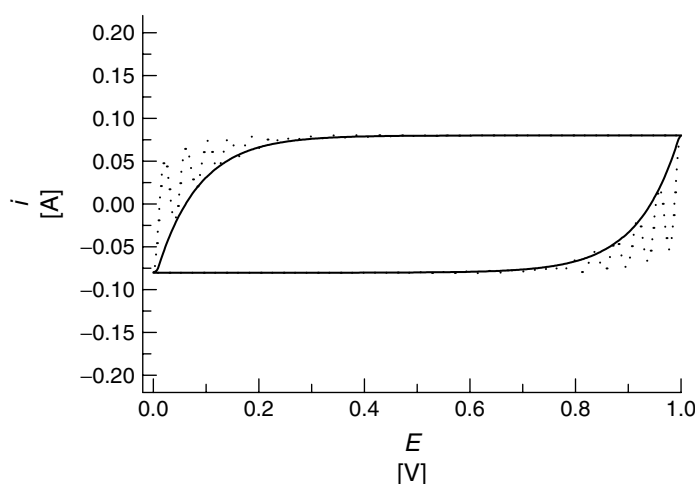


Fig. 21 Calculated CV curves with a 2000 V s^{-1} scan rate applied to the model potentiostat of Fig. 18. (—) $R_c = 1000 \Omega$, $R_u = 200 \Omega$, $C_{ST} = 10 \text{ pF}$, $C_{dl} = 0.2 \mu\text{F}$, $R_{RE} = 10 \text{ k}\Omega$; $C_{RE} = 1 \text{ pF}$; $R_f = 200 \Omega$; $C_f = 1 \text{ nF}$; (\cdots) $R_{RE} = 50 \text{ k}\Omega$; $C_{RE} = 300 \text{ pF}$.

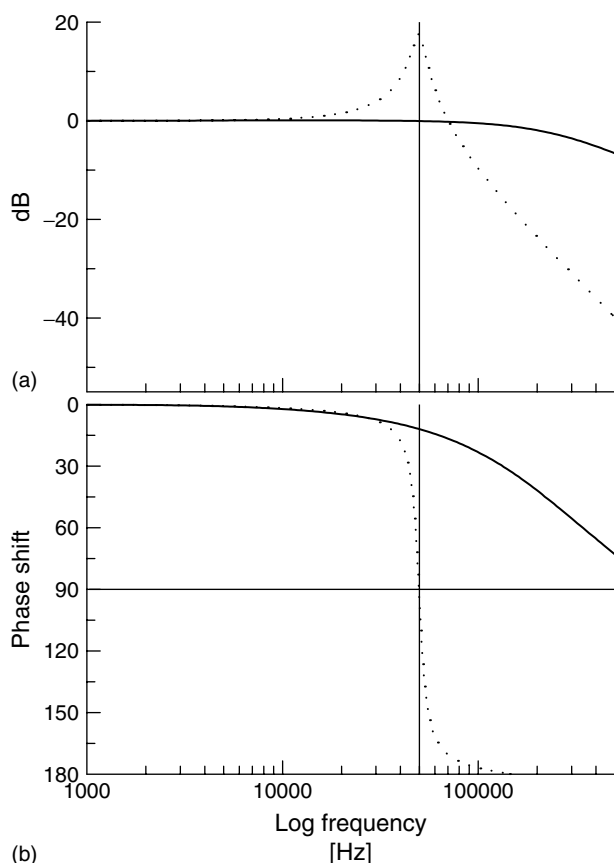


Fig. 22 Calculated (a) bode and (b) phase shift curves for the circuit of Fig. 18. Conditions are given in Fig. 21.

19 are essentially identical. Note the exception that the stabilizing capacitor is much less effective in reducing ringing in the positive feedback case. The Bode plots of Figs. 23(a) and 20(a) are quite different. Gain rises above unity over a larger range of frequencies in the positive feedback case. This reflects the fact that the frequencies necessary to reduce IR_u drop must be supplied at increased gain. Note also that the “job” of reducing IR_u drop is shifted to the current transducer, OA3, in positive feedback, which partly explains the reduced effectiveness of C_{ST} in minimizing ringing.

1.2.7.3 Other Destabilizing Conditions

The simple R_uC_{dl} model of the electrochemical cell provides a challenging control situation. The presence of diffusional faradaic current reduces the reactance of the working electrode interface by adding a parallel *noncapacitive* current path across C_{dl} . However, some electrode processes can transiently increase the reactance of the interface, thus decreasing the control loop stability. For example, potential-dependent adsorption or desorption of ions at the interface or passivation/depasivation phenomena can destabilize an otherwise

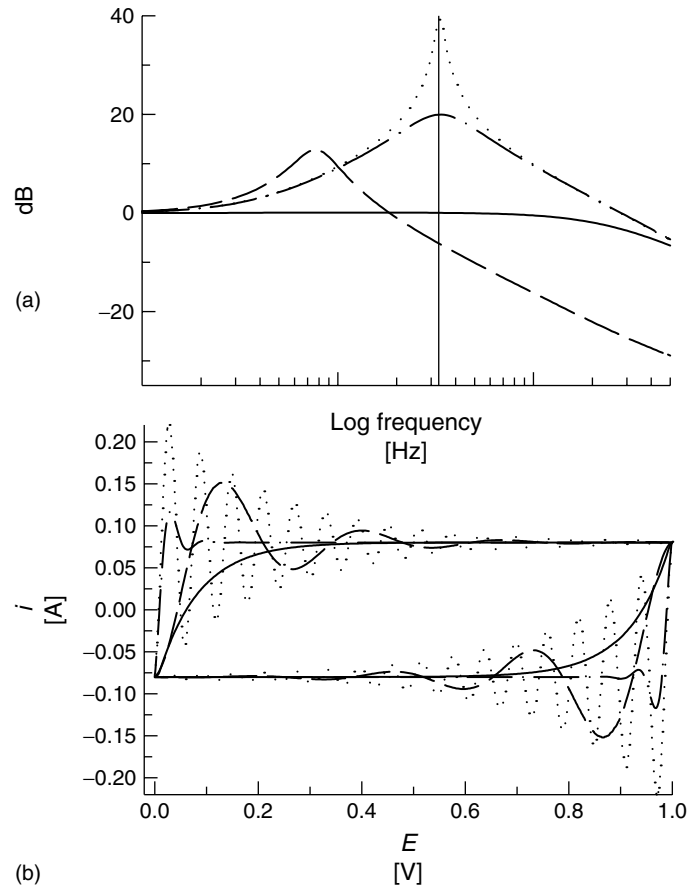


Fig. 23 Calculated (a) and (b) CV curves with a 2000 V s^{-1} scan rate applied to the model potentiostat of Fig. 18 using different amount of positive feedback IR compensation. (—) 0% compensation, $R_c = 1000 \Omega$, $R_u = 200 \Omega$, $C_{ST} = 10 \text{ pF}$, $C_{dl} = 0.2 \mu\text{F}$, $R_{RE} = 10 \text{ k}\Omega$; $C_{RE} = 1 \text{ pF}$; $R_f = 200 \Omega$; $C_f = 1 \text{ nF}$; (-.-.-) 90% compensation, $C_{ST} = 10 \text{ pF}$; ($\cdot \cdot \cdot \cdot$) 99% compensation, $C_{ST} = 10 \text{ pF}$; (- - -) 99% compensation, $C_{ST} = 1000 \text{ pF}$.

stable control loop. In such cases, the control loop must be further stabilized, often at the cost of a decreased frequency response.

Maintaining control is more difficult with certain potential excitation waveforms. Step functions (as in chronoamperometry) are particularly severe tests for potentiostats. As an example, consider the

requirements for a 1-V step applied to the test circuit of Fig. 18. With $R_c = 1000 \Omega$, $R_u = 200 \Omega$, and $C_{ST} = 10 \text{ pF}$, OA1 is required to supply a transient voltage and current greater than 35 V and 30 mA, respectively. This is excess of what most simple OAs can supply and a buffer amplifier (as in Fig. 11) would be required. Reducing R_u to 2Ω ($R_c = 1198 \Omega$) increases

the voltage and current required to greater than 350 V and 300 mA, respectively. However, this transient occurs during the first microsecond after a step. Degrading the frequency response of OA1 (e.g. by increasing C_{ST}) reduces the transient power requirements.

1.2.8

Excitation Signals and Data Acquisition

A variable voltage source is often used to *program* the magnitude and time course of the potential or current excitation signal applied to an electrochemical cell. The controlling voltage can be as simple as a battery connected to a manually adjusted potentiometer. The *output* signal of a potentiostatic or galvanostatic circuit is usually a voltage proportional to the current at the WE or cell voltage. Traditionally, the output of an electrochemical experiment would be recorded by hand in a laboratory notebook or with an electromechanical recorder using a pen on graph paper. Oscillographic recorders, storage oscilloscopes, or magnetic tape are used for transient experiments. However, the availability of inexpensive personal computers (PCs) has essentially eliminated these traditional *analog* recording methods in favor of more versatile *digital* recording. Similarly, analog methods of programming excitation signals have been supplanted by digital means. This section discusses digital methods of experiment control and data acquisition.

1.2.8.1 Excitation Signals

Signals for programming a controlling potential or current in an electrochemical cell include large amplitude potential sweeps or steps (as in cyclic voltammetry or chronoamperometry), sine and square waves, pulse sequences, pseudorandom

noise, and various combinations of these. Applications of some of these methods are discussed in the following chapters (e.g. Chapter 2.1 considers cyclic voltammetry and Chapter 2.2 describes chronoamperometry). Although traditional analog electronic methods were used to generate any of these excitation waveforms, digital methods are much more efficient and versatile and can replace nearly all traditional analog signal generation methods. The use of high-accuracy and very fast *digital-to-analog converters* (DACs) in consumer electronics, such as in compact disc players and in high-resolution PC graphics cards, has made DAC-based signal sources widely available and, in general, significantly less expensive and more precise than equivalent analog sources.

A DAC converts a set of binary digits into an analog current or voltage. The number of the binary digits used in each conversion sets the output resolution of a DAC. A typical DAC might have 12 bits of resolution, corresponding to 2^{12} (i.e. 4096) possible analog outputs. An internally or externally supplied *reference* sets the DAC output range. This allows a DAC to provide a wide range of possible outputs. For example, the DAC reference might be used to set an output range of ± 10 V or, alternately, 0 to -1 V. In either case, the DAC resolution (e.g. 12 bits) fixes the digital resolution but the accuracy of the analog output depends on the output range. The number of bits of resolution, n , sets the full-scale accuracy according to this equation $100\%/(2^n - 1)$. Thus, a 12-bit DAC has an accuracy of 0.024%, which corresponds to 4.9 mV or 0.24 mV accuracy on a ± 10 or 0–1 V range, respectively. Toggling the value of the *least significant bit* (*lsb*) produces the smallest possible output change. Increasing the output accuracy of a DAC

requires increasing the number of bits or decreasing the full-scale output range. The rate at which the digital codes are sent to the DAC is governed by a *clock*, which also, necessarily, sets the maximum rate at which the analog output can vary. The clock is simply a sequence of digital pulses occurring at regular intervals. The maximum rate at which a DAC can produce an output is typically limited by the ability of the analog output to settle to a fraction of the lsb value. In general, a DAC with greater resolution will not be able to generate output as rapidly as a DAC with lower resolution.

A concern with using a DAC-based signal source is the limited output resolution. Commonly, the DAC resolution is 12 bits on PC-based instrumentation. With a ± 10 -V scale, the lsb change is 4.9 mV, which means that a voltage sweep generated with this DAC has a staircase appearance. However, changing the output range to ± 2 V improves the resolution to less than 1 mV, which makes the sweep essentially identical to the ideal linear response. The ± 2 V range still permits most voltammetry experiments, but if necessary, using a second DAC provides an additional offset voltage. Using a higher-resolution DAC is an even better option. For example, a 16-bit DAC allows better than 0.3 mV accuracy with a full-scale range of ± 10 V.

1.2.8.2 Data Acquisition

In most cases, data from electrochemical experiments are acquired using *analog-to-digital converters* (ADCs) [18]. An ADC converts an analog signal (usually voltage) to a binary code. As in DACs, ADCs use a digital clock to set the rate at which digital codes are generated. The number of bits in the digital output is related to the accuracy with which the signal is encoded. For highest accuracy, the input

signal should be no smaller than one-half of the full-scale range. For example, an input signal of between ± 1 V presented to a 12-bit ADC with a ± 10 V input range will be digitized with only 9 bits of resolution, limiting the ultimate precision to 0.2% of the full scale. Most ADC systems provide on-board amplification that can be used to better match the input signal to the full-scale range of the data. More recently, inexpensive 16-bit and higher-resolution ADC systems have become available. A 16-bit ADC retains a precision of 0.01% over a ± 10 V range. The higher resolution also allows a “zoom” into the data to extract small signals from a large background.

Increased accuracy is possible with sample averaging. Rather than acquire a single sample at sample rate f , n samples are acquired at sample rate $n \times f$. The samples are then averaged to retain the effective sampling rate f . Averaging has a number of advantages. If a signal contains only white noise, the signal-to-noise ratio, SNR, is improved by a factor of $n^{1/2}$. In addition, the effective resolution in the digitized sample is increased by a factor of $0.5 \times \log_2(n)$. Averaging 16 12-bit samples, produces one sample with an effective 14-bit resolution. A point of diminishing returns occurs with this method since all ADC cards show a loss in their effective number of bits (ENOB) as the sampling rate increases. The sample rate must be proportionately increased to allow for averaging and the input circuitry may not completely settle at the highest acquisition rate, decreasing resolution. However, the ENOB often does not drop significantly until sample rates of greater than 10 kHz are used.

The Nyquist criterion states that an input signal can be recovered if it is sampled at least two times the bandwidth of the signal. Sampling slower than the Nyquist

rate leads to *aliasing*, where the undersampled signal appears as an artifact at lower frequencies. Aliasing is avoided by using a low-pass filter on the input to the ADC and sampling at twice the filter cutoff frequency or higher. Note that the filter will attenuate the signal power at frequencies higher than the filter cutoff but strong noise sources *above* the cutoff frequency may produce aliased signals. Failure to prevent aliasing will place the noise present at frequencies higher than the Nyquist rate into the digitized data samples.

1.2.8.3 Microcomputer Control and Storage

ADCs and DACs rely on a microcomputer or microcontroller to acquire and provide, respectively, the digital codes needed for their operation [19]. In some commercial instrumentation, a microcomputer is embedded into the instrument along with memory and other circuitry to provide for timing and external communication. Such integrated devices are referred to as microcontrollers. In addition to acquiring data and generating excitation signals, the microcontroller accepts user input from the front panel (e.g. pushbuttons or switches) or from a PC over a digital communication channel. The microcontroller also maintains displays and data output. The computer program for the microcontroller is highly specific for the hardware found in the instrument and is typically stored in read-only memory (ROM) where it is protected against user modification for both reliability and security reasons. Some instruments employ rewriteable ROM that allows the manufacturer to send out updated command sets or fix program bugs. Newer instruments will probably allow the manufacturer or vendor to enable features remotely via the Internet or special computer commands. This allows a user

to purchase an instrument with limited experimental capabilities and then enable a set of experiments if needed at a future date. The new feature set will be permanently enabled or leased for a specific time interval or number of experiment repetitions.

In other instruments, a general-purpose computer communicates with separate devices containing ADC and DAC circuitry. Often the ADC and DAC circuitry is on a computer board that plugs into an internal expansion slot of the PC. Alternately, the ADC and DAC might be part of a general-purpose test instrument such as an oscilloscope, high-resolution voltammeter, or an arbitrary waveform generator. In such cases, data and control signals are exchanged between the PC and the test instrument via an external bus. Serial busses, such as RS-232, are included as standard equipment on most PCs and have been a popular choice. The *general-purpose interface bus* (GPIB or standardized as the IEEE-488) is widely used on many types of test and measurement equipment. It has the advantage that up to 15 devices can be attached to one GPIB controller. GPIB busses are not standard equipment on PCs but can be added with a plug-in controller card.

A recent trend in PCs is towards “legacy-free” systems, which ultimately will lead to a loss of internal expansion slots. Introduction of standardized, high-speed communication ports compensates this loss. Importantly, test equipment will not be restricted for use with specific hardware or operating systems (such as plug-in data-acquisition boards). The *Universal Serial Bus*, *USB*, and *IEEE-1394* (FireWire) are examples of low- ($1.5\text{--}12\text{ Mb s}^{-1}$) and high-speed (up to 400 Mb s^{-1}), respectively, serial communication busses that are available on modern PCs [20]. These

are superior to RS-232 and GPIB busses since either is faster and both support more than 60 devices per controller while also supplying power to the device. Electrochemical equipment employing these or similar communication busses are likely to appear since the busses are now ubiquitous and commercialization has made interface circuitry inexpensive. Communication links can also be established using Internet or similar protocols (e.g. TCP/IP). Some test equipment is now available with Ethernet ports, allowing remote data collection. The use of wireless connections to test equipment is likely in the future given the rapid commercialization of computing in this area. An emerging technology is *Bluetooth*, which uses a 2.4 GHz RF link to provide a low-speed (1 Mb s^{-1}), short-range (10 m) data link to other Bluetooth devices [21]. Current Internet and wireless data connections are probably too unreliable and slow for many applications. For example, the 2.4 GHz band of Bluetooth and other RF links is susceptible to interference from microwave ovens, which operate at the same frequency and, ironically, are the reason for the availability of the 2.4 GHz communication band. However, several reports of remote or “teleoperated” experiments over Internet links are available and it is likely that these applications will rapidly increase in number [22–25].

Microcontroller systems and PCs use software programs to manage the hardware in electrochemical instruments. Microcontroller systems are designed to operate in “real time”. Data must be acquired and stored without interruption from other tasks, such as updating a display or accepting user input. For this reason, the control programs are usually designed to be the sole program running on the instrument’s microcontroller. In addition,

efficient coding of programs is necessary to minimize the expense in purchasing and preparing the ROM storage chips, especially for commercial instrumentation. For this reason, programming in assembly or in an efficient compiled language such as C is common. In contrast, PCs are general-purpose computers and, as such, are required to run an operating system as well as other programs that run simultaneously with the instrument control software. This requires the various programs to cooperate with each other and, thus, share hardware and processor resources. Modern operating systems, such as Windows, Macintosh, or Linux, enforce limits on the ability of a single program to directly control a piece of hardware or respond in a guaranteed time to a hardware signal. Thus, programming at a low level is inconvenient. The solution is to use a higher-level programming language that allows the user to interact with the hardware through vendor-supplied *drivers*. One example is *LabView* (National Instruments), a platform-independent *data-flow* language programmed by connecting iconic representations of functions, execution blocks, hardware, and so forth. Vendors also supply drivers for conventional programming languages such as Basic, C, and Fortran.

Use of a general-purpose computer for controlling an electrochemical instrument allows using computing power to perform many data manipulation and display functions. An example is the use of the computer to perform coulometric experiments by digital integration of the cell current. This task would require a separate circuit in a completely analog instrument but incorporation into a computer-controlled instrument requires only a few lines of computer code. The amount of analog circuitry in modern

and future instruments will be reduced to the bare minimum required to maintain electrical control with all other functions assigned to increasingly faster computers.

1.2.9

Example Instrument

There are many examples of electrochemical instrumentation in the literature. Unlike the basic ideas presented here, practical instruments often contain a great deal of additional circuitry. A concern, especially with commercial instruments, is that the circuit operates reliably and within specification. Circuitry to provide protection from input and output over-voltage/overcurrent is present. Often, addition of calibration circuitry allows the instrument to self-calibrate and report out-of-specification or fault conditions. Despite this additional complexity, the basic operation of the instrument follows the electronic principles outlined above. A block schematic diagram of the Solartron Instruments Model 1287 “Electrochemical Interface” illustrates a typical high-end commercial instrument (Fig. 24). The SI1287 is similar to other commercial instrumentation in that it is designed to provide an experimenter with a wide range of possible experiments. There is no direct control of the internal circuitry by the user; the internal microprocessor mediates all aspects of the instrument. Although manual operation of the SI1287 is possible with the front-panel controls, the designers clearly intended control of the instrument by a personal computer. To that end, a RS-232 or GPIB interface provides a communication bus. The block diagram is not intended to be a complete description and, for example, does not indicate the circuitry involved with the digital control or front-panel display.

The section of Fig. 24 to the left is marked “Polarization Control” and is involved in electrical control of the cell potential or current. Note that the instrument can operate as either a potentiostat or galvanostat and the potential or current applied to the cell is programmed by summing the internal sources, marked DC Ref and Sweep, with an external polarity input. The box marked Feedback/Bandwidth control represents actual control circuitry similar to that in Figs. 8 and 11. Relays and electronic switches, controlled by the internal microprocessor, allow switching between potentiostatic or galvanostatic mode. The microprocessor also sets the control loop bandwidth, which allows the experimenter to trade bandwidth for increased control loop stability. Other inputs to the feedback control circuitry are the RE potential and IR compensation (if necessary). A power amplifier is inserted at the counter (auxiliary) electrode connection. This allows currents of up to 2 A to be applied to the cell.

Current flow at the working electrode is determined from the voltage drop across a measuring resistor. Unlike in Fig. 9, a differential amplifier (cf. Fig. 12) measures the voltage drop, which permits a floating WE configuration. An optional offset, $\times 10$ gain, and low-pass filter is applied to the current signal before it is sent to the current output terminal. Voltage measurement with the SI1287 employs a somewhat unusual configuration. Two REs are provided and a differential amplifier measures the voltage difference between them (ΔRE). The use of two REs has a number of significant advantages. As discussed previously, using a measuring resistor at the working electrode introduces an additional voltage drop caused by the product of cell current and R_m . Connecting RE2 to the WE and RE1 to

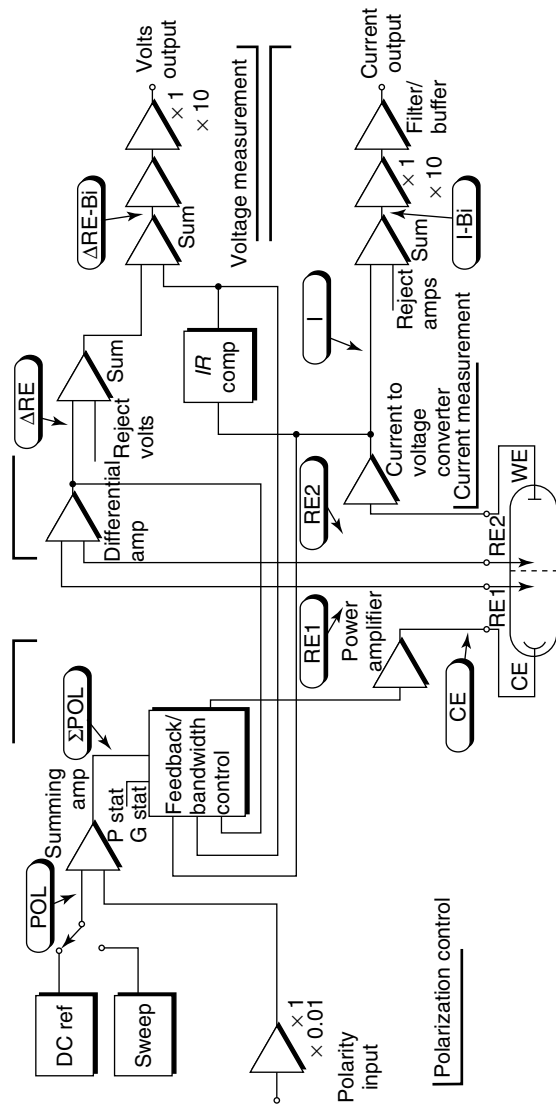


Fig. 24 Simplified schematic diagram of the Solartron model SI1287 instrument.

the RE avoids this problem. The voltage difference between references does not include the voltage drop produced by R_m . A second use for dual reference electrodes is to monitor the voltage dropped across a membrane or phase boundary. An optional offset, $\times 10$ gain, and low-pass filter is applied to the current signal before it is sent to the voltage output terminal. Either positive feedback or current-interruption methods is used for IR compensation.

The SI1287 uses two internal ADCs with accuracy greater than 16 bits for all measurements. The nine different measurement points are marked on the diagram by oval-shaped labels, that is, POL or ΔRE . Measurements are made by using the internal microprocessor to switch measurement points as required. The measurements are sent to the PC as they are collected or a small amount of internal memory is used to store measurements.

1.2.10

Conclusion

It was once said that there were more different types of electrochemical instruments than electrochemists to operate them. The nature of an electrochemist is to tinker in the desire to squeeze a bit more signal-to-noise or a few more ohms of IR drop out of an experiment. This section only presents a small portion of the information required to fully comprehend or construct instrumentation for electrochemistry. It is hoped that the information given will allow the reader to appreciate the design and operation of electrochemical instrumentation.

References

1. P. Horowitz, W. Hill, *The Art of Electronics*, Cambridge University Press, Cambridge, 1989, pp. 175–261.
2. P. T. Kissinger in *Laboratory Techniques in Electroanalytical Chemistry* (Eds.: P. T. Kissinger, W. R. Heineman), Marcel Dekker, New York, 1996, pp. 165–194.
3. R. M. Wightman, D. O. Wipf in *Electroanalytical Chemistry* (Ed.: A. J. Bard), Marcel Dekker, New York, 1989, pp. 267–353, Vol. 15.
4. D. Britz, *J. Electroanal. Chem.* **1978**, *88*, 309–352.
5. R. M. Souto, *Electroanalysis* **1994**, *6*, 531–542.
6. R. L. Deutscher, S. Fletcher, J. A. Hamilton, *Electrochim. Acta* **1986**, *31*, 585–589.
7. H. Yamagishi, *J. Electroanal. Chem.* **1992**, *326*, 129–137.
8. D. O. Wipf, *Anal. Chem.* **1996**, *68*, 1871–1876.
9. G. S. Popkirov, *J. Electroanal. Chem.* **1993**, *359*, 97–103.
10. J. D. McIntyre, W. F. Peck Jr, *J. Electrochem. Soc.* **1970**, *117*, 747–751.
11. R. Bezman, *Anal. Chem.* **1972**, *44*, 1781–1785.
12. D. Britz, W. A. Brocke, *J. Electroanal. Chem.* **1975**, *58*, 301–311.
13. W. J. Wruck, R. M. Machado, T. W. Chapman, *J. Electrochem. Soc.* **1987**, *134*, 539–546.
14. D. K. Roe in *Laboratory Techniques in Electroanalytical Chemistry* (Eds.: P. T. Kissinger, W. R. Heineman), Marcel Dekker, New York, 1986, pp. 195–236.
15. D. Garreau, P. Hapiot, J.-M. Savéant, *J. Electroanal. Chem.* **1989**, *272*, 1–16.
16. C. Amatore, E. Maisonhaute, G. Simonneau, *J. Electroanal. Chem.* **2000**, *486*, 141–155.
17. P. R. Gray, P. J. Hurst, S. H. Lewis et al., *Analysis and Design of Analog Integrated Circuits*, John Wiley & Sons, New York, 2001.
18. M. Tyler, *Sci. Comp. Instrum.* **2001**, *18*, 32–34.
19. C. G. Masi, *R&D* **2001**, *43*, 14–19.
20. B. Weaver, *Sci. Comp. Instrum.* **2001**, *18*, 27–30.
21. J. C. Haartsen, *IEEE Personal Commun.* **2000**, *7*, 28–36.
22. J. W. Overstreet, A. Tzes, *IEEE Control Syst. Mag.* **1999**, *19*, 19–34.
23. O. Frederik, J. R. Danaraj, B. Fleet et al., *Electroanalysis* **1999**, *11*, 1027–1032.
24. C. L. Enloe, W. A. Pakula, G. A. Finney et al., *IEEE Trans. Educ.* **1999**, *42*, 174–179.
25. M. Hadidahassan, S. J. Young, S. T. Peltier et al., *J. Struct. Biol.* **1999**, *125*, 235–245.

1.3 Digital Simulation in Electroanalytical Chemistry

Dieter Britz
Aarhus Universitet, Århus C, Denmark

1.3.1 Introduction

In this chapter, digital simulation, as applied in electroanalytical chemistry, will be described. The description must necessarily be brief, but references are provided for more detail. In particular, the classical chapter by Feldberg [1] and the more detailed (and more up-to-date) monograph [2], as well as the excellent review of the field by Speiser [3], going up to 1996, are recommended reading.

Very broadly speaking, digital simulation in electrochemistry is the numerical solution of Fick's second diffusion equation,

$$\frac{\partial c}{\partial t} = D \frac{\partial^2 c}{\partial x^2} \quad (1)$$

where c is the concentration of a diffusing species, t is the time, x is the distance from the electrode, and D is the diffusion coefficient of the diffusing species. The equation as given is one-dimensional and in Cartesian coordinates, and can take other forms according to the number of species considered and other coordinate systems. Except in some simple (model) cases, numerical solution is the only way to get results. The most popular electroanalytical techniques are linear sweep or cyclic voltammetry [LSV, CV, cf Chapter 1.1 and 2.1 in this volume] and potential step voltammetry [Chapter 2.2 in this volume]. In the sections to follow, there will be names and

techniques referred to without citation; these can all be found in the Refs. [1–3].

1.3.2 Historical

Electrochemists consider Feldberg as the person who introduced digital simulation to the field. The extensive chapter describing the method was written between the years 1964 [4] to 1969. This was the standard text for a long time. It is not always appreciated that Randles, in fact, used finite differences to solve the LSV problem in the year 1948 [5], thus making him the first electrochemist to do so. Finite differences (the technical term mathematicians use for digital simulation or, more precisely, for the implementation of one method of digital simulation), go back to about 1911 (Richardson) and the technique was formalized in 1924. Feldberg used what the present author calls the *box method* (see Sect. 1.3.4), yet the standard procedure in the mathematics/computer field is the point method. The box method will get brief treatment here but the accent is now on points. They make advanced methods (see Sect. 1.3.9), such as the implicit methods that have made possible great advances in efficiency, easier to implement.

Up to the writing of the present author's monograph [2], in 1988, there was a number of unsolved problems, mainly concerned with homogeneous chemical reactions, which introduce several problems such as thin reaction layers and coupled sets of equations. These problems have now been solved, at the cost of programming complexity. Bieniasz [6] introduced variable grids to enable dynamic gridding, thereby overcoming the reaction layer problem (and problems with sharp transients); and Rudolph [7]

solved the problem of coupled equations by introducing the block-tridiagonal notation (see Sect. 1.3.9). The next push is now into the area of ultramicroelectrodes (see Sect. 1.3.11).

1.3.3

Some Mathematics

In order to simulate an electroanalytical problem, it is necessary first to express it in a suitable mathematical form. For one-dimensional problems, Eq. (1) must be augmented by the boundary conditions, including initial conditions. There are some typical systems (experiments) that illustrate the procedure: potential step and controlled current experiments, and LSV of a reversible electrochemical reaction. These will suffice, although in later sections, other more complicated systems will be mentioned.

1.3.3.1 Three Model Systems

In a potential step experiment such as the Cottrell experiment, we must know the starting conditions, that is, the concentrations for the whole cell; since we are dealing (for the moment) in only one dimension, this means concentrations along the space variable x . As the experiment proceeds, the concentrations at a range of distances from the electrode will change, but at the electrode ($x = 0$), it will be fixed at zero, and at some sufficient distance from the electrode, it will retain the value c^* , the initial bulk concentration. All this is expressed formally as a set of boundary conditions:

$$\begin{aligned} t \leq 0, \text{ all } x: c &= c^* \\ t > 0, x = 0: c &= 0 \\ t > 0, x \longrightarrow \infty: c &= c^* \end{aligned} \quad (2)$$

This, classical Cottrell, system has an analytical solution that can be used to test methods and programs. That solution is in terms of concentrations (see Chapter 2.2 in this volume for the solution). What one normally wants is the current i at a given time, and this is derived from the concentration profile by using Fick's first diffusion equation, relating flux to concentration gradients:

$$i = nFADc \left. \frac{\partial c}{\partial x} \right|_{x=0} \quad (3)$$

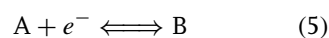
where n is the number of electrons transferred, F the Faraday constant, and A the electrode area. Differentiating the solution $c(x, t)$ as given in Chapter 2.2 in this volume and inserting this into Eq. (3), gives the well-known solution for the current. Equation (3) is also the basis for the calculation of current in digital simulation.

The constant current (chronopotentiometric) experiment has a different set of boundary conditions, the main difference being the imposition of a constant current or, via Eq. (3), a constant concentration gradient at the electrode. The set is

$$\begin{aligned} t \leq 0, \text{ all } x: c &= c^* \\ t > 0, x = 0: \left. \frac{\partial c}{\partial x} \right|_{x=0} &= \text{const} \\ t > 0, x \longrightarrow \infty: c &= c^* \end{aligned} \quad (4)$$

(note that it is only the middle one of the three equations that is different).

The above two cases involve only a single species of concern. In LSV or CV, however, one must follow the development in time and space of both species (if not more) of the electrochemical reaction, for example,



and we designate the respective concentrations by c_A and c_B . There are now two diffusion equations and more boundary conditions. If the system is reversible and there is no B present initially, and if the potential scan starts at E_1 and proceeds with the scan rate $-v$ (see Chapter 2.1, this volume) then the combined set of boundary conditions is

$$\begin{aligned} t \leq 0, \text{ all } x: c_A &= c^*, c_B = 0 \\ t > 0, x \longrightarrow \infty: c_A &= c^*, c_B = 0 \\ t \leq 0: E &= E_1 \\ t > 0: E &= E - vt \\ t > 0, x = 0: \frac{c_A}{c_B} &= \exp\left(\frac{nF}{RT}(E - E^0)\right) \end{aligned} \quad (6)$$

in which we note a form of the Nernst equation and the standard potential E^0 , and the bulk concentration c^* refers to species A (as is usual for a set of species involved in a reaction system). The two species each have some of their own boundary conditions and are also coupled by the Nernst condition.

1.3.3.2 Normalization

Normally, the equations as presented above, are rendered dimensionless (normalized) by expressing the variables as multiples of reference values. For the Cottrell system, the reference time value is the observation time, or duration of the experiment, τ ; concentrations are referred to c^* and distance x to a suitable length scale δ . In view of the solution of Eqs. (1 and 2) (see Chapter 2.2, this volume and Ref. [2]), this scale is conveniently defined as $\delta = \sqrt{D\tau}$, which means that the concentration profile will extend into the solution bulk by only a few δ -units. We then have the following

normalizing relations:

$$\begin{aligned} C &= \frac{c}{c^*} \\ T &= \frac{t}{\tau} \\ X &= \frac{x}{\delta} = \frac{x}{\sqrt{D\tau}} \end{aligned} \quad (7)$$

thus forming the new dimensionless variables C , T , and X . Equation (1) then transforms to the simpler form,

$$\frac{\partial C}{\partial T} = \frac{\partial^2 C}{\partial X^2} \quad (8)$$

and the boundary conditions for the Cottrell experiment also normalize to the set

$$\begin{aligned} T \leq 0, \text{ all } X: C &= 1 \\ T > 0, X = 0: C &= 0 \\ T > 0, X \longrightarrow \infty: C &= 1 \end{aligned} \quad (9)$$

The solution of this Eq. (8) with (9) now applies to all sets of experimental parameters c^* , D , and τ and is thus much more useful. In all cases, the solution will be within the bounds $0 \leq T \leq 1$ and $0 \leq X \leq m\delta$, in which m must be chosen suitably (this will be described in Sect. 1.3.7). Current is also expressed without dimensions, simply (in view of Eq. 3) as the dimensionless gradient $\left. \frac{\partial C}{\partial X} \right|_{X=0}$, which will be given the symbol G in this chapter.

For chronopotentiometry, a good choice for the observation time is the transition time itself, and this has the interesting consequence that the constant current reduces to constant $G = 1/2\sqrt{\pi}$, the

boundary conditions (4) becoming

$$\begin{aligned} T \leq 0, \text{ all } X, C &= 1 \\ T > 0, X = 0: G &= \frac{1}{2}\sqrt{\pi} \\ T > 0, X \longrightarrow \infty: C &= 1 \end{aligned} \quad (10)$$

and the solution must be that $C(X=0)$ falls to zero at $T = 1$.

The LSV system is also normalized, eliminating the scan rate as well. It was noted above (Equation set 6) that the swept potential changes at the rate $-v$, where v has units of Vs^{-1} . First, we refer voltages to units of RT/nF and shift it relative to E^0 :

$$p = \frac{nF}{RT}(E - E^0) \quad (11)$$

which makes the dimensionless unit p equal to about $25.69n$ mV and it is centered on the standard potential E^0 . The scan rate too is now expressed in terms of changes in p -units per s:

$$p = p_1 - at \quad (12)$$

with the new unit a defined as the inverse time

$$a = \frac{nF}{RT}v \quad (13)$$

We can now define a reference time τ , being the time taken for the potential to change by one p -unit. Normalizing time t as above (Eq. 8), that is $T = t/\tau$ ($\tau = a^{-1}$), we now have a sweep starting at p_1 and moving, for all experimental parameter sets, with the dimensionless sweep rate 1, as is seen in the new dimensionless

boundary conditions

$$\begin{aligned} T \leq 0, \text{ all } X: C_A &= 1; C_B = 0 \\ T > 0, X \longrightarrow \infty: C_A &= 1, C_B = 0 \\ T \leq 0: p &= p_1 \\ T > 0: p &= p_1 - T \\ T > 0, X = 0: \frac{C_A}{C_B} &= \exp(p) \end{aligned} \quad (14)$$

(note the much simpler form of the Nernst condition in the last line).

1.3.3.3 Denormalization

Having obtained a solution to a given problem in dimensionless terms, we might wish to go back to dimensioned variables, in order to compare with an experiment. This simply reverses the normalizing equations. Thus, we have

$$\begin{aligned} c &= c^*C \\ t &= \tau T \\ x &= \delta \cdot X \\ E &= E^0 + \frac{RT}{nF}p \end{aligned} \quad (15)$$

and the current through (computed) G :

$$i = nFAD^{1/2} \frac{c^*}{\sqrt{\tau}} G \quad (16)$$

The groundwork is now laid for the simulation methods themselves.

1.3.4

The Box Method

In this section, a very brief description of the “box method” is given. This is the method as originally devised by Feldberg [1]. It is, in the opinion of the present author, awkward and outdated, although many prefer it because it appears

to provide a closer definition for what is being done, in contrast with the “point method”, which is the way numerical mathematicians have always solved partial differential equations.

Consider Fig. 1, showing three boxes along a narrow tube representing the diffusion path in one dimension. The tube has been sectioned into short lengths (boxes) of equal length δx , and they are numbered consecutively, starting from 1. The essence of the box method is to use Fick’s first diffusion equation, relating the unit area flux f , in moles per second per m^2 , of the diffusing substance at a given point (or plane) to the concentration gradient there:

$$f = -D \frac{dc}{dx} \quad (17)$$

This is very intuitive and perhaps explains the appeal of the method. The problems begin with finding approximations to the derivative term. The boxes are considered to have uniform concentration within each box, and the gradient between two boxes is expressed by the concentration difference divided by the distance between adjacent boxes. For example, the flux of substance from box i into box $i + 1$ is approximated as $-D(c_{i+1} - c_i)/\delta x$ and this, combined with the analogous expression for the flux from box $i - 1$ into box i and converting to concentration change in the center box, gives the discrete explicit formula for the new concentration in the center box i after

a time interval δt ,

$$c_i(t + \delta t) = c_i(t) + D \frac{\delta t}{\delta x^2} (c_{i-1}(t) - 2c_i(t) + c_{i+1}(t)) \quad (18)$$

(for details of the derivation of this formula, see Refs. [1, 2]). It will be seen in Sect. 1.3.5 that this is identical with the expression derived there, using points. However, there are problems with the box method. First of all, consider the end elements close to the electrode, Fig. 2. At the electrode, how does one express the concentration gradient between the electrode and the first box? The way this has normally been handled is to assume a distance of half δx between these. As explained in [2], however, this gives rise to an incorrect formula that happens to work surprisingly well by accident. When dealing with geometries other than the simple ones depicted here – for example, boxes that do not all have the same length, or curved shells as one gets with a cylindrical or spherical diffusion space – the question of how far adjacent boxes are from each other becomes vexing. Feldberg and his coworkers have devised corrections for curved elements, to overcome such problems. It is the strong view of the present author that all these problems vanish with the use of points, and this method will be used in the rest of this chapter.

Fig. 1 Three boxes in the solution bulk.

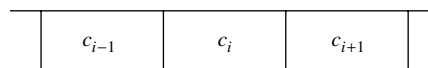
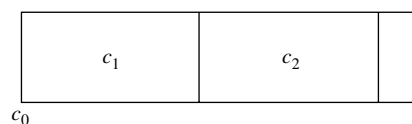


Fig. 2 End-boxes at the electrode.



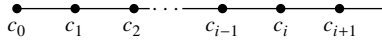


Fig. 3 Points distribution.

1.3.5

Point Discretizations

The point method proceeds from the discrete approximation of Fick's second diffusion equation, for example, Eq. (1) or, after normalization, Eq. (8) or variants of that equation according to the chosen geometry. Both time and space are sampled at a set of points, and approximations for the left-hand and the right-hand sides of the equation are sought. If the spacing of the points is even throughout time (intervals δt or, dimensionless, δT) and space (h , or H), then it is always straightforward to develop good approximations in terms of concentration values at these points. Consider Fig. 3, showing a number of points in space along the single dimension X with the corresponding concentration values, and intervals H between the points. The usual discrete approximation of the right-hand side of Eq. (8) is

$$\frac{\partial^2 C}{\partial X^2} \approx \frac{1}{H^2} (C_{i-1} - 2C_i + C_{i+1}) \quad (19)$$

applying at the point $X = iH$. If we represent (sample) the whole diffusion space by N points, placing the electrode at $X = 0$ and including one more point outside the diffusion space at $X = (N + 1)H$ (which will be the convention here), we then have N expressions of the type (19), for which the first ($i = 1$) uses the boundary point at the electrode and the last ($i = N$) uses the outer boundary, or the bulk of the solution. The latter will not normally change during an experiment. The approach described up to this point is called the *method of lines*, or *MOL*. It is also called the *semidiscretization approach*, because so far, we have only discretized the

right-hand side of the diffusion equation, and produced a set of ordinary differential equations. There are N of these:

$$\begin{aligned} \frac{dC_1}{dt} &= \frac{1}{H^2} (C_0 - 2C_1 + C_2) \\ \frac{dC_2}{dt} &= \frac{1}{H^2} (C_1 - 2C_2 + C_3) \\ &\dots \\ \frac{dC_i}{dt} &= \frac{1}{H^2} (C_{i-1} - 2C_i + C_{i+1}) \\ &\dots \\ \frac{dC_N}{dt} &= \frac{1}{H^2} (C_{N-1} - 2C_N + C_{N+1}) \end{aligned} \quad (20)$$

This is a useful approach, leading to a large variety of methods. Note that nothing has yet been said about how to handle the boundary values that are not subject to diffusion in themselves. The outer value is normally constant at the bulk value. The value at the electrode, C_0 , is the problem, and will be dealt with in the next section in detail. For the moment, let us dwell on the Set (20). We need to find discrete expressions for the left-hand sides, the time derivatives. Here, we can draw on the practice in the field of ordinary differential equations (*ode's*). Taking the i th equation out of (20) and expressing it in the simple form

$$\frac{dC_i}{dt} = f_i(t) \quad (21)$$

there are several common ways to discretize it. The Euler formula, or forward difference, is

$$\frac{C_i(t + \delta t) - C_i(t)}{\delta t} = f_i(t) \quad (22)$$

where the right-hand side indicates that the expression is intended to pertain to time t . This, as will be seen in Sect. 1.3.7, is the easiest – but least efficient – method to follow. By using Taylor expansions (see Ref. [2] for details), it can be shown that this scheme is first order with respect to time. This means that if we try to reduce the errors in a given computation by making the time interval δt smaller, the error will get smaller proportionally with δt . This is not very good. The method has another limitation, of stability, and this may be the point to mention this problem.

1.3.5.1 Stability

If we combine the above forward difference in time (22) with the discretization (19), we can get an explicit expression for the new concentration at the point $(iH, t + \delta t)$:

$$\frac{C_i(t + \delta t) - C_i(t)}{\delta t} = \frac{1}{H^2}(C_{i-1}(t) - 2C_i(t) + C_{i+1}(t)) \quad (23)$$

We now introduce some simplifying notation. Unless certain advanced methods are used, the situation is always that one has, at a given time, a row of known concentrations, at time t , and develops a new row of concentrations at time $(t + \delta t)$. It is necessary to mark the X -positions (the subscripts), but time can be marked more conveniently. If there is no time marked, this implies time t ; and time $(t + \delta t)$ will be indicated by a superscript dash on the concentration, for example C' . Using this notation and now also rearranging Eq. (23), we get the explicit expression for the new concentration

$$C'_i = C_i + \frac{\delta t}{H^2}(C_{i-1} - 2C_i + C_{i+1}) \quad (24)$$

and substituting the symbol λ , defined as

$$\lambda = \frac{\delta t}{H^2} \quad (25)$$

this becomes

$$C'_i = C_i + \lambda(C_{i-1} - 2C_i + C_{i+1}) \quad (26)$$

Now, without going into details, it is well known that the calculation will deviate from the proper values more and more within a few time steps, unless $\lambda \leq 0.5$ for this explicit method. Such a deviation (which might take the form of increasingly wild swings, or wide one-sided divergence) is called *instability*. Thus, the stable range for λ is $0 - 0.5$. This is inconvenient, as it makes for inefficient computation. If one attempts to lower errors by decreasing the spacing along X (that is, the value of H), one must also reduce δt such that λ remains within the stable range.

The explicit (Euler) method described above has this stability limitation. There are other methods that do not. One of them (reverting again to the *ode* 21) is the backward difference (or backward implicit, BI) formula:

$$\frac{C_i(t + \delta t) - C_i(t)}{\delta t} = f_i(t + \delta t) \quad (27)$$

Note that the left-hand side is identical with (22), which is the forward difference formula. The difference is in the right-hand side, which is a function of values at the next time level, to which the same left-hand-side approximation now pertains. Intuitively, one might expect this form to be about as inefficient as the forward difference and this is in fact true; this formula, too, is first order with respect to time, as is the forward difference formula. The big difference is that this formula, applied to the diffusion equation, yields a method that is stable for all λ . This is

the formula

$$C'_i = C_i + \lambda(C'_{i-1} - 2C'_i + C'_{i+1}) \quad (28)$$

and is known as the BI method, or the Laasonen method (see Ref. [2]). The reader will realize, on perusal of the system (20) that, if this formula is applied to that system, the result is a system of N unknowns, no longer explicit in each equation, and the system needs to be solved as a whole. The method is one of several *implicit* methods that will be discussed in Sect. 1.3.9. Despite its poor performance in its simple form, the BI method forms the basis for some highly efficient methods.

The last way to be mentioned here to discretize the *ode* (21) is what is called the *trapezium method*:

$$\frac{C_i(t + \delta t) - C_i(t)}{\delta t} = f_i\left(t + \frac{\delta t}{2}\right) \quad (29)$$

where the same left-hand-side expression now pertains to the midpoint (in time), and becomes a central difference. This one is second order with respect to time or $O(\delta t^2)$, meaning that the error is proportional to δt^2 . This is much more efficient than first-order methods. As with the BI (Laasonen) method, the application of this formula to system (20) (see Sect. 1.3.9) yields an implicit system of equations that must be solved as a whole. This is the Crank–Nicolson method; and it, like the Laasonen method, is stable for all values of λ . In fact, this statement can be misleading; there are problems with this method, to be discussed later.

One last example should suffice to illustrate the way the point method can be used. If we take the diffusion equation in cylindrical coordinates and add a homogeneous first-order chemical reaction,

$$\frac{\partial C}{\partial t} = \frac{\partial^2 C}{\partial R^2} + \frac{1}{R} \frac{\partial C}{\partial R} - KC \quad (30)$$

then, taking a shell i at some radius, the explicit discretization of the equation is

$$C'_i = \lambda(C_{i-1} - 2C_i + C_{i+1}) + \frac{\delta t}{2HR_i} \times (C_{i+1} - C_{i-1}) - K\delta t C_i \quad (31)$$

where the second term on the right-hand side of (30) has been replaced by a central difference (hence the division by $2H$). If we take $R_i = iH$, then this becomes

$$C'_i = \lambda(C_{i-1} - 2C_i + C_{i+1}) + \frac{\lambda}{2i}(C_{i+1} - C_{i-1}) - K\delta t C_i \quad (32)$$

1.3.5.2 Gradients at the Electrode

Equation (3) shows how the current is related to the gradient of concentration at the electrode, and in dimensionless computations, the gradient G , as defined above, is often required, either as an output (expression of current), or as a boundary condition (see the next section). Thus, a way of expressing it is needed. The simplest approximation is

$$G \approx \frac{C_1 - C_0}{H} \quad (33)$$

This is a forward difference, applied at one end of the interval. It is rather a poor approximation, first order with respect to H . It is nevertheless favored by many and may be justified, especially if that first interval is very small, in which case the approximation is not too bad (this argument comes in with unequal intervals, see Sect. 1.3.9). It is however rather easy to use better approximations. Formula (33) uses just two concentration points; if one uses more, the approximation becomes better, of higher order. The present author tends to use a six-point approximation, but there is reasonable argument for using the

three-point formula:

$$G \approx \frac{-\frac{3}{2}C_0 + 2C_1 - \frac{1}{2}C_2}{H} \quad (34)$$

which is $O(H^2)$ and thus matches the order of the approximation (19) used in simulations. In general, the formula for an n -point approximation is

$$G \approx \frac{1}{H} \sum_{i=0}^{n-1} \beta_i C_i \quad (35)$$

where the β -coefficients depend on n and are tabulated in Ref. [2]. The values, for example, for $n = 3$ (Eq. 34), are $(-1.5, 2, -0.5)$.

The reader should now have a good idea of how the various forms of the diffusion equation are discretized, using the point method.

1.3.6

Boundary Conditions

In the last section, discretization of the partial differentials away from the boundaries was described; those boundaries must now be added to complete the picture. In the last section, the convention was established that the diffusion space is represented by a number of points, counting from zero to $N + 1$, where the points numbered $1 \dots N$ are those at which concentrations will change as a result of diffusion, and the other two are boundaries, subject to other relationships. Thus, point $N + 1$ is normally held constant, at the initial bulk value for the species concerned (there are exceptions to this).

For the point at the electrode, there are technically three classes of conditions. The Dirichlet condition is that in which the concentration there has a certain value (perhaps time variant); the Cottrell experiment

is an example of this, the value C_0 being fixed at zero (see Equation sets 2 and 9).

A different boundary condition is the Neumann condition or derivative boundary condition. An example is seen with chronopotentiometry, Equation sets (4 and 10). The procedure here is that a value of C_0 is computed such that it fits with the concentration profile (set of points $C_1 \dots C_N$), so as to satisfy the gradient specification. Using the simple two-point approximation (33) and given a G value, this yields an explicit expression for C_0 ,

$$C_0 = C_1 - HG \quad (36)$$

Extensions to higher-order formulae, using (35), are obvious. Note however, that in more complex contexts, an equation like (36) might not be explicit; it might be one of a set of such equations for a number of species and the variables on the right-hand side might themselves be unknowns (see Sect. 1.3.9).

A third kind of boundary conditions lies in between the two presented above; they are the mixed boundary conditions and normally involve two species. Take Reaction (5), involving the two species A and B. In Sect. 1.3.3 (boundary conditions set 14), the reversible case was mentioned, and a boundary condition was

$$\frac{C_{A,0}}{C_{B,0}} = \exp(p) \quad (37)$$

better expressed as

$$C_{A,0} - C_{B,0} \exp(p) = 0 \quad (38)$$

where p was the dimensionless electrode potential. This condition couples the two species. It is not enough, however, there being the two unknowns, $C_{A,0}$ and $C_{B,0}$. The other required condition comes from the fact that the fluxes at the electrode of the two substances must be equal and opposite (B is generated at the same rate as

A is used up):

$$f_A + f_B = 0 \quad (39)$$

Flux was defined in (17) and we must here take note of the fact that the two species' diffusion coefficients might not be the same. For this reason, we define diffusion coefficient ratios, all referred to that of the main species, whose bulk concentration is also the reference, c^* . Thus, for species B, we have

$$d_B = \frac{D_B}{D_A} \quad (40)$$

The flux now being equal to the diffusion coefficient multiplied by the concentration gradient, Condition (39) becomes, in terms of dimensionless gradients.

$$G_A + d_B G_B = 0 \quad (41)$$

where we now have two different gradients G , both expressed in discrete terms by a form of Eq. (35). If, for illustration, the simple two-point formula (33) is chosen, the discretized boundary condition becomes

$$\frac{C_{A,1} - C_{A,0}}{H} + d_B \frac{C_{B,1} - C_{B,0}}{H} = 0 \quad (42)$$

and eliminating the H terms and rearranging the unknowns on the left-hand side, finally,

$$C_{A,0} + d_B C_{B,0} = C_{A,1} + d_B C_{B,1} \quad (43)$$

This now, taken together with Condition (38), determines the two unknowns. Note again, as with Eq. (36), that (43) need not be explicit but may, in complex situations, be merely one of several statements involving a larger set of unknowns.

Lastly, the system described by Reaction (5) might be quasireversible or even irreversible, in which case the boundary condition is given by the Butler–Volmer equation. It is preferable to express it in dimensionless form, using potential p , and the heterogeneous rate constant k_0

is normalized to the dimensionless K_0 by

$$K_0 = k_0 \sqrt{\frac{\tau}{D}} \quad (44)$$

where τ is the designated reference time and D the diffusion coefficient of the reference species. If we further define two convenient dimensionless rate constants, the forward and backward rates,

$$K_f = K_0 \exp(-\alpha p)$$

$$K_b = K_0 \exp((1 - \alpha)p) \quad (45)$$

then, the Butler–Volmer equation becomes

$$G_A = K_f C_{A,0} - K_b C_{B,0} \quad (46)$$

and if we again, for example, use the two-point approximation for G_A and rearrange, this gives the discrete expression

$$(1 + K_f H) C_{A,0} - K_b H C_{B,0} = C_{A,1} \quad (47)$$

This must be paired with the flux condition (43) to yield the two unknowns.

1.3.7

The Explicit Method

Here, the simple explicit method is briefly gone through, in practical detail. The example taken is the one-dimensional Cottrell system, diffusion Eq. (8) and boundary conditions (9). In writing a simulation program, some practical decisions have to be made. Normally, the time interval for a complete simulation is $0 \leq T \leq 1$, and that leaves only the number of steps N_T or its inverse δT to set. Then there is the interval H in X . This is related to the time interval by the important parameter λ (see Eq. 25), and it might be better to decide on its value, which then provides that for H . Another quantity is the distance along X to which the simulation is to extend. Here, experience (and the solution of the Cottrell equation, see Chapter 2.2 in this volume)

tells that a value of 6 units of δ as defined in Equation set (7) is sufficient. In case one wants to change it later for some reason, it is good practice to make it a program parameter, X_{lim} , and set that in the program preamble (or, if using Fortran 90, a module). This then determines the number of points N along X , and the required array(s) can be allocated. The present author prefers these steps:

1. Read in N_T and λ ;
2. Calculate H (needed for the calculation of G) and thus N ;
3. Allocate the concentration array $C_0 \dots C_{N+1}$ and initialize it (all $C_i = 1$, $C_0 = 0$);

4. For all N_T values of T , recalculate the concentration array using Eq. (26), outputting the desired quantities at chosen times; these might be $G(T)$ values and/or the errors in G .

There is a small point to watch in point 4. When moving along the points in X , it is important to use old concentrations only in applying Eq. (26). This is easily achieved using a moving trio of concentration scalars equal to the old values, while replacing the actual concentration array with the newly computed values. A short program in Fortran 90, which carries out the above steps, is given below.

```

module STUFF
  integer,parameter      :: dbl=selected_real_kind(14)
  real(kind=dbl),parameter :: Xlim=6.0, pi=3.14159265358979
end module

program COTTSIM
! To simulate the Cottrell experiment, outputting the current
! at doubling intervals. Current G is calculated as 3-pt approx.
use STUFF; implicit none
integer      :: NT, N, iT, iX, next_out
real(kind=dbl) :: dT, H, lambda, G, C1, C2, C3
real(kind=dbl),allocatable :: C(:)

print '("NT, lambda?")'; read*, NT, lambda
dT = 1.0_dbl / NT; H = SQRT(dT/lambda); N = CEILING (Xlim/H)
ALLOCATE (C(0:N+1)); C = 1; C(0) = 0; next_out = 1 ! C set up
print '(4x, "iT", 5x, "T", 7x, "G", 3x, "G(analyt)")' ! Header
do iT = 1, NT
! Grand T-loop
  C1 = C(0); C2 = C(1)
! Running scalars
  do iX = 1, N
! X-loop
    C3 = C(iX+1)
! Next scalar grabbed
    C(iX) = C2 + lambda * (C1 - 2*C2 + C3) ! new C in array
    C1 = C2; C2 = C3
! Scalars shifted along
  enddo
enddo
if (iT == next_out. OR. iT == NT) then
  G = (-3*C(0) + 4*C(1) - C(2)) / (2*H)
  print '(i6, 3f8.3)', iT, iT*dT, G, 1.0_dbl/SQRT(pi*iT*dT)
  next_out = 2 * next_out
endif
enddo
DEALLOCATE (C)
end program COTTSIM

```

This rather reduced program produces the following output (excluding the I/O dialogue) when run with the input parameters $N_T = 100$, $\lambda = 0.4$:

iT	T	G	G(analyt)
1	0.010	4.427	5.642
2	0.020	3.921	3.989
4	0.040	2.808	2.821
8	0.080	1.996	1.995
16	0.160	1.414	1.410
32	0.320	0.999	0.997
64	0.640	0.706	0.705
100	1.000	0.565	0.564

Clearly, we can do better, introducing error calculations and so forth, but this will suffice as a brief example. The program can be easily converted to doing a simulation of chronopotentiometry. Here, the quantity of interest is C_0 , which should fall to exactly zero at $T = 1$. Its value there, then, is the simulation error. The boundary conditions set (10) applies and, rather than Eq. (36), the three-point equivalent, obtained from Eq. (34) is used to set C_0 at the *beginning* of every iteration in T . This is a nontrivial point. The explicit method calculates a new array of concentration values from an old array. That old array must include the appropriate C_0 , whose value satisfies the boundary condition, such that Eq. (36) (or another, perhaps higher-point approximation of it) is satisfied. This causes some apparent redundancy in the program, arising from the fact that C_0 is set before and, whenever there is output, also after, an iteration. Here is the middle part of the program, in which it differs from the Cottrell one:

```
...
do iT = 1, NT ! Grand T-loop
C(0) = (4*C(1) - C(2) - 2*H*G)/3
! New C(0), 3-pt approx
C1 = C(0); C2 = C(1)
! Running scalars
```

```
do iX = 1, N ! X-loop
C3 = C(iX+1) ! Next scalar grabbed
C(iX) = C2 + lambda*(C1 - 2*C2 + C3)
! new C in array
C1 = C2; C2 = C3
! Scalars shifted along
enddo
if (iT == next_out .OR. iT == NT)
then
T = iT * dT
C(0) = (4*C(1) - C(2) - 2*H*G)/3
! C(0) again
print '(i6, 3f8.3)', iT, T, C(0),
1-SQRT(T)
next_out = 2 * next_out
endif
enddo
...
```

Using the same parameters as for the Cottrell program, this produces the output

iT	T	C(0)	C(0)(analyt)
1	0.010	0.857	0.900
2	0.020	0.825	0.859
4	0.040	0.774	0.800
8	0.080	0.698	0.717
16	0.160	0.586	0.600
32	0.320	0.424	0.434
64	0.640	0.193	0.200
100	1.000	-0.006	0.000

showing that the error is -0.006 at the end. The explicit method is first order with respect to the time interval δt . A run using the input $N_T = 200$ (double the previous) yielded the final error of -0.003 , confirming the order. As will be seen, there are better methods. Here, these two examples will have to suffice.

1.3.7.1 Fudging

There is, especially among adherents of the box method, a rather widespread custom of adjusting the time value, after a number of iterations, by subtracting half a time interval, and assigning that adjusted time to the calculated current.

Thus, after j iterations, when $T = j\delta T$, the current is presented as belonging to $(j - 0.5)\delta T$. The only argument for this is that it seems to work, providing more accurate current values for systems like the Cottrell experiment. However, there is no formal justification for the trick. This is a fudge and should not be used. The trick is also applied in the case of backward differentiation formula (BDF) (see Sect. 1.3.9) and there it is fully justified, as will be seen later.

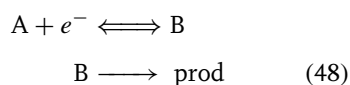
1.3.8

Homogeneous Chemical Reactions

The major reason for doing electrochemical digital simulations is the occurrence of chemical reactions taking place in the solution, involving either the starting substances or products of the electrochemical reactions at the electrode, called *heterogeneous reactions*. In contrast, reactions taking place in the solution are called *homogeneous*. These are of interest in several ways, either for themselves in mechanistic studies or, if they are known, their rates. These can in principle be determined from comparison of experimentally measured curves with those calculated. These calculations almost always involve simulation, since analytical solutions are known only for rather trivial and therefore uninteresting cases.

A systematic classification of homogeneous chemical reactions (hcr) in electrochemical cells can be read in Chapter 1 in Volume 8 and here, only some examples that impinge on simulations will be mentioned.

The following problems arise with hcrs. In a system such as



(in which the product of the decay of species B is of no interest), the concentration profiles of the two species A and B will have different extents into the solution, depending on the (often first-order) rate constant of the decay reaction. The faster this reaction runs, the more species B will be confined to a thin “reaction layer” near the electrode. This has been quantified; if the diffusion coefficient be D and the rate constant of the decay reaction (assumed irreversible) k , then the characteristic thickness μ of the reaction layer, (analogous to the diffusion layer) is given by

$$\mu = \sqrt{\frac{D}{k}} \quad (49)$$

steady state is often established. For first-order reactions, the rate constant can be normalized by the chosen time reference τ :

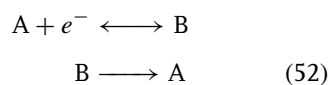
$$K = k\tau \quad (50)$$

and then the normalized reaction layer thickness, in terms of the unit δ , is

$$\mu^* = K^{-1/2} \quad (51)$$

This was, until recent years, a major problem for simulations, because large values of the rate constant can mean that there are few, or even no, points placed within the concentration profile of the species forming a reaction layer. This led to the use of unequal intervals (see Sect. 1.3.9) but this, too, is limited if a fixed distribution of the unequally placed points is used. That problem has been solved by using dynamic grids, also described briefly in Sect. 1.3.9.

Another problem, not solved until recently, comes from so-called *coupled systems*. Take the catalytic (EC') system



in which the product B reverts, in a (pseudo-) first-order reaction, to A. There will be two transport equations to describe this system (assume equal diffusion coefficients for simplicity, and a normalized rate constant K for the catalytic decay),

$$\begin{aligned}\frac{\partial C_A}{\partial T} &= \frac{\partial^2 C_A}{\partial X^2} + K C_B \\ \frac{\partial C_B}{\partial T} &= \frac{\partial^2 C_B}{\partial X^2} - K C_B\end{aligned}\quad (53)$$

Note that the first of the two equations has terms in both variables, C_A and C_B . This is not a problem when using an explicit method, but these are practically useless when hcrs are involved and implicit methods are normally chosen for their greater efficiency. However, while these produce tridiagonal systems of equations for single species or uncoupled multireactions, they produce more complicated systems for coupled reaction systems, which are not amenable to the usual solution techniques. This problem was solved recently by Rudolph [7] and references therein, who introduced the technique known as *block-tridiagonal solution* into electrochemical simulations, (see Ref. [2], 3rd edn. only) and Sect. 1.3.9.

Second-order reactions present a few small problems. They introduce nonlinear terms into the transport equations and one wishes to avoid these in the discretized equation systems. There are some tricks that work rather well, see Ref. [2]. Another problem associated with second-order reactions, such as



is that the associated discrete equation will approximate in some linear way the term $-K C_B^2$ into the transport equation. The result is that if C_B at some stage falls

below zero, it can never recover from that erroneous condition and the simulation deviates more and more from reality. This happens especially with methods that have oscillatory responses.

1.3.9

Advanced Methods

In this limited space, it is not possible to provide an exhaustive survey of the advanced techniques for simulations, for which see Ref. [2], especially the 3rd edition. Here, only those advances that have helped to overcome the major problems of thin reaction layers, coupled systems, and efficiency, will be mentioned. Such excellent methods as orthogonal collocation, finite elements, or other sophisticated methods are left out of necessity.

1.3.9.1 Unequal Intervals

In Sect. 1.3.8, the reaction layers often formed when homogeneous chemical reactions are involved, were mentioned. The higher the homogeneous reaction rates, the thinner the layers become, and it is harder and harder to ensure that even a few sample points are placed in that thin region. In practice, first-order reaction rates have an upper limit of (dimensionless) about 10^{10} , so that reaction layers can get as thin as 10^{-5} . Using equal intervals in the usual interval $0 \leq X \leq 6$, this would mean of the order of 10^6 points along X and, in order not to have too high a λ value (Eq. 25), a correspondingly large number of time intervals. However, the changes are most marked near the electrode and clearly it is of advantage to crowd more points into that region, loosening up further out. There are two ways to implement unequal intervals.

A simple transformation of the X -axis can do the trick, for example, the formula

$$Y = \ln(1 + aX) \quad (55)$$

with the adjustable parameter a ; the greater its value, the more compression there is of points near the electrode. Having chosen the value, it is then a simple matter to divide the Y -range into a small number of (equally spaced) points. Using this transformation, the diffusion equation must also be transformed, replacing derivatives with respect to X with those to Y , the new space variable. For details, see Ref. [2]; Eq. (8) transforms to a slightly different form, the details of which will not be gone into here, for the following reason. Numerical specialists regard transformation, and discretization on the (equally spaced) transformed grid, as the best method to use. However, Rudolph [10] has recently shown that direct discretization on the unequally spaced grid in fact yields better results. The transformation (55) is mathematically equivalent to a sequence of points x_i , $i = 1, N + 1$, spaced according to the expression

$$x_i = x_1 \frac{\beta^i - 1}{\beta - 1} \quad (56)$$

where x_1 is the first point away from the electrode and β a stretching parameter > 1 . However, the method does not require this specific placing of the points, and any suitable placing can be used. How this is implemented is explained below.

Both the transformation and direct techniques suffer from the fact that the placement of the points (or boxes) is static during a given simulation. If one is attempting, for example, to fit a reaction rate to an experimental curve, one cannot choose the transform parameter suitably.

Feldberg and Rudolph [7] handle this by always choosing a very unequal spacing (in effect, large β) that hopefully will be able to cope with the highest possible reaction rates. This means an extremely small first interval near the electrode, and then also justifies these authors' use of the simple two-point approximation for the current (G).

A better way is, clearly, to use a grid of points whose spacing dynamically adjusts itself suitably. This was introduced by Bieniasz [6], and see references therein who has concluded that his latest scheme, which he calls *the patch-adaptive strategy* [6], is to be preferred. It is apparently quite simple. One starts with a number of equally spaced points along X . The program calculates a new concentration array, and then it exactly halves all the intervals and calculates another new concentration array. The two solutions are then compared, enabling an error estimate. For those regions in which the error estimate exceeds some threshold, the points in that region (and in that region only) are doubled once more. Thus, locally, one always deals with equal intervals, but the intervals themselves vary with X . This algorithm will always adapt the point distribution to conditions. If a thin reaction layer is formed, points will be doubled up repeatedly in that region until satisfactory solutions are found there. Note that this will work, even when there are sharp concentration changes away from the electrode, whereas unequal intervals as normally used, will not. Clearly, this is not an easy programming job, but one must pay a price for progress. This is one reason that electrochemists will increasingly make use of commercial packages (see Sect. 1.3.10).

In general, Rudolph's recent findings point to an arbitrary grid of points,

set by some unspecified method, at the positions x_i , $i = 1, N + 1$. The second spatial derivative at each point x_i then deviates from the form in (19) and is a weighted sum of the three concentrations centered on that point,

$$\frac{\partial^2 C_i}{\partial X^2} \approx 2 \left(\frac{C_{i-1}}{(x_i - x_{i-1})(x_{i+1} - x_{i-1})} - \frac{C_i}{(x_i - x_{i-1})(x_{i+1} - x_i)} + \frac{C_{i+1}}{(x_{i+1} - x_i)(x_{i+1} - x_{i-1})} \right) \quad (57)$$

which is a first-order expression.

1.3.9.2 The Rudolph Method for Coupled Systems

If the single-species diffusion Eq. (8) is discretized in one of the implicit schemes such as that of Crank & Nicolson or of Laasonen (BI), the result is in effect a tridiagonal system of equations in the N unknown concentrations at the next time level. This can be solved using the Thomas algorithm, by attacking at the ends at which either values are known, or certain boundary conditions are given (see Ref. [2] for details). If an electrochemical reaction involves several species but the diffusion equation for each species contains terms in concentrations only of that one species, the Thomas algorithm can still be applied; the species will then be coupled by their boundary conditions (for example, the Nernst condition (37) and flux equality (39)), which is easy to handle. However, certain systems result in diffusion equations with terms in more than one species, with the result that the system of discrete equations has a bandwidth greater than three and is not amenable to the convenient Thomas algorithm. A standard example

will have to suffice to illustrate how Rudolph solved this problem [7]. Take the catalytic system (52) in Sect. 1.3.8, which yields the two coupled *pdes* shown in (53). On an unequally spaced grid, these equations are discretized to the form at the point x_i ,

$$\begin{aligned} C'_{A,i-1} + a_1(i)C'_{A,i} + a_k(i)C'_{B,i} \\ + a_2C'_{A,i+1} &= b_{A,i} \\ C'_{B,i-1} + [a_1(i) - a_k(i)]C'_{B,i} \\ + a_2C'_{B,i+1} &= b_{B,i} \end{aligned} \quad (58)$$

in which the a -coefficients arise from the discretization process (and depend on the algorithm used, for example, Crank–Nicolson or Laasonen, (see Ref. [2], 3rd edn. only for details). The point is that the first of the two equations includes terms for both species and the whole system of these equations is thus not amenable to the usual Thomas algorithm for a tridiagonal system (this is in fact not quite true, since a related strategy can be devised in this particular case but the statement is true in general for coupled systems). Rudolph, however, recognized that the two equations can be lumped into a single one in terms of vectors and a matrix, becoming

$$\underline{C}_{i-1} + \underline{A}_i \underline{C}_i + a_2 \underline{C}_{i+1} = \underline{B}_i \quad (59)$$

in which the vector \underline{C}_i now stands for both concentration terms, that is

$$\underline{C}_i \equiv \begin{bmatrix} C_{A,i} \\ C_{B,i} \end{bmatrix} \quad (60)$$

and similarly for the other three vectors, and the coefficient matrix is

$$\underline{A}_i \equiv \begin{bmatrix} a_1(i) & a_k(i) \\ 0 & (a_1(i) - a_k(i)) \end{bmatrix} \quad (61)$$

from equation pair (58). Clearly, Eq. (59) is now back to the form of the single-species discrete equation, with the difference that instead of a row of concentration scalars, we now have a row of concentration vectors and a coefficient matrix. This forms a system called *block-tridiagonal*, since the system has (vector, matrix) elements only on the three middle diagonals. It is thus amenable to a kind of extended Thomas algorithm, and even boundary conditions can be incorporated as vector/matrix expressions. This then solves completely the problem of coupled equation systems, at the price of a little extra complexity in the programming.

The Rudolph method has its limitations. Firstly, as mentioned above, it is harder to program. Secondly, it cannot be implemented effectively for two-dimensional systems. Both problems are overcome by what the present author calls the *brute force* method. This recognizes that computers are very fast these days and we can sometimes afford to be wasteful of computer time, especially if this makes programming easier (and thus, safer from programming errors). Take the discrete equation pair (58). If we simply write this for all N pairs and include the particular discrete expressions for the boundary conditions, the result is a possibly large linear equation system. There are rather efficient subroutines for solving such systems directly, and this is the easiest option. In its simplest implementation, this ignores the fact that the coefficient matrix is mostly empty and the calculation is wasteful. By appropriate ordering of the concentration arrays (specifically, in this case, using the order $C_{A,1}, C_{B,1}, C_{A,2}, C_{B,2}, \dots, C_{A,N}, C_{B,N}$), the matrix can be made tightly banded, which allows more efficient subroutines to be used that bypass all the zero elements. Some progress has been made

in this direction, notably by the Compton group, using Krylov methods. The reader is referred to Ref. [8] for details.

1.3.9.3 BDF(FIRM)

For many years, it was considered that if one wanted to use an implicit method, the method of Crank–Nicolson was the choice (see Ref. [2] for a description). However, although stable for all λ and having second-order accuracy, this method has the disadvantage that it reacts to initial transients, such as from a potential step, in an oscillatory manner; and the larger the value of λ , the longer these (error) oscillations persist. Oscillating errors are not necessarily a bad thing – they provide a visible sign of convergence as they are damped out – but if they are large and persist over a large fraction of the total simulation time, they render the simulation useless. So a method that has similar accuracy and stability as Crank–Nicolson, and has a smooth response to transients, is desirable. The Laasonen method almost does the trick; it fulfills all but one of these requirements, that is, it lacks accuracy being, like the explicit method, first order with respect to time. There are two tricks that can be employed to improve its accuracy, one of them being the BDF. This is the term used in the area of ordinary differential equations. The method was suggested for use with *pdes* and was recently revived by Feldberg and coworkers (see Ref. [2], 3rd edn. only, for references), who prefer to call it the “fully implicit Richtmyer method” (“FIRM”) for historical reasons.

Consider Eq. (27), which expresses the time derivative as a backward difference, that is, takes the simple two-point expression to pertain to the next point in time at $t + \delta t$. This has an error that is dominated by the first-order term in δt . It is

possible to increase this order and thus to get better accuracy for the derivative, by bringing in more points lying at earlier times; the more points that are brought in, the higher the order. The expressions for this are very similar to the multipoint expressions for G , as seen in Eqs. (34 and 35)—in fact, the coefficients are the same but in reverse order and sign, as we are now looking backwards. In all cases, what we get is a derivative that applies to the next time level. The simple three-point scheme serves to illustrate the method. The diffusion equation discretizes to

$$\begin{aligned} \frac{3}{2}C'_i - 2C_i + \frac{1}{2}C_i \\ = \lambda(C'_{i-1} - 2C'_i + C'_{i+1}) \quad (62) \end{aligned}$$

in which C'_i denotes the value at the previous time level $t - \delta t$. Note that the right-hand side is the Laasonen form. This again gives rise to a system of equations of the unknowns C' , which can be solved once the appropriate boundary conditions are applied. For coupled systems, the Rudolph method can be used. The result for the three-point scheme as seen above is a smooth stable response and second-order accuracy, the same as Crank–Nicolson. The three-point scheme is in fact a good match for the three-point expression (19) normally used, and experiments indeed show that using more points in time for BDF does not gain much accuracy, the limit being then set by the three-point derivative along X . Feldberg and coworkers nevertheless prefer a five-point BDF scheme. At about this number of points, the solution shows signs of small oscillations, which become worse for the six- and seven-point schemes; the scheme is unstable for more than seven points.

There is a problem with this method, however, in how to start it. In order to

calculate the very first new point at time δt using, say, the three-point scheme above, we not only need the initial concentration values but also values at time $-\delta t$, which do not exist. The problem is worse for higher-point schemes. There are several strategies to handle this. Feldberg and coworkers simply set all past values to the initial values and start from there. From the world of numerical solution of *odes*, we have a more rational start. Here, the first step is simply a BI step, using the two-point scheme, the same as the Laasonen method. This yields two concentration rows, the initial row and the new one at δt . These can now be used with a three-point scheme to generate the next row at $2\delta t$, and the resulting three rows with a four-point scheme and so forth. When the required number of rows has been generated, one goes on with that number. This method produces reasonable results, which are better than those from the rough start used by the Feldberg school, in itself (but see below). The result is still not as good as one might expect, however, as can be seen when one uses a better approximation than (19) for the derivative along X . It is then seen that the values do not, as expected, improve with the number of points used for the BDF scheme, beyond the three-point scheme.

There is a surprise here, however. The Feldberg school uses a trick that renders the simple start highly accurate. At each step n , the time corresponding to that step, which ought perhaps to be $n\delta t$, is instead corrected by half a time interval to $(n - 1/2)\delta t$. This is the same device previously used for the explicit box method, and described as a fudge in Sect. 1.3.7. In this case, however, there is rational basis for doing this, as was shown recently [9]. Briefly, it turns out

that the simple start, for any order BDF, shifts the time by precisely $1/2\delta t$ and thus the correction brings the simulated values exactly into line with the time. BDF might thus be regarded as a useful simulation method, if one is willing to put up with having to keep several concentration vectors in memory.

1.3.9.4 Extrapolation

The alternative to BDF, that still makes use of the pleasant properties of the Laasonen or BI method, is extrapolation. When one says that discretization (27) is first order with respect to δt , one means that the error e_i can be expressed as a polynomial like

$$e_i = a_1\delta t + a_2\delta t^2 + \dots \quad (63)$$

where, most often, the lowest order (here, the term in δt) dominates. If this could be eliminated, then a smaller error would result, dominated by the (much smaller) next order term. Briefly, this can be done with the following. First calculate the new value, with the time interval δt , getting an error approximately equal to $a_1\delta t$; call this error $e(1, 1)$, meaning that it is the error from one step of one whole δt interval. Then repeat the calculation, now using two steps of half a δt interval each. The resulting error, $e(2, 0.5)$, will be approximately equal to $0.5a_1\delta t$, since we have taken half- δt steps. Note that we do not know what these errors are, we only know their interrelationships. Now, if we subtract twice the error $e(2, 0.5)$ from $e(1, 1)$, the result should be close to zero. That is, using the same notation as for the errors, the calculation

$$C'_i = C_i(1, 1) - 2C_i(2, 0.5) \quad (64)$$

the lowest-order error term will be eliminated. The result is Crank–Nicolson-like accuracy, together with stability and a

smooth response to transients. Note that there are no starting problems to overcome here. The method can be driven to higher orders, by taking combinations of even smaller steps and using more complicated formulae than (64). As with BDF, however, given the second-order nature of (19), there is no appreciable gain in going to more than the two-step scheme described above. In fact, the efficiency falls off, because there is more calculation to do but no accuracy gained.

Extrapolation is an old technique going back to about 1927 and was suggested for general *pdes* in the 1980s, and revived for use with electrochemical simulations in recent years (see Ref. [2], 3rd edn. for details and references). It appears to be the best method at the time of writing.

1.3.9.5 Method of Lines

Increasingly, as the quest for efficiency accelerates and more sophisticated methods are used, the electrochemist who wants to do experiments and not spend all his/her time writing and debugging computer programs, will use program or subroutine packages. In the next section, some whole simulation packages will be mentioned. A cheaper solution however is to use professional subroutines as parts of the programs. One such approach is the MOL. This has already been mentioned in Sect. 1.3.5, in which only the derivative in X was discretized, leaving a set of *odes* (20). If the boundary conditions are added to this system, the result is a differential-algebraic equation (DAE) system, and there exist subroutines to solve such systems, written by experts. The problem then reduces to presenting the data in the form required by the subroutine, and it does the rest. Usually, these routines can either do a single step or a number of steps, perhaps even determine the best step size

or sizes itself. Ultimately, MOL may become the method of choice, supported by such professional routines.

1.3.10

Commercial Packages

A step further than using professional sub-routines as part of one's own program is to use the several available commercial whole packages for electrochemical simulation. A reasonably up-to-date listing of available simulation programs (including some online ones) can be seen at the website <ftp://electrochem.cwru.edu>, then going on to the directories *pub* and *estir*. Speiser [3] has described the main contenders in detail and compared them by computations. The reader is referred to his article for details of these programs. Speiser has himself produced such a program, and was one of the first to do so; it is the package EASI, and he is still working on it sporadically (available from the author, Bernd.Speiser@uni-tuebingen.de), now using the language C++. It uses a "menu" of reaction mechanisms to choose from. One of the next of such packages was that of Gosser, CVSIM, which comes with Gosser's book on cyclic voltammetry. It is written in Pascal and uses the explicit method. Bieniasz produces the more general and sophisticated ELSIM (also written in C++), which allows the user to enter a symbolic form of the differential equations to be solved as well as the boundary conditions; it now also allows entering mechanisms as one writes them normally. Bieniasz is developing, at the time of this writing, a PC Windows version of his program. His program is available through him, nbbienia@cyf-kr.edu.pl. ELSIM is very general and can handle practically any problem one is likely to encounter, including adsorption, but

it is a little demanding to learn to use. It presupposes some knowledge of such programs on the part of the user, who can choose the algorithm to be used, for example. It is Bieniasz' contention that different algorithms are best suited to different problems. This might be a bit of a challenge to the nonmathematical electrochemist, who just wants simulation results. At this time, too, ELSIM has only rather crude facilities for parameter fitting. This is taken to a high level in the commercial package DigiSim, written by Rudolph and Feldberg (in C++) and distributed by BAS (at a considerable price). This is a PC Windows program and rather easy to learn to use. It now uses the BDF (or, as they prefer, FIRM) method and strongly unequal intervals that are considered to enable computations of even the fastest homogeneous reactions. The program is able to compare simulations with experimental data files and adjust a number of parameters to best match the data. The program has suffered from bugs; these may have been removed by now. Another program is POLAR by Huang (info@electroanal.com or <http://www.electroanal.com>); its description promises many features. Nervi has a program, ESP, to be seen at <http://chpc06.ch.unito.it/chemistry/esp-manual.html>. There is an online service for simulation and data fitting at Oxford, <http://physchem.ox.ac.uk:8000/wwwda>, provided by the Compton group.

With all these packages, as pointed out by Speiser [3], there is an element of uncertainty as to the output. The best strategy is probably to run a given package (or two or more of them, if possible) not only on the problem at hand, with its (presumably) unknown result, but also on a similar problem, simplified to the point at which an analytical solution exists for comparison.

1.3.11

The Future

As was written in the foregoing, the major problems in electrochemical digital simulation in one dimension have now been solved. The new frontier is in two- and more-dimensional systems. During the last 20 years or so, ultramicroelectrodes have more or less replaced the mercury drop, and these form a two-dimensional diffusion space, whether they be single disks, or disk arrays, or (arrays of) strips or generator-collector strips, and so forth. Here, the problems include the fact of the large numbers of nodes required for reasonably accurate computations, and thus, long computation times and extreme computer memory needs, at the least; as well as the fact that discretization usually produces (widely) banded systems of equations, so that sophisticated methods of solution need to be used in order to have sufficient memory and realistic computation times. There is also a lack of theoretical work on the numerical methods used. It is by no means certain that the familiar stability criteria will apply with these systems, which often have

steep gradients at the electrode edges. Predictably, this is where new research efforts will be directed in the next decade, and one expects greater use of professional subroutines, at the least.

References

1. S. W. Feldberg in *Electroanalytical Chemistry* (Ed.: A. J. Bard), Marcel Dekker, New York, 1969, pp. 199–296, Vol. 3.
2. D. Britz, *Digital Simulation in Electrochemistry*, 2nd ed., Springer, Berlin, Germany, 1988. 3rd revised edition is expected to appear in 2003.
3. B. Speiser in *Electroanalytical Chemistry* (Eds.: A. J. Bard, I. Rubinstein), Marcel Dekker, New York, 1996, pp. 1–108, Vol. 19.
4. S. W. Feldberg, C. Auerbach, *Anal. Chem.* **1964**, 36, 505–509.
5. J. E. B. Randles, *Trans. Faraday Soc.* **1948**, 44, 327–338.
6. L. K. Bieniasz, *J. Electroanal. Chem.* **2000**, 481, 115–133.
7. M. Rudolph in *Physical Electrochemistry* (Ed.: I. Rubinstein), Marcel Dekker, New York, 1995, pp. 81–129.
8. J. A. Alden, R. G. Compton, *J. Phys. Chem. B* **1997**, 101, 8941–8954, 9606–9616.
9. D. Britz, *J. Electroanal. Chem.* **2001**, 515, 1–7.
10. M. Rudolph, *J. Electroanal. Chem.* **2002**, 529, 97–108.

2.1 Linear Sweep and Cyclic Voltammetry

Bernd Speiser
Institut für Organische Chemie, Tübingen,
Germany

2.1.1 Introduction

2.1.1.1 Historical Background

On the basis of polarography [1, 2], a variety of widely used instrumental electroanalytical techniques has been elaborated and used. Some of them are called *voltammetries* [3]. The basic experiments were initially performed by Matheson and Nichols [4] and independently advanced by Randles [5, 6] and Sevcik [7].

While a more physico-chemical definition will be provided in Sect. 2.1.1.2, we observe here, that a linearly changing (*scanned* or *swept*) potential is imposed on a working electrode, and the resulting current is recorded and analyzed. Hence, advances were related to the development of fast and accurate control of the electrode potential with potentiostats [8]. Since already in early work the potential was changed so fast that electrical recording devices had to be used, the term “cathode ray polarography” [5, 6, 9] or “oscillographic polarography” [7] appeared. Later, the technique

was called “potentiostatische Dreieckspannungsmethode” (potentiostatic triangular voltage method) [10, 11] owing to the characteristic triangular development of the working electrode potential when performing “cyclic” experiments. Stationary rather than dropping electrodes were used, and consequently the term “stationary electrode polarography” [12] became popular.

Already in the mid-1960s, there was rich potential of applying such experiments to the determination of concentrations but even more to the elucidation of reaction mechanisms and kinetics coupled to electron transfer at an electrode was recognized. Today the resulting linear sweep or cyclic voltammetries are employed as simple, flexible routine techniques in particular as sophisticated means to solve chemical and mechanistic problems. The combination with computer control, ultramicroelectrodes, and digital simulation has further contributed to their success.

2.1.1.2 Potential Scan Voltammetries – Definitions

The voltammetric [13] (*volt-ampero-metric*) techniques discussed here record the current i through a working electrode as a function of time t , while the potential E applied to this electrode is controlled as a linear function of t . During the experiment the electrode is stationary, and

usually the electrolyte is not agitated, but at rest. The excitation signal can consist of a single linear sweep (often called a scan) from a starting (E_{start}) to an end potential (Fig. 1a), of two such segments (two scans, often called a cycle) between a starting and a “switching” potential (E_{λ} ; Fig. 1b; the end potential is not necessarily the same as the starting potential), of three segments (Fig. 1c shows an often encountered case) or of several cycles (multicycle experiment; Fig. 1d).

If E is changed according to Fig. 1(a), the experiment is called linear scan or linear sweep voltammetry (LSV), while variants according to Figs. 1(b to d) are commonly called cyclic voltammetry (CV). Although in particular the latter term is widely used, IUPAC [14] recommends the more formal names “chronoamperometry with linear potential sweep” for LSV, while “triangular wave voltammetry” (“chronoamperometry with triangular potential sweep”) is reserved for an experiment according to Fig. 1(b), and CV

or “cyclic triangular wave voltammetry” (“chronoamperometry with multiple triangular potential sweeps”) is used for the multicycle variant. It seems, however, that the latter distinction is neither observed in common usage nor necessary.

The rate at which E changes is the *potential* (sometimes also: voltage) *scan rate*

$$v = \frac{dE}{dt} \quad (1)$$

(often simply termed “scan rate”). Although in most cases, the absolute value of v is the same for all scans of an experiment, a change of $|v|$ at E_{λ} (or other switching points) has been suggested [15]. This variation does not seem to have attracted much attention, however.

Owing to the linear relationship between E and t as given in Eq. (1), the current can be plotted versus time (as directly measured in the experiment; typical curves in Figs. 2a and 2b) or versus potential (typical results in Figs. 2c and 2d). The latter case is most common (“cyclic voltammogram”).

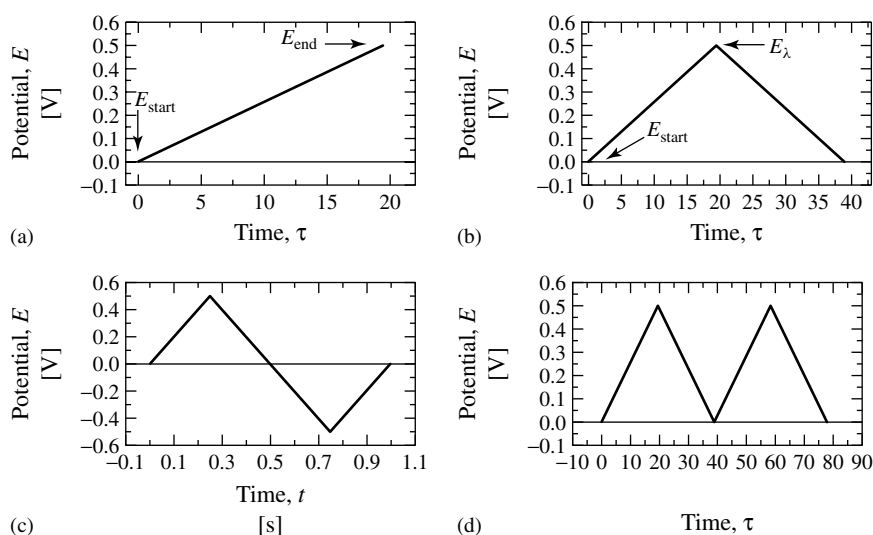


Fig. 1 Excitation signals for potential scan voltammetries: (a) linear sweep voltammetry (LSV); (b–d) cyclic voltammetry (CV).

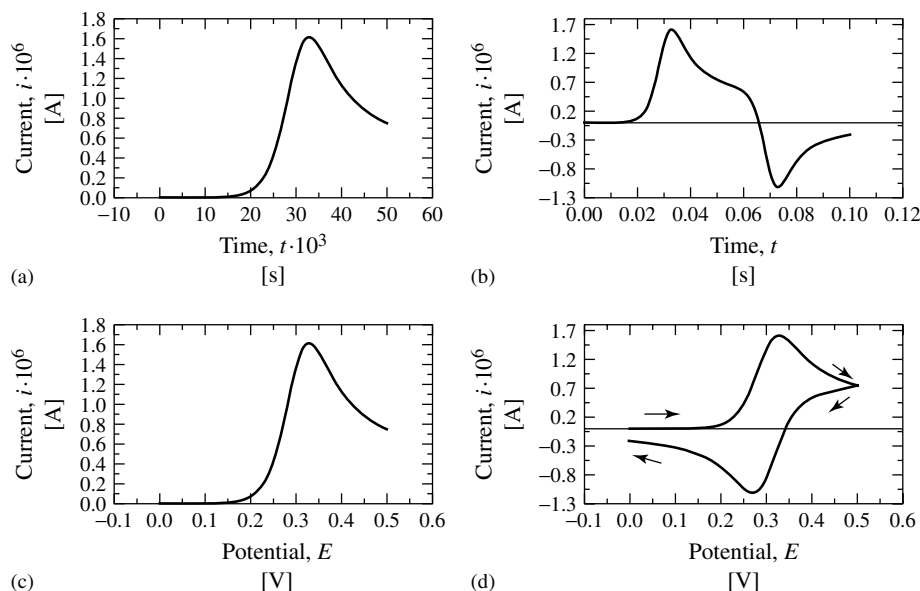


Fig. 2 Typical results of LSV (left) and CV (right) experiments plotted versus time (a, b) or potential (c, d).

When plotting i versus E , it has conventionally to be observed that the scan is presented clockwise as indicated by the arrows in Fig. 2(d). Still, however, two conventions for plotting potentials exist (either positive or negative potentials to the right). Likewise, the sign of currents (anodic currents defined positive or negative) is not unequivocal [16, 17]. Consequently, when interpreting a cyclic voltammogram one has to be careful as regards the exact direction of the individual scans.

2.1.1.3 Scope of the Chapter

The present chapter will first deal with the theoretical background of LSV and CV experiments. The basic equations describing the most important processes will be discussed. A short account of practical problems will lead to a discussion of the experimental limitations and the most common caveats to be observed when applying

these techniques. Some state-of-the-art developments will be described and finally applications will be demonstrated.

Space limitations do only allow a rather selective discussion. For further information, the reader is referred to review articles [13, 18–24].

2.1.2

Theory of Potential Scan Voltammetries

2.1.2.1 General

As already highlighted in Chapter 1.1, electrode processes are complex (see, e.g. Volume 8, Chapter 1), and usually consist of several coupled steps, among these at least transport to and from the electrode and electron transfer, often linked to chemical transformations. Each of these steps may influence the voltammetric response. In order to theoretically describe a voltammetric experiment, all pertinent processes have to be included.

Although it is possible to derive the necessary mathematical equations in “real”, dimensioned quantities, it is often advantageous to use a more general, “dimensionless” formulation. This may involve both the current, and the time/potential variables. Often, however, in the literature only the current is normalized, while the potential is retained as a dimensioned variable, only referred to the formal potential E^0 of the electrode process.

We assume a voltammetric experiment with equal scan rates for all scans and an excitation waveform as in Fig. 1(b). Furthermore, we assume that the substrate is present totally in its reduced form at E_{start} , i.e. the primary process is an oxidation. Conversion to the case of an initial reduction is easily possible.

The temporal development of the electrode potential will then be defined as [12]

$$\begin{aligned} E &= E_{\text{start}} + vt - (m - 1) \times vt_{\lambda} \\ &\quad \text{for odd } m \\ E &= E_{\text{start}} - vt + m \times vt_{\lambda} \\ &\quad \text{for even } m \end{aligned} \quad (2)$$

where m numbers successive scans and t_{λ} is the time needed to scan the potential from E_{start} to E_{λ} . Note that v is always taken positive for the oxidation case considered.

We calculate the concentration ratio for the reduced and oxidized redox partners at the electrode, as defined by the Nernst equation (n , F , R , and T have their usual meaning; x is the distance from the electrode surface)

$$\frac{c_{\text{ox}}(x=0)}{c_{\text{red}}(x=0)} = \exp \left[\frac{nF}{RT} (E - E^0) \right] = \theta S \quad (3)$$

where

$$\theta = \exp \left[\frac{nF}{RT} (E_{\text{start}} - E^0) \right] \quad (4)$$

contains all time-independent quantities, and

$$S = \begin{cases} \exp[at - (m - 1)at_{\lambda}] & \text{for odd } m \\ \exp[mat_{\lambda} - at] & \text{for even } m \end{cases} \quad (5)$$

(with $a = nF/RT \times v$) encapsulates the variation with t . Note the sign change in Eq. (5) as compared to Nicholson and Shain's [12] work, where reductions were considered.

2.1.2.2 Reversible Electron Transfer

We will first consider a simple system, and then include further complications.

Basic starting assumptions are the following:

- The electrode is a solid stationary disk of area A .
- The electrolyte is not in motion and extends virtually infinitely from the electrode. It contains an excess of supporting electrolyte.
- The (reduced) substrate of the electrode reaction is present in the electrolyte with homogeneous distribution in a concentration c^0 . It undergoes electron transfer (assumed to be in equilibrium at all times) with a formal potential E^0 and has a diffusion coefficient D .

Under such assumptions (“reversible” system), diffusion is the main mode of transport and semiinfinite linear diffusion conditions prevail. Thus, Fick's 2nd law describes the variation of concentrations with t and the space coordinate x (extending from the electrode surface, $x = 0$, into

the electrolyte):

$$\frac{\partial c_{\text{red}}}{\partial t} = D_{\text{red}} \frac{\partial^2 c_{\text{red}}}{\partial x^2} \quad (6)$$

$$\frac{\partial c_{\text{ox}}}{\partial t} = D_{\text{ox}} \frac{\partial^2 c_{\text{ox}}}{\partial x^2} \quad (7)$$

At the beginning of the experiment, $t = 0$,

$$c_{\text{red}}(x, 0) = c_{\text{red}}^0, \quad c_{\text{ox}}(x, 0) \longrightarrow 0 \quad (8)$$

i.e. only the reduced form is present. It is assumed that during the experiment there is no change of concentrations at a large distance from the electrode (bulk solution):

$$\begin{aligned} c_{\text{red}}(x \rightarrow \infty, t) &= c_{\text{red}}^0, \\ c_{\text{ox}}(x \rightarrow \infty, t) &\longrightarrow 0 \end{aligned} \quad (9)$$

while Eq. (3) applies at $x = 0$. Often it is further assumed that $D_{\text{ox}} = D_{\text{red}}$ for simplification.

Finally, Eq. (10) defines mass conservation at $x = 0$:

$$D_{\text{ox}} \left(\frac{\partial c_{\text{ox}}}{\partial x} \right)_{x=0} = -D_{\text{red}} \left(\frac{\partial c_{\text{red}}}{\partial x} \right)_{x=0} \quad (10)$$

Equations (6) to (10) and (3) form a system of second order partial differential equations with initial [Eq. (8)] and boundary conditions [Eqs. (3), (9) and (10)]. The presence of the time dependence in Eq. (3) prevents a closed form solution of this system. Several approaches have been used to calculate the concentrations c as a function of x and t , including Laplace transformation [7, 12] and digital simulation [25], all relying on numerical integration steps. Chapter 1.3 provides further information on digital simulation.

From *concentration profiles* $c = f(x, t)$ it is possible to calculate the temporal development of the current through

the electrode (see also Volume 8, Chapter 1) by

$$i = nFAD \left(\frac{\partial c_{\text{red}}}{\partial x} \right)_{x=0} = nFAf_{\text{red}, x=0} \quad (11)$$

($f_{\text{red}, x=0}$ is the flux of species red at $x = 0$).

A particular form of Eq. (11) is

$$i = nFADc_{\text{red}}^0 \sqrt{\pi D_{\text{red}} a} \chi(at) \quad (12)$$

as derived by Nicholson and Shain [12] where $\chi(at)$ is a dimensionless function obtained from the integration procedure (*current function*).

The result for a single scan is shown as a current–potential curve in Fig. 3(a). It exhibits the characteristic peak shape with a peak potential E_p and a peak current i_p . The potential where the current attains 50% of the peak value ($i_p/2$) on the rising flank is the half-peak potential $E_{p/2}$.

The form of the curve is qualitatively explained as follows: at the beginning of the experiment, essentially no current flows since we start from an equilibrium situation (see Sect. 2.1.3.4). Scanning E induces a change in $c_{\text{ox}}/c_{\text{red}}$ at $x = 0$ according to Eq. (3): Red is converted into ox at the electrode, resulting in a current. The concentration of red is depleted in the immediate vicinity of the electrode surface, while the concentration of ox increases. These changes of $c(x = 0)$ with respect to the bulk solution values induce diffusional transport. Thus, red diffuses towards the electrode, while ox diffuses to the bulk. The resulting flux f of material sustains the current flow.

Further increase of E causes a decrease of $c_{\text{red}}(x = 0)$ and an increase of $f_{\text{red}}(x = 0)$ with an increase of i . Simultaneously, according to Eq. (12) a diffusion layer develops that extends over a thickness $\delta \sim \sqrt{t}$. The increase in δ tends to decrease $f_{\text{red}}(x = 0)$. The two effects are

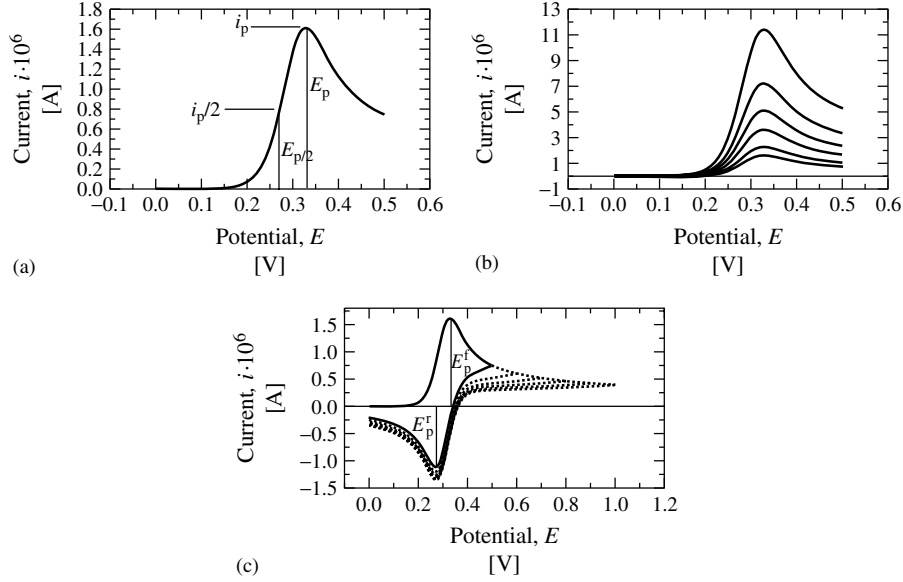


Fig. 3 Current–potential curves for a reversible electron transfer: (a) shape and important features of a linear sweep voltammogram; (b) linear sweep voltammograms as a function of the scan rate $\nu = 0.1, 0.2, 0.5, 1., 2., 5. \text{ V s}^{-1}$ with increasing i_p ; (c) cyclic voltammograms and their dependence on E_λ .

superimposed. If $c_{\text{red}}(x = 0)$ decreases to very small values, further changes of E have no more effect, and the current is mainly determined by the expansion of δ . About 180 mV after the peak, the decay of the voltammetric i/t curve can essentially be described by potential-step Cottrell behavior (see Chapter 2.2).

Quantitatively, the peak current is given by Ref. [12]

$$\sqrt{\pi} \chi_p = 0.4463 \quad \text{or} \quad i_p = nFAc_{\text{red}}^0 \sqrt{aD_{\text{red}}} \times 0.4463 \quad (13)$$

At $T = 298 \text{ K}$ the so-called Randles–Sevcik equation

$$i_p = (2.69 \times 10^5) n^{3/2} A c_{\text{red}}^0 \sqrt{\nu D_{\text{red}}} \quad (14)$$

follows. Note, that i_p in both Eqs. (13) and (14) is proportional to $\nu^{1/2}$. The scan rate defines the timescale of the experiment. For short timescales (high ν), the

diffusion-controlled current is increased over that for longer timescales (smaller ν). This is due to the fact that the concentration gradient and the flux of educt to the electrode increase with increasing ν . Figure 3(b) demonstrates this relationship that is often used to prove diffusion control of the current as opposed to currents due to surface-bound or adsorbed redox species (see Sect. 2.1.2.5).

The position of the peak on the potential axis is also of interest. For the reversible case,

$$E_p = E^0 + \frac{28}{n} \text{ mV} \quad (15)$$

for $T = 298 \text{ }^\circ\text{C}$ (oxidation) and

$$E_{p/2} = E^0 - \frac{28}{n} \text{ mV} \quad (16)$$

hold. Both relationships only apply if $D_{\text{red}} = D_{\text{ox}}$.

Obviously, the peak on the first scan of a cyclic voltammogram is identical to the one of a single scan experiment. The reverse (“back”) scan curve and the details of the reverse peak, however, depend on the exact position of E_λ (Fig. 3c). In this peak the product of the electrode reaction, which has accumulated in the diffusion layer during the forward scan, is transformed back to the starting species. For practical purposes, the peak *shape* is independent of E_λ for $n|E_\lambda - E^0| > 35$ mV [12]. For $n|E_\lambda - E_p| > 180$ mV, it is also true that $|E_p^f - E_p^b| \approx 58$ mV at $T = 298$ K. Still, the reverse peak *current* is a function of E_λ . An important characteristic of the cyclic voltammetric i/E curve is the current ratio [26]

$$\frac{i_p^b}{i_p^f} = \frac{i_{p,0}^b}{i_{p,0}^f} + 0.485 \frac{i_{\lambda,0}}{i_{p,0}^f} + 0.086 \quad (17)$$

where currents with subscript 0 are measured relative to the zero current line and $i_{\lambda,0}$ is the current at E_λ . This ratio is unity for the simple case considered here.

Note that the area under the curves, i.e. the charges transferred in the forward and reverse scans, are *not* equal, since not all starting material is regenerated during the reverse scan and some product (ox in the present discussion) escapes from the electrode.

If many cycles are performed, the successively recorded voltammograms gradually change until a steady state is reached since the concentrations at E_{start} shift between cycles [12]. However, only changes in peak current are essential while peak potentials are affected to a minor extent.

2.1.2.3 Kinetics of Electron Transfer

As a first complication, we consider a finite rate constant k_s of the electron transfer. In such a case, the kinetics of the electron

transfer step have to be included, most often by a Butler–Volmer relationship

$$i = i_0 \left\{ \exp \left[\frac{-\alpha n F}{RT} (E - E^0) \right] - \exp \left[\frac{(1 - \alpha) n F}{RT} (E - E^0) \right] \right\} \quad (18)$$

which is substituted for Eq. (3). Here, $i_0 = nFAk_s c_{\text{red}}^0$ is the exchange current (defined at $E = E^0$) and α is the transfer coefficient.

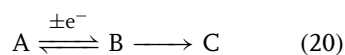
Depending on the relative magnitudes of D and k_s , we move from a situation in which diffusion control predominates (small D , large k_s ; reversible case, see Sect. 2.1.2.1) through a mixed-control regime (both diffusion and kinetics are important; quasi-reversible case [9, 27, 28]) to a situation in which the rate of electron transfer controls the overall reaction (large D , small k_s ; irreversible case [12]). This continuum of conditions is characterized in LSV or CV by the dimensionless quantity

$$\psi = \frac{k_s}{\sqrt{aD_{\text{red}}}} \quad (19)$$

The dependence of voltammograms on ψ has been analyzed by Matsuda and Ayabe [9] (LSV) as well as Nicholson and Shain [27] (CV) and characteristic voltammograms can be found in Volume 8 Chapter 1.

2.1.2.4 Coupled Homogeneous Chemical Kinetics

To consider coupled chemical reactions in the homogeneous electrolyte phase, the diffusion equations such as Eqs. (6) or (7) are augmented by the kinetic terms corresponding to the reaction of the species whose diffusion it describes (reaction–diffusion equations). For example, for a reaction



where the reduced form A of the redox couple is oxidized to B, which then reacts in a homogeneous chemical reaction, the governing equations become

$$\frac{\partial c_A}{\partial t} = D_A \frac{\partial^2 c_A}{\partial x^2} \quad (21)$$

$$\frac{\partial c_B}{\partial t} = D_B \frac{\partial^2 c_B}{\partial x^2} - k c_B \quad (22)$$

$$\frac{\partial c_C}{\partial t} = D_C \frac{\partial^2 c_C}{\partial x^2} + k c_B \quad (23)$$

In these equations, we assume that the chemical reaction is of first order and characterized by a rate constant k . B disappears as determined by $k c_B$, and each reacting molecule B generates one molecule C. Consequently, the concentration profiles of all species are modified, and the

resulting current depends on the homogeneous reaction.

Many types of coupled chemical reactions have been considered under LSV or CV conditions, and the resulting effects on voltammetric curves have been analyzed. This forms the basis for both qualitative derivation of mechanisms and quantitative determination of kinetic constants for electron transfer coupled reaction steps from LSV and CV. Some examples are discussed in Volume 8, Chapter 1.

2.1.2.5 Adsorption and Surface-Bound Redox Species

If the redox species is confined to the immediate vicinity of the electrode surface, either by adsorption forces or by covalent bonds (modified electrodes), there is no need for transport from the bulk of the electrolyte in order to induce the electrochemical reaction. No concentration profile develops. On the other hand, the number of molecules subject to electron transfer is limited to those attached to the surface. These facts lead to a characteristic voltammetric response, see e.g. Fig. 4.

The current–potential curve in the simplest case (Langmuir adsorption isotherm) [29, 30] is mirror-symmetric to the line normal to the potential axis at E^0 with a peak potential $E_p = E^0$. Furthermore, the current returns to zero after the peak. This is explained by the fact that *all* surface-bound material is converted according to Eq.(3). Since no diffusional loss is involved, all product can be converted back to the starting

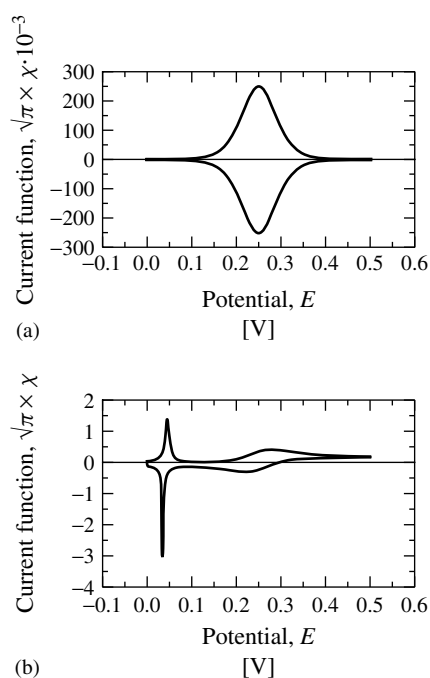


Fig. 4 Cyclic voltammograms for surface attached redox active molecules: (a) Langmuirian behavior; (b) Frumkin-type behavior with attractive interaction between oxidation product molecules.

material in the reverse scan. Thus, the areas under the two peaks will ideally be identical. The peak current for such a system will be proportional to v rather than $v^{1/2}$.

The exact shape and quantitative features of the voltammograms will depend on a variety of parameters, e.g. the adsorption isotherm followed, the surface concentration of the redox species, or the presence or absence of intermolecular forces between the adsorbed molecules (see Fig. 4b for an example with attractive forces between product molecules) [31–33]. Additional effects such as slow transport of counterions between bulk and the surface layer may further change the characteristics of the voltammograms [34].

2.1.2.6 Nonlinear Diffusion

At long timescales or for small dimensions of the electrode, the assumption of linear diffusion (see Sect. 2.1.2.2) no longer holds. The form of the partial differential equations [e.g. Eq. (6)] or the diffusion term therein, changes to, for example, spherical diffusion:

$$\frac{\partial c}{\partial t} = D \left(\frac{\partial^2 c}{\partial r^2} + \frac{2}{r} \frac{\partial c}{\partial r} \right) \quad (24)$$

where r is a coordinate parallel to the radius of the electrode disk. Thus, the flux and consequently the current increases over the linear case. At intermediate situations a mixture of linear and spherical diffusion applies:

$$\frac{\partial c}{\partial t} = D \left(\frac{\partial^2 c}{\partial r^2} + \frac{1}{r} \frac{\partial c}{\partial r} + \frac{\partial^2 c}{\partial z^2} \right) \quad (25)$$

Here, z is the coordinate perpendicular to the disk. The form of linear sweep voltammograms changes from peak to S-shaped, indicating that the diffusion layer quickly attains a steady state with a fixed thickness (Fig. 5).

In even more complex cases, three-dimensional forms of Fick's law such as Eq. (26) must be used

$$\frac{\partial c}{\partial t} = D \left(\frac{\partial^2 c}{\partial x^2} + \frac{\partial^2 c}{\partial y^2} + \frac{\partial^2 c}{\partial z^2} \right) \quad (26)$$

2.1.2.7 Restricted Diffusion

The assumption of semiinfinite diffusion becomes invalid if the diffusion space is

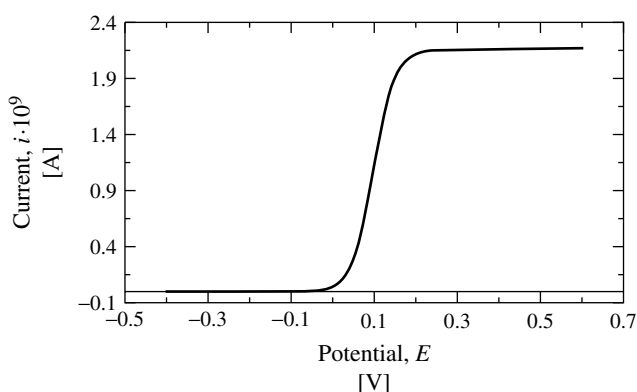


Fig. 5 Cyclic voltammogram of ferrocene ($c = 4 \times 10^{-4}$ M) at an ultramicroelectrode disk (10 μm diameter, Pt, $v = 10$ mV s $^{-1}$) with spherical diffusion.

limited, i.e. the electrolyte does not extend to virtual infinity from the electrode. In such situations, the boundary condition at large distances from the electrode is no longer constant with t . Rather, the diffusing material is being exhausted. Restricted diffusion is found for example in thin layer cells [35] under potential scan conditions.

2.1.2.8 Simulation

Solutions of the differential equation systems including initial and boundary conditions as discussed in the previous sections are generally provided by simulation. Mathematical models describing the basic physico-chemical processes are numerically resolved [25]. LSV and CV are among the main methods treated in electrochemical simulations. Further information on this subject can be found in Chapter 1.3 of this Volume and (with mechanistic background) in Chapter 1 of Volume 8.

2.1.3

Practical Considerations

2.1.3.1 Electrodes and Cells

While initially [4–7] often hanging mercury drop electrodes were employed, today the entire range of electrode materials, in particular Pt, Au, and C (glassy carbon, graphite) is used for LSV and CV. Consequently, not only spherical (drop) but also planar (disk) and cylindrical (wire) electrode geometries became important. This was already recognized early [12] by simultaneously treating planar and spherical systems. The choice of electrode material strongly depends on the application.

The characteristic size of electrodes is conventionally a few millimeters (radius for a planar disk) as a maximum. The current minimum for disk electrodes is in the

nanometer region [36], where, however, reproducibility may be a problem and the exact determination of the electroactive area is difficult [37].

The cells for voltammetric experiments usually comprise a three-electrode arrangement, with working and counter-electrodes sufficiently spaced, while the reference electrode is brought close to the working electrode surface with a Haber–Luggin capillary to minimize iR loss (see Sect. 2.1.3.4). The conventional cell volume is up to ≈ 20 ml, but only a small part of this total volume is affected during the experiment (diffusion layer). With sufficient mixing after a scan or cycle, a large number of voltammograms can be recorded in the same solution without interference in most cases. Smaller cells for microelectrode use [13] or cells for high-purity applications in organic solvents have been described [38].

2.1.3.2 Solvents and Supporting Electrolytes

The whole range of solvents (aqueous and nonaqueous) and supporting electrolytes (usually 0.1 M in order to avoid migration effects) including the popular tetra-alkyl ammonium salts are used in voltammetric studies. There are no particular restrictions from the voltammetric conditions. It must be noted, however, that for mechanistic studies high-purity electrolyte components are necessary. Since the substrates are often present in concentrations of 10^{-4} M or lower, even traces of impurities may have detrimental effects on the current–potential curves (see also Sect. 2.1.3.3). The choice of solvent and supporting electrolyte clearly depends on the application and factors such as solubility of the substrate.

2.1.3.3 Experimental Limitations

Applicability of voltammetric techniques is in some cases limited due to several factors which will be discussed in the following.

In a real system, we will observe the oxidation or reduction of electrolyte components, the electrode material itself, or of impurities in the electrolyte at certain potentials. These processes define the *accessible potential window* (Fig. 6), and the observable electrode reactions should yield voltammetric signals well inside this window to allow analysis without interference of background contributions.

At low scan rates, the tacit assumption that no convection takes place in the cell breaks down. For example, in a dichloromethane/0.1 M NBu₄PF₆ electrolyte at room temperature, convection effects are already observable at $v \approx 10 \text{ mV s}^{-1}$. This defines a lower limit of the applicable scan rates (see also edge effects below).

At high scan rates, in most cases sampling rates or potentiostat rise times, limit applicability of voltammetric experiments (see Chapter 1.2). Modern commercial

computer-controlled instruments allow scan rates up to several hundred volts per second. With electrodes in the mm radius range, however, often iR drop (see Sect. 2.1.3.4) reaches critical values making useful interpretation impossible, at least in organic electrolytes. Smaller electrode sizes may be used for larger scan rates (see Sect. 2.1.4.1).

Another inherent limitation becomes important if the size of the diffusion layer becomes comparable to that of the electrical double layer [39]. Thus, scan rates are limited to a practical maximum of $\approx 10^6 \text{ V s}^{-1}$ if such effects are not taken into account [39] (see, however, Ref. [40]).

2.1.3.4 Artifacts and How to Avoid Them

Although the voltammetric experiments discussed in this Chapter are rather simple to perform and reasonable protocols are incorporated into the control software of most modern computer controlled electrochemical instruments, there are several important points to observe in order to avoid artifacts.

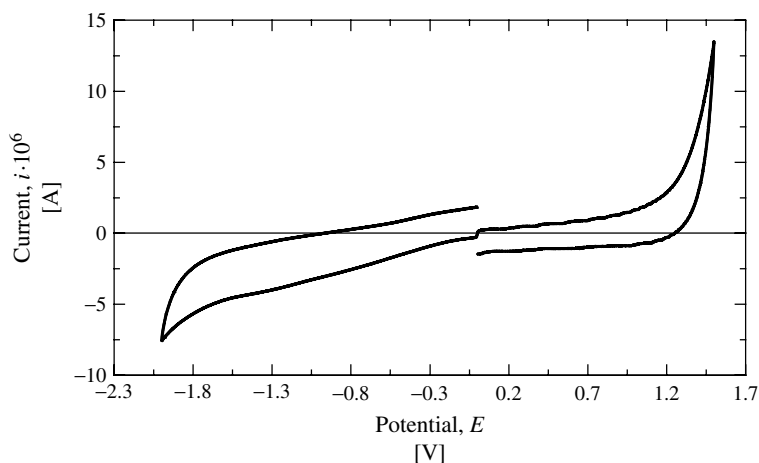


Fig. 6 Potential window in a dichloromethane/0.1 M NBu₄PF₆ electrolyte, potentials vs. a Ag/0.01 M Ag⁺ reference electrode.

Selection of starting and switching potentials. The end points of the potential scans have to be selected inside the potential window of the electrode/electrolyte combination. Furthermore, however, two guidelines should be observed if at all possible:

- The starting potential should be located at a potential where no current flows through the working electrode. Often this potential can be determined as the “open circuit” or “rest” potential of the solution. This ensures that the current/potential curve starts at $i = 0$. The initial condition of homogeneous distribution of the redox active species throughout the electrolyte is fulfilled. If this precaution is not taken, the product of the electron transfer is produced at the electrode before the start of the scan and diffuses towards the bulk electrolyte. Consequently, some distortion of the voltammetric curve may be observed. In practical terms, the recommended

selection means to choose E_{start} well (usually several hundred millivolts) before the first peak in the voltammogram.

- On the other hand, the selection of E_{λ} will only influence the reverse peaks. Depending on the actual problem, several choices of E_{λ} are meaningful (if e.g. several peaks are present in the current/potential curves). In general, however, for quantitative analyses of reverse peak features, E_{λ} should be at least 180 mV past the forward peak.

Selection of scan parameters. As mentioned earlier, the scan rate significantly influences the shape and quantitative features of voltammograms. Usually, a variation of v gives important information. There are, however, other scan-related parameters that may affect the current/potential curves. In computer controlled instruments, the ideal linear variation of E is often simulated using a staircase function (Fig. 7). The response from such an excitation function

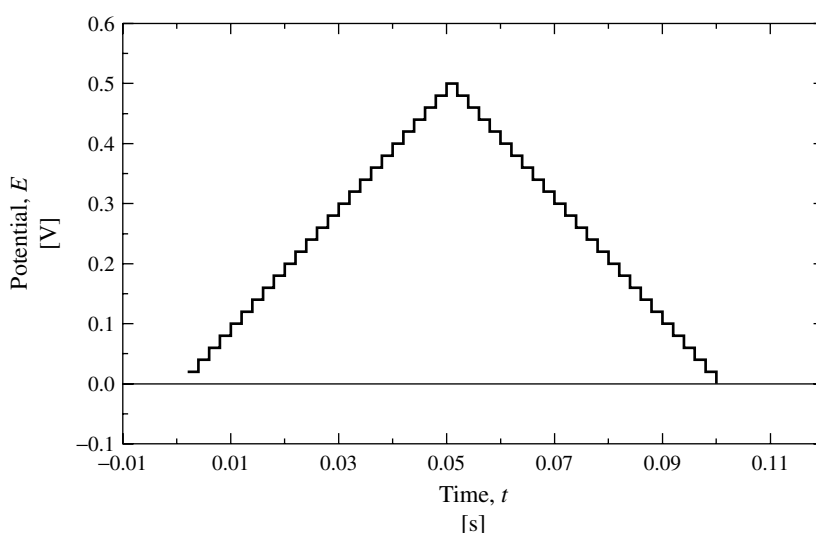


Fig. 7 Staircase type potential scans as substitute for linear scans; step size exaggerated.

is equivalent for practical purposes if the change of E during a step is small enough. What exactly is small enough, is a complex function of several experimental variables and the electrode reaction itself [41].

Selection of potential cycles. It has been mentioned earlier that multicycle experiments lead to a steady state current/potential curve eventually (to be distinguished from steady state microelectrode curves!). Often such curves are presented in the literature. However, quantitative analysis, in particular comparison to simulations, is greatly complicated with such steady state data and pristine curves should be preferred. Furthermore, product molecules produced after several cycles may induce additional chemical reactions or show additional peaks. If it is desired to study such effects, the variation of the voltammogram with the cycle number must be analyzed in greater detail.

Uncompensated resistance and double layer effects. In particular, in organic solvents and at high scan rates uncompensated resistance with the resulting iR drop and double layer effects may affect the voltammograms [42]. The iR drop distorts the linear E/t curve, usually assumed in LSV or CV. Of course, in turn, the current is affected. While this can be controlled to some extent by the use of ultramicroelectrodes, it does not entirely vanish. Thus, iR compensation [43, 44] or correction [45, 46] is strongly recommended. Further details on this topic are given in Chapter 1.2 (Sect. 1.2.6). Double layer charging adds in the most simple case a constant current i_d at constant v to the i/E curve. Since i_d is proportional to v , while the peak current i_p increases with $v^{1/2}$, i_d increasingly dominates the current signal at high v . Furthermore, remaining electrolyte impurities will distort the voltammograms in

some cases. Background subtraction may thus additionally be required.

Nonlinear diffusion. The voltammetric behavior related to linear (e.g. at short times) and spherical (e.g. at large times or small electrodes) diffusion has been discussed in Sect. 2.1.2. Of course, there are intermediate situations, in which mixed behavior is observed, which may be regarded as a distortion of either of the extreme types of transport. In particular, use of conventionally sized electrodes at slow scan rates causes the increase of peak currents (normalized to $v^{1/2}$) with decreasing v since additional nonlinear transport of material across the edge of the electrode occurs ("edge diffusion" or "edge effect" [47]). Consequently, too slow scan rates should be avoided.

2.1.4

Present Methodological Developments

2.1.4.1 Voltammetry at Ultramicroelectrodes

Ultramicroelectrodes (see Chapter 2.5) have attracted considerable attention for voltammetric experiments recently [39, 48]. Such devices are defined conventionally by size (disks with diameter $\leq 20 \mu\text{m}$ [48]) or by physico-chemical behavior [39]. Owing to their size, at ultramicroelectrodes the diffusion layer attains a steady state shortly after the beginning of the experiment. Thus, if the timescale is long enough, the i/E curves under LSV or CV conditions show a plateau type shape (see Sect. 2.1.2.6). On the other hand, in faster experiments, a peak still develops. The transport rate and, consequently, the current per unit area (current density) become very large because of the change from linear to spherical diffusion. Other processes than diffusion may become rate controlling under these

conditions. Consequently, ultramicroelectrode voltammetry may be used to determine heterogeneous electron transfer rate constants. Furthermore, the high transport rates render homogeneous chemical reactions less important and decrease their influence on the voltammograms.

The diffusion-controlled steady state current at an ultramicroelectrode of radius r_0 is given by

$$i_d = 4nFDc^0r_0 \quad (27)$$

Note that the functional relationship between current, c^0 and D in Eq. (27) is different from that in Eqs. (13) and (14). This has been used to determine c^0 and D simultaneously from steady state and non-steady state curves at the same ultramicroelectrode, e.g. in gel monoliths [49].

In the following two sections, further applications of LSV or CV at ultramicroelectrodes are discussed in brief.

2.1.4.2 Fast Scan Techniques

As mentioned already (Sect. 2.1.4.1), at short times scales, i.e. fast scan rates, LSV or CV curves at ultramicroelectrodes still attain the conventional peak shape related to linear diffusion. Under these conditions, another advantage of such electrodes becomes apparent: the small electrode area, resulting in a small double layer capacity C_d (hence a small time constant RC_d), and a small current i (hence a small iR drop). Artifacts due to double layer charging and uncompensated iR drop become less prominent, and consequently high scan rates up to 10^6 V s^{-1} can be used [39] as compared to the limit of a few 10 V s^{-1} at conventional electrodes. Furthermore, specific techniques allow the recording of iR -drop free voltammograms even at $v > 10^6 \text{ V s}^{-1}$ [50].

In such timescales, it is possible to study very fast heterogeneous electron transfer rate constants [48]. Diffusion layers as thin as a few nanometers are characteristic for such fast scan rates [50]. Coupled homogeneous chemical reaction steps become less important, and highly reactive intermediates can be detected [48]. The chemical reversibility of electrode reactions increases and thus redox potentials of electron transfer reactions involving extremely unstable species become available [48].

2.1.4.3 Voltammetry Without Supporting Electrolyte

The decreased iR drop in voltammetric experiments at ultramicroelectrodes has been exploited to perform electrochemistry under conditions in which no or only a small concentration of supporting electrolyte is added and allows measurements in low-polarity solvents (e.g. hydrocarbons), without the presence of excess ions, or even in the gas phase [51]. This topic is discussed further in Chapter 2.5 (Sect. 2.5.5.6). In these cases, the transport of charge in the electrolyte is realized by small amounts of impurities [48], by ions of the substrate material itself [52], or those generated in the electrode reaction [39]. Thus, migration has to be considered as an additional mode of transport, in particular for multiply charged species [52]. A recent modeling study [53] has provided evidence that LSV should be best suited to deal with situations of high uncompensated resistance as compared to chronopotentiometry and chronoamperometry.

Since nonpolar solvent based electrolytes cannot be used in conventional voltammetric experiments, solubility problems may arise for some organic compounds. Ultramicroelectrodes allow the use of benzene, toluene, and even hexane or supercritical CO_2 as solvents and the

study of electrode reactions or analytical determinations in such environments is now actively studied [48].

Furthermore, the polarity range for mechanistic or analytical studies is considerably broadened. The stability of intermediates under such unconventional conditions can be investigated.

2.1.4.4 Voltammetry Under Hydrodynamic Conditions

Usual conditions for LSV or CV experiments require a quiet solution in order to allow undisturbed development of the diffusion layer at the electrode. Some groups, however, have purposely used the interplay between diffusion and convection in electrolytes flowing in a channel or similar devices [23]. In these experiments (see also Chapter 2.4), mass transport to the electrode surface is dramatically enhanced. A steady state develops [54] with a diffusion layer of constant thickness. Thus, such conditions are in some way similar to the use of ultramicroelectrodes. Hydrodynamic voltammetry is advantageous in studying processes (heterogeneous electron transfer, homogeneous kinetics) that are faster than mass transport under usual CV or LSV conditions. A recent review provides several examples [22].

2.1.4.5 Voltammetric Spectroelectrochemistry

Although, in particular CV is ideally suited to detect the presence of intermediates in an electrode reaction and to define the kinetics and thermodynamics of the reaction, it is impossible to derive direct structural information about intermediates or products from voltammetric data. On the other hand, such information advantageously can be provided by spectroscopic experiments. Consequently,

both instrumental approaches were combined in the form of in situ spectroelectrochemistry [55, 56] under potential scan conditions.

Thus, a large number of spectra is recorded during the potential scan of an LSV or CV experiment. Each spectrum can be assigned to a situation of defined potential (i.e. concentration ratio at the electrode) and to a certain time since the start of the experiment (kinetics). If recorded fast enough, the spectral properties of even short lived intermediates are accessible. Further details on spectroelectrochemical measurements of this type are given in Chapter 3.4.

2.1.4.6 Derivative Voltammetry

The current signal in LSV or CV is rather broad even for the reversible electron transfer case. The width of the reversible peak at half height is about 96 mV. Thus, resolution is relatively low and exact determination of the peak potential is often difficult.

It is well known that features of signals can be enhanced by examining their derivative. Consequently, *derivative cyclic voltammetry* (DCV) was developed [57]. The derivative is usually calculated numerically by simple differencing ($\Delta i / \Delta t$) if the time step increments are small enough [58], by a Savitzky-Golay polynomial least-squares procedure [59], or by Fourier transformation [60]. Also, hardware based differentiation is possible [60].

Figure 8 shows simulated cyclic voltammograms and their derivatives. The peak potentials can easily be extracted with high accuracy from the derivative curve as the points at which the baseline is crossed.

It has been emphasized [61] that distortions by double layer charging (see Sect. 2.1.3.4) are eliminated in DCV curves, since their constant contribution disappears in the derivative signal.

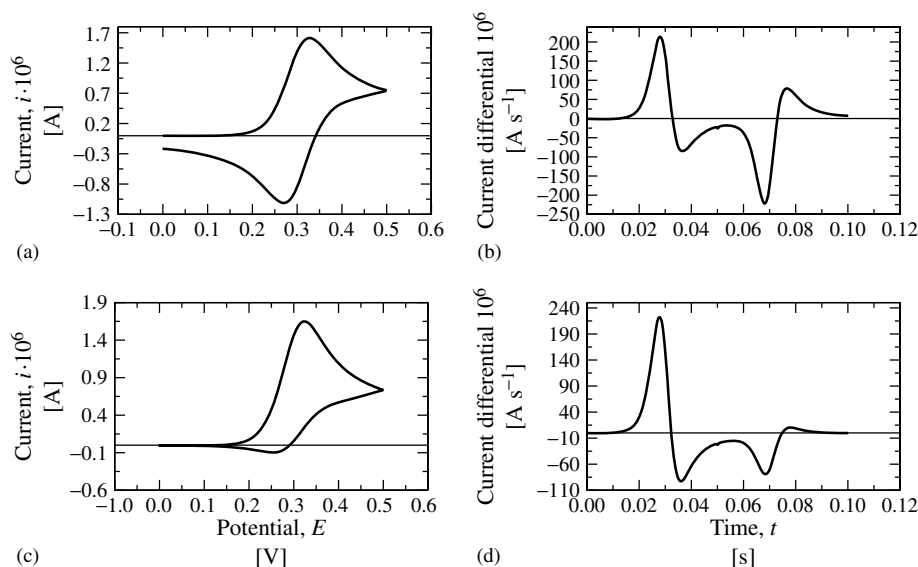


Fig. 8 Cyclic voltammograms of a reversible electron transfer without (a) and with a homogeneous follow-up reaction (c) and their derivatives (b, d).

Furthermore, DCV was employed for kinetic and mechanistic analyses of electrode reactions [57, 59, 61]. The ratio of the derivative peak intensities (see Fig. 8d) is a convenient measure of the original i/E curve shape and sensitive to homogeneous [57, 61] and heterogeneous kinetics [59].

2.1.4.7 Semiintegral (“Convolution”) and Semiderivative Voltammetry

Another transformation of high interest in LSV or CV is the calculation of the *semiintegral* [62] of the current, $m(t) = d^{-1/2}i(t)/dt^{-1/2}$. It is characterized by the fact that applying it twice in succession, the integral of the original function will be generated. This function is given by

$$m(t) = \frac{1}{\pi^{1/2}} \int_0^t \frac{i(\tau)}{(t - \tau)^{1/2}} d\tau = I(t) \quad (28)$$

with the dummy variable τ , and is thus identical to the convoluted current

$I(t)$ [63–65]. Recently, extended semiintegrals with a general convoluting function $g(t)$ have been defined:

$$m(t) = \int_0^t i(\tau)g(t - \tau)d\tau \quad (29)$$

where $g(t)$ depends on the electrode geometry and kinetics [66].

Transformation (Eq. 28) can be accomplished by analog circuits [67], but also several numerical algorithms have been provided [16, 17, 60, 68, 69].

The semiintegral of an LSV or CV voltammogram (Fig. 9) has some important properties. The sigmoidal branches of the forward and reverse part of the $m(t)$ curve for a reversible redox process exactly coincide [16, 17]. Moreover, the semiintegral and in particular its maximum value are independent of the exact E/t relationship under ideal conditions [46, 62]. Thus, effects of iR drop on the linearity of the potential scan excitation function in LSV or CV disappear, when considering

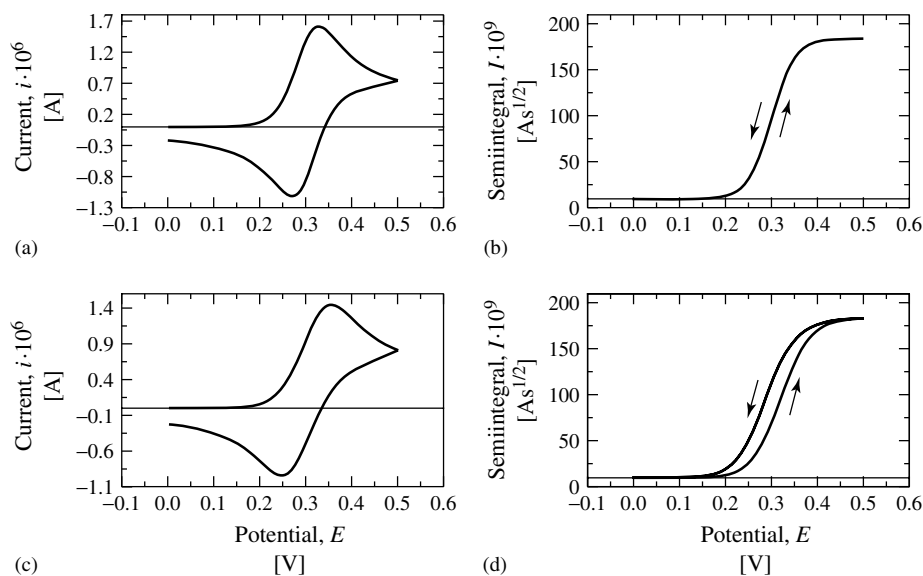


Fig. 9 Cyclic voltammograms of an electron transfer with fast (a) and slow (b) heterogeneous kinetics and their semiintegrals (b,d).

$m(t)$ [70]. Quasireversibility of the redox process or iR drop contributions cause the two branches of the semiintegral to split (Fig. 9d) providing an extremely sensitive test for reversibility and the absence of iR effects [70]. From the extent of separation of the two branches calculation of the uncompensated resistance was attempted [46].

Further applications of the $m(t)$ or $I(t)$ transform of LSV or CV curves are found in mechanistic analysis [63–65, 71]. In particular, the fact that no *a-priori* assumption of the rate law for the heterogeneous electron transfer is necessary for the calculations has been stressed. Thus, deviations from the simple Butler–Volmer behavior can be identified [64]. A sophisticated example for the use of such techniques will be discussed later.

Semiderivative or semidifferential voltammograms appear sharper than their non-transformed counterparts [60] and have

thus been used to improve resolution of closely spaced peaks with severe overlap [72].

2.1.5

Applications

In this section, a few examples have been selected from the literature to demonstrate the possibilities of the experimental techniques described in the present chapter. In the examples mostly CV will be used. Apart from the impossibility to detect intermediates and products during the reverse scan, similar arguments, however, apply to LSV.

2.1.5.1 Typical Voltammograms

– Classical Applications

Figure 10 shows three selected cyclic voltammograms that demonstrate the scope of the CV technique as a tool for the characterization of redox active chemical compounds.

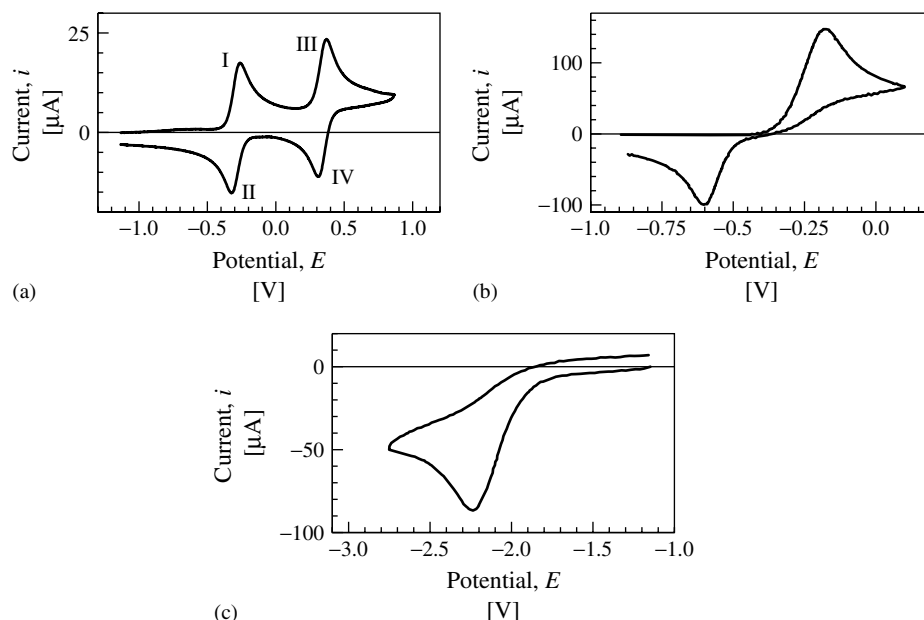


Fig. 10 Typical cyclic voltammograms of organic molecules. (a) *N, N, N', N'*-tetramethyl-*p*-phenylenediamine, TMPD, at Pt electrode, $c = 0.27$ mM in $\text{CH}_2\text{Cl}_2/\text{CH}_3\text{CN}$ (1 : 1)/0.1 M NBu_4PF_6 , $\nu = 0.5$ V s $^{-1}$;

(b) 3,6-bis(dimethylamino)durene, $\nu = 0.5$ V s $^{-1}$ (replotted from Ref. [73], in which further experimental details can be found); (c) benzylchloride (replotted from Ref. [74], in which further experimental details can be found).

N, N, N', N'-Tetramethyl-*p*-phenylenediamine **1** is a well-known example of a system with three stable redox states. The neutral starting species can be oxidized to a radical cation (also known as “Wurster’s Blue”, $1^{\bullet+}$) [75] and a dication 1^{2+} (see e.g. Refs. [76 and 77]). This two-step redox process results in a cyclic voltammogram as in Fig. 10(a) with two oxidation peaks I and III and two corresponding reduction signals II and IV. The two peak couples I/II and III/IV are well separated, and mirror the increasing potential needed to generate increasingly positively charged cationic species. The E^0 of the two steps ($E_1^0 = -0.29$ V, $E_2^0 = +0.34$ V; both values versus the ferrocene/ferricinium ion standard redox couple [78]) are simply calculated as mean values of the corresponding peak

potentials. The difference in E_p for two peaks related to the same redox process is close to 58 mV in both cases, as expected for a diffusion-controlled one-electron process (see Sect. 2.1.2.2). Equation 13 allows the calculation of $D = 1.6 \times 10^{-5}$ cm 2 s $^{-1}$.

There are some interesting cases, in which two successive one-electron steps give rise to only a single peak couple [79, 80] (see Fig. 10b for 3,6-bis(dimethylamino)durene). This was called “inverse” potential ordering [79], since in such a case oxidation of the intermediate is thermodynamically more easy as compared to that of the starting compound. In several examples, [73, 80, 81] this was attributed to substantial structural changes during the redox process.

An extreme form of structural reorganization is met in dissociative electron transfer [82], in which the electron transfer is accompanied by bond cleavage. Thus, the overall reaction, e.g.



appears totally irreversible, as presented in Fig. 10(c) for benzylchloride, $\text{R} = \text{C}_6\text{H}_5\text{CH}_2$ [74]. The passage from stepwise to concerted (dissociative) mechanisms was explored [82].

2.1.5.2 Selected Recent Examples

This section will selectively present some recent examples of LSV or CV use for the solution of chemical problems. The selection is by no means comprehensive and necessarily limited to only a small number of papers.

The first example shows the possibilities of ultramicroelectrodes (Sect. 2.1.4.1) at extremely fast scan rates (Sect. 2.1.4.2).

Under such conditions very thin diffusion layers (nanometers and below) are generated, offering the study of correspondingly small objects in detail. Thus, fourth generation polyamidoamide (PAMAM) dendrimers with 64 pendant $[\text{Ru}(\text{tpy})_2]^{2+}$ (tpy = terpyridyl) centers (radius ≈ 5 nm) were adsorbed on a Pt electrode immersed into an acetonitrile electrolyte [40, 83]. At (relatively) slow scan rates ($\nu = 36 \text{ kV s}^{-1}$) cyclic voltammograms are close to Langmuirian shape (Sect. 2.1.2.5) with $i_p \sim \nu$, and the dendrimers act as an adsorbed monolayer on the electrode surface (Fig. 11, top left). At high scan rates ($\nu \leq 2.52 \text{ MV s}^{-1}$) the shape of the i/E curves changes to that approaching diffusion control (Fig. 11, bottom) and i_p becomes proportional to $\nu^{1/2}$. Hence, by adjustment of the diffusion layer thickness through ν in molecular dimensions, the “squatted” spheres of the dendrimer molecules on the surface were studied (“electrochemical

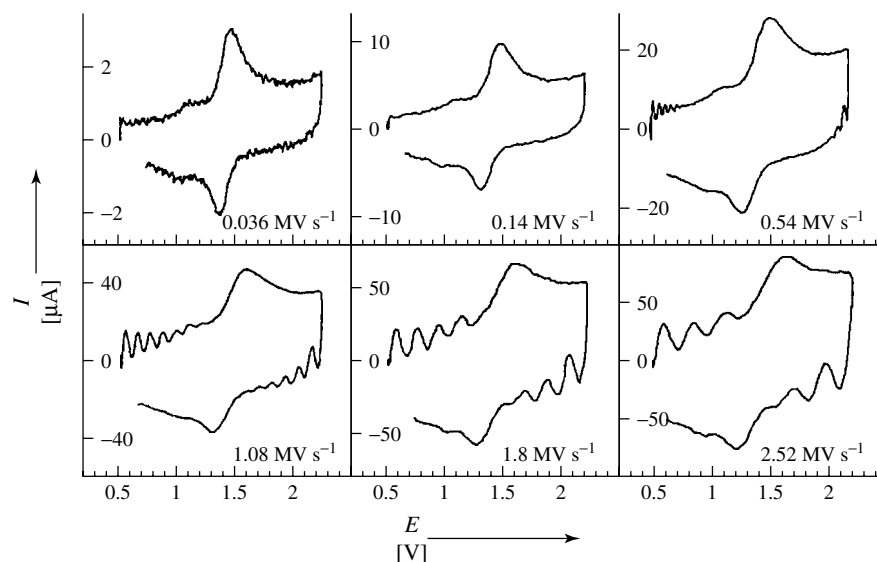
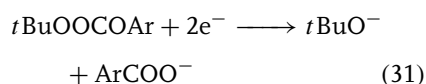


Fig. 11 Cyclic voltammograms of PAMAM dendrimer with 64 pendant $\text{Ru}(\text{tpy})_2^{2+}$ moieties ($\text{CH}_3\text{CN}/0.6 \text{ M } \text{NEt}_4\text{BF}_4$, Pt electrode with radius $5 \mu\text{m}$, scan rates as indicated); (with kind permission of Wiley-VCH from Ref. [40]).

microtome”). The rate of electron transfer between the redox centers in the dendrimer and the mobility of the Ru moieties within the polymer were determined.

The detailed analysis of LSV data using the convolution techniques (Sect. 2.1.4.7) is demonstrated by studies concerned with the electrochemical reduction of perbenzoate *tert*-butylesters [84]. The overall chemically irreversible two-electron reduction leads, by cleavage of the O–O bond, to *tert*-butoxy anion and benzoate anion:



One important question in the light of current electron transfer theories [85–87] is that of the transition between stepwise (electron transfer and bond cleavage as separate elementary steps) or concerted (dissociative electron transfer [88]) mechanisms. For the two extremes, one expects largely different activation parameters for the electron transfer at an electrode. In particular, in contrast to the simple Butler–Volmer relationship (Eq. 18) with a constant transfer coefficient, potential dependent α values become evident. The experimentally accessible apparent transfer coefficient

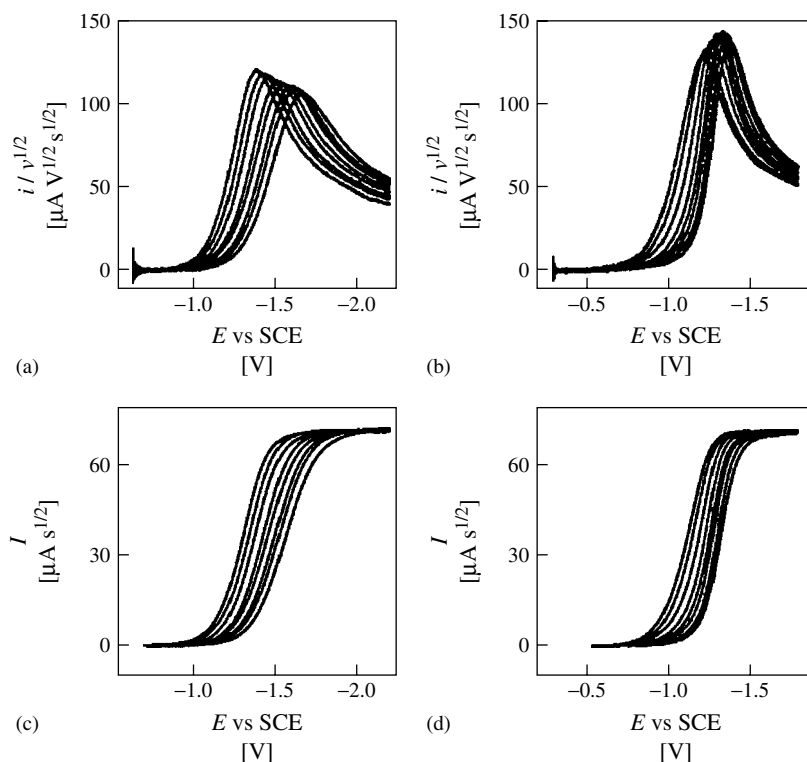


Fig. 12 Cyclic voltammograms (curves in a and b) and the corresponding convoluted semiintegrals (curves in c and d) for the reduction of *tert*-butyl-perbenzoate (a and c) and its *p*-acetyl derivative (b and d) in DMF/0.1 M NBu₄ClO₄ (currents in a and b normalized to $\nu^{1/2}$) at various scan rates. (Reprinted with permission from Ref. [84], Copyright 1999 American Chemical Society.)

$$\alpha_{\text{app}} = -\frac{RT}{F} \left(\frac{d \ln k}{dE} \right) \quad (32)$$

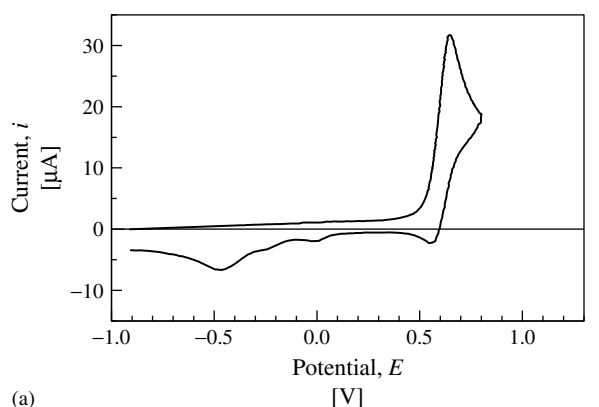
is related to the potential dependence of the heterogeneous electron transfer rate constant k [89]. The latter in turn can be determined from semiintegrated $I(t)$ and original $i(t)$ LSV data as [63, 64]

$$\ln k = \ln D^{1/2} - \ln \frac{I_{\text{lim}} - I(t)}{i(t)} \quad (33)$$

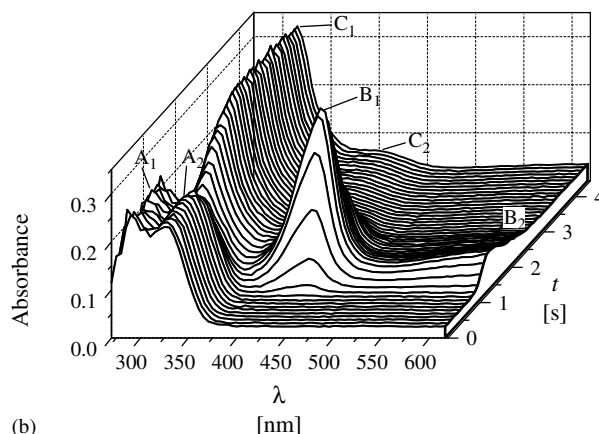
with I_{lim} being the limiting value of the semiintegral. Figure 12 shows LSV

and semiintegral curves for perbenzoic acid *tert*-butyl ester and the *p*-acetyl derivative [84]. Calculation of $\alpha_{\text{app}} = f(E)$ and analysis of this quantity revealed transition from a concerted mechanism in the unsubstituted parent molecule to a stepwise reaction in the *p*-nitro derivative.

Figure 13 shows an example in which UV/Vis-spectroscopy was coupled to CV in order to investigate the anodic oxidation of 1,1-dimethyl-3-aryltriazenes. While the *p*-dimethylamino derivative is reversibly oxidized to a radical cation in a first step,



(a)



(b)

Fig. 13 Cyclic voltammogram (a) and temporal development of UV/Vis spectra during potential scan (b) of 3-(*p*-ethoxyphenyl)-1,1-dimethyl-triazene (with kind permission of Wiley-VCH from Ref. [91]); further details see text and Ref. [91].

less electron-donating substituents lead to more reactive radical cations as primary oxidation products. These have been detected by ESR spectroscopy [90–91]. A detailed picture of the follow-up reaction is derived from the temporal development of UV/Vis-spectra during CV: maxima A₁ and A₂ correspond to the starting triazene, while B₁ and B₂ are assigned to the transient radical cation. The final reaction product exhibits signals C₁ and C₂, which remain stable during the reverse scan of the CV. A comparison to the UV/Vis-spectrum of an authentic sample of the correspondingly substituted phenyldiazonium ion proves the formation of this compound by cleavage of an N–N-bond in the radical cation.

2.1.6

Conclusion

Linear sweep and cyclic voltammetry are among the most widely used electroanalytical techniques for analysis of electron transfer related reactions. They are simple to apply, available in modern computer based electrochemical instruments and backed by extensive theoretical treatment. Besides classical applications in mechanistic analysis (see also Volume 8, Chapter 1), advances in data treatment, ultramicro-electrode use, and combination with other techniques allow the study of molecular electrochemical systems in great detail.

Acknowledgments

I thank Silke Buchmann and Steffen Heiss for technical help with Figs. 1, 5 and 6.

References

1. J. Heyrovský, *Chem. Listy* **1922**, 16, 256–264.
2. J. Heyrovský, *Recl. Trav. Chim.* **1925**, 44, 488–495.
3. J. C. Eklund, A. M. Bond, J. A. Alden et al., *Adv. Phys. Org. Chem.* **1999**, 32, 1–120.
4. L. A. Matheson, N. Nichols, *Trans. Electrochem. Soc.* **1938**, 73, 193–210.
5. J. E. B. Randles, *Trans. Faraday Soc.* **1948**, 44, 322–327.
6. J. E. B. Randles, *Trans. Faraday Soc.* **1948**, 44, 327–338.
7. A. Sevěik, *Collect. Czech. Chem. Commun.* **1948**, 13, 349–377.
8. R. S. Rodgers, *Today Chem. Work* **1995**, 4(6), 30–34.
9. H. Matsuda, Y. Ayabe, *Z. Electrochem.* **1955**, 59, 494–503.
10. F. G. Will, C. A. Knorr, *Z. Elektrochem.* **1960**, 64, 258–269.
11. H. Binder, A. Köhling, G. Sandstede, *Chem.-Ing.-Tech.* **1968**, 40, 543–548.
12. R. S. Nicholson, I. Shain, *Anal. Chem.* **1964**, 36, 706–723.
13. D. H. Evans in *Microelectrodes: Theory and Applications*, (Eds.: M. I. Montenegro et al.), NATO ASI Ser., Ser. E, Kluwer Academic Publishers, Dordrecht, 1991, pp. 17–32, Vol. 197.
14. J. Inczédy, T. Lengyel, A. M. Ure, A. Gelencsér and A. Hulanicki, *Compendium of Analytical Nomenclature*, 3rd ed., Blackwell Science, Oxford, 1998, pp. 8–45.
15. J. M. Savéant, *Electrochim. Acta* **1967**, 12, 999–1030.
16. A. J. Bard, L. R. Faulkner, *Electrochemical Methods. Fundamentals and Applications*, 2nd ed., Wiley, New York, 2001, p. 6.
17. A. J. Bard, L. R. Faulkner, *Electrochemical Methods. Fundamentals and Applications*, 2nd ed., Wiley, New York, 2001, p. 248ff.
18. B. Speiser, *Chem. in uns. Zeit* **1981**, 15, 62–67.
19. J. Heinze, *Angew. Chem.* **1984**, 96, 823–840; *Angew. Chem., Int. Ed. Engl.* **1984**, 23, 831–847.
20. D. H. Evans, *Acc. Chem. Res.* **1977**, 10, 313–319.
21. D. H. Evans, *Chem. Rev.* **1990**, 90, 739–751.
22. J. C. Eklund, A. M. Bond, R. Colton et al., *Inorg. Chem.* **1999**, 38, 2005–2011.
23. J. A. Alden, R. G. Compton, *Anal. Chem.* **2000**, 72, 199A–203A.
24. A. W. Bott, *Curr. Sep.* **1999**, 18, 9–16.
25. B. Speiser, in *Electroanalytical Chemistry*, (Eds.: A. J. Bard, I. Rubinstein), Marcel Dekker, New York, 1996, pp. 1–108, Vol. 19.

26. R. S. Nicholson, *Anal. Chem.* **1966**, 38, 1406.
27. R. S. Nicholson, I. Shain, *Anal. Chem.* **1965**, 37, 178–190.
28. T. W. Rosanske, D. H. Evans, *J. Electroanal. Chem.* **1976**, 72, 277–285.
29. R. H. Wopschall, I. Shain, *Anal. Chem.* **1967**, 39, 1514–1527.
30. E. Laviron, in *Electroanalytical Chemistry*, (Ed.: A. J. Bard), Marcel Dekker, New York 1982, pp. 53–157, Vol. 12.
31. C. Schulz, B. Speiser, *J. Electroanal. Chem.* **1993**, 354, 255–271.
32. E. Laviron, *J. Electroanal. Chem.* **1974**, 52, 395–402.
33. E. Laviron, L. Roullier, *J. Electroanal. Chem.* **1980**, 115, 65–74.
34. R. W. Murray, (Ed.), *Molecular Design of Electrode Surfaces, Techniques of Chemistry*, Wiley & Sons, New York, 1992, Vol. 22.
35. A. J. Bard, L. R. Faulkner, *Electrochemical Methods. Fundamentals and Applications*, 2nd ed., Wiley & Sons, New York, 2001, p. 455ff.
36. R. M. Penner, M. J. Heben, T. L. Longin et al., *Science* **1990**, 250, 1118–1121.
37. W. R. Fawcett, M. Opallo, *Angew. Chem.* **1994**, 106, 2239–2252; *Angew. Chem., Int. Ed. Engl.* **1994**, 33, 2131–2143.
38. H. Kiese, *Anal. Chem.* **1981**, 53, 1952–1954.
39. C. Amatore, in *Physical Electrochemistry. Principles, Methods, and Applications, Monographs in Electroanalytical Chemistry and Electrochemistry*, (Ed.: I. Rubinstein), Marcel Dekker, New York, 1995, pp. 131–208.
40. C. Amatore, Y. Bouret, E. Maisonhaute et al., *Chem. Phys. Chem.* **2001**, 2, 130–134.
41. A. W. Bott, *Curr. Sep.* **1997**, 16, 23–26.
42. J. C. Myland, K. B. Oldham, *Anal. Chem.* **2000**, 72, 3972–3980.
43. D. Britz, *J. Electroanal. Chem.* **1978**, 88, 309–352.
44. A. W. Bott, J. O. Howell, *Curr. Sep.* **1992**, 11, 21–24.
45. E. Eichhorn, A. Rieker, B. Speiser, *Anal. Chim. Acta* **1992**, 256, 243–249.
46. A. M. Bond, K. B. Oldham, G. A. Snook, *Anal. Chem.* **2000**, 72, 3492–3496.
47. J. B. Flanagan, L. Marcoux, *J. Phys. Chem.* **1973**, 77, 1051–1055.
48. J. Heinze, *Angew. Chem.* **1993**, 105, 1327–1349; *Angew. Chem., Int. Ed. Engl.* **1993**, 32, 1268–1288.
49. M. M. Collinson, P. J. Zambrano, H. Wang et al., *Langmuir* **1999**, 15, 662–668.
50. C. Amatore, E. Maisonhaute, G. Simonneau, *Electrochem. Commun.* **2000**, 2, 81–84.
51. J. Ghoroghchian, S. Pons, M. Fleischmann, *J. Electroanal. Chem.* **1991**, 317, 101–108.
52. A. M. Bond, D. C. Coomber, S. W. Feldberg et al., *Anal. Chem.* **2001**, 73, 352–359.
53. J. C. Myland, K. B. Oldham, *Anal. Chem.* **2000**, 72, 3210–3217.
54. R. G. Compton, P. R. Unwin, *J. Electroanal. Chem.* **1986**, 206, 57–67.
55. W. R. Heineman, *Anal. Chem.* **1978**, 50, 390A–402A.
56. W. R. Heineman, *J. Chem. Educ.* **1983**, 60, 305–308.
57. E. Ahlberg, V. D. Parker, *Acta Chem. Scand.* **1981**, B35, 117–121.
58. E. Ahlberg, V. D. Parker, *J. Electroanal. Chem.* **1981**, 121, 73–84.
59. H. Wang, O. Hammerich, *Acta Chem. Scand.* **1992**, 46, 563–573.
60. J.-S. Yu, Z.-X. Zhang, *J. Electroanal. Chem.* **1996**, 403, 1–9.
61. M. Tilset, in *Energ. Organometallic Species*, (Ed.: J. A. Martinho Simões), NATO ASI Ser., Ser. C, Kluwer Academic Publishers, Dordrecht 1992, pp. 109–129, Vol. 367.
62. M. Goto, K. B. Oldham, *Anal. Chem.* **1973**, 45, 2043–2050.
63. J. C. Imbeaux, J. M. Savéant, *J. Electroanal. Chem.* **1973**, 44, 169–187.
64. J. M. Savéant, D. Tessier, *J. Electroanal. Chem.* **1975**, 65, 57–66.
65. J. M. Savéant, D. Tessier, *J. Electroanal. Chem.* **1977**, 77, 225–235.
66. P. J. Mahon, K. B. Oldham, *J. Electroanal. Chem.* **1998**, 445, 179–195.
67. K. B. Oldham, *Anal. Chem.* **1973**, 45, 39–47.
68. J. M. Rodríguez Mellado, *Comput. Chem.* **1991**, 15, 235–236.
69. I. Prieto, J. M. Pedrosa, M. T. Martín et al., *J. Electroanal. Chem.* **2000**, 485, 7–12.
70. P. E. Whitson, H. W. VandenBorn, D. H. Evans, *Anal. Chem.* **1973**, 45, 1298–1306.
71. R. S. Rodgers, *Anal. Chem.* **1975**, 47, 281–285.
72. A. Bobrowski, G. Kasprzyk, J. Mocák, *Collect. Czech. Chem. Commun.* **2000**, 65, 979–994.
73. K. Hu, D. H. Evans, *J. Electroanal. Chem.* **1997**, 423, 29–35.
74. C. P. Andrieux, A. Le Gorand, J.-M. Savéant, *J. Am. Chem. Soc.* **1992**, 114, 6892–6904.
75. H. D. Roth, *Tetrahedron* **1986**, 42, 6097–6100.
76. T. Yao, S. Musha, M. Munemori, *Chem. Lett.* **1974**, 939–944.

77. M. A. Zón, H. Fernández, J. *Electroanal. Chem.* **1990**, 295, 41–58.
78. G. Gritzner, J. Kùta, *Pure Appl. Chem.* **1984**, 56, 461–466.
79. D. H. Evans, K. Hu, *J. Chem. Soc., Faraday Trans.* **1996**, 92, 3983–3990.
80. B. Speiser, M. Würde, C. Maichle-Mössmer, *Chem.-Eur. J.* **1998**, 4, 222–233.
81. K. Hu, D. H. Evans, *J. Phys. Chem.* **1996**, 100, 3030–3036.
82. J.-M. Savéant, *Adv. Phys. Org. Chem.* **1990**, 26, 1–130.
83. C. Amatore, Y. Bouret, E. Maisonhaute et al., *Chem.-Eur. J.* **2001**, 7, 2206–2226.
84. S. Antonello, F. Maran, *J. Am. Chem. Soc.* **1999**, 121, 9668–9676.
85. R. A. Marcus, *Angew. Chem.* **1993**, 105, 1161–1172; *Angew. Chem., Int. Ed. Engl.* **1993**, 32, 1111–1121.
86. R. A. Marcus, *J. Electroanal. Chem.* **1997**, 438, 251–259.
87. J.-M. Savéant, *Pure Appl. Chem.* **1997**, 69, 269–271.
88. J.-M. Savéant, *Adv. Electron Transfer Chem.* **1994**, 4, 53–116.
89. S. Antonello, F. Maran, *J. Am. Chem. Soc.* **1997**, 119, 12 595–12 600.
90. B. Gollas, B. Speiser, *Angew. Chem.* **1992**, 104, 336–338; *Angew. Chem. Int. Ed. Engl.* **1992**, 31, 332–334.
91. L. Dunsch, B. Gollas, A. Neudeck et al., *Chem. Ber.* **1994**, 127, 2423–2429.

2.2

Step and Pulse Techniques

Christopher M. A. Brett and Ana Maria Oliveira Brett
Universidade de Coimbra, Coimbra, Portugal

2.2.1

Introduction

Step and pulse techniques are now an essential part of the armory of techniques employed by the electrochemist. When first introduced, applications were essentially limited to discrete single or double steps in applied potential (or current), the response to the perturbation being monitored as a function of time – chronoamperometry (or chronopotentiometry). There were instrumental difficulties in implementing anything more complex, as has happened with the first version of square wave polarography in the 1950s [1]. A number of current sampling strategies were developed in connection with dropping mercury electrodes and synchronization with drop growth, and this led to the advent of normal pulse and differential pulse polarography in the 1970s, which were the first widely available pulse techniques [2]. Nevertheless, the instrumentation permitted very little flexibility in experimental conditions.

Developments in microprocessor-based instrumentation completely changed the situation. Nowadays, nearly all commercial instruments – potentiostats and galvanostats – are digitally based, which means that the programming of an almost infinite variety of step and pulse waveforms has become relatively easy to carry out. This opens up a multitude of exciting possibilities to the experimentalist, since he can adapt the applied waveforms to the kinetics and mechanism of the electrode reaction under study, so long as there

is an appropriate theoretical description. Nevertheless, two possible drawbacks of digital instruments should be pointed out. First, potential and current ramps have been replaced by staircases, which may or may not give an equivalent response depending on the step size. Secondly, the response is *sampled*, which may lead to an increase in noise. Both these problems and the strategy adopted in order to circumvent them will be discussed during the course of the chapter. Further details on analog and digital instrumentation can be found in Chapter 1.2.

The chapter begins with a theoretical description of the potential step and the resulting current response. This is then extended to a double potential step. Following this, pulse and square wave techniques are introduced and described, together with applications. Current step techniques are then discussed together with their application.

2.2.2

Potential Step

All potential pulse techniques are based on combinations of potential steps. It is therefore of importance to understand the current response to potential steps as a function of time. Further details can be found in Ref. [3].

2.2.2.1 Single Potential Step

We begin with the derivation of the response to a potential step from a value at which no current flows, to one at which the diffusion-limited current passes, Fig. 1(a). The response of the current to this perturbation will be a sharp change from zero current followed by relaxation to a value close to zero, the final steady state magnitude of which is determined by the flow of species to the electrode surface. As will

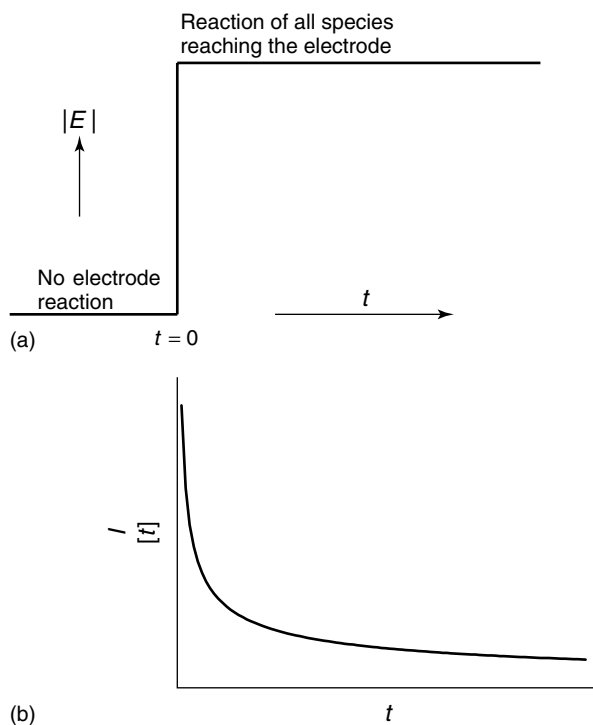


Fig. 1 Potential step chronoamperometry: (a) schematic application of potential step and (b) chronoamperometric response.

be seen, this varies according to electrode geometry and solution convection. In this section, we will consider only diffusion induced by concentration gradients of the electroactive species.

For a uniformly accessible planar electrode, the diffusion process is known as semi-infinite linear diffusion, since it can be assumed to occur only in one dimension perpendicular to the electrode surface. The observed current depends directly on the concentration gradient at the electrode surface, $(\partial c / \partial x)_0$. According to Fick's first law

$$I = nFAD \left(\frac{\partial c}{\partial x} \right)_0 \quad (1)$$

where x is the perpendicular distance from the electrode. Since the concentration

gradient changes with time, it is necessary to solve Fick's second law to obtain the chronoamperometric response

$$\frac{\partial c}{\partial t} = D \frac{\partial^2 c}{\partial x^2} \quad (2)$$

The boundary conditions are

$$t = 0 \quad \text{No electrode reaction } c_0 = c_\infty \quad (3a)$$

$$t \geq 0 \quad \text{Bulk solution } \lim_{x \rightarrow \infty} c = c_\infty \quad (3b)$$

$$t > 0 \quad \text{Diffusion-limited current, } I_d, \quad \text{at electrode surface} \quad (3c)$$

The mathematical solution of this equation is most easily carried out using Laplace transforms and leads to the expressions

- for the variation of concentration with distance from the electrode

$$c = c_{\infty} \left\{ 1 - \operatorname{erfc} \left[\frac{x}{x(Dt)^{1/2}} \right] \right\} \quad (4)$$

- for the concentration gradient at the electrode surface

$$\left(\frac{\partial c}{\partial x} \right)_0 = \frac{1}{(\pi Dt)^{1/2}} \quad (5)$$

The calculated current is therefore

$$I(t) = I_d(t) = \frac{nFAD^{1/2}c_{\infty}}{(\pi t)^{1/2}} \quad (6)$$

which is known as the *Cottrell equation* [4]. Note that the current decays with the square root of time, as illustrated in Fig. 1(b).

At a spherical electrode of radius r_0 , which corresponds to a first approximation to a mercury drop electrode, the form of Fick's second law to solve is

$$\frac{\partial c}{\partial t} = D \left\{ \frac{\partial^2 c}{\partial r^2} + \frac{2}{r} \frac{\partial c}{\partial r} \right\} \quad (7)$$

and the boundary conditions are

$$t = 0 \quad r \geq r_0 \quad \text{No electrode reaction } c_0 = c_{\infty} \quad (8a)$$

$$t \geq 0 \quad \text{Bulk solution } \lim_{r \rightarrow \infty} c = c_{\infty} \quad (8b)$$

$$t > 0 \quad r = r_0 \quad \text{Diffusion-limited current, } I_d, \text{ at electrode surface } (8c)$$

The calculated diffusion-limited current is

$$I_d(t) = nFADc_{\infty} \left[\frac{1}{(\pi Dt)^{1/2}} + \frac{1}{r_0} \right] \quad (9)$$

It can be seen by comparison with Eq. (6) that this is the Cottrell equation together with a correction term for spherical diffusion. The reason for these two terms can be easily understood in

that if the sphere is large (corresponding to small $1/r_0$), then the effects of sphericity are small and there is essentially only semiinfinite linear diffusion. The other extreme represents the situation at very small electrodes and a steady state current is predicted. The reason for this is that a very steep concentration gradient is created, which sucks in electroactive species; this situation occurs for microelectrodes.

Below the transport-limited current, kinetics have to be taken into account. The relevant expressions for the current are given in Table 1 for both planar and spherical electrodes, considering that only the reduced species is initially present in solution. This is what is usually encountered in practice. Details of the derivation of these expressions may be found in Ref. [3].

A point that has not been considered so far, but which becomes crucial on using pulse techniques that are combinations of potential steps, is that of capacitive currents. These are predominantly due to changes in the charge of the electrolyte double layer on applying a potential step ΔE . If a constant double layer differential capacity, C_d , is assumed, then the charging current is given by

$$I_C = \frac{\Delta E}{R} \exp \left(\frac{-t}{RC_d} \right) \quad (10)$$

where R is the solution resistance. Whereas R is independent of electrode area, C_d is directly dependent and so I_C is proportional exponentially to the electrode area. Since the voltammetric current is directly proportional to electrode area, the ratio I_f/I_C increases with decreasing electrode area. This is a good reason for using microelectrodes (Chapter 2.5).

Tab. 1 Current responses following application of a potential step to the system $R \rightarrow O + ne^-$ with only R initially present in solution

		Current [I]
Reversible	Plane	$\frac{nFADc_\infty}{(1+\theta)(\pi Dt)^{1/2}}$
	Sphere	$\frac{nFADc_\infty}{(1+\theta)} \left[\frac{1}{(\pi Dt)^{1/2}} + \frac{1}{r_0} \right]$
Irreversible	Plane	$nFAk_\infty \left[\exp \frac{k^2 t}{D} \operatorname{erfc} \left(\frac{kt^{1/2}}{D^{1/2}} \right) \right]$
	Sphere	$nFAk_\infty \left[\left(1 + \frac{D}{kr_0} \right) \exp \frac{k^2 t}{D} \operatorname{erfc} \left(\frac{kt^{1/2}}{D^{1/2}} \right) - \frac{D}{kr_0} \right]$
Irreversible (small t)	Plane and sphere	$nFAk_\infty \left(1 - \frac{2kt^{1/2}}{(\pi D)^{1/2}} \right)$
$\theta = \exp[(nF/RT)(E - E^{\theta'})]$		k rate constant of electrode reaction

2.2.2.2 Double Potential Step

The second step toward the development of a pulse technique is that of a double potential step in which the potential is altered between two values. The simplest case is to return to a value at which no electrode reaction occurs, the step being inverted after a time τ . The expressions that are obtained for initial oxidation of a species of concentration c to the region of the diffusion-limited current are

$$t < \tau \quad I = \frac{nFAD^{1/2}c_\infty}{(\pi t)^{1/2}} \quad (11)$$

$$t > \tau \quad I = nFAD^{1/2}c_\infty \times \left[\frac{1}{(\pi t)^{1/2}} - \frac{1}{\pi(t-\tau)^{1/2}} \right] \quad (12)$$

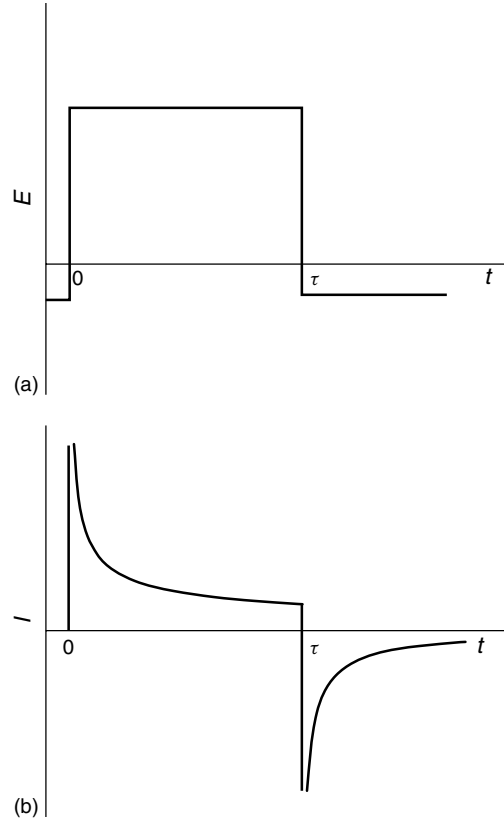
showing that the backward response is superimposed on the continuation of the forward response (Fig. 2). There is thus a memory effect that also appears in square wave voltammetry (SWV). Expressions for kinetic control in one of the two steps and in both steps exist in the literature [5].

There are situations in which interference effects can be removed by the use of a double potential step. For example, if two electroactive species are oxidized at the same potential and only one of them can be reduced, then more information can be gained.

2.2.2.3 Potential Step Chronocoulometry

In the previous subsections, the chronoamperometric response to a potential step or steps has been evaluated. However, experimentally it may be advantageous to study the variation of charge with time – chronocoulometry [6]. Although it may appear that integration of a chronoamperometric signal after the experiment, which is easy to do in a modern digitally based potentiostat, is equivalent, there are subtle differences that can be useful and concern the reduction of signal noise if the charge is registered directly. In particular, the recording of the charge leads to improved signal-to-noise ratios toward the end of the transients when the current is close to zero.

Fig. 2 Double potential step:
(a) potential-time waveform and
(b) current response.



Additionally, integration reduces signal noise in general.

If a potential step is applied from a region of zero current, the expressions given in Table 1 may be integrated to give the corresponding charge, Q .

In the case of a step to the diffusion-limited current region, the integrated Cottrell equation is obtained:

$$Q_t = \frac{2nFAD^{1/2}c_\infty t^{1/2}}{\pi^{1/2}} \quad (13)$$

When capacitive charges – and possibly oxidation or reduction of adsorbed species – are taken into account, there may be a nonzero intercept (see upper line in Fig. 3).

A double potential step, following from Eq. (12), leads to

$$Q_{t>\tau} = \frac{2nFAD^{1/2}c_\infty}{\pi^{1/2}} \left[t^{1/2} - (t - \tau)^{1/2} \right] \quad (14)$$

This can be particularly useful because when $t > \tau$, there is no net capacitive contribution to the charge, that is, the difference between the charges at time $(t - \tau)$ and time t . Thus, the adsorption phenomena can be probed. For this, the charge difference, Q_{dif} , between Q_τ and $Q_{t>\tau}$ is necessary and is given by

$$Q_{\text{dif}} = \frac{2nFAD^{1/2}c_\infty}{\pi^{1/2}} \times \left[\tau^{1/2} - t^{1/2} + (t - \tau)^{1/2} \right] \quad (15)$$

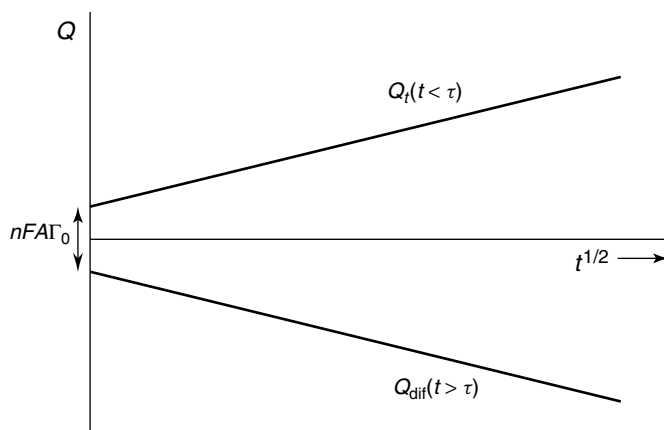


Fig. 3 Double potential step chronocoulometry, showing deduction of surface concentration of adsorbed species. See text for details.

Figure 3 shows plots of Q_t vs $t^{1/2}$ and of Q_{dif} vs $t^{1/2}$ and how the surface concentrations, Γ_0 , of adsorbed species may be deduced.

2.2.3

Staircase Voltammetry

The main importance of staircase voltammetry, in the context of this chapter, is that it forms an integral part of many widely practiced pulse techniques. In staircase voltammetry, a sequence of potential steps

of equal height is applied to the electrode, and the current is sampled toward the end of each step of width τ (Fig. 4). It was originally devised to work in conjunction with the dropping mercury electrode (*tast polarography*), and here the periodic renewal of the electrode at the end of each step precluded any memory effects between current sampling in the consecutive steps.

However, at a nonrenewed electrode, the response to a staircase waveform of this kind is similar to that from a linear

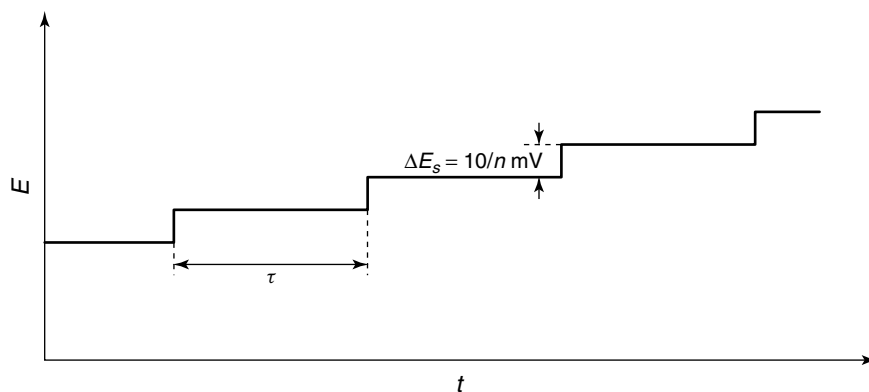


Fig. 4 Staircase voltammetry waveform.

ramp. In modern digital potentiostats, linear sweep, and cyclic voltammetry are usually implemented as a staircase waveform (Fig. 4). In this context, it is therefore important to quantify the conditions under which staircase and linear sweep/cyclic responses are equivalent. It has been shown in Ref. [7] for a simple electrode process that these criteria are that the current is sampled after 0.25 of the step width ($\tau/4$) and for more complicated cases from $\tau/4$ up to $\tau/2$ [8]. Obviously there is also a dependence on step height, ΔE_s . Whatever the mechanism of the reaction, theory shows that the differences between sampling times become insignificant if $n\Delta E_s < 0.26$ mV [9], a situation that is not easy to accomplish in practice, since a single linear sweep scan of 500 mV would require over 1900 current sampling points.

In fact, the error is usually not significant for $n\Delta E_s < 5$ mV and with sampling times close to the end of the step, this later sampling time ensuring a lesser, hopefully zero, capacitive contribution. Often, higher values are permitted by the instruments, although the justification for treating the experiment as linear scan in such cases, that is, whether the results should be analyzed as staircase voltammetry, should be addressed. Either a true linear ramp must be used or the current-time profile properly analyzed as a staircase voltammogram (see Sect. 2.2.2). Particular care must be exercised when studying adsorption phenomena, although recognizing the existence of a pulsed response can be used to good advantage for measuring rate constants of adsorbed species [10].

2.2.4

Pulse Techniques

Many pulse techniques have been devised on the basis of a succession of potential

steps of varying height and in forward or reverse direction, with current sampling. Much of the important work in this area has been summarized in literature reviews [11–13].

As seen in previous sections, the response to a potential step is a pulse of current, which decreases with time as the electroactive species near the electrode surface is consumed and consists of a faradaic, I_f , and a capacitive contribution, I_C . The advantage of most pulse techniques results from the measurement of the current flow near the end of the pulse when the faradaic current has decayed, often to a diffusion-limited value but when the capacitive current is insignificant. Pulse widths, t_p , are adjusted to satisfy this condition and the additional condition that time has not been allowed for natural convection effects to influence the response. There is a greatly improved signal-to-noise ratio (sensitivity) compared to steady state techniques and in many cases, greater selectivity. Detection limits are of the order of 10^{-7} M. Furthermore, for analytical purposes, most current-voltage profiles from the pulse techniques are faster to interpret than those of dc voltammograms, because they are peak-shaped rather than the typical step curve of conventional voltammetric methods.

Pulse voltammetric techniques, most used in electrochemistry, are normal pulse voltammetry (NPV) and differential pulse voltammetry (DPV). In square wave voltammetry (SWV), there may be a non-faradaic contribution to the individual currents but the current sampling strategy essentially eliminates this through subtraction, as will be seen in Sect. 2.2.4.3. SWV was pioneered by Barker [1] in the 1950s, but due to instrumentation development only 40 years

later did its use by electrochemists for analytical, kinetic, and mechanistic work become widespread.

2.2.4.1 Normal Pulse Voltammetry (NPV)

NPV involves the imposition of square wave voltage pulses (i.e. potential steps of fixed time duration) of increasing height upon a constant value of applied potential (Fig. 5a). This base potential, E_{base} , is chosen where $I = 0$, that is, no faradaic

reaction occurs. The potential increment, ΔE , between successive pulses is constant, and sufficient time should be left between pulses for the current on the reverse step to die away to zero and for all concentration gradients to disappear. The current is measured near the end of the pulse and a plot made of the successive current sampled points against the potential of the applied pulses. This gives a voltammetric profile of the same form as a steady state

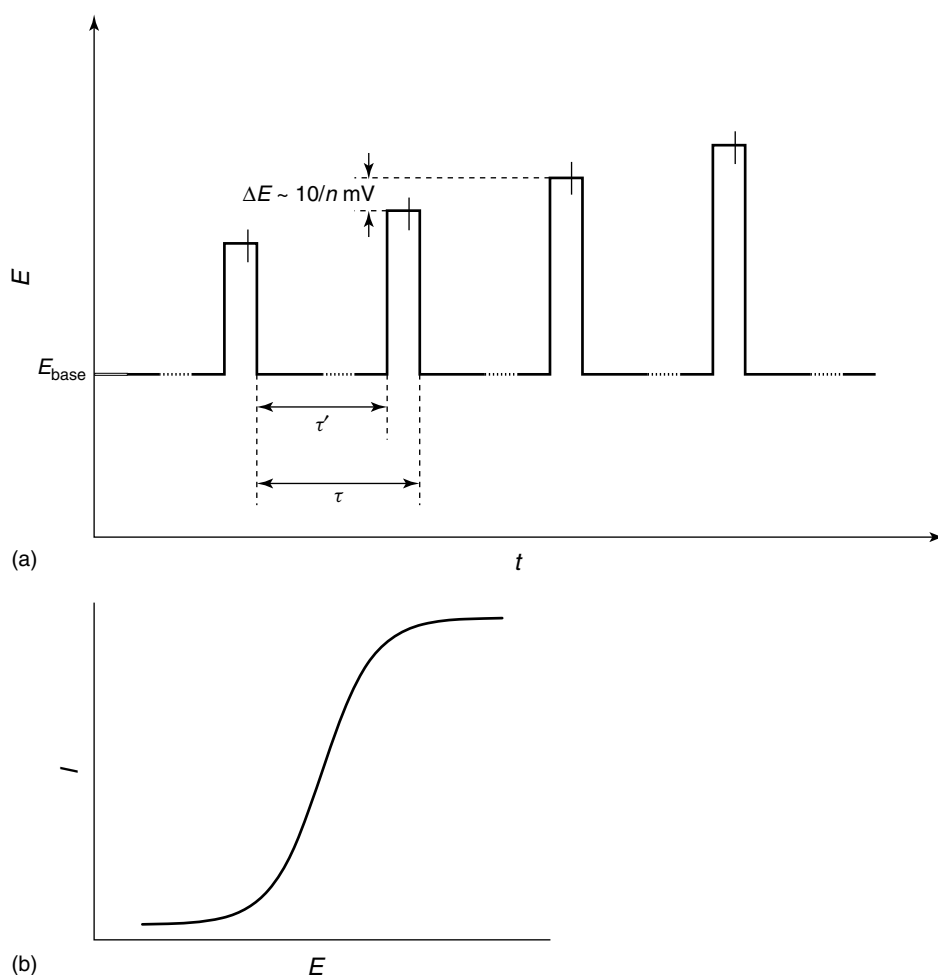


Fig. 5 Normal pulse voltammetry: (a) potential-time waveform and (b) schematic voltammogram.

voltammogram, Fig. 5(b), as can also be seen from the expressions in Table 1, which are directly applicable. Effective sweep rates, determined by the staircase period, τ , are generally of the order of 1 to 10 mV s⁻¹, corresponding to intervals between pulses of 2 to 4 s; pulse widths usually vary between 5 and 100 ms.

The maximum obtainable current is thus given by the Cottrell equation

$$I_{\max} = \frac{nFAD^{1/2}c_{\infty}}{(\pi t_m)^{1/2}} \quad (16)$$

where t_m is the sampling time after application of the pulse. If t_m is constant throughout the NP scan for a given electroactive species, then the current is directly proportional to concentration.

A pulse leads to higher mass transport than a hydrodynamic electrode (Chapter 2.4) owing to the sharply induced concentration gradient, so that kinetic effects may be more visible. In particular, an electrode reaction that appears reversible at a hydrodynamic electrode may become quasi-reversible under NPV conditions. Another important advantage of the use of pulses starting at the base potential is that irreversible adsorption of the product of the electrode reaction will be much reduced and the short timescale may mean that effects of coupled homogeneous reactions are not observed.

The NPV technique was first developed as NP polarography (NPP) at dropping mercury electrodes. In these cases, the pulses are synchronized with the drops, the pulse being applied near the end of drop life when the increase in the surface area of the drop is least. Current sampling in NPP also serves to remove the oscillations resulting from drop formation.

When there are parallel electrode reactions of the initial electroactive species or interfering species, a modification of NPV

may be useful. For this, the base potential is fixed at the potential corresponding to the diffusion-limited reaction and the pulses are applied in the reverse direction. This is called *reverse pulse voltammetry* (RPV).

The influence of reactant adsorption on the shape and height of the NP voltammogram has been investigated and is conveniently summarized in Ref. [14].

2.2.4.2 Differential Pulse Voltammetry (DPV)

In DPV, the difference between two sampled currents is measured, registered just before the end of the pulse and just before pulse application. In the first instruments to offer this technique, the pulses were superimposed on a linear ramp of potential. However, in digital potentiostats, it is simpler to superimpose the pulses on a staircase waveform. Thus, the base potential is incremented in a staircase (Fig. 4) and the pulse, of constant height, is of width 10 or more times smaller than the period of the staircase waveform (Fig. 6a). If these conditions are followed, the staircase width is generally the same as for NPV, so that once again the effective sweep rate is of the order of 1 to 10 mV s⁻¹.

The difference between the two sampled currents ($I(2) - I(1)$) is plotted against the staircase potential and leads to a peak-shaped waveform, as shown in Fig. 6(b).

The peak for a reversible system occurs at a potential

$$E_p = E_{1/2} - \frac{\Delta E}{2} \quad (17)$$

where ΔE is the pulse amplitude (with sign included). The reason for the difference between E_p and $E_{1/2}$ for fast kinetics is that the current is plotted as a function of E_{base} and not as a function of the potential halfway up the pulse.

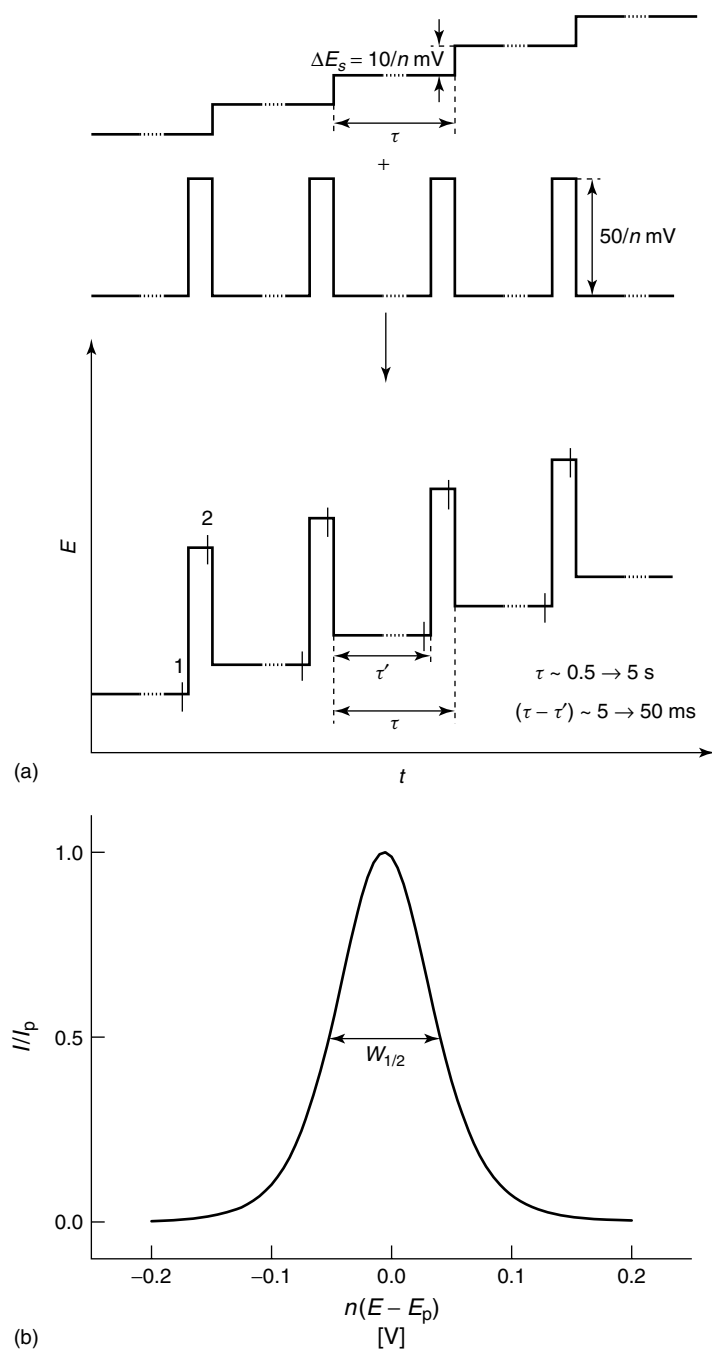


Fig. 6 Differential pulse voltammetry: (a) potential-time waveform: sum of staircase and synchronized pulses and (b) schematic voltammogram.

The corresponding current, I_p , is given by the expression

$$I_p = -\frac{nFAD^{1/2}c_\infty}{(\pi t_m)^{1/2}} \left(\frac{1-\sigma}{1+\sigma} \right) = I_{\text{Cot}} \left(\frac{1-\sigma}{1+\sigma} \right) \quad (18)$$

where

$$\sigma = \exp \left(\frac{nF}{RT} \frac{\Delta E}{2} \right) \quad (19)$$

and I_{Cot} is the current in the Cottrell equation at the sampling time t_m (Eq. 16). Two extreme cases of this expression can be considered:

- Large $|\Delta E|$, $\sigma \gg 1$. The term $(1-\sigma)/(1+\sigma)$ becomes ± 1 (reduction or oxidation, respectively), equal to the value for NPV (Eq. 16), and $I_p = I_{\text{Cot}}$.
- Small $|\Delta E|$. By expansion of $(1-\sigma)/(1+\sigma)$, one finds $\sigma \rightarrow (nF\Delta E/4RT)$.

$$I_p = -\frac{n^2 F^2 A D^{1/2} c_\infty}{4RT (\pi t_m)^{1/2}} \Delta E = I_{\text{Cot}} \left(\frac{nF\Delta E}{4RT} \right) \quad (20)$$

This latter equation is valid if ΔE is less than $(2RT/nF)$ but appears to be applicable for larger pulse heights.

The expression for the half-width at half-height, $W_{1/2}$

$$W_{1/2} = \frac{3.52RT}{nF} \quad (21)$$

is equal to a value of $90.4/n$ mV at 25°C , showing that peaks separated by $50/n$ mV can be resolved.

As the system becomes more irreversible, the difference between $E_{1/2}$ for a reversible system and E_p increases, the peak becomes wider and its height

decreases. Values of ΔE greater than 100 mV are not useful because the peak width increases with the pulse amplitude. Many applications have been described. An interesting example is the oxidation of the bases of single strand DNA, in which an oxidation scan followed by a reduction differential pulse scan clearly show the adsorption and blocking of the electrode surface [15]; the relatively slow timescale of the DP scan is appropriate for this purpose.

The effect of adsorption of reactants on peak shape and peak potential has been thoroughly studied and is summarized in Ref. [14].

2.2.4.3 Square Wave Voltammetry (SWV)

The form of SWV most electrochemists use today is based on work dating from 1969 [16] and principally developed by Osteryoung and coworkers using *large amplitude* pulses [11, 17], such that a steady state is not achieved, and it has taken over a large part of the traditional domain of application of DPV.

The potential waveform consists of a square wave superimposed on a staircase (Fig. 7). The current at the end of the forward pulse, I_f , and the current at the end of the reverse pulse, I_b , are both registered as a function of staircase potential, which is midway between the potentials corresponding to the forward and backward potential steps. Usually the net current, I_{net} , that is $(I_f - I_b)$, is plotted against E . Since I_f and I_b usually have opposite signs, the difference, I_{net} , is larger than each individual component in the region of the peak that is centered on the half-wave potential. At potentials corresponding to the diffusion-limited current, $I_{\text{net}} = 0$. Examples of square wave responses are shown in Fig. 8.

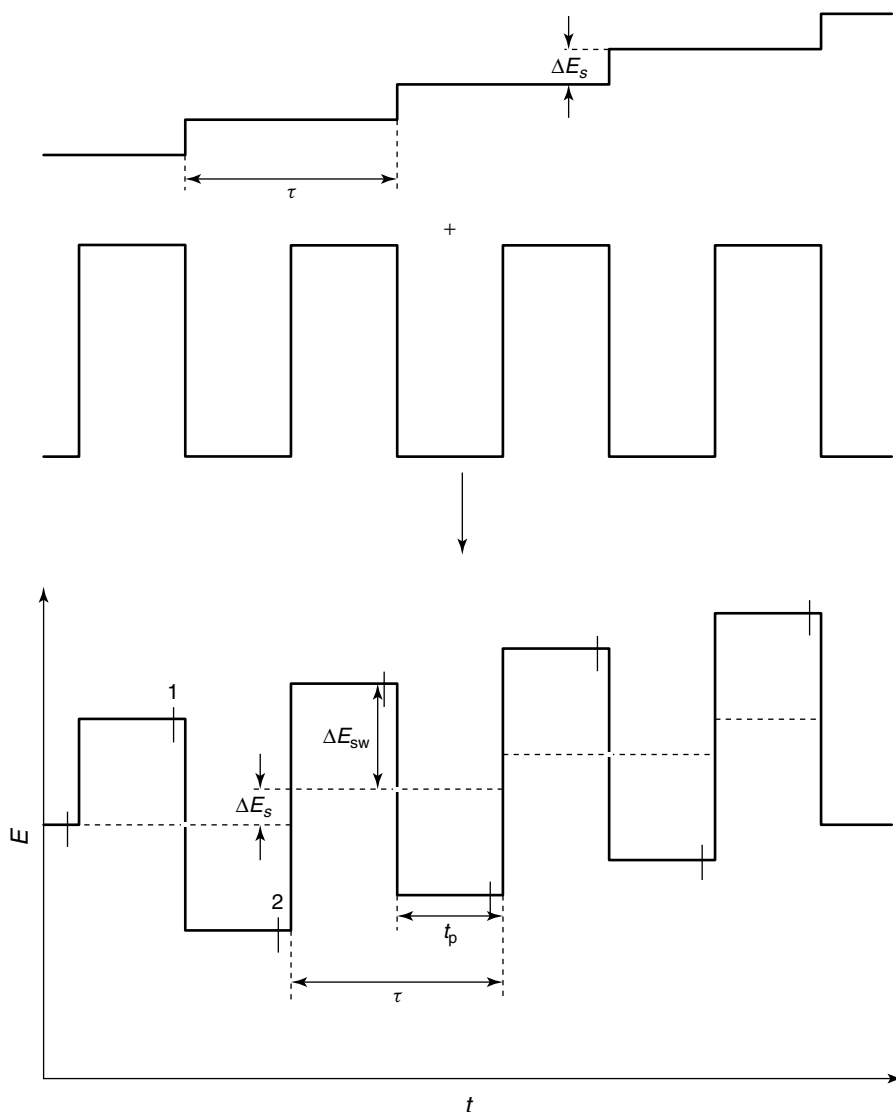


Fig. 7 Square wave voltammetry potential-time waveform: sum of staircase and synchronized square wave.

Over the small potential range between forward and reverse pulses, the interfacial capacity is normally constant, and thus calculation of the difference between responses from backward and forward pulses effectively annuls the capacitive contributions. It is not necessary to wait

until I_C dies away, which is a disadvantage of techniques such as fast scan cyclic voltammetry. Consequently, higher scan rates can be used in SWV because it effectively removes the background current from the measurements. This means that there is the possibility of

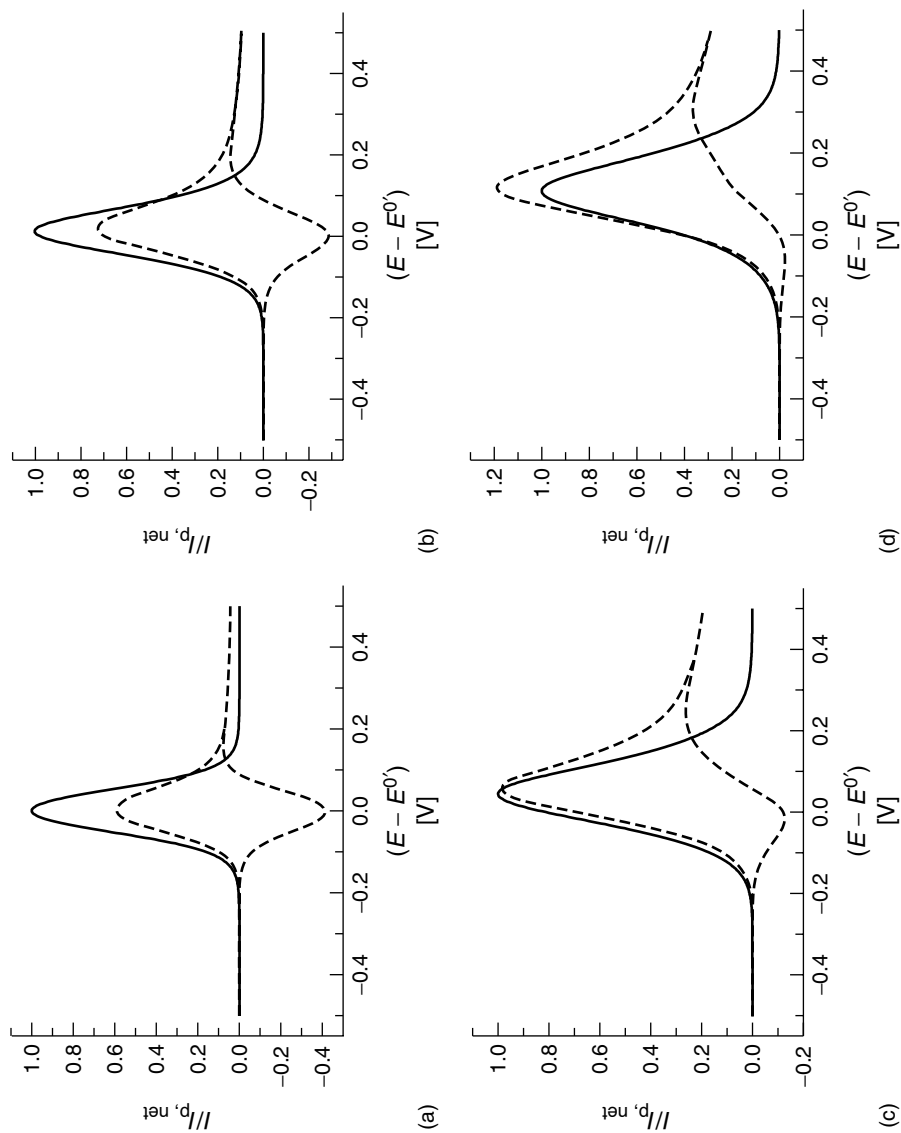


Fig. 8 Square wave voltammogram profiles for $R \rightarrow O + e^-$. (a) Reversible reaction and $k_0 =$ (b) 0.3, (c) 0.1, and (d) 0.03 cm s^{-1} . $\Delta E_{\text{sw}} = 50 \text{ mV}$, $f = 50 \text{ Hz}$, $\alpha_c = 0.5$. Dotted lines show forward and backward currents and solid line the net current.

investigating kinetic systems, in particular with fast reactions. The three different plots of I_f , I_b , and I_{net} may also be overlaid, the resulting combination plot, such as those in Fig. 8 having been suggested as the most useful form for investigating kinetics and mechanisms [18].

SWV is characterized by four parameters: square wave period, τ , pulse width, $t_p = \tau/2$, step height, ΔE_s , and pulse height, ΔE_{sw} . The pulse width is related to the square wave frequency, $f = 1/(2t_p)$ and as the staircase step at the beginning of each cycle is ΔE_s , it means that the effective scan rate is $v = \Delta E_s/2t_p = f \Delta E_s$.

A square wave can be described by the equation

$$E = -(-1)^m \Delta E_{\text{sw}} \quad (22)$$

and in combination with a staircase waveform, this leads to

$$E_m = E_i \pm \left[\text{Int} \left(\frac{m+1}{2} \right) - 1 \right] \times \Delta E_s \mu(-1)^m \Delta E_{\text{sw}} \quad (23)$$

where the upper signs refer to a positive-going scan and the lower to a negative-going scan, and “Int” refers to the integer part of the expression. Thus, odd values of m refer to the forward pulse and even values of m to the backward pulse.

Because there is a memory effect between each potential step, the current is given for each value of m at time t_p , after application of the step by

$$I_m = I_{\text{Cot}} \sum_{i=1}^m \frac{Q_i - Q_{i-1}}{(m-i+1)^{1/2}} = I_{\text{Cot}} \Psi_p \quad (24)$$

in which $Q_i = \theta_i/(1 + \theta_i)$, assuming equal diffusion coefficients for oxidized and reduced species, and is defined as in Table 1 for potential step. It can be seen that Ψ_p is a dimensionless current relating the observed current to that which would be obtained from the Cottrell equation.

Subtraction of neighboring values of I_m leads to the difference current. The peak current is given by

$$I_p = I_{\text{Cot}} \Delta \Psi_p \quad (25)$$

For a reversible reaction, the peak current is symmetrical about the peak potential, which is identical to the reversible half-wave potential. In this case, the form of the peak is the exact differential of the steady state voltammetric curve, as would be expected.

Some representative values of Ψ_p are shown in Table 2. It can be seen from the form of this equation that a peak shape will be obtained.

Tab. 2 Peak current dimensionless scaling factors, Ψ_p , for square wave voltammetry (see Eq. 25) [10]

$n\Delta E_{\text{sw}}[\text{mV}]$	$n\Delta E_s[\text{mV}]$			
	1	5	10	20
0	0.0053	0.0238	0.0437	0.0774
10	0.2376	0.2549	0.2726	0.2998
20	0.4531	0.4686	0.4845	0.5077
50	0.9098	0.9186	0.9281	0.9432
100	1.1619	1.1643	1.1675	1.1745

The pulse width, t_p , is usually varied over a large range 1 to 500 ms, that is, $f = 1$ to 500 Hz, and defines the experimental timescale, whereas ΔE_s is much smaller than ΔE_{sw} . Recommended values are $\Delta E_s = 10/n$ mV for staircase step height, and $\Delta E_{sw} = 50/n$ mV for pulse height. Thus, the pulses can be shorter than in DPV or NPV and a broader spectrum of scan rates can be applied. Since effective sweep rates of 1 to 10 mV s⁻¹, as in DPV, to scan rates of 1 V s⁻¹ or higher can be employed, this enables the achievement of kinetic and analytical data with the same technique. Because of the lower consumption of electroactive species by reaction in relation to DPV, there are less problems of blocking the electrode surface.

However, care must be taken with the interpretation of SWV data, as illustrated in Fig. 8. Figure 8(a) shows profiles for the forward and reverse and net currents for a reversible reaction. If the electrode kinetics are slow, then the forward current is shifted to higher overpotentials than the reverse current, which becomes relatively smaller, at the same time as the peak width becomes greater. This is demonstrated in Figs. 8(b) to (d).

In a multistep reaction with a first rate-determining quasi-reversible step, two peaks may appear. Unless the individual forward and backward current profiles are monitored, the erroneous conclusion that two species are reacting could be reached. Similarly, if there is adsorption, many different nuances of which have been investigated [19–22], then effects on the peaks become apparent, and the reverse peak can entirely disappear. The response at mercury film electrodes has also been deduced and tested [23]. Fortunately, fitting and simulation software packages exist that can aid in the task of unravelling mechanisms and kinetics and theoretical

approaches for more complex cases have been developed [24–26].

An important advantage of SWV for many electroanalytical applications is that in the negative potential region, oxygen does not have to be excluded from solution when using SWV, unless it directly interferes with the electrode reaction under study for two reasons. First, in the limiting-current region for oxygen reduction, the forward and reverse currents are equal leading to a zero net current. Second, during a scan from negative potentials in the positive direction, the fast effective scan rate means that no electroactive oxygen species have time to diffuse to the electrode surface from bulk solution. Thus, the experimental time is less and procedures are simplified because prior bubbling of nitrogen or argon in the solution is avoided. This is used to good effect in anodic stripping voltammetry, in particular in combination with square wave injection techniques [27, 28] or with ultrasound [29] in which simplifying protocols is a useful advantage.

SWV also allows the possibility of measurements over a wide dynamic range, defined as its ability to respond to both high and low concentrations of electroactive species. Additionally, the rapidity means that successive voltammograms can be recorded and a voltammetric profile with time registered, for example, for analysis of eluents from a high-pressure liquid chromatography column.

2.2.4.4 Other Pulse Techniques

There are several other pulse techniques that have been developed for particular situations, but are not widely employed. They include:

- *Reverse pulse voltammetry.* The base potential is held at a value in which

all electroactive species react at the diffusion-limited rate. Pulses of increasing height are then made, in the backward sense, so this has similarities with NPV. This can reduce problems of interference or parallel electrode reactions.

- *Differential normal pulse voltammetry.* As presently used, in this waveform each pulse corresponding to NPV (see Fig. 5a) is divided into two equal parts with a small increase in potential in the second half of the pulse. The difference between the currents sampled halfway through and at the end of the main pulse is displayed as a function of the potential of the first half of the pulse. Advantages relative to DPV are that less time is spent at potentials in which adsorption and so on can occur.

For a specific reaction scheme, it is now relatively simple to program a potentiostat in the desired fashion and many waveforms have appeared in the literature.

2.2.4.5 Comparison between Potential Pulse Techniques

It is useful to compare the relative advantages of the most used potential pulse techniques.

The advantage of NPV is short electrolysis time, the main disadvantage being that the charging current becomes larger as the pulse becomes of larger amplitude.

Concerning DPV, residual capacitive contributions will be subtracted out more effectively, since the pulses are of equal height, which means that DPV is better than NPV in the majority of situations, although the faradaic sensitivity is theoretically the same. Also, the peak response of DPV is more useful for resolving the signals due to two species with close half-wave potentials than wave shape of NPV response. The disadvantage relative to NPV

is that the time during which electrode reactions can occur is much larger and this may cause complications, especially from adsorption and electrode blocking.

SWV seeks to address the disadvantages of both NPV and DPV by being “differential” and also by being fast to minimize adsorption. It cannot always reach this goal. Indeed, there are situations in which SWV is too fast, given the slow kinetics of some reactions, to be able to register any electrode response. In these cases, DPV must be employed.

Many instruments allow the user complete freedom to choose the waveform parameters and to cover the whole transition range from DPV, as originally conceived, to SWV by reducing the interval between DPV pulses until it becomes equal to the pulse width. In this sense, SWV can be thought of as a special case of a DPV waveform when the interval between pulses is reduced until it is equal to the pulse width. However, although the waveform construction is very similar, the reasoning behind the conception of the techniques was rather different as has been previously discussed, particularly regarding effective scan rate and elimination of capacitive contributions. Another important difference is that in SWV the potential, at which the current is registered on SWV, is the staircase potential shifted in the scan direction by $|\Delta E/2|$ relative to DPV (see consequences in Eq. 17, for example).

2.2.5

Current Step and Chronopotentiometry

In current step techniques, a step in applied current at an electrode causes a change in the potential. After charging the double layer, faradaic reactions will begin to occur, giving rise to a chronopotentiogram.

2.2.5.1 Variation of Potential with Time

At a planar electrode, the equation to be solved under conditions of linear semi-infinite diffusion is the same as for a potential step. The difference is the third boundary condition, which instead of defining the diffusion-limited current expresses the concentration gradient resulting from the applied current at the electrode surface.

Thus the equation to solve is

$$\frac{\partial c}{\partial t} = D \frac{\partial^2 c}{\partial x^2} \quad (26)$$

with the boundary conditions

$$t = 0 \quad \text{No electrode reaction } c_0 = c_\infty \quad (27a)$$

$$t \geq 0 \quad \text{Bulk solution } \lim_{x \rightarrow \infty} c = c_\infty \quad (27b)$$

$$t > 0 \quad I = nFAD \left(\frac{\partial c}{\partial x} \right)_0 \quad (28)$$

The solution to the equation is

$$\frac{I\tau^{1/2}}{c_\infty} = \frac{nFAD^{1/2}\pi^{1/2}}{2} \quad (29)$$

which is known as the *Sand equation* [30]. The transition time, τ , corresponds to the situation when $c_0 = 0$ when all the electroactive species in the zone of the electrode have been consumed. If this is obeyed (i.e. a simple electrode process), then the quantity $(I\tau^{1/2}/c_\infty)$ is constant.

It can be shown, for a reversible system, by substituting the concentrations of O and R at the electrode surface together with the Sand equation in the relevant Nernst equation that the variation of potential with time for an oxidation is given by

$$E = E_{\tau/4} - \frac{RT}{nF} \ln \frac{\tau^{1/2} - t^{1/2}}{t^{1/2}} \quad (30)$$

and in which

$$E_{\tau/4} = E^{\theta'} + \frac{RT}{nF} \ln \left(\frac{D_R}{D_O} \right)^{1/2} \quad (31)$$

The parameter $E_{\tau/4}$ is identifiable with the reversible half-wave potential in a voltammogram and is thus usable as an identification parameter for the electroactive species in mixtures (see Fig. 9a). A plot of E vs $\lg [(t^{1/2} - \tau^{1/2})/t^{1/2}]$ gives a straight line of slope 59.2 mV at 25 °C for a reversible system (Fig. 9b). Another simple and useful diagnostic parameter for a reversible system at 25 °C is $|E_{3\tau/4} - E_{\tau/4}| = 47.9/n$ mV.

Table 3 shows these expressions and those obtained for quasi-reversible and irreversible systems. Further details are given in Ref. [3].

2.2.5.2 Current Steps and Potentiometric Stripping Analysis

The derivatives of the expressions in Table 3 are easily calculated and are

$$\begin{aligned} \left(\frac{dE}{dt} \right)_r &= \pm \frac{RT}{2nF} \frac{\tau^{1/2}}{t(\tau^{1/2} - t^{1/2})} \\ \left(\frac{dE}{dt} \right)_{irr} &= \pm \frac{RT}{2\alpha nF} \frac{t^{1/2}}{t(\tau^{1/2} - t^{1/2})} \end{aligned} \quad (32)$$

which correspond to minimum values of

$$\begin{aligned} \left(\frac{dE}{dt} \right)_{r,min} &= \pm \frac{27}{8} \frac{RT}{nF\tau} \quad t = 4\tau/9 \\ \left(\frac{dE}{dt} \right)_{irr,min} &= \pm \frac{2RT}{\alpha nF\tau} \quad t = \tau/4 \end{aligned} \quad (33)$$

Thus the transition time can be calculated from the derivatives.

A plot of (dt/dE) vs E , that is, the inverse expressions, leads to peaks that identify the species and the height of which are directly concentration dependent, since the transition time depends linearly on the concentration of electroactive species. This

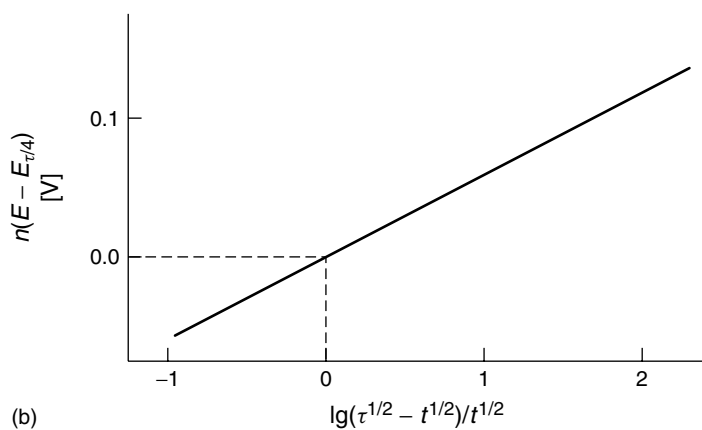
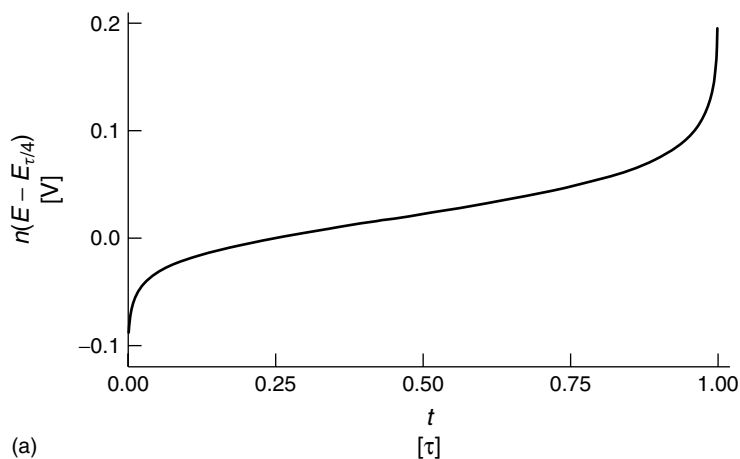
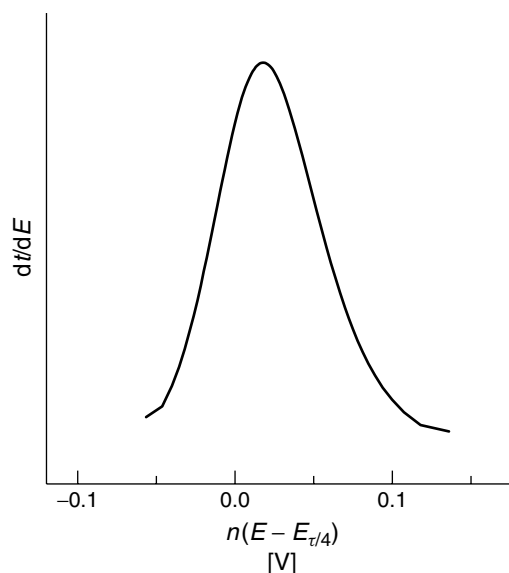


Fig. 9 Response to a current step for a reversible system, illustrated as an oxidation: (a) chronopotentiogram and (b) plot of E vs $\lg[(t^{1/2} - \tau^{1/2})/t^{1/2}]$.

Tab. 3 Variation of potential following application of a current step to the system $R \rightarrow O + ne^-$ with only R initially present in solution

	Potential (E)	$ E_{3\tau/4} - E_{\tau/4} [mV]$
Reversible	$E_{\tau/4} - \frac{RT}{nF} \ln \frac{\tau^{1/2} - t^{1/2}}{t^{1/2}}$	$47.9/n$
Irreversible	$E_{\tau/4} - \frac{RT}{\alpha_a nF} \ln \left[\frac{2k_0}{(\pi D)^{1/2}} (\tau^{1/2} - t^{1/2}) \right]$	$33.8/\alpha n$
	k_0 standard rate constant of electrode reaction	

Fig. 10 Plot of dt/dE vs E from chronopotentiograms as appears in potentiometric stripping analysis.



concept is used in *potentiometric stripping analysis* (PSA) [31]. After accumulation of the trace species to be measured on the electrode, reoxidation is carried out either by an oxidant in solution or by an applied current. Originally the results were presented in the form of chronopotentiograms such as those in Fig. 9(a), but now are commonly displayed as a plot of (dt/dE) vs E (Fig. 10). This makes identification and quantitation simpler and is more similar to results obtained from differential pulse and square wave voltammetry. Further details on PSA, sometimes termed stripping potentiometry, are given in Chapter 2.3 (Sect. 2.3.3).

2.2.6

Concluding Remarks

The purpose of this chapter was to show how the potential and current step and the various pulse techniques can be used to gain kinetic and mechanistic information concerning simple and complex electrode processes as well as to provide

useful electroanalytical data. The number of publications on these themes using pulse techniques is very large so it is not possible here to refer to the many studies undertaken in this area, and the interested reader is directed to the specialist literature.

References

1. G. C. Barker, I. L. Jenkins, *Analyst* **1952**, 77, 685–696.
2. J. B. Flato, *Anal. Chem.* **1972**, 44, 75A–87A.
3. C. M. A. Brett, A. M. Oliveira Brett, *Electrochemistry. Principles, Methods, and Applications*, Oxford University Press, Oxford, 1993, Chap. 10, pp. 199–223.
4. F. G. Cottrell, *Z. Phys. Chem.* **1902**, 42, 385.
5. F. Kimmeler, J. Chevalet, *J. Electroanal. Chem.* **1969**, 21, 237–255.
6. F. C. Anson, *Anal. Chem.* **1966**, 38, 54–57.
7. M. Serelathan, R. A. Osteryoung, J. G. Osteryoung, *J. Electroanal. Chem.* **1986**, 214, 141–156.
8. M. Serelathan, R. A. Osteryoung, J. G. Osteryoung, *J. Electroanal. Chem.* **1987**, 222, 69–100.
9. M. Penczek, Z. Stojek, J. Buffle, *J. Electroanal. Chem.* **1989**, 270, 1–6.

10. H. A. Heering, M. S. Mondal, F. A. Armstrong, *Anal. Chem.* **1999**, 71, 174–182.
11. J. Osteryoung, J. J. O'Dea, in *Electroanalytical Chemistry: A Series of Advances* (Ed.: A. J. Bard), Marcel Dekker, New York, 1986, pp. 209–308, Vol. 14.
12. J. G. Osteryoung, M. M. Schreiner, *Crit. Rev. Anal. Chem.* **1988**, 19, S1–S27.
13. J. Osteryoung, *Acc. Chem. Res.* **1993**, 26, 77–83.
14. H. P. van Leeuwen, J. Buffle, M. Lovrić, *Pure Appl. Chem.* **1992**, 64, 1015–1028.
15. C. M. A. Brett, A. M. Oliveira Brett, S. H. P. Serrano, *J. Electroanal. Chem.* **1994**, 366, 225–231.
16. L. Ramaley, M. S. Krause Jr., *Anal. Chem.* **1969**, 41, 1362–1365.
17. J. J. O'Dea, J. Osteryoung, R. A. Osteryoung, *Anal. Chem.* **1981**, 53, 695–701.
18. J. J. O'Dea, J. Osteryoung, T. Lane, *J. Phys. Chem.* **1986**, 90, 2761–2764.
19. M. Lovrić, S. Komorsky Lovrić, R. W. Murray, *Electrochim. Acta* **1988**, 33, 739–744.
20. J. J. O'Dea, A. Ribes, J. Osteryoung, *J. Electroanal. Chem.* **1993**, 345, 287–301.
21. J. H. Reeves, S. Song, E. F. Bowden, *Anal. Chem.* **1993**, 65, 683–688.
22. S. Komorsky-Lovrić, M. Lovrić, *J. Electroanal. Chem.* **1995**, 384, 115–122.
23. S. P. Kounaves, J. J. O'Dea, P. Chandreskhar et al., *Anal. Chem.* **1986**, 58, 3199–3202.
24. B. A. Brookes, R. G. Compton, *J. Phys. Chem. B* **1999**, 102, 5289–5295, 9020–9028.
25. A. B. Miles, R. G. Compton, *J. Phys. Chem. B* **2000**, 104, 5331–5342.
26. A. B. Miles, R. G. Compton, *J. Electroanal. Chem.* **2000**, 487, 75–89.
27. C. M. A. Brett, A. M. Oliveira Brett, L. C. Mitoseriu, *Anal. Chem.* **1994**, 66, 3145–3150.
28. C. M. A. Brett, A. M. Oliveira Brett, F.-M. Matysik et al., *Talanta* **1996**, 43, 2015–2022.
29. F.-M. Matysik, S. Matysik, A. M. Oliveira Brett et al., *Anal. Chem.* **1997**, 69, 1651–1656.
30. H. J. S. Sand, *Philos. Mag.* **1901**, 1, 45.
31. D. Jagner, *Trends Anal. Chem.* **1983**, 2, 53–56.

2.3 Stripping Analysis

Joseph Wang
New Mexico State University, Las Cruces,
New Mexico, U.S.A.

2.3.1 Introduction

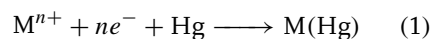
Stripping analysis is a powerful electro-analytical technique for trace metal measurements [1]. Its remarkable sensitivity is attributed to the “built-in” preconcentration step, during which the target metals are accumulated onto the working electrode. The combination of such an effective preconcentration step with advanced electrochemical measurements of the accumulated analytes generates favorable signal-to-background characteristics, and hence results in extremely low detection limits (down to the picomolar level). Other advantages of stripping analysis include its multielement and speciation capabilities, low cost, and suitability to on-site, in situ, and on-line applications. Different versions of stripping analysis, which differ mainly in the nature of the preconcentration step (electrolytic vs. adsorptive) and in the method of detection (voltammetric vs. potentiometric), are available [2]. Fundamental and practical aspects of these different stripping protocols are discussed in the following sections.

2.3.2 Anodic Stripping Voltammetry

2.3.2.1 Principles

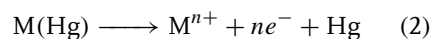
Anodic stripping voltammetry (ASV) is the oldest, and still the most widely used version of stripping analysis [3]. The technique is applicable to metal ions

that can be deposited at an electrode, and particularly for those metals that dissolve in mercury. Here, the metals are accumulated by potentiostatic deposition onto a small-volume mercury electrode (a thin mercury film or a hanging mercury drop), or onto a nonmercury surface (Fig. 1). This is accomplished by cathodic deposition at a controlled time and potential. The amalgam-forming deposition step is given by Eq. (1):



The deposition potential should be ca. 0.3 to 0.4 V more negative than the reduction potential of the metal analyte. Since the sensitivity of the stripping operation is dependent on the deposition time, the latter should be selected according to the concentration of the target metals (from around 0.5 min at the 10^{-7} M level to 10 min for 10^{-9} – 10^{-10} M concentrations). The deposition step is usually facilitated by convective transport of the analyte to the surface of the working electrode. This can be accomplished by stirring or flowing the solution or by rotating the electrode. Quiescent solutions can be used in connection to ultramicroelectrodes (described below). Only a small, and yet reproducible, fraction of the metal in the solution is being deposited.

Following the preselected deposition period, the forced convection is stopped, and a positive-going potential scan is initiated, during which the amalgamated metals are reoxidized and “stripped” away from the surface:



The excitation signals used during the “stripping” step are usually pulse-voltammetric waveforms (that discriminate against the charging-current background

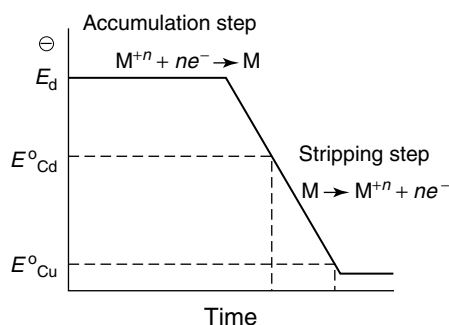


Fig. 1 The deposition and stripping steps of anodic stripping voltammetry.

contribution) or a linear potential ramp. The stripping voltammogram, recorded during this measurement step, consists of multiple current peaks, corresponding to the reoxidation of the amalgamated metals, and their “stripping” out of the electrode (Fig. 2). Such an output provides the qualitative and quantitative information through measurements of the peak potential and current, respectively. The ASV operation thus allows the simultaneous measurements of four to six trace metals.

The peak current depends upon various parameters of the preconcentration

and stripping steps. The exact behavior governing the shape of the stripping voltammogram depends on the type of electrode and stripping waveform employed. Various theoretical treatments are thus available [4, 5]. In all cases, the peak current is proportional to the deposition period and metal concentration:

$$i_p = K C t_{\text{dep}} \quad (3)$$

with K being a constant (including the electrode area (A), scan rate (v), number of electrons (n), diffusion coefficient (D), and convection rate). For example, the stripping peak current for a mercury film

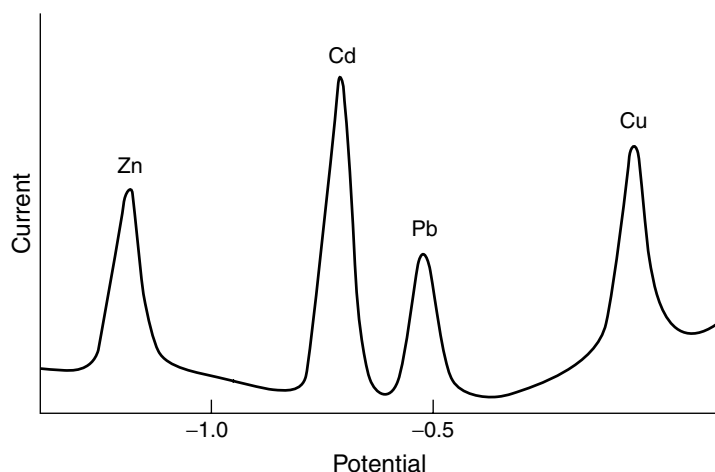


Fig. 2 Typical stripping voltammogram for a mixture containing 10^{-8} M zinc, cadmium, lead, and copper.

electrode (MFE) is given by

$$i_p = 1.1157 \times 10^6 n^2 A C_R l \nu \quad (4)$$

where l is the film thickness, and C_R is the concentration of the metal in the electrode (which is proportional to C and t_{dep}).

A “mirror image” of ASV is cathodic stripping voltammetry (CSV), which involves an anodic deposition of the analyte, followed by stripping in a negative-going potential scan.

2.3.2.2 Interferences

As with other voltammetric techniques, stripping voltammetry may suffer from insufficient resolution of neighboring peaks. Within a potential window of about 1.5 V, more than 15 metals may yield stripping peaks. Thus, it is often difficult to resolve metals that have peak potentials in close proximity to one another. The problem of overlapping peaks can be addressed by adding a masking agent or using a “medium-exchange” protocol. Stripping voltammetry can also be complicated by the formation of intermetallic compounds by two metals (e.g. Cu–Zn) that codeposit into the mercury electrode [6]. Such intermetallic interaction usually causes one of the stripping peaks to be depressed or shifted. This can be circumvented by plating only one of the metals (at a lower potential) or via a preferential formation of another intermetallic compound (e.g., Cu–Ga). Another problem is the presence of surfactants that adsorb on the working electrode and block the deposition [7]. Such adsorption may affect both the deposition and stripping steps, leading to lower or broader peaks, and shifts in the peak potential. The surfactant problem can be minimized through coverage with a permselective/protective film (e.g. Nafion, Agar), or using ultraviolet irradiation. The

analyst should also be aware that he is working with trace levels, and should thus employ a clean work practice for minimizing contamination risks or adsorption losses. The reagents and solutions used for preparing supporting electrolytes or standards should thus be of the highest purity possible.

2.3.3

Stripping Potentiometry

Stripping potentiometry (SP) is another attractive version of stripping analysis [8, 9]. This was introduced in Chapter 2.2 (Sect. 2.2.5). Like other stripping protocols, stripping potentiometry consists of two steps. The first (preconcentration) step, in which the metals are electrodeposited onto the working electrode (usually a mercury film), is followed by a stripping step in which the amalgamated metals are brought back to the solution with the aid of an oxidant (e.g. oxygen, mercury ion) or a constant anodic current. The resulting potentiogram (E vs. t plot) consists of stripping plateaus, as in a redox titration curve (Fig. 3a), with sharp potential changes accompanying the depletion of each metal from the surface. Such a potentiogram provides both the quantitative and qualitative information. The transition time needed for the oxidation of a given metal, t_M , is a quantitative measure of the sample concentration of the metal:

$$t_M \propto \frac{C_{M^{n+}} t_{\text{dep}}}{C_{\text{ox}}} \quad (5)$$

where C_{ox} is the concentration of the oxidant. The qualitative identification relies on potential measurements (in accordance with the Nernst equation for the amalgamated metal). Modern SP instruments use microcomputers to register fast stripping

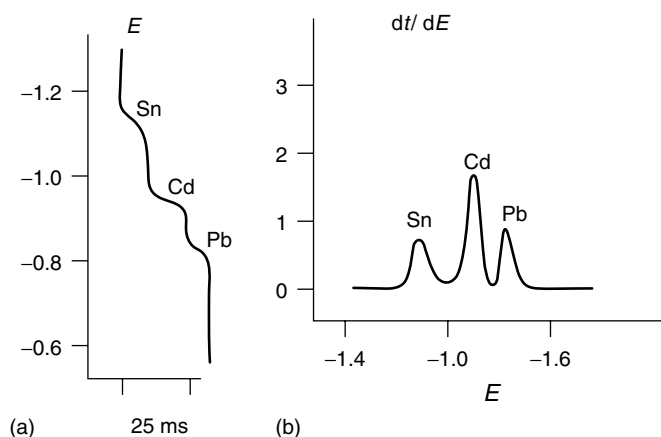


Fig. 3 Stripping potentiometric curves for $90 \mu\text{g L}^{-1}$ tin, cadmium, and lead following 90 s deposition at -1.4 V .

events and to convert the wave-shaped response to a more convenient peak over a flat baseline (i.e. to dt/dE versus E signals; Fig. 3b). Here, the peak area is proportional to the bulk concentration, with the peak potential providing the qualitative identification. Because of the short (millisecond) transition times, a fast rate of data acquisition (kilohertz) is required for obtaining a sufficient number of “counts” for a defined peak.

Stripping potentiometry offers several important advantages (over analogous ASV schemes), including reduced susceptibility to organic surfactants and reliable operation in nondeaerated samples.

2.3.4

Adsorptive Stripping Voltammetry

The power and scope of stripping analysis have been greatly enhanced during the past two decades owing to the introduction of adsorptive stripping procedures [10–12]. Such use of adsorptive accumulation permits convenient measurements of over two dozen trace metals that cannot be readily deposited (e.g. Cr, Al, U, Fe, Ti, V, Mo).

Adsorptive stripping protocols commonly rely on the formation of surface-active complexes of the target metal (in the presence of a suitable complexing agent) followed by the interfacial accumulation of the complex onto a mercury drop or film electrode (Fig. 4). Most procedures involve the reduction of the metal in the adsorbed complex during a negatively going potential scan. In few cases, it is possible to exploit the reduction of the ligand in the complex. This is usually accomplished by scanning the potential in the negative direction (using linear or pulse-scan modes) following the adsorptive accumulation step. The quantitation of extremely low levels of the target metals (10^{-10} M) can be realized in connection to short (3–5 min) adsorption times. Even lower concentrations, down to the 10^{-12} M level, can be achieved by combining the adsorptive stripping operation with catalytic effects [13, 14]. Such adsorptive-catalytic stripping voltammetric protocols commonly involve a catalytic cycle in the presence of a chemical oxidant (such as bromate, nitrite, or hydrogen peroxide). Different kinds of catalytic systems can be

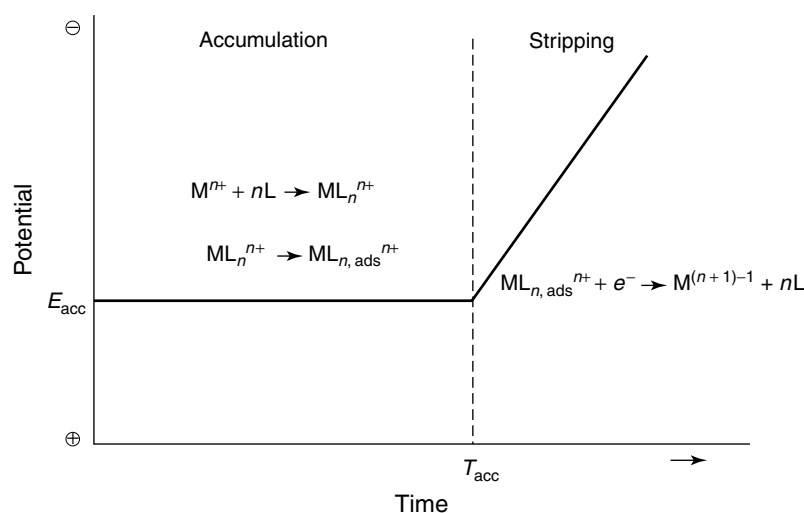


Fig. 4 Steps in adsorptive stripping voltammetry: formation of a metal complex, its adsorptive accumulation, and the reduction of the adsorbed complex.

considered depending upon the reaction mechanism [14]. The remarkably low detection limits of such operations are thus attributed to the dual current amplification effect (associated with the adsorption and catalytic processes).

The adsorptive stripping response (of the surface-confined species) is directly related to its surface concentration, with the adsorption isotherm – commonly that of Langmuir – providing the relationship between the surface and bulk concentrations of the adsorbate. As a result, calibration curves display an initial linear portion, followed by a curvature, and a leveling off at high concentrations. The response is dependent upon numerous other variables that affect the extent of adsorption, including the electrolyte, pH, accumulation potential and time, convection rate, and ligand concentration.

Besides expanding the scope of stripping analysis to numerous trace elements that cannot be electroplated (e.g. Table 1), adsorptive stripping procedures have been

used for detecting trace levels of organic compounds (e.g. pharmaceuticals) and biologically important compounds (including hormones and nucleic acids). Non-electroactive macromolecules may also be determined following their interfacial accumulation from tensiometric peaks (resulting from their adsorption–desorption mechanism).

2.3.5

Practical Considerations

2.3.5.1 Electrodes

Proper choice of the working electrode is crucial for the success of the stripping operation. The ideal working electrode should offer effective preconcentration, a favorable redox reaction of the target metal, reproducible and renewable surface, and a low background current over a wide potential range. Mercury is the electrode of choice for many stripping applications. Two types of mercury electrodes are commonly used, the hanging

Tab. 1 Common adsorptive stripping procedures for trace metals

<i>Metal</i>	<i>Complexing agent</i>	<i>Supporting electrolyte</i>	<i>Detection limit (M)</i>	<i>References</i>
Al	Dihydroxyanthraquinone-sulfonic acid	BES buffer	1×10^{-9}	15
Co	Nioxime	HEPES buffer	6×10^{-12}	16
Cr	Diethylenetriamine-pentaacetic acid	Acetate buffer	4×10^{-10}	17
Fe	Solochrome violet RS	Acetate buffer	7×10^{-10}	18
Mo	Oxine	Hydrochloric acid	1×10^{-10}	19
Ni	Dimethylglyoxime	Ammonia buffer	1×10^{-10}	20
Pt	Formazone	Sulfuric acid	1×10^{-12}	21
Sn	Tropolone	Acetate buffer	2×10^{-10}	22
Ti	Mandelic acid	Potassium chlorate	7×10^{-12}	23
U	Oxine	PIPES buffer	2×10^{-10}	24
V	Catechol	PIPES buffer	1×10^{-10}	25

mercury drop electrode (HMDE) and mercury film electrode (MFE). The HMDE relies on reproducible drop formation at the tip of a glass capillary. The MFE may be preplated (prior to the measurement) or codeposited with the target metal analytes. Glassy carbon, carbon fiber, iridium microdisks, and screen-printed carbon are the most common supports for the mercury film. MFEs possess higher surface-to-volume ratio (compare to the HMDE), and consequently offer a more efficient preconcentration [26]. Alternative “nonmercury” electrodes, including gold, carbon, silver, or bismuth ones, have been developed for addressing concerns regarding the toxicity and handling of mercury. Particularly attractive are the bismuth-film electrodes that offer an attractive stripping performance, similar to that of mercury electrodes, while eliminating toxicity problems [27]. Gold surfaces are characterized by a wider potential window (compare to mercury ones) to allow convenient detection of important metals, such as arsenic, selenium, or mercury.

Ultramicroelectrodes have been shown to be useful for eliminating the need for forced convection during the deposition step and for obviating the need for supporting electrolyte [28]. The latter is particularly attractive for speciation work in low ionic-strength natural waters and for minimizing the risk of contamination. Arrays of microelectrodes have been shown to be useful for measuring metal concentration profiles in high spatial resolution [29]. Further information is provided in Chapter 2.5. Microfabricated (mass-produced) electrodes, particularly screen-printed electrode strips, have been developed as low-cost disposable (“one-shot”) metal sensors [30]. The deliberate modification of conventional electrodes can benefit various stripping applications, by imparting higher selectivity, sensitivity, and stability. Various surface coatings have thus been used for protection against surface-active foulants or for preconcentration of target metals.

2.3.5.2 Cells and Instrumentation

Electrochemical stripping analysis is carried out in a conventional (“beaker-type”) three-electrode cell (of 5–50-ml volume). The three electrodes, as well as the tube used for bubbling the deoxygenating gas, are supported in five holes in the cell cover. Various microcells with 20 to 500 μ l volumes can be used when the sample volume is limited. Particularly attractive are thin-layer cells in which the entire sample is confined within a thin layer (of less than 10- μ m thickness) at the electrode surface [6]. Smaller sample volumes can be accommodated in connection with ultramicroelectrodes and advanced microfabrication processes. The latter result in planar strips that can be considered as disposable electrochemical cells onto which sample droplets are placed.

The adaptation of electrochemical stripping techniques to on-line flow systems provides several advantages, including high sample throughput, continuous monitoring capability, improved precision, lower risk of contamination, and convenient medium exchange. A wide range of flow-through stripping detectors has been developed for on-line monitoring of metals [1]. Fully automated flow systems, based on such detectors, have been described [31]. High-throughput stripping assays of small samples volumes have been realized in connection to flow-injection [32] and batch-injection [33] operations. Further information on several types of hydrodynamic electrodes is given in Chapter 2.4.

The portable instrumentation and low power demands of stripping analysis satisfy many of the requirements for on-site and in situ monitoring of trace metals. Efforts in this direction have led to the replacement of conventional stripping protocols and systems with remotely deployed

submersible stripping-based sensors [34] and submersible (“lab-on-cable”) stripping probes [35, 36]. Such devices offer a fast return of the chemical information (i.e. a direct and reliable assessment of the fate and gradient of metal contaminants) in a safe, timely, and cost-effective manner. These, along with the introduction of single-use (disposable) microfabricated metal-sensor strips [30] or micromachined handheld total stripping analyzers [35] would allow moving the measurements of trace metals to the field, and performing them more rapidly, reliably, and inexpensively.

Portable (handheld), battery-powered, easy-to-use stripping analyzers have also been developed, particularly in connection to decentralized screening of blood lead in children [37]. The operation of these compact stripping meters has been combined with disposable screen-printed electrodes, similar to those used by diabetes patients for monitoring their blood glucose [30].

2.3.6

Representative Examples

Numerous applications of stripping analysis to many environmental, clinical, or industrial problems have been reported. The technique has been widely used for the measurement of trace metals in natural waters, including pristine and polluted inland and marine waters [1, 36, 38]. The technique is particularly suitable for the study of chemical speciation, that is, the determination of different physical–chemical forms of the element [39]. Measurements of oxidation states, complexation capacity, stability constants, or “labile metal” concentration, represent typical stripping speciation experiments. Because of its fundamentally different detection principles, the

Tab. 2 Representative applications of stripping analysis

<i>Metal</i>	<i>Sample matrix</i>	<i>Stripping mode</i>	<i>Working electrode</i>	<i>References</i>
Antimony	Gunshot residue	ASV	MFE	40
Cadmium	Rain	ASV	MFE	41
Chromium	Soil	AdSV	HMDE	42
Cobalt	Seawater	AdSV	HMDE	16
Copper	Steel	ASV	HMDE	43
Iodide	Seawater	CSV	HMDE	44
Iron	Wine	AdSV	HMDE	45
Lead	Blood	SP	MFE	46
Manganese	Wastewater	SP	MFE	47
Mercury	Fish	ASV	Au	48
Nickel	Aerosols	AdSV	HMDE	49
Platinum	Gasoline	AdSV	HMDE	50
Selenium	Soil	CSV	HMDE	51
Thallium	Urine	ASV	HMDE	52
Titanium	Seawater	AdSV	HMDE	23
Uranium	Groundwater	AdSV	HMDE	53
Zinc	Eye tissue	ASV	HMDE	54

Note: AdSV: Adsorptive stripping voltammetry.

adsorptive stripping approach provides a different speciation information (based on ligand competition) compared to conventional ASV procedures. Recent advances in miniaturization and remote sensing have facilitated the application of stripping analysis for on-site monitoring of toxic metals, including in situ (real-time) profiling [35]. Other environmental applications of stripping analysis include assays of sediments, fly ash, rain, or airborne particulate matter (e.g. Table 2).

Stripping analysis has been widely used for measuring trace metals in biological fluids. The use of stripping analysis for decentralized testing of blood lead in children has been particularly successful [46]. Measurements of mercury in fish [48], of antimony in gunshot residues [40], or of cadmium impurities in zinc plant electrolyte [55], represent typical food, forensic, and industrial applications, respectively, of stripping analysis. These,

and other applications, are illustrated in Table 2.

References

1. J. Wang, *Stripping Analysis: Principles, Instrumentation and Applications*, VCH Publishers, Deerfield Beach, Fla., 1985, p. 160.
2. A. Fogg, J. Wang, *Pure Appl. Chem.* **1999**, 71, 891.
3. T. R. Copeland, R. K. Skogerboe, *Anal. Chem.* **1974**, 46, 1257A.
4. D. Roe, J. Toni, *Anal. Chem.* **1965**, 37, 1503.
5. W. T. de Vries, *J. Electroanal. Chem.* **1965**, 9, 448.
6. T. DeAngelis, R. Bond, E. Brook et al., *Anal. Chem.* **1977**, 49, 1792.
7. J. Wang, D. Luo, *Talanta* **1984**, 31, 703.
8. D. Jagner, *Trends Anal. Chem.* **1983**, 2(3), 53.
9. D. Jagner, *Analyst* **1982**, 107, 593.
10. C. M. G. van den Berg, *Anal. Chim. Acta* **1991**, 250, 265.
11. J. Wang, Voltammetry after nonelectrolytic preconcentration in *Electroanalytical Chemistry* (Ed.: A. J. Bard), Marcel Dekker, New York, 1989, pp. 1–88, Vol. 16.

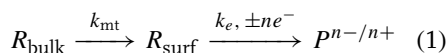
12. M. Paneli, A. Voulgaropoulos, *Electroanalysis* **1993**, 5, 355.
13. M. Czae, J. Wang, *Talanta* **1999**, 50, 921.
14. A. Bobrowski, J. Zarebski, *Electroanalysis* **2000**, 12, 1777.
15. C. M. G. van den Berg, K. Murphy, J. Riley, *Anal. Chim. Acta* **1986**, 188, 177.
16. J. Donat, K. Bruland, *Anal. Chem.* **1988**, 60, 240.
17. J. Golimowski, P. Valenta, H. W. Nürnberg, *Fresenius Z. Anal. Chem.* **1985**, 322, 315.
18. J. Wang, J. Mahmoud, *Fresenius Z. Anal. Chem.* **1987**, 327, 789.
19. C. M. C. van den Berg, *Anal. Chem.* **1985**, 57, 1532.
20. B. Pihlar, P. Valenta, H. W. Nürnberg, *Fresenius Z. Anal. Chem.* **1981**, 307, 337.
21. J. Wang, J. Zadeii, M. S. Lin, *J. Electroanal. Chem.* **1987**, 237, 281.
22. J. Wang, J. Zadeii, *Talanta* **1987**, 34, 909.
23. K. Yokoi, C. M. C. van den Berg, *Anal. Chim. Acta* **1991**, 245, 167.
24. C. M. G. van den Berg, N. Nimmo, *Anal. Chem.* **1987**, 59, 269.
25. C. M. G. van den Berg, *Anal. Chem.* **1984**, 56, 2383.
26. T. M. Florence, *J. Electroanal. Chem.* **1970**, 27, 273.
27. J. Wang, J. Lu, S. Hocevar et al., *Anal. Chem.* **2000**, 72, 3218.
28. J. Wang, P. Tuzhi, *Anal. Chim. Acta* **1987**, 197, 367.
29. M. L. Tercier-Waeber, J. Pei, J. Buffle et al., *Electroanalysis* **2000**, 12, 27.
30. J. Wang, B. Tian, *Anal. Chem.* **1992**, 64, 1706.
31. A. Zirino, S. Lieberman, C. Clavell, *Environ. Sci. Technol.* **1978**, 12, 73.
32. J. Wang, H. Dewald, *Anal. Chem.* **1994**, 56, 156.
33. C. M. Brett, A. M. Brett, L. Tugelea, *Electroanalysis* **1996**, 8, 639.
34. J. Wang, N. Foster, S. Armalis, D. Larson, A. Zirino, K. Olsen, *Anal. Chim. Acta* **1995**, 310, 223.
35. J. Wang, B. Tian, J. Lu et al., *Anal. Chim. Acta* **1999**, 385, 429.
36. M. Tercier, J. Buffle, *Electroanalysis* **1993**, 5, 187.
37. C. Yarnitzky, J. Wang, B. Tian, *Talanta* **2000**, 51, 333.
38. E. P. Acheterberg, C. Braungradt, *Anal. Chim. Acta* **1999**, 400, 381.
39. T. M. Florence, *Talanta* **1982**, 29, 345.
40. N. Komanur, G. van Loon, *Talanta* **1977**, 24, 184.
41. H. Emons, A. Baede, M. Schoning, *Electroanalysis* **2000**, 12, 1171.
42. J. Wang, J. Lu, J. K. Olsen, *Analyst* **1992**, 117, 1913.
43. S. Gottesfeld, M. Ariel, *J. Electroanal. Chem.* **1965**, 9, 112.
44. G. Luther, C. Swartz, W. Ullman, *Anal. Chem.* **1988**, 60, 1721.
45. J. Wang, S. Mannino, *Analyst* **1989**, 114, 643.
46. P. Ostapczuk, *Clin. Chem.* **1992**, 38, 195.
47. G. Scollary, G. Chen, T. Cardwell et al., *Electroanalysis* **1995**, 7, 386.
48. J. Golimoski, I. Gustavsson, *Fresenius Z. Anal. Chem.* **1984**, 317, 484.
49. M. Nimmo, G. Fones, *Anal. Chim. Acta* **1994**, 291, 321.
50. K. Hoppstock, M. Michulitz, *Anal. Chim. Acta* **1997**, 350, 135.
51. S. Porbes, G. Bound, T. West, *Talanta* **1979**, 26, 473.
52. D. L. Levit, *Anal. Chem.* **1973**, 45, 1291.
53. J. Wang, R. Setiadji, L. Chen et al., *Electroanalysis* **1992**, 4, 161.
54. T. Williams, O. Foy, C. Benson et al., *Anal. Chim. Acta* **1975**, 75, 250.
55. A. M. Bond, *Anal. Chim. Acta* **1999**, 400, 333.

2.4 Hydrodynamic Electrodes

Andrew R. Mount
The University of Edinburgh, Edinburgh,
United Kingdom

2.4.1 Introduction

A hydrodynamic electrode is an electrode system in which the solution near the electrode undergoes forced mechanical convection (stirring). This chapter is concerned with controlled hydrodynamic electrodes in which this mechanical convection is reproducible and leads to steady state currents. There are several advantages of using electrodes with controlled hydrodynamics. These are most easily seen by considering a general scheme for electrochemical reaction



where a reactant R is electrochemically converted to a product P at an electrode surface by accepting or donating n electrons (i.e. reduction or oxidation). The overall reaction requires the mass transport of R from the bulk of solution to the electrode surface, the rate of which can be considered to be governed by a first-order rate constant k_{mt} in cm s^{-1} . The rate of the mass transport reaction is then given by the flux of species ($\text{mol cm}^{-2} \text{s}^{-1}$) to the electrode surface

$$j_{\text{mt}} = k_{\text{mt}}(c_{\infty} - c_0) \quad (2)$$

where c is the concentration of R in the bulk (at a near infinite distance ∞ from the electrode) or at the electrode surface (at zero distance, 0, from the electrode). The maximum flux for this process is when $c_0 = 0$, when the rate of mass transfer is

relatively slow and rate-limiting and the overall flux is given by

$$j_{\text{mt}} = k_{\text{mt}}c_{\infty} \quad (3)$$

At the electrode, electrochemical reaction then occurs, governed by a characteristic first-order rate constant k_e . Under steady state conditions, the electrochemical reaction flux is also equal to the overall flux j , that is, $j_e = j = j_{\text{mt}}$. The electrochemical flux is given by

$$j_e = k_e c_0 \quad (4)$$

When the reaction is under electrochemical control, the electrochemical reaction is relatively slow and rate-limiting and $c_{\infty} = c_0$. Then the overall flux is given by

$$j_e = k_e c_{\infty} \quad (5)$$

In general, the overall flux j for the reaction is determined by the following equation:

$$\frac{1}{j} = \left[\frac{1}{k_{\text{mt}}} + \frac{1}{k_e} \right] \frac{1}{c_{\infty}} \quad (6)$$

with the smallest of the rate constants determining the overall reaction rate. The overall rate of reaction is measured experimentally as the current i where

$$i = \pm nFAj \quad (7)$$

where A is the electrode area (cm^2), F is Faraday's constant (C mol^{-1}), and the positive and negative signs correspond to oxidation and reduction, respectively. From Eqs. (6 and 7), it can therefore be seen that reproducible currents can only be obtained in systems in which both k_{mt} and k_e can be controlled.

k_e is easily controlled by controlling the electrode potential. However, in stagnant solutions, or solutions with irreproducible or unstable convection, k_{mt} is not constant

and is time-dependent, as the extent of depletion of reactant near the electrode governs the rate of mass transfer, and this changes with time. This often leads to irregular or unpredictable currents. The first advantage of controlled hydrodynamic electrodes is that they generate reproducible and predictable solution convection through mechanical stirring, which leads to control of k_{mt} and hence i , producing steady state (or time-independent) currents. Variation of k_{mt} is easily achieved by varying the convection rate, allowing the quantitative determination of the role of mass transport in the overall kinetics of electrode reaction. The second advantage is that the reproducible flow results in a reproducible and controllable flux of product away from the electrode surface. This allows the downstream detection and identification of these products, for example, by means of a second electrode [as in the rotating ring disc electrode (RRDE, see Sect. 2.4.2.2), which can be set up (by control of electrode type and potential) to detect and identify particular products, or by a suitable spectroscopic technique [such as electron spin resonance (esr)]. Applications of esr in electrochemistry are discussed further in Volume 2 of the *Encyclopedia*. The third advantage is that the controlled hydrodynamics allow the fraction of products that can be detected (or collected) downstream to be theoretically determined (e.g. the collection efficiency of the RRDE, see Sect. 2.4.2.2). Comparison of the amount of product detected experimentally and expected theoretically therefore allows quantitation of the amount of product produced by the reaction process (giving the efficiency of the reaction). Finally, control of product flux through stirring rate can be used to control the transit time from product generation to downstream collection or

detection. Measurement of the decrease in the amount of product detected as the flux (and hence the transit rate) is decreased experimentally therefore enables the reactivity of any unstable products generated upstream to be determined.

This chapter considers each of the major hydrodynamic electrode systems in turn. Only those systems at which steady state measurements can be achieved are considered, therefore excluding those systems with hydrodynamic regimes that inherently produce time-dependent oscillations superimposed on steady state behavior, such as vibrating electrodes [1] and sonicated electrode systems [2] in which ultrasound is used to produce fluid motion. The latter are discussed further in Chapters 2.8, 2.9 and 2.10 of this volume. For each system, the hydrodynamic regime is described, along with representative applications that demonstrate the applicability of the system to particular measurements of electrochemical kinetics and mechanism. The system characteristics are also discussed, to highlight the suitability of the system to particular applications, giving insight into the strengths and weaknesses of each system.

2.4.2

Rotating Disc Hydrodynamics

2.4.2.1 Rotating Disc Electrode(RDE)

The RDE (Fig. 1) is a disc electrode that is surrounded by a coplanar insulating mantle (typically made of poly(tetrafluoroethylene), PTFE). This is placed into a solution and rotated at a controlled rotation speed, W (Hz), which induces stirring in the solution [3].

The RDE acts as a pump (Fig. 2), drawing the solution up toward the electrode along the z -axis (Fig. 2a), then

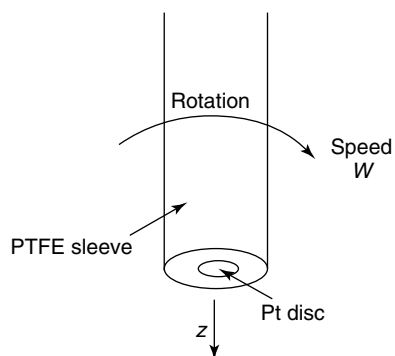


Fig. 1 The rotating disc electrode.

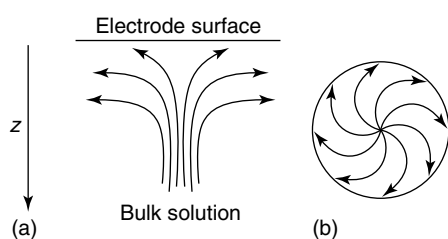


Fig. 2 Solution flow for RDE (a) along z -axis and (b) near disc surface.

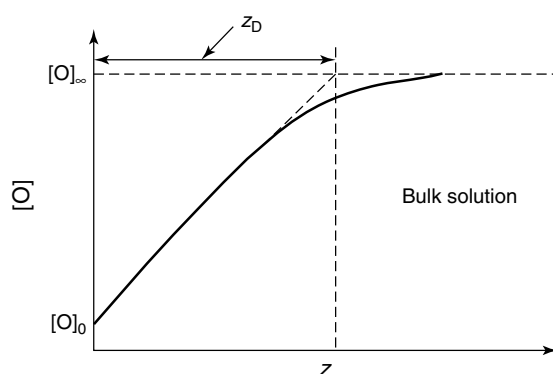


Fig. 3 Concentration profile for the RDE normal to the electrode. Reaction of O at the RDE produces a concentration $[O]_0$ at the electrode surface. Mass transport to the electrode occurs by diffusion across z_D . At $z > z_D$, the solution is well-stirred and the concentration of O is the bulk concentration $[O]_\infty$.

flinging it out radially across the electrode surface (Fig. 2b).

This electrode is uniformly accessible [4], in that during a reaction the flux (and hence the current density) is the same across the entire disc surface. Also, the system possesses circular symmetry about the z -axis. This greatly simplifies the mathematical description of the hydrodynamics, and allows an analytical solution of the convective-diffusion equation [5].

Viewed along the z -axis, there is a diffusion layer, z_D , across which the reactant diffuses to the electrode (Fig. 3).

It must be remembered that when $z < z_D$, although transport along the z -axis is by diffusion only, the diffusion layer is not totally stagnant, as there is significant radial convection (Fig. 2b) that sweeps products away from the electrode. This is utilized in product detection in the RRDE system (see Sect. 2.4.2.2).

The thickness of the diffusion layer is rotation speed–dependent, and is given by

$$z_D = 0.643D^{1/3}\nu^{1/6}W^{-1/2} \quad (8)$$

where D is the diffusion coefficient of the reacting species ($\text{cm}^2 \text{s}^{-1}$) and ν is the kinematic viscosity of the solvent ($\text{cm}^2 \text{s}^{-1}$). Since in the z -direction transport is only by diffusion,

$$j = -D \frac{\partial c}{\partial z} = D \frac{(c_\infty - c_0)}{z_D} \quad (9)$$

with

$$k_{\text{mt}} = \frac{D}{z_D} \quad (10)$$

The mass transport limiting current, i_L , on the electrode (which is the current when k_e is extremely large, the electrode is highly reactive, and $[O]_0 = 0$ i.e. $c_0 = 0$) is given by a combination of Eqs. (3, 7, 8, and 10). This is termed the *Levich equation* [5],

$$i_L = \pm 1.554nFAD^{2/3}\nu^{-1/6}W^{1/2}c_\infty \quad (11)$$

and more generally, the current is given by a combination of Eqs. (6, 7, 8, and 10) as the Koutecky–Levich equation [6],

$$\frac{1}{i} = \frac{1}{i_L} \pm \frac{1}{nFAk_e c_\infty} \quad (12)$$

From Eq. (11), the first term in Eq. (12) can be varied by changing W , while the second term can be varied by changing the electrode potential and hence k_e . Hence this relationship allows the relative effects of the rate of mass transport (the first term) and the rate of electrochemical reaction (the second term) on the overall reaction rate to be separated and quantified.

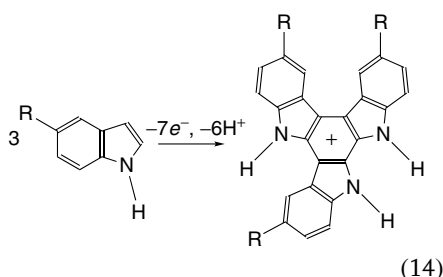
The RDE is a particularly good system for the measurement of the electrode kinetics of electrocatalytic films (modified electrodes), in which mediated electron transfer to substrate species in solution occurs via a surface-immobilized redox

couple. This is because the uniform accessibility of the RDE ensures that the flux of substrate to the electrode is constant across the surface, and the controlled hydrodynamics ensures a constant and reproducible substrate concentration at the surface of the electrocatalytic film. Both of these effects simplify kinetic modeling. In these experiments a general form of the Koutecky–Levich equation generally applies,

$$\frac{1}{i} = \frac{1}{i_L} + \frac{1}{i_\infty} \quad (13)$$

with the second term in Eq. (12) generalized to be a mass transfer–independent current i_∞ (independent of W). A value of i_∞ can generally be obtained from the y -intercept of a straight-line plot of $1/i$ against $W^{-1/2}$ (termed a *Koutecky–Levich plot*). The infinity subscript is used to indicate that this is the current that would be obtained at infinite rotation speed, when the first term is unimportant and $c_0 = c_\infty$. In each case, the theoretical parameters that make up i_∞ reflect the nature of the rate-determining step in the reaction at the surface, between the substrate and the immobilized redox species. For a simple catalytic reaction between a substrate and an electrocatalytic monolayer or thin film, the rate-determining step is often the kinetics of the electron transfer reaction between the substrate and the redox species and the rate constant for this reaction can be obtained from i_∞ . However, for thicker surface films (e.g. polymer modified electrodes), the rate of transport of electrons or substrate across the film can also become rate-determining, and terms for these processes are then included in i_∞ . Albery and Hillman [7, 8] and Andrieux and Saveant [9] have each produced general theoretical treatments that enable the rate-determining step for these electrocatalytic reactions to be identified and quantified.

This approach has also been extended to other modified electrode reactions and this has been the subject of a comprehensive review [10]; a good example is the reaction between an immobilized enzyme and its substrate, in which complexation between the immobilized enzyme (the redox species) and the substrate occurs [11, 12]. We have also shown [13] that the electropolymerization and trimer film formation of a range of 5-substituted indoles at the RDE



produce straight-line Koutecky–Levich plots, from which the rate constant for coupling of the indole monomer radical cations produced on the electrode surface (which form the redox-active film of indole trimers) can be obtained. Furthermore, use of the RDE ensures controlled flux of indole monomer to the whole of the electrode surface, which ensures a much more reproducible and homogenous film structure across the disc than in experiments with stationary electrodes.

2.4.2.2 The Rotating Ring Disc Electrode (RRDE)

The RRDE utilizes a second independent electrode positioned downstream of the

RDE (the ring electrode) to detect products from the RDE (Fig. 4). In this case, products are ejected outwards radially from the disc electrode, and so the ring electrode is positioned outside of and coplanar with the disc electrode, with a relatively narrow insulating gap separating them.

The crucial parameter for the rotating disc electrode is the collection efficiency N . This determines the fraction of stable product generated with 100% efficiency at the disc electrode that will be collected by the ring, under mass transport control, when there is a mass transport-limiting ring current. In general, under these conditions,

$$j_R = -Nj_D \quad (15)$$

where j_R and j_D are the ring and disc fluxes, respectively. The collection efficiency can either be determined experimentally or theoretically. It is independent of rotation speed and is merely a function of electrode geometry. Under most conditions it is generally denoted as N_0 , given by [14, 15]

$$N_0 = 1 - F\left(\frac{\alpha}{\beta}\right) + \beta^{2/3}[1 - F(\alpha)] - (1 + \alpha + \beta)^{2/3} \times \left\{1 - F\left[\left(\frac{\alpha}{\beta}\right)(1 + \alpha + \beta)\right]\right\} \quad (16)$$

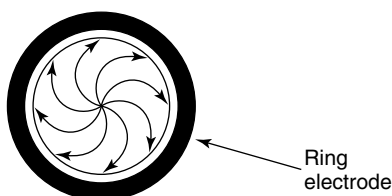


Fig. 4 The positioning of a ring electrode downstream of the rotating disc electrode.

with

$$F(\theta) = \frac{\sqrt{3}}{4\pi} \ln \left[\frac{(1 + \theta^{1/3})^3}{1 + \theta} \right] + \frac{3}{2\pi} \tan^{-1} \left[\frac{2\theta^{1/3} - 1}{\sqrt{3}} \right] + \frac{1}{4} \quad (17)$$

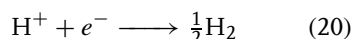
and

$$\alpha = \left(\frac{r_2}{r_1} \right)^3 - 1 \quad (18)$$

$$\beta = \left(\frac{r_3}{r_1} \right)^3 - \left(\frac{r_2}{r_1} \right)^3 \quad (19)$$

α and β are therefore merely functions of the disc radius r_1 , the inner ring radius r_2 , and the outer ring radius r_3 . N_0 typically has a value around 0.2 for most RRDE systems.

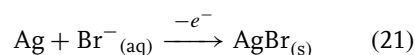
In our work on the polymerization of 5-substituted indoles [13], we have used the ring electrode of the RRDE to detect and quantify the amount of soluble trimer formed during electropolymerization (vide supra). Significant soluble fractions were obtained with indole monomers that contained solubilizing R groups, such as amino groups or hydroxy groups. Furthermore, judicious selection of the ring potential enabled the protons produced by the reaction in Eq. (14) to be detected on the ring as



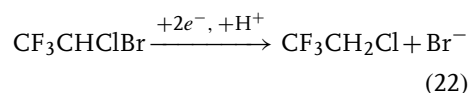
and the measured fluxes of protons on the ring were compared to the flux of electrons on the disc to establish the stoichiometry of Eq. (14).

The ring electrode can also be made from a different material to the disc, designed to selectively detect a particular species produced by the disc reaction. An example is the use of a silver ring electrode

to selectively detect the bromide ion produced by the electrochemical reduction of the inhalation anaesthetic, halothane (CF_3CHClBr), at an RDE [16]. The electrochemical reduction of halothane at an RDE is one potential method for sensing this inhalation anaesthetic. However, this reduction occurs at a very similar potential to the reduction of oxygen gas, which precludes deconvolution of the proportion of the reduction current due to oxygen, and that due to halothane. At a silver ring electrode, the selective mass transport-limited oxidation of bromide



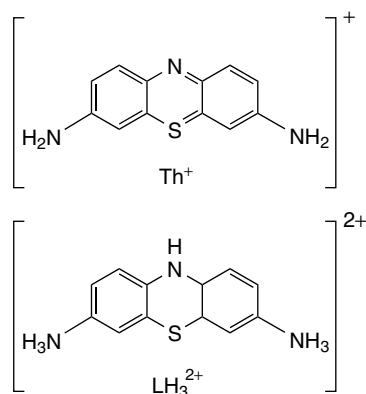
was shown to occur [16]. This produced solid silver bromide, which deposited on the ring surface at a characteristic potential. The oxidative current for this process and the reduction charge obtained from reducing the silver bromide formed on the ring electrode after a given period of time (by the reverse reaction of Eq. 21) were both shown to be a good measure of the flux of bromide produced at the disc. Comparison of the ring bromide flux and the disc electron flux established the stoichiometry of the halothane reduction reaction to be [16]



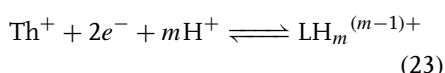
and the amount of bromide detected at the silver ring was shown to be a good measure of the proportion of halothane in the halothane/oxygen mixtures [17]. This, in combination with the overall disc current, allowed deconvolution of the relative amounts of halothane and oxygen in the mixture.

The ring electrode of an RRDE has also been used to selectively detect the

products from the redox reaction of a rotating disc-modified electrode. In this work, a thionine-coated electrode was produced by the electropolymerization of thionine. Thionine is a phenothiazine dye, and the resulting film is redox-active, with the thionine redox centers being able to be redox-cycled between their oxidized (thionine, Th) and reduced (leucothionine, L) forms, according to the



general equation

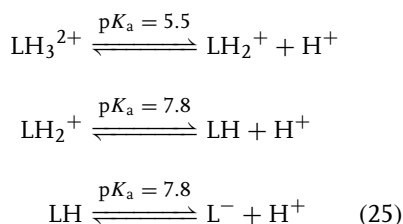


The value of m is dependent upon the pH of the solution. If $m \neq 0$, then redox reaction involves the incorporation and expulsion of protons during the redox reaction and this can be measured by a pH-sensitive bismuth oxide ring electrode [18, 19]. In the special case when the ring electrode is a potentiometric sensor with a low exchange current density, such as the bismuth oxide sensor for pH [18, 19], the ring electrode reaction does not significantly perturb the radial concentration profile of the disc product across the ring, and a different collection efficiency, termed the *detection efficiency*,

N_D , must be used [18], where

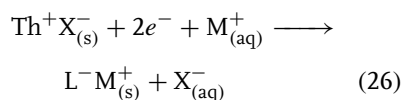
$$N_D = 1 - \frac{1}{6}F(\alpha) - \frac{2}{3} \left\{ F \left[\left(\frac{r_2 + r_3}{2r_1} \right)^3 \right] \right\} - \frac{1}{6}F(\alpha + \beta) \quad (24)$$

The exact form of the proton transients seen at the ring is determined by the degree of protonation of the L centers and their ability to act as a buffer, mopping up the protons produced in the redox reaction. This is determined by the pK_a s for deprotonation of the various protonated forms of L. Quantitative analysis of the proton transients observed at the bismuth oxide ring electrode enabled these pK_a values to be determined as



and the rate-determining step for the film redox reaction was shown to be the transport of electrons through the film.

When $m \neq 2$, then the redox reaction involves incorporation into the film or expulsion from the film of solution counteranions (and/or countercations) to maintain overall film electroneutrality during redox cycling. In unbuffered solution near pH 7, the reduction of Th⁺ rapidly causes the film pH to rise above 7.8, and the film redox reaction is



This flux of X[−] can be measured by an anion-sensitive ring electrode such as

the Ag/AgX potentiometric ring electrode, which shows a selective and quantifiable change in potential due to the local concentration of X^- anion [19]. Measurements have been made with X^- as Cl^- , using a silver/silver chloride ring electrode in an electrolyte solution of 50 mM $NaClO_4$, 1 mM $NaCl$ [19]. The magnitude of the ring transient, when compared to that expected from the disc current transient, indicated that, as expected, reaction occurred according to Eq. (26) and that the film was permselective to Cl^- over ClO_4^- by a factor of 20. Further general information on potentiometric measurements is given in Sect. 1.1.3 of Chapter 1 in this volume.

Such ring current measurements are of necessity not steady state, as the reaction involves the reduction of a redox-active film of finite thickness coated on the disc electrode. However, the ring response to a transient disc current has also been calculated. The time-dependent collection efficiency N_τ has been derived analytically for a galvanostatic (constant current and hence constant flux) step on the disc electrode [20] as a function of the dimensionless time

$$\tau = 4.0 \left(\frac{D}{\nu} \right)^{1/3} Wt \quad (27)$$

where t is the time, which allows the corresponding time-dependent variation of the ring flux to be calculated from Eqs. (7 and 15) (Fig. 5a and b) for a constant disc flux. This approach has been generalized to produce a computational method for predicting the ring flux for any form of disc flux transient [21], by considering any disc current transient as consisting of the sum of many discrete galvanostatic steps (Fig. 5d). The time-dependent ring flux can then be calculated

for each of these steps (Fig. 5e), and the responses added to give the overall ring flux transient (Fig. 5f). A similar procedure can often be applied in reverse to generate the disc flux that gave rise to an observed ring flux [22]. In this case, the parameters of a number of general disc current functions (usually \tanh and exponential functions) are adjusted so that when added, their calculated time-dependent ring flux response matches the experimentally observed ring flux. The sum of the disc flux functions then corresponds to the disc flux transient.

One final application of the RRDE is in the measurement of the kinetics of the following chemical reactions of species electrogenerated at the disc with other solution species (often termed *titration reactions*). In one of the simplest examples of these reactions, reactant A is generated electrochemically on the disc electrode, which then undergoes reaction with reactant B, present in solution, during transit between disc and ring. The ring electrode is set to detect reagent A, and because of reaction, the observed ring flux is typically less than that predicted from the disc flux and Eq. (15). A good example [23] is the use of the RRDE to study the kinetics of bromination of the fatty acids: oleic (or *cis*-9-octadecanoic) acid $[CH_3(CH_2)_7CH=CH(CH_2)_7COOH]$, erucic (or *cis*-13-docosenoic) acid $[CH_3CH_2CH=CH(CH_2)_{11}COOH]$, and linolic (or *cis,cis*-9,12-octadecanoic) acid $[CH_3(CH_2)_3(CH_2CH=CH)_2(CH_2)_7COOH]$ in a mixed solvent system of acetic acid and acetonitrile. Titration with bromine is one potential analytical method for measuring the amount of double bonds in an oil containing these unsaturated hydrocarbons in solution, but the kinetics of reaction must be sufficiently fast for this approach to be viable. In this work, bromine was

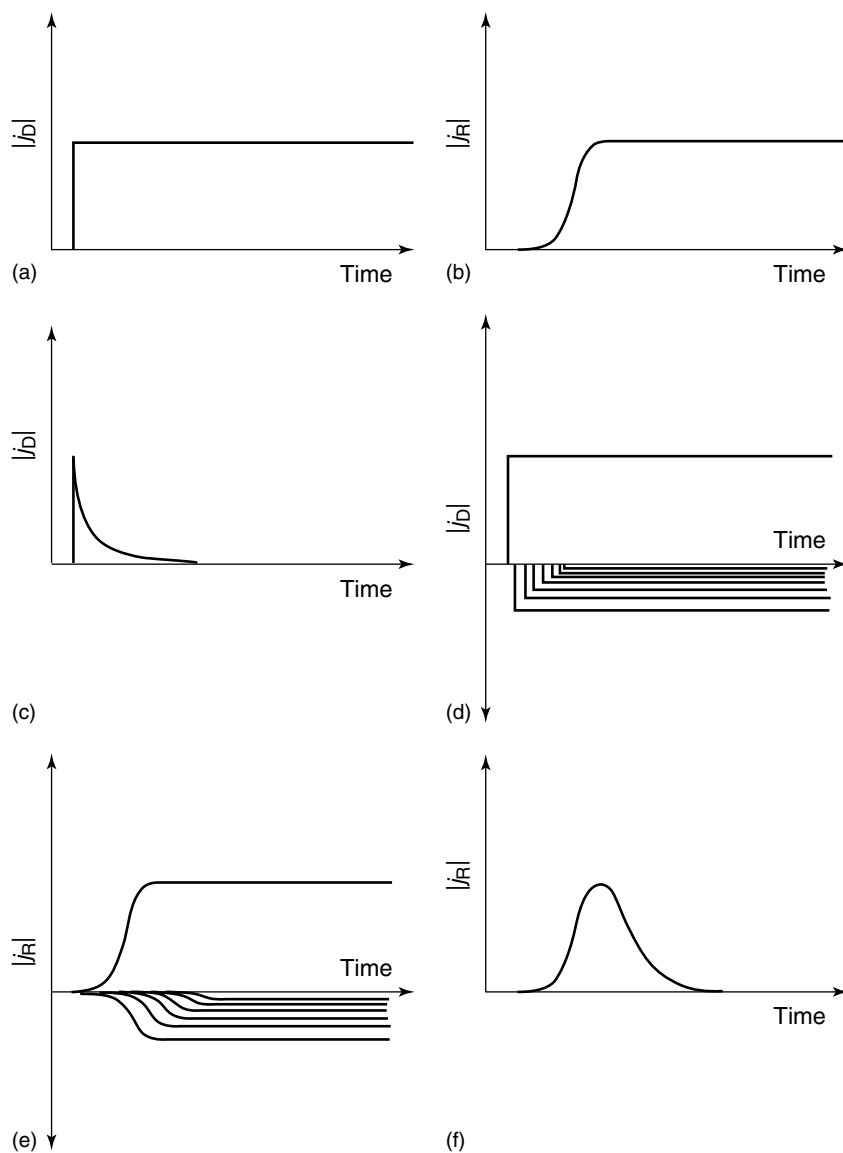
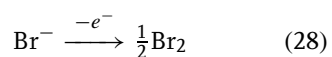


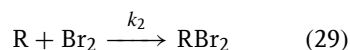
Fig. 5 The time-dependent ring flux (b) produced from a galvanostatic disc flux step (a) and N_r (d) the deconvolution of a disc flux transient (c) into a series of galvanostatic disc flux steps (e) the calculation of the time-dependent ring fluxes from these steps and their combination to produce (f), the theoretical ring flux for (c).

electrogenerated at the disc by the oxidation of Br^- according to the reaction



with the reverse reaction of being used at the ring to detect the amount of bromine. In the gap between disc and ring, reaction between bromine and the unsaturated

hydrocarbon R occurs



which reduces the amount of Br_2 available for detection at the ring, and hence the measured collection efficiency N_k , such that $N_k < N_0$. The concentration of unsaturated hydrocarbon was chosen to be greatly in excess [23] compared to the amount of Br_2 produced; therefore the reaction followed pseudo-first-order kinetics, with the first-order rate constant given by

$$k_1 = k_2 c_{org} \quad (30)$$

where c_{org} is the bulk concentration of organic hydrocarbon. For such a first-order homogeneous reaction, the relationship of N_k to N_0 has been derived analytically [24] as

$$\frac{N_0}{N_k} = \frac{0.20}{W} \left(\frac{\nu}{D} \right)^{1/3} k_1 \quad (31)$$

Measurements of N_k from the measured disc and ring currents

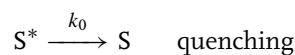
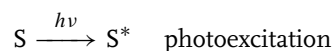
$$j_R = -N_k j_D \quad (32)$$

as a function of W were therefore used to determine k_1 and then k_2 from Eqs. (16 to 19, 30 and 31).

2.4.2.3 The Optical Rotating Disc Electrode (ORDE)

The ORDE consists of a quartz rod, polished at both ends, one of which is coated with a quasi-metallic antimony-doped tin oxide film to form a (semi-) transparent disc electrode. Light is shone down the rod and through the disc electrode as it is rotated in solution. The rotation of the ORDE imposes RDE hydrodynamics at the transparent

disc, enabling the electrochemistry of solution photoactive species excited by the light to be studied by measuring the steady state photocurrents obtained at the disc electrode. For stable species, these photocurrents tend to vary with $W^{-1/2}$, as only photoexcited species that are produced in the diffusion layer react at the electrode without being swept away, and the thickness of this diffusion layer varies with $W^{-1/2}$ (Eq. 8). Systems studied include photogalvanic cells [25] and photoactive colloids [26]. More recently, analytical expressions have been derived for analysis of the transient and steady state photocurrents for the PE process [27], where photoexcitation (P) of a sensitizer molecule (S) leads to its electrochemical oxidation (E) at an electrode surface



and these have been used to analyze the response of colloidal CdS particles [27]. This approach has been extended to the study of PCE processes [27], in which the photoexcited S^* chemically (C) reacts with a scavenger A to give A^- and S^+ , and it is A^- that is then electrochemically (E) oxidized on the disc.

A related experimental setup, the rotating optical ring-disc electrode (RORDE), has also been developed [28, 29]. Illumination in this case occurs through a quartz disc, with detection of the photosensitized products occurring on a platinum ring. This ring electrode has the advantage of being more chemically inert

than tin oxide, allowing it to be used to study a wider variety of photoactive species.

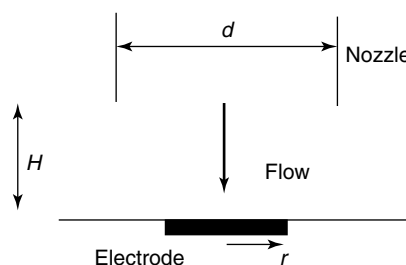
2.4.3

Solution Flow Hydrodynamic Systems

Although the RDE and RRDE systems are extremely widely utilized, there are some problems associated with them for some applications. One of these is that the disc electrode rotates, which makes it difficult to attach ancillary sensing devices such as spectrophotometers in close proximity to the electrode to monitor disc products. To overcome this, hydrodynamic systems have been developed in which the electrode remains stationary and the solution moves. These also have the advantage of being compatible detection systems for the flowing eluent from dynamic solvent separation systems such as chromatographic columns. Unlike the RDE and RRDE, a packed bed electrode can also easily be incorporated upstream of the system through which the solution must flow. This enables electrochemical redox reaction of reagents in the column, producing new species with 100% conversion in solution for subsequent analysis in the system. An interesting example of the use of the Packed Bed Wall-jet Electrode (PBWJE) [30] is the electrochemical detection of nitrate ion by means of the WJE (see Sect. 2.4.3.2). This involves the electrochemical production of Cu^{2+} ion from a copper packed bed, which is then deposited by reduction on the disc electrode of a wall-jet electrode (WJE), producing a fresh copper disc electrode. This fresh copper film is necessary for the electrochemical reduction and detection of nitrate at a WJE, as reduction leads to progressive poisoning of the copper electrode.

This section will focus on the major solution flow hydrodynamic systems, initially looking at those in which fluid exits a tube via a nozzle and impinges on a stationary electrode (or electrodes), and then at those in which an electrode (or electrodes) is (are) incorporated into the tube itself. It will be seen that many of these systems are not uniformly accessible; although this can be a disadvantage when studying systems such as modified electrodes (see Sect. 2.4.2.1), in which uniform mass transport simplifies analysis and ensures equivalence of reaction across the entire electrode, it has been argued that nonuniformly accessible systems should have greater inherent kinetic discrimination [31] when studying electrochemical reactions with coupled chemical reactions. This is because in many cases, analysis of these systems generally involves fitting experimental data to theoretical curves. These curves often predict the variation in the effective number of electrons, n_{eff} , passed during reaction with the velocity of the hydrodynamic solution [controlled by W for the RDE (see Sect. 2.4.2.1) and the volume flow rate V_f for the solution flow systems below]. Nonuniformly accessible electrodes show a variation in the mass transfer flux (and hence the balance of importance of kinetic and hydrodynamic terms) across the electrode surface, which results in a more gradual change in n_{eff} with V_f than for n_{eff} with W for the RDE. This more gradual change should enhance the distinction between differing coupled chemical reaction mechanisms and lead to greater accuracy in kinetic analysis. This has been demonstrated for measurements of the ECE reaction (electron transfer, chemical reaction, electron transfer) at both a WJE and an RDE [32]. Although

Fig. 6 The wall-tube electrode configuration.



Unwin and Compton [33] have shown no significant distinction for first-order chemical processes, they have postulated that this will not be the case for second- and higher-order processes.

2.4.3.1 The Wall-tube Electrode (WTE)

The wall-tube electrode system involves pumping the electrolyte solution through a nozzle onto a disc electrode as a jet of fluid (Fig. 6). In this arrangement, the nozzle diameter d is larger than the disc electrode diameter $2r$, and electrode and jet are arranged coaxially. Under these conditions, the factors controlling the mass transport hydrodynamics of a WTE are well established [34]. The mass transfer characteristics are analogous to the RDE, with essentially uniform accessibility across the electrode surface [35]. There is, however, a slight dependence of the mass transport-limited current on the nozzle-electrode separation H , with [34]

$$i_L = 12.08nFAD^{2/3}v^{-1/6}c_\infty \times \left(\frac{V_f}{\pi d^3}\right)^{1/2} \left(\frac{H}{d}\right)^{-0.054} \quad (33)$$

where V_f is the volume flow rate of fluid ($\text{cm}^3 \text{s}^{-1}$) through the nozzle. When comparing this equation to Eq. (11), it is clear that V_f is the equivalent variable for the WTE to W for the RDE, as is the case for all solution hydrodynamic systems.

2.4.3.2 The Wall-jet Electrode (WJE)

The WJE has a similar configuration to the WTE, but in this case the nozzle diameter d is very much smaller than the electrode diameter $2r$. This produces the hydrodynamic flow pattern shown in Fig. 7.

The limiting current for the WJE is (under conditions in which the electrode-cell wall separation is very much larger than the electrode-nozzle separation) [15, 36]

$$i_L = 1.38nFD^{2/3}v^{-5/12}d^{-1/2}r^{3/4}c_\infty V_f^{3/4} \quad (34)$$

As can be seen from Fig. 7, the electrode is not uniformly accessible; in fact the thickness of the diffusion layer varies with $r^{5/4}$ and hence from Eq. (9), the mass transport-limited flux at the electrode varies with $r^{-5/4}$. Figure 7 also shows

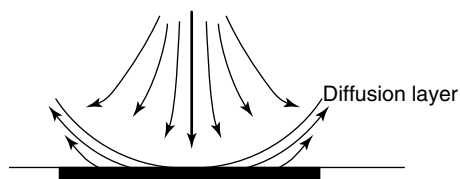


Fig. 7 The flow pattern at the WJE.

that away from the center of the jet in the diffusion layer, flow is away from the electrode, ensuring that a fresh electrolyte from the jet is efficiently brought to the electrode surface. Also, the relatively narrow jet decreases the volume flow rate of solution required for controlled hydrodynamics, decreasing the volume required for analysis compared with the WTE, and the jet spreads radially across the electrode surface, ensuring that a relatively large proportion of the reagent in the jet can be detected on the electrode, thereby increasing detection sensitivity. As a result, the WJE has been used as a sensitive analytical electrochemical detector in flow-through chromatographic systems [37, 38].

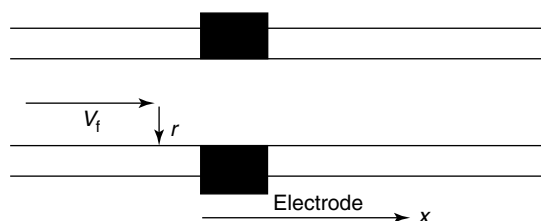
Two further applications demonstrate the relative ease of incorporation of ancillary electronic measurement systems at a stationary disc in the WJE compared with a rotating disc in the RDE. The first involves using the WJE configuration to measure the rate of deposition of colloidal particles on a (semi-) transparent doped tin oxide disc electrode as a function of electrode potential, by measuring the degree of light scattering of the adsorbed particles on the transparent electrode using total internal reflection microscopy [39, 40]. In this work, the predicted radial variation of the mass transport-limited flux across the electrode proved extremely useful in assessing whether deposition occurred under mass transport or surface electrochemical control. The second concerns measurement of the kinetics and mechanism of copper dissolution in acid chloride media [41]. This work involves the use of an electrochemical quartz crystal microbalance (EQCM) as the disc electrode in the WJE configuration. Controlled dissolution was achieved because of the WJE hydrodynamics,

and the EQCM allowed simultaneous measurement of the mass loss from the copper disc electrode and the current due to copper oxidation and dissolution. Correlation of these two measurements allowed direct determination of the variation of the overall copper dissolution valency (between 1 and 2) as a function of the chloride concentration and the hydrodynamic conditions employed. Although there has been one study of the deposition of clays using an EQCM disc system constructed in the RDE configuration [42], this is more of a technological and engineering challenge than using the WJE configuration. An overview of the EQCM and its applications is the subject of Chapter 2.7 of this volume.

2.4.3.3 The Wall-jet Ring-disc Electrode (WJRDE)

The WJRDE system has also been developed [43], and this has enabled still greater sensitivity in analytical detection. Fundamentally, the WJRDE is a WJE in which the disc electrode is replaced by a ring-disc electrode (see Sect. 2.4.2.2). The hydrodynamic regime of the WJE leads to lower collection efficiencies N for the WJRDE (from Eq. 15) compared to an RRDE of similar dimensions, as significant flow in the diffusion layer is away from the electrode surface. Also, unlike the RDE, this collection efficiency N varies (albeit predictably and reproducibly) with V_f . Despite this, the WJRDE configuration is particularly applicable to analytical detection of species in flow injection analysis and liquid chromatography [44], and particularly those species that take part in plating-stripping reactions [45]. This configuration enables reagents in the jet to be electrochemically deposited (plated) and accumulated on the surface

Fig. 8 The tube electrode system.



of the disc by maintaining a suitable disc potential. The reaction can then be reversed at the disc by changing potential, stripping the reagents off the electrode in a concentrated burst, to be detected by the downstream ring electrode. This preconcentration of reagents on the disc markedly increases the overall detection sensitivity of the system when compared to the WJE.

2.4.3.4 The Tube or Tubular Electrode (TE)

The TE system consists of an annular electrode that is inserted into the length of a cylindrical tube down which the solution under study flows (Fig. 8).

In this simple configuration, the volume flow rate V_f is chosen to ensure laminar flow of solution in the cylindrical tube. Because of friction with the tube walls, the velocity of liquid v in the tube varies in a parabolic manner with the distance r from the tube center [46, 47]

$$v = v_0 \left(1 - \left[\frac{r}{r_0} \right]^2 \right) \quad (35)$$

where v_0 is the velocity at the center of the tube and r_0 is the radius of the tube, so that $r \leq r_0$. As the flow is laminar, the diffusion layer thickness (the equivalent of z_D for the RDE, see Sect. 2.4.2.1) increases with the distance x , downstream from the upstream edge of the tube electrode, actually as $x^{1/3}$. The mass transport-controlled flux (from Eq. 9)

therefore varies with $x^{-1/3}$ across the electrode surface, and hence like the WJE, this electrode is not uniformly accessible. If long electrodes or slow flow conditions are avoided, so that the diffusion layer thickness does not become comparable to the tube radius (resulting in the depletion of reagents extending into the center of the tube), the limiting current is given by the Levich equation for the TE [5]

$$i_L = 5.43nF(Dl)^{2/3}V_f^{1/3}c_\infty \quad (36)$$

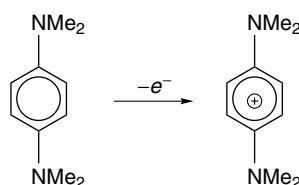
where l is the length of the electrode (i.e. it extends from $x = 0$ to $x = l$). This equation is derived assuming flow is sufficiently fast such that diffusion in the direction of convective flow can be considered to have a negligible effect, convection is sufficient to ensure that the concentration gradient of reactive species near the electrode can be linearized and the diffusion layer thickness is much smaller than the tube dimensions across the whole electrode surface [48]. Under these conditions, the limiting current does not depend upon either r_0 or (unlike the RDE and RRDE) the kinematic viscosity of the solvent. At the slow flow or long electrode limit (often termed the thin layer cell configuration), in which complete conversion of the reagents in the tube occurs by the end of the electrode, the simple expression

$$i_L = nFV_fc_\infty \quad (37)$$

applies. A transition therefore occurs between these two limiting analytical expressions (Eqs. 36 and 37) at intermediate values of V_f , but the complete theoretical description of the response of the TE can only be determined numerically (see Sect. 2.4.4) [48]. This does mean that the hydrodynamic conditions of the TE can be varied to control the degree of electrochemical conversion of reagents in solution and that unlike the systems considered previously, essentially 100% conversion of reagents to products can be achieved in the thin electrode configuration by judicious choice of electrode length and flow. This can often be useful in electroanalysis, for example, in the design of electrochemical chromatographic detectors.

The detection and generation efficiency and the controlled hydrodynamics of this system have also been utilized in the electrochemical generation, detection, and characterization of radicals. In this work, a TE was positioned just upstream of an esr spectrometer cavity, so that the radicals generated were transported into the cavity without the electrode destabilizing the cavity resonance. Not only does esr allow identification and characterization of the radical generated but the reproducible hydrodynamics allow the theoretical variation of esr signal intensity with V_f to be calculated. Initial work concentrated on stable radical systems, in which both steady state esr signal intensities [46] and the time-dependent response of the esr signal intensity to a step change in tube electrode current [49] were measured and compared with theory. In this work, good agreement was found between the theoretical and experimental signal intensities for the

one-electron oxidation of N, N, N', N' -tetramethyl-*p*-phenylenediamine (TMPD)



confirming both the stability of the radical and the viability of this approach. Theoretical and experimental studies were subsequently extended to unstable radicals that decompose by simple first-order kinetics [50] and those that decompose by second-order kinetics [47], for which the TE esr system allowed direct measurements of the first-order and second-order rate constants, respectively.

The analysis of steady state voltammetric curves at a TE has also been achieved for electrochemically reversible [51], quasi-reversible [52], and irreversible [52] electron transfer reactions by numerical methods (see Sect. 2.4.4), which enables experimental voltammetric curves to be analyzed to give electrochemical kinetic information.

2.4.3.5 The Channel Electrode (CE)

The CE system is shown in Fig. 9. In hydrodynamic terms it is closely related to the TE system.

It consists of an electrode embedded in the wall of a tube down which solution flows. Generally, $h \ll d$ to ensure edge effects on the flow are negligible. As with the TE (see Sect. 2.4.3.4), the solution is under laminar flow, with the parabolic variation in velocity with height given in this case by

$$v = v_0 \left[1 - \left(\frac{y}{h} \right)^2 \right] \quad (38)$$

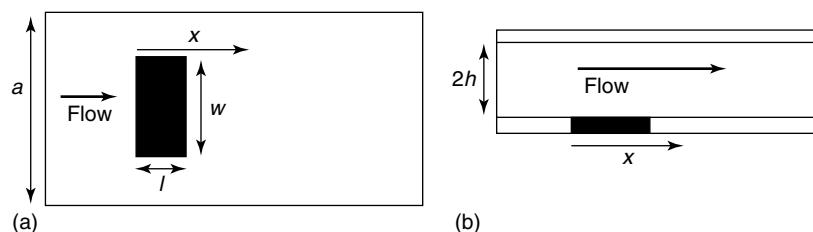


Fig. 9 The channel electrode system seen from (a) above and (b) the side. The electrode dimensions are width w and length l . The channel width and height are d and $2h$, respectively, with y , the height variable, ranging from $-h$ (at the electrode surface) to h and with $y = 0$ corresponding to the center of the channel.

The diffusion layer thickness also varies with $x^{1/3}$, which from Eq. (9) means that the mass transport-limited flux across the CE varies with $x^{-1/3}$, so that the electrode is nonuniformly accessible. An analogous Levich equation to the TE has been derived analytically for the CE. This gives the mass transport-limited current for fast flow (where as with the TE, diffusion in the direction of convective flow can be considered to be negligible and where convection is so efficient that the concentration gradient of reactive species near the electrode can be linearized [53]) and for short electrodes (in which the diffusion layer can be considered to be thin compared to the height of the channel) as

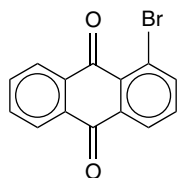
$$i_L = 0.925nFw \left(\frac{Dl}{h} \right)^{2/3} \left(\frac{V_f}{d} \right)^{1/3} c_\infty \quad (39)$$

As with the TE, at slow flow and for long electrodes, complete conversion of the electroactive species can occur, and under these conditions the TE thin layer cell equation (Eq. 37) applies. Like the TE, these are limiting cases, and the complete rigorous description of the response of the CE at all flows and electrode lengths requires numerical methods (see Sect. 2.4.4) [48]. However, for both these systems this is relatively straightforward [54] (see Sect. 2.4.4) and the resulting mass transport-limited

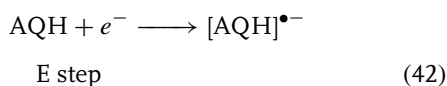
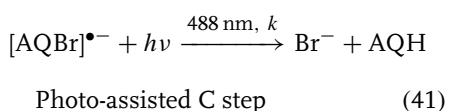
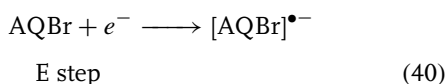
current shows a smooth transition between Eqs. (38 and 39) with decreasing flow and increasing electrode length. Thus, like the TE, the CE system can be used in the thin layer cell configuration for the complete detection of electrochemically active species in chromatographic separations [55]. The CE, like the TE, can also be employed for the efficient generation and detection of radicals, by combining the CE with radical detection and quantitation using an esr spectrometer. However, unlike the TE, the CE system can in fact be placed directly in the center of the cavity of the esr spectrometer without significant perturbation of the resonant sensitivity, as long as the cell is constructed of synthetic silica [56]. This enables detection of radical intermediates and products with much shorter lifetimes than in the TE configuration. Concentration distributions of electrogenerated radicals have therefore been calculated under steady state conditions for model electrode reaction mechanisms and have been used to produce the theoretical esr signal intensity [57–59]. Analysis of experimental data using this theory has then allowed electrode reaction mechanisms to be verified and radical lifetimes to be measured.

A further advantage of the CE system is that unlike the TE, a window of transparent material can be incorporated into

the channel unit in the region of the electrode [60–62]. Incorporation of this window either directly above or downstream of the electrode allows spectroscopic interrogation and/or photoexcitation of electrogenerated products or intermediates with light, while a window either above or upstream of the electrode allows spectroscopic interrogation and/or photoexcitation of reagents prior to electrochemical reaction. A good example of the use of such a system is in the electrochemical reduction of 1-bromoanthroquinone (AQBr),



which is simultaneously irradiated with 488-nm light [63]. Detection of the radical products of the reaction was by means of an esr spectrometer. This work established that reaction occurred by a photo-ECE mechanism



Identification of the esr spectrum and quantitative analysis of the esr signal intensity as a function of electrogeneration current and channel flow conditions established that the reaction given in Eq. (40) occurred in the absence of light, producing the stable $[\text{AQBr}]^{\bullet-}$ radical. Upon irradiation, the esr spectrum of $[\text{AQH}]^{\bullet-}$ was observed at slow flow; the loss of the esr intensity of the $[\text{AQBr}]^{\bullet-}$ radical was then quantitatively analyzed as V_f was varied, confirming the reaction mechanism and producing a value for the rate constant of the C reaction (Eq. 41) as $k = 0.047 \text{ s}^{-1}$, in good agreement with other independent measurements [64, 65].

2.4.3.6 The Double Channel Electrode (DCE) and Double Tube Electrode (DTE)

The DCE system (Fig. 10) is the equivalent configuration for the CE as the RRDE (see Sect. 2.4.2.2) is for the RDE (see Sect. 2.4.2.1).

In this configuration, a second or collector channel electrode is placed downstream of the first or generator CE to detect products from the electrogeneration reaction [66]. An analogous system can also be constructed for the TE, with a

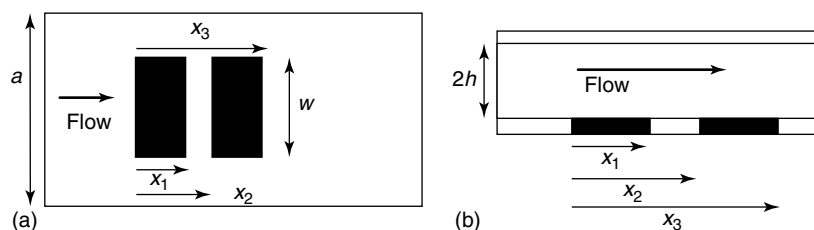


Fig. 10 The DCE system: (a) top view and (b) side view. x_1 , x_2 , and x_3 are the first or generating channel length, the distance to the inner edge of the second or collecting channel electrode and the distance to the outer edge of the collecting channel electrode, respectively, along the flow path.

second tube electrode positioned with its inner and outer edges at distances of x_2 and x_3 downstream of a generating electrode of length x_1 (Fig. 8), producing a DTE [67, 68]. As the hydrodynamics of the TE and CE are essentially the same, the DCE and DTE have similar characteristics; hence, in this section, only the DCE will be discussed.

The collector channel electrode of the DCE performs a similar function to the ring electrode of the RRDE (see Sect. 2.4.2.2), electrochemically detecting products electrogenerated on the upstream electrode, in this case the generator channel electrode. Usually, the generator electrode is held at a potential that ensures mass transport-limited electrogeneration of product and the collector electrode is held at a potential to ensure mass transport-limited electrochemical reaction of this product. [Like the RRDE (see Sect. 2.4.2.2), when more than one product is formed, the collector electrode material and the potential can be chosen to selectively detect the product of choice.]

As with the RRDE, the theoretical collection efficiency N of the collector electrode (see Eq. 15) has been determined for the simplest case in which one stable electroactive product is formed at 100% efficiency

$$j_{\text{coll}} = -Nj_{\text{gen}} \quad (43)$$

where j_{coll} and j_{gen} are the collector and generator electrode fluxes, respectively, determined from the currents by Eq. (7) [66, 69–71]. In the first treatment [66, 69, 70], a uniform surface concentration was assumed across the generator electrode, applicable to electrochemically reversible systems. This produces the following relationship

for N :

$$N = 1 + \lambda^{2/3}[1 - F(\theta)] - (1 + \lambda + \theta)^{2/3} \times \left\{ 1 - F\left[\left(\frac{\theta}{\lambda}\right)(1 + \lambda + \theta)\right] \right\} - F\left(\frac{\theta}{\lambda}\right) \quad (44)$$

which has been experimentally verified for the reversible ferri/ferrocyanide couple [72], whereas the second treatment [71], which assumes a uniform current distribution on the generator electrode, applicable to electrochemically irreversible systems, gives

$$N = 1 - (1 + \lambda + \theta)F\left(\frac{1 + \theta}{\lambda}\right) + (\lambda + \theta)F\left(\frac{\theta}{\lambda}\right) + \frac{3^{3/2}\lambda^{2/3}}{2\pi} \left[(1 + \theta)^{1/3} - \lambda^{1/3} \right] \quad (45)$$

In both cases

$$\theta = \frac{x_2 - x_1}{x_1} \quad (46)$$

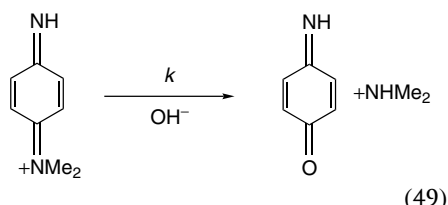
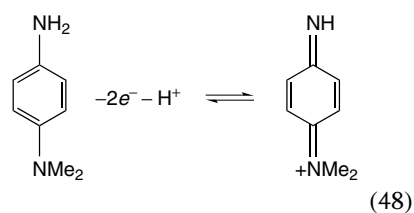
and

$$\lambda = \frac{x_3 - x_2}{x_1} \quad (47)$$

and $F(\theta)$ is the function defined in Eq. (17). It should be noted that as for the RRDE, both treatments predict N to be dependent only on electrode geometry and not on flow conditions. However, the nonuniform accessibility of the channel configuration results in a nonuniform current distribution of the channel electrode, which leads to different values of N for reversible and irreversible electrochemistry at the generator electrode. This is because the reversible system (the first treatment) assumes rapid electrode kinetics and a

constant concentration of reactant and product across the electrode surface, which results in more current being passed at the upstream end of the generator electrode than in the irreversible case. Products have more chance of escaping from the upstream part of the generator electrode into bulk solution and evading the collector electrode. As a consequence, the collection efficiency is greater for the irreversible system. This variation in collection efficiency can in principle be used to determine the electrochemical kinetics on the generator electrode for those reagents in which the electrochemical and mass transfer rate constants are comparable at the generator electrode. Under slow flow conditions, the rate of mass transfer is rate-limiting and the system can be considered reversible, with N given by Eq. (44); however, for fast flow, if the surface electrochemical reaction becomes rate-limiting, the reaction can be considered irreversible, with N given by Eq. (45). The flow condition at which the transition between these two limiting values occurs is therefore a useful measure of the electrochemical kinetics [48].

Like the RRDE (see Sect. 2.4.2.2), the DCE has also been extensively used to study the kinetics and mechanisms of electrode reactions involving following chemical reactions. A good example is the electrooxidation of 4-amino-*N,N*-dimethylaniline (ADMA), which proceeds by an EC reaction in basic aqueous solution [71].



The aromatic products of both the first step (i.e. oxidized ADMA) and the second step (following deamination) are electrochemically active, and can be detected under mass transport control at 0.0 V and -0.2 V, respectively, versus the saturated calomel electrode on the collector electrode. Setting the potential at -0.2 V therefore detects the current due to *both* the products. As expected, when this current was used to calculate the experimental collection efficiency N , it closely coincided with that expected for a stable reversible electrochemical reaction (Eq. 44). However, measurement of the current at 0.0 V also enabled the relative fluxes at the collector electrode due to oxidized ADMA and the product of the chemical reaction to be deconvoluted. Increasing V_f allowed the transit time from generator to collector to be decreased, which decreased the importance of the following chemical reaction. Comparison of the experimental variation of N with V_f for each product with the theoretical response solved through numerical methods [73] allowed a value of k to be determined as $k = 1.8 \times 10^4 \text{ dm}^3 \text{ mol}^{-1} \text{ s}^{-1}$. This was in good agreement with previous spectrophotometric measurements [72], demonstrating the applicability of this approach.

As with the RRDE (see Sect. 2.4.2.2), transient collection measurements are also possible with the DCE. Transient data collection and analysis is extremely

important for measuring fluxes due to the redox reaction of finite amounts of species adsorbed on the generator electrode (e.g. for modified electrodes, see Sect. 2.4.2.2) or for reactions in which generation is accompanied by adsorption of products on the generator electrode. The time-dependent collection efficiency N_τ , has been calculated for a stable species generated under electrochemically reversible conditions and collected under mass transport-controlled conditions with 100% efficiency. This allows the time-dependent variation of the collector electrode current to be calculated from Eqs. (7 and 15) for a constant generator electrode current. N_τ is the collection efficiency as a function of the dimensionless time τ , which is related to the time t , by

$$\tau = \left(\frac{4v_0^2 D}{h^2 l^2} \right)^{1/3} t \quad (50)$$

Analytical expressions have been derived both at short τ and long τ [74], and these have been shown to correlate closely with the general N_τ function determined numerically (see Sect. 2.4.4), applicable at all τ [74]. This general function can be reproduced to within 4.5% by the simple analytical expression

$$\frac{N_\tau}{N} = \frac{1 + \tanh \Xi}{2} \quad (51)$$

in the range $0.1 \leq \theta \leq 1.0$ and $0.5 \leq \lambda \leq 1.5$, where

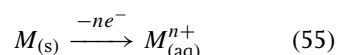
$$\Xi = \left[E - \left(\frac{1}{B} \right)^2 \right] \tau - (E)(B)^{2/3} + \frac{1.5}{B^{4/3}} - \frac{1}{2\tau} \quad (52)$$

$$E = 1.44 - 0.386\lambda \quad (53)$$

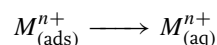
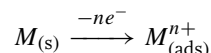
$$B = 2.53\theta + 0.38\lambda + 0.9 \quad (54)$$

and θ , λ , and N are given by Eqs. (46, 47 and 44), respectively.

Transient current DCE studies have been utilized in the investigation of the mechanism of anodic metal dissolution. This reaction may be simply written as



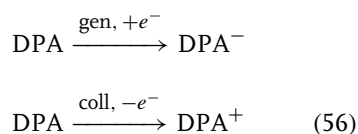
but for many metals the actual mechanism is much more complex, often involving adsorbed intermediates. Such processes have been studied using transient measurements on the RRDE ([75], see Sect. 2.4.2.2), but transient measurements have also successfully been carried out using the DCE [76, 77]. In this work, a galvanic current step on the metal generator electrode was used to induce oxidation and dissolution of the metal according to Eq. (55). The collector electrode was then set to a potential to cause mass transport-limited reduction and detection of the metal ions, and the transient collection current recorded. Some of these reactions take place via adsorbed intermediates



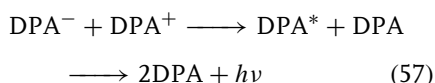
in which case adsorption on the generator electrode causes the experimental collector current to rise more slowly with time to its steady state value, after the onset of metal oxidation, than would be expected in the absence of adsorption. The expected collector current, in the absence of adsorption, can be calculated from the generator electrode current and Eqs. (7, 15, 44, and 51) (or, more accurately, the current predicted using the general N_τ function calculated numerically, rather than Eq. 51). The difference in charge (produced by

integrating the current with time) between the expected collection in the absence of adsorption and the experimental collection has therefore been used not only as a method for determining whether adsorption takes place but also as a quantitative measure of the total number of moles of adsorbed intermediate on the generator electrode [76, 77].

An interesting application of the DCE is in the study of electrochemiluminescent reactions [78]. In this work, the generator and collector electrodes were used to generate the reduced and oxidized forms of diphenylaniline (DPA) according to the equations



These species were then mixed under the controlled hydrodynamics of the DCE. This gave the excited state, DPA^* , which luminesces because of the following reactions:



Luminescence was measured through a transparent window (see Sect. 2.4.3.5) using a charge coupled device (CCD) detector. The variation of ECL intensity as a function of V_f permitted kinetic and mechanistic modeling of the ECL reaction.

2.4.4

Numerical Calculations

Although analytical solutions can be derived for many reactions using the RRDE (see Sect. 2.4.2.2), owing to the simplifications afforded by its circular symmetry [3], there are many reactions, particularly those with complicated homogeneous kinetics, for which the theoretical response of the RRDE requires a numerical solution. An introduction and overview of numerical methods was given in Chapter 1.3 of this volume. Bard and Prater [79] and Feldberg [80, 81] were the first to develop suitable methodology. Their approach was to divide the solution in the vicinity of the RRDE into a grid (Fig. 11). The circular symmetry of the system ensures that all variables are circularly symmetric, which reduces the numerical analysis to a two-dimensional problem, requiring a two-dimensional grid

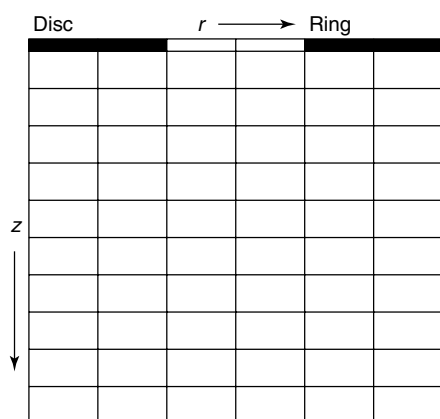


Fig. 11 The division of the solution near the RRDE into a two-dimensional grid.

as shown. As long as one chooses a grid with enough elements, any smooth function, $f(r, z)$, (such as concentration) can then be approximated to a series of discrete values, one of which is assigned to each box location r, z . The derivatives of these functions can then simply be obtained from the differences between the neighboring boxes.

Simulation occurs with successive time steps, Δt from $t = 0$. The initial conditions (at $t = 0$) define the starting configuration of the system. Boundary conditions at the disc and the ring and in the gap ensure that the simulation remains physically realistic (typical boundary conditions are that the concentration gradient of electrochemically active species at the disc is set by the current at the disc, that this concentration gradient must be zero at the insulator between disc and ring and that the concentrations in the bulk solution must remain constant at the bulk concentration value at all t). Numerical calculation then typically involves the calculation of the concentration differences between neighboring boxes at the initial time, $t = 0$, to give the concentration gradients $\partial c_i / \partial z$, $\partial c_i / \partial r$, $\partial^2 c_i / \partial z^2$, and $\partial^2 c_i / \partial r^2$ for the redox-active species i . The convective-diffusion equation for the system is then used to calculate dc_i/dt for each box, with the controlled hydrodynamics of each system ensuring reproducible, known, time-independent solution convection. For example, for the RDE, the convective-diffusion equation for species i is

$$\frac{dc_i}{dt} = D_i \frac{\partial^2 c_i}{\partial z^2} + C z^2 \frac{\partial c_i}{\partial z} - C r z \frac{\partial c}{\partial r} \pm k c_i^m c_j^m \dots \quad (58)$$

where

$$C = -8.0 \left(\frac{W^3}{\nu} \right)^{1/2} \quad (59)$$

The final term in Eq. (58) is present when analyzing electron transfer processes that include a coupled homogeneous chemical reaction. For example, for first-order decay of i , the term is negative, $m = 1$, $n = 0$, and k is a first-order rate constant (s^{-1}), whereas for bimolecular decay of i by reaction with j , $m = 1$, $n = 1$, and k is a second-order rate constant ($cm^3 mol^{-1} s^{-1}$). A similar convective-diffusion equation exists for each species, i , j , and so on; these can be solved to give $\partial c / \partial t$ for all boxes and all species. These $\partial c / \partial t$ terms then enable the overall changes in concentration in each box over a short time step Δt to be determined, which gives the new concentrations of each species in each box at time Δt .

This process can be successively repeated, generating concentration profiles for all species at times $2\Delta t$, $3\Delta t$, and so on until steady state conditions have been reached. The flux (and hence the current from Eq. 7) at the ring electrode at any time at any point on the ring electrode surface is then simply determined by Fick's first law at the electrode surface ($z = 0$) for the redox-active species i

$$j = -D \left[\frac{\partial c_i}{\partial z} \right]_{z=0} \quad (60)$$

To produce the most accurate values of ring current, the concentration gradients must be most accurately determined at and near the ring electrode, where these gradients are usually the steepest. A finer grid is often used on the innermost box, near the ring electrode [82], to achieve this. Also, non-Cartesian space has been used, replacing the Cartesian coordinate z with

w , where [83]

$$w = \frac{\int_0^x \exp\left(\frac{-x^3}{3}\right) dx}{\int_0^\infty \exp\left(\frac{-x^3}{3}\right) dx} \quad (61)$$

where

$$x = 2 \left(\frac{W^{1/2}}{D^{1/3} \nu^{1/6}} \right) z \quad (62)$$

This has two effects. Firstly, instead of the z variable extending from 0 to infinity, the w variable extends from 0 to 1, thereby reducing the number of boxes required in the calculation. Secondly, this transformation linearizes the concentration gradients, which makes the contribution of each box to the total calculation more equal. These effects combine to greatly enhance the efficiency of the calculation.

Similar numerical calculations can also be carried out on the WJRDE and the WTE because of their similar circularly symmetric geometry. These involve using the appropriate convective-diffusion equation for the hydrodynamic system of study. For the WJRDE this is [84]

$$\frac{dc_i}{dt} = D_i \frac{\partial^2 c_i}{\partial z^2} + v_z \frac{\partial c_i}{\partial z} - v_r \frac{\partial c}{\partial r} \pm kc_i^m c_j^m \quad (63)$$

where v_z and v_r are the solution velocity components in the z - and r -directions, respectively. As for all these hydrodynamic electrodes, the variation of v_z and v_r with r and z are well established.

For the DCE (and the DTE), such circular symmetry does not apply. In this case, a two-dimensional grid in x and y is again constructed as in Fig. 11, but with the x -component, which is the channel length variable (see Sect. 2.4.3.6), replacing the

variable r in Fig. 11 and the y -component, which is the channel height variable (Fig. 9 and see Sect. 2.4.3.5), replacing z in Fig. 11 [55, 85, 86]. The generator and collector channel electrodes then occupy similar positions in this grid as the ring and disc, respectively, in Fig. 11. In order to make the simulation two-dimensional and hence simple, the electrode width (w in Fig. 10) is usually assumed to be sufficiently large to ensure uniformity in this dimension (although if this is not the case, simulation, although more complicated, is still perfectly feasible). As long as the system has laminar flow, the convective-diffusion equation for this system is

$$\frac{dc_i}{dt} = D_i \frac{\partial^2 c_i}{\partial y^2} - v_0 \left(1 - \frac{y^2}{h^2} \right) \frac{\partial c}{\partial r} \pm kc_i^m c_j^m \quad (64)$$

as the convective flow in the system is determined by Eq. (38). The backwards implicit method has been found to be the best method of calculation for the DCE system [55].

2.4.5

Microhydrodynamic Systems

With recent improvements in micromachining and microfabrication, solution flow hydrodynamic systems have been produced on the micrometer scale. A micrometer scale WTE (MWTE) system has recently been developed [87], as has a microjet electrode (MJE) [88–90]. This has similar dimensions to the MWTE, but in the MJE the nozzle has been placed off-axis to enhance mass transport to the electrode. A micromachined WJRDE (MWJRDE) has also been produced and characterized [91] and microchannel electrode (MCE) and microchannel double electrode (MCDE)

systems have been made both by a sandwiching method [92] and by lithography [93]. The fundamental question is “why is there this drive toward fabrication on the microscale?”

The first and most obvious answer is the reduction in volume inherent in reducing the hydrodynamic electrode scale. It has been shown (see Sect. 2.4.3) that all solution flow hydrodynamic systems produce fluxes that are directly proportional to V_f (usually to some fractional power) and inversely proportional to electrode scale. This is because it is the solution *velocity* that determines the hydrodynamic regime. Reduction in electrode scale therefore leads to a comparable solution velocity at lower V_f , which allows experimental measurement and theoretical analysis of lower volumes of solution. This is compatible with microanalysis in, for example, biological systems and microchromatography. Furthermore, the lower V_f values required enable less technologically complex pumping systems to be employed. The second answer is that the collection efficiency of detector electrodes (such as in the DCE, the DTE, and the WJRDE systems) is increased as the gap between generator and collector electrodes is reduced. Thus, micromachined systems offer the possibility of enhanced detection. The final answer is that as the distance between generator and collector electrodes is reduced, the transit time between electrodes at a given solution velocity is decreased. This transit time often determines the fastest kinetic rate constant that can be measured by the system for unstable species, for if the kinetics are so fast that the reaction is completed in the zone between generator and collector, a rate constant cannot accurately be

determined (see Sect. 2.4.3.6). There is a viable solution velocity range for any hydrodynamic system; for example, if the velocity is too low, irreproducible stirring occurs, whereas if it is too high, turbulent rather than radial flow occurs, which again causes instability and irreproducibility. Reduction of system dimension therefore allows shorter transit times and faster reaction kinetics to be accessed within this viable solution velocity range [94]. The shortest response time for any system can also be determined in transient studies by the electrode double layer charging time, and this is also reduced with electrode dimension. It is to be expected that these advantages will ensure an increase in the use of microhydrodynamic electrode systems. Further applications of microelectrochemical systems are the subject of the next chapter.

References

1. D. E. Williams, K. Ellis, A. Colville et al., *J. Electroanal. Chem.* **1997**, 432, 159.
2. G. Macfie, R. G. Compton, *J. Electroanal. Chem.* **2001**, 503, 125.
3. W. J. Albery, M. L. Hitchman, *Ring-Disc Electrodes*, Clarendon Press, Oxford, 1971.
4. W. J. Albery, S. Bruckenstein, *J. Electroanal. Chem.* **1983**, 144, 105.
5. V. G. Levich, *Physicochemical Hydrodynamics*, Prentice Hall, Englewood Cliffs, N.J., 1962, pp. 60–78.
6. J. Koutecky, V. G. Levich, *Zh. Fiz. Khim.* **1956**, 32, 1565.
7. W. J. Albery, A. R. Hillman, *Annu. Rep. C* **1981**, 78, 377.
8. W. J. Albery, A. R. Hillman, *J. Electroanal. Chem.* **1984**, 170, 27.
9. C. P. Andrieux, J. M. Saveant, *Molecular Design of Electrode Surfaces*, Wiley Interscience, New York, pp. 207–270.
10. M. E. G. Lyons, *Electroactive Polymer Electrochemistry Part 1; Fundamentals*, Plenum Press, New York, 1994, pp. 237–371.
11. W. J. Albery, P. N. Bartlett, *J. Electroanal. Chem.* **1985**, 194, 211.

12. M. Sharp, B. Lindholm, E. Lotta-Lind, *J. Electroanal. Chem.* **1989**, 274, 35.
13. P. Jennings, A. C. Jones, A. R. Mount et al., *J. Chem. Soc., Faraday Trans.* **1997**, 93, 3791.
14. W. J. Albery, S. Bruckenstein, *Trans. Faraday Soc.* **1965**, 62, 1920.
15. W. J. Albery, C. M. A. Brett, *J. Electroanal. Chem.* **1983**, 148, 201.
16. A. R. Mount, D. Clark, M. S. Appleton et al., *J. Electroanal. Chem.* **1992**, 334, 155.
17. A. R. Mount, D. Clark, M. S. Appleton et al., *J. Electroanal. Chem.* **1992**, 340, 287.
18. W. J. Albery, E. J. Calvo, *J. Chem. Soc., Faraday Trans. 1* **1983**, 79, 2583.
19. W. J. Albery, A. R. Mount, *J. Chem. Soc., Faraday Trans. 1* **1989**, 85, 1181, 1189, 3717.
20. W. J. Albery, J. S. Drury, M. L. Hitchman, *Trans. Faraday Soc.* **1971**, 67, 2162.
21. P. J. Colby, Ph.D. thesis, University of London, London, 1983.
22. W. J. Albery, M. G. Boutelle, P. J. Colby et al., *J. Chem. Soc., Faraday Trans. 1* **1982**, 78, 2757.
23. J. Malyszko, E. Malyszko, E. Rutkowska-Ferchichi et al., *Anal. Chim. Acta* **1998**, 376, 357.
24. W. J. Albery, S. Buckenstein, *Trans. Faraday Soc.* **1966**, 62, 1946.
25. W. J. Albery, *Acc. Chem. Res.* **1982**, 15, 142.
26. W. J. Albery, P. N. Bartlett, J. D. Porter, *J. Electrochem. Soc.* **1984**, 131, 2892, 2896.
27. C. Boxall, W. J. Albery, *Phys. Chem. Chem. Phys.* **2000**, 2, 3631, 3641, 3651.
28. D. C. Johnson, E. W. Resnic, *Anal. Chem.* **1972**, 44, 637.
29. P. R. Gaines, V. E. Peacock, D. C. Johnson, *Anal. Chem.* **1975**, 47, 1393.
30. D. Pletcher, Z. Poorabedi, *Electrochim. Acta* **1979**, 24, 1253.
31. R. G. Compton, P. R. Unwin, *J. Electroanal. Chem.* **1986**, 205, 1.
32. R. G. Compton, A. C. Fisher, G. P. Tyley, *J. Appl. Electrochem.* **1991**, 21, 295.
33. R. G. Compton, P. R. Unwin, *J. Electroanal. Chem.* **1988**, 245, 287.
34. D. T. Chin, C. H. Tsang, *J. Electrochem. Soc.* **1978**, 125, 1461.
35. W. J. Albery, S. Bruckenstein, *J. Electroanal. Chem.* **1983**, 144, 105.
36. M. B. Glauert, *J. Fluid Mech.* **1956**, 1, 625.
37. B. Soucaze-Guillous, W. Kutner, *Electroanalysis* **1997**, 9, 31.
38. T. McCreedy, P. R. Fielden, *Analyst* **1995**, 120, 2343.
39. W. J. Albery, R. A. Fredlein, G. R. Kneebone et al., *Colloids Surf.* **1990**, 44, 337.
40. M. Itagaki, M. Tagaki, K. Watanabe, *J. Electroanal. Chem.* **1997**, 440, 139.
41. A. Göransson, C. Trägårdh, *J. Colloid Interface Sci.* **2000**, 231, 228.
42. N. Shirtcliffe, *Colloids Surf.* **1999**, 155, 277.
43. W. J. Albery, C. M. A. Brett, *J. Electroanal. Chem.* **1983**, 148, 201, 211.
44. J. C. Hoogvliet, F. Elferink, C. J. Van Der Pool et al., *Anal. Chim. Acta* **1983**, 153, 149.
45. C. M. A. Brett, M. M. P. M. Neto, *J. Chem. Soc., Faraday Trans. 1* **1986**, 82, 1071.
46. W. J. Albery, B. A. Coles, A. M. Couper, *J. Electroanal. Chem.* **1975**, 65, 901.
47. W. J. Albery, A. T. Chadwick, B. A. Coles et al., *J. Electroanal. Chem.* **1977**, 75, 229.
48. P. R. Unwin, R. G. Compton, *Comp. Chem. Kin.* **1989**, 29, 290.
49. W. J. Albery, R. G. Compton, A. T. Chadwick et al., *J. Chem. Soc., Faraday Trans. 1* **1980**, 76, 1391.
50. W. J. Albery, R. G. Compton, *J. Chem. Soc., Faraday Trans. 1* **1982**, 78, 1561.
51. W. J. Blaedel, L. N. Klatt, *Anal. Chem.* **1966**, 38, 879.
52. W. J. Blaedel, L. N. Klatt, *Anal. Chem.* **1966**, 39, 1065.
53. M. A. Lèvêque, *Ann. Mines Mem. Ser. 12* **1928**, 13, 201.
54. J. Lankelma, H. Poppe, *J. Chromatogr.* **1976**, 125, 375.
55. J. L. Anderson, S. Moldoveanu, *J. Electroanal. Chem.* **1984**, 179, 107.
56. B. A. Coles, R. G. Compton, *J. Electroanal. Chem.* **1983**, 144, 87.
57. R. G. Compton, B. A. Coles, G. M. Stearn et al., *J. Chem. Soc., Faraday Trans. 1* **1988**, 84, 2357.
58. R. G. Compton, B. A. Coles, M. B. G. Pilkington, *J. Chem. Soc., Faraday Trans. 1*, **1988**, 84, 4347.
59. A. M. Waller, R. J. Northing, R. G. Compton, *J. Chem. Soc., Faraday Trans. 1* **1990**, 86, 335.
60. T. R. Beck, *Corrosion* **1977**, 33, 9.
61. T. R. Beck, S. G. Chan, *Corrosion* **1981**, 37, 665.
62. J. N. Harb, *J. Electrochem. Soc.* **1986**, 133, 439C.
63. R. D. Webster, R. A. W. Dryfe, J. C. Eklund et al., *J. Electroanal. Chem.* **1996**, 402, 167.
64. R. G. Compton, J. C. Eklund, L. Nei, *J. Electroanal. Chem.* **1995**, 381, 87.

65. R. G. Compton, B. A. Coles, M. B. G. Pilkington, *J. Chem. Soc., Faraday Trans. 1* **1990**, 86, 663.
66. H. Gerischer, I. Mattes, R. Braun, *J. Electroanal. Chem.* **1965**, 10, 553.
67. G. W. Schieffer, W. J. Blaedel, *Anal. Chem.* **1977**, 49, 49.
68. J. Hermann, H. Schmidt, W. Vielstich, *Z. Phys. Chem.* **1984**, 139, 83.
69. H. Matsuda, *J. Electroanal. Chem.* **1968**, 16, 153.
70. R. Braun, *J. Electroanal. Chem.* **1968**, 19, 23.
71. R. N. Cook, D. Phil. thesis, University of Oxford, 1973, 313.
72. K. Aoki, H. Matsuda, *J. Electroanal. Chem.* **1978**, 94, 157.
73. K. Aoki, K. Tokuda, H. Matsuda, *J. Electroanal. Chem.* **1977**, 79, 49.
74. K. Aoki, K. Tokuda, H. Matsuda, *J. Electroanal. Chem.* **1986**, 195, 229.
75. S. Bruckenstein, D. T. Knapp, *J. Am. Chem. Soc.* **1968**, 90, 6303.
76. T. Tsuru, T. Nishimura, S. Haruyama, *Denki Kagaku* **1984**, 52, 532.
77. T. Tsuru, T. Nishimura, K. Aoki et al., *Denki Kagaku* **1982**, 50, 712.
78. Q. Fulian, A. C. Fisher, D. J. Riley, *Electroanalysis* **2000**, 12, 503.
79. A. J. Bard, K. B. Prater, *J. Electrochem. Soc.* **1970**, 117, 207.
80. S. W. Feldberg, *J. Electroanal. Chem.* **1969**, 3, 199.
81. S. W. Feldberg, M. L. Bowers, F. C. Anson, *J. Electroanal. Chem.* **1986**, 215, 11.
82. W. J. Albery, C. C. Jones, A. R. Mount, *Comp. Chem. Kin.* **1989**, 29, 129.
83. J. M. Hale, *Batteries Vol. 2*, Pergamon Press, Oxford, 1965, p. 147.
84. P. Laevers, A. Hubin, H. Terryn et al., *J. Appl. Electrochem.* **1995**, 25, 1023.
85. S. Moldoveanu, J. L. Anderson, *J. Electroanal. Chem.* **1984**, 175, 67.
86. J. L. Anderson, S. Moldoveanu, *J. Electroanal. Chem.* **1984**, 179, 119.
87. F. Bjrefors, J. Gadomska, M. Donten et al., *Anal. Chem.* **1999**, 71, 4926.
88. J. V. Macpherson, M. A. Beaton, P. R. Unwin, *J. Chem. Soc., Faraday Trans.* **1995**, 91, 889.
89. R. D. Martin, P. R. Unwin, *J. Electroanal. Chem.* **1995**, 397, 325.
90. J. V. Macpherson, S. Marcar, P. R. Unwin, *Anal. Chem.* **1994**, 66, 2175.
91. K. Toda, S. Oguni, Y. Takamatsu et al., *J. Electroanal. Chem.* **1999**, 479, 57.
92. N. V. Rees, J. A. Alden, R. A. W. Dryfe et al., *J. Phys. Chem.* **1995**, 99, 14 813.
93. R. G. Compton, A. C. Fisher, R. G. Welling-ton et al., *J. Phys. Chem.* **1993**, 97, 10 410.
94. J. A. Alden, S. Hakoura, R. G. Compton, *Anal. Chem.* **1999**, 71, 806.

2.5

Microelectrodes – Retrospect and Prospect*Robert J. Forster**Dublin City University, Dublin, Ireland*

2.5.1

Background and Introduction

Microelectrodes, also commonly known as ultramicroelectrodes, may be defined as electrodes whose critical dimension is in the micrometer range [1–5]. Strictly, all electrode dimensions should be smaller than the thickness of the diffusion layer on the timescale of the electrochemical experiment. Microelectrodes have several attractive features, including small currents, steady state responses in quiescent solutions, and short response times [6]. Microelectrodes have been used since the 1940s, for example, to measure oxygen concentrations within tissue [7]. However, it is only since the 1980s that the wide availability of microscopic wires and fibers, as well as sensitive instrumentation, has allowed them to be used extensively. Traditionally, electrochemistry suffered relative to spectroscopy because electrochemical measurements could be made only in highly conducting media such as aqueous solutions containing a salt as supporting electrolyte. This restriction arose because resistance between the working or sensing electrode and the reference electrode limited the precision with which the applied potential could be controlled. However, the currents observed at microelectrodes typically lie in the picoamp to nanoamp range, which is several orders of magnitude smaller than those observed at conventional millimeter-dimensioned macroelectrodes. These small electrolysis currents often completely eliminate ohmic effects. Thus, electrochemical processes

can be investigated in high resistance solvents, in solids, in supercritical fluids, and in gases. Moreover, they facilitate measurements at short timescales and at low temperatures and allow *redox mapping* to be performed with extraordinary spatial resolution. Microscopic sensors and arrays impact the development of areas as diverse as the manipulation of individual nanoparticles and the mapping of brain functions.

2.5.2

Microelectrode Fabrication and Characterization

We define microelectrodes as miniature electrodes in which the critical electrode dimension is of the order of $10\ \mu\text{m}$ yet it remains much greater than the thickness of the electrical double layer, which is typically 10 to $100\ \text{\AA}$.

2.5.2.1 **Microelectrodes**

Figure 1 illustrates the five common microelectrode geometries. The microdisc is the most popular geometry and is employed in approximately 50% of all investigations. Other common geometries include cylinders (20%) and arrays (20%), with the remaining 10% comprising bands and rings and less frequently spheres, hemispheres, and more unusual assemblies. The most popular materials include platinum, carbon fibers, and gold, although mercury, iridium, nickel, silver, and superconducting ceramics have also been used. Microdisc electrodes predominate because of their ease of construction, and because the sensing surface of the electrode can be mechanically polished. Microelectrodes in the form of discs, cylinders, and bands are commonly fabricated by sealing a fine wire or foil into a nonconducting electrode body such

Fig. 1 The most common microelectrode geometries and their associated diffusion fields.

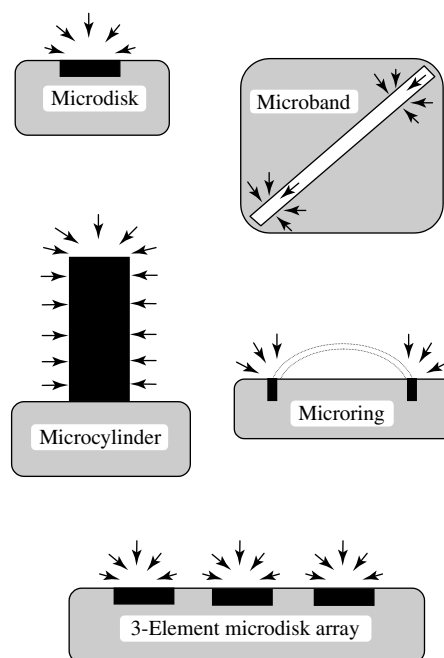
as glass. Spherical and hemispherical microelectrodes are typically formed by electrodepositing mercury onto platinum or iridium microdisks.

2.5.2.2 Nanodes

The term *nanode* has been introduced to describe electrodes with at least one dimension in the nanometer size range [8]. Although their fabrication and characterization remain challenging, these ultras small probes with critical dimensions approaching those of individual molecules are now an integral part of the field.

A procedure commonly used to fabricate nanodes uses the electrochemical etching approaches originally developed for the production of STM tips [9]. For example, applying a 2 V root-mean-square AC waveform to a platinum wire immersed in a solution of saturated CaCl_2 (60% v/v), H_2O (36%), and HCl (4%) produces an atomically sharp tip [10]. These tips can then be sealed in glass and the tip exposed by careful polishing. However, a disadvantage of this approach is that the height-to-radius ratio of the tip cannot be varied over a wide range causing the electrode radius to increase significantly as one polishes down through the cone.

Unwin and coworkers [11] have developed a straightforward approach for fabricating platinum microelectrodes with tip sizes as small as a few nanometers. Their innovation is to use an electrophoretic paint to insulate the electrode walls while leaving an electrochemically active tip exposed. These electrodes have excellent properties for use in scanning electrochemical microscopy (SECM), discussed further in Chapter 3.3.



Approaches based on micropipette pullers allow the height-to-radius ratio of the conical shaped nanode to be controlled over a much wider range than is accessible using electrochemical sharpening. Wong and Xu [12] have described an elegant approach to the fabrication of carbon disk nanodes using a laser-based micropipette puller. First, quartz capillaries are pulled using a laser-based micropipette puller to form a small tip. A carbon deposit is then formed by pyrolyzing methane, and finally electrical contact is made with the disk using mercury. The carbon nanodes exhibit a well-defined response for dopamine with a low background charging current. Mirkin, Lewis and coworkers [13] have also employed a laser-based micropipette puller but to fabricate platinum nanodes. In their approach, the laser simultaneously heats both the glass electrode body and the platinum microwire while it is mechanically stretched to a nanometer-dimensioned tip.

The tip is exposed either by chemical etching or micropolishing and ranges from 2 to 500 nm in radius. The voltammetric performance of these nanodes is excellent, with close to theoretical resistances and interfacial capacitances being observed.

Carbon fiber nanodes have been fabricated by first etching a single fiber using an argon ion beam thinner [14]. Then a single fiber with a tip diameter of approximately 50 nm is inserted into a glass capillary and sealed by heating under a vacuum. The analytical performance of these electrodes is excellent with wide dynamic ranges and low limits of detection being observed for dopamine and 5-hydroxytryptamine.

Although the voltammetric performance of some nanodes is excellent, it is important to note that when the thicknesses of the depletion and double layers become comparable, classical theories are not likely to be applicable [15].

2.5.2.3 Microelectrode Arrays

A microelectrode array consists of a series of microelectrodes separated by an insulating material. The small size of microelectrodes facilitates the use of arrays, because several elements can fit into a small surface area. Within these arrays, individual electrodes may all be connected in parallel, that is, coupled electrodes, or they may be independently addressable.

2.5.2.3.1 Arrays of Coupled Electrodes

Two significant objectives in using microarrays are to increase the magnitude of the observed current and to improve the ratio of the Faradaic to charging currents. Arrays of microelectrodes achieve the first objective simply by increasing the area at which Faradaic reactions can occur compared to a single microelectrode. Microarrays achieve the second objective

because the double-layer charging current depends simply on the area exposed to the electrolytic solution. In contrast, at long experimental timescales, the diffusion layers associated with the Faradaic reaction coalesce and the total Faradaic current is given by the area of the microelectrodes plus the insulator. In this way, the contribution from capacitance to the total current is reduced compared to a uniformly accessible surface.

The first approach to fabricating an array of coupled microelectrodes consists of sealing a bundle of individually conducting microwires or fibers in an insulating material and making a single electrical connection to the assembly. Alternatively, a conventional macroelectrode may be modified with an insulating layer that has microscopic faults through which analytes can diffuse to the electrode surface. Electrodes of this kind are known as random-array microelectrodes or RAM electrodes. Although both approaches give robust devices, they suffer from the problem of ill-defined spacing between the individual elements. This irregular spacing causes the diffusion layers to overlap at different times making correlations with theory difficult. However, Amatore and coworkers developed a theory to allow the size and intersite separation of these *microelectrodes* to be estimated from transient electrochemical data. Self-assembled monolayers have been used to create RAM electrodes, for example, Crooks and Baker [16] formed arrays of nanometer scale electrodes by cyanide etching hexadecanethiol monolayers confined to Au(111) that was modified by underpotential deposition of copper. The electrode radii ranged from 6 to 80 nm. While the theoretical limiting current correlated with the experimental value, there was significant scatter in the

data due to the wide distribution of electrode size and pitch. Other approaches to partially blocking an electrode surface include membrane-covered electrodes in which the pores are filled with carbon paste or other conducting material using mechanical or electrochemical approaches.

There is considerable interest in using microlithography, microcontact printing, and micromachining to fabricate arrays. For example, Whitesides and coworkers [17] described a laser direct write method for generating micrometer-dimensioned patterns for microanalytical applications. An elastomeric stamp was used to fabricate a microelectrode array by printing on a silicon wafer. Other approaches to fabricating well-defined coupled arrays include the use of the atomic force microscope [18] or electron beam lithography [19] to pattern spontaneously adsorbed or self-assembled monolayers followed by electrodeposition. For example, microelectrode arrays with electrode widths and spacings of 500 and 250 nm have been created using deep UV photolithography [20]. Comparable resolution can be obtained using hot embossing lithography or nanoimprinting with liftoff

using anisotropically etched silicon masters [21]. Arrays of interdigitated electrodes with interelectrode spacings as small as 3 nm can be fabricated using a shadow evaporation technique [22].

2.5.2.3.2 Independently Addressable Arrays

Microfabrication technology, which takes advantage of the thin- and thick-film techniques developed for the integrated circuit (IC) industry, allows the microelectrode size, shape, material, and pitch to be precisely controlled [23, 24]. Moreover, it allows a separate electrical contact to be made to each microelectrode so that it can be addressed independently. Table 1 details the main microfabrication techniques that are commonly used for microelectrode and microsensor fabrication [25]. As illustrated in Fig. 2, photolithography and chemical etching or liftoff are indispensable for this purpose [26]. A key distinguishing feature of microelectrode arrays compared to conventional integrated circuits is the need to package the device in a way that protects it from the sample and the chemical environment [27]. The production of packaging approaches that

Tab. 1 Microfabrication techniques that can be used to produce microelectrode arrays and microchemical sensors and biosensors

Component	Techniques or materials
Electrode pattern	Photolithography etching, liftoff, metal masking, screen printing
Insulation	Chemical vapor deposition, hydrophobic polymer
Electrolyte layer pattern	Screen printing, photosensitive polymer
Container	Anisotropic etching, field-assisted bonding, photosensitive polymer
Flow cell	Anisotropic etching, isotropic etching, field-assisted bonding, photosensitive polymer, dicing-saw
Liquid junction	Anisotropic etching, porous silicon, hydrophilic polymer
Immobilization of enzyme	Liftoff, ink-jet printing, screen printing
Needle structure	Anisotropic etching, etch-stop

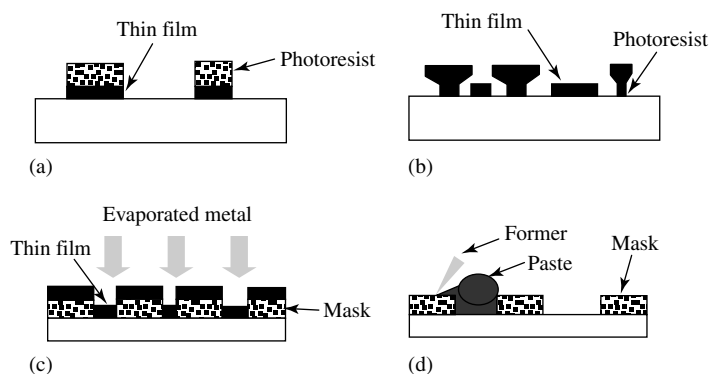


Fig. 2 Schematic representation of the approaches used to fabricate microelectrode arrays and sensors. (a) Etching; (b) liftoff; (c) metal masking; and (d) screen printing.

yield highly stable devices with long lifetimes, but avoid problems with sample contamination because of leaching from the encapsulant, remains a technological challenge [28].

2.5.3

Properties of Microelectrodes

2.5.3.1 Reduced Ohmic Effects

When Faradaic and charging currents flow through a solution, they generate a potential that acts to diminish the applied potential by an amount iR , where i is the total current and R is the cell resistance. This is an undesirable process that leads to distorted voltammetric responses.

As discussed in detail by Newman [29], the solution resistance for a disc-shaped ultramicroelectrode is inversely proportional to the electrode radius,

$$R = \frac{1}{4\kappa r} \quad (1)$$

where κ is the conductivity of the solution and r is the radius of the microdisc. Equation (1) shows that R increases as the electrode radius decreases. However, the currents observed at microelectrodes are

typically six orders of magnitude smaller than those observed at macroelectrodes. These small currents often completely eliminate ohmic drop effects even when working in organic solvents. For example, the steady state current observed at a 5- μm -radius microdisc is approximately 2 nA for a 1.0 mM solution of ferrocene. Taking a reasonable value of $0.01 \Omega^{-1} \text{cm}^{-1}$ as the specific conductivity, then Eq. (1) indicates that the resistance will be of the order of 50 000 Ω . This analysis suggests that the iR drop in this organic solvent is a negligible 0.09 mV. In contrast, for a conventional macroelectrode the iR drop would be of the order of 5 to 10 mV. Under these circumstances, distorted current responses and shifted peak potentials would be observed in cyclic voltammetry.

It is useful to investigate the effect of an experimental timescale on the iR drop observed at microelectrodes. In a subsequent section, we discuss in more detail how the diffusion field at microelectrodes depends on the characteristic time of the experiment. At short times, the dominant mass transport mechanism is planar diffusion and the microelectrode behaves like a macroelectrode. Therefore, at short times,

the current i decreases with decreasing electrode area ($\propto r^2$). Since the resistance increases with decreasing electrode radius rather than area, the product iR decreases with decreasing electrode radius in short timescale experiments. In contrast, at long experimental timescales, the Faradaic current depends directly of the radius making the product iR independent of the electrode radius.

2.5.3.2 Interfacial Capacitance

Altering the potential that is applied to an electrode causes the charge on the metal side of the interface to change and some reorganization of the ions and solvent dipoles in the double layer on the solution side of the interface will occur. This process causes electrons to flow into or out of the surface, giving rise to a charging or capacitive response. The double-layer capacitance for a disc-shaped ultramicroelectrode is proportional to the area of the electrode surface and is given by:

$$C = \pi r^2 C_o \quad (2)$$

where C_o is the specific double-layer capacitance of the electrode. Thus, shrinking the size of the electrode causes the interfacial capacitance to decrease with decreasing r^2 . These low capacitive currents are particularly important for analytical applications in which the ability to discriminate a Faradaic signal above background charging often dictates the limit of detection that can be achieved.

2.5.3.3 Electrode Response Times

Beyond chemical analysis, a major application of microelectrodes is the investigation of chemical reactivity. Therefore, it is important to consider the effect of shrinking the electrode size on its response time. Every electrochemical measurement has a

lower timescale limit that is imposed by the RC cell time constant, that is, the product of the solution resistance, R , and the double-layer capacitance, C , of the working electrode. Meaningful electrochemical data can only be extracted at timescales that are typically five to ten times longer than the RC time constant [30]. Therefore, an important objective when seeking to make high-speed-transient measurements is to minimize the cell time constant.

The existence of the double-layer capacitance at the working electrode complicates electrochemical measurements at short timescales. Specifically, the double-layer capacitance must be charged through the solution resistance in order to change the potential across the Faradaic impedance, and this process cannot be achieved instantaneously.

The time constant for this charging process is given by Eq. (3),

$$RC = \frac{\pi r C_o}{4\kappa} \quad (3)$$

and is typically hundreds of microseconds for a conventional millimeter-sized electrode placing a lower limit on the useful timescale of the order of several milliseconds. In contrast, as illustrated in Fig. 3, the cell time constant decreases linearly from approximately 2 μ s to 80 ns as the electrode radius is reduced from 25 to 1 μ m. The RC time constant can also be decreased by making measurements in highly conducting solutions, for example, response times as short as 5 ns can be achieved for an ideal 5- μ m-radius microelectrode by making measurements in highly concentrated acidic solutions [31].

However, there are a number of practical problems associated with the design and fabrication of microelectrodes that cause them to have RC time constants that greatly exceed those predicted by Eq. (3).

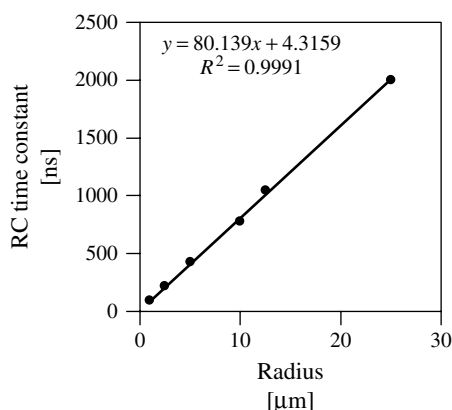


Fig. 3 Relationship between the RC cell time constant and the radius of platinum microdiscs in which the supporting electrolyte is 0.1 M HCl. Cell time constants were measured using chronoamperometry conducted on a microsecond to submicrosecond timescale by stepping the potential from 0.200 to 0.250 V versus Ag/AgCl.

An important cause of nonideal responses is stray capacitance within the electrochemical system that may arise from the electrode itself, the leads, or electrical connections. Stray capacitance will increase the cell time constant as described by Eq. (4).

$$RC = \frac{1}{4\kappa r}(\pi r^2 C_o + C_{\text{Stray}}) \quad (4)$$

where C_{Stray} is the stray capacitance. Although it depends on the microelectrode design and the experimental setup, this stray capacitance is typically between a few pF and several tens of pF. The cell time constant observed in these circumstances depends strongly on the relative magnitudes of the double-layer and stray capacitances. At a normal size electrode, the stray capacitance is negligible compared to the double-layer capacitance, and therefore, does not significantly affect the observed cell time constant. However, when the magnitude of the double-layer capacitance is reduced by shrinking the size of the electrode to micron and submicron dimensions, the stray and double-layer capacitances can become comparable. For example, taking a typical value of $40 \mu\text{F cm}^{-2}$ as the specific double-layer capacitance for a platinum electrode in contact with 1 M

aqueous electrolyte solution, the double-layer capacitance of a 1-mm-radius disc will be approximately 1 μF . This value is very significantly larger than the pF stray capacitance found in a typical electrochemical experiment. However, for a 1- μm -radius microdisc, the interfacial capacitance will decrease by six orders of magnitude to approximately 1 pF. Therefore, stray capacitance of even a few pF will cause the observed RC time constant to increase significantly beyond the minimum value dictated by double-layer charging alone. Thus, in seeking to implement ultrafast transient techniques, it is vital to minimize the stray capacitance.

There are two major sources of stray capacitance. First, the capacitance of the potentiostat and leads. By using high-quality cable of minimum length, for example, by mounting the current-to-voltage converter directly over the electrochemical cell, and by avoiding the use of switches as far as possible, stray capacitance from the electrochemical system can be minimized. Second, the microelectrode itself. For example, if there is a small imperfection in the seal between the insulator and the electrode material, then solution leakage will cause the RC cell time constant to increase massively and the Faradaic response may

become obscured by charging/discharging processes. Moreover, as shown by Wightman [32], as well as Faulkner and coworkers [33], using silver epoxy or mercury to make the electrical connection between the microwire and a larger hook-up wire can cause the RC cell time constant to increase dramatically. This increase arises because the electronically conducting mercury/glass insulator/ionically conducting solution junctions cause significant stray capacitance. It is important to note that these effects may only become apparent in high-frequency measurements.

2.5.4

Mass Transport

Oxidation or reduction of a redox-active species at an electrode surface generates a concentration gradient between the interface and the bulk solution. This redox process requires electron transfer across the electrode–solution interface. The rate at which electron transfer takes place across the interface is described by the heterogeneous electron transfer rate constant, k . If this rate constant is large, then diffusional mass transport will control the current observed. Our objective is to describe how the diffusion field evolves in time. The experiment of interest involves stepping the potential from an initial value at which no electrode reaction occurs, to one at which electrolysis proceeds at a diffusion-controlled rate. We consider the case of a spherical electrode of radius r_s placed in a solution that contains only supporting electrolyte and a redox-active species of concentration C . The concentration gradient at the electrode surface is obtained by solving Fick's second law in spherical coordinates.

$$\frac{\partial C(r, t)}{\partial t} = D \left[\frac{\partial^2 C(r, t)}{\partial r^2} + \frac{2}{r} \frac{\partial C(r, t)}{\partial r} \right] \quad (5)$$

The boundary conditions for the potential step experiments described above are

$$\begin{aligned} \lim_{r \rightarrow \infty} C(r, t) &= C^\infty \\ C(r, 0) &= C^\infty \\ C(r, t) &= 0 \text{ for } t > 0 \end{aligned}$$

where r is the distance from the center of the sphere, D is the diffusion coefficient for the redox-active species, and C is the concentration as a function of distance r and time t .

Equation (5) can be solved using Laplace transform techniques to give the time evolution of the current, $i(t)$, subject to the boundary conditions described resulting in Eq. (6),

$$i(t) = \frac{nFADC^\infty}{r_s} + \frac{nFAD^{1/2}C^\infty}{\pi^{1/2}t^{1/2}} \quad (6)$$

where n is the number of electrons transferred in the redox reaction, F is Faraday's constant, and A is the geometric electrode area.

Equation (6) shows that the current response following a potential step contains both time-independent and time-dependent terms. The differences in the electrochemical responses observed at macroscopic and microscopic electrodes arise because of the relative importance of these terms at conventional electrochemical timescales. It is possible to distinguish two limiting regimes depending on whether the experimental timescale is short or long.

1. **Short times.** At sufficiently short times, the thickness of the diffusion layer that is depleted of reactant is much smaller than the electrode radius and

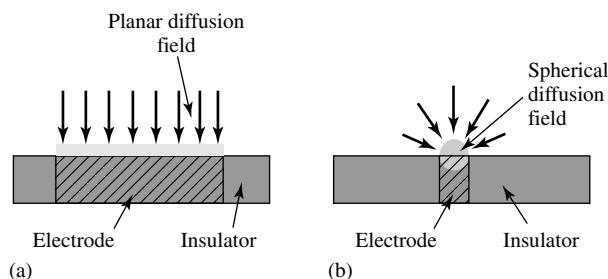


Fig. 4 Diffusion fields observed at microelectrodes. (a) Linear diffusion observed at short times and (b) radial (convergent) diffusion observed at long times.

the spherical electrode appears to be planar to a molecule at the edge of this diffusion layer. Under these conditions, the electrode behaves like a macroelectrode and mass transport is dominated by linear diffusion to the electrode surface as illustrated in Fig. 4(a). At these short times, the $t^{-1/2}$ dependence of the second term in Eq. (6) makes it significantly

larger than the first and the current response induced by the potential step initially decays in time according to the Cottrell equation.

$$i(t) = \frac{nFAD^{1/2}C^\infty}{\pi^{1/2}t^{1/2}} \quad (7)$$

Figure 5 shows the relationship that exists between the range of useable scan

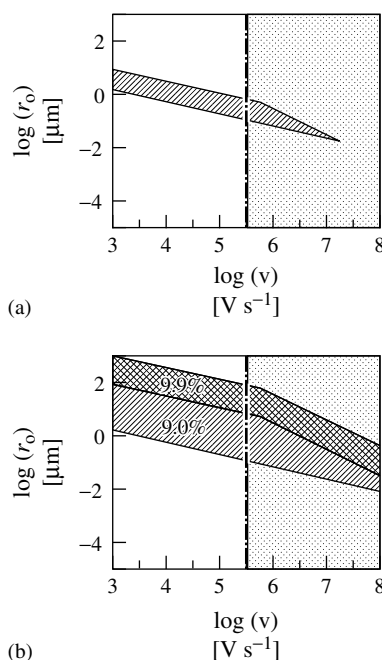


Fig. 5 Theoretical limitations on ultrafast cyclic voltammetry. The shaded area between the slanted lines represents the radius that a microdisc must have if the ohmic drop is to be less than 15 mV and distortions due to nonplanar diffusion account for less than 10% of the peak current.

(a) Without iR drop compensation by positive feedback and (b) with 90% and 99% ohmic drop compensation. The dotted areas in (a) and (b) represent the regions in which transport within the double layer affects the voltammetric response. Limits are indicative and correspond approximately to a 5 mM anthracene solution in acetonitrile, 0.3 M tetrafluoroborate as supporting electrolyte. (Reproduced by permission of Marcel Dekker from C. Amatore, *Electrochemistry at Microelectrodes*, Ed. I. Rubenstein, Chap. 4, 1995.)

rates and electrode radius subject to the condition that ohmic drop is negligible and that the dominant mass transport regime is linear diffusion [34].

2. **Long times.** At long times, the transient contribution given by the second term of Eq. (6) has decayed to the point at which its contribution to the overall current is negligible. At these long times, the spherical character of the electrode becomes important and the mass transport process is dominated by radial (spherical) diffusion as illustrated in Fig. 4(b).

The current attains a time-independent steady state value given by Eq. (8).

$$i_{ss} = \frac{nFADC^\infty}{r_s} \quad (8)$$

The steady state response arises because the electrolysis rate is equal to the rate at which molecules diffuse to the electrode surface.

Since *short* and *long* times are relative terms, it is useful to determine the times over which transient and steady state behaviors will predominate and how this time regime is affected by the electrode radius.

This objective can be achieved by considering the ratio of the transient to steady state current contributions (Eqs. 7 and 8, respectively). This analysis gives a dimensionless parameter $(\pi Dt)^{1/2}/r_s$ that can be used to calculate a lower time limit at which the steady state contribution will dominate the total current to a specified extent. For example, the time required for the steady state current contribution, i_{ss} , to be ten times larger than the transient component, i_t , can be calculated. Taking a typical value of D as $1 \times 10^{-5} \text{ cm}^2 \text{ s}^{-1}$ for a redox couple dissolved in an aqueous solution, then for an electrode of 5-mm

radius, the experimental timescale must be longer than 80 s. Therefore, steady state is not observed for macroelectrodes at the tens of mV s^{-1} timescale typical of conventional cyclic voltammetry experiments. However, reducing the electrode radius by a factor of a thousand to $5 \mu\text{m}$, means that a steady state response can be observed for times longer than $80 \mu\text{s}$. Since the steady state current becomes more dominant with increasing time, steady state responses are easily observed for microelectrodes in electrochemical experiments run at conventional timescales. Figure 6(a) shows the sigmoidal-shaped responses that characterize steady state mass transfer in slow scan-rate cyclic voltammetry. In contrast, as illustrated in Fig. 6(b), at short experimental timescales (high scan rates), peaked responses similar to those observed at conventional macroelectrodes are seen. It is important to emphasize that there is no theoretical barrier to observing steady state behavior for any size of electrode. However, for conventional millimeter-dimensioned macroelectrodes, the time taken is too long to be experimentally practical. Moreover, unintentional convection, for example, caused by building vibration, will play an important role in the mass transport process at these long timescales.

The preceding analysis considered a spherical electrode because its surface is uniformly accessible, and a simple closed-form solution to the diffusion equation exists [35]. The microdisc is the most widely used geometry, but the derivation of rigorous expressions describing their experimental response is complicated because the surface is not uniformly accessible. For discs, electrolysis at the outer circumference of the disc diminishes the flux of the electroactive material to the center of the electrode. However, microdisc

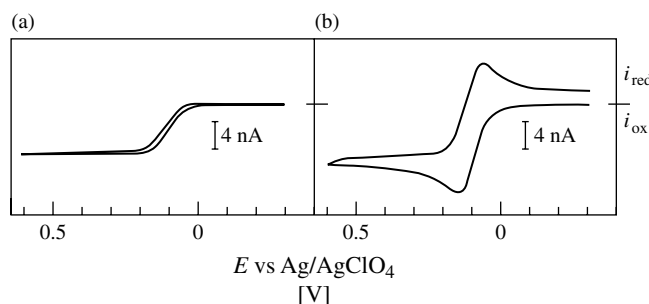


Fig. 6 Effect of scan rate on the cyclic voltammetry of 1.0 mM ferrocene at a 6.5- μm gold microdisc where the supporting electrolyte is 0.1 M tetrabutyl ammonium perchlorate in acetonitrile. (a) Scan rate is 0.1 V s^{-1} and (b) scan rate is 10 V s^{-1} . (Reproduced with the permission of the American Chemical Society from J. O. Howell and R. M. Wightman, *Anal. Chem.* **1984**, 56, 524.)

and microring geometries share the advantage of spherical microelectrodes in that quasi-spherical diffusion fields are established in relatively short periods of time. The steady state current is given by,

$$i_{\text{ss}} = \gamma n F D C r \quad (9)$$

where γ is 4 and 2π for disk and hemispherical shaped electrodes, respectively.

Observing a steady state response depends on all the electrode dimensions being small, not just the radius, and is therefore not achieved for every geometry at the timescales considered above. For example, band electrodes whose thickness is in the micrometer range, but whose length is several millimeters, do not exhibit true steady state responses. However, a high analyte flux to the ends of the band often makes it possible to observe a pseudo-steady state condition in a practical sense. Radial diffusion gives very high rates of mass transport to the electrode surface with a mass transport coefficient of the order of D/r . Therefore, even at rotation rates of 10^4 rpm , convective transport to a rotating macroelectrode is smaller than diffusion to a $1\text{-}\mu\text{m}$ microdisc.

2.5.4.1 Instrumental Challenges

Taking typical values of 1 mM and $1 \times 10^{-5} \text{ cm}^2 \text{ s}^{-1}$ for the concentration and diffusion coefficient, respectively, the steady state current is of the order of 2 nA for a $5\text{-}\mu\text{m}$ -radius microdisc. As described by Eq. (9), the magnitude of this current will decrease with decreasing electrode radius and picoamp currents will be observed for a 10-nm -radius electrode. These are certainly small currents but can be measured with relatively simple circuits based on operational amplifiers. This success can only be achieved because the measurement is performed at long timescales. The ability to measure nA to pA currents at nanosecond timescales remains a challenge.

2.5.5

Applications

2.5.5.1 Electroanalysis

The advantages of microelectrodes are exploited in many different areas of electroanalysis, with the environmental, food quality assurance, and biomedical applications being the most active. Portability

represents one of the key advantages of electrochemistry over spectroscopy, especially for on-site analysis.

Bond and coworkers [36] have probed the ability of microelectrodes to determine low concentrations of electroactive species using flow injection analysis. Ferrocene was chosen as a test system to avoid any complications associated with irreversible reactions. Measuring concentrations of the order of 10 nM proved challenging and required the use of a battery operated two-electrode potentiostat because of 50-Hz noise coming from the mains power supply. Bond has also shown that it may be easier to realize low limits of detection using macro- rather than microelectrodes [37]. For example, the electrochemical detection of As(III) at a platinum electrode in an HPLC system becomes less favorable as the electrode radius decreases. Thus, while 10 nM As(III) could be detected at a 50- μ m-radius microelectrode, the limit of detection increased to 500 nM when a 2.5- μ m-radius electrode was used. This falloff in performance appears to arise because of imperfect seals and high stray capacitance for the smaller electrodes.

Electrochemical-stripping techniques promise not only portability but also high sensitivity with disposable one-shot systems, as already highlighted in Chapter 2.3. Wang and Tian [38] have used screen-printed electrodes for stripping measurements of trace mercury. This research group has also demonstrated the significant benefits of performing anodic stripping voltammetry (ASV) of trace metals at lithographically fabricated pyrolytic carbon interdigitated microelectrode arrays [39]. Their innovation was to collect the soluble metal ions generated at one set of electrodes by applying a reducing

potential at the other. This approach gives enhanced performance under steady state conditions with improved baselines due to reduced charging currents. Square-wave ASV has already been conducted using microfabricated mercury microelectrode arrays for the detection of Cd^{2+} , Pb^{2+} , Cu^{2+} , and Zn^{2+} [40, 41].

When dealing with complex matrices such as those encountered in food and medical samples, it is often difficult to develop a sensor that exhibits a sufficiently selective response for the target analyte. Under these circumstances, arrays and mathematical modeling, for example, principal components analysis, artificial neural networks, or other pattern recognition approaches, may be required [42].

Recently, a number of papers have appeared describing novel approaches to the detection of analytes based on principles traditionally associated with biological systems or semiconductors. For example, Amatore and coworkers [43] described assemblies of paired microband electrodes that behave like neuronal synapses. The generator electrode mimics a synaptic terminal while the collector functions as a postsynaptic membrane. These artificial synapses can be designed in several configurations allowing Boolean functions such as AND or OR operations to be performed. Bartlett and coworkers have reported a molecular electronic device that is based on direct electrical communication between an enzyme (horseradish Peroxidase, HRP) and a conducting polymer [44]. The system uses two carbon microband electrodes separated by a 20- μ m gap that is bridged by poly(aniline) coated with an enzyme-containing layer. In the presence of hydrogen peroxide, the polymer is driven into its nonconducting state. This analyte-induced switching from conducting to insulating states is reminiscent of transistor

operation and represents a novel molecular electronics approach to chemical sensing.

2.5.5.2 Small Sample Volumes

Microelectrodes open up the possibility of probing redox processes in small sample volumes or physically small spaces. For example, the redox properties of sample volumes as small as a few picoliters have been interrogated. Experiments of this kind are possible because, as described by Eq. (10), for solution phase reactants, the depletion layer thickness, δ , depends on the experimental timescale.

$$\delta = (\pi Dt)^{1/2} \quad (10)$$

For a 5- μm -radius microelectrode and a 1- μs electrolysis time, the volume that is depleted of reactant will be less than 5 pL!

Wightman and coworkers have exploited this method to probe electrochemiluminescent reactions involving individual reactant pairs [45]. Their approach is to use 50- μs potential steps at a 5- μm -radius microelectrode to electrolyze a few femtoliters of a 9,10-diphenylanthracene solution so as to generate a small population of radical anions. By allowing these radical anions to diffuse into a solution containing the radical cation of the same molecule, singlet-excited states of 9,10-diphenylanthracene were created. This electronically excited state then decays back to the ground state by emission. Because of the low concentrations involved, these reactions are seen as individual light-producing events.

Bard and Fan developed an approach to allow single redox-active molecules to be detected by using a piezoelectric positioner to move a microelectrode toward a large counterelectrode so as to create a microvolume electrochemical cell [46]. When a redox-active molecule moves from bulk solution into the microvolume defined

by the two electrodes, it is repeatedly electrolyzed so as to generate a measurable current. Transport of the electroactive species is dictated by Brownian motion causing the events to be infrequent.

Rather than rely on controlling the experimental timescale to probe only a tiny volume, Wightman and coworkers have demonstrated that microcapillaries can be used to create vials with a volume of 100 pL [47]. Evaporation of the sample can be a particular problem when working with such small volumes, but it can be minimized by placing a drop of mineral oil on top of the aqueous solution. Another difficulty with measurements in ultrasmall volumes is depletion of the reactants causing the responses to deviate from those found in conventional bulk experiments [48]. Recently, lithography [49–51] and UV laser photoablation [52] have been used to create vials with picoliter volumes. For example, as illustrated in Fig. 7, Ewing and coworkers [53] have used a template produced using lithography to imprint microvials with volumes between 300 and 0.4 pL. Steady state voltammograms for ferrocenecarboxylic acid show close to ideal behavior even for vials with 1-pL volumes. Microvials of this kind are particularly important for biological applications since they facilitate the detection of redox-active messengers from single cells without significant dilution.

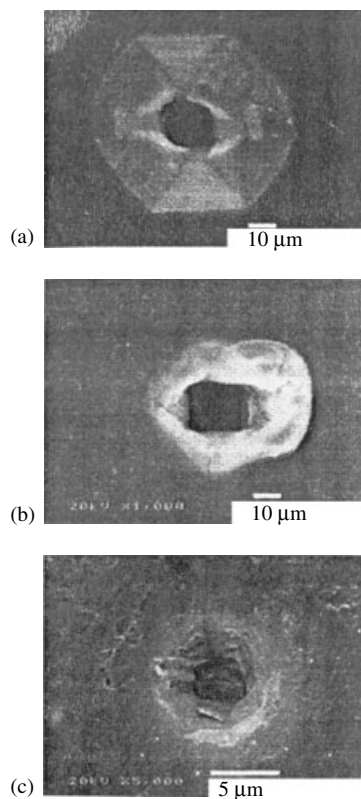
2.5.5.3 Biosystems

Since the pioneering work of Davies and Brink [7] in 1942 that measured the concentration of oxygen in animal muscle, microelectrodes have been instrumental in providing information about the concentration and temporal release of redox-active biomolecules. This research is becoming more important in the light of evidence that not only is the absolute concentration

Fig. 7 Scanning electron micrographs of polystyrene microvials: (a) 75; (b) 20; and (c) 0.4 pL. The microvials were sputtered with Pd/Au prior to imaging. (Reproduced with the permission of the American Chemical Society from R. A. Clark, P. B. Hietpas, A. G. Ewing, *Anal. Chem.* **1997**, *69*, 259.)

of a chemical messenger important in dictating a cellular response, so too is the time profile (frequency) of the output. The chemical events of interest are often restricted to the interior or exterior surfaces of single cells. Therefore, to provide useful information about in vivo biochemistry, these measurements must be performed with a high degree of spatial and temporal resolution, as well as a high degree of sensitivity and selectivity [54]. Spectroscopic techniques such as fluorescence microscopy, magnetic resonance imaging, ion mass spectrometry, and even X-ray emission imaging can provide useful information about the two-dimensional structure of biosystems. However, they are typically restricted to high analyte concentrations, millimeter rather than micrometer resolution, and slow ($> \text{ms}$) time responses.

The mammalian brain has been the focus of a significant research effort over the last 25 years and represents an extraordinarily challenging environment in which to perform analytical chemistry. At every level of organization, the brain is temporally and spatially heterogeneous with neuronal structures of differing sizes (from nanometer to millimeter) communicating with each other at timescales ranging from the microseconds to hours or days. When the objective is to elucidate the structure-function relationship of these assemblies, the ability to make spatially resolved measurements across a wide range of timescales is paramount [55, 56].



2.5.5.3.1 Spatial Sampling and Timescale

The first challenge is to ensure that measurements of the neurotransmitter concentration are sufficiently spatially localized to provide a meaningful insight into the brain's structure. Of particular importance is the volume of tissue that is sampled, since this dictates the size of structure that may be examined. For example, a microdialysis loop combining two 0.4-mm stainless steel cannulae cannot provide information on a micron length scale. In contrast, Eq. (10) indicates that by using microelectrodes and experimental timescales less than 100 μs , the diffusion layer thickness will be less than 1 μm and a high degree of spatial resolution can be achieved. For example, Lu and Gratzl [57]

investigated the drug resistance of individual cancer cells by voltammetrically monitoring the efflux of the anticancer drug, doxorubicin, from the cells. This approach promises to provide information about the heterogeneity of individual cancer cell resistance on a length scale not previously attainable.

Wightman and coworkers, have demonstrated that the distance between the microelectrode and the source cell can dramatically affect the nature of the microelectrode response [58–60]. As illustrated in Fig. 8, driving the electrode toward the cell causes the amplitude of the current spikes associated with catecholamines release to increase in amplitude and become narrower. This behavior arises because the neurotransmitter rapidly diffuses in the extracellular medium giving rise to smaller, broader peaks when the microelectrode is far from the release site.

2.5.5.3.2 Sensitivity A second key issue in bioelectrochemistry is sensitivity [61]. In the case of localized release, for example, neurotransmitter release through exocytosis, the local concentration may be

high, but the total number of molecules released will be very small. In this regard, the high mass rather than concentration sensitivity of electrochemical techniques, and the ability to routinely measure small currents, ≤ 1 pA, is important.

2.5.5.4 Neuronal Networks for Drug Evaluations

Beyond *in vivo* studies of fundamental biochemistry, microelectrode arrays have been used as platforms for growing active neuronal networks [62–65]. These cultures continue to grow and remain active for extended periods, exceeding three months under some conditions. These *in vitro* networks display complex spatiotemporal spike and burst patterns that are highly sensitive to their chemical environment. For example, Gross and coworkers [66] have grown networks of embryonic spinal cord and auditory cortex tissues on 64 element arrays and performed quantitative investigations into the effects of cannabinoid mimetics, for example, anandamide and methanandamide, on cell activity. These investigations reveal that the agonists generate specific, concentration-dependent spontaneous activity that can

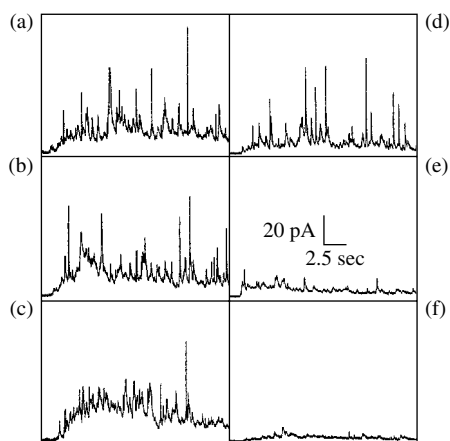


Fig. 8 Amperometric detection at isolated bovine adrenal medullary cells detected at glass encased (a–c) and etched (d–f) carbon fiber electrodes at 1 (A, D), 5 (B, E) and 10 μm (C, F). Measurements at each position were made simultaneously with the large and small electrode. Release of catecholamines was induced by a 3-s, 100- μM nicotine exposure applied at 1.25 s. (Reproduced with the permission of the American Chemical Society from K. T. Kawagoe, J. A. Jankowski, R. M. Wightman, *Anal. Chem.* **1991**, *63*, 1589.)

be reversibly turned on and off. The intra- and interculture response is highly reproducible suggesting that the cultures provide reliable quantitative information about drug interactions with neuronal tissues.

While these investigations are likely to play pivotal roles in identifying new chemical treatments for neuroconditions ranging from Parkinson's disease to schizophrenia and depression, microelectrodes will continue to play important roles in invasive surgery. For example, ablative procedures, deep brain stimulation, and cell transplantation are all emerging treatments for Parkinson's disease. Microelectrodes, especially devices in which the conducting wire or fiber is coated with a microscopically thin insulating layer, provide important information about the physical and chemical structure of the brain making surgical intervention in the basal ganglia considerably more precise [67].

2.5.5.5 Artificial Noses

Another area of substantial interest is the development of the electronic nose [68, 69]. Microarrays modified with conducting polymers coupled with pattern recognition or neural networks, represent a useful approach to analyzing or at least characterizing gas mixtures [70]. The most popular detection mechanism is based on the changes in electronic resistance when the conducting polymers are exposed to different volatile compounds. The sensitivity to different volatiles can be altered by changing the counterion incorporated into the polymer at the time of synthesis or by adding functional groups to the polymer backbone. The ease with which the physicochemical properties of these materials can be changed contrasts with conventional pellistor or metal oxide technologies.

Moreover, the ability to deposit a coating on a microstructure without the need for precise positioning equipment, for example, *drop-on-demand* technology, makes electropolymerization especially attractive.

Resistance is often the measurement of choice, since reference and counterelectrodes are not required and the measurement can be performed in both solution and gas phases. Typically, two adjacent microelectrodes are connected and polymer deposited from the solution across the gap separating the two elements. For analysis, the resistance between adjacent electrodes is measured as the device is exposed to the gases of interest. Because the responses are typically sparingly selective rather than specific, each electrode or collection of electrodes within the array is functionalized in a slightly different way, for example, chemically distinct polymers, or simply different morphologies induced by the deposition rate.

This technology has spawned at least five commercial instruments: the AromaScan (Alphatech International), the NOSE (Neotronics Olfactory Sensing Equipment; Neotronics), the Bloodhound (University of Leeds Innovations Ltd.), and the Electronic Nose (Nordic Sensor Technologies). The MOSE-nose (Metal Oxide Sensor Electronic nose) system (Alpha) is based on metal oxide sensors. The principal target of these arrays is quality control in the food and beverage industries (notably, cheeses and wines), in which the subjectivity of the human nose can sometimes create problems with traditional analytical techniques. However, medical applications are emerging in which body odors are used for the diagnosis of various diseases and infections. The ability of these devices to accurately mimic the human nose has been discussed in Ref. [71]

along with *artificial intelligence* approaches to data mining [72–74].

2.5.5.6 Low Conductivity Media

The ability to make electrochemical measurements in low ionic strength media allows analyses to be performed in unusual media, for example, solids, frozen solutions, low ionic strength media, and so on, and facilitates comparison of spectroscopic and electrochemical information [75].

2.5.5.6.1 Theoretical Descriptions The first successful attempt to predict the current for a redox reaction in the absence of a supporting electrolyte was presented by Amatore and coworkers [76, 77]. Oldham also produced seminal work in this area and presented a rigorous treatment, including an analysis of the ohmic drop [78]. These mathematical treatments reveal that the total solute concentration is uniform throughout the solution if electroneutrality is maintained within the depletion layer. However, Feldberg, White, and coworkers [15, 79] have shown that electroneutrality may not be maintained when a significant part of the depletion layer lies within the double layer. This situation may arise when nanodes or electrodes with dimensions approaching that of the double layer (100 Å to 1 μm in the absence of supporting electrolyte) are used. It is perhaps important to note that even in the absence of deliberately added electrolytes, the ion concentration is typically of the order of 10^{-6} M and electroneutrality will be maintained even for electrodes of micron dimension. Moreover, charged species are typically created within the depletion layer during electrolysis. Thus, as the Faradaic reaction proceeds, the ionic strength within the depletion layer increases.

2.5.5.6.2 Voltammetry in the Absence of Deliberately Added Electrolyte

Voltammetry in highly pure water without added electrolyte is now well established [80–83]. The ability to perform stripping analysis of metals without the need to add potentially contaminating supporting electrolyte is a particularly important application [80]. As illustrated in Fig. 9, Ciszewska and Osteryoung [84] have probed the voltammetric reduction of three metal cations: thallium, cadmium, and lead, in solutions of various salts {TlNO₃, Tl₂SO₄, Cd(NO₃)₂, Pb(NO₃)₂, and CdSO₄}, containing either no supporting electrolyte or where LiClO₄ or Ca(NO₃)₂ were added at various concentrations. The influence of migration was studied under a wide range of concentrations of the electroactive species and supporting electrolyte [77, 85].

2.5.5.6.3 Voltammetry in Pure Liquid Organics

White and coworkers pioneered the use of microelectrodes in neat organic liquids and the theoretical interpretation of the voltammetric responses [86–93]. A very low level of electrolyte helps to lower the ohmic drop and permits well-defined voltammetric waves to be obtained. Voltammograms have been obtained for redox processes of several organic compounds, including nitrobenzene [86, 87], 4-cyanopyridine [88], aniline and pyrrole [94], acetonitrile [95], simple alcohols [96], dimethylsulfoxide [97], and DMF [98]. Significantly, because the analyte concentration is so high in these experiments, water and other impurities do not influence the observed responses to any great extent.

Perhaps the most specific feature of voltammetry of pure organics is the formation of a microlayer of an ionic liquid at the electrode surface [88]. This thin layer of

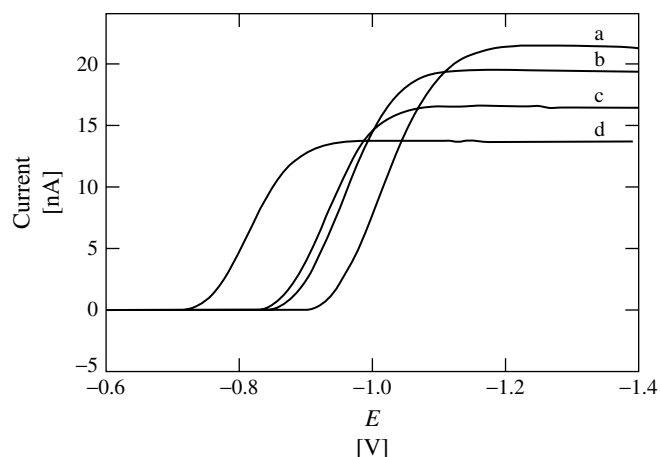


Fig. 9 Staircase voltammograms for reduction of 0.65 mM TlSO_4 at a silver-based mercury film microelectrode. The concentration of supporting electrolyte (LiClO_4) is 0 (a), 0.1 (b), 1 (c) and 100 mM (d). (Reproduced with the permission of the American Chemical Society from K. M. Ciszowska, J. G. Osteryoung, *Anal. Chem.* **1995**, *67*, 1125.)

ionic liquid also leads to large differences in the viscosity of the media, which change both the activities of all species close to the electrode surface and their diffusion coefficients. These layers can be very stable, especially for the electrooxidation of simple alcohols and the electroreduction of nitrobenzene. In extreme situations, precipitation may occur at the electrode surface. White and coworkers have used interferometry [90] and voltammetry at elevated pressure [91] to probe the interfacial structure in these systems. These careful studies allow the pressure dependence of molecular transport to be investigated and have demonstrated that the interfacial layer can be compressed [91]. White and Ragsdale [93] used the Cullinan–Vignes equation to predict the reduction wave height of nitrobenzene in acetonitrile over a wide range of compositions. Significantly, the deviations of experimental data from the theoretical predictions for mole fractions of nitrobenzene less than 0.4

allowed self-association of the solution components to be detected.

2.5.5.6.4 Complexation Equilibria Traditionally, voltammetric investigations of complexation suffered relative to spectroscopy because an excess of supporting electrolyte had to be added. A high concentration of electrolyte can cause contamination or can compete with the analyte of interest in the complexation reaction. Moreover, the high ionic strength can cause the activity of the analyte to deviate significantly from its concentration. Also, the ability to perform electrochemical measurements without deliberately adding supporting electrolyte may extend the range of analyte : ligand concentrations that can be investigated.

Palys and coworkers [99] have extended the work of Myland and Oldham [100] to develop a model that describes the steady state microelectrode response for

a wide range of complexes that are inert on the experimental timescale. Theory indicates that the steady state limiting current depends on the type of complexation equilibrium, the type of the change in the reactant charge number, and the complex formation constant, β . The theory provides a good description of the experimental data found for the complexation of europium(III) with 1,4,8,11-tetraazacyclotetradecane (cyclam) in a 4 : 1 mixture (v/v) of methanol and dimethylsulfoxide.

2.5.5.6.5 Electron Transfer Mechanisms

Beyond its relevance for understanding reaction energetics and dynamics, elucidating the mechanism of electron transfer reactions allows devices, materials, and synthetic pathways to be rationally designed. The effect of low ionic strength on the reaction mechanism of a wide variety of organic [101–103], organometallic [104], and inorganic species [105–110] has been explored. When attempting to extract accurate thermodynamic information under these low ionic strength conditions, it is essential to accurately correct for ohmic drop effects [111, 112].

Amatore and coworkers have developed a theory describing successive electron transfers in low ionic strength solutions and explored the coupling of migration and homogeneous electron transfer reactions [113]. The analytical solutions obtained allow the limiting currents to be calculated for any stepwise electron transfer reaction as a function of the ratio of the redox to supporting electrolyte concentrations. This work provides a dramatic insight into the importance of considering the homogeneous electron transfer reactions between species that differ by +2 in oxidation state, that is, disproportionation reactions. For example, the

authors demonstrate that the experimentally observed current for the reduction of $[\text{Ru}(2,2'\text{-dipyridyl})_3]^{2+}$ is approximately 50% smaller than that expected for a direct two-electron reduction reaction. In contrast, the theory that includes disproportionation effects accurately models the experimental response.

Measurement of reaction kinetics can also be facilitated by employing microelectrodes and low ionic strength solutions. For example, in an elegant investigation, Unwin and Macpherson probed the kinetics of silver chloride dissolution in aqueous solutions containing no supporting electrolyte using the scanning electrochemical microscope (SECM) [114]. They also used the alternating direction implicit finite difference method to solve the mass transport equation for the system and demonstrated that steady state current-distance measurements allow the order of the reaction to be determined. Significantly, this investigation suggests that rate constants, particularly in the fast kinetic limit, can be measured with greater precision in the absence of an *inert* electrolyte. Further information on SECM is given in Chapter 3.3.

2.5.5.6.6 Analytical Applications

ASV is a sensitive technique that often provides excellent selectivity in the detection of metal ions (see Chapter 2.3). In an elegant analytical study, Ewing and coworkers [80] used ASV to determine Pb^{2+} concentrations in solution. The microelectrodes were thin mercury films deposited on ultrasmall carbon-ring electrodes. Thin ring electrodes can have effective diffusional areas that are more than one hundred times larger than microdisks of the same geometrical area. This increase in accessibility to diffusing species gives a higher current efficiency that can reduce the limit of detection by an order of magnitude.

The authors report the effects of several experimental variables on the anodic stripping current including, potential scan rate, preconcentration duration, deposition potential, concentration of Hg^+ during the in situ deposition step, and Pb^{2+} concentration. Performing ASV in the absence of deliberately added supporting electrolyte was investigated as a means of reducing impurity levels in the samples.

The high analyte flux at microelectrodes, and their short response times, can be exploited to increase the speed and sensitivity of stripping analysis. Baranski and Harman [115] used fast cathodic stripping analysis at microelectrodes for the determination of various anions including iodide, bromide, sulfide, and cysteine. The results obtained using electrodes of conventional size at slow scan rates (ca. 100 mV s^{-1}) were compared with those obtained using microelectrodes under fast linear scan conditions (ca. 700 V s^{-1}). This study suggests that fast scan methods can simultaneously decrease the analysis time and improve sensitivity since larger currents are observed at high scan rate.

As discussed by Tercier and Buffle [116], when trying to carry out ASV in samples of low or variable ionic strength, it can be difficult to correlate peak heights and analyte concentration. This difficulty arises because counterion transport is coupled to oxidation of the metal that is concentrated within the mercury or polymeric film. Therefore, the peak height, width, and position can depend significantly on the identity and concentration of the counterions in the sample.

Buffle and coworkers [117] have investigated iridium-based mercury-plated microelectrodes for the determination of trace metals including Pb^{2+} and Cd^{2+} at nM levels. These electrodes give analytically reproducible results and have

many desirable properties for analysis in low ionic strength media such as lake waters. The determination of lead and cadmium was also investigated by Daniele and Mazzocchin [118] on a mercury film deposited on a platinum disk electrode. The influence of the solution resistance and migration on the peak position, peak width at half-height, and the peak current were investigated. The results obtained reveal that even a small ohmic drop leads to larger fwhm values. Moreover, their investigations emphasize the importance of considering the impact of ionic strength-dependent liquid junction potentials when attempting to determine peak potentials accurately [119].

2.5.5.7 Solid State Investigations

Voltammetry at microelectrodes without supporting electrolyte has proven to be a very useful technique for studying the transport of electroactive ions and molecules in complex systems including polyelectrolytes, molten salts [120], solutions of high molecular weight polymers that contain ionic groups [121–123], colloidal suspensions [124], and polymeric gels [125]. Beyond the traditional objective of understanding ionic conductivity, microelectrodes also allow the dynamics of segmental polymer chain motion to be investigated. One approach to probing these dynamics is to dissolve redox-active molecules in the polymer and then to measure their diffusion rates through the matrix. The high viscosity of these media gives diffusion coefficients of the order of $10^{-7} \text{ cm}^2 \text{ s}^{-1}$, which is almost two orders of magnitude smaller than values typically observed in aqueous solution.

In recent years, there has been growing interest in electrochemical studies in the solid state, that is, in the absence of liquid electrolyte phase [126–128].

Suitable candidates for these investigations have mobile charge compensating counterions and contain mixed-valence redox centers. Beyond its theoretical importance, solid networks are important for chemical sensing [128], as well as for the development of charge storage, electrochromic, and molecular electronics devices [129]. Faulkner and Kulesza have successfully applied microelectrodes to study solid-state redox transitions in

bulk mixed-valence materials, such as single crystals of silicotungstic acid [130, 131]. These crystals contain highly mobile protons at a high concentration, which serve the same purpose as supporting electrolytes in conventional electrochemistry. Potential step and cyclic voltammetry have been performed using a three-electrode solid-state electrochemical cell of the type illustrated in Fig. 10. As shown in Fig. 11, the solid-state voltammetry of a single

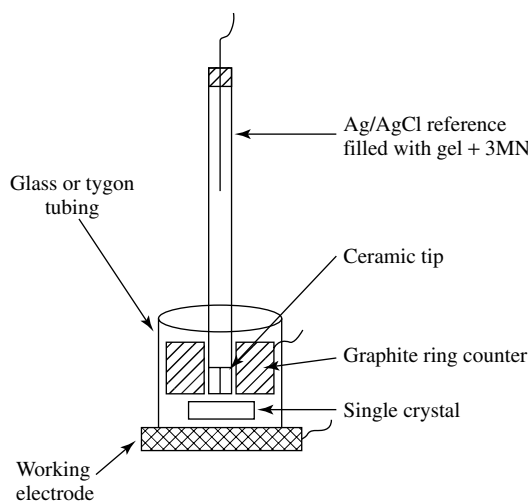


Fig. 10 Schematic representation of a three-electrode cell for probing solid-state redox processes. (Reproduced with the permission of the American Chemical Society from P. J. Kulesza, L. R. Faulkner, J. Chen, W. G. Klemperer, *J. Am. Chem. Soc.* **1991**, 113, 379.)

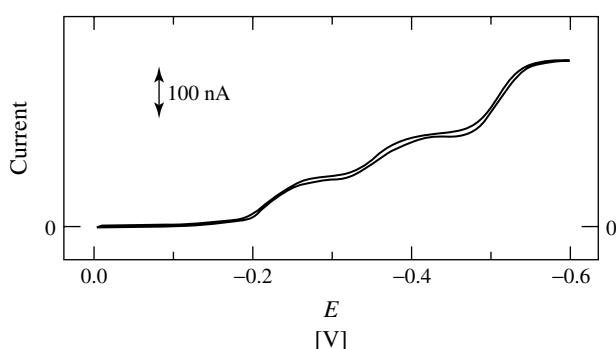


Fig. 11 Solid-state voltammetry of a silicotungstic acid single crystal using a 5- μm -radius carbon fiber microdisk. The scan rate is 5 mV s^{-1} . (Reproduced with the permission of the American Chemical Society from P. J. Kulesza, L. R. Faulkner, *J. Am. Chem. Soc.* **1994**, 115, 11 878.)

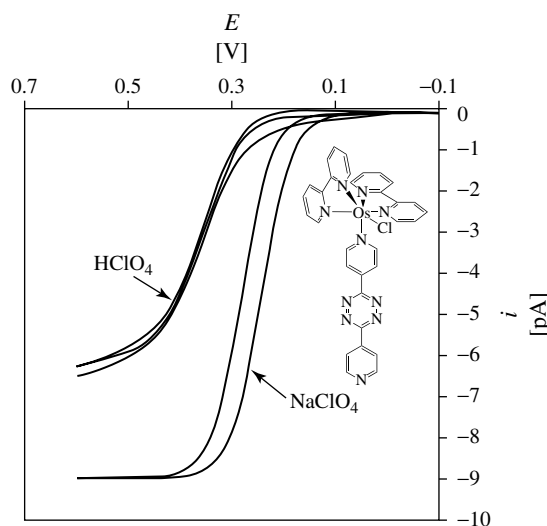
crystal of silicotungstic acid exhibits three well-defined redox transitions corresponding to the injection of one, two, or four electrons to hexavalent tungsten atoms, depending on the applied potential. Steady state plateau currents are observed, which is consistent with predominantly radial mass transport to the microelectrode surface. Solid-state electrochemical measurements have allowed the mixed-valence redox site concentration C_o , the effective diffusion coefficient $D_{app.}$, the standard heterogeneous electron transfer rate constant k^o , and the formal potential E^o , to be measured for this fast redox conducting molecular solid. Recently, Kulesza and coworkers [132] further developed this approach and prepared a single crystal of 12-tungstophosphoric acid, which contains traces of chloroplatinic acid in its secondary hydrated structure. Following partial reduction of the system, metallic Pt microcenters are generated. While these particles do not adversely affect the voltammetry of the polytungstate, at sufficiently negative potentials, the dispersed Pt

particles efficiently catalyze the discharge of intrastructural protons.

Recently, Bond and coworkers developed a very versatile method of studying the voltammetry of solids in which insoluble microcrystals are immobilized on an electrode surface that is then placed in an electrolyte. Voltammetry reveals that nucleation and crystal growth phenomena can accompany redox switching [133]. Systems of this kind have been used to probe the dynamics of crystal growth, the effect of the charge, and structure of the complex on crystallization [134] as well as the dynamics of charge transport through the films [135].

In collaboration with the Bond group [136], we have investigated the voltammetric properties of microcrystals of $[\text{Os}(\text{bpy})_2 \text{ 4-tet-Cl}](\text{ClO}_4)$ (Fig. 12) (where bpy is 2,2'-bipyridyl and 4-tet is 3,6-bis(4-pyridyl)-1,2,4,5-tetrazine) that are mechanically attached to macro- and microdisk electrodes. The complex is insoluble in water, allowing the solid-state redox properties to

Fig. 12 Structure of $[\text{Os}(\text{bpy})_2 \text{ 4-tet-Cl}]\text{ClO}_4$ used to form solid deposits on microelectrode. The voltammograms are steady state responses recorded at 1 mV s^{-1} using a $2\text{-}\mu\text{m}$ -radius microelectrode. The supporting electrolyte is 1.0 M HClO_4 and 1.0 M NaClO_4 for the smaller and larger limiting currents, respectively. (Reproduced with the permission of the American Chemical Society from R. J. Forster, T. E. Keyes, A. M. Bond, *J. Phys. Chem. B* **2000**, 104, 6389.)



be probed by placing the modified electrode in an aqueous electrolyte media. Scanning electron microscopy reveals that repeated voltammetric cycling in sodium perchlorate electrolyte can induce crystallization of the material on the electrode surface. In contrast, in perchloric acid, the films remain amorphous even after several thousand voltammetric scans. We have used voltammetry conducted at slow (1 mV s^{-1}) and fast (1 V s^{-1}) scan rates to determine the absolute concentrations of redox centers within the film (1.8 and 1.6 M for NaClO_4 and HClO_4 electrolytes, respectively) and the apparent diffusion coefficients for homogeneous charge transport (2.7×10^{-11} and $5.0 \times 10^{-11} \text{ cm}^2 \text{ s}^{-1}$ for NaClO_4 and HClO_4 electrolytes, respectively). The dependence of the voltammetric peak current on the pH of the contacting electrolyte was used to estimate the $\text{p}K_a$ of the unbound pyridine moiety of the tetrazine ligand as 3.5 ± 0.1 in the solid state as compared to 2.7 ± 0.2 in essentially aqueous solution.

2.5.5.8 Ultrafast Electrochemical Techniques

Many significant electrochemical events, such as electron and proton transfers, ligand exchanges, isomerizations, and ejection of leaving groups, occur on the low microsecond and nanosecond time domains. To achieve a meaningful insight into these redox processes, it must be possible to measure large rate constants. However, conventional electrochemical methods cannot fulfill this role since they are restricted to millisecond, or longer, timescales [137]. Thus, while modern pulsed laser spectroscopy has provided a powerful new insight into chemical processes that occur at picosecond and even femtosecond timescales, it is only recently that electrochemists have meaningfully

probed redox processes occurring on the submicrosecond timescale [31, 138].

Ultrafast electrochemical techniques provide information about the kinetics and thermodynamics of redox processes that occur at microsecond or even nanosecond timescales. This short timescale is achieved either by making very rapid changes in the applied potential or by using ultrasensitive probes to achieve very high rates of diffusion under steady state conditions. The former approach was introduced in the context of LSV and CV in Chapter 2.1. Microelectrodes play pivotal roles in both approaches. Electrochemistry has several advantages over spectroscopy in that it provides *direct* information about electron transfer and coupled chemical reactions. In transient measurements, decreasing the lower accessible timescale depends critically on fabricating ultramicroelectrodes that continue to respond ideally as their critical dimension, for example, the radius of a microdisk, decreases. The second difficulty is with ohmic drop since a small diffusion layer corresponds to a large concentration gradient, and hence large currents. In steady state approaches, ultrasensitive probes are required to make short timescale measurements. As discussed in Sect. 2.5.2.2, various approaches that yield *nanodes*, that is, electrodes of nanometer dimension, have been developed but the production of well-characterized nanodes remains a challenge.

2.5.5.8.1 Transient Techniques In transient electrochemical measurements involving a solution phase redox couple, one seeks to create a competition between the reaction of interest, that is, electron transfer at the electrode surface or coupled homogeneous steps, and diffusion of the species to and from the electrode surface [139].

Heterogeneous electron transfer dynamics.

Understanding the factors that impact the rate of heterogeneous electron transfer across a metal–solution interface underpins the development of advanced sensors, batteries, and molecular electronic devices. As shown in Table 2, the heterogeneous electron transfer dynamics of a diverse range of organic and inorganic species have been investigated using transient techniques [140–153]. However, cyclic voltammetry of the anthracene–anthracene anion radical has been used extensively as a reference system for characterizing new electrodes and instruments. This focus arises because the aromatic nature of the molecule leads to very small changes in the bond lengths and

angles, that is, the Marcus inner sphere reorganization energy is small [154], causing the heterogeneous electron transfer rate constant to be large. Wightman [155] has studied this reaction using cyclic voltammetry at scan rates up to 10^5 V s^{-1} and found good agreement between the predictions of the Nicholson and Shain theory and experiment after correcting for the nonspherical nature of the microdisc used.

Despite the many elegant investigations that have been conducted into the heterogeneous electron transfer dynamics of solution phase reactants, the magnitude of the diffusion-controlled current at short times ultimately places a lower limit on the accessible timescale. As described by Eq. (10), the thickness of the diffusion layer

Tab. 2 Rate constants for heterogeneous electron transfer as determined using transient methods

Analyte	Electrode ^a	$k^0 [\text{cm s}^{-1}]$	References
Anthracene	Au, 6.5 μm	3.46 ± 0.55	155
	Au, 5 μm	3.3	140
	Au, 5 μm	2.6	141
	Au, 3, 8.5 μm	3–4.8	142, 143
	Au, 6 μm	10	144
Anthraquinone	Pt cylinder, $r = 25.4 \mu\text{m}$, $l < 0.25 \text{ cm}$	1.78 ± 0.35	155
	Pt, 5 μm	1.5	141
	Au, 6.5 μm	2.4	145
Benzoquinone	Pt, 5 μm	0.14	141
Ferrocene	Pt, 5 μm	1.1	141
	Au, 5 μm	3.1 ± 1.1	146
	Pt, 5 to 25 μm	1.4–3.6	145
	Pt, 10 μm		147
Ferrocyaniide	C cylinder, $r = 15 \mu\text{m}$, $l = 500 \mu\text{m}$	0.0114 ± 0.0022	148
	Pt, 10, 50 μm	0.42 ± 0.03	149
	C, 5 μm	0.06 ± 0.05	150
	Pt, 1 to 30 μm	0.64–0.79	151
	Pt, 20 μm	0.2	152
9-fluorenone	Pt, 6 μm	3	153
$[\text{Ru}(\text{bpy})_3]^{2+}$	Hg, 5.5 μm	0.45	146
	Au, 5 μm	2.5	146

^aDimension given is the radius of a microdisc electrode unless otherwise stated.

is proportional to the square root of the polarization time. One can estimate that the diffusion layer thickness is approximately 50 Å if the diffusion coefficient is $1 \times 10^{-5} \text{ cm}^2 \text{ s}^{-1}$ and the polarization time is 10 ns. Given a typical bulk concentration of the electroactive species of 1 mM, this analysis reveals that only 10 000 molecules would be oxidized or reduced at a 1- μm -radius microdisc under these conditions. The average current for this experiment is only 170 nA, which is too small to be detected with low nanosecond time resolution.

Therefore, in order to probe the dynamics and energetics of ultrafast heterogeneous electron transfer dynamics this diffusion limitation must be eliminated. One successful approach to achieving this objective is to use self-assembled or spontaneously adsorbed monolayers. When immobilized on an electrode surface, the electroactive species no longer needs to diffuse to the electrode to undergo electron transfer. Moreover, the electroactive species is preconcentrated on the electrode surface. For example, in the situation considered above, there will be approximately $1.7 \times 10^{-20} \text{ mol}$ of electroactive material within the diffusion layer. Given that the area of a 1- μm disc is approximately $3.1 \times 10^{-8} \text{ cm}^2$, this translates into an *equivalent surface coverage* of about $5.4 \times 10^{-13} \text{ mol cm}^{-2}$. In contrast, the surface coverage, Γ , observed for dense monolayers of adsorbates is typically more than two orders of magnitude larger with coverages of the order of $10^{-10} \text{ mol cm}^{-2}$ typically being observed. This higher concentration gives rise to much larger currents that are easier to detect at short timescales. As exemplified by the work of Chidsey [156], Abr  na [157], Faulkner [158], and Finklea [159], electroactive adsorbed monolayers have been

developed that exhibit close to ideal reversible electrochemical behavior under a wide variety of experimental conditions of timescale, temperature, solvent, and electrolyte.

We have investigated the redox properties of the ground and electronically excited states of $[\text{Ru}(\text{bpy})_2 \text{Qbpy}]^{2+}$ (Fig. 13) monolayers using a combination of a nanosecond pulsed laser and cyclic voltammetry at megavolt per second scan rates [160]. The ground state voltammetry of these monolayers in acetonitrile is nearly ideal, and five redox states are accessible over the potential range from +1.3 to -2.0 V . Chronoamperometry conducted on a microsecond timescale was used to measure the heterogeneous electron transfer rate constant, k , for both metal and ligand-based redox reactions. Standard heterogeneous electron transfer rate constants, k^0 , were $5.1 \pm 0.3 \times 10^5 \text{ s}^{-1}$, $3.0 \pm 0.1 \times 10^6 \text{ s}^{-1}$ and $3.4 \pm 0.2 \times 10^6 \text{ s}^{-1}$ for the $3+/2+$, $2+/1+$, and $1+/0$ couples, respectively. Significantly, the free energy of activation is constant at $6.9 \pm 0.6 \text{ kJ mol}^{-1}$ for all three redox couples investigated.

Following photoexcitation using a laser pulse at 355 nm, emission is observed from the monolayers with an excited state lifetime (6.2 μs) that exceeds that of the complex in solution (1.4 μs). It appears that weak electronic coupling between the adsorbates and the electrode means that the excited states are not completely deactivated by radiationless energy transfer to the metal. As illustrated in Fig. 13, in the first report of its kind, we used voltammetry at megavolt per second scan rates to directly probe the redox potentials and electron transfer characteristics of electronically excited species.

Homogeneous chemical kinetics. The decrease in the lower accessible time limit

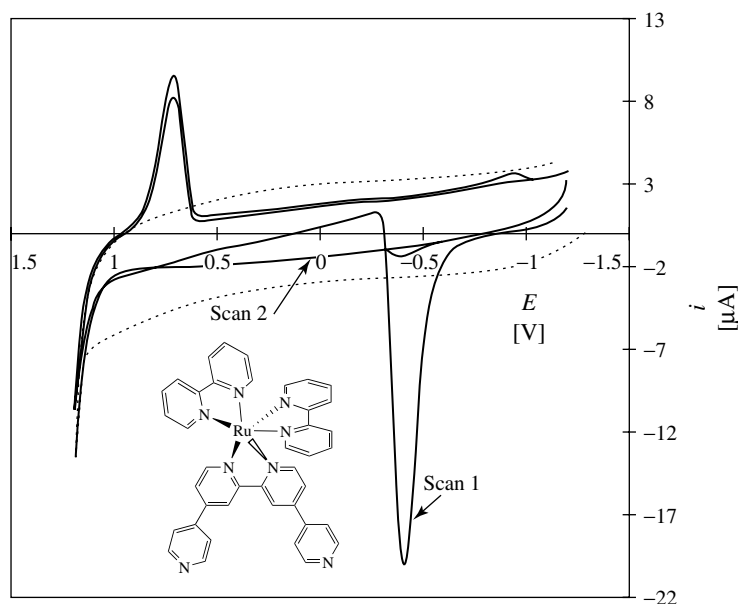


Fig. 13 Structure of the $[\text{Ru}(\text{bpy})_2 \text{Qbpy}]^{2+}$ complex used to form luminescent monolayers on platinum microelectrodes. The electrode radius is $5 \mu\text{m}$ and the response shown is immediately following laser excitation at 355 nm . The scan rate is $3 \times 10^5 \text{ V s}^{-1}$, the surface coverage is $1.1 \times 10^{-10} \text{ mol cm}^{-2}$ and the supporting electrolyte is 0.1 M TBABF_4 in acetonitrile. The initial potential is -1.2 V . (Reproduced with the permission of the American Chemical Society from R. J. Forster, T. E. Keyes, *J. Phys. Chem. B* **1998**, *102*, 10 004.)

possible using microelectrodes also has important implications for probing the dynamics of rapid homogeneous chemical reactions. For example, bimolecular reactions in solution cannot proceed faster than the rate at which molecules come into close contact. Thus, bimolecular rate constants cannot exceed the diffusion-limited rate constant that is of the order of 10^9 to $10^{10} \text{ M}^{-1} \text{ s}^{-1}$ in most organic solvents. Since the characteristic time of cyclic voltammetry is $RT/F\nu$, where ν is the scan rate, experiments performed at MV s^{-1} scan rates allow kinetic information, such as lifetimes that are close to the diffusion limit, to be obtained [161]. For example, as illustrated in Fig. 14, Wightman [162] has shown that the irreversible

response observed for the oxidation of anthracene at slow scan rates becomes fully reversible at a scan rate of 10^4 V s^{-1} . This behavior is opposite to that expected when heterogeneous electron transfer is slow and suggests that the cation radical undergoes a following chemical reaction. The ability to make the voltammetric response reversible means that the formal potentials of highly reactive species can be accurately measured.

The kinetics and mechanism of the homogeneous reactions following the reduction of NAD^+ and synthetic analogs continue to be extensively investigated. Several reaction mechanisms have been observed for NAD^+ analogs, with molecules containing at least one

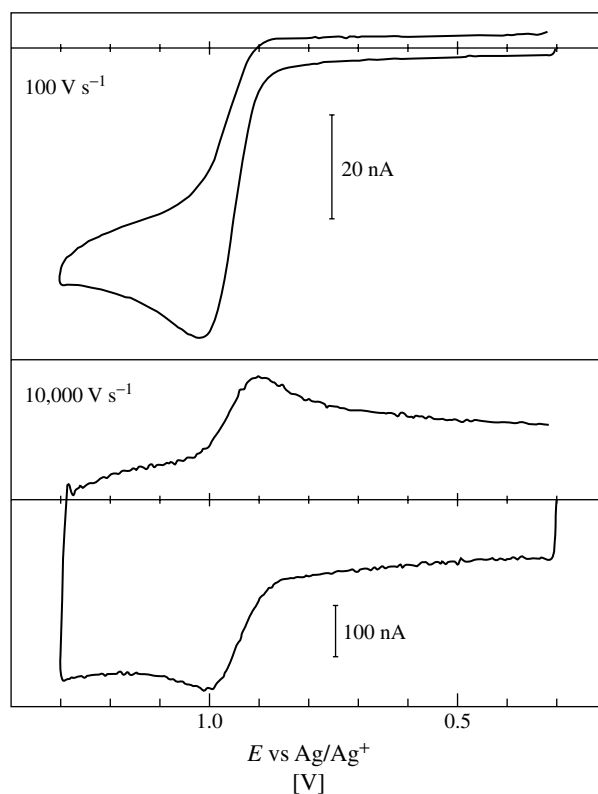


Fig. 14 Cyclic voltammograms obtained at a 50- μm -radius platinum microelectrode for the oxidation of anthracene (2.36 mM) in acetonitrile containing 0.6 M TEAP. (Reproduced with the permission of the American Chemical Society from J. O. Howell, R. M. Wightman, *J. Phys. Chem.* **1984**, *88*, 3915.)

hydrogen at the 4-position, that is, direct analogs of NAD^+ , typically undergoing a dimerization reaction [163]. We have probed the effect of changing the substitution pattern on the mechanism and kinetics of the homogeneous solution reactions of electrogenerated 1-Methyl-carbamidopyridinyl radicals. Fast scan cyclic voltammetry and double potential step chronoamperometry conducted on a microsecond timescale reveal that 1-Methyl-3-carbamidopyridinyl radicals react via a dimerization mechanism involving direct coupling of the

electrogenerated neutral radicals at a rate of approximately $1.6 \pm 0.1 \times 10^7 \text{ M}^{-1} \text{ s}^{-1}$ in DMF. The 1-Methyl-4-carbamidopyridinyl and 1-Methyl-3,4-dicarbamidopyridinyl radicals react via a pH-dependent ECE-DISP1 mechanism, E, C and DISP denote electron transfer, following chemical and disproportionation reactions, respectively. These high-speed investigations not only provide accurate thermodynamic and kinetic information but also allow the effect of substitution patterns on reaction mechanisms to be elucidated.

2.5.5.9 Steady State Electrochemistry

Under steady state conditions, the critical timescale for diffusion, t_D , is *not* related to the actual duration of the experiment since the diffusion layer thickness depends only on the electrode radius. Under these conditions, t_D is approximately equal to r^2/D . This result has a profound impact on the size of microelectrodes required to make measurements at steady state, for example, given a typical diffusion coefficient of $10^{-5} \text{ cm}^2 \text{ s}^{-1}$, microelectrodes with radii of less than 30 nm are required to address submicrosecond timescales.

Heterogeneous electron transfer dynamics.

Steady state voltammetry has been widely used to probe the dynamics of heterogeneous electron transfer for a wide range

of solution phase redox-active molecules and a representative sample is given in Table 3 [113, 164–173]. These data show that the rate of electron transfer across the electrode–solution interface varies significantly, rate constants up to 220 cm s^{-1} being observed for ferrocene. These variations reflect differences in the reaction adiabaticity and activation barriers that exist for the individual systems.

Homogeneous chemical kinetics. A second important application of steady state measurements is in studies of chemical reactivity. Steady state measurements using electrodes of different radii can provide a powerful insight into the kinetics of homogeneous reactions where the limiting current density depends on the magnitude

Tab. 3 Rate constants for heterogeneous electron transfer determined using steady state methods

Analyte	Electrode ^a	k^0 [cm s^{-1}]	References
Anthracene	Au ring $\Delta r = 0.09 \mu\text{m}$ $r = 5 \mu\text{m}$	3.33 ± 0.05	164
(C ₆ H ₆) Cr (CO) ₃ ⁺	Pt, 25 μm	≥ 0.3	165
Cytochrome c	C, 6.3 μm	> 0.4	166
9,10-diphenylanthracene	Au ring $\Delta r = 90 \mu\text{m}$ $r = 5 \text{ mm}$	5.7 ± 0.1	164
Ferrocene	C, 6 μm	2.3 ± 0.8	167
	Pt, 0.3 to 25 μm	≥ 6	168
	Pt, 1 μm	> 2	169
	Pt, 16 Å to 2.6 μm	220 ± 120	
Fe(OEP)(N-Melm) ₂ ⁺	Pt, 1 to 25 μm	0.4	170
	Pt, 0.5 to 12.5 μm	0.38	171
	Pt, 1 to 25 μm	0.35	170
Fe(TPP) (HIm) ₂ ⁺	Pt, 1 to 25 μm	0.5	170
Fe (TPP) py ₂ ⁺	Pt, 1 to 25 μm	0.6	170
MV ^{2+(F)}	Pt, 22 Å to 0.21 μm	170 ± 90	
Naphthalene	Au ring $\Delta r = 0.2 \mu\text{m}$ $r = 20.5 \mu\text{m}$	0.88 ± 0.02	164
Oxygen	Pt, 12.7 to 250 μm	0.63 ± 0.05	172
Ru (NH ₃) ₆ ³⁺	Au, 5 μm	0.076	173
	Pt, 11 Å to 11.1 μm	79 ± 44	
[Ru(bpy) ₃] ²⁺	Pt, 11.2 μm		113
Tetracyanoquinodimethane	Au ring $\Delta r = 0.2 \mu\text{m}$ $r = 20.5 \mu\text{m}$	0.23 ± 0.01	164
Zn(TPP)	Pt, 1 to 25 μm	> 1	170

^aDimension given is the radius of a microdisc electrode unless otherwise stated.

Tab. 4 Rate constants for homogeneous chemical reactions determined using steady state methods

Analyte	Electrode ^a	<i>k</i>	References
Anthracene oxidation	Pt, 0.3 to 62.5 μm	$190 \pm 50 \text{ s}^{-1}$	174
Ascorbic acid oxidation at a Prussian blue film	Pt, 2.5 to 25 μm	$1.3 \times 10^5 \text{ M}^{-1} \text{ s}^{-1}$	175
Ferrocyanide oxidation in the presence of ascorbic acid	Pt band pair, gap = 2 to 12 μm	$27 \pm 4 \text{ M}^{-1} \text{ s}^{-1}$	176
9,10-diphenylanthracene + 4,4-dibromodiphenyl	C, 6 to 9 μm	$3.9 \pm 0.6 \text{ M}^{-1} \text{ s}^{-1}$	177
Anion radicals + alkyl halides	Pt, 0.25 μm	$9 \times 10^{-4} \text{ to } 1.7 \times 10^4$	178, 179
[Fe(CN) ₆] ³⁻ + aminopyridine	Pt, 0.3 to 25 μm	$3.0 \pm 0.6 \times 10^3 \text{ M}^{-1} \text{ s}^{-1}$	180
	Pt, 2.5 to 432 μm	$1.8 \times 10^3 \text{ M}^{-1} \text{ s}^{-1}$	181
	Pt band pair, gap = 2 to 12 μm	$8 \pm 1 \times 10^2 \text{ M}^{-1} \text{ s}^{-1}$	176
Hexamethylbenzene oxidation	Pt, 0.3 to 25 μm	$720 \pm 100 \text{ s}^{-1}$	174
H ₂ evolution on Pt from acetic acid solution	Pt, 0.3 to 25 μm	$4.1 \times 10^{10} \text{ M}^{-1} \text{ s}^{-1}$	180
1-naphthylamine oxidation	Pt, 0.5 to 12.5 μm	$4.1 \times 10^3 \text{ s}^{-1}$	182
Triphenylamine oxidation	Pt, 0.3 to 20 μm	$>3 \times 10^4 \text{ M}^{-1} \text{ s}^{-1}$	174
Thioselenanthrene		$8.87 \pm 1.1 \text{ s}^{-1}$	183
Dibenzo-1,2-diselenine		$20.7 \pm 2.8 \text{ s}^{-1}$	184

^aDimension given is the radius of a microdisc electrode unless otherwise stated.

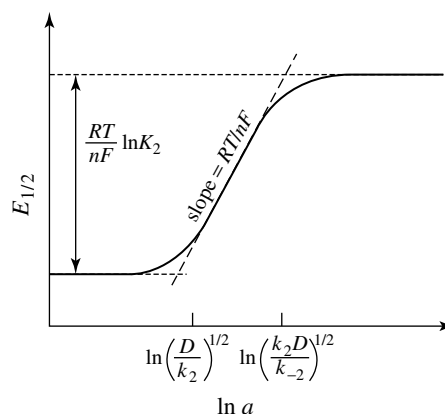
of the homogeneous rate constant. Hence, as described in Table 4 coupled chemical (C) and electron transfer (E) reactions, for example, CE mechanisms, catalytic follow-up processes, as well as reactions involving disproportionation (DISP) have been characterized [174–184]. As illustrated in Fig. 15, the position of the wave on the potential axis depends on the homogeneous reaction rate and kinetic information can be obtained by probing how $E_{1/2}$ depends on the electrode radius [185].

The dissociation of protons from organic acids followed by reduction of the protons to hydrogen is an archetypal example of a CE mechanism. However, despite their ubiquity and importance, it is only recently that this family of CE

reactions has been rigorously treated in the literature. Osteryoung and coworkers [186] used steady state voltammetry and simulations in the presence and absence of supporting electrolyte to describe the reactions under diffusional and migrational transport conditions. The treatment covers cases ranging from strong acids (essentially an E mechanism) to weak acids in which the dissociation step is important.

It is important to note that SECM plays an important role not only in topographical imaging but also in probing chemical reactivity [187, 188]. A comprehensive description of the design, functioning, and application of the SECM is given in Chapter 3.3.

Fig. 15 Dependence of $E_{1/2}$ for an EC reaction on the logarithm of the electrode radius. (Reproduced with the permission of Elsevier publishers from K. B. Oldham, *J. Electroanal. Chem.* **1991**, 313, 3.)



2.5.5.10 AC Electrokinetics

One of the defining themes of the next ten years will be molecular electronics, especially nanotechnology. Electrochemistry has a key role to play in this emerging area. Electrochemistry can be used to produce and characterize clean surfaces, for example, electrochemical cleaning of metals. It can direct the assembly of supramolecular structures, for example, by using self-assembled or spontaneously adsorbed monolayers. It can address molecular components, for example, by switching their oxidation state. It can read their state, for example, through measurements of the open circuit potential. Moreover, microelectrodes offer the possibility of selecting and precisely moving nanometer-dimensioned objects using AC electrokinetics. AC electrokinetics offers advantages over scanning-probe methods of nanoparticle manipulation in that the equipment used is simple, cheap, and has no moving parts, relying entirely on the electrostatic interactions between the particle and dynamic electric field. Furthermore, there is theoretical evidence that as manufacturing technology further improves, single nanoparticles may be manipulated using this approach.

As illustrated in Fig. 16, AC electrokinetics uses an electric field created between two or more microelectrodes to induce a dipole within a cell, particle, or macromolecule. With a suitable electrode design, a variety of motions including pushing, pulling, and rotation can be induced by changing the nature of the dynamic field. In many ways, these forces may be viewed as an electrostatic equivalent of optical tweezers [189] and optical spanners [190] in that they exert translational and rotational forces due to the interaction between the particle and the applied field. AC electrokinetic techniques such as dielectrophoresis [191] and electrorotation [192] have been utilized for many years for the manipulation, separation, and analysis of cellular-scale particles. However, recent advances in semiconductor manufacturing technology have enabled researchers to develop electrodes for manipulating macromolecules as small as 9 kDa using both attractive [193] and repulsive AC electrostatic forces, and to concentrate 14-nm beads from solution [194]. Trapping of single particles such as viruses and nanometer-diameter latex spheres in contactless potential energy wells [195] has also been demonstrated. Ultimately, this

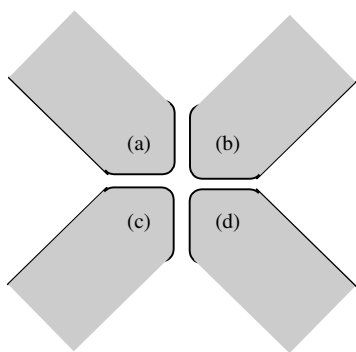


Fig. 16 A schematic of typical array of four microelectrodes used in dielectrophoresis experiments. The gap between opposing electrodes in the center of the array is typically of the order 10 to 50 μm across, but can be as small as 500 nm or as large as 1 mm. To induce dielectrophoretic motion in particles suspended near the electrode array, the electrodes are polarized such that a and c are of the same phase, while b and d are antiphase. To cause electrorotation in particles within the central gap, electrodes B, C, and D would be phase-shifted by 90° , 180° , and 270° with respect to electrode A.

technology may be applied for the manipulation of single molecules [196].

2.5.6

Future Directions

This review has attempted to convey a sense of the many significant new insights and opportunities that have been made possible by microelectrodes. This revolution in electrochemistry has greatly extended the range of solvents, temperatures, and timescales under which it is now possible to obtain direct information about redox processes. In particular, today microelectrodes allow experiments, for example, voltammetry in oil or concrete, to be performed that would simply have been impossible a few years ago. This advance has not only revolutionized the field internally, it has broadened the impact of electrochemistry into new dimensions of space and time, for example, microsecond monitoring of neurotransmitter release with single cell spatial resolution.

There are significant opportunities both within the field and other disciplines for electrochemists to make pivotal contributions. We consider some of them below.

2.5.6.1 Electron Transfer Mechanisms

A profound understanding of those factors that influence the dynamics of electron transfer across electrode/solution and homogeneous chemical reactions has been achieved. However, a level of experimental and theoretical insight into coupled chemical and electron transfer reactions, for example, coupled proton and electron transfer, remains elusive. It is probable that new approaches and models will emerge in this key area over the next five years.

2.5.6.2 Neurochemistry

Major advances are likely in the area of intrasynaptic detection of both electrical and chemical messengers. In particular, electrochemical measurements at microelectrodes and nanodes promise to provide powerful new insights into cognitive brain function including learning, memory, and perhaps even consciousness itself. However, given that neurotransmitter release can occur at frequencies of the order of 10 kHz, success in this area will only be possible if ideally responding nanodes can be produced. While approaches to correcting seal and other defects have been developed for metallic microelectrodes,

they have not been widely investigated for the carbon fiber microelectrodes that are often preferred for biochemical investigations.

2.5.6.3 Medicine

2.5.6.3.1 Nonanimal-based Drug Testing

Microelectrode arrays are proving to be useful platforms on which collections of fully functioning cells can be grown and manipulated. Moreover, there is increasing evidence that these cell cultures react to chemical stimulation in a similar way to their parent tissue in fully functional animals. Therefore, it is likely that these microarray methods will play increasingly important roles in determining the efficacy, toxicity, and therapeutic levels for new drug treatments.

2.5.6.3.2 Prosthetic Devices To reach for an object of interest, primates typically use their visual system to determine where the object is located and how to move the arm while avoiding obstacles. Plans to move the arm are then formulated in the posterior parietal cortex. Then the motor areas develop these plans into precise movement instructions that are normally conveyed down the spinal cord to the muscles in the arm. When the spinal cord is injured, neural commands can no longer reach the arm. On the basis of the current state of the art in microelectrodes, it seems likely that it will be possible to tap into these signals and reroute them around the damaged area to the natural arm, by microstimulating muscles, or to a prosthetic arm. Microelectrodes have a key role to play in this process by providing a fundamental understanding of the underlying neurobiology of this process, and by allowing the nerve impulses to be

precisely delivered to their intended site of action.

2.5.6.4 Analysis

Many key problems in chemical sensing can be solved by using microelectronics and micromechanics to fabricate systems that convert biological or chemical responses into an electrical signal. For instance, a well-known DNA chip already allows infectious diseases or genetic alterations associated with many cancers to be detected. It seems likely that electrochemical detection of mutations in human DNA using microelectrode arrays will continue to develop so as to offer high-speed sequencing and detection of pathogenic DNA.

2.5.6.5 Nanodevices and Circuits

Molecular electronics represents a powerful approach to the continued miniaturization of electronic circuits down to the lower nanometer scale. One significant challenge is the electrical connection of molecular devices by nanowires. In this regard, the ability of microelectrodes, to both image, for example, through SECM and fabricate, for example, through spatially controlled electrodeposition, micro- and nano-structures will continue to be invaluable.

References

1. A. M. Bond, *Analyst* **1994**, 119, R1.
2. R. J. Forster, *Chem. Soc. Rev.* **1994**, 289.
3. M. I. Montenegro, M. A. Queiros, J. L. Daschbach, (Eds.), *Microelectrodes: Theory and Applications*, Kluwer Academic Press, Dordrecht, The Netherlands, 1991.
4. J. Heinze, *Angew. Chem., Int. Ed. Engl.* **1993**, 105, 1327.
5. R. M. Wightman, D. O. Wipf, *Electroanalytical Chemistry* (Ed.: A. J. Bard), Marcel Dekker, New York, 1989, pp. 267–353, Vol. 15.

6. J. Heinze, *Angew. Chem., Int. Ed. Engl.* **1993**, 32, 1268.
7. P. W. Davies, F. Brink, *Rev. Sci. Instrum.* **1942**, 13, 524.
8. R. M. Penner, M. J. Heben, T. L. Longin et al., *Science* **1990**, 250, 688.
9. P. A. Christensen, *Chem. Rev.* **1992**, 197.
10. C. Lee, C. J. Miller, A. J. Bard, *Anal. Chem.* **1991**, 63, 78.
11. C. J. Slevin, N. J. Gray, J. V. MacPherson et al., *Electrochem. Commun.* **1999**, 1, 282.
12. D. K. Y. Wong, L. Y. F. Xu, *Anal. Chem.* **1995**, 67, 4086.
13. Y. H. Shao, M. V. Mirkin, G. Fish et al., *Anal. Chem.* **1997**, 69, 1627.
14. X. J. Zhang, W. M. Zhang, X. Y. Zhou et al., *Anal. Chem.* **1996**, 68, 3338.
15. C. P. Smith, H. S. White, *Anal. Chem.* **1993**, 65, 3343.
16. W. S. Baker, R. M. Crooks, *J. Phys. Chem. B* **1998**, 102, 10 041.
17. B. A. Grzybowski, R. Haag, N. Bowden et al., *Anal. Chem.* **1998**, 70, 4645.
18. H. Sugimura, O. Takai, N. Nakagiri, *J. Electroanal. Chem.* **1999**, 473, 230.
19. M. A. Guillorn, D. W. Carr, R. C. Tiberio et al., *J. Vac. Sci. Technol., B* **2000**, 18, 1177.
20. P. Van Gerwen, W. Laureyn, W. Laureys et al., *Sens. Actuators, B* **1998**, B48, 73.
21. H. Schiff, R. W. Jaszewski, C. David et al., *Microelectron. Eng.* **1999**, 46, 121.
22. G. Philipp, T. Weinmann, P. Hinze et al., *Microelectron. Eng.* **1999**, 46, 157.
23. M. Madou, *Fundamentals of Microfabrication*, CRC Press, Boca Raton, Fla., 1997.
24. P. J. Holmes, R. G. Loasby, *Handbook of Thick Film Technology*, Electrochemical Publications, Port Erin, Great Britain, 1976.
25. H. Suzuki, *Mater. Sci. Eng., C* **2000**, 12, 55.
26. M. Hatzakis, B. J. Canavello, J. M. Shaw, *IBM J. Res. Dev.* **1980**, 24, 452.
27. W. K. Ko, *Mater. Chem. Phys.* **1995**, 42, 169.
28. G. Schmitt, J. W. Schultze, F. Fassbender et al., *Electrochim. Acta* **1999**, 44, 3865.
29. J. Newman, *J. Electrochem. Soc.* **1968**, 113, 501.
30. A. J. Bard, L. R. Faulkner, *Electrochemical Methods: Fundamentals and Applications*, John Wiley & Sons, New York, 1980.
31. R. J. Forster, Ultrafast electrochemical techniques in *Encyclopedia of Analytical Chemistry* (Ed.: R. Meyers), John Wiley & Sons, New York, 2000, pp. 10 142–10 171.
32. D. O. Wipf, A. C. Michael, R. M. Wightman, *J. Electroanal. Chem.* **1989**, 15, 269.
33. L. R. Faulkner, M. R. Walsh, C. Xu in *Contemporary Electroanalytical Chemistry* (Ed.: A. Ivaska), Plenum Press, New York, 1990, pp. 5–12.
34. W. J. Bowyer, E. E. Engelman, D. H. Evans, *J. Electroanal. Chem.* **1989**, 67, 262.
35. C. Amatore, B. Fosset, *Anal. Chem.* **1996**, 68, 4377.
36. J. W. Bixler, A. M. Bond, *Anal. Chem.* **1986**, 58, 2859.
37. R. S. Stojanovic, A. M. Bond, E. C. V. Butler, *Anal. Chem.* **1990**, 62, 2692.
38. J. Wang, B. Tian, *Anal. Chim. Acta* **1993**, 274, 1.
39. J. Wang, D.-B. Luo, T. Horiuchi, *Electroanalysis* **1998**, 10, 107.
40. G. T. A. Kovacs, C. W. Storment, S. P. Kounaves, *Sens. Actuators, B* **1995**, 23, 41.
41. C. Belmont, M.-L. Tercier, J. Buffle et al., *Anal. Chim. Acta* **1996**, 329, 203.
42. R. I. Stefan, J. F. van Staden, H. Y. Aboul-Enien, *Crit. Rev. Anal. Chem.* **1999**, 29, 133.
43. C. Amatore, L. Thouin, J. Warkocz, *J. Chem.-Eur. J.* **1999**, 5, 456.
44. P. N. Bartlett, P. R. Birkin, J. H. Wang et al., *Anal. Chem.* **1998**, 70, 3685.
45. M. M. Collinson, R. M. Wightman, *Science* **1994**, 268, 1883.
46. F.-R. F. Fan, A. J. Bard, *Science* **1995**, 267, 871.
47. B. Giros, M. Jaber, S. Jones et al., *Nature* **1996**, 379, 606.
48. R. Kashyap, M. Gratzl, *Anal. Chem.* **1998**, 70, 1468.
49. R. A. Clark, A. G. Ewing, *Anal. Chem.* **1998**, 70, 1119.
50. A. Vogel, J. W. Schulze, *Electrochim. Acta* **1999**, 44, 3751.
51. C. S. Henry, I. Fritsch, *J. Electrochem. Soc.* **1999**, 146, 3367.
52. J. S. Rossier, M. A. Roberts, R. Ferrigno et al., *Anal. Chem.* **1999**, 71, 4294.
53. R. A. Clark, P. B. Hietpas, A. G. Ewing, *Anal. Chem.* **1997**, 69, 259.
54. R. M. Wightman, P. Runnels, K. Troyer, *Anal. Chim. Acta* **1999**, 400, 5.
55. G. Chen, A. G. Ewing, *Crit. Rev. Neurobiol.* **1997**, 11, 59.
56. P. C. Garell, M. A. Granner, M. D. Noh, et al., *Rev. Sci. Instrum.* **1998**, 69, 4027.
57. H. Lu, M. Gratzl, *Anal. Chem.* **1999**, 71, 2821.

58. K. T. Kawagoe, J. A. Jankowski, R. M. Wightman, *Anal. Chem.* **1991**, 63, 1589.
59. R. M. Wightman, T. J. Schroeder, J. F. Finnegan et al., *Biophys. J.* **1995**, 68, 383.
60. D. J. Michael, R. M. Wightman, *J. Pharm. Biomed. Anal.* **1999**, 19, 33.
61. D. M. Cannon, N. Winograd, A. G. Ewing, *Annu. Rev. Biophys. Biomol. Struct.* **2000**, 29, 239.
62. G. W. Gross in *Enabling Technologies for Cultured Neural Networks* (Eds.: D. A. Stenger, T. M. McKenna), Academic Press, New York, 1994, pp. 277–317.
63. K. S. Guillery, R. A. Normann, *J. Neurosci. Methods* **1999**, 9, 21.
64. G. W. Gross, F. U. Schwalm, *J. Neurosci. Methods* **1994**, 52, 73.
65. G. W. Gross, H. M. E. Azzazy, M.-C. Wu et al., *Biosens. Bioelectron.* **1995**, 10, 553.
66. S. I. Morefield, E. W. Keefer, K. D. Chapman et al., *Biosens. Bioelectron.* **2000**, 15, 383.
67. P. A. Starr, J. L. Vitek, R. A. E. Bakay, *Neurosurgery* **1998**, 43, 989.
68. J. W. Gardner, P. N. Bartlett, *Electronic Noses, Principles and Applications*, Oxford University Press, Oxford, 1999.
69. W. Göpel, *Sens. Actuators, B* **2000**, 65, 70.
70. M. S. Freund, N. S. Lewis, *Proc. Natl. Acad. Sci. U.S.A.* **1995**, 92, 2652.
71. J. W. Gardner, P. N. Bartlett, *Sens. Actuators, B* **1994**, 18, 21.
72. T. Bachinger, C. F. Mandenius, *Trends Biotechnol.* **2000**, 18, 494.
73. L. B. Kish, R. Vajtai, C. G. Granqvist, *Sens. Actuators, B* **2000**, 71, 55.
74. C. Distantea, P. Sicilianob, L. Vasanellib, *Sens. Actuators, B* **2000**, 69, 248.
75. M. Ciszowska, Z. Stojek, *J. Electroanal. Chem.* **1999**, 466, 129.
76. C. Amatore, M. R. Deakin, R. M. Wightman, *J. Electroanal. Chem.* **1987**, 225, 49.
77. C. Amatore, B. Fosset, J. Bartelt et al., *J. Electroanal. Chem.* **1988**, 256, 255.
78. K. B. Oldham, *J. Electroanal. Chem.* **1988**, 250, 1.
79. J. D. Norton, H. S. White, S. W. Feldberg, *J. Phys. Chem.* **1990**, 94, 6772.
80. D. K. Y. Wong, A. G. Ewing, *Anal. Chem.* **1990**, 62, 2697.
81. A. M. Bond, F. G. Thomas, *Langmuir* **1988**, 4, 341.
82. L. Nyholm, G. Wikmark, *Anal. Chim. Acta* **1993**, 273, 41.
83. J. Wang, J. M. Zadeii, *J. Electroanal. Chem.* **1988**, 246, 297.
84. M. Ciszowska, J. G. Osteryoung, *Anal. Chem.* **1995**, 67, 1125.
85. J. B. Cooper, A. M. Bond, K. B. Oldham, *J. Electroanal. Chem.* **1992**, 331, 877.
86. R. A. Malmsten, H. S. White, *J. Electrochem. Soc.* **1986**, 133, 1067.
87. R. A. Malmsten, C. P. Smith, H. S. White, *J. Electroanal. Chem.* **1986**, 215, 223.
88. R. B. Morris, K. F. Fischer, H. S. White, *J. Phys. Chem.* **1988**, 92, 5306.
89. J. D. Norton, S. A. Anderson, H. S. White, *J. Phys. Chem.* **1992**, 96, 3.
90. Q. Li, H. S. White, *Anal. Chem.* **1995**, 67, 561.
91. K. J. Stevenson, H. S. White, *J. Phys. Chem.* **1996**, 100, 18 818.
92. S. C. Paulson, N. D. Okerlund, H. S. White, *Anal. Chem.* **1996**, 68, 581.
93. S. R. Ragsdale, H. S. White, *J. Electroanal. Chem.* **1997**, 432, 199.
94. R. L. McCarley, M. Morita, K. O. Wilbourn et al., *J. Electroanal. Chem.* **1988**, 245, 321.
95. J. Cassidy, S. B. Khoo, S. Pons et al., *J. Phys. Chem.* **1985**, 89, 3933.
96. M. Ciszowska, Z. Stojek, *J. Electroanal. Chem.* **1993**, 344, 135.
97. M. Koncka, Z. Stojek, *Electroanalysis* **1995**, 7, 1010.
98. J. Gadomska, Z. Stojek, *Electroanalysis* **1998**, 10, 307.
99. M. Palys, Z. Stojek, M. Bos et al., *Anal. Chim. Acta* **1997**, 337, 5.
100. J. C. Myland, K. B. Oldham, *J. Electroanal. Chem.* **1993**, 347, 49.
101. M. F. Bento, M. J. Medeiros, M. I. Montenegro et al., *J. Electroanal. Chem.* **1993**, 345, 273.
102. J. D. Norton, H. S. White, *J. Electroanal. Chem.* **1992**, 325, 341.
103. R. T. Robertson, B. D. Pendley, *J. Electroanal. Chem.* **1994**, 374, 173.
104. F. Rourke, R. Gash, J. A. Crayston, *J. Organomet. Chem.* **1992**, 423, 223.
105. J. B. Cooper, A. M. Bond, *Anal. Chem.* **1993**, 65, 2724.
106. B. Soucaze-Guillous, W. Kutner, K. M. Kadish, *J. Electrochem. Soc.* **1996**, 143, 550.
107. D. Pletcher, S. Sotiropoulos, *J. Electroanal. Chem.* **1993**, 356, 109.
108. D. Pletcher, S. Sotiropoulos, *J. Chem. Soc., Faraday Trans.* **1995**, 91, 457.

109. D. R. Rolison, J. Z. Stemple, *J. Chem. Soc., Chem. Commun.* **1993**, 25.
110. Y. Takeoka, T. Aoki, K. Sanui et al., *J. Electroanal. Chem.* **1997**, 438, 153.
111. M. F. Bento, L. Thouin, C. Amatore et al., *J. Electroanal. Chem.* **1998**, 446, 91.
112. M. F. Bento, L. Thouin, I. Montenegro et al., *J. Electroanal. Chem.* **1998**, 443, 137.
113. C. Amatore, S. C. Paulson, H. S. White, *J. Electroanal. Chem.* **1997**, 439, 173.
114. J. V. Macpherson, P. R. Unwin, *J. Phys. Chem.* **1996**, 100, 19 475.
115. A. R. Harman, A. S. Baranski, *Anal. Chim. Acta* **1990**, 239, 35.
116. M. L. Tercier, J. Buffle, *Electroanalysis* **1993**, 5, 187.
117. R. R. De Vitre, M. L. Tercier, M. Tsacopoulos et al., *Anal. Chim. Acta* **1991**, 249, 419.
118. S. Daniele, G. A. Mazzocchin, *Anal. Chim. Acta* **1993**, 273, 3.
119. T. T. Wooster, M. L. Longmire, H. Zhang et al., *Anal. Chem.* **1992**, 64, 1132.
120. M. E. Williams, H. Masui, R. W. Murray, *J. Phys. Chem. B* **2000**, 104, 10 699.
121. S. E. Morris, M. Ciszowska, J. G. Osteryoung, *J. Phys. Chem.* **1993**, 97, 10 453.
122. C. Scordilis-Kelley, J. G. Osteryoung, *J. Phys. Chem.* **1996**, 100, 797.
123. M. Ciszowska, J. G. Osteryoung, *J. Phys. Chem.* **1998**, 102, 291.
124. J. M. Roberts, P. Linse, J. G. Osteryoung, *Langmuir* **1998**, 14, 204.
125. M. Ciszowska, M. D. Guillaume, *J. Phys. Chem. A* **1999**, 103, 607.
126. P. J. Kulesza, J. A. Cox, *Electroanalysis* **1998**, 10, 73.
127. E. F. Dalton, N. A. Surridge, J. C. Jernigan et al., *Chem. Phys.* **1990**, 141, 143.
128. J. A. Cox, K. S. Alber, C. A. Brockway et al., *Anal. Chem.* **1995**, 67, 993.
129. C. E. D. Chidsey, R. W. Murray, *Science* **1986**, 231, 25.
130. P. J. Kulesza, L. R. Faulkner, J. Chen et al., *J. Am. Chem. Soc.* **1991**, 113, 379.
131. P. J. Kulesza, L. R. Faulkner, *J. Am. Chem. Soc.* **1994**, 115, 11 878.
132. P. J. Kulesza, B. Karwowska, B. Grzybowska et al., *Electrochim. Acta* **1998**, 44, 1295.
133. A. M. Bond, F. Scholtz, *J. Phys. Chem.* **1991**, 95, 7640.
134. S. Fletcher, C. S. Halliday, D. Gates et al., *J. Electroanal. Chem.* **1983**, 159, 267.
135. P. G. Bruce, (Ed.), *Solid State Electrochemistry*, Cambridge University Press, Cambridge, UK, 1995.
136. R. J. Forster, T. E. Keyes, A. M. Bond, *J. Phys. Chem. B* **2000**, 104, 6389.
137. C. Amatore in *Electrochemistry at Ultramicroelectrodes* (Ed.: I. Rubinstein), Marcel Dekker, New York, 1995, Chap. 4, pp. 131–208.
138. F. Magno, I. Lavagnini, *Anal. Chim. Acta* **1995**, 305, 96.
139. M. I. Montenegro, Applications of microelectrodes in kinetics in *Research in Chemical Kinetics* (Eds.: R. G. Compton, G. Hancock), 1994, pp. 1–80, Vol. 2.
140. C. P. Andrieux, D. Garreau, P. Hapiot et al., *J. Electroanal. Chem.* **1988**, 243, 321.
141. M. I. Montenegro, D. Pletcher, *J. Electroanal. Chem.* **1986**, 200, 371.
142. C. Amatore, C. Lefrou, F. Pfluger, *J. Electroanal. Chem.* **1989**, 270, 43.
143. C. Amatore, C. Lefrou, *J. Electroanal. Chem.* **1992**, 324, 33.
144. D. O. Wipf, R. M. Wightman, *J. Phys. Chem.* **1989**, 93, 4286.
145. I. Lavagnini, P. Pastore, F. Magno, *J. Electroanal. Chem.* **1992**, 333, 1.
146. D. O. Wipf, E. W. Kristensen, M. R. Deakin et al., *Anal. Chem.* **1988**, 60, 306.
147. H. F. Zhou, N. Y. Gu, S. J. Dong, *J. Electroanal. Chem.* **1998**, 441, 153.
148. A. Neudeck, J. Dittrich, *J. Electroanal. Chem.* **1991**, 313, 37.
149. W. Huang, R. McCreery, *J. Electroanal. Chem.* **1992**, 326, 1.
150. N. Oyama, T. Ohsaka, N. Yamamoto et al., *J. Electroanal. Chem.* **1989**, 265, 297.
151. C. Beriet, D. Pletcher, *J. Electroanal. Chem.* **1994**, 375, 213.
152. K. Winkler, *J. Electroanal. Chem.* **1995**, 388, 151.
153. D. O. Wipf, M. R. Wightman, *Anal. Chem.* **1988**, 60, 2460.
154. R. A. Marcus, *J. Chem. Phys.* **1965**, 43, 679.
155. J. O. Howell, R. M. Wightman, *Anal. Chem.* **1984**, 56, 524.
156. C. E. D. Chidsey, *Science* **1991**, 251, 919.
157. D. Acevedo, H. D. Abruña, *J. Phys. Chem.* **1991**, 95, 9590.
158. R. J. Forster, L. R. Faulkner, *J. Am. Chem. Soc.* **1994**, 116, 5444.
159. H. O. Finklea, D. D. Hanshew, *J. Am. Chem. Soc.* **1992**, 114, 3173.
160. R. J. Forster, T. E. Keyes, *J. Phys. Chem. B* **1998**, 102, 10 004.

161. C. A. Amatore, A. Jutand, F. Pflüger, *J. Electroanal. Chem.* **1987**, 218, 361.
162. J. O. Howell, R. M. Wightman, *J. Phys. Chem.* **1984**, 88, 3915.
163. P. Hapiot, J. Moiroux, J. M. Savéant, *J. Am. Chem. Soc.* **1990**, 112, 1337.
164. A. Russell, K. Repka, T. Dibble et al., *Anal. Chem.* **1986**, 58, 2961.
165. C. G. Zoski, D. A. Sweigart, N. J. Stone et al., *J. Am. Chem. Soc.* **1988**, 110, 2109.
166. F. N. Büchi, A. M. Bond, *J. Electroanal. Chem.* **1991**, 314, 191.
167. A. Owlia, J. F. Rusling, *Electroanalysis* **1989**, 1, 141.
168. A. M. Bond, T. L. E. Henderson, D. R. Mann et al., *Anal. Chem.* **1988**, 60, 1878.
169. J. Daschbach, D. Blackwood, J. W. Pons et al., *J. Electroanal. Chem.* **1987**, 237, 269.
170. Y. Zhang, C. D. Baer, C. Camaioni-Neto et al., *Inorg. Chem.* **1991**, 30, 1682.
171. K. B. Oldham, C. G. Zoski, A. M. Bond, *J. Electroanal. Chem.* **1988**, 248, 467.
172. B. R. Scharifker, P. Zelenay, J. O. 'M. Bockris, *J. Electrochem. Soc.* **1987**, 134, 2714.
173. A. J. Bard, M. V. Mirkin, P. R. Unwin et al., *J. Phys. Chem.* **1992**, 96, 1861.
174. M. Fleischmann, F. Lassere, J. Robinson, *J. Electroanal. Chem.* **1984**, 177, 115.
175. S. Dong, G. Che, *J. Electroanal. Chem.* **1991**, 315, 191.
176. T. V. Shea, A. J. Bard, *Anal. Chem.* **1987**, 59, 2101.
177. C. L. Miaw, J. F. Rusling, A. Owlia, *Anal. Chem.* **1990**, 62, 268.
178. S. U. Pedersen, K. Daasbjerg, *Acta Chem. Scand.* **1989**, 43, 301.
179. K. Daasbjerg, S. U. Pedersen, H. Lund, *Acta Chem. Scand.* **1989**, 43, 876.
180. M. Fleischmann, F. Lassere, J. Robinson et al., *J. Electroanal. Chem.* **1984**, 177, 97.
181. S. Dong, G. Che, *Electrochim. Acta* **1992**, 37, 2701.
182. S. Daniele, P. Ugo, G. A. Mazzocchin, *J. Electroanal. Chem.* **1989**, 267, 129.
183. R. Muller, L. Lamberts, M. Evers, *J. Electroanal. Chem.* **1996**, 417, 35.
184. R. Muller, L. Lamberts, M. Evers, *J. Electroanal. Chem.* **1996**, 401, 183.
185. K. B. Oldham, *J. Electroanal. Chem.* **1991**, 313, 3.
186. A. Jaworski, J. G. Osteryoung, M. Donten et al., *Anal. Chem.* **1999**, 71, 3853.
187. P. T. Lillehei, L. A. Bottomley, *Anal. Chem.* **2000**, 72, 189R.
188. M. V. Mirkin, B. R. Horrocks, *Anal. Chim. Acta* **2000**, 406, 119.
189. A. Ashkin, J. M. Dziedzic, J. E. Bjorkholm et al., *Opt. Lett.* **1986**, 11, 288.
190. N. B. Simpson, K. Dholakia, L. Allen et al., *Opt. Lett.* **1997**, 22, 52.
191. T. B. Jones, *Electromechanics of Particles*, Cambridge University Press, Cambridge, UK, 1995.
192. U. Zimmermann, G. A. Neil, *Electromanipulation of Cells*, CRC Press, Boca Raton, Fla., 1996.
193. M. Washizu, S. Suzuki, O. Kurosawa et al., *IEEE Trans. Ind. Appl.* **1994**, 30, 835.
194. T. Müller, A. Gerardino, T. Schnelle et al., *J. Phys. D: Appl. Phys.* **1996**, 29, 340.
195. M. P. Hughes, *Phys. Med. Biol.* **1998**, 12, 3639.
196. M. P. Hughes, H. Morgan, *J. Phys. D: Appl. Phys.* **1998**, 31, 2205.

2.6

Impedance Methods

Steffi Krause

University of Sheffield, Sheffield, United Kingdom

2.6.1

Introduction

Impedance spectroscopy is a powerful technique for investigating electrochemical systems and processes. Its main strength lies in its ability to interrogate relaxation phenomena, whose time constants range over several orders of magnitude. In contrast to other electrochemical techniques, it is noninvasive and can be used for investigating bulk as well as interfacial processes connected with time constants ranging from minutes down to microseconds.

There is a vast amount of literature on the subject of impedance measurements comprising a large number of different applications, such as corrosion, characterization of thin films and coatings, batteries, semiconductor electrodes, sensors, biological systems, and many more. It is beyond the scope of this article to cover all of these applications comprehensively. This chapter, therefore, concentrates on the description of the main principles and theories and selected applications of impedance methods. A more thorough treatment of the subject from the point of view of corrosion can be found in [1, 2], impedance spectroscopy of solid systems is described in [3]. The fundamentals of impedance spectroscopy of electrochemical systems are also explained in [4, 5].

Linear sweep or potential step techniques described in previous chapters (see Chapters 2.1 and 2.2) usually drive

electrodes to a condition far from equilibrium. In contrast, impedance methods are based on perturbation of the electrochemical cell with an alternating signal of small magnitude allowing measurements at equilibrium or steady state. The perturbation can be of a wide range of parameters such as the applied potential, the applied current, the convection rate at hydrodynamic electrodes, or light intensity. The main advantage of these techniques is that the response can be regarded as approximately linear as long as the perturbations are sufficiently small.

2.6.2

Impedance – A Complex Quantity

2.6.2.1 Definition

The perturbations applied to an electrochemical system are usually sinusoidal. For simplification, we will only consider sinusoidal perturbations of the applied voltage

$$V(t) = V_0 \sin \omega t \quad (1)$$

where $V(t)$ is the voltage at time t , V_0 is the voltage amplitude, and ω is the radial frequency (in rad s^{-1}). The relationship between the radial frequency and the frequency f (in Hz) is $\omega = 2\pi f$. The current response $I(t)$ will be a sinusoid at the same frequency but shifted in phase

$$I(t) = I_0 \sin(\omega t + \Phi) \quad (2)$$

where $I(t)$ is the current at time t , I_0 is the current amplitude, and Φ is the phase shift by which the voltage lags the current (see Fig. 1). Analogous to Ohm's law for a dc circuit, the impedance is defined as the ratio of voltage and current

$$Z = \frac{V(t)}{I(t)} \quad (3)$$

The impedance has a magnitude ($Z_0 = V_0/I_0$) and a phase (Φ) and is thus a

Fig. 1 Sinusoidal voltage perturbation and current response.

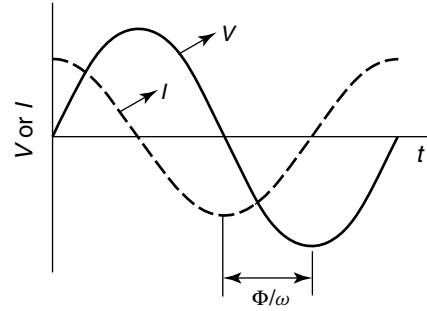
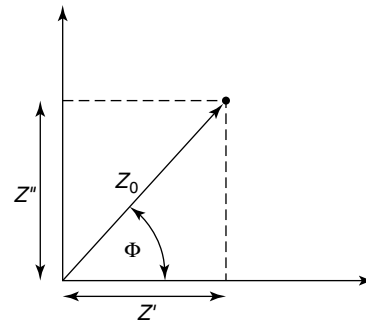


Fig. 2 Impedance presentation in the complex plane. Z'' and Z' are the imaginary and real parts of the impedance, Z_0 is the magnitude of the impedance, and Φ is the phase angle.



vector quantity. It is therefore convenient to present impedance in complex notation (see Fig. 2)

$$Z = Z_0(\cos \Phi + j \sin \Phi) = Z' + jZ'' \quad (4)$$

where $j = \sqrt{-1}$, Z' is the real part and Z'' the imaginary part of the impedance.

Using Euler's relationship, we can also write

$$Z = Z_0 e^{j\Phi} \quad (5)$$

The complex plane diagram presented in Fig. 2 shows the interrelationship between the two different forms of presentation.

2.6.2.2 Impedance Response of Selected Circuit Elements and Their Combinations

2.6.2.2.1 Resistance If a sinusoidal voltage is applied to a pure resistor of value R , then $Z_0 = R$ and $\Phi = 0$ for all frequencies.

This is shown in a plot of the imaginary part versus the real part of the impedance (Fig. 3a), which is also called a *complex plane* or *Nyquist plot*.

2.6.2.2.2 Capacitance If a sinusoidal voltage is applied across a pure capacitor, the impedance can be calculated according to the relationship

$$Z = \frac{1}{j\omega C} = -\frac{j}{\omega C} \quad (6)$$

where C is the capacitance. The magnitude of the impedance for a pure capacitor is

$$Z_0 = \frac{1}{\omega C} \quad (7)$$

and the phase angle is $\Phi = -\pi/2$, that is, the impedance depends on the frequency and is entirely imaginary (Fig. 3b).

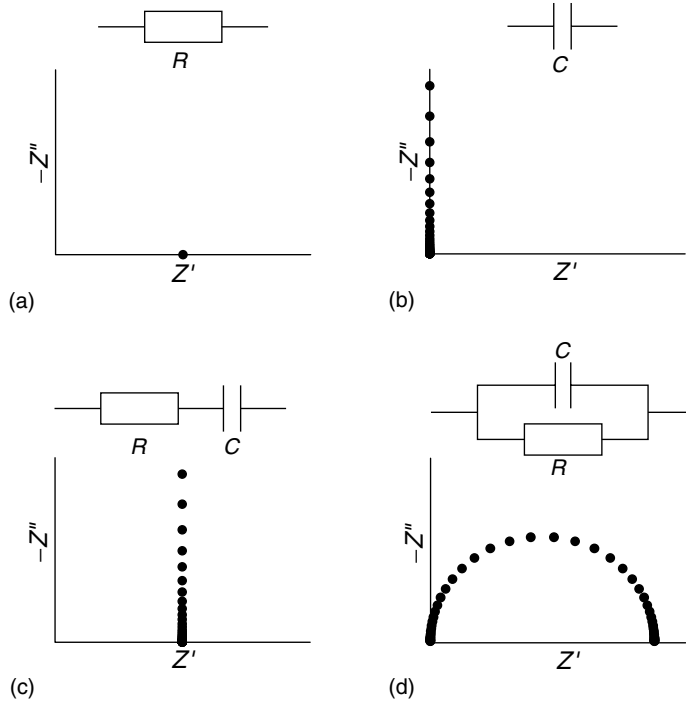


Fig. 3 Nyquist plots for different equivalent circuits.

2.6.2.2.3 Resistance and Capacitance in Series For the serial combination of a resistor and capacitor, the result is shown in Fig. 3(c). According to Kirchhoff's law, the currents through both elements are the same. The total potential equals the sum of the potentials across the capacitor and resistor

$$V(t) = I(t)R - \frac{jI(t)}{\omega C} \quad (8)$$

and the total impedance can be calculated according to

$$Z = R - \frac{j}{\omega C} \quad (9)$$

The magnitude of the impedance is

$$Z_0 = \sqrt{R^2 + \frac{1}{\omega^2 C^2}} \quad (10)$$

and the phase angle is

$$\Phi = \arctan\left(-\frac{1}{R\omega C}\right) \quad (11)$$

2.6.2.2.4 Resistance and Capacitance in Parallel The impedance for a resistor and a capacitor in parallel shows the shape of a semicircle in the complex plane diagram (Fig. 3d). According to Kirchhoff's law for a parallel circuit, the potentials across both circuit elements are equal, while the total current can be calculated from the sum of the currents flowing through resistor and capacitor

$$I(t) = \frac{V(t)}{R} - \frac{\omega C V(t)}{j} \quad (12)$$

For the impedance, we can write

$$\frac{1}{Z} = \frac{1}{R} - \frac{\omega C}{j} \quad Z = \left(\frac{1}{R} - \frac{\omega C}{j} \right)^{-1} \quad (13)$$

The magnitude of the impedance is

$$Z_0 = \left(\frac{1}{R^2} + \omega^2 C^2 \right)^{-1/2} \quad (14)$$

and the phase angle is

$$\Phi = \arctan(-R\omega C) \quad (15)$$

2.6.2.3 Equivalent Circuit Elements and the Electrochemical Cell

Many researchers take the view that the transfer function for a given system should be derived from the equations governing the kinetics of the electrochemical reactions involved. This will be demonstrated for a simple charge-transfer reaction in Sect. 2.6.3. A second method for modeling electrochemical processes involves the use of networks of electrical circuit elements, so-called *equivalent circuits*, which can be selected on the basis of an intuitive understanding of the electrochemical system. It has been shown many times that for simple systems, equivalent circuits can be used to derive useful information from impedance spectra as long as they are based on the physical and chemical properties of the system and do not contain arbitrarily chosen circuit elements.

In order to express a simple three-electrode electrochemical cell in terms of an equivalent circuit, at least three quantities need to be taken into account. One of them is the resistance of the electrolyte solution between the reference and the working electrodes R_e , another is the

electrochemical double layer that can be expressed as the double-layer capacitance C_{dl} , and finally the impedance of the charge-transfer process also called *faradaic impedance*. The equivalent circuit consists of a parallel combination of double-layer capacitance and faradaic impedance Z_f with the electrolyte resistance in series (Fig. 4a). In the absence of any electroactive species, the faradaic impedance becomes infinitely large, and the equivalent circuit in Fig. 4(a) simplifies to a serial combination of electrolyte resistance and double-layer capacitance. In the presence of electroactive species, the faradaic impedance can often be described by a simple resistor R_{ct} (Fig. 4b).

AC-impedance measurements at a series of different frequencies can be used to identify and separate the different circuit components. This can be done graphically

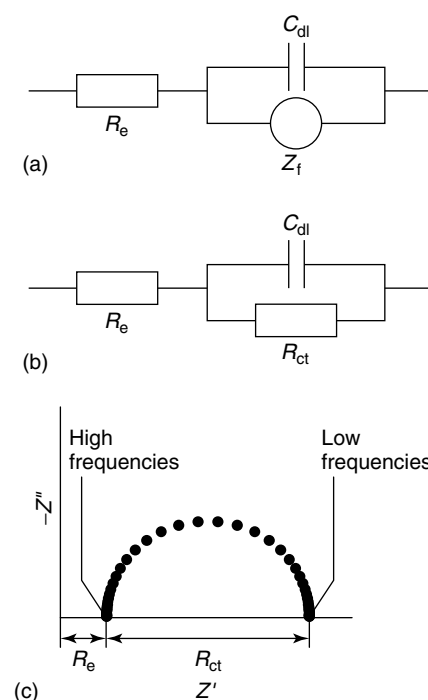


Fig. 4 Equivalent circuits [(a) general electrochemical cell; (b) simple electrochemical cell without diffusion]; and (c) Nyquist plot for a simple electrochemical cell without diffusion.

from the Nyquist plot (Fig. 4c). At high frequencies, the impedance of the double-layer capacitance is very small (Eq. 6) and the charge-transfer resistance is effectively shorted out, that is, the intercept of the semicircle with the real axis at high frequencies represents the resistance of the electrolyte solution. With decreasing frequency, the impedance of the double-layer capacitance becomes greater and the impact of the charge-transfer resistance on the total impedance increases. At sufficiently low frequencies, the impedance of the double-layer capacitance becomes significantly larger than the charge-transfer resistance, and the impedance spectrum is dominated by electrolyte and charge-transfer resistance (low-frequency intercept of the semicircle with the real axis, Fig. 4c). The diameter of the semicircle is given by the charge-transfer resistance R_{ct} . The frequency at the top of the semicircle, where the imaginary part of the impedance reaches its maximum, is

$$\omega_{\max} = \frac{1}{R_{ct}C_{dl}} \quad (16)$$

From this, the time constant τ for the faradaic process can be defined as

$$\tau = R_{ct}C_{dl} \quad (17)$$

A more accurate method of determining values for the equivalent circuit elements is to use one of the many commercial software packages for fitting ac-impedance data to user-defined equivalent circuits. Most fitting programs require very accurate guesses of the initial parameters, that is, the graphical approach is still very useful for initial estimates of equivalent circuit parameters.

The simple approach described above can be used for estimating the double-layer capacitance and the rate of the electrode

reaction. R_{ct} can be related to the exchange current of a reversible electrode reaction as well as to the corrosion rate in a steady state system. Frequently however, the behavior of electrochemical systems is governed by more complicated reaction mechanisms. Particularly at lower frequencies, diffusion and adsorption processes are picked up by ac-impedance measurements that require the derivation of more complex models. Examples for this are given in Sect. 2.6.3.

2.6.2.4 Forms of Data Presentation

As described in Sect. 2.6.2.1, impedance is a vector quantity and as such can be expressed either in terms of real and imaginary parts or in terms of magnitude and phase. From these two forms of mathematical expression, the two most common forms of data presentation can be derived. The complex plane or Nyquist diagrams, which plot the real versus the imaginary part of the impedance, have already been shown for a variety of different equivalent circuits in the previous paragraphs (see Figs. 3 and 4c). Nyquist plots have proven very useful for estimating impedance parameters from impedance spectra appearing as single or multiple arcs in the complex plane as explained above. However, the information they present is not complete since there is no indication of the frequency the impedance was measured at. For the presentation of experimental data, the points in the Nyquist plot must be labeled with the frequencies they correspond to.

Another form of data presentation is the Bode plot. Most commonly, it shows a plot of the phase angle and the logarithm of the magnitude of the impedance versus the logarithm of the frequency (Fig. 5a). When resistive behavior dominates the impedance behavior, a horizontal line is observed in the presentation of $\log Z_0$

Fig. 5 Bode plots for the equivalent circuit shown in Fig. 4(b).

versus $\log f$. When the impedance response is determined by a capacitance, a straight line with a slope of -1 is observed (Fig. 5a). Sometimes alternative Bode plots are presented, which show $\log Z'$ and $\log Z''$ versus $\log f$ (Fig. 5b). In contrast to Nyquist plots, both types of Bode plot include all of the information obtained by ac-impedance measurements.

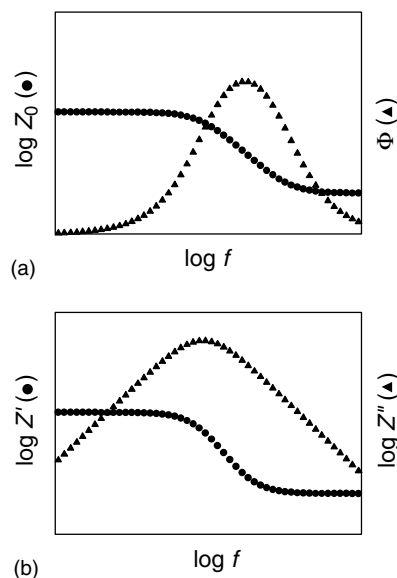
2.6.3

Description of Electrochemical Processes

2.6.3.1 Faradaic Processes and Diffusion-related Phenomena

It was shown that an electrochemical cell could be described with a simple equivalent circuit (Fig. 4a) containing the electrolyte resistance, the double-layer capacitance, and the impedance of the faradaic process. Previously, the faradaic process was described in terms of a simple charge-transfer resistance (Sect. 2.6.2.3) neglecting the diffusion of electroactive species.

For the interpretation of the faradaic impedance in the presence of diffusion-related phenomena, it is convenient to subdivide it into two circuit elements. This can be done in two different ways. Z_f can be presented by a resistance R_s in series with a pseudocapacitance C_s according to Fig. 6(a), or it can be subdivided into the charge-transfer resistance and the



mass-transfer impedance Z_W (Fig. 6b), also called the *Warburg impedance*.

For the circuit shown in Fig. 6(a), the total voltage drop is

$$V(t) = I(t)R_s + \frac{Q}{C_s} \quad (18)$$

where Q is the charge.

After differentiation, it can be written that

$$\frac{dV(t)}{dt} = R_s \frac{dI(t)}{dt} + \frac{I(t)}{C_s} \quad (19)$$

For a sinusoidal perturbation of the current according to

$$I(t) = I_0 \sin \omega t \quad (20)$$

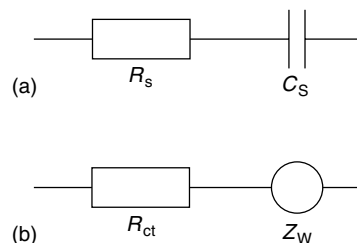
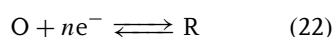


Fig. 6 Two possible presentations of the faradaic impedance Z_f as an equivalent circuit [5].

Eq. (19) changes to

$$\frac{dV(t)}{dt} = R_s I_0 \omega \cos \omega t + \frac{I_0}{C_s} \sin \omega t \quad (21)$$

For the simple charge-transfer reaction



where O and R are both soluble, it can be written that

$$V(t) = f[I(t), c_O(0, t), c_R(0, t)] \quad (23)$$

where $c_O(0, t)$ and $c_R(0, t)$ are the surface concentrations of the oxidized and the reduced species at times t .

Hence,

$$\begin{aligned} \frac{dV(t)}{dt} = & \left(\frac{\partial V(t)}{\partial I(t)} \right) \frac{dI(t)}{dt} \\ & + \left(\frac{\partial V(t)}{\partial c_O(0, t)} \right) \frac{dc_O(0, t)}{dt} \\ & + \left(\frac{\partial V(t)}{\partial c_R(0, t)} \right) \frac{dc_R(0, t)}{dt} \quad (24) \end{aligned}$$

In order to obtain an analytic expression for dV/dt , the six factors on the right-hand side of Eq. (24) have to be evaluated. The three partial differentials are determined by the kinetics of the electrode reaction and can therefore be derived from the current-overpotential equation

$$\begin{aligned} \frac{I(t)}{i_0} = & -\frac{c_O(0, t)}{c_O^*} e^{-\frac{\alpha n F}{RT} \eta} \\ & -\frac{c_R(0, t)}{c_R^*} e^{-\frac{(1-\alpha) n F}{RT} \eta} \quad (25) \end{aligned}$$

where c_O^* and c_R^* are the bulk concentrations of oxidized and reduced species, η is the overpotential, i_0 is the exchange current, F is the Faraday constant, R is the gas constant, T is the temperature, and α is the transfer coefficient.

Provided that the time averaged potential is the equilibrium potential for

Reaction (22) and the amplitude of the ac perturbation is small, Eq. (25) can be linearized using the Taylor series expansion

$$\eta = \frac{RT}{nF} \left[\frac{c_O(0, t)}{c_O^*} - \frac{c_R(0, t)}{c_R^*} + \frac{I(t)}{i_0} \right] \quad (26)$$

The first partial differential in Eq. (24) $\partial V/\partial I$ is the charge-transfer resistance and can be calculated to

$$\frac{\partial V(t)}{\partial I(t)} = R_{ct} = \frac{RT}{nF i_0} \quad (27)$$

The other partial differentials can be derived from Eq. (26) to

$$\begin{aligned} \frac{\partial V(t)}{\partial c_O(0, t)} &= \frac{RT}{nF c_O^*} \\ \frac{\partial V(t)}{\partial c_R(0, t)} &= -\frac{RT}{nF c_R^*} \quad (28) \end{aligned}$$

The other three factors have to be evaluated for the current-time relationship in Eq. (20)

$$\frac{dI(t)}{dt} = I_0 \omega \cos \omega t \quad (29)$$

Expressions for the other factors are derived considering mass transfer assuming semi-infinite linear diffusion with the initial conditions $c_O(x, 0) = c_O^*$ and $c_R(x, 0) = c_R^*$. Details of this derivation can be found in [5], Chapter 9.2.

The derivatives of the surface concentrations are

$$\begin{aligned} \frac{dc_O(0, t)}{dt} &= \frac{I_0}{nFA} \left(\frac{\omega}{2D_O} \right)^{1/2} \\ &\times (\sin \omega t + \cos \omega t) \quad (30) \end{aligned}$$

$$\begin{aligned} \frac{dc_R(0, t)}{dt} &= -\frac{I_0}{nFA} \left(\frac{\omega}{2D_R} \right)^{1/2} \\ &\times (\sin \omega t + \cos \omega t) \quad (31) \end{aligned}$$

where D_O and D_R are the diffusion coefficients of oxidized and reduced species.

Equation (24) then becomes

$$\frac{dV(t)}{dt} = \left(R_{ct} + \frac{\sigma}{\omega^{1/2}} \right) I_0 \omega \cos \omega t + I_0 \sigma \omega^{1/2} \sin \omega t \quad (32)$$

where

$$\sigma = \frac{RT}{n^2 F^2 A \sqrt{2}} \left(\frac{1}{D_O^{1/2} c_O^*} + \frac{1}{D_R^{1/2} c_R^*} \right) \quad (33)$$

By comparison of Eqs. (21 and 32), we obtain

$$R_s = R_{ct} + \frac{\sigma}{\omega^{1/2}} \quad (34)$$

and

$$\frac{1}{C_s} = \sigma \omega^{1/2} \quad (35)$$

From Eqs. (34 and 35), the Warburg impedance can be identified. A comparison with the two forms of presentation of the faradaic impedance in Figs. 6(a and b) shows that the second term in Eq. (34) is identical to the real part of the Warburg impedance

$$Z'_W = \frac{\sigma}{\omega^{1/2}} \quad (36)$$

and the imaginary part of the Warburg impedance results from C_s

$$Z''_W = -\frac{1}{\omega C_s} = -\frac{\sigma}{\omega^{1/2}} \quad (37)$$

that is,

$$Z_W = \frac{\sigma}{\omega^{1/2}} - j \frac{\sigma}{\omega^{1/2}} \quad (38)$$

Since real and imaginary parts of the Warburg impedance Z_W have the same value, a plot of Z''_W versus Z'_W would show a straight line with a phase angle of 45° (Fig. 9a). The impedance of an electrochemical cell in which the faradaic impedance in Fig. 4(a) is expressed as a serial combination of charge-transfer resistance and Warburg impedance (see Fig. 6b) is presented in Fig. 7. The resulting equivalent circuit is also known as *Randles circuit*. The semicircle is caused by a charge-transfer-controlled reaction and can be interpreted as discussed in Sect. 2.6.2.3. The straight line with a slope of 1 is due to the Warburg impedance and indicates a purely diffusion-controlled reaction at the low-frequency limit.

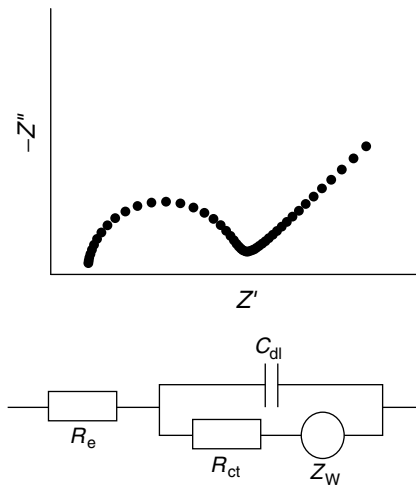


Fig. 7 Randles circuit and Nyquist plot for reversible electrochemical system with diffusion-limited behavior at low frequencies.

The analysis above has shown that it is possible to derive kinetic parameters from the impedance spectra of a redox system. The charge-transfer resistance is directly related to the exchange current (Eq. 27) and a medium diffusion coefficient for oxidized and reduced species can be calculated from the coefficient σ of the Warburg impedance (Eq. 33).

Because of the assumption of semi-infinite diffusion made by Warburg for the derivation of the diffusion impedance, it predicts that the impedance diverges from the real axis at low frequencies, that is, according to the above analysis, the dc-impedance of the electrochemical cell would be infinitely large. It can be shown that the Warburg impedance is analogous to a semi-infinite transmission line composed of capacitors and resistors (Fig. 8) [3]. However, in many practical cases, a finite diffusion layer thickness has to be taken into consideration. The first case to be considered is that of enforced or natural convection in an

electrolyte solution, which would cause the concentrations of solution species to be constant at a certain distance from the electrode surface ($c(\delta, t) = c^*$ for all t , in which c^* is the bulk concentration). In this case, the impedance is given by the expression

$$Z_W^{\text{finite}} = R_0 \frac{\tanh(\delta\sqrt{j\omega/D})}{\delta\sqrt{j\omega/D}} \quad (39)$$

where δ is the diffusion layer thickness, R_0 is the diffusion resistance for $\omega \rightarrow 0$, and D is the diffusion coefficient of the diffusing particle. This behavior is analogous to a finite length transmission line terminated with a resistance. In contrast to the Warburg impedance for semi-infinite diffusion, the finite Warburg impedance as described in Eq. (39) will bend over to the real axis at low frequencies giving rise to a distorted semicircle (Fig. 9b). This concurs with the fact that electrochemical cells usually have a finite dc-resistance.

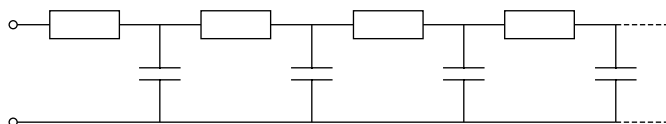


Fig. 8 Infinite length transmission line that describes the behavior of semi-infinite diffusion ([3] Chapter 2.1).

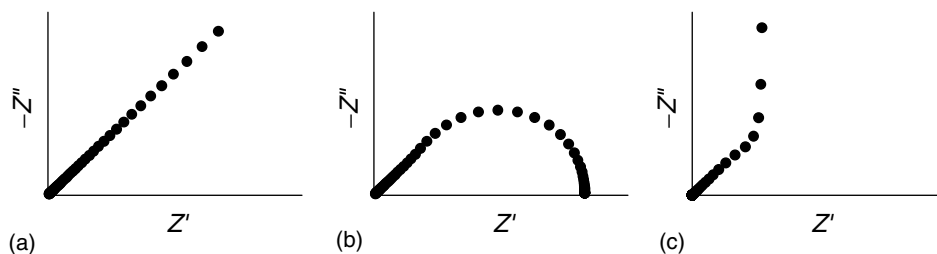


Fig. 9 Impedance spectra for diffusion-limited behavior (a) semi-infinite diffusion; (b) finite diffusion with unhindered ion transfer at the far end of the diffusion region; and (c) finite diffusion with blocked ion transfer at the far end of the diffusion layer.

A finite length diffusion layer thickness cannot only be caused by constant concentrations of species in the bulk of the solution but also by a reflective boundary, that is, a boundary that cannot be penetrated by electroactive species ($dc/dx = 0$). This can happen when blocking occurs at the far end of the diffusion region and no dc current can flow through the system, for example, a thin film of a conducting polymer sandwiched between a metal and an electrolyte solution [6]. The impedance in this case can be described with the expression

$$Z_D^{\text{finite}} = \frac{\delta^2}{DC_0} \frac{\coth(\delta\sqrt{j\omega/D})}{\delta\sqrt{j\omega/D}} \quad (40)$$

where C_0 is the limiting capacitance for $\omega \rightarrow 0$. This behavior is analogous to a finite length transmission line terminated with an open circuit, that is, at low frequencies capacitive behavior is observed (Fig. 9c).

In this section, the behavior of a redox system at the equilibrium potential has been discussed. It should, however, be noted that impedance spectroscopy of irreversible systems can also yield useful information. For example, the charge-transfer resistance determined at the corrosion potential corresponds to the slope of the current–potential curve ($R_{\text{ct}} = dV(t)/dI(t)$) at that potential and allows calculation of the rate of corrosion [1].

2.6.3.2 Validation of Experimental Data

Impedance is only properly defined as a transfer function when the system under investigation fulfills the conditions of linearity, causality, and stability during the measurement. However, as the current voltage characteristic of any electrode shows (see Eq. 25), electrochemical systems are nonlinear. Deviation from

causality can arise when the response is not caused by the input but for example, by a concentration, current, or potential relaxation upon departure of the system from equilibrium. Causality can also be disturbed as result of instrument artifacts or noise. The stability of an electrochemical system is usually not guaranteed when continually changing systems such as corroding electrodes or batteries are investigated.

To assess whether meaningful data that fulfill the above conditions have been obtained, a range of techniques and diagnostic tools have been developed to validate impedance data. The problem of nonlinearity can generally be overcome by making the amplitude of the perturbation signal small enough to approach quasi-linear conditions. This can be achieved by measuring impedance spectra at different perturbation amplitudes. The amplitude can be regarded sufficiently small when it has no significant effect on the impedance spectrum measured. In electrochemical systems, nonlinearity mainly affects the low-frequency part of the spectrum, which is determined by the faradaic current. The high-frequency part of the spectrum determined by the electrolyte resistance and the double-layer capacitance shows approximately linear behavior [7].

Depending on the technique used for data acquisition, different methods for data validation can be applied. If a sinusoidal signal were applied to a nonlinear system, the response function would contain multiples (harmonics) of the excitation signal. Popkirov and Schindler utilized this effect to develop a technique for assessing the linearity of an impedance measurement obtained using a time-domain technique (see Sect. 2.6.7.2) [8]. They compared the frequencies contained in the perturbation and the response

signals by performing a Fast Fourier Transform (FFT) on the response signal. When the system behaves nonlinearly, harmonics of the frequencies contained in the perturbation signal appear in the response spectrum.

Erroneous impedance data cannot only be caused by nonlinearity but very frequently by a lack of stability of the system under investigation. The easiest way to establish whether a system has changed during the course of an impedance measurement is to repeat the experiment and compare both sets of data. For most applications, instabilities could and should be eliminated by adjusting the measuring conditions accordingly. However, it may also be desirable to characterize systems, which are known to change over time, or even to measure changes of the complex impedance in real time [9, 10]. As long as the measurement time is short compared to the time constant of relaxation of the system, valid impedance data can be obtained. Since the lower the measurement frequency, the greater the measurement time, it is generally accepted that high-frequency data can be valid even when low-frequency data are affected by non-stationary behavior of the electrochemical system.

Kramers–Kronig relations have been used by a large number of scientists as a diagnostic tool for the validation of impedance data to establish which frequency range contains consistent data [2]. Originally developed for optical applications, they can also be applied to electrochemical impedance spectroscopy. The Kramers–Kronig relations are a series of integral equations that govern the relationship between the real and imaginary parts of complex quantities for systems fulfilling the conditions of linearity, causality, and stability.

The imaginary part of the impedance can be calculated from the real part of the impedance from

$$Z''(\omega) = -\frac{2\omega}{\pi} \int_0^{\infty} \frac{Z'(x) - Z'(\omega)}{x^2 - \omega^2} dx \quad (41)$$

If the high-frequency limit of the real part of the impedance is known, the real part of the impedance can be obtained from the imaginary part of the impedance using

$$Z'(\omega) = Z'(\infty) + \frac{2}{\pi} \int_0^{\infty} \frac{xZ''(x) - \omega Z''(\omega)}{x^2 - \omega^2} dx \quad (42)$$

If the zero frequency limit of the real part of the impedance is known, the real part of the impedance can be obtained at any frequency from the imaginary part using

$$Z'(\omega) = Z'(0) + \frac{2\omega}{\pi} \times \int_0^{\infty} \frac{x/\omega Z''(x) - \omega Z''(\omega)}{x^2 - \omega^2} dx \quad (43)$$

The relationship between phase angle and modulus of the impedance is

$$\Phi(\omega) = \frac{2\omega}{\pi} \int_0^{\infty} \frac{\ln Z_0(x)}{x^2 - \omega^2} dx \quad (44)$$

To assess whether experimental data fulfill the Kramers–Kronig relations, one part of the impedance is calculated from the other part of the impedance, which has been experimentally determined. For example, the imaginary part can be calculated from the measured real part of the impedance using Eq. (41). The calculated imaginary part of the impedance can then be compared with the measured imaginary part of the impedance. Any difference between calculated and measured values would indicate a deviation from one of the conditions of linearity, causality, or

stability. This method, however, requires that at least one part of the impedance is known between the frequency limits of zero and infinity.

In most cases, the frequency range is not sufficiently large to integrate over the frequency limits zero and infinity. To overcome this problem, various models for extrapolating the experimental data sets to the frequency limits have been suggested. These methods were reviewed by Agarwal and coworkers in [2] and will only be summarized in this chapter. Kendig and coworkers suggested extrapolating impedance data to low frequencies assuming that the imaginary impedance is symmetrical (see for example, Fig. 5b) [11]. However, this can only be applied to simple systems with one time constant. Macdonald and coworkers extrapolated polynomial fits to the data into the unmeasured frequency range [12]. Esteban and coworkers calculated impedance data below the lowest measured frequency by using Eqs. 41 and 42 (or 43) simultaneously forcing the measured data set to satisfy the Kramers–Kronig relations [13]. Any discontinuity between the measured and the calculated data set would then indicate erroneous impedance data.

A method that does not require extrapolating data to frequency ranges not accessible by experiment is the fit of the data with an equivalent circuit. Equivalent circuits consisting of passive circuit elements satisfy the Kramers–Kronig relations. Any successful fit of such an equivalent circuit to a data set would confirm that the data is consistent with the Kramers–Kronig relations. A generalization of this approach, which suggests the use of a so-called *measurement model*, was described by Agarwal and coworkers [14]. The measurement model is of

the form

$$Z(\omega) = Z_0 + \sum_k \frac{\Delta_k}{(1 + j\tau_k\omega)} \quad (45)$$

It is equivalent to a series of a number of RC parallel combinations in series with the solution resistance, which is also known as the *Voigt model*. If a sufficient number of terms is included, the model should be able to fit impedance data of any stationary electrochemical cell. Since the model is consistent with the Kramers–Kronig relations, any failure to fit experimental data using this model indicates a violation of the Kramers–Kronig relations.

2.6.4

Distributed Circuit Elements

Impedance data are frequently fitted with an equivalent circuit made up of circuit elements, which are related to the physical processes in the system under investigation. In many cases, ideal circuit elements such as resistors and capacitors can be applied. Mostly, however, distributed circuit elements are required in addition to the ideal circuit elements to describe the impedance response of real systems adequately. Various distributed circuit elements and their applications are discussed in [3, 15].

Historically, the Warburg impedance, which models semi-infinite diffusion of electroactive species, was the first distributed circuit element introduced to describe the behavior of an electrochemical cell. As described above (see Sect. 2.6.3.1), the Warburg impedance (Eq. 38) is also analogous to a uniform, semi-infinite transmission line. In order to take account of the finite character of a real electrochemical cell, which causes deviations from the Warburg impedance at low frequencies,

the finite length Warburg impedance was introduced (Eq. 39).

In all real systems, some deviation from ideal behavior can be observed. If a potential is applied to a macroscopic system, the total current is the sum of a large number of microscopic current filaments, which originate and end at the electrodes. If the electrode surfaces are rough or one or more of the dielectric materials in the system are inhomogeneous, then all these microscopic current filaments would be different. In a response to a small-amplitude excitation signal, this would lead to frequency-dependent effects that can often be modeled with simple distributed circuit elements. One of these elements, which have found widespread use in the modeling of impedance spectra, is the so-called *constant phase element* (CPE). A CPE is defined as

$$Z_{\text{CPE}} = A_0(j\omega)^{-\alpha} \quad (46)$$

where A_0 and α are frequency-independent parameters and $0 \leq \alpha \leq 1$. The name *constant phase element* stems from the fact that the phase angle is frequency independent. In the complex plane diagram, a CPE would appear as a straight line at a constant phase angle of $\Phi = -(\alpha \times 90^\circ)$. For $\alpha = 0$, the CPE describes an ideal resistor, and for $\alpha = 1$, it describes an ideal capacitor. The CPE has been used to describe different processes. For $\alpha = 0.5$, the CPE represents homogeneous diffusion, that is, Eqs. (38 and 46) are mathematically equivalent for $\alpha = 0.5$. For other values of α , the CPE can be used to describe inhomogeneous diffusion.

The CPE has also been interpreted as a distribution of relaxation times due to inhomogeneities in dielectric materials, that is, materials that can pass an alternating current but not a dc current. The main problem associated with the CPE is that

it is only valid over a limited frequency range. In any physically valid model, there should be a shortest and a longest relaxation time. This is, however not true for the CPE. Therefore, the CPE usually needs to be modified at both ends of the frequency spectrum. In many cases, this does not pose a problem, since impedance measurements are not carried out at extreme frequencies.

Other empirical distributed elements have been described, which can be expressed as a combination of a CPE and one or more ideal circuit elements. Cole and Cole found that frequency dispersion in dielectrics results in an arc in the complex ε plane (an alternative form of presentation) with its center below the real axis (Fig. 10a) [16]. They suggested the equivalent circuit shown in Fig. 10(b), which includes a CPE and two capacitors. For $\omega \rightarrow 0$, the model yields capacitance C_0 and for $\omega \rightarrow \infty$ the model yields capacitance C_∞ . The model can be expressed with the following empirical formula for the complex dielectric constant

$$\varepsilon = \varepsilon_\infty + \frac{\varepsilon_0 - \varepsilon_\infty}{1 + (j\omega\tau_0)^{1-\alpha_\varepsilon}} \quad (47)$$

where ε_∞ and ε_0 are the dielectric constants for $\omega \rightarrow \infty$ and $\omega \rightarrow 0$, and τ_0 is a generalized relaxation time. The CPE parameter A_0 (Eq. 46) is correlated to τ_0 through

$$\tau_0 \equiv [A_0(C_0 - C_\infty)]^{1/1-\alpha} \quad (48)$$

Analogous behavior has been described for conducting systems, that is, systems that can pass a direct current. In this case, a semicircle with its center below the real axis can be found in the complex impedance plane (Fig. 11a). The equivalent circuit (Fig. 11b) contains a combination of a CPE and two resistors,

Fig. 10 (a) Cole–Cole plot showing a depressed arc in the complex ε plane and (b) equivalent circuit describing the frequency dispersion in dielectrics [16].

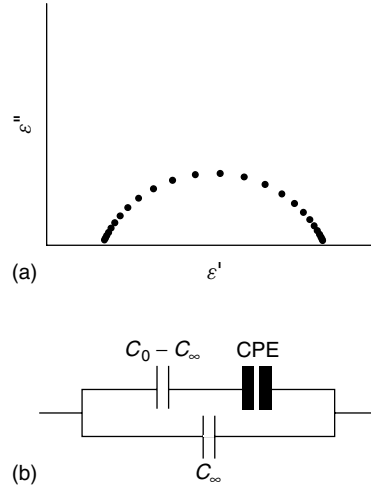
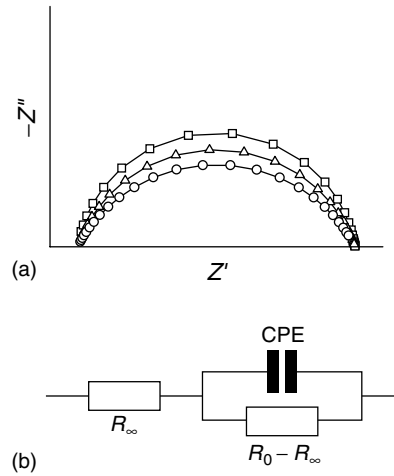


Fig. 11 (a) Frequency dispersion in electrochemical systems leads to a depressed semicircle in the complex impedance plane (shown for different values of the exponent α of the CPE (Eq. 46), $\square \alpha = 0.9$, $\triangle \alpha = 0.8$, $\circ \alpha = 0.7$), (b) equivalent circuit describing the frequency dispersion in electrochemical systems [3].



R_0 and R_∞ , which represent the low and high-frequency limits. The impedance of this circuit can be expressed as

$$Z = R_\infty + \frac{R_0 - R_\infty}{1 + (R_0 - R_\infty)A_0^{-1}(j\omega)^\alpha} \quad (49)$$

A comparison between the circuit shown in Fig. 11(b) and the equivalent circuit of a simple electrochemical cell (Fig. 4b) shows that they are analogous, with $R_\infty \equiv R_e$, $R_0 - R_\infty \equiv R_{ct}$, and $C_{dl} \equiv CPE$.

Impedance spectra of real electrochemical cells will usually not show a perfect semicircle as the one presented in Fig. 4(c) but depressed semicircles as shown in Fig. 11(a).

This behavior is observed when the surface of an electrode is not perfectly flat. In the simple equivalent circuits for electrochemical cells discussed in Sects. 2.6.2 and 2.6.3, the double-layer capacitance (see Figs. 3c, 4b, and 7) is

therefore frequently replaced by a CPE, although the parameters α and A_0 in Eq. (46) can often not be accurately correlated to physical properties of the system under investigation. A few special cases in which the parameters of the CPE can be derived directly from the electrode morphology are discussed in Sect. 2.6.5.

For further information regarding distributed circuit elements, refer to [3, 15].

2.6.5

The Effect of Electrode Morphology

As indicated in Sect. 2.6.4, modeling of real electrochemical systems usually requires the aid of distributed circuit elements. In this section, the relationship between the morphological properties of rough or porous electrodes and their impedance behavior will be discussed.

As established by a large number of authors, the impedance of solid electrodes in the absence of faradaic processes usually deviates from pure capacitive behavior. Only for smooth and clean surfaces like that of liquid mercury, a pure capacitance can be used to describe the impedance behavior (Fig. 13, curve a). The deviation from ideality has frequently been attributed to surface roughness or porosity. In the case of rough electrodes, the impedance behavior is usually approximated using a CPE (see Eq. 46) with $0.5 < \alpha < 1$. Several attempts have been made to derive a relationship between the CPE and a fractal surface morphology [17, 18]. However, the relationships between

the exponent α of the CPE and the fractal dimension are contradictory, and there is some controversy about the validity of these theories since there is little experimental evidence to support them [19, 20]. More recently, models have been suggested that are based on the assumption that the frequency dependence of capacitance on solid electrodes is due to the atomic scale inhomogeneities rather than the geometric aspects of surface roughness [21].

2.6.5.1 Porous Electrodes

De Levie was the first to develop a transmission line model to describe the frequency dispersion in porous electrodes [22]. Here, only the effect of double-layer charging in the absence of a faradaic process will be discussed. De Levie's model is based on the assumption that the pores are cylindrical, of uniform diameter, and semi-infinite length, not interconnected and homogeneously filled with electrolyte. The electrode material is assumed to have no resistance. Under these conditions, a pore behaves like a uniform RC transmission line as shown in Fig. 12. If a sinusoidal excitation is applied, the transmission line behavior causes the amplitude of the signal to decrease the further the distance from the opening of the pore, that is, only a fraction of the pore is effectively taking part in the double-layer charging process. From that, a penetration depth λ of the signal can be defined, which is inversely proportional to the square root of frequency and

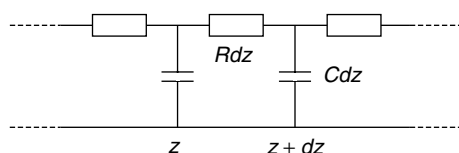
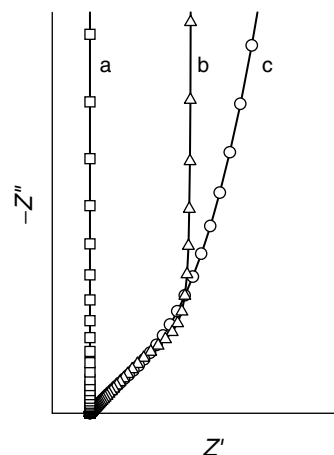


Fig. 12 Section of the equivalent circuit of a pore, in which z is the distance from the pore entrance. Solution resistance and double-layer capacitance are uniformly distributed [22].

Fig. 13 Impedance behavior of an electrode in the absence of electroactive species for (a) a perfectly flat electrode; (b) a porous electrode with uniformly sized pores according to de Levie's model; and (c) an electrode with a pore size distribution [23].



directly proportional to the square root of the radius of the pores

$$\lambda = \frac{1}{2} \sqrt{\frac{\kappa r}{C_{dl} \omega}} \quad (50)$$

where r is the radius of a pore, κ is the electrolyte conductivity, and C_{dl} is the double-layer capacitance.

At very high frequencies, the penetration depth is negligible and only the capacitance effects of the flat external electrode surface are measured. At lower frequencies, the penetration depth and therefore the influence of the pores become progressively more important since the inner surface of the electrode is very large compared with the outer surface. Hence, a decrease of the frequency is accompanied by an increase in capacitance. The result is a straight line in the complex plane diagram at a phase angle of -45° , which is equivalent to a Warburg impedance or a CPE with $\alpha = 0.5$.

If the model is extended to pores with finite and uniform length, the penetration depth will eventually reach the length of the pores when the frequency is sufficiently low. A further decrease in frequency would result in pure capacitive

behavior since the electrode surface taking part in the double-layer charging process is now frequency independent (Fig. 13, curve b).

Experimental results match the predictions of de Levie's model at high frequencies. At low frequencies, however, deviations from ideal capacitive behavior are frequently observed (Fig. 13, curve c). Song and coworkers suggested that the nonideal behavior might be due to pore size distribution [23, 24]. This leads to a distribution of the penetration depth even at a single frequency since each pore would have a different penetration depth depending on its dimensions. The model developed by Song and coworkers integrates dispersion due to pore size distribution as well as in-the-pore dispersion described by de Levie. It successfully describes the low-frequency branch of the impedance data for a porous electrode and can also be used to assess the average radius of pores, the width of the pore size distribution, the average pore length, and the surface area. Song and coworkers also suggested that the model might allow the use of impedance spectroscopy for porosimetry.

2.6.6

Characterization of Coatings and Membranes

In the previous sections, the impedance behavior of electrochemical cells was described, with a view of how kinetic parameters of electrochemical reactions or electrode properties such as the morphology might be extracted from an impedance spectrum. However, electrochemical impedance spectroscopy has been utilized for a vast number of applications and is not limited to mechanistic investigations of electrode reactions. A large number of studies have been dedicated to the investigation of coated electrode surfaces. In this chapter, a few selected examples will be given of how impedance spectra of coated electrodes can be evaluated and what information can be gained from them.

2.6.6.1 Insulating Coatings

Insulating coatings have been of particular interest in corrosion protection. A large number of papers deal with the characterization of polymer layers and their degradation [25–27]. An electrode with a perfectly insulating coating shows

the simple impedance behavior of the electrolyte resistance in series with the geometric capacitance of the polymer film (Fig. 14b), which can be calculated according to

$$C_{\text{geom}} = \frac{\varepsilon \times \varepsilon_0 \times A}{l} \quad (51)$$

where ε is the dielectric constant of the polymer, ε_0 is the dielectric constant of vacuum, A is the surface area of the electrode, and l the thickness of the polymer film. Measured values of the geometric capacitance can be used to calculate the dielectric constant or the thickness of the polymer if one of both parameters is known.

Impedance spectroscopy can be used to distinguish between different processes of degradation. A dissolution of a polymer film layer-by-layer would only lead to a reduction in the film thickness l in Eq. (51), that is, the geometric capacitance of the film would increase, but the principle shape of the impedance spectrum would stay the same (Fig. 14a) [28]. Frequently, however, the formation of pores is the main reason for coating failure. This behavior can be approximated with the equivalent circuit shown in Fig. 15(b) [25],

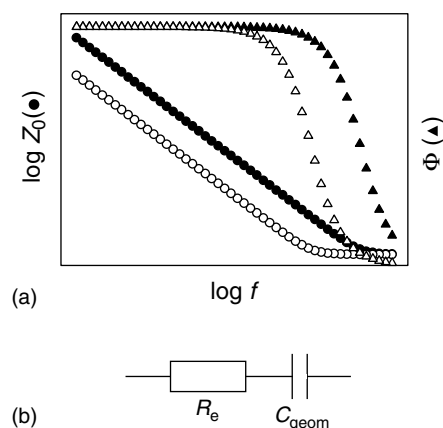


Fig. 14 (a) Change of impedance during degradation of an insulating coating layer-by-layer (simulated data, solid symbols: before degradation, open symbols: after partial degradation) and (b) equivalent circuit of coated electrode before and after partial degradation.

Fig. 15 (a) Change of impedance during degradation of an insulating coating by pore formation (simulated data, solid symbols: before degradation, open symbols: after partial degradation) and (b) equivalent circuit of a partially degraded film [25].

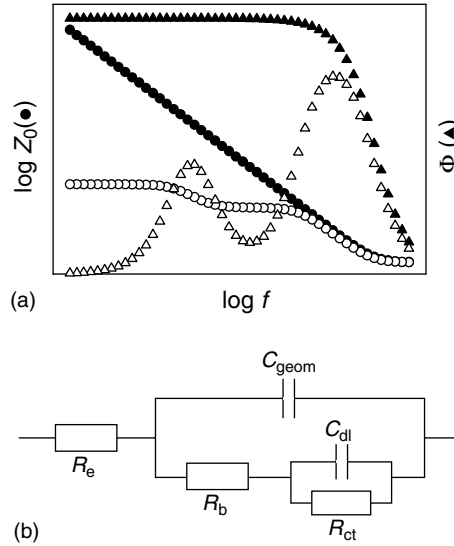
and the impedance spectrum changes as shown in Fig. 15(a). If a coating has electrolyte-filled pores that extend through the entire thickness of the coating, then an apparent bulk resistance R_b can be observed, which corresponds to the resistance of the electrolyte in the pores. The ratio of the resistance R_{bt} of an electrolyte layer that occupies the same space as the polymer layer to the bulk resistance R_b is equivalent to the fraction of the film, which consists of electrolyte-filled pores, and therefore to the porosity P of the coating

$$P = \frac{R_{bt}}{R_b} \quad (52)$$

Impedance spectra of partially degraded coatings cannot only be used to estimate the porosity of the film but also to estimate the area of the metal electrode wetted by electrolyte. Since the interface metal–electrolyte is represented by the parallel combination of the charge-transfer resistance and the double-layer capacitance; both of these can be used to estimate the fraction of the electrode surface W wetted by electrolyte

$$W = \frac{C_{dl}}{C_{dl}^0} = \frac{R_{ct}^0}{R_{ct}} \quad (53)$$

where R_{ct}^0 and C_{dl}^0 are the charge-transfer resistance and double-layer capacitance of an uncoated electrode. Frequently, the wetted surface area is considerable larger than the porosity of the coating indicating that the electrolyte spreads along the



metal–polymer interface after penetrating the film. The relationship given in Eq. (53) can only be regarded as a rough estimate of the wetted metal area since the spreading of electrolyte along the electrode surface leads to a nonuniform current distribution that can best be described with a linear transmission line [25].

The degradation of coatings, although an unwanted effect in corrosion protection, has been exploited for sensor development. Disposable electrodes were coated with biodegradable films. In the presence of either an enzyme or the product of an enzymatic reaction, the polymer degraded. The change of impedance observed during the enzyme catalyzed degradation of the polymer films has been used as a sensor signal to detect analytes such as urea, creatinine, and a variety of different enzymes [28–30].

2.6.6.2 Noninsulating Films

There has been great interest in the characterization of conducting

polymers using impedance spectroscopy. Johnson and coworkers described the theoretical response of a metal-polythiophene-electrolyte system and a metal-polythiophene-metal system [6]. For the metal-conducting polymer-electrolyte arrangement, the following regions in the impedance spectrum were predicted (Fig. 16):

- A high-frequency semicircle corresponds to the bulk resistance R_b of the polymer layer in parallel to its geometric capacitance. The bulk resistance reflects the concentration and mobility of charge carriers in the conducting polymer.
- Two charge-transfer semicircles are expected, which correspond to two RC parallel combinations of the double-layer capacitance and charge-transfer resistance at the electrode-polymer interface and the double-layer capacitance and charge-transfer resistance at the polymer-electrolyte interface. At the metal-polymer interface, electron transfer would occur while at the polymer-electrolyte interface anion transfer is expected.
- At low frequencies, a diffusion-limited region appears, which, if fitted to a Warburg impedance, can be used to determine diffusion coefficients of charge carriers in the conducting polymer. At the low-frequency limit, capacitive behavior can be observed indicating that no dc current can flow through the system.

The impedance spectrum of the metal-conducting polymer-metal system was predicted to show the following regions (Fig. 17):

- The high-frequency semicircle is again caused by a parallel combination of the bulk resistance and geometric capacitance of the film.
- Only one semicircle is predicted for the metal-polymer interfaces, since only electron transfer can occur.
- Since electron transfer occurs at both metal-polymer interfaces, a dc current can flow through the system, that is, the low-frequency limit is not a capacitance as in the case of the metal-conducting polymer-electrolyte system but the impedance response bends over to the real axis after the Warburg region.

In principle, a large number of parameters such as conductivity, charge-transfer resistors, and diffusion coefficients can be determined from the impedance spectra discussed above. However, in practice, it is only possible to resolve the different processes and their characteristic shapes in the impedance spectrum if their time

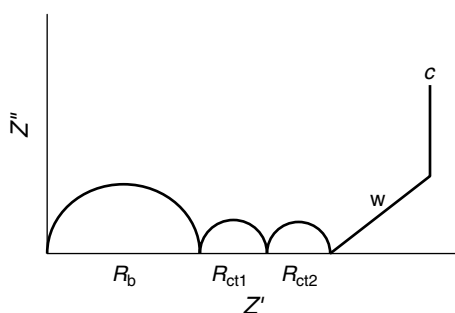
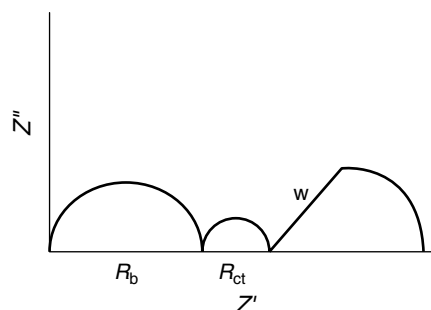


Fig. 16 Theoretical impedance response of a metal-polythiophene-electrolyte structure [6].

Fig. 17 Theoretical impedance response of a metal-polythiophene-metal structure [6].



constants are sufficiently different. Frequently, the time constants of interface and bulk processes are not as clearly separated as shown in Figs. 16 and 17, and mixed impedance behavior is observed making an interpretation of the impedance spectra more difficult.

Other examples for the characterization of films and membranes using impedance spectroscopy are the investigation of electrolyte uptake of polymer films [31–33] and the determination of exchange currents at ion-selective membranes for potentiometric sensors [32, 34].

2.6.7

Instrumentation

Impedance test equipment usually comprises an ac measurement unit and a potentiostat or galvanostat. For many applications, such as biomedical investigations or the characterization of thin films in which it is not essential to maintain a dc-voltage level during the impedance measurement, a potentiostat is not required. In cases like this, the ac-measurement unit can be used more efficiently by itself since it usually allows more accurate measurements and the use of higher frequencies. Potentiostats, however, are a useful addition to the impedance test equipment when the system under investigation has a high impedance, since they have high-input

impedance and good current sensitivity. Further information analog and digital instrumentation is given in Chapter 1.2.

The techniques commonly utilized for ac-impedance measurements in modern equipment can be subdivided into two main groups – single-sine and multiple-sine techniques. The lock-in technique and frequency-response analysis will be described as representatives of the single-sine techniques and FFTs will be introduced as an example for multiple-sine techniques.

2.6.7.1 Single-sine Techniques

In single-sine techniques, a small-amplitude sinusoidal signal with a fixed frequency is applied to the test cell. The response signal is then analyzed to extract the two components of the impedance (real and imaginary parts or magnitude and phase). This experiment is then repeated at a series of different test frequencies usually starting at the highest frequency and finishing at the lowest in order to minimize sample perturbation. The main advantages of single-sine techniques are

- that they produce high-quality data,
- that fast measurements can be performed at high frequencies since the measurements can be performed during one cycle of the sine wave,

- that the instrumentation is simple since the sine wave can be produced with a frequency generator, and
- that measurements can be carried out at very high frequencies.

2.6.7.1.1 Phase-sensitive Detectors – Lock-in Amplifiers Lock-in amplifiers are designed for signal detection in a high-noise background and are therefore capable of very accurate readings. A schematic of a lock-in amplifier is shown in Fig. 18. An oscillator produces a sinusoidal waveform, which is simultaneously applied to the electrochemical cell and fed into the reference input. The response wave is applied to the signal input and amplified including noise. The bandwidth of the noise is reduced by passing the amplified signal through a band pass filter [35, 36].

A lock-in amplifier usually provides a dc output that is proportional to the ac input signal. The rectifier, which performs this ac to dc conversion, is called a *Phase-Sensitive Detector (PSD)*. The detector multiplies input and reference signal with each other. If the reference signal is a voltage according to

$$V^{\text{ref}} = V_0^{\text{ref}} \cos \omega t \quad (54)$$

and the input signal is a voltage proportional to the ac current flowing through the

system under investigation according to

$$V^{\text{in}} = V_0^{\text{in}} \cos(\omega t + \Phi) \quad (55)$$

then the product of these two signals would be a sinusoid at twice the reference frequency

$$V^{\text{PSD}} = \frac{1}{2} V_0^{\text{ref}} V_0^{\text{in}} \cos \Phi + \frac{1}{2} V_0^{\text{ref}} V_0^{\text{in}} \times \cos(2\omega t + \Phi) \quad (56)$$

Figure 19 shows the case in which $\Phi = 0$.

The mean level of V^{PSD} , which is the dc component of the detector signal, can be calculated to

$$V_{\text{mean}}^{\text{PSD}} = \frac{1}{2} V_0^{\text{ref}} V_0^{\text{in}} \cos \Phi \quad (57)$$

In a lock-in amplifier, the reference signal is passed through a phase shifter that compensates for any phase shift between input and reference signal introduced by the system under investigation. Since there is no phase shift between input and reference signals ($\Phi = 0$) after passing through the phase shifter, the mean level of the detector signal assumes its maximum possible value of $1/2 V_0^{\text{ref}} V_0^{\text{in}}$ according to Eq. (57). If the reference signal is fixed at a constant level, the input signal and therefore the impedance can be calculated from the mean level of the detector signal. The dc component of the detector signal is

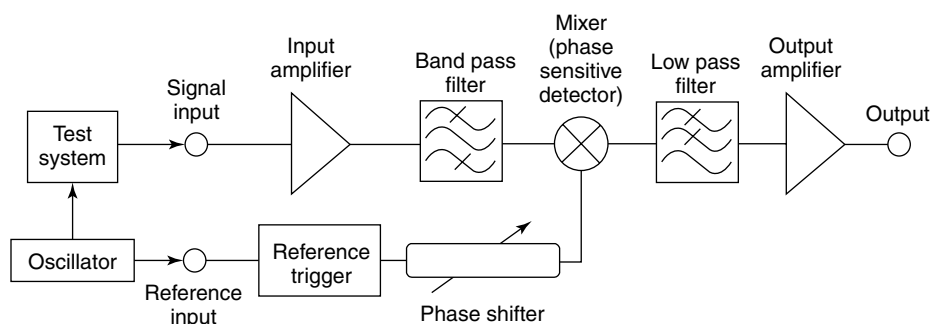


Fig. 18 Schematic of a lock-in amplifier [35].

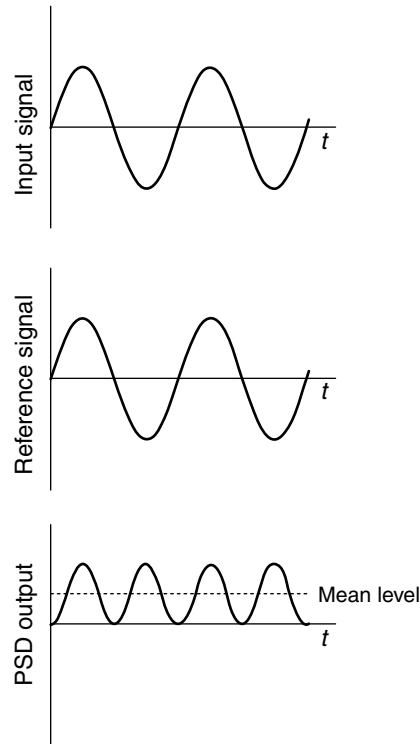
Fig. 19 Detection principle of a lock-in amplifier [35].

isolated from the signal by using a low pass filter and by measuring the filtered output with a dc-voltmeter. Noise associated with the input signal would also be multiplied with the reference signal. However, since noise does not have a fixed frequency or phase relationship to the reference signal, it does not cause a change of the mean dc level, that is, lock-in amplifiers are highly frequency selective.

There are different types of PSDs, three of which will be discussed briefly. The first one is an analog multiplier in which the input signal is multiplied with the reference signal via an electronic circuit. In the presence of large noise, it is difficult to guarantee linear operation of analog multipliers that therefore often show poor noise rejection.

The simplest form of PSD is a digital switching multiplier. Its operation is shown in Fig. 20. During the first half cycle, while the reference signal is positive, the input signal remains unchanged. During the second half cycle, the reference signal becomes negative, and the input signal is inverted. This type of PSD usually operates linearly. However, the main disadvantage of switching multipliers is, that they do not only detect signals at the frequency of the reference signal but also at odd harmonics of the reference frequency.

The PSD found in digital lock-in amplifiers is the digital multiplier. In this case, the input signal is first amplified and then digitized. This digitized signal is multiplied with a digitized version of the reference signal using a digital signal processor (DSP). This technology provides perfect multiplication and excludes odd harmonics of the reference frequency. A problem associated with instruments



using DSPs is the dynamic range that is inherent to all digital instruments (see Chapter 1.2).

Many modern lock-in amplifiers include a microprocessor to perform simple mathematical manipulations, and can easily be incorporated into a computer-controlled setup. Measurements using a lock-in amplifier provide high-quality data but are usually more time consuming than those carried out with a frequency response analyzer (FRA).

2.6.7.1.2 Frequency Response Analysis

Frequency Response Analysis is the most widely used technique for impedance testing. Similar to the lock-in technique, it can extract a small signal from a very high background of noise automatically

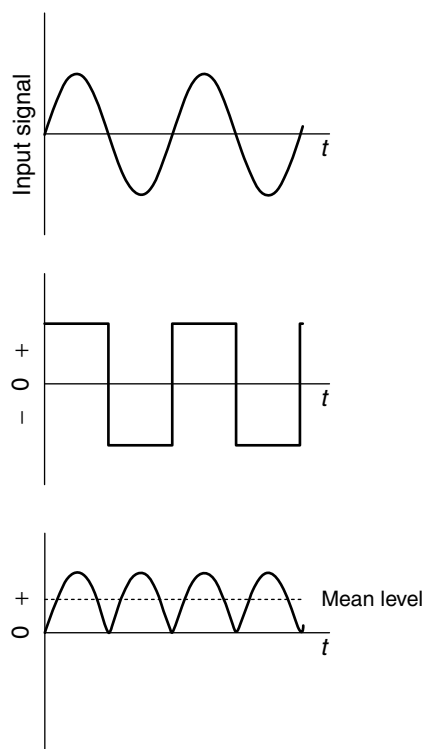


Fig. 20 The digital-switching multiplier is the simplest form of the phase-sensitive detector [36].

used to reject these spurious components is analogous to the digital multiplication of the input signal with a reference waveform performed by a phase-sensitive detector (see Sect. 2.6.7.1.1). However, in the case of an FRA, no phase shifter is needed to compensate for the phase shift between input and reference signals, but the integrated waveforms are immediately correlated by multiplying them by sine and cosine reference waveforms, and the resulting signals are integrated.

For a pure sinusoidal input signal

$$V^{\text{in}} = r \sin(\omega t + \Phi) = a \sin \omega t + b \cos \omega t \quad (58)$$

the results of the integrations would be

$$\frac{1}{T} \int_0^{2\pi/\omega} (V^{\text{in}} \sin \omega t) dt = \frac{a}{2} \quad (59)$$

which corresponds to the real component of the input signal and

$$\frac{1}{T} \int_0^{2\pi/\omega} (V^{\text{in}} \cos \omega t) dt = \frac{b}{2} \quad (60)$$

which corresponds to the imaginary component of the input signal. Once real and imaginary parts of the input signals have been determined by correlation, the complex impedance of the test object can be calculated. It can be mathematically proven that all the spurious components are rejected by this technique of correlation provided that a sufficiently large number of cycles have been used for the integration.

Some FRAs are also capable of analyzing harmonics. This could be achieved by multiplying the input signal with a waveform of the appropriate frequency or by carrying out an FFT on the input signal.

rejecting dc and harmonic responses. An FRA correlates the input signal with reference sine waves. To achieve fast measurements, FRAs are usually equipped with separate analyzers for each input.

FRAs have a sine wave generator that outputs a small-amplitude voltage signal to the system under investigation. The response signals, usually the voltage measured between two reference points in the electrochemical cell and a voltage signal proportional to the current flowing through the cell, are fed into the input channels, digitalized, and then integrated over several cycles in order to reject noise.

In addition to the waveform at the frequency of interest, the measured signals usually contain a dc component, harmonics, and noise (see Eq. 67). The process

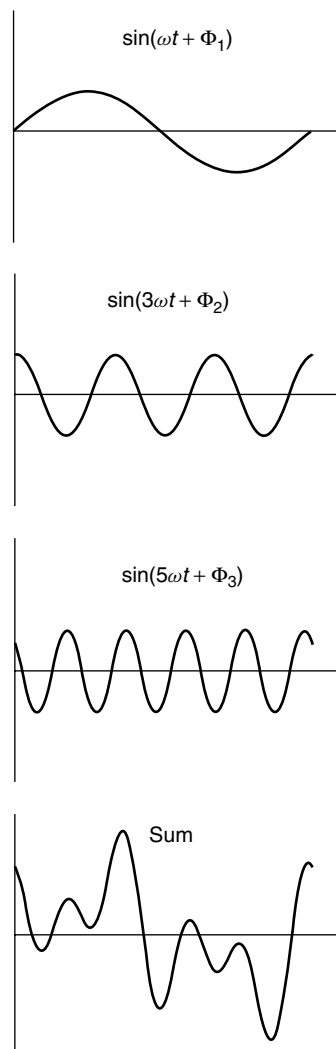
Fig. 21 FFT waveform composed of three different frequencies [36].

The technique of digital correlation can be applied to a large range of frequencies. However, to allow easier analysis at high frequencies, the measured signal is shifted to lower frequencies using a technique called *heterodyning*. The input signal is multiplied with a reference signal of slightly different frequency. The resulting signal has two components, one at the sum of both frequencies and one low-frequency component at the difference of both frequencies. The high-frequency signal can easily be filtered out, and the low-frequency signal is then analyzed by correlation as described above.

2.6.7.2 Multiple-sine Techniques

Impedance spectroscopy is frequently used to characterize systems that change with time. In Sect. 2.6.3.2, it was shown how inconsistent impedance data could be eliminated using Kramers–Kronig transforms. Another way to reduce the effects of a system changing during the measurement is to reduce the total measurement time by using a multisine technique, which is also frequently called *time-domain* or *FFT technique*.

In the case of multisine techniques, a measurement is carried out at several frequencies simultaneously. Analogous to white noise, waveforms of typically 15 to 20 different frequencies and equal amplitudes are superimposed as demonstrated in Fig. 21 [36]. The phases of the superimposed signals are randomized to minimize the amplitude of the composite signal. In contrast to single-sine techniques, multisine techniques do not require waiting for a full cycle to be completed for each of the frequencies used. For a multisine technique, a full experiment can be



carried out during a full cycle of the lowest frequency resulting in a reduced measurement time. This advantage can be utilized to investigate electrochemical processes in real time provided that time required for data acquisition is shorter than the time constants of the system under investigation.

The voltage across the system under investigation and the current, which contains

information about the response of the system to each of the frequencies contained in the perturbation signal, are measured in the time domain. The time-domain signals are digitized and transferred into the frequency domain by carrying out an FFT. The resulting data for each discrete frequency can be treated the same way as the impedance data obtained with a single-sine technique. Repeated application of the waveform and averaging of the signal before FFT is applied can improve the signal-to-noise ratio of the multisine technique, although it also increases the measurement time required.

It is worth considering the effect of a change of the system during the experiment. Because of the fact that the perturbation signal is a superposition of different frequencies, data are acquired for each frequency throughout the entire experiment. The result for one frequency is then obtained by averaging all the data sampled for this particular frequency. If the system under investigation changes during the experiment, the data averaged for each frequency would vary noticeably resulting in an impedance plot with considerable scatter. This scatter can be taken as a clear indication of unreliable data, but it also makes the entire data set unusable. As described in Sect. 2.6.3.2, the effect of a change of the system during the measurement can frequently be eliminated by discarding low-frequency data. For a multisine technique, this means that the experiment has to be repeated with a higher low-frequency limit in order to further reduce the measuring time.

As discussed in Sect. 2.6.10, electrochemical systems can show a nonlinear response, that is, the current response of an electrochemical system can be composed of a response at the excitation frequency

and responses at harmonics of the excitation frequency. Therefore, the frequencies superimposed for a multisine experiment have to be chosen very carefully. To prevent faulty results, the frequencies chosen are usually odd harmonics of the lowest frequency in order to eliminate the second harmonics components that may be caused by a nonlinear response of the system. Nonlinear behavior of the system would cause additional frequencies to appear in the response signal. The response at these additional frequencies would appear in the time-domain signal at places not occupied by the frequencies of the excitation waveform and at places already occupied by the excitation waveform. As shown by Popkrov and coworkers, this would cause a distortion of the response and data scattering [9]. Hence, not only nonstationary effects but also nonlinearity of the response appear in the FFT spectra as additional scatter.

2.6.7.3 Experimental Setup

For impedance measurements on electrochemical systems, frequently a potentiostat of suitably high bandwidth is integrated into the impedance measurement system. The operation of a potentiostat has been described in Chapter 1.2 of this volume. In the case of electrochemical impedance measurements, the potentiostat is not only responsible for maintaining a defined dc level but also for applying the correct ac voltage to the working electrode. A typical measurement setup with an FRA and a potentiostat is shown in Fig. 22 [37]. The polarization potential and the ac perturbation are added together and applied to the electrochemical cell at the counter electrode (CE terminal). The voltage difference between the two reference electrodes RE1 and RE2 is measured and fed back to

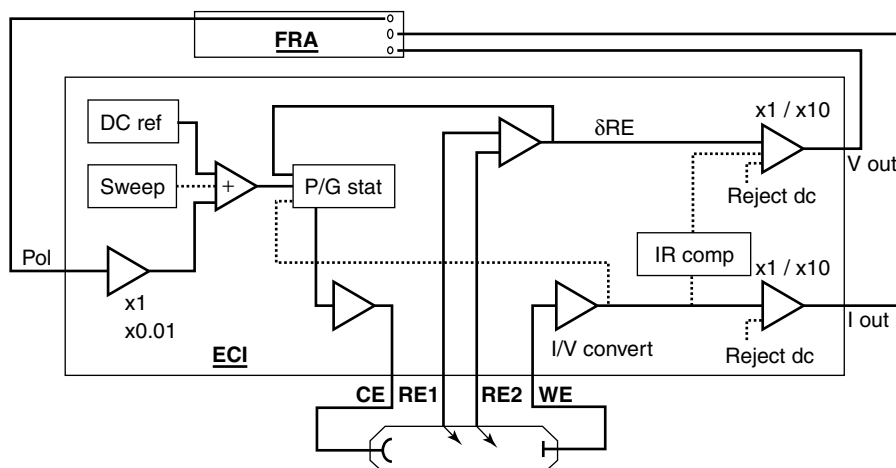


Fig. 22 Example for impedance measurement setup with an FRA [37]. (ECI: electrochemical interface, P/G stat: potentiostat/galvanostat).

the control loop, which corrects the voltage applied to the counter electrode until the required potential difference between RE1 and RE2 is established. The voltage measured between RE1 and RE2 and the current measured at the working electrode are amplified by the potentiostat and fed into the FRA as voltage signals. The potentiostat can provide dc rejection as well as compensate for the solution resistance if required (IR compensation).

In an experimental setup as described above, there is usually a choice between a two-, three-, or four-electrode cell. These options determine which part of the electrochemical cell is characterized by the impedance measurements.

In a *two-electrode cell*, terminal RE1 is connected to the counter electrode CE, and terminal RE2 is connected to the working electrode (Fig. 23a). The impedance is always measured between RE1 and RE2, that is, the impedance measured includes that of the counter electrode, the electrolyte solution, and the working electrode. This type of electrode arrangement is typically used if it is impossible to position a

reference electrode in the electrochemical cell, for example, in the characterization of batteries, or when it is important to maintain a homogeneous current distribution as, for example, in low-conductivity media, in which an inhomogeneous current distribution can lead to measurement artifacts [38]. If the properties of a single electrode (the working electrode) are to be investigated using a two-electrode arrangement, the impedance of the counter electrode has to be minimized by giving it a considerably larger surface area than that of the working electrode.

For the characterization of electrode properties, a *three-electrode cell* is superior. In this case, terminal RE1 is connected to a reference electrode placed close to the working electrode, which itself is connected to terminal RE2 (Fig. 23b). Since the impedance is now measured between reference and working electrodes, the impedance obtained will only be influenced by the properties of the working electrode and the properties of the electrolyte solution between working and

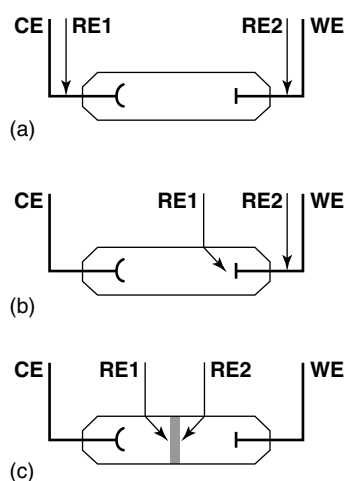


Fig. 23 (a) Two-electrode cell; (b) three-electrode cell; and (c) four-electrode cell.

reference electrodes, that is, the influence of the counter electrode on the impedance spectrum is eliminated and that of the resistance of the electrolyte solution is minimized.

The applications of impedance spectroscopy are not limited to the characterization of electrode properties. Sometimes it is desirable to investigate the properties of membranes, solutions, or dielectrics. For this kind of application, *four-electrode cells* provide the best results. Two reference electrodes are placed in the electrochemical cell between counter and working electrodes (Fig. 23c). The impedance measured depends purely on the properties of the electrolyte or membrane between the two reference electrodes, and the electrode properties are completely eliminated from the impedance spectrum.

2.6.8

Spatially Resolved Impedance Measurements

As demonstrated repeatedly in this chapter, ac-impedance spectroscopy is a valuable tool in the characterization of

electrochemical systems and new materials as it provides information over a large range of frequencies simultaneously. However, the results obtained using this method are always surface averaged. This can lead to difficulties when the properties of an electrode or a thin film are not uniform over the entire sample area. Several attempts have been made to develop methods that can detect impedance of electrochemical systems with local resolution. Two of these techniques will be described in this section.

2.6.8.1 Local Electrochemical Impedance Spectroscopy (LEIS)

Lillard and coworkers developed a method called *Local Electrochemical Impedance Spectroscopy LEIS* [39]. It relies on the fact that ac current densities in the solution very near to the working electrode are proportional to the local impedance properties of the electrode. In order to determine the current densities normal to the surface, the ac potential drop was measured between planes parallel to the electrode surface employing a two-electrode microprobe. A schematic of a commercially available experimental setup for LEIS is

shown in Fig. 24. The ac current density can be calculated from the potential drop $\Delta V(\omega)_{\text{probe}}$ using the following relationship:

$$I(\omega)_{\text{local}} = \frac{\Delta V(\omega)_{\text{probe}} \sigma}{l} \quad (61)$$

where σ is the conductivity of the electrolyte and l is the distance between the two microelectrodes normal to the surface. The area-normalized magnitude of the local impedance is then obtained from

$$Z_0(\omega)_{\text{local}} = \frac{V_0(\omega)}{\Delta V(\omega)_{\text{probe}}} \frac{l}{\sigma} \quad (62)$$

where $V_0(\omega)$ is the magnitude of the ac potential applied between working and reference electrodes.

The assumption made in the derivation of Eq. (62) is that the current density at the tip of the two-electrode probe and the current density at the electrode surface are the same, which means that all the current measured at the two-electrode probe is assumed to be flowing normal

to the surface of the working electrode. In reality, however, the ac currents spreads in the solution as a function of the distance from the electrode surface, that is, the resolution of LEIS depends on the distance of the two-electrode probe from the electrode surface. The spatial resolution of LEIS is also limited by the size of the two-electrode probe, since it is not possible to resolve features smaller than the probe. A reduction in size of the probe is also accompanied by an increase of its impedance, which makes it more difficult to measure the current density accurately. Lillard and coworkers therefore indicated that these competing effects needed to be optimized in order to achieve maximum spatial resolution [39]. Bayet and coworkers modified LEIS by replacing the two-electrode microprobe with a single vibrating probe to improve the local resolution [40].

LEIS has been applied successfully to study defects in organic coatings [41, 42] and passivation of metal surfaces [43].

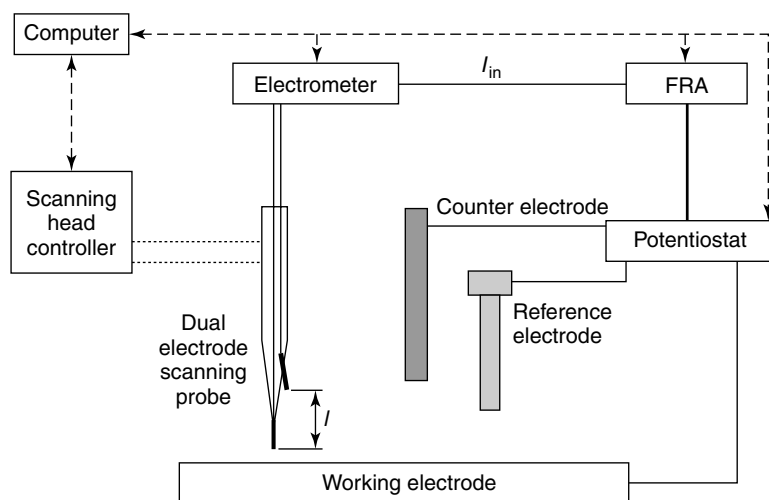


Fig. 24 Schematic of an experimental setup for LEIS (provided by Uniscan instruments).

2.6.8.2 Scanning Photo-induced Impedance Microscopy (SPIM)

Another impedance-based imaging technique for laterally resolved characterization of thin films or electrochemical systems is Scanning Photo-induced Impedance Microscopy (SPIM) [44]. It is based on photocurrent measurements at field-effect structures. In their simplest arrangement, field-effect structures consist of a semiconductor substrate with a thin insulator, and a gate electrode. This gate electrode can be a metal film resulting in the structure Metal Insulator Semiconductor (MIS) or, alternatively, Electrolyte Insulator Semiconductor structures are used, in which the electrolyte is in direct contact with the insulator, and a reference electrode is required to fulfill the function of the gate electrode.

Different regions of the semiconductor in a field-effect structure can be addressed with light. A dc voltage is applied between the semiconductor substrate and the gate electrode. Because of the presence of an insulator, this does not produce a dc current but controls the space charge region in the semiconductor at the interface between the semiconductor and the insulator. Electron hole pairs created during illumination of the semiconductor separate in the field of the space charge region if it is biased towards inversion.

The resulting current causes electrons and holes to collect on both sides of the insulator effectively charging the capacitor. When the illumination is turned off, the capacitor discharges and a current flows in the opposite direction. A modulated or chopped light beam focused on one region of the semiconductor substrate results in a local ac current. When the space charge region is biased towards accumulation, no photocurrent flows. Figure 25 (curve a) schematically shows the change of the photocurrent with the dc voltage.

If the system under investigation, for example a thin film, is deposited on a semiconductor insulator structure, the photocurrent decreases as shown in Fig. 25 (curve b). The difference in photocurrent is a function of the complex impedance of the layer added. Local differences in the impedance can be detected in the scanning mode. An additional variation of the modulation frequency of the light results in ac-impedance spectra with lateral resolution.

In classical ac-impedance spectroscopy, a small-amplitude ac-voltage signal is applied to the system under investigation, and the resulting ac current is measured. In the case of SPIM, a local ac voltage is created as a result of the photo-effect within the semiconductor by a focused, modulated light beam leading to a localized ac current. In contrast to other

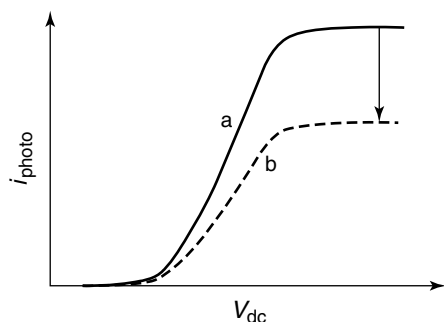


Fig. 25 Curve (a) photocurrent of a field-effect structure as a function of the dc voltage; curve (b) decrease of the saturation current of the photocurrent curve upon deposition of a thin film on the field-effect structure.

localized impedance techniques such as LEIS, no probe or microelectrode needs to be positioned above the sample. It is however required that the system under investigation be deposited on a field-effect structure. This can be done in two different arrangements: (1) The film is deposited onto a semiconductor insulator structure followed by the deposition of a thin metal film (Fig. 26a). This allows measurements in the gas phase. (2) The film is deposited onto a semiconductor insulator structure and is then exposed to an electrolyte solution (Fig. 26b).

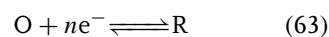
2.6.9

AC Voltammetry

AC voltammetry is an extension of classical linear sweep techniques such as cyclic voltammetry. Its main strength lies in the quantitative characterization of electrode processes, and it can also be used for analytical purposes. A dc ramp with a comparatively slow sweep rate and an ac signal are superimposed and applied to a working electrode, and the

response ac current and its phase angle are registered. The function of the dc potential is to enforce and change the surface concentrations of the electroactive species at the electrode surface. A simplification of the theoretical treatment can be achieved when the perturbation frequency is sufficiently high to separate the ac and dc contributions of the response signal. Because of the different timescales of the long term diffusion caused by the dc potential and the rapid diffusional fluctuations caused by the ac potential, the surface concentration set up by the dc potential has the same effect as a bulk concentration on the ac process.

In this chapter, only the response of a reversible system will be described. Linear sweep ac voltammetry of a Nernstian system is considered.



The mean surface concentrations of the electroactive species are exactly the same as they would be in a linear sweep experiment without a superimposed ac

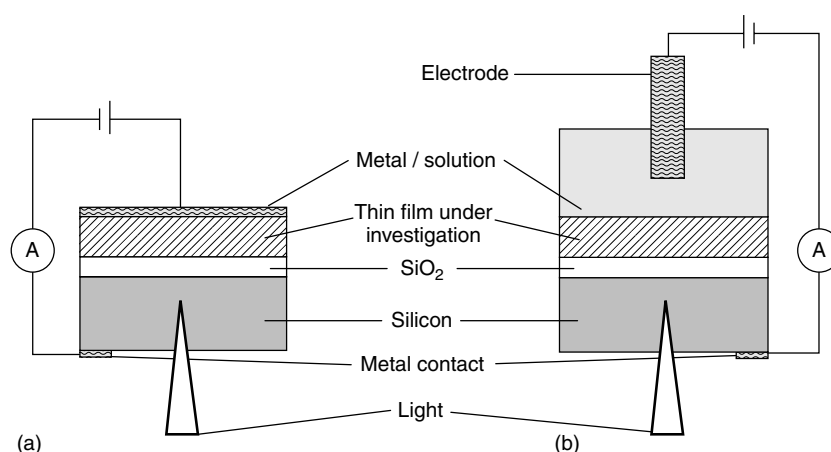


Fig. 26 Experimental arrangements for SPIM for (a) gas phase measurements and (b) measurements in electrolyte solutions.

potential (see Chapter 2.1 of this volume). The amplitude of the ac current can be derived according to

$$I_0 = \frac{E_0}{Z_f} = \frac{n^2 F^2 A \omega^{1/2} D_O^{1/2} c_O^* E_0}{4RT \cosh^2(a/2)} \quad (64)$$

where $a = nF/RT(E_{dc} - E_{1/2})$, E_0 is the amplitude of the ac potential, Z_f is the faradaic impedance, E_{dc} is the dc potential, and $E_{1/2}$ is the reversible half wave potential [5]. The bell shaped ac voltammogram described by Eq. (64) is shown in Fig. 27. At the peak maximum, the applied dc potential equals the half wave potential.

The peak current can be expressed as

$$I_p = \frac{n^2 F^2 A \omega^{1/2} D_O^{1/2} c_O^* E_0}{4RT} \quad (65)$$

From Eq. (65), it can be seen that the peak current is proportional to n^2 , $\omega^{1/2}$, and c_O^* [5]. The latter is utilized for the application of ac voltammetry for analytical purposes. The peak current is also proportional to the amplitude of the ac potential E_0 . This is, however, limited to small amplitudes, that is, to quasi-linear conditions. More recent simulations have shown that ac voltammetry can be carried out at considerably larger ac-potentials in order to increase

the sensitivity of ac voltammetry as an analytical technique [45, 46]. Although under these conditions, the peak current is not proportional to the ac-amplitude anymore, it could be demonstrated that the area under the peak is proportional to the perturbation amplitude and the analyte concentration [45]. Since the rules for semi-infinite diffusion apply, a phase angle of -45° can be observed for any reversible electrode reaction (see Sect. 2.6.3.1).

By extending ac linear sweep voltammetry by a reverse scan, ac-cyclic voltammetry is obtained. Surface concentrations of the electroactive species are the same at the same potential for forward and reverse scans. Hence, the peaks for forward and reverse scans are identical. In contrast to classical cyclic voltammograms, ac-cyclic voltammograms have a clear baseline that is advantageous for quantitative measurements.

If the dc process is not fully reversible, the surface concentrations of the electroactive species are different at a given dc potential for forward and reverse scans, that is, for quasi-reversible systems a displacement of the peaks for forward and reverse scan can be observed. This displacement can be used to derive kinetic parameters of the electrode reaction. For

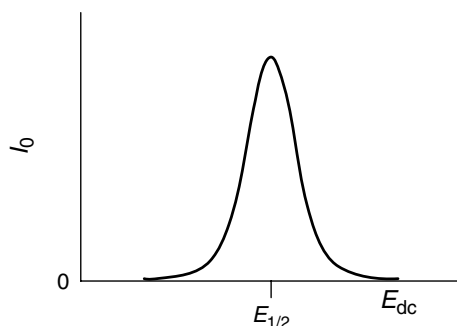


Fig. 27 Characteristic shape of an ac voltammogram for a reversible system.

a detailed discussion of the behavior of quasi-reversible and irreversible systems, see Bard and Faulkner [5].

2.6.10

Nonlinearity of Electrochemical Systems – Analysis of Higher Harmonics

In previous chapters only the linearized form of the current–potential relation has been used. The other terms of the Taylor series expansion were dropped. However, in reality, current–potential relationships show a considerable amount of curvature. The Taylor series expansion of the Butler–Volmer equation predicts that

$$\Delta I = \left(\frac{\partial I}{\partial E} \right)_{E_0} \Delta E + \frac{1}{2} \left(\frac{\partial^2 I}{\partial E^2} \right)_{E_0} \Delta E^2 + \dots \quad (66)$$

When a pure sinusoidal voltage is applied to an electrochemical cell, the waveform of the resulting current is very often distorted due to this nonlinear current–potential relationship unless the excitation voltage is sufficiently small. The response signal can be described as

$$I = I_{dc} + I_0 \sin(\omega t + \Phi) + I_1 \sin(2\omega t + \Phi_1) + I_2 \sin(3\omega t + \Phi_2) + \dots + \text{Noise} \quad (67)$$

where I_{dc} is the dc component of the current and $I_1, I_2, I_3 \dots$ are harmonic distortion components.

It is useful to consider the second and higher harmonics for the characterization of electrochemical systems. The advantage

of techniques based on the nonlinearity of electrochemical systems is, that the second and higher harmonic signals are relatively free of charging currents. Since the double-layer capacitance behaves in much more linear fashion than the faradaic processes, the charging currents of the double layer can mainly be found at the excitation frequency ω . Hence, the determination of kinetic parameters is frequently easier at higher harmonics. Harmonic analysis has been used widely for determining corrosion rates (see, for example, Jafar and coworkers in [2]).

Higher harmonics can be detected by FRAs or lock-in amplifiers, which can be tuned to detect a multiple of the excitation frequency. An alternative is to extract the harmonic signals from the response using FFT.

Second- or higher-order effects have not only been utilized for impedance spectroscopy but also for ac voltammetry [45, 47, 48]. While an ac voltammogram (shown

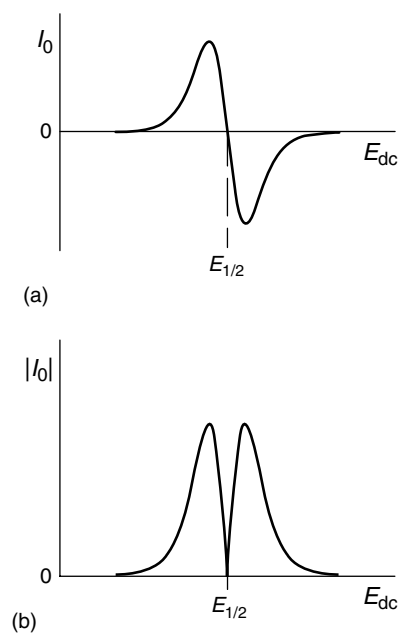


Fig. 28 Second harmonic ac voltammogram for a reversible system (a) phase-sensitive current detection and (b) modulus of the current.

in Fig. 27) corresponds to the first derivative of the current–potential relationship (first term in Eq. 66), the higher harmonics ac voltammograms that depend on the curvature of the current–potential relationship, correspond to that of the second and higher derivatives (Fig. 28a). The sign inversion of the current at $E_{1/2}$ can be detected in phase-sensitive measurement as a phase shift of 180° . A measurement of the magnitude of the ac-current amplitude would result in a voltammogram of the shape shown in Fig. 28(b).

Acknowledgments

I would like to thank Werner Moritz, Ron Armstrong, and Andrea Sabot for their suggestions for improving this chapter. I am also very grateful to Ed Holden (Perkin Elmer), Andrew Hinton (Solartron Analytical), Graham Johnson (Uniscan Instruments), and Timoer Frelink (Eco Chemie) for providing me with up-to-date technical information.

References

1. B. Cottis, S. Turgoose, R. Newman, *Corrosion Testing Made Easy: Impedance and Noise Analysis*, NACE International, Houston, Tex., 2000.
2. John R. Scully, David C. Silverman, M. Kendig, *Electrochemical Impedance: Analysis and Interpretation*, American Society for Testing and Materials, West Conshohocken, 1993.
3. J. R. Macdonald, *Impedance Spectroscopy Emphasizing Solid Materials and Systems*, 1st ed., John Wiley & Sons, New York, 1987.
4. C. M. Brett, A. M. Oliveira Brett, *Electrochemistry: Principles, Methods, and Applications*, Oxford University Press, New York, 1993.
5. A. J. Bard, L. R. Faulkner, *Electrochemical Methods: Fundamentals and Applications*, 1st ed., John Wiley & Sons, New York, 1980.
6. B. W. Johnson, D. C. Read, P. Christensen et al., *J. Electroanal. Chem.* **1994**, 364, 103–109.
7. G. S. Popkurov, R. N. Schindler, *Electrochim. Acta* **1995**, 40, 2511–2517.
8. G. S. Popkurov, R. N. Schindler, *Electrochim. Acta* **1993**, 38, 861–867.
9. G. S. Popkurov, *Electrochim. Acta* **1996**, 41, 1023–1027.
10. M. E. Orazem, P. T. Wojcik, M. Durbha et al., *Mater. Sci. Forum* **1998**, 289-2, 813–828.
11. M. Kendig, F. Mansfeld, *Corrosion* **1983**, 39, 466, 467.
12. D. D. Macdonald, M. Urquidimacdonald, *J. Electrochem. Soc.* **1985**, 132, 2316–2319.
13. J. M. Esteban, M. E. Orazem, *J. Electrochem. Soc.* **1991**, 138, 67–76.
14. P. Agarwal, M. E. Orazem, L. H. Garciarubio, *J. Electrochem. Soc.* **1992**, 139, 1917–1927.
15. R. L. Hurt, J. R. Macdonald, *Solid State Ionics* **1986**, 20, 111–124.
16. K. S. Cole, R. H. Cole, *J. Chem. Phys.* **1941**, 9, 341–351.
17. S. H. Liu, *Phys. Rev. Lett.* **1985**, 55, 529–532.
18. A. Lemehaute, G. Crepy, *Solid State Ionics* **1983**, 9–10, 17–30.
19. G. Kahanda, M. Tomkiewicz, *J. Electrochem. Soc.* **1990**, 137, 3423–3429.
20. T. Pajkossy, *J. Electroanal. Chem.* **1994**, 364, 111–125.
21. Z. Kerner, T. Pajkossy, *Electrochim. Acta* **2000**, 46, 207–211.
22. R. de Levie, *Electrochim. Acta* **1963**, 8, 751–780.
23. H. K. Song, H. Y. Hwang, K. H. Lee et al., *Electrochim. Acta* **2000**, 45, 2241–2257.
24. H. K. Song, Y. H. Jung, K. H. Lee et al., *Electrochim. Acta* **1999**, 44, 3513–3519.
25. R. D. Armstrong, D. Wright, *Electrochim. Acta* **1993**, 38, 1799–1801.
26. F. Mansfeld, C. H. Tsai, *Corrosion* **1991**, 47, 958–963.
27. S. Krause, C. J. McNeil, R. D. Armstrong et al., *J. Appl. Electrochem.* **1997**, 27, 291–298.
28. C. Sumner, A. Sabot, K. Turner et al., *Anal. Chem.* **2000**, 72, 5225–5232.
29. C. J. McNeil, D. Athey, M. Ball et al., *Anal. Chem.* **1995**, 67, 3928–3935.
30. W. O. Ho, S. Krause, C. J. McNeil et al., *Anal. Chem.* **1999**, 71, 1940–1946.
31. B. Malmgren-Hansen, T. S. Sorensen, J. B. Jensen et al., *J. Colloid Interface Sci.* **1989**, 130, 359–385.

32. R. D. Armstrong, A. K. Covington, G. P. Evans et al., *Electrochim. Acta* **1984**, 29, 1127–1131.
33. A. Friebe, W. Moritz, *J. Appl. Polym. Sci.* **1994**, 51, 625–634.
34. J. Szeponik, W. Moritz, F. Sellam, *Ber. Bunsen-Ges. Phys. Chem. Chem. Phys.* **1991**, 95, 1448–1453.
35. PerkinElmer Instruments, What is a lock-in amplifier?, Technical Note TN1000.
36. EG&G Princeton Applied Research Electrochemical Impedance Measurements: Instrumentation and Techniques, Application Note AC-3.
37. Solartron, Materials Test Products, Version 1.6.4.
38. G. Hsieh, S. J. Ford, T. O. Mason et al., *Solid State Ionics* **1996**, 91, 191–201.
39. R. S. Lillard, P. J. Moran, H. S. Isaacs, *J. Electrochem. Soc.* **1992**, 139, 1007–1012.
40. E. Bayet, F. Huet, M. Keddam et al., *Electrochemical Methods in Corrosion Research* V, Pts 1 and 2, Transtec Publications, Zurich, Uetikon, 1998, pp. 57–68, Vol. 289-2.
41. F. Zou, D. Thierry, *Electrochim. Acta* **1997**, 42, 3293–3301.
42. R. S. Lillard, J. Kruger, W. S. Tait et al., *Corrosion* **1995**, 51, 251–259.
43. J. Kruger, R. S. Lillard, C. C. Streinz et al., *Mater. Sci. Eng., A Struct. Mater. Properties Microstruct. Process.* **1995**, 198, 11–18.
44. S. Krause, H. Talabani, M. Xu et al., *Electrochim. Acta* **2002**, 47, 2143–2148.
45. S. O. Engblom, J. C. Myland, K. B. Oldham, *J. Electroanal. Chem.* **2000**, 480, 120–132.
46. D. J. Gavaghan, A. M. Bond, *J. Electroanal. Chem.* **2000**, 480, 133–149.
47. W. T. Yap, *J. Electroanal. Chem.* **1998**, 454, 33–38.
48. D. A. Brevnov, H. O. Finklea, *J. Electroanal. Chem.* **2000**, 488, 133–139.

2.7

The Electrochemical Quartz Crystal Microbalance

A. Robert Hillman

University of Leicester, Leicester, United Kingdom

Abstract

This chapter reviews the development and use of the electrochemical quartz crystal microbalance (EQCM) as an in situ probe of interfacial processes involving the formation, properties, and redox switching of multilayer films. For films that are sufficiently rigid and/or thin (termed *acoustically thin*), the EQCM functions as a quantitative gravimetric probe of surface population changes. This well-established methodology is now being used to explore both thermodynamic and kinetic aspects of film compositional changes, for example, in response to electrochemical stimuli. Correlation of mobile species (ion and solvent) population changes – within the effectively static film matrix – with electrochemical control and response functions (potential, current, and charge) now provides mechanistic information. Combination with other in situ (e.g. optical or spectroscopic) techniques is a developing area and can facilitate separation of individual ion and solvent transfers. For films that are softer and/or thicker (termed *acoustically thick*), the acoustic wave is attenuated during passage across the film, which in turn undergoes acoustic deformation. The EQCM now responds primarily to film viscoelastic properties, that is, film (rather than mobile species) dynamics. This is a developing area, but it is now possible to extract film shear modulus components (storage and loss moduli); these are found to respond significantly

to the film redox state (controlled via potential or charge), temperature, timescale (frequency), and environment (both solvent and electrolyte ions). These effects are reviewed with selected examples from a diverse range of materials, encompassing metals, metal oxides, semiconductors, metal coordination complexes, and redox, conducting, and insulating polymers.

2.7.1

Introduction2.7.1.1 **Overview**

The quartz crystal microbalance (QCM) is one of a large family of acoustic wave devices, whose utility is based on the sensitivity of resonant frequency and amplitude responses to their environment [1]. The common feature of all the devices is that they use excitation of a piezoelectric element (commonly, but not universally, quartz) to launch an acoustic wave that interacts with the medium immediately adjacent to the piezoelectric element. The nature of this interaction – generally characterized through phase and amplitude shifts (as functions of frequency) – is determined by the local composition and properties of the medium. Different devices use different crystal cuts to generate different crystal modes that propagate in different ways. However, the common feature is that the acoustic waves generally only propagate a short distance into the contacting medium, so that the frequency response of the device is predominantly determined by interfacial properties; this is ideal for electrochemical systems.

In this review, we discuss the development and application to electrochemical problems of a bulk acoustic wave device, the thickness shear mode (TSM) resonator, whose operation (in the simplest case of a

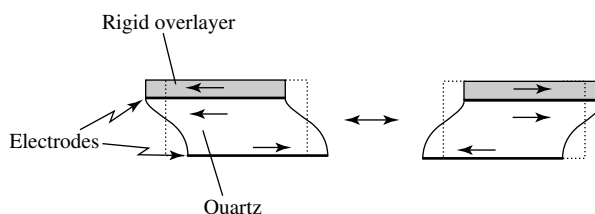


Fig. 1 Schematic diagram of the shear motion of a TSM resonator loaded with a rigid overlayer.

rigid overlayer) is schematically indicated in Fig. 1. Generically, the utility of the device exploits the fact that almost any surface process – whether chemically or physically originated – will result in a change in surface composition and/or species population(s). The consequent change in acoustically coupled mass causes a change in the resonant frequency of the oscillator. Through suitable analysis, expounded in this article, one can invert this process and attribute the frequency response to the underlying interfacial physicochemical process(es) and materials properties.

2.7.1.2 History and Prior Reviews

The growth of EQCM studies as an independent field has been remarkable. Following the extension of the *ex situ* QCM method to *in situ* operation as EQCM in 1985, annual publication rates were at single figures for the first few years, rising steadily through the 1990s to around 100 per year at present. This does not include the huge number of (nonelectrochemical) QCM publications, presently running at over 300 per year and totaling well over 2000 to date. There are also a considerable number of publications that report studies in which the (E)QCM was used as a supporting (rather than primary) technique, to the extent that it is not always listed in abstracts; this is testament to the speed with which the

EQCM has become accepted as a standard tool in the armory of the interfacial electrochemist.

Although this is a relatively new field, the rapid increases in capability and areas of application of the EQCM have prompted a number of reviews in journals and books [2–6]. The reader entering the field will find these helpful, although it is noteworthy that over half of the literature in this field has been published from 1998 onwards, that is, after all but one of these reviews; the most significant consequence of this is the necessarily low coverage given to viscoelastic effects (see below). There are also special issues of primary journals related to the topic [7, 8] and those interested in keeping abreast of recent developments should consult the outputs of two established series of biannual meetings [9, 10].

2.7.1.3 Organization and Coverage of Topics

Since full listings of the numerous EQCM-based publications can readily be generated by computer-based literature searches, this article is selective with the goal of clearly illustrating specific phenomena or processes. A companion article in this series [11] focuses on the more overtly interfacial aspects (such as fluid coupling – including roughness and “slip” phenomena – and double-layer effects) and monolayer films (including

simple adsorption, self-assembled monolayers, and underpotential deposition of metals). It provides important updates of topics that were the focus of previous reviews [2–6]. In contrast, the present article focuses on thicker (multilayer) interfacial systems, which those reviews covered in less detail.

For sufficiently thin films, the general concepts applied to monolayer systems apply; in particular, the EQCM functions as a simple gravimetric probe of interfacial populations and processes. For thicker films, factors other than inertial mass can exert a significant influence on EQCM response. Prominent among these are film viscoelastic properties, whose influence is commonly dominant for thick polymer films. Accordingly, the next section covers the principles and practice of operation of the EQCM under conditions in which it functions as a gravimetric probe and then as a viscoelastic probe. As will become apparent, a given system can show either type of response (according to such parameters as temperature, solvent, and potential). Thus, the account of experimental application of the EQCM is organized on the basis of the (electro)chemistry involved.

2.7.2

The EQCM Technique

2.7.2.1 Principles

Detailed explanations of the operation of TSM resonator devices have been given elsewhere [1, 12]; here, we summarize the principles in only as much detail as required to understand their capabilities and limitations in the electrochemical context. As a complement to the above electronically oriented descriptions, Kanazawa's physical model [13] is extremely helpful in visualizing the mechanical aspects,

such as film displacement, that underlie viscoelastic phenomena (discussed in Sects. 2.7.2.1.2 and 2.7.3.7).

When loaded with a thin film, a TSM resonator functions as a gravimetric probe of the populations of surface-attached species. In this context, “thin” implies a film whose combination of thickness and shear stiffness is such that the acoustic wave does not deform it; consequently, the film moves synchronously with the resonator. Such a film is termed *acoustically thin*. Monolayer adsorbates can generally be expected to conform to this requirement. Since such systems have been described in a companion article in this series, we describe this simpler case (as it relates to multilayer films) first and in less detail.

In contrast, when loaded with a sufficiently thick film, a TSM resonator functions as a rheological probe of the properties of surface-attached species. An acoustically thick film is one whose combination of thickness and shear stiffness is such that the acoustic wave significantly deforms it. Consequently, displacement of the outer regions of the film exhibits a phase delay with respect to displacement of the underlying resonator. Multilayer adsorbates may behave in this manner if they are either intrinsically “soft” or are plasticized by the permeation of a solvent or other small molecules. This situation is more complicated and it is only recently that the theoretical aspects have been treated in quantitative fashion for fluid-immersed films. Accordingly, this case is described subsequently to the simpler gravimetric case and in greater detail.

2.7.2.1.1 The EQCM as a Gravimetric Probe

Application of an AC voltage across an AT-cut [1] quartz crystal results in the crystal undergoing the shear motion illustrated

in Fig. 1. Resonance occurs when there is constructive interference from the wave fronts propagating from the upper and lower surfaces of the resonator, that is, the outgoing and reflected waves. This criterion is satisfied when the thickness of the crystal corresponds to half the acoustic wavelength. Thus the thickness of the crystal defines the base operating frequency.

The central tenet behind all the applications discussed in this review is that a change in surface composition and/or species populations leads to a change in the acoustic loading, which is detectable via a change in resonator frequency response. In the simplest case, one can readily envisage that a change in the mass of the mechanically oscillating system (the quartz resonator plus associated surface-attached material) will lead to a change in resonant frequency. For TSM resonators, the frequency responds to the change in areal mass density (i.e. change in mass per unit area, $(\Delta M/\text{g cm}^{-2})$) rather than the change in mass ($\Delta m/\text{g}$) per se. For a change in elastically coupled (“rigid”) inertial mass, the resonant frequency change ($\Delta f/\text{Hz}$) of an AT-cut quartz crystal resonator from its initial value (f_0) is given by

$$\Delta f = - \left(\frac{2}{\rho_q v_q} \right) f_0^2 \Delta M \quad (1)$$

where ρ_q and v_q , respectively, are the density and shear wave velocity within the quartz. The simple form of Eq. (1), known as the *Sauerbrey equation* [14], is a result of making the approximation that the overlayer producing the added mass can be treated as an extension of the quartz. This is strictly only true when the layer is thin, elastic, and has the same acoustic impedance as quartz. In practice, the acoustic mismatch problem (differing film and quartz characteristic acoustic

impedances) is generally not significant for mass changes involving rigid films that are less than 1% of the mass of the quartz crystal; most problems encountered in interfacial studies of rigid films conform to this.

Implicit in the derivation of the Sauerbrey equation is the idea that the medium into which the acoustic wave propagates does not dissipate energy. It has long been recognized that if the ambient medium were a liquid, then this would no longer be true – indeed it was commonly presumed that the energy dissipation would be so great that attenuation of the shear wave would so severely damp the oscillation as to prevent in situ use of the QCM. In the 1980s, it was shown that, although significant, fluid damping is not fatal to in situ operation of the QCM [15] – thus its electrochemical extension, the EQCM, became a reality [16]. Furthermore, the effective viscous coupling of the fluid (the decay length, x_L , of the wave in the fluid) was calculable [17] in terms of fluid properties (viscosity (η_L) and density (ρ_L)) and the crystal operating frequency:

$$x_L = \left(\frac{\eta_L}{\pi \rho_L f_0} \right)^{1/2} = \left(\frac{2\nu_L}{\omega} \right)^{1/2} \quad (2)$$

where $\nu_L (= \eta_L/\rho_L)$ is the kinematic viscosity of the fluid and $\omega (= 2\pi f_0)$ is the angular frequency of the resonator.

2.7.2.1.2 The EQCM as a Viscoelastic Probe

The Sauerbrey equation was developed to describe films that are thin and elastic (in common parlance, “rigid”). In this situation, the addition of more of the same material or of a second rigid material can be described in a linear additive manner. This is because the “new” layer experiences the same displacement as the existing layer, that is, there is no

decay or phase shift of the acoustic wave across the inner layer. However, if the material immediately adjacent to the resonator surface is nonrigid, the effect(s) of additional loading(s) on the resonator are not linearly additive. This is because the material immediately adjacent to the resonator now suffers a deformation across its thickness. Thus, any additional material on the outer surface will not experience the same displacement as when overlaid on a rigid inner layer. Instead, the acoustic wave it experiences from the inner layer will be subject to a phase shift and significant attenuation with respect to the wave initially launched by the resonator.

One common experimental approach to this situation (described in Sect. 2.7.2.2.2) is based on impedance methods. An AC electrical excitation drives the resonator, whose mechanical response is determined by the viscoelastic characteristics of the loading (in this context, surface films and electrolyte solutions). The measured electrical driving and response functions are related by the electrical impedance, and analogous mechanical functions can be defined; the electrical and mechanical analogs are linked through the piezoelectric effect, quantified by the electromechanical coupling factor of the resonator (usually quartz, for which $K^2 = 7.74 \times 10^{-3}$). Here we summarize the general concepts, developed by Martin and a series of coworkers [1, 18, 19], and illustrate them for surface loadings typical of electrochemical systems.

In electrical/electrochemical impedance, it is common practice to represent the system under study by an electrical equivalent circuit, in which a combination of resistors, capacitors, and inductors represents the physical components of the system. For the system as a whole, the impedance is the quotient of the applied potential (the

driving force) and the resultant current (the response). An analogous approach can be used for the surface mechanical impedance of the resonator loading. For the system as a whole, the mechanical impedance (Z_S) is the quotient of the surface stress (T_{xy} , driving the motion) and the particle velocity (v_x , the motion) at the resonator surface ($y = 0$):

$$Z_S = \left. \frac{T_{xy}}{v_x} \right|_{y=0} \quad (3)$$

Pursuing this analogy, components in the electrical equivalent circuit can be assigned direct mechanical significance: resistance represents energy loss, capacitance represents energy storage, and inductance represents inertial mass. Thus, one overall strategy is to model the electrical response in terms of an equivalent circuit and then to transform the components into their mechanical analogs.

There are two electrical equivalent circuits in common usage, the transmission line model (TLM) and a lumped element model (LEM) commonly referred to as the Butterworth–van Dyke (BvD) model; these are illustrated in Figs. 2(a and b), respectively. In the TLM, there are two acoustic ports that represent the two crystal faces: one is exposed to air (i.e. is stress-free, indicated by the electrical short) and the other carries the mechanical loading (here, a film and the electrolyte solution, represented below by the mechanical loading Z_S). These acoustic ports are connected by a transmission line, which is in turn connected to the electrical circuitry by a transformer representing the piezoelectric coupling. For the TLM, one can show [18, 19] that the motional impedance (Z_m^1) associated with the surface loading can be related to the mechanical impedances of

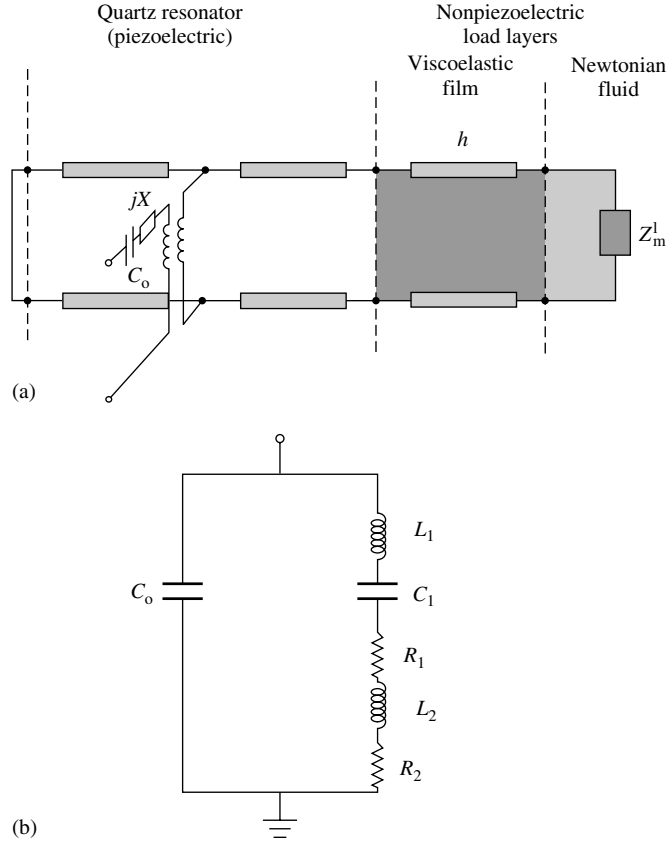


Fig. 2 Electrical equivalent circuit models for a TSM resonator: (a) transmission line model (TLM) and (b) Butterworth–vanDyke lumped element model (LEM). Circuit elements are defined in the main text.

quartz (Z_q) and the loading (Z_s) by

$$Z_m^1 = \frac{\phi_q(Z_s/Z_q)}{4K^2\omega C_0} \left[1 - \frac{j(Z_s/Z_q)}{2 \tan(\phi_q/2)} \right] \quad (4)$$

In practice, one is always interested in measurements close to resonance ($\omega \simeq \omega_s$), so that the phase shift, $\phi_q \simeq \pi$. For most systems of interest, the loading is generally a small perturbation on the total impedance ($Z_s/Z_q \ll 1$). Under these conditions, the second term in the bracket in Eq. (4) is small compared to

unity. Hence,

$$Z_m^1 \approx \frac{\pi}{4K^2\omega_s C_0} \left(\frac{Z_s}{Z_q} \right) = R_2 + j\omega L_2 \quad (5)$$

In Eq. (5), we have indicated that the simplified expression for Z_m^1 can be expressed as a series combination of a resistor and an inductor. In the mechanical context, these represent energy loss and inertial mass, respectively. Equation (5) in fact describes the BvD LEM; in other words, the LEM (Fig. 2b) is a low loading/near resonance approximation of the more general TLM

(Fig. 2a). Simple considerations show that the vast majority of electrochemical experiments correspond to this low loading case and that the error incurred by the use of the simpler Eq. (5) [as opposed to the more cumbersome Eq. (4)] is less than 1% – comparable to or better than the precision of experimental data.

In the earlier literature, there was a tendency to ascribe anomalous EQCM behavior to viscoelastic effects; in the absence of quantitative models for these phenomena, this was not surprising. This problem no longer exists, since Eq. (5) suggests a simple test for “rigid” layer behavior. An elastic film does not dissipate energy, that is, will contribute nothing to the electrical equivalent circuit resistance. In this case, in Eq. (5), $R_2 = 0$ and L_2 is proportional to the inertial mass of the film. One can then show [19] that

$$\Delta f = -\frac{L_2 f_s}{2L_1} = \frac{2f_s^2 \Delta M}{\sqrt{\rho_q \mu_q}} \quad (6)$$

where L_1 and L_2 are represented in Fig. 2(b), f_s is the series resonant

frequency, ρ_q is the density of quartz, and μ_q is the shear elastic constant for quartz. In fact, since the mass loading exerts only a small perturbation on the resonant frequency ($f_0 \simeq f_s$) and $v_q = (\mu_q \rho_q)^{1/2}$, it can be seen that Eq. (6) is a restatement of the Sauerbrey equation. Thus, an unequivocal test for film rigidity is a crystal impedance measurement that returns a zero value for R_2 ; in the event that R_2 is nonzero but constant with changing conditions (e.g. film redox state), then the film is nonrigid but frequency changes (e.g. with redox state) are not viscoelastically driven.

Aspects of loading with nonrigid films have been considered by several authors [18–22]. The primary case of interest in the electrochemical context is loading with a rigid layer (the electrode), a viscoelastic film (commonly, though not necessarily, a polymer), and then a Newtonian fluid, schematically illustrated in Fig. 3. (The rigid layer component may also include material entrapped within surface features [23].) The characteristic mechanical impedances of the two nonrigid

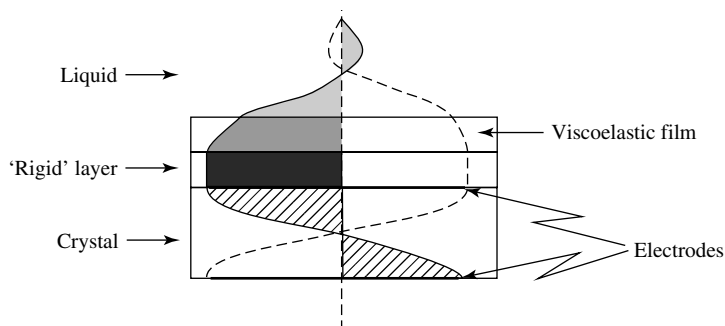


Fig. 3 Schematic diagram of the propagation of an acoustic shear wave launched by a TSM resonator loaded with a viscoelastic overlayer and exposed to a fluid. Note the progressive zero, significant, and dramatic attenuations of the wave on moving from the rigid layer (electrode plus surface feature-entrapped material) to the viscoelastic solid to the fluid. The acoustic decay lengths in these three regions are, respectively, infinity, $[2G/(1 - G'/G)]^{1/2}/(\omega\sqrt{\rho_f})$, and $1.4[G''/\rho_f]^{1/2}/\omega$; in the latter two instances, typical values are 2 and 0.2 μm .

components are

$$Z_L = \left(\frac{\omega \rho_L \eta_L}{2} \right)^{1/2} (1 + j) \quad (7)$$

for the liquid and

$$Z_f = (G \rho_f)^{1/2} \quad (8)$$

for the film, where ρ_f is the film density and G its shear modulus:

$$G = G' + jG'' \quad (9)$$

in which G' is the shear storage modulus, G'' is the shear loss modulus, and $j = \sqrt{-1}$.

One implication of the treatment of Sect. 2.7.2.1.1 is that the impedances of serially deposited rigid layers are additive; this is because each successive layer experiences the full acoustic motion for the resonator, transmitted without loss through each underlying layer. However, nonrigid layers do not behave in this fashion: as one moves away from the resonator surface, each successive layer experiences only a fraction of the acoustic displacement entering the underlying layer. Consequently, the component impedances of the separate loadings (here, film and fluid) are no longer simply additive. For a viscoelastic film of thickness h_f immersed in a semi-infinite Newtonian fluid, the total surface mechanical impedance is given by [18, 19]

$$Z_S = Z_f \left[\frac{Z_L \cosh(\gamma h_f) + Z_f \sinh(\gamma h_f)}{Z_f \cosh(\gamma h_f) + Z_L \sinh(\gamma h_f)} \right] \quad (10)$$

where the complex wave propagation constant γ is defined as $j\omega(\rho_f/G)^{1/2}$. A little algebra reveals that Eq. (10) has the “required” limiting forms: (1) when the film is very thick the term in brackets approaches unity and $Z_S \rightarrow Z_f$, so the resonator sees only film and no fluid; and (2) when the film is very thin $Z_S \rightarrow Z_L$ +

$j\omega h_f \rho_f$, which corresponds to additivity of a rigid film and the fluid. In the latter case, the film is sufficiently thin (acoustically thin) that there is negligible acoustic deformation across it. Bandey and coworkers have generalized Eq. (10) to the case of an arbitrary number of nonrigid layers [19]. As will now be revealed, one can use such an equation to predict the behavior of multiple nonpiezoelectric layers of known properties, but not to determine (from experimental data) unknown layer properties.

There is an additional phenomenon worthy of mention for viscoelastic films – film resonance. As film thickness increases, an acoustic phase delay (ϕ) develops across the film. One can show [1, 24] that the phase shift developed across a film of thickness h_f and shear modulus G is given by

$$\begin{aligned} \phi &= \omega h_f \operatorname{Re} \left\{ \sqrt{\frac{\rho_f}{G}} \right\} \\ &= \omega h_f \sqrt{\rho_f} \sqrt{\frac{1 + G'/G}{2|G|}} \quad (11) \end{aligned}$$

When the phase shift reaches a quarter of the acoustic wavelength ($\phi = \pi/2$), bearing in mind that reflection at the outer (film/solution) interface introduces a phase shift of π , the “round trip” for a wave launched at and returning to the resonator surface corresponds to one wavelength. This results in constructive interference between the returning wave and the next outgoing wave. Provided that the reflectivity coefficient at the film/solution interface is close to unity (a condition fulfilled when the film and fluid characteristic impedances are very different), there will then be a dramatic change in coupling of energy from the resonator into the film; this is termed *film resonance*. In terms of the observed frequency response, there is a sharp

increase in admittance and an increase in resonant frequency. As the system passes through resonance, for example, with further increase in film thickness, the response returns back to the preresonance trend of decreasing resonant frequency and admittance.

The sequence of events as the system passes through film resonance is illustrated schematically in Fig. 4 [25], in which the total (observed) impedance (full line) is the combination of the crystal (dotted line), and film (dashed line) components. As film thickness increases (moving from frame 1 to frame 5), the film component moves rapidly downwards in frequency. As it passes through the crystal component, the prediction is that the total resonance will – transiently – split into two peaks (frame 3). As the resonance condition is passed (frame 5), the response returns to a more “normal” appearance. More detailed theoretical exploration of this phenomenon [25] shows that both the absolute and relative values of the shear modulus components have significant influence over the resonator response. In particular, the double-peak nature of the response shown in Fig. 4 is only predicted for low loss films (i.e. films for which the loss tangent, $G''/G' < 1$).

2.7.2.2 Experimental Methodology

2.7.2.2.1 Basic EQCM Technique The usual configuration is for one of the electrodes on the crystal to be exposed to air and the other to be exposed to the electrolyte; the latter is then the working electrode in a standard three-electrode electrochemical cell. The basic electronic circuitry suitable for driving a TSM resonator exposed to a liquid and maintained under electrochemical potential control, and measuring the resonant frequency, was

first described by Bruckenstein [16]. Since then, several variants on this have been described and commercial instrumentation is now readily available. Significant extensions of the original design include low noise circuitry [26], rapid data acquisition [27], a purpose-built cell [28], and a dual QCM in which a fluid-exposed reference crystal compensates for changing fluid properties [29].

Beyond this, but still restricting attention to frequency measurement (i.e. gravimetric mode), the concept of AC electrogravimetry has been developed in a series of papers by Gabrielli and coworkers. Although applications of this methodology to specific systems are discussed in Sect. 2.7.3, some of the papers provide specific details on the generic principles [30] and instrumentation [31, 32]. The essential concept is that, analogous to conventional electrochemical admittance, $\tilde{i}/\tilde{E}(\omega)$, one can define an electrogravimetric-transfer function, $\Delta\tilde{m}/\tilde{E}(\omega)$, as a function of frequency, ω . Other useful quantities are the mass/charge-transfer function, $(\Delta m/\Delta q)(\omega)$, and the partial mass/charge-transfer functions [32]:

$$\frac{\Delta m_{iS}}{\Delta E}(\omega) = \frac{\Delta m}{\Delta E}(\omega) \mp \frac{m_i}{j\omega F Z_F(\omega)} \quad (12)$$

for the anion ($i = A$; minus sign) and the cation ($i = C$; plus sign), where $Z_F(\omega)$ is the conventional electrochemical impedance. The mass/charge-transfer function can be regarded (with the inclusion of appropriate constants) as a generalized version of the normalized mass change, $\Delta MF/Q$, and the partial mass/charge-transfer functions are analogous to the quantity ϕ_i defined [33, 34] as the algebraic sum of the total mass change and the contribution of either the anion (leaving the cation, $i = C$) or cation (leaving the anion, $i = A$) contribution to

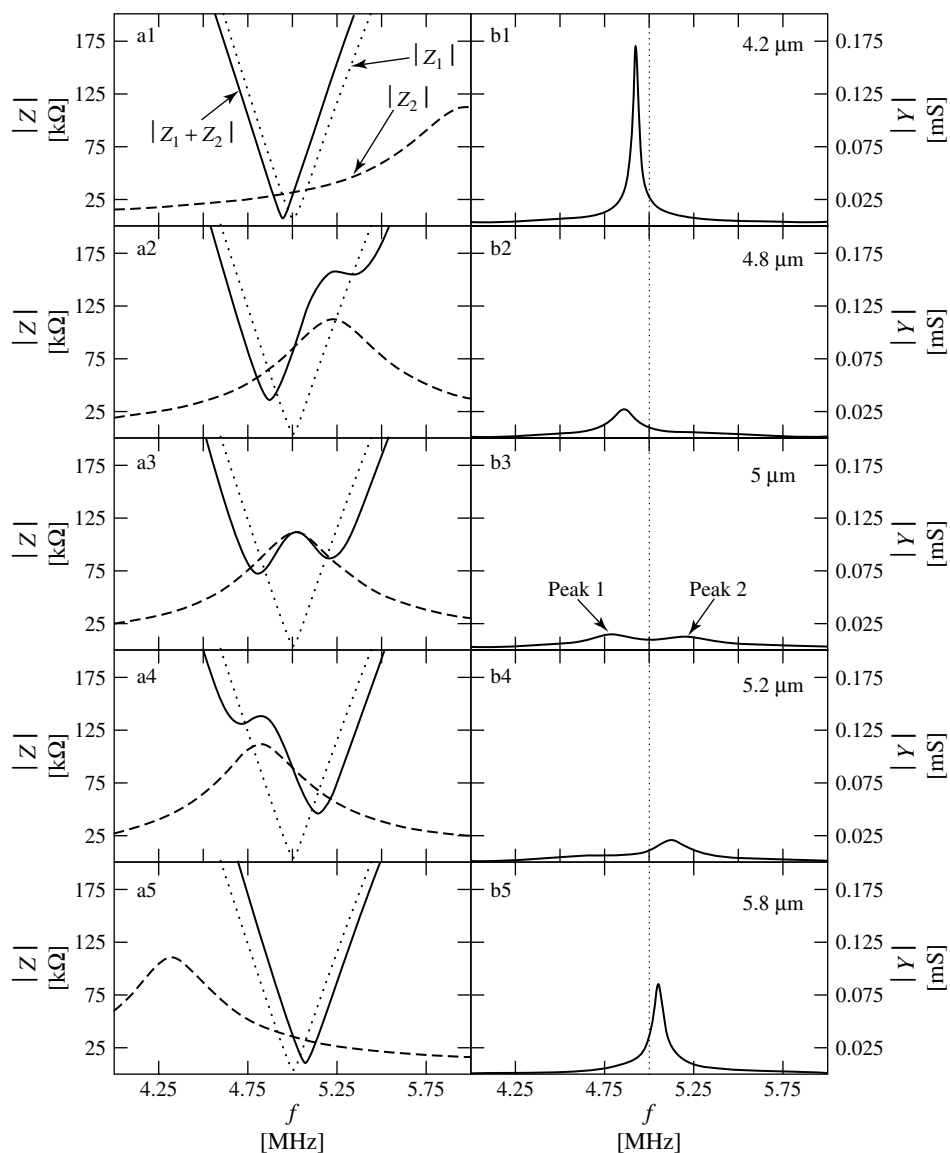


Fig. 4 Simulation of TSM resonator frequency response in the vicinity of film resonance. Panels 1–5 represent increasing film thickness (as labeled). Panels a show impedance components for the resonator (dotted line), the film (dashed line), and the composite resonator (full line). Panels b show calculated admittance (as would

be measured experimentally). Resonator base frequency: 5 MHz. Film parameters: $\rho_f = 1 \text{ g cm}^{-3}$, $G' = 10^8 \text{ dyn cm}^{-2}$, $G''/G' = 0.1$. (Reproduced from Ref. [25] with permission from the American Chemical Society.)

the mass change. In principle, the dynamics of different contributory processes (e.g. ion and solvent transfers) can be resolved in the frequency domain, analogous to their resolution in the time domain in, for example, a chronoamperometric experiment. Through the use of complex plane representations of the admittance, one can in principle identify the individual mobile species contributions. Although this technique is unquestionably instrumentally more complicated, it allows detailed exploration of timescale effects (via the frequency domain) with all the usual advantages of impedance methods.

The resonant condition for the TSM device is that the crystal thickness be an odd multiple of half the acoustic wavelength, $\lambda = v_s/f$. Since the shear wave velocity, v_s , is equal to $(\mu_q/\rho_q)^{1/2}$ (presuming quartz, q, as the piezoelectric material):

$$h_s = \frac{1}{2f} \sqrt{\frac{\mu_q}{\rho_q}} \quad (13)$$

for the 5 and 10 MHz crystals most commonly used in electrochemical applications of the QCM, practical devices have nominal thicknesses of 0.0334 and 0.0167 mm, respectively. Selection of crystal operating frequency is based upon a trade-off between sensitivity and mechanical robustness: decreasing thickness leads to higher sensitivity (see Eq. 1) but at the cost of increased fragility, which makes mounting the crystal in the cell more difficult. One way to gain increased sensitivity is to use higher (necessarily odd) harmonics, for example, 30 MHz for a 10 MHz fundamental frequency device, although in this case the sensitivity only increases linearly with frequency, rather than the quadratic dependence of the fundamental mode (see Eq. 1). A chemically milled

30 MHz fundamental QCM for in situ application has been described [35] and shown to have the appropriately increased sensitivity. Although the sensitivity gain is clearly significant, in fact this is commonly not the limiting factor for studies of multilayer films. The issue of making measurements at higher harmonics will be returned to in the context of acoustically thick films (see Sect. 2.7.3.7.2), in which the intention is to use variations of frequency as a means of varying timescale.

Generally, on the basis of the above compromises, the operating frequency is in the range 5 to 10 MHz. For resonators using AT-cut quartz crystals with $f_0 = 10$ MHz, the Sauerbrey equation reduces to

$$\Delta M(\text{g cm}^{-2}) = -4.426 \times 10^{-9} \Delta f(\text{Hz}) \quad (14)$$

Typically, the electrode area is on the order of 0.2 cm², so the mass sensitivity is on the order of 1 ng (ca. 10 pmol for a “typical” adsorbate). In addition to the quantitative aspects of the Sauerbrey equation (high sensitivity), Eq. (14) highlights the generality of detection and absolute nature of the sensing process. These attractive features contributed to a long and successful history of TSM resonators being used for a range of gas sensing and gas/solid interfacial applications, in which surface accumulation of material from the gas phase was the underlying physicochemical process [1, 12]. For comparison purposes, we note that the gaseous environment is rather less demanding in two respects than the liquid environment inherent to electrochemical applications: if one wishes to use a bulk shear acoustic wave, the more fragile thinner crystals can be used in a gas; the lower attenuation associated with a gas allows one to use surface acoustic wave (SAW) devices.

For typical fluids (water and most organic solvents), x_L (at 10 MHz) is on the order of 170 nm. The effectively coupled mass of this fluid layer, expressed as an areal mass density, is simply the product of x_L and the fluid density. For a smooth 10-MHz resonator, immersion in an aqueous solution couples ca. $17 \mu\text{g cm}^{-2}$ of fluid, resulting in a decrease in the resonant frequency of ca. 3.8 kHz. Beyond this relatively small (cf. 10 MHz operating frequency) baseline “shift”, the EQCM can then be used in situ to study interfacial processes under potential control.

Two practical issues arise at this stage. First, it is important to maintain fluid properties constant during the experiment; in practice, this generally amounts to good temperature control. For example, if the liquid density changed by 1% (due to temperature drift of ca. 1 K), then the component of Δf due to the liquid (see above) would change by ca. 40 Hz: this would be fatal for monolayer adsorption studies and significant, but not fatal, for studies of thick (e.g. polymeric) layers. In some cases, notably when the time intervals are extended or when the surface mass changes are small, this – rather than the sensitivity of frequency measurement per se – can become the limiting factor. One obvious solution to this problem is to measure frequency shifts with respect to a reference crystal immersed in the same solution. In practice, electrical connection between the “working” and “reference” crystals makes this nontrivial, but a dual quartz crystal microbalance (DQCM) achieving compensation for fluid-based changes has been demonstrated [29, 36]. Second, most crystal – and thus overlying electrode – surfaces are not smooth at the atomic level. Simplistically, fluid entrained within surface features behaves as though rigidly coupled to the resonator. This issue

has been considered at varying levels of sophistication [4, 37] and we do not consider it further here, except where it impinges directly on the study of other interfacial processes, notably viscoelastic film dynamics (see below).

2.7.2.2.2 Crystal Impedance Technique

Section 2.7.2.1.2 described the principles by which film viscoelastic properties (shear moduli) could be determined from the surface mechanical impedance. Experimentally, the latter can be determined by measuring the electrical impedance of the resonator in the vicinity of resonance, exploiting the piezoelectric effect to transform the electrical driving function and the mechanical response function. A less well-explored variant on this steady state approach is to drive the system with an ac function, then open the circuit and monitor the transient decay. These complementary approaches have recently been brought within an elegant general framework by Kanazawa [38]. Comparison of the various methods is made in Fig. 5 [38]; the reader is referred to the original paper for a detailed exposition of the strategies summarized by this figure. Essentially, what the figure shows is that there are two transient solutions (depending upon whether one goes to a condition of open circuit or short circuit) and a steady state solution. In the latter case, one can either proceed via an electrically based approach (to determine the equivalent circuit parameters) or a physically based model that leads to the displacements in the system. To date, the predominant source of film viscoelastic properties is impedance data, so coverage of this topic here will focus on steady state methods, but one can expect the transient methods to assume increasing importance. As

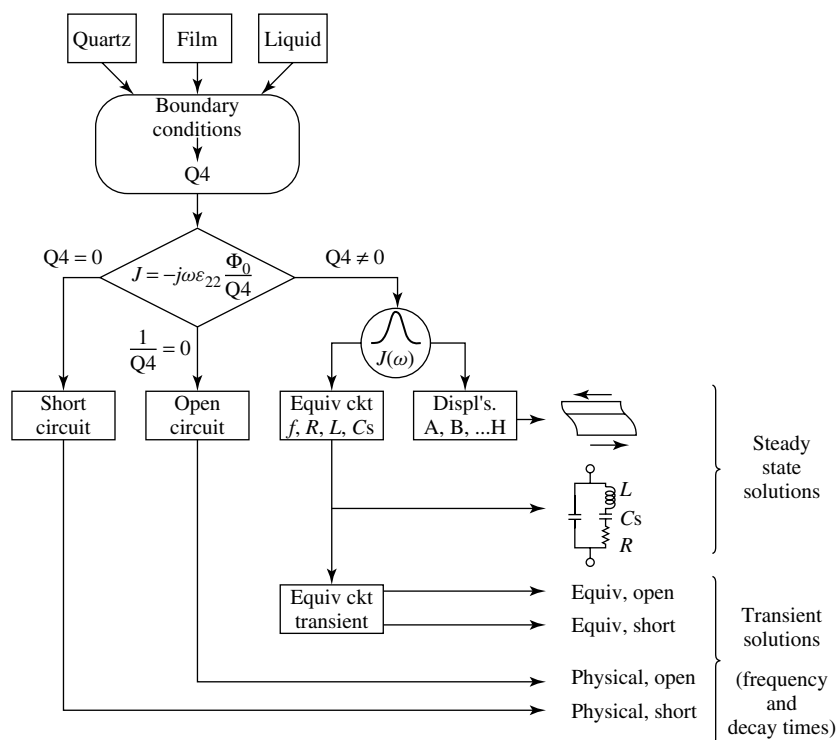


Fig. 5 Schematic routes to transient and steady state solutions for the frequency response of a TSM resonator upon the application of different electrical control functions. Symbols explained in main text. Q4 defines the current–voltage relationship for the resonator. (Reproduced from Ref. [38] with permission from The Electrochemical Society.)

this powerful methodology is developed, experience of analogous electrochemical control functions leads one to speculate that the different approaches represented in Fig. 5 will yield subtly different insights, so that they will in fact be complementary rather than competitive.

In a “typical” EQCM experiment, one could envisage being able to characterize: (1) the bare crystal in air; (2) the “immersed” bare crystal (by which it is implied that one face is exposed to the electrolyte solution and the other to air, so that the crystal is not electrically shorted); and (3) the immersed film-coated crystal. The first experiment will provide parameters

associated with the crystal (e.g. R_1 , C_0 , C_1 , and L_1 in the LEM). The second experiment will provide parameters associated with the liquid (η_L and ρ_L). In principle, one would then hope that the third measurement would provide appropriate parameters for the electroactive film.

In the case of a rigid (acoustically thin) film, the frequency shift provides film mass (Eq. 1); this will be the sum of the masses of the electroactive material (e.g. metal, polymer, or metal oxide) and the liquid that permeates it. Coulometric assay – which may be based on film deposition or subsequent redox chemistry – provides the amount of electroactive

material, via Faraday's law. Thus Q and Δf provide the two unknowns – the amounts of electroactive material and of solution within the film. If required, the amounts of the two components (of known individual density) can be used to deconvolute the film mass into film thickness and density; this requires the reasonable approximation of additive volumes, that is, a zero volume of mixing.

In the case of a nonrigid (acoustically thick) film, the problem is underdetermined: there are four unknowns (film thickness, film density, and the two shear moduli components) and less than four measurands. Several approaches to this problem have been adopted. One argument is that viscoelastic behavior is due to high solvent swelling, so the film is liquidlike, that is, $\eta_f \simeq \eta_L$ and $G' \ll G''$ [22, 39]. An alternative approach is to assume a value for ρ_f and to fix the loss tangent, $\tan \alpha = G''/G'$ [22, 39, 40]. Another approach is to constrain ρ_f and h_f according to additional information [23, 41, 42], for example, ρ_f must lie between ρ_L and ρ_P (density of pure polymer) and coulometric assay provides a lower bound (h_f^0) for h_f corresponding to a slab of pure polymer. In various ways, all these approaches are attempts to reduce a four-parameter problem (in ρ_f , h_f , G' , and G'') to a two-parameter problem, which is amenable to an “unambiguous” solution based on crystal impedance data (frequency response of the loaded crystal in the vicinity of resonance).

Although each of these procedures has some merit, none of them can claim to be mathematically rigorous or totally physically defensible. A recent solution to the problem [24] is to split this four-parameter problem into two separate two-parameter problems, as follows. First, one operates in the acoustically thin

regime, in which the Sauerbrey equation applies. With the additional input of the electrochemical charge data (or indeed, any other direct measure of film thickness), one can then determine film thickness and density (as described above) in this regime in which viscoelastic parameters have no bearing on the response. Second, one operates in the acoustically thick regime, in which viscoelastic properties do govern the response. The tactic is to make the assumption – which is in fact made for all of the approaches described – that the film is homogeneous at all coverages. Firstly, this allows one to carry the acoustically thin regime data-derived film density into the acoustically thick regime. Secondly, it allows one to project the charge–thickness relationship from the acoustically thin regime into the acoustically thick regime, so that coulometric data – even in the acoustically thick regime – provide film thickness. Now, there is a unique solution in terms of film shear moduli for crystal impedance responses.

A flow chart demonstrating the protocol is shown in Fig. 6. The procedure has been demonstrated for poly(3-methylthiophene) films, by analysis of frequency response as a function of time during film electropolymerization: short (long) time responses represent the acoustically thin (thick) film scenario [24]. Film mass (whether or not directly accessible from Δf data) defines the product $h_f \rho_f$, so (as shown in Fig. 6 [24]) a plot of h_f versus ρ_f is a hyperbola. As film mass (polymer coverage) increases, a series of hyperbolae are generated. The acoustically thin film data (Δf and Q) define the unique solution (of the infinity of solutions on the hyperbola) for ρ_f as indicated in Fig. 6 [24]; this value is projected across all the hyperbolae. The procedure is reliant upon two factors: knowing Faraday's law for the system

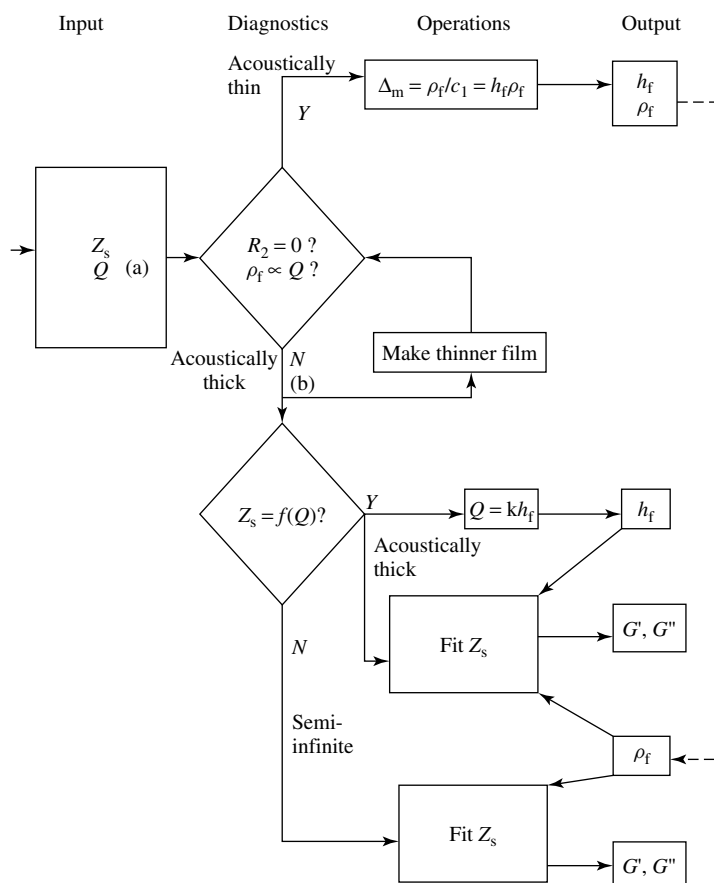


Fig. 6 Summary of data interpretation strategy (described in main text) for extracting viscoelastic parameters from film-loaded TSM resonator frequency response. Input parameters (at left of diagram) are resonator impedance and any selected parameter representative of film thickness (here, charge, interpreted using Faraday's law). Upper part of the scheme relates to acoustically thin films (yielding h_f and ρ_f). Lower part of diagram relates to acoustically thick films (yielding, with the help of h_f and ρ_f , G' and G''). (Reproduced from Ref. [24] with permission from the American Chemical Society.)

and film homogeneity. It worked well for the system used, poly(3-methylthiophene), suggesting that the uniform film model was physically reasonable and that the doping level was accurately known. It is recommended that the approach be tried for other systems; in cases in which it does not yield physically reasonable solutions,

one implication is that the uniform film model is inappropriate. Previous methodologies (see above) would presumably also have returned physically unreasonable (and nonunique?) data, but could provide no insight into the underlying physical reason, if indeed they gave any direct indication of a problem.

2.7.2.2.3 Combination of the EQCM with Other In situ Techniques

The QCM has now attained a status comparable with many other in situ techniques: electrochemistry drives the interfacial chemistry and the QCM probes the constituent processes. Although the combination of electrochemical and gravimetric data is very powerful, it is sometimes inadequate for solving complicated problems. For example, if an electroactive film is nonpermselective (e.g. at high electrolyte concentration), one would generally expect redox switching to be accompanied by the exchange of anions, cations, and the solvent. On the basis of electrochemical (charge, Q) and gravimetric (mass change, ΔM) data only, this three-parameter problem is underdetermined. One approach is to vary the concentration [34] (see Sect. 2.7.3.7.1), but this is lengthy and vulnerable to film aging effects. Another approach is the simultaneous introduction of an additional technique to provide the third piece of information. One example of this is the combination of the EQCM with probe beam deflection (PBD; sometimes called the *mirage effect*) [43–47].

The advantages of controlled mass transport have long been recognized in electrochemistry, as discussed in Chapter 2.4. In the present context, the elegant combination of the rotating disk electrode (RDE) [48–50] and wall-jet electrode (WJE) [51, 52] solution hydrodynamics with EQCM interfacial detection has proved to be very effective.

Combination with scanning electrochemical microscopy (SECM), the subject of Chapter 3.3, has also been explored and the tip–surface separation was found to influence the crystal impedance [53]. Viewed from the opposite perspective, the observation of stress effects on crystal resonant

frequency have been shown to be a means of calibrating tip–surface separation [54].

There have been relatively few combinations of the EQCM with the spectroscopic and optical techniques that have revolutionized interfacial electrochemistry over the last two decades. Some of these are considered further in Sect. 3 of this volume. Of these, simultaneous use of visible spectroscopy [55], Fourier transform infrared (FTIR) spectroscopy [56], and ellipsometry [57] are significant examples that should be more generally exploited. A more specialized example is the combination, via a special dual thin layer cell, of the EQCM and differential electrochemical mass spectrometry DEMS for real-time determination of volatile products and deposited or dissolved species [58]. The combination of the EQCM with UV–visible spectroscopy is particularly interesting: electrochemistry (via charge) provides the total change in electron population within the film, electronic spectroscopy provides insight into the partition of this charge among the various source(s) or sink(s), and the QCM provides the identities of the ions required (by electroneutrality) to move in response to this change in film charge. A very nice example of this is given by a study of polypyrrole redox switching [55], in which the electroactive film was deposited on an indium tin oxide (ITO) electrode supported on a quartz TSM resonator, with an uncoated ITO electrode/quartz crystal used to provide a “blank” for the spectroscopic data. This particular study was in fact rather more sophisticated, since it also explored the viscoelastic properties of the polymer film using simultaneous resonant resistance measurements. The authors systematically explored all relationships between the electrochemical, acoustic, and optical data, of which a representative example is shown in Fig. 7 [55]. Through

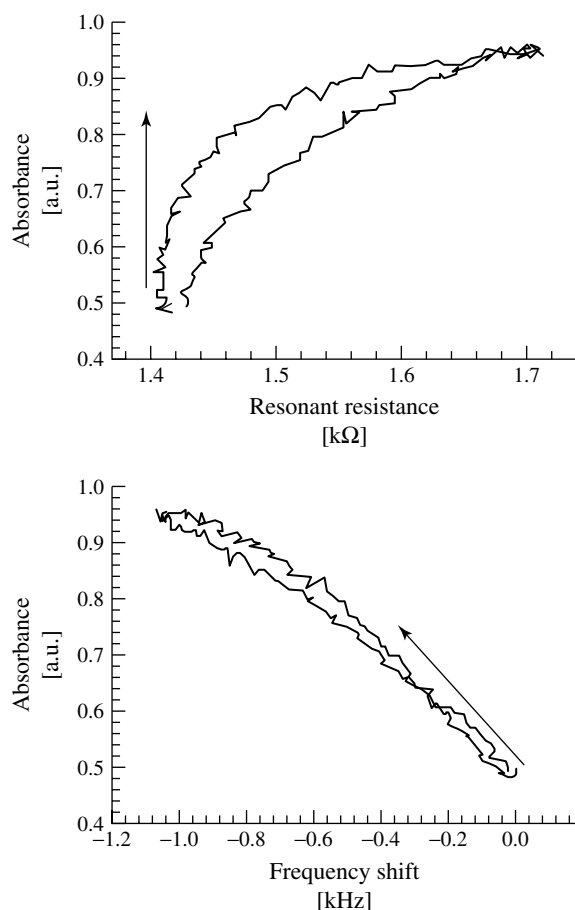


Fig. 7 Correlation of absorbance (at 800 nm) with resonant resistance (left-hand panel) and frequency shift (right-hand panel) during redox cycling of a polypyrrole film on an ITO electrode supported on a 9-MHz TSM resonator. Voltammetric experiment: scan rate 50 mV s^{-1} . Solution: aqueous $0.1 \text{ mol dm}^{-3} \text{ KClO}_4$. (Reproduced from Ref. [55] with permission from The Electrochemical Society.)

this, they were able to demonstrate a clear correlation between the film color change (represented by a specific electronic band) and its mass (represented by the crystal resonant frequency); given the different possible mechanisms for maintaining electroneutrality and the very different kinetics for electron, cation, anion, and solvent transfers, this is a significant outcome.

Low-resolution imaging of polymer film profiles has been achieved using a scanning-electrode quartz crystal analyzer (SEQCA) method [59]. In this technique, illustrated in Fig. 8 [59], one uses a small probe electrode, whose location can be effectively rastered over the surface (although, in practice, this was achieved by keeping the probe stationary and moving

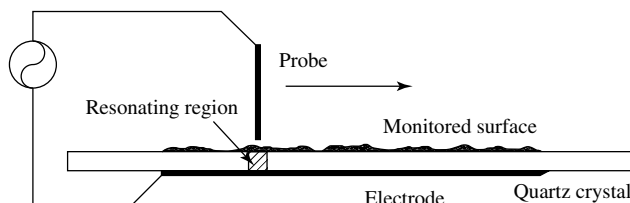


Fig. 8 Schematic illustration of the principle of the scanning-electrode quartz crystal analyzer (SEQCA) operating in “overscanning” mode, with a small probe electrode on the polymer/solution loaded side of the resonator; in “underscanning” mode, the full electrode and the small probe locations are reversed. (Reproduced from Ref. [59] with permission from the Royal Society of Chemistry.)

the sample), to excite the crystal at selective locations. Figure 8 [59] illustrates a mode in which a small probe scans over a polymer-coated crystal upper surface, with a normal electrode on the lower surface. Since this approach will fail when the electrolyte concentration is high, a suggested variant of the mode illustrated is one in which the small probe scans under a crystal with a bare lower surface and a normal film-coated electrode on the upper surface. Although this method lacks the high spatial resolution of some other (e.g. scanning tunneling microscopy (STM) or SECM) imaging methods, one could imagine it might in future provide different information such as local film viscoelasticity associated with local variations in film solvation or redox state.

2.7.3

Electrochemical Systems

2.7.3.1 Strategy and Organization

Having considered the types of phenomena one might expect to see using the EQCM, we now consider application of the EQCM to interfacial electrochemistry and see how material properties influence the nature of the response. In broad terms, the EQCM has three attractive attributes:

in situ applicability, high sensitivity, and generality of detection; in the acoustically thin regime, there is the additional analytical advantage that quantitation is absolute. Consequently, the technique has been applied to almost every class of electrochemical system. This contrasts with many spectroscopic techniques, in which aspects of selectivity can yield considerable detail, but only for a restricted set of systems.

As will become apparent, the use of the EQCM as a gravimetric probe – operating in the acoustically thin regime – is a mature area, providing a broad coverage of materials, properties, and chemistry. Viscoelastic studies are a newer avenue of enquiry that provide new challenges and novel insights; since this topic necessarily has a lower profile in previous reviews [2–6], it is given greater coverage here. The facility to extract unequivocal physically meaningful materials parameters (shear modulus values) [24] (see Sect. 2.7.2.2.2) should provide an impetus for rapid future development.

2.7.3.2 Metals

Metal films are, at first sight, obvious candidates for the application of the EQCM as a gravimetric sensor: these materials are rigid, have relatively high relative atomic

mass, and the application of Faraday's law to coulometric data should be unequivocal. Commonly, metal redox systems of known redox chemistry ($M^{z+/0}$) are used to calibrate the EQCM. The EQCM "nano" version of Faraday's classic $Ag^{+/0}$ experiment [16, 28, 60] is an obvious example and the $Cu^{2+/0}$ system has been similarly exploited [53]. Figure 9 [43] illustrates this calibration experiment for an EQCM combined with a PBD instrument. Simplistically, one anticipates that the current represents the electron flux, the mass represents the Ag deposited/dissolved, and the optical deflection (2) of the laser beam passing across the face of the electrode is the response of the concentration gradient in solution. Correlation of the three responses (in either integral or differential mode) unequivocally demonstrates that $Ag^{+/0}$ redox chemistry is the sole interfacial process [43].

As is well known for the QCM [12], the mass sensitivity of the resonant frequency is not uniform across the resonator surface: it is radially dependent, with a maximum at the center of the electrode and falling to effectively zero (we do not discuss fringing effects here) at the edge of the electrode. The carryover of this spatial distribution result to the EQCM has been demonstrated using the deposition of Cu [61–63] or Ag [64] "dots" across the electrode surface. In a mirror-image experiment, localized laser-induced dissolution of a Ni–Cu alloy has been used to map the spatial distribution of EQCM mass sensitivity [65].

In other cases, the EQCM can provide a means of differentiating between metal deposition and other processes. This is clearly critical in electrowinning and a good example is the deposition of Co, which has been distinguished from the accompanying process of hydrogen evolution by the elegant

use of a rotating EQCM [66]. Another technologically important example of this is electroless deposition. The generic situation is that metal ions (whether free or complexed) are reduced to the elemental metal by a solution reducing agent, Red (e.g. formaldehyde). Under operating conditions, the net current flow is zero, as a consequence of balanced currents for M^{z+} reduction and Red oxidation. Mechanistically, the common requirement is to obtain the partial currents as a function of potential (and other chemical variables) from the measured $i-E$ curve. In an EQCM experiment, the electrochemical data provides the total (net) current and application of Faraday's law to the QCM (mass) response provides the partial current for M^{z+} reduction; the Red partial oxidation current is then obtained by difference. A classic example is electroless Cu deposition, illustrated in Fig. 10 [67]. In the more complicated case of Au electroless deposition from dimethylborane solutions, the EQCM has been used to provide evidence for formation and reduction of an oxide layer and for adsorption of a reactive intermediate [68] and shown to be a powerful technique for screening plating bath formulations [69].

More detailed examination of metal deposition, using crystal impedance measurements, shows that there can also be damping effects [70]. In the case of Cu and Ag, these were shown to be attributable to film morphology through the associated increase in viscous coupling to the liquid. An attractive goal is the manipulation of metal surface morphology, and crystal impedance measurements have been shown to provide useful insights during electrodeposition of nanostructured Pt from liquid crystalline plating baths [71].

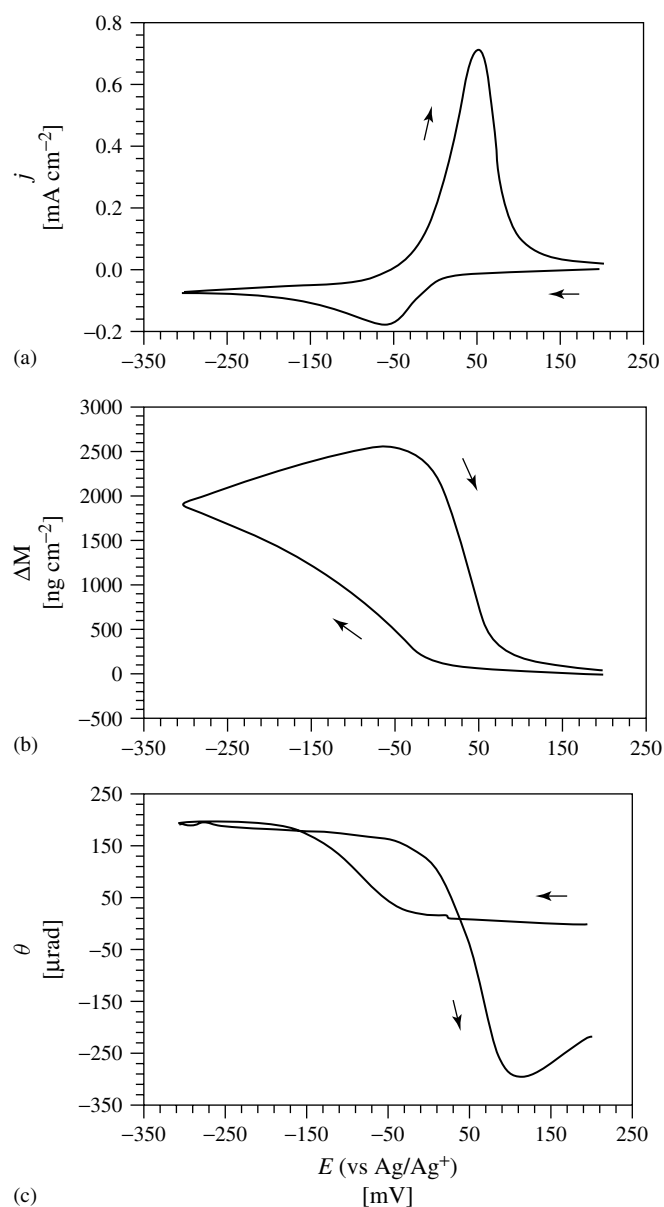


Fig. 9 Calibration experiment for a combined EQCM/PBD instrument, using the electrodeposition of Ag. Panels (a), (b), and (c), respectively, show current, mass change, and beam deflection responses to a cyclic voltammetric experiment (scan rate: 20 mV s^{-1}). Working electrode: Au (area 0.22 cm^2) on a 10-MHz AT-cut quartz crystal. Probe beam: 633 nm He–Ne laser parallel to Au electrode at a distance of $155 \mu\text{m}$. Solution: $1 \text{ mmol dm}^{-3} \text{ AgNO}_3/0.2 \text{ mol dm}^{-3} \text{ HClO}_4$. (Reproduced from Ref. [43] with permission from Elsevier.)

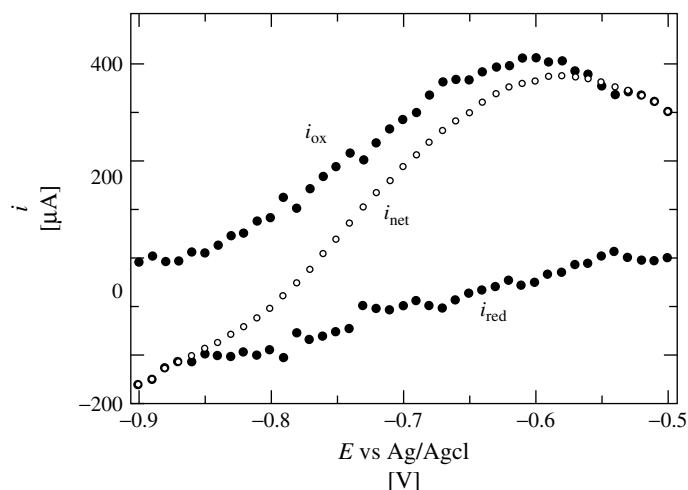


Fig. 10 Mixed potential diagram for an electroless Cu deposition bath. i_{net} is the measured (total) current, i_{red} is the determined from the rate of Cu deposition (rate of QCM frequency change) using Faraday's law, and i_{ox} was then determined by the difference. Working electrode: Cu (area 0.34 cm^2) on 5-MHz quartz crystal. Solution contained 5 mmol dm^{-3} CuSO_4 , 10 mmol dm^{-3} Na_2EDTA , 50 mmol dm^{-3} Na_2SO_4 , and 50 mmol dm^{-3} HCHO at pH 10.8. Temperature: 70°C . (Reproduced from Ref. [67] with permission from The Electrochemical Society.)

2.7.3.3 Metal Oxides

For broadly the same reasons as metals, metal oxides/hydroxides are amenable to study by the EQCM. This is true for films that are electroactive or passivating, and which may be formed by chemical, electrochemical, or thermal routes. Given the fraction of elements in the periodic table forming such materials and the breadth of applications – including corrosion, energy storage, and electronic devices – the technological importance of this area is immense.

Prominent among the electroactive metal (hydr)oxides studied is nickel hydroxide. The EQCM has proved to be extremely useful in exploring aspects of the electrochemically driven precipitation of $\text{Ni}(\text{OH})_2$ and its subsequent redox chemistry. Figure 11 [72] shows EQCM data for $\text{Ni}(\text{OH})_2$ deposition from $\text{Ni}(\text{NO}_3)_2$

solution, consequent upon the interfacial pH change driven by electrochemical hydrogen generation. The data show how the deposition rate can be varied by current control. The slope of the plot, in conjunction with the value of the current value, was fitted to an empirical model for deposition efficiency. More generally, one could consider it as providing an effective molar mass (defined as $\Delta MF/Q$) for the deposit, for example (under different experimental conditions to those employed in the cited study) providing film water content. In the context of $\text{Ni}(\text{OH})_2$ film redox chemistry, a key mechanistic issue is the competition between the interfacial transfers of metal cation (commonly K^+ or Li^+) and hydroxide anion or protons in order to satisfy electroneutrality and of the solvent in order to satisfy activity constraints. The EQCM [73, 74] has been extremely

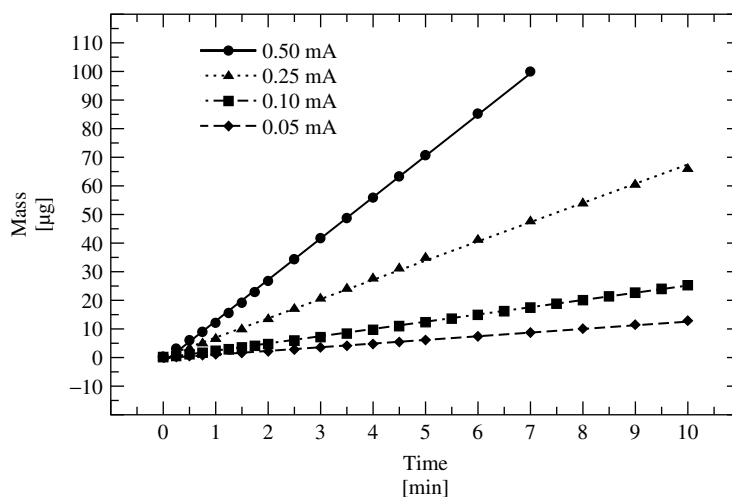


Fig. 11 Plots of electrode mass change versus time for the electrochemical deposition of $\text{Ni}(\text{OH})_2$ from 0.2 mol dm^{-3} $\text{Ni}(\text{OH})_2$ solution at different imposed currents (as indicated). Electrode: Au (area 0.2 cm^2) on 10-MHz quartz crystal. (Reproduced from Ref. [72] with permission from The Electrochemical Society.)

informative in this respect, especially when coupled with a laser-deflection technique to monitor stress effects [75] or probe beam deflection to extract individual ion and solvent fluxes as functions of potential or timescale [76]. This system is also complicated by phase changes; the structural changes (predominantly between α - and β - $\text{Ni}(\text{OH})_2$) result in significant changes in internal volume, which dramatically influence the gravimetrically observable solvent exchange signature [77, 78].

In the search for battery materials with better performance characteristics, the parent nickel hydroxide system has been modified by the inclusion of other metal ions. The EQCM has been used to monitor redox-driven ion and solvent transfers in sol-gel derived nickel-cobalt oxide films [79] and, through the solvent-transfer signature shown in Fig. 12, phase changes in electroprecipitated Co-Ni(OH)₂ films [78]. An as-prepared Co-Ni(OH)₂

film, like α -Ni(OH)₂, shows a mass increase upon oxidation, but redox cycling progressively converts it to the β -form, which shows a mass decrease upon oxidation. There is, however, a subtle contrast between the phase change behavior of the Co-modified material and the parent Ni(OH)₂, studied earlier by Scherson and coworkers [77], in that the inclusion of Co prevents the shift in oxidation potential (i - E response) to more positive potentials, even though it has virtually no effect on the α - to β -phase transition that is so graphically seen through the redox-driven solvent-transfer process (seen in the ΔM - E response of Fig. 12). The salutary lesson from this example is that the electrochemical goals may tempt one to interpret the gravimetric data in terms of the charge carrying species (ions), but in fact a neutral species (solvent) can be dominant. The unexpected positive outcome is that one learns, indirectly from the solvent

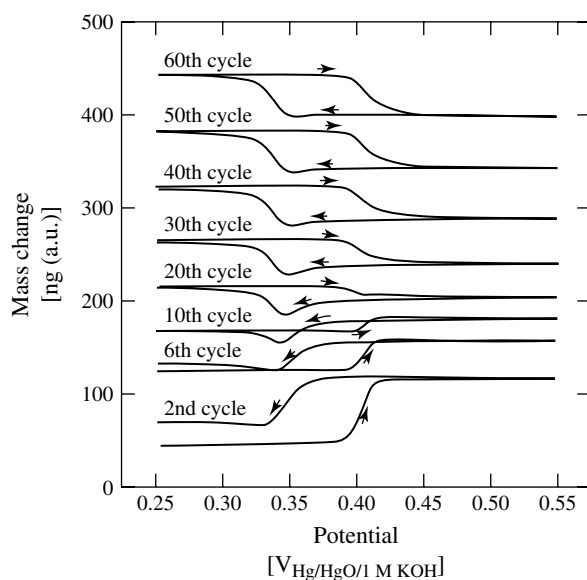


Fig. 12 Mass change versus potential responses to multiple redox cycling of an electroprecipitated Co/Ni(OH)_2 film (containing 10.2% Co) supported on an Au electrode. Solution: 1 mol dm^{-3} KOH. Potential scan rate: 10 mV s^{-1} . (Reproduced from Ref. [78] with permission from The Electrochemical Society.)

population changes, as much about the film structural as about the film redox changes; the former controls the dynamics of the latter.

The EQCM has also been used to study other metal oxide systems of relevance to energy storage and other applications, including MnO_2 [80], PbO_2 [81, 82], and sol-gel derived films of V_2O_5 [83], WO_3 [84], and Nb_2O_5 [85]. Although film deposition (e.g. nucleation and growth of PbO_2 [81]) can obviously be studied, the primary exploitation of the technique has been probing the redox-driven surface composition changes, for example, associated with lithium insertion: correlation of charge and mass data provides access to solvent effects that would be difficult to observe by other means. A system of long-standing interest is MnO_2 ,

and Yu and coworkers have used the EQCM to study both electrochemically [86] and chemically [80] deposited films. The electrochemical performance is critically dependent upon the “microtexture” of the film, that is, the presence of solvent-filled pores and cavities. The EQCM, as illustrated by the data of Fig. 13 [80] for chemically deposited material, is able to separate out the charge and solvation effects. By comparing the current and mass responses shown in Fig. 13 [80], along with the analogous anodic half-cycle data, it was shown that micropores within the film are filled with solvent, electrolyte, and dissolved manganese species when the film is oxidized (to MnO_2), but that these pores are emptied when the film is reduced (to Mn(OH)_2). The authors highlighted the fact that expulsion of species from the

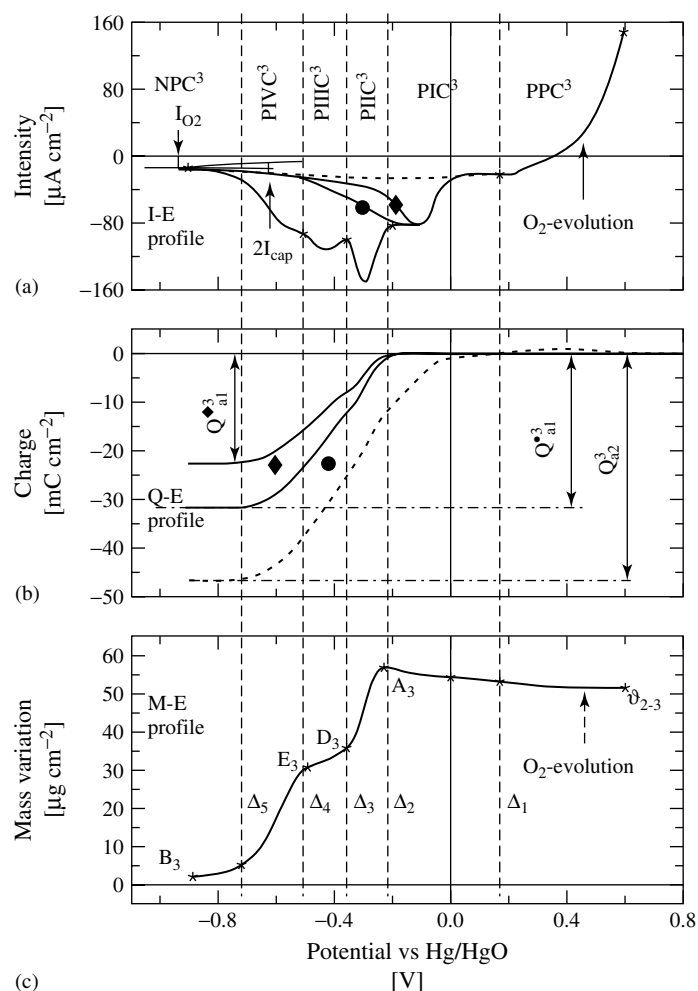


Fig. 13 Responses of (a) current; (b) charge; and (c) film mass change to a linear cathodic potential sweep of a chemically deposited (via MnSO_4 reduction of KMnO_4) MnO_2 film. Electrodes: Au (electroactive area 1.37 cm^2 , piezoactive area 0.34 cm^2) on 5-MHz quartz crystal. Solution: 1 mol dm^{-3} KOH. Potential scan rate: 1 mV s^{-1} . Lines marked with filled circle and diamond symbols, respectively, represent contributions due to oxygen reduction and capacitive currents, respectively. Vertical dashed lines separate different regimes, represented by the annotations and described in detail in the original work. (Reproduced from Ref. [80] with permission from The Electrochemical Society.)

oxide structure into the fluid phase does not necessarily correspond to mass loss (as perceived by the EQCM), since these species may be trapped within pores that

are effectively inertially coupled to the underlying resonator.

A rather different oxide system is the Cu_2O film electrodeposited from alkaline

copper lactate solution. At constant current, the potential undergoes periodic oscillations. These are reflected in changing QCM $f-t$ slopes (equivalent, under constant current conditions, to $\Delta f-Q$ slopes) that were interpreted in terms of the formation of an alternating Cu/Cu₂O multilayer nanostructure [87].

In other systems, oxide films can be passivating. An elegant example of the power of the EQCM is the use of frequency change data to calculate the fraction of the total current associated with oxide film growth on Cr [88]. Analogous to the approach in electroless deposition (see above), the EQCM can be used to provide selectivity in terms of the process of interest, here oxide film growth. Film thickness data estimated using the EQCM were in excellent agreement with X-ray photoelectron spectroscopy measurements, but of course the EQCM has the advantage that the data are acquired in situ, in time-resolved fashion, and at a fraction of the instrumental cost. Potential steps were executed in two stages across the passive domain and the film growth responses compared with two models: the interface model (growth limited by growth/dissolution at the film/solution interface) and the high-field model (growth limited by ion conductivity through the film). As Fig. 14 [88] shows, either model can explain growth at lower potentials (0.0–0.4 V) but only the interfacial model can describe growth at higher potentials (0.4–0.8 V). The method has been extended to stainless steels containing Cr, Mo, or W [89–91].

The closely related process of corrosion is also amenable to study by the EQCM. Since the species transferred across the interface (metal ions) are generally relatively heavy, a gravimetric sensor is very sensitive. An excellent example of this

is shown in Fig. 15 [92], which depicts the frequency increase (mass loss) for a zinc film (representative of the surface of a galvanized steel) upon exposure to an industrial alkaline cleaner, as part of a cleaning and chromating procedure. The response clearly has two components. By examining their pH and oxygen sensitivities, it was possible to deduce that the faster process is associated with chemical dissolution of an oxide layer on the outer zinc surface and that the slower process is anodic dissolution of zinc. As Fig. 15 shows, the first stage is unaffected by the age of the bath, but the second stage is dramatically slower in a “used” bath; this is attributable to increased solution zincate concentration in the latter case. The EQCM has also been used to show that zinc corrosion is significantly affected by illumination [93]. (As an aside, it is worth mentioning that in both of these studies the complications of Au/Zn alloy formation were avoided by deposition of an intervening layer of Cu between the Au electrode and the Zn overlayer.)

Corrosion is generally recognized to involve spatially localized and temporally discrete events. This is significant in the context of using the EQCM as a probe, since the Sauerbrey equation represents a spatially averaged sensitivity, use of metal deposition/dissolution to establish the bell-shaped spatial sensitivity function across the resonator surface was discussed in Sect. 2.7.3.2. Consequently, mass loss (corrosion) will give rise to a frequency change (increase) that is dependent upon the location of the event on the surface. Furthermore, the appearance of pits on the surface will change the coupling to the fluid. This complicated situation has begun to be considered recently by Gabrielli and coworkers [94], who attached thin foils of authentic 304 stainless steel (rather than depositing model layers) to

Fig. 14 Passive film growth on Cr following application of a potential step from: (a) 0.0 to 0.4 V and (b) 0.4 to 0.8 V. Full line is film thickness calculated from QCM frequency response (with widely spaced dots indicating uncertainty, 2σ). The predictions of the interface and high-field models (explained in main text) are also indicated by the line-styles marked IFM and HFM, respectively. Electrodes: Cr film on Au supported on 10-MHz AT quartz crystal. Solution: $0.1 \text{ mol dm}^{-3} \text{ H}_2\text{SO}_4 + 0.4 \text{ mol dm}^{-3} \text{ Na}_2\text{SO}_4$. (Reproduced from Ref. [88] with permission from The Electrochemical Society.)

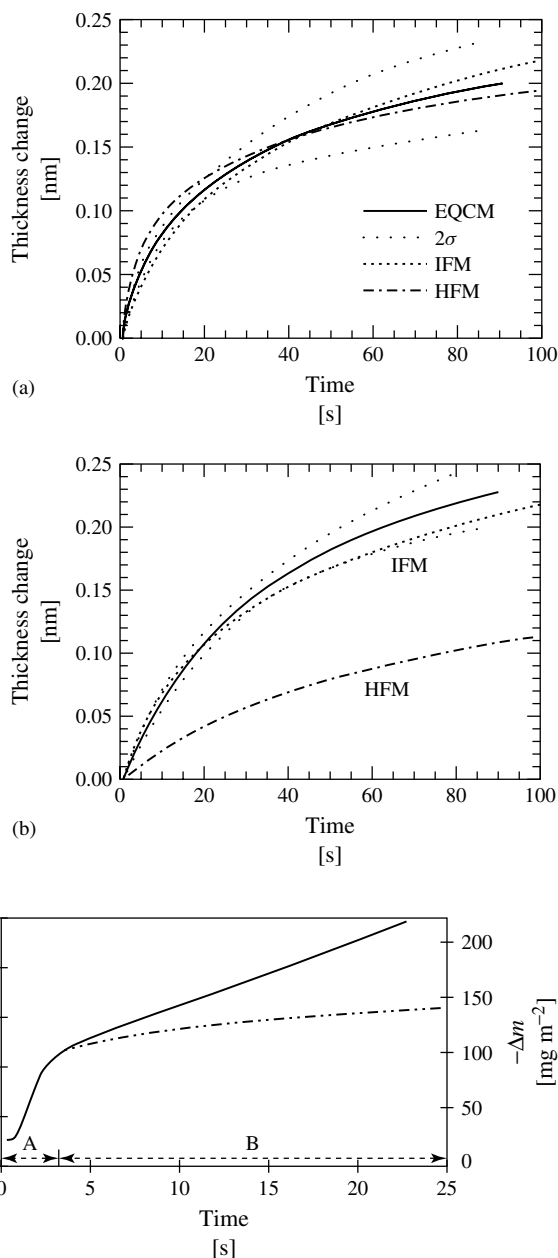


Fig. 15 Mass changes of Zn films at open-circuit potential exposed to new (full line) and used (dash-dot line) alkaline cleaning solution. Electrodes: Zn film on Au (with Cu overlayer) supported on 10-MHz AT-cut quartz crystal. Solution: RIDOLINE industrial alkaline cleaner, pH 12.43. Temperature: 316 K. (Reproduced from Ref. [92] with permission from the Royal Society of Chemistry.)

an EQCM, then observed transient frequency change events. Scanning electron microscopy (SEM) images showed both large and small pits, with the latter predominating to the extent that the spatial averaging intrinsic to use of the Sauerbrey equation was a reasonable approximation.

Inhibition of corrosion (through deliberate addition of organic inhibitors) has been studied on Ni [95] and Fe [50]; in many respects this aspect is an adsorption problem, and indeed Landolt and coworkers used the EQCM to test different isotherms for the selected inhibitors.

Chemically more complex oxide systems studied by the EQCM include barium and strontium tungstates and molybdates on W and Mo, in which dissolution and precipitation processes result in the formation of surface ternary oxide layers [96].

2.7.3.4 Semiconductors

Electrochemical methods can be used for the preparation of semiconductor materials in thin film form. This class of preparation methods generally centers on a redox-driven electrodeposition and is thus amenable to study by the EQCM. Chemically, the complications arise because the stoichiometry of the materials may be variable, according to the particular conditions employed. For example, Rajeshwar and coworkers and Kemell and coworkers have studied the complexities of deposition (by oxidation or reduction of solution precursors) of a range of chalcogenides, including CdS, In_2S_3 , and CdTe [97], CdSe [98], PbS [99], PbSe [100], PbTe [101], CuInSe₂ [102], and $\text{Cu}_{(2-x)}\text{Se}$ [103]. Generally, electrogravimetric data can provide insight into the processes involved and the composition of the resultant material by the application – at the nanogram level – of Faraday's law to the frequency response to charge

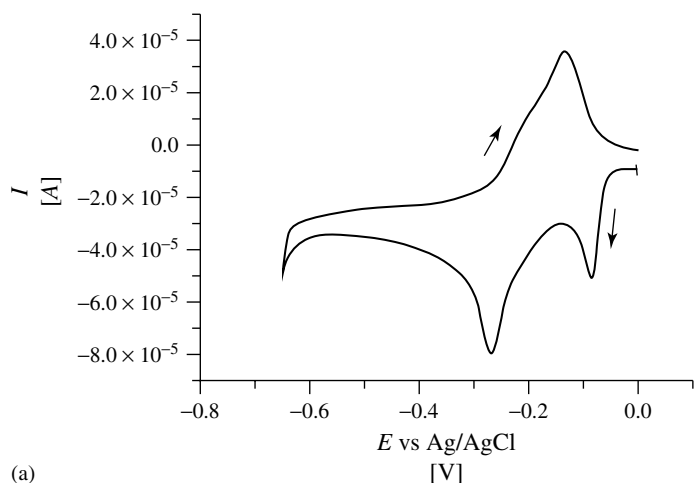
passage. Effectively, the slope of a $\Delta M - Q$ plot is used to provide an effective molar mass that can be compared with the stoichiometries of various model processes. In one case, coupling the EQCM with a flow injection stripping method was used to obtain the composition of CdSe films [98].

The case of cathodic deposition of $\text{Cu}_{(2-x)}\text{Se}$ from a $\text{Cu}(\text{SCN})_4^{3-}/\text{HSeO}_3^-$ solution is interesting, in that deposition at -0.1 V gives a $\Delta M - Q$ relationship consistent with four-electron reduction of HSeO_3^- to Se, and at slightly more negative potentials yields the desired $\text{Cu}_{(2-x)}\text{Se}$. At much more negative potentials ($E < -0.65\text{ V}$) metallic Cu is deposited. In a voltammetric experiment, illustrated in Fig. 16 [103], one thus sees a mass (frequency) versus charge signature that is attributable to the initial deposition of Se, then a chemical process that consumes surface Se to produce a $\text{Cu}_{(2-x)}\text{Se}$ film, and eventually the codeposition of Cu and Se as $\text{Cu}_{(2-x)}\text{Se}$. When $\text{Cu}_{(2-x)}\text{Se}$ was deposited, the composition was found to be independent of potential, but morphological (simplistically, roughness) changes occurred and (presumably through liquid coupling effects) lead to changes in the $\Delta f - Q$ slope with potential.

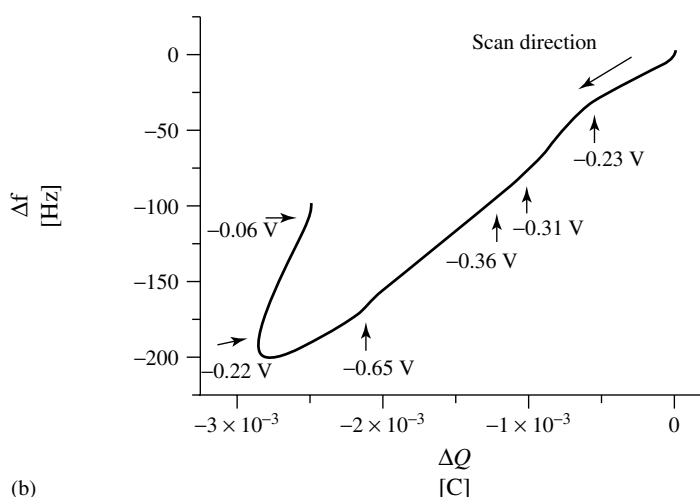
2.7.3.5 Metal Complexes

Most of the electroactive metal complexes studied using the EQCM are in fact polymeric materials, which are discussed in Sect. 2.7.3.7. A few examples that highlight nonpolymeric metal complex chemistry are presented here.

Surface-attached microcrystals of $\text{Fe}(\eta_5\text{-C}_5\text{Ph}_5)$ exposed to aqueous and water/acetonitrile media can be made to undergo Fe(III/II) redox chemistry. In addition to the expected ion and solvent transfers accompanying the redox chemistry, the EQCM revealed some unexpected



(a)



(b)

Fig. 16 Data from a voltammetric deposition study of the Cu_{2-x}Se system: (a) current versus potential and (b) frequency change versus charge plots. Electrode: Au (area = 0.236 cm^2) on 5-MHz AT-cut quartz crystal. Solution: $50 \text{ mmol dm}^{-3} \text{ CuCl} + 1 \text{ mmol dm}^{-3} \text{ SeO}_2 + 4 \text{ mol dm}^{-3} \text{ KSCN/pH } 3$. Potential scan rate: 10 mV s^{-1} . (Reproduced from Ref. [103] with permission from Elsevier.)

characteristics associated with phase behavior [104]. Co(II)-ethylenediamine complexes have been explored as reducing agents in electroless deposition baths (see also Sect. 2.7.3.2). As part of this process, the EQCM, in a wall-jet configuration, has been used to extract partial currents for

the Co complex redox chemistry and for Cu electrode dissolution in the presence of halides, which are believed to act as bridges in the adsorption of the Co complex on the Cu surface [52].

Electrocrystallization, as an example of an electrochemically driven deposition

process, is amenable to study using the EQCM. The technique has been used to show that electrocrystallization of the partially oxidized cyanoplatinum complexes $K_{1.75}Pt(CN)_4(H_2O)_{1.5}$ and $K_2Pt(CN)_4Cl_{0.3}(H_2O)_3$ from aqueous solutions of $K_2Pt(CN)_4$ occurs by progressive nucleation and one-dimensional growth and that their dissolution occurs at open circuit [105].

A rather clever use of the EQCM in a molecular recognition context is the binding of ferrocene species to surface-bound β -cyclodextrin hosts [106]. By using a carboxylate-substituted ferrocene and changing the solution pH and/or applied electrode potential, it was possible to control the guest charge type (negative, neutral, or positive, visualized in a Pourbaix diagram) and thereby manipulate the host–guest interactions.

2.7.3.6 Other Inorganic Materials

Although, in the context of electrode surface modifiers, inorganic materials are sometimes perceived to lack some of the synthetic flexibility associated with polymeric materials (see Sect. 2.7.3.7), they commonly possess greater stability and robustness to physicochemical manipulation. This has provided the motivation to study the interfacial properties of a number of electroactive inorganic materials using the EQCM.

Prominent among these is Prussian Blue (simplistically, “ferric ferrocyanide”), which can undergo reduction to a “ferrous ferrocyanide” material, known as *Everitt’s salt*. There are three issues relating to the redox chemistry of this material upon which the EQCM has shed light: irreversible compositional changes accompanying redox cycling of freshly deposited Prussian Blue, ion transfer required to maintain electroneutrality upon

redox switching, and solvation changes. Although other techniques have undoubtedly contributed to our understanding of this material, recent EQCM studies show in quantitative manner that initially formed Prussian Blue corresponds to $Fe_4^{3+}[Fe(CN)_6] \cdot 6H_2O$ (referred to as “insoluble Prussian Blue”) and that reduction (in potassium-containing electrolytes) to Everitt’s salt generates $K_2Fe^{2+}[Fe(CN)_6]$ [107, 108]. The product of reoxidation is $KFe^{3+}[Fe(CN)_6]$ (referred to as “soluble Prussian Blue”). Subsequent redox cycling then corresponds to reversible switching between soluble Prussian Blue and Everitt’s salt. One consequence of the high stability of this system is that EQCM data are generally of extremely high-quality: ΔM –(or Δf)– Q plots are linear, show little hysteresis and are very reproducible, allowing one to pursue mechanistic issues in some detail.

Complete redox switching (after the initial “insoluble/soluble Prussian Blue” conversion) in aqueous solutions of alkali metal and ammonium cations was found [108] to yield effective molar mass changes $\Delta MF/Q$ close to, but distinguishable from, the cation molar mass. The inference was that there was a small amount of solvent transfer (less than one water per transferred cation), the direction of which was dependent upon the electrolyte cation. (It is worth noting that the effective molar mass change for reduction in K^+ solution was found to be essentially identical in the two studies reported (30 [107] and 31 [108] $g\ mol^{-1}$), a level of agreement seldom seen in studies of polymer films (see Sect. 2.7.3.7) for which minor variations in film preparation, handling, and aging result in apparent inconsistencies between different studies.) In the case of Prussian Blue films immersed in NaCl solution (but

protected by a Nafion layer), the more sophisticated ac electrogravimetric method was able to show that sodium ions are desolvated prior to entry into the Prussian Blue film [109].

In contrast with reversible redox switching of precycled films, the initial redox cycle of Prussian Blue yielded more complex mass responses with much greater irreversible solvation changes. This is dramatically illustrated by the data of Fig. 17 [108], which shows the $i-E$ and $\Delta M-E$ responses to the first redox cycle for each of two nominally identical films, one exposed to H_2O and the other to D_2O . Although the difference in solvent molar masses is quite small (11%), solvent transfer is such a large component of this initial redox-driven structural change that the overall responses are very different. Somewhat reminiscent of the α/β -Ni(OH)₂ case, this underscores the fact that when the observed response is a sum of individual transfer components (commonly in opposing directions, for example, in response to a volume constraint), a relatively small variation in one component

may result in a major change in the observed (net) mass response.

In an extension of their Prussian Blue study, Ogura and coworkers [110] prepared bilayers in which a polyaniline film was overlaid onto a Prussian Blue inner layer. The interesting feature here is that, on charge grounds, polyaniline (see Sect. 2.7.3.7.2) is a barrier to the normal cation-transfer-based electroneutrality mechanism exhibited by the Prussian Blue/Everitt's salt redox chemistry (see above). For thin polyaniline outer layers, the cation-transfer mechanism is achieved, but thick polyaniline films preclude this. At intermediate outer layer thicknesses, there is a more complex mechanism in which redox-driven K^+ cation expulsion (on oxidation of the Everitt's salt form of the inner layer) from the inner layer to the outer layer is electrically balanced by Cl^- anion entry into the outer layer. Further oxidation of the bilayer (oxidizing the polyaniline) results in expulsion of the K^+ ("inherited" from the inner layer), the Cl^- normally incorporated in this polyaniline oxidation process already being present to neutralize

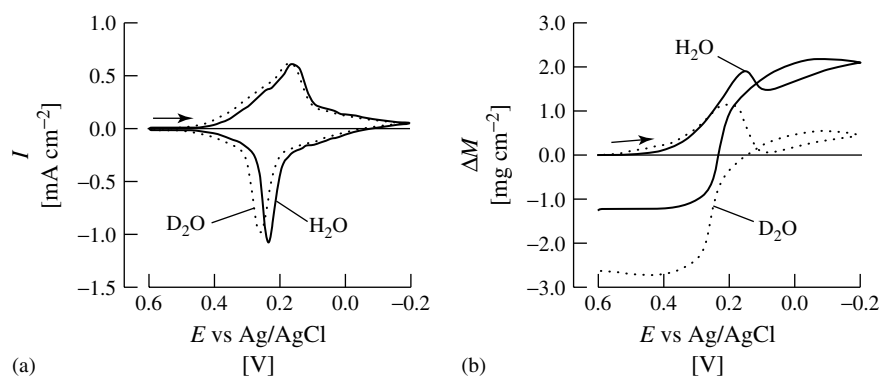


Fig. 17 Current (left panel) and mass change (right panel) responses during the first redox cycle of Prussian Blue films (deposition charge 10 mC cm^{-2}). Electrodes: Au (area = 0.32 cm^2) on 6-MHz AT-cut quartz crystals. Solution: $0.5 \text{ mol dm}^{-3} \text{ KNO}_3$ in H_2O (full lines) or D_2O (dotted lines). Potential scan rate: 10 mV s^{-1} . (Reproduced from Ref. [108] with permission from Elsevier.)

the previously internally transferred K^+ ions. Polymer/polymer bilayers will be discussed in Sect. 2.7.3.7.2, but this example neatly shows how spatial configuration of materials at the interface can alter the responses normally associated with the individual components.

The EQCM has also been used to study redox-driven ion and solvent transfers in Prussian Blue–related materials, in which one or other of the iron species is replaced by another metal. These include ferric ruthenocyanide (“ruthenium purple”) [111], silver hexacyanoferrate [112], and nickel hexacyanoferrate [113, 114]. EQCM data for the latter case – the best characterized of this set – was shown to be consistent with a broadly electrolyte cation-dominated electroneutrality mechanism (as for the parent Prussian Blue material), but with some evidence for electrolyte anion participation, in the redox process.

An interesting example of the use of the EQCM to monitor both interfacial electrochemical and subsequent chemical processes is the deposition of Hg on thin TSM resonator-immobilized graphite electrodes [115]. As the authors conceded, there are a variety of complicating factors – notably spatially inhomogeneous deposition of Hg droplets and viscoelastic phenomena associated with these fluid deposits. Nevertheless, in chloride media, when electrodeposition of elemental Hg was followed by setting the electrode to open circuit, the electrode unequivocally continued to gain mass; this was interpreted in terms of the comproportionation of deposited Hg(0) and dissolved Hg(II), to produce surface-immobilized Hg_2Cl_2 .

There are a number of other inorganic systems that have been studied using the EQCM, although in somewhat less detail. These include electrochemical

deposition of calcium carbonate scale on Au [116], the electrodeposition of clays [48], and the redox chemistry of electroactive metal coordination complexes ($[Ru(bpy)_3]^{2+/3+}$, $[Ru(NH_3)_6]^{2+/3+}$, and $[Fe(CN)_6]^{4-/3-}$) ion-exchanged into clay films [117]. The EQCM has also been applied to the study of C_{60} [118, 119] and carbon nanotubes [120, 121], although the data have not yet lead to clear or specific conclusions.

2.7.3.7 Polymers

In terms of electrochemical systems, polymer films are arguably the main class of material to which the EQCM has been applied. This section is split into a separate discussion of redox, conducting, and insulating polymer films; this is to some extent a matter of organizational convenience and the recurrence of similar phenomena and properties should be noted. Some attention has been given to film electrodeposition, but most studies relate to ion and solvent transfers accompanying film redox switching. As will become clear from the examples selected, the EQCM has been central to a fundamental change in the way electroactive polymer films are now viewed, particularly with regard to the role of competitive (anion versus cation) ion transfers, solvation effects, and polymer dynamics (as manifested through viscoelastic phenomena). It is unlikely that these insights would have resulted from purely electrochemical measurements, such as the voltammetric experiments that dominate the study of these systems.

2.7.3.7.1 Redox Polymers The term “redox polymer” is used to denote a polymer that contains electroactive groups that are discrete, localized entities. The

electroactive groups may be pendant to the polymer backbone, as in polyvinylferrocene, or may be an integral part of it, as in poly(xylylviologen) [PXV]. In either case, they function as essentially independent entities, and charge transport is by a hopping-type mechanism, involving sequential self-exchange between groups in the oxidized and reduced forms of the couple that are in appropriately close proximity.

A wide range of electrochemical (i - V - t) methods has been used to study the overall extent and dynamics of redox polymer film switching, as manifested through the electron flux (current) or population (charge). However, these methods cannot provide insight into the associated transfers of ions and solvent: this has been one of the main contributions of the EQCM to this area. The electroneutrality constraint is generally appreciated: the film must overall be electrically neutral, so electron transfer (in this context, electrochemically driven) into or out of the film at the electrode/polymer interface must be balanced by an electrically equivalent ion transfer at the polymer/solution interface. Under permselective conditions, the transferred ion will be the counterion (anion for a positively charged film and cation for a negatively charged film). However, this is strictly only true at very low ionic strength – a situation deliberately violated in most electrochemical experiments – and at equilibrium – a situation generally violated in potentiodynamic experiments. In concentrated electrolytes (in principle, above ca. 0.1 mol dm^{-3}), activity arguments can be used to show that there may be significant amounts of coion (and an equivalent amount of counterion, commonly referred to as *salt* in the ion-exchange literature) partitioned into the film. Consequently, the system has

a choice of mechanisms by which it can satisfy electroneutrality upon redox switching: anion ejection or cation injection upon reduction and vice versa upon oxidation. Quite generally, the balance of these competing ion transfers may be dependent upon applied potential, film charge state, experimental timescale, and solution ionic strength. The power of the EQCM is its ability to distinguish between them, under either thermodynamically controlled (long timescale) or kinetically controlled (short timescale) conditions. At the crudest level, anion and cation transfers must be in opposite directions, so the sign of the mass change will be different. At a more sophisticated level, one can interpret the EQCM frequency response to extract quantitative population changes and fluxes of the ions involved as functions of applied potential or film charge.

A very graphic example of this facility to distinguish anion- versus cation-based mechanisms for maintaining electroneutrality is given in Fig. 18 [122] for the poly(1-hydroxyphenazine) system. In this example, the cation is proton so the competing ions have very different mobilities – a feature that will be returned to shortly. Beyond the fact that it clearly has two distinct components, the i – E curve is relatively featureless, that is, unhelpful. In this particular case, the film is sufficiently thin (acoustically thin) that the EQCM frequency response can be interpreted in gravimetric terms. During the first part of polymer oxidation (“step I” in the figure), the frequency decreases (mass increases): this is consistent with anion entry. During the second part of polymer oxidation (“step II” in the figure), the frequency increases (mass decreases): this is consistent with cation exit. This qualitative conclusion is supported by the PBD data in panel (b) of Fig. 18. Quantitative analysis

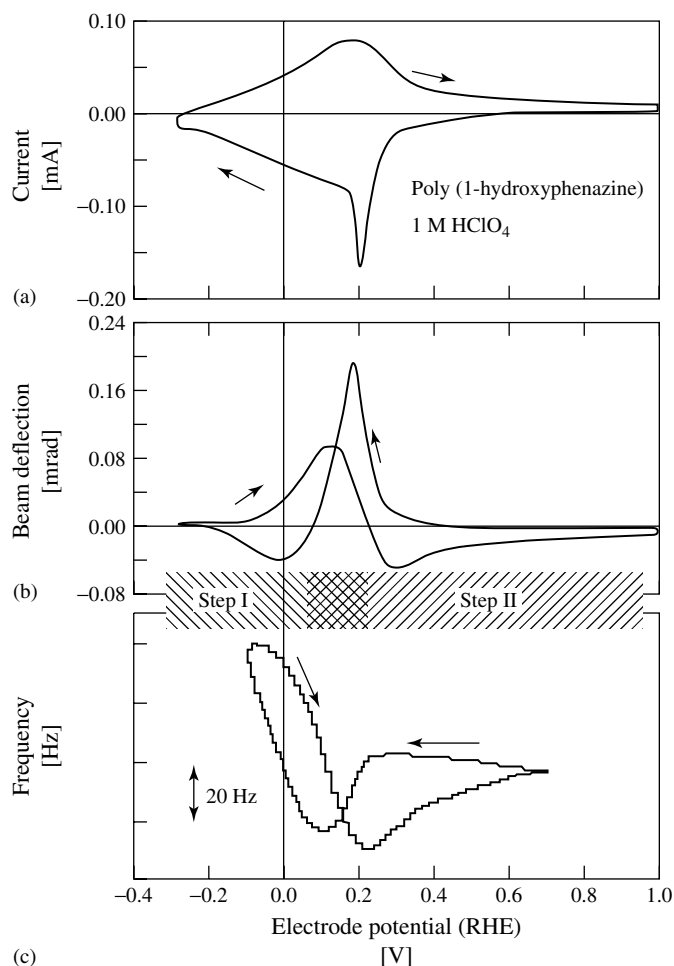


Fig. 18 Current, beam deflection, and frequency change responses (panels (a–c), respectively) of a poly(1-hydroxyphenazine) film to a redox cycle under cyclic voltammetric conditions. Electrodes: glassy carbon (probe beam experiment) and Au (area = 0.36 cm²) on 5-MHz AT-cut quartz crystals (QCM experiment). Solution: 1 mol dm⁻³ HClO₄. Potential scan rate: 50 mV s⁻¹. (Reproduced from Ref. [122] with permission from Elsevier.)

of the mass change data reveals that a counterflux of solvent occurs (to which the probe beam is insensitive), to an extent that broadly maintains a constant film volume. Interestingly, shorter timescale experiments than those of Fig. 18 reveal that oxidation using a potential step across

the full potential range transiently drives within the film an excess anion population change, which then relaxes on longer timescales.

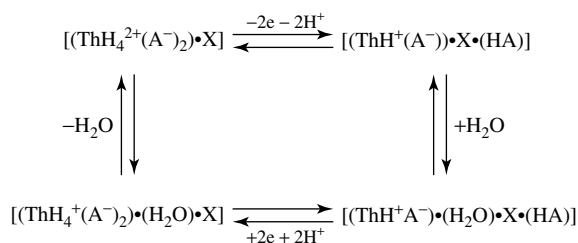
Many organic redox species have protonatable groups (e.g. amines), so in aqueous media one might expect proton

transfer to be a plausible means of satisfying electroneutrality, even if only transiently. An interesting, and slightly unusual, example of coupled electron/proton transfers is provided by the polythionine system. In strong acid media, there is a complicated electrolyte-dependent competition between anion and proton transfers [123]. However, in acetic acid media, the coordinating power of the carboxylic acid is such that it remains in the film, regardless of the polymer redox state, and proton (nominally the coion) transfers rather than acetate (nominally the counterion) [124]. The system (under these conditions) is further unusual in that volume constraints restrict the amount of solvent that can enter the film, to the extent that a simple coordination model with integer solvation stoichiometry applies. The overall redox process is associated with an effective molar mass change of 16 g mol^{-1} , interpreted as a coupled $2\text{e}^-/2\text{H}^+$ transfer in one direction and a single solvent molecule transfer in the opposite direction, as represented by the scheme-of-squares mechanism shown in Scheme 1. Chemically, this is rationalized by considering that the solvent molecule entering upon polymer oxidation takes up a coordination site made available by an internal (acetate/acetic acid) proton transfer and, upon polymer reduction, the water must leave the film to make this site available to the more coordinatively powerful

acetate species. Kinetically, this promises a very neat – albeit unexpected – situation since proton transfer in the aquated acidic medium of the film is about as fast as an ion transfer as one could expect in a redox polymer, whereas transfer of the solvent (a larger species, whose motion is not field-assisted) is expected to be much slower. The mass-charge data shown in Fig. 19 [124] allow one to test this speculation. The linear $\Delta M-Q$ relationship during film reduction indicates that solvent expulsion is rapid enough to keep pace with the coupled e^-/H^+ transfers, but the dramatic curvature and hysteresis associated with film oxidation indicates that solvent entry is very slow; given the compactness of the film, this is entirely plausible.

The behavior described above for polythionine is a simple and helpful introduction to the concepts of redox-driven solvation change, participation of coion, kinetic effects (in terms of entry vs. exit rates for a given species and of charged vs. neutral species transfers), and temporal resolution of mobile species transfers. However, this level of simplicity is rare. Quite generally, the extent of solvent transfer is governed by an activity constraint [125, 126]: at equilibrium, the activity of the solvent within the film must equal the activity of the solvent in the solution (an effectively constant value, given the huge excess present). A change in film redox (charge) state results in a change in solvent activity coefficient

Scheme 1 Scheme-of-squares representation of the redox-switching mechanism of a polythionine film exposed to acetic acid solution. Th represents a monomeric thionine unit, A represents acetate, and X can be either a water or acetic acid molecule. (Reproduced from Ref. [124] with permission from the American Chemical Society.)



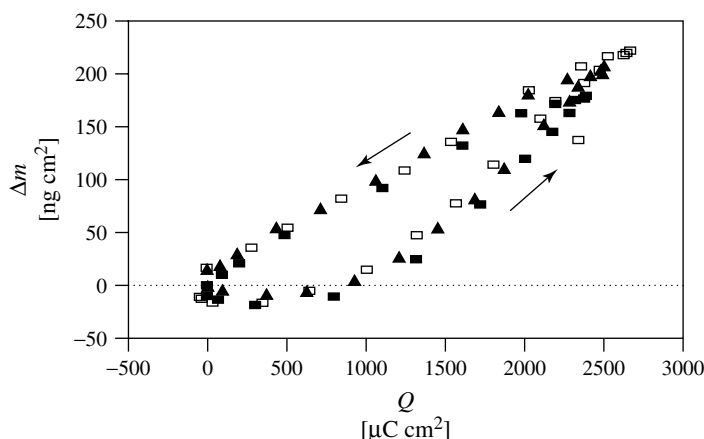


Fig. 19 Mass change versus charge plots for redox cycling under voltammetric conditions of a polythionine film ($\Gamma = 13.8 \text{ nmol cm}^{-2}$) in aqueous acetate solution. Electrode: Au (area = 0.23 cm^2) on 10-MHz AT-cut quartz crystals. Solution: 0.1 mol dm^{-3} total acetate, buffered to pH 4.5. Potential scan rates: 5 (\square), 50 (\blacktriangle), 100 (\blacksquare) mV s^{-1} . (Reproduced from Ref. [124] with permission from the American Chemical Society.)

within the film, thus requiring a change in solvent concentration (population) within the film. At the present state of knowledge, there is no prospect of being able to calculate a priori values of solvent activity coefficients within an electroactive polymer film. Given the diversity of chemical species involved in this class of materials, one must anticipate diverse behavior and at best hope to rationalize the experimental observations; EQCM measurements can provide the data to facilitate this approach.

One of the most widely studied electroactive polymer film systems is polyvinylferrocene (PVF). PVF films can be deposited by electroprecipitation from organic solvents (as discussed below) then studied as surface-immobilized films in aqueous media. Redox switching between the two ferrocene (Fc) states can be represented as a $\text{Fc}^{+/0}$ process. On electroneutrality grounds, one would then expect anion transfer into (out of) the film upon oxidation (reduction), and indeed a very early

study in this field [127] established this to be the case for PVF films exposed to aqueous ClO_4^- and PF_6^- electrolytes. Subsequent studies explored this system in more detail, showing that solvent entry accompanied anion entry (to the extent of a few water molecules per anion) and that, at higher electrolyte concentrations (typically in excess of 1 mol dm^{-3}), permselectivity failure occurred, that is, salt also partitioned into the film. Somewhat similar to the case of polythionine discussed above, the individual mobile species transfers (ClO_4^- , H_2O , and $\text{Na}^+\text{ClO}_4^-$) consequent upon redox switching of PVF were resolved by monitoring the current and frequency (mass) responses to a potential step [34]. The current response is complete relatively rapidly and is accompanied by a rapid mass change; on electroneutrality grounds, this is dominated by the transfer of a charged species, shown by the $\Delta M-Q$ relationship to be ClO_4^- . Thereafter, at essentially zero current,

there is continued substantial mass change; on electroneutrality grounds, this must be the transfer of a net neutral species – solvent under permselective conditions and solvent + salt under nonpermselective conditions. Thus, it was possible to separate out, using time and electrolyte concentration as variables, the individual contributions to the overall redox process.

It is intuitively obvious that while thermodynamic studies (focused upon populations, when the fluxes have decayed to zero) will benefit from considerations of the integral quantities charge and mass, kinetic studies will benefit from considerations of the corresponding differential quantities current and mass flux. A recent study of PVF redox-switching dynamics has shown how the charge (or potential) dependence of the ratio of the fluxes of solvent to counterion ($\rho = j_{\text{solvent}}/j_{\text{anion}}$) can be of particular benefit [128]. The variations (or independence) of ρ with potential, charge, or scan direction as functions of timescale (e.g. potential scan rate in a voltammetric experiment) have mechanistic diagnostic value. Plots of ρ versus Q and E provide qualitative identification (even on immediate visual inspection) of the rate-limiting process, and more detailed quantitative exploration can be expected to yield kinetic parameters. Given that most modern data acquisition systems store directly (or give facile access to) the relevant fluxes, future utilization of this analytical methodology is encouraged.

PVF is one of the few systems for which quantitative data have been obtained in any detail; since this must be the ultimate aspiration for any useful study, it is worth noting how far the present state of knowledge allows one to proceed. In rationalizing observed solvent transfers, there is a common tendency to consider

that one driver for solvent transfer is to fill/vacate space within the film in order to facilitate ion transfers. To the extent that the film is a kinetically frozen matrix – the dynamics and elasticity of polymer film matrices will be considered shortly – this is a qualitatively reasonable notion. On the other hand, the exchange of ions and solvent between the film and the solution phase are often considered without regard to any film volume constraint. There is thus a clear need to establish a means to test whether the volume is fixed and to explore the consequences of the result. In a recent study, the effect of imposing or removing a volume constraint on the partition of the solvent and salt was studied [129]. Theoretically, this was represented through a permselectivity index (R), defined as the ratio of the concentrations of coion and polymer charge sites. Experimentally, this was explored through the change in permselectivity index (ΔR), derived from redox-driven film mass changes under nonpermselective (high electrolyte concentration) conditions. It was shown that R , under given conditions, can be expressed in terms of a concentration parameter (S) and a thermodynamic parameter (T), where S is the ratio of the solution electrolyte concentration to the film charge site concentration, and T contains the salt partition coefficient and activity coefficients. For the simple case of a “+1/0”-type redox polymer (e.g. PVF) exposed to a 1:1 electrolyte, one can show that

$$\Delta R = 0.5[-1 + (1 + 4S^2T_{\text{Ox}}^2)^{1/2}] \quad (15)$$

Thus, a plot of $(\Delta R + 1/2)^2$ (from the EQCM data) versus S^2 should yield a straight line, from which the salt partition coefficient (within the thermodynamic parameter, T) might be estimated. More detailed criteria (described within

the original work [129] and based on the sensitivity of the film concentrations involved in Eq. (15) to film volume changes) determine whether or not this simple plot will be linear. For the case of PVF exposed to concentrated solutions of NaClO_4 , it was deduced that the films shrink significantly (ca. 35%). The partition coefficients for the net neutral species into the oxidized form of the polymer were found to be $K_{\text{salt, Ox}} \simeq 1.0$ and $K_{\text{solv, Ox}} \simeq 0.15$. Given the concentration of water in the bulk solution (55.5 mol dm^{-3}), the latter corresponds to a water concentration in the film of ca. 9 mol dm^{-3} . When compared with the redox site concentration of ca. 3 mol dm^{-3} , this indicates that even the oxidized form of PVF is quite hydrophobic.

Even in the light of the above advances, if one were to identify a limitation in the EQCM methodology, it would probably be that it is a differential method, that is, the measured frequency changes can only lead directly to film population changes (whatever the species involved). In many cases, this is adequate for the application. However, there are cases in which absolute populations are helpful. For example, in the case of the PVF films discussed here, oxidation is usually associated with an increase within the film of a few (5–10, according to the electrolyte and other conditions) solvent molecules per redox site. However, placing a physical interpretation on this is somewhat reliant upon knowing the “baseline” for this change, that is, whether it represents a relatively minor or major population change. The experimental problem is the absence of a suitable “reference” point. An instrumental approach designed to provide this is the DQCM [29, 36] discussed in Sect. 2.7.2.2.1. This device uses a reference crystal exposed to the same solution,

thereby automatically compensating for changes in fluid properties, for example, viscosity and density. The value of this facility has been demonstrated for the case of PVF films exposed to the 1:2 electrolyte disodium naphthalene-1,5-disulfonate (Na_2NDS) [130], a relatively rare example of an EQCM study using anything other than a 1:1 electrolyte. The crucial added capability provided by the DQCM (cf. EQCM) is that one can expose the modified electrode to a series of solutions (here, of different concentration) and attribute the change in frequency response to a change in film composition, free of any change in solution properties. By this means, it was possible to demonstrate film permselectivity for $[\text{Na}_2\text{NDS}] < 64 \text{ mmol dm}^{-3}$ and progressive permselectivity failure at higher concentrations. The salt permeation characteristics were such that film oxidation resulted in electroneutrality maintenance by ingress of a mixture of NDS^{2-} and NaNDS^- in the high concentration regime; while one might have arrived at this qualitative notion by other means, the DQCM has for the first time provided quantitative information.

A rather neat example of the manipulation of film electroneutrality maintenance mechanism is provided by the redox behavior of poly(xylylviologen) (PXV) films, in which the nominal counterion is poly(styrenesulfonate) (PSS). In this case, the “counterion” is effectively immobile, and the question arises as to whether the PXV and PSS ion charges compensate each other or are separately compensated by (other) electrolyte ions. This will clearly have implications for the possible sources and sinks of ionic charge available to satisfy electroneutrality upon PXV redox switching, and the EQCM is ideally placed to make the distinction. It was found that

the result was very dependent upon the ratio of PXV:PSS in the film as cast [131]. The $\Delta f-E$ traces for voltammetric redox conversion of the viologen were interestingly complex: in all cases, they were nonmonotonic within a given half-cycle and showed substantial mass changes well beyond completion of the redox process as indicated by the cessation of current passage. The short timescale (kinetically controlled) mechanism must therefore involve both anion and cation transfers. The long timescale (thermodynamically controlled) situation was interpreted as predominant – but not exclusive – cation transfer for PXV:PSS = 1:2 films and vice versa for PXV:PSS = 2:1 films.

All the ion and solvation changes discussed so far in this section relate to chemically reversible processes. Anecdotally, it is widely accepted in the redox polymer modified electrode literature that the first redox cycle of a newly deposited film is atypical. Although the reasons and processes are chemically rather different, this is reminiscent of the “first cycle” effect discussed in Sect. 2.7.3.6 for Prussian Blue films. PVF provides a typical example of this first cycle, or “break-in”, effect. The initial EQCM response to PVF oxidation in water (after its deposition from an organic solvent, typically dichloromethane) is quite different from that of a previously cycled film [132]. The result is most clearly demonstrated by considering the mass flux – or, better still, the difference between the total mass flux and the electron/ion flux – as a function of applied potential or film charge. Such plots show a once-only pulse of solvent into a new film; this solvent (typically ca. five solvent molecules per ferrocene redox site) is retained (“trapped”) within the film thereafter and provides the baseline upon which subsequent redox-driven solvation

changes occur. From an electrochemical perspective, the consequence of solvent within the film is the more facile electron/ion motion, manifested by a less positive anodic peak potential on subsequent redox cycling.

All the above applications of the EQCM to study redox polymer films have relied upon the TSM resonator as a gravimetric probe of surface populations and changes therein, that is, have been for acoustically thin films (see Sect. 2.7.2.2.1). The same was true for the inorganic films discussed in Sects. 2.7.3.2–2.7.3.6. However, the effect of solvent entry is very different for polymer films: in this case, the solvent can act as a plasticizer, ultimately resulting in the film becoming sufficiently softened so that it is acoustically deformed by the TSM resonator motion. In other words, one moves from the acoustically thin regime to the acoustically thick regime. Under these circumstances, the TSM resonator no longer responds predominantly to film mass; rather, the frequency response is viscoelastically controlled. In the context of film redox chemistry (cf. deposition), this means that the response provides insight into the polymer matrix – often perceived to be the “fixed” component of the system – rather than the mobile species (ions and solvent) that permeate it. Consequently, measurements on the same system in both the acoustically thin and thick regimes provide complementary insights into film dynamics.

Theoretical treatments for the acoustically thick film case have only recently been developed (see Sect. 2.7.2.1.2); thus this topic has not been reviewed previously. The field is at an interesting stage of development: the existence of viscoelastic phenomena in this context are generally accepted, the basic theoretical concepts have been delineated [18–20, 22, 23, 25],

and these analyses have been applied to a small number of experimental studies. We now consider some representative examples of redox polymer films that show these effects.

The TSM resonator frequency response shows a peak admittance (resonance), whose location on the frequency axis is determined by the capacitive and inductive elements of the system and whose magnitude is determined by the resistive elements in the system (in which these elements can, for example, be represented by the equivalent circuits in Fig. 2). An acoustically thin ("rigid") film will contribute nothing to the resistance of the system, that is, will not provide a mechanism for energy dissipation. Consequently, film population (mass) changes will be manifested by a translation at constant shape and amplitude of the resonance peak along the frequency axis; this translation will be described by the Sauerbrey equation (see Eq. 6 for parameterization in terms of the inductive element in the equivalent circuit of Fig. 2b). Contrastingly, an acoustically thick film will contribute additional resistance to the system; that is, internal friction will be a mechanism for energy dissipation. Consequently, film population or composition changes will be manifested by changes in shape and amplitude (as well as location) of the resonance peak. These contrasting variations in peak shape characteristics provide a diagnostic for film (non)rigidity.

PVF provides a good example of how the EQCM can be used to explore solvation processes via their influence over film viscoelastic properties. It also provides a representative example of progress in this area: an early study [133] of PVF electrodeposition clearly identified the presence of film viscoelastic phenomena, which were subsequently parameterized in terms of

equivalent circuit parameters [134], but only more recently have the tools to extract physically useful parameters (shear modulus components) been developed. The earlier discussions in this section on the use of the EQCM as a probe of mobile species transfers accompanying PVF redox chemistry in aqueous media were based on the notion of film rigidity; for the studies described, crystal impedance spectra support this idea. However, when exposed to the dichloromethane solutions typically used for the electroprecipitation of PVF films, the situation is very different. The basis of the film deposition strategy is that reduced PVF (PVF^0) is soluble in CH_2Cl_2 , but oxidized PVF (PVF^+) is not. However, although $\text{PVF}^+ \text{A}^-$ (where A^- represents the electrolyte anion, e.g. ClO_4^- or PF_6^-) is insoluble, it is relatively lyophilic, that is, highly solvated. The consequences of this are seen in crystal impedance spectra acquired dynamically during deposition, as shown in Fig. 20 [134]. Progressive deposition of polymer on the electrode surface results in an increase in inertial mass and thus the anticipated decrease in resonant frequency. However, there is also a dramatic decrease in admittance, which can be parameterized as an increase in the resistance in the motional arm of the equivalent circuit of Fig. 2(b). When the film is sufficiently thick, acoustic deformation can also be seen in aqueous electrolytes. This is nicely illustrated by a crystal impedance study of PVF break-in (for thicker films than those discussed above and in acid, rather than salt, media), in which the irreversibly incorporated solvent can lead to viscoelastic behavior [135].

The sensitivity of film viscoelastic properties to the ambient medium applies not only to the solvent but also to the electrolyte. This is illustrated for the case of $\text{poly}[\text{Os}(\text{bipy})_2\text{Cl}(\text{PVP})_{10}]$ (where

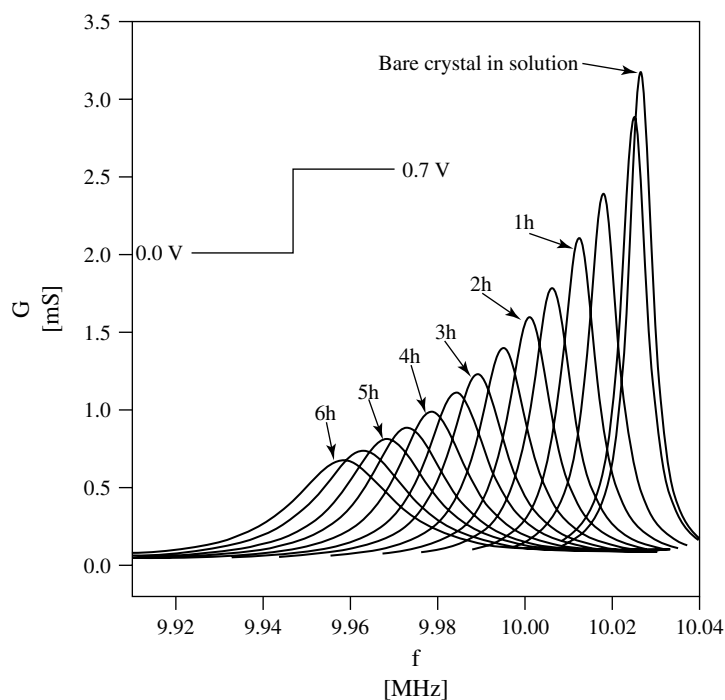


Fig. 20 Crystal admittance spectra acquired during the deposition of a PVF film. Electrode: Au (area = 0.23 cm^2) on 10-MHz AT-cut quartz crystal. Solution: PVF (2 mmol dm^{-3} in ferrocene units)/ 0.1 mol dm^{-3} TPA⁺ ClO₄⁻/CH₂Cl₂. At $t = 0$, potential stepped from 0.0 to 0.7 V. Numbers adjacent to spectra indicate deposition times. (Reproduced from Ref. [134] with permission from Elsevier.)

PVP represents polyvinylpyridine) films. These “OsPVP” films are rigid when exposed to aqueous sodium perchlorate solution, but viscoelastic when exposed to sodium *p*-toluenesulfonate (in certain concentrations) [136]. This is immediately discerned by inspection of the crystal impedance spectra for films in the two media [136], but it is a salutary warning that the variations of resonant frequency – as one would monitor in a “simple” EQCM experiment – show contrasting responses despite the essentially identical underlying physical phenomena. In perchlorate solution (and for solutions of moderate *p*-toluenesulfonate

concentration), the OsPVP-loaded TSM device resonant frequency decreases upon film oxidation, indicating a mass increase consequent upon anion and a little solvent entry (essentially as for PVF redox chemistry). Contrastingly, in concentrated *p*-toluenesulfonate solution, the Au/OsPVP-loaded TSM device resonant frequency increases upon film oxidation: a gravimetric interpretation would – inappropriately – suggest mobile species expulsion.

An additional driver of viscoelasticity changes is temperature, either for reasons based on free volume at constant film composition (see the brief discussion

of Williams–Landel–Ferry (WLF) theory in Sect. 2.7.3.7.2) or through temperature-dependent film composition (e.g. solvation). An example of the latter phenomenon is the behavior of poly(vinylferrocene-co-*N*-isopropylacrylamide) films as a function of temperature, illustrated in Fig. 21 [137]. There is a transition temperature (T_t) below which the film is highly solvated (“swollen”) and above which it is poorly solvated (“shrunk”). In these two solvation states, both film thermodynamics (formal potential) and dynamics (mobile species diffusion coefficients) are very different. For each redox state, the change in solvation state can be monitored through the change in TSM resonant

frequency and resistance with temperature (Fig. 21). Starting with the high temperature (collapsed, and thus rigid) form and progressively decreasing the temperature, entry of the solvent softens the film and results in an increase in energy dissipation and a decrease in resonant frequency; this is consistent with a shift from a rigid to a viscoelastic film. Further decrease of the temperature, and entry of more solvent, eventually results in a drop in resonant resistance and an increase in resonant frequency. Presumably, this is a consequence of decoupling the more distant regions of the film from the underlying resonator; in terms of the model of Bandey and coworkers [19], this might be interpreted as a shift

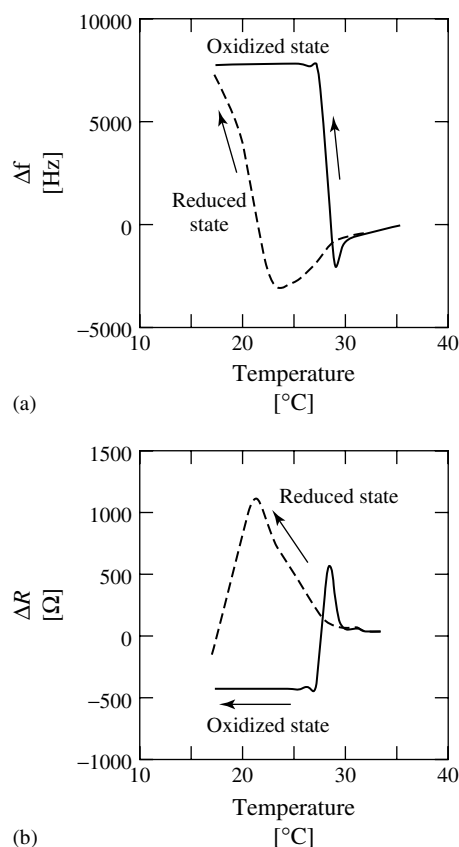


Fig. 21 Changes in resonant frequency (panel A) and resonant resistance (panel B) for a poly(vinylferrocene-co-*N*-isopropylacrylamide) film (VF :NIPAA = 1 : 13; dry film thickness ca. 5 μm) as a function of temperature, with the film maintained in the reduced state ($E = 0.0$ V; dashed line) and in the oxidized state ($E = 0.5$ V; full line). Electrode: Pt (area = 0.2 cm^2) on 9-MHz AT-cut quartz crystal. Solution: 0.1 mol dm^{-3} NaClO_4 . Temperature scanned from 35 to 10 $^\circ\text{C}$ over the course of ca. 1 h. (Reproduced from Ref. [137] with permission from the American Chemical Society.)

from a finite to a semi-infinite viscoelastic film, of which only a portion is sampled by the acoustic wave. As seen in Fig. 21, the transition temperatures are different for the two film redox states: $T_{t,Red} < T_{t,Ox}$. Thus, high temperatures ($T_{t,Red} < T_{t,Ox} < T$) result in the redox-driven interconversion of two rigid films (the simple case, interpretable in gravimetric terms), low temperatures ($T < T_{t,Red} < T_{t,Ox}$) result in the redox-driven interconversion of two viscoelastic films, and intermediate temperatures ($T_{t,Red} < T < T_{t,Ox}$) result in the redox-driven interconversion of a rigid (oxidized) and a viscoelastic (reduced) film. In summary, it is now possible to achieve, and to monitor through the EQCM, combined thermal and electrochemical control of film viscoelasticity.

2.7.3.7.2 Conducting Polymers The term “conducting polymer” is used here to refer to polymers with electronic charge delocalization along the spine of the polymer; the electroactive functionality is thus a delocalized system, contrasting with the discrete electroactive functionalities of “redox” polymers. From an applications viewpoint, the *raison d'être* for conducting polymers is that they show high (and controllable) electronic conductivity. It is not the purpose of this review to discuss these electronic aspects of conduction processes, but rather to explore two associated phenomena into which the EQCM brings insight. First, injection of electronic charge into a conducting polymer is intimately coupled to ion dynamics: injection or removal of a charge-compensating ion (“dopant”). Second, both the electronic motion along the polymer spine and the ionic motion through the polymer matrix are functions of the polymer dynamics: respectively, the rates at which the polymer strands achieve internal planarity

for π -delocalization and create space for accompanying ion motion. In the first case, the EQCM – as a gravimetric sensor – responds to ion transfer into/out of a conducting polymer film and in the second case – as a viscoelastic probe – it responds to polymer dynamics, exactly as described in Sect. 2.7.3.7.1 for redox polymers.

In the earlier electrochemical conducting polymer literature, the emphasis was on coupled electron/ion motion. Accordingly, within the EQCM literature in this area, the gravimetric capability to probe ion transfers, for example, distinguishing opposing anion versus cation motion, was predominant. This gravimetric approach was consistent with the simpler instrumentation in use at that time, but more recently, the capabilities of the EQCM with regard to characterizing viscoelastic phenomena have assumed a higher profile in this field.

Given that the generic issues are the same, it is not surprising that the EQCM has been applied to all the key types of materials in this category, including parent compounds and derivatives based on polypyrrole [32, 138–151], polyaniline [46, 57, 152–156], and polythiophene [41, 45, 157–162]. In this review, selected examples (from over 100 papers on polypyrroles, ca. 70 papers on polyanilines, and ca. 30 papers on polythiophenes) are chosen to provide specific illustrations of the types of phenomena observed and amenable to exploration using the EQCM.

An early example of the diagnostic value of the EQCM for exploring doping mechanisms of conducting polymer films is the study by Naoi and coworkers [138] of polypyrrole films prepared with anions of different sizes. In the case of films prepared with small anions, typified by perchlorate and tetrafluoroborate, electrochemical injection of positive charge

sites (oxidation) of the polymer had the anticipated predominant effect of intercalating anionic dopant ions (along with some solvent). At the other extreme, film deposition in the presence of very large polymeric anions, typified by polystyrenesulfonate and polyvinylsulfonate, resulted in the anion being trapped within the film in both polypyrrole oxidation states. Consequently, polypyrrole redox chemistry resulted in cation transfer, but of course in the opposite sense to the transfer of small anions. The use of intermediate-sized anions, represented by *p*-toluenesulfonate, was found to result in mixed redox-driven anion and cation transfers.

Qualitatively, this picture is relatively simple to understand in terms of the mobilities of the anions involved. Quantitatively, the picture is rather complex, particularly when the ion sizes are not too different. In the case of *p*-toluenesulfonate (with a small solution cation), anion transfer is the thermodynamically “preferred” process, but the greater mobility of a small cation makes the latter transfer kinetically more facile. Consequently, the dominant process is timescale dependent. Furthermore, as indicated in Sect. 2.7.3.7.1, the presence of “salt” within the film is electrolyte concentration dependent. Cations (coions) can only be ejected from the film if they are present in the first place, that is, if the film is nonpermselective. The complexities of this process have only recently been unraveled [149, 150] and the EQCM response (film composition) is dependent upon the experimental timescale (e.g. voltammetric scan rate), film history (first or subsequent redox cycle after equilibration), and electrolyte concentration. Film mass changes during redox cycling are nonmonotonic: on short timescales cation (sodium) transfer is the predominant mode of satisfying electroneutrality

and on long timescales *p*-toluenesulfonate transfer predominates.

At low electrolyte concentration (typically $c < 0.1 \text{ mol dm}^{-3}$), polypyrrole films in both redox states are permselective at equilibrium, that is, exclude “salt”, but the undoped film accumulates salt under kinetically controlled conditions [149]. Thus, the first redox cycle from an equilibrated reduced film must result in anion entry, but the accumulation of some cation (salt) during the redox cycle allows a mixed anion/cation mechanism to occur in a subsequent redox cycle. This is a consequence of the typical experimental timescale (10–100 s) being much shorter than the equilibration time for salt and/or solvent transfer (up to 1000 s); extended holding of the film at a given potential eventually restores equilibrium. When one moves to thermodynamically nonpermselective conditions ($c < 0.1 \text{ mol dm}^{-3}$), the situation becomes much more complicated [150] since the presence of both anions and cations in both redox states opens up all the mechanistic possibilities.

A significant difficulty in this type of problem is visualizing film compositional changes. This is facilitated by the use of the scheme-of-cubes [163], in which three orthogonal axes can be used to represent three elementary steps in film redox switching, here film redox state (electron/anion population), solvation state (solvent population), and permselectivity failure (salt population). The concept is illustrated for the case of polypyrrole films exposed to sodium *p*-toluenesulfonate solution in Fig. 22 [150], in which there is the added subtlety of representing cation transfer (a “fourth dimension”) as the algebraic sum of anion and salt transfers in opposite direction, that is, a diagonal transfer across a cube face. The attractions of this model are its greater

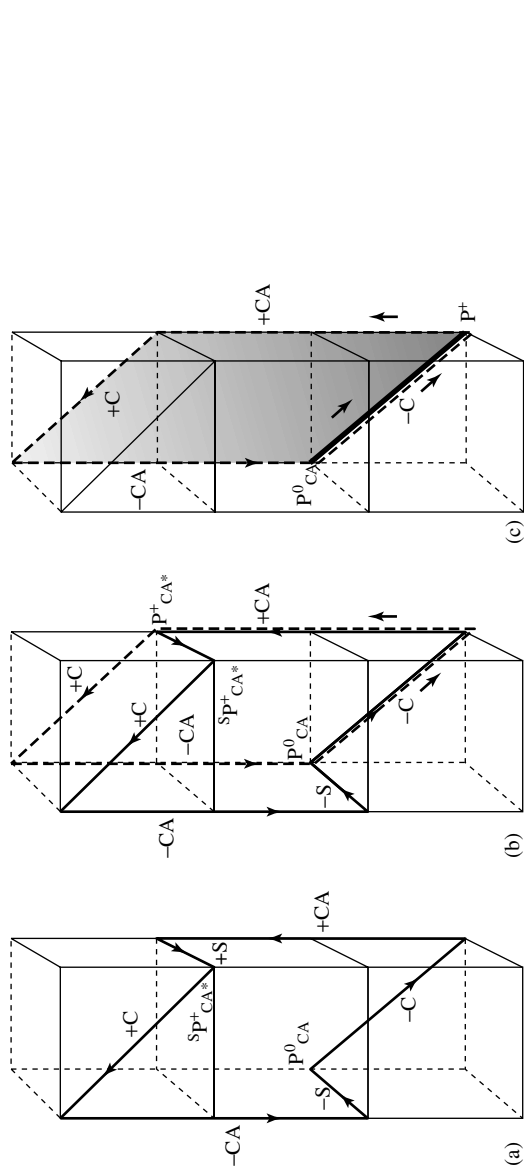


Fig. 22 Scheme-of-cubes [163] representations of mechanistic pathways for polypyrrole film redox switching on: (a) long; (b) intermediate; and (c) short timescale. The (x, y, z) -coordinate system represents (film redox state, solvent population, salt population): the left (right) hand cube faces represent reduced (oxidized) polymer; the rear (front) faces represent less (more) solvated film; lower (higher) faces represent lower (higher) salt population. Translations along the x, y, z -coordinates, respectively, represent E, C, and C' processes in a traditional EC-type model; E' is used to represent an electrochemical step, but with electroneutrality maintained by cation transfer (cf. anion transfer for an E-type elementary step). A, C, and S annotations, respectively, indicate transfers of anion, cation, and solvent species. The mechanisms indicated by the heavy lines are (a) E'C'C repetitively, (b) E'C'C in the first half-cycle, subsequently reducing to E'C', (c) E'C', progressively reducing to E' as the C' (salt transfer) step is progressively kinetically frozen on decreasing timescales. (Reproduced from Ref. [150] with permission from the Royal Society of Chemistry.)

palatability rather than long sequences of stoichiometric equations, and the fact that the “axes” are directly related to selected components of the EQCM frequency response (which may be directly or only indirectly related to the charge). The particular feature highlighted in Fig. 22 is the effect of decreasing the experimental timescale (here, by increasing voltammetric scan rate): this progressively “freezes out” each elementary step, starting with the slowest (here, solvent entry), then the next slowest (here, salt entry) until only the fastest step (here, field-driven coupled electron/cation transfers) remains. Since the effective timescale is also a function of film thickness, this provides a means of correlating data for different polymer coverages.

It will be clear from the foregoing paragraphs that the ion transfer satisfying electroneutrality upon redox switching of polypyrrole films can be manipulated by an appropriate choice of physical and chemical parameters. This has led to exploration of the ability to deliver ions from the film under electrochemical control. Obvious candidates of interest are ions with therapeutic activity: since these tend to be relatively large – but not polymeric – such systems are almost inevitably of the “mixed-transfer” type, so the EQCM has proved invaluable in studying them. Examples include salicylate [146, 147], naproxen [146], nicoside [146], chlorpromazine [141], and heparin [142]. Figure 23 [147] provides an example of the time-dependent competition between opposing anion and cation transfers, in this case with the additional help of the PBD experiment. The goal was to achieve dominant salicylate transfer, but the short time response is cation dominated, as graphically shown by the nonmonotonic mass transients and, using

this data, comparison of the observed probe beam response with that calculated for pure anion transfer.

The above applications were targeted on ion delivery. Complementary to this is targeted ion uptake. The EQCM has been used to explore polypyrrole as a material for facilitating removal from solution of heavy metal ions, such as lead, cadmium, cobalt, and nickel [140, 143].

At a more sophisticated instrumental level than monitoring EQCM resonant frequency at constant or linearly swept potential (as used for the studies discussed above) is the use of electrogravimetric impedance. The concept is essentially the same as conventional electrochemical impedance, except that the response function is the film mass (TSM device resonant frequency). This is a powerful diagnostic technique, firstly through the location of different species’ responses in different quadrants of the traditional complex plane plot and, secondly, through the facility to vary the timescale (see above) over a wide range. Using this approach, rather detailed kinetic and isotherm data were obtained for various anion and cation and water (solvent) transfers into/out of polypyrrole [32]. Interestingly, with the benefit of the detailed information obtainable from this ac technique, one cannot only confirm that all species participate (as deduced from detailed analysis of voltammetric data [150]), but can also extract quantitative kinetic parameters and further show that they are film charge-state dependent. Kwak and coworkers have used this approach to study ion dynamics of polypyrrole containing small (nitrate) [151] and large (poly(styrenesulfonate)) [144] anions. These measurements again provide additional detail and sophistication compared to the simpler voltammetric

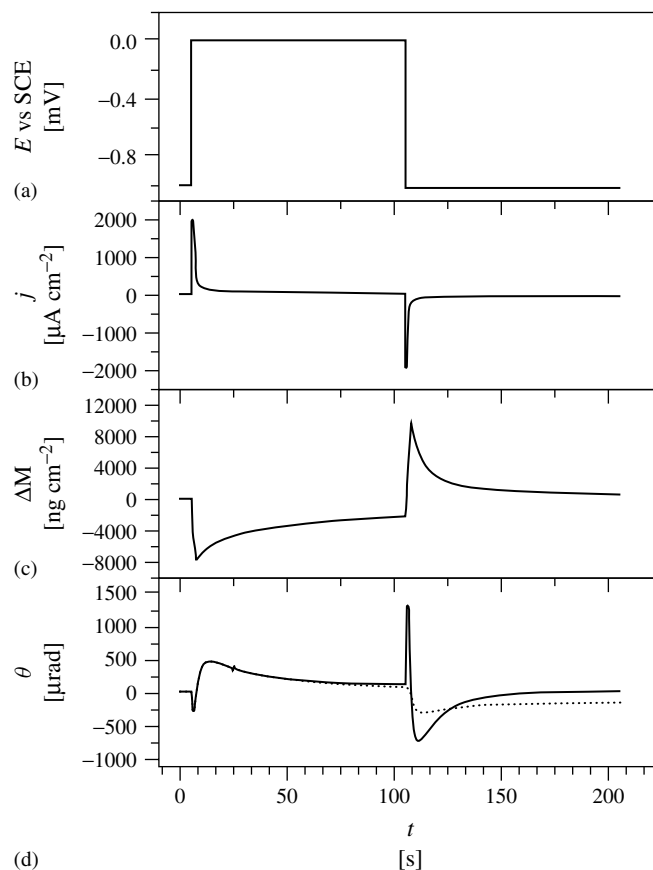


Fig. 23 Combined EQCM/PBD responses of a polypyrrole film to redox switching in sodium salicylate solution. Electrode: Au (area = 0.23 cm²) on 10-MHz AT-cut quartz crystal. Solution: aqueous 0.5 mol dm⁻³ sodium salicylate. Potential step program as shown in panel (a). Dotted line in panel (d) represents prediction, based on current trace of panel (b), of salicylate but no sodium transfer to satisfy electroneutrality. (Reproduced from Ref. [147] with permission from The Electrochemical Society.)

measurements, for example, revealing different types of charge site (“fast” and “slow”) and associated ion population dynamics [151]. Detailed modeling of voltammetric EQCM responses to ion transfers has also been used to deduce the presence of ions in two environments, labeled “free” and “bound” [145], whose dynamics are different.

In Sect. 2.7.3.7.1, appropriate control of polymer composition of a redox polymer (PVF) was shown to lead to the introduction of viscoelastic phenomena and to thermal sensitivity. For polypyrrole, deposition from micellar surfactant media (dodecylsulfate and dodecylbenzenesulfonate) also leads to changes in film morphology and viscoelastic behavior [139].

Thermal sensitivity, based on temperature-dependent swelling as monitored using the EQCM, resulted from deposition in the presence of such polymers as 2-acrylamido-2-methyl-1-propane sulfonic acid (AMPS) [148].

Polyaniline has proved an attractive electroactive material in part because of its stability in aqueous media and the possibility of (rapid) ionic charge transport by protons. Thus, most of the EQCM studies of polyaniline relate to film redox switching, with the now familiar goal of identifying the ion(s) responsible for maintaining electroneutrality and the extent of solvent transfer. Although transfer of protons, as the cations in this system, is difficult to detect on a gravimetric basis, the near absence of a rapid mass response associated with rapid charge transfer is a signature – albeit near invisible – of proton transfer (for those who read the Sherlock Holmes stories, it is like “the dog that did not bark in the night”). The situation is rather complex, since there are two redox processes whose behaviors are dependent upon pH, so one must be careful to restrict conclusions to the conditions under which they were deduced. In aqueous perchloric acid medium, charge transfer in the first oxidation process was found to be compensated by anion injection and in the second oxidation process by cation (proton) ejection, in each case accompanied by some solvent transfer [152]. A recent ac electrogravimetric study [156] of polyaniline redox switching in various aqueous acid media shows how far this technique has now advanced, by direct comparison of the rather featureless mass–potential responses to cyclic voltage scans with the complex plane representation of the electrogravimetric-transfer function, $(\Delta m/\Delta E)(\omega)$. In the latter case, one sees features (semicircles)

that respond to film thickness, DC potential (film charge state), and electrolyte composition. By implementing the partial electrogravimetric-transfer function approach (see Eq. 12), this leads to isotherm data for individual mobile species as functions of potential. This is a clear example of detailed analysis of high-quality data providing a rich source of mechanistic information.

The deposition of polyaniline has also been studied using a rather elegant combination of the EQCM with ellipsometry, as shown in Fig. 24 [57]. The data compare the simultaneously determined gravimetric (Δf) and optical (thickness) data during the electrochemical deposition of polyaniline from an aqueous solution of the monomer. Since, in the acoustically thin regime, $\Delta f \propto \Delta M$ (via the Sauerbrey equation), the instantaneous slope of the plot provides the film density. The linearity of the plot shown clearly signals constant composition (polymer and solvent volume fractions) with film thickness and provides an alternative route to separating the areal density ($\Delta M/\text{g cm}^{-2}$) into the volumetric film density and thickness components, cf. the method outlined in Sect. 2.7.2.2.2.

One of the other attractions of polyaniline is the ease of preparing (or even commercial availability) of substituted derivatives. The simplest example is the methyl derivative poly(*o*-toluidine), for which the EQCM in conjunction with PBD has been used to obtain the individual anion, cation, and solvent fluxes/film populations. By comparing the EQCM frequency responses to a potential sweep [46] and a potential step [154], it is possible to show that the competing ion transfers have intrinsic potential and timescale dependencies; the contributions of the protons and perchlorate ions are also pH dependent. One interesting feature is that anion

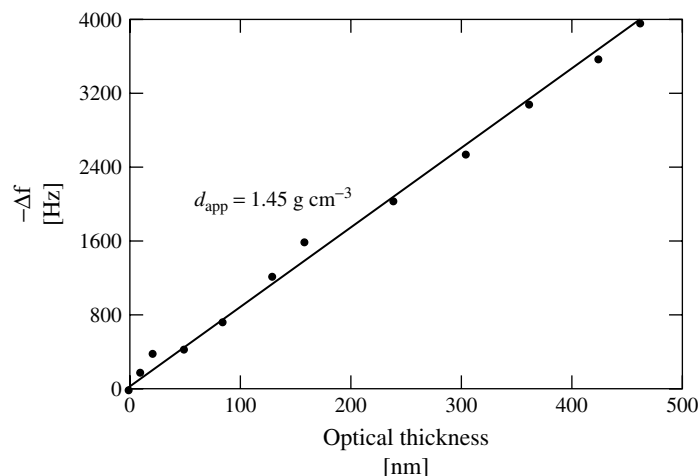


Fig. 24 Variation of EQCM resonant frequency with simultaneously ellipsometrically determined film thickness during deposition of polyaniline. Electrode: Pt on 5-MHz AT-cut quartz crystal. Solution: 1 mol dm^{-3} aniline/ 2 mol dm^{-3} HCl. Galvanostatic control: $i = 77 \mu\text{A cm}^{-2}$. Optical measurements at $\lambda = 550 \text{ nm}$. (Reproduced from Ref. [57] with permission from Elsevier.)

transfer is accompanied by solvent transfer in the opposite direction, suggesting that in this case film rigidity imposes a volume constraint. Another derivative of polyaniline, this time with a fused aromatic ring, is poly(1,8-diaminonaphthalene) [153]. In this case, the EQCM was used to show how amine groups on the polymer can be used to extract Hg^{2+} ions from solution; detailed considerations of the data suggest a 1:1 monomer:metal ion stoichiometry. A rather more exotic derivative is poly(aniline-co-*N*-propane sulfonic acid aniline), a so-called *self-doped* system in which the parent aniline and sulfonic acid aniline comonomers carry opposite charges [155]. EQCM and supporting crystal impedance measurements were obtained for such films exposed to propylene carbonate and acetonitrile solutions, in which the electrolyte anion and cation sizes were varied. In all cases, a mixed ion-transfer process was observed:

with the larger cations, the contribution to electroneutrality maintenance (transport number) decreased with ionic radius.

In most cases, stability and oxidation potential issues mean that polythiophenes are prepared, studied, and used in non-aqueous media, and the influence of the solvent can be significant. The extent of solvent swelling is determined by polymer-solvent interactions, which can be manipulated both by choice of solvent and introduction of substituents, here in the 3- and 4-positions. Electropolymerization of alkyl-substituted thiophenes provides good examples of the effects one can observe. EQCM (with PBD) measurements of potentiodynamic deposition from acetonitrile:benzonitrile (4:1) of poly(didodecylterthiophene) (with the substituents in the 3',4'- or 3,3''-positions) showed that film deposition occurred primarily during the reductive half-cycle, in the form of short chain oligomers of the

neutral polymer [45, 157]. These studies were focused on the early stages of film deposition, that is, nucleation, so a gravimetric interpretation was appropriate, in contrast to other studies discussed below.

In terms of ion and solvent transfers, polythiophenes provide some of the more complex examples of acoustic wave behavior and thus more sophisticated examples of data interpretation. In the simpler, gravimetric regime early measurements of ion, solvent, and cation (“salt”) transfer at acoustically thin poly(2,2'-bithiophene) [33] films have been shown to be typical; for example, the presence of salt in reduced poly(1,4-ethylenedioxythiophene) films is implied by a substantial contribution from cation expulsion during polymer oxidation [159].

A more complicated scenario is presented by an electroactive bilayer, in which a poly(2,2'-bithiophene) (PBT) film is overlaid with a PXV redox polymer film [162]. Individually, the two layers (here, both acoustically thin) behave exactly as one would expect: the PBT film undergoes predominant anion (cation) exchange upon *p*-doping (*n*-doping), albeit with some coion participation, and the PXV film is a cation exchanger. The difference when one moves to the bilayer is that the usual ion-transfer requirements of the inner PBT layer are not generally consistent with the permselective properties of the outer PXV layer. The result is a transient accumulation of electrolyte in the film upon redox cycling. In this case, the EQCM is able to reveal the mechanism of bilayer redox switching, by using gravimetrically determined ion transfer – in conjunction with the electroneutrality condition – as the marker for locating the destination of injected electronic charge. Variation of timescale (potential scan rate) shows,

Fig. 25 [162], that complete redox conversion of either layer does not occur before commencement of redox conversion of the other layer. Rather, minor conversion of the inner layer to its conducting state occurs first (signaled by cation transfer to balance PBT *n*-doping; see mass flux at high scan rate), opening up conducting pathways to completely convert the outer layer (signaled by anion transfer to balance PXV redox conversion; see opposite mass flux at slow scan rate). This ability of the EQCM to diagnose ion-transfer mechanisms in bilayers has been further demonstrated for [polypyrrole – poly(styrenesulfonate)]/poly(3-octylthiophene) [164] and [polypyrrole – poly(styrenesulfonate)]/poly(vinylferrocene) [165] systems.

As described in Sect. 2.7.2.1, there is no sharp distinction between “rigid” and “nonrigid” behavior, but rather a continuous variation between films that are acoustically thin ($h_f < \delta$) and acoustically thick ($h_f \geq \delta$). Since the decay length, δ , is a function of shear modulus and thereby of film solvent content, medium effects are critical. The discussion of polythiophene systems above was deliberately restricted to examples of acoustically thin films, but we now move to a consideration of acoustically thick polythiophene-based films.

The transition between the acoustically thin and thick situations is illustrated by the redox-switching (doping) behavior of poly(3-methylthiophene) films exposed to acetonitrile [158]. At low coverages, parameterized through deposition charge ($Q_{\text{dep}} \leq 12 \text{ mC cm}^{-2}$), the films are acoustically thin and the resonator frequency response can be interpreted in gravimetric terms Δf converted to ΔM , according to the Sauerbrey equation). In this particular case, the film was found to contain two different regions (“zones”)

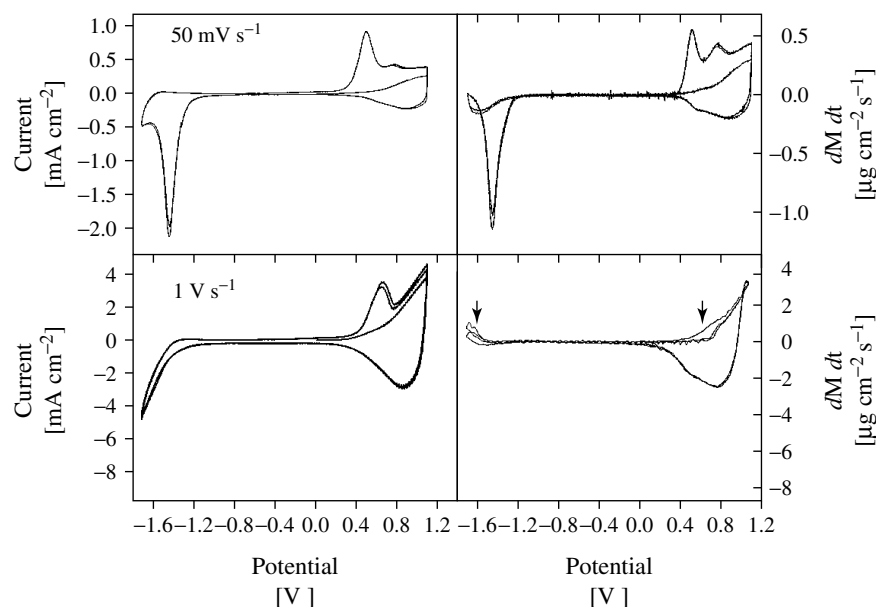


Fig. 25 Current (left panels) and mass flux (right panels) responses for a polybithiophene/polyxylylviologen (PBT/PXV) bilayer. Electrode: Au (area = 0.23 cm^2) on 10-MHz AT-cut quartz crystal. Solution: 1 mol dm^{-3} tetraethylammonium perchlorate/acetonitrile. Voltammetric experiment, scan rate 50 mV s^{-1} (upper panels), 1 V s^{-1} (lower panels). (Reproduced from Ref. [162] with permission from the Royal Society of Chemistry.)

with different solvation characteristics and ion dynamics. For somewhat thicker films (Q_{dep} ca. $30\text{--}50 \text{ mC cm}^{-2}$), viscoelastic characteristics were visible in the crystal admittance spectra, but not dramatic. In this regime, a gravimetric interpretation is inappropriate, but modeling in terms of viscoelastic parameters is inaccurate, since the acoustic deformation is not large. Much thicker films ($Q_{\text{dep}} > 80 \text{ mC cm}^{-2}$) showed dramatic viscoelastic effects, from which shear moduli could be extracted.

A similar pattern can be expected for other systems, such as the more elaborate trimeric fused ring dithioenothiophene-based polymers [160]. Admittance spectra for films of these materials deposited with $5 < Q_{\text{dep}}/\text{mC cm}^{-2} < 120$ showed the dramatic effects of film viscoelasticity

and were parameterized through equivalent circuit parameters for the BvD model of Fig. 2(b).

The absolute value of film thickness at which one sees the shift from acoustically thin to thick behavior will depend significantly on the polymer itself, the solvent, and other physicochemical parameters, notably temperature, applied potential, and timescale. An example of the importance of the latter two control parameters is provided by a study of poly(3-hexylthiophene) films exposed to propylene carbonate [161]. Storage and loss moduli, derived from the admittance spectra, for a film held at different applied potentials (effectively, controlling charge) are shown in Fig. 26 [161]. Immediate observations are that the film is

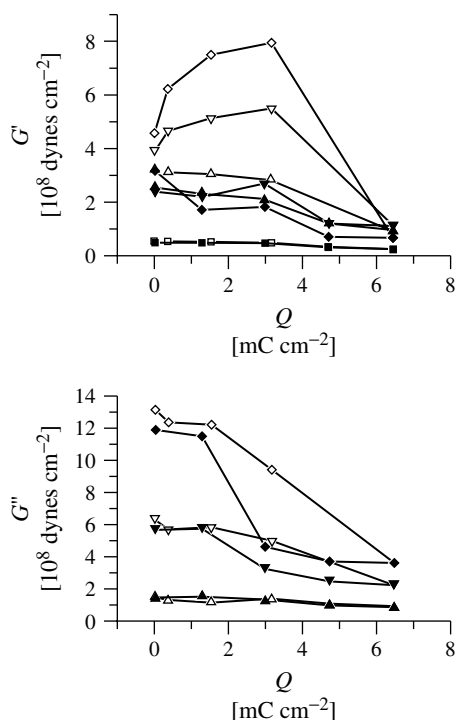


Fig. 26 Viscoelastic properties of electropolymerized poly(3-hexylthiophene). Fitted (a) storage modulus (G') and (b) loss modulus (G'') as functions of charge and frequency. Frequency dependence obtained by use of harmonics of polished 10 MHz fundamental Au-coated TSM resonator; open (filled) symbols for increasing (decreasing) potential measurement sequence (lines are merely a guide to the eye). Frequency (MHz): 10 (\square , \blacksquare), 30 (\triangle , \blacktriangle), 50 (∇ , \blacktriangledown), 70 (\diamond , \blacklozenge). Electrode: Au (area = 0.23 cm^2) on polished 10-MHz AT-cut quartz crystal. Solution: 0.1 mol dm^{-3} tetraethylammonium hexafluorophosphate/propylene carbonate. (Reproduced from Ref. [161] with permission from the Royal Society of Chemistry.)

in the middle of the viscoelastic range ($G \sim 10^8 \text{ dyn cm}^{-2}$) and is lossy ($G' < G''$). Although these were anticipated to represent equilibrium measurements, by holding the applied potential at a series of constant values for times on the order of minutes, there is clearly hysteresis. This is not a matter of slow charge (coupled electron/ion) transport, since the data are plotted as functions of resultant electrochemical charge (obtained by integrating the current response) not of applied potential. The conclusion reached was that this is a consequence of slow solvent transfer. Thus, mobile species dynamics – which one commonly monitors directly through gravimetric experiments – are here observed indirectly through polymer dynamics in a viscoelastic experiment.

Figure 26 also shows shear modulus data as functions of frequency, obtained

by making admittance measurements at the fundamental frequency (10 MHz) and higher harmonics (30, 50, and 70 MHz). Over this frequency (timescale) range, the shear modulus components vary by approximately an order of magnitude. In polymer science, it is common to use “spring and dashpot” mechanical models to explain the frequency dependence of viscoelastic parameters. The exchange between the polymer and solution of ions and solvent might be expected to be associated, respectively, with electrostatic stiffening and plasticization effects. In the case of poly(3-hexylthiophene) films [41, 161], the increase in G' with frequency is qualitatively consistent with a Maxwell model (spring and dashpot in series) and inconsistent with a Voigt model (spring and dashpot in parallel). Although neither model can quantitatively describe the

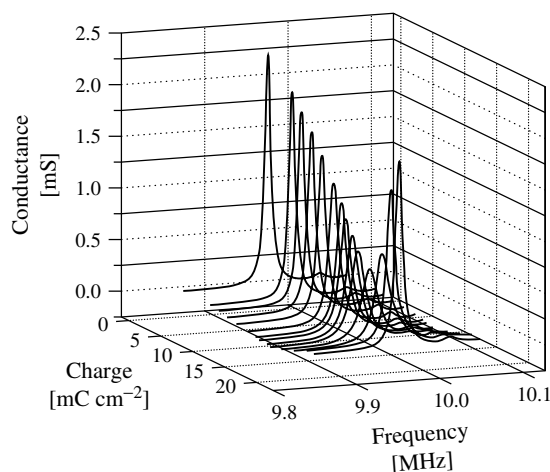
observed responses, this avenue of enquiry is at an early stage. Certainly, TSM resonators can provide viscoelastic parameters in a frequency range inaccessible to bulk mechanical techniques, which typically operate in the sub-kHz range.

Although temperature has not been systematically explored as a variable in this context, this will unquestionably prove a fruitful future avenue of enquiry and the associated effects might be rationalized in terms of the concept of time-temperature superposition and the WLF model that are commonly used in polymer science.

In Sect. 2.7.2.1.2, the phenomenon of film resonance was discussed. In this special situation, the film thickness corresponds to one quarter of the acoustic wavelength, that is, the acoustic phase shift defined by Eq. (11) has the numerical value $\phi = \pi/2$. For a film of given shear modulus, progressive increase in thickness will eventually result in this condition being satisfied. This phenomenon is illustrated in Fig. 27 [41] for a poly(3-hexylthiophene) film as a function of the polymerization charge during deposition. As can be seen, the resonant frequency transiently moves sharply upwards and the peak amplitude

increases with increasing loading of the TSM resonator; once resonance is passed, the anticipated pattern of response is resumed. In enquiring why more observations of film resonance have not been reported, three corollaries are highlighted. First, an additional requirement is that the reflectivity coefficient for the acoustic wave at the film/solution interface must be close to unity. This corresponds to a sharp gradient of acoustic properties, that is, a sharp polymer/solution interface, a condition that may commonly not be fulfilled. Second, if the polymer is lossy, attenuation of the acoustic wave in passage twice across the required film thickness may be too great for a significant effect. Third, there is an interesting effect in terms of the operating frequency. In the case of poly(3-hexylthiophene), the film thickness required to achieve film resonance was essentially independent of frequency (comparing data for the fundamental and third harmonic, 10 and 30 MHz, respectively). Inspection of Eq. (11) shows that this requires a frequency-dependent shear modulus (in the simplest situation, increasing with the square of frequency), consistent with a viscoelastic polymer in

Fig. 27 Crystal admittance spectra as a function of charge density, acquired dynamically during potentiodynamic electropolymerization of a poly(3-hexylthiophene) film. Solution: 3.7 mmol dm⁻³ 3-hexylthiophene/0.1 mol dm⁻³ tetraethylammonium hexafluorophosphate/propylene carbonate. Electrode: Au (area = 0.23 cm²) on polished 10-MHz AT-cut quartz crystal. Spectra acquired at $E = 0.4$ V following each potential cycle. (Reproduced from Ref. [41] with permission from the American Chemical Society.)



the transition region between rubbery and glassy regimes.

Several other polymers with delocalized systems have been studied. One example is poly(*p*-phenylenevinylene), for which the EQCM was used to study ion motion during *n*-doping [166]. The case of an electropolymerized nickel-salen-based complex, poly[Ni(saltMe)], studied using the combined EQCM/PBD technique, is rather interesting in terms of the chemistry involved [47]. Although one might expect to classify the material as a “metal complex” (and indeed the monomer behaves in this fashion), spectroscopic studies show the polymer redox chemistry to be ligand-, rather than metal-based, and to involve a delocalized system, that is, it should be classed as a “conducting polymer”. Crystal impedance spectra showed the polymer films to behave rigidly, so a gravimetric interpretation of EQCM data could be used; from this it was possible to demonstrate dominance of anion (cf. cation) transfer in maintaining electroneutrality during redox switching and to quantify the associated transfer of solvent. Film resonance has been observed in crystal admittance spectra of poly(carbazole) [42]. In this case, the film thickness satisfying the resonance condition was inversely related to frequency (comparing data for the fundamental and the third harmonic). According to Eq. (11), this is consistent with a frequency-independent shear modulus, contrasting with the behavior of poly-(3-hexylthiophene).

2.7.3.7.3 Insulating Polymers Electrochemical polymerization has been used to generate insulating polymeric coatings on electrode surfaces, usually for the purposes of surface protection. In these cases, there can be no use of electrochemistry to characterize the deposited material

per se – at best, one can only determine film performance electrochemically using solution redox probes to seek out its imperfections. Consequently, the determination of polymer coverage using a gravimetric probe is attractive. The EQCM has been used to study a number of acrylate-based insulating films, such as acrylonitrile [167], methylmethacrylate [167], methacrylonitrile [168], and *N*-vinyl-2-pyrrolidone [168]. The EQCM was used to explore the efficiency of deposition during the polymerization process [168] and, postdeposition, issues of film solubility [167].

2.7.3.8 Other Organic Materials

The redox chemistry of solid-state lattices based on TCNQ, prepared by oxidizing crystallites of 9-aminoacridinium (TCNQ)₂ exposed to calcium or potassium acetate solutions, has been studied using the EQCM [169]. EQCM frequency responses to redox conversion of the TCNQ^{0/-} and TCNQ^{-/2-} states were interpreted in terms of permselective cation transfer of CaOAc⁺ and K(H₂O)₄⁺. The first reduction half-cycle was associated with an anomalously large frequency change, suggesting a one-off solvation process or structural change. Chronoamperometric experiments (associated with shorter timescales) suggested that oxidation proceeds by anion insertion from the electrolyte, then diffusional loss of neutral electrolyte from the solid-state lattice. Although the physical nature of the film is rather different from a redox polymer or a metal oxide film, the parallels in behavior are clear.

There has been considerable interest in the coupling to electrode surfaces of DNA which, as a large electroinactive molecule, is amenable to gravimetric detection by the QCM. Following immobilization onto Au electrodes, electrochemically triggered

release of DNA has been monitored using the EQCM [170]; the longer-term goal is on-demand gene delivery. Oligonucleotides have also been immobilized within polypyrrole films on electrode surfaces, for example, by incorporating an electropolymerizable pyrrole functionality onto the oligonucleotide [171–173]. (Although one could categorize these as “polypyrrole” systems, the entity of interest is the oligonucleotide, and the primary role of the polypyrrole is the provision of an immobilization matrix.) These studies are at a relatively early stage, but offer the promise of sophisticated biosensing devices.

2.7.3.9 Miscellaneous

The phenomenon of oscillating reactions is widely recognized in chemistry. In those cases in which a surface-bound species or the surface itself is involved in the complex sequence of steps, the EQCM offers the prospect of additional information. An example of this is the role of an oxide layer in the oxidation of formaldehyde at Pt and Rh [174]. Similarly, in the oxidation of 2-propanol at Pt electrodes, it was found that the oscillations (in potential and mass, at constant current) increased in amplitude until the positive extreme of the potential excursion reached a value consistent with PtOH and/or PtO formation [175]. Oscillations in mass at open-circuit potential were also observed during the dissolution of Cu in sulfate media when the solution concentration of Cu^{2+} was sufficiently high ($c > 0.045 \text{ mol dm}^{-3}$) [176], although in this case the potential excursions were such that oxide formation/dissolution was ruled out.

With the notable exception of corrosion, most of the processes and systems discussed in this review occur essentially uniformly across the electrode surface.

Since the QCM sensitivity is spatially variant – maximum at the center and falling to effectively zero at the edges of the exciting electrode – this means that there is no error incurred by using the usual spatially averaged sensitivity function of frequency to mass change (the Sauerbrey equation). Another exception to this lateral uniformity is the case of heterogeneous bubble evolution. Simplistically, the concept is that nucleation of a bubble at the interface results in the replacement of fluid with gas, so that the coupling of the ambient medium to the resonator is locally changed. Since the characteristic size of a bubble (typically in excess of $1 \mu\text{m}$) is likely to be much larger than the decay length of the acoustic wave in the fluid (typically $0.2 \mu\text{m}$, for a 10-MHz resonator in aqueous solution), there is effectively complete (local) decoupling of the resonator and fluid. This situation has been studied for electrolytically generated hydrogen [177–179] and chlorine [179]. In the latter case, the situation is complicated by the formation/removal of oxide layers and electrode dissolution, to both of which the EQCM responds. In addition to the lateral sensitivity issue, that is, the fact that the frequency response is dependent upon the spatial location of the bubble, the QCM response is dependent upon interfacial energetics, which determine the contact angle and thus the bubble shape. Although this case has not subsequently been explored in great detail, spectral analysis of the frequency response was shown to be a powerful tool in extracting kinetic information [178].

2.7.4

Conclusion and Future Prospects

The EQCM is now firmly established as a generic probe of interfacial processes, providing valuable information for rational

interfacial design. Integration into the electrochemist's armory of techniques has in some cases gone as far as simultaneous utilization with other interfacial probes, such as ellipsometry, probe beam deflection, and visible spectroscopy. Significant attributes include *in situ* capability, rapid (down to millisecond) data acquisition, high (submonolayer) sensitivity, generality of detection, and known sensitivity. According to whether a surface film is acoustically thin or thick, the frequency response provides gravimetric or viscoelastic information; in many cases, control of coverage can be used to explore both regimes.

In the case of acoustically thin films, the EQCM frequency response can be simply interpreted in terms of film mass changes, and thus surface population changes. This has been widely exploited for deposition and dissolution processes, and for redox-driven exchange of ions and neutral species (predominantly solvent) between a surface film and its bathing solution. In the case of ion transfer(s), required to maintain electroneutrality within the film, the "simple" permselective result of purely counterion (no coion) transfer is commonly observed, but is by no means to be considered as the "expected" result. At the higher electrolyte concentrations typical of electrochemical experiments, permselectivity failure occurs and "salt" (electrically equivalent amounts of counter and coion) within the film provides a mechanism for transfer of either ion. Additionally, when the ion mobilities are very different, for example, as a consequence of different size and/or charge number, it may be kinetically expedient for the faster moving ion to transfer on short timescales and subsequent transfer of "salt" to restore the equilibrium populations somewhat later, following completion of charge transfer.

As a consequence of this, mixed ion transfer is a likely scenario. Furthermore, the relative amounts of anion and cation transferred have been shown for a number of systems to be dependent upon potential (film charge state). Hence, the assumption that the overall (end-to-end) compositional change is a good representation of events at intermediate redox composition may be rather poor. This has important consequences for many applications of modified electrodes, for example, in charge storage (batteries and supercapacitors), optical displays, and controlled delivery/uptake. Recent developments in both experimental and interpretational methodologies offer the prospects of significant advances here. Exploration of the time (frequency) domain through potential step and ac electrogravimetry methods can be significantly superior to the most commonly used electrochemical control function, a linear (cyclic) potential scan.

Despite the undoubted progress in data acquisition, it is slightly disappointing that the interpretation of EQCM mass changes is commonly only qualitative, for example, determining whether cation or anion transfer predominates in a film redox-switching experiment. Since conversion of the measured quantity (frequency change) to mass change is trivial via the Sauerbrey equation, and since the sensitivity function for conversion to a population change (molar mass) is known *a priori*, this lack of interpretation is surprising. Also, it is generally more common for the mass (interpreted as population) change to be correlated with the potential, but by far the more informative correlation is with charge, analogous to Faraday's classical experiment, since this is the route to specification. Adoption of recent progress in data analysis, for example, correlating fluxes of

solvent and ions (derived from differential mass change and charge data), promises considerable new mechanistic insights.

From the origins of the EQCM technique, the notion that it can provide solvent population changes in surface films has been widely appreciated. With the quantitative approaches now available, this offers two significant areas of application. First, in a rather classical vein, the solvent population change – at constant activity, defined by the bathing solution – can provide information on solvent activity coefficient changes within the film, for example, a polymer. While such effects have been generally appreciated from the ion-exchange literature, acquisition of data has been nontrivial. Second, since the solvent can function as a plasticizer for some materials (notably polymers), correlation of solvation population changes with interfacial rheology opens previously unexplored avenues of study.

This leads to what is undoubtedly the emerging area of study – viscoelastic phenomena. A decade ago, viscoelasticity represented the “unknown” (in this context) to which anomalies were frequently – though perhaps not always correctly – attributed. This is no longer the case. Basic theoretical models are now well established; these may be expressed through either electrically or mechanically based representations, ultimately linked through the piezoelectric effect. These models provide the qualitative means to distinguish acoustically thin (“rigid”) and acoustically thick films and the quantitative means to extract materials properties. In the latter context, the issue of data fitting has received attention and reliable means now exist to extract film shear moduli from the resonator frequency response. The phenomenon of film resonance – well known for films exposed to gaseous

media – has also been reported and described; this is a phenomenon that should receive greater consideration in future.

Most of the viscoelastic studies to date have involved steady state impedance measurements. More recently, transient measurements have been reported; these appear to offer some advantages over steady state measurements. Unquestionably, comparison of the two methods – now united by a general theory – should be pursued.

Many applications of the QCM involve soft matter and exploitation of the technique in a biological context, for example, involving DNA, will undoubtedly highlight this aspect. This will heighten the need to develop and test models for viscoelastic behavior. Polymer science provides a rich source of such information, but generally developed in the context of bulk materials and explored by rheological experiments at relatively low frequency (<1 kHz). The EQCM is invariably applied in the context of thin films (microns, not millimeters) and provides access to high frequencies (>1 MHz). It therefore offers a unique opportunity to determine materials properties and the applicability of various standard models and concepts in polymer science (e.g. Maxwell and Voigt “spring and dashpot” models, the WLF theory, and time-temperature superposition) should be explored.

Acknowledgments

The author wishes to acknowledge the contributions of Prof. S. Bruckenstein and Dr. S. J. Martin as senior collaborators over an extended period of time, the many other coworkers who have contributed greatly to progress in this field, and to those authors who kindly provided illustrative material for this review.

References

1. D. S. Ballantine, R. M. White, S. J. Martin et al., *Acoustic Wave Sensors*, Academic Press, San Diego, Calif., 1997.
2. D. A. Buttry in *Electroanalytical Chemistry* (Ed.: A. J. Bard), Marcel Dekker, New York, 1991, pp. 1–85, Vol. 13.
3. D. A. Buttry, M. D. Ward, *Chem. Rev.* **1992**, 92, 1355–1379.
4. R. Schumacher, *Angew. Chem., Int. Ed. Engl.* **1990**, 29, 329–343.
5. S. Bruckenstein, A. R. Hillman in *Handbook of Surface Imaging and Visualization* (Ed.: A. T. Hubbard), CRC Press, Boca Raton, Fla., 1995, pp. 101–113.
6. M. Hepel in *Interfacial Electrochemistry* (Ed.: A. Wieckowski), Marcel Dekker, New York, 1999, pp. 599–630.
7. *Faraday Discuss.* **1997**, 107.
8. A. R. Hillman, *Electrochim. Acta* **2000**, 45(22–23).
9. Acoustic Wave Sensor Workshops.
10. The Electrochemical Society, *Acoustic Wave Sensor Symposia*, Electrochemical Society Meetings.
11. M. Urbakh, E. Gileadi in *Encyclopedia of Electrochemistry* (Eds.: A. J. Bard, M. Stratmann), Wiley-VCH, Weinheim, Germany, 2002, Vol. 3.
12. C. Lu, A. W. Czanderna, (Eds.), *Applications of Piezoelectric Quartz Crystal Microbalances*, Elsevier, Amsterdam, 1984.
13. K. K. Kanazawa, *Faraday Discuss.* **1997**, 107, 77–90.
14. G. Sauerbrey, *Z. Phys.* **1959**, 155, 202–222.
15. T. Nomura, M. Iijima, *Anal. Chim. Acta* **1981**, 131, 97–102.
16. S. Bruckenstein, M. Shay, *Electrochim. Acta* **1985**, 30, 1295–1300.
17. K. K. Kanazawa, J. G. Gordon, *Anal. Chim. Acta* **1985**, 175, 99–105.
18. V. E. Granstaff, S. J. Martin, *J. Appl. Phys.* **1994**, 75, 1319–1329.
19. H. L. Bandey, S. J. Martin, R. W. Cernosek et al., *Anal. Chem.* **1999**, 71, 2205–2214.
20. D. M. Soares, M. A. Tenan, S. Wasle, *Electrochim. Acta* **1998**, 44, 263–268.
21. M. A. Tenan, D. M. Soares, *Braz. J. Phys.* **1998**, 28, 405–412.
22. R. A. Etchenique, E. J. Calvo, *Electrochem. Commun.* **1999**, 1, 167–170.
23. H. L. Bandey, A. R. Hillman, M. J. Brown et al., *Faraday Discuss.* **1997**, 107, 105–121.
24. A. R. Hillman, A. Jackson, S. J. Martin, *Anal. Chem.* **2001**, 73, 540–549.
25. S. J. Martin, H. L. Bandey, R. W. Cernosek et al., *Anal. Chem.* **2000**, 72, 141–149.
26. E. Hwang, Y. Lim, *Bull. Korean Chem. Soc.* **1996**, 17, 39–42.
27. C. Dusemund, G. Schwitzgebel, *Ber. Bunsen-Ges. Phys. Chem. Chem. Phys.* **1991**, 95, 1543–1546.
28. Y. Ratieuville, P. Viers, J. Alexandre et al., *Electrochem. Commun.* **2000**, 2, 839–844.
29. S. Bruckenstein, M. Michalski, A. Fensore et al., *Anal. Chem.* **1994**, 66, 1847–1852.
30. C. Gabrielli, M. Keddad, N. Nadi et al., *Electrochim. Acta* **1999**, 44, 2095–2103.
31. S. Bourkane, C. Gabrielli, M. Keddad, *Electrochim. Acta* **1989**, 34, 1081–1092.
32. C. Gabrielli, J. J. Garcia-Jareno, H. Perrot, *Electrochim. Acta* **2001**, 46, 4095–4103.
33. A. R. Hillman, M. J. Swann, S. Bruckenstein, *J. Phys. Chem.* **1991**, 95, 3271–3277.
34. A. R. Hillman, D. C. Loveday, S. Bruckenstein, *J. Electroanal. Chem.* **1991**, 300, 67–83.
35. Z. X. Lin, C. M. Yip, I. S. Joseph et al., *Anal. Chem.* **1993**, 65, 1546–1551.
36. S. Bruckenstein, A. Fensore, Z. F. Li et al., *J. Electroanal. Chem.* **1994**, 370, 189–195.
37. M. Urbakh, L. Daikhin, *Phys. Rev. B* **1994**, 49, 4866–4870.
38. S. J. Geelhood, C. W. Frank, K. Kanazawa, *J. Electrochem. Soc.* **2002**, 149, H33–H38.
39. E. J. Calvo, R. Etchenique, P. N. Bartlett et al., *Faraday Discuss.* **1997**, 107, 141–157.
40. E. J. Calvo, R. Etchenique, *J. Phys. Chem. B* **1999**, 103, 8944–8950.
41. A. R. Hillman, M. J. Brown, S. J. Martin, *J. Am. Chem. Soc.* **1998**, 120, 12 968, 12 969.
42. R. Saraswathi, A. R. Hillman, S. J. Martin, *J. Electroanal. Chem.* **1999**, 460, 267–272.
43. M. J. Henderson, A. R. Hillman, E. Vieil et al., *J. Electroanal. Chem.* **1998**, 458, 241–248.
44. M. J. Henderson, A. R. Hillman, E. Vieil, *J. Electroanal. Chem.* **1998**, 454, 1–8.
45. D. Dini, F. Decker, G. Zotti, *Electrochem. Solid State Lett.* **1998**, 1, 217–219.
46. M. J. Henderson, A. R. Hillman, E. Vieil, *J. Phys. Chem. B* **1999**, 103, 8899–8907.
47. M. Vilas-Boas, M. J. Henderson, C. Freire et al., *Chem. – Eur. J.* **2000**, 6, 1160–1167.
48. N. Shirtcliffe, *Colloids Surf. Physicochem. Eng. Aspects* **1999**, 155, 277–285.
49. P. Kern, D. Landolt, *J. Electrochem. Soc.* **2000**, 147, 318–325.

50. P. Kern, D. Landolt, *J. Electrochem. Soc.* **2001**, 148, B228–B235.
51. M. Itagaki, M. Tagaki, K. Watanabe, *J. Electroanal. Chem.* **1997**, 440, 139–143.
52. Z. Jusys, G. Stalnionis, *Electrochim. Acta* **2000**, 45, 3675–3682.
53. B. Gollas, P. N. Bartlett, G. Denuault, *Anal. Chem.* **2000**, 72, 349–356.
54. M. S. Shin, I. C. Jeon, *Bull. Korean Chem. Soc.* **1998**, 19, 1227–1232.
55. J. M. Kim, S. M. Chang, H. Muramatsu, *J. Electrochem. Soc.* **1999**, 146, 4544–4550.
56. K. Shimazu, S. Ye, Y. Sato et al., *J. Electroanal. Chem.* **1994**, 375, 409–413.
57. J. Rishpon, A. Redondo, C. Derouin et al., *J. Electroanal. Chem.* **1990**, 294, 73–85.
58. Z. Jusys, H. Massong, H. Baltruschat, *J. Electrochem. Soc.* **1999**, 146, 1093–1098.
59. T. Tatsuma, S. Yamaguchi, I. Wakabayashi et al., *Faraday Discuss.* **1997**, 107, 53–60.
60. W. Koh, W. Kutner, M. T. Jones et al., *Electroanalysis* **1993**, 5, 209–214.
61. M. D. Ward, E. J. Delawski, *Anal. Chem.* **1991**, 63, 886–890.
62. A. C. Hillier, M. D. Ward, *Anal. Chem.* **1992**, 64, 2539–2554.
63. J. J. Kelly, K. M. A. Rahman, C. J. Durning et al., *J. Electrochem. Soc.* **1998**, 145, 492–497.
64. C. Gabrielli, M. Keddam, R. Torresi, *J. Electrochem. Soc.* **1991**, 138, 2657–2660.
65. R. Oltra, I. O. Efimov, *J. Electrochem. Soc.* **1994**, 141, 1838–1842.
66. M. I. Jeffrey, W. L. Choo, P. L. Breuer, *Miner. Eng.* **2000**, 13, 1231–1241.
67. B. J. Feldman, O. R. Melroy, *J. Electrochem. Soc.* **1989**, 136, 640–643.
68. A. Sargent, O. A. Sadik, L. J. Matienzo, *J. Electrochem. Soc.* **2001**, 148, C257–C265.
69. A. Sargent, O. A. Sadik, *J. Electrochem. Soc.* **2001**, 148, C413–C420.
70. A. Bund, G. Schwitzgebel, *Electrochim. Acta* **2000**, 45, 3703–3710.
71. B. Gollas, J. M. Elliott, P. N. Bartlett, *Electrochim. Acta* **2000**, 45, 3711–3724.
72. C. C. Streinz, A. P. Hartman, S. Motupally et al., *J. Electrochem. Soc.* **1995**, 142, 1084–1089.
73. M. S. Kim, T. S. Hwang, K. B. Kim, *J. Electrochem. Soc.* **1997**, 144, 1537–1543.
74. M. Gonsalves, A. R. Hillman, *J. Electroanal. Chem.* **1998**, 454, 183–202.
75. S. I. Pyun, K. H. Kim, J. N. Han, *J. Power Sources* **2000**, 91, 92–98.
76. H. M. French, M. J. Henderson, A. R. Hillman et al., *J. Electroanal. Chem.* **2001**, 500, 192–207.
77. Y. B. Mo, E. Hwang, D. A. Scherson, *J. Electrochem. Soc.* **1996**, 143, 37–43.
78. M. S. Kim, K. B. Kim, *J. Electrochem. Soc.* **1998**, 145, 507–511.
79. I. Serebrennikova, V. I. Birss, *J. Electroanal. Chem.* **2000**, 493, 108–116.
80. Y. Ratieuville, W. L. Wu, D. Lincot et al., *J. Electrochem. Soc.* **1999**, 146, 3161–3167.
81. J. S. Gordon, V. G. Young, D. C. Johnson, *J. Electrochem. Soc.* **1994**, 141, 652–660.
82. J. Lee, H. Varela, S. Uhm et al., *Electrochem. Commun.* **2000**, 2, 646–652.
83. E. Shouji, D. A. Buttry, *Electrochim. Acta* **2000**, 45, 3757–3764.
84. C. O. Avellaneda, P. R. Bueno, R. C. Faria et al., *Electrochim. Acta* **2001**, 46, 1977–1981.
85. P. R. Bueno, C. O. Avellaneda, R. C. Faria et al., *Electrochim. Acta* **2001**, 46, 2113–2118.
86. B. L. Wu, D. Lincot, J. Vedel et al., *J. Electroanal. Chem.* **1997**, 420, 159–165.
87. E. W. Bohannon, L. Y. Huang, F. S. Miller et al., *Langmuir* **1999**, 15, 813–818.
88. C. O. A. Olsson, D. Hamm, D. Landolt, *J. Electrochem. Soc.* **2000**, 147, 4093–4102.
89. P. Schmutz, D. Landolt, *Electrochim. Acta* **1999**, 45, 899–911.
90. P. Schmutz, D. Landolt, *Corros. Sci.* **1999**, 41, 2143–2163.
91. C. O. A. Olsson, D. Landolt, *J. Electrochem. Soc.* **2001**, 148, B438–B449.
92. K. H. Stellnberger, M. Wolpers, T. Fili et al., *Faraday Discuss.* **1997**, 107, 307–322.
93. E. Juzeliunas, P. Kalinauskas, P. Miecinskis, *J. Electrochem. Soc.* **1996**, 143, 1525–1531.
94. H. Ehahoun, C. Gabrielli, M. Keddam et al., *J. Electrochem. Soc.* **2001**, 148, B333–B336.
95. F. Zucchi, M. Fonsati, G. Trabanelli, *J. Appl. Electrochem.* **1998**, 28, 441–447.
96. P. Krtíl, S. Nishimura, M. Yoshimura, *Electrochim. Acta* **1999**, 44, 3911–3920.
97. N. Myung, S. Kim, D. Lincot et al., *Electrochim. Acta* **2000**, 45, 3749–3756.
98. N. Myung, J. H. Jun, H. B. Ku et al., *Microchem. J.* **1999**, 62, 15–25.
99. H. Saloniemi, M. Kemell, M. Ritala et al., *Thin Solid Films* **2001**, 386, 32–40.
100. H. Saloniemi, M. Kemell, M. Ritala et al., *J. Mater. Chem.* **2000**, 10, 519–525.
101. H. Saloniemi, M. Kemell, P. Ritala et al., *J. Electroanal. Chem.* **2000**, 482, 139–148.

102. M. Kemell, H. Saloniemi, M. Ritala et al., *J. Electrochem. Soc.* **2001**, 148, C110–C118.
103. M. Kemell, H. Saloniemi, M. Ritala et al., *Electrochim. Acta* **2000**, 45, 3737–3748.
104. A. M. Bond, A. Lamprecht, V. Tedesco et al., *Inorg. Chim. Acta* **1999**, 291, 21–31.
105. D. C. Loveday, A. R. Hillman, A. G. Orpen et al., *J. Mater. Chem.* **1996**, 6, 993–998.
106. W. Kutner, K. Doblhofer, *J. Electroanal. Chem.* **1992**, 326, 139–160.
107. K. Ogura, M. Nakayama, K. Nakaoka, *J. Electroanal. Chem.* **1999**, 474, 101–106.
108. I. Oh, H. Lee, H. Yang et al., *Electrochem. Commun.* **2001**, 3, 274–280.
109. J. J. Garcia-Jareno, A. Sanmatias, F. Vicente et al., *Electrochim. Acta* **2000**, 45, 3765–3776.
110. K. Ogura, K. Nakaoka, M. Nakayama, *J. Electroanal. Chem.* **2000**, 486, 119–125.
111. T. R. I. Cataldi, G. E. de Benedetto, C. Campa, *J. Electroanal. Chem.* **1997**, 437, 93–98.
112. U. Schroder, F. Scholz, *Inorg. Chem.* **2000**, 39, 1006–1015.
113. J. Bbcskai, K. Martinusz, E. Czirok et al., *J. Electroanal. Chem.* **1995**, 385, 241–248.
114. M. A. Malik, K. Miecznikowski, P. J. Kulesza, *Electrochim. Acta* **2000**, 45, 3777–3784.
115. C. D. Evans, I. Nicic, J. Q. Chambers, *Electrochim. Acta* **1995**, 40, 2611–2615.
116. C. Gabrielli, G. Maurin, G. Poindessous et al., *J. Cryst. Growth* **1999**, 200, 236–250.
117. K. Yao, K. Shimazu, M. Nakata et al., *J. Electroanal. Chem.* **1998**, 443, 253–261.
118. F. M. Zhou, S. L. Yau, C. Jehoulet et al., *J. Phys. Chem.* **1992**, 96, 4160–4162.
119. W. Y. Koh, D. Dubois, W. Kutner et al., *J. Phys. Chem.* **1993**, 97, 6871–6879.
120. J. N. Barisci, G. G. Wallace, R. H. Baughman, *Electrochim. Acta* **2000**, 46, 509–517.
121. J. N. Barisci, G. G. Wallace, R. H. Baughman, *J. Electrochem. Soc.* **2000**, 147, 4580–4583.
122. M. C. Miras, C. Barbero, R. Kotz et al., *J. Electroanal. Chem.* **1992**, 338, 279–297.
123. S. Bruckenstein, C. P. Wilde, M. Shay et al., *J. Phys. Chem.* **1990**, 94, 787–793.
124. S. Bruckenstein, C. P. Wilde, A. R. Hillman, *J. Phys. Chem.* **1993**, 97, 6853–6858.
125. S. Bruckenstein, A. R. Hillman, *J. Phys. Chem.* **1988**, 92, 4837–4839.
126. S. Bruckenstein, A. R. Hillman, *J. Phys. Chem.* **1991**, 95, 10 748–10 752.
127. P. T. Varineau, D. A. Buttry, *J. Phys. Chem.* **1987**, 91, 1292–1295.
128. I. Jureviciute, S. Bruckenstein, A. R. Hillman et al., *Phys. Chem. Chem. Phys.* **2000**, 2, 4193–4198.
129. E. M. Pater, S. Bruckenstein, A. R. Hillman, *J. Chem. Soc., Faraday Trans.* **1998**, 94, 1097–1103.
130. S. Bruckenstein, A. Fensore, A. R. Hillman, *Faraday Discuss.* **1997**, 107, 323–336.
131. G. S. Ostrom, D. A. Buttry, *J. Phys. Chem.* **1995**, 99, 15 236–15 240.
132. A. R. Hillman, N. A. Hughes, S. Bruckenstein, *J. Electrochem. Soc.* **1992**, 139, 74–77.
133. A. R. Hillman, D. C. Loveday, S. Bruckenstein, *Langmuir* **1991**, 7, 191–194.
134. H. L. Bandey, M. Gonsalves, A. R. Hillman et al., *J. Electroanal. Chem.* **1996**, 410, 219–227.
135. C. Barbero, E. J. Calvo, R. Etchenique et al., *Electrochim. Acta* **2000**, 45, 3895–3906.
136. A. P. Clarke, J. G. Vos, A. R. Hillman et al., *J. Electroanal. Chem.* **1995**, 389, 129–140.
137. N. Oyama, T. Tatsuma, K. Takahashi, *J. Phys. Chem.* **1993**, 97, 10 504–10 508.
138. K. Naoi, M. Lien, W. H. Smyrl, *J. Electrochem. Soc.* **1991**, 138, 440–445.
139. K. Naoi, Y. Oura, M. Maeda et al., *J. Electrochem. Soc.* **1995**, 142, 417–422.
140. M. Hepel, L. Dentrone, *Electroanalysis* **1996**, 8, 996–1005.
141. M. Hepel, F. Mahdavi, *Microchem. J.* **1997**, 56, 54–64.
142. J. Hepel, S. Bruckenstein, M. Hepel, *Microchem. J.* **1997**, 55, 179–191.
143. M. Hepel, X. M. Zhang, R. Stephenson, S. Perkins, *Microchem. J.* **1997**, 56, 79–92.
144. H. Yang, J. Kwak, *J. Phys. Chem. B* **1998**, 102, 1982–1988.
145. M. A. Vorotyntsev, E. Vieil, J. Heinze, *J. Electroanal. Chem.* **1998**, 450, 121–141.
146. K. Kontturi, P. Pentti, G. Sundholm, *J. Electroanal. Chem.* **1998**, 453, 231–238.
147. M. J. Henderson, H. French, A. R. Hillman et al., *Electrochem. Solid State Lett.* **1999**, 2, 631–633.
148. W. S. Shim, Y. H. Lee, I. H. Yeo et al., *Synth. Met.* **1999**, 104, 119–127.
149. S. Bruckenstein, K. Brzezinska, A. R. Hillman, *Electrochim. Acta* **2000**, 45, 3801–3811.
150. S. Bruckenstein, K. Brzezinska, A. R. Hillman, *Phys. Chem. Chem. Phys.* **2000**, 2, 1221–1229.
151. H. Yang, H. Lee, Y. T. Kim et al., *J. Electrochem. Soc.* **2000**, 147, 4239–4246.

152. H. Daifuku, T. Kawagoe, N. Yamamoto et al., *J. Electroanal. Chem.* **1989**, 274, 313–318.
153. M. Skompska, A. R. Hillman, *J. Chem. Soc., Faraday Trans.* **1996**, 92, 4101–4108.
154. M. J. Henderson, A. R. Hillman, E. Vieil, *Electrochim. Acta* **2000**, 45, 3885–3894.
155. H. Varela, R. M. Torresi, D. A. Buttry, *J. Electrochem. Soc.* **2000**, 147, 4217–4223.
156. C. Gabrielli, M. Keddam, N. Nadi et al., *J. Electroanal. Chem.* **2000**, 485, 101–113.
157. D. Dini, F. Decker, G. Zotti et al., *Electrochim. Acta* **1999**, 44, 1911–1917.
158. M. Skompska, A. Jackson, A. R. Hillman, *Phys. Chem. Chem. Phys.* **2000**, 2, 4748–4757.
159. C. Kvarnstrom, H. Neugebauer, S. Blomquist et al., *Electrochim. Acta* **1999**, 44, 2739–2750.
160. F. Soavi, C. Arbizzani, M. Mastragostino, *Phys. Chem. Chem. Phys.* **2000**, 2, 2993–2998.
161. M. J. Brown, A. R. Hillman, S. J. Martin et al., *J. Mater. Chem.* **2000**, 10, 115–126.
162. A. R. Hillman, A. Glidle, *Phys. Chem. Chem. Phys.* **2001**, 3, 3447–3458.
163. A. R. Hillman, S. Bruckenstein, *J. Chem. Soc., Faraday Trans.* **1993**, 89, 339–348, 3779–3782.
164. S. Demoustierchampagne, J. R. Reynolds, M. Pomerantz, *Chem. Mater.* **1995**, 7, 277–283.
165. M. Pyo, J. R. Reynolds, *J. Phys. Chem.* **1995**, 99, 8249–8254.
166. P. Damlin, C. Kvarnstrom, A. Ivaska, *Anal. Chim. Acta* **1999**, 385, 175–186.
167. N. Baute, L. Martinot, R. Jerome, *J. Electroanal. Chem.* **1999**, 472, 83–90.
168. J. Charlier, C. Bureau, G. Lecayon, *J. Electroanal. Chem.* **1999**, 465, 200–208.
169. C. D. Evans, J. Q. Chambers, *Chem. Mater.* **1994**, 6, 454–460.
170. J. Wang, M. Jiang, B. Mukherjee, *Bioelectrochemistry* **2000**, 52, 111–114.
171. K. Galasso, T. Livache, A. Roget et al., *J. Chim. Phys. Phys. -Chim. Biol.* **1998**, 95, 1514–1517.
172. N. Lassalle, A. Roget, T. Livache et al., *Talanta* **2001**, 55, 993–1004.
173. N. Lassalle, P. Mailley, E. Vieil et al., *J. Electroanal. Chem.* **2001**, 509, 48–57.
174. M. T. M. Koper, M. Hachkar, B. Beden, *J. Chem. Soc., Faraday Trans.* **1996**, 92, 3975–3982.
175. G. Inzelt, V. Kertesz, G. Lang, *J. Phys. Chem.* **1993**, 97, 6104–6106.
176. G. Inzelt, *J. Electroanal. Chem.* **1993**, 348, 465–471.
177. M. W. Carr, A. R. Hillman, S. D. Lubetkin et al., *J. Electroanal. Chem.* **1989**, 267, 313–320.
178. C. Gabrielli, F. Huet, M. Keddam et al., *J. Electroanal. Chem.* **1991**, 297, 515–522.
179. F. B. Li, A. R. Hillman, S. D. Lubetkin et al., *J. Electroanal. Chem.* **1992**, 335, 345–362.

2.8

Sonoelectrochemistry: Physical Aspects

*Richard G. Compton, Joanna L. Hardcastle,
Javier del Campo
Physical and Theoretical Chemistry Laboratory,
University of Oxford, South Parks Road,
Oxford, UK*

2.8.1

Introduction to Power Ultrasound

Normal human hearing is capable of detecting sound waves of frequencies between 16 Hz and 16 kHz. Ultrasound is defined as sound waves of frequencies higher than the human ear can detect (i.e. greater than 16 kHz). The frequencies of ultrasonic sources cover a huge range, from 16 kHz to 500 MHz. The lower-frequency, high-power ultrasound region lies between 20 and 500 kHz. It is this region of the sonic spectrum that provides beneficial effects when coupled with electrochemistry.

Ultrasound is generated by utilizing the inverse piezoelectric effect discovered in 1880 [1, 2]. The ultrasonic transducer produces a change in the dimension of a material by the application of an electrical potential across opposite faces. By alternating the potential across the faces at high frequency, the crystal converts the electrical energy to mechanical energy. At sufficiently high frequency of alternating potential, this will result in the generation of ultrasound [3].

The natural resonance frequency of response to piezoelectric stimulation provides the optimum ultrasonic performance. Target ultrasonic frequencies can be generated by the use of different crystal size, material, and cut. Examples of commonly used materials are barium

titanate, BaTiO_3 , and lead zirconate titanate, $\text{Pb}(\text{Zr,Ti})\text{O}_3$ [4].

Ultrasound has long been used for a wide range of applications [5]. These include *inter alia* the welding of plastics [6], ultrasonic imaging in medicine [7], the dispersion of pigments and solids [8], cleaning both on an industrial scale [9] and in precision applications such as dentistry [10], and in catalyst manufacture [11]. Sonoelectrochemistry [3, 12–15] is concerned with the coupling of power ultrasound to electrochemical systems in order to both achieve and develop new processes and applications.

2.8.2

Approaches to the Coupling of Ultrasound with Electrochemical Methods

There are numerous methods of introducing ultrasound into an electrochemical cell. These include whistle reactors, ultrasonic baths, and ultrasonic horns (also known as probes) [3, 16]. Of these techniques, the ultrasonic bath is of great commercial use in cleaning applications and in sonochemical reactors. An ultrasonic bath normally consists of a number of fixed frequency (typically 20–100 kHz) transducers beneath the physical exterior of the bath unit. The bath unit is filled with distilled water and an electrochemical cell can be immersed in the bath in a fixed position [17]. The transducer is electrically separated from the cell, which is advantageous. However, the results have been found to depend strongly on positioning and design, which is clearly undesirable [18]. The ultrasonic horn transducer provides an alternative to the bath; it delivers ultrasound directly to the solution within the cell using a metal horn tip. The horn acts as an amplifier with the shape of the tip determining the mechanical

amplification of the piezoelectric vibration. For this reason, the tip has a length (typically 12.5 cm for a 20-kHz horn) that corresponds to a multiple of half wavelengths of the ultrasonic wave. The most common material for horn construction is a titanium alloy ($\text{Ti}_6\text{Al}_4\text{V}$). This is chosen because of its strength, durability, and relative chemical inertness. The horn is then placed in the electroactive solution of interest to a depth of not less than 1 to 2 cm. This arrangement results in the delivery of high-intensity ultrasound at, and in the vicinity of, the tip of the horn.

The advantages of the use of the horn over the bath are: the higher ultrasonic intensities available (up to 1000 W cm^{-2}), the ease with which the intensity delivered to the system can be varied, and the small effect on observed electrode processes resulting from the variation of cell geometry and dimensions. Problems arising from the heating of the cell, resulting from high-intensity ultrasound, can be regulated by the introduction of a cooling coil connected to a thermostatted water bath. The need for bipotentiometric [19] control is removed by the insulating the horn from the electrochemical cell by a screw thread machined from Delrin[®]. The ultrasonic frequency of a piezo-driven horn is fixed and the most commonly used frequency is 20 kHz. Such equipment is readily available commercially and is easily introduced into the electrochemical cell. A simple design for a three-electrode cell is shown in Fig. 1.

Experiments may be conducted using alternative geometries of the ultrasonic horn relative to the working electrode. This permits the study of the processes governing sonovoltammetry. The “face-on”, “side-on”, and “sonotrode” geometries are illustrated in Fig. 2. The “face-on” geometry is the most conventional and analytically

useful. It is primarily this geometry that is exploited and described in subsequent sections. The “side-on” geometry comprises the electrode placed perpendicularly to the tip of the ultrasonic horn [20]. In the sonotrode arrangement, the working electrode is incorporated in the tip of the ultrasonic horn [21]. It is proposed that in this arrangement, mass transport to the electrode surface can be maximized and extreme limiting currents corresponding to diffusion layer thicknesses of less than $1 \mu\text{m}$ have been observed [21–23].

2.8.3

The Influence of Ultrasound on Mass Transport at the Electrode

Power ultrasound, of frequencies between 20 and 500 kHz is known to cause a multitude of complex phenomena in solution; these include acoustic streaming [24], bubble oscillation, and cavitation [25, 26], resulting in the generation of microjets [27–30] and shock waves which occur preferentially at the solid–liquid interface. Figure 3 is a schematic diagram of the most significant effects observed in sonoelectrochemical systems; acoustic streaming and cavitation.

The application of power ultrasound in solution drastically increases the rate of mass transport of material to the solid surface. Figure 4 shows two voltammograms obtained at a 3-mm glassy carbon electrode for the reduction of 1.0 mM $\text{Ru}(\text{NH}_3)_6\text{Cl}_3$ in aqueous solution with 0.1 M KCl as supporting electrolyte, which is a well-defined model voltammetric system:

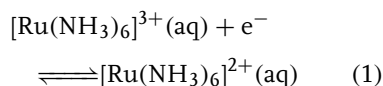


Figure 4(a) shows a cyclic voltammogram recorded under silent conditions, which

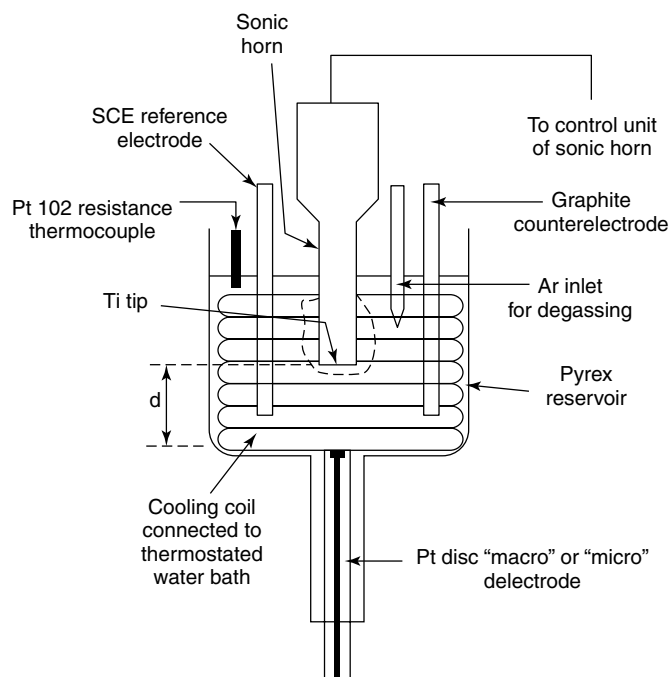


Fig. 1 Thermostatted sonoelectrochemical three-electrode cell in which the working electrode is located a distance d from the horn tip of the transducer. The cut away section through the cooling coil reveals the Ti tip.

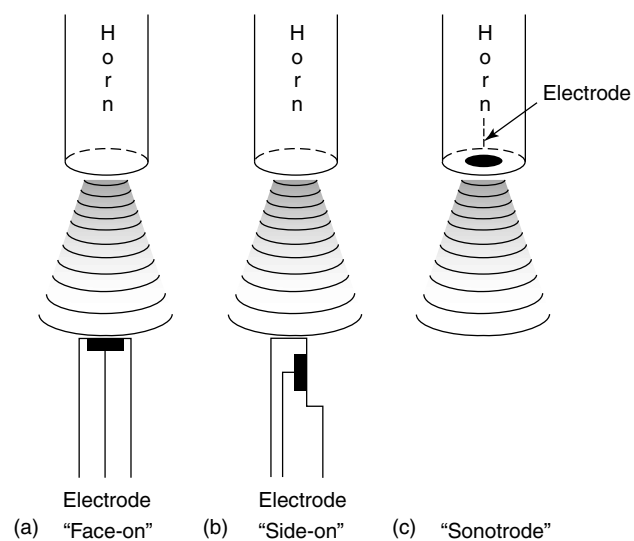


Fig. 2 Three-electrode geometries commonly used in sonovoltammetric measurements.

Fig. 3 Representation of (a) acoustic streaming; and (b) an ultrasonically induced cavitation bubble collapsing in the vicinity of a surface.

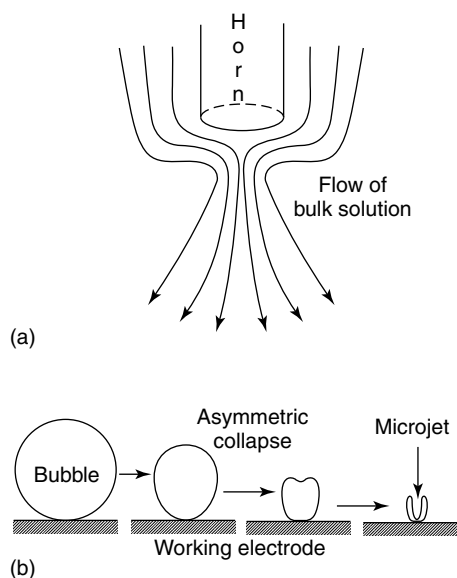
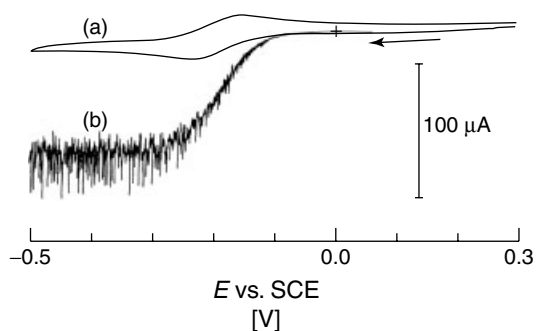


Fig. 4 (a) Cyclic voltammogram and (b) sonovoltammogram, at a horn to electrode separation of 20 mm and ultrasound intensity 15 W cm^{-2} , for the reduction of $1 \text{ mM Ru(NH}_3)_6^{3+}$ at a Pt disc electrode.



has the characteristic peak shape appearance expected for a reversible one-electron reduction with a half wave potential $E_{1/2} = -0.2 \text{ V}$ versus saturated calomel electrode (SCE) and a magnitude consistent with a value of $D_{\text{Ru}} = 0.91 \times 10^{-9} \text{ m}^2 \text{ s}^{-1}$ [31]. Figure 4(b) shows an analogous measurement in the presence of 20-kHz ultrasound of intensity $15 \pm 5 \text{ W cm}^{-2}$ directed in a face-on arrangement with the electrode surface at $10 \pm 2 \text{ mm}$ horn to electrode separation. It can be seen that the average transport limited current is significantly enhanced when compared to the

silent case. Furthermore, the form of the voltammogram has qualitatively changed. A familiar cyclic voltammogram is no longer observed but a sigmoidal voltammogram indicative of a constant rate of transport of electroactive species to the electrode surface, thus sustaining an average steady current. The magnitude of the limiting current observed in the presence of ultrasound is found to increase on the reduction of the horn to electrode separation or an increase in the magnitude of the ultrasonic intensity applied to the system [32]. A quantitative

model used to parameterize the mass transport to both insonated microdisc and macrodisc electrodes assumes that the application of power ultrasound results in a truncated or thinned Nernst diffusion layer. The diffusion layer model (Fig. 5) allows a crude description of the mass transport at the electrode–liquid interface by assuming a laminar sublayer close to the surface and an approximately linear concentration gradient across a thin layer adjacent to the electrode. Equation (2) consequently describes transport to the insonated electrode.

$$I_{\text{lim}} = \frac{nFDAc_{\text{bulk}}}{\delta} \quad (2)$$

where the limiting current, I_{lim} , is related to the number of transferred electrons, n , the Faraday constant, F , the diffusion coefficient, D , the electrode area, A , the concentration, c , and the diffusion layer thickness, δ . Under these conditions, all the electroactive material transported to the electrode is converted into products. It is found experimentally for the “face-on” geometry [22] that:

$$I_{\text{lim}} \propto D^{2/3}Ac_{\text{bulk}} \quad (3)$$

hence,

$$\delta \propto D^{1/3} \quad (4)$$

This result implies that the diffusion layer thickness is controlled by both diffusion and convection. By comparison with experimental results for hydrodynamic electrodes such as the rotating disc electrode [33], it can be shown that I_{lim} at stationary electrodes with convective mass transport to the electrode surface exhibits a $D^{2/3}$ dependence. In the case of the insonated electrode, acoustic streaming contributes significantly to this convective flux [31].

A major factor in ultrasound-induced processes is the presence of cavitation both in the bulk solution and at interfaces. The phenomenon caused by voids or gas bubbles in the solution phase being coupled to the oscillating pressure field, is responsible for “hot spot” processes and microjetting. There are different types of cavitation, notably stable cavitation (violently oscillating bubbles), or transient cavitation (collapsing bubbles) [34]. The ultrasound frequency and intensity determine the type and violence of the process. Cavitation occurs more readily in the vicinity of the electrode surface

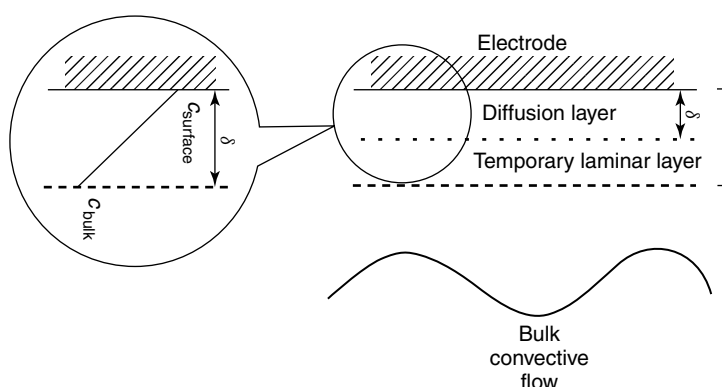


Fig. 5 Schematic representation of the diffusion and boundary layers at the electrode–solution interface as applied in the diffusion layer model.

compared to that in the bulk solution due to the typically weaker molecular interactions. At the interface, crevices and active sites also exist where vapor bubbles readily form. In the presence of hydrodynamic flow, the interfacial tension is increased and the cavities collapse asymmetrically resulting in a microjet of electrolyte being cast against the surface. The nature of the microjets generated by cavitation events in the vicinity of the solid–liquid interface has been the focus of much attention with both experimental and theoretical approaches; increased mass transport and depassivation of electrodes resulting from jet speeds of up to 100 m s^{-1} have been reported [35–38].

Chronoamperometry at microelectrodes (see Chapter 2.5) and macroelectrodes permits a direct comparison between the effects of cavitation in different solvents and at different ultrasound intensities. Figure 6 shows current–time measurements recorded at an insonated $50\text{-}\mu\text{m}$ diameter platinum electrode in ammonia, water, and dimethyl formamide (DMF) (at 298 and 218 K). In each case, a well-characterized simple one-electron redox couple was employed as given in Table 1. The electrode was held at a potential corresponding to the transport-limited electrolysis of the substrate of interest. Sharp spikes are observed, superimposed on a background current much enhanced in comparison with the steady state current seen under silent conditions. The background or baseline current is attributed to enhanced mass transport brought about by acoustic streaming. The spikes are caused by the collapse of single cavitation bubbles in the vicinity of the electrode. On the collapse of a cavitation bubble the jet of electrolyte, which is cast against the electrode surface, brings new electroactive material giving an enhanced current. In

this way, one can record direct hits or near misses of these microjets of solution as individual current transients of differing height and shape. For example, for a microjet impinging directly on the electrode surface, the current observed in the corresponding spike may be higher than if the jet had hit the edge of the electrode.

The frequency and violence of cavitation events is different from one medium to the next reflecting the differences in physical properties between solvents, primarily vapor pressure and viscosity. Cavitation bubbles are allowed to grow larger in media of high vapor pressure [39], and therefore when the bubble collapses, the implosion is less violent as a result of the cushioning effect arising from its larger size. Large bubbles may also have more chance to move away from the surface of the electrode reducing the frequency of events. Conversely, much more violent events are brought about in solvents of low vapor pressure [39]. More energy is required to disrupt the medium in order to create a void resulting in small bubbles and a reduction in the “cushioning effect”. The chance of the smaller bubbles escaping from the surface is lessened, the resulting cavitation collapses are not only more violent but also more frequent. Greater stability of bubbles in low vapor pressure can result in prolonged stability of oscillating bubbles on the surface as in the case of liquid ammonia. The viscosity is also a contributing factor with a higher viscosity resulting in much less efficient replacement of solution at the electrode surface on cavitation collapse and therefore, a smaller current enhancement. Interplay between these physical properties permits the elucidation of the overall scheme shown in Fig. 7.

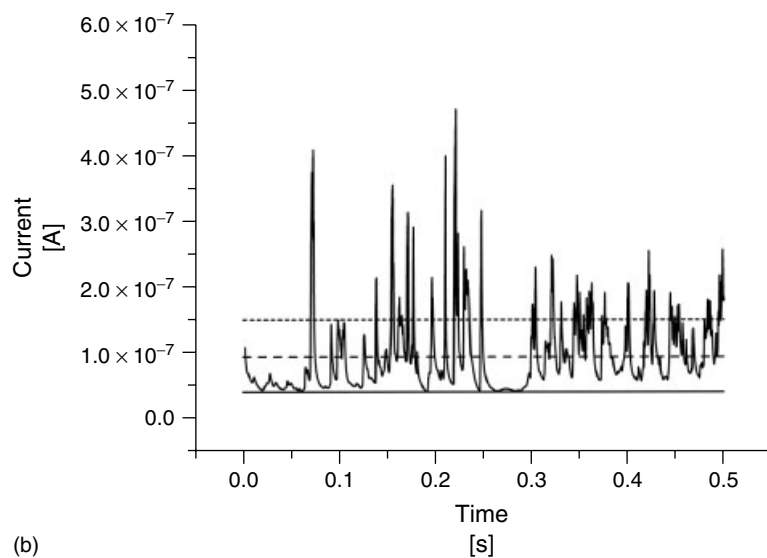
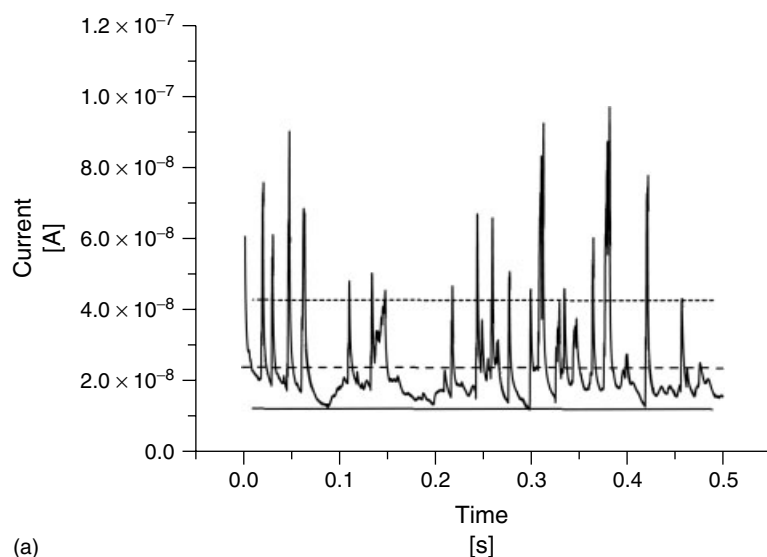


Fig. 6 Chronoamperometric experiments at a 50- μm diameter Pt disc in the presence of ca. 250 W cm^{-2} ultrasound in different media and temperatures. (a) 1 mM ferrocene in DMF at 218 K; (b) 1 mM ferrocene in DMF at 298 K; (c) 1 mM $\text{Ru}(\text{NH}_3)_6^{3+}$ in water at 298 K; and (d) 1 mM nitrotoluene in liquid ammonia at 218 K. The additional lines superimposed on the traces correspond to the calculated baseline current (—), calculated average current (-----), and standard deviation (— —).

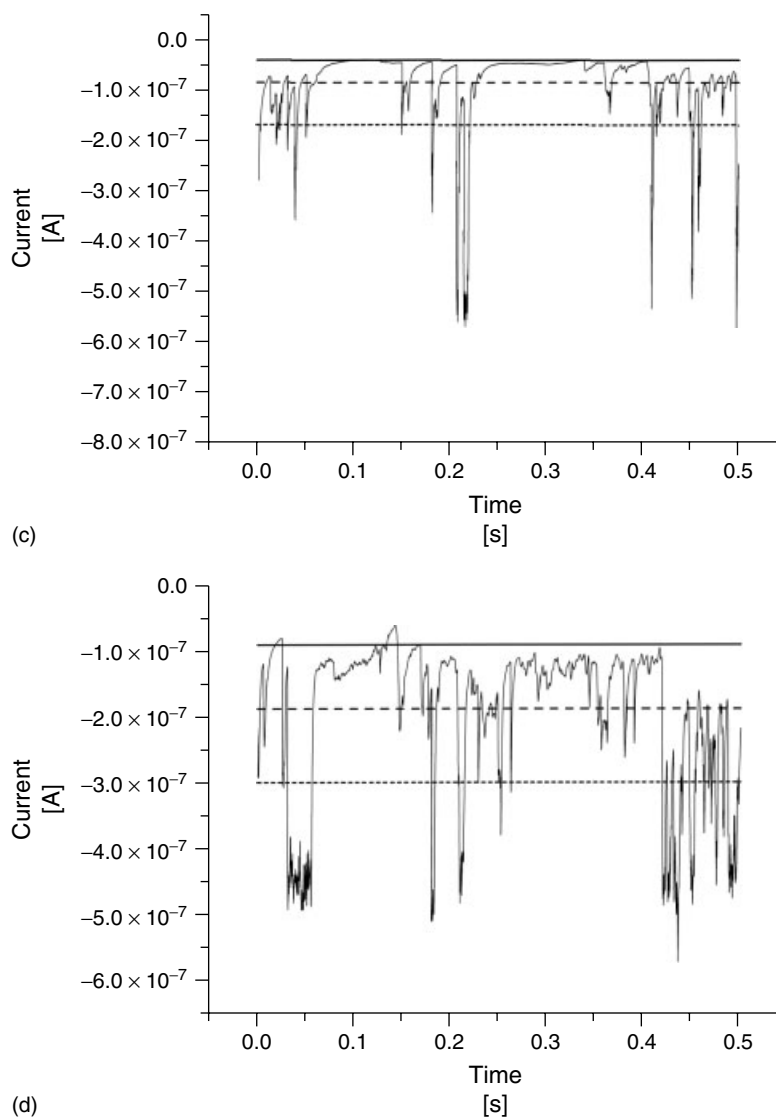


Fig. 6 (Continued)

Macroelectrodes have been used to investigate the variation of cavitation processes with ultrasound intensity with the advantage that the most violent conditions can be attained with only small effects of the local erosion damage on the overall current response [40]. Chronoamperometry

at a macroelectrode permits quantitative analysis of cavitation events occurring at the surface of the electrode at differing ultrasound powers by recording the deviation of individual current data points from the mean background current. Figure 8 shows a plot of the percentage of current

Tab. 1 Redox systems studied at a 50- μm platinum disc electrode under silent conditions

Solvent	Redox system	Supporting electrolyte	Silent current [nA]	$D [\text{cm}^2 \text{ s}^{-1}]$	$E_{1/2} [\text{V}]$
NH_3 (218 K)	Nitrotoluene	KI	18	1.4×10^{-5}	−0.390 vs Ag
H_2O (298 K)	$\text{Ru}(\text{NH}_3)_6^{3+}$	KCl	13	9.1×10^{-6}	−0.171 vs SCE
DMF (298 K)	Ferrocene	TBAHFP	12	1.2×10^{-5}	0.470 vs Ag
DMF (218 K)	Ferrocene	TBAHFP	4	2.6×10^{-6}	0.774 vs Ag

Note: TBAHFP: tetrabutyl ammonium hexafluorophosphate.

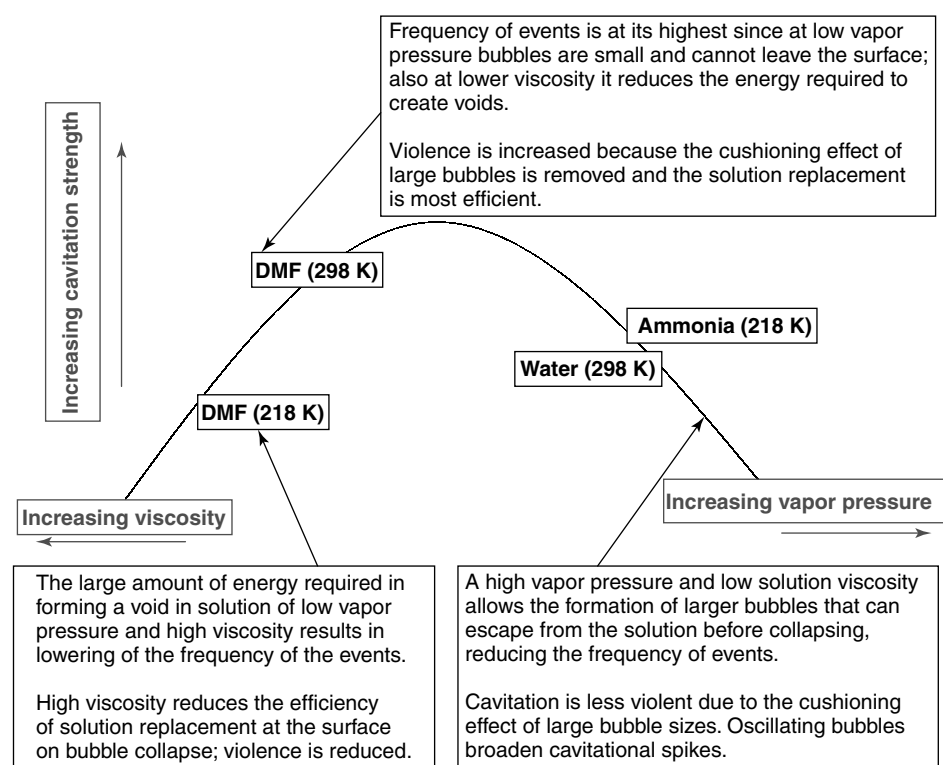
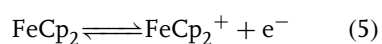


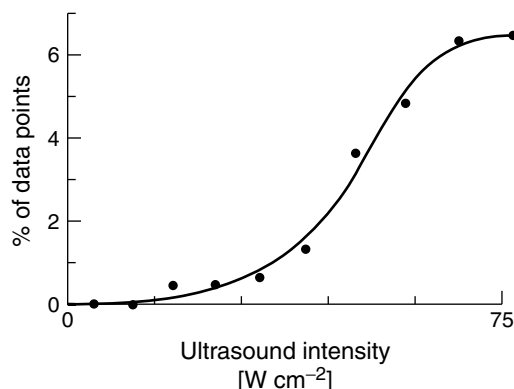
Fig. 7 Schematic describing the relationship between cavitation strength and the physical properties of the solvent.

data points deviating more than 10% from the mean for the simple one-electron oxidation of ferrocene in DMF with a background electrolyte of 0.1 M NBu_4PF_6 .



It can be seen that the effect of increasing ultrasound intensity is to promote a nonlinear increase in the deviation from the mean with an appearance consistent with the existence of a cavitation threshold [3].

Fig. 8 Plot of the fraction of current readings for the sonoelectrochemical oxidation of 1 mM ferrocene in DMF at a Pt disc macroelectrode with a deviation from the average current response of more than 10% versus the ultrasound intensity employed.



2.8.4

Ultrasound-induced Surface Effects

The cleaning effect of ultrasound harnessed in the use of ultrasonic baths is dependent upon cavitation. The same is true at the surface of an electrode. The combination of ultrasonic frequency, intensity, and the electrochemical solvent as described above can give rise to considerable release of energy occurring during cavitation events and damage to a metallic electrode surface is possible. There is also evidence for the surface activation of insonated glassy carbon electrodes [41, 42]. A wide range of *ex situ* and *in situ* methods are available for the investigation of surface properties. Atomic force microscopy (AFM) may be used for the investigation of various types of electrode surfaces [43, 44], as discussed in Chapter 3.2 in this volume. Images of a platinum electrode polished (Fig. 9a) and after 2 min of sonication (Fig. 9b) demonstrate a slow but significant roughening due to pitting which depends on the applied intensity. As well as the intensity and solvent used in the experiments, the erosion process depends on the hardness of the electrode material [45]. For glassy carbon and gold electrodes, considerable damage occurs at high intensities

in aqueous electrolyte. In voltammetric experiments however, the timescale is much shorter and the ultrasound intensity much lower meaning that the effect of erosion effect remains acceptable [43] and subtler changes in the surface properties are observed.

Associated with electrode damage, the “cleaning” or “depasivation” of electrode surfaces is an important aspect of sono-electrochemistry. This effect has been documented for the depasivation of iron electrodes [35], the removal of deposits [45], and observed when polymer films are present at the electrode surface [46]. It is also vital to sonoelectroanalytical methods (see Sect. 2.8.1.2). The oxidation of the carbonyl complex $\text{Cr}(\text{CO})_6$ is an example of an electrochemical system that is prone to electrode passivation [42]. In the presence of ultrasound, sustained voltammetric currents can be obtained, which suggested both depasivation and/or a suppression of precipitation; this is in contrast with corresponding silent voltammetry in which these phenomena preclude “clean” voltammetry.

Electrochemical AC impedance methods are well suited for *in situ* monitoring of changes in surface roughness and capacitance [43], as discussed in Chapter 2.6 in

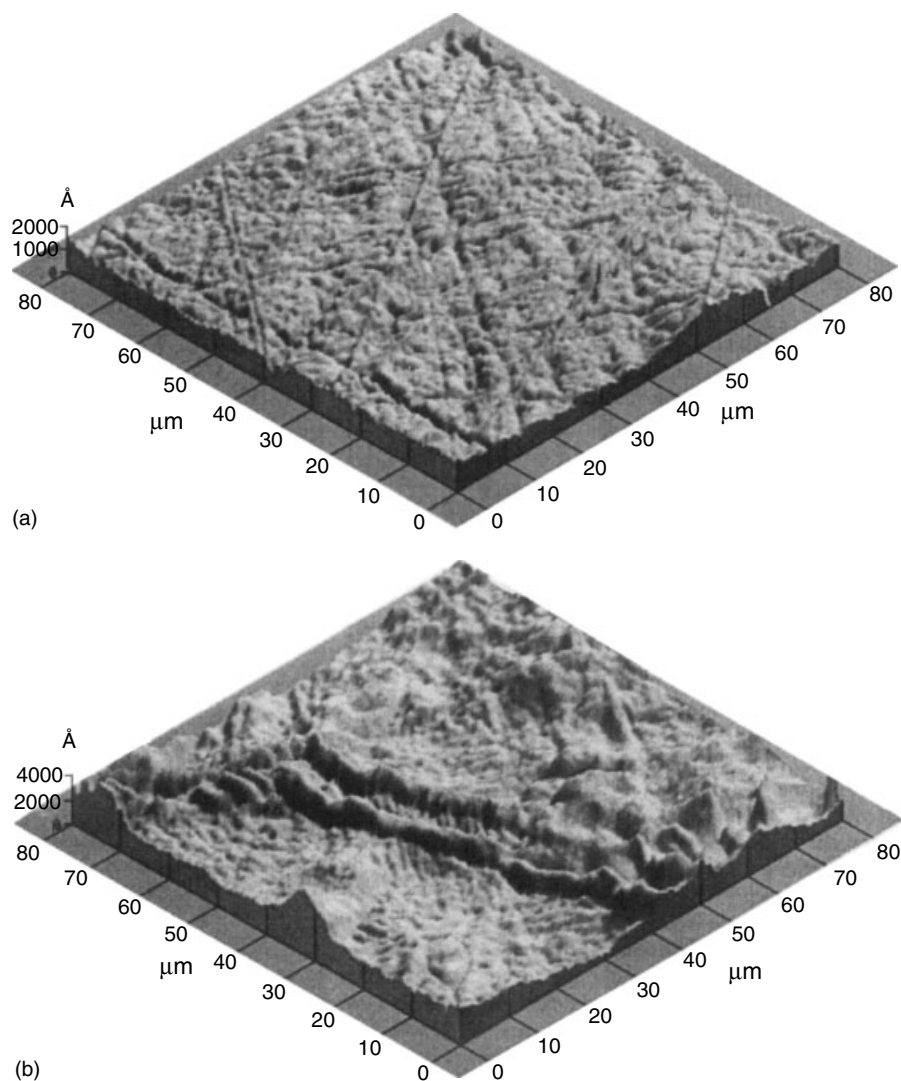


Fig. 9 AFM images of: (a) a Pt electrode surface freshly polished with 0.1 μm diamond lapping compound and (b) the same Pt electrode after application of power ultrasound in a solution of acetonitrile. Note the difference in scale in (a) 2000 Å and (b) 4000 Å.

this volume. Cole–Cole plots obtained at 0.0 V (vs. SCE) for an insolated glassy carbon surface immersed in argon-saturated 0.1 M NaOH solution show a marked deviation from the ideal behavior. This occurs as a direct result of cavitationally induced surface roughening. Further

electrochemical manifestation of the effect is seen for the oxidation of a nickel electrode surface in alkaline aqueous media [42]. In the presence of ultrasound, the magnitude of the observed current and overall shape of the signal remains unchanged, which is consistent with

surface-confined processes independent of mass transport in the solution phase. It is known that a surface oxidized layer is formed at the Fladé potential. This potential, however, is shifted up to 60 mV toward more anodic potentials when the surface is insonated. This shift has been attributed to ultrasound causing surface erosion, which competes with the growth of the oxide film.

2.8.5

The Influence of Ultrasound on Chemical Processes

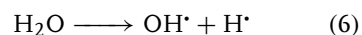
The use of ultrasound to enhance the rate or change the pathway of both homogeneous and heterogeneous chemical reactions has been exploited for a number of years [47–49]. There are a wide variety of processes involved in the alteration of reaction rate or pathway. These vary from surface activation of solid reactants to the generation of active radical species. It is possible to bring about gross changes in the transport leading to new dominant reaction pathways and in many cases the processes behind such changes are not fully understood. Ultrasound may affect chemical reactions that occur in a simple liquid phase via four possible routes:

- enhanced mass transport;
- thermal fluctuations caused by cavitation or “hot spots”;
- the formation of highly reactive intermediates, for example, radical species in the solution near a “hot spot”; and
- strong shear forces that can affect large molecules, particles, or surfaces.

2.8.5.1 Generation of Active Radical Species

The hydroxyl radical has been shown to be responsible for many of the chemical

effects of ultrasound in homogeneous systems. This has recently been harnessed for the treatment of wastewater [50, 51]. In particular, the sonochemical degradation of chlorophenols [52, 53], chlorohydrocarbons [54, 55], and cyanide [56] has been the focus of studies aimed at the development of new methods for the elimination of traces of toxic materials. The mechanism proposed for these sonochemical processes is based on the formation of short-lived radical species (Eq. 6), which are generated in violent cavitation events.



Elegant spin trapping work by Riesz and coworkers [57, 58] comparing pulse radiolysis and sonolysis has provided firm evidence for the proposed intermediates. In the absence of reactive organic compounds, the sonochemical formation of OH^\bullet radicals is followed by recombination processes that lead to the formation of hydrogen peroxide [59]. The production of hydrogen peroxide can therefore provide an indirect indication of the presence of high-energy intermediates allowing the measurement of a relative sonochemical activity index [56]. Other reaction pathways are likely to be complementary, such as the direct pyrolysis of unstable compounds, for example, nitrophenol [60] and direct oxidation induced by supercritical water [51, 61].

The effect of 20-kHz ultrasound on the concentration of cyanide in aqueous 0.1 M NaOH is first-order decay in the cyanide concentration over a period of 2.5 h with an apparent rate constant $1.3 (\pm 0.2) \times 10^{-4} \text{ s}^{-1}$ for a solution volume of 400 mL and ultrasound intensity of 60 W cm^{-2} . However, changing the volume of solution undergoing sonication in the reactor dramatically changes the apparent rate constant with a decrease in volume causing

an approximately inversely proportional increase in the rate constant for cyanide destruction. This can be understood if the sonochemical reaction does not proceed homogeneously throughout the reactor volume but is localized in a volume close to the ultrasound emitting horn tip. This volume is approximately $3 \times 10^{-6} \text{ m}^3$, with a rate constant for the destruction of cyanide within this reaction volume of $\approx 2 \times 10^{-2} \text{ s}^{-1}$.

2.8.5.2 Rates of Heterogeneous Electron Transfer

The kinetics of heterogeneous electron transfer reaction in the presence of insonation at the electrode surface has been quantified by analyzing the wave shape of the sonovoltammetric signal. Huck [18] investigated one-electron redox systems such as $\text{Fe}^{3+/2+}$ and $\text{Fe}(\text{CN})_6^{3-/4-}$ and reported consistent results between silent rotating disc voltammetry and sonovoltammetry performed in an ultrasonic bath. Measurements performed in the cell described in Fig. 1 with the working electrode placed opposite the immersed ultrasonic horn have also been carried out [62]. The limiting currents that are observed for the simple one-electron reduction of $\text{Ru}(\text{NH}_3)_6^{3+}$ and of Eu^{3+} in aqueous media at various electrode materials can be used to determine the diffusion layer thickness, δ , by applying Eq. (2). Calculation of the rate of electron transfer was found to give good agreement with analogous measurements under silent conditions [31]. In all cases, the sole effect of ultrasound within experimental error was to change the apparent reversibility of the electron transfer process by promoting mass transport. When the effect of the latter is corrected for, no change in the

heterogeneous rate constants for electron transfer was seen in the presence of ultrasound. Consistent with these observations, Fontana and coworkers [63] reported for two reversible systems, $\text{Fe}(\text{CN})_6^{3-}/\text{Fe}(\text{CN})_6^{4-}$ and $\text{Fe}^{2+}/\text{Fe}^{3+}$, that ultrasound improves only the mass transport. However, for a less reversible quinone–hydroquinone system, ultrasound improved the reversibility by a factor of 2. This improvement may be due to either an increase in the exchange current density or to an increase in the speed of the intermediate chemical steps.

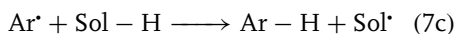
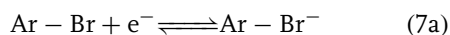
2.8.5.3 Sonovoltammetric Study of Homogeneous Chemical Reactions

The use of well-known model systems has been undertaken to confirm the validity and define the limits of the treatment of sonovoltammetry in line with the model of a uniformly accessible electrode and also to assess the influence of ultrasound on homogeneous chemical reactions coupled to the electron transfer. The uniformly accessible electrode model allows the introduction of a reaction layer, which has also been successfully employed for rotating disc voltammetry, in studies using channel electrodes [64] and in a slightly more complex form for studies in turbulent voltammetry [65].

A physical model has been proposed [35–38], which may be used to describe the processes that occur within the electrochemically important layer of ca. $100 \mu\text{m}$ adjacent to the electrode surface in the presence of power ultrasound. The current may be separated into a steady component and a transient component suggesting a significant local fluctuation of the current density. The physical process responsible for the fluctuations is the collapse of cavitation bubbles and the formation of microjets. The number

and magnitude of these jets impinging onto the electrode surface determines whether the simple stagnant diffusion layer model or a more sophisticated model is necessary.

A great many model systems that have been studied by electroanalytical methods are available for comparison with sonovoltammetric measurements. The reduction of halogenated aromatic compounds is known to cause in many cases the cleavage of the carbon halide bond with a first-order rate constant determined by the properties of the molecule. From the known range of accessible diffusion layer thicknesses in sonovoltammetry, ca. 1–15 μm , unimolecular rate constants ranging from 10 to 10^4 s^{-1} are accessible. The reduction of 3-bromobenzophenone and *ortho*-bromonitrobenzene in DMF [66] may be described by the ECE type mechanism given in Eqs. 7(a–d).



Of the two chemical reaction steps, Eqs. 7(b and c), usually Eq. 7(b) is rate limiting [67, 68]. In this mechanism, an electron transfer step at the electrode surface is followed by a chemical step in homogeneous solution, in this case the cleavage of a carbon bromide bond. The sigma radical Ar^\bullet is very reactive and may undergo H-atom transfer with the solvent or electrolyte present [69] to form the parent aromatic compound. This molecule can undergo further reduction at the electrode surface permitting a second electron to be transferred where the kinetics of the chemical step is fast enough to compete with the mass transport at the electrode surface.

Two voltammetric signals are observed for the reduction of 3-bromobenzophenone in DMF (0.1 M NBu_4PF_6) at a 3-mm glassy carbon electrode in silent conditions. The first process with $E_p^{\text{red}} = -1.56 \text{ V}$ (vs SCE) corresponds to the one-electron reduction process described in Eq. 7(a). The second chemically reversible reduction process occurs at a potential at which benzophenone itself is reduced and therefore corresponds to the process described in Eq. 7(d). At the insonated electrode, the ratio between the measured limiting current for the first and second processes decreases with decreasing horn to electrode separation, hence thinner diffusion layer thickness. A quantitative description for the effective number of electrons, n_{eff} , transferred at a uniformly accessible electrode for variable diffusion layer thickness is given in Eq. (8) [70].

$$n_{\text{eff}} = \frac{I_{\text{lim}}}{I_{\text{lim}}^0} = 2 - \frac{\sqrt{\tanh(\delta^2 k/D)}}{\sqrt{\delta^2 k/D}} \quad (8)$$

In this equation I_{lim}^0 is the purely transport controlled limiting current, D is the diffusion coefficient assumed to be identical for all species, and k is the first-order rate constant for the chemical reaction step. A plot of the observed limiting currents versus δ^{-1} determined from the first one-electrode process is shown in Fig. 10. A theoretical line can be fitted to the experimental points and a rate constant of $k = 600 \pm 100 \text{ s}^{-1}$ is in good agreement with the value reported in the literature, $k = 740 \pm 200 \text{ s}^{-1}$ [67]. For the reduction of *ortho*-bromonitrobenzene, a rate constant of $k = 200 \pm 50 \text{ s}^{-1}$ was determined, which is also in close agreement with the literature value of $k = 250 \text{ s}^{-1}$ [71]. The implication is that ultrasound facilitates the measurement of fast rate constants under steady state conditions at

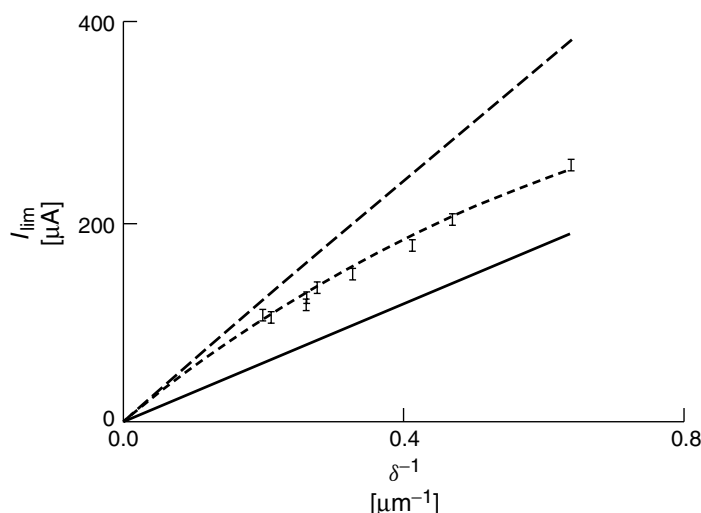


Fig. 10 Plot of sonovoltammetrically obtained limiting currents versus the reciprocal diffusion layer thickness for reduction of 3-bromobenzophenone in DMF at a glassy carbon electrode. The theoretically predicted curves for $k \rightarrow \infty$ and for $k = 6 \times 10^2 \text{ s}^{-1}$ are also shown.

macroelectrodes. These would otherwise only be measurable using steady state microelectrode studies or via transient techniques such as fast scan cyclic voltammetry. Furthermore, the results suggest, first, a physical reality to the diffusion layer concept, and second, no sonochemical enhancement of the reaction, at least in the two cases reported, as compared to silent conditions.

2.8.6

Extreme Conditions and Deviation from Hydrodynamic Behavior

It has been shown in Sect. 2.8.3 that when the source of ultrasound is brought very close to the working electrode, 5-mm horn to electrode separation or less, then the cavitation events induced can be very violent generating sharp spikes in the current transient. On systematic variation of horn to electrode separation and ultrasound power, it becomes

apparent that there is a threshold for the detection of violent cavitation activity [40]; see Fig. 8. This leads to the hypothesis that the cavitation threshold may coincide with the breakdown of the simple planar diffusion layer model, even when calibration of the diffusion layer thickness is employed. The transition to a more complex mass transport model would obviously be expected for very extreme conditions with strong cavitation interference. The calculated rates for the reduction of reduction of 3-bromobenzophenone at a range of diffusion layer thicknesses from 0.6 to 1.5 μm exhibited a marked deviation from the simple diffusion layer model under extreme conditions at low diffusion layer thickness with an apparently smaller number of electrons transferred. A purely thermal effect [72] would result in the opposite, suggesting that the negative deviation may be attributed to a breakdown of the mass transport model.

In practice, the diffusion layer prevailing under insonated conditions arises from an interplay between the effects of acoustic streaming and cavitationally induced microjetting, which control the overall sonovoltammetric response. Differential pulse voltammetry (DPV) has been used as a sensitive means of exploring the diffusion layer under steady state electrolysis at insonated electrodes. In DPV (see Chapter 2.2, Sect. 2.2.3 in this volume), the current is measured immediately before each pulse is applied and again at the end of the pulse; the difference between the two currents is recorded as a function of the voltage on the underlying staircase. Given that it is a difference in current that is monitored, it follows that the technique will be sensitive to the transport conditions prevailing during the interval between current sampling times. In particular, in a cavitation-free sonovoltammetric experiment, it would be expected [22, 32, 40] that a diffusion layer would be established in which convection was reduced as compared to the bulk solution. The transport of material within this diffusion layer would therefore control the DPV response. However, in a cavitationally highly active situation, the frequent disruption of the diffusion layer by bubble activity would reduce the voltammetric sensitivity if the frequency is such that bubbles are regularly formed in the interval between sampling times.

The effect of convection on the DPV response can be predicted by a theoretical comparison between the limit of a Nernstian diffusion layer in which the solution is fully stagnant and a rotating disc electrode [73, 74]. The general trend is as the speed of rotation increases (which corresponds to a reduction in diffusion layer thickness in the static simulation), the peak

height increases, because of convection increasing mass transport to the electrode (see Chapter 2.4 in this volume). Turning to sonovoltammetry, the simulations predict, by analogy, that at a given diffusion layer thickness, if the main effect of sonication is an enhancement of mass transport to the electrode via convection from acoustic streaming, a larger peak current will flow than that which would be measured under pure, entirely stagnant “Nernstian” diffusion layer conditions.

Differential pulse voltammograms were recorded for the well-characterized simple one-electron redox couples given in Table 1 at an insonated 1-mm Pt electrode over a calibrated range of diffusion layer thicknesses. For each of the experimental diffusion layer thickness, the theoretical peak current was simulated for an equivalent stagnant Nernstian diffusion layer [73] with the parameters of the DPV simulation corresponding with those employed experimentally. Figure 11(a–d) shows a comparison of experimental peak currents and theoretical peak currents for the solvents DMF, water and ammonia at a range of diffusion layer thicknesses. It is evident from Fig. 11 that experimentally obtained peak currents are smaller than those theoretically predicted at a given diffusion layer thickness, deviating most markedly at small diffusion layer thicknesses in which the ultrasonic perturbation is greatest. This is the opposite of the predictions of the rotating disc in which increasing mass transport via pure convection (higher rotation speeds) would lead to a larger peak current than that which would be measured under “Nernstian” diffusion layer conditions. It is therefore likely that cavitation not acoustic streaming is responsible for this deviation due to the turbulent collapse of bubbles perturbing or even replacing the diffusion layer. The conditions in which it

is believed that cavitation is strongest (see Fig. 7) result in the greatest deviation between theory and experiment. For all the solvents, the largest deviation is observed

at the smallest diffusion layer thickness, corresponding to the smallest horn to electrode separation and highest power of ultrasound. The correlation between

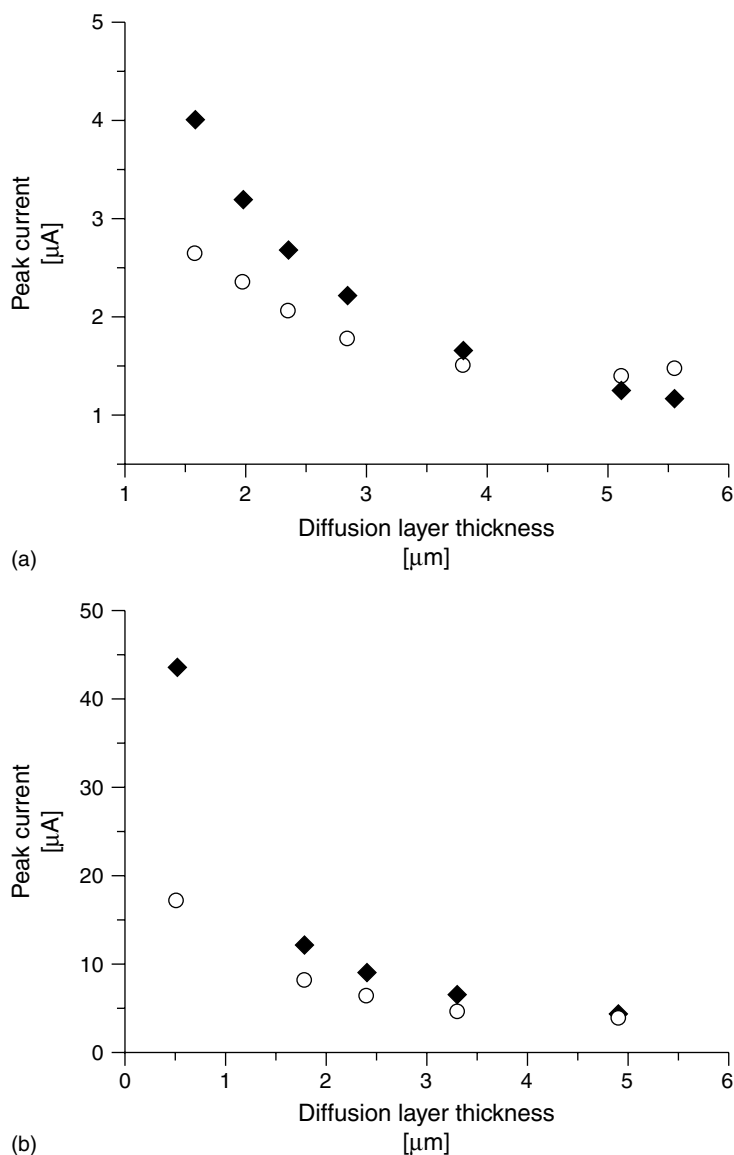


Fig. 11 Theoretical stagnant Nernst diffusion model (◆) and experimental (○) DPV peak currents for: (a) 1 mM ferrocene in DMF at 218 K; (b) 1 mM ferrocene in DMF at 298 K; (c) 1 mM $\text{Ru}(\text{NH}_3)_6^{3+}$ in water at 298 K; and (d) 1 mM nitrotoluene in liquid ammonia at 218 K.

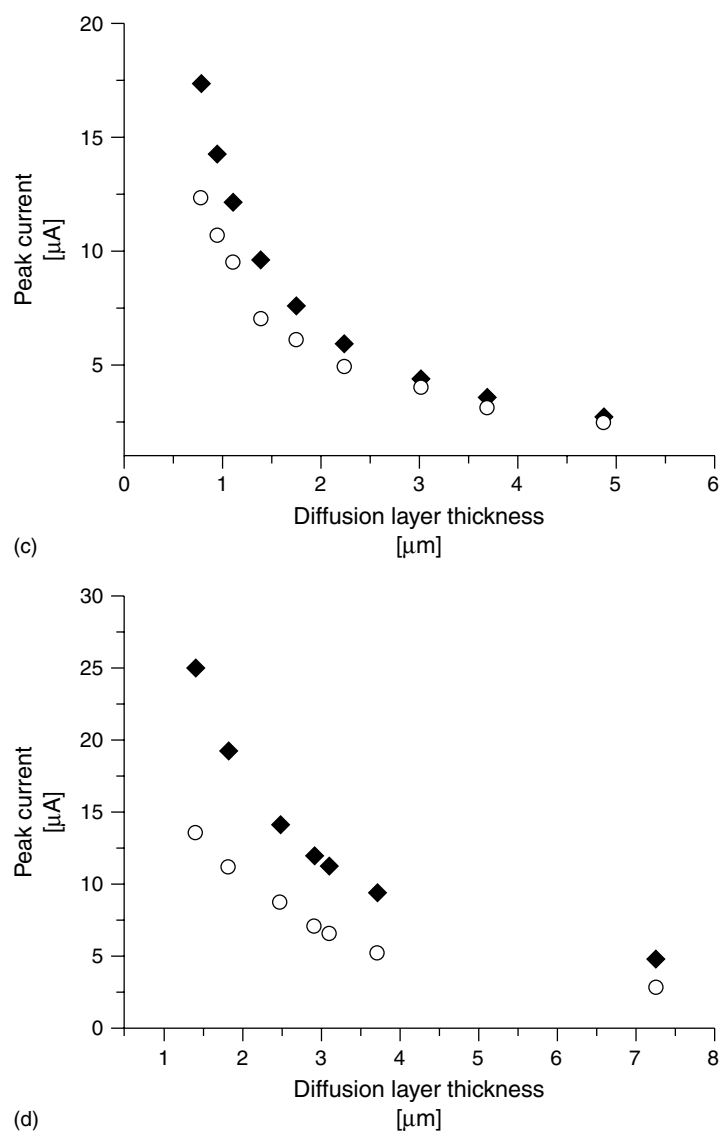


Fig. 11 (Continued)

cavitation and the deviation observed in the DPV confirms that the contribution from cavitation perturbation of the diffusion layer, from both bubble formation and microjetting, is significant in comparison with acoustic streaming under more extreme conditions. Nevertheless, it is also

clear that for mild ultrasonic stimulation, in which the diffusion layer thickness is relatively large, the Nernst diffusion model is physically realistic as testified by the good agreement between theory and experiment in the high diffusion layer thickness limit.

The resulting physical model of an insonated electrode can be described as a steady diffusion layer a few microns thick brought about by acoustic streaming, which is occasionally and randomly punctuated by a cavitation event the frequency and violence of which is dependent on the solvent and ultrasound intensity. At high intensity and short horn to electrode separation, the cavitation contribution becomes substantial with violent cavitation activity giving a pronounced deviation from the steady diffusion layer model.

2.8.7

The Effects of High-Frequency Power Ultrasound

The majority of studies coupling electrochemistry with ultrasound have employed ultrasonic emitters in the frequency range 20–40 kHz, primarily because of their ease of implementation and use. Although measurements of Faradaic currents based on electrochemical oxidation or reduction of redox-active solution species have been employed for the characterization of high-frequency sonochemical systems [45, 75], less is known about the physical nature of the effects prevailing at the surface of the electrode under these conditions. High-frequency ultrasound has been studied by microelectrode voltammetry [76], employed in electrosynthetic applications [77], and used in the modification of the properties and growth of electrochemically formed polymer films [78]. It has been shown that sonoelectrochemistry at high frequency is based on distinctly different processes than those governing sonoelectrochemistry at 20–40 kHz [79]. In particular, processes involving slowly diffusing species are especially enhanced in 500-kHz systems relative to their 20–40-kHz counterparts. At high frequencies, the

physical nature of the phenomena occurring at the electrode–solution interface is found to be considerably different from 20 kHz. As a result, some of the benefits observed in sonoelectrochemistry at lower frequencies are changed dramatically. The strong macroscopic acoustic streaming effect observed with a 20-kHz probe at 60 W cm^{-2} is absent, which can be attributed to the far lower ultrasonic intensity, $\sim 1.4 \text{ W cm}^{-2}$ and the change in geometry on going to a 500-kHz system. The use of an aqueous suspension of Mearlmaid OL permitted the visualization of the flow pattern in the liquid phase at 1.4 W cm^{-2} intensity and was indicative of a macroscopic toroidal and turbulent flow away from the transducer in the center of the reactor and back at the walls of the reactor. The flow rate is low, of the order of 5 cm s^{-1} , and is therefore only a minor factor contributing to mass transport effects. As a result of the much shorter wavelength associated with 500-kHz ultrasound in comparison with 20 kHz, the sound propagation is subject to reflection and interference phenomena, which give rise to a characteristic pattern of sonochemical activity. The implication of this is a ring-shaped zone of activity that has been detected by the chemiluminescence of luminol induced by cavitation activity [75]. When compared with systems employing low-frequency ultrasound, 500-kHz power ultrasound is known to give better efficiency in sonochemical processes due to the number and timescale of cavitation events, which reaches an optimum around 0.5 MHz [80]. This has led to the exploitation of 500 kHz for the sonochemical mineralization of organic waste products [81].

The positioning of the electrode in the reactor is a crucial factor in determining the origin of the enhanced mass transport

observed for simple one-electron redox processes at the electrode surface [75, 79]. It was found that current enhancement is not maximized by positioning the electrode in the center of the cell as would be predicted if macroscopic acoustic streaming is the predominant effect. However, the intensity pattern attributed to high cavitation activity, which peaks in a ring-shaped pattern half way between the center and the reactor walls is reproduced. This clearly suggests that cavitation is an important factor in inducing mass transport at the electrode–solution interface.

The magnitude of the average limiting currents observed at a glass-mounted Pt disc electrode is proportional to the concentration of reactant c_{bulk} , and to the area of the electrode, A , for a range of electrode diameters from 0.25 to 6.0 mm consistent with Eqn. (2). However, the effect of the diffusion coefficient, D , on the observed limiting current has been shown [25–30] to reveal the subtleties of the nature of mass transport observed. A linear relationship, $I_{\text{lim}} \propto D$, is indicative of a truly stagnant diffusion layer, in the presence of 20 kHz, $I_{\text{lim}} \propto D^{2/3}$, is consistent with hydrodynamic flow or acoustic streaming. In the case of 500-kHz ultrasound, the effect of the diffusion coefficient on the limiting current is much smaller than anticipated on the basis of existing mass transport models for ultrasonically enhanced processes with $I_{\text{lim}} \propto D^{0.24}$. A simplistic model, allowing the observations to be rationalized, must account for a mechanism other than diffusion dominating the mass transport. If at a rate of 500 kHz microjetting or micromixing phenomena occur at the electrode–solution interface, then the timescale for diffusion is reduced and the distance that molecules can travel, δ_{diff} ,

becomes short (Eqn. 9).

$$\delta_{\text{diff}} = \sqrt{\frac{D}{500 \text{ kHz}}} \approx 0.05 \text{ } \mu\text{m} \quad (9)$$

Therefore, at high ultrasound frequencies and at electrodes of slow time constant (large diameter), transport due to mixing on a microscopic scale may effectively compete with transport due to diffusion.

Although the mass transport at higher frequencies such as 500 kHz has been shown to be dominated by cavitation and microstreaming, there is little damage to conventional electrodes made from platinum, gold, or carbon even after prolonged periods of sonication. This is advantageous if mechanically less robust electrode materials such as lead, graphite, or metal oxide have to be used. The erosion process, although subtle still leads to significant surface effects as has been shown for an electrochemically deposited film of Prussian blue [79]. Under silent conditions the films are stable over many potential cycles. However, the diminishing area under the voltammetric signal observed after several minutes of sonication at 500 KHz suggests that the film is gradually removed. Furthermore, a change in the shape of the voltammetric response suggests that the rate of transport of ions into the film, or electrons out of the film becomes slower. A comparison of film degradation observed in the presence of 500-kHz ultrasound with and without degassing the solution prior to insonation reveals a dramatic increase in film degradation after degassing. A plausible interpretation associates this with the increase in violence of cavitation processes after degassing. Gas and gas bubbles present in the solution phase act to cushion the violence of the implosion process. In the degassed solution, the colored Prussian blue film is completely

removed from the electrode surface after approximately 15 min of insonation.

Electrochemical processes in the presence of high-frequency 500-kHz ultrasound are governed by processes considerably different from those that are important at lower frequencies. The basis of the mass transport model is suggested to be microjetting and micromixing. The relatively low dependence of the mass transport controlled limiting current on the diffusion coefficient suggests that even at higher ultrasound frequencies, ultrasound processes could become independent of the diffusion coefficient, thereby relatively favoring processes involving very slowly diffusing species such as proteins [23, 82].

References

1. J. Curie, P. Curie, *Compt. Rend.* **1880**, 91, 294.
2. J. Curie, P. Curie, *Compt. Rend.* **1881**, 93, 1137.
3. T. J. Mason, J. P. Lorimer, *Sonochemistry: Theory Applications and Uses of Ultrasound in Chemistry*, Ellis Horwood, Chichester, UK, 1988.
4. Y. I. Goltzov, V. E. Yurkevich, *Ferroelectrics* **1992**, 129, 67.
5. J. R. Frederick, *Ultrasonic Engineering*, John Wiley & Sons, New York, NY, 1996.
6. J. Tsujino, T. Ueoka, K. Hasegawa et al., *Ultrasonics* **1996**, 34, 177.
7. M. Halliwell, *IEEE Proc. Sci. Meas. Technol.* **1987**, 134, 179.
8. J. P. Lorimer, T. J. Mason, D. Kershaw et al., *Colloid Polym. Sci.* **1991**, 269, 392.
9. G. W. Gale, A. A. Busnaina, *Particulate Sci. Technol.* **1996**, 13, 197.
10. E. Westfelt, *J. Clin. Periodontol.* **1996**, 23, 263.
11. A. Tai, T. Kikukawa, T. Sugimura et al., *Bull. Chem. Soc. Jpn.* **1994**, 67, 2473.
12. P. D. Lickiss, V. E. McGrath, *Chem. Br.* **1996**, 32, 47.
13. A. A. Kaplin, V. A. Bramin, I. E. Stas, Z. Anal. Khim. **1998**, 43, 921.
14. E. Yeager, F. Hovorka, *J. Acoust. Soc. Am.* **1953**, 25, 47.
15. V. Yegnaraman, S. Bharathi, *Bull. Electrochem.* **1992**, 8, 84.
16. R. G. Compton, J. C. Eklund, F. Marken, *Electroanalysis* **1997**, 9, 509.
17. D. J. Walton, S. S. Phull, A. Chyla et al., *J. Appl. Electrochem.* **1995**, 25, 1083.
18. H. Huck, *Ber. Bunsen-Ges Phys. Chem.* **1987**, 91, 648.
19. F. Marken, R. G. Compton, *Ultrasonics Sonochem.* **1996**, 3, 5131.
20. J. C. Eklund, F. Marken, D. N. Waller et al., *Electrochim. Acta* **1996**, 41, 1541.
21. R. G. Compton, J. C. Eklund, F. Marken et al., *Electrochim. Acta* **1996**, 41, 315.
22. F. Marken, R. P. Akkermans, R. G. Compton, *J. Electroanal. Chem.* **1996**, 55, 415.
23. H. A. O. Hill, Y. Nakagawa, F. Marken et al., *J. Phys. Chem.* **1996**, 100, 17 395.
24. J. Lighthill, *Waves in Fluids*, Cambridge University Press, Cambridge, UK, 1978, p. 337.
25. K. S. Suslick, *Science* **1990**, 247, 1439.
26. A. Henglein, *Ultrasonics* **1987**, 25, 6.
27. R. Penn, E. Yeager, F. Hovorka, *J. Acoust. Soc. Am.* **1959**, 31, 1372.
28. E. Kowalska, J. Mizera, *Ultrasonics* **1971**, 9, 81.
29. C. R. S. Hagan, L. A. Coury Jr., *Anal. Chem.* **1994**, 66, 399.
30. R. G. Hickmann, *Plating* **1965**, 52, 407.
31. F. Marken, J. C. Eklund, R. G. Compton, *J. Electroanal. Chem.* **1995**, 395, 335.
32. R. G. Compton, J. C. Eklund, S. D. Page et al., *J. Appl. Electrochem.* **1996**, 26, 775.
33. P. H. Reiger, *Electrochemistry*, Chapman & Hall, New York, NY, 1994.
34. T. G. Leighton, *The Acoustic Bubble*, Academic Press, London, 1994.
35. S. A. Peruisch, R. C. Alkire, *J. Electrochem. Soc.* **1991**, 138, 700, 708.
36. J. Klima, C. Bernard, C. Degrand, *J. Electroanal. Chem.* **1995**, 339, 147.
37. P. R. Birkin, S. Silva-Martinez, *Chem. Commun.* **1995**, 1807.
38. P. R. Birkin, S. Silva-Martinez, *J. Electroanal. Chem.* **1996**, 416, 127.
39. L. Pastore, F. Magno, C. A. Amatore, *J. Electroanal. Chem.* **1989**, 26, 33.
40. J. L. Hardcastle, J. C. Ball, Q. Hong et al., *Ultrasonics Sonochem.* **2000**, 7, 7.
41. H. Zhang, L. A. Coury Jr., *Anal. Chem.* **1993**, 65, 1552.
42. R. G. Compton, J. C. Eklund, S. D. Page et al., *J. Phys. Chem.* **1994**, 98, 12 410.

43. F. Marken, S. Kumbhat, G. H. W. Sanders et al., *J. Electroanal. Chem.* **1996**, 414, 95.
44. W. J. Tomlinson, *Adv. Sonochem.* **1990**, 1, 173.
45. A. Benahcene, C. Petrier, G. Reverdy et al., *New J. Chem.* **1995**, 19, 989.
46. N. A. Madigan, C. R. S. Hagan, L. A. Coury Jr., *J. Electrochem. Soc.* **1994**, L23, 141.
47. S. V. Ley, C. M. R. Low, *Ultrasound in Synthesis*, Springer, Berlin, 1989.
48. G. J. Price, (Ed.), *Current Trends in Sonochemistry*, The Royal Society of Chemistry, London, 1992.
49. K. S. Suslick, (Ed.), *Ultrasound: its Chemical, Physical and Biological Effects*, Wiley-VCH, Weinheim, Germany, 1988.
50. P. Colarusso, N. Serpone, *Res. Chem. Intermed.* **1996**, 22, 61.
51. M. R. Hoffmann, I. Hua, R. Höchemer, *Ultrasonics Sonochem.* **1996**, 3, S163.
52. N. Serpone, R. Terzian, H. Hidaka et al., *J. Phys. Chem.* **1994**, 98, 2634.
53. N. Gondrexon, V. Renaudin, A. Bernis et al., *Environ. Technol.* **1993**, 14, 587.
54. C. Petrier, Y. Jiang, M.-F. Lamy, *Environ. Sci. Technol.* **1998**, 32, 1316.
55. A. J. Colussi, H.-M. Hung, M. R. Hoffmann, *J. Phys. Chem.* **1999**, 103, 2696.
56. Q. Hong, J. L. Hardcastle, R. A. J. McKeown et al., *New J. Chem.* **1999**, 23, 845.
57. K. Makino, M. M. Mossoba, P. Riesz, *J. Phys. Chem.* **1983**, 87, 1369.
58. V. Misik, P. Riesz, *Sonochemistry and Sonoluminescence*, Nato ASI Series, Kluwer Academic Publishers, Boston, Mass., 1997, p. 225, Vol. 524.
59. A. Henglein, *Adv. Sonochem.* **1993**, 3, 17.
60. A. Kotronarou, G. Mills, M. R. Hoffmann, *J. Phys. Chem.* **1991**, 95, 3630.
61. A. Henglein, *Ultrasonics Sonochem.* **1995**, 2, S115.
62. R. G. Compton, J. C. Eklund, F. Marken et al., *Electrochim. Acta* **1997**, 42, 2919.
63. C. G. Jung, F. Chapelle, A. Fontana, *Ultrasonics Sonochem.* **1997**, 4, 117.
64. P. R. Unwin, R. G. Compton, *J. Electroanal. Chem.* **1988**, 8, 107.
65. F. Barz, C. Bernstein, W. Vielstich, *Adv. Electrochem. Electrochem. Eng.* **1984**, 13, 261.
66. R. G. Compton, F. Marken, T. O. Rebbitt, *Chem. Commun.* **1996**, 1017.
67. L. Nadjo, J. M. Savéant, *J. Electroanal. Chem.* **1971**, 30, 41.
68. C. P. Andrieux, J. M. Savéant, D. Zann, *New J. Chem.* **1984**, 8, 107.
69. R. G. Compton, J. C. Eklund, L. Nei, *J. Electroanal. Chem.* **1995**, 381, 87.
70. S. Karp, *J. Phys. Chem.* **1968**, 72, 1082.
71. R. G. Compton, R. G. Wellington, P. J. Dobson et al., *J. Electroanal. Chem.* **1994**, 370, 129.
72. N. A. Madigan, L. A. Coury, *Anal. Chem.* **1997**, 69, 5.
73. J. L. Melville, R. G. Compton, *J. Electroanal. Chem.* **2001**, 501, 114.
74. F. J. Del Campo, J. Melville, J. L. Hardcastle et al., *J. Phys. Chem. A* **2001**, 105, 666.
75. F. Trabelsi, H. Ait-lyazidi, J. Berlan et al., *Ultrasonics Sonochem.* **1996**, 3, S125.
76. P. R. Birkin, C. L. Delaplace, C. R. Bowen, *J. Phys. Chem.* **1998**, 102, 10885.
77. J. P. Lorimer, B. Pollet, S. S. Phull et al., *Electrochim. Acta* **1996**, 41, 2737.
78. D. J. Walton, U. Geissler, S. S. Phull et al., *Chemical Processes and Reactions Under Extreme or Non-Classic Conditions*, European Communities Publication COST Action D6, European Communities Publication, 1998, p. 83.
79. F. J. Del Campo, B. A. Coles, F. Marken et al., *Ultrasonics Sonochem.* **1999**, 6, 189.
80. T. J. Mason, J. P. Lorimer, D. M. Bates, *Ultrasonics* **1992**, 30, 1.
81. J. D. Schramm, I. Hua, *Water Res.* **2001**, 35, 665.
82. A. V. Sokirko, K. B. Oldham, *J. Electroanal. Chem.* **1997**, 1430, 15.

2.9

Sonoelectroanalysis: Applications

*Richard G. Compton, Joanna L. Hardcastle,
Javier del Campo
Physical and Theoretical Chemistry Laboratory,
University of Oxford, South Parks Road,
Oxford, UK*

2.9.1

Analysis by Classical Electrochemical Techniques

Electrochemical methods of analysis are extremely sensitive and have been exploited to permit the detection of a wide range of analytical targets down to concentrations of the order 10^{-10} M in favorable conditions. The relative low cost of these electroanalytical techniques when compared with conventional techniques such as Inductively Coupled Plasma-Mass Spectrometry (ICP-MS) and Atomic Absorption Spectroscopy (AAS) has led to the use of electrochemical stripping voltammetry (Chapter 2.3) and linear sweep voltammetry (Chapter 2.1) for the detection of both inorganic and organic species [1–6]. Target analytes that have been documented include heavy metals (Bi, Cu, Cd, Ga, Mn, Pb, Sb, Sn, V, Zn), cardiac and anticancer drugs, vitamins, and pesticides. However, the limits of applicability for these “silent” classical electrochemical techniques have been compromised by four main drawbacks:

- lack of rapidity with long accumulation steps [7, 8];
- deactivation and complete fouling of the electrode surfaces due to passivating adsorbates [9–17];
- low sensitivity in “real media” in the absence of time-consuming substrate pretreatments [14–18];
- techniques are often dependent on environmentally unacceptable mercury electrodes.

In attempts to overcome these problems, a range of techniques have been employed. The use of rotating disk electrodes (Chapter 2.4) reduces the accumulation time required for sensitive stripping analysis, however, the benefits are restricted to rotation speeds up to the limit where nonlaminar flow hinders reliable quantification [19]. Microelectrodes (Chapter 2.5), with diameters of 1–100 μm have further enhanced the applicability of electroanalysis but not without drawbacks. The main difficulties are primarily their fragility, with consequent complications for cell design, and also dimensional instability resulting from erosion or the dissolution of electrode substrate into deposited metals [20]. The use of either of these techniques is limited in environmental, biological or food samples due to the surface passivating effects of proteins, sugars, soluble polymers, and solid particulate matter. Such electrode fouling can be overcome in part by the use of a hanging mercury drop electrode (HMDE), which permits continuous regeneration of the surface by slowly allowing mercury to drop from the electrode. The technique has been used for a wide range of applications, but is still plagued by the drawbacks associated with long accumulation times. Furthermore, the use of mercury in high quantities is undesirable because of its toxicity and future restrictions on its use [21, 22].

2.9.2

Coupling Ultrasound with Electroanalysis

The synergistic coupling of ultrasound with electroanalytical measurements has been the subject of detailed study for many years [23, 24] and the technique is now

emerging as a powerful electroanalytical tool [7, 24–31]. The cavitation and acoustic streaming effects of ultrasound are reported in Sects. 2.9.1.3 and 2.9.1.4 [21, 24, 30–32] and have been shown to facilitate the determination of trace metals in highly passivating media such as alcoholic beverages [21, 24–26, 28, 33]. Ultrasonically enhanced stripping and linear sweep voltammetry (LSV) has therefore been successfully applied to *inter alia* the determination of lead in wine [33], copper in beer [21], lead in river sediment [34], manganese in tea [35], nitrite in egg [36], and copper in blood [37]. Table 1 provides an overview of the scope of sonoelectroanalysis demonstrating the diversity of targets and the accuracy of results.

2.9.3

Sono-anodic Stripping Voltammetry (sono-ASV)

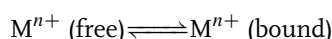
Targeting analytes in “real” media containing organics such as sugars, proteins, fats, and soluble polymers using classical, silent ASV is plagued by long accumulation times and the passivating effects of adsorbed species on the surface of the electrode. Typically this leads to insensitivity or even complete blocking of the electrode. The applications described below exemplify both the benefits afforded by ultrasound and the versatility of this novel technique, demonstrating accurate and rapid analyses in media previously inaccessible to the electrochemist.

2.9.3.1 The Determination of Heavy Metals in Alcoholic Beverages

Lead in wine An early target for interrogation by sono-ASV was monitoring trace amounts of heavy metals in alcoholic beverages [33]. Quantification of lead in a

white Italian Chardonnay was shown to be possible. The enhanced mass transport associated with power ultrasound yields efficient preconcentration of lead over a short period of time at a Hg/Pt electrode, this step was followed by a linear anodic potential sweep. The standard microaddition technique [33] was implemented with a 10-min sonication period between each deposition step in order to clean and activate the surface and ensure efficient mixing of the cell contents. The lead concentration yielded by sono-ASV was compared with an independent assay by AAS, the current standard method [38], for total lead detection in wine samples, and the sono-ASV results were found to be in excellent agreement (see Table 1). Previous attempts to employ ASV for lead detection have been unsuccessful with typically only ~50% of the true lead level detected by AAS being recorded [13].

The benefits of insonation are first, maintenance of the equilibrium between “free” and “bound” ions as described by the equilibrium constant K_{eq} for the following equilibrium:



Second, and most importantly, the maintenance of a clean, active electrode surface to ensure the uptake of metal from the range of complex lead cation species labeled Pb^{2+} (free). In the absence of ultrasound, there is a much reduced signal because of blocking by organic species.

Copper in beer Leaching of copper ions from the fermentation vessel into beer is a side effect of the brewing process [21], its rapid evaluation is therefore of importance to the industry. Mercury-free electrodes were used to determine the amount of copper in Marstons “Pedigree

Tab. 1 Overview of the scope of Sonoelectroanalysis demonstrating a diverse range of targets and the accuracy of results that can be achieved.

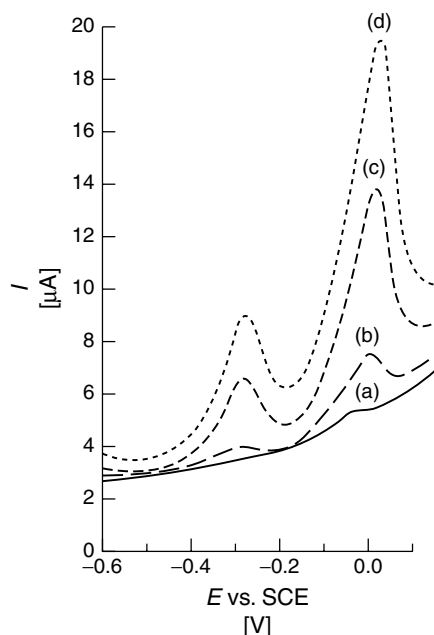
Analytical target	Voltammetric method	Concentration via sono method	Detection limit [M]	Independent method	Concentration via independent method
Lead in wine	Sono-ASV	22 ± 6 µg L ⁻¹	3 × 10 ⁻⁸	AAS	24 ± 4 µg L ⁻¹ 27 ± 4 µg L ⁻¹
Copper in beer	Sono-ASV	222 ± 31 µg L ⁻¹ 139 ± 4 µg L ⁻¹	5 × 10 ⁻⁷	AAS	230 ± 6 µg L ⁻¹ 140 ± 6 µg L ⁻¹
Copper in blood	Sono-ASV	1300 ± 300 µg L ⁻¹ 620 ± 60 µg L ⁻¹	3 × 10 ⁻⁶	AAS	1300 µg L ⁻¹ 690 µg L ⁻¹
Copper in fish gill mucus	Sono-ASV	16 ± 4 µg L ⁻¹ 21 ± 4 µg L ⁻¹	6 × 10 ⁻⁸	AAS	17 ± 4 µg L ⁻¹ 25 ± 4 µg L ⁻¹
Lead in river sediment	Sono-CSV	187.1 mg kg ⁻¹	1 × 10 ⁻⁸	ICP-MS	206.1 mg kg ⁻¹
Manganese in instant tea	Sono-CSV	1859 µg g ⁻¹ 914 µg g ⁻¹	1 × 10 ⁻¹¹	AAS	1800 µg g ⁻¹ 1000 µg g ⁻¹
Nitrite in egg	Sono-LSV	1.20 ± 0.05 mg kg ⁻¹ 1.40 ± 0.05 mg kg ⁻¹	1 × 10 ⁻⁶	MAFF data	1.0–2.5 mg kg ⁻¹ Mean 1.7 ± 0.4 mg kg ⁻¹
Nitrate in effluent	Sono-LSV	469 µM		Griess assay	479 µM
Lead in petrol	Biphasic sono-ASV	380 ± 40 µg L ⁻¹	2 × 10 ⁻⁷	AAS	400 ± 20 µg L ⁻¹
Vanillin in vanilla essence	Biphasic sono-SWV	9.09 ± 0.2 mM 9.24 ± 0.2 mM	2 × 10 ⁻⁵	HPLC-UV	9.17 mM 9.13 mM

Note: AAS: Atomic absorption spectroscopy; ICP-MS: Inductively coupled plasma–mass spectrometry; MAFF: Ministry of agriculture fisheries and food; HPLC-UV: High performance liquid chromatography with UV detection; ASV: Anodic stripping voltammetry; CSV: Cathodic stripping voltammetry.

Fig. 1 Square wave anodic stripping voltammograms of aqueous solutions of “Pedigree” beer following deposition: (a) beer under silent conditions; (b) beer under insonated conditions; (c) insonated deposition following the first microaddition of copper; (d) insonated deposition following the second microaddition of copper.

Bitter” (Marston’s Brewery, Burton-on-Trent, Staffs., UK) using a glassy carbon electrode. Deposition of copper on the glassy carbon substrate was performed under power ultrasound and was followed by an anodic stripping step which employed a square wave scan [CR]. Typical square wave voltammograms are shown in Fig. 1 for microadditions to the beer sample. The wave at ca. 0 V (vs. SCE) increases with added copper concentration and corresponds to the anodic stripping peak of solid copper deposited on the electrode surface. It can clearly be seen that in the absence of ultrasound (scan a) no measurable stripping peak for copper is obtained because of the passivation of the electrode by sugars and other organic material in the beer. Total copper content levels were determined using this technique with the calculated results within one standard deviation of the independent AAS analysis (see Table 1).

The successful determination of copper in beer, a complex system that precludes meaningful measurements under silent conditions, opened up the possibility for analysis in even more inaccessible media such as biological samples. Cavitation depassivation provides a remarkable enhancement in measured Faradaic currents whilst the increased mass transport due to acoustic streaming lowered the accumulation times below those required for other hydrodynamic voltammetric techniques such as rotating disk electrodes.



2.9.3.2 The Determination of Copper in Biological Samples

Liberation and determination of copper in whole blood Copper is an essential mineral present in the bloodstream which is vital for infant growth [37], host defense mechanisms, bone strength, red and white cell maturation, iron transport, cholesterol and glucose metabolism, myocardial contractility, and brain developments [39–42]. Studies have shown that the variation in trace copper content in whole human blood usually varies between 800 and 1400 $\mu\text{g L}^{-1}$ [43] depending on age and sex. More than 90% of this copper is bound to ceruloplasmin, an α_2 -globulin [44, 45]. The diagnosis of marginal copper deficiency by traditional methods (AAS or serum ceruloplasmin levels) has not been perfected and can be highly unreliable, underlining the need for a technique to accurately and rapidly determine copper stores in whole blood that is cheaper than spectroscopic or enzymatic

techniques and requires little or no sample pretreatment.

In order to investigate the role of ultrasound in the extraction of copper from a solution of whole blood, the accumulation step followed a pretreating insonation period. Subsequently, silent accumulation was performed at a bare glassy carbon electrode, followed by a square wave–stripping step. It was observed that the size of the stripping peak is related to the duration

of insonation prior to the deposition, with an increase in peak size reaching a plateau after 960 s. We conclude that ultrasound facilitates the liberation of copper from the active sites where it is bound within the ceruloplasmin and, accordingly, enhanced peak heights are obtained (see Table 2). The insonated deposition and pretreatment is contrasted with the response obtained in silent conditions in Fig. 2, which demonstrates a large current

Tab. 2 Approximate peak heights for SWASV (amplitude of 50 mV, step potential 2 mV and frequency 60 Hz) in a 10% by volume solution of horse blood in 0.1 M nitric acid for a range of pretreatment and deposition stages

Experimental details				Approximate SWASV peak height [μA]
Pretreatment duration [s]	Ultrasound power [W cm^{-2}]	Deposition duration [s]	Ultrasound power [W cm^{-2}]	
0	0	240	0	5
240	300	240	0	8
480	300	240	0	14
720	300	240	0	19
960	300	240	0	20
960	300	240	300	60

Note: SWASV: Square wave anodic stripping voltammogram.

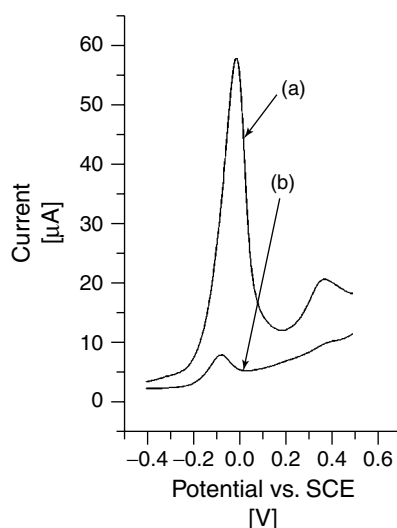


Fig. 2 Square wave anodic stripping voltammogram of 10% by volume whole blood in 0.1 M nitric acid on a glassy carbon electrode following deposition at -1.5 V for: (a) 240 s insonated; (b) 240 s silent.

enhancement in the sono case. The total copper content obtained using sono-ASV exhibited close agreement with independent analyses of both samples (Table 1).

When coupled with heightened mass transport and cavitation cleaning, this previously unreported type of ion liberation resulting from insonation removes the necessity for complex and degradative sample pretreatments in biological samples. The result is a facile and inexpensive technique that can provide an accurate measure of copper status from an appropriate volume of blood without incurring undue time or cost.

2.9.3.3 Determination of Copper in Fish Gill Mucus

Fish are commonly used as environmental biomarkers to assess the levels of pollution in waterways [46]. Of the existing methods of test available, direct determination of metal concentrations in fish tissue samples is the most universal indicator of metal pollution levels since it is the least species specific and provides precise elemental values. It is, however, a destructive technique that involves complicated methodology and dissection. Histopathological studies of fish exposed to pollutants have shown that fish gills are efficient indicators of water quality [47–49]. Aqueous metal interactions at fish gills have been modeled to demonstrate the binding and rate of uptake of different heavy metals into the gills [50, 51] and it has been proposed that gill mucus plays a large part in these interactions via the glycoproteins within the layer of mucus covering these organs [52].

The application of power ultrasound to mucus solution extracted from *Salmo gairdneri* (rainbow trout) into borate buffer followed by SWASV has been shown to directly facilitate a rapid, quantitative

determination of total copper content and qualitative heavy metal contamination within the extract. The results demonstrate good intrasample reproducibility and compare favorably with independent analysis by AAS (Table 1).

In an insonated system, it is possible to optimize the ultrasound power and deposition potential in order to target a specific heavy metal. Fig. 3(a,b) shows the variation in ultrasound power and deposition potential for copper and lead from a dilute mucous solution. It is evident that the optimum deposition of copper is effected at 200 W cm^{-2} ultrasound power and potential of -1.6 V . For lead, this is found to be 100 W cm^{-2} ultrasound power and a potential of -1.7 V . We conclude that stability of the deposit on the surface of the electrode is dependent on the interaction between the deposit and the electrode surface and the cavitation activity, which also acts to depassivate the electrode in the presence of glycoproteins from the mucus.

The versatility of sono-ASV has developed from the modes by which individual metals can be targeted, such as horn power and horn to electrode separation in synergy with deposition potential and electrode material. The use of insonated solid electrodes that can effect preferential plating of the target analyte over competing species even when such species are in excess is a powerful analytical prospect.

2.9.3.4 Silver Analysis at a Boron-doped Diamond Electrode

The use of an insonated boron-doped diamond (BDD) electrode [53] permitted the quantitative measurement of silver ions. This chemically and mechanically robust surface is unaffected even by high ultrasound powers and very short

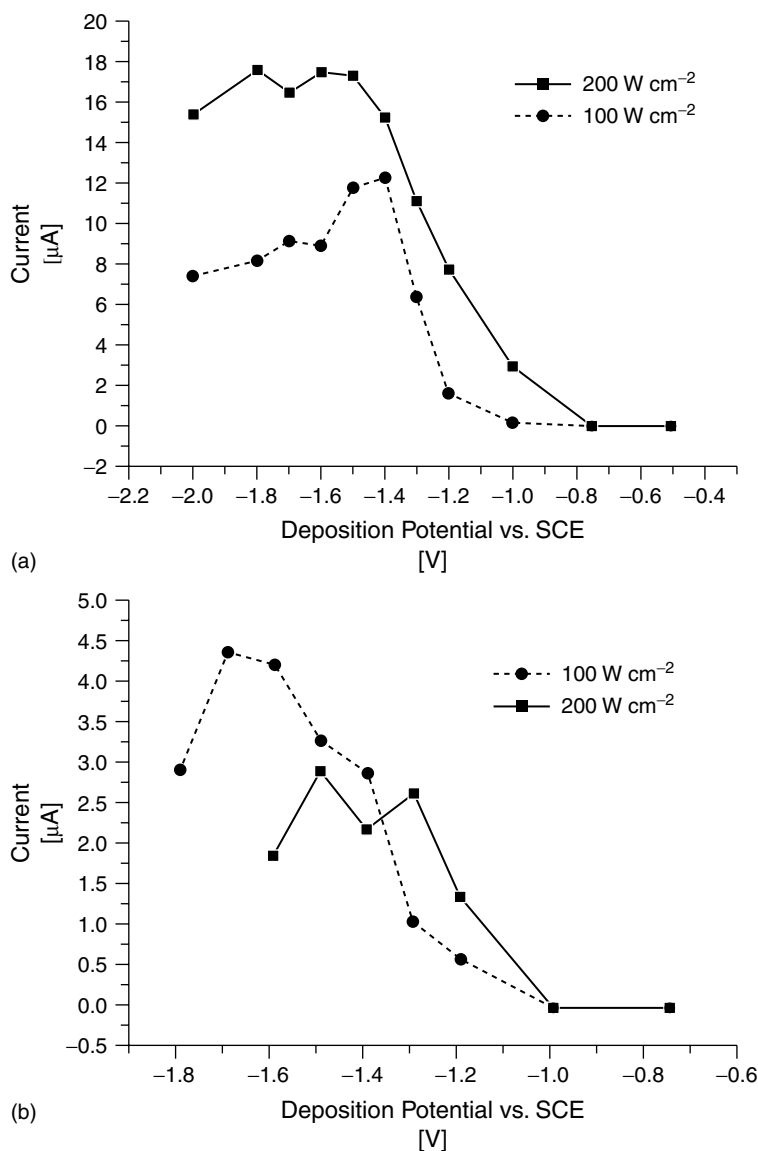


Fig. 3 Variation in square wave anodic stripping peak currents from a dilute solution of rainbow trout mucous in 0.1 M nitric acid at a glassy carbon electrode for: (a) copper at varying deposition potentials and ultrasound intensity; (b) lead at varying deposition potentials and ultrasound intensity.

horn to electrode separations [54]. A linear anodic stripping scan was employed to monitor the concentration of silver ions following an insonated accumulation at

the electrode surface. The practical lower limit of detection for a deposition time of 300 s was 10^{-9} M, and it is reasonable to predict that detection limits below 10^{-9} M

would be possible as peak response scaled with deposition time and ultrasound power.

The determination of silver concentration using ASV has been limited by its strong interaction with mercury, their similar stripping potentials, and poor irreproducible deposition on other materials. The use of novel surface materials such as BDD, which can endure ultrasound of extremely high intensity for longer periods of time, has further highlighted the specificity that can be achieved by the correct combination of experimental parameters without the necessity for complexing agents or separation techniques.

2.9.3.5 Determination of Cadmium in the Presence of Surfactant

The effect of applying ultrasound to the anodic stripping voltammetric analysis of the toxic heavy metal cadmium [55], in the presence of the surfactant Triton X-100, has been explored at a mercury thin film glassy carbon electrode. Manipulation of the horn intensity and the horn to electrode separation effectively reduced the deleterious influence of the surfactant on the height of the cadmium peak, which became less susceptible to the influence of Triton-X with decreasing horn to electrode separation. The optimal configuration was found to reduce the suppressive influence of Triton-X on the Cd stripping peak height from 58 to 14 %. The analytical performance of the system towards the detection of Cd^{2+} in solutions containing Triton-X was assessed. As a result, facile detection of Cd^{2+} ($0.05\text{--}4.00\text{ }\mu\text{M}$) in solutions containing $10\text{ }\mu\text{g mL}^{-1}$ Triton-X can be achieved without recourse to sample pretreatments or electrode modification.

The technique is directly applicable to the online analysis of wastewater, which

typically contains a high concentration of detergents that would, under silent conditions, rapidly foul the electrode by forming an adsorbed layer on the surface.

2.9.4

Applications of Sono-adsorptive Stripping Voltammetry (Sono-AdSV)

AdSV (Chapter 2.3) has been applied to the detection of metals such as Co, Ni, Mo, U, and V (following their preconcentration as metal complexes) and a wide variety of organic compounds including drugs such as codeine, herbicides such as atrazine, and vitamins such as folic acid and riboflavin [1]. The preconcentration step is crucial for AdSV analysis and its rapidity affects the selectivity and sensitivity of the method [8]. The extent of preconcentration and hence the detection limit depends on the length of time over which the adsorption is allowed to proceed. Consequently, insonation was found to significantly improve the sensitivity of the AdSV of a vanadium (V) catechol complex by increasing the rate at which the complex was deposited onto a mercury surface. Maximum responses can be achieved for an insonated system in less than one-tenth the time required for conventional AdSV under silent conditions.

In cases in which the target cannot be usefully preconcentrated by electrolysis at electrode surfaces, such as transition metals with numerous high stable oxidation states or metals which show complicated amalgam formation, AdSV (Chapter 2.3) can be a valuable alternative. Exploiting the enhanced mass transport afforded by insonation in this way offers improved levels of sensitivity.

2.9.5

Applications of Sono-cathodic Stripping Voltammetry (Sono-CSV)

Cathodic stripping voltammetry of metal ions is a complementary technique to ASV. Its benefits include the avoidance of interactions between metals, such as the formation of alloys on the surface of solid electrodes [21], and an alternative to the use of mercury electrodes. However, the applications of CSV reported in literature are relatively few, considering the potential benefits of the technique. Early studies of CSV utilized platinum electrodes although these methods invariably involved lengthy deposition times and a limited range of applications [56–59]. Alternative electrode materials such as conducting glass [60] and tin oxide [61] proved to be more successful although the applications were limited to relatively clean samples such as rain water. The following applications describe the use of ultrasound to broaden the range of analytical targets accessible by CSV when coupled with the mechanically and chemically robust BDD electrode [54].

2.9.5.1 Determination of Lead in River Bed Sediment

In the determination of lead by ASV, inter-metallic species and overlapping signals can often lead to complications [34]. The effect of possible interferences when using sono-CSV, from other ionic metallic species often found in industrial waste, such as chromium, copper, nickel, iron, cadmium, and zinc, was investigated on a BDD electrode. The results demonstrated that Cr, Ni, Cd, and Zn were not detected by this technique. However, both Cu and Fe were detected at potentials more cathodic than for Pb reduction but had no effect on the Pb response. Figure 4 shows the responses observed for Cu, Pb and Fe, demonstrating a very high elemental specificity for lead ($1\ \mu\text{M}$) over Cu ($150\ \mu\text{M}$) and Fe ($300\ \mu\text{M}$).

The river sediment sample used for quantitative analysis was taken from a region downstream of a location extensively exploited for metalliferous mining, which consequently contained significant heavy metal contamination. Following ultrasonic digestion in a mixture of concentrated

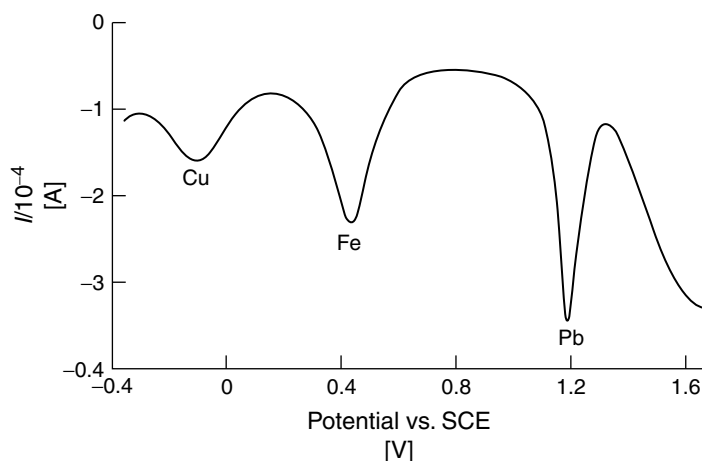


Fig. 4 Square wave sono-CSV demonstrating the simultaneous detection of copper ($150\ \mu\text{M}$), iron ($300\ \mu\text{M}$), and lead ($1\ \mu\text{M}$) at a BDD electrode.

nitric and perchloric acid, an aliquot of the digest was diluted with dilute nitric acid and introduced to the electrochemical cell. The microaddition technique facilitated quantification of the lead in the acid digest via sono-CSV, giving a result that is in agreement with an independent analysis by ICP-MS (see Table 1).

The very high elemental specificity of the sono-CSV of lead is apparent and is promising for the analysis of metallic targets that have alloying properties. By facilitating the removal of excess lead oxide remaining on the surface, high intensity ultrasound combined with the inertness and mechanical stability of BDD promotes both intersample and intrasample reproducibility, factors that have hindered meaningful measurements using CSV in the past.

2.9.5.2 Determination of Manganese in Instant Tea

Tea is a popular beverage, in its various forms [35], on a global scale and is a rich source of dietary manganese [62], with tea drinkers ingesting between 21 and 45% more manganese than in the average diet [63].

The analytical stripping response of Mn^{2+} was measured using differential-pulse sono-CSV (sono-DPCSV) in two steps. First accumulation of MnO_2 via an insonated deposition, secondly, quantification of the deposited MnO_2 using an insonated-differential pulse-stripping scan. The electrode was cleaned ultrasonically between each scan to ensure complete mixing and removal of any surface material prior to the next scan. This technique was found to give a linear increase in peak height for increasing concentration of aqueous Mn^{2+} over the range $1 \times 10^{-11} - 3 \times 10^{-7}$ M.

Quantitative analysis of manganese in instant tea was compared with independent analysis with good correlation being observed between sono-DPCSV, AAS, and the reported MAFF, UK data [64] (see Table 1).

The use of ultrasound in both stages of the sono-CSV of manganese is essential to the efficiency of the technique, with corresponding silent deposition of MnO_2 resulting in near total loss of analytical signal, highlighting the dramatic effect of ultrasound on mass transport. An insonated stripping step promotes rapid removal of reduced Mn^{2+} ions from the surface of the electrode ensuring a sharp analytical stripping peak is obtained.

2.9.6 Sonoelectroanalytical Linear Sweep Voltammetry

2.9.6.1 Detection of Nitrite in Egg The potential for nitrite [36] to be metabolized to carcinogenic *N*-nitroso compounds [65, 66] and its widespread presence in food products and beverages has necessitated its monitoring [65, 66]. Attempts to analyze whole eggs are complicated by the presence of high concentrations of protein and fat, which serve to foul the electrode and have traditionally prevented direct electrochemical probing of such foodstuffs without recourse to substantial sample pretreatment. Ultrasound in combination with linear sweep voltammetry (Chapter 2.1 in this volume) provides an alternative to sample manipulation beyond simple homogenization.

Detection is based upon the reaction of acidified nitrite with an activated phenolic compound (phloroglucinol) where the reduction of the resulting nitroso species at a glassy carbon electrode provides the analytical signal [67, 68]. In the absence of

ultrasound, the electrode response to these microadditions is nonlinear and shows no consistent increase in the magnitude of the nitroso reduction peak. This is attributed to electrode fouling, which is further complicated by the reduction of other electroactive constituents in the egg adsorbed to the surface of the electrode being reduced at a similar potential to the nitroso reduction. When insonated, ablation of the electrode surface by cavitation events, both during and prior to the linear sweep, exerts an *in situ* cleaning action and is responsible for an improvement in the resolution of the nitroso reduction signal permitting quantitative measurements to be obtained. The results from two different batches of egg are shown in Table 1 and were found to be in accordance with MAFF estimates of nitrite levels in egg [69].

The determination of nitrite in egg highlights the beneficial aspects of sonoelectrochemical analysis in difficult matrices. Moreover, the advantages of the technique include significant simplification over the liquid chromatographic procedure currently employed for nitrite detection [69], which involves hot water extraction, protein precipitation and solid-phase extraction/purification.

2.9.6.2 Detection of Nitrate at a Copper-modified Electrode

The importance of nitrate [70, 71] monitoring is recognized by most health authorities due to legislation restricting permissible levels in drinking water and food produce [72]. Existing silent electrochemical methods are based on an electrodeposited copper layer that can provide a linear response over 10–200 μM nitrate [73]. While this range is acceptable for a number of applications, it is inadequate when considering the analysis of

physiological nitrate concentrations [74]. Surface fouling, whether in physiological or environmental samples can also severely restrict the application of the system [75].

The stability of electrodeposited copper under the influence of ultrasound was examined using a low power setting, mild conditions were selected to minimize cavitation erosion of the surface. Introduction of ultrasound removed the fern like growth of electrodeposited copper, but the response to nitrate remained greater than that for a bare electrode suggesting that a catalytic compact layer persists. The layer was found to be stable to repeated pulses of ultrasound facilitating a comparison between silent linear sweep voltammetry and sonovoltammograms recorded at the copper-modified electrode. The introduction of ultrasound provides a dramatic improvement in the sensitivity of the electrode towards nitrate above the silent response obtained with the compact copper layer, which is illustrated by Fig. 5. The sonochemical response is also significantly greater than that obtained with the intact, macroporous surface suggesting that lower detection limits may be possible. The analytical utility of the sonochemical approach was assessed by evaluation of nitrate in treated sewage effluent. The calculated results compared favorably with an independent spectroscopic analysis based on Cu–Cd reduction/Griess assay [70] (see Table 1).

The fragility of the macroporous electrode is a drawback to its utility and therefore the ability to use the more robust compact layer, when coupled with the depassivating and mass transport phenomena introduced by ultrasound, is a major advantage. It is conceivable that such a system may be suitable for nitrate analysis in oil-based products in which the

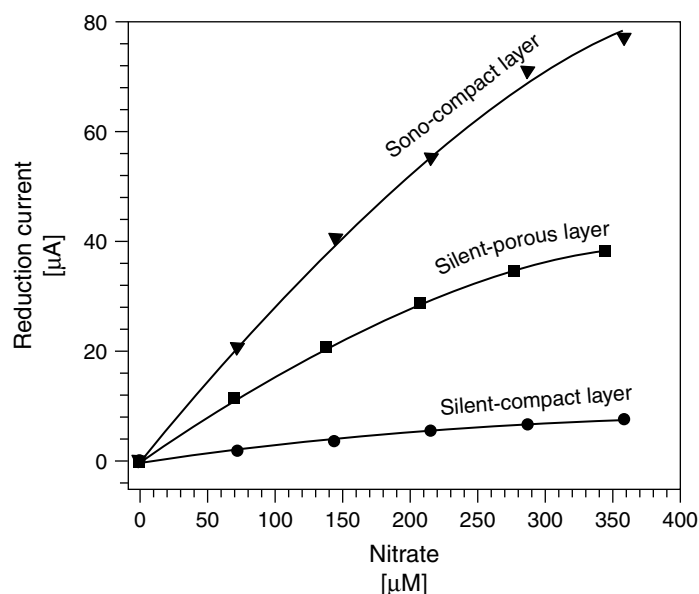


Fig. 5 A quantitative comparison of the compact deposit modified electrode response to increasing nitrate concentration under silent and sonicated conditions. The response obtained at an intact porous, copper-modified electrode under silent conditions is also included.

application of ultrasound could be used to both generate the microemulsion needed to release the analyte and provide the enhanced detection.

2.9.7

Biphasic Sonoelectroanalysis

Ultrasound is known to facilitate emulsification in biphasic systems [76] with benefits including smaller drop sizes down to 0.3 μm [77], lower energy consumption and more stable emulsions that are less polydispersed than conventional mechanical techniques [78]. Cavitational processes occur preferentially at the phase boundary [78, 79] causing intensive shock waves in the surrounding liquid and the formation of liquid jets of high velocity [80]. These mechanical forces act to divide droplets again and again

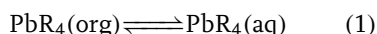
forming microdroplets and eventually “homogenizing” even in the absence of surfactant.

2.9.7.1 Determination of Lead in Petrol

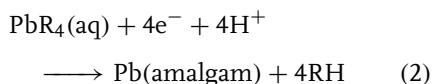
Owing to the continuing focus on total lead concentrations in petrol in recent years [78], there is increasing demand for simple and rapid methods of determination. Existing methods include AAS [81–83], ICP-MS [84], and electrochemical stripping voltammetry although these techniques involve elaborate sample preparation, for example, decomposition of the organolead compounds with concentrated nitric acid and then ashing at 300 °C [85] or dilution in ethanol, nitric acid, mercury ions, and detergent [86]. To provide a rapid and facile alternative the determination of lead using biphasic

sono-ASV has been established. Addition of aliquots of petrol to the cell prior to each accumulation step resulted in the formation of an emulsion on insonation from which Pb could be plated onto the surface of the electrode. The peak area increased with increasing petrol additions and also behaved linearly with accumulation time over the range 7–240 s. The mechanism proposed for the detection of lead in the petrol aliquots involves the following steps:

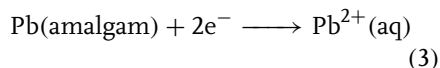
First, the sono-extraction of the tetra-alkyl lead from the petrol phase.



This is followed by reduction of lead at the surface of the electrode.



The final step is analytically sensitive stripping of Pb to form Pb^{2+} in solution.



Determination of total lead was compared to independent analysis using AAS according to the Institute of Petroleum method no. 362/93 [87]. Excellent quantitative agreement was observed (see Table 1).

2.9.7.2 Determination of Vanillin in Vanilla Extract

Biphasic sonoelectroanalysis was employed in the detection of vanillin (4-hydroxy-3-methoxybenzaldehyde) using the novel electrochemical and sonoelectrochemical solvent ethyl acetoacetate [88]. The electrochemical oxidation of vanillin in this medium was shown to give oxidative linear sweep voltammetric signals sensitive to microadditions. In addition,

the near reversible kinetics of vanillin in ethyl acetoacetate facilitated sensitive square wave voltammetry.

Problems of electrode passivation led to typically diminishing peak heights for square wave voltammetry in silent conditions for a constant concentration of vanillin. Employing ultrasound between each scan, ensured that peak heights were maintained by quantitative depassivation of the electrode surface. Background corrected square wave voltammetric scans can be seen in Fig. 6 along with a linear calibration graph of $r = 0.9987$ (Fig. 6 inset). The method permitted a detection limit in clean conditions of 0.016 mM.

The determination of vanillin in natural vanilla essence is achieved by the exploitation of biphasic sonoelectroanalysis in aqueous ethanolic vanilla pod extract and ethyl acetoacetate. In contrast with silent voltammetry, which gave no measurable signal for the oxidation of vanillin, ultrasound facilitated emulsification and extraction of vanillin from the flavoring, permitting an analytical square wave voltammetric signal to be obtained. Microadditions to two separate samples of vanilla essence facilitated the quantification of vanillin in the extract. Close agreement with a blind analysis of the samples using HPLC-UV is observed with a limit of detection in the biphasic medium of 0.020 mM (see Table 1).

Electroanalysis in biphasic systems is an area that has limited success due to the difficulties in creating and maintaining emulsions in the absence of surfactant, which can detrimentally affect the analysis [55]. The use of ultrasound to form emulsions ensures that regardless of the relative densities of the two liquids, droplets of both are in constant contact with the electrode surface during voltammetric analysis. This

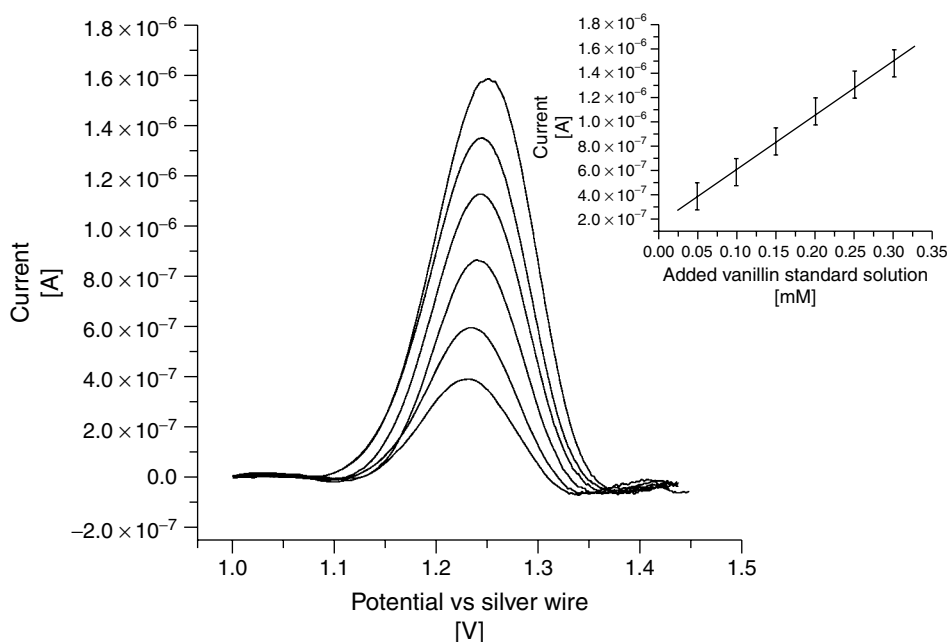


Fig. 6 Background corrected square wave voltammetry of microadditions of vanillin to ethyl acetoacetate with electrode conditioning at +2 V for 4 s and insonation for 30 s prior to each scan. Inset: linear calibration graph ($r = 0.9987$).

permits meaningful quantitative measurements to be obtained efficiently and rapidly in nonaqueous media.

2.9.8 Conclusion

The advantages of sonoelectroanalysis, explored in the above applications, can be summarized as:

1. *Acoustic streaming*: promotes mass transport to the electrode surface, actively reducing sampling times and consequently increasing sensitivity.
2. *Cavitation*:
 - continuously depassivates and activates the electrode surface, during or between electrochemical deposition steps; permitting electrochemistry where in silent

voltammetry complete fouling of the electrode would occur;

- effects rapid in situ degradation of proteins and organic matrices bound to the target analyte precluding the necessity for elaborate pretreatment methods;
- facilitates the use of novel electrode materials such as BDD with wide potential windows and robust mechanical properties;
- promotes emulsification enabling biphasic analyses to be conducted in the absence of surfactant;
- minimizes the use of mercury electrodes by activating the surface of solid electrodes to specific metal deposition.

3. *Portability*: handheld ultrasonic horns expand the potential for field apparatus.
4. *Cost*: relative low cost of sonoelectrochemical instrumentation provides a more cost-effective method of analysis than conventional AAS or ICP-MS.

References

1. J. Wang, *Stripping Analysis: Principles Instrumentation and Applications*, VCH Publishers, Deerfield Beach, Florida, 1985.
2. M. Jiang, F. C. Meng, C. Gong et al., *Analyst* **1990**, 115, 49.
3. J. Wang, J. Huiliangand, W. Kubiak, *Electroanalysis* **1990**, 2, 127.
4. L. Z. Wang, C. S. Ma, X. L. Zhang et al., *Anal. Lett.* **1993**, 26, 1711.
5. A. Romanus, H. Müller, D. Kirsch, *Fresenius' J. Anal. Chem.* **1991**, 340, 363.
6. J. Wang, J. M. Lu, *Talanta* **1995**, 42, 331.
7. C. Agra-Gutiérrez, R. G. Compton, *Electroanalysis* **1998**, 10, 204, 603.
8. S. Sander, G. Henze, *Fresenius' J. Anal. Chem.* **1996**, 356, 259.
9. B. Hoyer, N. Jensen, *Talanta* **1995**, 42, 767.
10. B. Hoyer, T. M. Florence, G. M. Batley, *Anal. Chem.* **1987**, 59, 1608.
11. B. Hoyer, T. M. Florence, *Anal. Chem.* **1987**, 59, 2839.
12. A. Aliakbar, M. Popl, *Collect. Czech. Chem. Commun.* **1985**, 50, 1141.
13. M. A. Baldo, C. Bragato, S. Daniele, *Analyst* **1997**, 122, 1.
14. S. K. C. Chang, E. Holm, J. Schwartz et al., *Anal. Chem.* **1979**, 168, 353.
15. L. Sipos, J. Golimoski, P. Valenta et al., *Fresenius' Z. Anal. Chem.* **1979**, 298, 1.
16. J. Golimoski, K. Golimoski, *Anal. Chim. Acta* **1996**, 325, 111.
17. D. Jagner, S. Westerlund, *Anal. Chim. Acta* **1980**, 117, 159.
18. W. H. Nurnberg in *Electrochemistry in Research and Development* (Eds.: R. Kalvoda, R. Parsons), Plenum Press, New York, 1985.
19. M. E. R. Dam, K. H. Schröder, *Electroanalysis* **1996**, 8, 1040.
20. C. Wetcher, J. Osteryoung, *Anal. Chim. Acta* **1990**, 234, 275.
21. C. Agra-Gutiérrez, J. L. Hardcastle, J. C. Ball et al., *Analyst* **1999**, 124, 1053.
22. E. Gustafsson, *Water, Air Soil Pollut.* **1995**, 80, 99.
23. D. J. Walton, S. S. Phull, *Adv. Sonochem.* **1996**, 4, 205.
24. R. G. Compton, J. C. Eklund, F. Marken, *Electroanalysis* **1997**, 7, 509.
25. A. M. Oliveira Brett, C. M. A. Brett, F.-M. Matysik et al., *Ultrasonics Sonochem.* **1997**, 4, 123.
26. F.-M. Matysik, S. Matysik, A. M. Oliveira Brett et al., *Anal. Chem.* **1997**, 69, 1651.
27. N. A. Madigan, T. J. Murphy, J. M. Fortune et al., *Anal. Chem.* **1995**, 67, 2781.
28. F. Marken, T. O. Rebbitt, J. Booth et al., *Electroanalysis* **1997**, 9, 19.
29. R. G. Compton, J. C. Eklund, S. D. Page et al., *J. Appl. Electrochem.* **1996**, 26, 775.
30. R. G. Compton, J. C. Eklund, S. D. Page et al., *J. Phys. Chem.* **1994**, 98, 12 410.
31. A. M. Oliveira Brett, F.-M. Matysik, *Bioelectrochem. Bioenerg.* **1997**, 42, 111.
32. Q. Hong, J. L. Hardcastle, R. A. J. McKeown et al., *New J. Chem.* **1999**, 23, 845.
33. R. P. Akkermans, J. C. Ball, T. O. Rebbitt et al., *Electrochim. Acta* **1998**, 43, 3443.
34. A. J. Saterlay, C. Agra-Gutiérrez, M. P. Taylor et al., *Electroanalysis* **1999**, 11, 1083.
35. A. J. Saterlay, J. S. Foord, R. G. Compton, *Analyst* **1999**, 12, 1791.
36. J. D. Davis, R. G. Compton, *Anal. Chim. Acta* **2000**, 404, 241.
37. J. L. Hardcastle, G. G. Murcott, R. G. Compton *Electroanalysis* **2000**, 12, 559.
38. P. M. Bersier, J. Howell, C. Bruntlett, *Analyst* **1994**, 119, 219.
39. J. Camakaris, I. Voskoboinik, J. F. Mercer, *Biochem. Biophys. Res. Commun.* **1999**, 261, 225.
40. V. Juturu, *Trace Elements Electrolytes* **1999**, 16, 55.
41. J. Aggett, *Bibliotheca Nutritio et Dieta* **1998**, 54, 18.
42. K. Cashman, A. Flynn, *Bibliotheca Nutritio et Dieta* **1998**, 54, 150.
43. M. A. Moreno, C. Marin, F. Vinagre et al., *Sci. Total Environ.* **1999**, 229, 209.
44. C. A. Burtis, E. R. Ashwood, *Tietz Fundamentals of Clinical Chemistry*, Harcourt Brace, Philadelphia, Pennsylvania, USA, 1995.
45. I. Zaitseva, V. Zaitsev, G. Card et al., *J. Biol. Inorg. Chem.* **1996**, 1, 15.
46. J. L. Hardcastle, R. G. Compton, *Electroanalysis* **2001**, 13, 89.

47. B. M. Alazemi, J. W. Lewis, E. B. Andrews, *Environ. Technol.* **1996**, 17, 225.
48. V. Roncero, J. A. Vincente, E. Redondo et al., *Environ. Health. Perspect.* **1990**, 89, 137.
49. G. H. Satchell, *Aquatic Toxicology*, Raven Press, New York, 1984, pp. 1–50.
50. R. C. Payle, *Sci. Total Environ.* **1998**, 219, 147.
51. P. Pärt, R. A. C. Lock, *Comp. Biochem. Physiol.* **1983**, 76C, 259.
52. T. L. Coombs, T. C. Fletcher, A. White, *Biochem. J.* **1972**, 128, 128.
53. A. J. Saterlay, F. Marken, J. S. Foord et al., *Talanta* **2000**, 53, 403.
54. J. Xu, M. C. Granger, Q. Chen et al., *Anal. Chem.* **1997**, 69, 591A.
55. Y.-C. Tsai, J. Davis, R. G. Compton, *Frese-nius' J. Anal. Chem.* **2000**, 368, 415.
56. C. M. G. van den Berg, Z. Q. Huang, *Anal. Chem.* **1984**, 56, 2383.
57. E. Hrabánková, J. Dolezal, P. Beran, *J. Electroanal. Chem.* **1969**, 22, 203.
58. T. Miwa, H. Motosugi, A. Mizuike, *Chem. Abstr.* **1971**, 75, 126 053.
59. T. Miwa, H. Motosugi, A. Mizuike, *Bunseki Kagaku* **1971**, 20, 846.
60. R. C. Propst, J. T. Kinard, *Anal. Chem.* **1974**, 46, 1106.
61. H. A. Laitinen, H. Watkins, *Anal. Chem.* **1975**, 47, 1352.
62. J. J. Powell, T. J. Burden, R. P. H. Thompson, *Analyst* **1998**, 123, 1721.
63. J. J. Fardy, G. D. McOrist, Y. J. Farrar, *J. Radioanal. Nucl. Chem.* **1992**, 163, 195.
64. <http://www.maff.gov.ac.uk/maffhome.htm>.
65. S. S. Mirvish, *Cancer Lett.* **1995**, 92, 17.
66. S. D. Gangoli, P. A. van den Brandt, V. J. Feron et al., *Eur. J. Pharmacol. Environ. Toxicol. Pharmacol.* **1994**, 292, 1.
67. M. Bader, K. McKeegan, M. F. Cardosi et al., *Talanta* **1999**, 50, 103.
68. A. J. Dombroski, L. Meites, K. Rose, *J. Electroanal. Chem.* **1982**, 137, 67.
69. MAFF Food Surveillance Information Sheet, FS1S 137, December 1997.
70. J. Davis, M. J. Moorcroft, S. J. Wilkins et al., *Electroanalysis* **2000**, 12, 1363.
71. M. Moorcroft, J. Davis, R. G. Compton, *Talanta* **2001**, 54, 785.
72. Statutory Instrument No. 1147/1989, Water Supply Regulations, HMSO, London, 1989.
73. J. Davis, M. J. Moorcroft, S. J. Wilkins et al., *Analyst* **2000**, 125, 737.
74. H. Moshage, B. Kok, J. R. Huizenga et al., *Clin. Chem.* **1995**, 41, 892.
75. R. N. Sah Commum, *Soil Sci. Plant Anal.* **1994**, 25, 2841.
76. R. W. Wood, A. L. Loomis, *Philos. Mag.* **1927**, 4, 417.
77. B. Abismaïl, J. P. Canselier, A. M. Wilhelm et al., *Ultrasonics Sonochem.* **1999**, 6, 75.
78. A. N. Blythe, R. P. Akkermans, R. G. Compton, *Electroanalysis* **2000**, 12, 16.
79. H.-J. Ladwig, H. Oelmann, W. Pippel, *Wiss. Z. Techn. Univers. Dresden* **1990**, 39, 163.
80. W. Lauterborn, C. D. Ohl, *Ultrasonics Sonochem.* **1997**, 4, 65.
81. M. Kashiki, S. Yamazoe, S. Oshima, *Anal. Chim. Acta* **1971**, 53, 95.
82. E. Cardelli, M. Cifani, M. Mecozzi et al., *Talanta* **1986**, 33, 279.
83. C. G. Taylor, J. M. Trevaskis, *Anal. Chim. Acta* **1986**, 179, 491.
84. *Varian Instrum. Appl.* **1991**, 20, 7.
85. M. H. Pournaghi-Azar, A. H. Ansary-Fard, *Talanta* **1998**, 46, 607.
86. D. Jagner, L. Renman, Y. Wang, *Anal. Chim. Acta* **1992**, 267, 165.
87. Institute of Petroleum (Great Britain), *Standard Methods for Analysis and Testing of Petroleum and Related Products*, John Wiley & Sons, Chichester, UK, 1995.
88. J. L. Hardcastle, C. J. Paterson, R. G. Compton, *Electroanalysis* **2001**, 13, 899.

2.10**Ultrasound and Electrosynthesis**

*Richard G. Compton, Joanna L. Hardcastle,
Javier del Campo, Jay D. Wadhawan
Physical and Theoretical Chemistry Laboratory,
University of Oxford, South Parks Road,
Oxford, UK*

2.10.1**Introduction**

Electrochemical methods offer selective transformations of considerable potential value to the organic chemist [1] by the coupling of electron-transfer processes at the electrode surface with homogeneous chemical transformations. In organic systems, this leads to ion-radicals and other useful intermediates, which may be produced in controlled fashion by the manipulation of the electrode potential, the nature of the electrode material, the cell design, and other reaction variables [2]. A benefit of this arrangement is that highly reactive species may be generated in conditions that are otherwise chemically mild. This allows the generation of these species at different rates or in different conditions to those encountered in corresponding thermal systems, so that the course of subsequent reaction may be entirely different to that of a nonelectrochemical system. This can lead to the production and isolation of novel compounds that might be otherwise impossible or difficult to prepare; see Ref. [3] and references therein, and there is now a wide range of synthetically valuable electroorganic systems [4] so that over 100 electroorganic reductions and oxidations are either used as steps in commercial synthesis or are under investigation for this purpose [5, 6].

The introduction of ultrasound into electrosynthesis can offer several advantages. First, the resulting increase in

mass transport offers not only more rapid reaction times, but in cases in which useful Faradaic processes compete with background currents, the former can be amplified relative to the latter, leading to improved yields. Second, cavitation action can lead to electrode depassivation, permitting synthetically useful heterogeneous procedures in which under silent conditions no or little reaction could occur. Third, the use of ultrasound can promote emulsification, allowing electrolysis of, for example, organic material in the form of microdroplets in water where under silent conditions a two-phase system would result. These benefits, and others, are illustrated by the examples covered in the following section. First, however, we consider the issue of cell design for sonoelectrosynthesis.

2.10.2**Cell Design in Sonoelectrosynthesis**

Various cells have been introduced for the practice of sonoelectrosynthesis. Two different cells are described in this section. First, a small volume cell, typically 20–50 mL (see Fig. 1a), in which an ultrasonic horn probe is immersed in order to obtain fast circulation of the liquid. This cell is placed in a thermostatic bath in order to control its temperature. The counterelectrode compartment, which is equipped with a gas outlet, is separated by means of a fine frit.

Second, a cell of larger dimensions (200–500 mL) is shown in Fig. 1(b) in which both the counterelectrode compartment and a thermostating coil surround the ultrasonic horn. The working electrode, typically a gauze or cloth of suitable material [7], is placed directly underneath the ultrasonic probe.

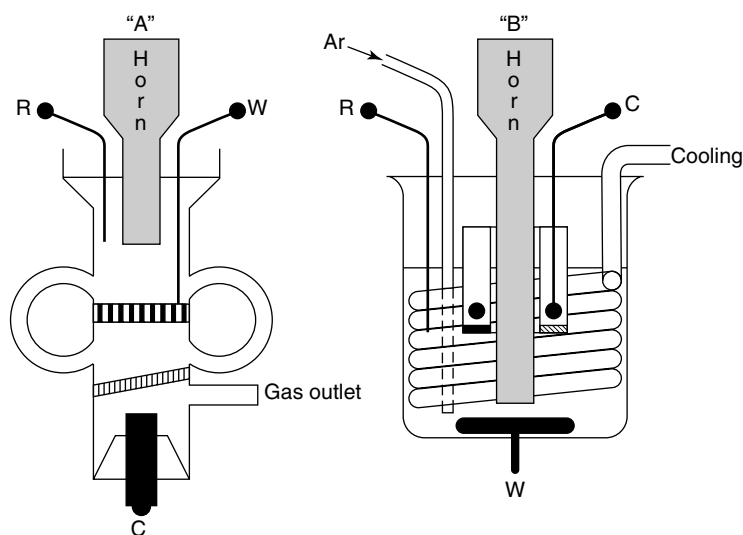
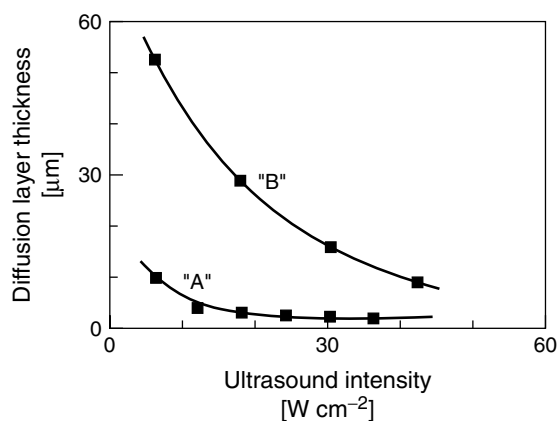


Fig. 1 (a) Small volume cell "A" for electrolysis in the presence of high-power ultrasound. (b) Cell "B" (500 mL) used for larger scale bulk electrolysis experiments. R, W, and C denote the reference, working, and counterelectrodes, respectively.

Fig. 2 Plot of the average diffusion layer thickness versus ultrasound intensity calculated from the limiting currents observed for the reduction of cobalticenium cations in acetonitrile at various ultrasound intensities and in cells "A" and "B".



In the smaller cell, ultrasound causes a much larger increase in mass transport than in the larger cell. This means that, as shown in Fig. 2, to achieve diffusion layers of any given thicknesses, ultrasonic radiation of a much higher intensity is required in the case of the larger cell. In order to quantify mass transport, limiting currents

obtained under sonication are analyzed using Eq. (1) [8–10], see reviews [11, 12] and Chapter 2.8.

$$I = \frac{nFADc}{\delta} \quad (1)$$

I corresponds is the limiting current in amperes, n the number of electrons

transferred, F the Faraday constant, A the electrode area, D the diffusion coefficient of the electroactive species, c the concentration, and finally, δ , the diffusion layer thickness. This equation is based on the simple Nernstian diffusion model, which has been shown to give satisfactory experimental parameterization [13, 14]. Depending on the applied ultrasonic power ($6\text{--}30\text{ W cm}^{-2}$), it is possible to adjust the diffusion layer thickness to between 50 and $15\text{ }\mu\text{m}$ using ultrasonic intensities of 6 and 30 W cm^{-2} for the case of the larger cell, and between 10 and $3\text{ }\mu\text{m}$ in the smaller one. Figure 2 shows the relation between diffusion layer thickness and ultrasonic intensity for the two cells described. For comparison, mechanical stirring diffusion layer thicknesses typically range between 100 and $50\text{ }\mu\text{m}$ [7].

For both cells under potentiostatic conditions, the diffusion-controlled currents depend on the concentration of the electroactive species in the bulk of the solution. The latter will gradually decrease as material is depleted. The current decays exponentially, according to [15]

$$i(t) = i_0 \exp\left(-\frac{nAD}{V\delta}t\right) \quad (2)$$

where i_0 is the initial limiting current in amperes, n is the number of electrons involved, A the electrode area in m^2 , D the diffusion coefficient of the electroactive species in $\text{m}^2\text{ s}^{-1}$, V the volume of solution in m^3 , and δ the diffusion layer thickness in m.

The reductive ring opening of α, β -epoxyketones (see Fig. 3) was used to exemplify the positive and beneficial effects of ultrasound in the cells described [13, 14]. This reaction was carried out at a glassy carbon electrode in the presence of power ultrasound. Isophorone oxide was chosen as a model system. Using the larger cell containing 150 mL of solution and using an ultrasonic intensity such that $\delta = 15\text{ }\mu\text{m}$, the time required to attain the conversion of half the starting material was less than 7.5 mins. under insonation. Under mechanical stirring, assuming a diffusion layer thickness of $50\text{ }\mu\text{m}$, the same level of conversion would have taken almost 25 mins. to be reached. This led to improved yield and current efficiency for the electrochemical ring opening of isophorone oxide in the presence of power ultrasound, since the Faradaic process competes against background currents and the relative importance of the latter is reduced in shorter time electrolyses.

2.10.3

Examples of Sonoelectrosynthetic Reactions

Representative organic electrosynthetic reactions of different characteristics, in which power ultrasound proves itself to be beneficial, will be described in this section as examples. In some cases, ultrasound dramatically enhances mass transport rates, thus leading to shorter reaction times and enhanced current efficiencies by means of minimizing background processes thanks to the massive decrease in

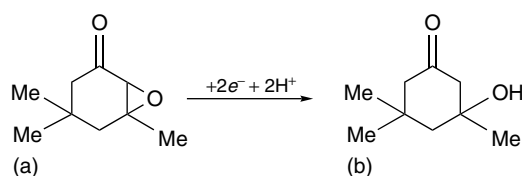


Fig. 3 Reaction scheme for the electrochemical ring opening of isophorone oxide (a) to yield 3-hydroxy-3,5,5-trimethylcyclohexanone (b).

the diffusion layer thickness on the electrode surface. Examples of this include the reductive ring opening of the α, β -epoxyketone isophorone oxide to yield the corresponding β -hydroxyketone, and the low temperature dimerization of 2-nitrobenzylchloride in liquid ammonia; both these examples will be covered in the following sections.

However, ultrasound does much more than stirring and mixing a reaction mixture. Specifically, the phenomenon of cavitation is an always-present feature, which is in itself very useful since it can remove adsorbates or precipitation products that would, otherwise, completely block and passivate the electrode. For instance, Methylene Green (MG) is reduced in a two-electron process to *leuco*-Methylene Green (*l*-MG), which is insoluble in aqueous media. This is addressed in Sect. 2.10.3.4. Passivation problems not only arise in aqueous media, but also in other solvents such as liquid ammonia, in which trace water or other impurities eventually cause the electrode to passivate. Ultrasound can often avoid the blockage of electrode surfaces in most media.

Ultrasound also presents the capacity to emulsify a mixture of immiscible liquids due to cavitation processes occurring at the liquid/liquid phase boundary effectively dispersing the biphasic system. This sonoemulsification allows product extraction from the aqueous phase, but at the same time may also prevent electrode passivation whilst keeping very fast rates of mass transport. The reduction of MG in the presence of a sonoemulsion of toluene (see Sect. 2.10.3.4) is one fine example of this. Another example of successful electroorganic process in a sonoemulsified mixture is the oxidation of carboxylic acids, known as Kolbe processes (see Sect. 2.10.3.5).

Finally, ultrasound can also be used to switch between reaction pathways in certain electroorganic reactions. During cavitation, because of the extreme conditions given, very reactive radical species are formed, which can readily react and change the product distribution. Also, higher mass transport regimes and desorption processes may affect the final products distribution. A controversial example of this ultrasound-induced product switching is, again, the Kolbe processes (Sect. 2.10.3.5).

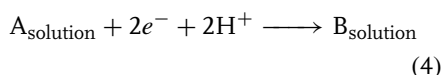
All these beneficial effects of ultrasound will be explored in more detail in the following section with the aim of giving a better and more comprehensive picture of what ultrasound can help achieve to the electrochemist interested in the study of synthetic reactions.

2.10.3.1 Electrochemical Reductions in Ultrasonically Emulsified Media: Electroreduction of Maleates, Fumarates, and Acetylenes

Water is an ideal solvent for organic electrosynthesis. It has good conductivity and polarity, and product recovery is relatively easy [16]. Water is also highly preferable from an environmental point of view. However, most organic compounds are poorly soluble in it, or have limited solubilities [17, 18]. Therefore, the extension of the range of systems undergoing electrochemical transformations in water is of considerable interest and studies employing surfactant-stabilized emulsions and suspensions have been described [17–20].

Ultrasound emitted by a horn source situated in a conventional cell allows the formation of emulsions without stabilizing agents simply by mechanical forces, which arise at the liquid/liquid phase boundary. An illustration of how this approach allows direct voltammetry and

electrolysis in aqueous media of materials with limited, mutual solubility has been made using emulsions of diethylfumarate, diethylmaleate, and cyclohex-2-en-1-one in water containing suitable supporting electrolyte formed by applying ultrasound [17]. Reduction of the carbon–carbon double bond following a two-electron-two-proton reaction pathway led to large currents and products formed consistent with the following mechanism [17]:



Diethylacetylene dicarboxylate was reduced in a four-electron process to diethylsuccinate. Yields of the isolated product typically ranged from 50 to 70%, with hydrogen evolution identified as the main cause for the drop in current efficiency. Side products arising from hydrodimerization or polymerization were not observed.

In conclusion, ultrasound promoted the emulsification of the medium, thus facilitating otherwise impossible electrochemistry.

2.10.3.2 Electrodimerization of 2-Nitrobenzylchloride in the Presence of Ultrasound

Dinitrobenzyls are key intermediate species in certain drug syntheses [21, 22]. They can be formed by the electrochemical reduction of nitrobenzyl halides in various solvents [23–25]. In liquid ammonia at -60°C , the mechanism involves a one-electron reduction and dechlorination followed by coupling of the neutral radical intermediate species (see Fig. 4). Once the dimer is formed, it can undergo two one-electron reductions at more negative

voltages, corresponding to the reduction of the two aromatic nitro groups (see voltammetry in Fig. 5). Potentiostatic reduction at a voltage of -0.35 V (vs Ag wire) in the presence of ultrasound yields the dimer 2,2-dinitrobenzyl (>95%) and very little or no side products. On the other hand, the duration of experiments depended on the distance between the ultrasonic probe and the working electrode. This is due to the difference in thickness of the diffusion layer caused by insonation, as suggested by Eq. (2) in Sect. 2.10.2.

Ultrasound was beneficial for the following reasons:

1. The dissolution kinetics of the starting material is faster in the presence of ultrasound.
2. Mass transport from the bulk towards the electrode, and vice versa, is greatly enhanced and reaction times are considerably reduced.
3. Current efficiency and product yields are optimized.

2.10.3.3 Ultrasonically Enhanced Birch Reductions

The Birch reaction involves the partial reduction of an aromatic ring [26, 27], as shown in Fig. 6. These reductions constitute an important class of reactions in organic synthesis, in which conventional procedure involves dissolving an alkali metal as reducing agent in liquid ammonia and organic cosolvent mixtures, in which the appropriate proton source is included. This procedure in principle poses both a safety and a pollution problem. Alternatively, the direct electrochemical generation of solvated electrons in liquid ammonia [28–31] may be used to replace alkali metal reagents [32] and power ultrasound may be employed to overcome

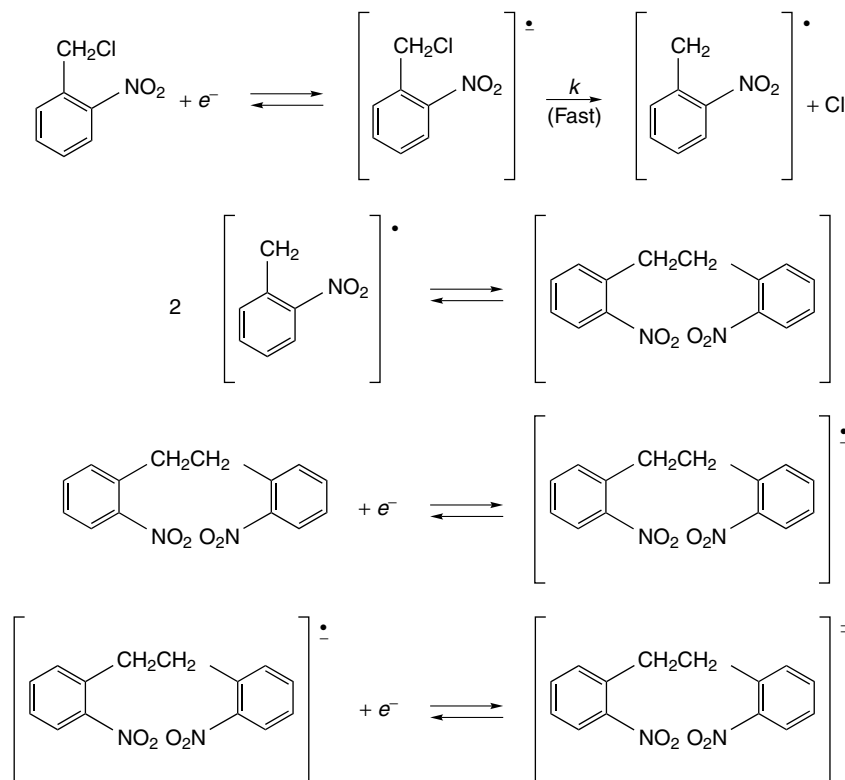
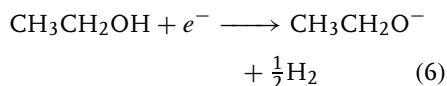


Fig. 4 Mechanism for the cathodic formation of the dimer 2,2-dinitrobibenzyl from 2-nitrobenzylchloride and further one-electron reductions of the aromatic nitro groups within the dimer molecule.

solubility problems, the need for cosolvents, and slow reaction rates.

Ethanol is used as a source of protons in the Birch reduction. However, proton sources such as ethanol are known to also react directly with solvated electrons to give hydrogen gas and the alkoxy anion (Eq. 6)



Ultrasound brings about homogeneous mixing of the electrode products with the bulk solution, so that the reaction of electrons with ethanol is minimized since the Birch process is much faster.

Birch conducted the first electrochemically driven reduction process in liquid ammonia and demonstrated that the same type of products are obtained compared with the alkali metal dissolution method [33]. However, a common problem when carrying out electrochemical studies in liquid ammonia is the passivation of the working electrode by trace water present in the system [34]. This problem can be overcome by applying ultrasound. Asymmetric cavitation and collapse at the electrode surface casts microjets of solution towards it, thus depassivating by removing blocking material. In a typical procedure applied to 3-methylanisole in

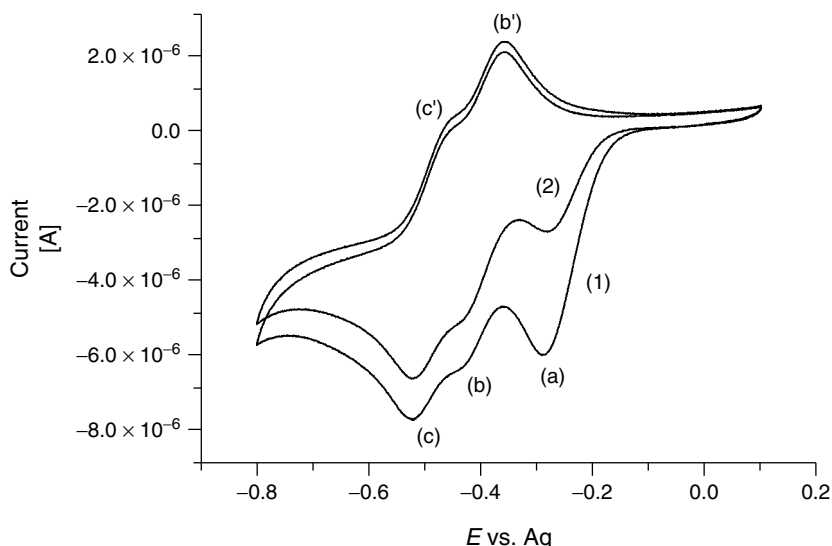
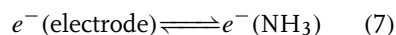


Fig. 5 Cyclic voltammetry (500 mV s^{-1}) of 1 mM 2-nitrobenzylchloride in 0.1 M KI in liquid ammonia at -60°C . (1) and (2) correspond to the first and second scans. Peak (a) is associated with the dechlorination step, while (b), (b') and (c), (c') correspond to the two successive one-electron reductions of the formed dimer.

liquid ammonia containing suitable supporting electrolyte at -60°C , solvated electrons were generated (see Fig. 7) at a potential of -2.3 V versus Ag wire. The formation of solvated electrons is seen as a reversible process with a peak-shaped feature detected after reversal of the scan direction.



The electrons so formed are stabilized by interaction with the supporting electrolyte.

Both LiCl and KI have been used: the former has rather limited solubility in liquid ammonia, whilst the latter, although significantly more soluble, shows a greater tendency to passivate the electrode in the presence of trace water under silent conditions. Electrolysis under galvanostatic conditions allows solvated electrons to be generated at the electrode surface. In the presence of power ultrasound, rapid mass transport and mixing produces a deep blue solution stable over a period in excess of an hour.

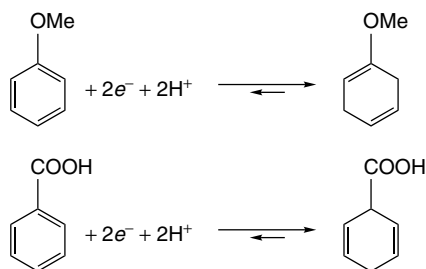


Fig. 6 Reaction schemes for the Birch reduction. The regioselectivity depends on the nature of the substituting groups bonded to the benzene ring.

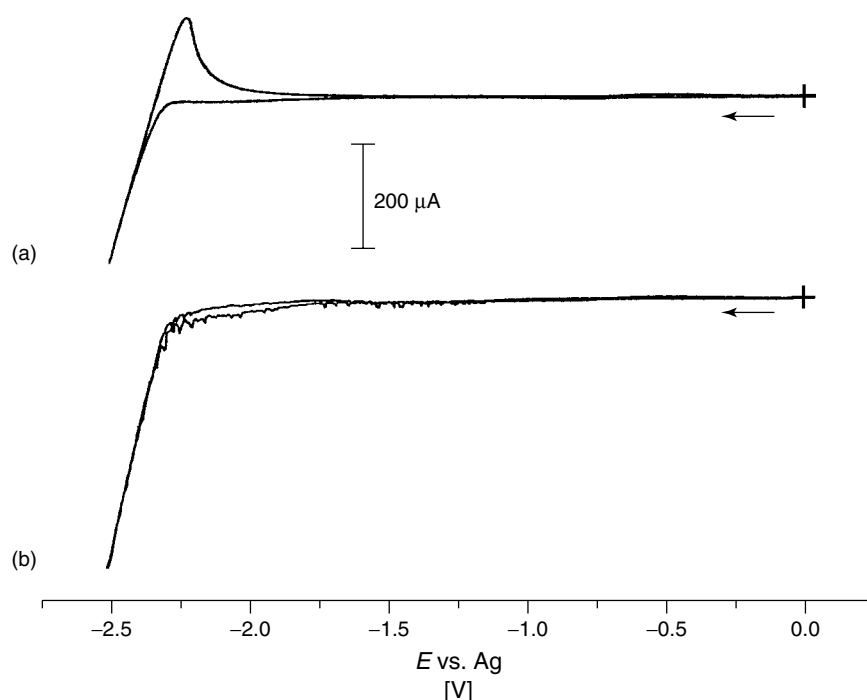


Fig. 7 Cyclic voltammograms (500 mV s^{-1}) for the formation of solvated electrons at a 1 mm Pt disk electrode in liquid ammonia at -60°C under: (a) silent conditions and (b) in the presence of ca. 150 W cm^{-2} ultrasound.

Experimental results are shown in Table 1, in which both supporting electrolytes and different concentrations of starting material have been used. Potassium iodide proved itself to be the best choice of supporting electrolyte despite the already mentioned passivation problems, which were avoided by the use of power ultrasound.

To summarize, the advantages of ultrasound in the Birch reduction are as follows:

1. Improved current efficiency and product yields (see Table 1).
2. Suppression of the need for cosolvents facilitating product recovery.
3. Greatly enhanced mass transport rates.
4. Most crucially, electrode depassivation.

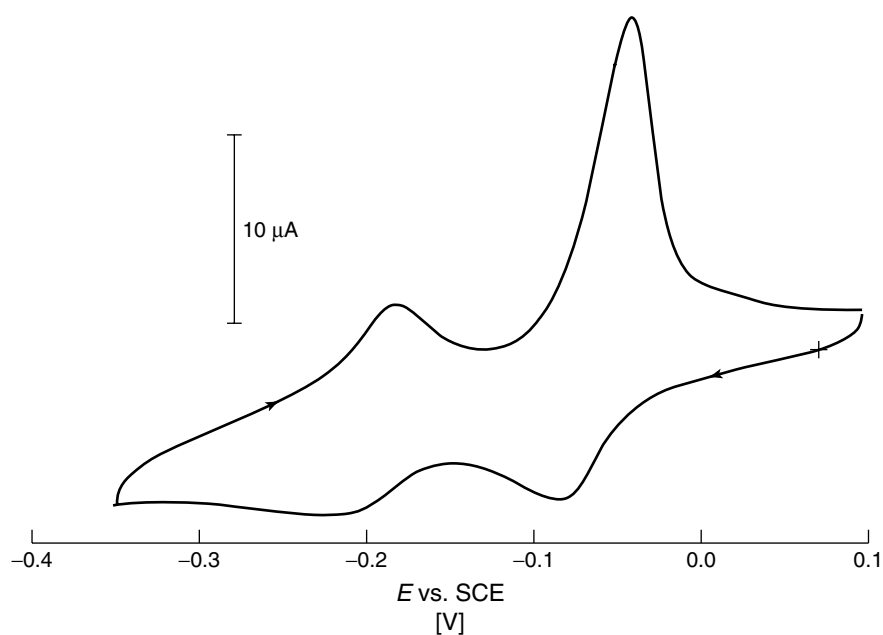
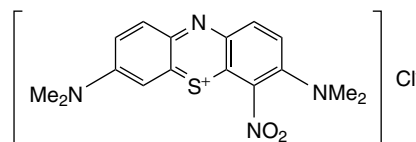
2.10.3.4 Ultrasonically Induced Electrode Depassivation: Reduction of Methylene Green

Many useful synthetic reactions cannot be carried out electrochemically because of the passivation of the electrode by the starting materials, reaction intermediates, or products [8, 11]. One possible solution is the ultrasound-induced formation of emulsions from biphasic systems so that the electrode process of interest occurs in the aqueous phase but the organic component constantly dissolves and removes the electrode passivating species. An example is the electroreduction of MG (see Fig. 8). MG is soluble in water, but the product of its two-electron reduction, *l*-MG, is not [19, 35]. Silent cyclic voltammetry of a 0.2 mM solution of MG in

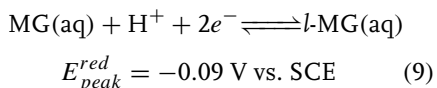
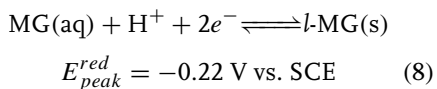
Tab. 1 Results from bulk electrolysis experiments for the Birch reduction of 3-methylanisole (3-MA) in a 50 mL one-compartment cell in liquid ammonia at -60°C . Galvanostatic conditions with 320 mA cm^{-2} current density at a 1-cm diameter platinum disk working electrode and in the presence of pulsed (1 s on/1 s off) 150 W cm^{-2} (3-mm diameter horn) or 12 W cm^{-2} (13-mm diameter horn) power ultrasound

Type of supporting electrolyte	Concentration of supporting electrolyte [M]	Concentration of 3-methylanisole [M]	Concentration of ethanol [M]	Charge passed [C]	Electrons per 3-MA	Product yield based on 3-MA %
LiCl	Saturated (0.03)	10^{-2}	$2.5 \times [3\text{-MA}]$	116	2.1	30
LiCl	Saturated (0.03)	5×10^{-2}	$2.2 \times [3\text{-MA}]$	580	2.1	25
LiCl/KI	Saturated (0.03)/0.5 M KI	5×10^{-2}	$2.2 \times [3\text{-MA}]$	580	2.1	35
LiCl/KI	0.03 M LiCl/0.5 M KI	75×10^{-2}	$10 \times [3\text{-MA}]$	870	2.1	40
KI	0.2	10^{-2}	$2.5 \times [3\text{-MA}]$	116	2.1	95
KI	0.3	5×10^{-2}	$2.2 \times [3\text{-MA}]$	580	2.1	65
KI	0.5	0.1	$2.2 \times [3\text{-MA}]$	1160	2.1	77

Fig. 8 Methylene green.

Fig. 9 Silent cyclic voltammogram (10 mV s^{-1} ; 6 mm Pt disk electrode) of 0.2 mM MG in 0.1 M KCl/0.2 M KH_2PO_4 (aq) at pH 6.5.

0.1 M KCl, 0.2 M KH_2PO_4 (pH 6.5) is shown in Fig. 9. Both reduction waves correspond to two-electron, one-proton reductions:



Cyclic voltammetry of this same system in the presence of ultrasound is illustrated in Fig. 10. It can be seen how the two peaks turn into waves under insonation as mass transport is increased by acoustic

streaming and cavitation. It is also possible to observe a steady decay in the current after the second wave. This is due to passivation of the electrode caused by adsorption and precipitation of large amounts of *l*-MG and confirmed by the larger stripping peak. If the electrosynthesis of *l*-MG is attempted, full electrode passivation is rapidly attained and the exercise proves impossible. In contrast, if voltammetry is carried out in a 20% (v/v) mixture of toluene and water, and ultrasound (18 W cm^{-2}) is used to form an emulsion, the stripping peak disappears, and the two waves present the features of reversible, steady-state voltammetry, as

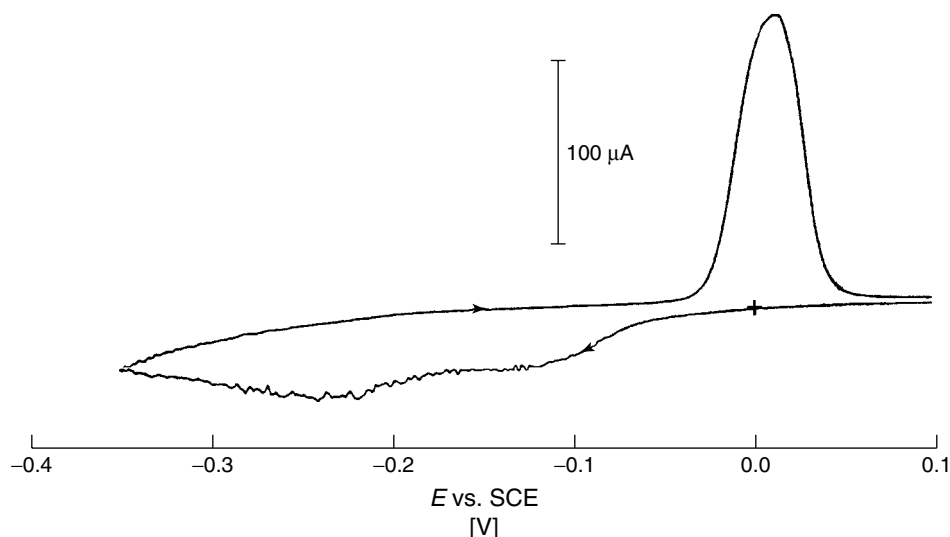


Fig. 10 Cyclic voltammogram (10 mV s^{-1} ; 6 mm Pt disk electrode) of 0.2 mM MG in 0.1 M KCl/0.2 M KH_2PO_4 (aq) at pH 6.5 in the presence of 25 W cm^{-2} ultrasound. The horn-to-electrode distance was 22 mm.

seen from Fig. 11. The vanishing of the stripping peak can be explained through *l*-MG being dissolved by microdroplets of organic solvent dispersed in the emulsion. From these observations, it becomes evident that ultrasound is extremely beneficial in the prevention of electrode passivation.

2.10.3.5 Ultrasonically Enhanced Kolbe Processes

Carboxylic acids can be oxidized in mixtures of water and methanol to give a range of products (see Fig. 12) depending on experimental conditions [36–41]. These products may arise from either one- or two-electron oxidation leading to the corresponding alkyl radicals or carbocations. Product selectivity depends not only on the experimental conditions such as solvent mixture, current densities, or electrode material but also on the carboxylic acid used in the study [42]. It is thought that the mechanism of the

reaction and, therefore, product selectivity, is controlled by adsorption of intermediate radical species on the anode surface [43]. Thus, it is suspected that desorbed radical species give the coupling (Kolbe) and disproportionation products, whereas more strongly adsorbed species undergo a second electron oxidation; see Ref. [43] and references therein. This is summarized in Fig. 12, in which a general scheme for the Kolbe process is shown. It is worth pointing out that the alkene is both a one- and a two-electron product. In the former case, it occurs via disproportionation of the intermediate radical species so that the yield of the “one-electron” alkene is matched by an equal yield of the corresponding alkane.

As an illustration, let us take the case of cyclohexane carboxylic acid (*c*- $\text{C}_6\text{H}_{11}\text{COOH}$). This system does not have a clear preference, according to the literature [44, 45], for either one- or two-electron products. This process is

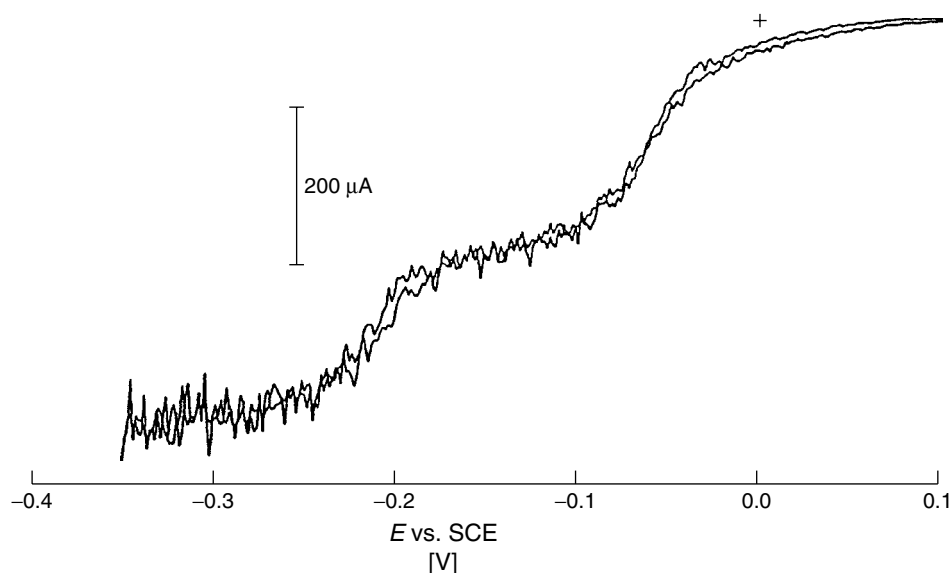


Fig. 11 Cyclic voltammogram (10 mV s^{-1} ; 6 mm Pt disk electrode) of 0.2 mM MG in 0.1 M KCl/0.2 M KH_2PO_4 (aq) at pH 6.5 and 20% (v/v) toluene (emulsified); 18 W cm^{-2} ultrasound was employed. The horn-to-electrode distance was 19 mm.

typically carried out in a mixture of water and methanol. The products from the one-electron oxidation are the dimer, $(c\text{-C}_6\text{H}_{11})_2$ and cyclohexane, $c\text{-C}_6\text{H}_{12}$. The two-electron process yields the ether $c\text{-C}_6\text{H}_{11}\text{OCH}_3$ and 1-cyclohexene, $c\text{-C}_6\text{H}_{10}$, which is also produced via a one-electron oxidation process. It has been observed by Nonaka and coworkers that, as the current density is increased, the ratio of one- to two-electron products [43] increases. As shown in Fig. 13, Nonaka [43] passed ca. 0.25 F of charge per mol of substrate and under these conditions the influence of sonication as opposed to silent conditions was small. In contrast, Walton and coworkers [46, 47] have claimed a major increase in the two-electron products on sonication, a result that at first sight appears paradoxical since the introduction of ultrasound was accompanied by a reduction in the cell voltage from 8.3

to 7.3 V! [47]. However, Walton passed 2 F mol^{-1} of charge and so this “apparent” sonoelectrochemical effect likely reflects competition with background reactions in the latter stage of the reaction as it is driven to completion; the work of Nonaka [43] under conditions of small reagent consumption (Fig. 13) testifies to the minimal sonoelectrochemical effect in this particular system and emphasizes the need for careful and systematic study before claiming a positive *sonoelectrochemical* effect.

A system showing a much clearer sonochemical influence was the crossed Kolbe electrolysis [43] of a mixture containing $\text{C}_5\text{H}_{11}\text{COOH}$ and $\text{C}_6\text{H}_{13}\text{OCH}_2\text{COOH}$ (10:1 molar ratio), known to give both one- and two-electron products, respectively. Current densities ranging from 50 up to 400 mA cm^{-2} were used both in silent conditions and under sonication. It was seen that the two-electron

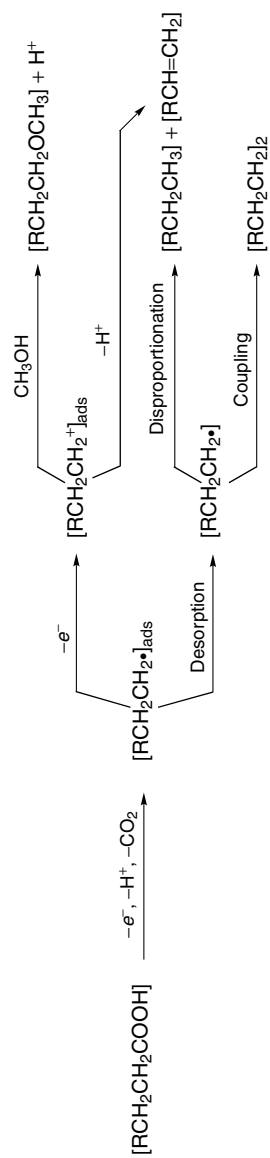


Fig. 12 Possible reaction pathways for the Kolbe electrooxidation of carboxylic acids in an ultrasonically emulsified medium.

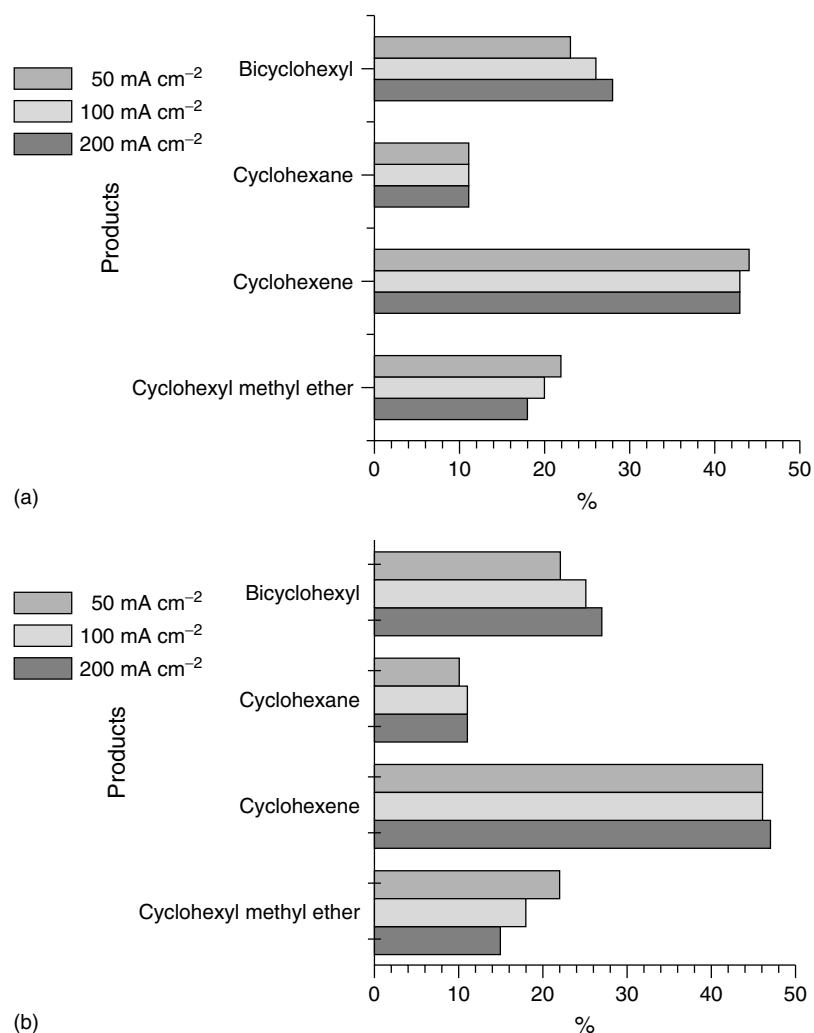


Fig. 13 Product distribution for the Kolbe oxidation of cyclohexanoic acid [43] at different current densities both under: (a) silent and (b) sonicated conditions.

products were formed under ultrasonic irradiation at low current densities. In contrast, one-electron products are formed by sonication at high current densities (see Fig. 1 in Ref. [43]). The fact that the one-electron products are favored at higher current densities under sonication can be explained in terms of enhancement of mass transport between the electrode

and the electrolyte. The decrease at low current density with ultrasonic irradiation can be rationalized as follows [43]. According to the mechanism proposed in Fig. 12, carboxylate anions ($\text{RCH}_2\text{CH}_2\text{COO}^-$) are physically adsorbed, forming an electrical double layer. Some of these carboxylate moieties then undergo a one-electron oxidation and the resulting carboxyl radical

($\text{RCH}_2\text{CH}_2\text{COO}^\bullet$) becomes chemically adsorbed. This adsorbed radical loses a CO_2 group, thus becoming $\text{RCH}_2\text{CH}_2^\bullet$, which after desorption, yields both the dimer and the products of disproportionation. The fraction of carboxyl radicals that did not lose a CO_2 group can undergo a second one-electron oxidation to give the cation $\text{RCH}_2\text{CH}_2^+$, which is desorbed by electrostatic repulsion to react either with methanol in the bulk of the solution or else lose a proton to form alkene via the two-electron route. At low current densities, chemisorption of $\text{RCH}_2\text{CH}_2^\bullet$ competes with the adsorption of the initial carboxylate anion. When ultrasound is applied, acoustic streaming and cavitation disrupt the electrode–solution interface and can remove physically adsorbed species ($\text{RCH}_2\text{CH}_2\text{COO}^-$) more easily from the surface. Therefore, chemical adsorption of $\text{RCH}_2\text{CH}_2^\bullet$ followed by the second one-electron oxidation predominates. Consequently, the two-electron oxidation products of $\text{RCH}_2\text{CH}_2\text{COO}^-$ are favored under ultrasonic irradiation at low current densities.

One significant capability of ultrasound is that of emulsifying water/organic

systems, which under silent conditions form two separate immiscible phases. Preparative voltammetry is viable in such media [17–20, 42] and this approach has been used to study the Kolbe oxidation of hexanoic or heptanoic acids under sonoemulsification conditions. With this procedure, the organic phase can continuously extract the products. The latter are summarized in Table 2 for the case of hexanoic acid using either a platinum anode or, alternatively, a free-standing polycrystalline boron-doped chemical vapor deposited (CVD) diamond electrode. Only the dimer is seen with the ester amyl capronate as the sole by-product.

The products observed in conventional monophasic Kolbe electrolysis reveal that the electrode material exerts a strong control, with products predominantly formed from carbocation intermediates detected at carbon anodes [48, 49] but one-electron products formed at platinum electrodes [36, 40]. Surprisingly, under biphasic conditions, as seen in Table 3, the electrode material did not affect the type or ratio of products formed, and the current efficiencies and product yields observed are only slightly lower using

Tab. 2 Experimental conditions used in the biphasic Kolbe electrooxidation of hexanoic and heptanoic acids

Water/decane ratio	3/1
Supporting electrolyte	1 M NaOH
Working electrode	12-mm diameter Pt disk or 5 × 5 mm free-standing polycrystalline BDD
Counter electrode	Pt wire
Reference electrode	None ^a
Charge passed	1 F mol ^{−1}
Temperature	20 °C
Ultrasonic power	190 W cm ^{−2}

^aMost experiments were carried out under galvanostatic conditions, for which no reference electrode was required.

Note: BDD: boron-doped diamond.

Tab. 3 A single-compartment cell was used, so the hydrogen evolution at the cathode helped to keep pH at a constant value throughout the duration of the experiment. After passing one equivalent of charge (1 F mol^{-1}), the reaction was stopped and the organic products were extracted and analyzed

Starting material	Concentration of NaOH [M]	Current density [A cm^{-2}]	Temperature [K]	Yield of Kolbe dimer 3 [%]
1.1 cm^2 platinum disk electrode				
1.72 g Hexanoic acid	1.0	0.08	293	0
1.72 g Hexanoic acid	1.0	0.13	293	24 ± 3
1.83 g Hexanoic acid	1.0	0.18	293	45 ± 5
1.82 g Hexanoic acid	1.0	0.35	293	45 ± 5
1.67 g Hexanoic acid	0.1	0.18	293	17 ± 2
1.87 g Hexanoic acid	1.0	0.18	313	3 ± 1
2.0 g Heptanoic acid	1.0	0.18	293	15 ± 2
2.0 g Heptanoic acid	1.0	0.35	293	6 ± 2
0.25 cm^2 polycrystalline boron-doped diamond electrode				
1.80 g Hexanoic acid	1.0	0.35	293	40 ± 5
1.80 g Hexanoic acid	1.0	0.70	293	14 ± 5

diamond instead of platinum. Thus, under conditions of sonoemulsification, for the first time in 150 years [50], the electrode material used and conditions employed were observed to have only little effect upon the type of products formed in a Kolbe reaction. Although the mechanism of the reaction is not clear, it likely involves the trapping of intermediates by the organic component of the emulsion. This type of electrosynthetic methodology shows promise for wider application.

In the Kolbe reaction, using ultrasound has proved advantageous because of the following reasons:

1. Aqueous electrolyte solutions may be coemulsified with a sparingly soluble liquid depolarizer, resulting in a medium of high conductivity.
2. There is no need for emulsion stabilizing reagents.
3. The electrode surface is continuously activated.
4. High rates of mass transport are easily achieved.
5. Separation of products is facile.
6. The process is insensitive to the electrode material.

2.10.3.6 Inorganic Sonoelectrosynthesis: Production of Metallic Nanopowders

Metallic powders have a vast range of applications in chemistry [51]. Amongst these lie their use in catalysis [52] and organometallic chemistry [53, 54]. However, whilst larger particles are readily available, until now the preparation of nanosized powders has been difficult and expensive, limiting their commercial viability.

Electrochemistry has, for some time, been used industrially to produce metallic powders with particle sizes ranging from 10 to 100 μm ; see for example Refs. [55, 56]. Different approaches have been taken with the aim of further reducing the particle size: increased agitation, increased current densities, and the addition of organic electrocrystallization inhibitors among others [57, 58]. Using these techniques, powders of 1–10 μm

have been produced, but sometimes they can be contaminated by trace amounts of inhibitors.

In this section, it will be shown that it is possible to produce powders (iron, cobalt, nickel, copper, and zinc) of particle size ranging from 10 to 100 nm [59]. By simultaneously using pulsed electrochemistry and pulsed ultrasound, the ultrasonic pulses are triggered from the potentiostat, and typically last for 100 ms or 1 s, depending on the conditions. The duration of the electrochemical pulse, which precedes the ultrasonic one, ranges from 1 ms up to 1 s, and is followed by a rest period of between 100 ms and 1 s. A 20-kHz ultrasonic titanium horn such as those described earlier in this chapter is connected to a potentiostat and used as the cathode at which the metal is deposited. The anode is usually a rod of the material to be deposited. The procedure is as follows. First, during the electrochemical pulse, three-dimensional nuclei are formed on the surface of the tip. It has been observed that the higher the current density or overpotential used, the smaller these nuclei are. Sonication comes immediately after the electrochemical pulse. During this stage, the particles previously formed are removed into the bulk of the solution due to the action of

asymmetrical collapse of cavitation bubbles. It is possible to observe a cloud of metallic particles leaving the tip on application of ultrasound. The average particle size achieved this way is around 50 nm. After the powders are collected, they are characterized by scanning electron microscopy, X-ray fluorescence, and atomic absorption spectrometry. The magnetic properties of powders containing iron were assessed by Mössbauer spectroscopy.

Binary and ternary alloy powders are also possible to produce using this technique. Table 4 summarizes experimental conditions and the different alloys prepared using pulsed electrochemistry and sonication in Refs. [59–61].

Sonoelectrochemistry has been shown to provide an efficient and low cost way of synthesizing metallic nano-powders in aqueous media, thus presenting an easy alternative to more conventional and expensive methods.

2.10.4

Sonoelectrosynthesis: An Overview

A diverse range of chemical systems have been explored for sonoelectrochemical effects. A selected list of papers of possible electrosynthetic value are listed in Table 5.

Tab. 4 Summary of the different metallic nano-powders synthesized using sonoelectrochemistry [59]

Metal used	Current density [mA cm ⁻²]	Electrochemical pulse		Ultrasonic pulse Time on [ms]	Particle size achieved [nm]	Current efficiency
		Time on [ms]	Time off [ms]			
Fe, Co, Ni, Cu, Zn	200	600	400	300	50	60%
Binary alloy (Co–Ni) or (Fe–Ni)	800	300	300	200	100	Not quoted
Ternary alloy (Fe–Co–Ni)	800	300	300	200	100	Not quoted

Tab. 5 Overview of sonoelectrosynthetic work carried out by different research groups between 1985 and 1999

No.	Chemical system used	Main technique	Insonation method and ultrasonic frequency	Notes	References
1	Kolbe oxidation of cyclohexanecarboxylic acid in MeOH	Galvanostatic control	35 kHz cleaning bath	Reported promotion of two-electron products vs one-electron products under insonation. But see Sect. 2.8.3.3.5 in this chapter	46
2	Kolbe oxidation of phenylacetate and <i>p</i> -Cl-phenylacetate	Galvanostatic control	35 kHz cleaning bath	Ultrasonically enhanced current efficiency and electrode depassivation	62
3	Chlorine, hydrogen, and oxygen evolution at a sonicated Pt electrode	Cyclic voltammetry	38 kHz cleaning bath	Gas evolution is enhanced under sonication due to removal of adsorbed species; oxygen evolution shows little ultrasonic effect	63
4	Organo-selenium and tellurium are synthesized in an ultrasonic field	Potentiostatic control	Not mentioned	Ultrasound enhanced current efficiencies and mass transport rates in acetonitrile	64
5	Selective oxidation of diuron in a MeOH–water mixture	Potentiostatic control	35 kHz cleaning bath and 20 kHz ultrasonic probe	Sonication improves current efficiencies, mass transport rates, and depassivates; the probe was reported to be a much more reliable and effective method of insonation	65
6	Oxidation of hexamethyldisilane in acetonitrile	Potentiostatic control	20 and 500 kHz probes	Ultrasound promotes anion exchange and greatly enhances mass transport	66
7	Copper electrodeposition on a titanium ultrasonic probe	Cyclic voltammetry studies; galvanostatic electrolysis	20 kHz sonotrode	Mass transport is greatly enhanced and the overpotential required for copper to nucleate is higher under sonication	67

(continued overleaf)

Tab. 5 (continued)

No.	Chemical system used	Main technique	Insonation method and ultrasonic frequency	Notes	References
8	Cathodic reduction of benzaldehyde and benzoquinone in water, THF, and acetonitrile	Cyclic voltammetry and potentiostatic electrolysis	20 kHz probe	Ultrasound enhances mass transport and current efficiencies without affecting the reaction mechanism; however, THF is reported to decompose under insonation	68
9	Lead dioxide is deposited on a glassy carbon electrode from a lead nitrate solution	Cyclic voltammetry and chronoamperometric studies; galvanostatic electrolysis	30 kHz ultrasonic bath	OH radicals caused by ultrasound are reported to be the cause of electrode activation. Ultrasound is also reported to enhance mass transport. The bath is recommended for fragile electrode materials prone to severe damage by power ultrasonic horns	69
10	Lead deposition on a copper gauze for galvanostatic synthesis of L-homocysteine	Chronoamperometry	30 kHz ultrasonic bath	Although ultrasound enhances mass transport more than mechanical stirring, a combination of both is reported to be optimal for lead deposition at 35 °C	70
11	Cathodic reduction of benzaldehydes in a MeOH–water mixture	Galvanostatic electrolysis	20 kHz sonotrode immersed in a 38 kHz ultrasonic bath	Ultrasound greatly enhances mass transport and promotes the formation of the hydrodimer in opposition to the hydromonomer; different ultrasonic power setups are reported	71
12	Cathodic reduction of benzaldehyde in a MeOH–water mixture	Galvanostatic electrolysis	36 kHz ultrasonic bath	Ultrasound affects product selectivity compared to mechanical stirring; ultrasound favors the formation of the hydrodimer	72
13	Reduction of benzaldehydes in a MeOH–water mixture	Galvanostatic electrolysis	20 kHz sonotrode	Yields for different current densities are presented in the presence of different ultrasonic powers	73

14	Oxidation of hydroquinone and reduction of <i>p</i> -methylbenzaldehyde	Galvanostatic electrolysis	20 kHz probe	A threshold is reported for ultrasound-induced cavitation, which affects both current efficiency and product selectivity	74
15	Cupric carboxylate is formed from a copper anode in a carboxylic acid solution	Galvanostatic electrolysis	20 kHz probe	Ultrasound improves current efficiency by greatly enhancing mass transport rates	75
16	Reduction of methylhalides at a Sn cathode	Galvanostatic electrolysis	20 kHz probe	Ultrasonically induced mass transport improves current efficiency	76
17	Cathodic reduction of benzoic acid in a MeOH–water mixture	Galvanostatic electrolysis	20 kHz probe	Product selectivity is reported to be greatly affected by ultrasonically controlled mass transport rates	77
18	Aniline is electrochemically polymerized at an electrode surface in aqueous acidic medium	Cyclic voltammetry	20 kHz probe	Although polymerization is slower under ultrasound than in silent conditions. On the other hand, the surface presented by the polymeric film is more regular in the sonicated case. It is proposed that ultrasound modifies the deposition mechanism	78
19	Indirect electrooxidation of <i>p</i> -methylbenzyl alcohol is carried out in a sono-emulsion	Galvanostatic electrolysis	45 kHz ultrasonic bath	Current efficiencies increase for electrochemical processes in an ultrasonically induced emulsion	79
20	Electrooxidative polymerization of aniline in acidic aqueous medium	Electropolymerization of aniline by cyclic voltammetry	20 kHz probe	Ultrasound facilitates the growth of polyaniline in a more homogeneous fashion than in silent conditions although growth rates were slower	80

References

1. M. M. Baizer, *Organic Electrochemistry: An Introduction and a Guide*, Marcel Dekker, New York, 1973.
2. S. Torii, *Electro-Organic Syntheses: Methods and Applications*, Kodansha, Tokyo, 1985.
3. D. M. G. Lloyd, C. A. Vincent, D. J. Walton, *J. Chem. Soc., Perkin Trans. 2* **1980**, 10, 1441.
4. R. D. Little, N. Weinberg, *Electro-Organic Synthesis*, Marcel Dekker, New York, 1992.
5. D. J. Walton, *Manufact. Chemist* **1981**, 52, 44.
6. D. Pletcher, F. Walsh, *Industrial Electrochemistry*, Chapman & Hall, London, 1990.
7. F. Marken, R. G. Compton, S. G. Davies et al., *J. Chem. Soc., Perkin Trans. 2* **1997**, 2055.
8. R. G. Compton, J. C. Eklund, S. D. Page et al., *J. Phys. Chem.* **1994**, 98, 12 410.
9. R. G. Compton, J. C. Eklund, S. D. Page, *J. Phys. Chem.* **1995**, 99, 4211.
10. J. Booth, R. G. Compton, E. Hill et al., *Ultrasonics Sonochem.* **1997**, 4, 1.
11. R. G. Compton, J. C. Eklund, F. Marken et al., *Electrochim. Acta* **1997**, 42, 2919.
12. R. G. Compton, J. C. Eklund, F. Marken, *Electroanalysis* **1997**, 9, 509.
13. F. Marken, S. Kumbhat, G. H. W. Sanders et al., *J. Electroanal. Chem.* **1996**, 414, 95.
14. R. G. Compton, F. Marken, T. O. Rebbitt, *Chem. Commun.* **1996**, 1017.
15. A. J. Bard, L. R. Faulkner, *Electrochemical Methods: Fundamentals and Applications*, John Wiley & Sons, New York, 1980.
16. H. Fees, H. Wendt in *Techniques of Chemistry* (Eds.: N. L. Weinberg, B. V. Tilak), John Wiley & Sons, New York, 1982, pp. 1–81, Version 5, Vol. Part III.
17. F. Marken, R. G. Compton, S. D. Bull et al., *Chem. Commun.* **1997**, 995.
18. F. Marken, R. G. Compton, *Electrochim. Acta* **1998**, 43, 2157.
19. R. P. Akkermans, S. L. Roberts, F. Marken et al., *J. Phys. Chem. B* **1999**, 103, 9987.
20. R. P. Akkermans, S. L. Roberts, R. G. Compton, *Chem. Commun.* **1999**, 1115.
21. D. J. Milner, Eur. Pat. Appl., Zeneca Ltd., UK, EP 1993 p. 4.
22. P. M. S. Chauhan, R. N. Iyer, D. S. Bhakuni, *Indian J. Chem., Sect. B* **1988**, 27B, 144.
23. J. G. Lawless, D. E. Bartak, M. D. Hawley, *J. Am. Chem. Soc.* **1969**, 91, 7121.
24. P. Peterson, A. K. Carpenter, R. F. Nelson, *J. Electroanal. Chem. Interfacial Electrochem.* **1970**, 27, 1.
25. W. F. Jarvis, M. D. Hoey, A. L. Finocchio et al., *J. Org. Chem.* **1988**, 53, 5750.
26. A. J. Birch, *J. Chem. Soc.* **1944**, 430.
27. A. J. Birch, *J. Chem. Soc.* **1945**, 809.
28. D. Postl, U. Schindewolf, *Ber. Bunsen-Ges. Phys. Chem.* **1971**, 75, 602.
29. T. Teherani, K. Itaya, A. J. Bard, *Nouv. J. Chim.* **1978**, 2, 481.
30. U. Schindewolf, *Ber. Bunsen Ges. Phys. Chem.* **1982**, 86, 887.
31. F. J. Del Campo, C. H. Goeting, D. Morris et al., *Electrochem. Solid State Lett.* **2000**, 3, 224.
32. J. Chaussard, C. Combellas, A. Thiebault, *Tetrahedron Lett.* **1987**, 28, 1173.
33. A. J. Birch, *Nature* **1946**, 158, 60.
34. F. J. Del Campo, A. Neudeck, R. G. Compton et al., *J. Electroanal. Chem.* **1999**, 477, 71.
35. R. P. Akkermans, J. C. Ball, T. O. Rebbitt et al., *Electrochim. Acta* **1998**, 43, 3443.
36. M. J. Allen, (ed.), *Organic Electrode Processes*, Chapman and Hall, London, 1958, p. 95.
37. H. J. Schäfer, *Angew. Chem., Int. Ed. Engl.* **1981**, 20, 911.
38. H. Kolbe, *Ann. Chem. Pharm.* **1849**, 69, 257.
39. Y. B. Vassilieb, V. A. Grinberg, *J. Electroanal. Chem.* **1991**, 308, 1.
40. B. C. L. Weedon, *Q. Rev.* **1952**, 6, 380.
41. B. C. L. Weedon, *Adv. Org. Chem.* **1963**, 1, 1.
42. J. D. Wadhawan, F. J. Del Campo, R. G. Compton et al., *J. Electroanal. Chem.* **2001**, 507, 135.
43. H. Fujiwara, M. Atobe, H. Nanetsuna et al., *J. Chin. Chem. Soc.* **1998**, 45, 175.
44. L. Ebersson, J. H. P. Utley, *Organic Electrochemistry*, Marcel Dekker, New York, 1983, pp. 435–531.
45. S. Torii, H. Tanaka in *Organic Electrochemistry* (Eds.: H. Lund, M. M. Baizer), Marcel Dekker, New York, 1991, pp. 535–572.
46. A. Chyla, J. P. Lorimer, T. J. Mason et al., *Chem. Commun.* **1989**, 603.
47. D. J. Walton, S. S. Phull, U. Geissler et al., *Electrochem. Commun.* **2000**, 2, 431.
48. J. H. P. Utley in *Techniques of Electroorganic Synthesis* (Ed.: N. L. Weinberg), Part I, John Wiley & Sons, New York, 1981.
49. C. J. Brockman, *Electroorganic Chemistry*, John Wiley & Sons, New York, 1926.
50. J. D. Wadhawan, F. Marken, R. G. Compton et al., *Chem. Commun.* **2001**, 87.

51. I. Malsch, European Commission-JRC Institute for Prospective Technological Studies, Brussels (1997).
52. J. Reisse, T. Caulier, C. Deckerkheer et al., *Ultrasonics Sonochem.* **1996**, 3, S147.
53. A. Durant, J.-L. Delplancke, R. Winand et al., *Tetrahedron Lett.* **1995**, 36, 4257.
54. A. Durant, J. L. Delplancke, V. Libert et al., *Eur. J. Org. Chem.* **1999**, 2845.
55. J. O. M. Bockris, B. E. Conway, *Modern Aspects of Electrochemistry*, Butterworths Scientific, London, 1954.
56. N. Ibl, *Advances in Electrochemistry and Electrochemical Engineering*, John Wiley & Sons, New York, 1961.
57. C. M. Chu, C. C. Wan, *J. Mater. Sci.* **1992**, 27, 6700.
58. U. Erb, *Can. Metallurg. Q.* **1995**, 34, 275.
59. J.-L. Delplancke, J. Dille, J. Reisse et al., *Chem. Mater.* **2000**, 12, 946.
60. J. L. Delplancke, V. Di Bella, J. Reisse et al., *Mater. Res. Soc. Symp. Proc.* **1995**, 372, 75.
61. J. L. Delplancke, O. Bouesnard, J. Reisse et al., *Mater. Res. Soc. Symp. Proc.* **1997**, 451, 383.
62. D. J. Walton, A. Chyla, J. P. Lorimer et al., *Synth. Commun.* **1990**, 20, 1843.
63. D. J. Walton, L. D. Burke, M. M. Murphy, *Electrochim. Acta* **1996**, 41, 2747.
64. B. Gautheron, G. Tainturier, C. Degrand, *J. Am. Chem. Soc.* **1985**, 107, 5579.
65. K. Macounova, J. Klima, C. Bernard et al., *J. Electroanal. Chem.* **1998**, 457, 141.
66. V. Jouikov, C. Bernard, C. Degrand, *New J. Chem.* **1999**, 23, 287.
67. J. Reisse, H. Francois, J. Vandercammen et al., *Electrochim. Acta* **1994**, 39, 37.
68. A. Durant, H. Francois, J. Reisse et al., *Electrochim. Acta* **1996**, 41, 277.
69. J. Gonzalez-Garcia, J. Iniesta, A. Aldaz et al., *New J. Chem.* **1998**, 22, 343.
70. E. Agullo, J. Gonzalez-Garcia, E. Exposito et al., *New J. Chem.* **1999**, 23, 95.
71. M. Atobe, T. Nonaka, *J. Electroanal. Chem.* **1997**, 425, 161.
72. K. Matsuda, M. Atobe, T. Nonaka, *Chem. Lett.* **1994**, 1619.
73. M. Atobe, T. Nonaka, *Chem. Lett.* **1995**, 669.
74. M. Atobe, T. Nonaka, *Chem. Lett.* **1997**, 323.
75. M. Atobe, T. Nonaka, *Ultrasonics Sonochem.* **1997**, 4, 17.
76. M. Atobe, K. Matsuda, T. Nonaka, *Denki Kagaku* **1994**, 62, 1298.
77. M. Atobe, K. Matsuda, T. Nonaka, *Electroanalysis*, **1996**, 8, 784.
78. M. Atobe, S. Fuwa, N. Sato et al., *Denki Kagaku* **1997**, 65, 495.
79. M. Atobe, P.-C. Chen, T. Nonaka, *Denki Kagaku* **1998**, 66, 556.
80. M. Atobe, T. Tono, T. Nonaka, *Electrochem. Commun.* **1999**, 1, 593.

2.11 Biosensors

Wolfgang Schuhmann, Eva Maria Bensen
Anal. Chem. – Elektroanalytik & Sensorik,
Ruhr-Universität Bochum, D-44780 Bochum,
Germany

2.11.1 Introduction

2.11.1.1 Basic Principles and Setup

A biosensor is defined as a sensing device consisting of a biological recognition element (enzymes, microorganisms, cells, antibodies, tissues, etc.) in intimate contact with a suitable transducer, which is able to convert the biological recognition reaction or eventually the biocatalytic process into a measurable electronic signal. Thus, a biosensor is able to deliver information about the concentration of a target analyte. The quality of this information is highly dependent on the complexity of the analyte solution, the inherent specific features of the complementary biological recognition process, the design of the sensor architecture, and the properties of the physical transducer (Fig. 1).

The target analyte, which is one compound among many others in a complex sample, is recognized by a specific biological element in a complementary recognition process leading to the binding of the analyte either to a catalytic site followed by a specific reaction and the release of the formed products (metabolism sensors) or to the recognition site with a specificity defined by the binding constant of the recognition reaction (affinity sensors). Generally, biorecognition elements can be divided into two groups: the biocatalytic and the bioaffinity recognition elements [1, 2].

In the first case, the biological recognition element is in general an enzyme

or a sequence of coupled enzymes, and the analyte in question is catalytically converted within the active site of the enzyme. The product formed is released, thus regenerating the active binding site, which is the major prerequisite for the inherent reversibility of enzyme-based biosensors. The catalytic reaction imposes a change in the concentration of the analyte itself, of the formed product, and of cofactors involved in the reaction. These concentration changes lead, for example, to the variation in the redox state, the potential, and the pH value that may be recognized by the physical transducer. The main advantage of enzyme-based sensors is the implemented regeneration of the enzyme's active site, implying an amplification of the signal concomitantly with an intrinsic reversibility of the sensor.

In contrast, the second type of biosensor is based on an affinant binding of the analyte to a recognition site. The specificity is defined by the equilibrium constant of the binding process, which suggests that these sensors are intrinsically not reversible and that they have to be regenerated prior to a second measurement.

Both metabolism sensors and affinity sensors can be designed using electrochemical transducers for the signal generation, as will be discussed in detail below. However, before evaluating specific features of electrochemical biosensors, some general aspects of the qualification of biosensor properties have to be discussed.

The *selectivity* of biosensors mainly derives from the role the biorecognition elements play in nature. Enzymes not only often exhibit a selectivity for the binding of a single substrate (or sometimes a class of compounds) but they additionally exclusively catalyze a single type of reaction, sometimes with high stereoselectivity. However, in addition to the selectivity

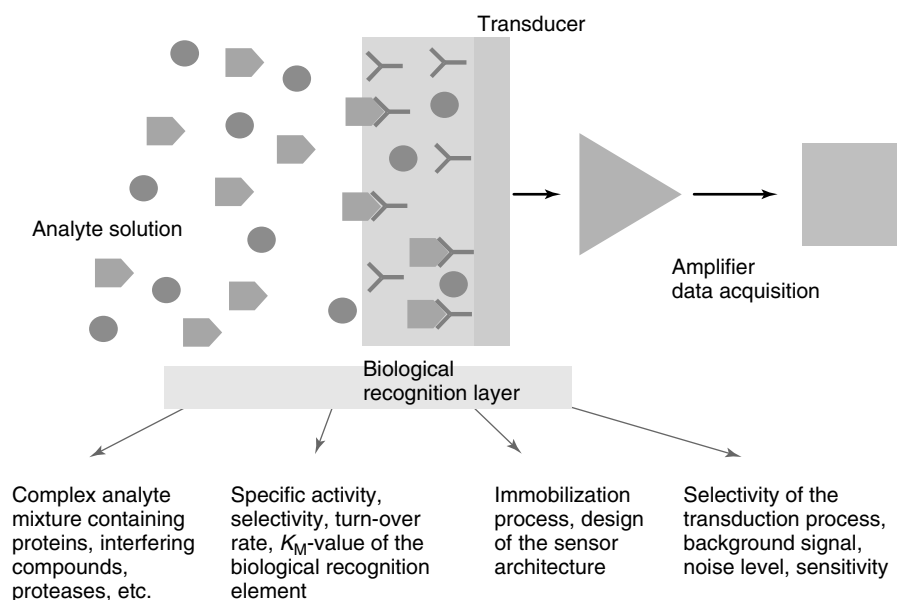


Fig. 1 Schematic view of a biosensor.

of the biological recognition process, the physical transducer imposes a selectivity for the transduction process. In general, the selectivity of the biological recognition process is superior to the selectivity of chemosensors based on supramolecular recognition elements such as ionophores.

The *linear dynamic range* of biosensors is highly dependent on the biological recognition process and the biocompound involved. For enzymes, the linear range extends from 2 to 5 concentration decades, depending on the turnover rate of the enzyme and its affinity constant. For non-catalytic biocompounds the linear range is dependent on the immobilized concentration of the biocompound and the affinity constant. Both the *detection limit* (defined as three times the noise level) and the *sensitivity* (defined as the slope of the calibration graph) depend on the complementary recognition and the transduction process. For enzyme-based sensors the

detection limit lies between 100 nmol L^{-1} in the case of amperometric electrodes and $100 \text{ } \mu\text{mol L}^{-1}$ in the case of potentiometric sensors. The *response time* of biosensors is highly dependent on the overall sensor architecture defining substrate diffusion to the recognition site, the transduction pathway, and in the case of a metabolism sensor the nature of the biological conversion process. Hence, the response time varies in the range of less than one second (in specifically designed amperometric enzyme electrodes and enzyme-based field-effect transistors) and more than 30 min (for substrate-induced changes in the metabolism of intact cells used as biological recognition elements). The *recovery time*, which is the shortest time between two subsequent measurements, depends on the properties of the whole analytical system. The recovery time can be decreased by rinsing of the biosensor with sample-free buffer

solution, which is advantageously done in flow-injection analysis (FIA) systems. For affinity sensors an active recovery has to be done (e.g. by rinsing the sensor with a buffer of low pH value), which is also usually done in flow-injection systems [3].

2.11.1.2 Application of Biosensors. Principal Considerations

Biosensors are of growing importance as a widely used analytical tool. However, biosensors or analytical instrumentation with integrated biosensors are not supposed to replace conventional analytical methods, but can serve as an additional tool for fast screening, for on-site determinations, or for the specific quantification of compounds that are difficult to analyze using conventional analytical methods. The main advantage of biosensors is their inherent selectivity, which is mainly dependent on the biological recognition element, allowing the determination of the target analyte without any separation steps in complex matrices. Their in general fast response and easiness of handling allows their application for preliminary screening to select those samples that have to be submitted to a detailed (and expensive) analytical procedure. A further advantage of biosensors is the possibility of their miniaturization (Sect. 2.11.3). The application of biosensors integrated into microsystems is especially appealing as a means to reduce costs as both reagents and sample volumes can be substantially reduced. Further, miniaturization enables the construction of portable, easy to use analytical instruments. Another important feature is the construction of sensor arrays with different biorecognition elements immobilized at the sensor surface for the simultaneous determination of several analytes. Clear disadvantages of biosensors are, in general, the insufficient long-term stability of

the biological recognition component [4, 5] and the sometimes difficult calibration of the sensor. Biosensors can be employed, for example, in environmental, clinical and food analysis [6–10]. Numerous compounds such as phenols [11, 12], phosphates [13], DMF [14], cyanide [15, 16], nitrite and methane [17], and various pesticides [16–20] can already be determined. The most applied biosensors are enzyme electrodes [11–13, 14, 19]. But also immunosensors [21, 22] and sensors based on whole cells [23] and plant tissue [12] have been intensively investigated.

2.11.1.3 Biorecognition Elements

As has been already discussed, the biological recognition element is the selective part in biosensors; however, the overall function of the biosensor is determined by the proper combination of the biological recognition element with the transducer, with respect to the signal-transduction process. Thus, after the discussion of the nature, the properties, and the applicability of different biological compounds, suitable combinations of biorecognition elements with electrochemical transducers are described in Sect. 2.11.1.4.

2.11.1.3.1 Catalytic Biorecognition Elements

For catalytic biological or biomimetic recognition elements such as enzymes, whole cells (or parts of them), tissues [2], or catalytic antibodies [24, 25], an easy kinetic treatment of the biological recognition and catalysis processes is derived following the Michaelis–Menten approach (see Chapter 13 in Volume 9). It is assumed that the analyte forms a complex within the active site of the biological recognition compound in a dynamic equilibrium reaction, while a quasi-irreversible follow-up reaction leads to the formation of the product and its release from the active

site under regeneration of the enzyme. Although this treatment holds for a simple recognition and conversion of one substrate molecule by the enzyme without the action of cosubstrates or coenzymes, it is generally applied for the description of biocatalytic and inhibitoric reactions in biosensors. These considerations explain the observed saturation characteristics at high substrate concentrations, and, as a matter of fact, the derived values for the K_M value (which reflects the substrate concentration at half-maximum reaction rate) and the maximal signal have a significant impact on the proper design of a biosensor.

In biocatalytic sensors usually the change in concentration of either a substrate, a cosubstrate or coenzyme, or a product is monitored by a suitable transduction process at the transducer. Because of the catalytic activity of the biorecognition element, the substrate (analyte) is consumed continuously, leading to a signal amplification in dependence from the turnover rate of the biocatalytic element and hence a steady state or transient signal. The utilization of biocatalytic recognition elements in biosensors is not restricted to the determination of biogenic materials, but due to their inherent selectivity they can also be employed for the analysis of nonbiogenic analytes [26].

The most often used recognition elements for the construction of biosensors are enzymes. Their catalytic activity usually derives from prosthetic groups (nonproteins such as heme, FAD, or pyridoxalphosphate) or metal ions. The prosthetic groups are usually covalently bound to the enzyme, while coenzymes or cosubstrates are only associated with it, binding in close proximity to the substrate binding site during the catalytic action. For their application in biosensors, enzymes have to be isolated from the biological

source, purified, characterized concerning their specific activity and possible coactivity for other substrates, and either freeze-dried or formulated together with preservatives. The isolation, purification, and characterization of novel enzymes for possible sensor applications are of growing importance. In addition, the large-scale fabrication of new enzymes using genetically modified host organisms has opened the route for the reproducible production of enzymes with well-defined properties [27–29]. However, since the amount of immobilized enzyme on a transducer surface is limited, the stability of the enzyme highly influences the overall stability of the sensor. Enzymes are classified according to the type of reaction they catalyze [30] (Table 1).

In contrast to isolated enzymes, intact organisms possess the inherent ability to regenerate eventually lost activity by their metabolic action. In addition, in living organisms, signal-transduction and signal-amplification pathways are established in complicated spatial and steric arrangements. In order to make use of these complex metabolic pathways in biosensors, different types of intact cells (microorganisms, such as bacteria, fungi, or yeast [2, 26], and body cells, such as neural cells, heart muscle cells, or pancreas beta cells [31]) can be of interest in sensor design.

Microorganisms, such as bacteria, have certain advantages over pure enzymes when employed as the recognition element in biosensors. At first they can be cheaper, as the enzyme does not have to be isolated. Since microorganisms have to take up the analyte (pollutant, drug, nutrient), information about bioavailability is provided. Further, they are more tolerant to assay conditions as they regulate their internal environment. Disadvantages are their

Tab. 1 International classification of enzymes, and examples for enzymes employed in electrochemical biosensors

Enzyme class	Enzyme subclass	Examples	Type of reaction catalyzed	Target analyte	Species detected
1. Oxidoreductases	Oxidases Dehydrogenases Peroxidases	Glucose oxidase Glucose dehydrogenase Horseradish peroxidase	Transfer of electrons	β -D-glucose β -D-glucose H_2O_2	H_2O_2 or O_2 NADH Redox mediator
3. Hydrolases	Amidohydrolases Esterases	Urease Acetylcholine esterase	Hydrolysis reactions	Urea Acetylcholine	NH_3 , CO_2 or H^+ H^+
4. Lyases	Decarboxylases	Amino acid Decarboxylases	Addition of groups to double bonds or abstraction of groups accompanied by formation of double bonds	Amino acid	CO_2
2. Transferases, transfer of groups used in combination with other enzymes					
5. Isomerases, transfer of groups within the same molecule and formation of isomers used in combination with other enzymes					
6. Ligases, formation of bonds from C to either C, S, O, or N by condensation reactions accompanied by cleavage of ATP					

low stability and lifetime, their in general long response time, and the problems to maintain a constant sensor architecture. In general, one can distinguish between two signal generation schemes using whole cells. In the first, the metabolic action of the microorganism is modulated by the presence of a substrate or an inhibitor in the sample. In the second, the generation of the signal involves the production of a suitable induction (e.g. binding of an inducer or a toxin to a regulatory protein) leading to the release of a reporter gene, its transcription, and finally the production of an enzyme switching on the catalytic conversion of a specific substrate [32].

Cells of more complex organisms can be used either as single cells, cell layers, cell networks, tissue, or even whole animals. These cells can show changes in conductivity or excrete metabolic products (receptor-mediated) upon contact with the analyte. In neural cells grown in networks, changes of the membrane potential can be observed upon stimulation with neurotransmitters or neuromodulators such as strychnine [31].

Further, cell parts like lipid membranes or mitochondria have been used for complementary recognition processes [2, 33, 34]. *Lipid membranes* can be considered rather to bioaffinity recognition elements, but the signal gained is amplified by the membrane constituents utilized. For example, receptors controlling ion channels or membrane-transport proteins can be employed. *Mitochondria* are cell organelles that are responsible for respiration and energy storage of the cell. They are permeable for molecules up to a certain size and this permeability is subject to alteration. Their inner walls (cristae) contain enzymes involved in respiration and ATP production and specific transport proteins (transport into and out of their matrix).

Their matrix contains enzymes, mainly of the tricarboxylic acid cycle [35].

2.11.1.3.2 Bioaffinity Recognition Elements

Bioaffinity recognition is based on non-catalytic complementary interaction with the analyte. The specificity of the complementary recognition process is mainly determined by the binding constant of the complex-formation reaction. The analyte quantification is usually done at equilibrium (when no further consumption of the analyte takes place) using a suitable transduction process modulated by the complementary recognition reaction.

Immunochemical reactions using the interaction between antibodies and antigens are the bioaffinity reactions most often found in biosensors. For the determination of an antigen the specific antibody has to be produced, isolated, and purified. This reaction is very selective and extremely sensitive and the binding is strong and often nearly irreversible. In this respect, the antibody-antigen reaction is superior to the enzyme reaction; however, signal transduction is more difficult since after the complementary binding no further reaction takes place. In addition, the strong binding of the antigen to the antibody limits the reversibility, leading to the main applications of immuno-reactions in single-use biosensors or FIA systems in which regeneration of the recognition element, for example, by changing the binding constant using pH changes is possible.

Another affinity process is the recognition of analytes (agonists) by receptors. The agonist may, for example, bind to the receptor of an ion channel, which then triggers the opening of the channel to ions such as Na^+ or Ca^{2+} . Here, an ion flux may be detected by the transducer. By means of receptors as

biorecognition elements, agonists can be distinguished from their antagonists. Often, structurally related compounds are similarly recognized by the receptor. Further, membrane-transport proteins that are involved in active transport phenomena over the lipid-bilayer membrane can be used as specific recognition elements. Carrier-mediated transport is highly specific, and the carriers exhibit a certain affinity for either a single kind of molecule or for molecule classes. For example, Na^+/K^+ -ATPase is able to act as an electrogenic transporter system, building up a potential across the membrane. If a bilayer membrane with integrated Na^+/K^+ -ATPase is covering a suitable transducer, the established membrane potential can be measured. Na^+/K^+ -ATPase is inhibited by a specific glucoside, and hence the potential change can be correlated with the glucoside concentration [36].

Nucleic acid recognition layers such as single-stranded DNA (ssDNA) are highly specific as they only bind to the complementary ssDNA or oligonucleotides with the same sequence. The process of formation of a duplex nucleic acid molecule with strands derived from different sources by complementary base pairing is called *hybridization* [35]. Even single mismatches in the sequence significantly change the complementary binding constant, as is reflected by differences in the melting behavior of double-stranded DNA (dsDNA) with and without mismatches. Hence, specific oligonucleotides can be designed (and synthesized) for complementary hybridization with a target ssDNA. If hybridization occurs, the presence of nucleic acid sequences can be identified, and the number of molecular probes (oligonucleotides) employed enables high analytical precision [37]. Among many others, infectious

microbes are an example of potential analytes [38]. Advantages of DNA probes over enzyme and immunosensors is their significantly better stability.

Another approach of biosensors utilizing nucleic acids are those containing dsDNA. Here, the intercalation of small pollutants such as metal ions or organic toxins is monitored (non-electroactive compounds) or competitive binding and displacement of redox markers (electroactive analytes) is determined. Generally, DNA probes could be useful in genetic testing, for environmental analysis, for detection of microorganisms, or for food testing [39].

2.11.1.4 Transducers and Instrumentation

Mainly electrochemical (amperometric, potentiometric, impedimetric, or conductometric) and optical (IR, Raman, fluorescence, absorption, reflection, evanescence field, or surface plasmon resonance) transducers are used as the basis for biosensors. However, beside these there are other, less often employed transducers that make use of the piezoelectric effect, surface acoustic waves, or detection of heat generated in enzyme reactions [40, 41]. In the context of this work, the focus is on the specific features of electrochemical transducers. An overview showing the different fields of application can be found in Sect. 2.11.1.5 (Table 2).

2.11.1.4.1 Amperometric Electrodes

In an amperometric setup (Fig. 2) a working electrode (usually the biosensor itself) is immersed in an electrolyte together with a reference electrode and a low-resistance counter electrode. At the working electrode a fixed (amperometric) or modulated (voltammetric) potential with respect to the reference electrode is

Tab. 2 Biorecognition elements, their classification, and suitable transducers for the effects observed

<i>Biorecognition element</i>	<i>Mechanism of recognition</i>	<i>Observed effect</i>	<i>Suitable electrochemical transducer</i>
Enzyme	Biocatalytic	Catalyzed decrease of substrate or increase of product concentration	Amperometric, conductometric potentiometric, FETs
Cells			
Microorganisms		Release of enzymes, biocatalytic reactions	Amperometric, potentiometric
Body cells/cellular networks		Cell–cell interaction (resistance)	Conductometric, impedimetric
		Metabolic products	Amperometric, potentiometric
		Direct electric response (e.g. neurons, heart muscle)	ISFETs, FETs
Membrane			
	Bioaffinity (signal amplification)	Receptor induced reaction: opening of ion channel invoking the flux of ions across the membrane;	Conductometric, amperometric, potentiometric
		Active transport by means of membrane-transport proteins	Potentiometric
Mitochondria	Biocatalytic	Release of enzymes, biocatalytic reactions	See above
Antibody/antigen (enzyme-labeled)	Bioaffinity (biocatalytic)	Formation of complex (catalyzed decrease of substrate or increase of product concentration)	Potentiometric (amperometric)
Receptor	Bioaffinity	Opening of ion channel, hence flux of ions – current across the membrane	Conductometric, amperometric, potentiometric
Nucleic acid	Bioaffinity /biocatalytic	Binding of oligonucleotides	Amperometric via enzyme labels

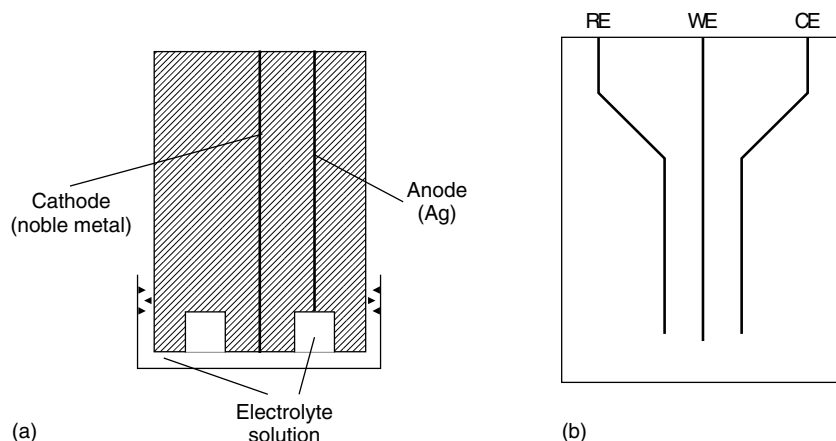


Fig. 2 (a) Amperometric electrode for the determination of dissolved O_2 (Clark electrode) and (b) screen-printed three-electrode setup.

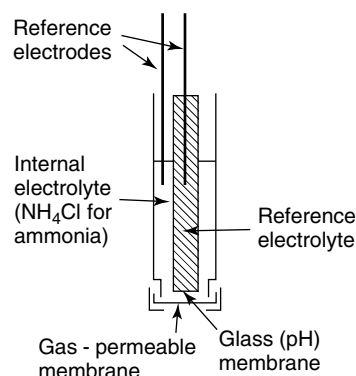
applied using a potentiostat (see Chapters 1.1 and 1.2). The current flows between the counter electrode and the working electrode, reflecting the heterogeneous electron-transfer reaction that is taking place over the electrode–electrolyte interface. In amperometry, the current at constant potential is measured over time, whereas in voltammetry, the current is measured with respect to the actual electrode potential. The current observed is dependent on the electrode area, the number of electrons transferred in the redox reactions, the diffusion coefficient of the electroactive species, as well as on their concentration (Cottrell equation; see Chapter 2.2). As reference electrodes, usually $Ag/AgCl$ or saturated calomel electrodes (SCE) are employed, while as counter electrodes, platinum wires or carbon strips are used in most cases. Working electrodes may consist either of noble metals (Au, Pt) or of carbonaceous materials (glassy carbon, carbon paste, or screen-printed carbon ink) [40, 41].

More detailed information about amperometry and voltammetry can be found in Chapters 2.1–2.5 of this volume.

2.11.1.4.2 Potentiometric Sensors The potential difference between two half-cells connected internally by an electrically conducting bridge can be measured using a high-impedance digital voltmeter. The electrode potential E for each half-cell is, according to the Nernst equation, dependent on the standard potential E° of the redox couple involved and on the concentration ratio between oxidized and reduced species (see Chapter 1.1). If one of the half-cells is a reference electrode, the potential generated at the second one is used as analytical information.

Ion-selective electrodes (ISEs) can be designed using various ion-selective elements, such as glass membranes (for pH electrodes), solid membranes (for ions such as F^- , Cl^- , Br^- , I^- , SCN^- , or S^{2-}), liquid ion-exchange membranes (for ions such as NO_3^- , Cl^- , BF_4^- , or K^+), or gas-sensitive electrodes on the basis of pH electrodes, containing a hydrophobic, gas-permeable membrane (for acidic or basic gases such as NH_3 or CO_2). An example of the latter is depicted in Fig. 3 [40–42].

Fig. 3 Gas-permeable membrane electrode containing H^+ -selective electrode (pH electrode).



Problems occurring in chemical analyses using ISEs are mainly caused by the chemical environment of the analyte. The ionic strength of the solution must be kept constant by the use of a total ionic strength adjustment buffer (TISAB). This TISAB should contain additives to adjust the pH and compounds masking possible interferences [40, 41]. For more detailed information on the function of potentiometric sensors, see Chapter 1.1 (Sect. 1.3) in this volume.

In field-effect transistors (FET) a potential is applied via metal contacts between two *n*-type semiconductor areas – called *source* and *drain* – in a bulk of otherwise *p*-type semiconductor material. A metal layer – called the *gate* – in contact with a thin insulating layer placed on top of the semiconductor (between source and drain) forms a metal/insulator/semiconductor (MIS) capacitor. If the gate is charged, the semiconductor region below the insulator is influenced by the electric field. The electric field thus affects the current flowing between source and drain. In ion-sensitive FETs (ISFETs) the metal layer on top of the insulating layer is replaced by an ion-sensitive material. This ion-sensitive layer is in contact with the analyte solution, and a reference electrode is placed close to it.

In Fig. 4 a schematic drawing of an ISFET is shown [40–42].

Basically, every kind of potentiometric ion-sensitive electrode can be miniaturized using a FET as potentiometric transducer; especially, ion-selective polymer membranes have been used. In addition, utilizing enzyme systems, enzyme-modified FETs (ENFETs) can be realized, opening up possibilities for miniaturized biosensors (see Sect. 2.11.3, Miniaturization).

2.11.1.4.3 Conductometric and Impedimetric Transducers

Conductance is the inverse of resistance, and thus related to current and potential by Ohm's law. As conductivity is nonspecifically influenced by many parameters, conductometric transducers do not measure absolute conductance values but rather changes in the conductance. Conductance changes are invoked by altering the number of ions in the solution (e.g. by dissociation reactions or cleavage of bonds), changes in the mobility of ions, or changes in the kind of ions (ions of higher/lower equivalent conductivity or higher/lower charge). If enzymes are used as an additional selectivity element in combination with a conductometric transducer, conductance changes

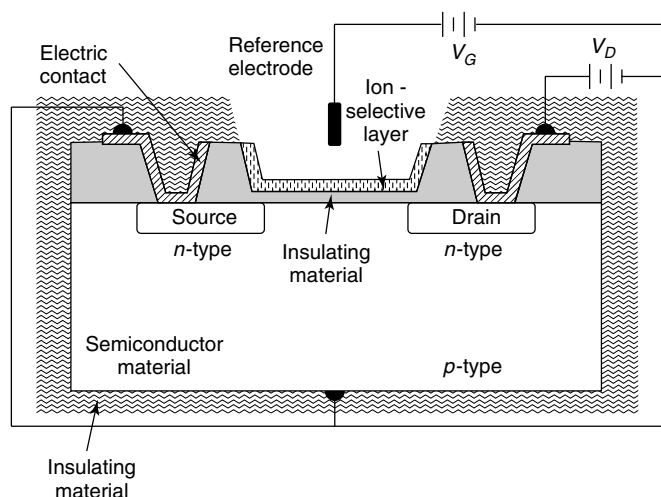


Fig. 4 ISFET with an ion-sensitive layer.

are observed after catalytic formation of ions or transfer of ionic groups (e.g. urease-catalyzed cleavage of urea into NH_4^+ and HCO_3^-). For biosensor applications, the conductivity cell usually consists of two metal electrodes (working and reference/counter electrode) that are covered by a polymer containing the biorecognition element. Measurements are carried out in a differential mode (Fig. 5a) using a standard conductivity bridge and a potentiostat for potential application. In order to minimize faradaic processes and a charging of the double layer, alternating current is usually applied. Varying the frequency of the alternating current, admittance (the inverse of impedance) can be measured,

which not only depends on conductance but also on capacitance and inductance (see Chapter 2.6 in this volume).

As a matter of fact, the cell parameters of the conductance cell have to be known. Hence, in order to optimize the ratio between interface area and electrode distance, miniaturized, serpentine, and interdigitated electrodes have been used (see Fig. 5b) [40, 41].

2.11.1.5 Coupling of Biorecognition Elements and Transducers

Biosensor design has to start with the actual analytical problem and possible biological recognition processes to select a suitable selectivity element. As a matter of

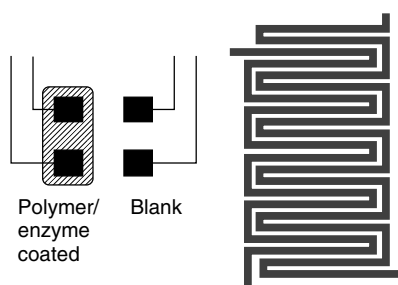


Fig. 5 (a) Differential conductivity measurement and (b) interdigitated microelectrodes for miniaturized conductivity cell.

fact, the choice of the biorecognition reaction suggests possible signal-transduction pathways and hence a selection of a suitable transducer and a sensor architecture that allows signal transduction to take place. In Table 1, biorecognition elements are listed, along with the effects observed on recognition of a specific analyte, and suitable electrochemical transducers.

The immobilization of the biological recognition element on the transducer surface by adsorption, cross-linking, entrapment in a polymer matrix, or covalent binding is a crucial step in biosensor development. On the one hand, the secure immobilization should guarantee the long-term stability of the sensor, avoiding loss of the biological recognition element to the bulk of the analyte solution. On the other hand, the chosen immobilization procedure predefines the overall sensor architecture and hence the possible signal-transduction process. As a matter of fact, a suitable immobilization procedure has to be adapted to the specific features of the biological recognition element such as its intrinsic stability, presence of functional groups for covalent binding and inhibition due to modification of the active site by reagent molecules. In addition, the immobilization procedure has a significant impact on the diffusion of the analyte to the recognition site (defining the linear range of the calibration graph), the local concentration of the biorecognition element (defining the maximum signal), and the location of the biorecognition element with respect to the transducer surface (monolayer versus multilayer immobilization). From these considerations, it is obvious that a vast variety of different immobilization protocols have been developed for biosensor application, specifically adapted to the demands imposed by the biological

recognition element, the analytical application, the nature of the sample solution, and the method of detection.

A further prerequisite has to be considered if a specific sensor configuration is to be commercially produced. In this case, besides the above-mentioned constraints, the immobilization procedure has to be mass-production compatible, with high reproducibility implying nonmanual immobilization techniques, addressing exclusively the transducer surface. Here, lithographic structuring of polymer membranes [43, 44], local electrochemical formation of conducting [45, 46] and nonconducting [47] polymer films in the presence of the biological recognition element, electrocoagulation [48], screen printing [49] or printing by using piezo-jets [50] have to be mentioned.

In electrochemical detection schemes the signal-transduction pathway is often highly dependent, or even directly related to the immobilization matrix, which may be modified with redox relays to allow for an optimal electron transfer from the active center of the biomolecule to the transducer surface. Specific immobilization methods, with the main focus on the simultaneous design of appropriate electron-transfer pathways, are discussed in detail in Sect. 2.11.2.

2.11.2

Specific Features of Electrochemical Biosensors

2.11.2.1 Amperometric Biosensors

In amperometric biosensors a current is measured, which arises from the oxidation or reduction of a compound generated in direct relation to the concentration of the envisaged analyte in a reaction catalyzed by the biological recognition

element. Thus, the fundamental question that arises concerning the function, the design, and the optimization of amperometric biosensors is related to the electron transfer between the biorecognition element and the electrode. In the following text, the discussion of the basic principles is restricted to amperometric biosensors based on redox enzymes (oxidoreductases with or without integrated prosthetic groups) as a biological recognition element in intimate contact with an electrode surface (usually a Pt, Au, or C electrode).

The electron-transfer kinetics between two redox species (one may also be a suitable electrode surface) are – according to Marcus' theory [51, 52] – determined by the driving force (which is the potential difference), the reorganization energy (which qualitatively reflects the structural rigidity of the redox species), and the distance between the two redox centers. Further information on interfacial kinetics is given in Volume 2 of the *Encyclopedia*. Obviously, regarding the complexity of the sensor architecture, the direct electrochemical recycling of the prosthetic group of an immobilized redox enzyme at the electrode surface, involving a tunneling mechanism (Fig. 6), appears to be the easiest way of electron transfer in an amperometric sensor.

However, the protein shell in many redox enzymes has been designed by nature to ensure an insulation of the redox center within the active site, thus preventing thermodynamically driven reactions caused by the interaction of redox centers having significantly different formal potentials until equilibrium is reached. Moreover, the size of the protein shell of many redox enzymes leads to a comparatively long distance between the electrode surface and the prosthetic group, thus significantly decreasing the electron-transfer kinetics. Nevertheless, some enzymes show a direct communication with the electrode either after direct adsorption at electrode surfaces or immobilized on self-assembled monolayers (SAMs) with precise distances between protein and electrode (see Sect. 2.11.2.1.6).

However, for most redox enzymes more elaborate electron-transfer pathways have to be considered in biosensor design. As this problem is crucial for understanding amperometric biosensors, the following sections deal with the complex features of electron-transfer mechanisms and sensor architecture [53].

2.11.2.1.1 Shuttle Mechanism Using Free-diffusing Natural Redox Mediators “Recycling” of the prosthetic group of an enzyme by a cosubstrate (such as molecular oxygen or NAD^+) is a natural process that was

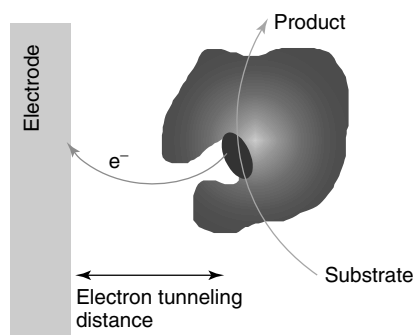


Fig. 6 Direct electron transfer (tunneling mechanism) from the active site of an enzyme to the electrode surface.

used in *biosensors of the “first generation”*. Those cosubstrates, which undergo a redox conversion in the catalytic cycle of the enzymatic reaction, diffuse to the electrode surface where they can be directly reduced or oxidized, thus acting as *electron-transfer shuttles* (Fig. 7) between the enzyme and the transducer. At a suitable working potential a change in current can be measured after addition of the enzyme’s substrate, and this current change is correlated to the increase of the coproduct or to the decrease of the cosubstrate, respectively. In the very first biosensor configuration, which was reported in 1962, glucose oxidase (GOx) was immobilized on the semipermeable membrane of a Clark-oxygen electrode by physical entrapment behind a dialysis membrane with a molecular-weight cut-off to retain the enzyme, simultaneously allowing the diffusion of the substrate to the enzyme [54]. The consumption of the free-diffusing cosubstrate O_2 at the underlying Pt electrode was measured. However, since the O_2 partial pressure varies, depending on the sample itself and the temperature, the background current for the O_2 determination fluctuates. In addition, the high-sensitive determination of small current changes on top of a high background signal is difficult. As a matter of fact, using a similar biosensor

configuration, but poisoning the electrode to a potential sufficiently high to oxidize enzymatically produced H_2O_2 , the coproduct can be detected electrochemically. Despite the rather high working potential implying problems with the cooxidation of potentially interfering compounds that may be present in the analyte solution (ascorbic acid, uric acid, paracetamol, etc.), such sensors have significant advantages including the small and stable background current. Today, these approaches are still used in commercially available analytical systems with integrated biosensors.

Oxygen reduction and H_2O_2 oxidation have been investigated for many sensor configurations, which mainly differ with respect to the transducer materials used, electrode size, and electrode integration, as well as the technique applied for the immobilization of the enzyme on the transducer surface. For the immobilization of GOx, various methods, such as physical fixation behind a membrane [55–59], entrapment into different kinds of gels [60, 61], mixing into a carbon paste [62–64], cross-linking with glutaraldehyde [65–67], electrochemically aided adsorption [49], controlled deposition based on avidin/biotin recognition [68], or using photo-polymerizable materials [69], as well as electrochemical formation of polymers in the presence of the enzyme [70–74], have been applied. In

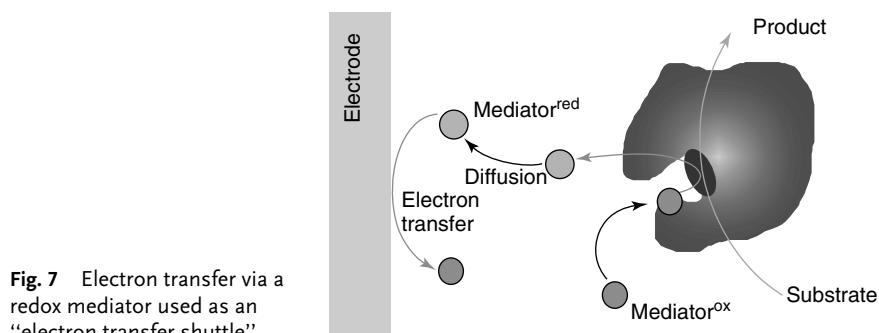


Fig. 7 Electron transfer via a redox mediator used as an “electron transfer shuttle”.

amperometric biosensors with O_2 or H_2O_2 as electron-transfer mediators, further oxidases consuming O_2 or producing H_2O_2 in their catalytic cycle – among these lactate oxidase [75, 76], glutamate oxidase [77], galactose oxidase [78, 79], or xanthine oxidase [80, 81] – have been used for the analysis of the related analytically relevant substrates.

As the concentration of the natural cosubstrates limits the overall enzyme-catalyzed reaction, and thus the linear range of the sensor, applications using this kind of biosensor under unpredictable cosubstrate concentration, such as in environmental analysis or in-vivo measurements, can lead to unreliable results. Especially for in-vivo applications of biosensors, the dependence on the O_2 partial pressure in blood or tissue is an extremely important issue. Use of elaborate sensor designs like a cylindrical sensor allowing axial diffusion of oxygen and glucose and additional radial diffusion of O_2 [56] have been proposed to overcome this problem. Anyhow, since the O_2 partial pressure often shows uncontrolled significant variations over time resulting in changes in the concentration-dependent sensor output, electron-transfer pathways that are independent from the natural cosubstrates have to be considered.

2.11.2.1.2 Artificial Redox Compounds as Free-diffusing Electron-Transfer Mediators

Artificial redox mediators have been used in the so-called “second generation” of biosensors to substitute the cosubstrate and thus circumvent the O_2 dependence. A suitable redox mediator has to be able to regenerate the active site of the enzyme with fast kinetics, to diffuse back to the electrode to be reconverted there to its initial stage. Thus, redox mediators have to be stable in both oxidation states, they should not

be toxic, their formal potential should be low to avoid cooxidation or coreduction of interfering compounds [82, 83], and they have to diffuse with a high diffusion coefficient between enzyme and electrode. For oxidase-based sensors, however, a more or less pronounced dependence on the O_2 partial pressure is still observed since electron-transfer kinetics between the enzyme and the artificial redox mediator have to be very fast to successfully compete with the regeneration of the enzyme via reduction of O_2 . Soluble low molecular weight compounds such as ferrocene derivatives, $K_4[Fe(CN)_6]$, quinones, or Os-complexes have been used as free-diffusing electron-transfer shuttles [84–90] (Fig. 7). The enzyme is usually immobilized in a second layer [86–92] after adsorption of the redox mediator at the electrode surface. Since – as has been shown above – the shuttle mechanism is dependent on the diffusional mass transport of the redox mediator between enzyme and electrode, and moreover the molecular weight of the redox compounds are close to that of the enzyme’s substrate, there are only limited possibilities to retain the redox mediator at the electrode surface. Thus, mediator leakage affecting the long-term stability of these biosensors and the danger of sample contamination, which is crucial especially for implantable sensors, are major disadvantages [93, 94]. Attempts to solve this inherent problem have made use of dissolved high-molecular weight redox mediators, such as polyethyleneglycol-bound ferrocene derivatives, physically entrapped behind a membrane [95, 96].

In case of the application of NAD^+ -depending dehydrogenases, the prerequisites for the design of an optimal sensor architecture are completely different. On the one hand, NAD^+ cannot be easily replaced by artificial species,

although attempts have been made to propose NAD^+ analogues by means of molecular modeling [97]. On the other hand, regeneration of NADH under the formation of enzymatically active NAD^+ occurs at bare electrodes only at high overpotentials via intermediate radicals that tend to dimerize under the formation of insoluble products leading to electrode fouling. Thus, the electrode has to be designed to enable catalytic oxidation of NADH optimally by means of a simultaneous two-electron transfer reaction at low potential. For this, electrodes are modified with suitable redox catalysts, the most efficient one being quinone-like compounds enabling the simultaneous two-electron transfer reaction in a sandwich-type configuration with NADH such as phenoxazines, phenothiazines, and so on [98–102]. In addition, attempts have been made to increase the local concentration of the negatively charged coenzyme using negatively charged polyelectrolytes (e.g. Nafion) or to synthesize so-called holo-dehydrogenases with NAD^+ bound via long and flexible spacers at the outer surface of the enzyme [103]. However, since NAD^+ has to be added to the analyte solution, dehydrogenase-based biosensors have been mostly used in flow-injection systems either providing the coenzyme in the background buffer or spiking the sample by injection of the coenzyme.

A first step toward the decrease of mediator leakage and hence concomitant increase in the sensor stability has been seen in the development of *carbon-paste electrodes* [104]. A graphite powder is thoroughly mixed with mineral oil, and the paste obtained is pressed into a tube and contacted from the back by the insertion of a copper wire. To

this basic carbon paste redox mediators, the biological recognition element, if necessary additives for enzyme stabilization are mixed providing a comparably simple and nevertheless well-working method [105–112]. The enzyme can also be immobilized on top of the carbon-paste surface and the sensor may additionally be covered with semipermeable or biocompatible membranes. Additives (stabilizers [113], polyelectrolytes [106]) can be applied to improve long-term stability and response time.

Regarding the electron-transfer mechanism in carbon-paste electrodes, it can be assumed that the carbon-paste-integrated mediator molecules slowly dissolve from the paste into the reaction layer on the electrode surface or overlying enzyme layer. Provided that leakage of the mediator from this reaction zone is slow, and a steady state concentration of the mediator is attained close to the electrode surface, the electron-transfer mechanism is comparable to the case of free-diffusing redox mediators [111]. As concentration profiles recorded using scanning electrochemical microscopy (SECM, see Chapter 3.3 in this volume) showed, contamination by leakage of the sensor components thus cannot be excluded [114]. However, owing to the readiness of their formation, and since it could be shown that the hydrophobic environment and large counteranions eventually used [115] within the carbon paste decrease the mediator leakage, carbon-paste electrodes have found increasing attention.

Biosensors based on free-diffusing redox mediators are presently applied in most of the disposable sensors for glucose self-monitoring [116–118]; however, they are not suitable for long-term applications or if the analyte must not be contaminated.

Hence, more complicated sensor architectures have to be investigated, which allow, on the one hand, the electron transfer between enzyme and electrode to take place and, on the other hand, tightly integrate all necessary sensor compounds to prevent leakage. The tight fixation of all sensor components in a specific sensor architecture designed with respect to an optimized electron-transfer pathway between immobilized enzyme and electrode is the main focus in the development of the so-called *reagentless* biosensors [119].

2.11.2.1.3 Immobilized Redox Mediators – “Electroenzymes” As the movement of the redox mediator is an absolutely necessary requirement for a productive electron transfer in amperometric biosensors, mechanisms have to be formulated that concomitantly provide a fast electrochemical communication between immobilized enzyme and electrode, as well as a safe attachment of the redox mediator to the sensor surface. One possibility can be seen in the modification of the enzyme itself by covalent binding of redox mediators either to its surface or site-directed in close proximity to the prosthetic group. The enzymes directly modified with redox mediators are called *electroenzymes*. The electron-transfer distance between the prosthetic group within the redox protein and the electrode surface may be decreased in order to accelerate the electron-transfer kinetics according to Marcus’ theory. Redox mediators have been bound to the outer surface of the protein shell using functional side chains of the amino acids forming the protein backbone [120–122], via imidazol side chains of histidine as ligands for Ru- or Os-complexes at the outer surface [123], preferentially in close proximity to the redox-active cofactor at the inner surface of the protein [124–126],

or at the cofactor [127] of the enzyme. The so-created redox relays are designed to allow “electron-hopping”, thus bringing the deeply buried active site virtually “closer” to the protein surface. While this works for dissolved “electroenzymes”, as can be proved by the catalytic effect using cyclic voltammetry, a productive electron-transfer pathway via the protein-bound redox relays is hardly encountered when the modified enzyme is integrated into an electrochemically inert matrix.

In order to regenerate the covalently bound redox mediator, it is required for the modified enzyme to get very close to the electrode surface, as the charge is intermediately located in the enzyme-bound redox species from which the electrons have to be transferred to the electrode surface. To solve this problem, long and flexible spacer chains have been integrated either to the electrode surface (*seaweed mechanism*) [128], a suitable matrix, or to the enzyme itself (*whip mechanism*) [120] (Fig. 8). These sensor configurations assure productive electron transfer, first between the redox mediator and the enzyme and finally between the redox mediator and the electrode surface, owing to the quasi-diffusional movement of the spacer-bound redox relays.

Electron transfer between electrodes and immobilized modified “electroenzymes” could be established via a “whipping” process, into and out of the active center, then in close distance to secondary mediator molecules, and finally toward the electrode surface [129]. The observed currents were small, owing to the overall small concentration of redox relays taking part in the electron-transfer chain.

2.11.2.1.4 “Wired” Enzymes by Means of Redox Hydrogels *Redox polymers* suitable to *wire* enzymes with the electrode

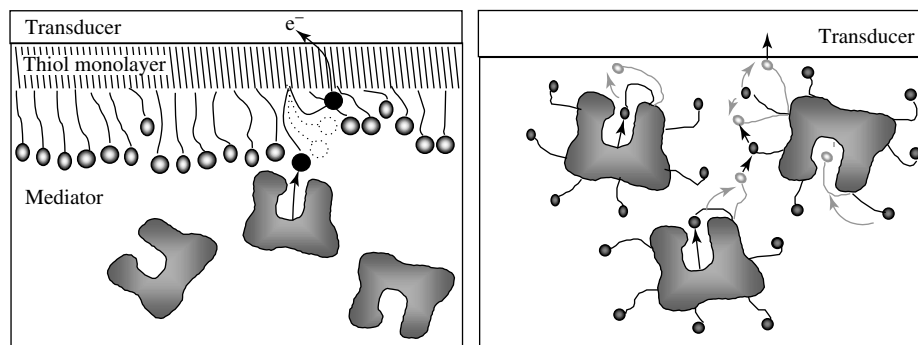


Fig. 8 Electron-transfer mechanisms with spacer-bound redox mediators (left) seaweed mechanism, mediator-bound via a flexible chain to the transducer surface and (right) whip

mechanism, mediator-bound via a flexible chain to the enzyme surface (black arrows: electron transfer, grey arrows: “whipping”).

surface are one of the most successful ways to generate reagentless amperometric biosensors. Redox polymers or redox hydrogels can be created by covalent binding of a suitable redox mediator to the (flexible) backbone of an immobilization matrix, hence providing a high local concentration of redox relays. The electron transfer process is divided into a number of sequential *electron-hopping* reactions between adjacently located redox relays (Fig. 9). The self-exchange reactions between adjacent redox relays thus play the dominating role in the overall electron-transfer mechanism. However, it has to be taken into account that the “first”

electron-transfer reaction occurring between the prosthetic group of the enzyme and the “first” mediator molecule is often the rate-determining step, rather than the sequence of self-exchange reactions between the mediator molecules. There are two obvious advantages in the modification at the immobilization matrix. On the one hand, since there is no need to modify the enzyme molecule itself, the requirements of the stability of the enzyme are less restricting. On the other hand, for the immobilization of the redox mediators to the matrix, more drastic conditions, such as heating and organic solvents, can be applied.

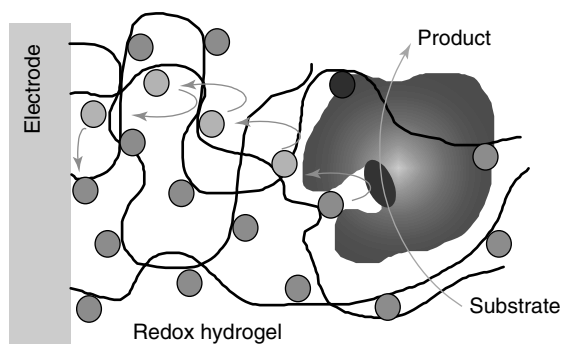


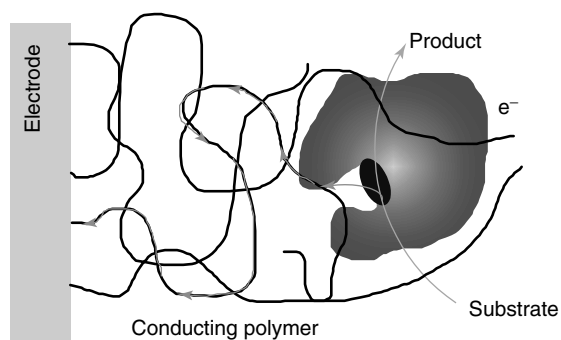
Fig. 9 Electron-hopping mechanism from “wired” enzymes in a redox polymer.

High mediator loading can be achieved by covalent binding of Os-complexes to a poly(vinyl pyridine) [130–137], a poly(vinyl imidazole) [138, 139], a poly(acrylic acid) [140], or a poly(allyl amine) [141] backbone. Because of the good swelling properties of the polymers used, the polymer layers thus obtained are called *redox hydrogels*. Alternatively, ferrocene units could be similarly bound to poly(siloxane) backbones [142]. By (manually) dispensing a solution containing the mediator-modified polymer, a cross-linker, and the enzyme on top of the electrode surface, the preparation of the sensing layers is initiated. The cross-linking process takes place when the solvent is evaporated leading to well-adhering hydrophilic redox-polymer films. The flexibility of the polymer backbone is increased as the film swells in water owing to its hydrogel character. Additionally, the diffusion of the enzyme's substrate and its reaction product within the polymer film is improved as well as the mobility of the counteranions, which is necessary for a fast charge transfer through the film [143, 144]. Although sensors prepared using these redox hydrogels show high substrate-dependent currents, and enable the development of multilayer architectures in order to remove interferences [145], the electrode-modification procedure still has to be improved as the covering of the electrode surface with the solution containing the hydrogel components involves (mostly manual) dispensing that lacks both precision and reproducibility. Obviously, nonmanual electrode-modification procedures have to be developed allowing the spatial addressing of individual electrode surfaces for the deposition of the sensing chemistry in question.

2.11.2.1.5 Conducting Polymers One possibility to selectively address an electrode surface for the modification reaction is seen in the initiation of a suitable reaction by an electrochemical process invoked at the electrode surface, for example, by application of a suitable potential or current. *Conducting polymers* are electrochemically formed on electrode surfaces by oxidation of the monomers (such as pyrrole and its derivatives, thiophene, phenol, aniline) to the radical cations that dimerize in subsequent chemical follow-up reactions (see Volume 10 for further details). Owing to its water solubility, the formation of polypyrrole is compatible with the entrapment of enzymes during the electrochemical formation of the conducting-polymer film [146–149], and polypyrrole-based biosensors have been intensively investigated. However, especially for enzymes with a deeply buried active site, a direct electron transfer from the enzyme via the conducting polymer (“molecular wire”; see Fig. 10) to the electrode has not been possible, and mostly, the conducting polymer was exclusively used as an inactive immobilization matrix. There had been reports on the direct electron transfer from glucose oxidase via the polypyrrole matrix generated in track-etched membranes [150, 151]; however, the electron transfer mechanism is not fully understood. Recently, evidence was obtained that using multifactor enzymes such as quinoprotein alcohol dehydrogenase (a PQQ-heme enzyme), a direct wiring of heme groups, which are located close to the outer surface of the protein shell, is possible [152] (see also the following section).

The combination of the advantages of the above-mentioned redox hydrogels with the possibility to electrochemically initiate their deposition exclusively on an electrode surface would be an optimal

Fig. 10 Ideal representation of the electron transfer from an enzyme via “molecular wires” in a conducting-polymer film to the electrode surface.



way to the formation of *conducting redox hydrogels* that are obtained by modifying the monomer with the chosen mediator prior to the electrochemical deposition of the related conducting polymer [153, 154], or in a heterogeneous polymer–analogue reaction after the formation of the polymer film [155, 156]. Because of the steric demand of the redox mediators attached to monomer side chains, copolymerization of the modified monomers with the unmodified parent monomer is favorable over homo-polymerization. In this case, the different radical-cation-formation potentials of the different monomers have to be considered. Thus, to achieve a statistical distribution of the monomers according to their concentration ratio in the electrolyte solution, an elaborate multipulse deposition procedure has been proposed [157]. Polypyrrole-based biosensors with Os-complexes covalently linked via flexible spacer chains to the polymer backbone could be obtained [158–160]; however, the electron transfer is still slow because of the stiffness of the polymer backbone.

2.11.2.1.6 Direct Electron Transfer between Redox Enzymes and Electrodes As already pointed out, reagentless biosensors making use of a direct communication between the enzyme and the transducer

would be optimal. Direct electron transfer between redox proteins and a variety of electrode materials was reviewed comprehensively [161, 162]. By avoiding intermediate electron transfer steps, the electron-transfer kinetic should be predominantly limited by the rate of the enzymatic reaction itself. It is indicative of a nonmediated electron transfer that the redox process takes place at the redox potential of the prosthetic group; often however, in the literature no clear distinction is made between direct electron transfer and electron transfer via a bound redox relay.

Considering Marcus' theory [51, 52], the shortest possible distance between the immobilized redox protein and the electrode surface (see Fig. 10) has to be realized for direct electron transfer. Mostly, the redox enzyme, in which the prosthetic group should be located in close proximity to the protein surface, is adsorbed directly on a bare or modified electrode material, implying a high risk of deterioration of the protein. As a matter of fact, supposing a proper orientation of the enzyme with the prosthetic group pointing toward the electrode, direct electrochemical communication can only be expected from the first monolayer. Thus, only a very small amount of enzyme is used, leading to severe restrictions concerning sensitivity

and especially long-term stability of related sensor designs.

Until now, mostly peroxidases adsorbed on carbon surfaces were used in sensor configurations with direct electron transfer such as cytochrome *c* peroxidase [163], horseradish peroxidase [164–169], fungal peroxidase [170, 171], lactoperoxidase [172], microperoxidase [173, 174], and chloroperoxidase [175].

Recently, multifactor enzymes having a primary prosthetic group internally connected with a series of redox center have been used for biosensors based on direct electron transfer [176–180].

Another possibility to keep the distance between an immobilized redox protein and an electrode surface small is seen in using SAMs for modification of mostly Au electrodes. SAM provides an interface with specific functions such as functional headgroups for binding of proteins, suitable charges for anisotropic orientation of proteins, and often they prevent denaturation of the proteins. Astonishingly, even direct electron transfer from SAM-immobilized glucose oxidase has been proved, although the mechanism remains unclear [181].

On the basis of the work by Hill and coworkers regarding promoted orientation of small redox proteins at electrode surfaces as a prerequisite for fast heterogeneous electron transfer [182], and the work by Armstrong [183, 184] and Bowden [185, 186] elucidating the electrochemistry of cytochrome *c*, it is evident that direct the electron-transfer rate is

dramatically enhanced, if the prosthetic group of the proteins is directed toward the electrode surface. This anisotropic orientation of the enzyme molecules in the monolayer allows a majority of the immobilized enzyme molecules to contribute to the overall electron-transfer reaction (Fig. 11b), while in the case of isotropic adsorption (Fig. 11a) most enzymes are in an unfavorable orientation for direct electron transfer.

For enzymes such as cytochrome *c*, which exhibit an anisotropic charge distribution on the protein surface, an orientation can be induced prior to covalent binding by means of a charged monolayer [187, 188]. The electrocatalytic reduction of H_2O_2 by cytochrome *c* was shown to be significantly improved after proper orientation of the protein on a negatively charged SAM.

Another possibility, which was first attempted by Wingard [189], is to bind an enzyme via its primarily bound prosthetic group. However, the reconstitution of the apo-enzyme using the prosthetic group bound, has to be done using a long spacer in order to allow the penetration of the prosthetic group into the active site of the enzyme. An orientation of the prosthetic group toward the electrode surface could be realized by reconstitution of apo-glucose oxidase on an FAD-modified SAM [190, 191] and of apo-horseradish peroxidase on a hemin-terminated SAM [192].

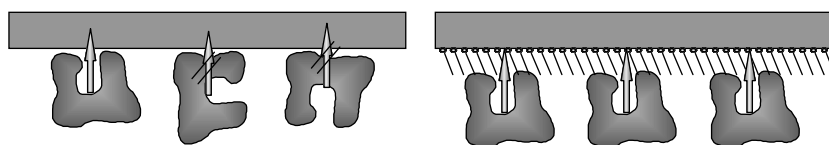


Fig. 11 (a) Enzymes immobilized by unspecific adsorption and (b) in an orientated way on the surface of a monolayer.

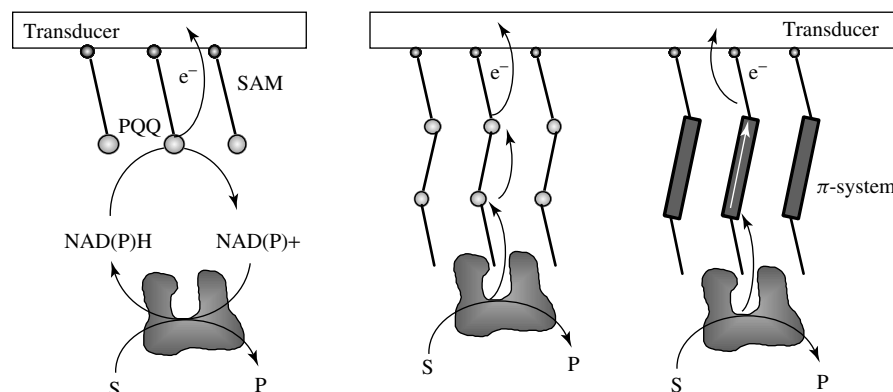


Fig. 12 Electron transfer pathways in self-assembled monolayers: (a) communication of immobilized dehydrogenases via the oxidation of NADH at PQQ-modified SAMs and (b) possible designs for “molecular cables” through a SAM.

Catalytic oxidation of NADH at low electrode potentials was achieved using pyrroloquinolinequinone (PQQ) modified SAM [193, 194] (Fig. 12a). Further information about the preparation, characterization, and application of SAM can be found in Volume 9.

Future challenging aspects involve the design of *molecular cables* in order to directly connect the active site of an enzyme with the electrode surface. For this purpose, either the overall electron-transfer distance can be subdivided by integration of redox relays into the monolayer (Fig. 12b) or parts of the nonconducting alkyl spacer may be replaced by conducting oligomers (Fig. 12c).

The entrapment of enzymes in conducting materials opens further perspectives in the optimization of direct electron transfer in amperometric biosensors as the “virtual” electrode surface is increased. Even enzyme molecules immobilized far away from the electrode surface may be connected by the conducting matrix, and thus are able to participate in “direct” electron-transfer reactions.

Enzymes were immobilized using various conducting materials such as *sol-gel composites* with integrated graphite particles [195]; however, there are still problems regarding a low sensitivity and undefined electron transfer. Moreover, in the case of the entrapment of enzymes into conducting-polymer films, possible direct electron transfer [150, 151] is still under discussion [196–198].

A direct electron transfer from entrapped quinoxinohemoprotein alcohol dehydrogenase (QH-ADH) to a Pt electrode, via chains of the polypyrrole, acting as immobilization matrix, was demonstrated [152]. QH-ADH is able to translocate in a fast inner-enzymatic reaction, the electrons primarily accepted by PQQ to heme units located close to the outer protein shell, from where they can be transferred on the conducting-polymer chains (Fig. 13). A similarity between the electron-transfer pathway in multicofactor proteins and that of mediator-modified “electroenzymes” is apparent, if one considers that a multicofactor enzyme can be regarded as a combination of a primary redox site and protein-integrated electron-transfer relays.

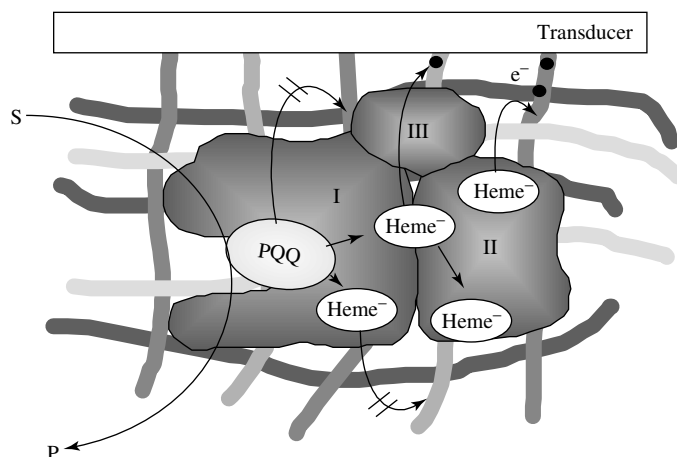


Fig. 13 Direct electron transfer in an alcohol sensor based on QH-ADH entrapped within a polypyrrole film.

2.11.2.2 Potentiometric Biosensors

In potentiometric biosensors the biological recognition reaction has to cause a modulation of a redox potential, a transmembrane potential, or the activity of an ion.

2.11.2.2.1 Potentiometric Enzyme Biosensors

In biocatalytic recognition reactions coupled with potentiometric transducers, ISEs were mostly used for detecting the modulation of the activity of an ionic species in relation to the conversion of the substrate in question. The change of the membrane potential of an ion-selective membrane is detected using a symmetric two-reference electrode setup, for example, using a pH glass electrode, a liquid ion-exchange membrane, or a crystal membrane as selective unit. In early potentiometric biosensors, enzymes that liberated free acids in their biocatalytic reaction sequence, such as penicillinase or glucose oxidase, were directly immobilized on the surface of pH-sensitive electrodes. The local pH modulation detected is correlated with the substrate concentration; however, in addition, the ionic strength

and the buffer capacity severely influence the signal obtained. In order to cope with the limited long-term stability of most enzymes in later sensor configurations, the enzyme was immobilized within the pores of a sintered glass frit, entrapped behind a cellulose membrane, or into gelatine membranes. A drastic improvement of the sensor stability was achieved by inclusion of the enzyme in a gel matrix. Cross-linking, for example, polyacrylamide hydrazine with dialdehydes such as glyoxal, leads to porous gels that present a very low diffusion barrier and show optimum adhesion. Much thinner, more stable and transparent films were obtained by copolymerization of acrylamide with methacrylamide. For example, an acetylquinolin esterase containing sensor was stable for up to six months and had a response time of about three minutes [40].

A strong limitation of these biosensors is their dependence on the pH conditions in the analyte solution. Thus, gas-sensitive electrodes were developed in which the pH electrode is separated from the analyte

solution by a hydrophobic, gas-permeable polypropylene or Teflon membrane. NH_3 or CO_2 , which are reaction products of decarboxylases or hydrolases, can penetrate through these membranes and then change the pH value of a weak internal buffer. Since only gaseous compounds can penetrate into the internal buffer reservoir, most interferences can be excluded. In addition to pH electrodes, ionophore-containing liquid-membrane electrodes can also be employed in potentiometric gas sensors. For example, a urea sensor was designed utilizing an NH_4^+ -selective nonactin-containing PVC membrane in combination with a gas-permeable membrane [41].

Another possible way for potentiometric transduction implies the detection of the redox potential using a metal electrode. According to Nernst equation, the electrode potential is governed by the ratio between oxidized and reduced form of the potential-determining redox species (see Chapter 1.1, Sect. 1.3). As a matter of fact, enzyme-catalyzed reactions leading to a change of the oxidation state of a redox species may be detected. However, the electrode potential is influenced by all redox systems depending on their exchange current density. Thus, it can be expected that influences by the complex $\text{O}_2/\text{H}_2\text{O}_2/\text{H}_2\text{O}$ system lead to long response times before a stable potential is attained. To overcome this problem, an electrode architecture has to be designed in which a redox species with fast electron-exchange kinetics exclusively dominates the electrode potential [199]. However, despite these considerations, a number of so-called *coated-wire* potentiometric sensors were described in which an enzyme was immobilized on a metal wire detecting the weak mixing potential

of O_2 and H_2O_2 [200, 201]. One possibility to overcome the inherent problems of poorly defined mixing potentials is to choose a potential-determining redox species having a high electron-exchange density with the metal electrode, which is simultaneously involved in the enzymatic reaction [202]. The use of redox mediators can be avoided by using enzymes that are in direct electrochemical communication with the electrode surface such as peroxidase or lactase (molecular transduction). In a peroxidase/glucose oxidase layer the H_2O_2 formed as a consequence of the catalytic oxidation of glucose is immediately reduced by the peroxidase. Hence, the initial potential, which is about 0.5 V lower than the redox potential of $\text{H}_2\text{O}_2/\text{H}_2\text{O}$, shows a sharp increase approaching the $\text{H}_2\text{O}_2/\text{H}_2\text{O}$ potential. The rate of this potential increase ($\Delta E/\Delta t$) is proportional to the formation of H_2O_2 and hence directly related to the glucose concentration [203, 204].

Enzyme-inhibition analysis based on mediatorless multienzyme electrodes was proposed making use of the cholinesterase/choline oxidase/peroxidase system. The cholinesterase reaction (hydrolysis of a cholinester into choline and the corresponding carboxylic acid) is known to be inhibited by organophosphorous pesticides. The decrease in the activity of the cholinesterase can be measured by means of a potentiometric choline electrode with molecular transduction using reduction of H_2O_2 by means of horseradish peroxidase [205, 206].

2.11.2.2.2 Potentiometric Immunosensors

In direct potentiometric immunosensors the biological recognition reaction is transduced by the modulation of the potential of a membrane, in which the biorecognition element is integrated. However, the

transduction mechanism is still questionable. In a recently proposed alternative mechanism the antibody forms a complex with a component integrated within a membrane. Upon addition of the antigen, for which the antibody exhibits a higher affinity than for the membrane-integrated compound, the antibody is dissolved from the membrane causing a potential change [207, 208].

In indirect immunosensors, either the antigen or the antibody is labeled with an enzyme. As a matter of fact, the transduction process is implied by the enzyme used leading to the possibilities for potentiometric detection described earlier. For example, potentiometric detection based on molecular transduction was described. The antigens are immobilized at the electrode surface and the corresponding antibody is labeled with peroxidase. Upon biological recognition, the antibody-bound peroxidase attaches to the electrode surface inducing a shift of the electrode potential owing to biocatalytic H_2O_2 reduction. After addition of a sample containing the free antigen, competition for the labeled antibody is initiated, leading to a liberation of the antibody from the electrode surface and hence to a decrease of the potential shift [207].

2.11.2.2.3 Field-effect Transistors Enzyme FETs and immuno FETs (IMFETs) are based on principles similar to those valid in potentiometric membrane biosensors. The enzyme is immobilized on top of the ion-selective membrane on the gate of the FET. For construction of ENFETs, usually double-gate FETs are used employing one gate as a reference system, covered only with a layer of the immobilization matrix, and allowing for the real-time compensation of pH modulations, temperature, and drift. Mostly, pH-sensitive FETs (ISFET)

are used in analogy to the potentiometric biosensors based on the glass-membrane electrode. In the ENFETs obtained the pH value in the sensing layer is altered upon the biocatalytic reaction, and this change is measured by the ENFET as a change in the gate potential [209]. To overcome problems occurring from the buffer properties of samples, theoretical models were established describing the influence of catalytic reaction products on the enzyme's kinetics [40]. Penicillinase, glucose oxidase, and urease are among the enzymes applied most often in ENFETs [41].

For the development of glucose biosensors employing ENFETs, glucose oxidase was covalently bound using polyacrylamide. The influence of O_2 and H^+ on the signal measured was quantified using a theoretical model, and enzymatically formed H_2O_2 was destroyed by means of catalase. An advanced method for the protection of the sensor against the buffer capacity of the sample solution is the use of Nafion membranes as sensor top layer prepared by spin coating. Furthermore, the use of photolithographic techniques has been described for immobilization of glucose oxidase in a photopolymer on top of a silanized gate region. Glucose oxidase and BSA are cross-linked within the polymer using glutaraldehyde to increase adhesion of the polymer layer [40].

Compensation of the buffer properties of the sample was achieved by integration of a pH actuator controlling the pH value in the immobilized layer based on a feedback loop and the electrochemical splitting of water releasing either H^+ or OH^- . This ENFET system was successfully employed in a urea sensor based on urease cross-linked with glutaraldehyde within a polysiloxane membrane. Bienzyme ENFETs for the determination of glucose and urea, employing glucose

oxidase and urease as biological recognition elements, were designed including a multigate FET using photolithographic techniques [40].

Direct binding of urease at the NH_4^+ -sensing layer of an ISFET was applied to overcome problems of activity loss during immobilization. The covalently bound enzyme did not cause any deterioration in sensitivity of a PVC-COOH coating serving as NH_4^+ -sensing membrane, whereas cross-linking of the enzyme decreases H_3O^+ sensitivity in pH-FET biosensors [210]. Protection of urea by means of an overlaying Nafion membrane led to an increase in sensitivity and storage stability of urea ENFETs as compared to immobilization into BSA membranes [210]. Silanization of the Al_2O_3 gate with 3-aminopropyltriethoxysilane and subsequent activation of the amino groups with glutaraldehyde for covalent attachment of enzymes such as urease, glucose oxidase, acetylcholine esterase leads to enzyme monolayers showing fast response characteristics. In addition, these enzyme layers, although not protected by additional membranes, exhibit good stability. Within several days, only about 30% loss in activity was observed with not more than 50% loss even after one month of operation [209]. NAD^+ -dependent ENFETs for the determination of lactate were realized modifying the aminosilanized gate of the FET with PQQ. A synthetic NAD^+ derivative is covalently bound to a PQQ monolayer, and NAD^+ -dependent lactate dehydrogenase is cross-linked on top. The integrated ENFET device detects the lactate-induced change of the pH value near the gate [211]. Fields of application for ENFET biosensors are, for example, the determination of glucose in diluted blood samples [212] and environmental analysis

such as determination of organophosphorous pesticides [213].

In an IMFET the antibodies are covalently bound to the sensitive surface of a FET as the molecules involved in the immune reaction are usually too large for selective permeation through an ion-selective membrane. This way the antibodies are part of the double layer and a change in charge density is directly measured. In a FET, changes in charge distribution in the interfacial layer can be observed upon adsorption of a molecule at the insulating interface causing a charge transfer through the double layer to the interface. If the interface layer between the membrane and the solution is ideally polarized, the sensitivity of an IMFET can be calculated theoretically. An application of an IMFET is the use of the antigen-binding membrane for Wassermann antibodies that is suitable for direct coating of the gate of a CHEMFET [40].

Additional information on potentiometric measurements of proteins is given in Volume 9.

2.11.2.3 Conductometric and Impedimetric Biosensors

Biosensors based on conductometric or impedimetric measurements are comparably rarely described in literature. They have two main fields of application: sensors utilizing enzyme reactions in which ionic substances are formed and sensors employing receptors (or bilayer lipid membranes containing receptors) or intact cells of higher organisms.

In enzyme-based conductometric biosensors the modulation of the conductivity of a conducting layer connecting two electrodes upon enzymatically catalyzed formation of ionic species is measured. In these conductometric enzyme sensors which are often miniaturized,

interdigitated electrodes of serpentine or comb-shaped electrode structures are applied. The conducting layer on top of these electrodes containing immobilized enzymes can be generated using gel layers [214], sol–gel-derived thick films [215], or fixation of conducting polymers using Langmuir–Blodgett films [40]. Couples of interdigitated electrodes have been produced among other techniques by screen printing [215], by using metal wires [214], or by means of photolithography [216]. A typical example is the detection of conductivity changes caused by immobilized urease. The biocatalytic cleavage of urea leads to the liberation of NH_3 and CO_2 . The related ions formed at a finite distance of the surface contribute to an increase in conductivity in the immobilization layer of the enzyme [217].

In conductometric receptor and membrane biosensors utilizing conductivity modulation caused by a bioaffinity reaction of a receptor molecule with its ligand, the complexation reaction leads to opening of ion channels, inducing a flux of ions over a membrane. This current across the membrane can be detected electrochemically. Another example for the application of conductometric transducers in biosensors is the measurement of impedance changes across a number of cells that are in contact with each other. The resistance is changed by variation of the contact between the cells. The impedance modulation is then measured either between interdigitated electrodes on top of which the cells have been cultivated or between two compartments that are separated by a membrane on which the cells are growing [31].

For additional information concerning the topics discussed above, several chapters in Volume 9 of this series are recommended, for example, Chapter 13 on

enzyme electrodes, Chapter 5 on electrochemical immunoassays, or Chapter 17 on mediated electron transfer.

2.11.3

Miniaturization and Future Aspects

Miniaturization is intensively studied in present biosensor research [218] aiming at the development of total microelectrochemical systems for local detection, multisensor arrays, implantable or portable devices. Not only the relevance of the items but also the electrochemical properties of microelectrodes that often make them superior to macroelectrodes allows miniaturization to become a necessity [219]; see also Chapter 2.5 in this volume.

2.11.3.1 **Miniaturized Transducers**

There are basically two groups of transducers suitable for the application in electrochemical microbiosensors: needle-type and planar electrodes. The former are mainly employed in neuro-biological research, both for direct electrochemical [220, 221] or enzymatic [77, 222–225] detection of neurotransmitters, and in medical applications, such as glucose sensors [226–231].

Conducting materials, mostly carbon fibers [33, 77, 222, 228, 230, 232–235] or Pt wires [222, 227, 236, 237], embedded within a glass capillary or an insulating coating, serve as a basis for the construction of needle-type electrodes with cylinder or planar disk-shaped active electrode surfaces. They are fabricated manually using pipette pullers or a variety of etching methods. Planar transducers can generally be produced using either thin-film or thick-film technology.

Thick-film electrodes are obtained using different printing techniques, such

as screen printing, microcontact printing, or ink-jet printing [238], while thin-film electrodes are produced using photolithographic techniques such as the well-elaborated methodology of current semiconductor technology in clean-room facilities such as the standard CMOS process (complementary metal oxide semiconductor) or bipolar technology. In combination with micromachining or lift-off techniques, even three-dimensional transducer structures can be reproducibly fabricated.

A great variety of planar transducer designs are currently available, including single free-standing electrodes [76, 239–241], microelectrode arrays [242–247], FET [247–250], light addressable potentiometric sensors (LAPS) [251–253], and potentiometric alternating biosensing systems (PAB) [31, 254, 255], or amperometric microelectrochemical enzyme transistors [256], as well as miniaturized electrochemical cells/chambers [45, 257–260].

2.11.3.2 Advantages and Problems of Miniaturized Biosensors

Although microbiosensors have a vast variety of potential applications and obvious advantages, they are often not commercialized.

Microelectrodes exhibit faster response, reduced iR-drop as a consequence of reduced capacitance, and lower currents. However, owing to the hemispherical diffusion profile in front of the microelectrode the mass transfer is enhanced leading to a higher current density and an improved signal-to-noise ratio (see Chapter 2.5). They not only permit measurements in small volumes and very low concentrations but additionally in samples with low conductivity. Because of the reduced size of miniaturized sensors, smaller amounts of rare and expensive

biological compound are needed, lowering development and production costs. Unfortunately, at the same time the smaller number of immobilized biological recognition elements on the smaller surface area of miniaturized transducers results in a reduced long-term stability.

The limits of independently addressable microbiosensors in an array have been explored on the basis of microdisc electrode arrays fabricated by thin-film technology. Cross-talk between the discrete enzyme-containing sensor elements was observed and the proximity limit was found to be about 100 μm [261].

The reliability of the biological compound is the main problem, not only in development and use of miniaturized systems, but of all biosensors. Thus, current research is aiming at optimized immobilization methods.

2.11.3.3 Multisensor Arrays and Sensor Chips

Multisensor arrays were designed using different types of transducers. Miniaturized multianalyte enzyme sensors for the determination of three different substrates, using three different enzymes, were realized employing interdigitated microelectrodes and conductometric analysis [216, 248]. In contrast to the signal in amperometric transducers, the one in potentiometric measurements does not depend on the electrode surface area. ISFETs show in general a lower long-time stability as compared to LAPSs, which are additionally more easy to integrate in measuring microchambers due to their flat surface [262]. Nevertheless, sensor chips making use of two ISFETs for differential measurement in a urea sensor (ENFET) with an ammonium-sensitive reference FET (REFET) were designed for further use in in-vitro and

in-vivo analysis [250]. Miniaturized whole cell biosensors were constructed on the basis of LAPS with a capacity for 32 different cell types on one chip [251]. Even a portable cell-based biosensor system was developed. Here, the communication between excitable cells immobilized on platinized gold-microelectrode arrays were investigated [32]. On microelectrode culture plates neuronal networks were grown to serve as specific sensing units after modification with novel receptors. These self-contained devices are able to detect dissolved compounds of low vapor pressure and even resist hostile environments [263].

Chips for electrochemical detection of DNA hybridization incorporate whole chemistry laboratories including DNA extraction, amplification, labeling, and fragmentation, followed by electrochemical array detection [264]. Complete miniaturized systems for bedside blood analysis utilizing potentiometric (ion-selective for Na^+ , NH_4^+ , pH, etc.; enzyme-based for urea), amperometric (enzyme-based for glucose), and conductometric (for hematocrit) sensors are commercially exploited [265]. A miniaturized total chemical analysis system utilizing electrochemical biosensors (μTAS) was first proposed in 1990 [266]. A further version developed includes a miniaturized measuring cell incorporated into a silicon microstructure flow stack [267]. Employing a high-efficiency microdialysis sampling system, it has already been implanted for in vivo on-line monitoring of glucose and lactate with amperometric enzyme sensors [268].

Certainly the most lucrative application for miniaturized biosensors appears to be clinical analysis [269, 270] in which patient self-control, especially for diabetic patients, the establishment of so-called

bedside diagnostics in intensive care, and the real-time control of important metabolites during operations, play a crucial role.

References

1. T. Vo-Dinh, B. Cullum, *Fresenius' J. Anal. Chem.* **2000**, 366, 540–551.
2. D. R. Thévenot, K. Toth, R. A. Durst et al., *Pure Appl. Chem.* **1999**, 71, 2333–2348.
3. H.-L. Schmidt, W. Schuhmann, F. W. Scheller et al. in *Sensors. A Comprehensive Survey* (Eds.: W. Göpel, J. Hesse, J. N. Zemel), Part II, Wiley-VCH, Weinheim, Germany, 1991, pp. 717–817, Vol. 3.
4. T. D. Gibson, *Analysis* **1999**, 27, 630–638.
5. N. Wisniewski, F. Moussy, W. M. Reichert, *Fresenius' J. Anal. Chem.* **2000**, 366, 611–621.
6. R. D. Schmid, *GBF-Monogr.* **1989**, 13, 271–280.
7. F. Scheller, K. Riedel, B. Neumann et al., *DECHEMA Biotechnol. Conf.* **1990**, 4, 1045–1048.
8. E. B. Nikolaskaya, G. A. Evtyugin, T. N. Shekhovtsova, *J. Anal. Chem. USSR* **1994**, 49, 408–416.
9. K. R. Rogers, L. R. Williams, *Trends Anal. Chem.* **1995**, 14, 289–294.
10. I. Karube, Y. Nomura, Y. Arikawa, *Trends Anal. Chem.* **1995**, 14, 295–299.
11. T. Ruzgas, J. Emneus, L. Gorton et al., *Anal. Chim. Acta* **1995**, 311, 245–253.
12. F. Mazzei, F. Botre, G. Lorenti et al., *Anal. Chim. Acta* **1995**, 316, 79–82.
13. E. M. d'Urso, P. R. Coulet, *Anal. Chim. Acta* **1990**, 239, 1–5.
14. H. Lüdi, M. B. Garn, M. Bataillard et al., *J. Biotechnol.* **1990**, 14, 71–79.
15. J. I. Lee, I. Karube, *Anal. Chim. Acta* **1995**, 313, 69–74.
16. J. L. Besombes, S. Cosnier, P. Labbe et al., *Anal. Chim. Acta* **1995**, 311, 255–263.
17. L. R. Damgaard, H. Larsen, N. P. Revsbech, *Trends Anal. Chem.* **1995**, 14, 300–303.
18. J. L. Marty, N. Mionetto, S. Lacorte et al., *Anal. Chim. Acta* **1995**, 311, 265–271.
19. C. Colapicchioni, A. Barbaro, F. Porcelli, *Sens. Actuators, B* **1992**, 6, 202–207.
20. Y. S. Su, A. Cagnini, M. Mascini, *Chem. Anal.* **1995**, 40, 579–585.

21. M. P. Marco, S. Gee, B. D. Hammock, *Trends Anal. Chem.* **1995**, *14*, 341–350.
22. O. A. Sadik, J. M. van Emon, *Biosens. Bioelectron.* **1996**, *14*, AR1–AR11.
23. D. M. Rawson, A. J. Willmer, A. P. F. Turner, *Biosensors* **1989**, *4*, 299–311.
24. P. G. Schultz, *Angew. Chem.* **1989**, *101*, 1336–1348.
25. A. G. Cochran, T. Pham, R. Sugawara et al., *J. Am. Chem. Soc.* **1991**, *113*, 6670–6672.
26. S. Ramanathan, M. Ensor, S. Daunert, *Trends Biotechnol.* **1997**, *15*, 500–506.
27. G. Siest, T. Oster, A. Viskis et al., *Clin. Chem.* **1993**, *39*, 1573–1589.
28. S. Pedersen, B. F. Jørgensen, S. T. Jørgensen, *Genet. Modif. Foods* **1995**, *605*, 196–208.
29. A. Pandey, P. Selvakumar, C. R. Soccol et al., *Curr. Sci.* **1999**, *77*, 149–162.
30. A. L. Lehninger, *Principles of Biochemistry*, Worth Publishers, New York, 1982.
31. C. Ziegler, *Fresenius J. Anal. Chem.* **2000**, *366*, 552–559.
32. L. Bousse, *Sens. Actuators, B* **1996**, *34*, 270–275.
33. D. P. Nikolelis, U. J. Krull, *Electroanalysis* **1993**, *5*, 539–545.
34. D. Nikolelis, T. Hianik, U. J. Krull, *Electroanalysis* **1999**, *11*, 7–15.
35. T. D. Brock, M. T. Madigan, J. M. Martinko et al., *Biology of Microorganisms*, 7th ed., Prentice Hall, Englewood Cliffs, N.J., 1995.
36. H. Kiefer, B. Klee, E. John et al., *Biosens. Bioelectron.* **1991**, *6*, 233–237.
37. S. Zhang, G. Wright, Y. Yang, *Biosens. Bioelectron.* **2000**, *15*, 273–282.
38. E. Souteyrand, *Analysis* **1999**, *27*, 639–646.
39. J. Wang, G. Rivas, X. Cai et al., *Anal. Chim. Acta* **1997**, *347*, 1–8.
40. E. A. H. Hall, *Biosensors*, Open University Press, 1990.
41. B. R. Eggins, *Biosensors: An Introduction*, Wiley/Teubner, Chichester/Stuttgart, 1996.
42. K. Camman, B. Ross, W. Haase et al., *Ullmann's Encyclopedia of Industrial Chemistry*, 6th ed., Wiley-VCH, Weinheim, Germany, 1998.
43. G. Jobst, I. Moser, M. Varaham et al., *Anal. Chem.* **1996**, *68*, 3173–3179.
44. C. Jiménez, J. Bartol, N. F. de Rooij et al., *Anal. Chim. Acta* **1997**, *351*, 169–176.
45. C. Kranz, M. Ludwig, H. E. Gaub et al., *Adv. Mater.* **1995**, *7*, 38–40.
46. C. Kranz, H. E. Gaub, W. Schuhmann, *Adv. Mater.* **1996**, *8*, 634–637.
47. C. Kurzawa, Ph.D. thesis, Ruhr-Universität Bochum, Bochum, Germany, 2001.
48. D. J. Strike, N. F. Roij, M. Koudelka-Hep, *Biosens. Bioelectron.* **1995**, *10*, 61–66.
49. U. Bilitewski, P. Rueger, W. Drewes et al., *GBF Monogr.* **1992**, *17*, 199–204.
50. M. Mosbach, H. Zimmermann, T. Laurell, J. Nilsson, E. Csöregi, W. Schuhmann, *Biosensors & Bioelectronics* **2001**, *16*, 827–837.
51. R. A. Marcus, N. Sutin, *Biochim. Biophys. Acta* **1985**, *811*, 265–322.
52. R. A. Marcus, *Angew. Chem., Int. Ed. Engl.* **1993**, *32*, 1111–1121.
53. K. Habermüller, M. Mosbach, W. Schuhmann, *Fresenius' J. Anal. Chem.* **2000**, *366*, 560–568.
54. L. C. Clark, C. Lyons, *Ann. N.Y. Acad. Sci.* **1962**, *102*, 29–45.
55. D. R. Thevenot, R. Sternberg, P. Coulet, *Diabetes Care* **1982**, *5*, 203–206.
56. M. Shichiri, R. Kawamori, Y. Yamasaki et al., *Lancet* **1982**, 1129–1131.
57. U. Wollenberger, F. Scheller, D. Pfeiffer et al., *Anal. Chim. Acta* **1986**, *187*, 39–45.
58. J. Brueckel, H. Zier, W. Kerner et al., *Horm. Metab. Res.* **1990**, *22*, 382–384.
59. D. A. Gough, J. Y. Lucisano, P. H. S. Tse, *Anal. Chem.* **1995**, *57*, 2351–2357.
60. S. J. Updike, G. P. Hicks, *Nature* **1967**, *214*, 986–988.
61. S. A. M. Van Stroe-Biezen, F. M. Everaerts, L. J. J. Janssen et al., *Anal. Chim. Acta* **1993**, *273*, 553–560.
62. W. Matuszewski, M. Trojanowicz, *Analyst* **1988**, *113*, 735–738.
63. A. Amine, J. K. Kauffmann, G. J. Patriarche, *Talanta* **1991**, *38*, 107–110.
64. J. Wang, F. Lu, *J. Am. Chem. Soc.* **1998**, *120*, 1048–1050.
65. S. J. Churchouse, C. M. Battersby, W. H. Mullen et al., *Biosensors* **1986**, *2*, 325–342.
66. M. Koudelka, F. Rohner-Jeanrenaud, J. Terrettaz et al., *Biomed. Biochim. Acta* **1989**, *48*, 935–942.
67. X. Yang, G. Johansson, L. Gorton, *Mikrochim. Acta* **1989**, *4*, 9–16.
68. T. Hoshi, J. Anzai, T. Osa, *Anal. Chem.* **1995**, *67*, 770–774.
69. C. Jiménez, J. Bartolí, N. F. de Rooij et al., *Sens. Actuators, B* **1995**, *26–27*, 421–424.
70. M. Umana, J. Waller, *Anal. Chem.* **1986**, *58*, 2979–2983.

71. N. C. Foulds, C. R. Lowe, *J. Chem. Soc., Faraday Trans.* **1986**, 82, 1259–1264.
72. P. N. Bartlett, R. G. Whitaker, *J. Electroanal. Chem.* **1987**, 224, 37–48.
73. M. Hämmerle, W. Schuhmann, H. L. Schmidt, *Sens. Actuators, B* **1992**, 6, 106–112.
74. L. Coche-Guerente, A. Deronzier, P. Mailley et al., *Anal. Chim. Acta* **1994**, 289, 143–153.
75. K. Hajizadeh, H. B. Halsall, W. R. Heinemann, *Talanta* **1991**, 38, 37–47.
76. N. Ito, T. Matsumoto, H. Fujiwara et al., *Anal. Chim. Acta* **1995**, 312, 323–328.
77. S. Cosnier, C. Innocent, S. Allien et al., *Anal. Chem.* **1997**, 69, 968–971.
78. G. Fortier, R. Beliveau, E. Leblond et al., *Anal. Lett.* **1990**, 23, 1607–1619.
79. S. Cosnier, C. Innocent, *Anal. Lett.* **1994**, 27, 1429–1442.
80. J. M. Kim, M. Suzuki, R. D. Schmid, *Anal. Lett.* **1989**, 22, 2433–2443.
81. S. D. Haemmerli, A. A. Suleiman, G. G. Guilbault, *Anal. Lett.* **1990**, 23, 577–588.
82. J. J. Kulys, A. S. Samalius, G. J. S. Svirnickas, *FEBS Lett.* **1980**, 114, 7–10.
83. A. G. Cass, G. Davis, G. D. Francis et al., *Anal. Chem.* **1984**, 56, 667–671.
84. P. Schläpfer, W. Mindt, P. H. Racine, *Clin. Chim. Acta* **1974**, 57, 283–289.
85. J. T. Kulys, N. K. Cenas, *Biochim. Biophys. Acta* **1983**, 744, 57–63.
86. A. E. G. Cass, G. Davis, M. J. Green et al., *J. Electroanal. Chem.* **1985**, 190, 117–127.
87. K. Yokoyama, E. Tamiya, I. Karube, *J. Electroanal. Chem.* **1989**, 273, 107–117.
88. M. Koudelka, S. Gernet, N. F. De Rooij, *Sens. Actuators, B* **1989**, 18, 157–165.
89. A. J. Thornton, D. E. Brown, *Biotechnol. Tech.* **1991**, 5, 363–366.
90. F. Battaglini, E. J. Calvo, *J. Chem. Soc., Faraday Trans.* **1994**, 90, 987–995.
91. D. J. Claremont, I. E. Sambrook, J. C. Pickup, *Diabetologia* **1986**, 29, 817–821.
92. G. Jönsson, L. Gorton, L. Pettersson, *Electroanalysis* **1989**, 1, 49–55.
93. S. L. Brooks, A. P. F. Turner, *Meas. Contr.* **1987**, 20, 37–43.
94. W. Schuhmann, H. Wohlschläger, R. Lammer et al., *Sens. Actuators, B* **1990**, 1, 537–541.
95. M. Frede, E. Steckhan, *Tetrahedron Lett.* **1991**, 32, 5063–5066.
96. W. Schuhmann, *Biosens. Bioelectron.* **1993**, 8, 191–196.
97. H.-L. Schmidt, W. Schuhmann, R. Medina et al., *GBF-Monographie* (Eds.: F. Scheller, R. D. Schmid), Wiley-VCH, Weinheim, Germany, 1992, pp. 97–106, Vol. 17.
98. G. Marko-Varga, R. Appelquist, L. Gorton, *J. Electroanal. Chem.* **1984**, 161, 103–120.
99. H. Huck, A. Schelter-Graf, J. Danzer et al., *Analyst* **1984**, 109, 147–150.
100. B. Persson, L. Gorton, *J. Electroanal. Chem.* **1990**, 292, 115–138.
101. L. Gorton, B. Persson, *Polym. Mater. Sci. Eng.* **1991**, 64, 326–328.
102. A. A. Karyakin, E. E. Karyakina, W. Schuhmann et al., *Electroanalysis* **1994**, 6, 821–829.
103. H.-L. Schmidt, F. Gutberlet, W. Schuhmann, *Sens. Actuators, B* **1993**, 13–14, 366–371.
104. L. Gorton, *Electroanalysis* **1995**, 7, 23–45.
105. W. Matuszewski, M. Trojanowicz, *Analyst* **1988**, 113, 735–738.
106. P. C. Pandey, *Enzyme and Microbial Biosensors*, Humana Press, Totowa, N.J., 1998.
107. M. Senda, T. Ikeda, H. Hiasa et al., *Anal. Sci.* **1986**, 2, 501–506.
108. J. M. Dicks, W. J. Aston, G. Davis et al., *Anal. Chim. Acta* **1986**, 182, 103–112.
109. J. Wang, L. H. Wu, Z. Lu et al., *Anal. Chim. Acta* **1990**, 228, 251–257.
110. J. Kulys, W. Schuhmann, H. L. Schmidt, *Anal. Lett.* **1992**, 25, 1011–1024.
111. V. Kacaniklic, K. Johansson, G. Marko-Varga et al., *Electroanalysis* **1994**, 6, 381–390.
112. M. Hedenmo, A. Narvaez, E. Dominguez et al., *J. Electroanal. Chem.* **1997**, 425, 1–11.
113. R. P. Baldwin, K. N. Thomsen, *Talanta* **1990**, 38, 1–16.
114. G. Wittstock, B. Grundig, B. Strehlitz et al., *Electroanalysis* **1998**, 10, 526–531.
115. B. Gründig, G. Wittstock, U. Rudel et al., *J. Electroanal. Chem.* **1995**, 395, 143–157.
116. W. F. Crismore, N. A. Surridge, D. R. McMinn et al., Roche Diagnostics Corporation, US Patent 5,997,817, 1999.
117. K. Hildenbrandt, H.-U. Siegmung, A. G. Bayer, US Patent 5,916,156, 1999.
118. E. Saurer, S. A. Asulab, US Patent 5,407,554, 1995.
119. H.-L. Schmidt, W. Schuhmann, *Biosens. Bioelectron.* **1996**, 11, 127–135.
120. W. Schuhmann, T. J. Ohara, H. L. Schmidt et al., *J. Am. Chem. Soc.* **1991**, 113, 1394–1397.

121. A. D. Riabov, A. M. Trushkin, L. I. Baksheeva et al., *Angew. Chem., Int. Ed. Engl.* **1992**, 31, 789–791.
122. W. C. Tsai, A. E. G. Cass, *Analyst* **1995**, 120, 2249–2254.
123. E. S. Ryabova, V. N. Goral, E. Csöregi et al., *Angew. Chem., Int. Ed. Engl.* **1999**, 38, 804–807.
124. Y. Degani, A. Heller, *J. Phys. Chem.* **1987**, 91, 1285–1289.
125. P. N. Bartlett, R. G. Whitaker, M. J. Green et al., *J. Chem. Soc. Chem. Commun.* **1987**, 1603–1604.
126. S. Sampath, O. Lev, *Electroanalysis* **1996**, 8, 1112–1116.
127. E. Katz, A. Riklin, V. Heleg-Shabtai et al., *Anal. Chim. Acta* **1999**, 385, 45–58.
128. T. Lötzbeyer, Ph.D. thesis, Technische Universität München, München, Germany, 1996.
129. W. Schuhmann, *Biosens. Bioelectron.* **1995**, 10, 181–193.
130. Y. Degani, A. Heller, *J. Am. Chem. Soc.* **1989**, 111, 2357–2358.
131. B. A. Gregg, A. Heller, *Anal. Chem.* **1990**, 62, 258–263.
132. A. Heller, *Acc. Chem. Res.* **1990**, 23, 128–33.
133. A. Heller, *J. Phys. Chem.* **1992**, 96, 3579–3587.
134. M. V. Pishko, A. C. Michael, A. Heller, *Anal. Chem.* **1991**, 63, 2269–2272.
135. E. J. Calvo, R. Etchenique, C. Danilowicz et al., *Anal. Chem.* **1996**, 68, 4186–4193.
136. D. Leech, R. J. Forster, M. R. Smyth et al., *J. Mater. Chem.* **1991**, 1, 629–635.
137. A. P. Doherty, R. J. Forster, M. R. Smyth et al., *Anal. Chim. Acta* **1991**, 255, 45–52.
138. C. Taylor, G. Kenausis, I. Katakis et al., *J. Electroanal. Chem.* **1995**, 396, 511–515.
139. N. Larson, T. Ruzgas, L. Gorton et al., *Electrochim. Acta* **1999**, 3, 3551–3554.
140. Y. Kashiwagi, Q. Pan, Y. Yanagisawa et al., *Denki Kagaku* **1994**, 62, 1240–1246.
141. C. Danilowicz, E. Corton, F. Battaglini et al., *Electrochim. Acta* **1999**, 43, 3525–3531.
142. T. Inagaki, T. A. Skotheim, Y. Okamoto, *J. Chem. Soc., Chem. Commun.* **1989**, 1181–1183.
143. A. Aoki, A. Heller, *J. Phys. Chem.* **1993**, 97, 11 014–11 019.
144. A. Aoki, R. Rajagopalan, A. Heller, *J. Phys. Chem.* **1995**, 99, 5102–5110.
145. A. Heller, R. Maidan, D. Wang, *Sens. Actuators, B* **1993**, 13–14, 180–183.
146. P. N. Bartlett, J. M. Cooper, *J. Electroanal. Chem.* **1993**, 362, 1–12.
147. W. Schuhmann, *Mikrochim. Acta.* **1995**, 121, 1–29.
148. M. Trojanovicz, T. Krawczynski vel Krawczyk, *Mikrochim. Acta* **1995**, 121, 167–181.
149. S. Cosnier, *Biosens. Bioelectron.* **1999**, 14, 443–456.
150. C. G. J. Koopal, B. De Ruiter, R. J. M. Nolte, *J. Chem. Soc., Chem. Commun.* **1991**, 1691–1692.
151. C. G. J. Koopal, M. C. Feiters, R. J. M. Nolte et al., *Biosens. Bioelectron.* **1992**, 7, 461–471.
152. A. Ramanavicius, K. Habermüller, E. Csöregi et al., *Anal. Chem.* **1999**, 71, 3581–3586.
153. S. Cosnier, A. Deronzier, J. C. Moutet, *J. Electroanal. Chem.* **1985**, 193, 193–204.
154. W. Schuhmann, R. Lammert, M. Hammerle et al., *Biosens. Bioelectron.* **1991**, 6, 689–697.
155. W. Schuhmann in *Immobilized Biomolecules in Analysis. A Practical Approach* (Eds.: T. Cass, F. S. Ligler), Oxford University Press, New York, 1998, pp. 187–210.
156. M. Hiller, C. Kranz, J. Huber et al., *Adv. Mater.* **1996**, 8, 219–222.
157. W. Schuhmann, C. Kranz, H. Wohlschläger et al., *Biosens. Bioelectron.* **1997**, 12, 1157–1167.
158. W. Schuhmann, C. Kranz, J. Huber et al., *Synth. Met.* **1993**, 61, 31–35.
159. K. Habermüller, A. Ramanavicius, V. Laurinavicius et al., *Electroanalysis* **2000**, 12, 1383–1389.
160. S. Gaspar, K. Habermüller, E. Csöregi et al., *Sens. Actuators, B* **2001**, 72, 63–68.
161. F. A. Armstrong, *Adv. Inorg. Chem.* **1992**, 38, 117–163.
162. A. L. Ghindilis, P. Antanasov, E. Wilkins, *Electroanalysis* **1997**, 9, 661–675.
163. F. A. Armstrong, A. M. Lannon, *J. Am. Chem. Soc.* **1987**, 109, 7211–7212.
164. A. J. Yaropolov, V. Malovik, S. D. Varfolomeev et al., *Doklady Akad. Nauk USSR* **1979**, 249, 1399–1401.
165. L. Gorton, G. Jonsson-Pettersson, E. Csöregi et al., *Analyst* **1992**, 117, 1235–1241.
166. T. Ruzgas, E. Csöregi, J. Emneus et al., *Anal. Chim. Acta* **1996**, 330, 123–138.
167. T. Ferri, A. Poscia, R. Santucci, *Biochem. Bioenerg.* **1998**, 45, 221–226.

168. A. Lindgren, F. D. Munteanu, I. Gazaryan et al., *J. Electroanal. Chem.* **1998**, 458, 113–120.
169. A. Lindgren, M. Tanaka, T. Ruzgas et al., *Electrochem. Commun.* **1999**, 1, 171–175.
170. J. Kulys, R. D. Schmid, *Bioelectrochem. Bioenerg.* **1990**, 24, 305–311.
171. U. Wollenberger, J. Wang, M. Ozsoz et al., *Bioelectrochem. Bioenerg.* **1991**, 26, 287–296.
172. E. Csöregi, G. Jönsson-Pettersson, L. Gorton, *J. Biotechnol.* **1993**, 30, 315–317.
173. V. Razumas, J. Kazlauskaitė, T. Ruzgas et al., *Bioelectrochem. Bioenerg.* **1992**, 28, 159–176.
174. T. Ruzgas, A. Gaigalas, L. Gorton, *J. Electroanal. Chem.* **1999**, 468, 123–131.
175. T. Ruzgas, L. Gorton, J. Emnéus et al., *Anal. Proc.* **1995**, 32, 207–208.
176. T. Larsson, M. Elmgren, S. E. Lindquist et al., *Anal. Chim. Acta* **1996**, 331, 207–215.
177. T. Ikeda in *Frontiers in Biosensorics I. Fundamental Aspects* (Eds.: F. W. Scheller, F. Schubert, J. Fedrowitz), Birkhäuser, Basel, Switzerland, 1997, pp. 243–266.
178. L. Gorton, A. Lindgren, T. Larsson et al., *Anal. Chim. Acta* **1999**, 400, 91–108.
179. A. Lindgren, L. Gorton, T. Ruzgas et al., *J. Electroanal. Chem.* **2001**, 496, 76–81.
180. W. Schuhmann, H. Zimmermann, K. Habermüller et al., *Faraday Discuss.* **2000**, 116, 245–255.
181. L. Jiang, C. J. McNeil, J. M. Cooper, *J. Chem. Soc., Chem. Commun.* **1995**, 1293–1295.
182. M. J. Eddowes, H. A. O. Hill, K. Uosaki, *J. Electroanal. Chem.* **1980**, 116, 527–537.
183. F. A. Armstrong, *Bioinorg. Chem.* **1990**, 72, 137–230.
184. F. A. Armstrong, H. A. O. Hill, N. J. Walton, *Q. Rev. Biophys.* **1986**, 18, 261–322.
185. M. Collinson, E. F. Bowden, M. J. Tarlov, *Langmuir* **1992**, 8, 1247–1250.
186. S. Song, R. A. Clark, E. F. Bowden et al., *J. Phys. Chem.* **1993**, 97, 6564–6572.
187. T. Lötzbeyer, W. Schuhmann, H. L. Schmidt, *Sens. Actuators, B* **1996**, 33, 50–54.
188. T. Lötzbeyer, W. Schuhmann, H. L. Schmidt, *J. Electroanal. Chem.* **1994**, 377, 291–294.
189. L. B. Wingard, *Trends Anal. Chem.* **1984**, 3, 235–238.
190. A. Riklin, E. Katz, I. Willner et al., *Nature* **1995**, 376, 672–675.
191. I. Willner, V. Helegshabtai, R. Blonder et al., *J. Am. Chem. Soc.* **1996**, 118, 10 321–10 322.
192. H. Zimmermann, A. Lindgren, L. Gorton et al., *Chem. Eur. J.* **2000**, 6, 592–599.
193. E. Katz, T. Lötzbeyer, D. D. Schlereth et al., *J. Electroanal. Chem.* **1994**, 373, 189–200.
194. I. Willner, A. Riklin, *Anal. Chem.* **1994**, 66, 1535–1539.
195. L. Coche-Guerente, S. Cosnier, L. Labbe, *Chem. Mater.* **1997**, 9, 1348–1352.
196. D. Belanger, J. Nadreau, G. Fortier, *J. Electroanal. Chem.* **1989**, 274, 143–155.
197. J. M. Cooper, D. Bloor, *Electroanalysis* **1993**, 5, 883–886.
198. S. Yabuki, H. Shinohara, M. Aizawa, *J. Chem. Soc., Chem. Commun.* **1989**, 945–946.
199. B. Uhe, W. Schuhmann, J. Janata et al., *Sens. Actuators, B* **1992**, 7, 389–392.
200. H. Freiser, *J. Chem. Soc., Faraday Trans.* **1986**, 82, 1217–1221.
201. E. S. Wilkins, M. G. Wilkins, *Horm. Metab. Res. Suppl. Ser.* **1988**, 20, 50–55.
202. L. Piras, M. Adami, S. Fenu et al., *Anal. Chim. Acta* **1996**, 335, 127–135.
203. A. Lindgren, T. Ruzgas, L. Gorton et al., *Biosens. Bioelectron.* **2000**, 15, 491–497.
204. S. D. Varfolomeev, I. N. Kurochkin, A. I. Yaropolov, *Biosens. Bioelectron.* **1996**, 9, 863–871.
205. A. L. Ghindilis, T. G. Morzunova, A. V. Barmin et al., *Biosens. Bioelectron.* **1996**, 11, 873–880.
206. J. Diehl-Faxon, A. L. Ghindilis, P. Atanasov, *Sens. Actuators, B* **1996**, 35–36, 448–457.
207. A. Warsinke, A. Benkert, F. W. Scheller, *Fresenius' J. Anal. Chem.* **2000**, 366, 622–634.
208. R.-I. Stefan, J. F. van Staden, H. Y. Abdoul-Enein, *Fresenius' J. Anal. Chem.* **2000**, 366, 659–668.
209. A. B. Kharitonov, M. Zayats, A. Lichtenstein et al., *Sens. Actuators, B* **2000**, 70, 222–231.
210. N. Jaffrezic-Renault, K. Wan, A. Sensillou et al., *Analysis* **1999**, 27, 578–586.
211. M. Zayats, A. B. Kharitonov, E. Katz et al., *Biosens. Bioelectron.* **2000**, 15, 671–680.
212. S. V. Dzyadevich, Y. I. Korpan, V. N. Arkhipova et al., *Biosens. Bioelectron.* **1999**, 14, 283–287.
213. N. Jaffrezic-Renault, A. Senillou, C. Martelet et al., *Sens. Actuators, B* **1999**, 59, 154–164.

214. S. R. Mikkelsen, G. A. Rechnitz, *Anal. Chem.* **1989**, 61, 1737–1742.
215. W.-Y. Lee, S.-R. Kim, T.-H. Kim et al., *Anal. Chim. Acta* **2000**, 404, 195–203.
216. D. C. Cullen, R. S. Sethi, C. R. Lowe, *Anal. Chim. Acta* **1990**, 231, 33–40.
217. N. F. Sheppard Jr., D. J. Mears, *Biosens. Bioelectron.* **1996**, 11, 967–979.
218. H. Suzuki, *Mater. Sci. Eng., C* **2000**, 12, 55–61.
219. W. Schuhmann, K. Habermüller in *Electrochemical Microsystem Technologies* (Eds.: J. W. Schulze, T. Osaka, M. Datta), Taylor & Francis, Andover, UK, in press.
220. D. Bruns, R. Jahn, *Nature* **1995**, 377, 62–65.
221. P. S. Cahill, Q. D. Walker, J. M. Finnegan et al., *Anal. Chem.* **1996**, 68, 3180–3186.
222. I. Karube, K. Yokoyama, E. Tamiya, *Biosens. Bioelectron.* **1993**, 8, 219–228.
223. Q. Xin, R. M. Wightman, *Brain Res.* **1997**, 776, 126–132.
224. J. M. Cooper, P. L. Foreman, A. Glidle et al., *J. Electroanal. Chem.* **1995**, 388, 143–149.
225. P. Pantano, W. G. Kuhr, *Electroanalysis* **1995**, 7, 405–416.
226. D. S. Bindra, Y. Zhang, G. S. Wilson et al., *Anal. Chem.* **1991**, 63, 1692–1696.
227. C. Cronenberg, B. Van Groen, D. De Beer et al., *Anal. Chim. Acta* **1991**, 242, 275–278.
228. J. W. Furbee Jr., T. Kuwana, R. S. Kelly, *Anal. Chem.* **1994**, 66, 1575–1577.
229. M. A. McRipley, R. A. Linsenmeier, *J. Electroanal. Chem.* **1996**, 414, 235–246.
230. L. I. Netchiporouk, N. F. Shram, N. Jaffrezic-Renault et al., *Anal. Chem.* **1996**, 68, 4358–4364.
231. H. Sakslund, J. Wang, O. Hammerich, *J. Electroanal. Chem.* **1996**, 402, 149–160.
232. J. Wang, G. Rivas, M. Chicharro, *J. Electroanal. Chem.* **1997**, 439, 55–62.
233. X. J. Zhang, J. Wang, B. Ogorevc et al., *Electroanalysis* **1999**, 11, 945–949.
234. E. Csöregi, L. Gorton, G. Marko-Varga et al., *Anal. Chem.* **1994**, 66, 3640–3610.
235. E. Tamiya, Y. Sugiura, E. N. Navera et al., *Anal. Chim. Acta* **1991**, 251, 129–134.
236. J. Motonaka, L. R. Faulkner, *Anal. Chem.* **1993**, 65, 3258–3261.
237. S. Poitry, C. Poitry-Yamate, C. Innocent et al., *Electrochim. Acta* **1997**, 42, 3217–3233.
238. M. Lambrechts, W. Sansen, *Biosensors: Microelectrochemical Devices*, Institute of Physics Publishing, Bristol, 1992.
239. D. Wilke, H. Muller, N. Kolytsheva, *Frese-nius J. Anal. Chem.* **1997**, 357, 534–538.
240. T. Matsumoto, M. Furusawa, H. Fujiwara et al., *Sens. Actuators, B* **1998**, 49, 68–72.
241. H. Tap, P. Gros, A. M. Gue, *Electroanalysis* **1999**, 11, 973–977.
242. J. Wang, Q. Chen, *Anal. Chem.* **1994**, 66, 1007–1011.
243. H. Sangodkar, S. Sukeerthi, R. S. Srinivasa et al., *Anal. Chem.* **1996**, 68, 779–783.
244. A. Guiseppi-Elie, J. M. Tour, D. L. Allara et al., *Mater. Res. Soc. Symp. Proc.* **1996**, 413, 439–444.
245. S. P. Yang, Y. F. Lu, P. Atanassov et al., *Talanta* **1998**, 47, 735–743.
246. T. Hermes, M. Buehner, S. Buecher et al., *Sens. Actuators, B* **1994**, 21, 33–37.
247. W. H. Baumann, M. Lehmann, A. Schwinde et al., *Sens. Actuators, B* **1999**, 55, 77–89.
248. M. J. Schöning, F. Ronkel, M. Crott et al., *Electrochim. Acta* **1997**, 42, 3185–3193.
249. C. Puig-Lleixa, C. Jimenez, J. Alonso et al., *Anal. Chim. Acta* **1999**, 389, 179–188.
250. A. Senillou, N. Jaffrezic-Renault, C. Martelet et al., *Talanta* **1999**, 50, 219–226.
251. F. Hafner, *Biosens. Bioelectron.* **2000**, 15, 149–158.
252. M. George, W. J. Parak, H. E. Gaub, *Sens. Actuators, B* **2000**, 69, 266–275.
253. A. B. M. Ismail, H. Sugihara, T. Yoshinobu et al., *Sens. Actuators, B* **2001**, 74, 112–116.
254. A. Seki, S.-I. Ikeda, I. Kubo et al., *Anal. Chim. Acta* **1998**, 373, 9–13.
255. M. Adami, M. Sartore, C. Nicolini, *Biosens. Bioelectron.* **1995**, 10, 155–167.
256. P. N. Bartlett, Y. Astier, *Chem. Commun.* **2000**, 105–112.
257. E. Mann-Buxbaum, F. Pittner, T. Schalkhammer et al., *Sens. Actuators, B* **1990**, 1, 518–522.
258. C. Y. Tian, N. Q. Jia, R. Wang et al., *Sens. Actuators, B* **1998**, 52, 119–124.
259. J. M. Cooper, *Trends Biotechnol.* **1999**, 17, 226–230.
260. B. Wolf, M. Brischwein, W. Baumann et al., *Biosens. Bioelectron.* **1998**, 13, 501–509.
261. P. Yu, G. S. Wilson, *Faraday Discuss.* **2000**, 116, 305–317.
262. A. Fanigiulo, P. Accossato, M. Adami et al., *Sens. Actuators, B* **1996**, 32, 41–48.
263. G. W. Gross, B. K. Rhoades, H. M. E. Azzazy et al., *Biosens. Bioelectron.* **1995**, 10, 553–567.

264. J. Wang, *Chem. Eur. J.* **1999**, 5, 1681–1685.
265. I. R. Lauks, *Acc. Chem. Res.* **1998**, 31, 317–324.
266. A. Manz, N. Graber, H. M. Widmer, *Sens. Actuators, B* **1990**, 1, 244.
267. E. Dempsey, D. Diamond, M. R. Smyth et al., *Anal. Chim. Acta* **1997**, 346, 341–349.
268. R. Freaney, A. Mc Shane, T. V. Keaveny et al., *Ann. Clin. Biochim.* **1997**, 34, 291–302.
269. W. Göpel, *Mikrochim. Acta* **1997**, 125, 179–196.
270. J. Wang, *J. Pharm. Biomed. Anal.* **1999**, 19, 47–53.

3.1 Electrochemical STM

*Thomas Polk Moffat
National Institute of Standards and Technology,
Gaithersburg, Maryland, U.S.A.*

3.1.1 Introduction

Scanning tunneling microscopy (STM) may be used to directly image the electron density of surfaces with atomic resolution and to follow the dynamics of surface processes in real time in a variety of environments. This capability, in combination with the simplicity and accessibility of the method, has contributed to major advances in surface science over the last 20 years [1–8]. Following the early vacuum STM work, spectacular atomically resolved images of immersed surface ranging from van der Waals solids to metals and semiconductors were presented in the early 1990s [9–11]. More recently, the lure of the aesthetic quality and novelty of atomically resolved imaging of electron density has given way to a more detailed and quantitative assessment of STM images of solid–liquid interfaces. In this sense, perhaps the most unique capability of STM began to emerge, namely,

the ability to image localized phenomena on an atomic scale. Defects such as vacancies, dislocation, surface steps, kinks, ad-atoms, and their effect on phase transitions may now be studied in real time and space [8]. Likewise, the ability to probe the electronic states of individual adsorbed redox molecules via resonant tunneling has been demonstrated [12]. In addition to imaging applications, the sensitivity of the tunneling junction may be implemented as either a displacement or conductance sensor for quantifying the effect(s) of interfacial stress or sensing the presence of different chemical species within the tunnel junction, respectively. Finally, the STM has also been implemented as a synthesis tool for building a variety of novel structures by etching, deposition, or oxidation, in which the spatial extent of the reaction is more or less defined by the tunnel gap [13, 14].

The purpose of this chapter is to describe the operation and utility of in situ STM as a technique for probing the structure and dynamics of electrode surfaces. This limited effort provides only a brief glimpse of the possibilities and the interested reader may wish to consult one or more of the textbooks, monographs, and/or review articles to obtain a more complete view of this expansive field [3–8, 15–26].

3.1.1.1 STM and Modes of Operation

The STM uses an atomically sharp probe tip to map contours of the local density of electronic states on the surface. This is accomplished by monitoring quantum transmission of electrons between the tip and substrate while piezoelectric devices raster the tip relative to the substrate as shown schematically in Fig. 1 [27]. The remarkable vertical resolution of the device arises from the roughly exponential dependence of the electron tunneling process on the tip–substrate separation, d . In the simplest approximation, the tunneling current, I , can be simply written in terms of the local density of states (LDOS; $\rho_s(z, E)$) at the Fermi level ($E = E_F$) of the sample in which V is the bias voltage between the tip and substrate

$$I = V\rho_s(0, E_F) \exp(-2\kappa d) \quad (1)$$

and κ is the decay constant, which is related to the magnitude and the shape of the potential barrier. The decay constant may be described by an effective barrier height, ϕ (eV), according to $\kappa = (\pi(8m_e\phi)^{1/2})/h \approx 0.51(\phi \text{ (eV)})^{1/2}$. A value of $\kappa \sim 1 \text{ \AA}^{-1}$ results in an order

of magnitude decrease of the tunneling current per angstrom of electrode separation. The influence of an electrolyte on the characteristics of the tunnel junction has been investigated both experimentally and theoretically [28]. Measurements, such as those shown in Fig. 2 reveal the anticipated distance dependence for an immersed Au–PtIr junction [29]. The effective barrier height is found to be less than that for related vacuum junctions, $0.75 \text{ \AA}^{-1} \sim 2.15 \text{ eV}$ in this instance, (vacuum junction is typically $\sim 1.0 \text{ \AA}^{-1} \sim 4 \text{ eV}$). The diminished barrier has been associated with tunneling via the “ V_0 ” level or loosely speaking the “conduction band”, of the solvent [30]. In a similar fashion, the expected ohmic behavior for a fixed metal tip–metal sample distance has been verified as shown in Fig. 3 [29]. Tunneling junctions may also be described in terms of the tunneling conductance, G ,

$$G \approx G_0 \exp(-2\kappa d) \quad (2)$$

where G_0 is associated with quantum-point contact at which the barrier has collapsed ($d = 0$, which corresponds to

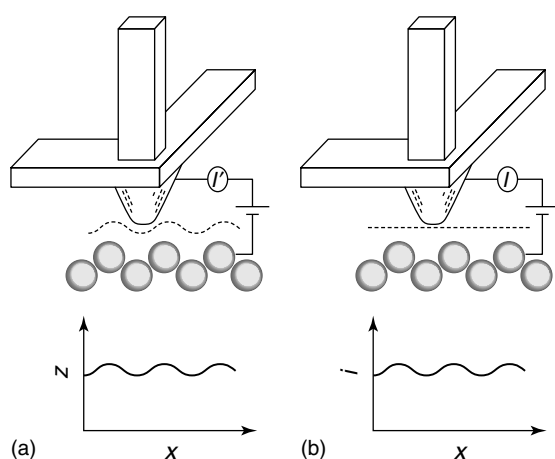


Fig. 1 Schematic representation of the: (a) constant current; and (b) constant height modes of operation of an STM. (Reprinted with permission from Ref. [27], Copyright 1987 by American Institute of Physics.)

Fig. 2 The dependence of the tunnel resistance on z-piezo voltage or movement, s , for a junction immersed in 0.01 M HClO_4 . Negative displacement corresponds to a diminishing gap between the Au(111) substrate and the Pt–Ir tip. Extrapolation of the data to point contact $\sim R = 10^4 \Omega$ may be used to estimate the size of the tunnel junction (note there are certain ambiguities and pitfalls associated with this procedure). The long–short dash corresponds to extrapolation from the slope at $10^9 \Omega$, while the other lines correspond to extrapolation from $10^7 \Omega$. These results reveal a distance dependence on the barrier height and also indicate a dependence on polarity. The inset figure shows data for vacuum tunneling. (Reprinted with permission from Ref. [29], Copyright 1995 by Elsevier.)

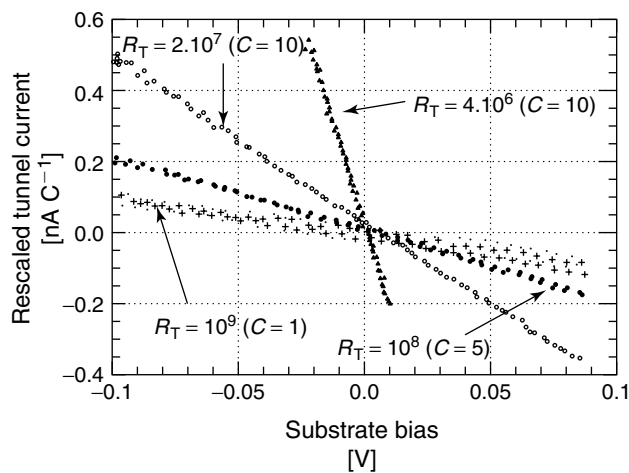
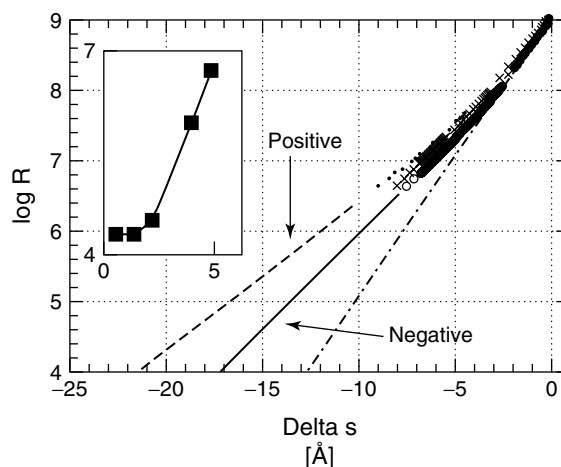


Fig. 3 Current–voltage plots taken at a variety of tunnel gap dimensions. The linear ohmic response suggests the absence of sharp resonant tunneling phenomena occurring in the Pt–Ir tip/0.01 M HClO_4 /Au(111) junction. The gap dimensions were set according to a specific tunnel resistance (R_T), after which the feedback was disengaged to collect the $i - V$ data. The currents were rescaled, (C), for display purposes. (Reprinted with permission from Ref. [29], Copyright 1995 by Elsevier.)

2–3 Å internuclear separation) ($G_0 = 1/R_0$, where $R_0 = h/2e^2 = 12.9 \text{ k}\Omega$) [2]. Point contact has also been treated classically as the Sharvin resistance in which the contact aperture has a radius, α , which is much less than the mean free path λ ($\lambda/\alpha \gg 1$), $R_s = 4\rho\lambda/3\pi\alpha^2$ where ρ is the resistivity of the metal such that a contact 3 Å in diameter corresponding to a resistance of $\sim 10 \text{ k}\Omega$ [2].

For imaging purposes, the STM may be used to follow contours of constant electron density or alternatively, the tunneling current may be monitored while the tip is rastered at a fixed distance from the substrate. The first imaging mode operates using negative feedback to adjust the z -piezo voltage to maintain a set tunneling conductance and is typically referred to as constant current imaging. A plot of the voltage applied to the z -piezo versus the tip raster position yields an image of contours of constant electron density of the surface as indicated in Fig. 1. On the mesoscopic level, this technique gives a measure of the surface topography of a bare metal surface; while at the atomic level a more sophisticated description is required that correlates local electron density at the Fermi level with the atomic surface structure. In the second imaging mode, the tip is rastered rapidly over the surface at a fixed height while the tunneling current is monitored. This method is referred to as constant height imaging. In this instance, higher scan rates are accessible since the electronics only have to measure the tunneling current fluctuations as opposed to controlling the movement of the z -piezoelectric scanner. This method is only used for imaging flat surfaces.

The STM may also be used to characterize the local electronic properties of the surface in terms of the effective tunneling barrier or decay constant (κ) as described

above (Eqs. (1 or 2), respectively). Experimentally, κ may be derived from dc or ac measurements. The more accurate ac modulation method is implemented by applying a small, $\sim 0.05 \text{ Å}$, modulation, Δs , to the z -piezo at approximately kilohertz frequency and using a lock-in amplifier to measure the corresponding current modulation (di/ds) where $\kappa = -1/i(di/ds) = -1/2(d(\ln(i))/ds)$ [29].

Similarly, the energy distribution of the density of states may be examined via tunneling spectroscopy in which the bias dependence of the tunneling current is measured at a fixed tip-substrate distance. This has proven to be particularly useful for examining surfaces that exhibit large changes in the LDOS with bias, such as semiconductors and the information gained may be used to optimize imaging conditions [7, 15]. In a similar vein, the potential-dependent resonant tunneling through adsorbed molecules may be studied, which offers a unique window for examining electron-transfer reactions involving surface-confined species [12].

Well-defined *in situ* STM experiments require the use of a bipotentiostat to independently control the electrochemical potential of the tip and substrate relative to some reference electrode. This configuration is distinct from an ultrahigh vacuum (UHV) experiment in which only the bias between the electrodes needs to be specified. In the electrochemical environment, the tip electrode is simultaneously a tunneling probe and an ultramicroelectrode. Consequently, suitable attention must be given to possible faradaic reactions proceeding at the tip as suggested in Fig. 4. These reactions may include redox events as well as deposition and dissolution processes. Under constant current imaging conditions, the set point current is maintained by a combination

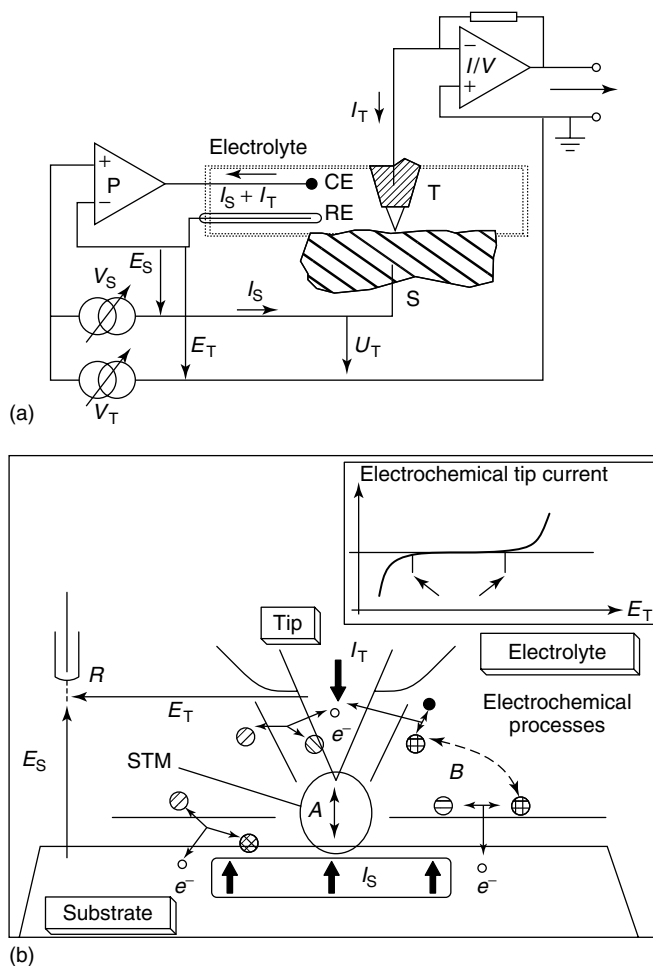


Fig. 4 (a) A bipotentiostat allows independent control of the tip (E_T) and substrate (E_S) potential relative to a reference electrode (RE). (Reprinted with permission from Ref. [26], Copyright 1992 by Springer-Verlag.) (b) Schematic presentation of an immersed tunnel junction, at which in addition to direct tunneling between the tip and substrate, there is also the possibility of electrochemical reactions occurring at the tip and substrate. The broken arrow indicates the possibility of linkage between the electrochemical reactions occurring at the tip and substrate, which is the basis of SECM. (Reprinted with permission from Ref. [16], Copyright 1992 by Springer-Verlag.)

of electron tunneling and the faradaic process occurring at the tip. Typically, an attempt is made to minimize the faradaic contribution at the tip by coating the probe with an insulating substance leaving only

the apex of the tip directly exposed to the electrolyte as indicated in Fig. 4. A typical set point current for atomically resolved STM imaging is on the order of ~ 1 to 20 nA. This corresponds to an extremely

large current flux $\sim 10^6 \text{ A cm}^{-2}$ between the apex of the tip and the substrate area being probed, $< 10^{-14} \text{ cm}^2$. In contrast, any faradaic process would be distributed over the exposed area of the tip, which is often in the range of $\sim 10^{-8}$ to 10^{-10} cm^2 such that a 10-nA faradaic current would correspond to a current density of 1 to 100 A cm^{-2} . Thus, provided the tip electrode is suitably coated, a large faradaic perturbation is required to destabilize the tunneling-based imaging process. In contrast, the exponential decrease in the tunneling current with increasing tip–substrate separation eventually leads to the limiting case in which $i_{\text{faradaic}} \gg i_{\text{tunnel}}$. Under appropriate conditions, the faradaic current may be used to form images of the electrochemical reactivity of a surface. This is known as *scanning electrochemical microscopy (SECM)* in which the transport and heterogeneous redox activity of species within the junction mediate the tip–substrate interaction (see Chapter 3.3 of this volume).

From a different perspective, electrochemical processes are also evident in certain two-electrode STM experiments performed in air. It is well known that water is absorbed on surfaces exposed to humid environments [31, 32]. When such conditions arise in combination with certain bias conditions, the conventional two-electrode STM exhibits some of the characteristics of a two-electrode electrochemical cell [33].

3.1.1.2 Atomically Resolved Imaging

The ability of STM to resolve the electronic density of individual atoms requires a lateral resolution of $\sim 2 \text{ \AA}$. To obtain such resolution requires the tip–sample distance be very short ~ 3 to 7 \AA (distance between the nucleus of the apex atom of the tip and nuclei of the top

layer of the sample surface). The STM has been likened to a giant molecule consisting of two component molecules with the relationship between tunneling and junction forces being closely related to the theory of chemical bonding [2]. Atomically resolved imaging proceeds via the interaction of the d-states of the tip and the substrate with a typical tunneling resistance of $< 10^7 \Omega$ [2, 3]. Theory indicates that at small tip–substrate separations, the barrier collapses as a result of attractive resonance and image forces between the tip and sample such that the barrier height is either very close to or lower than the Fermi level [2, 3, 34]. Under these conditions, the electrolyte is largely displaced from the gap resulting in physics not unlike that of the vacuum junction. Experimentally, the dependence of the barrier height on tip–sample separation is revealed as a changing slope of the resistance–separation curve such as that shown in Fig. 2 [29]. Likewise, the measured corrugation amplitude of a metal surface is known to be a strong function of tip–sample separation as well as the electronic state of the tip [2, 3, 35]. For example, an exponential dependence of corrugation amplitude with distance was clearly observed for Al(111) in UHV as shown in Fig. 5. Importantly, the measured amplitude was found to be more than an order of magnitude greater than the corrugation determined by helium scattering experiments, the latter providing an assessment of the total charge density integrated over all occupied states while STM probes only states at the Fermi level.

The role of solvated ions in the tunneling process has received little attention since these species are unlikely to exist in the junction during atomically resolved imaging. In contrast, ions that are specifically absorbed on either the tip or substrate

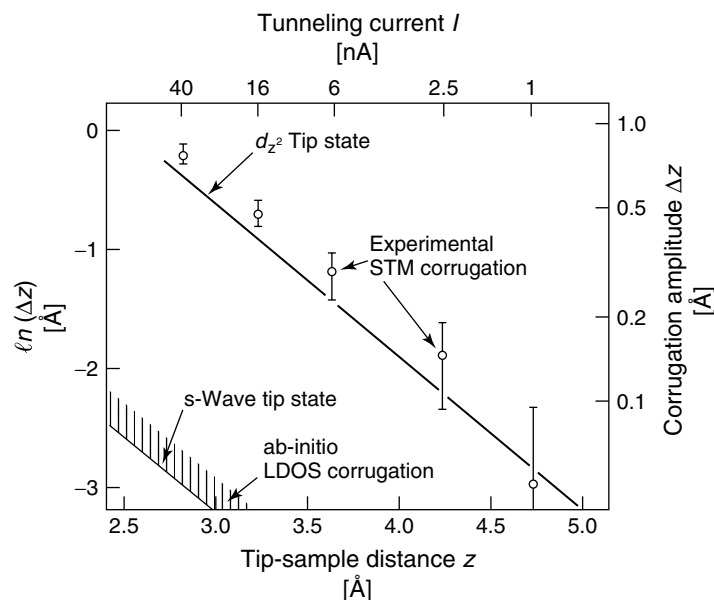


Fig. 5 The corrugation observed while imaging Al(111) is a strong function of tip-sample separation as well as the electronic structure of the tip. Theoretical results for an s and d_{z^2} tip state are shown in comparison with experimental data from Ref. [35] ($V_{\text{bias}} = -50$ mV). (Reprinted with permission from Ref. [3], Copyright 1998 by Cambridge University Press.)

will change the LDOS and the surface dipole thereby altering the distribution of the electrostatic potential within the gap in a manner analogous to the vacuum junctions [37, 38]. In cases in which the atomic resonance of an adsorbate lies far above the Fermi level [37], the adsorbate still contributes to the LDOS due to significant broadening of the resonance upon adsorption. If the size of the orbital is such that it extends considerably further out from the surface than the bare substrate wave functions, it will significantly contribute to image formation [37, 39, 40]. For simple anions adsorbed on metal surfaces, it is generally found that the extension of the orbitals in space is more important to image formation than the energy of the adsorbate orbitals [39, 40]. However, recent studies show that image formation

in such systems can be highly sensitive to the tunneling conductance. As shown in Fig. 6, the image shifts from revealing the anion overlayer to the underlying metal as the tunneling resistance is decreased from 7.2 to 1.7 M Ω . Optimization allows both the ordered halide adlayer and underlying metal to be simultaneously resolved and subsequent Fourier analysis yields information on the geometry of the adsorption site [41]. Similar effects of the imaging conductance have been reported for molecules adsorbed on metallic surfaces. For example, TMPyP on Au(111)-I the iodine underlayer is imaged at tunnel resistance of 5 M Ω while the electron density of TMPyP was observed at 800 M Ω [42]. Careful consideration needs to be given to the effect of tip-induced perturbations and imaging of large molecules, such as

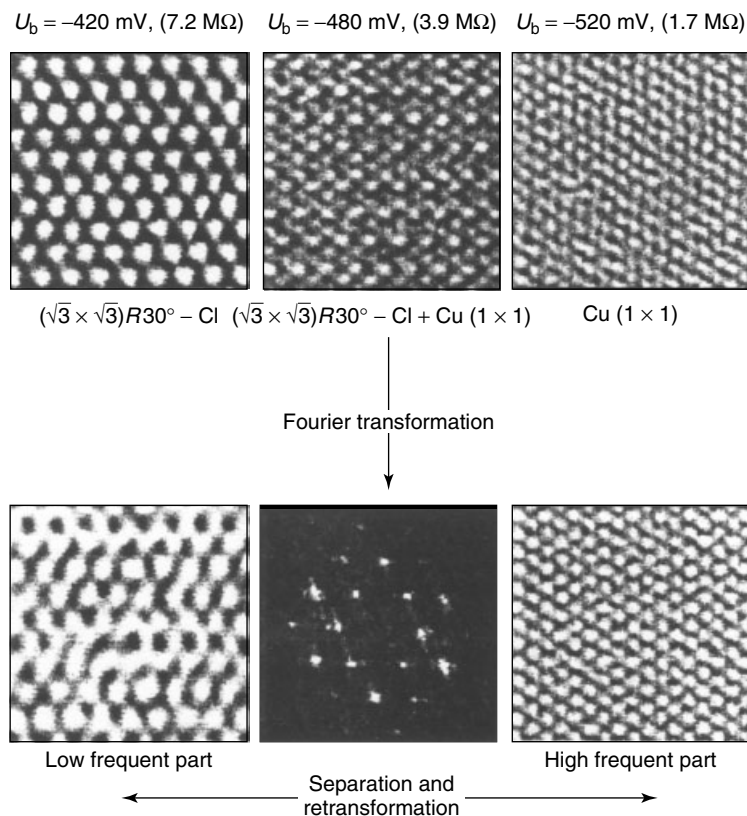


Fig. 6 STM images of Cu(111) in 10 mM HCl showing the dependence of image formation on the tunnel conductance. Fourier analysis of the convoluted images can help identify adsorption sites, $3.8 \text{ nm} \times 3.8 \text{ nm}$, $I_t = 18 \text{ nA}$, $E = -0.550 \text{ V}$ saturated mercurous sulfate electrode (SSE). (Reprinted with permission from Ref. [41], Copyright 1999 by Elsevier.)

extended amphiphile monolayers, in a low perturbation usually requires tunneling impedance in the gigaohm range [43].

Elastic resonant tunneling and/or through bond tunneling has also become a central theme in the interpretation and theoretical development of STM imaging of molecules adsorbed on metal surfaces [2, 3, 39, 44, 45]. Numerous images of molecules adsorbed on metallic surfaces display a likeness to the shape of the highest occupied (HOMO) and lowest unoccupied (LUMO) molecular orbitals of

the molecules. As noted above, this simply reflects the participation of the frontier orbitals in the tunneling process [46]. Since the tunneling probability depends on the LDOS at the Fermi level, the imaging of the adsorbate with a large separation between its electronic states and the Fermi level, $> \sim 0.5 \text{ eV}$, is found not to depend strongly on tunneling bias. In contrast, if the molecule's electronic states are within $\sim 0.5 \text{ eV}$ of the Fermi level strong resonant tunneling may be expected. An elegant example is provided

by the observation of potential-dependent resonant tunneling associated with the LUMO of a redox center embedded in a porphyrin molecules as shown in Fig. 7 [12].

Further progress in understanding atomically resolved STM images requires a close coupling between theory and experiment. The LDOS of many surfaces have been studied by first principle calculations while, in contrast, the lack of detailed knowledge of the geometry and electronic structure of probe tips (outside of vacuum conditions) usually limits a more in depth or sophisticated evaluation of images and the imaging mechanism.

3.1.1.3 Double-layer Overlap and Tip-screening Effects

As the dimensions of the tip–substrate gap change, the contribution of the electrolyte to the tunneling barrier will vary as well its effect on double-layer structure and thereby the dynamics of electrode processes. For typical electrolytes concentrations, 0.01 to 0.1 mol L⁻¹, the dimensions of the tunnel junction are less than the Debye screening length (3 to 1 nm, respectively) and not surprisingly the overlapping double layers of the tip and substrate are severely perturbed [47]. A significant perspective on this problem is provided by a simple calculation that indicates that the electron density emanating 2 to 3 Å from the metal is significantly higher than the ionic density in a 0.1 mol L⁻¹ solution [48]. Strong hydration and resonance forces are known to dominate the junction at this length scale [49], and simultaneous measurement of the force and tunnel conductance, in a manner analogous to prior vacuum experiments [50], should provide further insight into the structural and electronic properties of the immersed tunnel junction (see Volume 1; this series).

Likewise, the influence of the tip screening upon the electrochemical potential of the substrate requires further investigation in order to understand the appropriate conditions for imaging as well as to guide the rational development of various tip-induced surface modification and synthesis schemes [13, 14]. At present, the successful observation of intelligible potential-dependent phase transitions (typically at small tip-sample bias) provides much optimism as to the relevance of analytical in situ STM studies [4–26]. In contrast, studies of metal deposition, dissolution, and oxidation have revealed a strong influence of tip potential, that is, inhibition or catalysis of the respective reaction [51–56]. Electrostatic shielding by the tip can result in a nonuniform current distribution around the junction and the tip may also limit access of metal ions in solution to the growth centers being studied [56, 57]. A particularly easy check for possible imaging related artifacts is to make significant changes in the area being investigated in order to reveal the presence or absence of surface modification. For example, under certain conditions, a marked shielding effect has been noted for copper deposition on Au(111) as shown in Fig. 8 [57]. The potential screening effect also generates a surface tension gradient, which in the case of liquid metals, for example Hg, results in destabilization or “waving” of the junction [58]. For solid metals, similar effects may be responsible for the reported tip-induced lifting of the surface reconstruction of gold, which occurs under certain bias conditions [59, 60]. Thus, the influence of the probe on the electrochemical conditions within the tunnel junction [51–56] remains a significant issue in the development of STM.

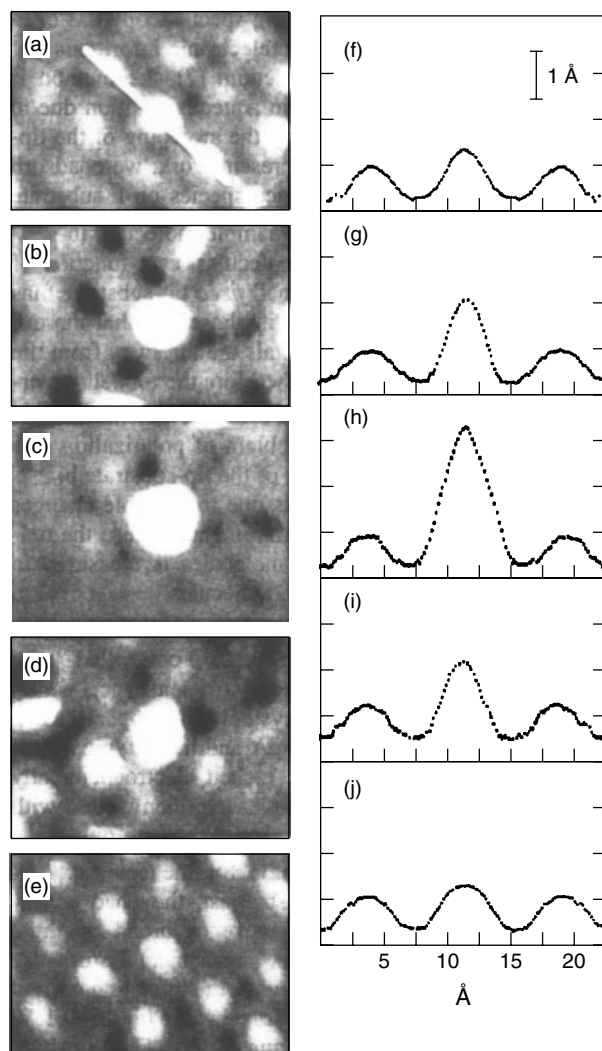


Fig. 7 A demonstration of resonant tunneling is provided by studying the effect of bias on the imaging of an Fe-protoporphyrin IX (Fe-PP) molecule embedded in an ordered array of protoporphyrin IX (PP) molecules. The addition of Fe(III) to the protoporphyrin (Fe-PP) causes little change in the protoporphyrin (PP) energy levels. A quantitative measure of the contribution of various resonant tunneling channels may be obtained by examining the apparent height of the Fe-PP relative to PP as a function of the substrate potential. The substrate was held at (a) -0.15 , (b) -0.30 , (c) -0.42 , (d) -0.55 , and (e) -0.65 V, respectively, (f)–(j) are the corresponding plots of the cross-sections along the white line indicated in (a). (Reprinted with permission from Ref. [12], Copyright 1996 by American Physical Society.)

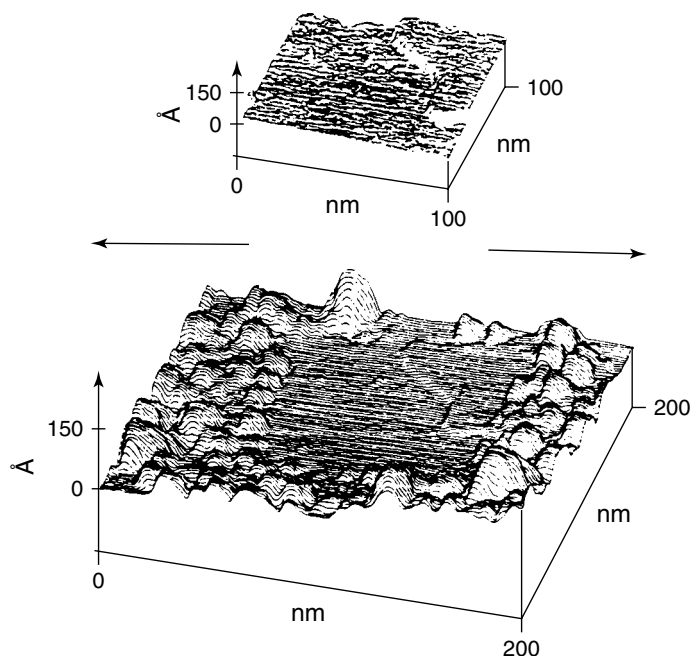


Fig. 8 STM image demonstrating the shielding effect of a positive tip potential on bulk copper deposition on Au(111). Substrate potential ~ -375 versus Cu/Cu^{2+} , in $50\ \mu\text{M}\ \text{CuSO}_4$ and $5\ \text{mM}\ \text{H}_2\text{SO}_4$. (Reprinted with permission from Ref. [57], Copyright 1993 by The Royal Society of Chemistry.)

3.1.2

Experimental Considerations

The relative simplicity and low cost of STM instrumentation has contributed significantly to the rapid increase in the number of in situ electrochemical studies. An excellent discussion of the general aspects of STM design and construction is available in a recent textbook [2, 3]. In the last decade, several reliable instruments have also become available from commercial vendors. The instruments incorporate bipotentiostatic operation, for independent control of the tip and substrate relative to some reference electrode, and, more recently, some degree of atmospheric control is usually implemented. Nevertheless,

optimization of instrument design and construction for electrochemical studies continues with a focus on increased stability, scanning speed, and compatibility with our analytical techniques [36, 61, 62]. Beyond instrumentation, insightful experiments depend on the preparation of a flat, well-defined substrate and the formation of a stable tip capable of atomically resolved imaging. In many respects, the ability to reliably produce high-quality noble metal electrodes outside UHV has been central to success of most electrochemical STM studies [4–26, 63–65]. In contrast, our knowledge of the structure, chemistry, and operation of the immersed probe tip may be optimistically viewed as a slowly advancing art form.

3.1.2.1 Electrochemical Cell

As with any experiment, the design and construction of an electrochemical cell derives from consideration of the system being examined. Potential sources of contamination must be carefully evaluated. In commercial cells, inert materials such as Teflon and Kel-F are typically used for electrolyte containment while a hanging meniscus cell has also been explored [66]. Good electrochemical engineering practice requires proper consideration to be given to the current distribution in the electrochemical cell. The theory for treating this problem is well developed although the important screening effects associated with the tip–substrate geometry have just begun to be examined [51–57] as noted earlier.

Experiments may be performed in either separated or unseparated cells, which typically have an electrolyte volume in the range of 0.1 to 1 mL, although larger cells have been used. A typical (unseparated) cell, for example, Fig. 4, is composed of a platinum wire counterelectrode, and a simple reference electrode, such as metal/metal ion, metal/metal hydride, metal/metal oxide, and/or Ag/AgCl/Cl[−]. To date, unseparated cells have proven to be remarkably effective although care must be given to possible interference and/or contamination effects between the various electrodes. When a quasi-reference (metal wire) electrode is used, it is usual practice to compare the voltammetric results obtained in the unseparated STM cell with that obtained in a conventional cell in order to verify the accuracy and precision of the potential scale.

In many early STM studies, limited effort has been made to control the atmosphere within the electrochemical cell, yet oxygen is known to exert a major role in the chemistry and corrosion of many

transition metals. For example, the copper/copper ion reference electrode has been widely used despite the electrode being polarized from its reversible condition by oxygen, which leads to significant dissolution [67]. Such effects become significant in studies of metal deposition and dissolution reactions at small overpotentials where precise knowledge of the supersaturation is important for detailed analysis. Oxygen reduction also complicates voltammetric analysis and may obscure certain adsorption reactions, as well as alter the surface chemistry of the system being investigated. Thus, deaeration of electrolytes prior to use and blanketing the cell with inert gas during the experiment has become a standard in most laboratories. In a similar vein, isolation from water is critical for stable operation in many nonaqueous and molten salt experiments.

Accurate atomically resolved STM studies require stable thermal conditions otherwise differential thermal expansion and contraction of the various components of the device will lead to significant image distortion or “drift”. Thus, it is usual practice to isolate the microscope from convective air currents associated with most laboratory environments. Furthermore, following assembly or sample exchange, it is important to allow the device to thermally equilibrate prior to performing an experiment. Another potential source of image drift may be associated with slow relaxation of the mechanical devices used to position the sample and/or scanner. For example, coarse positioning in many microscopes incorporates fine-pitch screws, which have a certain degree of backlash associated with their operation. Wobbling the screws at their final setting may be effective in reducing this effect. The slow relaxation of the tip/sample positioning

devices along with thermal perturbations account for much of the commonly observed drift as well as its diminution with time-following device assembly.

3.1.2.2 Tip Selection and Preparation

The tip is the source of the greatest uncertainty in STM as a result of a combination of its ill-defined structure and electronic properties as well as instability associated with interactions with the sample, electrolyte, and/or surface contaminants. Almost any conductive material may be used as a tip although electrochemical studies have largely focused on Pt, Pt–Ir, Ir, and W wire, which may be easily fashioned into tips by etching or mechanical fracture. In the mechanical processes, the tip is formed by either cutting the wire at 45° with pliers or straining the wire to failure in tension. Tips have also been prepared by mechanical polishing [68]. In the case of etching, a wide variety of electrochemical methods have been used ranging from ac to dc processes. A summary of the appropriate etching conditions for a variety of materials is available [2, 3, 16, 69]. Etching of W in KOH and Pt–Ir in CaCl₂ solutions appears to be the most extensively used. Interestingly, the final apex may be formed by chemo-mechanical fracture of the narrowing ligament that forms during etching. The precision of the process is dependent on the design of the electrochemical cell and sample geometry. In certain protocols, the fractured apex receives a final polishing step. Bipotentiostatic operation during STM enables the tip to be biased in a potential regime that minimizes faradaic processes occurring at the tip. However, many studies are now performed under conditions of constant tunneling bias in which the former conditions are not necessarily fulfilled. The faradaic component of the tip current is

minimized by coating the tip with an insulating coating, such that the residual background current in inert electrolytes is at least below 0.1 nA. A wide variety of coatings have been developed ranging from inorganic glasses to polymers [16]. However, the pace of development has slowed with most papers reporting the use of either a piezon wax or polyethylene. Typically, the coating is applied by immersion of the tip in the liquid phase followed by controlled removal while monitoring the solidification or glass transition process [16, 70, 71]. In another procedure, the tip is rotated about its axis while molten wax is transferred to the tip from an adjacent heated wire. An alternative scheme involves electrophoretic painting of the coating followed by subsequent polymerization [72]. The effectiveness of any coating may be examined by monitoring the voltammetric response of the ultramicroelectrode tip in an electrolyte containing a well-defined redox couple. Estimates of the exposed or electroactive area of the coated tip range from 10 μm down to ~10 nm. Finally, in some studies, substrate contamination as a result of degradation of tip coating material has been noted and this possibility must always be carefully considered, particularly as experiments move beyond simple, well-studied aqueous electrolytes. Currently, the figure of merit defining a suitable tip is simply the demonstrated ability to obtain atomically resolved images of graphite or a noble metal. One not uncommon problem is the formation of ghost images, usually of steps, due to tunneling from multiple points on the tip, that is, the “double-tip effect”. This effect may dissipate with scanning although tip replacement is usually required.

Although some effort has been made to formalize the engineering of tips, the

scientific foundation for the etching, coating, and characterization of the tips has hardly progressed in the last 10 years [16]. In UHV experiments, a variety of post-etch treatments have been used to ensure that the tip is well formed as well as oxide- or contamination-free. In contrast, exposure of the commonly used tungsten tip to an electrolyte and air results in the formation of a hydrated WO_3 -based oxide. It is worthwhile to note that freshly etched W tips typically do not provide atomically resolved imaging when first engaged in UHV studies [2]. Rather, effective imaging usually begins spontaneously after repeated tunneling and/or scanning, although the onset occurs in an unpredictable way. A variety of phenomena ranging from oxide removal to transfer of material from the substrate have been used to rationalize this observation. In a similar manner, optimal image resolution in some of the earliest *in situ* STM studies was associated with copper deposition on the W tip [21, 73]. This effect in combination with other reports suggests that controlled alteration of the surface chemistry of the tip may be a profitable way to probe the electronic structure of the tunnel junction [39].

3.1.2.3 Substrate Preparation

Atomically resolved STM studies require preparation of a flat surface with well-defined crystallography. Studies to date have focused on either single-crystal or highly textured thin film noble metal electrodes. The traditional approach to single-crystal preparation involves growing an ingot or boule by solidification from a melt using a seed crystal to control the orientation. Alternatively, a remarkably simple and inexpensive technique has been developed whereby a H_2 - O_2 flame is used to melt the end of a polycrystalline

noble metal wire and then allowing the grain at the end of the wire to seed subsequent crystallization during solidification of the molten sphere [63–65]. By allowing the bead to solidify slowly, followed by remelting and/or annealing, symmetric facets develop that reveal the formation and orientation of a single crystal. This method has been widely used for producing gold and platinum electrodes and, more recently, has been extended to other noble metals such as Rh, Pd, and Ag [74]. Thin film deposition methods, such as e-beam evaporation and sputtering, provide another avenue for producing flat, highly oriented thin films. The substrate and deposition conditions exert a major influence on the evolution of roughness and texture during film growth. Highly textured (111) fcc crystals [75] may be grown by vapor deposition on freshly cleaved mica while (100) fcc textured films may be obtained by evaporation on a variety of substrate with cubic symmetry, and so forth. [76]. Bulk single crystals as well as thin films may also be prepared by the electrolytic deposition. For example, a capillary-growth technique has been used extensively in the study of the deposition and dissolution of silver [77, 78].

Electrochemical studies of solid electrodes require that the surface be routinely restored to its original conditions. Flame annealing, in which the noble metal surface is annealed in a hydrogen-oxygen flame, has proven to be particularly convenient for rapidly refurbishing crystals. This method has been used for thin film electrodes [79] as well as bulk crystals [63–65, 79–81]. Crystal quality is a sensitive function of the cooling procedure with slow cooling in air or inert gas being recommended over rapid quenching in water [3, 4, 82]. Alternatively, furnace annealing or

resistive heating under a controlled atmosphere may be used. For reactive materials, control of the partial pressure of the gas phase species is critical to providing a clean surface. Electrochemical or chemical polishing may be used as an alternative, or additional step, to thermal annealing. This method has found wide application in the preparation of copper electrodes. However, it is important to note that the different preparation methods can lead to different mesoscopic structures, for example, step bunching, that depend on specific procedures employed.

3.1.3

Applications

3.1.3.1 Imaging Two-dimensional Structures

STM has been used to reveal the structure of several noble metals and ordered adlayers, such as anions and/or underpotential deposited metals. At low coverages, the anion adlayers appear to be disordered, (or a two-dimensional lattice gas) since surface X-ray scattering and STM reveal only the ordered electron density associated with the underlying metal lattice. At more positive potentials, a critical value is reached in which the adlayer transforms into an ordered structure. This typically corresponds to anion coverage of ~70 to 80% of the saturation value. The potential dependence of adlayer structure may be followed by performing potential step or sweep experiments in which discontinuities in the STM image dimensions and symmetry become readily apparent ("composite-domain" imaging [4–26]) A representative example is shown in Fig. 9. This method, in combination with that outlined in Fig. 6, may be helpful for determining adsorbate–substrate registry [4–26, 83]. The ordered adlayer

may form commensurate, incommensurate, or higher-order commensurate structures. Incommensurate structures usually exhibit potential-dependent in-plane dimensions as a consequence of electrocompression [83, 84]. In comparing surface X-ray diffraction and STM, the precision of lattice parameter measurements by surface X-ray diffraction greatly exceeds that associated with STM due to thermal drift and imperfect calibration of the piezoelectric drives. However, the mismatch between the substrate and the incommensurate adlattice usually creates a long-range modulation or Moiré pattern, such as that shown in Fig. 9 for bromide adsorption on Au(111), which may be used for a reasonably accurate view of in-plane dimensions [83]. The relationship between the superlattice period, Λ , of the Moiré pattern, the lattice spacing of the overlayer, a , and substrate, b , and the rotation angle between them, Ω , [83] is given by

$$\Lambda = \frac{ab}{\sqrt{a^2 + b^2 - 2ab \cos \Omega}} \quad (3)$$

Images may be analyzed by approximating the adlattice structure as a high-order commensurate overlayer and comparing the result with the simulated Moiré patterns. Reasonable agreement with the X-ray data for electrocompression has been found for the case of bromide adsorption on Au(111) [83]. Similar effects have been extensively investigated for other noble metal–anion systems, for example, Au–I, [6, 7].

Not surprisingly, ordered metal adlayers exhibit many of the characteristics already noted for anion adsorption such as electrocompression, Moiré patterns, faceting transitions, as well as additional effects such as two-dimensional alloying [4–26]. Of course, for many ordered upd systems, structural assignment of the imaged

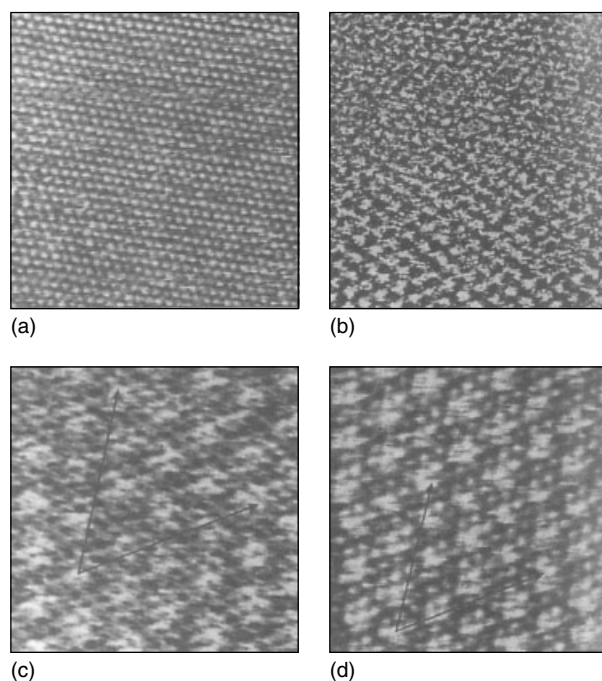


Fig. 9 STM images revealing the formation of a sequence of ordered hexagonal bromide adlayers on Au(111) in 1 mM NaBr + 0.1 M HClO₄. ((a, c, d) 8.0 nm × 8.0 nm (b) 6.5 nm × 6.5 nm) (a) At 0.44 V only the Au substrate is visible; (b) Upon increasing the potential from 0.48 V (upper edge of image) to 0.59 V (lower edge), a rotated-hexagonal bromide adlayer is formed; (c) A Moiré pattern is evident as a result of the mismatch between the adlattice and the substrates; (d) The dimensions of the pattern change as the potential (coverage) is increased from 0.59 to 0.74 V (c, d). (Reprinted with permission from Ref. [83], Copyright 1996 by American Chemical Society.)

electron density can be particularly difficult due to coadsorption. This was clearly demonstrated for Cu upd on Au(111) in H₂SO₄ where resolution of the multi-component coadsorbed “ $\sqrt{3} \times \sqrt{3} R^{30}$ ” Cu/SO₄[−] “honeycomb” adlayer structure required corroborating evidence in order to assign tunneling contrast to atomic species [4, 5, 10, 17, 19, 21, 24]. More recently, the composition and structure of the mixed (HSO₄[−], SO₄^{2−})/(H₃O⁺, H₂O) layer on Au(111), Pt(111), Rh(111),

and Cu(111) has been resolved using the same strategy; Refs. [4, 7, 41] and reference therein.

3.1.3.2 Imaging Surface Dynamics

One of the most important attributes of STM is the ability to quantitatively evaluate the rate parameters associated with various surface processes. The dynamics of individual surface atoms, that is, terrace and step edge diffusion, have been monitored with STM, although for many

processes of technical interest, the rate of individual atomic events often exceeds the response time of conventional instruments. Information obtained under such conditions represents the convolution of the surface dynamics with the imaging raster [8]. A number of strategies have been pursued to surmount this problem. The most obvious is performing experiments at lower temperatures at which the processes of interest become coincident with the instrumental response. More challenging is the construction of faster microscopes. Recently, a video rate STM capable of acquiring ~ 25 atomic resolution images per second was described [61]. The instrument was used to image the dynamics of individual kinks as shown in Fig. 10. Other novel imaging modes that allow the direct observation of individual atomic events have also been reported in UHV-STM. The “atom tracker” technique employs lateral-positioning feedback to lock the STM probe tip into position above a selected atom with sub-Angstrom precision [85]. This device has been used to follow the random walk of surface species whereby the temporal resolution is increased by a factor $\sim 10^3$ over conventional STM imaging techniques. Care must be taken to avoid tip-induced artifacts in such measurements. Alternative approaches to increase time resolution involve experimental design combined with developments in the statistical physics of surface transport at the mesoscopic length scale [8, 86, 87]. Time resolution is en-

hanced by reducing the dimensionality of the experiment by disabling the y-raster to follow the movement of well-defined one-dimensional surface features, for example, an array of steps [8]. This extremely powerful methodology has revealed much about the kinetics and mechanisms of surface transport in both vacuum and more recently in electrolytes. Phenomena ranging from equilibrium step fluctuations [8, 86, 87], to roughness evolution during film growth [88, 89] to surface alloy formation [89, 90], and so forth, have been successfully examined from both a theoretical and experimental perspective. In particular, comparison between scaling and spectral analysis of experimental images and simulations has been used to infer the underlying atomic mechanisms. For example, thermally driven equilibrium

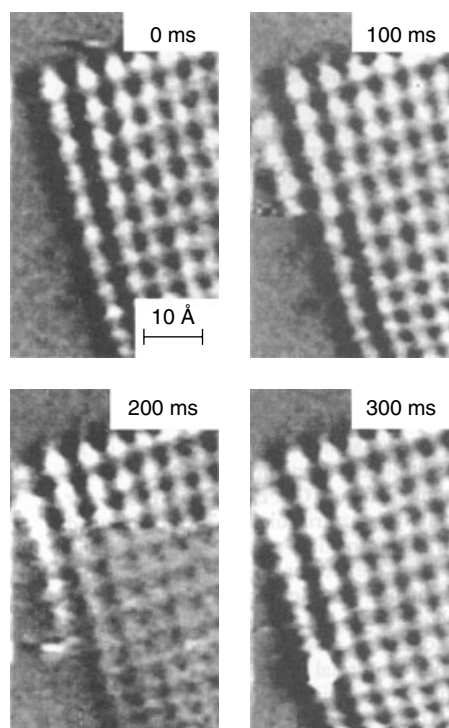


Fig. 10 Video-STM sequence of Cu(100) in 0.01 M HCl solution at -0.23 V SCE. The image shows the nucleation and rapid growth of an individual ad-row from the corner of an island. (Reprinted from Ref. [61], Copyright 1999 by The Electrochemical Society.)

step fluctuations have been observed for both Ag and Cu surfaces in both vacuum and electrolytes [8]. As shown in Fig. 11, the steps on an immersed Ag(111) actually appear to be “frizzy” due to kink motion, which is rapid compared to the tip raster speed [8, 91, 92]. In $x-t$ images, the fluctuations can be quantitatively analyzed by means of a step correlation function, $G(t) = \langle [x(t) - x(0)]^2 \rangle$, where x defines the step position at a particular time, t . If image drift is a problem, the step pair correlation function may be used [8, 93]. The evolution of the correlation function and its dependence on step spacing is a reflection of the mass transport mechanism, which is dependent on both the potential and electrolyte composition. Furthermore, an assessment of the temperature dependence of the fluctuations allows the activation energy of the rate-limiting process to be evaluated. As shown in Fig. 11,

the step fluctuations for Ag(111) in a sulfuric acid electrolyte increase markedly as the potential is moved towards the reversible value of the Ag/Ag^+ electrode [8, 91, 92]. At negative potentials, the fluctuations follow a $t^{0.25}$ power law independent of step spacing, which is similar to that observed in vacuum studies. This suggests that the electrolyte exerts negligible influence on mass transport along step edges. In contrast, at higher potentials, a $t^{0.5}$ power law is observed with the fluctuations being dependent on step separation as shown in Fig. 11. This is rationalized in terms of the exchange of ad-atoms between steps and terraces as well as transfer between the terraces and electrolyte. These fluctuations amplify sharply as the reversible potential for Ag/Ag^+ is approached [8, 91, 92].

More recently, the strong influence of anion adsorption on surface transport has been quantitatively evaluated in this

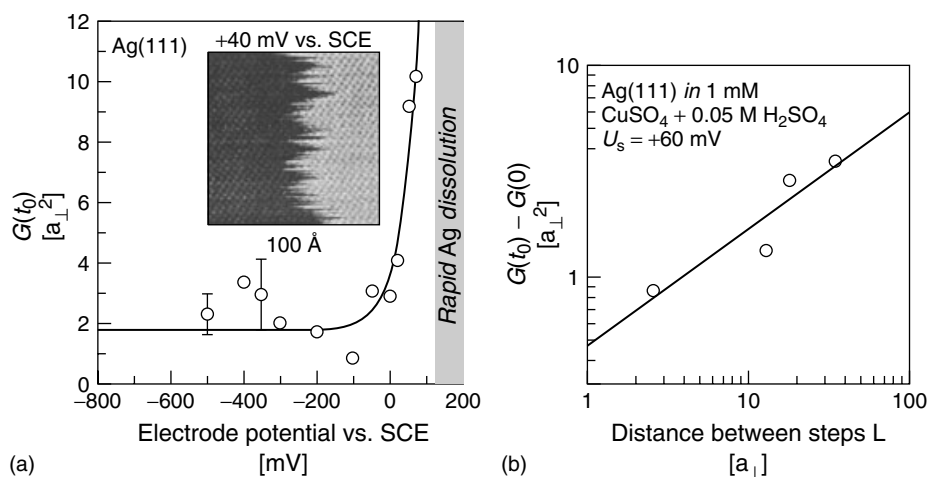


Fig. 11 (a) The influence of potential on step fluctuation, $x(t)$, may be described by means of a time correlation function $G(t)$. At negative potentials, fluctuations are due solely to mass transport along the steps while at more positive potentials, the magnitude of the fluctuation increases rapidly. This is attributed to the onset

of ad-atom exchange with terraces as well as the electrolyte, which occurs even at the potential well below the reversible value for Ag/Ag^+ . (b) The fluctuations in the latter case are dependent on step spacing. (Reprinted from Ref. [8], in press, Elsevier.)

manner [8, 93]. Analysis of the influence of chloride on step fluctuations on Au(111) in sulfuric acid suggests that the adsorption of halide at the steps yields enhanced mobility to kink diffusion. It has been recognized that analysis of the effect of adsorbates is complicated by the fact that the anions as well as metal ad-atom may be the mediating species [8, 93].

The methods outlined above focus on measuring changes in the step position to derive information about the kink mobility. More recently, a method known as “*time of walk, (TOW)*,” has been developed for the direct observation of kink migration [62]. In this instance, enhanced time resolution is gained by repetitive line scanning, at two locations along a step separated by a distance Δy . The passage of a kink is indicated by a displacement of Δx thereby allowing the average velocity to be determined. This method is particularly effective for characterizing systems that exhibit strong step faceting. Average kink propagation and reaction rates in the range of 10^3 and 10^5 atom/s have been measured for Cu(100) in hydrochloric acid giving the first direct glimpse of the exchange process that characterizes ion-transfer reaction at small overpotentials [62].

3.1.3.3 Morphological Evolution during Phase Transitions

The STM has been widely employed for examining a wide range of phase transitions, such as potential-induced reconstruction, adsorption, underpotential deposition and overpotential deposition, oxide formation, etching, and so on [4–26] (see Volume 1, 4, and 10 of this series). Most of these studies involved stepping or sweeping the potential of a fresh electrode into a regime in which the phase transition occurs and imaging the evolution of the surface. Phenomena ranging from step faceting and

island ripening to strain relief and alloy formation have been studied. The important role of site bias in the nucleation and subsequent morphological evolution has also been examined. Likewise, studies that probe the transition from two- to three-dimensional growth in both homo- and heteroepitaxial growth as well as the effect of electrolyte additives on growth have been widely reported [94–96]. Importantly, the high z -resolution of the STM permits detection of single misfit dislocation glide lines making STM a highly precise tool for studying strain accommodation [97]. Images of strained overlayer structures and misfit accommodation during electrodeposition have been published [68, 98]. Many other wonderful examples of the utility of STM may be found in the literature [4–26].

In summary, STM studies represent a central element in the convergence of theory, simulation, and experiment that enables the impact of individual rate processes on the evolution of the surfaces and their reactivity to be evaluated. This represents a timely opportunity for electrochemists to examine many long-standing questions concerning the interplay between electrode structure and electrochemical kinetics.

3.1.3.4 Surface Modification

In addition to its role as a surface analytical technique, STM has proven to be a unique tool for the synthesis of novel structures ranging from cluster deposition to positioning of single atoms. In vacuum studies, tip-sample interactions have generally been attributed to the influence of atomic forces, the electric field and/or the tunneling current [99]. In addition to these “physical” interactions, the tip may also be used to alter the local electrochemical conditions within the tunnel junction. Three

different tip-directed schemes have been reported for producing small clusters and nanometer features electrochemically. In the first method, the material of interest is first concentrated by overpotential deposition on the tip and subsequently transferred to the substrate by bringing the tip into close proximity at which a “jump to contact” between the tip and sample occurs. When the tip is retracted, the connecting neck breaks leaving a cluster behind [3, 4, 14]. In a second method, the material concentrated on the tip is dissolved electrochemically into the tunnel junction at which the constraint of geometry and applied potential result in deposition on the immediately adjacent substrate area. In certain cases, deposition on the substrate is further constrained by defects induced by prior tip–substrate interactions [13]. A third electrochemical modification scheme involves using a two-electrode STM. When operated under humid ambient conditions, a thin layer of water may be adsorbed on the surface, which effectively creates an electrochemical cell between the tip and substrate. In comparison to the operation of a conventional SECM immersed in an electrolytic solution, the geometry of the cell formed by the thin layer of water confines or limits the surface modification to the tens of nanometer range. To date, this scheme has been largely used to perform etching and anodization [100, 101].

References

1. G. Binnig, H. Rohrer, *Rev. Mod. Phys.* **1987**, 56, 615.
2. C. J. Chen, *Introduction to Scanning Tunneling Microscopy*, Oxford University Press, New York, 1993.
3. R. Wisendanger, *Scanning Probe Microscopy and Spectroscopy, Methods and Applications*, Cambridge University Press, Cambridge, UK, 1998.
4. D. M. Kolb, *Angew. Chem., Int. Ed.* **2001**, 40, 1162.
5. D. M. Kolb, *Electrochim. Acta* **2000**, 45, 2387.
6. M. J. Weaver, X. Gao, *Annu. Rev. Phys. Chem.* **1993**, 44, 459.
7. K. Itaya, *Prog. Surf. Sci.* **1998**, 58, 121.
8. M. Giesen, *Prog. Surf. Sci.* **2001**, 68, 1–153.
9. D. J. Trevor, C. E. D. Chidsey, D. N. Loiacono, *Phys. Rev. Lett.* **1989**, 62, 929.
10. O. M. Magnussen, J. Hotlos, R. J. Nichols et al., *Phys. Rev. Lett.* **1990**, 64, 2929–2932.
11. S. L. Yau, C. M. Vitus, B. C. Schardt, *J. Am. Chem. Soc.* **1990**, 112, 3677.
12. N. J. Tao, *Phys. Rev. Lett.* **1996**, 76, 4066.
13. R. M. Nyffenegger, R. M. Penner, *Chem. Rev.* **1997**, 97, 1195.
14. D. M. Kolb, R. Ullmann, T. Will, *Science* **1997**, 275, 1097.
15. P. Allongue in *Advances in Electrochemical Science and Engineering* (Eds.: H. Gersischer, C. W. Tobias), VCH Publishers, New York, 1995, Vol. 1.
16. H. Siegenthaler, *STM in Electrochemistry in Scanning Tunneling Microscopy II* (Eds.: R. Wiesendanger, H. J. Gunterodt), Springer-Verlag, New York, 1992.
17. A. A. Gewirth, H. Siegenthaler, (Eds.), *Nanoscale Probes of the Solid/Liquid Interface*, NATO ASI Series E, Kluwer Academic Publishers, Boston, Mass., 1995, Vol. 288.
18. W. J. Lorenz, (Ed.), *Electrochim. Acta* **1995**, 40, 10.
19. D. Kolb, (Ed.), *Electrochim. Acta* **1995**, 40, 1.
20. E. Budevski, G. Staikov, W. J. Lorenz, *Electrochemical Phase Formation and Growth*, VCH Publishers, New York, 1996.
21. A. S. Dakkouri, M. Dietterle, D. M. Kolb, *Adv. Solid State Phys.* **1997**, 36, 1.
22. A. A. Gewirth, B. K. Niece, *Chem. Rev.* **1997**, 97, 1129.
23. W. J. Lorenz, W. Plieth, (Eds.), *In-situ Local Probe Techniques for Studies of Electrochemical Interfaces*, Wiley-VCH, New York, 1998.
24. A. Dakkouri, D. M. Kolb, (Eds.), *Electrolytic Metal Deposition: Fundamental Aspects and Applications*, 5. Ulmer Electrochemische Tage, R. Uldenbourg Verlag, Munchen, 1999; This is reprinted from Zeitschrift fur Physikalische Chemie, Bd. 208 1999.
25. T. P. Moffat, *Electroanal. Chem.* **1999**, 21, 211.

26. J. Lipkowski, P. N. Ross, (Eds.), *Imaging of Surfaces and Interfaces*, Wiley-VCH, New York, 1999.
27. P. K. Hansma, J. Tersoff, *J. Appl. Phys.* **1987**, 61, R1.
28. W. Schmickler, *Chem. Rev.* **1996**, 96, 3177.
29. A. Vaught, T. W. Jing, S. M. Lindsay, *Chem. Phys. Lett.* **1995**, 236, 306.
30. W. Schmickler, D. Henderson, *J. Electroanal. Chem.* **1990**, 290, 283.
31. S. P. Sharma, J. H. Thomas, *J. Vac. Sci. Technol.* **1977**, 14, 825.
32. M. Salmeron, L. Xu, J. Hu et al., *MRS Bull.* **1997**, 22, 8, 36.
33. F.-R. F. Fan, A. J. Bard, *Science* **1995**, 270, 1850.
34. S. Ciraci, E. Tekman, A. Baratoff et al., *Phys. Rev. B* **1992**, 46, 10 411.
35. J. Wintterlin, J. Wiechers, H. Brune et al., *Phys. Rev. Lett.* **1989**, 62, 59–62.
36. M. Wilms, M. Kruft, G. Bermes et al., *Rev. Sci. Instrum.* **1998**, 69, 2696.
37. D. M. Eigler, P. S. Weiss, E. K. Schweizer et al., *Phys. Rev. Lett.* **1991**, 66, 1189.
38. W. Schmickler, *J. Electroanal. Chem.* **1990**, 296, 283.
39. P. Sautet, *Chem. Rev.* **1997**, 97, 1097.
40. P. Sautet, *Surf. Sci.* **1997**, 374, 406.
41. P. Broekmann, M. Wilms, M. Kruft et al., *J. Electroanal. Chem.* **1999**, 467, 307.
42. M. Kunitake, N. Batina, K. Itaya, *Langmuir* **1995**, 11, 2337.
43. G. E. Poirier, *Chem. Rev.* **1997**, 97, 1117.
44. R. Guckenberger, T. Hartmann, W. Wieg-rabe et al. in *Scanning Tunneling Microscopy II* (Eds.: R. Wisendanger, H. J. Guntherodt), Springer-Verlag, New York, 1992.
45. C. Joachim, P. Sautet in *Scanning Tunneling Microscopy and Related Methods* (Eds.: R. J. Behm, N. Garcia, H. Rohrer), NATO ASI Series, Kluwer Academic Publishers, Norwell, Mass., 1990.
46. S. Chiang in *Scanning Tunneling Microscopy I* (Eds.: H. J. Gunterodt, R. Wisendanger), Springer-Verlag, New York, 1992.
47. D. Henderson, K.-Y. Chan, *J. Electroanal. Chem.* **1992**, 330, 395.
48. W. Schmickler in *Nanoscale Probes of the Solid/Liquid Interface* (Eds.: A. A. Gewirth, H. Siegenthaler), NATO ASI Series E, Kluwer Academic Publishers, Boston, Mass., 1995, pp. 5–24, Vol. 288.
49. R. Wisendanger, H. J. Guntherodt, (Eds.), *Scanning Tunneling Microscopy III*, Springer-Verlag, New York, 1993.
50. U. Durig, O. Zuger, B. Michel et al., *Phys. Rev. B* **1993**, 48, 1711.
51. X.-P. Gao, M. J. Weaver, *J. Electroanal. Chem.* **1994**, 367, 259.
52. N. Breuer, U. Stimming, R. Vogel, *Electrochim. Acta* **1995**, 40, 1401.
53. S. A. Hendricks, Y. T. Kim, A. J. Bard, *J. Electrochem. Soc.* **1992**, 139, 2818.
54. A. M. Bittner, J. Wintterlin, G. Ertl, *Surf. Sci.* **1997**, 376, 267.
55. Y.-Q. Li, O. Chailapakul, R. M. Crooks, *J. Vac. Sci. Technol., B* **1995**, 13, 1300.
56. J. Divisek, B. Steffer, U. Stimming et al., *J. Electroanal. Chem.* **1997**, 440, 169.
57. N. Batina, D. Kolb, *The Liquid/Solid Interface at High Resolution*, Faraday Discussions, The Royal Society of Chemistry, London, 1992, pp. 93–106, Vol. 94.
58. J. F. T. Conroy, K. Caldwell, C. J. Bruckner-Lea et al., *J. Phys. Chem.* **1996**, 100, 18 222.
59. J. Buisset, H.-P. Rust, E. K. Schweizer et al., *J. Vac. Sci. Technol., B* **1996**, 14, 1117.
60. J. H. Schott, H. S. White, *Langmuir* **1992**, 8, 1955.
61. L. Zitzler, B. Gleich, O. M. Magnussen et al., Proc. Electrochem. Soc. in *Localized In Situ Methods for Investigating Electrochemical Interfaces*, Eds.: A. C. Hillier, M. Seo and S. R. Taylor, Electrochemical Society, Washington, 1999, p. 38, Vol. 99-28.
62. O. M. Magnussen, M. R. Vogt, *Phys. Rev. Lett.* **2000**, 85, 357.
63. J. Clavilier, R. Faure, G. Guinet et al., *J. Electroanal. Chem.* **1980**, 107, 205.
64. J. Clavilier, *J. Electroanal. Chem.* **1980**, 107, 211.
65. A. Hamelin in *Modern Aspects of Electrochemistry* (Eds.: B. E. Conway, R. E. White, J. O'M. Bockris), Plenum Press, New York, 1985, pp. 1–101, Vol. 16.
66. C. P. Wade, H. Luo, W. L. Dunbar et al., *MRS Symp. Proc. V 451*, MRS Pittsburgh, Pittsburgh, Pa., 1997.
67. L. H. Jenkins, U. Bertocci, *J. Electrochem. Soc.* **1965**, 112, 517.
68. A. M. Bittner, J. Wintterlin, G. Ertl, *Surf. Sci.* **1997**, 376, 267.
69. A. J. Melmed, *J. Vac. Sci. Technol., B* **1991**, 9, 601.
70. L. A. Nagahara, T. Thundat, S. M. Lindsay, *Rev. Sci. Instrum.* **1989**, 60, 3128.

71. B. Zhang, E. Wang, *Electrochim. Acta* **1994**, 39, 103.
72. C. E. Bach, R. J. Nichols, W. Beckmann et al., *J. Electrochem. Soc.* **1993**, 140, 1281.
73. R. J. Nichols, W. Beckmann, H. Meyer et al., *J. Electroanal. Chem.* **1992**, 330, 381.
74. K. Sashikata, N. Furuya, K. Itaya, *J. Vac. Sci. Technol., B* **1991**, 9, 457.
75. G. L. Borges, M. G. Samant, K. Ashley, *J. Electrochem. Soc.* **1992**, 139, 1565.
76. J. W. Matthews, (Ed.), *Epitaxial Growth*, Volume A and B, Academic Press, New York, 1975.
77. M. Hopfner, W. Obretenov, K. Juttner et al., *Surf. Sci.* **1991**, 248, 225.
78. W. Obretenov, M. Hopfner, W. J. Lorenz et al., *Surf. Sci.* **1992**, 271, 191.
79. T. Will, M. Dietterle, D. M. Kolb, pg. 137–162 in Ref. 17.
80. M. Dietterle, T. Will, D. M. Kolb, *Surf. Sci.* **1995**, 342, 29.
81. R. Gomez, M. J. Weaver, *J. Electroanal. Chem.* **1997**, 435, 205.
82. N. Batina, A. S. Dakkouri, D. M. Kolb, *J. Electroanal. Chem.* **1994**, 370, 87.
83. O. M. Magnussen, B. M. Ocko, J. X. Wang et al., *J. Phys. Chem.* **1996**, 100, 5500.
84. M. F. Toney, J. G. Gordon, G. L. Borges et al., *Phys. Rev. B* **1994**, 49, 7793.
85. B. S. Swartzentruber, *Phys. Rev. Lett.* **1996**, 76, 459.
86. E. D. Williams, *Surf. Sci.* **1994**, 299/300, 502.
87. A. Pimpinelli, J. Villain, D. E. Wolf et al., *Surf. Sci.* **1993**, 295, 143.
88. A.-L. Barabasi, H. E. Stanley, *Fractal Concepts in Surface Growth*, Cambridge University Press, New York, 1995.
89. R. Q. Hwang, M. C. Bartelt, *Chem. Rev.* **1997**, 97, 1063.
90. H. Ibach, M. Giesen, T. Flores et al., *Surf. Sci.* **1996**, 364, 453.
91. M. Dietterle, T. Will, D. M. Kolb, *Surf. Sci.* **1995**, 327, L495.
92. M. Giesen, M. Dietterle, D. Stapel et al., *Surf. Sci.* **1997**, 384, 168.
93. M. Giesen, D. M. Kolb, *Surf. Sci.* **2000**, 468, 149.
94. F. A. Mollers, O. M. Magnussen, R. J. Behm, *Phys. Rev. Lett.* **1996**, 5249, Vol. 77.
95. S. Morin, A. Lachenwitzer, O. M. Magnussen et al., *Phys. Rev. Lett.* **1999**, 83, 5066.
96. R. Nichols, pg. 99 in Ref. 26.
97. N. Frank, G. Springholz, G. Bauer, *Phys. Rev. Lett.* **1994**, 73, 2236.
98. M. Dietterle, T. Will, D. M. Kolb, *Surf. Sci.* **1998**, 396, 189.
99. P. Avouris, *Acc. Chem. Res.* **1995**, 28, 95.
100. C. Lebreton, Z. Z. Wang, *J. Vac. Sci. Technol., B* **1996**, 14, 1356.
101. K. Matsumoto, M. Ishii, K. Segawa, *J. Vac. Sci. Technol., B* **1996**, 14, 1331.

3.2 Electrochemical-AFM

*Julie V. Macpherson
University of Warwick, Coventry, United
Kingdom*

3.2.1 Introduction

The advent of the scanned probe microscope (SPM) [1], such as the atomic force microscope (AFM) and the scanning tunneling microscope (STM), has greatly enhanced our understanding of the structure and reactivity of interfaces at the solid–liquid interface. This comprehension stems primarily from the unprecedented spatial resolution offered by these devices; atomic resolution images of well-defined surfaces in ultrahigh vacuum (UHV), air, and even under solution are routinely observed. Such techniques are of vital importance in electrochemistry as they can be used to address in situ, atomic-level structural changes that occur at the electrode–electrolyte interface, in response to a change in the applied potential and/or the nature of the surrounding solution. This has not been possible using the wide range of UHV-based surface techniques in existence, which are strictly of an “ex situ” nature; the electrode is removed from solution and placed into the UHV chamber for subsequent analysis.

Although both STM and AFM have proved equally valuable in probing the solid–liquid interface, this review will focus primarily on the electrochemical applications of the AFM; electrochemical STM is discussed in detail in Chapter 3.1 of this volume. This review will consist of two main parts. (1) The use of AFM to investigate the electrified solid–liquid interface.

High-resolution structural and force data obtained with this technique can provide a powerful insight into many electrochemical interfacial phenomena such as; the role of the electrolyte in determining the activity of the electrode, the underpotential deposition (upd) process, the nature of the diffuse double layer (DL), corrosion, and the activity of molecular adsorbates on electrode surfaces. (2) The use of electrochemically active AFM probes to investigate the structure–activity relationship of a wide range of interfacial processes.

3.2.2 Principles of AFM

The AFM is a force measuring instrument [2]. It operates on broadly similar principles to the surface force apparatus [3], except that instead of probing the interaction forces between two macroscopic surfaces, the forces measured are those between a very sharp tip and a surface. The tip is attached to a cantilever – the spring – which, as the sample is scanned under the tip (or the tip scanned with respect to the sample), or moved in a direction normal to the tip, deflects in accordance with the force experienced between the tip and the surface. This basic concept is depicted in Fig. 1. Importantly, the AFM can be used to image any surface irrespective of sample conductivity – this is in contrast to STM where the substrate must be (semi)conducting. AFM probes are typically microfabricated from Si_3N_4 or Si [4].

The sample (or tip) is moved using a piezoelectric tube similar to that employed in STM instrumentation. Deflections of the cantilever are monitored using a suitable detection system. The most common is the optical lever detection system in which a laser beam is reflected off the rear of the cantilever and into a multisegment

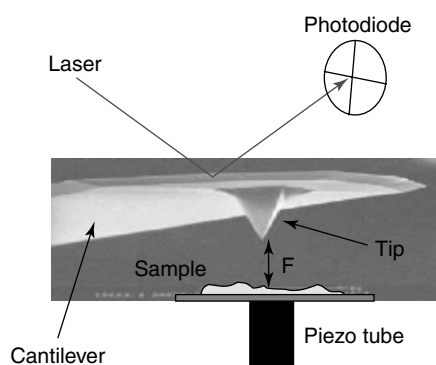


Fig. 1 The basic concept of AFM. A sharp tip, attached to the end of a force-sensing cantilever, deflects in accordance with the force, F , experienced between the tip and the substrate, as the tip scans across the surface of the sample, or is moved in a direction normal to the substrate. In most cases, the deflection of the cantilever is monitored by reflecting a laser beam off the rear of the cantilever and into a multisegment photodiode.

photodiode, which serves as a position sensitive detector, see Fig. 1 [5]. The deflection characteristics of the cantilever as the tip approaches, retracts, and/or scans a surface can ultimately be used to determine some property of the interface under investigation, such as topography, surface charge, elasticity, or tip-sample adhesion.

For imaging experiments, the tip can be employed in either contact, intermittent, or noncontact mode with the surface. This is often in conjunction with a feedback loop that operates to maintain a constant cantilever deflection (or vibration amplitude), by adjusting the tip-sample separation.

3.2.2.1 Substrate Preparation

For atomic-level resolution imaging of electrode surfaces, it is essential that the metal surface is prepared so that it is clean and ordered (preferably monocrystalline). Prior to the discovery of flame annealing by Clavilier in 1980 [6, 7], most surfaces could only be prepared and maintained in such a way by the employment of a UHV imaging environment. However, with the finding that high-temperature flame annealing, followed by quenching in water and/or an inert gas stream, resulted in smooth, clean contamination-free surfaces, it is now possible to routinely prepare electrodes for atomic-level SPM imaging under ambient

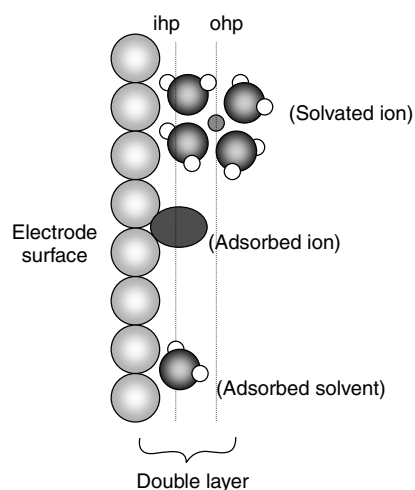
conditions. Ordered surfaces of the metals Au, Pt, Ir, Rh, and Ag can all be reliably produced using this procedure.

3.2.3

AFM Investigation of the Electrified Solid-solution Interface

Before detailing examples of AFM studies, it is useful to first consider the universally accepted model of the interfacial region between a metal electrode (or any charged surface) and electrolyte solution – the so-called *electrochemical double layer* [8], as depicted in Fig. 2. The double layer plays an important part in many aspects of physical chemistry and biology. In particular, the double layer is responsible for controlling processes such as the stability of colloidal particles in electrolyte solutions and ion partitioning at biological membranes. The layer closest to the electrode – the *inner Helmholtz plane* – *ihp* contains solvent molecules and other species (ions or molecules), which are said to be specifically adsorbed. Completely solvated ions can only approach within a certain distance of the electrode surface and are thus referred to as nonspecifically adsorbed species. The closest distance of approach for these ions signifies the *outer Helmholtz plane* – *ohp*.

Fig. 2 Schematic representation of the electrochemical double layer, at the electrode–electrolyte interface.



The thickness of the double layer varies with the concentration of the supporting electrolyte, but for a typical (1:1) electrolyte concentration of 0.1 mol dm^{-3} , the double layer is only some 10 \AA thick (a few atomic diameters) [8]. Importantly, the interfacial charge distribution in this region strongly controls electrochemical activity, which is in turn linked to the spatial distribution of chemical species. Thus, techniques that can provide insight into the structural arrangement of the metal substrate, adsorbates, and interfacial solvent molecules in this region, and information on the charge distribution in the double layer, are extremely powerful. Further details on the electrochemical double layer can be found in several chapters in Volume 1 of the *Encyclopedia*.

One of the main attractions of electrochemical interfaces is the ability to externally control the electrode potential and hence electrical potential drop across the interface. This in turn enables charge-transfer reactions and adsorption processes that occur at the surface of the electrified interface to be altered, usually in a controlled fashion.

Structural information on the electrified interface, under real conditions, can be “reliably” obtained at the atomic level by AFM (as well as STM – see Chapter 3.1 of this volume). However, it should be noted that caution is often required with interpretation of the image, as the technique in standard use is relatively insensitive to chemical identification. Moreover, for very weakly bound adsorbates, the pressure exerted by the tip as it images the surface has been thought to, in some cases, lead to adsorbate detachment or surface deformation [9]. For the most powerful interpretation of interfacial structure, it is often useful to correlate AFM images with complementary techniques, such as voltammetry and in situ X-ray methodologies.

Although, as it appears in the literature, STM is used more frequently than AFM for atomic-level imaging of electrode surfaces, AFM does have some obvious advantages over STM. One major strength of electrochemical AFM is the ability to quantitatively measure DL forces at the electrode–electrolyte surface, with the electrode held under potential control. This is extremely useful for understanding

charge distribution in the interfacial region and will be discussed in detail later in Sect. 3.2.3.2. Moreover, preparation of the probe for electrochemical AFM is much less technically challenging than for electrochemical STM, the latter requires the insulation of an etched sharp wire, such that only a small area of the tip is exposed [10]. Control of the substrate electrode potential is also relatively straightforward with AFM, an external potentiostat system normally suffices. The situation is slightly more complicated for STM, where it is necessary to control the potential at the STM probe in addition to that of the sample.

In general, *in situ* AFM solution studies of the electrode–electrolyte interface have, to date, yielded a plethora of information on the structure and charge distribution of the interfacial region at the highest spatial resolution, enabling previously unanswered questions to be addressed. Some of these studies will be highlighted in the chapter here, but for further examples and excellent reviews of electrochemical SPMs, refer to Refs. [11–14] and Chapters 3.1 and 3.3 of this volume.

3.2.3.1 Imaging Applications of Electrochemical AFM

3.2.3.1.1 The Role of Ionic Adsorbates in Electrode Behavior Ionic species are an integral component of the electrolyte solution, either due to the presence of a supporting electrolyte or as a result of solution impurities. Thus, understanding the role that ionic adsorption on the electrode surface plays in influencing the activity and structure of the electrode is essential. One of the most widely studied group of ionic species investigated both by electrochemical SPM and the more traditional UHV techniques (such as X-ray scattering) are the halide ions. These

ions often form a major component of electrolyte solutions and the resulting halide adlayers can be imaged relatively easily using scanned probe methods.

In one interesting study, Sneddon and Gewirth [15] used *in situ* AFM to investigate the structure and growth of halide adlayers and bulk Ag-halide deposits on the surface of Ag(111), as a function of electrode potential. For solutions containing F^- and Cl^- (in acidic media), cycling the potential of the Ag(111) substrate between -0.50 and $+0.50$ V versus a $Hg/Hg_2SO_4/K_2SO_4$ reference electrode resulted in no discernible change to the atomic-level structure of the Ag(111) surface. Images such as those displayed in Fig. 3(a) were obtained, at all potentials, depicting a hexagonal arrangement of atoms with a Ag interatomic spacing of 0.29 ± 0.02 nm, consistent with the expected value of 0.289 nm for the Ag(111) lattice.

In Br^- -containing solutions, a similar structural arrangement of atoms was observed in the potential range -0.35 to 0.20 V. However, upon sweeping the potential positive to $+0.26$ V a larger lattice structure was seen, as shown in Fig. 3(b), exhibiting a spacing of 0.41 ± 0.03 nm and no rotation relative to the Ag substrate. This was thought to correspond to a Br^- adlattice exhibiting a (3×3) structure and 44% monolayer coverage. Cyclic voltammograms (CVs) recorded in the same solution media, depicted a sharp peak at 0.24 V, as shown in Fig. 3(c), which was also thought to indicate the formation of the ordered halide overlayer. This (3×3) structure could be reductively desorbed by a cathodic potential sweep. In I^- -containing solutions, the Ag(111) lattice was never observed, instead at all potentials, one structure corresponding to I^- chemisorption on Ag(111) was seen, as shown in Fig. 3(d). Here, the structure

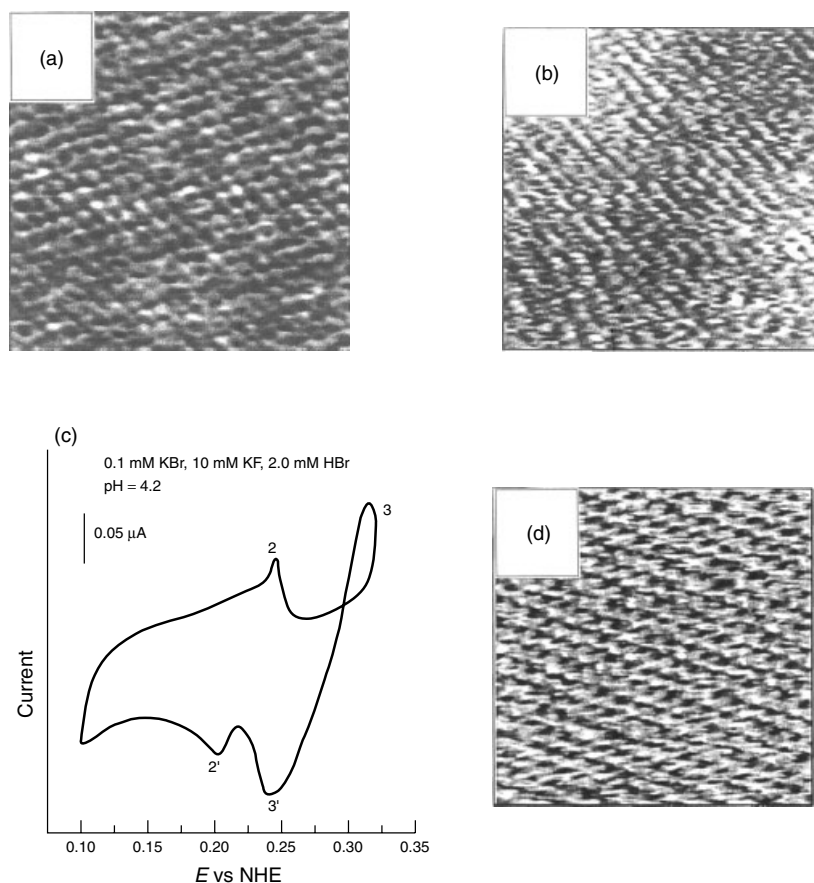


Fig. 3 AFM investigation of halide adsorption on Ag(111) (after Ref. [15]): (a) 6 nm \times 6 nm AFM image of Ag(111) in a solution of 10×10^{-3} mol dm $^{-3}$ KF and 1.5×10^{-3} mol dm $^{-3}$ HF at an applied potential of -0.21 V versus NHE. The structure is hexagonal with an atomic spacing of 0.29 ± 0.02 nm. Identical images were obtained between -0.50 and 0.50 V and in Cl $^{-}$ -containing solutions; (b) 8 nm \times 8 nm AFM image of Ag(111) in a solution of 0.1×10^{-3} mol dm $^{-3}$ KBr, 10×10^{-3} mol dm $^{-3}$ KF, and 2×10^{-3} mol dm $^{-3}$ HBr, at an applied potential of $+0.26$ V. A lattice exhibiting a spacing of 0.41 ± 0.03 nm and no rotation relative to the Ag substrate is observed; (c) Cyclic voltammogram of Ag(111) in 0.1×10^{-3} mol dm $^{-3}$ KBr, 10×10^{-3} mol dm $^{-3}$ KF, and 2×10^{-3} mol dm $^{-3}$ HBr, pH 4.2, recorded at a potential sweep rate of 5 mV s $^{-1}$; (d) 8 nm \times 8 nm AFM image of Ag(111) in a solution of 0.1×10^{-3} mol dm $^{-3}$ KI, 10×10^{-3} mol dm $^{-3}$ KF, and 1.5×10^{-3} mol dm $^{-3}$ HF. The image was unchanged at all potentials studied. The structure is hexagonal with a lattice spacing of 0.48 ± 0.03 nm.

displayed a hexagonal ($\sqrt{3} \times \sqrt{3}$)R30 $^{\circ}$ arrangement of ions with a lattice spacing of 0.48 ± 0.03 nm, corresponding to a 33% monolayer coverage.

The differences in the observed behavior of the four halide ions was thought to be due to the strength of the Ag–X (where X represents the halide ion)

interaction. For the more strongly solvated halide ions (such as the F^- and Cl^- , high electronegativity ions), the surface interaction is weak and no evidence for halide ion adsorption was seen. However, as the electronegativity of the ion decreases, and thus the degree to which these ions are solvated decreases, the strength of the Ag–X surface interaction increases. For both the Br^- and I^- case, adlayer structure was observed. In the case of I^- , where the Ag–I interaction is the strongest, the adlayer was observed at all potentials.

3.2.3.1.2 Underpotential deposition Underpotential deposition (upd) occurs when monolayers (or submonolayers) of a metal ad-atom are deposited on a foreign metal substrate at potentials positive of the reversible Nernst potential for bulk deposition [16]. Monolayers will only form when a low work function metal is deposited onto the surface of a higher work function substrate. In this case, the metal ad-atom–substrate bond is greater than the ad-atom–ad-atom bond formed in bulk metal deposition. Upd phenomena have been the subject of extensive work using SPMs and of particular interest is the role of coadsorbed anions on this process, as a function of electrode potential.

The most widely studied upd process is the deposition of Cu on Au(111) – particularly in sulfate-containing media [17]. In fact, one of the first examples of atomic resolution using electrochemical SPM [18] was obtained using this system. Various investigations have used electrochemical AFM to examine the role of the counteranion in this particular upd process. One of the first examples, from this wide area of research, was the elegant work of S. Manne and coworkers, who used the AFM in contact mode to investigate the behavior of

copper electrodeposition and subsequent dissolution at the surface of a Au(111) electrode in $1 \times 10^{-3} \text{ mol dm}^{-3} \text{ Cu}^{2+}$ solutions, as a function of applied potential and anionic component of the electrolyte (ClO_4^- and SO_4^{2-} , respectively) [19].

In both electrolyte solutions, upon sweeping the potential at the Au electrode to -0.100 V at 10 mV s^{-1} , bulk deposition of the Cu (resulting from reduction of aqueous Cu^{2+} to Cu) occurred and stable images of a close packed Cu(111) surface, were observed (atom–atom distance of $0.26 \pm 0.02 \text{ nm}$). Upon sweeping the potential positive to $+0.110 \text{ V}$, the bulk Cu was removed from the surface, leaving behind only an upd monolayer of Cu (and in some media, coadsorbed counteranions). In the presence of perchloric acid (ClO_4^- anion), the adlayer structure was found to have the same interatomic spacing associated with the underlying Au(111) surface (atom–atom distance $0.29 \pm 0.02 \text{ nm}$), but rotated at 30° to the Au(111) surface [19]. The imaged structure was assumed to be due to the Cu ad-atoms, where the slight mismatch between the two lattices was attributed to subtle strain effects, as the covalent radius of Cu is slightly greater than that of Au. No evidence for ClO_4^- coadsorption was observed here, although non-SPM techniques have suggested otherwise [20].

In the presence of sulfuric acid (SO_4^{2-} anion), at $+0.100 \text{ V}$, the structure of the adlayer was found to be completely different from that in ClO_4^- media. The adlayer interatomic distance was significantly larger ($0.49 \pm 0.02 \text{ nm}$) indicating a substantially more open structure, although the atoms were still rotated 30° with respect to the underlying Au(111) surface [19]. This open-packed structure was thought to be due to coadsorption of the SO_4^{2-} ions with the Cu. In

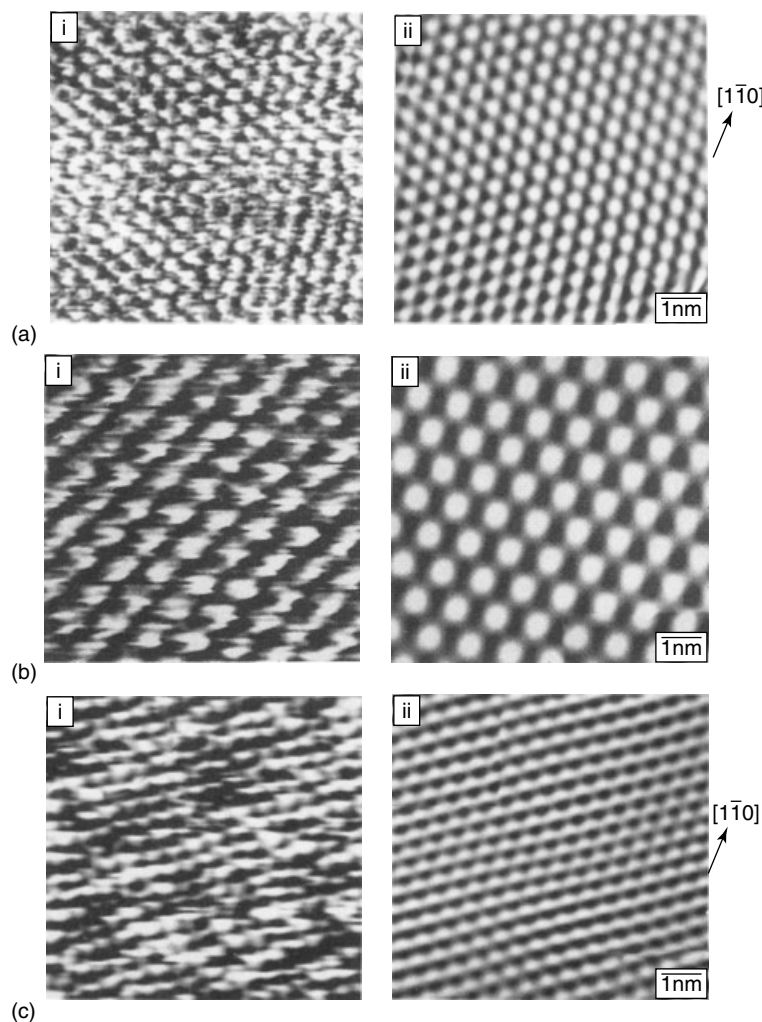


Fig. 4 AFM study of Cu upd on Au(111) in sulfate-containing electrolyte solution (after Ref. [23]): (ai) unfiltered, and (aii) filtered atomic resolution AFM images ($4 \text{ nm} \times 4 \text{ nm}$) of Au(111) in $0.05 \text{ mol dm}^{-3} \text{ H}_2\text{SO}_4$ and $1 \times 10^{-3} \text{ mol dm}^{-3} \text{ CuSO}_4$ solution, at an electrode potential of $+0.5 \text{ V}$. The images show the unreconstructed Au surface, with an Au–Au lattice spacing of 0.29 nm ; (bi) First Cu upd region. Unfiltered (i), and filtered (ii) AFM images ($4 \text{ nm} \times 4 \text{ nm}$) at a Au(111) electrode potential of $+0.25 \text{ V}$. The image shows the coadsorbed SO_4^{2-} , with a $\text{SO}_4^{2-} - \text{SO}_4^{2-}$ lattice spacing of 0.49 nm , arranged in a triangular ($\sqrt{3} \times \sqrt{3}$) $R30^\circ$ structure on the surface of Au(111). Around each SO_4^{2-} ion (and not detected by the AFM) are six Cu ad-atoms, which form a honeycomb-shaped network; (c) Second Cu upd region. Unfiltered (i), and filtered (ii) AFM images ($4 \text{ nm} \times 4 \text{ nm}$) at a Au(111) electrode potential of $+0.07 \text{ V}$. The structure corresponds to the Cu (1×1) adlayer on Au(111).

these initial studies, the imaged adlayer was assumed to be due to Cu ad-atoms, as was documented by many other researchers at that time, using electrochemical-SPM techniques.

Although this general hypothesis was correct, later work [21, 22], using complementary techniques, disproved the image interpretation, again highlighting the lack of chemical specificity associated with conventional AFM imaging. In fact, it is now known that the imaged adlayer actually corresponds to the coadsorbed SO_4^{2-} ions that form the triangular ($\sqrt{3} \times \sqrt{3}$) $R30^\circ$ structure (surface coverage 33%) on the surface of the Au(111). Around each central SO_4^{2-} ion sit six Cu ad-atoms forming a honeycomb lattice (surface coverage 66%) over the Au(111) substrate. These atoms are not detected by the AFM imaging tip. Further work [23] has shown that Cu upd, in SO_4^{2-} -containing media, takes place in two distinct steps; the first is the honeycomb lattice structure (as described above) and the second, on sweeping the substrate electrode potential more negative, is the formation of a commensurate full (1×1) monolayer. The two processes can also be detected in CVs [23]. Figure 4 shows AFM images pertaining to (a) the underlying Au(111) substrate, (b) the first and (c) second Cu upd regions on Au(111) in SO_4^{2-} -containing media.

3.2.3.1.3 Corrosion Studies In order to fully understand the phenomena underpinning corrosion processes, a detailed structural and chemical understanding of the dissolution activity of metals, alloys, and semiconductors is required [24]. Volume 4 of the *Encyclopedia* is concerned with corrosion and oxide films. The ability of SPMs to provide high-level resolution structural information and to map shape evolution in real time

makes these techniques ideally suited to tackling such issues. As stated earlier, use of these methodologies in conjunction with alternative spectroscopic (for chemical analysis) and voltammetric techniques provides the most powerful approach to studying the interfacial process of interest.

Corroding systems are, however, technically more challenging to work with compared to the systems described above, which mostly employ ordered metal electrode substrates, operating under well-defined conditions. In contrast, it is much more difficult to prepare the corrosion materials of interest (such as steel, metal alloys, Al) so that atomic resolution is possible. Electrochemical or mechanical polishing, prior to use, often results in rougher surface conditions and a slightly lower limit of resolution [25]. Moreover, the behavior of the substrate in response to a change in potential is often more unpredictable. This particularly applies to materials that possess a passivation layer, such as stainless steels, Al, or Ti. Once a sufficiently high overpotential has been applied to break down the insulating layer, the dissolution rate can proceed very quickly, in a relatively uncontrolled manner.

In order to successfully understand corrosion, it is necessary to consider factors such as: what are the characteristics of the passivation film; what mechanism operates in the “early stage” of the corrosion process; and how does the substrate of interest maintain the corrosion process? In particular, the identification of active sites on the surface at which pits will nucleate and develop further – pitting precursor sites – is of particular importance. It is these sites that often sustain corrosion activity on a surface, over a prolonged period of time. Many corrosion systems involve the presence of a nonconductive

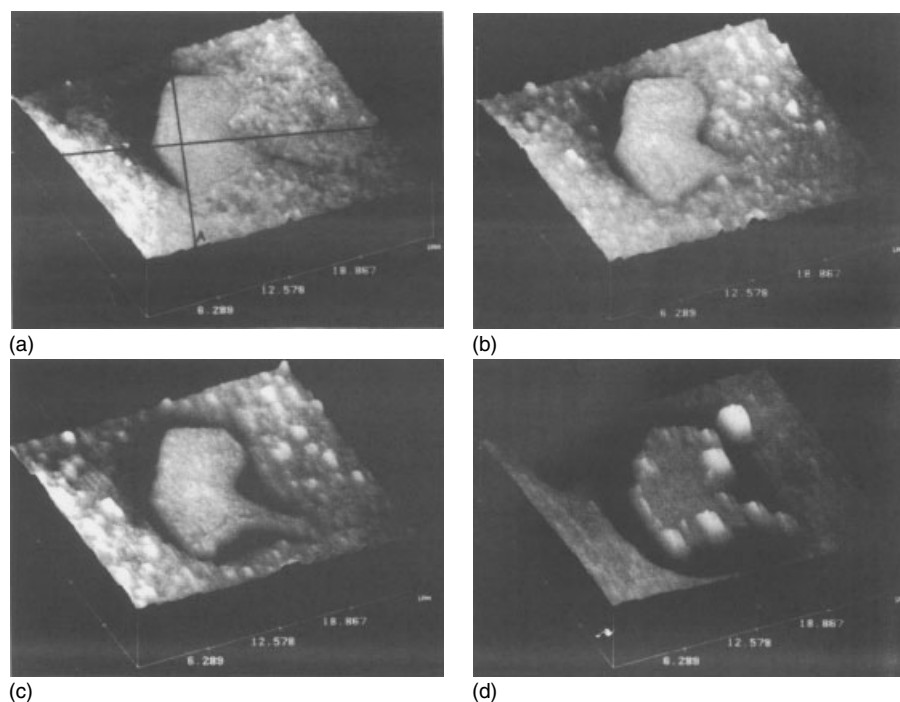


Fig. 5 AFM images ($z = 250 \text{ nm div}^{-1}$) of Al-6061-T6 and an iron-rich inclusion: (a) in air; (b) in situ after exposure to 0.6 mol dm^{-3} NaCl at the corrosion potential for 1 h; (c) 2 h; and (d) 24 h (after Ref. [26]).

oxide film, and given that STM is incapable of directly imaging insulating surfaces, in many cases AFM is more suited to providing topographical information on the surface of interest.

Most AFM studies of dissolution and corrosion processes have focused on technologically relevant materials such as aluminum alloys [25–27], copper [28], and steel [29–32]. For example, in situ electrochemical-AFM was used to investigate the corrosion activity of Al-6061-T6 (alloyed with Fe) immersed in 0.6 mol dm^{-3} NaCl, near iron-rich intermetallic (Al_3Fe) inclusion sites [26]. Inclusion sites are thought to be favorable areas for pit initiation and represent an important area of corrosion research. By marking the sample using a photoresist grid, it was

possible to preselect an inclusion site, analyze the area using Auger electron spectroscopy, and then relocate the site for AFM analysis.

Figure 5 displays a series of in situ AFM images that were recorded over a 24-h period at the corrosion potential, around the selected inclusion. Figure 5(a) shows the surface prior to exposure to solution. The location of the Al_3Fe inclusion is clearly evident. One hour after addition of solution (Fig. 5b), the beginnings of the formation of a trench, around the inclusion site, is observed. Over a further period of time, as the metal adjacent to the inclusion site dissolves further, the trench widens, resulting in the formation of a circular pit (Fig. 5c, d). This behavior was attributed to oxygen reduction taking

place at the inclusion (cathodic) site, resulting in a rise in the local pH. This in turn causes degradation of the passive oxide film surrounding the inclusion, and dissolution proceeds. Electrolysis is thought to take place preferentially at the inclusion sites as a result of their increased conductivity compared with the surrounding passivated layer.

By using a combination of AFM and fluorescence microscopy, further studies on this substrate demonstrated that a small percentage of the inclusions on the surface (ca. 5%) also acted as anodic dissolution sites [27]. This was confirmed by the addition of a fluorescent dye (fluorescein) to the Cl^- -containing solution media. At the dissolution sites, the dye complexes with the corrosion products to form a precipitate on the surface, which is detected optically using fluorescence imaging. The structure of the surface in this area was obtained using AFM. Around a small number of inclusions, fluorescent rings were observed, which signified the anodic nature of these sites.

3.2.3.1.4 Molecular Adsorbates on Electrode Surfaces The modification of electrode surfaces, due to the presence of a molecular adsorbed layer is of great scientific importance due to the potential applications of such systems as wide ranging as: barrier films for corrosion protection, chemical and biological sensors, lubricating films, lithographic resists, and photoelectronic materials. SPMs have been used most widely to probe the structural and electronic properties of the film. For completely insulating films, AFM is obviously the preferred SPM. For atomic-level resolution imaging of the adsorbed film, well-ordered flame annealed metal substrates are often employed.

Perhaps the most widely studied molecular layers are the self-assembled monolayers (SAMs) [33] that offer a highly ordered structure, are stable and can be functionalized easily to offer a rich chemistry of functional end groups. The most common SAMs are the *n*-alkanethiols adsorbed on gold, through a Au–S linkage. By employing *in situ* AFM, it is possible to follow the adsorption process in real time, enabling information on the kinetics and the mechanism of the process to be elucidated [34].

As an example, time-dependent AFM imaging of the adsorption of $0.2 \times 10^{-3} \text{ mol dm}^{-3} \text{ CH}_3(\text{CH}_2)_{17}\text{SH}$ (C_{18}SH) in 2-butanol on Au(111) revealed that initially the C_{18}SH molecules adsorbed on gold with their molecular axis orientated parallel to the surface (i.e. lying down). As the coverage of the alkanethiols increased to near saturation, a two-dimensional phase transition occurred to form islands composed of molecules with their molecular axis orientated 30° from the surface normal (i.e. standing up). This sequence of images, recorded over a time period of 80.5 min is shown in Fig. 6. Continuous exposure to the thiol solution resulted in the appearance of more islands, and the growth of these nuclei. The process continued until a complete SAM was formed, which adopted a commensurate $(\sqrt{3} \times \sqrt{3})R30^\circ$ structure, as shown in Fig. 7. This arrangement is the expected final structure for the *n*-alkanethiol monolayer coverage of a Au(111) surface [35]. By changing the chemical nature of the functional group (and molecular size), it is possible to alter the structural properties of the SAM, as observed using AFM [36].

Control of the substrate potential can, in some cases, induce morphological (and electronic [37]) changes in the adsorbed molecular film [38]. For example, the effect

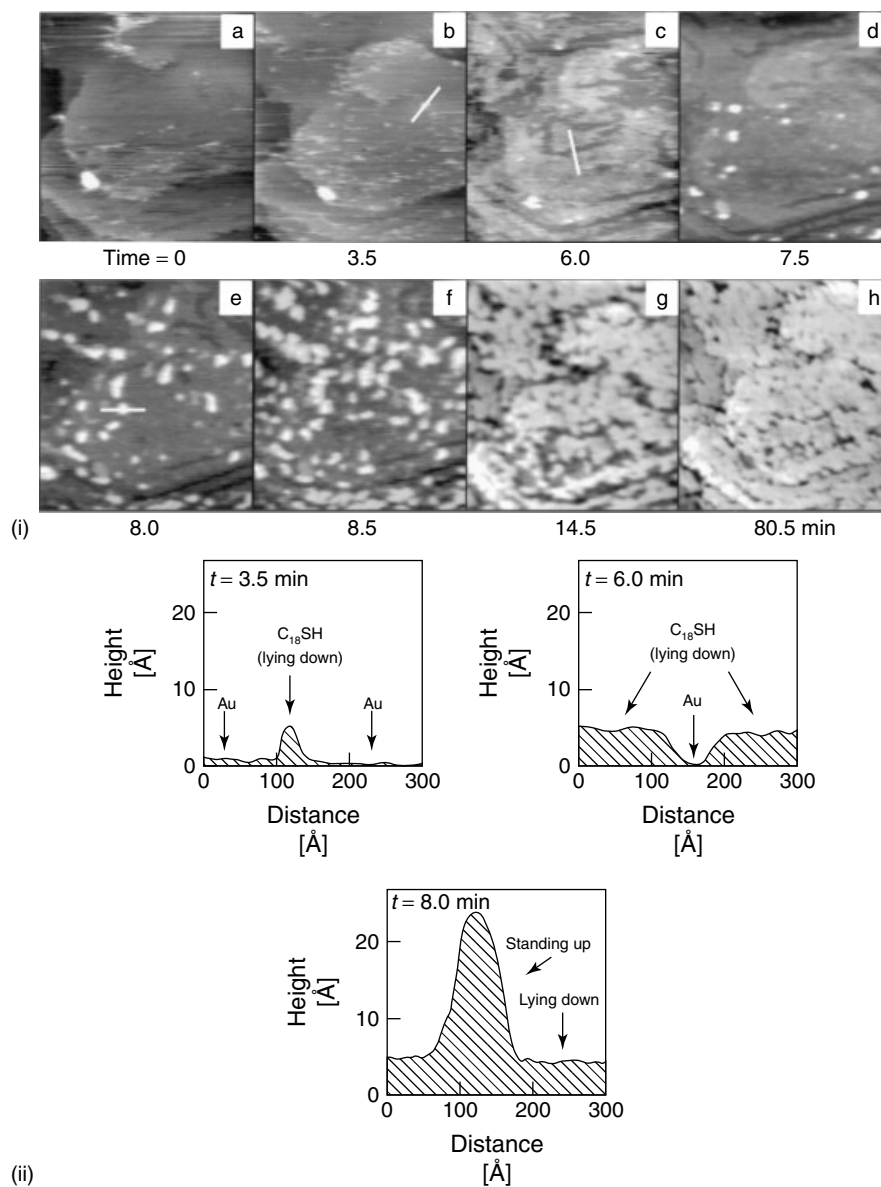


Fig. 6 Kinetics of thiol assembly on Au(111) (after Ref. [34]): (i) In situ topographic AFM images (a–h) of Au(111) at various times after injection of a solution of $\text{CH}_3(\text{CH}_2)_{17}\text{SH}$ in 2-butanol. The concentration of thiol in the liquid cell was 0.2 mol dm^{-3} . The area of each frame is $150 \text{ nm} \times 150 \text{ nm}$. The bright spot in the lower left-hand corner and the Au(111) steps, at the bottom of each frame provide topographic landmarks for comparison of these images. (ii) The apparent heights of the cursors in (b), (c), and (e) are shown.

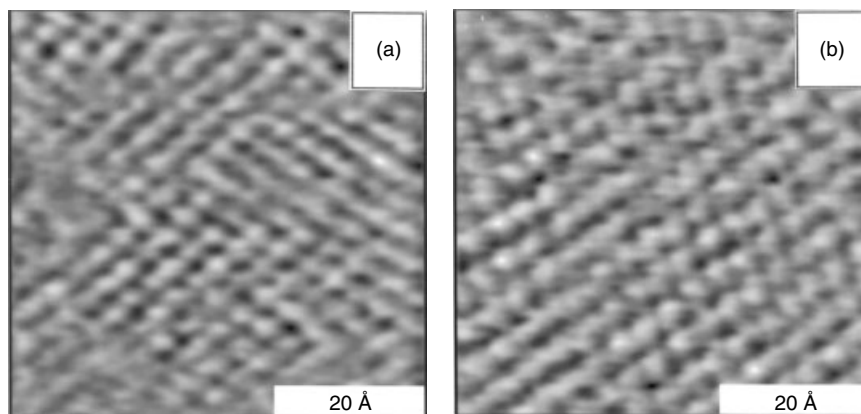


Fig. 7 Higher resolution AFM images of the same scanning area as in Fig. 6 after 3.5 h of immersion of Au(111) in a solution of $\text{CH}_3(\text{CH}_2)_{17}\text{SH}$ in 2-butanol. These images indicate a triangular ($\sqrt{3} \times \sqrt{3}$) $R30^\circ$ periodicity, denoting complete monolayer coverage of the SAM (after Ref. [34]).

of electrode potential on the orientation of thiol-derivatized DNA duplexes (60% monolayer coverage) adsorbed on gold, was investigated using AFM [38]. At open-circuit potential, DNA helices were observed to form, with a film depth of 45 Å. This was thought to correspond to an average 45° orientation of the helical DNA axis, with respect to the gold substrate. With the electrode potential poised at values either side of the potential of zero charge (pzc), the height of the film was observed to vary dramatically. At potentials negative of the pzc, the film height increased from its open-circuit value to 55 Å. In contrast, when the potential was increased positive of the pzc, the film height dropped considerably to a limiting value of ca. 20 Å. This process was found to be reversible. The change in molecular height was attributed to electrostatic effects modulating the surface coverage. At potentials negative of the pzc, the DNA duplexes were thought to be aligned normal to the surface, in order to minimize electrostatic repulsion, whereas, at negative potentials of the pzc, the duplexes were able to lie

flat as a result of electrostatic attraction. The observed voltage-induced morphology change was thought to effectively constitute a nanoscale molecular switch.

As a word of caution, when imaging molecular adsorbates using AFM, care is often taken to apply a minimum tip–substrate loading force. This is in order to avoid unwanted effects such as displacement of molecules from the surface (which may only require loading forces in the nanonewton range) or compression of the molecular film. In fact, increasing the tip applied force in order to wipe the imaged area clean of adsorbate is commonly used in AFM as a method for both estimating the thickness of a molecular film [38] and surface microlithography [39].

3.2.3.2 Electrochemical Force Data Acquired Using the AFM

Although AFM is clearly capable of atomic-level topographical imaging of surfaces, it is important to recognize that the instrument is in essence a very sensitive,

highly localized force measuring device. By monitoring the deflection of the cantilever, as the AFM tip and a sample substrate are brought together and then retracted, in the vertical z direction, it is possible to obtain information on the tip–substrate interaction force [40]. This requires that the spring constant of the force-sensing cantilever is known precisely. From these approach and retract “force curves”, it is possible to obtain a wealth of information about the elasticity, charge, and adhesive properties of the surface.

3.2.3.2.1 Approach Curve Measurements

Of particular interest in electrochemical systems, is the role of the electrostatic DL. The electrical DL arises as a consequence of the structured ordering of dissolved counterions in response to a surface charge, as depicted in Fig. 2. Perturbation of the DL, for example, as a result of an approaching surface, gives rise to the DL force. By using AFM, it is possible to directly probe the diffuse DL at an electrode surface with nanometer resolution, enabling the surface charge and potential on the electrode surface to be determined unambiguously. Prior to the introduction of AFM, direct measurement of the structure and forces at the electrode–electrolyte interface had been severely limited.

One of the first AFM studies of DL forces was carried out by Hillier and Bard [41]. They measured the interaction force between a gold electrode and a modified AFM probe, as a function of electrode potential, electrolyte concentration, and chemical identity of the anion. A silica sphere (10–20 μm nominal diameter) attached to the end of the AFM cantilever functioned as the tip. This probe geometry is often adopted in AFM force measurements, in conjunction with a planar substrate, as the tip–sample geometry is well

defined. This is an important prerequisite for the quantitative interpretation of the experimental results. Although conventional AFM pyramidal tips offer very high lateral resolution, the true probe geometry is often quite difficult to determine, over the 10-nm range at the apex.

Under the solution conditions employed (pH ca. 5.5), the silica probe surface had a fixed negative charge (–41 mV). In contrast, the charge on the gold surface and thus the resulting structure of the double layer (which consists of counterions that balance the charge injected into the electrode) could easily be controlled by altering the applied electrode potential. Figure 8 shows force–distance approach curves obtained in 0.001 and 0.01 mol dm^{-3} (inset) KCl solutions for a range of gold electrode potentials varying between –700 and +100 mV versus a saturated calomel reference electrode.

In all cases, for a negative electrode potential, the interaction force between the tip and the substrate was seen to be purely repulsive, indicating that the electrode surface was also negatively charged. Under these conditions, a diffuse DL structure forms by increasing the local concentration of K^+ (thought to be nonspecifically adsorbed) and decreasing the local concentration of Cl^- (specifically adsorbed), in the vicinity of the electrode. Repulsion between the positive DL of the silica probe and the gold surface, as the tip and substrate are brought close together, causes the AFM cantilever to deflect upwards and a force of positive magnitude is recorded.

As the applied potential was made positive, the net surface charge of the electrode became more positive and a negative DL formed, by the repulsion of K^+ and the attraction of Cl^- . Under these conditions, the attractive interaction

between the negatively charged DL of the electrode and positively charged DL of the silica results in a downwards deflection of the cantilever and thus a force of negative magnitude. The size of the applied electrode potential was found to govern the size of the force–distance gradient. Similar results were obtained by Butt and coworkers [42, 43] who measured the force between a Si_3N_4 tip and a gold, platinum, and highly oriented pyrolytic graphite (HOPG) surface, as a function of substrate potential.

In the more dilute KCl solution, the force versus distance curve extended beyond a 30-nm separation whilst in the $1 \times 10^{-2} \text{ mol dm}^{-3}$ KCl solution, the force interaction decayed within the first 8 nm (see Fig. 8). This behavior was

indicative of the size of the double layer, which is more compressed in higher ionic strength solutions. In general, the force–distance data were found to agree well with the theoretical Derjaguin–Landau–Verwey–Overbeek (DLVO) theory, which assumes that for many interactions between small particles in aqueous electrolyte solutions, the total interaction force between two surfaces can be described by the sum of the van der Waals (VdWs) force and the electrostatic DL force. At close probe–surface separations of less than 5 to 10 nm, the model was found to underestimate the observed force, which was attributed to solvent ordering resulting in an additional repulsive force, which is not accounted for in DLVO theory.

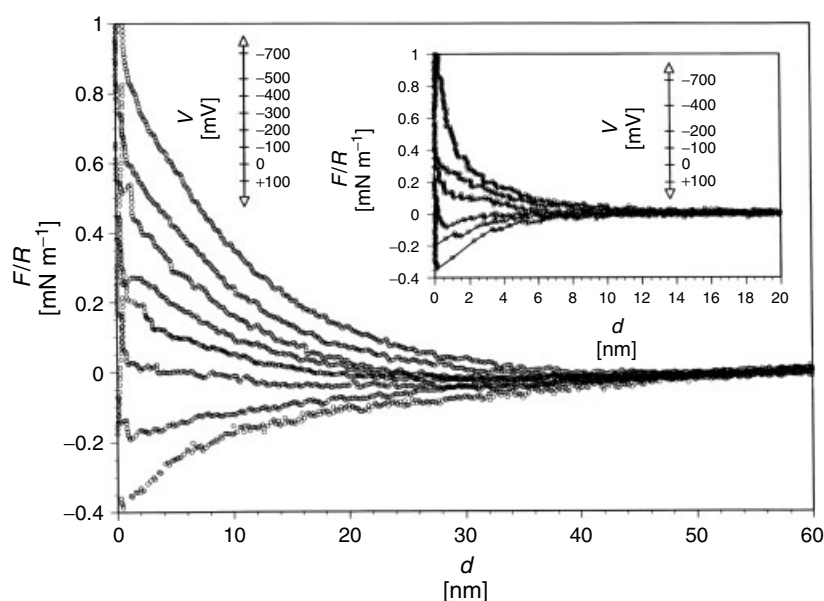


Fig. 8 Force between a silica sphere and a gold electrode in an aqueous solution of $1 \times 10^{-3} \text{ mol dm}^{-3}$ KCl, and $1 \times 10^{-2} \text{ mol dm}^{-3}$ (inset) KCl at 25 °C, and pH 5.5, as a function of the applied electrode potential. The curves correspond to, from top to bottom, electrode potentials of -700, -500, -400, -300, -200, -100, 0, and +100 mV (versus SCE). Electrostatic repulsion decreases as the electrode potential increases from -700 to 100 mV (after Ref. [41]).

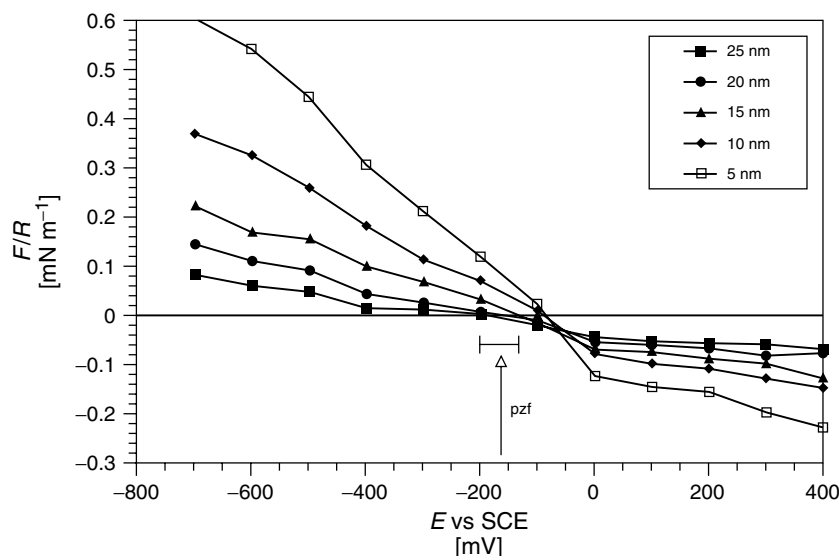


Fig. 9 Force between a silica sphere and the gold electrode in 1×10^{-3} mol dm $^{-3}$ KCl solution, at fixed separations of 5, 10, 15, 20, and 25 nm as a function of electrode potential. The potential of zero force (pzf) is shown (after Ref. [41]).

The electrode potential at which the measured electrostatic force changed from repulsive to attractive was indicative of the point of zero force (pzf), a parameter that strongly relates to the pzc, of the electrode surface. The pzc of an electrode depends upon the nature of the electrolyte, in particular the extent of specific adsorption of anions at the interface. At the pzc, the charge resulting from ion adsorption is totally compensated by charge on the metal electrode and no diffuse DL forms. Figure 9 depicts the experimentally measured force as a function of gold electrode potential for five different probe-substrate separations in a 1×10^{-3} mol dm $^{-3}$ solution of KCl. Electrostatic force data recorded at the larger distances (15–25 nm) were expected to be more reliable than force measurements recorded over smaller separations, as contributions from VdWs forces and solvent interactions were negligible at these larger distances. As shown in Fig. 9, the

measured force decreased monotonically from repulsive to attractive as the electrode potential was increased from negative to positive values. At electrode potentials far positive, the attractive force was observed to plateau. This effect arose as a consequence of the “jump-to-contact” behavior of the cantilever, which often renders near surface attractive forces inaccessible to measurement.

Overall, Fig. 9 demonstrates that in 1×10^{-3} mol dm $^{-3}$ KCl solution, the pzf for the gold substrate electrode falls in the potential range -150 to -200 mV for silica–gold separations greater than or equal to 15 nm. This value was found to be strongly governed by the surface adsorption characteristics of the dominant anion in solution. For example, when the KCl solution was replaced with solutions containing 1×10^{-3} mol dm $^{-3}$ I $^{-}$, Br $^{-}$, and F $^{-}$ the pzf measured at a tip–substrate separation of 15 nm was found to vary

between 0 and 400 mV (F^-), -250 and -350 mV (Br^-), and -600 and -650 mV (I^-). In general, the more strongly adsorbing the anion, the more negative the surface charge of the electrode at the pzc. The data presented here qualitatively agree with the AFM topography data presented earlier in Sect. 3.2.3.1.1, which demonstrated structurally that the metal-halide ion surface interaction was strongest for the larger, poorly solvated halide ions [15]. Other studies have also used AFM force curves to confirm that specific anion adsorption has taken place at the electrode-electrolyte interface [44, 45].

Surface force measurements have also been carried under much higher ionic strength conditions, in which the solution conditions and substrates employed are more akin to those encountered in industrial electrochemical processes. In one set of experiments [46], the surface force was measured between a silica sphere and a copper electrode, as a function of electrode potential, in concentrated (0.01 and 0.1 mol dm^{-3}) solutions of

$MgSO_4$ at pH 3.4. Despite the high ionic strength conditions, which acts to decrease the size of the DL to a range at which VdWs forces are expected to dominate, the interaction was found to be controlled, as above for the lower concentration electrolyte solutions, by the electrostatic DL force. In this case, it was thought that a strong repulsive hydration force between the copper substrate and silica probe was counterbalancing the effect of the VdWs attractive force, at short separations. At pH 3.4 and open-circuit potential, the copper electrode was found to be positively charged, whereas on increasing the pH to 5.8, the surface became negatively charged. This phenomenon was attributed to the presence of a layer of chemisorbed oxygen that was thought to be chemically stable under the higher pH solution conditions.

In an interesting set of experiments, force-curve measurements were used to provide information on the nature of the conductive polymer film-aqueous solution interface [47]. Although electronically conductive polymers, grown on electrode surfaces, are often described as displaying metallic behavior, there have been very few studies that address the surface charge of the film as a function of the applied potential. Force curves recorded between a negatively charged silica sphere and a conductive poly(3-methylthiophene) film (grown on a Pt substrate electrode) at different applied substrate potentials, in $0.001 \text{ mol dm}^{-3} \text{ KClO}_4$, are shown in Fig. 10. At a potential of -0.4 V , the film is in a reduced (uncharged state) and thus no diffuse DL exists at the film-solution interface. This is reflected in the characteristics

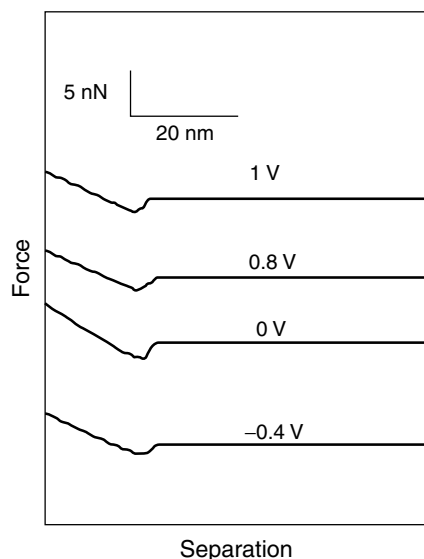
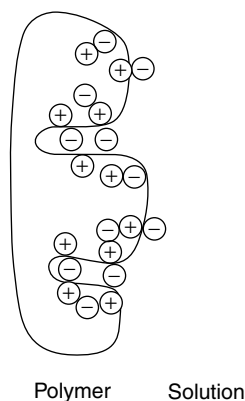


Fig. 10 Force between a silica sphere and a conductive poly(3-methylthiophene) film in $0.001 \text{ mol dm}^{-3} \text{ KClO}_4$, as a function of electrode potential (after Ref. [47]).

Fig. 11 Schematic of the electrode–electrolyte interface for a conductive polymer film electrode (after Ref. [47]).



of the force curve. The curve remains flat until at a sufficiently small tip–substrate separation, VdWs forces are dominant and the tip is pulled abruptly into contact with the surface. Importantly, there is no evidence for electrostatic interactions between the tip and the conductive polymer.

Interestingly, when the potential is made more positive so that the film becomes oxidized, the observed force–distance data remain the same. Similar effects were observed with polypyrrole films. This suggests that the positive charge in the film is fully compensated by negatively charged solution ions that can penetrate the polymer matrix either within the polymer strands or within pores in the polymer, as depicted in Fig. 11. Thus, at the conductive polymer–solution interface, no DL exists. This is in stark contrast to the behavior of metal electrodes in contact with aqueous electrolytes.

AFM has also been employed to probe DL forces at the interface between an SAM (on gold) and the surrounding electrolyte [48, 49]. In one particular study, by employing an electroactive SAM, it was possible to investigate structural changes in the diffuse DL in response to a change in the charge of the surface layer, imposed by controlling the substrate

potential. Alkanethiol SAMs, synthesized with a ferrocenesulfonate terminal group, were interrogated with a silica sphere AFM probe, in $0.001 \text{ mol dm}^{-3} \text{ NaClO}_4$ at pH 6.0. Under potential conditions in which oxidation of the ferrocene did not occur, a strong electrostatic repulsive force was observed between the negatively charged silica sphere and the modified Au surface. This interaction dictated that the substrate was negatively charged, a factor attributed primarily to the anchored terminal sulfonate anions of the SAM.

On increasing the substrate potential more positive, to values in which the surface ferrocene groups could be oxidized to form cationic species, the electrostatic repulsive force was seen to decrease. This is as expected, given that each oxidized ferrocene group will compensate a surface negative charge from the sulfonate group. On reaching $+0.45 \text{ V}$, no measurable long-range electrostatic interaction was observed, indicating that the modified Au substrate no longer had a net charge. From the observed diffuse DL forces, it was possible to calculate the magnitude of the surface charge of the SAM modified Au substrate, immersed in aqueous solution. The surface charge measured using AFM was found to be considerably smaller

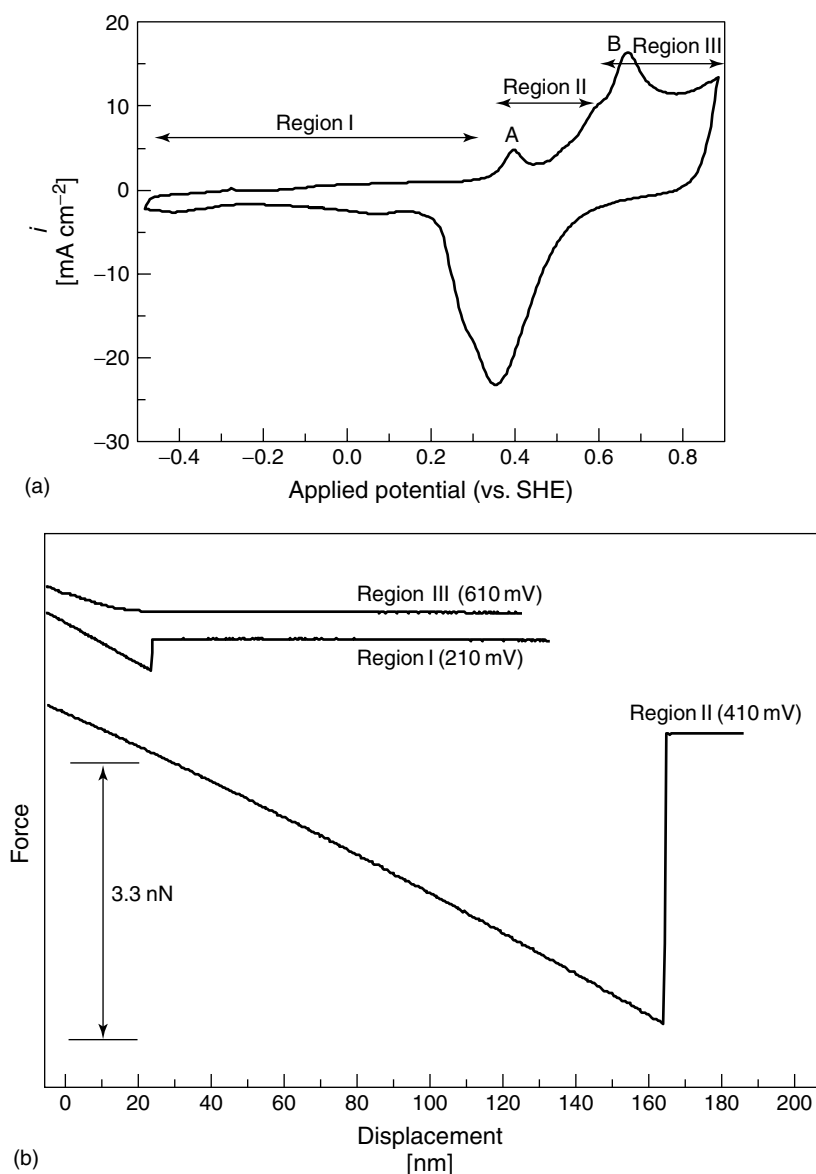


Fig. 12 (a) Cyclic voltammogram of $0.01 \text{ mol dm}^{-3} \text{ NaOH}$ on $\text{Au}(111)$. The scan rate was 50 mV s^{-1} . The oxidation feature “A” at $+0.4 \text{ V}$ corresponds to the specific adsorption of OH^- . The second oxidation feature “B” corresponds to the formation of gold oxide. Scanning the potential from negative to positive potentials, the voltammetry can be divided into three potential regions: Region I corresponds to the bare gold, region II corresponds to the presence of AuOH , and region III corresponds to gold oxide; (b) Representative adhesion force versus pull out displacement curves for potential regions I–III. The zero of displacement corresponds to the onset of constant compliance for the tip–surface approach curves (after Ref. [52]).

than the value obtained using electrochemical measurements (via integration of the voltammogram obtained for oxidation of the ferrocene group located in the end terminal of the SAM). This difference was attributed to the presence of counterion binding at the charged SAM–electrolyte interface, which acts to screen (considerably so in this case) the SAM charge during AFM DL force measurements.

3.2.3.2.2 Retract Curve Measurements

The response of the cantilever as the AFM tip is moved away from a sample substrate provides information on the adhesive properties of a surface. As the tip approaches and then touches the surface, bonds may be made that, on retraction of the tip from the substrate, are eventually broken when the force applied to the probe exceeds the adhesive pull of the surface. As such this technique, often using chemically modified tips, has received considerable attention as a way of measuring specific molecular and intermolecular interactions and even mechanical molecular properties, at the single molecule level [50, 51]. Adhesion measurements in electrochemical systems, of which there have been a number of studies, are of interest to this review.

Adhesion measurements can often provide very sensitive information on the chemical nature of the substrate of interest, enabling values for the interfacial free energy of the surface to be elucidated. As such, AFM force curves have been used to directly determine the chemical identity of adsorbates on an electrode surface, subject to potential control [42, 52, 53]. For example, AFM adhesion measurements were used to provide direct evidence for the surface composition of Au(111), as a function of the applied potential in basic solution. Figure 12(a) displays the CV for Au(111)

in $0.01 \text{ mol dm}^{-3} \text{ NaOH}$. The oxidation peak at A corresponds to the specific adsorption of OH^- onto the bare Au(111) surface, whilst the second peak B signals the onset of the gold oxide layer. Adhesion curves were also recorded at three different electrode potentials corresponding to the three different surface states of the Au(111), as shown in Fig. 12(b). Curve I at +210 mV signifies a bare Au(111) surface, curve II at +410 mV denotes the presence of AuOH, and curve III at 610 mV corresponds to gold oxide. Adhesion was always found to be much larger in region II than in regions I and III. It was thought that the large interaction force (in region II) was due to the occurrence of significant hydrogen bonding between the AuOH surface and the Si–O $^-$ groups of the Si_3N_4 AFM tip, which dominate under the basic solution conditions of the experiment. The measured interaction energy -2 kJ mol^{-1} – agreed well with the expected strength of a hydrogen bond between O $^-$ groups on the tip and AuOH on the surface. In regions I and III in which the Au(111) crystallite surface is composed of Au atoms, the force-curve characteristics were thought to be largely dominated by VdWs forces and as such the tip–substrate interaction was significantly minimized, compared with region II.

Through the employment of polymer- or SAM-modified electrodes, it is possible to monitor electrochemical transformations in the film using AFM adhesion-based measurements [54, 55]. For example, Hudson and Abruña demonstrated the ability to directly control the adhesion force between a tip and substrate surface, both coated with an electroactive polymer, via the selective oxidation or reduction of the polymer film [54]. In these studies, both a gold-coated tip and gold foil were modified

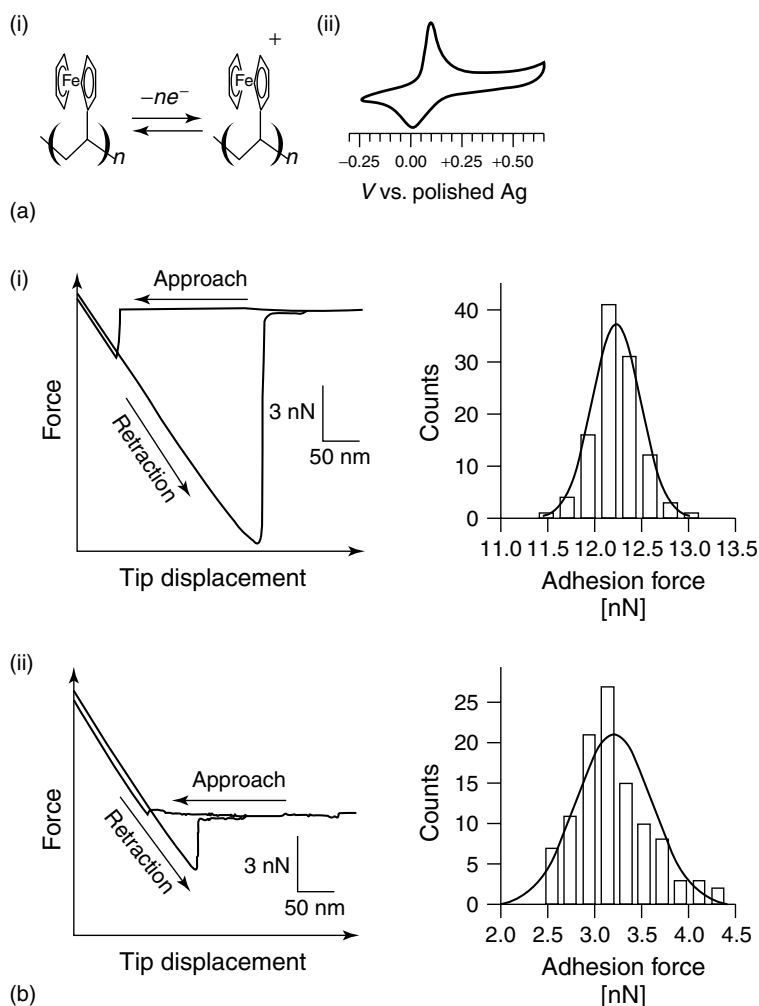


Fig. 13 (ai) Reaction scheme for oxidation of PVF to PVF⁺, (aii) Cyclic voltammogram of the tip and sample taken in the fluid cell in 0.1 mol dm⁻³ KClO₄ at a scan rate of 50 mV s⁻¹; (b) Typical force curves and histograms showing the number of times a given force was observed (fitted by a Gaussian distribution) for, (i) interactions between neutral polymer films ($E = -0.25$ V versus polished silver), and (ii) interactions between oxidized polymer films ($E = +0.30$ V versus polished silver) (after Ref. [54]).

with an approximately 35-nm thick film of poly(vinylferrocene) (PVF) and immersed in a solution of 0.1 mol dm⁻³ KClO₄.

Figure 13(a) shows the electrochemical characteristics of the PVF electroactive film

as the potential was swept positive from -0.25 to +0.50 V and back again. The peak in the forward direction, at $E = +0.05$ V, corresponds to the one-electron oxidation of each of the ferrocene subunits on PVF, resulting in the production of a

positively charged species. On reversing the potential, the return peak is characteristic of the reversible one-electron reduction of the positively charged PVF^+ species to form a neutral complex. Hence, by holding the potential of the tip or substrate either negative or positive of the PVF oxidation wave, it is possible to confer neutrality or a positive charge on the PVF-coated surface of interest.

Figure 13(b) depicts typical force curves that were obtained when the interaction between neutral polymer films (both tip and substrate biased at -0.25 V versus polished silver reference electrode) and oxidized polymer films ($E = +0.30$ V) was measured. Statistical analysis of over 100 consecutive approach and retract plots yielded an average adhesive force of 12.2 ± 0.3 nN for the neutral films and 3.2 ± 0.4 nN for the oxidized surfaces. As the surface of the neutral polymer is far more hydrophobic in nature than the positively charged polymer, this variance in measured interactive force was linked to differences in the solvation energies of the two surfaces. Oxidation of the polymer results in solvent and electrolyte incorporation into the film (see Fig. 11) and an increase in surface hydrophilicity, which significantly reduces adhesion between the two oxidized polymer films.

Similar results were observed on monitoring the adhesive interaction between a ferrocene-terminated alkanethiolate SAM chemisorbed at a Au(111) substrate and a probe tip modified with a methyl-terminated alkanethiolate SAM [55] in 1.0 mol dm^{-3} HClO_4 . As the potential of the substrate was gradually made more positive and the fraction of oxidized ferrocene groups in the SAM increased, the adhesive interaction between tip and sample was seen to decrease. Oxidation of the ferrocene group was thus

thought to result in a surface that was notably more hydrophilic after electrochemical transformation, thereby leading to smaller magnitude adhesive interactions with the methyl-terminated SAM on the tip.

3.2.4

Electrochemically Active AFM Probes

As the images in Sect. 3.2.3.1 elegantly demonstrate, the AFM can function as an extremely high resolution probe of surface topography. Unfortunately, as noted earlier, in its conventional form the technique does lack chemical specificity and it is for this reason that AFM is often used in conjunction with other chemically sensitive surface techniques, when probing the electrode–electrolyte interface. However, it has long been recognized in AFM methodology that chemical modification of the tip confers molecular specificity on the probe. This is particularly evident in AFM measurements of the binding force between two species, using the force-curve approach (the principles of which were described in Sect. 3.2.3.2.2 [56, 57]). However, specific tailoring of the chemical functionality of the tip is essential in order to probe the molecular interaction of interest.

Electrochemical analysis represents an extremely attractive tool for the chemical identification of electroactive ions and molecules, with each species having a characteristic voltammetric “fingerprint”. As such, it is becoming increasingly recognized that scanned probe techniques based on electrochemical principles, have a strength in imaging that AFM lacks: the ability to identify regions of differing electrochemical properties and by implication chemical reactivity, with one probe [58]. The scanning electrochemical

microscope (SECM) [59–61] outlined in Chapter 3.3 of this volume, is one such technique, in which a tiny electrode – ultramicroelectrode (UME: typically having a characteristic dimension in the micrometer to submicrometer range) – functions as the imaging tip. The topographical resolution limit of the device is governed by the size of the electrode, which is typically in the range 0.1 to 10 μm , although nanometer-sized electrodes can be fabricated [62–64]. SECM differs from STM in that a faradaic signal resulting from electrolysis of electroactive species in solution is recorded. This is in contrast to STM, which measures a tunneling current, originating from electrons tunneling between the gap of two very closely spaced (angstrom-level separations) (semi)conducting surfaces, held under potential control.

SECM has provided considerable new insights into quantifying chemical processes at condensed phase interfaces, including metals, semiconductors, and inorganic materials in contact with liquid phases, liquid–liquid interfaces, and even liquid–gas interfaces. Moreover, in the biomedical field, SECM has proved powerful in exploring single cells and enzyme activity, as well as determining transport pathways in tissues, all of which are discussed in detail in Chapter 3.3 of this volume. However, one of the major problems with the technique is that the probe response (often a current, but can also be a potential) contains information about both the topography and reactivity of a surface.

One way to enhance both the chemical-sensing capabilities of AFM and the topographical-imaging qualities of SECM is to integrate an electrode component into an AFM probe in order to confer dual functionality – the cantilever functions as the force sensor, which in conjunction

with a sharp tip, is capable of providing very high resolution topographical measurements, whilst the electrode serves as a very sensitive probe of (electro)chemical reactivity, akin to the SECM. This type of imaging device is potentially very powerful as it enables: (1) structural information to be correlated directly with surface activity, with chemical specificity or alternatively, (2) topographical and structural changes to be mapped, in response to a local chemical perturbation (induced electrochemically).

Of interest to this review is the development and application of electrochemically active AFM probes. Two types of probes will be discussed here: (1) metal-coated conventional microfabricated AFM tips; and (2) homemade probes produced from a metal microwire etched to a fine point (to form the tip), bent and in some cases flattened (to form the cantilever) and insulated at all but the tip end [65, 66].

3.2.4.1 Microfabricated Conducting AFM Probes

Electrically conducting AFM probes are conventionally employed, in air or under vacuum, to measure a wide range of electrical characteristics of a sample, such as electrostatic and voltage drop properties, charge distribution, capacitance, or resistance, all at sub-100 nm length scales [67]. In the literature, this hybrid-AFM technique is often named according to the electrical property of the sample under investigation, for example, conducting-AFM (C-AFM) [68], scanning capacitance microscopy [69], scanning potentiometry [70], or electric force microscopy [71] (or as it is sometimes known, Kelvin force probe microscopy). In all cases, the dual functionality of the probe means that high-resolution topographic images and electrical measurements can

be achieved simultaneously, enabling the direct correlation of electrical properties of the substrate with specific topographic features.

Of vital importance to these electrical (and electrochemical) measurements is the preparation of the conducting tip (or electrode). This typically involves modification of a conventional Si_3N_4 or Si AFM probe so that the conductivity of the device is increased, ideally to a level representing minimum probe resistance. This is often achieved in one of two ways. (1) By coating the probe with a thin conducting film, using sputter deposition or evaporation. Typically, Pt or Au is deposited in this manner [68] although Ag and NbN have also been used [72]. (2) By heavily doping either the probe (Si) or a hard-wearing film (diamond), already deposited on the probe [73]. The latter is less common as the contact resistance of the probe is normally much higher than for the metal-coated tips.

When imaging, with the tip held in direct contact with the surface, metal-coated tips are prone to wear over a prolonged period of time. This process that can affect the validity of the electrical measurement. In order to minimize this potential problem, some workers have advocated the use of tapping mode imaging for identifying topographical features of interest [74]. However, this makes simultaneous collection of topography and conductance data (where ideally the tip should remain in contact with the surface) virtually impossible.

When using these conducting tips in solution, with the probe externally connected to a voltage source, so that the device can function as an electrode, the size of the electroactive area becomes a very important issue. This is because it effectively governs the “electrochemical” resolution limit of the probe. This is

especially important for imaging applications in which the tip is used either as a passive (electro)chemical sensor of a surface process or for local perturbation of solution conditions, in order to induce changes in the surface topography. However, for force-sensing applications, employing force-curve measurements, the geometry of the end of the tip is important not the size of the electrode. Similar force studies to those outlined in Sect. 3.2.3.2, have been carried out with metal-coated AFM probes, in electrolyte solution, with the tip held under potential control.

Initial work on the development of electrochemically active AFM probes for solution work, employed Pt-coated Si_3N_4 AFM tips, with the main body of the probe insulated with a nail varnish–super glue mixture, applied manually. In this case, the electroactive area was effectively governed by the surface area of the exposed Pt-coated cantilever (and tip). Using this manual application procedure, it was very difficult to further reduce the active electrode area, without significantly affecting the force-sensing and imaging capabilities of the cantilever and tip. The employment of insulating electrodeposited paints was also problematic [75], due to the number of sharp edges that exist on microfabricated AFM probes (in addition to the tip end). During curing or air-drying, the insulating film tends to retract from sharp points, resulting in the uncontrolled formation of micrometer-sized electrodes all over the probe [76].

These probes were, however, found to be very effective for high-resolution mapping of topographical and structural changes of a substrate immersed in fluid, in response to a local chemical perturbation (induced electrochemically). In particular, the probes were used to electrochemically induce dissolution from a specific region of

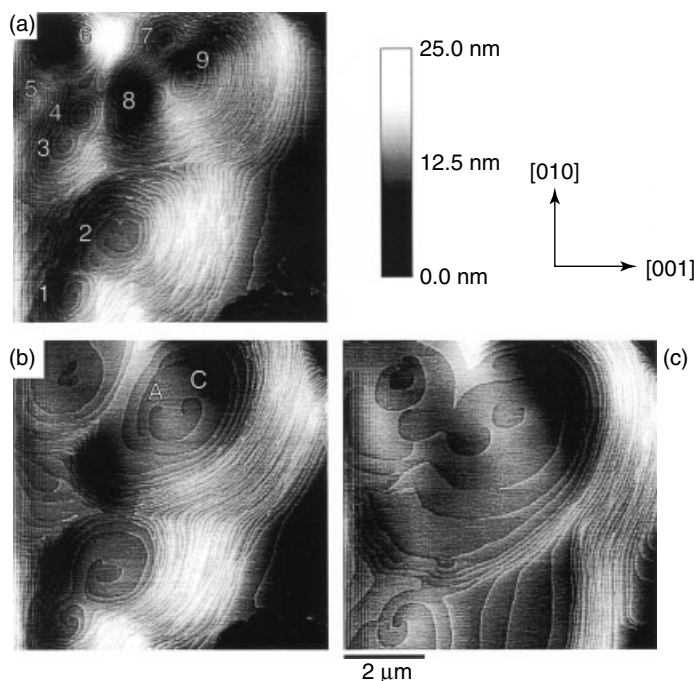


Fig. 14 AFM topography images recorded on KBr(100) immediately after the application of a 1 s potential pulse (from +0.5 to +1.1 V) to the electrochemically active probe. The images were recorded sequentially at a rate of 21 s per frame: Clockwise (C); and anticlockwise (A); rotating spiral are identified in (b) (after Ref. [77]).

the surface of an ionic crystal, and monitor the evolving change in sample topography as the crystal dissolved [77, 78]. Dissolution was achieved electrochemically by stepping the potential of the Pt-coated AFM tip and cantilever from a value at which no electrochemical reactions occurred, and the solution was saturated with respect to the crystalline material, to a value at which electrolysis of one of the lattice ionic species in solution occurred. As the concentration of lattice ions in the solution gap between the probe and surface became depleted, this resulted in a corresponding undersaturation at the crystal–solution interface, which provided the thermodynamic driving force for dissolution.

Figure 14 shows a sequence of AFM topography images recorded on KBr(100), initially in contact with a saturated solution of KBr in acetonitrile, after the application of a 1 s potential pulse (from +0.5 to +1.1 V) to the electrochemically active AFM probe [77]. This is sufficient to induce dissolution by the electrochemical removal of bromide ions (by oxidation to tribromide) in the probe–substrate gap. The images were recorded sequentially at a rate of 21 s per frame, clearly showing that dissolution occurred via a spiral mechanism, in which steps of unit cell height unwind from screw dislocations emerging on the crystal surface. These images provided the first direct experimental evidence

for the operation of the spiral mechanism in the dissolution of an ionic crystal.

3.2.4.2 Microwire Conducting AFM Probes

Homemade AFM probes fabricated from metal microwires [79–81] (such as W, Ni, Pt, or Pt/Ir) where the end of the wire has been etched to form a sharp tip and then bent to form the cantilever, have also found much use as probes of the electrical, frictional, and topographical properties of sample substrates, in air or under vacuum. In many cases, the microwires are electrochemically etched using dissolution procedures borrowed from STM methodology for the production of sharp STM tips [10]. In some cases, the bent wire is flattened to form a beam- (or even V-)shaped cantilever [65, 82]. For C-AFM imaging measurements, solid metal microwire AFM probes are an attractive alternative to the metal-coated conventional AFM tips, as loss of probe conductivity due to wear, no longer poses a problem.

For high resolution electrochemical imaging under solution, an insulating film is applied to the probe so that only the very end of the tip remains exposed. This is possible using etched microwires, as the tip end is the only sharp point on the probe. A similar approach is used for the production of submicrometer UMEs [83] and STM tips, for imaging under solution [84, 85]. Using an electrodeposited insulating paint [64, 75], effective cone-shaped tip electrodes (with integrated cantilevers) with radii in the range 1 nm to 1 μm have been fabricated [64–66]. Optical and scanning electron micrographs (SEMs) of typical electrochemically active AFM (SECM-AFM) microwire probes are shown in Fig. 15.

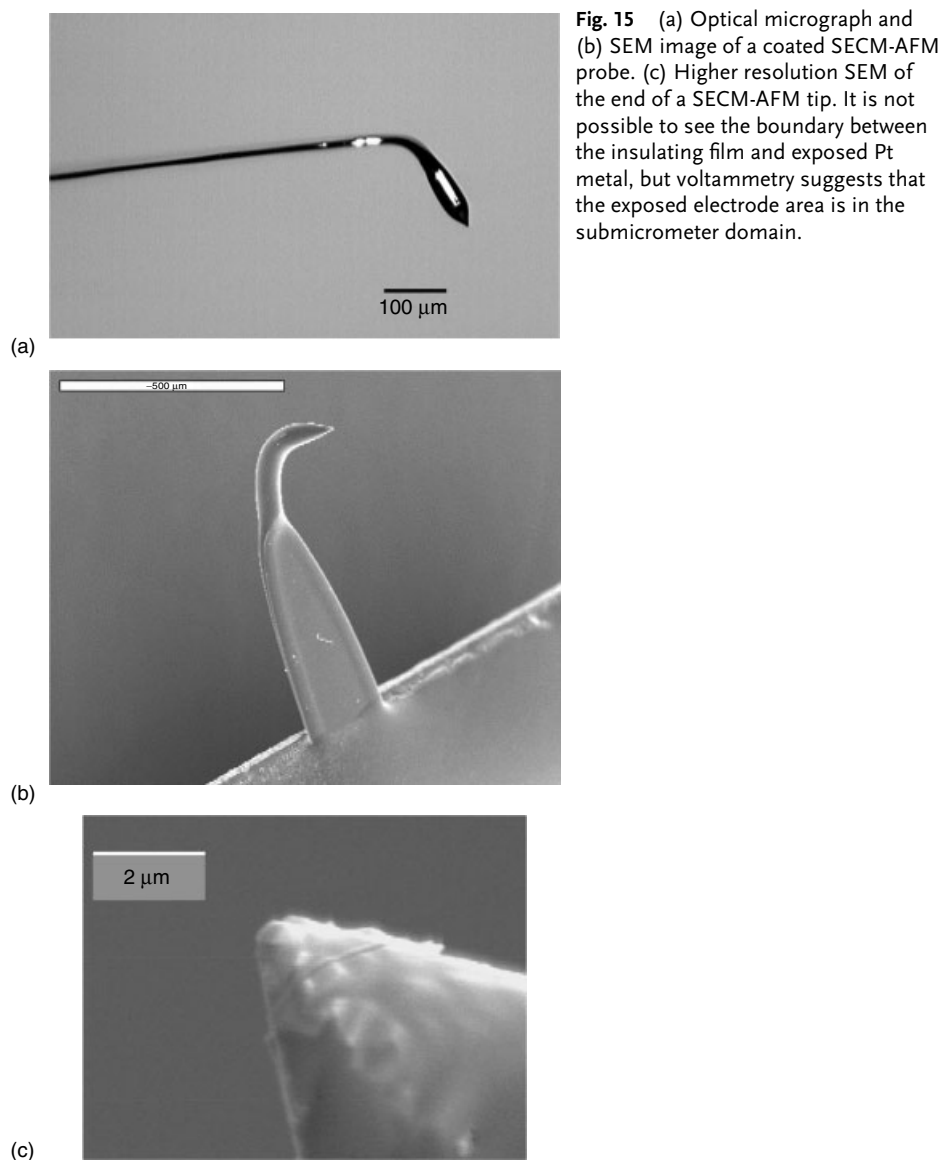
Using these probes, it is possible to simultaneously map the topography and

(electro)chemical (or conducting) properties of a surface under solution (or in air), with both high electrochemical and topographical resolution. For example, the SECM-AFM probe has been used to image both the topography and electrochemical activity of an 10- μm diameter Pt UME sealed in glass [66]. The substrate UME was biased at a potential sufficient to oxidize the electrolyte solution component (IrCl_6^{3-}) at a diffusion-controlled rate, whilst the tip was biased at a potential sufficient to detect the product of substrate electrolysis, also at a diffusion-controlled rate. As Fig. 16 demonstrates, the zone over which tip collection of the electro-generated species occurs is clearly evident and correlates well with the underlying location of the electrode, identified by topographical imaging. The magnitude of the current measured at the tip electrode, can be quantified in terms of the activity of the substrate UME. Although still in their infancy, SECM-AFM tips have also been employed to (1) correlate the transport activity of electroactive species diffusing through pores in a synthetic membrane, with the structure of the surface of the membrane [65]; and (2) to etch (using the equilibrium perturbation approach outlined above) and image pre- and postdissolution, topographically selected zones on a crystal surface [65].

3.2.5

Conclusion

The ability of AFM to provide atomic-level resolution images of electrode surfaces under solution has proved invaluable in providing a greater understanding of the electrode–electrolyte interface, especially when used in conjunction with chemically sensitive surface techniques. The capability to topographically image any surface



irrespective of substrate conductivity at high spatial resolution ideally lends the technique to the investigation of corrosive systems (which often possess a passive insulating layer) or molecularly adsorbed films on electrode surfaces. However, it must not be forgotten that the AFM is in

essence a highly sensitive force-measuring instrument and it is the ability of the device to measure the interaction force between the probe and an electrode surface in which the AFM system excels over other SPM techniques. As such, AFM can provide a detailed understanding of the

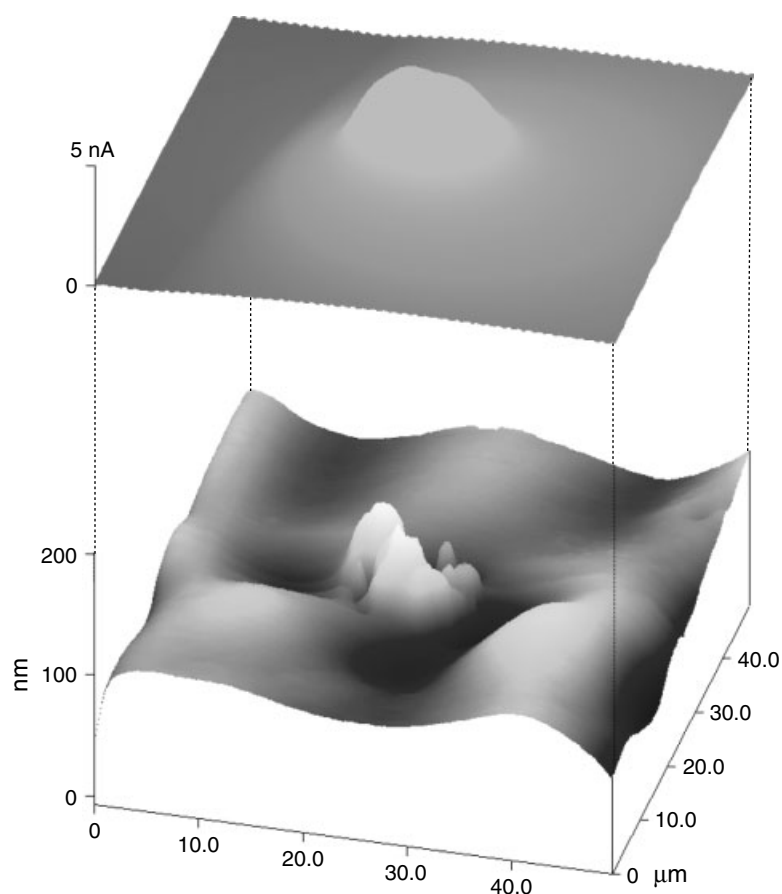


Fig. 16 Topography (flattened) and fixed-height current maps for the diffusion-controlled tip detection of IrCl_6^{2-} (tip potential +0.5 V vs. AgQRE), generated from the transport-limited oxidation of IrCl_6^{3-} , at a 10- μm diameter substrate electrode (substrate potential +0.9 V vs. AgQRE). The scan size was 50.7 $\mu\text{m} \times 50.7 \mu\text{m}$ imaged at a rate of 25.4 $\mu\text{m s}^{-1}$, in a solution containing 0.01 mol dm^{-3} IrCl_6^{3-} and 0.5 mol dm^{-3} KNO_3 . The SECM-AFM tip was characterized by an effective tip radius of 0.93 μm . Both images were recorded in the same area. For topographical imaging, the tip was held in contact with the surface (unbiased), while electrochemical data were acquired with the tip imaging at a fixed height of 1 μm from the surface of the substrate (after Ref. [66]).

electrostatic DL and the charge properties of an electrode surface.

Although it has long been recognized that functionalization of the AFM probe, often with a SAM, is one way of conferring chemical specificity on the tip, an alternative approach is to integrate an electrode

component into the device. By careful tuning of the potential of the electrode, the probe becomes sensitive to any electroactive species (molecules or ions). In this way, it is possible to correlate structural information directly with surface activity and/or map topographical changes in

response to a local chemical perturbation (induced electrochemically). To date, electroactive AFM probes have been fabricated by metal-coating conventional AFM probes and/or home producing the tips from etched (to form the tip) metal microwires, which have been bent (and in some cases flattened) to form the cantilever. The exposed electrode area can be greatly reduced by the application of an electrodeposited insulating film, which on curing exposes just the apex of the metal tip.

Acknowledgments

I would like to thank the Royal Society for support through a University Research Fellowship and Molecular Imaging for a Young Electrochemical Scanned Probe Microscopist award. I would also like to thank those who contributed figures to this review. Their efforts in sending the figures so promptly were much appreciated.

References

1. R. Wiesendanger, *Scanning Probe Microscopy and Spectroscopy*, Cambridge University Press, Cambridge, UK, 1994.
2. G. Binnig, C. F. Quate, Ch. Gerber, *Phys. Rev. Lett.* **1986**, 56, 930.
3. J. Israelachvili, *Intermolecular and Surface Forces*, Academic Press, San Diego, Calif., 1992, p. 169–172.
4. T. R. Albrecht, S. Akamine, T. E. Carver et al., *J. Vac. Sci. Technol., A* **1990**, 8, 3386.
5. S. Alexander, L. Hellemans, O. Marti et al., *J. Appl. Phys.* **1989**, 65, 165.
6. J. Clavilier, R. Faure, G. Guinet et al., *J. Electroanal. Chem.* **1980**, 107, 205.
7. J. Clavilier, *J. Electroanal. Chem.* **1980**, 107, 211.
8. A. J. Bard, L. R. Faulkner, *Electrochemical Methods*, John Wiley & Sons, New York, 1980, p. 8–10.
9. C.-H. Chen, K. D. Kepler, A. A. Gewirth et al., *J. Phys. Chem.* **1993**, 97, 7290.
10. H. Siegenthaler, in *Scanning Tunneling Microscopy II* (Eds.: R. Wiesendanger, H.-J. Guntherodt), Springer-Verlag, Berlin, Germany, 1992, Vol. 28, pp. 7–49.
11. A. A. Gewirth, B. K. Niece, *Chem. Rev.* **1997**, 97, 1129.
12. M. J. Weaver, *J. Phys. Chem.* **1996**, 100, 13079.
13. S. R. Snyder, H. S. White, *Anal. Chem.* **1992**, 64, R116.
14. A. J. Bard, H. D. Abruna, C. E. D. Chidsey et al., *J. Phys. Chem.* **1993**, 97, 7147.
15. D. D. Sneddon, A. A. Gewirth, *Surf. Sci.* **1995**, 343, 185.
16. D. M. Kolb, in *Advances in Electrochemistry and Electrochemical Engineering* (Eds.: H. Gerischer, C. W. Tobias), Wiley-Interscience, New York, 1978, Vol. 11, pp. 125–271.
17. M. A. Schneeweiss, D. M. Kolb, *Phys. Status Solidi* **1999**, 173, 51.
18. O. M. Magnussen, J. Hotlos, R. J. Nichols et al., *Phys. Rev. Lett.* **1990**, 63, 2929.
19. S. Manne, P. K. Hansma, J. Massie et al., *Science* **1991**, 251, 183.
20. H. Uchida, N. Ikeda, M. Watanabe, *J. Electroanal. Chem.* **1997**, 424, 5.
21. M. F. Toney, J. N. Howard, J. Richer et al., *Phys. Rev. Lett.* **1995**, 75, 4472.
22. Z. Shi, J. Lipkowski, *J. Electroanal. Chem.* **1994**, 365, 303.
23. N. Ikemiya, S. Miyaoka, S. Hara, *Surf. Sci.* **1994**, 311, L641.
24. G. S. Frankel, *J. Electrochem. Soc.* **1998**, 145, 2186.
25. K. Shimizu, K. Kobayashi, P. Skeldon et al., *Corros. Sci.* **1997**, 39, 701.
26. R. M. Rynders, C.-H. Paik, R. Ke et al., *J. Electrochem. Soc.* **1994**, 141, 1439.
27. M. Büchler, T. Watari, W. H. Smyrl, *Corros. Sci.* **2000**, 42, 1661.
28. J. Y. Josefowicz, L. Xie, G. C. Farrington, *J. Phys. Chem.* **1993**, 97, 11995.
29. R. E. Williford, C. F. Windisch, Jr., R. H. Jones, *Mater. Sci. Eng., A* **2000**, 288, 54.
30. F. Katsuki, M. Matsuda, M. Matsumoto et al., *J. Vac. Sci. Technol., A* **1999**, 17, 3481.
31. M. G. Walls, A. Ponthieux, B. Rondot et al., *J. Vac. Sci. Technol., A* **1996**, 14, 1362.
32. E. Schmidt-Rieder, X. Q. Tong, J. P. G. Farr et al., *Br. Corros. J.* **1996**, 31, 139.
33. A. Ullman, *An Introduction to Ultrathin Organic Films: From Langmuir-Blodgett to Self-Assembly*, Academic Press, Boston, Mass., 1991.

34. S. Xu, S. J. N. Cruchon-Dupeyrat, J. C. Garno et al., *J. Chem. Phys.* **1998**, *108*, 5002.
35. J. Pan, N. J. Tao, S. M. Lindsay, *Langmuir* **1993**, *9*, 1556.
36. K. Tamada, J. Nagasawa, F. Nakanishi et al., *Thin Solid Films* **1998**, *150–155*, 327.
37. W. Han, E. N. Durantinit, T. A. Moore et al., *J. Phys. Chem. B* **1997**, *101*, 10719.
38. S. O. Kelley, J. K. Barton, N. M. Jackson et al., *Langmuir* **1998**, *14*, 6781.
39. T. A. Jung, A. Moser, H. J. Hug et al., *Ultra-microscopy* **1992**, *42–44*, 1446.
40. B. Capella, G. Dietler, *Surf. Sci. Rep.* **1999**, *34*, 1.
41. A. C. Hillier, S. Kim, A. J. Bard, *J. Phys. Chem.* **1996**, *100*, 18808.
42. R. Raiteri, M. Grattarola, H.-J. Butt, *J. Phys. Chem.* **1996**, *100*, 16700.
43. A. Döppenschmidt, H.-J. Butt, *Surf. Colloids A* **1999**, *149*, 145.
44. T. Arai, M. Fujihira, *J. Vac. Sci. Technol., B* **1996**, *14*, 1378.
45. S. Biggs, P. Mulvaney, C. F. Zukoski et al., *J. Am. Chem. Soc.* **1994**, *116*, 9150.
46. C. Dedeloudis, J. Fransaer, J.-P. Celis, *J. Phys. Chem. B* **2000**, *104*, 2060.
47. J. Wang, A. J. Bard, *J. Am. Chem. Soc.* **2001**, *123*, 498.
48. K. Hu, A. J. Bard, *Langmuir* **1997**, *13*, 5114.
49. K. Hu, Z. Chai, J. K. Whitesell et al., *Langmuir* **1999**, *15*, 3343.
50. A. Noy, D. V. Vezenov, C. M. Lieber, *Annu. Rev. Mater. Sci.* **1997**, *27*, 381.
51. A. Engel, H. E. Gaub, D. J. Müller, *Curr. Biol.* **1999**, *9*, R133.
52. J. M. Serafin, A. A. Gewirth, *J. Phys. Chem. B* **1997**, *101*, 10833.
53. J. M. Serafin, H. J. Hsieh, J. Monahan et al., *J. Phys. Chem. B* **1998**, *102*, 10027.
54. J. E. Hudson, H. D. Abruña, *J. Am. Chem. Soc.* **1996**, *118*, 6303.
55. J.-B. D. Green, M. T. McDermott, M. D. Porter, *J. Phys. Chem.* **1996**, *100*, 13342.
56. E.-L. Florin, V. T. Moy, H. E. Gaub, *Science* **1994**, *264*, 415.
57. C. D. Frisbie, L. F. Rozsnyai, A. Noy et al., *Science* **1994**, *265*, 2071.
58. H. G. Hansma, *Proc. Natl. Acad. Sci.* **1999**, *96*, 14678.
59. A. J. Bard, F.-R. F. Fan, D. T. Pierce et al., *Science* **1991**, *254*, 68.
60. M. V. Mirkin, *Anal. Chem.* **1996**, *68*, A177.
61. A. L. Barker, M. Gonsalves, J. V. Macpherson et al., *Anal. Chim. Acta* **1999**, *385*, 223.
62. Y. Shao, M. V. Mirkin, G. Fish et al., *Anal. Chem.* **1997**, *69*, 1627.
63. B. D. Pendley, H. D. Abruña, *Anal. Chem.* **1990**, *62*, 782.
64. C. J. Slevin, N. J. Gray, J. V. Macpherson et al., *Electrochem. Commun.* **1999**, *1*, 282.
65. J. V. Macpherson, P. R. Unwin, *Anal. Chem.* **2000**, *72*, 276.
66. J. V. Macpherson, P. R. Unwin, *Anal. Chem.* **2001**, *73*, 550.
67. T. W. Kelley, E. L. Granstrom, C. D. Frisbie, *Adv. Mater.* **1999**, *11*, 261.
68. S. J. O'Shea, R. M. Atta, M. E. Welland, *Rev. Sci. Instrum.* **1995**, *66*, 2508.
69. Y. Martin, D. Abraham, H. Wickramasinghe, *Appl. Phys. Lett.* **1988**, *52*, 1103.
70. M. Hersam, A. Hoole, S. O'Shea et al., *Appl. Phys. Lett.* **1998**, *72*, 915.
71. H. Bluhm, A. Wadas, R. Weisendanger et al., *Phys. Rev. B* **1997**, *55*, 4.
72. H. Dai, E. Wong, C. M. Lieber, *Science* **1996**, *272*, 523.
73. Ph. Niedermann, N. Blanc, R. Christoph et al., *J. Vac. Sci. Technol., A* **1996**, *14*, 1233.
74. R. E. Thomson, J. Moreland, *J. Vac. Sci. Technol., B* **1995**, *13*, 1123.
75. C. E. Bach, R. J. Nichols, H. Meyer et al., *Surf. Coat. Tech.* **1994**, *67*, 139.
76. J. V. Macpherson, P. R. Unwin, unpublished results.
77. J. V. Macpherson, P. R. Unwin, A. C. Hillier et al., *J. Am. Chem. Soc.* **1996**, *118*, 6445.
78. C. E. Jones, J. V. Macpherson, P. R. Unwin, *J. Phys. Chem. B* **2000**, *104*, 2351.
79. J. E. Stern, B. D. Terris, H. J. Mamin et al., *Appl. Phys. Lett.* **1988**, *53*, 2717.
80. C. M. Mate, G. M. McClelland, R. Erlandsson et al., *Phys. Rev. Lett.* **1987**, *59*, 1942.
81. A. H. Sørensen, U. Hvid, M. W. Mortensen et al., *Rev. Sci. Instrum.* **1999**, *70*, 3059.
82. C. A. Peterson, R. K. Workman, X. Yao et al., *Nanotechnology* **1998**, *9*, 331.
83. R. M. Penner, M. J. Heben, T. L. Longin et al., *Science* **1990**, *250*, 1118.
84. L. A. Nagahara, T. Thundat, S. M. Lindsay, *Rev. Sci. Instrum.* **1989**, *60*, 3128.
85. A. A. Gewirth, D. H. Craston, A. J. Bard, *J. Electroanal. Chem.* **1989**, *261*, 477.

3.3**Scanning Electrochemical Microscopy***Benjamin R. Horrocks**University of Newcastle upon Tyne,
Newcastle upon Tyne, United Kingdom***3.3.1****Introduction**

Scanning electrochemical microscopy (SECM) arose from experiments aiming to probe the diffusion layer directly with an ultramicroelectrode (UME) [1–4]. Related techniques such as the scanning vibrating electrode technique (SVET) were also being used to study localized corrosion, albeit on a coarser length scale [5]. In the mid to late 1980s, scanning tunneling microscopy (STM) was making an impact in electrochemistry (see Chapter 3.1) and it was natural to combine STM-like positioning technology with UMEs to image electrochemical activity in addition to topography (Fig. 1). With the development of the feedback mode, 2D imaging of samples of a general nature, not only electrode surfaces, became possible [4, 6]. The use of the SECM for microfabrication by deposition of thin metal lines and etching of semiconductors also appeared early in its history [7–9]. Although most of the early work employed home-built apparatus, assembled from piezoelectric actuators and a bipotentiostat, a commercial SECM is now available. The lateral spatial resolution typically achieved is on the μm scale, which is higher than that of the related scanning reference electrode technique (SRET) and SVET techniques, but does not routinely approach the resolution of scanning tunneling (STM) and atomic force microscopes (AFM). The major limiting factor is the tip size. However, under certain conditions (thin water films on mica in humid air) molecular scale resolution can

be obtained, though the imaging mechanism is disputed (see Sect. 3.3.5.3). The resolution of SECM in the direction normal to the surface (z -axis) is somewhat higher and probably only limited by the stability of the positioning technology and the capability of the electronics to resolve small changes in the signal from the tip. The utility of SECM is not related merely to spatial resolution, in fact most applications take advantage of the chemical selectivity possible and the kinetic modes of operation that allow new kinds of electrochemical experiment to be performed. A judicious choice of the solution-phase reagents has enabled the imaging and kinetic analysis of a wide range of systems including electrode surfaces, semiconductors (Sect. 3.3.4.1.2.), conducting polymers (Sect. 3.3.4.1.3.), immobilized enzymes (Sect. 3.3.4.1.4.), liquid–liquid and liquid–gas interfaces (Sect. 3.3.4.2), biological specimens (Sect. 3.3.4.3), homogeneous reaction kinetics, and heterogeneous electron and ion transfer. Some workers have also applied SECM as a fabrication tool. The spatial resolution of the technique is not usually greater than photolithography. However, there are promising applications in which chemical or biochemical functionality is patterned on a surface for which the conventional techniques, which employ vapor deposition and/or high temperatures, are often unsuitable [10]. The various applications of the SECM will be reviewed after a description of the operating principles (Sect. 3.3.1.1.) and instrumentation (Sect. 3.3.2.).

Quantitative theoretical models are available for many of the possible SECM experiments (Sect. 3.3.3.). In the simplest case, the variation of tip current with tip/substrate distance provides an accurate calibration of the distance scale, d , in

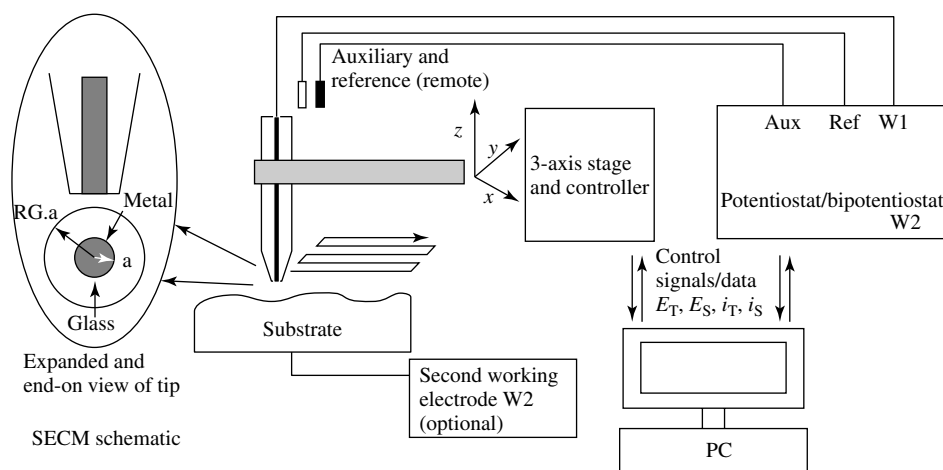


Fig. 1 Schematic diagram of the scanning electrochemical microscope (SECM).

units of tip radius, a . Quantitative SECM experiments have been used to characterize various interfaces, evaluate the kinetics of electron transfer (ET) at liquid–liquid interfaces (Sect. 3.3.4.2.1), metal [11] and semiconductor electrodes [12], redox and conductive polymers (Sect. 3.3.4.1.3), and immobilized enzymes [13–18]. Complex heterogeneous processes, such as corrosion and crystal dissolution reactions, have also been studied [19–24].

Several limitations of the SECM technique remain although they may be overcome as the technology develops. First, the smallest tip size, which is routinely employed, is limited by the diameter of available microwire to ca. 1 μm . Strategies for fabricating much smaller tips have been reported, however, considerable effort is still required to characterize the tip geometry (Sect. 3.3.2.2). Laser-pulled micropipette tips have some promise for the production of submicrometer tips of well-defined geometry [25]. Second, the time required to capture an image is much longer than other scanning probe microscopes (SPMs), for example, STM or AFM,

and these in turn are slower than optical methods. Depending on the tip size, number of linescans, and the area scanned, the typical image-acquisition times range from a few minutes to an hour. Again, smaller tips would improve the capture rate, though the technique will probably remain slow compared to other SPMs. Third, it may often be difficult to deconvolute topographic information and chemical reactivity; for example, determining tip height information over a mixed conductive/insulating sample. This remains an area of significant activity and approaches based on tip height modulation, the development of current-independent distance calibration methods and hyphenated SECM techniques (e.g., SECM-AFM) have been reported (Sect. 3.3.5 and Chapter 3.2 in this volume).

3.3.1.1 Principles of Operation

Figure 1 shows a schematic diagram of the SECM apparatus. The scanning probe, known as the tip, is usually a UME fabricated in the form of a disk by sealing a metal wire in glass and exposing the

cross section (see Chapter 2.5 in this volume). The tip is typically mounted on a three-axis positioning stage that is driven by piezoelectric actuators under software control. As the tip is scanned in a raster pattern across the sample surface (substrate), the software produces a map of the electrochemical response of the tip. Generally the tip current, i_T , is displayed, although the tip voltage, E_T can just as easily be acquired. In the case in which the substrate is another electrode whose electrochemical properties are of interest, a bipotentiostat is required and the substrate current i_S and potential E_S can also be recorded. Otherwise, a standard potentiostat or even a two-electrode cell can be used. The reference and auxiliary electrode are usually placed relatively far from the tip. Almost any conventional electrochemical experiment, for example, cyclic voltammetry (CV), ac voltammetry or potentiometry can be

carried out in the SECM. In addition, there is flexibility in choosing the manner in which the tip interacts with the substrate; this gives rise to the different modes of operation (Fig. 2) that are discussed next.

3.3.1.1.1 Feedback Mode In the feedback mode [6], the tip potential is set to a value at which a particular molecule in the solution, for example, a redox mediator, is consumed. Feedback is the term used to indicate that the measured tip current is influenced by the rate at which the mediator is regenerated at the substrate. The substrate may also be biased independently and serve as a second working electrode; however, it is not essential for the substrate to be another electrode or even for it to be conductive (Fig. 3). The feedback effect is sensitive to the tip-substrate separation, d , often expressed in units of tip radius, a , as $L = d/a$. At large values of

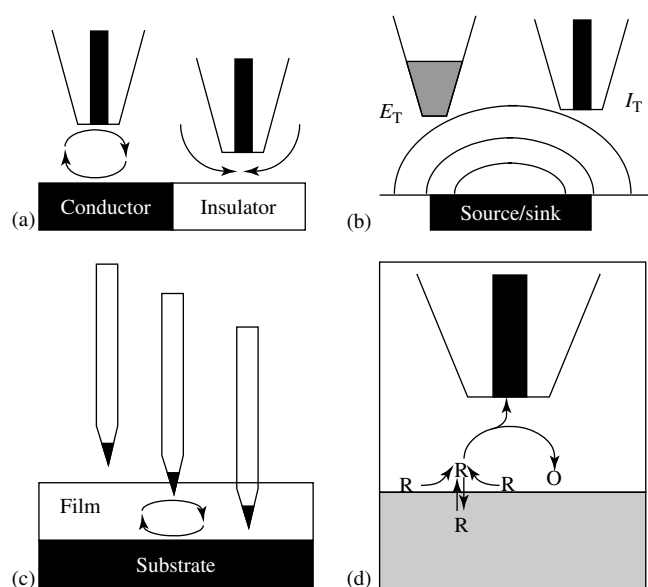


Fig. 2 Various types of SECM experiment (modes). (a) feedback; (b) generation-collection; (c) penetration; and (d) equilibrium perturbation.

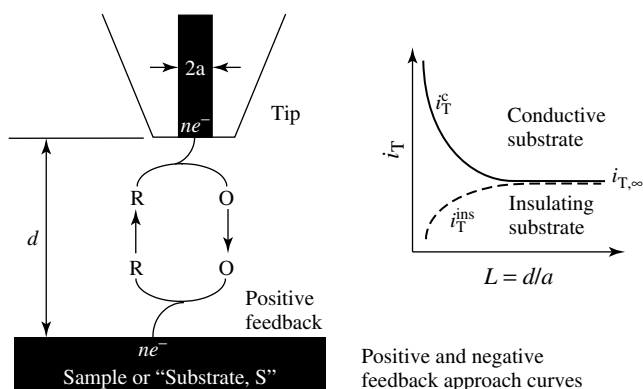
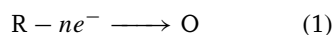


Fig. 3 The feedback effect (schematic).

L , the tip diffusion layer is not affected by the substrate and the current is $i_{T,\infty}$ and is independent of L . The standard type of tip is the cross section of a micron-sized wire sealed in an insulator such as glass that is beveled to allow close approach of the tip to the substrate. This tip geometry is most frequently employed because the tip surface is parallel to the substrate and maximizes the feedback effect discussed below. Conical electrodes such as etched STM-like tips are occasionally used when a disk geometry is not feasible, although the feedback ($i_T/i_{T,\infty}$) is smaller [26].

For an oxidizable redox mediator, R , the process at the tip during a feedback experiment is



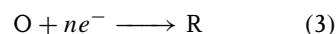
If E_T is sufficiently positive, then the rate of the reaction is governed by the diffusion of R to the tip. For large L and a microdisk tip with a thick insulating sheath, the steady state current, $i_{T,\infty}$, is given by

$$i_{T,\infty} = 4nFDca \quad (2)$$

F is the Faraday constant, n is the number of electrons transferred in the tip reaction, D is the diffusion coefficient of R , c is the

bulk concentration of R , and a is the tip radius. Equation (2) applies to a microdisk tip, but the functional form is the same for other geometries.

When the tip-substrate separation is less than a few tip radii, the O species formed in the Reaction (1) can diffuse to the substrate where it may be reduced back to R



This reaction produces an additional flux of R to the tip and hence an increase in tip current ($i_T > i_{T,\infty}$). When this reaction is also diffusion-limited, the tip current reaches a maximum value. This phenomenon is termed “positive feedback” (Fig. 3). As the tip-substrate distance (d) decreases, i_T increases without limit. In order for this to occur, it is not necessary for E_S to be controlled by an external voltage source, since a conductive substrate will be biased by electron exchange with reduced mediator, R , outside the area beneath the tip. However, if the size of the conductive features on the substrate is comparable to the tip radius, a , then a bipotentiostat is necessary. Finally, it is worth noting that in many topical applications, Reaction (3)

is not an electrode process at all. It may be an enzymatic redox reaction [27, 28], an ion transfer [29, 30], or the transfer of a neutral molecule involved in the overall electrochemical process [31, 32].

“Negative feedback” is the conventional terminology for situations when Reaction (3) does not occur; the substrate may be an inert, electrical insulator or the oxidation of R may be irreversible. At small L , $i_T < i_{T,\infty}$ because the substrate now simply hinders diffusion of species R to the tip from the bulk solution (Fig. 3). Indeed, the closer the tip to the substrate, the smaller will be the i_T . For both positive and negative feedback, variations of i_T can be related to changes in L and used to image the substrate topography by scanning the tip over the substrate surface. Since the mass transport rate in positive feedback experiments at small L is of order D/d , which is typically $\sim 0.1 \text{ cm s}^{-1}$, convective effects owing to the motion of the tip during imaging at typical speeds of $10 \mu\text{m s}^{-1}$ are not usually important.

Since the magnitude of the feedback is sensitive to the rate of mediator regeneration at the substrate, the measured feedback-distance behavior (“approach curve”) provides information on the kinetics of the process at the substrate [13–18, 33]. During imaging, the Z -position of the tip is usually fixed and therefore an independent measurement of the tip-substrate distance is useful to deconvolute substrate kinetics from the effects of topography [34]. For this reason, feedback-mode kinetic studies are often made at fixed X - Y lateral positions, but with the tip scanning over a range of Z values to generate an approach curve.

3.3.1.1.2 Generation/Collection Mode and Potentiometric SECM Generation/collection (G/C) mode refers to experiments in

which species are generated at the substrate independent of the tip reaction and are subsequently detected at the tip, or vice versa (Fig. 2). These two different G/C modes are referred to as substrate generation/tip collection (SG/TC) and tip-generation/substrate collection (TG/SC). The ratio of fluxes at the tip and the substrate defines the collection efficiency. Owing to the relative sizes of tip and substrate, the collection efficiency approaches 100% in the TG/SC mode. Deviations of the collection efficiency from 100% can be used to investigate homogeneous chemical kinetics of unstable species in the tip/substrate gap [35–39]. The rates of chemical reactions following an initial electron transfer may be determined by measuring the distance dependence of the collection efficiency; at small L , the reverse reaction at the substrate competes with the homogeneous chemical reaction. An example is the dimerization of the radical anion of acrylonitrile [37].

In SG/TC experiments, the tip travels within a thick diffusion layer generated by the substrate. In fact, the first SECM-type measurements were aimed at probing such a layer [1, 40, 41]. The reason that the Generation-collection (GC) mode is less often used than feedback is that the tip may disturb the diffusion layer at the substrate either through the consumption of species at the tip or by hindering the supply of reagents to the substrate. Convective effects are also sometimes observed as a result of stirring by the tip. The SG/TC mode is often simplest with a potentiometric tip, which reduces the disturbance of the substrate diffusion layer. An analytical treatment of the steady state SG/TC experiment is available when a small substrate (a microdisk or a spherical cap) generates stable species that

are sensed by a smaller tip, for example, an ion-selective microelectrode [42–46].

For large substrates, the diffusion field of the substrate does not attain a steady state; however, for reversible electrode kinetics at tip and substrate, the transient response to a potential step has been treated numerically and the tip attains a pseudo-steady state [47]. This experiment is able to distinguish the diffusion coefficients of the oxidized and reduced forms of the redox couple and may be useful in cases in which the usual assumption, that these are equal, breaks down. A treatment of the feedback mode for this problem has also been reported [48]. One advantage of the SG/TC mode is that the tip response is zero when there is no substrate reaction, whereas in feedback experiments, the tip current is measured on top of a background owing to the diffusion of species from the bulk solution. While feedback mode is certainly advisable for heterogeneous kinetic measurements, SG/TC can be used for monitoring many heterogeneous processes such as corrosion and enzymatic reactions (Sects. 3.3.4.1.1 and 3.3.4.1.4).

3.3.1.1.3 Penetration Experiments In a few studies, the SECM tip has been used to penetrate the substrate, for example, the polymeric film of a polymer-modified electrode. Some information about the variation of concentrations, kinetic and mass transport parameters with depth, can be obtained from straightforward voltammetric measurements [49, 50]. When the tip approaches the underlying metal electrode, feedback effects occur and the current-distance curves are similar to those obtained in solution as long as the film is homogeneous and reasonably conductive. Eventually, tunneling effects may be important for very short distances; $d < 1$ nm.

3.3.1.1.4 Equilibrium Perturbation Mode

This mode, pioneered by Unwin and coworkers [18], uses the reaction at the tip to perturb an equilibrium at a second interface, by depletion of a component of the solution. The tip current transient is sensitive to the flux of that component as the position of the equilibrium adjusts. The steady state tip current will lie between the values for negative feedback and diffusion-limited positive feedback depending on the kinetics of the equilibrium. If the kinetics are rapid, the same tip current as for a simple redox couple at a metallic substrate is observed. The use of smaller tips and decreased tip/substrate distances results in higher mass transport rates and increases the range of measurable rate constants. This mode is a flexible method for obtaining heterogeneous kinetic information about nonelectrochemical processes. It has been applied to, amongst other systems, adsorption/desorption, solubility, and partition equilibria as well as biophysical applications such as lateral proton transport in models of cell membranes [51].

A related technique is double potential step chronoamperometric SECM in which the first potential step generates a reactive species that diffuses to the interface of interest and then undergoes a reaction or is adsorbed or transferred to a second phase. The second potential step collects the remaining reactive species. The fraction of reactive species “lost” as a function of the time delay gives a measure of the interfacial kinetics.

3.3.1.2 SECM Imaging

The SECM may be used in different ways: as an imaging tool in which the feedback current or tip potential reflects both topography and chemical reactivity or with a stationary tip as a means to initiate and monitor chemical reactions

with high spatial localization (μm – nm) and high mass transport rates up to $\text{ca. } 1 \text{ cm s}^{-1}$. Imaging experiments are generally carried out in feedback mode since the mass transport rate is high and the chemical reactions are confined to the tip/substrate gap. A high mass transport rate is important to maximize the tip velocity and minimize the time required to collect an image. Even so, the image acquisition times for typical experiments are usually 15 min or longer. SECM imaging therefore requires that the condition of the substrate is not changing on this at such a timescale. In the case of samples in which there are large areas of the image with no contrast, there are possibilities to increase the frame acquisition rate by altering the tip velocity according to the amount of detail present [52]. A feedback mode can be applied to almost any sample, though it may not resolve small (compared to a), unbiased conductive areas in a generally insulating surface [53]. GC mode imaging works best when the sources and sinks of reagents are spatially localized and sufficiently small and well separated to set up steady state diffusion fields that do not overlap. It has been used successfully for the study of immobilized enzymes deliberately spotted for applications in, for example, immunoassay [54].

3.3.2

Instrumentation

3.3.2.1 Apparatus

Figure 1 is a schematic of a basic SECM apparatus comprising a tip position controller, an electrochemical cell (including tip, substrate, counterelectrode, and reference electrode), bipotentiostat, and data acquisition system. The tip is usually mounted on the z -axis of an x - y - z stage

controlled by piezoelectric actuators, although DC servomotors or stepper motors have also been employed. The substrate is fixed horizontally in an electrochemical cell that is mounted on a stable platform. A vibration-isolation table may be required for high-resolution work, though it is often unnecessary for imaging on the micrometer scale. For air-sensitive or controlled-atmosphere work, the SECM can be housed inside a glove box or bag.

SECM instruments suitable for imaging require a PC equipped with an interface board to synchronize acquisition of the electrochemical data with the movement of the tip. Building an SECM for kinetic experiments at fixed tip position or approach curve measurements is relatively easy, but fairly sophisticated software and some electronic work is necessary to construct a computer-controlled apparatus for imaging applications. Details on the construction of SECM instruments can be found elsewhere [6, 13–18, 53, 55]. An SECM is now available commercially from CH Instruments, Inc. (Austin, TX, USA). The instrument employs piezoelectric actuators, a three-axis stage, and a bipotentiostat controlled by an external PC under a 32-bit Windows environment. Various standard electrochemical techniques are incorporated along with SECM imaging, approach curves, and the modes described in Sect. 3.3.1.1.

3.3.2.2 Tips

Most SECM experiments have employed μm -sized metal disks (Fig. 4). Such tips are fabricated by heat-sealing a metal wire or a carbon fiber in a glass capillary with application of a vacuum using a simple oil pump. The glass is subsequently polished to expose the cross section of the wire, and the glass wall surrounding the conductive disk is beveled to allow the tip to approach

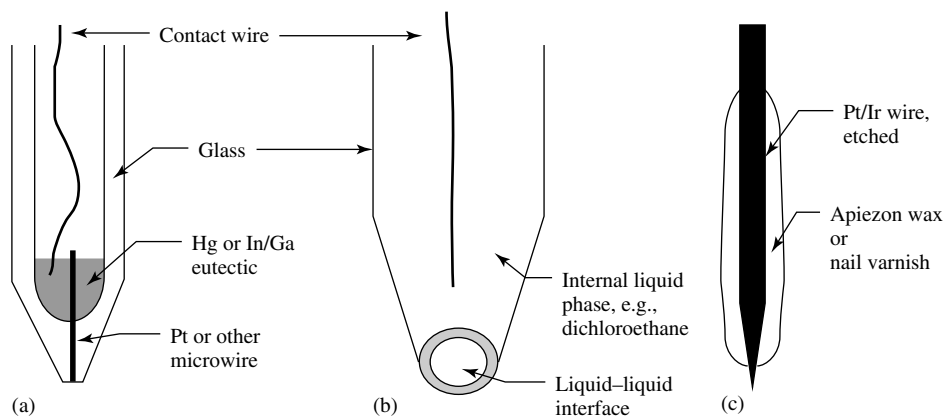


Fig. 4 SECM tips (not an exhaustive list). (a) standard voltammetric microdisk; (b) micropipette; and (c) etched metal tip.

close to the substrate. The ratio of the radius of metal and glass to metal alone is termed RG and is typically ca. 10. Detailed information on the preparation of such tips can be found elsewhere [4, 16]. The tip radius is limited by the available wire to $>0.3\ \mu\text{m}$ for Pt tips.

Nanometer-scale tips have been fabricated by electrochemically etching $125\ \mu\text{m}$ diameter Pt/Ir rods in a solution of saturated CaCl_2 and HCl at about 20 V rms ac [26, 56]. The tip was insulated with molten Apiezon wax and the very end of the tip was exposed by placing it in a scanning tunneling microscope (STM) and setting the tunneling current. These nm-sized conical tips are useful for penetration of soft interfacial films and for imaging [49]. The precise geometry of these tips is not usually known although the approach curves certainly depart from the theory for microdisks and have been modeled as spherical caps or cones [26].

Another technique prepares small disk-shaped tips by sealing metal wires in glass using a laser-based micropipette puller [25]. The metal was exposed either by etching the glass insulator or

by micropolishing. Several of these tips exhibited well-behaved voltammetry with effective radii from 2 to 500 nm. However, only relatively large tips ($a > 100\ \text{nm}$) were found to be suitable for quantitative electrochemical measurements based on voltammetric, scanning electron microscopy (SEM), and SECM feedback characterization.

A novel method for the preparation of micrometer and submicrometer spherical tips based on self-assembly from Au sols was reported by Demaille and coworkers [57]. The self-assembly of ca. 8 nm diameter Au particles occurred at the tip of a 0.1- to $1\ \mu\text{m}$ glass pipette containing a solution of 1,9-nonanedithiol. A spherical Au tip was formed in two hours. Steady state voltammograms and SECM approach curves obtained with these tips were in good agreement with the theory.

Other tips that extend the range of analytes to species not accessible to metal tips have been reported. Biosensor tips for hydrogen peroxide have been prepared by coating carbon fibers with an electrically wired enzyme (horseradish peroxidase) [58]. A small ac perturbation

applied to the tip was used to measure the conductance in the tip/substrate gap, and this was shown to generate an approach curve identical to the usual feedback effect. The liquid-membrane (micropipette-type) ion-selective electrodes (ISEs) can also serve as SECM tips. Micropipette ISEs for K^+ , Zn^{2+} , and NH_4^+ have been used to map local concentrations of ions with micrometer resolution [44]. A disadvantage of a potentiometric SECM probe is the difficulty in the determination of the tip-substrate distance, which is often required for quantitative data analysis. Antimony tips can be used as both amperometric electrodes and potentiometric pH sensors [43]. Another approach is to make a dual-channel tip, in which one channel operates as an ISE and the other as a distance sensor [44]. Recently, small potentiometric tips have been made by etching an Ag wire to a fine point and then insulating the tip using an electrophoretic paint. The effective radii were measured by voltammetry as 50 nm–1 μ m. Anodization in the presence of Cl^- produced tips with Nernstian response to Cl^- over the range 10^{-4} – 10^{-1} mol dm $^{-3}$ [59]. Pulled tips can also be used to prepare Ag/AgI μ ISEs and these can be coated with NaFion to improve selectivity [25].

A combined optical/electrochemical microelectrode can be used as the tip to study, for example, photoelectrochemical reactions on semiconductors [60–63]. This tip consists of a several micron diameter optical fiber coated with gold and insulated with a polymer film [60]. The optical fiber creates a focused light spot on the substrate surface and the concentric gold ring serves as an electrode to monitor the products of the photoelectrochemical reaction at a substrate. If i_T and E_S (the substrate photocurrent) are acquired, it is possible to image the photoelectrochemical response

of the substrate as well as the SECM (SG/TC-like) response.

A micropipette filled with a solvent immiscible with the outer solution can also serve as an amperometric UME. In Ref. [64], interfacial electron transfer occurred between the aqueous ferrocyanide inside a micropipette and tetracyanoquinodimethane (TCNQ) in the outer dichloroethane solution. Such pipettes show feedback effects just as for conventional metal tips. However, the equivalent RG (insulating sheath radius/active electrode radius) is typically rather small and this particularly affects the shape of the approach curve in negative feedback experiments [30, 65]. These tips may have some advantages – submicron pipettes tend to have more regular geometry metal tips of comparable size. There is also the possibility to use ion transfer at the liquid–liquid interface as the i_T . This enables one to study ion transfer processes and opens the possibility to study many non-redox-active systems. For example, SECM experiments with the tip current produced by ion transfer of K^+ from water to 1,2-dichloroethane facilitated by dibenzo-18-crown-6 (DB18C6) were carried out [29]. The resulting approach curves at a second liquid–liquid interface, which was a source of K^+ , showed normal positive feedback. Selectivity can also be introduced into these tips using the commercially available ionophores for liquid-membrane ISEs [66]. The tips can be operated amperometrically, though care must be taken to minimize the uncompensated resistance in the organic phase inside the tip using a nonaqueous reference electrode such as Ag/AgB[ClPh] $_4$ [30]. An alternative method to fabricate ion transfer (IT)-type tips uses a recessed metal microdisk electrode to support the liquid

phase, producing a tip more robust than the pulled pipettes [67].

3.3.3

Theory

This section is a brief survey of the quantitative modeling of SECM experiments. The theoretical approach curves are usually expressed in terms of the normalized tip/substrate distance, $L = d/a$, and a current, I_T , normalized by the diffusion-limited current to a disk-shaped UME, $I_T = i_T/4nFDac$. It should be noted that the common experimental practice of normalizing by the tip current at large L , $i_{T,\infty}$, is not equivalent, especially for small values of RG .

3.3.3.1 Numerical Simulation of SECM Experiments

Extraction of quantitative chemical information from SECM requires a mathematical model of the interaction of the tip and substrate. Such modeling typically involves numerical solution of a reaction-diffusion equation with the boundary conditions appropriate to the interfacial kinetics. Simulation of SECM experiments is computationally much more demanding than for standard electrochemical experiments (discussed in Chapter 1.3). This is because diffusion in at least two dimensions must be considered and the discontinuity in the boundary condition between the tip metal and insulating sheath necessitates a fine mesh.

3.3.3.1.1 Finite Difference Methods Finite difference techniques have frequently been applied to the simulation of the SECM in the axisymmetric cylindrical geometry encountered with microdisk tips. Often an exponentially expanding grid is used in order to produce a fine mesh near

the edge of the microdisk and a comparatively coarse mesh further away in both the radial and perpendicular directions. Depending on whether steady state or time-dependent phenomena are of interest, several approaches have been employed to solve the difference equations. The most popular technique is undoubtedly the alternating direction implicit (ADI) method applied to the computation of the tip response to a potential step [35–39]. Since the ADI method generates the current-time response, the steady state approach curves are obtained from the long-time limit of the current transient. Unwin and coworkers have applied this technique to the simulation of many different interfacial kinetic experiments with the SECM, including finite heterogeneous electron transfer kinetics, following chemical reactions, crystal dissolution, and several types of equilibrium perturbation experiments [68]. Successive overrelaxation has also been used to obtain the steady state concentration profile at polymer-coated electrodes [69, 70]. This technique is very simple to implement either in code or using the iteration facilities of a spreadsheet. However, it is not particularly efficient nor does it provide directly the transient response, although it may be used to do so in combination with a fully implicit time step. Some simulations are possible with explicit time stepping methods [71]; these are however restricted to short time steps if a fine mesh is used, or conversely suffer from poor accuracy if the mesh is coarsened. The fast quasi-explicit finite difference (FQEFD) method was employed by Matsue and coworkers in their treatment of enzyme-mediated feedback [72]. This method updates the concentration profile using concentration values at the previous two time points. Although several efficient methods are available, for example, multigrid or Krylov

integrators [73], for most axisymmetric SECM problems, the techniques above are sufficient to find a solution on a modern PC within a reasonable period of time.

3.3.3.1.2 Integral Equations An analytical solution for the typical SECM problem of a disc-shaped tip over a flat substrate, with quasireversible electron transfer at both tip and substrate, can be expressed in terms of multidimensional integral equations through the application of integral transforms to the diffusion equation [74, 75]. This solution applies to both transient and steady state feedback experiments. The integral equations, however, must be solved numerically. This was carried out using a finite difference technique and the computations were observed to be in good agreement with a standard finite difference solution of the diffusion equation. Although this technique has not been widely applied, it does offer some advantages at the cost of some mathematical complexity. Since one spatial variable may be integrated out exactly, the dimensionality of the problem is reduced. As for convolution voltammetry at planar macroscopic electrodes, the basic equations are written in a form independent of the shape of the applied voltage perturbation. Recently, another analytical approach to the SECM problem has been to expand the solution as a dual series and truncating this series appropriately provided simple and accurate analytical approximations to the feedback approach curve. The functional form of these approximations is in fact rather similar to those obtained by fitting to the numerical simulations, but more accurate [76].

3.3.3.1.3 Finite Element Methods Although the first numerical treatment of the SECM feedback experiment was carried

out by the finite element method (FEM) [6], it has subsequently been used on relatively few occasions. The major reason for this is that the finite difference techniques mentioned above are easy to implement and very familiar to most electrochemists. The FEM is however well suited to handle complex geometries, and adaptive algorithms are able to refine the mesh in which the concentration profiles are steep at boundaries between conductive and insulating regions. Although most workers have written their own code to solve SECM diffusion problems, finite element programs are widely available and some have proven useful for the simulation of microelectrode and cylindrically symmetrical SECM problems (2D) [29, 30, 77]. Such programs easily generate concentration profiles, however, not all of these programs may be suited to electrochemical simulation in which the concentration gradient is required and routines to integrate this over the electrode surface may need to be written.

In two papers, the boundary element method (BEM) has been employed to model SECM [78]. In this technique, the weighting function is chosen so that the weighted residual formulation of the problem can be written in terms of quantities evaluated only on the boundary of the simulation domain. The advantage of the method is the reduction of the dimensionality of the problem, which enabled the simulation of SECM linescans and images. Since the mesh is generated only on the boundaries, that is, the surface of the electrode and insulator, the number of elements required is reduced (Fig. 5). The SECM image of a inlaid disc electrode and raised or recessed hemispherical electrodes in an insulating plane was computed assuming a steady state condition during imaging,

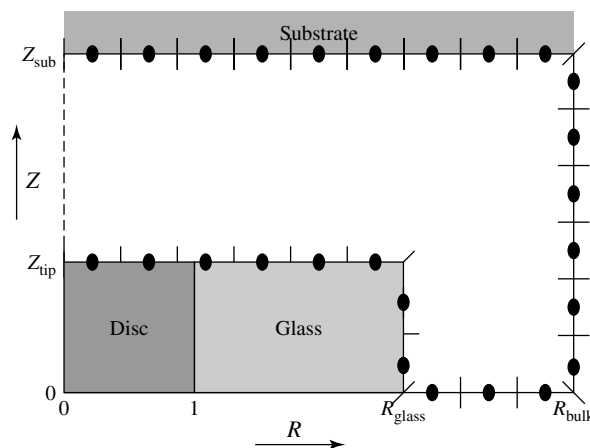


Fig. 5 Schematic of the BEM grid and geometry employed for microdisk approach curve simulations. (Reprinted with permission from Ref. [78], Copyright 1999 by American Chemical Society.)

that is, tip speed less than the diffusion mass transport coefficient. This type of simulation is not as easily carried out by the finite difference method since the symmetry of the problem is reduced when the tip moves away from the center of the substrate disc. This would require a complex 3D grid and therefore greatly increase the computational expense.

3.3.3.2 Steady State SECM Experiments

Steady state SECM measurements are relatively immune to problems of uncompensated resistance and charging current, quantitative studies are therefore usually carried out under steady state conditions as long as the chemical nature of the system permits. The steady state theory is simpler than for transient techniques and several useful analytical expressions suitable for least squares fitting of data are available.

3.3.3.2.1 Diffusion-controlled Reactions

Numerical simulations of the dimensionless current-distance curves for steady

state processes at both insulating and conductive substrates have been reported for several values of RG [6]. These calculations assume a diffusion-controlled mediator turnover, equal diffusion coefficients, and an infinitely large substrate. Current-distance curves for the case in which the substrate is of comparable size to the tip are given in Ref. [75]. An often-used analytical expression for an infinite conductive substrate is [26]

$$I_T^c(L) = \frac{i_T}{i_{T,\infty}} = \frac{0.78377}{L} + 0.3315e^{-1.0672/L} + 0.68 \quad (4)$$

which fits the simulated I_T-L curve over an L range 0.05 to 20 to within 0.7%, that is, better than typical experimental accuracy. For negative feedback at an infinite substrate, Eq. (5) is accurate to within 0.5% over the same L interval.

$$I_T^{\text{ins}}(L) = \frac{1}{0.15 + 1.5385/L + 0.58e^{-1.14/L} + 0.0908e^{(L-6.3)/(1.017L)}} \quad (5)$$

By fitting an experimental current-distance curve to theory, one can determine the tip-substrate separation, L , and the mass transport coefficient, which are essential for many quantitative SECM measurements.

Both Eqs. (4 and 5) were derived using the data tabulated in Ref. [6] for $RG = 10$. Galceran and coworkers have also provided very accurate alternative equations of similar form [76]. Although the effect of RG is often ignored, when $RG < 10$ it may be significant, especially with negative feedback. Very small RG values (~ 1.1) occur for micropipette-based tips and the appropriate values of the normalized steady state SECM current for various values of RG have been calculated using a finite element technique [30].

If a small (submicrometer) tip is to be used in quantitative measurements, it is important to show that the metal surface is not recessed into the insulator since the mass transport coefficient will be altered. This is possible via a study of the approach curve; a recessed tip does not produce as large a positive feedback [26]. Recessed tips have also been produced intentionally for single molecule experiments [79, 80]. Fan and coworkers [80] simulated a special case of the recessed electrode with the radius of the circular hole in the insulator equal to the disk radius. An analytical approximation for recessed tips with the hole in the insulator sheath different from the disk radius is also available [25]. The feedback effect is also reduced for tips, which are conical or spherical caps, but the shape of the approach curve provides some information on the tip geometry, for example, the solid angle [26]. Accurate numerical simulations of such tips by the finite difference method are more costly than for microdisks, but have been

reported using the BEM with similar conclusions [78].

3.3.3.2.2 Finite Kinetics The case of finite tip kinetics and diffusion-controlled mediator regeneration at the substrate can be treated as for a thin-layer cell as long as the tip/substrate separation is small enough ($L < 1$) for the current distribution to be uniform [81]:

$$I_T(E, L) = \frac{0.68 + 0.78377/L + 0.3315e^{-1.0672/L}}{\theta + 1/\kappa} \quad (6)$$

where $\theta = 1 + \exp[nf(E - E^{\circ})]D_O/D_R$, $\kappa = k^{\circ} \exp[-\alpha n f(E - E^{\circ})]/m_O$, k° is the standard rate constant, E is the tip potential, E° is the formal potential, α is the transfer coefficient, n is the number of electrons transferred per redox event, and $f = F/RT$ (where F is the Faraday, R is the gas constant, and T is temperature), and the effective mass-transfer coefficient for SECM is

$$m_O = \frac{4D_O}{\pi a} \left[0.68 + \frac{0.78377}{L} + 0.3315e^{-1.0672/L} \right] = \frac{i_T(L)}{\pi a^2 n F c} \quad (7)$$

At constant L , Eqs. (6 and 7) describe a quasireversible steady state tip voltammogram, as may be obtained by scanning the potential of the tip while the substrate potential is held constant. If a series of voltammograms is recorded at decreasing values of L , the effect of increased mass transport rate can be observed whilst preserving the advantages of steady state methods, that is, the absence of problems associated with ohmic drop, adsorption, and charging current. This approach was used to determine a

value of $3.7 \pm 0.6 \text{ cm s}^{-1}$ for the oxidation of ferrocene at Pt in acetonitrile [11].

The effect of finite substrate heterogeneous kinetics has also been studied (Fig. 6) [33]. When the kinetics of the tip reaction are fast, the local rate of an irreversible heterogeneous reaction occurring at a substrate can be extracted by fitting an experimental approach curve to Eq. (8) [82]:

$$I_T(L) = I_S \left(1 - \frac{I_T^{\text{ins}}}{I_T^c} \right) + I_T^{\text{ins}} \quad (8a)$$

$$I_S = \frac{0.78377}{L(1 + 1/\Lambda)} + \frac{0.68 + 0.3315e^{-1.0672/L}}{1 + F(L, \Lambda)} \quad (8b)$$

where I_T^c and I_T^{ins} are given by Eqs. (4 and 5), respectively, and I_S is the kinetically controlled substrate current. $\Lambda = k_f d/D$ where k_f is the apparent heterogeneous rate constant (cm s^{-1}), and $F(L, \Lambda) = (11/\Lambda + 7.3)/(110 - 40L)$. The numerical results fit Eq. (8) over an L interval from 0.1 to 1.5 and $-2 \leq \log \Lambda \leq 3$ within $\sim 1\text{--}2\%$. Equation (8) is equally applicable to finite electrochemical and chemical kinetics at the substrate. The only difference is that

for a chemical process k_f is potential-independent.

Equation (8a) splits I_T into two components; the fraction of the substrate current, I_S , which is collected by the tip, plus the contribution due to diffusion into the tip/substrate gap, I_T^{ins} . This is exact for a simple positive feedback experiment over a conductive substrate when all of the tip current is collected at the substrate, $I_T^c = I_S$. However, it can be applied approximately as long as the product of the substrate reaction is stable and forms the basis for a semi-analytical treatment of chemical reactions following electron transfer at the tip [38].

Mandler and coworkers have studied the case of twin microdisks (tip and substrate) in which the substrate is unbiased and acts to catalyze the reaction of the product formed at the tip (methyl viologen cation radical) with $\text{H}^+(\text{aq})$ [83]. This arrangement allows the determination of the substrate potential and exchange current density and was used to analyze the kinetics of proton reduction at the Pt substrate.

3.3.3.2.3 Generation-collection Mode In SG/TC mode, the rate of generation ($\text{mol cm}^{-2} \text{ s}^{-1}$) can be evaluated from the

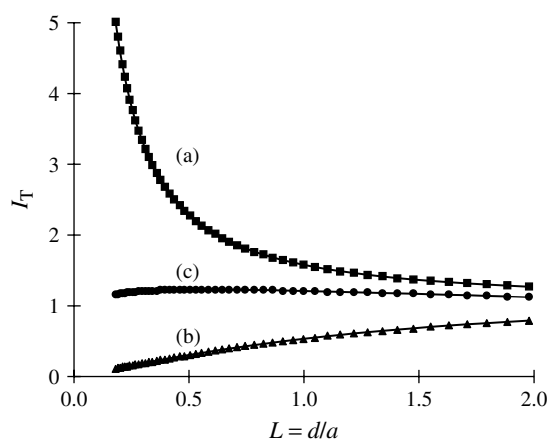


Fig. 6 Effect of substrate kinetics on feedback in approach curves. (a) diffusion-limited substrate kinetics, pure “positive feedback”; (b) inert substrate, pure “negative feedback”; and (c) an intermediate case for which substrate kinetics can be quantified.

concentration profile of generated species if the diffusion coefficient is known. A typical experimental situation is a collection mode measurement of the products of a reaction at a microdisk substrate. Under appropriate assumptions for the flux distribution, the concentration profile can be expressed as an integral and evaluated numerically [43]. Closed-form approximations are also available [44]. When the flux is uniform across the substrate, the concentration profile over the center of the disk is exactly Eq. (9):

$$c(Z) = \frac{rf}{D} \left[\sqrt{(Z^2 + 1)} - Z \right] \quad (9)$$

Where r is the substrate radius, $Z = d/r$, D is the diffusion coefficient of the species sensed by the tip, and f is the reaction flux/mol cm⁻² s⁻¹. The corresponding concentration profiles for nonuniform flux at the substrate have been computed [46]. Such a situation might correspond to electrolytic generation of H⁺ by oxidation of an organic molecule at the diffusion-limited rate or to an enzymatic process limited by the supply of the enzyme substrate. This can often be tested by comparing the extracted flux with the diffusion-limited flux to the substrate. Although, it would be straightforward to extend the theory to other than disk-shaped substrates, there are comparatively few relevant applications as yet. If the substrate is too large to generate a steady state concentration profile, then transient techniques such as cyclic voltammetry [84] or potential steps [47, 48] have been employed. A time-of-flight experiment, in which a pulse is applied to the substrate and the time delay before the tip detects the products, is another possibility and may be used to determine the tip/substrate separation.

3.3.3.3 Transient SECM Experiments

In general, transient SECM experiments require numerical simulation for a quantitative analysis of the data although much can often be gained from qualitative studies, for example, the use of the tip to detect ejected ions at polymer-modified electrodes during cyclic voltammetry [85, 86]. The possible influence of charging current and uncompensated resistance must also be considered, although this does not appear to be a severe problem in practice. Coupling between tip and substrate through the solution resistance can occur since part of the potential between the tip and the reference electrode can be affected by the substrate current flowing through the solution resistance. This is not a cause for concern if the tip is poised at a potential at which the tip reaction is diffusion-limited. Occasionally, a tip-substrate coupling at high frequencies has been observed when both are metallic electrodes, the origin of the effect is not entirely certain, but it may interfere with transient generation-collection experiments or time-of-flight measurements [47, 48]. Despite the possible complications, equilibrium perturbation and other transient experiments have become popular because they enable a wide range of chemical systems and processes to be investigated.

3.3.3.3.1 Potential Step Techniques The i_T response to a potential step under a condition of positive feedback is similar to that of an isolated UME; initially the current decays $\propto t^{-1/2}$ before reaching a steady state at times determined by the tip-substrate separation, d , and the diffusion coefficient [73]. The transient response for negative feedback is slower since the characteristic length scale involved is determined by the diffusion of material from outside the tip/substrate region to

replenish that depleted underneath the tip. Equilibrium perturbation methods, such as the SECM-induced transfer (SECMIT) experiments of Unwin and coworkers [68], are based on the use of potential steps to rapidly deplete the tip/substrate gap of particular species. The flux from bulk solutions is low, therefore many other sources of material will produce a detectable signal and the SECM can be used to study reactions at any nearby interface, which can act as a source. Examples include the dissolution of CuSO_4 induced by the reduction of $\text{Cu}^{2+}(\text{aq})$, desorption of H^+ from oxides induced by the reduction of $\text{H}^+(\text{aq})$ [35], charge transfer from a second liquid phase [87], and proton transport along a monolayer at the air–liquid interface [51]. The detailed shape of the current transients depends on the distance, d , the rates of diffusion in the solution and in the second liquid phase, or across the surface of the substrate in addition to any kinetic limitations. Since either the interfacial kinetics or the mass transport rates themselves may be of interest, means to separate these quantities are required. When the SECM is used to study electron or ion transfer at liquid–liquid interfaces, it is the interfacial rate constants that are of interest and the concentration of species in the second phase are often increased to allow a constant composition approximation in which there is no diffusion limitation in the lower phase. Alternatively, if the aim is to make analytical measurements in a second phase, which cannot be directly probed by the tip, then rapid interfacial kinetics are necessary [68]. The various possibilities must be differentiated on the basis of comparison to simulated working curves and through their characteristic dependence on the bulk concentrations, interfacial potentials, and surface excesses.

A second type of transient SECM experiment is double potential step chronoamperometry in which the species generated at the tip under diffusion control in the first potential step reacts at or is transferred across a nearby interface. As the rate of the interfacial reaction increases, the fraction collected in the reverse potential step is reduced. At short times, the current during the reverse step varies linearly with $t^{-1/2}$ and there are two limiting slopes corresponding to the cases of no reaction at the interface to that of diffusion-controlled reaction at the interface. For intermediate cases, the interfacial kinetics may be extracted [88].

3.3.3.3.2 Miscellaneous Techniques Substrate generation–tip collection experiments have been simulated for the case of reversible redox reactions in which case they can be used to obtain separately the diffusion coefficients of both forms of the redox couple [47]. SG/TC experiments have also been used to study following chemical reactions [84]. This method may be limited in scope owing to the large charging current that flows at the macroscopic substrate shortly after the step. Another transient technique is the MEMED (microelectrochemical measurements at expanding droplets) method in which a liquid drop grows in a second phase at the tip of a fine capillary. The SECM is used to position a detector electrode near the drop and used to detect products of the interfacial reaction that diffuse into the receiving phase. The drops were observed to be near spherical and the mass transport problem is analogous to classical polarography with the difference that the drop is not the working electrode, but a source of reactants. The potentiometric transients for Cl^- production were analyzed to determine the rate of

hydrolysis of triphenylmethyl chloride in dichloroethane dropping into water [89]. More recently, the same technique has been used to study the kinetics of Cu^{2+} stripping in an oil/water system [90].

3.3.4

Selected Applications

SECM has been applied to the investigation of various technologically important materials and interfaces, for example, metallic corrosion [91–96], fuel cell electrocatalysts [97], semiconductor photocatalysts [12, 60–63, 98], conducting polymers [49, 50, 85, 86, 99–103], liquid–liquid and liquid–gas interfaces [29, 30, 68]. The SECM may be used to image the substrate topography and/or reactivity, or with the tip at a fixed location, to study the local kinetics of the interfacial reactions of interest.

3.3.4.1 Solid–Liquid Interfaces

3.3.4.1.1 Corrosion The SECM has been employed to study the corrosion of metals such as steel and oxide films on titanium in aqueous solutions. Previously, the SRET provided direct evidence for the existence of local anodes and cathodes on corroding iron surfaces and potentiometric microelectrodes were used to monitor pH and Cl^- in corrosion pits [104, 105]. Localized corrosion processes have also been imaged at higher resolution by SECM [91–96]. An interesting result from these studies was the observation of very high current densities ($>1 \text{ A cm}^{-2}$) at MnS inclusions in stainless steel. This effect was catalyzed by Cl^- and it was suggested that the high local current density could lead to an increased concentration of Cl^- and a decrease in pH sufficient to act as a trigger for a pitting event [93, 106]. Dissolution products

of MnS inclusions have also been observed using a carbon fiber SECM tip and I^-/I_3^- as the redox mediator [107]. Strong enhancement of the SECM feedback was observed at a small number of microscopic sites on oxide-covered titanium foils for the redox couples $\text{Fe}(\text{CN})_6^{4-/3-}$ and Br^-/Br_2 . The diameters of these active sites were $10\text{--}50 \mu\text{m}$ at an areal density of between $20 \pm 5 \text{ sites cm}^{-2}$ and in a later report $3\text{--}30 \mu\text{m}$ at $180 \text{ sites cm}^{-2}$ [108, 109]. Application of a positive potential to initiate pitting and subsequent examination by a range of techniques (energy dispersive X-ray analysis, SEM, AFM, and confocal laser microscopy) showed that the active sites were usually associated with inclusions of Al and Si [94]. A probe consisting of an optical fiber with a concentric gold microring electrode was used as the SECM tip to image simultaneously the electrochemical (via i_T) and photoelectrochemical activity (via i_S) of the oxide film. The use of the optical fiber to provide a scanning light spot provides similar information to the scanning laser spot techniques for mapping photoelectrochemical activity across a surface [110]. The photocurrent was found to be lower over the inclusions, consistent with metallic behavior [61]. Pitting precursors have also been identified on nitrogen-bearing austenitic steel [111]. The SECM was used to monitor pH and Cl^- at the pit precursors in combination with Raman spectroscopy. An increase in pitting resistance was observed as the nitrogen content increased. The authors concluded from the SECM and Raman data that nitrate ions were formed and incorporated into the passive film.

Individual pitting events are difficult to study since they often occur at unpredictable locations and times. An SECM approach has been reported that allows the experimenter to attempt to initiate

pitting events at predetermined locations on aluminum and steel [91, 112]. The basis of the technique is the generation of a pulse of Cl^- via reduction of trichloroacetic acid at the tip. This technique enabled the study of the effect of the time and potential of passivation as well as spatial location on the ease with which corrosion could be induced. The large tip current fluctuations observed were assigned to the reduction of soluble iron(II) species produced as precursors to breakdown of the passive film on the metal.

3.3.4.1.2 Semiconductors SECM images of the dark electrochemical behavior of WSe_2 , TiO_2 , and Ta_2O_5 have shown that the ET rate is nonuniform when the semiconductor is in depletion [12, 108, 109, 113, 114]. In the case of iodide, bromide, and ferrocyanide on $n\text{-TiO}_2$, the SECM images showed active sites for oxidations that occurred positive of the flatband potential. Conversely, reduction of ferricyanide at $n\text{-TiO}_2$ under conditions of accumulation was observed to be spatially uniform. The current at the active sites is not resolved unless the semiconductor is in depletion and the mean current across the semiconductor–liquid interface is small. In the case of ET at the interface $p\text{-WSe}_2/\text{Ru}(\text{NH}_3)_6^{3+}$, the feedback current as a function of substrate potential was determined by the Boltzmann factor for the concentration of majority carriers at the interface at potentials negative of the flatband potential. This corresponds experimentally to an apparent transfer coefficient of 1. Such ideal behavior was observed only on undamaged portions of the van-der Waal's surface; at steps or pits, the currents were much greater and increased less steeply with potential [12].

The photoelectrochemical behavior of titanium dioxide has also been studied;

the scanning microring/optical fiber tip of Smyrl and coworkers was used to map the photoactivity of titanium dioxide films [61]. More recently, SECM was used to study the mechanisms of oxidation and reduction at unbiased titanium dioxide photocatalysts [98]. A model for metallized TiO_2 photocatalysts was prepared by spray pyrolysis of titanyl acetylacetonate onto indium tin oxide glass (ITO). The half of the ITO uncoated with TiO_2 served to mimic the action of metallic particles deposited on TiO_2 particles. With the tip far from the semiconductor surface and oxidizing ferrocyanide at the diffusion-limited rate, band gap illumination of the semiconductor caused a depletion of ferrocyanide and a reduction in the tip current. However, when the tip was within feedback range of the substrate, the tip current increased upon illumination indicating feedback of ferrocyanide via reduction of ferricyanide at the TiO_2 . This result demonstrated that both oxidation and reduction reactions occur on the illuminated semiconductor and that any Schottky barrier at the photocatalyst surface must therefore be relatively small. The extent of the increase in feedback current was greater when the bare ITO portion was insulated with epoxy. Saturation of the solution with oxygen inhibited the positive feedback and in fact, the tip current now decreased on illumination. The role of oxygen and the ITO is similar to that of an external bias, removing photogenerated electrons and favoring the oxidation reaction at the TiO_2 surface. These studies provided support for the mechanism of the enhancement of activity of TiO_2 photocatalysts by deposition of small noble metal particles.

3.3.4.1.3 Conductive Polymers Characterization of charge and mass transport in ionically conducting polymers (e.g.,

perfluorinated sulfonate polymers and dialysis membranes) and electronically conductive polymers (e.g., polyvinylferrocene and polypyrrole) is an ongoing area of research. The various steps involved in charge and mass transport processes in these systems may include interfacial electron transfer (ET), ion transfer (IT), diffusion, migration, and conformational changes in the polymeric structure. A complete understanding of such a complex process requires not only kinetic measurements, but also a determination of the location of the rate limiting processes, that is, in the bulk polymer, at the electrode–polymer interface or the polymer–solution interface. SECM images of ionic fluxes from polymeric films on electrode surfaces show that there may also be lateral variations in the flux caused by nonuniformity in the film [99].

The ion transfer that occurs on electrochemical switching of redox-active polymers has been studied by a variant of the GC mode, tip/substrate cyclic voltammetry (T/S CV). In this experiment, i_T is monitored as E_S is cycled to switch the polymer film. E_T is poised at a constant value to detect particular ions near the polymer film–solution interface. Ejection of $\text{Os}(\text{bpy})_3^{2+/3+}$ from NaFion-coated electrodes showed that the ions ejected from the film were mostly $\text{Os}(\text{III})$ [115]. T/S CV was also used to detect proton fluxes during the redox cycling of polyaniline and to differentiate Cl^- and H^+ fluxes [116, 117]. Potentiometric tips were also used to detect Cl^- fluxes and provided direct evidence in support of the accepted mechanism of polyaniline oxidation [42–46]. Electrochemical reduction of polypyrrole (PPY) similarly requires a transfer of ions to maintain electroneutrality. Using a platinum tip poised at a potential sufficient to oxidize Br^- , the reduction of PPYBr was

shown to occur first with influx of cations and that Br^- is ejected later in the CV ($E_S < -0.3$ V vs SCE) [85, 86]. Polypyrrole doped with styrene-methacrylate copolymer micelles was studied using T/S CV to determine the flux of ejected cations. Cd^{2+} was monitored amperometrically by reduction at an amalgamated Au tip and K^+ using a BME-44-based potentiometric liquid-membrane ion-selective microelectrode [118]. The block copolymer micelles act as immobile polyanions inside the film and charge compensation on redox switching occurs through cation transport.

The SECM can obtain spatially resolved information in the direction parallel to the film surface in a straightforward manner. In one recent example, it was used to image the variation in conductivity of poly[3-ethoxy-thiophene] and poly[ethylenedioxy-thiophene] after ion bombardment. This process converts the topmost layers (ca. 30 nm) to an insulating material and has applications to lithography and printed circuits [119]. However, it is also possible to probe the location of reactions inside the film in two ways: (1) through penetration experiments with nm-scale tips and (2) through approach curves. The penetration experiments are feasible for soft films that are able to relax and adjust to the presence of the tip. A 30 nm radius Pt tip was used to study the voltammetry of $\text{Os}(\text{bpy})_3^{2+}$ inside a 218-nm thick NaFion film [49]. The diffusion coefficient and kinetic parameters of the redox couple inside the film were determined directly without the complication of accounting for processes at the polymer–liquid interface. In addition, the film thickness is measured by approaching to within tunneling distance. The same method was applied in a study of the redox switching of polyvinylferrocene and the depth variation of the kinetic properties

in a 300 nm film [50]. On a coarser scale, SECM has been used to study the transport of ruthenium hexaamine and methylene blue in polyacrylamide gels using a 25 micron Pt tip [120]. A chronoamperometric experiment inside the gel yields the diffusion coefficient directly, independent of concentration and was used to observe the interaction of the redox species with DNA in the gel by measurement of the decrease in effective diffusion coefficient.

The second method for studying spatial location of reactions in polymer films via approach curves is based on the idea that the magnitude of the feedback depends on the distance between the tip and the site at which the regeneration of the mediator takes place. For example, the effective tip/substrate distance appearing in the equation for feedback may correspond to the distance between the tip and the polymer–solution interface or the tip and the buried polymer–metal interface. A set of diagnostic criteria has been produced, which enables the experimenter to distinguish between regeneration of the mediator at the polymer–solution interface or in the bulk polymer [85, 86]. An analysis of approach curves was used to show that reduction of ferrocenium and $\text{Os}(\text{bpy})_3^{3+}$ at oxidized polypyrrole occurs within a submicrometer layer of polymer at the polymer–solution interface [86]. A study of polyalkylterthiophenes using similar methodology has also been reported and the electron transfer to methylviologen at these films was found to occur at the polymer–solution interface [121]. This methodology works well when an independent measurement of the film thickness and the tip–film–solution interface separation is available to calibrate the distance scale. The latter can sometimes be obtained by directly touching the film and then retracting the tip [50, 118].

3.3.4.1.4 Immobilized Enzymes The SECM has been employed to detect the catalytic activity of a variety of immobilized enzymes or enzyme labels including glucose oxidase [27, 58, 122–124], urease [44, 125], nitrate reductase [126], diaphorase [72, 127, 128], horse radish peroxidase [129], NADH-cytochrome C reductase [28], and alkaline phosphatase [54]. When the enzyme kinetics are too slow for feedback measurements, generation/collection mode can be used. In this section, we discuss kinetic investigations and analytical applications, but leave patterning of activity to Sect. 3.3.4.4 on microfabrication.

The study of immobilized enzymes by SECM by Pierce and coworkers concerned the catalytic oxidation of β -D-glucose to D-glucono- δ -lactone inside a micrometer-thick porous layer of immobilized glucose oxidase (GOx) using a feedback approach [27]. The oxidized form of the mediator produced by the tip reaction was reduced at the substrate surface by GOx when a sufficient concentration of glucose was present. Zero-order enzyme-mediator kinetics were observed and similar apparent heterogeneous rate constants evaluated for several mediators indicating saturation of the enzyme by glucose and mediator under the conditions of the experiment. For the feedback approach to be successful, the flux of mediator owing to the enzymatic process must be comparable to the diffusion flux of mediator from the bulk solution; low mediator concentrations and large tip radius decrease the limit of detection. This was expressed quantitatively in Eq. (10):

$$k_{\text{cat}}\Gamma_{\text{enz}} \geq 10^{-3} \frac{D_{\text{Red}}C_{\text{Red}}}{a} \quad (10)$$

where $k_{\text{cat}}\Gamma_{\text{enz}}$ is the maximum flux of the enzyme reaction and the right-hand

side is proportional to the flux of mediator from the bulk solution to the tip. This flux should be less than $k_{\text{cat}}\Gamma_{\text{enz}}$ if the enzyme is to be detected. Feedback detection was also used to observe the localized reaction of GOx in the pores of track-etched polycarbonate membranes and membrane-bound NADH-cytochrome c reductase in rat liver mitochondria [28].

Studies of antibody-antigen complexation and DNA-protein interactions have used enzyme-labeling techniques to generate redox-active species. Wittstock and coworkers imaged alkaline phosphatase-labeled digoxin, which was observed to bind to the corresponding antidigoxin antibody immobilized on a glass slide [54]. 4-aminophenol, an electroactive product of the enzymatic hydrolysis of 4-aminophenyl phosphate, was detected by an amperometric SECM tip. Figure 7 shows a schematic of the approach of Matsue and coworkers to SECM immunoassay applied to the immunoassay of leukocidin, a toxic protein produced by methicillin-resistant *Staphylococcus aureus* (MRSA) [130]. An antibody-chip for leukocidin was prepared by self-assembly of antileukocidin on a protein A-coated glass substrate. These workers also demonstrated a dual immunoassay for the polypeptide hormones human placental lactogen (HPL) and human chorionic gonadotropin (HCG) [131]. A glass substrate was spotted with anti-HPL and anti-HCG. After incubating the substrate in a solution containing the antigens, horseradish peroxidase (HRP)-labeled antibodies were used to form sandwich complexes as in standard enzyme-linked immunosorbent assay (ELISA). HRP was detected using a Pt tip to observe production of ferrocenium in a solution containing hydrogen peroxide and a soluble ferrocene derivative. The amount of HRP, and hence antigen, was

quantified using i_T and the two antigens were distinguished by their spatial position on the substrate using the SECM to image ferrocenium. This strategy for SECM immunoassay has some different, potentially useful, characteristics compared to conventional methods since the product generated by the enzyme label is detected close to the site of production. The time required to produce a detectable signal is reduced and the use of patterned substrates should allow arrays for multianalyte assays to be developed.

An interesting new approach to SECM immunoassay [132] has used commercial paramagnetic beads of 1–3 μm mean diameter to prepare microspots loaded with biochemical reagents (Fig. 8). The bead suspension can be mixed with reagents and applied as if it were a liquid reagent. A magnet placed underneath a hydrophobic substrate (silanized glass or plastic film on glass) was used to attract the beads from a 1 μL drop at the tip of a micropipette positioned over the substrate using the SECM. The pipette was approached slowly towards surface and the beads collected at the bottom of the drop under the influence of the magnet. On contacting the surface, the drop remains attached to the tip, but the beads are transferred to the surface and form mounds of quite regular geometry. The size of each mound is determined by the number of beads, but not by the area wetted by the drop. The biochemical activity of the assembled bead structures was imaged in GC mode using alkaline phosphatase as the enzyme label and also in the feedback mode using glucose oxidase.

The study of nonredox enzymes by SECM is possible using a potentiometric collection mode [125]. An ammonium selective SECM tip was used to monitor

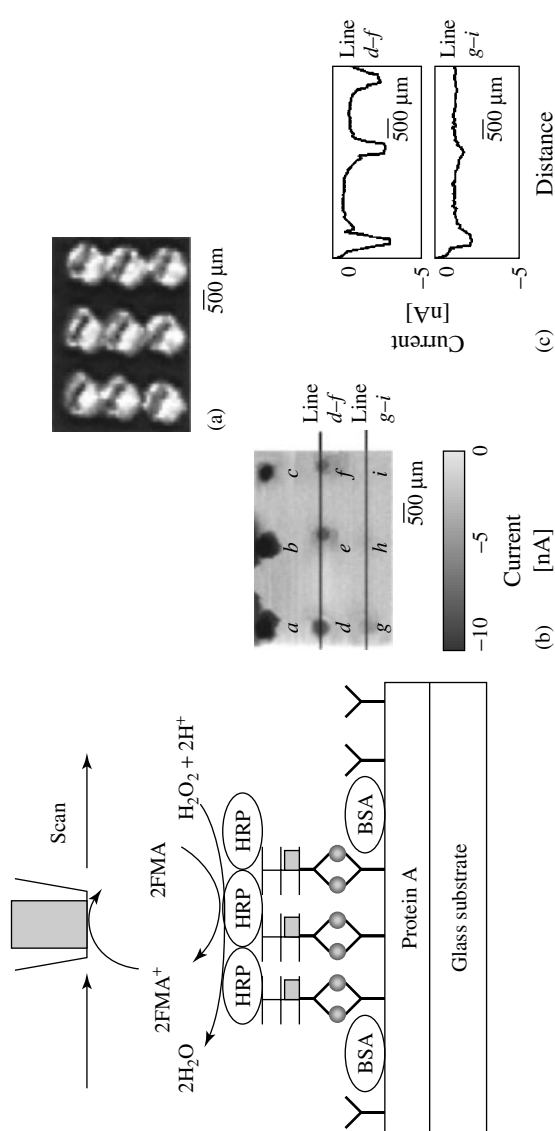


Fig. 7 Schematic diagram showing the operating principle of the SECM-ELISA system. (a) 3×3 array of vials formed on a glass plate; (b) SECM image of leukocidin spots formed at each vial using different concentration of leukocidin: (1) $52.5 \mu\text{g mL}^{-1}$, (2) $5.25 \mu\text{g mL}^{-1}$, (3) 525 ng mL^{-1} , (4) 52.5 ng mL^{-1} , (5) 5.25 ng mL^{-1} , (6) 525 pg mL^{-1} , (7) 52.5 pg mL^{-1} , (8) 5.25 pg mL^{-1} , and (9) 0 pg mL^{-1} ; and (c) line data across vials d-f and vials g-i. Au microelectrode (diameter, 0.3 mm) was scanned at $73 \mu\text{m s}^{-1}$ with the tip-substrate distance of $50 \mu\text{m}$. Images were taken at 0.05 V versus Ag/AgCl in a 0.1 M phosphate buffer solution ($\text{pH } 7.0$) containing 1.0 mM FMA , $0.5 \text{ mM H}_2\text{O}_2$, and 0.1 M KCl . A carbon microelectrode was scanned at $48.8 \mu\text{m s}^{-1}$. The distance between the tip and the substrate surface was $\sim 10 \mu\text{m}$. (Reprinted with permission from Ref. [130], Copyright 2000 by American Chemical Society.)

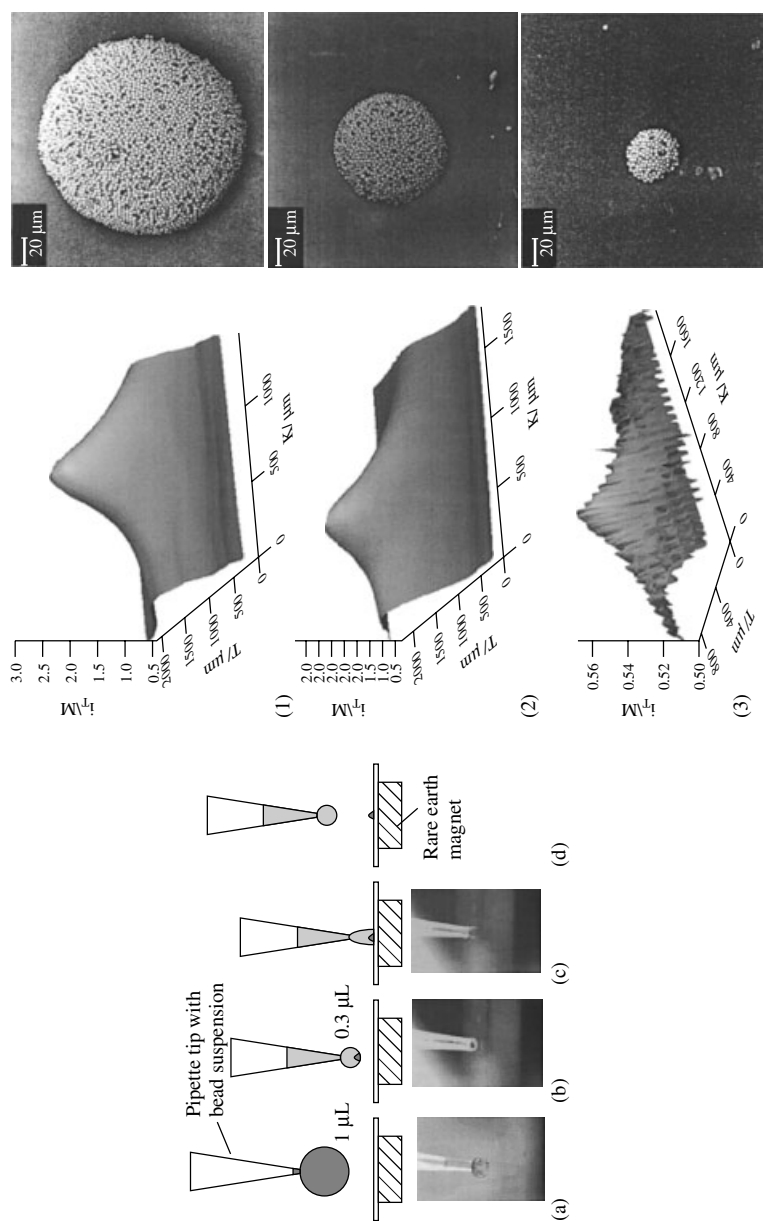


Fig. 8 Schematic representation of the bead-deposition protocol and images obtained with a CCD camera. (a) Drop of bead suspension is extruded out of the micropipette; (b) after concentrating the beads in the drop tip, the drop size is reduced to 0.3 μL ; (c) the drop is set on the hydrophobic surface; (d) the drop will stay at the pipette tip if the pipette is retracted slowly from the surface, leaving the beads behind. Series of SEM images of bead agglomerations. The beads were coated with antimouse Ab saturated with a conjugate of mouse IgG and alkaline phosphatase. The SEM images were obtained in the GC mode by oxidizing enzyme-generated para-aminophenol (PAP). SEM images of representative bead agglomerations illustrate the size of the deposits from which the SECM images were obtained. Particle concentration in the suspension in particles per milliliter: (1) 4.1×10^6 , (2) 4.1×10^5 , and (3) 4.1×10^4 . (Reprinted with permission from Ref. [132], Copyright 2000 by American Chemical Society.)

the flux of ammonium ions produced via enzymatic hydrolysis of urea by urease immobilized on a gold microdisc substrate. Reversible inactivation of the enzyme, but no faradic current, was observed when the potential of the gold substrate was scanned across the range 0.0 to +0.4 V versus Ag/AgCl. These phenomena were attributed to changes in the enzyme quaternary structure due to the changing electric field and ionic composition at the interface.

3.3.4.1.5 Dissolution of Ionic Crystals

The kinetics of dissolution of ionic solids has traditionally been studied via the measurement of bulk concentration changes in, for example, stirred suspensions. Using the equilibrium perturbation mode of the SECM, the experimenter can control directly the interfacial undersaturation and make measurements at single crystal surfaces or with micrometer spatial resolution [24].

Investigation of the dissolution of ionic solids by SECM is based on the use of the UME tip to oxidize or reduce a component of the crystal in order to generate a controllable undersaturation at the crystal surface [20–24]. This induces crystal dissolution and the rate of dissolution determines the extent of feedback [20]. Two limiting cases of the Burton–Cabrera–Frank Model corresponding to detachment ($n = 1$) and surface diffusion ($n = 2$) as the rate limiting steps were simulated in Eq. (11):

$$j = k_n \sigma^n \quad (11)$$

where j is the flux of dissolving species, k_n is the rate constant, n is the reaction order, and σ is the undersaturation produced by the tip reaction. The reaction orders were determined for the dissolution of

several different salts, for example, $n = 1$ for the (100) face of copper sulfate pentahydrate [20] and $n = 2$ for the (010) face of potassium ferrocyanide [22].

The spatial distribution of dissolution activity can also be imaged by scanning the SECM tip over the surface. Images of the dissolution rate around a single pit on the surface of potassium ferrocyanide trihydrate showed an increase in tip current near the edge of the pit indicated that the local dissolution rate there was more rapid than for the planar surface [22]. Higher resolution images were achieved using a combined AFM-SECM probe in which the dissolution was initiated on an SECM scale by the faradic tip current, but with simultaneous AFM imaging of the KBr crystal surface [23]. Recently, these authors also applied their integrated AFM-SECM to the study of the (010) surface of potassium ferrocyanide trihydrate in aqueous solution [133].

The dissolution rate experiments and theory have also been extended to the case of salt dissolution in a solution containing no supporting electrolyte [22]. Although the theory describing mass transport via diffusion/migration in such systems is more complicated, it was possible to fit the experimental current-distance curves for AgCl dissolution and to show that the rate is second order in interfacial undersaturation and to determine the rate constant.

3.3.4.2 Liquid–Liquid and Liquid–Gas Interfaces

The reproducibility and smoothness of liquid–liquid interfaces makes the interface between two immiscible electrolyte solutions (ITIES) an interesting object for fundamental studies of charge transfer. Electron transfer at liquid–liquid interfaces differs from electron transfer at metal

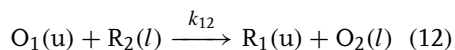
or semiconductor electrodes in which there is a continuum of electronic states in the solid and therefore has some characteristics of homogeneous electron transfer. Since the liquid–liquid interface may be supported at the opening of a micropipette, it is also possible to study ion transfer reactions using SECM with such pipette-based tips. In addition, adsorption of surface-active molecules can make a useful model of biological membranes. In this section, we discuss selected SECM studies of ET, IT, and chemical reactions at the liquid–liquid interface and some studies of the transfer of neutral molecules occurring at the liquid–air interface.

3.3.4.2.1 Electron Transfer at the ITIES

The SECM is capable of quantitative determination of ET rates at the ITIES in a straightforward manner as long as appropriate account of possible coupled ion transfer processes is taken [82]. The study of ET kinetics at the liquid–liquid interface is an area of topical interest [134–138]. Conventional electrochemical measurements employ a four-electrode cell to drive the ET reaction, however, in the SECM studies, the electrodes are all in one phase and the problems associated with double layer capacitance, iR drop, and restricted potential window are therefore avoided. In particular, the study of ET rates at high driving force is possible.

In the experiments used to probe ET at the ITIES, a metal tip is placed in the upper liquid phase (organic solvent) containing, for example, the reduced form, R_1 , of a redox species. At positive tip potentials, the oxidized form, O_1 , is produced. As the tip approaches the ITIES, R_1 can be regenerated at the interface via the bimolecular ET reaction between O_1 in the upper phase (u) and R_2 in the lower

phase (l)



and positive feedback is observed. In SECM measurements, a nonpolarizable ITIES is poised by the concentrations of the potential-determining ions, which, in addition to the difference in formal potential of the two redox couples, defines the driving force for the ET process [134, 139–143]. A suitable charge-diffuse ion such as ClO_4^- is often employed for this purpose. The tip current may be limited by one of four steps: mediator diffusion between the tip and the ITIES, interfacial reaction Eq. (12), diffusion of R_2 in the lower phase, and charge compensation by ion transfer. At small L when the current distribution is uniform, the current across the ITIES (i_s) can be expressed as [82]

$$\frac{1}{i_s} = \frac{1}{i_T^c} + \frac{1}{i_{ET}} + \frac{1}{i_d} + \frac{1}{i_{IT}} \quad (13)$$

in which i_T^c , i_{ET} , i_d , and i_{IT} in Eq. (13) are the characteristic limiting currents for the above four stages, respectively. The concentration of R_2 is usually made sufficiently high to exclude the possibility of diffusion limitations in the bottom phase, that is, to allow a constant composition approximation. If the common ion, for example, ClO_4^- , concentration in both phases is sufficiently high, then IT is also fast. Under these conditions, the effective heterogeneous ET rate constant can be obtained by fitting experimental current-distance curves to Eq. (8) [82, 139, 140]. The driving force dependence and the potential dependence of the ET rate are of theoretical interest. If the potential is dropped across a sharp interface, then the Butler–Volmer equation should be obeyed (see Volume 2). However, the accepted three-layer model

of the interface due to Schiffrin, Girault, and developed by Schmickler predicts that the ET rate is potential-independent since the potential is largely dropped in the diffuse layers [141–143]. An apparent transfer coefficient of ca. 0.5 for reactions of $\text{Zn}(\text{porphyrin})^+$ with $\text{Ru}(\text{CN})_6^{4-}$ has been observed [139, 140]. The reverse reaction between the neutral porphyrin and $\text{Ru}(\text{CN})_6^{3-}$ was in fact found to be potential-independent (Fig. 9). The potential dependence may therefore be a diffuse layer effect analogous to the Frumkin correction [137].

In a study of ET from aqueous redox couples to zinc porphyrin in benzene, phospholipids were adsorbed at the

interface and found to reduce the ET rate, thus facilitating the study of large driving forces. The monolayer also prevents the reactants from approaching close to the phase boundary. The ET rate decreased as the number of methylene groups in the lipids increased, consistent with ET through the monolayer rather than at pinholes. The driving force dependence of the ET rate followed the prediction of Marcus theory (see Volume 2) with a transfer coefficient ca. 0.59 at low driving force and a decrease in ET rate at a very high driving force at which Marcus inverted behavior was obtained [140]. Such behavior is not observed at metallic electrodes because of the continuum of electronic states

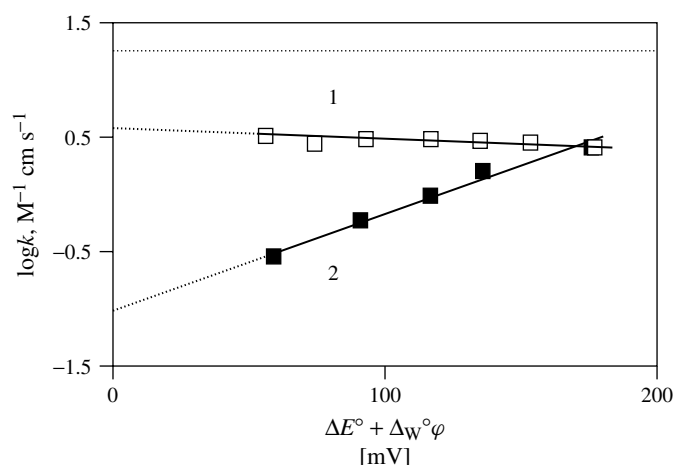


Fig. 9 Potential dependence ($\Delta W^\circ \phi + \Delta E^\circ$) of the ET rate between ZnPorphyrin (ZnPor) in benzene (BZ) and $\text{Ru}(\text{CN})_6^{3-}$ in water (curve 1) and an analogous dependence for the reverse ET reaction replotted from (ref 98). BZ contained (1) 2 mM ZnPor and 50 mM THAClO_4 and (2) 0.5 mM ZnPor and 0.25 M THAClO_4 . The aqueous solution contained 0.01–2.0 M NaClO_4 , 0.1 M NaCl and (1) 0.1 mM $\text{Ru}(\text{CN})_6^{4-}$ or (2) 7 mM $\text{Ru}(\text{CN})_6^{4-}$. ΔE° is the difference between standard potentials of two redox couples and k is the bimolecular ET rate constant. Horizontal dotted line shows the diffusion limit for the ET rate measurements by SECM under conditions corresponding to curve 1. The tip was biased at a potential corresponding to the plateau current of the oxidation wave of $\text{Ru}(\text{CN})_6^{4-}$ (0.8 V vs Ag/AgCl; curve 1) or ZnPor (0.9 V vs Ag/AgCl; curve 2). (Reprinted with permission from Ref. [137], Copyright 1999 by American Chemical Society.)

and cannot be explained as a diffuse layer effect.

Although the analysis of the data is simplified by the procedure of employing high concentrations of R_2 in the lower phase, this leads to a high rate for Reaction (12) and therefore renders high-rate constants harder to distinguish from diffusion-controlled feedback. A numerical treatment of the full system has been carried out, which enabled measurements at low concentrations of R_2 [87, 138]. This enabled a study of the driving force dependence of the rate constant using $\text{Zn}(\text{porphyrin})^+$ as oxidant and $\text{Ru}(\text{CN})_6^{4-}$, $\text{Mo}(\text{CN})_6^{4-}$, $\text{Fe}(\text{CN})_6^{4-}$, and FeEDTA^- as reductants. The data was in rough agreement with Marcus theory for a maximum ET rate constant of $50 \text{ cm s}^{-1} \text{ M}^{-1}$ and a reorganization energy of 0.55 eV [138]. The measured rate for $\text{Zn}(\text{porphyrin})^+/\text{FeEDTA}^-$ was suggestive of inverted region behavior and this is supported by the observation of electrochemiluminescence at a bare ITIES [144]. The SECM studies of ET processes have highlighted several sources of mechanistic complexity, such as ion-pairing and competitive adsorption at the interface, in systems previously assumed to be simple models [135, 137]. This area remains one of considerable activity and further details of the ET process will doubtless be investigated. For example, the first indication of solvent dynamics effects has been reported [137].

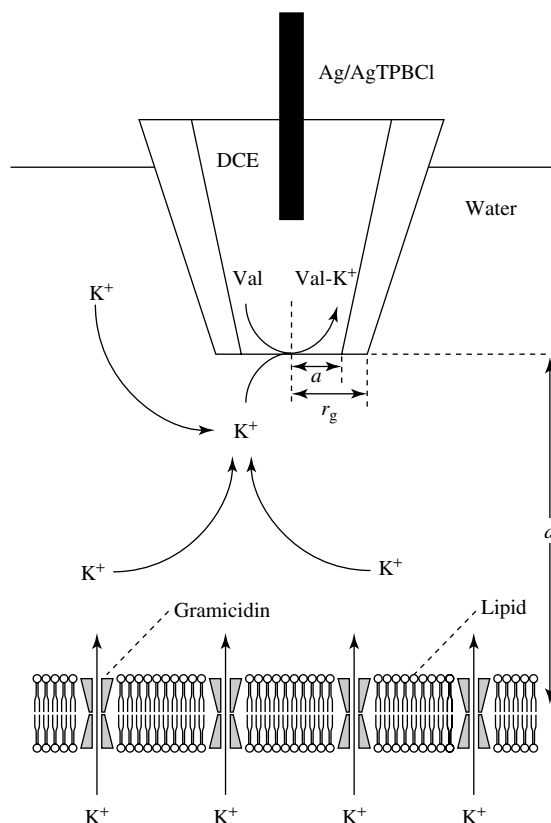
3.3.4.2.2 Ion Transfer at the ITIES The ion transfer mode of the SECM extends the applicability of SECM techniques to many processes that cannot be studied by conventional metal electrodes [29, 30]. The tip is a micropipette, and the tip current is produced by transfer of ions from the liquid phase inside the pipette to

an external, immiscible liquid phase. An example is the facilitated transfer of K^+ from aqueous solution inside the pipette into 1,2-dichloroethane (DCE) assisted by dibenzo-18-crown-6 (DB18C6) [29]. With the internal concentration of K^+ at least 50 times higher than the concentration of DB18C6 in DCE, the tip current becomes limited by the diffusion of DB18C6 to the pipette orifice. When the tip approached the interface between DCE and an aqueous layer, the regeneration of DB18C6 occurred via an interfacial dissociation mechanism in which K^+ transferred to the aqueous phase, releasing a free DB18C6 molecule [142]. A positive feedback current was therefore observed when the tip approached the water–DCE interface and negative feedback was observed when the tip approached a glass insulator.

The SECM response depends on rates of both heterogeneous reactions at the mouth of the pipette and at a second liquid–liquid or other interface. Thus the kinetics of facilitated IT and reverse IT reactions can be measured using methodologies developed previously for studies of ET processes [82, 139, 140]. While facilitated transfer of potassium is rapid, giving diffusion-controlled feedback, a kinetically controlled regeneration of the mediator was observed for proton transfer assisted by 1,10-phenanthroline [29]. The mass-transfer rate for IT measurements by SECM is similar to that for heterogeneous ET measurements, and the standard rate constants of the order of 1 cm s^{-1} should be measurable. Recently, pipettes based on valinomycin have been described. These are selective for K^+ and were used to study transport through gramicidin channels in a lipid bilayer (Fig. 10) [66].

SECM experiments can be performed using a simple (unassisted) IT process [30]. In this case, both the top and the bottom

Fig. 10 Schematic diagram of the voltammetric responses and SECM experiments at a black lipid membrane (BLM) using a K^+ -selective micropipette electrode based on valinomycin. The micropipette electrode is characterized by the electrode radius, a , and r_g is the distance from the center to the edge of the pipette. The BLM is located at the distance d . (Reprinted with permission from Ref. [66], Copyright 2000 by American Chemical Society.)



phases contain the same ion at equilibrium. The micropipette tip is used to deplete concentration of this common ion in the top solvent near the ITIES in a type of equilibrium perturbation experiment. This depletion causes ion transfer across the ITIES, which is observed as positive feedback. Dual pipettes based on theta glass have also been constructed and these can be used for generation-collection experiments in which ions ejected from one barrel are collected at the other, subject of course to any reactions they undergo in the external liquid phase [145, 146]. This technique also enabled the observation of the direct unassisted transfer of K^+ from water to DCE.

3.3.4.2.3 Transfer of Neutral Molecules

The SECM tip can be used to locally deplete the concentration of an electroactive species at a liquid–liquid interface and induce the transfer of this species from the second liquid phase. If the interfacial transfer is known to be rapid, this provides a methodology (called SECM-induced transfer by the original authors) for analysis of species in the second liquid phase without the tip penetrating this phase [87]. Detailed theoretical modeling of this mode was carried out using a finite difference technique (ADI), however for the particular case of slow interfacial transfer, the problem is analogous to unassisted ion transfer experiments [30]. If the partition coefficient

or diffusion coefficient ratio is known, the interfacial kinetics can be determined. The method was applied to oxygen transfer between water and nonaqueous solvents [87] or water and laryngeal cartilage [31, 32] as well as charged species, for example, the transfer of copper(II) ions between water and a 1,2-dichloroethane solution of an oxime ligand [87].

Transfer of oxygen across the air–water interface in the presence of a monolayer of 1-octadecanol was studied by steady state SECMIT. The depletion of oxygen in the interfacial region by reduction at an inverted UME tip in the aqueous phase was used to drive the transfer of oxygen from air into water. The dependence of the tip current on the monolayer compression showed that the monolayer strongly reduced the transfer rate and the rate was in fact essentially determined by the fraction of accessible interface [147]. Liquid–gas interfaces have also been studied by double potential step chronoamperometry, the reagent produced in the forward step may be lost by transfer out of the liquid phase and therefore less current is observed in the reverse step. Since the tip reaction is diffusion-controlled, problems of uncompensated resistance are not serious. The transfer of tip-generated bromine across the water–air interface was however observed to be diffusion-controlled with heterogeneous rate constant $>0.5 \text{ cm s}^{-1}$ [88]. The dual pipette technique of Liu and coworkers has also been applied to study gas phase processes using a thin liquid phase between the two pipette openings [145, 146].

3.3.4.3 Applications in the Life Sciences

In this section, selected applications of the SECM to problems of physiology and cell biology are discussed. The examples are chosen from widely differing biological systems: cartilage, excised skin, dentine,

photosynthesis in the leaves of *Tradescantia fluminensis*, respiratory and redox activity of cultivated cells, and the resorption of bone matrix in mammals; this reflects the increasing number of applications in the life sciences. Electrochemical methods such as ion-selective microelectrodes and patch-clamp techniques have been of long standing importance in these fields and the flexibility of the SECM approach has enabled many new kinds of experiments and information to be obtained.

3.3.4.3.1 Intact Plants and Single Cultivated Cells

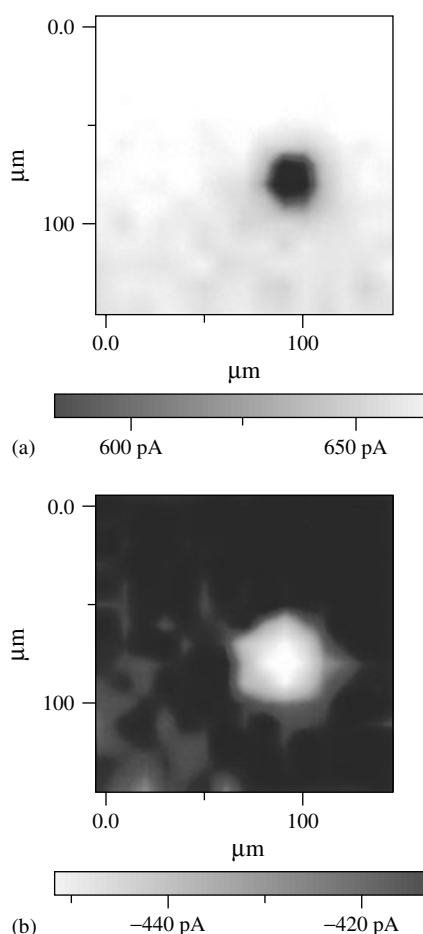
The SECM has been used both to map the topography and the rate of photosynthetic oxygen production in vivo on the leaves of an intact plant, *T. fluminensis*. A leaf, which was alive and still attached to the plant, was held against the base of the electrochemical cell using mounting tape or soft O-rings. The whole experiment, SECM and plant, was placed inside a glove bag to allow control of the gas composition. Illumination of the leaf was achieved using a 1 mm diameter optical fiber and a xenon lamp. Since conventional electrochemical redox mediators are often toxic, the choice of mediator for feedback imaging of the topography was restricted. Previous work had utilized ferrocyanide as the redox mediator [148], however for the study of the living plant, oxygen was chosen [149]. As long as the tip potential is poised at a sufficiently negative value to ensure a diffusion-controlled tip current, standard SECM theory for negative feedback applies. The solution was also buffered to ensure a stable local pH at the leaf surface. Topographic images based on the negative feedback mode were obtained in the dark so that the contribution of oxygen fluxes as a result of photosynthesis was negligible. Individual stomatal complexes were clearly resolved with the guard cells

appearing as depressions in the tip current image and the stomatal pore in the center of the complex as a current peak. Illumination of the leaf caused the production of an oxygen flux as a result of photosynthesis and i_T rose above the value observed in the bulk solution as the tip approached the leaf surface. Tsionsky and coworkers were able to image the photosynthetic oxygen production in a stomatal complex of a white leaf region and demonstrate directly the photosynthetic electron transport in single guard cells of an intact living plant. This work illustrates the flexibility of the SECM technique; the experimenter can image topography and biochemical reactivity and then choose a particular location on the sample to make kinetic studies of the response of a specific portion of the system to an external stimulus in essentially one experiment. Matsue and coworkers have also used SECM to study the photosynthetic activity of single algal protoplasts. A dual Pt microelectrode was used to simultaneously image topography using the feedback effect for $\text{Fe}(\text{CN})_6^{4-}$ oxidation with one electrode and the other to record the local oxygen concentration (Fig. 11) [150–152].

Another approach was applied to the response of cultivated cancer cells (cell line SW-480) on addition of cyanide to the culture medium [153]. In cyanide-free solution, the concentration of oxygen is

reduced around the cells; the difference in the oxygen reduction current directly above a cell and in bulk solution was used to assay the cellular activity. After the addition of cyanide, the cellular activity could be followed on the minute timescale. Cyanide blocks the electron transport of the respiratory chain in mitochondria leading to cell death. However, it was found that cellular activity first remained constant for 500 s, then rose until 800 s before decreasing until cell death [153]. Because the CN^- ion has to pass the cell and mitochondria membranes, the local concentration inside

Fig. 11 Dual-SECM images of a single, living protoplast (radius, 25 μm) based on the oxidation current for $\text{Fe}(\text{CN})_6^{4-}$ (a, W1, leveled) and the reduction current for oxygen (b, W2, beveled). Probe, dual-microdisk electrode. Scan rate: 9.8 $\mu\text{m s}^{-1}$. Concentration of $\text{Fe}(\text{CN})_6^{4-}$, 1.0 mM. The radii of disks are 2.8 μm for W1 and 1.2 μm for W2. (Reprinted with permission from Ref. [151], Copyright 1999 by American Chemical Society.)



the mitochondria lags behind the CN^- extracellular concentration. Modeling of the mass transport and comparison with the observed lag time suggested that the permeability of the membranes for CN^- in vivo is about $(1-3) \times 10^{-7} \text{ cm s}^{-1}$.

The final example in this section employed many of the concepts of charge transfer at liquid–liquid interfaces to analyze the intracellular redox activity of non-metastatic and metastatic human breast cells as well as highly motile breast cells engendered by overexpression of protein kinase $\text{C}\alpha$ [154]. A selection of highly charged mediators was found not to be regenerated at the cells, consistent with the usual assumption that they do not penetrate the cell membrane. The mediators, menadione and naphthaquinone, in which both forms are neutral, showed a different behavior. The apparent rate constants for reoxidation of these species was extracted from the SECM approach curves. Figure 12 shows several possible mechanisms for the SECM response. The rate of the multistep reaction underlying the observed SECM response can be influenced by a number of factors including the following: (1) the rate of intracellular ET, which is governed either by the intracellular redox potential or concentrations of redox species; (2) the rate of mass/charge transport across the membrane; and (3) the kinetics of heterogeneous ET occurring on both sides of the membrane. The intracellular redox potential was probably not rate limiting since the rate constant for menadione was less than for anthraquinone in opposition to the expectation based on the order of the redox potentials. A detailed analysis of the data led the authors to suggest that a bimolecular ET mechanism is in operation inside the cell (Fig. 12). The comparison between normal and metastatic cells showed an

interesting difference in rate constants; the slower mediator regeneration rates observed for 11α and MDA-MB-231 cells may be related to a high level of $\text{PKC}\alpha$ expression compared with MCF-10A (normal) cells. Since 11α and MDA-MB-231 cell lines are highly motile and exhibit slower proliferation rates, a reduced metabolic activity overall is expected [154].

3.3.4.3.2 Calcium and Superoxide Measurements

SECM and microelectrode techniques have been applied to the study of the resorption of bone by specialized cells known as osteoclasts, OCLs [155]. Bone comprises calcium phosphate-based minerals (hydroxyapatite), organic material (mostly collagen), and various cells. The osteoclast carries out the resorption of bone by the secretion of protons and hydrolytic enzymes that break down the matrix releasing, among other species, Ca^{2+} . The conventional assays for the resorptive activity of OCLs requires 18 to 20 h incubation on bone slices. The area and number of resorption pits can be determined from SEM micrographs. The rate of resorption has been probed more directly using a simplified SECM apparatus and liquid-membrane calcium-selective microelectrodes to directly determine Ca^{2+} released from the hydroxyapatite into the extracellular medium during resorption. A significant background Ca^{2+} concentration ($0.21 \pm 0.08 \text{ mM}$) always exists in the culture medium near the bone surface as a result of dissolution of the bone by a purely chemical mechanism; however, the elevated Ca^{2+} due to the resorptive activity of the cells was detectable within approximately 10 min of incubation. Fluoride treatment (soaking in 10 mM NH_4F for 24 h) of the bone slice dramatically reduces the chemical dissolution pathway, but the OCL can still resorb. The SEM assay that

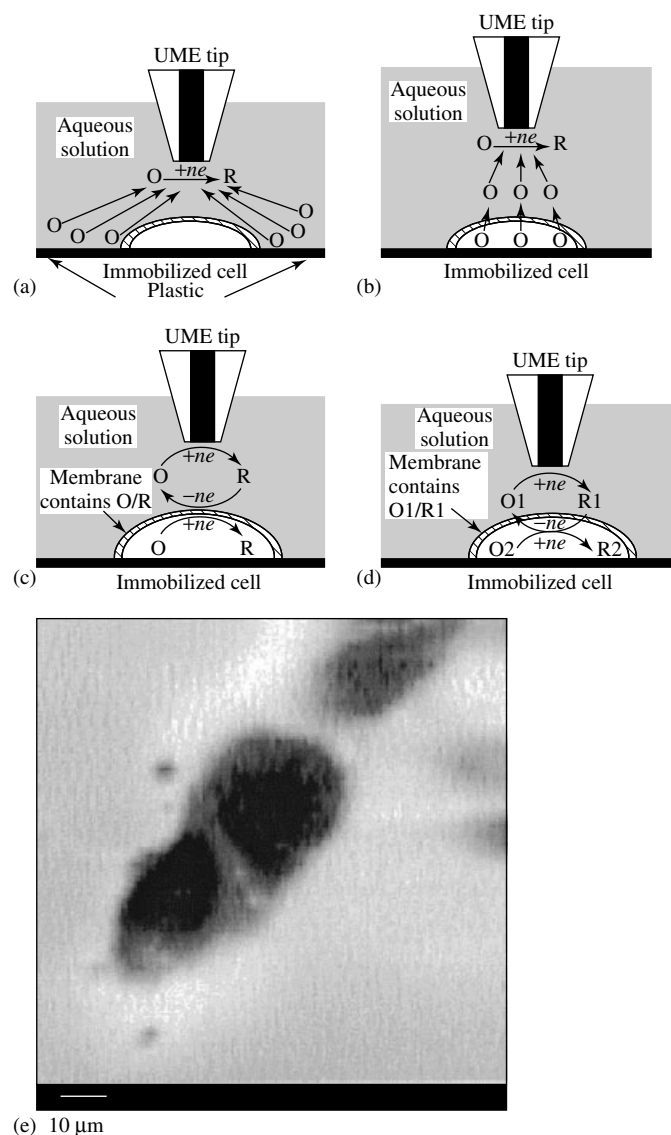


Fig. 12 Schematic diagrams of the SECM experiments with four different types of mediator regeneration by a cell. (a) The tip is positioned in the solution close to the cell surface. The lipid cell membrane is impermeable for a hydrophilic redox mediator. Negative feedback is due to the hindered diffusion of redox species to the tip electrode. (b) The UME tip induces the ejection of the redox species, O, from the cell by depleting its concentration near the cell surface via electrolysis. (c) Mediator regeneration proceeds via a self-exchange ET reaction. The charge is shuttled across the membrane by the same hydrophobic redox species (O/R). (d) Bimolecular ET between hydrophobic redox mediator (O1/R1) and cell-bound redox moieties (O2/R2). (e) Normal human breast (MCF-10A) cells imaged by the SECM with a 1 μm -radius Pt tip and 40 μM 1,2-naphthoquinone as mediator. (Reprinted with permission from Ref. [154], Copyright 2000 by National Academy of Sciences, USA.)

the cells were not inhibited from attaching to the treated bone or by any fluoride released into the medium on resorption; the resorption process is slowed simply by the greater resistance of fluorapatite to acidic dissolution.

Superoxide anion produced in the respiratory burst of OCLs in response to parathyroid hormone, PTH, can be detected using an amperometric sensor consisting of cytochrome c covalently attached to a gold electrode [156–158]. Such microelectrodes have also been used to study regulation of the membrane-bound NADPH-dependent oxidase responsible for superoxide generation. The SECM was used to position the superoxide-selective tip near OCLs on a bovine cortical bone slice. The effects of inhibitors of protein kinases, membrane-permeable analogues of cAMP, and cholera toxin on the stimulation of superoxide anion production by PTH, pertussis toxin, and ionomycin were studied [159, 160]. The SECM data shows that cAMP-dependent inhibition is dominant in controlling the superoxide anion production. In these collection mode experiments, the SECM provided information on much shorter timescales than conventional assays and demonstrates that the O_2^- burst following stimulation by PTH was too fast to be mediated indirectly by other cells, such as osteoblasts, as had previously been accepted. In combination with the short timescale of the response and the effects of cholera and pertussis toxin, this suggests that the superoxide anion burst results from a direct action of PTH on the osteoclast via a G-protein coupled receptor. In fact, there is some direct evidence for cell membrane receptors for PTH in the osteoclast [161]. The same type of argument based on the use of SECM to detect faster processes than accessible by traditional assays enabled the observation

of acute effects of steroid hormones, for example, vit D₃, which stimulate a burst of O_2^- on a timescale of a few seconds, too fast for the mechanism to involve the usual nuclear receptor for this hormone [159].

3.3.4.3.3 Imaging Mass Transport in Biological Systems

Several workers have used the fact that the imaging mechanism of SECM is strongly dependent on mass transport to image local rates of diffusion, convection, and migration. Examples include the transport of oxygen and electroactive ions in cartilage [31, 32], convective [162, 163], and diffusional [71] transport in dentinal tubules and iontophoretic fluxes through skin [164–169]. Often these experiments have employed a two-compartment SECM cell in which the tissue under investigation (substrate) is oriented horizontally and separates two liquid phases. Diffusion is then driven by raising the concentration of the species of interest in the lower compartment and a generation-collection type of SECM experiment can be used to detect localized transport. Although the porosity of dentine is such that the diffusion layers at individual tubules rapidly overlap, it is possible to observe blocked tubules [71]. Convective transport through dentine is also of interest and this can be monitored using a hydrostatic pressure gradient to drive solution from the lower compartment. The pressure can be controlled by adjusting the height of a column of liquid connected to the lower compartment of the cell. The combination of the small pore size of dentine (a few μm) and the tip facing the stream of liquid exiting the pore creates a small wall-jet or wall-tube type of electrochemical cell. The theory for conventional hydrodynamic electrodes can be adapted to this situation to determine locally the flow rate on a micron scale [162, 163]. In

a series of papers, White and coworkers have reported studies of iontophoretic transport through excised skin tissues. An electric field drives transport of charged, redox-active species across the skin and the SECM tip can be used in collection mode to detect ions such as Fe^{2+} and $\text{Fe}(\text{CN})_6^{4-}$ and molecules such as hydroquinone amperometrically. The technique was used to image the distribution of iontophoresis in hairless mouse skin and it was observed that the fluxes of hydroquinone are localized to hair follicles [169]. The transport can be quantitated using measurements of the concentration profile in the upper compartment and analysis via the standard generation-collection theory [164–169]. More recently, this work has been extended to take account of electric field-driven convection, that is, electroosmosis that is employed in drug-delivery technology [170]. It was found that the transport rates are strongly dependent on interactions between the transported species and pore-walls and not simply the electroosmotic flow rate, for example, neutral molecules move much faster through membrane materials bearing anionic groups than do cations.

An alternative strategy to study mass transport is based on the equilibrium perturbation mode; the tip is used to deplete a component of the solution above the specimen and this drives transport of the corresponding species. Articular cartilage is essentially impermeable to the highly negatively charged mediator, $\text{Ru}(\text{CN})_6^{4-}$ and this was used to image the topography and detect the locations of chondrocytes as areas of reduced i_T . Subsequent images using oxygen as the probe molecule could then be compared to show that areas with elevated rates of oxygen permeation correspond to cellular and pericellular regions [32]. Another example is the lateral

transport of protons between phosphate groups on the surface of biological membranes, which has been suggested to be very fast [171, 172]. A model system, the stearic acid monolayer at the air–water interface, was studied by Slevin and Unwin [51], who measured directly the surface diffusion coefficient and found that it is dependent on the compression of the monolayer, but that the maximum value is no more than 15% of that in bulk solution (Fig. 13).

3.3.4.4 Microfabrication

Microfabrication by SPMs is in part motivated by their potential to beat the diffraction limitations of optical methods for electronics applications. The spatial resolution of SPM is limited only by the tip size and STM has been used to manipulate individual atoms. However, the typical tip size in SECM is ca. $1\ \mu\text{m}$ and therefore a significant improvement over photolithographic resolution is not routinely obtained. Further, SPMs are rather slow since they are limited by the speed of the tip and this is especially so for SECM. Instead, SECM microfabrication is often more useful as a technique for patterning surfaces with chemical or biochemical functionality and fabricating microscopic structures with particular chemical properties.

SECM microfabrication is based on the use of the tip to alter local chemical properties in small (micrometer or submicrometer-sized) domains. Several approaches to surface modification by SECM are outlined in this section. These may be divided roughly into methods in which the tip and substrate are the working electrode and auxiliary electrodes of a cell and methods in which the chemistry of the system is chosen so that the SECM feedback process leads to deposition or

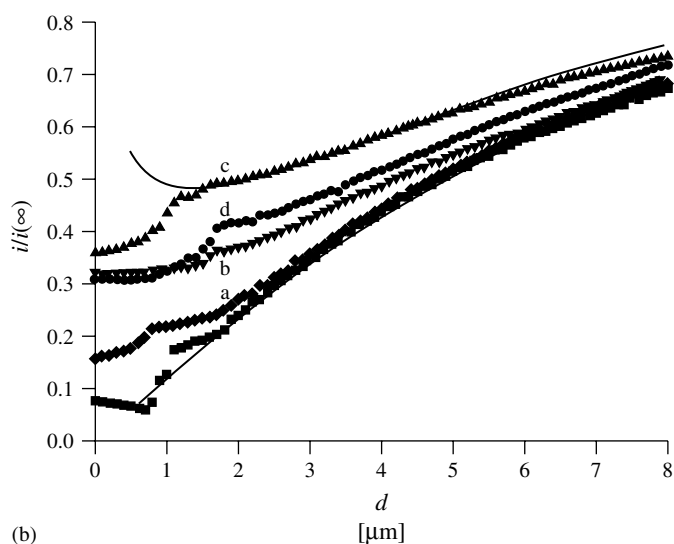
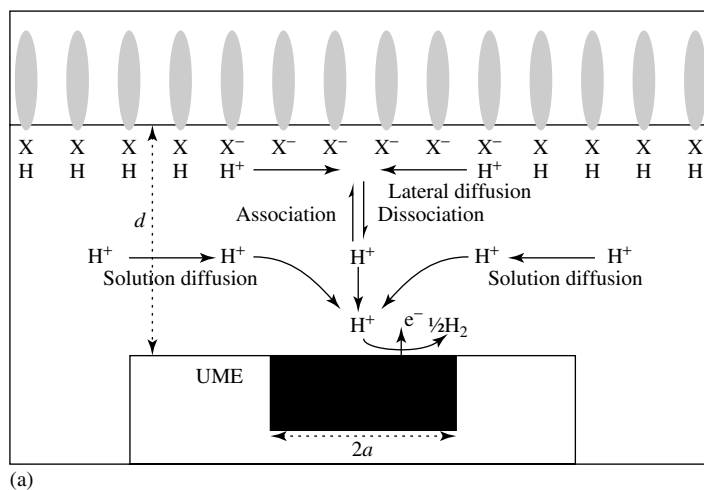


Fig. 13 (a) Schematic (not to scale) of the arrangement for SECM measurements of proton transport at a stearic acid monolayer deposited at the air–water interface. The UME typically had a diameter, $2a$, in the range 10–25 μm and the tip/interface distance, d , was typically $<2a$. (b) Normalized steady state diffusion-limited current versus UME–interface separation for the reduction of $5 \times 10^{-5} \text{ mol dm}^{-3} \text{ H}^+$ at a 10 μm diameter platinum UME approaching an air–water interface, for (■) a clean surface and with a stearic acid monolayer at a surface coverage of (◆) 35 (a), (▼) 28 (b), (▲) 26 (c), and (●) 24 $\text{\AA}^2 \text{ molecule}^{-1}$ (d). The lower solid line is the theoretical curve for hindered solution diffusion only, while the upper solid line is for a stearic acid covered interface (26 $\text{\AA}^2 \text{ molecule}^{-1}$) with a surface diffusion coefficient of $1.2 \times 10^{-5} \text{ cm}^2 \text{ s}^{-1}$. (Reprinted with permission from Ref. [51], Copyright 2000 by American Chemical Society.)

etching. For example, metals such as Cu, Ag, and Au may be deposited locally to form lines and microstructures [173]. In addition, chemical and biochemical functionality may be altered or introduced on the substrate and methods for patterning organic and biological molecules have recently been reviewed [10].

3.3.4.4.1 Methods Based on Direct Current Flow Between Tip and Substrate

When the tip and substrate are set up as the working and counterelectrodes of a cell, the current can be used to drive deposition or etching reactions directly [7]. In this way, lines were etched in illuminated *n*-GaAs with the tip biased negative [9]. Since there is no feedback mechanism, the usual method of sensing the tip/substrate distance was not possible. This was overcome by coating the substrate with an ionically conductive polymer (NaFion) and a constant current was maintained using an electronic feedback loop to adjust the penetration of the STM-like tip into the polymer. Etched lines and high-resolution deposition of Cu, Ag, and Au were obtained by choosing the sign of the potential between tip and substrate. The tip scan rate however was limited to ca. $0.1 \mu\text{m s}^{-1}$ [8]. A similar strategy was used to deposit silver particles on mica substrates in a humid atmosphere in which a thin water film on the substrate replaced the NaFion in the previous example (see Sect. 3.3.5.3) [174]. Microfabrication of conductive polymers has also been carried out by SECM and this may have some practical importance in sensor technology since polypyrrole, polyaniline, and related compounds cannot be deposited by evaporation [175]. A constant potential or current technique suffers from problems due to depletion of monomer in the tip/substrate gap, but a galvanostatic

pulse method of Schuhmann and coworkers is effective and was used to connect two gold microelectrodes with a line of polypyrrole drawn on the insulator in between [176]. This technique was combined with a current-independent distance measurement and a feedback loop to create polypyrrole towers of several hundred microns height and about 80 microns diameter [176]. An important area of SECM fabrication in which conventional methods suffer from serious problems is the patterning of biological molecules for biosensor development, for example, SECM immunoassay. In general, photolithographic methods can denature or disrupt the function of many enzymes and proteins. Patterning of glucose oxidase was demonstrated using the tip to electrochemically desorb alkanethiols from a self-assembled monolayer (SAM) on a gold substrate. Well-defined areas of desorbed thiol were obtained in alkaline media (0.2 M KOH) on which cystamine could subsequently be adsorbed. Periodate-treated glucose oxidase was then attached via Schiff-base chemistry and the enzyme activity was imaged by detection of hydrogen peroxide in the generation/collection mode [122]. This method has been refined using an ac voltage (kHz frequency), in which case, the desorption stops when the area of bare gold approaches that of the UME and the current becomes dominantly non-faradic [177]. Another approach to enzyme micropatterning was developed by Shiku and coworkers [129], who used a scanning micropipette to create an array of $\sim 20\text{-}\mu\text{m}$ sized droplets of deposition solution on a glass slide. Two different immobilization mechanisms (i.e., direct immobilization from solutions containing albumin and glutaraldehyde, and an antigen-antibody-based method) resulted in a formation of well-defined micrometer-sized spots of

horseradish peroxidase, which was then imaged with the SECM.

3.3.4.4.2 Methods Based on Feedback or Localized Generation of Reagents

Micro-fabrication using the feedback mode is straightforward in the case of etching; strong oxidants generated at the tip will etch metals or semiconductors [178, 179]. The approach curve can be used to study the etching kinetics and in the case of semiconductors is sensitive to the position of the band edges and the majority carrier type [178, 180]. Injection of holes into *n*-type semiconductors by oxidants produced at the tip leads to the local buildup of positive charge in the semiconductor and the etching reaction proceeds with regeneration of the reduced form of the mediator. This results in positive feedback at the tip and the etching rate can in principle be obtained by analyzing the tip current. On the other hand, injection of holes into *p*-type material does not lead to etching even though positive feedback is observed; the reason is that the charge rapidly diffuses away. It is also possible for this process to happen at *n*-type material if the oxidant produces an inversion layer at the surface. A partial list of semiconductors, which have been etched by SECM feedback methods includes GaAs, CdTe, $\text{Hg}_{1-x}\text{Cd}_x\text{Te}$, and GaP. In more recent work, Mandler and coworkers succeeded in etching silicon by oxidation of bromine at the tip in acidic fluoride solutions, which ensure the surface is not covered by an insulating and inert oxide layer [181]. One-electron oxidants were not able to etch silicon, presumably due to inversion of the surface layer and rapid dissipation of the injected charge. The authors suggested that bromine succeeds in etching silicon through the trapping of holes at surface

Si–Br bonds. Etching of metals in feedback mode is possible and a kinetic study of Cu etching by generation of $\text{Fe}(\text{phen})_3^{3+}$ and $\text{Os}(\text{bipy})_3^{3+}$ was made. Again, there is the possibility for the injected charge to diffuse laterally. Using two microdisc electrodes (one of Cu) in a twin electrode thin-layer cell configuration, the rapid dissipation of the injected charge is prevented and it was shown that in fact the etching of Cu by $\text{Ru}(\text{bipy})_3^{3+}$ and bromine was diffusion-controlled at the available mass transport rates for SECM [182].

Metal deposition in the feedback mode involves generation of reductants in solutions of metal ions and may therefore lead to deposition on the tip as well as the substrate. However, gold structures were electrodeposited in this way in polymer films containing AuCl_4^- through generation of $\text{Ru}(\text{NH}_3)_6^{2+}$, at the tip [178]. An alternative is to produce the metal ions locally by anodic dissolution of a gold tip in bromide-containing solution [183]. Positive feedback was observed because the bromide ions are regenerated when the AuBr_4^- plates out on the substrate. The resolution obtained in this mode is of the order of the tip diameter. Another approach is to use the tip to alter the local chemical composition of the solution in the tip/substrate gap [184]. Ag was deposited on Au using the oxidation of nitrite at the tip to lower the pH and induce dissociation of $\text{Ag}(\text{NH}_3)_2^+$. The free Ag^+ ions are then reduced at the substrate. This system is an example of a “chemical lens”; the concentration profile of Ag^+ is focused to a zone of radius smaller than the tip because diffusion of ammonia from the bulk solution continuously removes free Ag^+ and this improves the spatial resolution. The technique was also applied to writing lines of Ag in AgCl films by generation of hydroquinone at the tip with free Ag^+

in solution as the “focusing” agent [185]. The chemical lens has similarities to the confined etchant layer technique (CELT), though in CELT the focusing agent is consumed at the tip and the resolution of the technique is determined by the tip diameter [186, 187]. Inorganic materials can also be deposited through the use of the tip to generate a reagent at the substrate; deposition of $\text{Ni}(\text{OH})_2$ on Pt from a solution of Ni^{2+} was obtained by reduction of methylviologen (MV^{2+}) at the tip. The reduced form in turn produced H_2 at an unbiased Pt substrate with consumption of H^+ . This produced a higher pH at the substrate than the tip or the bulk and $\text{Ni}(\text{OH})_2$ deposited chemically on the Pt [188]. Tungsten-oxide materials have also been studied and their reversible chemistry allows “writing”, “reading”, and “erasing” of patterns [189].

Feedback-mode strategies have been reported for the deposition of conductive polymers. Heinze and coworkers coated the substrate with the water-insoluble monomer (2,5-bis(1-methyl-pyrrol-2-yl)-thiophene) by thermal evaporation and polymerized it by generation of oxidants in aqueous solution by feedback SECM [184]. The substrate was then washed in organic solvent to remove the excess monomer. The polymerized patterns were insoluble and remained on the substrate. Wipf and Zhou deposited polyaniline onto noble metals by applying a positive potential to the substrate and consuming protons at the tip in order to locally shift the oxidation potential of the monomer to a value negative of the substrate potential [190].

Several methods have been developed for the patterning of biomolecules or locally modulating their activity on surfaces [10]. Local generation of bromine or chlorine can be used to inactivate immobilized enzymes. The system studied

was diaphorase, which catalyzes the oxidation of NADH, and its activity was therefore imaged by the SECM using ferrocenemethanol as the mediator [72]. The inactivated lines and spots showed up in the feedback-mode images as low currents. Diaphorase micropatterned on Au microarrays has also been imaged [191]. The technique of deactivating the enzyme locally is ingenious, though rather wasteful, and the same group has reported a different strategy in which SAMs of alkyltrichlorosilanes on glass were locally modified [192]. Fenton chemistry was used to attack the SAM by generating hydroxyl radicals at the tip through reduction of Fe^{3+} in peroxide-containing solutions. Amino-terminated silanes were used to covalently immobilize the enzyme and the SECM-generated hydroxyl radical could make a “negative image” by destruction of the amino-terminated SAM. Alternatively, spots of hydroxylic surface in a thiol-terminated monolayer could be produced, leaving the surrounding monolayer terminated by unreactive sulphonate groups. Subsequent adsorption of (3-aminopropyl)trimethoxysilane in the etch spots enabled the formation of positive patterns of enzymatic activity. These patterns of enzymatic activity were also imaged using the SECM. It is also possible to locally activate an enzyme; this was demonstrated using alcohol dehydrogenase immobilized on agarose beads. The pH in the tip/substrate gap was raised from the bulk value of 6 towards the optimum for the enzyme, that is, 9, by reduction of oxygen and water, though in this case the enzymatic activity was observed by monitoring the reduced cofactor, NADH, via fluorescence microscopy [193].

Another strategy for the immobilization of enzymes has been described in which the galvanostatic pulse method of

deposition of conductive polymers was used to pattern functionalized pyrroles for subsequent attachment of glucose oxidase [194, 195]. The authors were also able to image the enzyme activity by SECM and discussed the possibilities for fabrication of miniaturized biosensors by this method. The use of the specific and strong binding between biotin and streptavidin is common method for immobilization of biochemical reagents by conjugation of the biomolecule to avidin. An SECM strategy has been demonstrated on the basis of this chemistry [196]; biotin hydrazine oxidized at the tip was observed to attach to carbon substrates and retained its ability to bind avidin. The substrate potential had to be carefully controlled to prevent extensive deposition of biotin and the tip/substrate distance was kept small because of the instability of the oxidized biotin. The authors also showed that tip-generated hydroxide was capable of removing the biotin/avidin complex. Despite the considerable technical difficulties, the area of biosensor miniaturization using SECM techniques seems to offer promise for the future since the conventional lithographic methods often involve harsh chemical treatments and/or high temperatures, whereas the strategies outlined above function in aqueous solution under ambient temperature. A useful feature of the technique is that SECM may also be used to image chemical reactivity and therefore can be used to study microfabricated biosensors as well as to construct them; Schuhmann and coworkers have studied the crosstalk between sensing elements [197].

In all modes of surface modification mentioned above, the spatial resolution is governed by the size of the SECM microprobe. With the commonly used micrometer-sized tips, fabricating sub-micrometer structures is difficult even

employing “chemical-lens” ideas. Further advances in spatial resolution will probably require smaller metal tips [25] or micropipette tips that can be made with radii of a few nm [30].

3.3.4.5 Single Molecule Electrochemistry

As the radius, a , of SECM tips is reduced, the number of molecules in the tip/substrate gap decreases in proportion to a^3 . The current is proportional to radius and therefore each molecule of the redox mediator makes many more trips between the tip and substrate per second. In fact, the single molecule limit can be reached using nm-sized tips fabricated by electrochemical etching of Pt-Ir wires [79, 80]. The etched Pt-Ir tip was coated with apiezon wax and the apex of the tip exposed by placing the insulated tip in the feedback loop of an STM. These tips exhibited normal voltammetry in bulk solution, however, for several tips, the approach curve showed a decrease near a conductive substrate (ITO-glass) rather than the expected positive feedback. This was attributed to compression of the wax insulator resulting in a reduction of the volume of solution under the tip. For these tips, the tip height could be fixed in the region of decreasing i_T and discrete current fluctuations between current values of ca. 1.6 pA were found. These fluctuations were interpreted as the presence of zero, one, or two molecules in the tip/substrate gap making 10^7 tip/substrate trips per second. The statistics of the current fluctuations were studied and an approximate theoretical model of the experiment was proposed [80].

Other approaches to single molecule experiments have been discussed; the mean number of molecules in the diffusion field around a nm-scale UME may be of the

order of unity and this suggests that individual electrochemical events could be distinguished if the current is observed with sufficient time resolution. A variation of this idea, which has been implemented, is to observe Electrogenerated chemiluminescence (ECL) at a UME with a sample rate of ca. 125 kHz [198]. Potentiometric experiments may also be possible with a suitable high-impedance voltmeter as long as the double layer capacitance scales with electrode area for the nm-scale tips [199]. The coulomb staircase, which arises from the finite voltage change produced by single electron charging of the tip double layer capacitance, has in fact been observed at nm UMEs in dilute (μM) solutions of redox couples at room temperature [201]. In this experiment, the linear region of the current–voltage curve around the rest potential shows discrete steps of roughly equal height as the interfacial potential responds to single electron charging events.

3.3.5

Advances in SECM Imaging

SECM images are generally obtained by rastering the tip above the substrate and recording the variations in the tip current; in the language of scanning tunneling microscopy, this is constant height mode. Other SPMs such as scanning tunneling microscopy also employ a feedback loop to fix the tip signal by adjusting the height, and the image consists of a map of the z -coordinate (constant current mode). Since constant height mode is simpler to implement, it is the usual method; however, it does not provide any protection against tip crashes. The constant current mode may therefore be more suitable for high-resolution work.

3.3.5.1 Constant Height Imaging

In constant height imaging, variations in the current or potential at the tip during the scanning are converted to grayscale images or 3D plots. Samples imaged in the constant height mode include, among others, metals [4, 6, 64, 200], ionic crystals [20–24, 202], polymer films [99, 203–205], and biological specimens [27, 28, 72, 129, 148]. An image recorded in feedback mode can be processed to yield the substrate topography (height) using Eq. (4) for a conducting substrate or Eq. (5) for an insulator. This is not possible if the reactivity or conductivity of the substrate is nonuniform.

The image resolution depends upon the tip radius, and the distance between tip and sample [203]. The use of nm-sized tips has been used to increase the lateral resolution from the usual range micrometer range to ca. 30–50 nm [206]. The scope for further improvements in the resolution of the positive feedback mode at conductive substrates is modest because, smaller tips would require tip/substrate separations within tunneling range. The resolution at insulating substrates is usually not as good because the diffusion field spreads laterally within the tip/substrate gap to a greater extent. Some improvement in resolution is possible using the “chemical lens” [187, 203]. The apparent size of an object in SECM images is overestimated owing to lateral diffusion of the mediator. If the mediator is chemically unstable, its diffusion length is reduced and the image is sharpened. This can be achieved using a bulk concentration of a reagent, which reacts with the form of the mediator generated at the tip. The trade-off is that the feedback effect decreases if the mediator is too unstable. A somewhat similar approach has been previously discussed by Engstrom and coworkers [84] and also

in generation-collection experiments in which pH images were sharpened by manipulating the buffer capacity of the solution [12]. Finally, it is worth remarking that the limitations of the feedback mode arising from tunneling at small distances do not apply to new tips employing ion transfer at micropipettes [29, 30] or the experiments in thin water films on mica in humid air [174].

SECM imaging of surface reactivity, as opposed to topography, can be done either in feedback or GC mode. The former provides the spatial distribution of the rate of a redox reaction responsible for mediator regeneration at the substrate. Using the collection mode of the SECM, one can image fluxes of species produced or consumed at the substrate, for example, localized iontophoretic fluxes of electroactive species through porous polycarbonate membrane or hairless mouse skin [164–169]. The rate of ion transport and radius of membrane pores can be determined from the analysis of SECM images. The SECM has recently been applied to the size-selective imaging of permeation through micropatterned thin films [207].

In GC mode, the diffusional broadening of the image is dependent on the flux at the substrate and is therefore virtually independent of the tip size. If the features on the substrate are too large, a steady state condition is not reached. However, in certain situations in which the substrate kinetics are slow, GC mode may be essential. Enzymes immobilized on a metallic surface, on which redox mediator regeneration is fast and dominates the feedback, are a common situation in which GC mode imaging has been preferred. An example is the collection mode imaging of H_2O_2 fluxes produced by GOx adsorbed on Au [122]. The image resolution was enhanced by the addition of small

amounts of catalase to the medium. Aside from the “chemical-lens” effect, the action of catalase is specific and confirms that the species being imaged is hydrogen peroxide.

3.3.5.2 Constant Current Imaging

In constant current imaging, the piezoelectric actuator is part of an electronic feedback loop, which maintains a fixed set point tip current. A difficulty arises for mixed insulating and conducting substrates for which the feedback loop cannot simply withdraw the tip according to increases in current (conductors) or decreases in current (insulators). Constant current imaging, which is routine in scanning tunneling microscopy, is therefore harder to implement unless the conductivity of the sample is uniform.

Essentially, one needs a method for recognizing the local nature of the substrate. Wipf and coworkers have described a constant current imaging device that uses an automatically switched servosystem in combination with tip position modulation (TPM) [53, 55]. In TPM-SECM, the tip-substrate distance is modulated by application of a small amplitude a.c. perturbation to a piezoelectric pusher. The modulated tip current that results is detected by a lock-in amplifier and the phase angle of this signal discriminates between conductors (in-phase) and insulators (antiphase). A TPM image of a Kel-F/Au composite surface was able to accurately show the topography of both conductive (Au) and insulating (Kel-F) regions. However, artefacts can be produced in the image at the boundaries of the insulating and conducting domains as the phase angle changes.

More recent work has instead concentrated on the development of tip current-independent distance measurements [100–103]. One possibility would be

to utilize the frequency change of a quartz tuning fork to control tip/substrate distance [208, 209]. Another idea is to oscillate the UME tip laterally at its resonant frequency with an amplitude of a few tens of nm. When the tip approaches the sample, hydrodynamic forces damp the vibration. Using a laser beam focused on the tip and a photodiode, it is possible to lock-in to the vibration and the change in tip oscillations can be used to regulate the tip/substrate distance. This shear force method has also been used in constant distance mode with tips that are not electrodes, but rather act to supply a reagent [34].

3.3.5.3 High-Resolution SECM Imaging

The highest-resolution images to date have employed a type of penetration mode in which an etched tip partially penetrates the Å-thick layer of water that is typically present on a solid surface in humid air. In fact, images of insulating surfaces, for example, mica, were obtained in which nm-scale lateral resolution was achieved and monoatomic steps can be resolved. There is however still discussion about the imaging mechanism in these experiments. Originally Guckenberger and coworkers obtained DNA images on mica and attributed the tip current to tunneling processes although the distance between the tip and the metallic contact on the sample was of the order of mm [210]. Fan and Bard [205] proposed instead that the images occurred by an electrochemical mechanism and suggested that a faradic current begins to flow when a nm-sized conical tip, positioned 1 to 2 mm laterally from the Au contact, touches the liquid layer on the atomically smooth surface of mica [205]. Other workers have also observed that a water bridge between the tip and the sample surface is necessary for successful imaging in this way [211].

Ag clusters have also been deposited on mica and provide direct evidence for a faradic component to the imaging mechanism [174].

Hyphenated SECM techniques are also being developed, such as SECM-QCM (see Chapter 2.7 in this volume), SECM-ECL, and SECM-AFM. The SECM-QCM combination has the problem that the motion of the tip can induce a frequency change, though the technique has been used for mechanistic studies of surface patterning reactions [212–217]. ECL has been combined with SECM to produce a new type of optical microscopy [218]. A small metal tip was used to generate ECL in close proximity to the substrate and the transmitted or reflected light was detected with a photomultiplier. The ECL and tip current provide topographic and chemical information. Although this technique may solve the problem of fabricating a small light source, the resolution currently remains at the micrometer level. A combination of SECM and ECL has been used to image the activity of immobilized horse radish peroxidase [219].

A highly significant recent development is the integration of atomic force microscopy with SECM (AFM-SECM) [220]. Further details are described in Chapter 3.2 of this volume. An etched Pt wire was flattened and then insulated with electrophoretic paint. This probe acts as the cantilever in AFM and as the SECM tip providing dual force-sensing and electrochemical capabilities. Submicron resolution for SECM and for topography by AFM was achieved for test samples of track-etched polycarbonate membranes and ionic crystal surfaces. As the resolution of the technique improves and it is combined with other scanning probes, it seems likely that SECM can be applied in an ever-wider spectrum of scientific fields.

Acknowledgments

Grants from NATO (95-0009), the Royal Society, and Action Research in the area of SECM are gratefully acknowledged.

References

1. R. C. Engstrom, M. Weber, D. J. Wunder et al., *Anal. Chem.* **1986**, 58, 844–848.
2. R. M. Wightman, D. O. Wipf in *Electroanalytical Chemistry* (Ed.: A. J. Bard), Marcel Dekker, New York, 1988, pp. 267–353, Vol. 15.
3. A. J. Bard, L. R. Faulkner, *Electrochemical Methods*, John Wiley & Sons, New York, 1980.
4. A. J. Bard, F.-R. F. Fan, J. Kwak et al., *Anal. Chem.* **1989**, 61, 132–138.
5. H. S. Isaacs, *Corros. Sci.* **1988**, 28, 547–558.
6. J. Kwak, A. J. Bard, *Anal. Chem.* **1989**, 61, 1221–1227, 1794–1799.
7. D. H. Craston, C. W. Lin, A. J. Bard, *J. Electrochem. Soc.* **1988**, 135, 785, 786.
8. O. E. Husser, D. H. Craston, A. J. Bard, *J. Vac. Sci. Technol., B* **1988**, 6, 1873.
9. C. W. Lin, F.-R. F. Fan, A. J. Bard, *J. Electrochem. Soc., ABC* **1987**, 134, 1038.
10. I. Turyan, T. Matsue, D. Mandler, *Anal. Chem.* **2000**, 72, 3431–3435.
11. M. V. Mirkin, T. C. Richards, A. J. Bard, *J. Phys. Chem.* **1993**, 97, 7672–7677.
12. B. R. Horrocks, M. V. Mirkin, A. J. Bard, *J. Phys. Chem.* **1994**, 98, 9106–9114.
13. M. V. Mirkin, *Anal. Chem.* **1996**, 68, 177A.
14. A. J. Bard, F.-R. F. Fan, M. V. Mirkin in *Physical Electrochemistry: Principles, Methods and Applications* (Ed.: I. Rubinstein), Marcel Dekker, New York, 1995, pp. 209–242.
15. M. Arca, A. J. Bard, B. R. Horrocks et al., *Analyst* **1994**, 119, 719–726.
16. A. J. Bard, F.-R. F. Fan, M. V. Mirkin in *Electroanalytical Chemistry* (Ed.: A. J. Bard), Marcel Dekker, New York, 1993, pp. 243–273, Vol. 18.
17. A. J. Bard, F.-R. F. Fan, D. T. Pierce et al., *Science* **1991**, 254, 68–74.
18. A. L. Barker, M. Gonsalves, J. V. Macpherson et al., *Anal. Chim. Acta* **1999**, 385, 223–240.
19. N. Casillas, S. Charlebois, W. H. Smyrl et al., *J. Electrochem. Soc.* **1994**, 141, 636–642.
20. J. V. Macpherson, P. R. Unwin, *Phys. Chem.* **1994**, 98, 1704–1713, 11 764–11 770.
21. J. V. Macpherson, P. R. Unwin, *Phys. Chem.* **1995**, 99, 3338–3351, 14 824–14 831.
22. J. V. Macpherson, P. R. Unwin, *Phys. Chem.* **1996**, 100, 19 475–19 483.
23. J. V. Macpherson, P. R. Unwin, A. C. Hillier et al., *J. Am. Chem. Soc.* **1996**, 118, 6445–6452.
24. P. R. Unwin, J. V. Macpherson, *Chem. Soc. Rev.* **1995**, 24, 109–119.
25. Y. Shao, M. V. Mirkin, G. Fish et al., *Anal. Chem.* **1997**, 69, 1627–1634.
26. M. V. Mirkin, F.-R. F. Fan, A. J. Bard, *J. Electroanal. Chem.* **1992**, 328, 47–62.
27. D. T. Pierce, P. R. Unwin, A. J. Bard, *Anal. Chem.* **1992**, 64, 1795–1804.
28. D. T. Pierce, A. J. Bard, *Anal. Chem.* **1993**, 65, 3598–3604.
29. Y. Shao, M. V. Mirkin, *J. Electroanal. Chem.* **1997**, 439, 137–143.
30. Y. Shao, M. V. Mirkin, *J. Phys. Chem.* **1998**, 102, 9915–9921.
31. J. V. Macpherson, D. O'Hare, P. R. Unwin et al., *Biophys. J.* **1997**, 73, 2771–2781.
32. M. Gonsalves, A. L. Barker, J. V. Macpherson et al., *Biophys. J.* **2000**, 78, 1578–1588.
33. D. O. Wipf, A. J. Bard, *J. Electrochem. Soc.* **1991**, 138, 469–474.
34. A. Hengstenberg, C. Kranz, W. Schuhmann, *Chem. – Eur. J.* **2000**, 6, 1547–1554.
35. P. R. Unwin, A. J. Bard, *J. Phys. Chem.* **1991**, 95, 7814–7824.
36. F. Zhou, P. R. Unwin, A. J. Bard, *J. Phys. Chem.* **1992**, 96, 4917–4924.
37. F. Zhou, A. J. Bard, *J. Am. Chem. Soc.* **1994**, 116, 393, 394.
38. D. A. Treichel, M. V. Mirkin, A. J. Bard, *J. Phys. Chem.* **1994**, 98, 5751–5757.
39. P. R. Unwin, A. J. Bard, C. Demaille, *J. Phys. Chem.* **1996**, 100(33), 14 137–14 143.
40. R. C. Engstrom, T. Meaney, R. Tople et al., *Anal. Chem.* **1987**, 59, 2005–2010.
41. R. C. Engstrom, R. M. Wightman, E. W. Kristensen, *Anal. Chem.* **1988**, 60, 652–656.
42. G. Denuault, M. H. Troise-Frank, L. M. Peter, *Faraday Discuss. Chem. Soc.* **1992**, 94, 23–35.
43. B. R. Horrocks, M. V. Mirkin, D. T. Pierce et al., *Anal. Chem.* **1993**, 65, 1213–1224.

44. C. Wei, A. J. Bard, G. Nagy et al., *Anal. Chem.* **1995**, 67, 1346–1356.
45. C. Wei, A. J. Bard, I. Kapui et al., *Anal. Chem.* **1996**, 68, 2651–2655.
46. E. Klusmann, J. W. Schultze, *Electrochim. Acta* **1997**, 42, 3123–3134.
47. R. D. Martin, P. R. Unwin, *Anal. Chem.* **1998**, 70, 276–284.
48. R. D. Martin, P. R. Unwin, *J. Electroanal. Chem.* **1997**, 419, 123–136.
49. M. V. Mirkin, F.-R. F. Fan, A. J. Bard, *Science* **1992**, 257, 364–366.
50. F.-R. F. Fan, M. V. Mirkin, A. J. Bard, *J. Phys. Chem.* **1994**, 98, 1475–1481.
51. C. J. Slevin, P. R. Unwin *J. Am. Chem. Soc.* **2000**, 122(11), 2597–2602.
52. B. R. Horrocks, G. Wittstock, *Scanning Electrochemical Microscopy: Biological Applications* (Eds.: A. J. Bard, M. V. Mirkin), Marcel Dekker, NY, April 2001, Chapter 11, pp. 445–519.
53. D. O. Wipf, A. J. Bard, D. E. Tallman, *Anal. Chem.* **1993**, 65, 1373–1377.
54. G. Wittstock, K. Yu, H. B. Halsall et al., *Anal. Chem.* **1995**, 67, 3578–3582.
55. D. O. Wipf, A. J. Bard, *Anal. Chem.* **1992**, 64, 1362–1367.
56. L. A. Nagahara, T. Thundat, S. M. Lindsay, *Rev. Sci. Instrum.* **1989**, 60, 3128–3130.
57. C. Demaille, M. Brust, M. Tsionsky et al., *Anal. Chem.* **1997**, 69, 2323–2328.
58. B. R. Horrocks, D. Schmidtke, A. Heller et al., *Anal. Chem.* **1993**, 65, 3605–3614.
59. N. J. Gray, P. R. Unwin, *Analyst* **2000**, 125, 889–893.
60. N. Casillas, P. James, W. H. Smyrl, *J. Electrochem. Soc.* **1995**, 142, L16.
61. P. James, N. Casillas, W. H. Smyrl, *J. Electrochem. Soc.* **1996**, 143, 3853–3865.
62. G. I. Pennarun, C. Boxall, D. O'Hare, *Analyst* **1996**, 121, 1779–1788.
63. G. D. Shi, L. F. GarfiasMesias, W. H. Smyrl, *J. Electrochem. Soc.* **1998**, 145, 2011–2016.
64. T. Solomon, A. J. Bard, *Anal. Chem.* **1995**, 67, 2787–2790.
65. J. L. Amphlett, G. Denuault, *J. Phys. Chem. B* **1998**, 102, 9946–9951.
66. S. Amemiya, A. J. Bard, *Anal. Chem.* **2000**, 72, 4940–4948.
67. N. J. Evans, M. Gonsalves, N. J. Gray et al., *Electrochem. Commun.* **2000**, 2, 201–206.
68. P. R. Unwin, *J. Chem. Soc., Faraday Trans.* **1998**, 94, 3183–3195.
69. D. Jeffrey, B. R. Horrocks, R. D. Armstrong et al., *Electrochim. Acta* **1997**, 42, 3637–3640.
70. <http://www.staff.ncl.ac.uk/b.r.horrocks/>.
71. S. Nagues, G. Denuault, *J. Electroanal. Chem.* **1997**, 408, 125–140.
72. H. Shiku, T. Takeda, H. Yamada et al., *Anal. Chem.* **1995**, 67, 312–317.
73. A. J. Bard, G. Denuault, R. A. Friesner et al., *Anal. Chem.* **1991**, 63, 1282–1288.
74. M. V. Mirkin, A. J. Bard, *J. Electroanal. Chem.* **1992**, 323, 29–51.
75. A. J. Bard, M. V. Mirkin, P. R. Unwin et al., *J. Phys. Chem.* **1992**, 96, 1861–1868.
76. J. Galceran, J. Cecilia, E. Companys et al., *J. Phys. Chem. B* **2000**, 104, 7993–8000.
77. <http://www.fortranlib.com/>.
78. Q. Fulian, A. C. Fisher, G. Denuault, *J. Phys. Chem. B* **1999**, 103, 4387–4392, 4393–4398.
79. F.-R. F. Fan, A. J. Bard, *Science* **1995**, 267, 871–874.
80. F.-R. F. Fan, J. Kwak, A. J. Bard, *J. Am. Chem. Soc.* **1996**, 118, 9669–9675.
81. M. V. Mirkin, A. J. Bard, *Anal. Chem.* **1992**, 64, 2293–2302.
82. C. Wei, A. J. Bard, M. V. Mirkin, *J. Phys. Chem.* **1995**, 99, 16 033–16 042.
83. Y. Selzer, D. Mandler, *J. Phys. Chem. B* **2000**, 104, 4903–4910.
84. R. C. Engstrom, B. Small, L. Kattan, *Anal. Chem.* **1992**, 64, 241–244.
85. M. V. Mirkin, M. Arca, A. J. Bard, *J. Phys. Chem.* **1993**, 97, 10 790–10 795.
86. M. Arca, M. V. Mirkin, A. J. Bard, *J. Phys. Chem.* **1995**, 99, 5040–5050.
87. A. L. Barker, J. V. Macpherson, C. J. Slevin et al., *J. Phys. Chem. B* **1998**, 102, 1586–1598.
88. C. J. Slevin, J. V. Macpherson, P. R. Unwin, *J. Phys. Chem. B* **1997**, 101, 10 851–10 859.
89. C. J. Slevin, P. R. Unwin, *Langmuir* **1997**, 13, 4799–4803.
90. J. Zhang, P. R. Unwin, *Phys. Chem. Chem. Phys.* **2000**, 2, 1267–1271.
91. D. O. Wipf, *Colloids Surf., A* **1994**, 93, 251–261.
92. K. Fushimi, K. Azumi, M. Seo, *ISIJ Int.* **1999**, 39, 346–351.
93. Y. Y. Zhu, D. E. Williams, *J. Electrochem. Soc.* **1997**, 144, L43–L45.
94. L. F. GarfiasMesias, M. Alodan, P. I. James et al., *J. Electrochem. Soc.* **1998**, 145, 2005–2010.

95. H. Tanabe, K. Togashi, T. Misawa et al., *J. Mater. Sci. Lett.* **1998**, 17, 551–553.
96. G. Razzini, S. Maffi, G. Mussati et al., *Corros. Sci.* **1997**, 39, 613–625.
97. A. R. Kucernak, P. B. Chowdhury, C. P. Wilde et al., *Electrochim. Acta* **2000**, 45, 4483–4491.
98. H. Maeda, K. Ikeda, K. Hashimoto et al., *J. Phys. Chem. B* **1999**, 103, 3213–3217.
99. I. C. Jeon, F. C. Anson, *Anal. Chem.* **1992**, 64, 2021–2028.
100. M. Ludwig, C. Kranz, W. Schuhmann et al., *Rev. Sci. Instrum.* **1995**, 66, 2857–2860.
101. C. Kranz, H. E. Gaub, W. Schuhmann, *Adv. Mater.* **1996**, 8, 634.
102. P. I. James, L. F. Garfias-Mesias, P. J. Moyer et al., *J. Electrochem. Soc.* **1998**, 145, L64.
103. M. Buchler, S. C. Kelley, W. H. Smyrl, *Electrochem. Solid State Lett.* **2000**, 3, 35–38.
104. J. L. Luo, Y. C. Lu, M. B. Ives, *J. Electroanal. Chem.* **1992**, 326, 51–68.
105. J. L. Luo, Y. C. Lu, M. B. Ives, *Mater. Performance* **1992**, 31, 44–47.
106. D. E. Williams, T. F. Mohiuddin, Y. Y. Zhu, *J. Electrochem. Soc.* **1998**, 145, 2664–2672.
107. C. H. Paik, H. S. White, R. C. Alkire, *J. Electrochem. Soc.* **2000**, 147, 4120–4124.
108. S. B. Basame, H. S. White, *J. Phys. Chem.* **1995**, 99, 16 430–16 435.
109. S. B. Basame, H. S. White, *J. Phys. Chem.* **1998**, 102, 9812–9819.
110. R. S. Hutton, D. E. Williams, *J. Chem. Soc., Faraday Trans.* **1996**, 92, 4033–4040.
111. T. Misawa, H. Tanabe, *ISIJ Int.* **1996**, 36, 787–792.
112. J. W. Still, D. O. Wipf, *J. Electrochem. Soc.* **1997**, 144, 2657–2665.
113. S. B. Basame, H. S. White, *Langmuir* **1999**, 15, 819–825.
114. S. B. Basame, H. S. White, *Anal. Chem.* **1999**, 71, 3166–3170.
115. C. Lee, F. C. Anson, *Anal. Chem.* **1992**, 64, 528–533.
116. M. H. Troise Frank, G. Denuault, *J. Electroanal. Chem.* **1993**, 354, 331–339.
117. M. H. Troise Frank, G. Denuault, *J. Electroanal. Chem.* **1994**, 379, 399–406.
118. I. Kapui, R. E. Gyurcsanyi, G. Nagy et al., *J. Phys. Chem. B* **1998**, 102, 9934–9939.
119. G. Wittstock, T. Asmus, T. Wilhelm, *Fresenius' J. Anal. Chem.* **2000**, 367, 346–351.
120. M. Pyo, A. J. Bard, *Electrochim. Acta* **1997**, 42, 3077–3083.
121. M. Tsionsky, A. J. Bard, D. Dini et al., *Chem. Mater.* **1998**, 10, 2120–2126.
122. G. Wittstock, W. Schuhmann, *Anal. Chem.* **1997**, 69, 5059–5066.
123. G. Wittstock, R. Hesse, W. Schuhmann, *Electroanalysis* **1997**, 9, 746–750.
124. T. Wilhelm, G. Wittstock, R. Szargan, *Fresenius' J. Anal. Chem.* **1999**, 365, 163–167.
125. B. R. Horrocks, M. V. Mirkin, *J. Chem. Soc., Faraday Trans.* **1998**, 94, 1115–1118.
126. J. Zaumseil, G. Wittstock, S. Bahrs et al., *Fresenius' J. Anal. Chem.* **2000**, 367, 352–355.
127. H. Yamada, H. Shiku, T. Matsue et al., *Bioelectrochem. Bioenerg.* **1994**, 33, 91–93.
128. T. Sawaguchi, T. Matsue, I. Uchida, *Bioelectrochem. Bioenerg.* **1992**, 29, 127–133.
129. H. Shiku, T. Matsue, I. Uchida, *Anal. Chem.* **1996**, 68, 1276–1278.
130. S. Kasai, A. Yokota, H. Zhou et al., *Anal. Chem.* **2000**, 72, 5761–5765.
131. H. Shiku, Y. Hara, T. Matsue et al., *J. Electroanal. Chem.* **1997**, 438, 187–190.
132. C. A. Wijayawardhana, G. Wittstock, H. B. Halsall et al., *Anal. Chem.* **2000**, 72, 333–338.
133. C. E. Jones, J. V. Macpherson, P. R. Unwin, *J. Phys. Chem. B* **2000**, 104, 2351–2359.
134. S. Amemiya, Z. F. Ding, J. F. Zhou et al., *J. Electroanal. Chem.* **2000**, 483, 7–17.
135. J. Zhang, A. L. Barker, P. R. Unwin, *J. Electroanal. Chem.* **2000**, 483, 95–107.
136. J. Zhang, P. R. Unwin, *J. Phys. Chem. B* **2000**, 104, 2341–2347.
137. B. Liu, M. V. Mirkin, *J. Am. Chem. Soc.* **1999**, 121, 8352–8355.
138. A. L. Barker, P. R. Unwin, S. Amemiya et al., *J. Phys. Chem.* **1999**, 103, 7260–7269.
139. M. Tsionsky, A. J. Bard, M. V. Mirkin, *J. Phys. Chem.* **1996**, 100, 17 881–17 888.
140. M. Tsionsky, A. J. Bard, M. V. Mirkin, *J. Am. Chem. Soc.* **1997**, 119, 10 785–10 792.
141. H. H. Girault, D. J. Schiffrin in *Electroanalytical Chemistry* (Ed.: A. J. Bard), Marcel Dekker, New York, 1989, Vol. 15, pp. 1–141.
142. H. H. Girault in *Modern Aspects of Electrochemistry* (Eds.: J. O. 'M. Bockris, B. E. Conway, R. E. White), Plenum Press, New York, 1993, Vol. 25, pp. 1–62.
143. A. G. Volkov, D. W. Deamer, (Eds.), *Liquid-Liquid Interfaces. Theory and Methods*, CRC Press, Boca Raton, Fla., 1996.

144. Y. Zu, F.-R. F. Fan, A. J. Bard, *J. Phys. Chem.* **1999**, 103, 6272–6276.
145. Y. H. Shao, B. Liu, M. V. Mirkin, *J. Am. Chem. Soc.* **1998**, 120, 12 700–12 701.
146. B. Liu, Y. H. Shao, M. V. Mirkin, *Anal. Chem.* **2000**, 72, 510–519.
147. C. J. Slevin, S. Ryley, D. J. Walton et al., *Langmuir* **1998**, 14, 5331–5334.
148. C. Lee, J. Kwak, A. J. Bard, *Proc. Natl. Acad. Sci. U.S.A.* **1990**, 87, 1740–1743.
149. M. Tsionsky, Z. G. Cardon, A. J. Bard et al., *Plant Physiol.* **1997**, 113, 895–901.
150. T. Yasukawa, T. Kaya, T. Matsue, *Chem. Lett.* **1999**, (9), 975–976.
151. T. Yasukawa, T. Kaya, T. Matsue, *Anal. Chem.* **1999**, 71, 4637–4641.
152. T. Yasukawa, T. Kaya, T. Matsue, *Electroanalysis* **2000**, 12, 653–659.
153. T. Yasukawa, Y. Kondo, I. Uchida et al., *Chem. Lett.* **1998**, 767, 768.
154. B. Liu, S. A. Rotenberg, M. V. Mirkin, *Proc. Natl. Acad. Sci. U.S.A.* **2000**, 97, 9855–9860.
155. C. E. M. Berger, B. R. Horrocks, H. K. Datta, *Electrochim. Acta* **1999**, 44, 2677–2683.
156. C. J. McNeil, K. A. Smith, P. Bellavite et al., *Free Radical Res. Commun.* **1989**, 7, 89–96.
157. H. K. Datta, P. Manning, H. Rathod et al., *Exp. Physiol.* **1995**, 80, 713–719.
158. H. K. Datta, H. Rathod, P. Manning et al., *J. Endocrinol.* **1996**, 149, 269–275.
159. C. E. M. Berger, B. R. Horrocks, H. K. Datta, *Mol. Cell. Endocrinol.*, **1999**, 149, 53–59.
160. C. E. M. Berger, B. R. Horrocks, H. K. Datta, *J. Endocrinol.* **1998**, 158, 311–318.
161. N. Agarwala, C. V. Gay, *J. Bone Miner. Res.* **1992**, 7, 531–539.
162. J. V. Macpherson, M. A. Beeston, P. R. Unwin et al., *J. Chem. Soc., Faraday Trans.* **1995**, 91, 1407–1410.
163. J. V. Macpherson, M. A. Beeston, P. R. Unwin et al., *Langmuir* **1995**, 11, 3959–3963.
164. E. R. Scott, H. S. White, *Anal. Chem.* **1993**, 65, 1537–1545.
165. E. R. Scott, H. S. White, J. B. Phipps, *J. Membr. Sci.* **1991**, 58, 71–87.
166. E. R. Scott, H. S. White, J. B. Phipps, *Pharm. Res.* **1993**, 10, 1699.
167. R. D. Lee, H. S. White, E. R. Scott, *J. Pharm. Sci.* **1996**, 85, 1186–1190.
168. B. D. Bath, R. D. Lee, H. S. White et al., *Anal. Chem.* **1998**, 70, 1047–1058.
169. B. D. Bath, H. S. White, E. R. Scott, *Pharm. Res.* **2000**, 17, 471–475.
170. B. D. Bath, H. S. White, E. R. Scott, *Anal. Chem.* **2000**, 72, 433–442.
171. A. Cavalli, O. N. Oliveira Jr., *Rev. Sci. Instrum.* **1995**, 66, 5567.
172. V. B. P. Leite, A. Cavalli, O. N. Oliveira Jr., *Phys. Rev. E* **1998**, 57, 6835–6839.
173. E. M. El-Giar, R. A. Said, G. E. Bridges et al., *J. Electrochem. Soc.* **2000**, 147, 586–591.
174. F. Forouzan, A. J. Bard, *J. Phys. Chem. B* **1997**, 101, 10 876–10 879.
175. Y.-M. Wu, F.-R. F. Fan, A. J. Bard, *J. Electrochem. Soc., ABC* **1989**, 136, 885, 886.
176. C. Kranz, M. Ludwig, H. E. Gaub et al., *Adv. Mater.* **1995**, 7, 38–40, 568–571.
177. T. Wilhelm, G. Wittstock, *Mikrochim. Acta* **2000**, 133, 1–9.
178. D. Mandler, A. J. Bard, *J. Electrochem. Soc.* **1990**, 137, 1079–1086, 2468–2472.
179. D. Mandler, A. J. Bard, *J. Electrochem. Soc.* **1989**, 136, 3143, 3144.
180. D. Mandler, A. J. Bard, *Langmuir* **1990**, 6, 1489–1494.
181. S. Meltzer, D. Mandler, *J. Chem. Soc., Faraday Trans.* **1995**, 91, 1019–1024.
182. J. V. Macpherson, C. J. Slevin, P. R. Unwin, *J. Chem. Soc., Faraday Trans.* **1996**, 92, 3799–3805.
183. S. Meltzer, D. Mandler, *J. Electrochem. Soc.* **1995**, 142, L82–L84.
184. K. Borgwarth, C. Ricken, D. G. Ebling et al., *Ber. Bunsen-Ges. Phys. Chem.* **1995**, 99, 1421–1426.
185. C. Hess, K. Borgwarth, C. Ricken et al., *Electrochim. Acta* **1997**, 42, 3065–3073.
186. Y. B. Zu, L. Xie, B. W. Mao et al., *Electrochim. Acta* **1998**, 43, 1683–1690.
187. Z. W. Tian, *Faraday Discuss.* **1992**, 94, 37.
188. I. Shohat, D. Mandler, *J. Electrochem. Soc.* **1994**, 141, 995–999.
189. I. Turyan, U. O. Krasovec, B. Orel et al., *Adv. Mater.* **2000**, 12, 330–334.
190. J. Zhou, D. O. Wipf, *J. Electrochem. Soc.* **1997**, 144, 1202–1207.
191. T. Yasukawa, N. Kanaya, D. Mandler et al., *Chem. Lett.* **2000**, (5), 458–459.
192. H. Shiku, I. Uchida, T. Matsue, *Langmuir* **1997**, 13, 7239–7244.
193. J. C. O'Brien, J. Shumaker-Parry, R. C. Engstrom, *Anal. Chem.* **1998**, 70, 1307–1311.
194. C. Kranz, G. Wittstock, H. Wohlschlager et al., *Electrochim. Acta* **1997**, 42, 3105–3111.

195. W. Schuhmann, C. Kranz, H. Wohlschlagger et al., *Biosens. Bioelectron.* **1997**, 12, 157–167.
196. W. B. Nowall, D. O. Wipf, W. G. Kuhr, *Anal. Chem.* **1998**, 70, 2601–2606.
197. D. J. Strike, A. Hengstenberg, M. Quinto et al., *Mikrochim. Acta* **1999**, 131, 47–55.
198. M. M. Collinson, R. M. Wightman, *Science* **1995**, 268, 1883–1885.
199. A. J. Bard, F.-R. F. Fan, *Acc. Chem. Res.* **1996**, 29, 572–578.
200. D. O. Wipf, A. J. Bard, *J. Electrochem. Soc.* **1991**, 138, L4.
201. F.-R. F. Fan, A. J. Bard, *Science* **1997**, 277, 1791–1793.
202. P. R. Unwin, A. J. Bard, *J. Phys. Chem.* **1992**, 96, 5035–5045.
203. K. Borgwarth, C. Ricken, D. G. Ebling et al., *Fresenius' J. Anal. Chem.* **1996**, 356, 288–294.
204. C. Lee, A. J. Bard, *Anal. Chem.* **1990**, 62, 1906–1913.
205. F.-R. F. Fan, A. J. Bard, *Science* **1995**, 270, 1849–1851.
206. A. J. Bard, F.-R. F. Fan, *Faraday Discuss. Chem. Soc.* **1992**, 94, 1.
207. M. E. Williams, K. J. Stevenson, A. M. Massari et al., *Anal. Chem.* **2000**, 72, 3122–3128.
208. K. Karrai, R. D. Grober, *Appl. Phys. Lett.* **1995**, 66, 1842–1844.
209. H. Edwards, L. Taylor, W. Duncan et al., *J. Appl. Phys.* **1997**, 82, 980–984.
210. R. Guckenberger, M. Heim, G. Cevc et al., *Science* **1994**, 266, 1538–1540.
211. N. Patel, M. C. Davies, M. Lomas et al., *J. Phys. Chem. B* **1997**, 101, 5138–5142.
212. B. Gollas, P. N. Bartlett, G. Denuault, *Anal. Chem.* **2000**, 72, 349–356.
213. M. S. Shin, I. C. Jeon, *Bull. Korean Chem. Soc.* **1998**, 19, 1227–1232.
214. A. J. Bard, D. E. Cliffel, C. Demaille et al., *Ann. Chim.* **1997**, 87, 15–31.
215. C. Hess, K. Borgwarth, J. Heinze, *Electrochim. Acta* **2000**, 45, 3725–3736.
216. D. E. Cliffel, A. J. Bard, S. Shinkai, *Anal. Chem.* **1998**, 70, 4146–4151.
217. D. E. Cliffel, A. J. Bard, *Anal. Chem.* **1998**, 70, 1993–1998.
218. F.-R. F. Fan, D. Cliffel, A. J. Bard, *Anal. Chem.* **1998**, 70, 2941–2948.
219. H. F. Zhou, S. Kasai, T. Yasukawa et al., *Electrochemistry* **1999**, 67, 1135–1137.
220. J. V. Macpherson, P. R. Unwin, *Anal. Chem.* **2000**, 72, 276–285.

3.4 Spectroelectrochemistry: In situ UV-visible Spectroscopy

Joe A. Crayston
University of St. Andrews, Fife, United Kingdom

3.4.1 Introduction and Principles

3.4.1.1 Introductory Remarks

Of all the multitudinous spectroelectrochemistry techniques available today, perhaps UV-visible spectroelectrochemistry can claim to be the oldest. Apart from early reports of the use of ellipsometry, a reflectance technique, the first report of the absorption spectrum of an electrogenerated chromophore is probably that of Heineman. Though as Heineman relates in his entertaining account of the development of the optically transparent thin-layer electrode (OTTLE) [1], it was in the late 1950s that Ted Kuwana, Ralph Adams's first graduate student, mused that it would be nice to have "a see-through electrode to spectrally identify the colored species being formed" during the oxidation of *p*-toluidine. The early cells were developed using technology from the electronics industry, which allowed the painting of metallic layers onto glass to lend a degree of conductivity while retaining some optical transparency. The prototype cells did not work very well as the cell was so thin that air bubbles could not be dislodged. Later on, the designs used demountable thin-layer cells, including the famous minigrid design. At its simplest, this design involves the sandwiching of a gold minigrid between two microscope slides, as shown in Fig. 1 [2, 3].

Today, UV-visible spectroelectrochemistry has become an essential tool in the study of redox processes, particularly when the processes are reversible and the reagents or products of electrolysis are colored. For example, the technique is of enormous value in the study of the electrochemistry of porphyrins and phthalocyanines, though it took some time to catch on. A review of porphyrin electrochemistry from 1986 barely mentions the technique, now an essential, even routine, tool in this field [4]. Another area of chemistry in which spectroelectrochemistry has been extremely important is conducting polymers, a field that had barely started 20 years ago. Spectroelectrochemistry has also been developing rapidly as the technology of electronic and optical detection has advanced. For example, we shall see later how time-resolved spectroelectrochemistry is now able to provide a wealth of information about electrochemical processes.

Since the comprehensive reviews published some time ago in *Electroanalytical chemistry* [5, 6], and a concise version of these in 1976 [7], there have been many recent reviews covering spectroelectrochemistry, using radiation other than in the visible region [8–11]. However, there are far fewer reviews exclusively covering UV-visible spectroelectrochemistry. The most recent and complete review (with 390 references) was published in 1996 [12]. Other surveys include those by Pragst [13], McCreery and coworkers [14] and Plieth and coworkers [15]. There are also the well-known biennial reviews in *Analytical Chemistry* within the Dynamic Electrochemistry sections [16, 17]. Various book chapters and monographs provide excellent summaries on the techniques/theory and the applications of optically transparent electrodes [18–21]. Although we shall

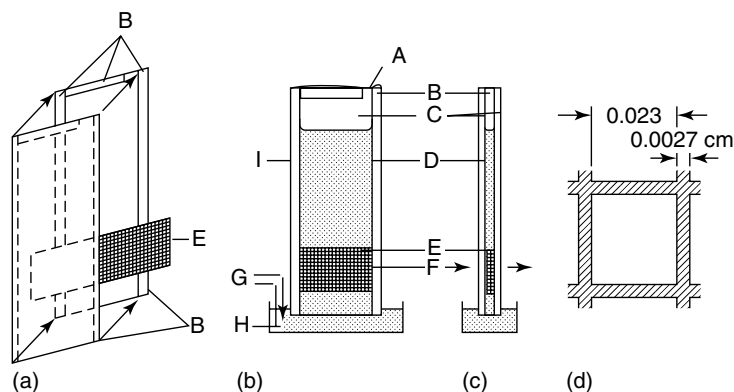


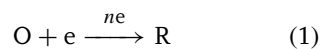
Fig. 1 Minigrid OTTLE cell. (a) Assembly of the cell; (b) front view; (c) side view; and (d) dimensions of 100 wires per inch gold minigrid. (A) Point of suction application to change solution, (B) Teflon tape spacers, (C) microscope slides (1 × 3 in.), (D) solution, (E) transparent fold minigrid electrode, (F) optical path of spectrometer, (G) reference and auxiliary electrodes, (H) solution cup, and (I) epoxy holding cell together. (Used with permission from *J. Chem. Educ.*, **1976**, 53, 594–597; Copyright (c) 1976, Division of Chemical Education, Inc.)

focus primarily on the spectroscopic detection of solution-generated species, we shall also discuss briefly the techniques used to look at thick films on electrode surfaces, such as conducting polymer films. While the pace of development of the basic theory has slowed, there is no shortage of new geometries stemming from ingenious new cell designs (e.g. channel-flow and long optical path-length cells), which demand new analysis. Similarly, optical responses for ever-more complex mechanistic schemes are steadily being developed.

This chapter does not cover probe-beam deflection used for spectroscopy [22], reflection spectroscopy [23, 24], surface plasmon resonance [23], second harmonic generation [25, 26], ellipsometry (Muller in Refs. [10, 27]), internal reflection [28], photoacoustic and photothermal spectroscopy [29] (neither of which has enjoyed widespread application in electrochemistry), or waveguides [30–32].

3.4.1.2 Theory and Techniques: Steady State Measurement

3.4.1.2.1 Cell Transmission for a Simple Electron Transfer Reaction: Determination of E and n The principles of UV-visible spectroelectrochemistry will be illustrated for transmission, as this is the most mature area. Suppose O, a colorless compound is reduced by n electrons to R, which does absorb,



For a fast electron transfer reaction, the surface concentration ratio will be given by the Nernst equation (see Chapter 1.1, Sect. 1.3):

$$E = E^{o'} + \frac{RT}{nF} \ln \frac{[\text{O}]}{[\text{R}]} \quad (2)$$

or

$$E = E^{o'} + 0.059n \log_{10} \frac{[\text{O}]}{[\text{R}]} \quad (3)$$

If we wait long enough, and there is sufficient mixing, then through electrolysis this surface concentration ratio will extend throughout the solution. At this point, the concentration ratio can be obtained by assuming Beer's law holds at the wavelength of choice. Normally, the wavelength at which there is maximum absorbance change is chosen. According to Beer's law, the total absorbance at this wavelength and potential E will be related to the extinction coefficients of each species at this wavelength and their concentrations:

$$A_E = \varepsilon_{\text{O}} c_{\text{O}} l + \varepsilon_{\text{R}} c_{\text{R}} l \quad (4)$$

Assuming that we have a single redox reaction without chemical reactions, then using

$$c_{\text{O}} + c_{\text{R}} = c \quad (5)$$

where c is the original bulk concentration of O, it can be easily shown that the Nernst equation becomes

$$E = E^{o'} + 0.059n \log_{10} \frac{A_E - A_{\text{R}}}{A_{\text{O}} - A_E} \quad (6)$$

where

$$A_{\text{O}} = \varepsilon_{\text{O}} c_{\text{O}} l \quad (7)$$

and

$$A_{\text{R}} = \varepsilon_{\text{R}} c_{\text{R}} l \quad (8)$$

More details on how to obtain the absorbance ratio from the spectra have been given previously [33]. A plot of the absorbance ratio versus E should then be a straight line with a y-axis intercept giving $E^{o'}$ and the slope giving n (Fig. 2) [34]. Note that a great attraction of the technique is that neither the extinction coefficients nor the path-length, nor even

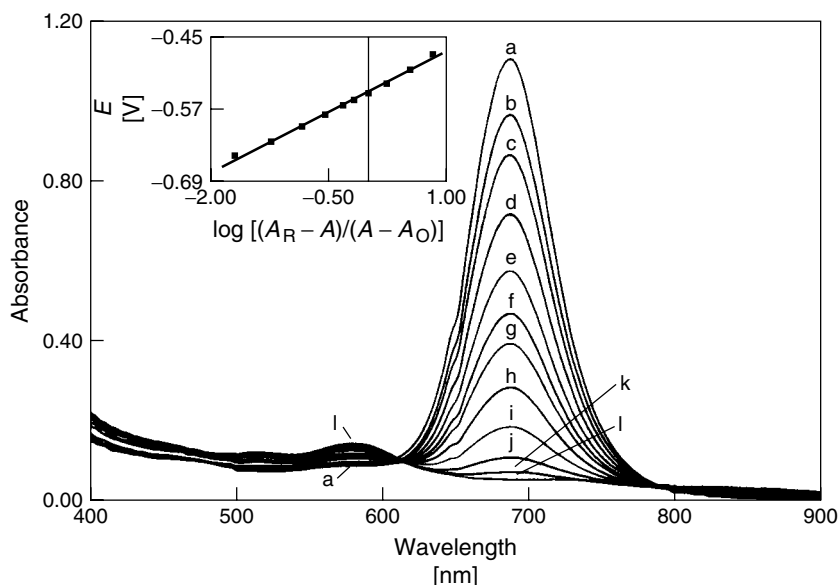


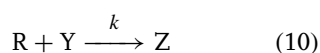
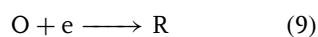
Fig. 2 Absorption spectra of a 6.08 mM solution of Re_3Cl_9 in the 49 mol% AlCl_3 –MeTmCl salt at 40 °C at various applied potentials (V): (a) open circuit, (b) –0.266, (c) –0.303, (d) –0.325, (e) –0.340, (f) –0.352, (g) –0.364, (h) –0.383, (i) –0.405, and (j) –0.550. Inset: Nernst plot constructed from the spectra. (Reprinted with permission from S. K. D. Strubinger, I. W. Sun, W. E. Cleland et al., *Inorg. Chem.* **1990**, 29, 993–999. Copyright 1990, American Chemical Society.)

the initial concentration are required as long as the limiting absorbances in each redox state (at sufficiently reducing and oxidizing potentials) can be measured. This analysis applies to any steady state method, such as rotating disk voltammetry or the channel electrode.

For a sequential reaction without any branching pathways (such as decomposition of a reactive intermediate), one would expect [35] to see isosbestic points in the thin-layer electrolysis, as in Fig. 2. It is an excellent idea to carry out several oxidation–reduction cycles to test the stability of the spectral responses, in other words, to see if the starting material is always fully regenerated. If not, the kinetics of the follow-up chemical reactions could be explored as described below.

The OTTLE method is very useful for slow electron transfer kinetics such as those of biological redox processes, in which a mediator is frequently used in an indirect coulometric titration [6, 36] and metal complexes with slow heterogeneous kinetics. An example of the latter is a copper complex in which the Cu(II/I) couple very often shows a broad quasi-reversible wave due to slow heterogeneous kinetics. In this case, spectroelectrochemistry is a useful method for obtaining accurate $E^{o'}$ values [37].

3.4.1.2.2 Effect of Follow-up Reactions in OTTLE Cells OTTLE cells are useful for looking at slow follow-up reactions, such as the EC reaction (Eqs. 9 and 10).



The volume inside the thin layer is completely electrolyzed by a potential step beyond the O/R wave within typically

30 s and after this time, the absorbance of the electrogenerated product R can be monitored (with potential maintained or at open circuit – it should not matter unless the reaction regenerates the starting material).

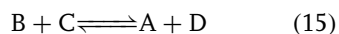
$$\ln(A_t - A_\infty) = -kt + \ln(A_0 - A_\infty) \quad (11)$$

It is possible to slow down the observed rate to a more convenient time-scale by generating less R. This may be done by stepping the potential to a point near the redox potential. If the Nernst ratio $q = [\text{O}]/[\text{R}]$ is $\exp[nF/RT(E - E^{o'})]$, then the rate constant will be reduced by a ratio of $q/(q + 1)$. This approach was successfully used in the classic *p*-aminophenol EC reaction example [38], discussed elsewhere in detail [6].

The open-circuit method is useful if the electrode reaction is complicated by slow heterogeneous kinetics, adsorption, double-layer charging, and so on. The open-circuit method also has the advantage that it can be used in thin-layer cells that have too great an *IR* drop to be used in electrochemical experiments for determination of follow-up reaction rate constants. A similar open-circuit experiment is commonly employed for in situ electron paramagnetic resonance (EPR) spectroelectrochemistry if radicals are being generated (see Chapter 3.2 in Volume 2). The treatment is particularly simple to apply in the case of first-order or pseudo-first-order reactions, since only the change in concentration, rather than the absolute concentration needs to be determined. It does not require simulation of the concentration profiles [39] (a check on the first-order nature of the reaction is made by varying the concentration or by varying the electrolysis time). There is also no need to determine the extinction coefficient of

the electrogenerated species. A plot of $\log(\text{absorbance})$ versus t yields k or kc_Z as the slope. Alternatively, $\log(\text{normalized absorbance})$ is plotted, in which the normalized absorbance is A/A_{off} and A_{off} is the absorbance when the current is turned off (it will be a maximum absorbance and would have remained constant in the absence of the reaction). For second-order (e.g. dimerization) and higher-order reactions, the concentration profiles must be estimated by digital simulation, unless the diffusion/mixing time is small compared to the reaction time.

The open-circuit method can, in certain cases, distinguish between two different reaction types. ECE and DISP1 are two mechanisms that are not easy to distinguish using purely electrochemical methods. Consider the following scheme:



Of the limiting cases, it is easy to distinguish DISP2 (Reaction 14 is unimportant and Reaction 15 the rate-determining step (RDS)) as it has a second-order dependence on B. But it is difficult to distinguish ECE (Reaction 15 unimportant) from DISP1 (Reaction 14 unimportant and Reaction 13 the RDS). However, the spectroelectrochemical experiment shows a rapid falloff in absorbance for the ECE reaction after the cell is switched to open circuit (Fig. 3). Species D, the carbocation radical in this case, decays rapidly when the electrode is unable to oxidize C [21, 40].

The copper-catalyzed decomposition of sulfite takes place by a catalytic regeneration reaction ($E_r C_i'$) and the open-circuit decay spectroelectrochemistry suggests it is second order in copper ion [41]. The following mechanism was proposed in a

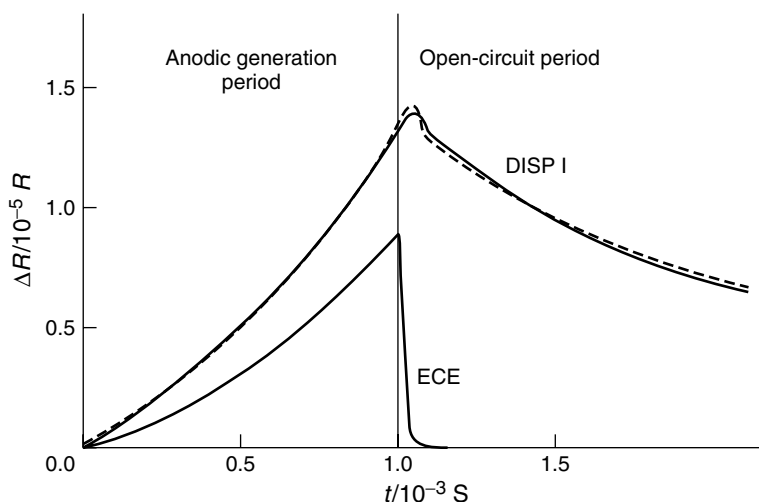
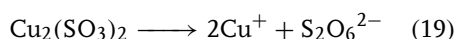
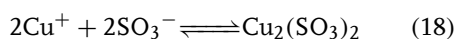
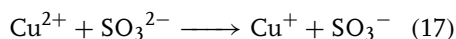
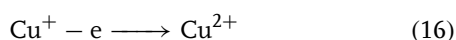


Fig. 3 Absorbance–time transients for the carbonium ion generated in a potential step followed by an open-circuit decay period. Full lines: curves computed for the DISP1 and ECE mechanisms. Dashed line: the experimental transient obtained for pentamethylbenzene at 467 nm. (Reprinted from *Electrochim. Acta*. **1980**, 25, 931. Copyright 1980, with permission from Elsevier Science.)

later paper, with the last step being rate determining [42]:

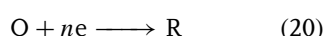


A small, horizontally mounted electrolysis cell of volume 8 cm^3 was fitted with a rotating disc electrode (RDE) or stirrer and an optical-fiber probe inserted to monitor the electrolysis. The first-order decay of electrogenerated $[\text{Fe}(\text{bpy})_3]^{3+}$ was monitored at open circuit [43].

Greater time resolution can be gained by coupling pulse electrolysis to stopped-flow apparatus [44]. This technique has been used in the study of anthracene radical cation reactions with nucleophiles described later [45]. Electrochemical techniques are considered rather slow for studying these reactions; the radical cations are much more conveniently generated and studied by laser flash photolysis.

3.4.1.3 Theory and Techniques: Kinetic Measurements

3.4.1.3.1 Chronoabsorptometry The technique of chronoabsorptometry, also known as potential step chronoamperospectrometry (PSCAS) and chrono-coulo-spectrometry (PSCCS), monitors the time dependence of the absorbance. We consider the case of an optically transparent electrode. Suppose O, which we shall assume to be colorless or to have negligible change in absorbance at the monitoring wavelength, is reduced by n electrons to R:



At any given time, the absorbance of R at the monitoring wavelength, λ (again chosen experimentally for the maximum absorbance change), corrected for any background absorbance, is given by

$$A_R(t) = \varepsilon_R l \int_{x=0}^l c_R(x, t) dx \quad (21)$$

where ε_R is the extinction coefficient or R at that wavelength. If we assume Beer's law and assume that the total (integrated) concentration of R at time t arising from the electrochemical reaction is simply related to the charge passed up to time t , we have

$$A_R(t) = \frac{10^3 \varepsilon_R Q(t)}{nFS} \quad (22)$$

where S is the electrode area, and the 10^3 factor arises from the conversion from cm^3 to dm^3 . Now, if we step the potential of the electrode beyond the wave to a potential at which O is fully reduced, then the boundary condition $c_R(x=0, t)=0$ is set up. $Q(t)$, the charge passed at the electrode, is simply given by the integrated Cottrell equation (see Chapter 2.2 in this volume).

$$Q(t) = \frac{2nFS c \sqrt{D_O t}}{\sqrt{\pi}} \quad (23)$$

Now this solution, of course, assumes semi-infinite conditions at the electrode. In order to use the integrated Cottrell result, we must assume that at some distance from the electrode, the absorbance reaches zero and we can replace l in the integration by infinity, though we note, in passing, that the case of a finite diffusion space has now been treated [46]. Inserting this into the previous equation, we have

$$A_R(t) = \frac{2 \times 10^3 \varepsilon_{RC} \sqrt{D_O t}}{\sqrt{\pi}} \quad (24)$$

Note the lack of dependence on electrode area or the number of electrons passed, both unknown quantities that have to be assumed or determined in the Cottrell determination of the diffusion coefficient. As Kuwana points out, the solution is identical to Beer's law if we allow the path-length l to be given by

$$l = 2\sqrt{\frac{D_O t}{\pi}} \quad (25)$$

To electrochemists this expression is clearly related to the diffusion length or Nernst diffusion layer thickness. So the potential step chronoabsorptometry experiment can be regarded as setting up an optical cell with the thickness equal to the Nernst diffusion layer. As time increases, not only does the diffusion layer thickness increase, but so does the amount of light-absorbing product generated in the layer.

Note that the slope of the absorbance-time plot allows the determination of the (usually) unknown extinction coefficient ε_R for the electrogenerated species, providing that c and D_O are known. No knowledge of the electrogenerated species' diffusion coefficient D_R is necessary. Usually the concentration is known and it is a simple matter to determine D_O from a chronoamperometry, chronocoulometry, or ultramicroelectrode experiment. If both c and D_O are unknown, then they can be obtained from a potential step experiment at an ultramicroelectrode [47, 48].

Another advantage of the chronoabsorptometric method is that the area of the electrode does not enter into the equation. Equation (24) can then form the basis of a useful method to measure the diffusion coefficient D_O provided that the extinction coefficient or R is known (perhaps from OTTLE measurements of the

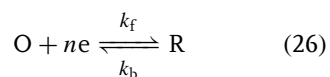
limiting absorbance A_R of a solution of known concentration).

3.4.1.3.2 Instrumentation for Chronoabsorptometry

It is relatively simple to set up an optical system for the measurement of the absorption decay at a single wavelength. Most standard spectrophotometers also offer this option ("time-drive") but at limited time resolution. For scanning the whole spectrum at once, the modern spectrometer is rather slow. For example, the popular Hewlett-Packard series of diode array spectrophotometers (HP 8452A) and Shimadzu (UVPC-1501) [49] were able to collect spectra every second [50], and nowadays a typical diode array instrument will collect a spectrum in as little as 5 ms. Commercial rapid-scanning spectrophotometers are available (e.g. Tracor-Northern spectrometer TN-1710 vibrating mirror instrument was used in the 1980s to collect spectra with a cycle time of only 12.5 ms) [51, 52]. It is possible to use rapid-scanning instruments to collect spectra in as little as 2 ms with 83 ms between spectra with a spinning grating monochromator [53]. Nevertheless, very often, signal averaging is required to achieve respectable signal-to-noise ratios. Nowadays, most rapid-scanning systems would use a multichannel detection system with an intensified charge coupled device (CCD), allowing the collection of a whole spectrum in 10 ms [54].

3.4.1.3.3 Slow Heterogeneous Kinetics

Chronoabsorptometry has been applied to the determination of heterogeneous electron-transfer parameters in single-step irreversible [55] and quasi-irreversible kinetics [56] and in double potential step modes [57]. In the case of a single potential step for the reaction



irreversible kinetics with $k_f \gg k_b$ will yield a time-dependent normalized absorbance:

$$A_R(\zeta) = \frac{\varepsilon_{RC} D_O}{\sqrt{\pi}} \left[\frac{2\zeta}{\sqrt{\pi}} + \exp(\zeta^2) \text{erfc}(\zeta) - 1 \right] \quad (27)$$

where

$$\zeta = \frac{k_f t^{(1/2)}}{\sqrt{D_O}} \quad (28)$$

Equation (27) may be rewritten in terms of the normalized absorbance:

$$A_N(\zeta) = 1 + \frac{\sqrt{\pi}}{2\zeta} [\exp(\zeta^2) \text{erfc}(\zeta) - 1] \quad (29)$$

which is plotted in Fig. 4, used as a working curve for the determination of k_f . Similar curves are available for quasi-reversible kinetics [6]. If desired, the rate constant may be tested for Butler–Volmer type dependence on potential. Although there are several nonspectroscopic methods

for measuring kinetic parameters, once again, the advantage of the spectroscopic method is the selectivity in the presence of interfering reactions, such as O_2 reduction.

3.4.1.3.4 Effect of Follow-up Reactions

The effect of follow-up reactions has been comprehensively examined (see the previous reviews [5, 6]). In general, there are few analytical solutions and so numerical methods must be used. For the simple EC reaction (where Z is neither electroactive, nor colored),



the time dependence of the absorbance is given by the Cottrell-type decay [derivative of Eq. (23)] coupled with the chemical reaction:

$$\frac{dA_R(t)}{dt} = \frac{2\varepsilon_{RC}\sqrt{D_O}}{\sqrt{\pi t}} - kA_R(t) \quad (32)$$

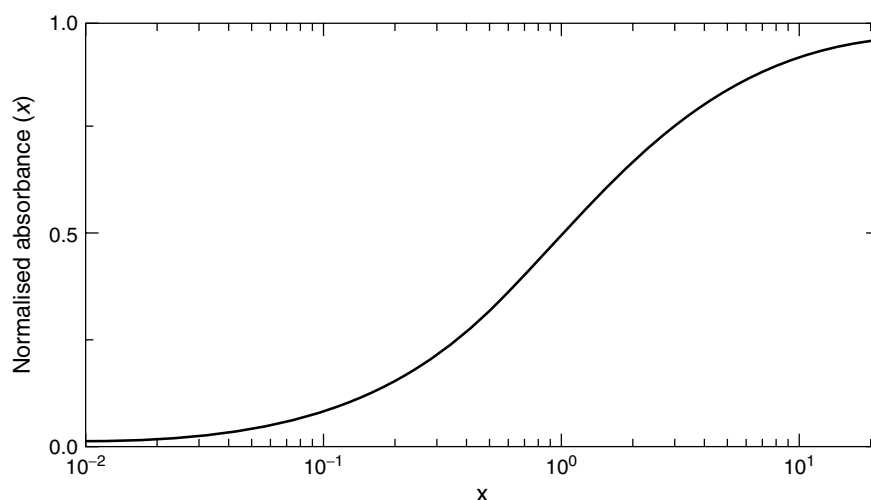


Fig. 4 Plot of Eq. (27) for the normalized absorbance dependence on the heterogeneous rate parameter.

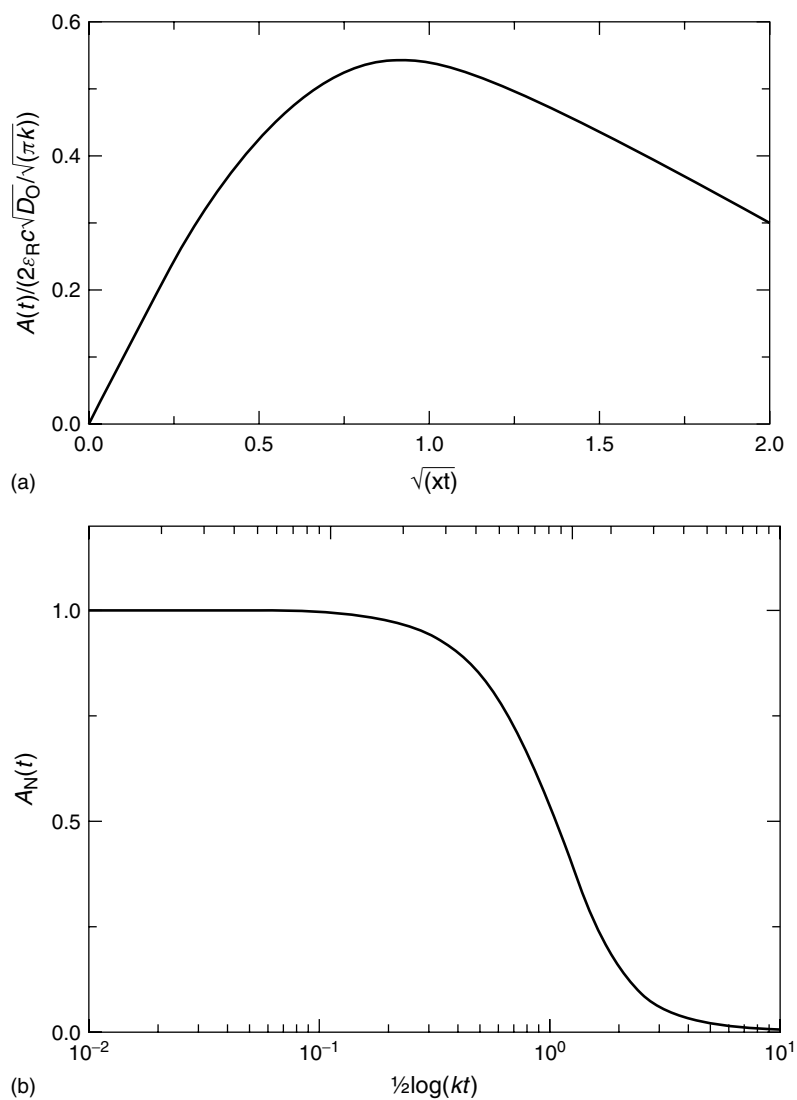


Fig. 5 Plots of (a) Eq. (33) for the absorbance dependence on rate parameter for a homogeneous EC reaction and (b) normalized absorbance plot (Eq. 34).

The solution obtained using Laplace transformations is [39]

$$A_R(t) = \frac{2\varepsilon_R c \sqrt{D_O}}{\sqrt{\pi k}} \times \left[\exp(-kt) \int_0^{\sqrt{kt}} \exp(\vartheta^2) d\vartheta \right] \quad (33)$$

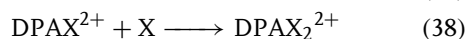
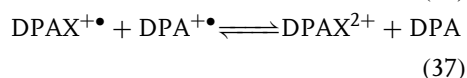
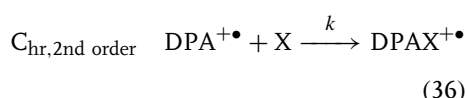
As shown in Fig. 5(a), the consumption of R causes the absorbance to pass through a maximum. A rate constant can be derived from this maximum or from the working curve of the normalized absorbance (absorbance in the presence of Reaction 31 divided by the diffusion-controlled

absorbance in the absence of Z) as given by Eq. (34) [Fig. 5(b)].

$$A_N(t) = \frac{1}{\sqrt{kt}} \left[\exp(-kt) \int_0^{\sqrt{kt}} \exp(\vartheta^2) d\vartheta \right] \quad (34)$$

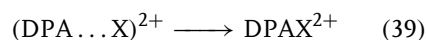
Finite difference method digital simulation (see Chapter 1.2 in this volume) has been performed for many different reaction mechanisms, and normalized absorbance working curves have been presented for not only current and charge but also absorbance of the various species assumed by the mechanism [58, 59]. For first-order or pseudo-first-order reactions, a little-used method for graphical analysis of the data is to plot the absorption–time transients according to Eq. (32) [40, 60].

A celebrated example of a more complicated follow-up reaction studied by chronoabsorptometry is the reaction of pyridine on the diphenylanthracene cation DPA^+ to give $\text{DPA}(\text{py})_2^{2+}$ [61]. This reaction follows the second-order half regeneration mechanism (EC_{hr}) with the reaction between $\text{DPA}^{+\bullet}$ and pyridine (X) being the RDS.



The chronoabsorptometric response fits the digital simulation of this reaction well (Fig. 6) [62, 63]. However, as Parker has pointed out [64], later findings on the rate law of the reaction suggest a subtle modification. The $\text{DPAX}^{+\bullet}$ adduct in the scheme should be regarded as a cation radical–nucleophile complex

$(\text{DPA} \dots \text{X})^{+\bullet}$. Then the final reaction in the scheme forming the covalent bond to X does not involve pyridine and should be written as



Nevertheless, these reactions still generate much controversy, as reactions between radical cations and nucleophiles should be forbidden unless electron transfer intervenes. Parker has suggested that the radical and cationic centers may be on different atoms [65]. Recent investigations on substituted DPA reactions show a strong substituent effect on the rate and, in some cases, the mechanism, as demonstrated in a recent pulse-electrolysis stopped-flow study [45].

3.4.1.3.5 Derivative Cyclic Voltabsorptometry (DCVA) This technique was first presented in 1981 for semi-infinite diffusion to an optically transparent electrode [66]. The theory has since been presented for the technique in a thin-layer (OTTLE) cell configuration [46]. Slow kinetics are often observed in electron transfer to biological molecules, and the chronoabsorptometric response was used to determine the heterogeneous rate constant for electron transfer to horse myoglobin [67]. The advantage of the optical technique is that the measurements can be made successfully in the presence of other faradaic processes or charging processes. This selectivity was demonstrated by the fact that residual oxygen gave rise to extra current, but the effect of oxygen was not, of course, evident in the DCVA trace recorded using visible wavelength light.

If we differentiate Eq. (22), after substituting dQ/dt by the current, we obtain,

$$\frac{dA_R(t)}{dt} = \frac{2 \times 10^3 \varepsilon_R c i(t)}{nFS} \quad (40)$$

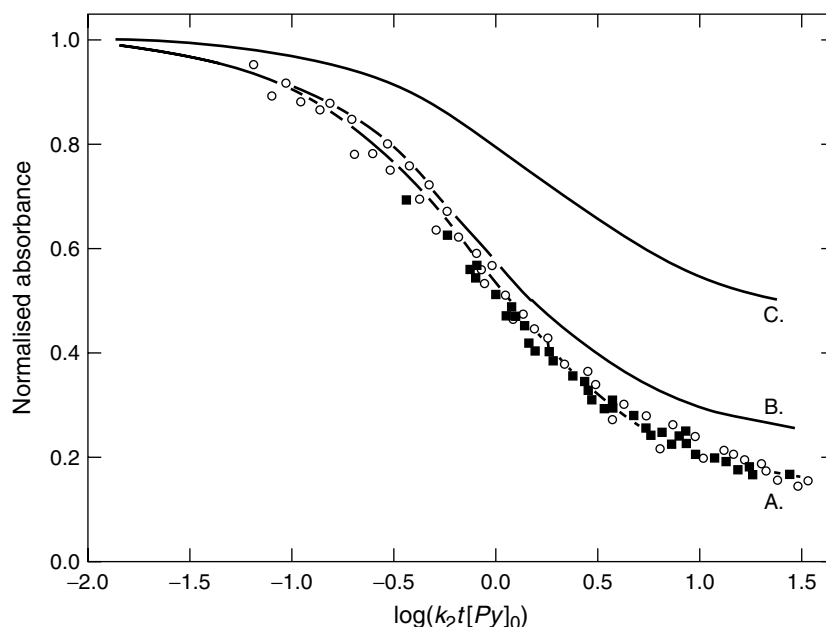


Fig. 6 Chronoabsorptometric plots for the reaction between $\text{DPA}^{+\bullet}$ and pyridine shown with simulated responses. Conditions: $[\text{DPA}] = 1.05 \text{ mM}$, $[\text{Py}] = 1.07 \text{ mM}$. Solid lines are simulated responses for (A), the second-order half regeneration mechanism (EC_{hr}); (B) ECE mechanism with “nuance”. (C) ECE mechanism with $k = 1.82 \times 10^4 \text{ M}^{-1} \text{ s}^{-1}$ [4, 5]. (Reprinted with permission from H. N. Blount, *J. Electroanal. Chem.* **1973**, 42, 271 and J. F. Evans, H. N. Blount, *J. Phys. Chem.* **1979**, 83, 1970. Copyright (1973, 1979) American Chemical Society. Solid squares from Blount, open circles from Evans et al.)

The absorbance change dA/dt will then follow the current, provided that species R has a measurable absorbance (depending, of course, on the concentration and the extinction coefficient). Instrumentally, it is also possible to plot dA/dE , which is related to dA/dt by the scan rate, ν :

$$\frac{dA_{\text{R}}(t)}{dt} = \nu \frac{dA_{\text{R}}(t)}{dE} \quad (41)$$

The usual expressions for the current peak-height in cyclic voltammetry (CV) (such as the Randles–Sevcik equation) are simply inserted into Eq. (40) to obtain the corresponding DCVA relations.

The strategy for the application of DCVA would seem to be to first record steady state

spectra (using an OTTLE) or alternatively, whole spectra as rapidly as possible in a semi-infinite diffusion cell. Once particular wavelengths can be assigned to particular species, perhaps through the judicious use of subtractions, or, in the case of overlapping species, more sophisticated chemometric methods, then the spectrophotometer can be set to “time-drive” at that wavelength while the potential is cycled (typically at up to 50 mV s^{-1}). If several species are being monitored by DCVA, it is important to remember that peak heights are proportional not only to concentration but also to the molar extinction coefficients, which in general are unknown.

Although it was mentioned earlier that oxygen is “silent” in absorption measurements in the visible region, in organic solvents it is possible to detect the superoxide ion (λ_{max} 271 and 305 nm, $\varepsilon = 2006 \text{ dm}^3 \text{ mol}^{-1} \text{ cm}^{-1}$). DCVA of oxygen reduction in DMSO and pyridine using a fiber-optic/reflection configuration shows that the wave is quasi-reversible (Fig. 7) [68]. These authors chose to use chronoabsorptometry to measure the heterogeneous rate constants, basing the analysis on the corresponding chronocoulometric case [69]. Of course, caution must be exercised in interpreting negative chronoabsorptometric intercepts in this way without being certain that uncompensated resistance (especially problematic with thin film electrodes) is fully accounted for.

Reduction of sulfur in DMSO gives two waves in the (CV). It was shown by reflection spectroelectrochemistry that the first reduction gives S_8^{2-} , which rapidly decomposes by follow-up reactions to S_6^{2-} , S_4^{2-} , S_3^{2-} , and S^{3-} . Three of these, S_8^{2-} , S_6^{2-} , and S^{3-} are further reduced at the second wave [52]. The reduction to S_3^{3-} has also been studied in dimethyl formamide (DMF) using time-resolved spectroscopy/DVCA using reflection with fiber-optic/CCD detection [54], and Raman spectroscopy [70], as has the corresponding Se system [71]. Further refinements to the sulfur mechanism have appeared [70].

3.4.1.4 Galvanostatic Conditions

The above theoretical treatments have involved the assumption of potential control; after all, this is the most useful and common approach in spectroelectrochemistry studies because the electrodes are very resistive and are not equipotential under galvanostatic conditions. Galvanostatic

techniques such as chronopotentiometry and its spectroscopic equivalent also suffer from the problem of how to correct for double-layer charging [69]. However, a few authors have considered galvanostatic transient absorption [72, 73], introducing the concept of the transition absorbance, analogous to the transition potential in chronopotentiometry. These theoretical treatments considered the effect of heterogeneous kinetics [72] and follow-up reactions [73]. Chronopotentiometry (see Chapter 2.2 in this volume) is very useful for background processes, stripping reactions, and for thin films. It has successfully been applied to the study of Prussian Blue modified electrodes and the results were consistent with the chronoabsorptometry results [74]. The transition times, τ , were well defined and a plot of i versus τ^{-1} was linear.

3.4.1.5 Adsorption

OTTLEs and the like may be used to monitor *irreversible* solute adsorption in a similar way to thin-layer cells with coulometric detection [75]. The concentration of the solution will be depleted by an amount $(\Gamma A)/V$ where Γ is the surface excess in mol cm^{-2} , A is the area and V is the volume of the thin-layer cell. This fall in concentration can be measured by coulometry [75] or by the change in absorbance of a spectroelectrochemical cell, in this case, a long optical path-length cell (see Sect. 3.4.2.4.3 in this chapter) chosen for its high surface area to volume ratio [76]. From the coverage Γ , it is possible to determine the area on the surface occupied per molecule, and, for example, that quinones lie flat on a carbon surface.

Yap and coworkers have considered the case when the product of the electrochemical reaction is *reversibly* adsorbed, and the

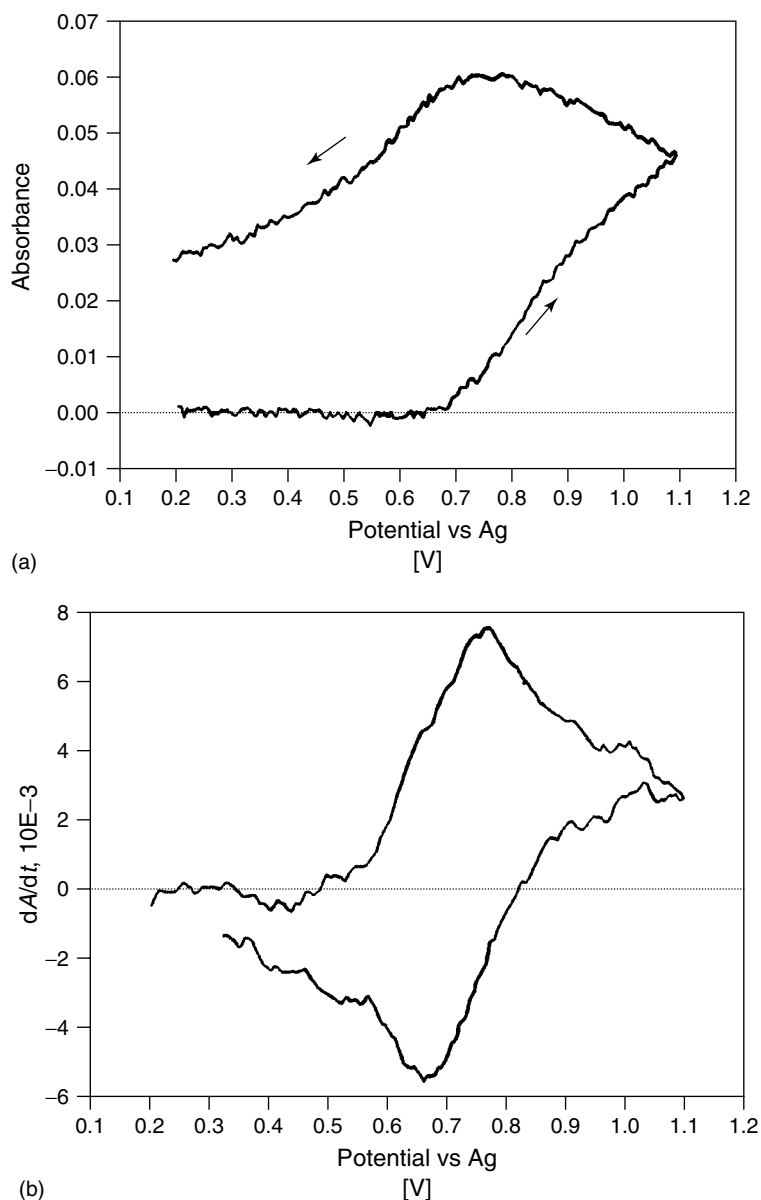


Fig. 7 DCVA of oxygen reduction in DMSO using a fiber-optic/reflection configuration with saturated O_2 solution (2.1 mM). (a) Absorbance and (b) dA/dt signals recorded at 270 nm as a function of the scanning potential. The A versus E signal was obtained simultaneously with the CV. The dA/dt signal was obtained from the absorbance with the application of a 10-point smoothing of the raw data. Potentials versus Ag wire pseudoreference. (Reprinted with permission from D. S. Shin, N. Doddapaneni, S. M. Park, *Inorg. Chem.* **1992**, 31, 4060–4064. Copyright 1992 American Chemical Society.)

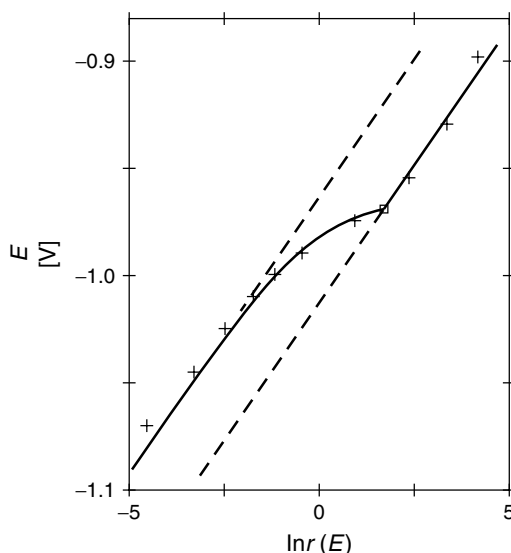


Fig. 8 Nernstian plot for system in which R is adsorbed reversibly. The x-axis, $\ln r(E)$ is equivalent to $\ln [O]/[R]$. The distance between the two lines gives $-\ln(s_R/c)$ and the circled point gives E_s . Laser dye concentration is 2.36 mM in 0.4 M KCl, potentials versus SCE (NaCl). (Reprinted from *J. Electroanal. Chem.* **1984**, 160, 73–78, Copyright 1984, with permission from Elsevier Science.)

adsorbate is not spectroscopically observable (as in the case when the minigrid electrode is used) [77]. In the reduction of O to R, there is a potential E_s , at which the concentration of R generated at the electrode exceeds the solubility. At this point, R will be adsorbed. The Nernstian plot then shows the behavior shown in Fig. 8. The distance between the two lines gives $-\ln(s_R/c)$ and the circled point gives E_s .

Irreversible electron transfer reactions followed by product adsorption may be studied in a thin-layer long optical path-length cell. Double logarithmic plots of absorbance versus potential help diagnose the type of adsorption [78].

3.4.2

Cell Geometries, Design, Techniques, and Instrumentation

3.4.2.1 General Considerations

Various optical arrangements for spectroelectrochemical experiments have been proposed. Figure 9 shows the options available. In addition to these in situ methods,

electrolysis outside the spectrometer sample compartment is perhaps the simplest approach and avoids the need for optically transparent electrodes (OTEs) and expensive cell design. Recent examples concern the generation of 1,4-benzoquinone dianion [79] and the nucleophilic substitution of diacyl disulfides [80]. External generation is also sometimes used in inorganic chemistry, for example, when a mercury electrode must be used, as in the electroreduction of $[\text{Os}(\text{CN})_5\text{NO}]^{2-}$ [81] and double-decker porphyrins [82]. This approach has even been used for protein redox potential measurements using a mediated continuous-flow column electrolytic spectroelectrochemical technique (CFCESET) [83, 84]. Geiger has used reflection optics for monitoring the solutions of bulk-generated air-sensitive complexes [85, 86].

We might also include in this discussion, cells that involve electrolysis of an entire 1 cm path-length cuvette. Although such cells are quite popular (e.g. Jones and coworkers [87] and Brewer and coworkers [88]), the long electrolysis time presents a disadvantage unless product

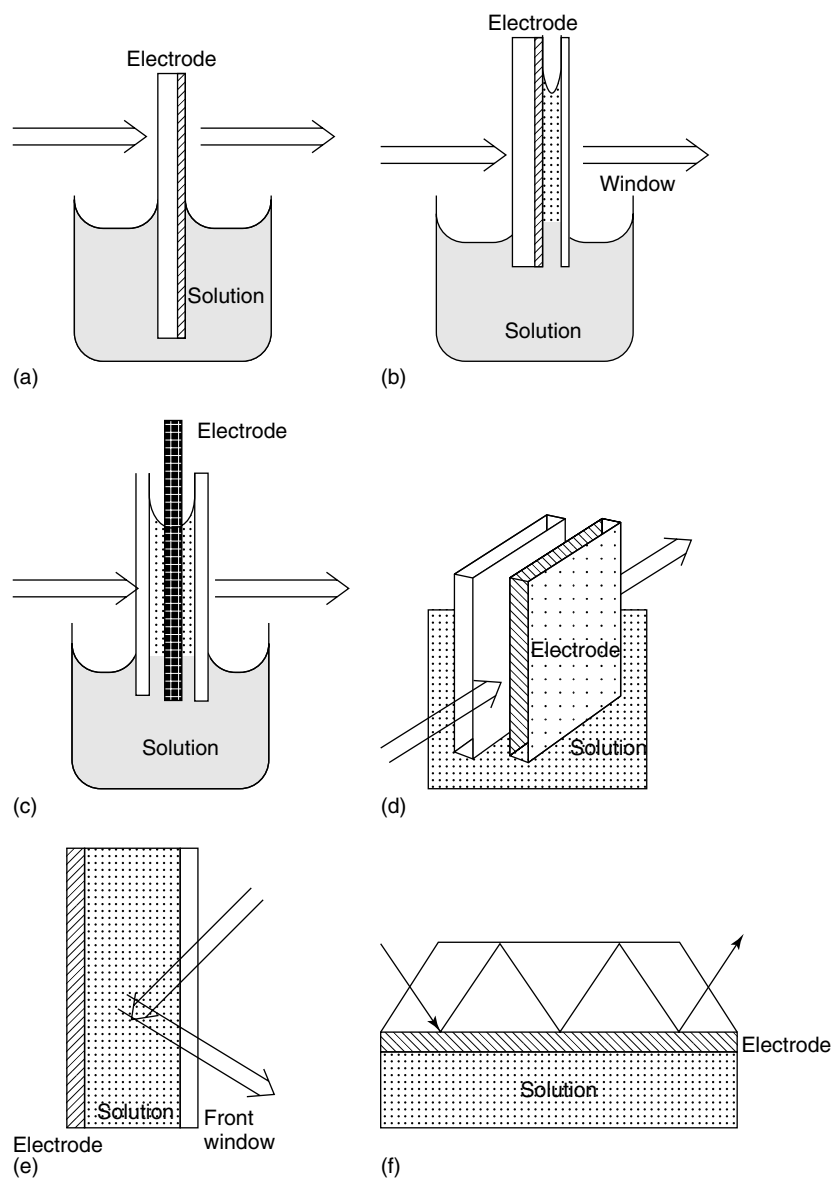


Fig. 9 Spectroelectrochemical cell configurations: (a) transmission cell with optically transparent electrode (OTE); (b) transmission optically transparent thin-layer electrode cell (OTTLE) with OTE; (c) sandwich OTTLE cell with minigrid or reticulated carbon (RVC) electrode; (d) long optical path-length cell (LOPTC) with light parallel to electrode surface; (e) double transmission reflection cell; and (f) internal reflection cell.

extraction for other spectroscopic analyses, such as nuclear magnetic resonance (NMR) is desired. Also, the working electrode must, of course, be separated from the counterelectrode by a medium porosity frit to prevent mixing.

Good general discussions of cell materials and design for *in situ* cells can be found in various textbooks [18, 89, 90]. The general considerations concerning the minimization of *IR* drop are particularly applicable in spectroelectrochemistry, although it is unavoidable in thin-layer designs. Materials used include glass, quartz, Teflon (DuPont), and modern plastics such as the fluoropolymer Kel-F (3M), and Delrin (distributed by RS, Goodfellows). The use of glass (or quartz as a window material for the UV region) is recommended whenever possible to avoid contamination and to allow for observation of the electrode. It is important to record a transmission spectrum of the transparent material used. It is also important to be aware of the absorption properties of the electrolyte and solvent combination. While modern instruments are quite capable of subtracting out small or moderate absorption bands, caution should be exercised in interpreting apparent peaks in regions of the spectrum at which the absorbance of solvent or electrolyte exceeds unity (10% transmission). Of the various plastic materials, Lucite (Perspex) has the advantage of optical transparency, which makes it easier to see what is going on. It is often used as the support structure for OTTLE cells (see below) but it should not generally be allowed to come into contact with non-aqueous solvents.

3.4.2.2 Transmission under Thin-layer Conditions: OTTLEs and Flow-cells

The great advantage of this design is that the small volume of analyte within

the layer is electrolyzed extremely rapidly, allowing the equilibrated spectrum to be recorded within minutes of applying the potential. The working electrode in these cells is usually a gauze or micromesh or minigrid. These are available from suppliers such as Goodfellows, Advent, and Aldrich. These suppliers may be able to suggest alternative suppliers if the desired mesh is not available. The very fine gold meshes (minigrids) are made by electroforming by Buckbee–Meers St Paul (<http://www.bmcind.com>). Currently, according to the website, 5- μm thick meshes of up to 2000 lines per inch with 36% transmission are available. Typically, the minigrids used in OTTLEs have 10 to 30- μm holes with 50% transmission. Other types of meshes have been used. Metal meshes modified by chemical vapor deposition of pyrolytic graphite exhibit sluggish electron transfer unless they are activated using a radio frequency (RF) plasma. It is believed that the treatment results in the exposure of a higher density of edge-plane carbon [91]. Mercury-plated gauzes can be prepared by immersing a Cu gauze into an aqueous saturated solution of $\text{Hg}_2(\text{NO})_2$ [92, 93]. A thicker cell is possible if reticulated vitreous carbon (RVC) is used; for example, transmission of 13 to 45% for 100 ppi (pores per inch) is possible for a 1.2 to 0.5-mm thick RVC plate. RVC has been used in a luminescence cell [94].

Perhaps the most detailed published description of OTTLE cell assembly is that intended for an undergraduate experiment, as shown in Fig. 1 [3, 33]. The spacers used are typically 50 μm to 0.02 cm. The working volume is 30 to 500 μl and complete electrolysis occurs in 30 to 60 s. The grid is mounted 4 to 6 mm from the bottom of the cell to minimize *IR* drop. Bulldog clips can be used to clamp

the electrode between the glass slides. A syringe hole is often provided to aid rinsing the cell and for “pumping” to remove bubbles. Another design uses a wax seal to mount the microscope slides and grid in between a lower glass reservoir and an upper glass compartment containing the reference electrode and the counterelectrode [95]. This was used to measure the partitioning of complexing agents between nonaqueous and aqueous phases. Finally, variable path-length cells have been reported [96, 97].

Although sandwiching the minigrid between microscope slides has been the traditional method, a more convenient method, which avoids the use of epoxy glue (especially if solvents are in use) and allows the use of the existing cuvette holders, is to place the mesh inside a thin (0.2 to 0.5 mm) cuvette, which is commercially available (Hellma). The path-length should not be smaller than 0.2 mm to avoid bubbles getting trapped. The top opening should be as wide as the grid. Another advantage of this cell is that it is relatively easy to keep out oxygen from the working electrode region, though this can be overcome by using a glove-box/bag or encasing the cell in a box that can be purged [preferably transparent Perspex (Lucite) to check what is going on inside] with quartz windows. Disadvantages of this method are that the cell is difficult to fill since capillary action cannot be used and the mesh can be damaged during insertion into the cell. It is also very difficult to clean the cells, although ultrasonic baths can be helpful in this regard. If the mesh is very fragile, then it can be reinforced by a Pt wire surround, or by lamination using a standard 100- μ m thick plastic ID card lamination (which resists acetonitrile, DMSO and DMF) with a hole punched through both sides as a window [98]. The laminated mesh is

cleaned by placing it in an ultrasonic bath containing diamond-polishing powder.

Another glue-free design uses Tefzel gaskets to seal the two microscope slides together [99]. The slides can also be held in a Kel-F (transparent fluoropolymer) clamp and lowered into a completely vacuum-tight cell [100]. Detailed descriptions of the vacuum procedures are provided [101]. For a less permanent seal, wax (such as that used in hair removal) may be used, though it does eventually succumb to solvent attack [102].

3.4.2.2.1 Variations on and Alternatives to the Basic OTTLE Design

The most popular variation on the basic OTTLE design houses the assembly within a normal UV-visible cuvette. This allows the cell to be used in the sample compartment using the usual cuvette holder. A Teflon lid may be adapted to take an indium tin oxide (ITO) electrode and the counter electrode and reference electrode. The ITO is brought up close to the front surface of the cell with Teflon tape if necessary [103]. Alternative designs have been proposed [104], including the one shown in Fig. 10 [105], and a design for looking at polymer modified electrodes [106]. An unusual cylindrical thin-layer cell geometry for spectrophotometry in a test tube-type cell has been reported [107].

More sophisticated OTTLE designs have been proposed. For example, a very successful variable temperature OTTLE cell has been used for many years by Heath at Canberra [108] and Yellowlees at Edinburgh, Fig. 11 [109]. The latter cell has been used in studying the spectroelectrochemistry of a porphyrin–viologen dyad. The first two reductions were viologen based while the second gave rise to a porphyrin anion radical, confirmed by EPR spectroscopy [110, 111]. A similar cell is

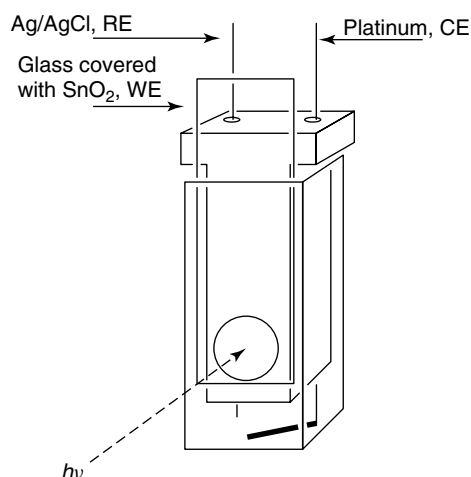


Fig. 10 Cuvette-based OTTLE cell using an ITO electrode. (Reprinted from *Inorg. Chim. Acta* **1995**, 228, 243–250, Copyright 1995, with permission from Elsevier Science.)

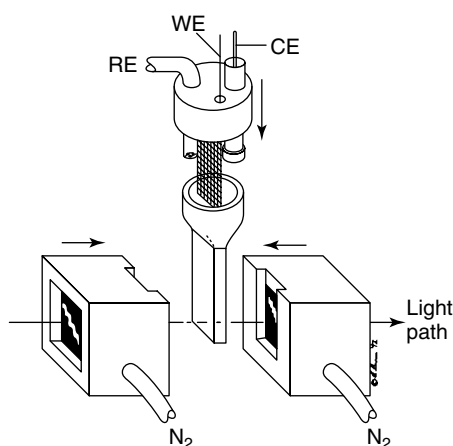


Fig. 11 Variable temperature OTTLE cell. (Reprinted from S. A. MacGregor, E. J. L. McInnes, R. J. Sorbie and coworkers in *Molecular Electrochemistry of Inorganic, Bioinorganic and Organometallic Compounds* (Eds.: A. J. L. Pombeiro, J. A. McCleverty), Kluwer Academic Publishers, New York, 1993, p. 503.)

in use elsewhere and has recently been used to look at porphyrin dimers [112]. Variable temperature cells generally have plenty of free volume to allow for expansion of the solvent and to prevent high pressures building up leading to leaks.

As a variation on the minigrid design, interdigitated, “filar” electrodes have been demonstrated [113]. This allows the independent control of the potentials of the two electrodes in the same way as having two electrodes placed opposite each other. This enhances the current and therefore,

the optical response as in the “collector” and “generator” electrodes. The design has the advantage of minimizing edge effects and *IR* drop, thus improving the transient response. Incidentally, edge effects (i.e. diffusion to the edges, which prevents the current in the cell reaching zero at long times – typically 1% residual current is regarded as acceptable) can also be minimized by limiting the optical area to a small central portion of the minigrid. Edge effects are particularly problematic for long experiment times.

Many biological studies use an OTTLE design based on that of Hawkridge [114] and Heineman [115]. Modifications to these basic designs have been proposed by Walker [116], who advocates the use of quartz windows and cell filling via Hamilton syringe valves. A low-volume cell for bioelectrochemical applications has been published [117]. Anaerobic cells for bioelectrochemical and other applications have also been described [118–120], and one design allows demounting of the electrodes [121].

3.4.2.2.2 OTTLE Cells Intended for Both UV-visible and FTIR Use

The thin-layer design of the OTTLE has much in common with liquid IR cells (see Chapter 3.5 in this volume). Kadish has described a thin-layer cell for Fourier Transform InfraRed (FTIR), UV-vis and ESR spectroelectrochemistry, which was used to study the redox behavior of [TPPRuCO] (TPP = tetraphenylporphyrin) in nonaqueous solution [122]. Other papers describe the modification of an old IR liquid cell [123], and a variable path-length IR cell [124], while an earlier, popular design is clearly inspired by IR cells [125, 126]. It was used to study the reduction of benzoquinone. An excellent cell design has been given by Krejčík and coworkers in which the minigrid is melt-sealed into the polyethylene spacer of the thin-layer FTIR cell [127], reminiscent of the lamination procedure described earlier. The cell was later modified to permit work at lower temperatures and has been used successfully in many investigations, for example, the radical anions of $[M(CO)_4(NN)]$, where $NN = 1,10$ -phenanthroline [128], and a low-temperature investigation of copper(II) Schiff base complexes [129]. The popular Mann cell design [130] and similar

cells [123, 131] can also be used for both UV-vis and FTIR regions of the spectrum.

Often CaF_2 is the window material of choice, transparent in both the visible and IR regions to allow simultaneous FTIR and visible monitoring using the same spectrometer (but with different beam-splitters) [132]. Another way to prepare a thin-layer cell is by ultrasonically machining a thin layer from a large block of calcium fluoride [133]. The cell was used to investigate the reduction product of bilirubin. A similar cell using a commercially available (Aldrich) block of KBr has been published [122]. Finally, reflection cells (see in the following text) are ideally suited to combined FTIR and UV-vis studies.

3.4.2.2.3 OTTLE Cell Electrochemical and Spectroscopic Response

The electrochemical response of the OTTLE cell should of course ideally be of the thin film variety with a peak separation close to zero and a symmetrical shape. The thin layer has restricted diffusion and exchange with the bulk solution, which leads to high uncompensated resistance and distorted responses at all but the lowest scan rates. Thus, cyclic voltammetry waves are often distorted with greater peak separations in the CVs than expected [134]. On the other hand, edge effects may mean that the edges are not at equilibrium so it is better to mask the area interrogated by the beam.

There have been surprisingly few simulations of the OTTLE response [135]. Recently, explicit finite difference digital simulation of an OTTLE with a platinum minigrid has shown that the critical ratio of the “parallel” diffusion path inside the mesh hole (half the hole size) and the “vertical diffusion path” (thin-layer thickness) is greater than 1.33; then there will be a

large, nonuniform concentration distribution inside the thin layer [136].

Overlapping bands can become a problem when, for example, there are two consecutive electron-transfer reactions [137]. One solution is to look at the time- or potential-resolved spectra [138]. Overlapping bands are often responsible for nonlinear Nernstian plots in OTTE studies [139]. There are only a few examples of the use of differentiating the absorbance [134], least-squares analysis [140], of the latest chemometric techniques [141]. In the latter study, evolutionary factor analysis of the spectra arising from the reduction of *E. coli* reductase hemoprotein (SiR-HP²⁻) in which three species are present and the reduction of the [Cl₂FeS₂MoS₂FeCl₂]²⁻ (four species present). The most challenging part of the work was the determination of the transformation matrix.

3.4.2.3 Semi-infinite Cells: Optically Transparent Electrodes (OTEs)

Pure tin and indium oxides have band gaps in excess of 3.7 eV and are transparent in the visible and near-UV regions. They also have insulating properties. However, when n-type doped the dopant levels just below the conduction band, they provide ample carriers for conduction, especially as the dopant levels can be much higher than in silicon [5]. ITO with 2 to 10 mol% tin doping of indium oxide and FTO (<5 mol% fluorine-doped tin oxide, supplied, for example, by Pilkington and called K-glass) are commonly used [5, 142]. Of the two, ITO is regarded as superior in optical and electronic properties, while FTO has somewhat greater chemical and thermal stability. These electrodes can also electrodeposit (or, as some propose, intercalate) lithium metal from lithium ion containing nonaqueous solutions when

the potential is sufficiently cathodic [143]. This will obviously lead to deterioration in optical properties and possible complications in the electrochemical response. Also, prolonged use in aqueous media under strongly oxidizing conditions may lead to etching away of the conducting surface. If desired, the ITO may be deliberately etched away [144]. ITO electrodes are not particularly easy to clean and it is best to use a fresh electrode for each experiment. Unlike metal grids, they do cut-off in the near-UV and the IR regions. Custom deposition on quartz rather than glass is recommended for full coverage of the spectrum. ITO is often preferred for studies on conducting polymer films that can block up the holes of micromeshes [145].

Interest in novel dopant atoms for SnO₂ itself has been reawakened following reports on the use of tin oxide as a replacement for graphite in lithium batteries [146–148]. Alternatively, thin films (100 to 5000 Å) of Au, Pt, or carbon on glass or quartz have been used successfully [19]. Platinum on mica was reported as showing promising characteristics as an OTE [149]. A new precursor for preparing carbon films on quartz gave films with low background currents but less than ideal reversibility for dopamine electrochemistry [150, 151].

A simple cell using RVC has been described in Ref. [94]. A bare and gold-plated RVC electrode has been used in the study of microperoxidase [152]. A bundle of cylindrical carbon fiber microelectrodes was used to monitor the catalytic reaction between ferrocyanide and ascorbic acid using the open-circuit kinetic method [153]. While boron-doped diamond has shown great promise as a new electrode material, its transparency has not yet been exploited in UV-vis spectroelectrochemistry [154].

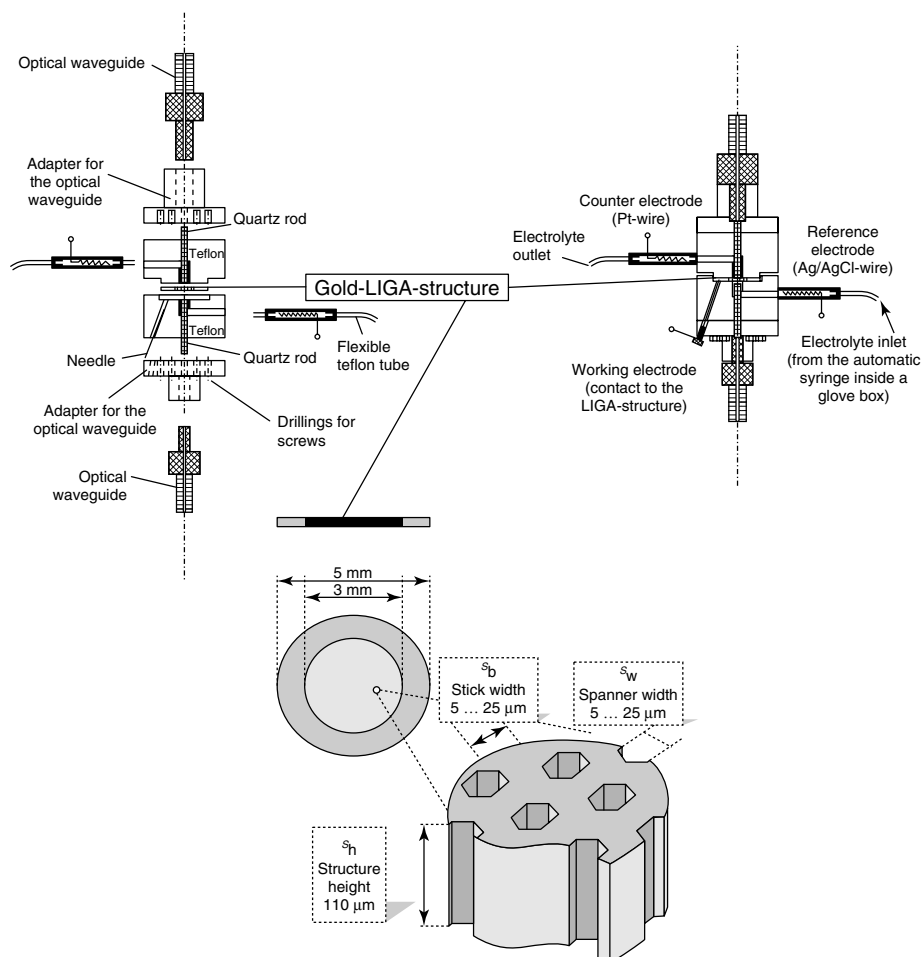


Fig. 12 LIGA electrodes and cells. (Reprinted from *Electrochim. Acta* **1995**, 40, 1427–1434, Copyright 1995, with permission from Elsevier Science.)

LIGAs are Lithographic-Galvanic structures (Fig. 12) that present some advantages over ITO and metal meshes, namely, improved stability, faster response times, and a greater range of electrode materials that can be used in the same cell. The electrodes are sandwiched between quartz rods coupled to the spectrometer using fiber optics [155]. Figure 13 shows the separated spectrum of the diazonium product from the oxidation of a triazene using a LIGA electrode [156].

3.4.2.4 Reflection from Electrodes and Liquid–Liquid Interfaces

Reflection techniques have been reviewed [23, 157]. Many of these cells are based on the established FTIR reflection cell design using a cylindrical cell and fiber-optic or external reflection accessory to deliver the light to the electrode surface. For example, the Salbeck cell has proved quite popular, as it allows operation under both thin-layer (15 μm, 1 s electrolysis time) and semi-infinite

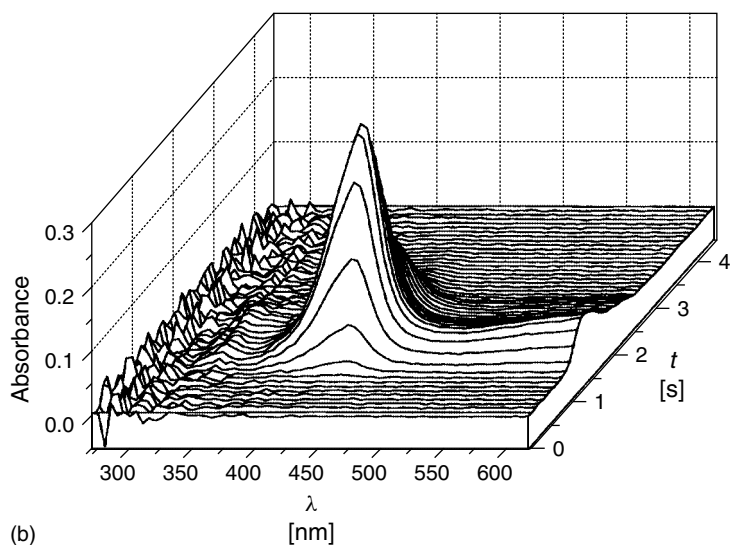
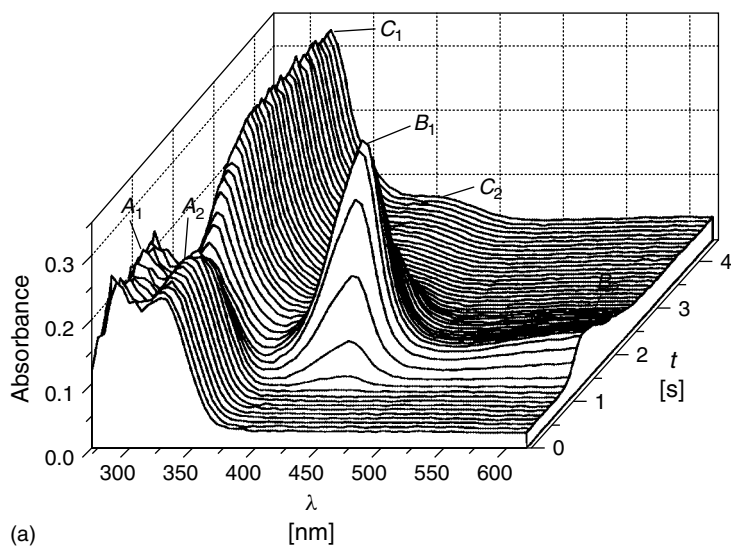
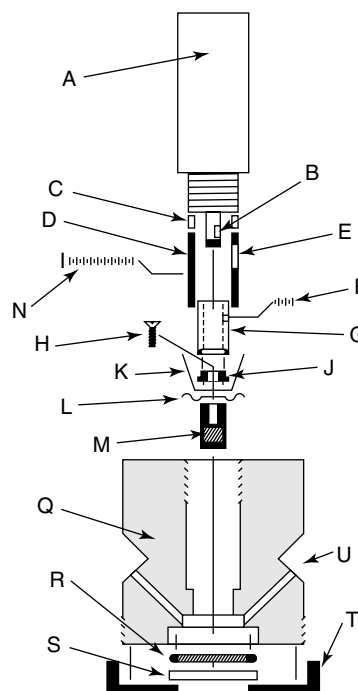


Fig. 13 Spectroelectrochemistry of Au LIGA electrodes. The one-electron oxidation of a triazene leads to an unstable radical cation that decomposes to the diazonium cation. (a) Time dependence of the spectra during a potential cycle with $\nu = 0.442 \text{ V s}^{-1}$ and $E_{\text{start}} = +0.1 \text{ V}$ ($t = 0$), $E_{\text{sw}} = +1.15 \text{ V}$ ($t = 2.38 \text{ s}$), $E_{\text{fin}} = 0.233 \text{ V}$ ($t = 4.45 \text{ s}$), $c = 1 \text{ mM}$. Bands A and C are due to starting material and diazonium ion product. (b) Separated spectrum of the radical cation intermediate, B. (Reprinted with permission from L. Dunsch, B. Gollas, A. Neudeck et al., *Chem. Berichte* **1994**, 127, 2423–2429. Copyright 1994 Wiley VCH.)

Fig. 14 Reflectance cell assembly consisting of (A) micrometer that has a shaft with a flat (B), (C) insulating ring, (D) brass cylinder that has a hole (E) for tightening the set screw (F) into the adapter sleeve (G), (H) assembly screw, (J) bearing and bearing adapter, (K) brass bushes, (L) diaphragm, (M) working electrode assembly, (N) electrical contact screw, (Q) Kel-F cell body, (R) Viton O-ring, (S) cell window, (T) cell cap and (U) three ports for electrodes and fittings. (Reprinted from *J. Electroanal. Chem.* **1991**, 313, 81–94. Copyright 1991, with permission from Elsevier Science.)



conditions [158]. The cell was also thermostatted to permit operation down to -40°C and, since no epoxy glue was used in the construction, the cell was useful for nonaqueous solvent electrochemistry. The Salbeck cell uses bifurcated optical fiber bundles as in a previous cell design [159]. A much more sophisticated and expensive design features stepper motor control of the electrode-window distance, Fig. 14 [160]. The critical distance for thin-layer behavior could accurately be determined. A new design, using a rectangular, rather than a cylindrical cell, permits both UV-vis and FTIR operation at variable temperatures down to -55°C [161].

For reflection experiments, the path-length, and hence, the absorbance of dissolved species is increased by the factor $(2/\cos\theta)$ where θ is the angle of incidence (angle between the beam and

the normal to the electrode surface). For greater sensitivity of surface species, such as the detection of very low concentrations of adsorbed species on the electrode, the potential of the electrode has been modulated [40, 60, 162, 163]. The sensitivities of the various techniques have been compared [162]. A recent paper addresses the theoretical background [164]. It is shown that all methods will discriminate between the surface and solution species on the basis of phase angle, and further that for parallel light techniques such as probe-beam deflection, the phase angle depends on the diffusion coefficient. Chronoabsorptometry of highly colored compounds (e.g. porphyrins) can be examined using reflectance and time-resolved difference spectroscopy. The light was reflected off the electrode using quartz rods mounted some distance away and at an angle of 45° to the normal [165].

3.4.2.4.1 Glancing Incidence Reflection, Near-parallel or Parallel Reflection, and Diffraction

If spectra of surface adsorption or deposition processes are *not* desired in a study, it may be worth considering a method in which the light beam passes parallel to the electrode surface such as LOPTLC or diffusion layer imaging techniques. McCreery's group showed that it was possible to observe absorbance changes around a cylindrical microelectrode wire by reflection. The changes appeared within 150 ns, providing the first real evidence for the small RC time constants at microelectrodes [166]. Grazing-angle laser reflection with 5- μ m resolution is useful for diffusion layer imaging [167]. The application of such an optical technique to the oxidation of catecholamines by chlorpromazine radicals was useful since the electrochemical transient methods contained interference from current due to the amine oxidation. Normalized absorbance plots (the ratio of the absorbance in the presence of reactant to that in the absence of reactant; mentioned above) were fitted to working curves derived from digital simulation [167]. This was later modified to have a broadband xenon lamp source to enable wavelength-dependent studies [168].

The 9,10-anthraquinone system is a classic example of an EE mechanism, which includes a synproportionation process. Absorbance versus distance profiles were measured for this reaction and the homogeneous and heterogeneous rate constants were in agreement with those derived from cyclic voltammetry [169]. Protonation of the benzophenone anion radical by benzoic acid and *o*-cresol was studied using this technique [170]. A variety of electrode geometries were explored in determining the heterogeneous

electron transfer kinetics of the *N,N,N,N*-tetramethyl-*p*-phenylenediamine redox reaction [171].

McCreery reported diffraction from the edge of an electrode using a laser [172]. Using electrode potential modulation, it was possible to detect species down to 2×10^{-8} M [173]. The technique was shown to work with a continuum source [174]. A recent paper has shown that it is possible to determine the source coherence from the diffraction pattern [175]. A flow-through spectroelectrochemical detector based on the diffraction principle, which had a detection limit of 40 μ M for MV^{+} , was described [176].

More popular methods such as probe-beam deflection in its nonspectrophotometric form [177, 178] are now used to profile the diffusion layer, and in conjunction with electrochemical quartz crystal microbalance (EQCM) measurements, are used to monitor the diffusion layer ingress and egress of ions, particularly protons. Further details can be found in Chapter 2.7 in this volume.

3.4.2.4.2 Liquid-Liquid Interface and Attenuated Total Reflection

Total internal reflection at a liquid-liquid interface can be used to monitor ion transfer across the interface. The kinetics of the reduction of TCNQ and the oxidation of 1,1'-dimethylferrocene by $[Fe(CN)_6]^{3-}$ in the aqueous phase has been considered [163]. The kinetics of these reactions were studied by chronoabsorptometry, assuming diffusion control [Eq. 23, allowing for the reflection correction, $(2/\cos \theta)$]. Ion-transfer kinetics across interfaces has been treated theoretically and applied to the study of indicator transfer [179]. Chronoabsorptometric studies show that ligand-assisted Cu(II) transfer is controlled by the diffusion of metal

ion to the interface [180]. $[\text{Ru}(\text{bpy})_3]^{3+}$ and eosin transfer have also been investigated [181].

Total internal reflection (or attenuated total reflection, ATR) is used a lot in FTIR spectroscopy of coatings. Heineman has carried out work in a series of papers, which uses ATR to detect the partitioning of the analyte into a selective membrane attached to the electrode surface. The sensor relies on three modes of selectivity: electrochemistry, spectroscopy, and partitioning [182, 183].

3.4.2.4.3 Long Optical Path-length Thin-layer Cell (LOPTLC) The optical path-length in an OTTLE cell is short and the optical sensitivity is low. In 1979, Tyson and West [184] proposed a new cell in which the light beam of the spectrometer passes parallel to the electrode surface, thereby sampling a greater path-length (typically 1 cm) of the region immediately in front (typically, up to 0.5 mm) of the electrode. Enhancements of about 100-fold are typically observed due to the increased surface area to volume ratio [185]. Another advantage is that, as in reflection spectroscopy, there is no requirement for the electrode to be transparent. Since that time many other designs have been presented in the literature [186, 187]. The electrode may be mounted vertically or horizontally, but vertically seems more sensible for matching modern spectrometer slits. An unusual design uses a block of graphite or glassy carbon with a 500- μm hole drilled through it [188]. The cylindrical geometry facilitated the simulation of the time response. Whilst in planar form, the LOPTLC is largely used in the same manner as the OTTLE, it is possible to compute the time-dependent absorbance either analytically or numerically [189].

LOPTLCs are often constructed to fit within a standard 1 cm^2 cuvette as shown in Fig. 15 [190, 191]. A cell that was specially designed for studying the adsorption of monolayers (see above) is easy to disassemble and clean [192]. A more sophisticated design has since been published [134].

A simplified method for the screening of the mechanisms involved during irreversible electron transfer and follow-up reactions has been proposed [193]. Since the current is exponentially dependent on the overvoltage when kinetically limited, the new method, based on standard thin-layer cell theory [194] involves plotting the double logarithm of the absorbance of the starting material against the potential. This is analogous to the Nernstian plots of the (single) log of absorbance versus potential for the thin-layer case.

LOPTLC for the study of homogeneous follow-up reactions has been reported for the classic cases of *o*-quinone and *p*-aminophenol. Because of the large ratio of the area of the electrode to the volume in these cells, the reactions were found to be sensitive to adsorption (on Pt working electrode) and the presence of active surface groups (glassy carbon working electrode). These complications were alleviated by preadsorbing iodide onto the Pt and oxidizing the glassy carbon electrode prior to use [195].

For the LOPTLC configuration, the first-order rate constant for the classic oxidation of *p*-aminophenol to the quinoneimine (which follows an EC reaction mechanism) was determined by digital simulation of the response [196]. Digital simulations have also been carried out for simple electron transfer [185, 189, 197, 198], catalytic reactions (the oxidation of ascorbic acid catalyzed by $[\text{Fe}(\text{CN})_6]^{3-}$ [199, 200], electrode

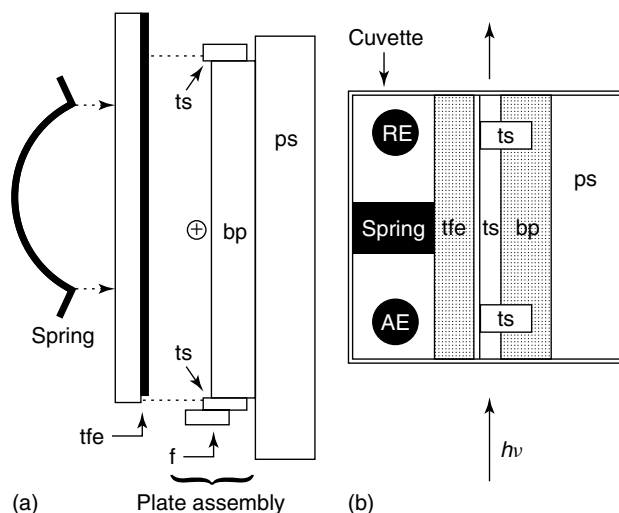


Fig. 15 LOPTLC mounted inside a standard quartz cuvette. (a) An exploded side view of all components down the optical axis of the cell (+) including the plate assembly, thickness spacers (ts), back plate (bp), electrode positioning foot (f), positional spacer (ps), thin-film electrode (tfe), and a compression spring; and (b) top view showing all components including the reference electrode (RE) and auxiliary electrode (AE) assembled inside the cuvette. (Reprinted with permission from N. J. Simmons, M. D. Porter, *Anal. Chem.* **1997**, 69, 2866–2869. Copyright 1997 American Chemical Society.)

position [201, 202]), and quasi-reversible electron transfer [191, 203]. In the latter study, equations for chronoabsorptometry at planar electrodes were shown to be directly transferable. The authors used a thick cell (150 μm) in order to observe semi-infinite behavior.

Unlike a transmission cell that samples both the solution and the electrode surface, the LOPTLC configuration allows the separation of surface and solution processes (indeed a cell that could be used in both transmission and LOPTLC modes simultaneously might be very interesting). For example, irreversible adsorption processes may be studied [78] using a double logarithmic method. Three experimental cases were

considered: self-blocking, self-inhibiting, and self-accelerating adsorbate.

3.4.2.5 Forced Convection, RDE and Channel Flow

The relatively long equilibration time of the stagnant thin layer of the OTTLE or reflection cell does not allow one to study the kinetics of fast reactions. Alternatively, the forced convection regimes of the RDE and the channel-flow cell allow production of steady state currents, and both have been investigated with optical detection of electrogenerated species. Further details can be found in Chapter 2.4 in this volume. The rotating OTE was investigated early on and the theory has recently been expanded [204]. The electrode is used

for photogeneration of species rather than spectroscopy. On the other hand, a rotating disk surrounded by an optically transparent, insulating ring has been constructed for the spectroscopic determination of intermediates [205]. The response has been digitally simulated [206]. Scherson has investigated the spectroscopy of electrogenerated species using a more convenient system: a light beam introduced by fiber-optics near normal to the RDE and reflected from the electrode [207]. The channel-flow cell has also been investigated; in this case, the steady state current is proportional to $V^{1/3}$, where V is the flow-rate, and hence the absorbance should be given by i/V , that is, proportional to $V^{-1/3}$. The absorbance also follows the Nernstian behavior of the current. Scherson has recently compared the two techniques for the determination of the faradaic efficiency of dithionite ($S_2O_4^{2-}$) generation from HSO_3^- (bisulfate) reduction. The RDE was judged to be better for this measurement since the measured absorbance is not dependent on the kinetics of follow-up reactions [208].

The channel-flow cell technique may also be used for transient absorption measurements (chronoabsorptometry) with numerical simulation of the data. The kinetics of the dimerization of $TMPD^+$ and MV^+ were both on the order of $10^4 \text{ M}^{-1} \text{ s}^{-1}$. The technique differs from the usual OTE method in that it allows the determination of the diffusion coefficient of the product, D_R [209].

3.4.2.6 UV-vis Combined with Other Spectroscopic Techniques

The combination of IR and UV-vis transmission techniques has been mentioned already. Raman spectroscopy (discussed in Chapter 3.6 in this volume) is very easily

carried out with an OTTLE cell or by reflection when the solvent does not scatter strongly. Other techniques that have been combined with UV-vis spectroscopy will now be mentioned.

There are surprisingly few published reports of using magnetic circular dichroism (MCD). The selection rules are different for MCD, depending on the magnetic dipole moment in addition to the electric dipole moment. Derivative shapes identify A-term transitions for degenerate excited states, Gaussian-shaped temperature independent transitions are due to B-terms, while C-term transitions are highly temperature dependent and they identify an orbitally degenerate ground state. Using conventional UV-vis spectroelectrochemical cells and an MCD spectrophotometer, the technique has mainly been used to investigate porphyrins, [210, 211], and phthalocyanines [212]. A novel cell using a reflection geometry has also been devised [207]. Double potential step circular dichroism (termed chronoelliptometry) was used to study the rate of conformational change of cytochrome *c* during electron transfer [213].

EPR and UV-vis spectroscopy have been combined; for example, in the study of anthraquinone reduction [214] and the evolution of species within conducting polymers [145, 215, 216]. The cell used a laminated grid as described above.

EQCM may be combined with spectroscopy (see Chapter 2.7 in this volume). Usually, the crystal is used in transmission mode [202, 217, 218]. Various plots, such as absorbance versus frequency, have been presented to help understand the complex electrochemical response of polypyrrole [219.] The growth of poly(1-naphthylamine) was monitored using a fiber-optic bundle in front of the crystal [220].

3.4.3

Applications3.4.3.1 **Solution Studies of Inorganic Species**

UV-vis spectroelectrochemistry took some time to catch on in the inorganic world but now it is seen as an indispensable technique, especially if it is coupled in certain cases with EPR and FTIR spectroscopy. It is of course, fairly easy to incorporate the latter into a UV-vis design, as in, for example, the design of Krejčík and coworkers [127]. One of the reasons for the growth in popularity is its use as an aid in characterizing a redox process as either largely metal or largely ligand-based (in those complexes in which it is meaningful or appropriate to do so). To some extent the inorganic electrochemist can guess at these assignments (based on previous work or the CV of the ligand alone) but the UV-vis spectroelectrochemistry is valuable confirmation. The OTTLE cell is the most popular as it offers a way to measure the redox potential and also the n -value. The use of OTTLEs in determining an accurate value for the redox potential, E° , of biological molecules with slow heterogeneous electron transfer rates can also be applied to inorganic complexes. For example, many Cu(II/I) waves are very broad because of the very different preferred coordination geometries for the two halves of the redox couple [37]. The accurate spectroelectrochemical determination of E° for a series of complexes shows a strong substituent effect, but only on the Cu(II/I) couple, and not on the further reductions.

A recent recognition of their role in biological redox processes has sparked a resurgence of interest in the electrochemistry of complexes of so-called “noninnocent” ligands, that is, ligands that can themselves undergo facile redox reactions,

for example, catecholate, which can be oxidized in two steps to the semiquinone and the quinone. More complex still are those analogous ligands that involve proton as well as electron transfer. UV-vis spectroelectrochemistry played an important role in unraveling the complexities of the oxidation of the 2-aminothiophenolato complex of Ru(II). The oxidation is shown to follow an ECE pathway, giving the appearance of “hysteresis” in the redox chemistry [221].

Spectroelectrochemical studies of analogues of the famous Creutz–Taube dimer are invaluable [222]. Thus, in the two complexes, $[(\text{CN})_4\text{FeLFe}(\text{CN})_4]$ L = bpym and bptz [223], it is the one with the longer bridging ligand that gives evidence for the greatest delocalization of metal charge (intervalence charge transfer, IVCT band at 2230 cm^{-1} observed), whereas the localized formulation $\text{Fe}^{\text{II}}, \text{Fe}^{\text{III}}$ is more appropriate for the other complex (no IVCT band observed). This is a consequence of the very low-lying π^* LUMO in the bptz ligand.

3.4.3.2 **Solution Studies of Organic Species**

Although not as widespread as in inorganic solution electrochemistry, UV-vis spectroelectrochemistry is finding use, as in the inorganic examples mentioned above, in locating the redox site in large organic molecules or in supramolecular systems containing several different linked redox-active groups. For example, spectroelectrochemical techniques have been used to show that the dimerization of viologen radical anions is suppressed in the presence of cyclodextrin [224]. Similar studies were performed with 4-amino-*N,N*-diphenylamine, the predominant dimer of aniline oxidation. Absorption spectra showed that the guest dimer was

deprotonated at higher pH than when unbound [225].

High spin organic molecules are of interest in preparing organic ferromagnetic materials [226]. UV-vis spectroelectrochemistry of the oxidation of polyamines [227] and the reduction of tricyanovinyl-substituted amines [228] leads to UV-vis spectra of intermediates containing strong, intervalence transfer (IVT) bands at long wavelength. Using Hush theory, the high-energy side of these bands is fitted to a Gaussian shape and the electronic coupling parameter may be determined.

3.4.3.3 Molten Salts Spectroelectrochemistry

There is an illuminating discussion of this topic in a recent book chapter [229]. An early OTTE cell design was essentially a vacuum tight version of the design in which a mesh is lowered into a thin cuvette [230]. This cell has been used with a multipass accessory to improve the signal [231]. This is necessary, as changing the solute concentration is far from trivial in these experiments. An example of the use of the latter cell is shown in Fig. 2 [34]. $[\text{YbCl}_6]^{3-}$ in basic AlCl_3 -1-methyl-imidazolium chloride molten salt can be reduced to Yb(II) . The shift in the Nernst-plot-derived $E^{o'}$ values with chloride concentration indicates loss of one chloride to give $[\text{YbCl}_5]^{3-}$ [232].

3.4.3.4 Studies of Species of Biological Interest

Reviews have appeared on the spectroelectrochemistry of biological molecules [104, 233]. Specialized reviews are also available on the direct electron transfer of cytochrome *c* [234] and potential inorganic redox reagents as mediators [235].

Rhodobacter photosynthetic reaction centers [236, 237], carbon monoxide

dehydrogenase corrinoid-enzyme complex [238, 239], and chronoabsorptometric methods were used to determine adsorption isotherms for cytochrome *c* on tin oxide electrodes [240]. The data were fitted to a Langmuir-type isotherm. DCVA has also been used to study cytochrome *c* electrochemistry at ITO [241, 242] and bilirubin oxidation in the presence of human serum albumin [243]. Cytochrome *c* electrochemistry has been studied by reflection from silver electrodes [244, 245].

The saliva of blood-sucking insects contains a variety of components that counteract blood clotting and vasoconstriction. A nitric oxide binding heme protein, nitrophorin 1 (NP1), was studied by UV-vis and FTIR spectroelectrochemistry. In the absence of NO, the spectroelectrochemistry of the $\text{Fe}^{\text{III/II}}$ process was clear. However, in the presence of NO, the changes were small for the $\text{Fe}^{\text{III}}\text{NO}$ and $\text{Fe}^{\text{II}}\text{NO}$ forms, and there was a larger than usual error (± 5 mV rather than 1 to 2 mV) on the redox potentials determined from Nernst plots [246].

3.4.3.5 Inorganic Thin Films and Modified Electrodes

Electrochromic windows have attracted interest not only from the point of view of displays but also, perhaps predominantly now, for use as reflection-control window materials ("smart windows") [247]. The large variety of inorganic and organic systems that have been studied has been reviewed recently in an excellent book [248].

Molecular films such as phthalocyanines are advantageously studied by such techniques as DCVA. Thus, ZnPC in a Nafion membrane shows both evidence of dimerization and, perhaps surprisingly, that the charge transport proceeds by monomer motion rather than charge hopping [249].

Prussian Blue and related inorganic redox films have proved very popular for spectroelectrochemical studies and electrochromic applications. Early investigations used rapid scan techniques to collect spectra as a function of potential [51]. Prussian Blue grows by a three-dimensional nucleation and growth mechanism, which includes surface diffusion of Prussian Blue particles to kinks at growing nuclei [250]. DCVA traces were better defined than the CVs [251], and allowed determination of the molar absorptivity and the amount of film on the electrode. A recent study used a waveguide to study the formation of Prussian Blue [30]. It showed that the technique could detect submonolayer deposition of Prussian Blue film. The technique is typically 10^4 times more sensitive than rival techniques.

Chronoabsorptometry has also been applied to studying reactions on surfaces rather than in solution. In a recent report, not only was the D_{app} for electron diffusion during oxidation of a layer of $[\text{Os}(\text{bpy})_2(\text{bpy}')]^{2+}$, where $\text{bpy}' = 4,4'-(\text{CO}_2\text{H})\text{bpy}$ reported, but also the rate of the mediated electron transfer from $[\text{Ru}(\text{bpy})_3]^{3+}$ in solution to the Os(II) on the surface [252].

3.4.3.6 Conducting Polymers and Oligomer Models

This field only came into being in the last 20 years and spectroelectrochemistry has played a major role in unravelling the intricacies of the redox and conformational processes occurring in these fascinating materials. Modified electrodes using conducting polymers have great potential in molecular electronics, sensors, displays, and batteries. Because of lack of space, the focus here is on polythiophene and the interesting insight given by model studies on thiophene oligomers. Conducting

polymers have also been widely studied as electrochromic materials. Brief accounts of the optical absorption of conducting polymers have appeared in conducting polymer reviews [253–255].

The attraction of using spectroelectrochemistry with conducting polymers is both in the attempt to observe new species that absorb within the band gap (polarons and bipolarons), and the potential to discriminate between “capacitive” charge and faradaic charge (only the latter will give rise to spectroscopic changes). The latter has turned out to be a red herring since the spectrum of the surface species contributing to the capacitive charge of the polymer fibrils are almost certainly identical to those of the bulk polymer.

The classic ITO electrode-based cell [106, 256] is still widely in use, its advantage being convenience and simplicity. It does suffer the disadvantage that it is difficult to keep out oxygen. Also, the resistance of the ITO means that the current distribution during the growth of a conducting polymer by electropolymerization may not be uniform over the surface. A fiber-optic-based cell has been described in Ref. [257–259].

We shall focus this discussion on polythiophene spectroelectrochemistry [260]. While simply monitoring the UV-vis spectrum of a coated ITO electrode can show evolution of polaron and bipolaron bands [255], for example, in poly(thiophene-3-methanol) [261], a DCVA experiment is even more revealing, showing that more regular and conjugated polymers generate bipolarons in much greater concentration early on in the CV [262, 263].

Chronoabsorptometry has also been used to determine the kinetics of doping/undoping reactions in thin films of poly(3-hexylthiophene) and

polyphenylenevinylenes (PPVs) [264]. Similar current–time transients with absorbance–time transients in polyaniline showed anomalous current–time behavior associated with a change in the physical state of the polymer [265, 266].

A key development in the understanding of conducting polymer electrochemistry has been the development of oligomeric models. Bauerle [267] showed, for example, that the redox potentials of the two successive oxidations of oligomers could be plotted against the reciprocal of chain length and converged to one potential for infinite chain length. He also noticed that the radical cations dimerized especially at room temperature to give characteristic bands near 650 nm. Others [268, 269] have shown that the dimer is EPR-silent. The formation of π -dimers is an alternative explanation to the usual polaron/bipolaron explanation given for polythiophene itself. These authors have obtained dimerization constants by in situ UV-vis spectroelectrochemistry using the following equations:



$$K_{eq} = \frac{[D]}{[M]^2} \quad (43)$$

$$\ln A_D = \ln \left[\frac{\epsilon_D}{\epsilon_M^2} l \right] + \ln K_{eq} + 2 \ln A_M \quad (44)$$

where l is the path-length. Thus, a log–log plot of the dimer versus the monomer absorbance should be linear with a slope of 2. Mann obtained a value of K_{eq} of 1.8 [268]. However, recently, data gathered for a bithiophene derivative gave plots of Eq. (44) with a slope of 1.25 rather than 2, and a hook-shaped curve at higher concentrations [270]. The problem is that the concentration is not

homogeneous throughout the solution, especially if during the wait to achieve full electrolysis and equilibration, the radical cation has reacted through dimerization or some other pathway. The authors minimized this problem by using a LIGA cell that has a very fast response time.

Polyanilines are very stable and very attractive for commercial applications. Their electrochromic and optical properties are well known [271, 272.] The most detailed study to date draws on both UV-vis and EPR data to map the concentration of species in the polymers as a function of potential [273]. Spectroelectrochemical techniques have also been applied to study polyaniline growth. The open-circuit method has been used in the study of the electropolymerization of anilines [274, 275]. For example, aniline cations can be shown to react with neutral aniline rather than with other cations [274]. Early stages of aniline oxidation have also been studied by employing spectroelectrochemical (DCVA) and rotating ring disk electrode experiments in 1 M H_2SO_4 . Results indicate that a large amount of the tail-to-tail dimer, benzidine, is produced in the initial stage of aniline oxidation, which is followed by the generation of the head-to-tail dimer, *N*-phenyl-*p*-phenylene diamine (PPD), as well as oligomers in solutions of high aniline concentrations [259.]

3.4.4

Conclusions

The advantages and disadvantages of UV-visible spectroelectrochemistry are summarized in Table 1. It seems that interest in the applications of UV-visible spectroelectrochemistry is very much alive, despite the attention of many

Tab. 1 Features of UV-visible spectroelectrochemistry

Advantages	Disadvantages
Established technique	High resistance of many optically transparent electrodes and/or thin-layer cells precludes kinetic measurements.
Solvent absorption usually not an issue	Overlapping bands, less species specificity and lower molecular bonding information content than vibrational spectroscopies
Useful for conducting polymers and thin films	Rapid scanning of entire spectrum is expensive
Insensitive to competing faradaic reactions generating colorless species	
Insensitive to non-faradaic charge consuming processes such as double-layer charging	
Species-specific through selection of appropriate wavelength	
Spectrometers inexpensive and widely available	
UV-vis OTTLE cells convenient and cheap to construct; common materials (glass, Teflon) used in cell construction	
OTTLE cells allow estimation of $E^{0'}$ and n without knowledge of concentration, extinction coefficients, path-length or diffusion coefficients	
OTTLE cells with mediator useful in bioelectrochemistry	
OTTLE cells separate working and counter electrode compartments automatically, provided that leakage ("edge effects") is minimized	
OTTLE cells useful for rapid electrolysis and investigation of slow follow-up reactions	
Open-circuit transients useful for kinetics of follow-up reactions	
Absorbance – time transient analysis does not require area of electrode to obtain diffusion coefficient	
More species-specific than electrochemical techniques	
More sensitive than FTIR or IR	
Not surface specific in transmission mode	

electrochemists having switched to surface processes and the use of probe microscopy. Thus, solution spectroelectrochemistry has experienced a renaissance in its application to the characterization of redox processes when there is ambiguity about the site of electron transfer in the molecule. Metal complexes

are the obvious examples for deciding whether ligand versus metal redox processes are occurring, but this is also becoming more important in molecular assemblies (supramolecular chemistry) and host–guest complexes (e.g. cyclodextrin or vesicle complexes) and the redox chemistry of multi–redox site

organic molecules. Spectroelectrochemistry has proved immensely powerful in the study of thick films such as conducting polymers and their soluble oligomer models. Considering the extra selectivity offered for the analysis of mixtures or complex matrices, the neglect of spectroelectrochemistry by analytical chemists is somewhat surprising and ought to be corrected.

Concerning the diagnostic and mechanistic applications of dynamic spectroelectrochemistry, there is certainly room for its more widespread use. The theory for the various predicted responses is as mature as that for cyclic voltammetry itself. However, where the results from CV are in any doubt, it is by no means a difficult proposition to carry out chronoabsorptometric studies to confirm the mechanism. Digital simulation programs (e.g. Digisim) are now much more widely available and allow almost unlimited freedom in the number of reactions in the mechanism and the techniques modelled (although Digisim itself does not as yet have a feature for absorbance plots). The great advantage of transient spectroelectrochemistry is in monitoring the fate of electrogenerated species in solution, perhaps generating nonelectroactive, but colored, species, and the availability of much slower timescales. For example, some reaction mechanisms give virtually the same double potential step current/charge responses, but these can be distinguished optically, for example, the DISP/ECE reactions mentioned above. Finally, it is possible that the use of DCVA as a diagnostic tool like cyclic voltammetry will grow, especially as optical systems, such as cheap fiber-optic spectrometers on a PC card, become inexpensive add-ons for electrochemical equipment, in the same way that EQCM is heading.

References

1. W. R. Heineman, W. B. Jensen, *ACS Symp. Ser.* **1989**, 390, 442–457.
2. R. W. Murray, W. R. Heineman, W. O. O'Dom, *Anal. Chem.* **1967**, 39, 1666.
3. W. R. Heineman, *J. Chem. Educ.* **1983**, 60, 305–308.
4. K. M. Kadish, *Prog. Inorg. Chem.* **1986**, 34, 435–605.
5. T. Kuwana, N. Winograd, *Electroanal. Chem.* **1974**, 7, 1.
6. W. R. Heineman, F. M. Hawkridge, H. N. Blount, *Electroanal. Chem.* **1984**, 13, 1–113.
7. T. Kuwana, W. R. Heineman, *Acc. Chem. Res.* **1976**, 9, 2421.
8. H. D. Abruna, (Ed.), *Electrochemical Interfaces: Modern Techniques for In-Situ Interface Characterization*, Wiley-VCH, New York, 1991.
9. C. Gutierrez, C. A. Melendres, (Eds.), *Spectroscopic and Diffraction Techniques in Interfacial Electrochemistry*, Kluwer, Amsterdam, 1990.
10. R. Varma, J. R. Selman, (Eds.), *Techniques for Characterization of Electrodes and Electrochemical Processes*, John Wiley & Sons, New York, 1991.
11. R. J. Gale, (Ed.), *Spectroelectrochemistry*, Plenum Press, New York, 1988.
12. J. J. Niu, S. J. Dong, *Rev. Anal. Chem.* **1996**, 15, 1–171.
13. F. Pragst, *Zeitschrift Fur Chemie* **1981**, 21, 241–249.
14. R. L. McCreery, in *Physical Methods of Chemistry, Volume 2, Electrochemical Methods*, B. W. Rossiter, S. F. Hamilton, (Eds.), John Wiley & Sons, New York, 1986, pp. 591–661.
15. W. Plieth, G. S. Wilson, C. G. de la Fe, *Pure Appl. Chem.* **1998**, 70, 2409–2412.
16. J. L. Anderson, L. A. Coury, J. Leddy, *Anal. Chem.* **1998**, 70, 519R–589R.
17. J. L. Anderson, L. A. Coury, J. Leddy, *Anal. Chem.* **2000**, 72, 4497–4520.
18. W. R. Heineman, P. T. Kissinger, in *Laboratory Techniques in Electroanalytical Chemistry* (Eds.: W. R. Heineman, P. T. Kissinger), Marcel Dekker, New York, 1984, pp. 51–124.
19. N. Winograd, in *Laboratory Techniques in Electroanalytical Chemistry* (Eds.: W. R. Heineman, P. T. Kissinger), Marcel Dekker, New York, 1984, pp. 321–335.

20. P. A. Christensen, A. Hamnett, *Techniques and Mechanisms in Electrochemistry*, Blackie, Glasgow, 1994.
21. R. Greef, R. Peat, L. M. Peter et al., *Instrumental Methods in Electrochemistry*, Ellis Horwood, Chichester, UK, 1985.
22. B. S. H. Royce, F. Sanchezsinencio, R. Goldstein et al., *J. Electrochem. Soc.* **1982**, 129, 2393–2395.
23. D. M. Kolb, in *Spectroelectrochemistry*, R. J. Gale, (Ed.), Plenum Press, New York, 1988.
24. J. Robinson, in *Electrochemistry (Specialist Periodical Report)* Vol. 9, (Ed.: D. Pletcher), Royal Society of Chemistry, London, 1984, pp. 101–161.
25. R. M. Corn, D. A. Higgins, *Chem. Rev.* **1994**, 94, 107.
26. G. L. Richmond, *Electroanal. Chem.* **1991**, 17, 87.
27. S. Gottesfeld, *Electroanal. Chem.* **1989**, 15, 143.
28. W. N. Hansen, *Adv. Electrochem. Electrochem. Eng.* **1973**, 9, 1.
29. A. Harata, Q. Shen, T. Sawada, *Annu. Rev. Phys. Chem.* **1999**, 50, 193–219.
30. D. R. Dunphy, S. B. Mendes, S. S. Saavedra et al., *Anal. Chem.* **1997**, 69, 3086–3094.
31. C. Piraud, E. Mwarania, G. Wylangowski et al., *Anal. Chem.* **1992**, 64, 651–655.
32. S. E. Ross, C. J. Seliskar, W. R. Heineman, *Anal. Chem.* **2000**, 72, 5549–5555.
33. T. DeAngelis, W. R. Heineman, *J. Chem. Educ.* **1976**, 53, 594.
34. S. K. D. Strubinger, I. W. Sun, W. E. Cleland et al., *Inorg. Chem.* **1990**, 29, 993–999.
35. R. S. Drago, 2nd ed., *Physical Methods in Inorganic Chemistry*, Saunders, Fort Worth, 1977.
36. K. Kano, T. Ikeda, *Anal. Sci.* **2000**, 16, 1013–1021.
37. G. Sanna, M. I. Pilo, M. A. Zoroddu et al., *Inorg. Chim. Acta* **1993**, 208, 153–158.
38. R. L. McCreery, *Anal. Chem.* **1977**, 49, 206.
39. G. C. Grant, T. Kuwana, *J. Electroanal. Chem.* **1970**, 24, 11.
40. A. Bewick, J. M. Mellor, B. S. Pons, *Electrochim. Acta* **1980**, 25, 931.
41. A. Katagiri, T. Matsubara, H. Arai et al., *J. Electrochem. Soc.* **1989**, 136, 101–108.
42. A. Katagiri, H. Arai, Z. I. Takehara et al., *Denki Kagaku* **1995**, 63, 669–674.
43. J. Mocak, M. Nemeth, M. Lapkowski et al., *Collect. Czech. Chem. Commun.* **1987**, 52, 1386–1396.
44. M. Oyama, K. Nozaki, S. Okazaki, *Anal. Chem.* **1991**, 63, 1387–1392.
45. M. Oyama, M. Yamanuki, T. Sasaki et al., *J. Chem. Soc., Perkin Trans. 2* **2000**, 1745–1748.
46. S. Zamponi, A. Czerwinski, G. Gambini et al., *J. Electroanal. Chem.* **1992**, 332, 63–71.
47. G. Denuault, M. V. Mirkin, A. J. Bard, *J. Electroanal. Chem.* **1991**, 308, 27–38.
48. A. S. Baranski, W. R. Fawcett, C. M. Gilbert, *Anal. Chem.* **1985**, 57, 166–170.
49. L. Kress, A. Neudeck, A. Petr et al., *J. Electroanal. Chem.* **1996**, 414, 31–40.
50. A. J. Paine, R. O. Loutfy, *Rev. Chem. Intermediates* **1984**, 5, 227–248.
51. C. A. Lundgren, R. W. Murray, *Inorg. Chem.* **1988**, 27, 933–939.
52. B. S. Kim, S. M. Park, *J. Electrochem. Soc.* **1993**, 140, 115–122.
53. D. H. Jones, A. S. Hinman, *Can. J. Chem. Rev. Can. Chim.* **1990**, 68, 2234–2238.
54. F. Gaillard, E. Levillain, *J. Electroanal. Chem.* **1995**, 398, 77–87.
55. D. E. Albertson, H. N. Blount, F. M. Hawkrig, *Anal. Chem.* **1979**, 51, 556.
56. E. E. Bancroft, H. N. Blount, F. M. Hawkrig, *Anal. Chem.* **1981**, 53, 1862–1866.
57. E. E. Bancroft, H. N. Blount, *Anal. Chem.* **1986**, 58, 2944–2949.
58. G. S. Wilson, C. Li, *Anal. Chem.* **1973**, 45, 2370.
59. M. K. Hanafey, R. L. Scott, T. H. Ridgway et al., *Anal. Chem.* **1978**, 50, 116.
60. M. Josowicz, J. Janata, K. Ashley et al., *Anal. Chem.* **1987**, 59, 253–258.
61. H. N. Blount, *J. Electroanal. Chem.* **1973**, 42, 271.
62. J. F. Evans, H. N. Blount, *J. Am. Chem. Soc.* **1978**, 100, 4191.
63. J. F. Evans, H. N. Blount, *J. Phys. Chem.* **1979**, 83, 1970.
64. V. D. Parker, *Acta Chem. Scand. Ser.-Phys. Inorg. Chem.* **1984**, 38, 671–677.
65. V. D. Parker, *Acta Chem. Scand.* **1998**, 52, 145–153.
66. E. E. Bancroft, J. S. Sidwell, H. N. Blount, *Anal. Chem.* **1981**, 53, 1390–1394.
67. D. J. Cohen, B. C. King, F. M. Hawkrig, *J. Electroanal. Chem.* **1998**, 447, 53–62.
68. D. S. Shin, N. Doddapaneni, S. M. Park, *Inorg. Chem.* **1992**, 31, 4060–4064.
69. A. J. Bard, L. R. Faulkner, *Electrochemical Methods*, John Wiley & Sons, New York, 2001.

70. F. Gaillard, E. Levillain, M. C. Dhamelin-court et al., *J. Raman Spectrosc.* **1997**, *28*, 511–517.
71. A. Ahriks, J. Paris, *New J. Chem.* **1999**, *23*, 1177–1180.
72. Z. Uziel, *Electrochim. Acta* **1987**, *32*, 489–495.
73. K. Ogura, T. Naito, *Electrochim. Acta* **1982**, *27*, 1243–1246.
74. G. J. Cheng, S. J. Dong, *Electrochim. Acta* **1987**, *32*, 1561–1565.
75. M. P. Soriaga, A. T. Hubbard, *J. Am. Chem. Soc.* **1982**, *104*, 2735–2742.
76. Y. P. Gui, M. D. Porter, T. Kuwana, *Anal. Chem.* **1985**, *57*, 1474–1476.
77. W. T. Yap, E. A. Blubaugh, R. A. Durst et al., *J. Electroanal. Chem.* **1984**, *160*, 73–78.
78. Y. C. Zhu, Y. J. Lu, G. J. Cheng et al., *J. Electrochem. Soc.* **1999**, *146*, 2954–2958.
79. N. Okumura, B. Uno, *Bull. Chem. Soc. Jpn.* **1999**, *72*, 1213–1217.
80. A. Ahriks, M. Anouti, J. E. Robert et al., *Can. J. Chem.-Rev. Can. Chim.* **1998**, *76*, 1867–1874.
81. F. Baumann, W. Kaim, L. M. Baraldo et al., *Inorg. Chim. Acta* **1999**, *285*, 129–133.
82. J. W. Buchler, P. Hammerschmitt, I. Kaufeld et al., *Chem. Ber.* **1991**, *124*, 2151–2159.
83. A. Sato, M. Torimura, K. Takagi et al., *Anal. Chem.* **2000**, *72*, 150–155.
84. M. Torimura, M. Mochizuki, K. Kano et al., *Anal. Chem.* **1998**, *70*, 4690–4695.
85. C. G. Atwood, W. E. Geiger, A. L. Rheingold, *J. Am. Chem. Soc.* **1993**, *115*, 5310–5311.
86. C. G. Atwood, W. E. Geiger, T. E. Bitterwolf, *J. Electroanal. Chem.* **1995**, *397*, 279–285.
87. S. W. Jones, L. M. Vrana, K. J. Brewer, *J. Organomet. Chem.* **1998**, *554*, 29–40.
88. K. J. Brewer, M. Calvin, R. S. Lumpkin et al., *Inorg. Chem.* **1989**, *28*, 4446–4451.
89. D. T. Sawyer, A. Sobkowiak, J. Roberts et al., 2nd ed., *Electrochemistry for Chemists*, John Wiley & Sons, New York, 1995.
90. H. Lund, in *Organic Electrochemistry* (Eds.: H. Lund, M. M. Baizer), Marcel Dekker, New York, 1991, pp. 253–327.
91. M. Kummer, J. R. Kirchhoff, *Electroanalysis* **1996**, *8*, 524–528.
92. A. Niemz, J. Imbriglio, V. M. Rotello, *J. Am. Chem. Soc.* **1997**, *119*, 887–892.
93. H. O. Finklea, R. K. Boggess, J. W. Trogon et al., *Anal. Chem.* **1983**, *55*, 1177–1179.
94. Y. F. Lee, J. R. Kirchhoff, *Anal. Chem.* **1993**, *65*, 3430–3434.
95. N. Jemaa, J. Yu, R. D. Noble et al., *Sep. Sci. Technol.* **1992**, *27*, 901–915.
96. P. A. Flowers, S. A. Callender, *Anal. Chem.* **1996**, *68*, 199–202.
97. M. D. Porter, S. J. Dong, Y. P. Gui et al., *Anal. Chem.* **1984**, *56*, 2263–2265.
98. A. Neudeck, L. Kress, *J. Electroanal. Chem.* **1997**, *437*, 141–156.
99. R. K. Rhodes, K. M. Kadish, *Anal. Chem.* **1981**, *53*, 1539–1541.
100. T. Watanabe, K. Honda, *J. Phys. Chem.* **1982**, *86*, 2617–2619.
101. E. A. Blubaugh, L. M. Doane, *Anal. Chem.* **1982**, *54*, 329–331.
102. M. B. G. Pilkington, B. A. Coles, R. G. Compton, *Anal. Chem.* **1989**, *61*, 1787–1789.
103. P. V. Kamat, S. K. Gupta, *Polymer* **1988**, *29*, 1329–1334.
104. W. R. Heineman, C. W. Anderson, H. B. Halsall et al., *Adv. Chem. Ser.* **1982**, *201*, 1–21.
105. W. S. Szulbinski, *Inorg. Chim. Acta* **1995**, *228*, 243–250.
106. P. M. Hoang, S. Holdcroft, B. L. Funt, *J. Electrochem. Soc.* **1985**, *132*, 2129–2133.
107. P. A. Flowers, G. Nealy, *Anal. Chem.* **1990**, *62*, 2740–2742.
108. C. M. Duff, G. A. Heath, *Inorg. Chem.* **1991**, *30*, 2528–2535.
109. S. A. MacGregor, E. J. L. McInnes, R. J. Sorbie et al., in *Molecular Electrochemistry of Inorganic, Bioinorganic and Organometallic Compounds* (Eds.: A. J. L. Pombeiro, J. A. McCleverty), Kluwer Academic Publishers, New York, 1993, pp. 503–517.
110. M. T. Barton, N. M. Rowley, P. R. Ashton et al., *J. Chem. Soc., Dalton Trans.* **2000**, 3170–3175.
111. M. T. Barton, N. M. Rowley, P. R. Ashton et al., *New J. Chem.* **2000**, *24*, 555–560.
112. D. P. Arnold, G. A. Heath, D. A. James, *J. Porphyr. Phthalocyanines* **1999**, *3*, 5–31.
113. D. G. Sanderson, L. B. Anderson, *Anal. Chem.* **1985**, *57*, 2388–2393.
114. E. F. Bowen, F. M. Hawkridge, *J. Electroanal. Chem.* **1981**, *125*, 367.
115. B. J. Norris, M. L. Meckstroth, W. R. Heineman, *Anal. Chem.* **1976**, *48*, 630.
116. F. A. Walker, D. Emrick, J. E. Rivera et al., *J. Am. Chem. Soc.* **1988**, *110*, 6234.
117. H. L. Landrum, R. T. Salmon, F. M. Hawkridge, *J. Am. Chem. Soc.* **1977**, *99*, 3154.

118. M. T. Stankovich, *Anal. Biochem.* **1980**, *109*, 295–308.
119. A. M. Bond, E. A. McLennan, R. S. Stojanovic et al., *Anal. Chem.* **1987**, *59*, 2853–2860.
120. D. M. Arciero, A. B. Hooper, M. J. Collins, *J. Electroanal. Chem.* **1994**, *371*, 277–281.
121. T. B. Jarbawi, M. T. Stankovich, *Anal. Chim. Acta* **1994**, *292*, 71–76.
122. X. H. Mu, K. M. Kadish, *Langmuir* **1990**, *6*, 51–56.
123. M. H. Barley, C. E. Anson, B. F. G. Johnson et al., *J. Organomet. Chem.* **1988**, *339*, 151–157.
124. J. S. Yu, C. Yang, H. Q. Fang, *Anal. Chim. Acta* **2000**, *420*, 45–55.
125. W. A. Nevin, A. B. P. Lever, *Anal. Chem.* **1988**, *60*, 727–730.
126. R. Gamage, S. Umapathy, A. J. McQuillan, *J. Electroanal. Chem.* **1990**, *284*, 229–235.
127. M. Krejčík, M. Danek, F. Hartl, *J. Electroanal. Chem.* **1991**, *317*, 179–187.
128. I. R. Farrell, F. Hartl, S. Zalis et al., *J. Chem. Soc., Dalton Trans.* **2000**, 4323–4331.
129. S. Knoblauch, F. Hartl, D. J. Stufkens et al., *Eur. J. Inorg. Chem.* **1999**, 303–312.
130. J. P. Bullock, D. C. Boyd, K. R. Mann, *Inorg. Chem.* **1987**, *26*, 3084–3086.
131. Y. J. Ma, J. M. Zheng, S. M. Zhu, *Chin. J. Inorg. Chem.* **1999**, *15*, 61–67.
132. R. E. Wittig, C. P. Kubiak, *J. Electroanal. Chem.* **1995**, *393*, 75–86.
133. J. J. Niu, S. J. Dong, *Electrochim. Acta* **1995**, *40*, 823–828.
134. J. J. Niu, S. J. Dong, *Electroanalysis* **1995**, *7*, 1059–1062.
135. S. W. Feldberg, C. Auerbach, *Anal. Chem.* **1964**, *36*, 505.
136. Y. C. Zhu, G. J. Cheng, S. J. Dong, *Electroanalysis* **2000**, *12*, 736–741.
137. W. T. Yap, G. Marbury, E. A. Blubaugh et al., *J. Electroanal. Chem.* **1989**, *271*, 325–329.
138. D. L. Langhus, G. S. Wilson, *Anal. Chem.* **1979**, *51*, 1139.
139. E. W. Kristensen, D. H. Igo, R. C. Elder et al., *J. Electroanal. Chem.* **1991**, *309*, 61–72.
140. A. Neudeck, L. Dunsch, *J. Electroanal. Chem.* **1995**, *386*, 135–148.
141. S. D. Brown, R. S. Bear, *Crit. Rev. Anal. Chem.* **1993**, *24*, 99–131.
142. N. R. Lynam, in *Symposium on Electrochromic Materials*, M. K. Carpenter, D. A. Corrigan (eds), Electrochemical Society, Pennington, NJ, USA, 1990, pp. 201–231.
143. P. Bressers, E. A. Meulenkaamp, *J. Electrochem. Soc.* **1998**, *145*, 2225–2230.
144. N. Leventis, Y. C. Chung, *J. Mater. Chem.* **1993**, *3*, 833–839.
145. P. Raptá, A. Neudeck, A. Petr et al., *J. Chem. Soc., Faraday Trans.* **1998**, *94*, 3625–3630.
146. Y. Idota, T. Kubota, A. Matsufuji et al., *Science* **1997**, *276*, 1395–1397.
147. I. A. Courtney, J. R. Dahn, *J. Electrochem. Soc.* **1997**, *144*, 2943–2948.
148. R. G. Egdel, A. Gulino, C. Rayden et al., *J. Mater. Chem.* **1995**, *5*, 499–504.
149. H. Y. Liu, F. R. F. Fan, A. J. Bard, *J. Electrochem. Soc.* **1985**, *132*, 2666–2668.
150. D. M. Anjo, K. Bogdon, S. Brown et al., *Anal. Lett.* **1993**, *26*, 2431–2442.
151. D. M. Anjo, S. Brown, L. Wang, *Anal. Chem.* **1993**, *65*, 317–319.
152. S. Zamponi, R. Santucci, M. Brunori et al., *Biochim. Biophys. Acta* **1990**, *1034*, 294–297.
153. Y. W. Xie, G. L. Che, S. J. Dong, *Electrochim. Acta* **1991**, *36*, 203–207.
154. J. Xu, M. C. Granger, Q. Chen et al., *Anal. Chem.* **1997**, *69*, 591A.
155. A. Neudeck, L. Dunsch, *Electrochim. Acta* **1995**, *40*, 1427–1434.
156. L. Dunsch, B. Gollas, A. Neudeck et al., *Chem. Ber.* **1994**, *127*, 2423–2429.
157. K. Ashley, S. Pons, *Trends Anal. Chem.* **1986**, *5*, 263–268.
158. J. Salbeck, *J. Electroanal. Chem.* **1992**, *340*, 169–195.
159. C. H. Pyun, S. M. Park, *Anal. Chem.* **1986**, *58*, 251–256.
160. T. M. Vess, D. W. Wertz, *J. Electroanal. Chem.* **1991**, *313*, 81–94.
161. I. S. Zavarine, C. P. Kubiak, *J. Electroanal. Chem.* **2001**, *495*, 106–109.
162. C. C. Jan, B. K. Lavine, R. L. McCreery, *Anal. Chem.* **1985**, *57*, 752–758.
163. Z. F. Ding, D. J. Fermin, P. F. Brevet et al., *J. Electroanal. Chem.* **1998**, *458*, 139–148.
164. I. C. Stefan, Y. V. Tolmachev, D. A. Scherson, *Anal. Chem.* **2001**, *73*, 527–532.
165. D. H. Jones, A. S. Hinman, *Can. J. Chem.-Rev. Can. Chim.* **1996**, *74*, 1403–1408.
166. R. S. Robinson, R. L. McCreery, *Anal. Chem.* **1981**, *53*, 997–1001.
167. J. S. Mayausky, R. L. McCreery, *Anal. Chem.* **1983**, *55*, 308–312.
168. H. P. Wu, R. L. McCreery, *J. Electrochem. Soc.* **1989**, *136*, 1375–1379.

169. J. Posdorfer, M. Olbrichstock, R. N. Schindler, *Z. Phys. Chem. Int. J. Res. Phys. Chem. Chem. Phys.* **1991**, 171, 33–52.
170. K. R. Walczyk, G. S. Popkirov, R. N. Schindler, *Ber. Bunsen-Ges. Phys. Chem. Chem. Phys.* **1995**, 99, 1546–1552.
171. J. Posdorfer, M. Olbrichstock, R. N. Schindler, *Electrochim. Acta* **1994**, 39, 2005–2013.
172. P. Rossi, C. W. McCurdy, R. L. McCreery, *J. Am. Chem. Soc.* **1981**, 103, 2524–2529.
173. C. C. Jan, R. L. McCreery, *Anal. Chem.* **1986**, 58, 2771–2777.
174. R. A. Fair, D. E. Ryan, P. K. Smith et al., *Anal. Chem.* **1986**, 58, 647–650.
175. S. B. Hudson, C. Riley, *J. Electroanal. Chem.* **1995**, 393, 1–6.
176. T. Demana, D. Peterman, J. Shaffer et al., *Anal. Chem.* **1989**, 61, 1216–1221.
177. M. A. Tamor, M. Zanini, *J. Electrochem. Soc.* **1986**, 133, 1399–1401.
178. J. Pawliszyn, M. F. Weber, M. J. Dignam et al., *Anal. Chem.* **1986**, 58, 239–242.
179. Z. F. Ding, F. Reymond, P. Baumgartner et al., *Electrochim. Acta* **1998**, 44, 3–13.
180. L. Tomaszewski, Z. F. Ding, D. J. Fermin et al., *J. Electroanal. Chem.* **1998**, 453, 171–177.
181. Z. F. Ding, R. G. Wellington, P. F. Brevet et al., *J. Electroanal. Chem.* **1997**, 420, 35–41.
182. A. F. Slaterbeck, M. L. Stegemiller, C. J. Seliskar et al., *Anal. Chem.* **2000**, 72, 5567–5575.
183. Y. N. Shi, A. F. Slaterbeck, C. J. Seliskar et al., *Anal. Chem.* **1997**, 69, 3679–3686.
184. J. F. Tyson, *Talanta* **1979**, 26, 117.
185. Q. J. Xie, W. Z. Wei, L. H. Nie et al., *Anal. Chem.* **1993**, 65, 1888–1892.
186. J. Zak, M. D. Porter, T. Kuwana, *Anal. Chem.* **1983**, 55, 2219–2222.
187. Y. P. Gui, T. Kuwana, *Langmuir* **1986**, 2, 471–476.
188. M. D. Porter, T. Kuwana, *Anal. Chem.* **1984**, 56, 529–534.
189. W. Z. Wei, Q. J. Xie, S. Z. Yao, *J. Electroanal. Chem.* **1992**, 328, 9–20.
190. W. S. Szulbinski, P. R. Warburton, D. H. Busch et al., *Inorg. Chem.* **1993**, 32, 297–302.
191. Y. Zhangyu, G. Tiande, Q. Mei, *Anal. Chem.* **1994**, 66, 497–502.
192. N. J. Simmons, M. D. Porter, *Anal. Chem.* **1997**, 69, 2866–2869.
193. Y. C. Zhu, G. J. Cheng, S. J. Dong, *J. Electrochem. Soc.* **1999**, 146, 3000–3003.
194. A. T. Hubbard, F. C. Anson, *Electroanal. Chem.* **1970**, 4, 129.
195. J. Y. Gui, G. W. Hance, T. Kuwana, *J. Electroanal. Chem.* **1991**, 309, 73–89.
196. J. D. Zhang, S. Z. Yao, L. H. Nie et al., *Anal. Sci.* **2000**, 16, 87–91.
197. Q. J. Xie, W. Z. Wei, L. H. Nie et al., *J. Electroanal. Chem.* **1993**, 348, 29–47.
198. Q. Xie, W. Wei, L. Nie et al., *J. Electroanal. Chem.* **1993**, 358, 359–360.
199. W. Z. Wei, Q. J. Xie, S. Z. Yao, *Electrochim. Acta* **1995**, 40, 1057–1061.
200. S. J. Dong, Y. W. Xie, *J. Electroanal. Chem.* **1992**, 335, 197–205.
201. Q. J. Xie, D. Z. Shen, L. H. Nie et al., *Electrochim. Acta* **1993**, 38, 2277–2280.
202. Q. J. Xie, X. Cheng, W. Z. Wei et al., *Talanta* **1994**, 41, 261–267.
203. Q. J. Xie, W. Z. Wei, X. Chen et al., *J. Electroanal. Chem.* **1993**, 351, 91–103.
204. C. Boxall, W. J. Albery, *PCCP Phys. Chem. Chem. Phys.* **2000**, 2, 3631–3639.
205. H. Debrodt, K. E. Heusler, *Ber. Bunsen-Ges. Phys. Chem. Chem. Phys.* **1977**, 81, 1172.
206. R. Dorr, E. W. Grabner, *Ber. Bunsen-Ges. Phys. Chem. Chem. Phys.* **1978**, 82, 104.
207. M. Zhao, D. A. Scherson, *Anal. Chem.* **1992**, 64, 3064–3067.
208. Y. V. Tolmachev, Z. H. Wang, Y. N. Hu et al., *Anal. Chem.* **1998**, 70, 1149–1155.
209. R. L. Wang, K. Y. Tam, R. G. Compton, *J. Electroanal. Chem.* **1997**, 434, 105–114.
210. N. Kobayashi, Y. Nishiyama, *J. Phys. Chem.* **1985**, 89, 1167–1170.
211. J. Mack, M. J. Stillman, *Inorg. Chem.* **1997**, 36, 413–425.
212. H. Isago, C. C. Leznoff, M. F. Ryan et al., *Bull. Chem. Soc. Jpn.* **1998**, 71, 1039–1047.
213. X. L. Yuan, S. C. Sun, F. M. Hawkridge et al., *J. Am. Chem. Soc.* **1990**, 112, 5380–5381.
214. R. Gamage, A. J. McQuillan, B. M. Peake, *J. Chem. Soc., Faraday Trans.* **1991**, 87, 3653–3660.
215. P. Rapt, R. Faber, L. Dunsch et al., *Spectrosc. Acta Pt. A–Mol. Biomol. Spectrosc.* **2000**, 56, 357–362.
216. A. Petr, L. Dunsch, A. Neudeck, *J. Electroanal. Chem.* **1996**, 412, 153–158.
217. Q. J. Xie, X. Y. Pang, D. Z. Shen et al., *Electrochim. Acta* **1994**, 39, 727–730.
218. K. Shimazu, M. Yanagida, K. Uosaki, *J. Electroanal. Chem.* **1993**, 350, 321–327.

219. J. M. Kim, S. M. Chang, H. Muramatsu, *J. Electrochem. Soc.* **1999**, 146, 4544–4550.
220. Y. J. Xu, Q. J. Xie, M. Q. Hu et al., *J. Electroanal. Chem.* **1995**, 389, 85–90.
221. M. Ebadi, A. B. P. Lever, *Inorg. Chem.* **1999**, 38, 467–474.
222. W. Kaim, A. Klein, M. Glockle, *Acc. Chem. Res.* **2000**, 33, 755–763.
223. M. Glockle, W. Kaim, N. E. Katz et al., *Inorg. Chem.* **1999**, 38, 3270–3274.
224. C. Lee, M. S. Moon, J. W. Park, *J. Inclusion Phenom. Mol. Recognit. Chem.* **1996**, 26, 219–232.
225. J. F. Bergamini, M. Belabbas, M. Jouini et al., *J. Electroanal. Chem.* **2000**, 482, 156–167.
226. J. A. Crayston, J. N. Devine, J. C. Walton, *Tetrahedron* **2000**, 56, 7829–7857.
227. C. Lambert, G. Noll, *J. Am. Chem. Soc.* **1999**, 121, 8434–8442.
228. C. Lambert, W. Gaschler, E. Schmalzlin et al., *J. Chem. Soc., Perkin Trans. 2* **1999**, 577–587.
229. C. L. Hussey, *Laboratory Techniques in Electroanalytical Chemistry*, 2nd ed., Marcel Dekker, New York, 1996.
230. G. Mamantov, V. E. Norvell, L. N. Klatt, *J. Electrochem. Soc.* **1980**, 127, 1768.
231. B. L. Harward, L. N. Klatt, G. Mamantov, *Anal. Chem.* **1985**, 57, 1773–1775.
232. W. J. Gau, I. W. Sun, *J. Electrochem. Soc.* **1996**, 143, 170–174.
233. S. J. Dong, J. J. Niu, T. M. Cotton, in *Methods in Biochemical Enzymology-Spectroscopy*, K. Saver, (ed), Vol. 246, Academic Press, Inc, Orlando, Florida, 1994, pp. 701–732.
234. F. M. Hawkrige, I. Taniguchi, *Comments Inorg. Chem.* **1995**, 17, 163–187.
235. N. G. Connelly, W. E. Geiger, *Chem. Rev.* **1996**, 96, 877–910.
236. V. Nagarajan, W. W. Parson, D. Davis et al., *Biochemistry* **1993**, 32, 12 324–12 336.
237. D. A. Moss, M. Leonhard, M. Bauscher et al., *FEBS Lett.* **1991**, 283, 33–36.
238. D. A. Grahame, *Biochemistry* **1993**, 32, 10 786–10 793.
239. N. J. Spangler, P. A. Lindahl, V. Bandarian et al., *J. Biol. Chem.* **1996**, 271, 7973–7977.
240. M. Collinson, E. F. Bowden, *Langmuir* **1992**, 8, 2552–2559.
241. E. F. Bowden, F. M. Hawkrige, J. F. Chlebowski et al., *J. Am. Chem. Soc.* **1982**, 104, 7641–7644.
242. E. E. Bancroft, H. N. Blount, F. M. Hawkrige, *Biochem. Biophys. Res. Commun.* **1981**, 101, 1331–1336.
243. G. J. Cheng, Y. Yang, S. J. Dong, *Bioelectrochem. Bioenerg.* **1994**, 34, 141–147.
244. D. E. Reed, S. Sun, K. B. Koller et al., *J. Electrochem. Soc.* **1987**, 134, C500–C501.
245. D. E. Reed, F. M. Hawkrige, *Anal. Chem.* **1987**, 59, 2334–2339.
246. X. D. Ding, A. Weichsel, J. F. Andersen et al., *J. Am. Chem. Soc.* **1999**, 121, 128–138.
247. S. K. Deb, *Symposium on Electrochromic Materials*, Electrochemical Society, Pennington, NJ, USA, 1990.
248. P. M. S. Monk, R. J. Mortimer, D. R. Rossinsky, *Electrochromism: Fundamentals and Applications*, Wiley-VCH, Weinheim, Germany, 1995.
249. M. Yagi, H. Fukiya, T. Kaneko et al., *J. Electroanal. Chem.* **2000**, 481, 69–75.
250. C. Kuhnhardt, *J. Electroanal. Chem.* **1994**, 369, 71–78.
251. P. J. Kulesza, S. Zamponi, M. A. Malik et al., *J. Solid State Electrochem.* **1997**, 1, 88–93.
252. S. A. Trammell, T. J. Meyer, *J. Phys. Chem. B* **1999**, 103, 104–107.
253. K. Doblhofer, K. Rajeshwar, in *Handbook of Conducting Polymers* (Eds.: T. A. Skotheim, R. L. Elsenbaumer, J. R. Reynolds), Marcel Dekker, New York, 1997, p. 531.
254. K. Hyodo, *Electrochim. Acta* **1994**, 39, 265–272.
255. A. O. Patil, A. J. Heeger, F. Wudl, *Chem. Rev.* **1988**, 88, 183–200.
256. J. Rault-Berthelot, V. Questaigne, J. Simonet et al., *New J. Chem.* **1989**, 13, 45–52.
257. J. Lukkari, J. Kankare, C. Visy, *Synth. Met.* **1992**, 48, 181–192.
258. J. Kankare, in *Contemporary Electroanalytical Chemistry* (Ed.: A. Ivaska), Plenum Press, New York, 1990, pp. 15–20.
259. B. J. Johnson, S. M. Park, *J. Electrochem. Soc.* **1996**, 143, 1277–1282.
260. A. R. Hillman, E. F. Mallen, *J. Electroanal. Chem.* **1988**, 243, 403–417.
261. E. Lankinen, M. Pohjakallio, G. Sundholm et al., *J. Electroanal. Chem.* **1997**, 437, 167–174.
262. P. Marque, J. Roncali, *J. Phys. Chem.* **1990**, 94, 8614–8617.
263. J. Roncali, P. Marque, R. Garreau et al., *Macromolecules* **1990**, 23, 1347–1352.
264. H. Nambu, M. Hamaguchi, K. Yoshino, *J. Appl. Phys.* **1997**, 82, 1847–1852.

265. S. Yonezawa, K. Kanamura, Z. Takehara, *J. Chem. Soc., Faraday Trans.* **1995**, 91, 3469–3474.
266. T. Amemiya, K. Hashimoto, A. Fujishima et al., *J. Electrochem. Soc.* **1991**, 138, 2845–2859.
267. P. Bauerle, U. Segelbacher, A. Maier et al., *J. Am. Chem. Soc.* **1993**, 115, 10 217–10 223.
268. M. G. Hill, J. F. Penneau, B. Zinger et al., *Chem. Mater.* **1992**, 4, 1106–1113.
269. G. Zotti, G. Schiavon, A. Berlin et al., *Adv. Mater.* **1993**, 5, 551–554.
270. A. Neudeck, P. Audebert, L. Guyard et al., *Acta Chem. Scand.* **1999**, 53, 867–875.
271. W. S. Huang, A. G. Macdiarmid, *Polymer* **1993**, 34, 1833–1845.
272. S. H. Glarum, J. H. Marshall, *J. Phys. Chem.* **1988**, 92, 4210–4217.
273. A. Neudeck, A. Petr, L. Dunsch, *J. Phys. Chem. B* **1999**, 103, 912–919.
274. A. Malinauskas, R. Holze, *Electrochim. Acta* **1999**, 44, 2613–2623.
275. A. Malinauskas, R. Holze, *J. Solid State Electrochem.* **1999**, 3, 429–436.

3.5**In situ Infrared Spectroelectrochemistry***Paul Andrew Christensen**The University, Newcastle upon Tyne, United Kingdom***3.5.1****Introduction**

Over the last two decades, in situ infrared spectroelectrochemistry has become an increasingly powerful analytical tool in electrochemistry, and has developed strongly in terms of sensitivity and the diversity of electrochemical systems that have been studied [1–12], (for a reasonably comprehensive list of papers 1997–2000, see <http://www.staff.ncl.ac.uk/p.a.christensen/ftir4.htm>). This transition may be associated with the ready availability of relatively inexpensive, research grade Fourier transform infrared (FTIR) spectrometers. In contrast to the early 1980s, the detection of organic monolayers is now commonplace [13–19], and there is other exciting work in fields as diverse as organometallic spectroelectrochemistry [20–22], in-depth studies of the double layer [23–25], time-resolved studies [26, 27], (photo)-electrocatalysis as a function of temperature [28–32], and the semiconductor–electrolyte interface [29, 33–35].

The wealth and diversity of the literature on in situ infrared spectroelectrochemistry renders an in-depth review outside the scope of this chapter. The aim of this treatise is hence to alert the electrochemical community to the possibilities opened up by in situ infrared techniques, to place the commonly employed methods in a historical context, and to provide a reasonably detailed overview of the practicalities of carrying out in situ infrared measurements.

Before proceeding, it may be helpful to review the aims that drove the development of in situ infrared spectroscopy, the problems that had to be overcome, and the means by which this was achieved.

3.5.2**Historical Context and Background**

By the latter half of the twentieth century, infrared spectroscopy had proved to be an invaluable tool in the study of the gas–solid interface, capable of identifying intermediates and products, as well as the orientation of adsorbed species. This success was being increasingly viewed with envious eyes by electrochemists eager to supplement the battery of conventional current/voltage/time techniques, which are incapable of providing such molecular information. However, two major problems had to be overcome if infrared spectra were to be obtained of species in the near-electrode region. Firstly, all common solvents, and especially water, absorb infrared light strongly; secondly, the amount of absorbing species of interest at or near an electrode is extremely small, rendering sensitivity a significant problem at a time when conventional infrared sources were weak, and detectors very noisy. These problems are discussed in turn below.

3.5.2.1 The Problem of Strong Solvent Absorption

There are two broad approaches to solving the problem of the absorption of light by the solvent when trying to collect vibrational spectra: (1) Use Raman spectroscopy, which has the advantage of employing radiation in the visible region, which is not absorbed by the solvents commonly employed in electrochemical studies. This is outside the scope of this

chapter, and details may be found elsewhere [1, 4, 5, 36]. (2) Use infrared spectroscopy, but minimize the path-length through which the infrared beam has to travel in the electrolyte, and this approach is the subject of the remainder of this chapter.

3.5.2.1.1 The Infrared Transmittance Approach

One obvious method of minimizing the path-length of the spectroelectrochemical cell is to employ a “transparent” electrode, such as a metal minigrid, as the working electrode, and sandwich it between two infrared transparent windows; the counter electrode and the reference electrode are then placed in the inlet/outlet tubes of the cell, or embedded in the thin section of cell wall between the two windows. Such a cell is termed an optically transparent thin-layer electrolyte (OTTLE) cell [20, 37]. However, this approach is insensitive to changes occurring at, or very near, the electrode surface, and so is usually employed to study the electrochemistry of solution species, formed via electrolysis [20, 37]; moreover, the very high attenuation of infrared light by water has so far prevented any significant exploitation of the approach in the study of aqueous electrochemical species, (although see Ref. [38] and Sect. 3.5.5.2 below).

3.5.2.1.2 The Infrared Internal Reflectance Approach

An interesting alternative method of minimizing the solution path-length is to employ internal reflectance or attenuated total reflectance (ATR) and this was the approach adopted by the authors of the first report on the acquisition of in situ infrared spectra; Mark and Pons [39] employed the ATR approach, [or, as they termed it, frustrated multiple internal reflection (MIR) – see below], to

study the electroreduction of 8-quinolinol and the tetramethylbenzidine free radical in dimethylformamide (DMF).

Internal reflection approaches rely upon the total reflection of the infrared beam one or more times, (*multiple* internal reflection, MIR), at the internal surface of an infrared transparent crystal or internal reflection element (IRE) such as Ge, Si, GaAs, or ZnSe, Medium 1 in Fig. 1(a)(i and ii). If the IRE is a semiconductor such as Ge, Si, or GaAs, it can serve as the working electrode, which was the case in the work of Mark and Pons, who employed a Ge IRE. More recently, Chazalviel and coworkers have published extensive and detailed studies on the GaAs, Ge, and Si electrolyte interfaces, (see, for example, Refs. [35, 40, 41]), using the semiconductor of interest as the IRE/working electrode.

For more general applications, the IRE is coated with a thin metal film, typically ca. 20 nm [26], Medium 2 in Fig. 1(a), and Medium 3 is the electrolyte. At angles of incidence greater than the critical angle, θ_c , total internal reflection occurs at the point of incidence on the inner surface of the IRE. In both the 3- and 2-layer cases, the critical angle is given by:

$$\theta_c = \sin^{-1} \left(\frac{n_{\text{elec}}}{n_{\text{IRE}}} \right) \quad (1)$$

where n_{elec} and n_{IRE} are the real parts of the refractive indices of the electrolyte and IRE, respectively. At the point of incidence, the incident and reflected infrared rays superimpose to form a standing, nonpropagating, or “evanescent” wave that decays exponentially out from the crystal surface, through the metal layer and out into the electrolyte (Fig. 1a). Both the electrolyte and the metal layer will damp the evanescent wave by absorbing energy from it; in a particular medium, the thickness over

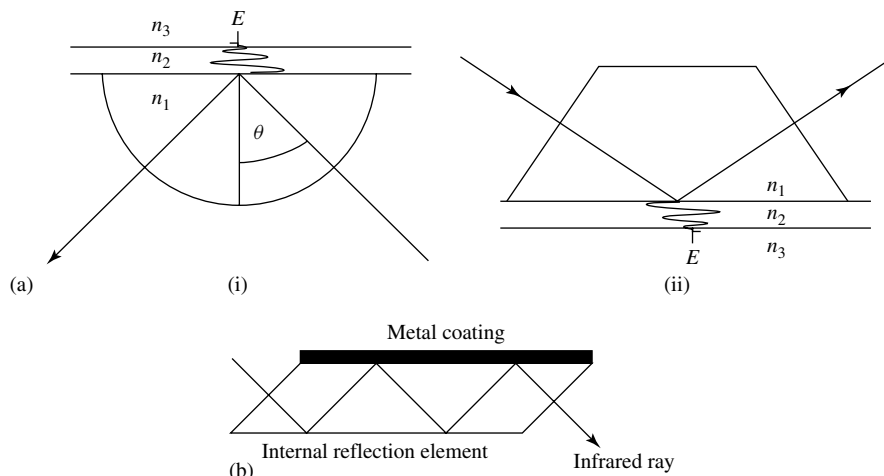


Fig. 1 (a) Schematic representation of the Kretschmann configuration ATR approach. Medium 1 is the single-reflection hemispherical (i) or (ii) Dove prism, Medium 2 is the thin metal overlayer, and Medium 3 is the electrolyte. (b) Schematic representation of the experimental arrangement employed in MIR.

which the intensity of the evanescent wave decays to $1/e$ of its value at the interface nearest the crystal is termed the *penetration depth*, τ ; for an absorbing medium such as a copper overlayer, the complex refractive index \tilde{n}_{Cu} is given by:

$$\tilde{n}_{\text{Cu}} = n_{\text{Cu}} - ik_{\text{Cu}} \quad (2)$$

and $n_{\text{Cu}} = 3$, $k_{\text{Cu}} = 30$ giving $\tau = 500 \text{ \AA}$ [4] at a wavelength of $5 \mu\text{m}$, that is 2000 cm^{-1} . Hence, it is crucial to ensure that the metal working electrode layer, whilst being thick enough to ensure metallic conduction, is not too thick that the evanescent wave is sufficiently damped it cannot sample the electrode–electrolyte interface. The difficulties associated with metal deposition, and with recycling the expensive IREs once the metal coating requires replacing, may explain the lower activity in research in this area compared to external reflectance infrared, (see in the following text).

The penetration depth of the evanescent wave into the electrolyte for in situ ATR infrared experiments is generally taken as ca. $\lambda/10$; on this basis, in the region of the O–H stretch of liquid water, $\epsilon = 55 \text{ mol}^{-1} \text{ dm}^3 \text{ cm}^{-1}$ [42], an absorbance of <0.1 would be expected, and this is the essence of the application of ATR techniques in in situ infrared spectroscopy.

ATR is highly surface sensitive, and this sensitivity may be further enhanced in two ways: 1. increase the effective path-length by employing thin IREs in which the infrared beam suffers MIR (Fig. 1b), and the effective path-length τ_{eff} is then given by:

$$\tau_{\text{eff}} = N\tau \quad (3)$$

where N is the number of internal reflections at which the evanescent wave probes the electrolyte, 2. Employ a thin metal overlayer and excite surface plasmon polaritons (SPPs) in the metal film [43] using the “Kretschmann” configuration [44], as shown in Fig. 1(a)(i and ii).

SPPs are collective electronic excitations at metal surfaces, which can be excited providing certain conditions are met [45]. By employing a Kretschmann configuration ATR cell, SPP excitation may be achieved by infrared illumination through the IRE, and the strong electromagnetic fields associated with this excitation provide a sensitive probe of the metal film–electrolyte interface, with tenfold enhancements in sensitivity being claimed over the more conventional external reflectance method [46] (see in following text). However, the presence of an infrared absorbing medium, such as water, would be expected to damp SPP excitation, and this has been modeled by Sass and coworkers [43]. The Kretschmann configuration was initially exploited for *in situ* infrared measurements by Sućetaka and coworkers [47] and Sass and coworkers [48].

Over recent years, internal reflectance infrared studies have tended to concentrate on the study of relatively “thick” films of conducting polymers or layers, (see, for example, the work of Pham and coworkers [49, 50], or Kvarnström, Nauer, Neugebauer and coworkers [51–54]) in which sensitivity was not a particular problem, or on the semiconductor–electrolyte interface, (see the work of Chazalviel and coworkers [35, 40, 41]), in which the SPP excitation approach is not appropriate. However, interest has focused again on this phenomenon with the surface-enhanced infrared absorption spectroscopy (SEIRAS) studies of Osawa and coworkers [19, 26, 27, 46, 55, 56], who have combined the application of the Kretschmann configuration with step-scan FTIR spectroscopy to study fast, reversible electrochemical processes on timescales down to microseconds [26, 46, 57–60].

3.5.2.1.3 The External Reflectance Approach

This is the most exploited *in situ* infrared approach, and simply involves trapping a thin layer of electrolyte, ca. 1–25 μm , between the polished, reflective working electrode and an infrared transparent window such as CaF_2 , ZnSe , and so on. One such cell, developed in Newcastle, is shown in Fig. 2 [31, 32], which allows the collection of *in situ* infrared data as a function of temperature [31]. Both plate and prismatic windows are employed, with the latter offering significant advantages in signal-to-noise, (S/N , see in following text), ratio. In contrast to the ATR approach, both the transmittance and external reflectance methods offer poor RC characteristics, and so are not suitable for the study of fast redox processes.

Although the solvent absorption can be reduced to some extent by applying one of the above techniques, it is generally still strong and needs to be annulled if the weak absorptions of near-electrode species are to be “picked out”, as do the detector response and the source emission envelope. This takes the discussion into the methods employed to solve the second major problem, that of sensitivity.

3.5.2.2 The Sensitivity Problem

The data collection protocol employed to “pick out” the absorptions of interest is generally a “difference” data manipulation, which varies according to the type of spectrometer employed. The early *in situ* infrared studies were carried out using dispersive infrared spectrometers with their attendant low power sources and noisy detectors. The simplest approach to the sensitivity problem is exemplified by the first *in situ* infrared paper by Mark and Pons [39], which reported a study of the reduction of 8-quinolinol solution by electrolysis at -1.8 V until sufficient

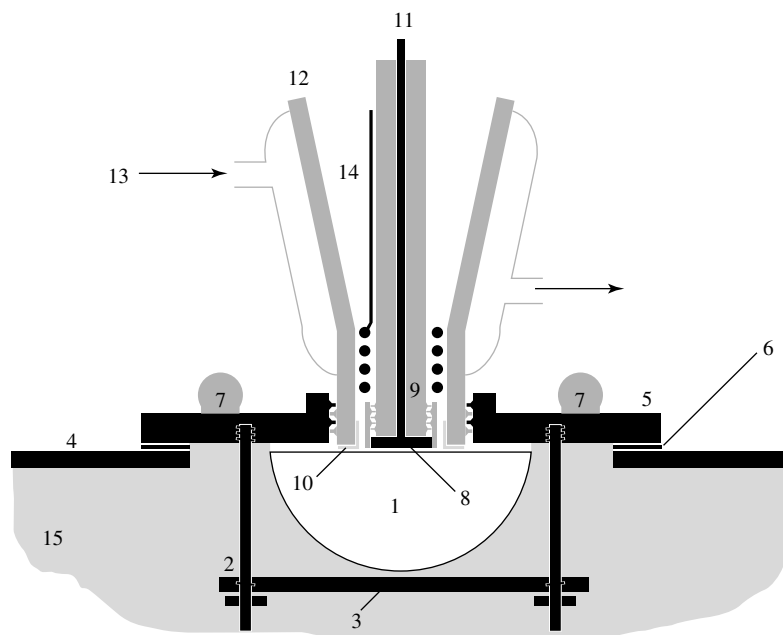


Fig. 2 Schematic representation of the in situ variable temperature FTIR spectroelectrochemical cell: (1) hemispherical CaF_2 window; (2) retaining plate + bolts for window; (3) Teflon cushion; (4) sample compartment lid; (5) cell mounting plate; (6) magnetic seal; (7) power resistors ($\times 4$); (8) reflective working electrode; (9) Teflon cell body; (10) Teflon seal; (11) working electrode connection and thermocouple leads; (12) glass cell body; (13) cooling/heating water inlet to cell jacket; (14) counter-electrode; and (15) spectrometer sample compartment. The reference electrode and cell inlet/outlet ports are not shown for clarity.

product, which the authors postulated was dihydro-8-quinolinol, had been produced to give product bands having relatively large absorbances of ca. 0.3 in the 1000 to 1200 cm^{-1} spectral region. A similar approach was adopted by Tallant and Evans [61] in their study of the electrochemical reduction of *p*-benzoquinone at a Ga-doped Ge IRE in DMSO.

3.5.2.2.1 The Lock-in Detection Approach

The sensitivity problem has been more generally addressed, particularly where adsorbed species were of interest, by exploiting the noise and instrumental drift-reducing capabilities of the lock-in

detection approach. In this approach, the potential at the working electrode is modulated, usually as a square wave at ca. 10 Hz, and the detector “locked in” to the frequency of this modulation; in this way, only the signal (and tiny component of the noise) modulated at the preset frequency is measured. The wavelength of the light reaching the detector is then scanned across a preset spectral range until the spectrum is complete. The external reflectance variant of this approach was termed electrochemically modulated infrared spectroscopy (EMIRS) [62, 63], and the data were generally presented as $(\Delta R/R)$ versus $\bar{\nu}$, where ΔR is the

difference between the intensity of light reaching the detector (reflectivity) at two potentials at each wavelength increment. ΔR is given by:

$$\Delta R = R_{(E+\Delta E)} - R_{(E-\Delta E)} \quad (4)$$

where $\pm\Delta E$ is the width of the potential modulation. The normalizing factor, R , was the difference in reflectivity between the electrode pulled back from the cell window to that pressed against the window. In the case of weak absorptions, the signal-to-noise ratio, S/N , could be increased by increasing the time over which ΔR was measured at each wavelength increment, since S/N increases as $\sqrt{t_m}$ [64], where t_m is the measurement time. The advantage of lock-in detection is that it is, in principle, highly sensitive, with the detection of relative reflectance changes ($\Delta R/R$) of ca. 10^{-5} [48] or even 10^{-6} [65] being claimed.

Lock-in detection was employed with both the internal and external reflectance approaches; although the early internal reflectance studies were generally straightforward investigations of electrolysis products [39, 61, 66, 67], the lock-in technique was employed where sensitivity was a problem, for example, to study the semiconductor–electrolyte interface [68] and metal–electrolyte interface [43, 48], with the sensitivity being further enhanced as necessary by employing a Kretschmann configuration ATR cell [44, 47, 48, 69]. In the latter studies, the potential modulation range, $2\Delta E$ in Eq. (4), was typically 10 to 100 mV, such that the spectra were described as being collected at potential E . In the analogous external reflectance EMIRS experiments, larger potential modulation ranges tended to be employed, of ca. 50 to 450 mV [70, 71].

Possibly one of the most critical in situ infrared experiments in establishing the importance of the in situ infrared

approach in the determination of electrochemical mechanisms was the paper by Beden and coworkers in 1981 on methanol electro-oxidation at Pt in acid electrolyte [71]. This paper sought to address a fundamental problem then extant in electrocatalysis, which was the identity of the poison formed during the chemisorption of methanol at Pt [72]. During methanol electro-oxidation at Pt in acid, the electrode is rapidly poisoned by the formation of a strongly adsorbed species that blocks the catalyst surface, and by the late 1970s, the two most likely candidates for this poison were adsorbed CO [73] or adsorbed COH [74]. In the EMIRS experiments reported by Beden and coworkers, the potential of the reflective Pt working electrode was modulated between +0.05 and +0.45 V versus normal hydrogen electrode (NHE) at a frequency of 8.5 Hz, that is, ΔR in Eq. (4) was $R_{(0.45 \text{ V})} - R_{(0.05)}$. The authors could not hope to interpret any spectral features attributable to irreversible reactions with certainty, because of the nature of the data collection process, but the technique may pick up absorption changes due to the adsorbed poison. The spectrum that Beden and coworkers obtained is shown in Fig. 3; the data collection and manipulation protocol results in *difference* spectra in which peaks pointing *up*, to $+\Delta R/R$, correspond to the loss of absorbing species as the potential is stepped from its reference value, (in this case +0.05 V), whilst peaks pointing *down*, to $-\Delta R/R$, correspond to the *gain* of absorbing species as the potential is stepped. On the basis of gas phase measurements, the band near 1850 cm^{-1} was assigned by the authors to the loss of bridge-bonded $\text{Pt}_2\text{C}=\text{O}$ on stepping from 0.05 to 0.45 V, whilst the bipolar band centered near 2070 cm^{-1} was attributed to

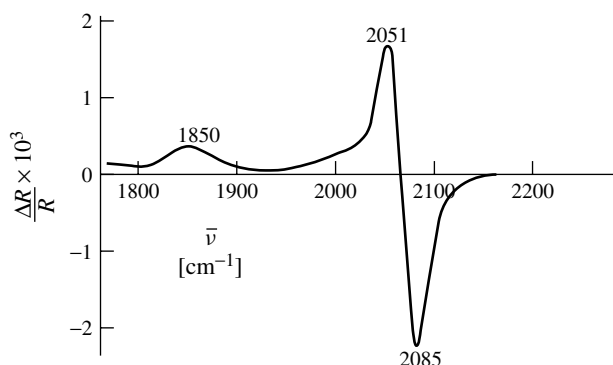


Fig. 3 EMIRS spectrum from a Pt electrode immersed in 1 M H_2SO_4 and 0.5 M CH_3OH . Potential modulation from 0.05 to 0.45 V versus NHE at 8.5 Hz. Scan rate was $0.0127 \mu\text{m s}^{-1}$. (From Beden and coworkers, Ref. [71] (see text for details).)

linearly bound $\text{Pt}-\text{C}\equiv\text{O}$. The bipolar nature of the band was interpreted in terms of a potential-dependent frequency shift with the energy of the $\text{C}\equiv\text{O}$ stretch being higher at more positive potentials; one later interpretation of this phenomenon [75] was that the electron back-donation into the $\text{C}\equiv\text{O}$ $2\pi^*$ levels is decreased as the electrode potential is made more positive.

The work by Beden and coworkers showed that, under the conditions of their experiment, there was a substantial coverage of adsorbed CO on Pt, which could be induced by the adsorption of CO gas directly, or via the adsorption of a range of organic molecules. In addition, they showed that the nature of the adsorbed CO, including the proportion of bridged to linear forms, is extremely sensitive to the crystal face of the Pt exposed to the electrolyte; they were then able to provide the outlines of an explanation as to why different single crystal surfaces of Pt show such markedly different activities towards the electrochemical oxidation of methanol [72, 76–78].

The success, and hence importance, of the experiment depicted in Fig. 3 lies

in the fact that the *irreversible* electro-oxidation of methanol resulted in an adsorbed fragment, $\text{C}\equiv\text{O}$, which showed a totally *reversible*, potential-dependent frequency shift that was able to respond fast enough to the frequency of the imposed potential modulation. However, the instrumentation is relatively complex compared to modern, straightforward FTIR methods, and is limited to the study of fast, reversible electrochemical systems; moreover, the spectra obtained using the technique were often of a lower quality than would be obtained using in situ FTIR methods [79]. Consequently, the EMIRS approach has been almost completely superseded by techniques based upon the application of FTIR spectrometers.

A second lock-in detection method that was employed is polarization modulation, which involves modulating the polarization state of the incident infrared beam, and is again an extension of an approach developed for the study of the gas–solid interface [80]. Polarization modulation infrared reflection–absorption spectroscopy (PM-IRRAS) relies upon the principles underlying the surface selection rule

(SSR) [4, 5, 81, 82], which is an important additional selection rule in infrared spectroscopy; thus, polarized light incident upon a reflective metal electrode surface can be thought of as comprising two perpendicular components (Figs. 4a and b), a component polarized such that its electric vector E_s vibrates perpendicular to the plane of incidence, (Fig. 4a), and a component vibrating parallel to the plane of incidence, E_p . On reflection, the incident and reflected rays interfere to set up a standing wave at the surface, (see, for example, Ref. [4]), the s-polarized component of which has a zero intensity at the surface, and a very small intensity over a distance up to that comparable to the wavelength of the incident infrared radiation, depending upon the reflectivity of the surface and any attenuation by the

solvent. Hence, if the surface is covered with an adsorbed layer whose thickness is small compared to the wavelength of the incident infrared light, then s-polarized light will be effectively “blind” to the adsorbate, as well as to any species in the near-electrode region, and will be attenuated only by any chromophores in the bulk of the solution. In contrast, p-polarized light is sensitive to species in the bulk and near-electrode regions of the electrolyte, as well as any adsorbed species, providing that the vibrations of the latter have a significant component of the dipole change perpendicular to the surface [4, 81, 82]; any infrared transitions associated with vibrations parallel to the surface will not be sampled by p-polarized infrared light, the intensity of such absorptions increase as $\cos^2 \theta$, where θ is the angle between the

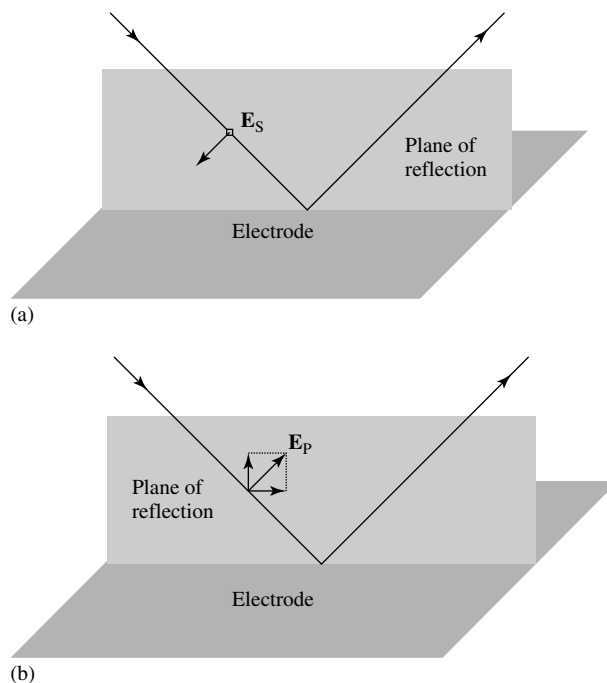


Fig. 4 Schematic representations of: (a) s- and (b) p-polarized light, incident at a reflective electrode surface.

vibration-induced dipole change and the oscillating electric vector of the incident infrared beam [83]. Thus, a molecule such as pyrene will, in principle, show strong infrared absorptions if adsorbed with the plane of the molecule perpendicular to the surface, but extremely weak absorptions if adsorbed flat. By studying an electrochemical reaction using s- and p-polarized infrared light, and applying the SSR, it should allow those species that are adsorbed, as opposed to those in solution, to be identified, and their orientation at the electrode deduced. Moreover, the intensities of the infrared absorptions of any adsorbed species may be enhanced by employing an angle of incidence as close as possible to the “Greenler angle” [5, 81, 82] of ca. 88° , where the absorption of the p-polarized light is at a maximum, that is up to $5000\times$ that at normal incidence [84]. High angles of incidence can be achieved at the electrode surface by employing hemispherical or Dove prisms, (Fig. 1(a)(i and ii)), as the cell windows [5]. Lipkowski and coworkers have elucidated the quantitative aspects of the SSR in an elegant series of papers [83, 85].

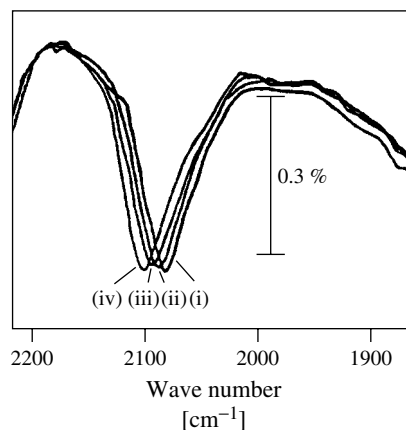
PM-IRRAS exploits the different attenuation of s- and p-polarized light by adsorbed species at a reflective (electrode) surface to annul the unchanging contributions to the infrared signal at the detector from the solvent, window, and so on, and produces an *absolute* rather than *difference* spectrum at a particular potential. In this approach, a photo-elastic modulator is employed to modulate the polarization state of the incident infrared ray between s- and p-states. On the basis of Greenler’s theory [81, 82], this polarization modulation gives rise to an AC signal at the detector, which is proportional $(I_p - I_s)$ – the difference in intensity of the two polarizations. Since, in principle, I_p is absorbed

by adsorbed species and solution species, and I_s only by solution species, $(I_p - I_s)$ contains the absolute spectrum of the adsorbed species at the electrode potential at which the spectrum was obtained. The incident light is also chopped mechanically to provide a normalizing factor, $(I_p + I_s)$, such that the final spectrum consists of a plot of $(I_p - I_s)/(I_p + I_s)$ versus $\bar{\nu}$.

PM-IRRAS data have been reported using both dispersive [86, 87] and FTIR spectrometers [88–90]. One of the earliest applications in electrochemistry was reported by Russell and coworkers [87], who employed the technique to substantiate the theory that the bipolar band observed by Beden and coworkers [71] in their EMIRS experiment on the electro-oxidation of methanol was due to $\text{Pt}-\text{C}\equiv\text{O}$ shifting its frequency as the potential was altered. The absolute spectra obtained by the authors clearly showed the monopolar $\text{Pt}-\text{C}\equiv\text{O}$ feature increasing in frequency as the potential of the Pt electrode was increased (Fig. 5).

The PM-IRRAS approach was employed in a large number of studies, but again has not been exploited as intensively as the more straightforward FTIR methods; this may be due to the complexity of the instrumentation required and/or for a second reason an indication of which is the sharply curving baseline in Fig. 5. As was stated above, the standing wave intensity of s-polarized light not only has zero intensity at the electrode surface, but also a very small intensity over a distance out into the solution, (ca. $0.1\ \mu\text{m}$ [4]), which represents a significant, uncompensated (and wavelength-dependent) absorption. Kunitatsu and coworkers [88, 91] drew attention to this problem, and it became the practice to annul the uncompensated solution absorption by subtracting PM-IRRAS spectra collected at different

Fig. 5 PM-IRRAS spectra of linearly adsorbed CO at a Pt electrode immersed in 1 M HClO₄ saturated with CO. The electrode potential was: (i) 50 mV versus NHE; (ii) 250 mV; (iii) 450 mV; and (iv) 640 mV. (From Russell and coworkers, Ref. [87] (see text for details).)



potentials, as in the standard difference techniques [90]. This procedure effectively removes the primary perceived advantage of PM-IRRAS of providing “absolute” spectra; coupled again with the relatively complex instrumentation required, the approach is not now widely exploited when compared to the more straightforward in situ FTIR methods.

Before moving on, one important exception to the SSR is worth noting, which arose from the work of Bewick, Pons and coworkers [92, 93] on the adsorption of acrylonitrile, and the later work of Korzeniewski and Pons [94–96]. In essence, the work showed that the vibrations of an adsorbed molecule that are parallel to the electrode surface may become activated as a result of the electric field, and this was termed the *electrochemical Stark effect* [94–96]; as would be expected, this effect depends very strongly on the nature of the adsorbed molecule. Thus, for example, Pons and coworkers [96] observed a bipolar band centered near 1600 cm⁻¹ in the in situ infrared spectrum of anthracene on reducing it to its radical anion; the band was attributed to the A_g C–C symmetric stretch of the anthracene shifting to lower $\bar{\nu}$ on reduction. As the molecule adsorbs

flat, this absorption is forbidden on the basis of the SSR. Rather confusingly, the potential-dependent frequency shift of adsorbed species such as CO is often also referred to as the *electrochemical Stark effect* or *Stark tuning effect*.

The advent of affordable, research grade FTIR spectrometers was followed by a rapid increase in the amount and diversity of in situ infrared studies, essentially as a result of their inherently high sensitivity, and rapid spectral collection times. As well as effectively solving the sensitivity problem, FTIR spectrometers facilitated the application of simple data collection and manipulation methods, and consequently greatly increased the experimental protocols that could be employed.

3.5.2.2.2 The Application of FTIR Spectrometers In essence, the routine use of FTIR spectrometers has meant that in situ infrared spectroscopic studies requiring high sensitivity, such as the study of adsorbed species, were no longer limited to the fast, reversible electrochemical systems dictated by lock-in detection techniques; infrared spectra could be collected during a slow linear voltammetric sweep, during a series of potential steps to higher

or lower potentials, or as a function of time after a single potential step. More recently, the advent of step-scan FTIR spectrometers have heralded a return to the study of reversible systems, but at much faster timescales, that is on the order of microseconds (see the work of Osawa and coworkers [26, 46, 56–60]).

The operation of FTIR spectrometers has been described in detail elsewhere, (see, for example, Refs. [4, 64]), as have the “advantages” of these over dispersive instruments [4, 5, 64]. Briefly, the heart of an FTIR spectrometer is the Michaelson interferometer (MI) (Fig. 6). The infrared beam leaves the source, S, and is incident on a beam-splitter, B. Fifty percent of the light is transmitted to a moving mirror, MM, and 50% to a fixed mirror, FM. On reflection, these rays recombine and interfere at the beam-splitter before reaching the detector, D, via the window, W, and reflective working electrode, WE, of the spectroelectrochemical cell. The system also includes a reference laser, RL, which follows the same path through the interferometer, after which it is intercepted and directed at the laser detector, LD.

Monochromatic light, such as the laser beam, passing through the interferometer

gives rise to a signal at the detector as shown in Fig. 7(a), as a result of constructive and destructive interference. x is the *retardation*, or distance the moving mirror is away from zero path difference. A plot of intensity versus retardation is termed an *interferogram*. By counting the maxima (fringes) in the separately monitored laser signal, the position of the moving mirror at any time is accurately determined.

When multiple wavelengths, that is from the infrared source, enter the interferometer, the combination of a variety of frequencies and intensities produces an interferogram such as that shown in Fig. 7(b); that is, the intensity at the detector dies off rapidly as x increases.

The interferogram is actually a series of data points (retardation, intensity) collected during the smooth movement of the mirror. Using a mathematical function known as a *Fourier transform*, the spectrometer computer is able to deconvolute (“Fourier transform”) all the individual cosine waves that contribute to the interferogram, and so produce a plot of intensity against wavelength, or more usually the frequency in cm^{-1} ; that is, the infrared single beam spectrum. All the

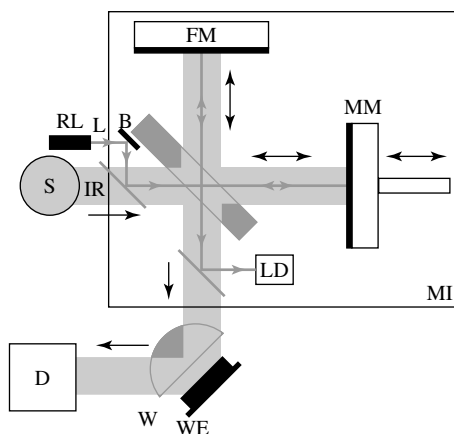
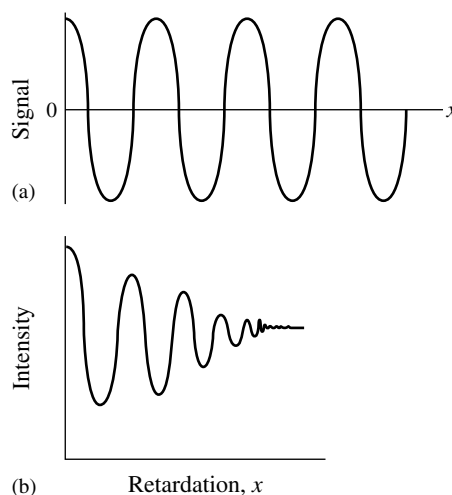


Fig. 6 Schematic representation of an FTIR spectrometer and spectroelectrochemical cell. B, beam-splitter; D, detector; FM, fixed mirror; IR, infrared beam; L, laser beam; LD, laser detector; MI, Michaelson interferometer; MM, moving mirror; RL, reference laser; S, infrared source; W, cell window; WE, working electrode.

Fig. 7 Schematic representation of the signal at the detector of an FTIR spectrometer using (a) a monochromatic source and (b) a “white” source.



retardation data points are necessary to obtain the spectrum.

In essence, the computational capacity of an FTIR spectrometer, and the accuracy of its laser referencing system, allows the coaddition and averaging of individual spectra, or “scans”, to produce spectra with improved S/N ; coupled with very rapid data collection times, routinely down to ca. 10 ms, and high throughput, (beam power in sample compartment typically ca. 100 mW), this means that a few seconds of data collection time are sufficient to generate a spectrum of sufficient sensitivity to detect adsorbed species at the electrode, a major goal since the 1980s. Thus, for example, Fig. 8 presents a spectrum [31] of CO adsorbed at a Ru(0001) electrode in 0.1 M HClO_4 [32] at 10°C ; the spectrum was collected at 0.2 V versus Ag/AgCl and normalized to the reference

taken at -0.2 V. The two bipolar bands in the figure, due to the potential-dependent shift in the frequencies of linearly adsorbed CO, (CO_L), and CO adsorbed at a threefold hollow site, (CO_H), have excellent S/N , despite the spectrum comprising only 16 scans and requiring ca. 3 s, representing a marked improvement over the data

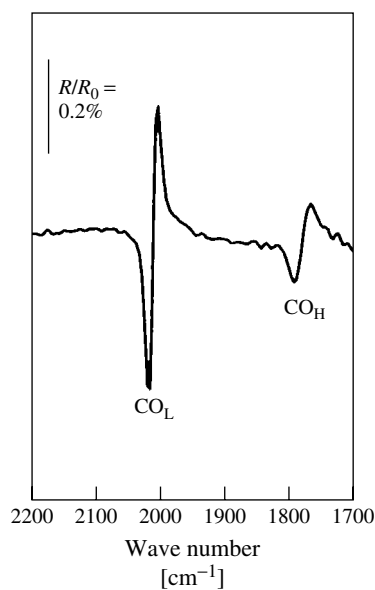


Fig. 8 An in situ FTIR spectrum of the CO adsorbate at a Ru(0001) electrode in 0.1 M HClO_4 at 10°C . The spectrum, comprising 16 coadded and averaged scans at 8 cm^{-1} resolution, was collected at 0.2 V versus Ag/AgCl and normalized to the reference taken at -0.2 V.

collection times of up to several hours required by the EMIRS approach.

Before proceeding to a consideration of data acquisition and manipulation protocols, it may be useful to review recent intensity-enhancement phenomena that have appeared in the literature, as these clearly have implications with respect to sensitivity, and hence data acquisition and manipulation.

3.5.3

Abnormal Infrared Effects, (AIRE), Surface-enhanced Infrared Spectroscopy, (SEIRAS), and Intensity Stealing Effects

In the early 1980s, despite the discovery of the surface-enhanced Raman (SER) effect [97] (see also Chapter 3.6 in this volume), there was no real expectation that such enhancement effects would be observed in *in situ* infrared spectra. That this was not necessarily to be the case could be gleaned from papers such as that by Christensen and coworkers [98] on the polymerization of thiophene at a Pt electrode in acetonitrile, who observed a somewhat more intense absorption than expected from the thiophene adsorbed on the electrode prior to polymerization. Recently, an increasing number of papers have appeared on AIREs, primarily from Sun and coworkers [99, 100] and SEIRAS, from Osawa and coworkers [19, 26, 46, 55, 58, 60, 101–106], a common factor of both effects is the enhancement of the infrared absorptions of adsorbed species.

3.5.3.1 **Abnormal Infrared Effects**

AIREs have been observed in the infrared spectra of adsorbates, CO and SCN^- , on thin metal films deposited on glassy carbon [99, 100], and are characterized by an inversion in the sign of the infrared band of the adsorbate and a change in

the shape of the band, in the form of a tail to lower energies, as well as a ca. $20\times$ enhancement in intensity [100]. The inversion in the sign of the infrared band in effect means that the spectrum shows the band as a *loss*, under the same experimental conditions in which it is a *gain* feature in the spectrum of adsorption at the bulk metal. Christensen and coworkers [107] reported such an effect in 1994 in *in situ* FTIR spectra collected during the electro-oxidation of methanol at small platinum particles deposited at a basal plane graphite, (BPG), electrode. The authors observed a bipolar Pt–C \equiv O band centered near 2055 cm^{-1} ; however, instead of the positive lobe occurring at a higher frequency than the negative lobe on stepping the potential more positive, as would be expected in terms of the decrease in back-donation to the π^* orbitals of the C \equiv O moiety, [for a discussion of the factors affecting the absorption frequency of adsorbed CO (see Refs. [31, 108]), the reverse was observed].

The result reported by Christensen and coworkers was in complete contrast to the significant literature concerning the electro-oxidation of small organic molecules at bulk Pt electrodes, which did not differ in terms of the Pt–C \equiv O from the first paper by Bewick and coworkers [71]. In fact, the band observed by Christensen and coworkers was not “bipolar”, but was clearly composed of a higher frequency loss feature, and a weaker, broader gain feature; that was not due to a potential-dependent frequency shift, but simply to the interchange/migration of adsorbed CO species at the surface as the potential was increased; this postulate was supported by the observation that the “bipolar” band was accompanied by the gain of a feature near 1820 cm^{-1} , which was attributed to multiply-bonded C=O. The fact that no

enhancement was observed, and that the spectral features could be interpreted in terms of a simple model argues against the presence of AIREs in the spectrum, and the work by Christensen and coworkers was the first to highlight the crucial role of CO migration to active sites, and that this may be rate limiting.

Gutiérrez and coworkers [109] have postulated that an infrared response such as that observed by Christensen and coworkers could be predicted in terms of a straightforward model based on Maxwell's equations; however, they could not carry

out any calculations, whilst calculations using the Fresnel equations and: $n = 1.25$ for water, $n = 10$ and $k = 15$ for Pt, $n = 2.3$ for carbon, (all at $4.6 \mu\text{m}$, data taken from Landolt-Bornstein, 6 Auflage, "Zahlenwerte und Funktionen", IIB 8 Teil), and $n = 1.3$ for carbon taken from Ref. [109], predicted no anomalous behavior.

The first report of an AIRE was by Sun and coworkers in 1997 [99] in a paper concerning the adsorption of CO at Pt and Pd thin layers dispersed on glassy carbon (GC). Figures 9(a) and (b) show spectra

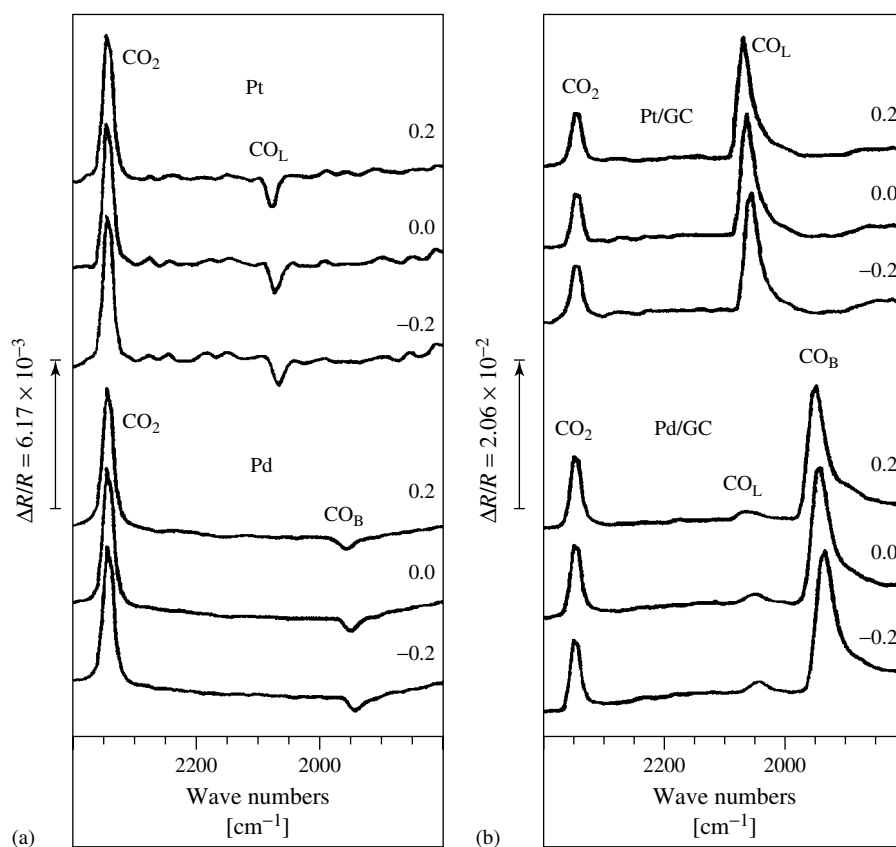


Fig. 9 In situ multiple step infrared spectra of: (a) CO adsorbed on smooth Pt and Pd electrodes and (b) CO adsorbed at Pt/GC and Pd/GC electrodes. The electrolyte was 0.5 M H_2SO_4 , and the reference spectrum was collected at +0.7 V versus SCE. (From Sun and coworkers, Ref. [99].)

collected during an experiment in which CO was adsorbed at (a) smooth Pt and Pd electrodes and (b) at Pt/GC and Pd/GC electrodes, after which the solution CO was removed and the potential stepped up from -0.2 V versus the saturated calomel electrode (SCE), with spectra being collected at each step. All the spectra were normalized to the reference spectrum collected at the end of the experiment at 0.7 V where all the adsorbed CO had been oxidized to CO_2 ; in effect, with respect to adsorbed CO species, the spectra in Figs. 9(a) and (b) are absolute spectra.

As expected, at the smooth electrodes, *gain* features attributed to both linearly adsorbed $\text{Pt-C}\equiv\text{O}$, CO_L , and bridged $\text{Pt}_2\text{C}=\text{O}$, CO_B , were observed, whose frequencies shifted to higher values as the potential was increased. At all four electrodes, the CO_2 feature near 2340 cm^{-1} was observed as a *loss* feature, due to the choice of reference spectrum. In contrast, at the thin film Pt/GC and Pd/GC electrodes, the CO_L and CO_B features appeared as *loss* features (Fig. 9b). Moreover, they were significantly more intense, showed a larger “Stark” shift and a larger full width at half maximum, (FWHM), than the corresponding features in the spectra of the bulk electrodes (Fig. 9a). This phenomenon was later given the acronym AIRE [100].

Sun and coworkers [99] showed that, even allowing for surface roughness, (1.2 and 1.6 for the Pd/GC and Pt/GC electrodes, respectively), the CO band intensities observed at the film electrodes was up to $20\times$ that observed at the bulk metal electrodes. In a later paper [100], the authors reported AIREs in the spectra of: CO adsorbed at thin films of Pt, Rh, and Pd supported on GC; of CO, SCN^- and poly-*o*-phenylenediamine at Pt/GC, (in the last

case, although the polymer absorptions were inverted, they were not enhanced), and CO at Pt/polypyrrole/GC and Pt at Pt/poly-*o*-phenylenediamine/GC, from which they concluded that the infrared absorption enhancement in AIREs is a localized effect, probably associated with the individual metal crystallites at the surface; it is clear that AIREs do not seem to depend on surface roughness and are not limited to the coinage metals Au, Ag, and Cu, unlike surface enhanced Raman spectroscopy (SERS) [5, 10]; however, the mechanism responsible for AIREs remains unclear [100].

3.5.3.2 Surface-enhanced Infrared Effects

The (nonelectrochemical) SEIRAS effect was first reported by Hartstein and coworkers in 1980 [110], after which Suëtaka and coworkers published a number of papers from 1982 exploiting Kretschmann coupling (Fig. 1a) to effect SPP excitation and the concomitant enhancement of the infrared absorptions of species adsorbed at the thin metal film electrode surface [69, 111–113], effectively SEIRAS. The authors commented that the short-range enhancement afforded by the technique enabled species at the metal–aqueous solution interfaces to be “preferentially observed”. Similarly, Neff and coworkers [48] reported the study of water at the electrode–electrolyte interface using SPP excitation. As with the SERS effect, SEIRAS is limited, so far, to the coinage metals [5, 10].

In 1991, Osawa and coworkers [101] employed the acronym SEIRAS to describe the Kretschmann coupling ATR technique, and have published a number of papers reporting the exploitation of the phenomenon along with step-scan interferometry (see Sect. 3.5.4.1.4) to study fast surface processes. As with

AIREs, SEIRAS spectra show marked enhancement of the infrared absorptions of adsorbed species, up to $40\times$ that expected on a smooth, bulk metal electrode. Thus, Sun and coworkers [106] investigated the adsorption of CO at thin Au films evaporated onto a hemispherical Si prism, and observed a $20\times$ enhancement over that expected at a conventional electrode; this increased by a further factor of two when the Au film electrode was flame-annealed to generate a highly ordered Au(111) surface, observed using ex situ scanning tunneling microscopy (STM).

The origin of the SEIRAS effect is still not completely understood [100], but understandable comparisons are being drawn with the electromagnetic (EM) theory [10] of the SERS effect.

3.5.3.3 Intensity Transfer Effects

In 1994, Villegas and Weaver [114] reported an elegant combined STM, and in situ FTIR study of CO adsorption at the Pt(111) electrode surface; this is a key paper in the area of in situ infrared spectroscopy. The work essentially showed that, in CO-saturated aqueous HClO_4 , the spatial structure of the compressed CO adlayer undergoes a phase transition from a close-packed (2×2) -3CO adlayer, ($\theta_{\text{CO}} = 0.75$), at potentials <0 V versus SCE, to a $(\sqrt{19} \times \sqrt{19})\text{R}23.4^\circ - 13\text{CO}$ unit cell structure, ($\theta_{\text{CO}} = 13/19$), at potentials between 0 V and the onset of CO oxidation at ca. 0.25 V. The STM data were supported by the infrared data in terms of the changing distribution of linearly adsorbed CO, (CO_L), and CO adsorbed at doubly bridging, (CO_B), and threefold hollow sites, (CO_H).

The key point of the paper may be drawn from the STM and infrared data on the

(2×2) -3CO adlayer observed at potentials <0 V, the structure of which is depicted schematically in Fig. 10 and consists of $1 \times \text{CO}_\text{L}$ and $2 \times \text{CO}_\text{H}$ per unit cell. Qualitatively, the infrared data were consistent with the structure in Fig. 10, since the spectra showed two CO_ads bands at potentials at which the STM data suggested the presence of the (2×2) -3CO adlayer, corresponding to CO_L and CO_H species, (that is bands at ca. 2066 and 1773 cm^{-1} , respectively, at -0.25 V). However, whilst the (2×2) -3CO structure contains a 1:2 ratio of CO_L to CO_H sites (Fig. 10), the ratio of the integrated intensities of the 2066 to 1773 cm^{-1} bands observed in the infrared spectra was ca. 2:1. This was interpreted by the authors as being due to intensity transfer, by which a higher frequency absorption of a species gains intensity at the expense of a lower frequency band [115, 116]. Using the dipole-coupling model of Persson and Ryberg [115], Villegas and Weaver were able to predict substantial intensity transfer from the CO_H to CO_L bands, in semiquantitative agreement with their experimental data. Thus, the authors showed that significant intensity transfer effects can occur between arrays of CO oscillators located in distinct, nearby sites, even when their frequencies are relatively far apart, (that is *c.* $200\text{--}300 \text{ cm}^{-1}$). The extent of intensity transfer will depend upon many factors, but was expected to be greatest for compressed monolayers.

This is a crucial paper in the field of in situ infrared spectroscopy, not simply because it reports an interesting observation, or since it elegantly shows the synergy between STM and in situ infrared, but as a result of its important, wider ramifications for the study of the electrode–electrolyte interface.

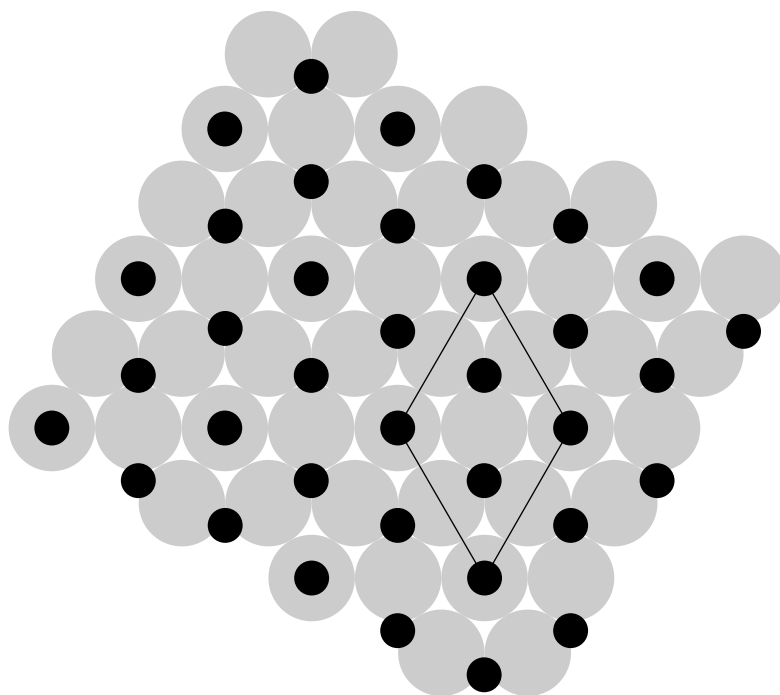


Fig. 10 The unit cell of the (2×2) -3CO surface adlayer on Pt(111), (redrawn from Ref. [114]).

3.5.4

The Practicalities of In situ FTIR Spectroscopy

3.5.4.1 Data Collection and Manipulation Protocols

3.5.4.1.1 Simple Potential Step Difference

Manipulations As was stated above, in order to “pick out” the potential-dependent, weak absorptions due to near-electrode and/or adsorbed species, those contributions to the signal at the detector that do not change with potential or time such as the solvent, detector response, source emission envelope, and so on must be annulled. This is generally achieved by adopting a difference protocol for the spectral data collection, the simplest of which was employed in the first paper

on in situ FTIR spectroscopy by Pons and coworkers [117], and involves a single potential step (Fig. 11a). The reference spectrum, S_1 , is collected at the base potential, E_1 , the latter usually chosen to be in a region in which no Faradaic processes occur. The potential is then stepped into a region in which the process of interest occurs, which can be Faradaic (electron transfer) or non-Faradaic (for example, see Refs. [13, 118]), and the sample spectrum S_2 collected. S_1 and S_2 consist of an identical number of coadded and averaged scans at identical spectral resolution, (typically ca. 100 and 4 or 8 cm^{-1} , respectively). The data are then presented as:

$$(-)\text{Absorbance} = \log_{10} \left(\frac{S_2}{S_1} \right) \text{ versus } \bar{\nu} \quad (5)$$

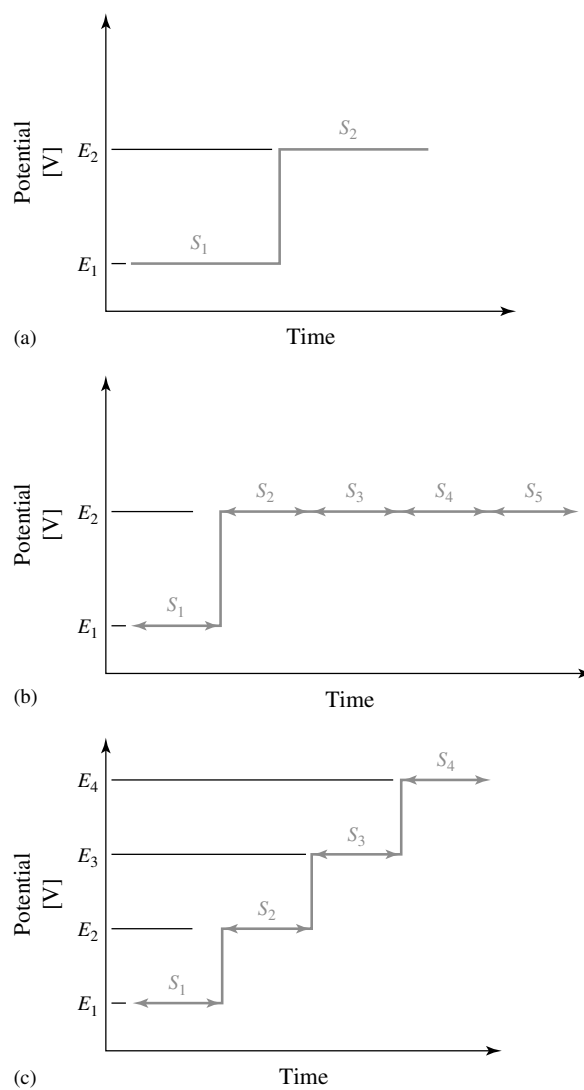


Fig. 11 Schematic representations of various in situ FTIR spectroscopy data collection protocols: (a) single step; (b) time-dependent; (c) “staircase”; (d) subtractively normalized interfacial Fourier transform infrared spectroscopy, SNIFTIRS; and (e) potential difference infrared spectroscopy, PDIRS.

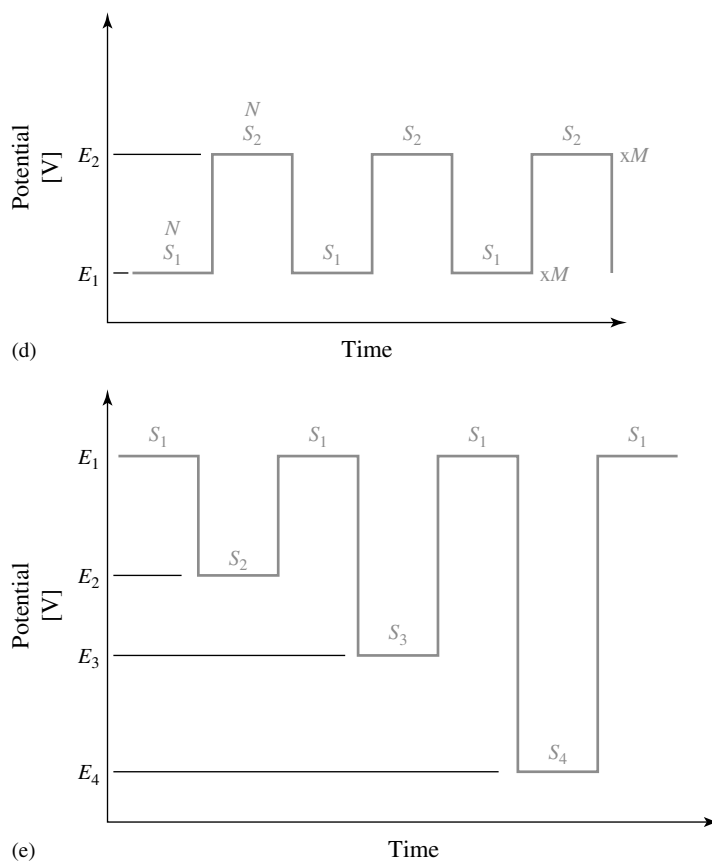


Fig. 11 (Continued)

$$\frac{\Delta R}{R} = \frac{(S_2 - S_1)}{S_1} \text{ versus } \bar{\nu} \quad (6)$$

$$\text{Reflectance} = \left(\frac{S_2}{S_1} \right) \text{ versus } \bar{\nu} \quad (7)$$

or

$$\text{Absorbance} = \log_{10} \left(\frac{S_1}{S_2} \right) \text{ versus } \bar{\nu} \quad (8)$$

All the data manipulations represented by Eqs. (5 to 8) result in difference spectra; in the case of the spectra produced using Eqs. (5 to 7), peaks pointing *up*, to + (–) *Abs.*, + *Refl.* or + $\Delta R/R$, are due to species whose concentration in the optical

path *decreases* at E_2 cff. E_1 , whilst peaks pointing *down* are due to species whose concentration *increases*. In the case of the difference spectra produced using Eq. (8), the convention is reversed. The number of coadded and averaged scans collected at E_1 and E_2 is chosen to give the required S/N ; this can range from ≤ 10 [32] to > 1000 [106, 119, 120].

The rapid data collection times of modern FTIR spectrometers allow irreversible reactions to be followed with time resolutions down to ca. 10 ms using the simple data collection protocols depicted in Figs. 11(a) and (b); in the

approach depicted in Fig. 11 (b), the potential is stepped up or down from the base potential E_1 to E_2 , and a series of sequential spectra, S_n , are then collected at E_2 , such that any process taking place at E_2 is monitored as a function of time. The short timescales are achieved at the expense of signal averaging, and so rely upon either strong chromophores, or enhancement via the Surface-Enhanced Infra Red (SEIR) effect discussed in Sect. 3.5.3; thus, Osawa and Yoshii [46] followed the reduction and reoxidation of 1,1'-di heptyl-4,4'-dipyridinium (heptyl viologen, MV^{2+}) at a Ag-coated Ge hemicylindrical prism with a 0.6 s data acquisition time by exploiting SEIRAS. Spectra were collected during the acquisition of a cyclic voltammogram, recorded at a scan rate of 10 mV s^{-1} ; this experimental protocol was earlier termed *SPAIRS* (single potential alteration infrared spectroscopy) by Weaver and coworkers [121] (see Sect. 3.5.4.1.3 in the following text).

Figures 11(a) and (b) are somewhat simplified as they do not show the time taken to transform the coadded and averaged (or single) interferograms (scans) into the resultant single beam spectra. Admittedly, this is typically only ca. 1 to 3 s, and is no problem when studying relatively slow reactions over minutes [122, 123], but is significant over a timescale such as that employed by Osawa and Yoshii [46]. However, modern FTIR spectrometers have the facility through the “kinetics” option to collect a large number of individual interferograms sequentially and to store them individually. At the end of the experiment, the individual interferograms can be retrieved and transformed, after which coaddition and averaging can be carried out or not, as required. This then

allows true time resolution down to that required for a single scan, ca. 10 ms.

The data acquisition protocols depicted in Figs. 11(a) and (b), as well as the “staircase” method shown in Fig. 11(c) are quite commonly employed [98, 124–126]. In the latter case, the potential is stepped to sequentially higher or lower values, spectra collected at each step and normalized to the reference spectrum, usually taken at the start or end of the experiment. As a result of the fact that the FTIR spectrometer allows the single beam spectra collected during any data acquisition protocol to be retained along with any normalized or otherwise manipulated spectra, the most suitable “reference” spectrum can be selected at the end of the experiment, usually after some preliminary manipulation. Thus, Lin and coworkers [31, 32] have investigated the adsorption and electro-oxidation of CO at Ru(0001) and, by selecting the spectrum collected at +1100 mV at the end of a stepping experiment from –200 mV as the reference, the authors were able to obtain “absolute” rather than difference spectra in the spectral region in which $\text{Pt-C}\equiv\text{O}$ absorbs, as all the adsorbed CO was stripped from the surface by the time the reference spectrum was collected.

It has been found that normalizing the spectra collected during a potential step or time-dependent experiment to the spectra collected at several different potentials or times during the experiment can be invaluable in elucidating complex mechanisms [127–129], particularly in the study of charge transport processes and so on in conducting polymers [98, 125, 130]. Thus, consider the following processes taking place at an electrode, for example the formation of polarons, bipolarons, or other charge carriers in a conducting polymer [131]:

$$A \longrightarrow B \quad (9)$$

$$B \longrightarrow C \quad (10)$$

$$C \longrightarrow D \quad (11)$$

If the data acquisition protocol depicted in Fig. 11(c) is employed, and process (9) is over by potential E_3 , (10) commences at E_3 but is over by E_6 , after which (11) begins, then four sets of spectra normalized to three different reference spectra would provide sufficient information to enable a clear picture of the processes taking place to be constructed. Thus, all the spectra collected at potentials $>E_1$ are normalized to the spectrum taken at E_1 ; the spectra collected at E_2 and E_3 are normalized to that taken at E_1 ; the spectra taken at E_4 to E_6 are normalized to that taken at E_3 , and the spectra collected at potentials $>E_6$ are normalized to that taken at E_6 . In situ infrared spectra of conducting polymers are usually dominated by broad and intense features extending from ca. 1600 cm^{-1} out into the near-infrared above 6000 cm^{-1} , (typically the upper spectral limit for most research grade FTIR spectrometers), due to low-lying electronic transitions [98, 132], and the potential variation of this feature can be employed to give a good indication of the potentials at which such changes in behavior occur [125].

3.5.4.1.2 Subtractively Normalized Fourier Transform Infrared Spectroscopy and Potential Difference Infrared Spectroscopy In 1983, Pons [133] reported a slightly more sophisticated data acquisition protocol, which he termed SNIFTIRS (subtractively normalized interfacial Fourier transform infrared spectroscopy), which involved stepping the potential of the reflective working electrode repeatedly between two preset values, as shown in Fig. 11(d). The

scans collected at the sample potential, E_2 , are coadded and averaged, as are all the spectra collected at E_2 ; the resultant S_2 is then normalized to all the spectra taken at the base potential E_1 , S_1 , according to Eq. (6) mentioned above. The number of scans, N , collected at each step is kept low to minimize the effects of instrumental drift, whilst the required S/N is achieved through the number of steps M . In order to allow some settlement time, spectral acquisition can be delayed for a period after the potential step [134, 135], and/or the potential can be ramped rather than stepped between spectral acquisitions, for example, to protect the surface structure of single crystal electrodes [136].

The SNIFTIRS approach is clearly related in some ways to the EMIRS technique, in that it does involve potential modulation, (but not lock-in detection), albeit at a much lower frequency; ca. 0.01–to 0.02 Hz [83, 85, 137], than the ca. 10 Hz typically employed in EMIRS experiments. Consequently, SNIFTIRS is also restricted to electrochemical systems that are essentially *reversible over the timescale of the potential modulation*, but has proved extremely sensitive, and is generally reported as being surface specific, only detecting potential-induced changes in adsorbed species [119, 138]. One specific exception to this generalization is where E_1 and E_2 are chosen such that the species of interest are fully adsorbed at one potential, and fully desorbed at the other potential [16, 85]. This led Weaver and Corrigan [139] to coin the general acronym PDIRS, for those approaches that involve multiple reference spectra as well as multiple sample spectra. Thus, Fig. 11(d) is an example of the PDIRS approach, as is Fig. 11(e), in which the sample potential is sequentially decreased

(or increased) after each step back to the base potential and a new reference spectrum collected [121, 140].

3.5.4.1.3 Single Potential Alteration Infrared Spectroscopy Single reference/multiple sample protocols were termed single potential alteration infrared spectroscopy (SPAIRS) by Weaver [121]. Such an experiment usually involves collecting the reference spectrum at the beginning or end of the experiment; in the former case, the potential is slowly ramped (ca. 1 mV s^{-1}) up or down from the base potential and spectra collected sequentially during the voltammetric sweep [109, 141–143]. This approach is sometimes referred to as linear potential sweep (LPS), or linear sweep voltammetry (LVS), -SPAIRS.

3.5.4.1.4 Time-resolved Spectroscopy Finally in this section, the advent of step-scan interferometers has opened up exciting opportunities to study fast, reversible surface processes. Details on step-scan interferometry may be found elsewhere [144]; briefly: in conventional mode (see in previous text), the mirror moves essentially continuously, with intensity measurements taken at regular intervals (Fig. 12). In “step-scan” mode, the mirror is paused at each position (retardation), allowing the exploitation of the “time-resolved spectroscopy” option of the spectrometer. Once the mirror has settled at a particular position, a reference point can be taken, after which a reaction can be triggered, that is via a light pulse or potential step, and the intensity measured at regular intervals (Fig. 13).

Fig. 12 Schematic representation of the mirror movement (retardation), during conventional versus step-scan spectral data acquisition by an FTIR spectrometer.

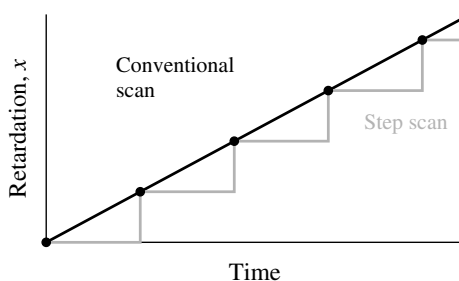
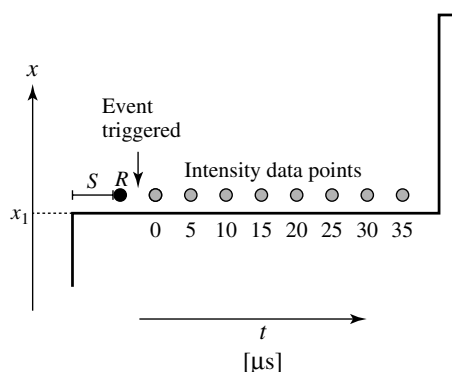


Fig. 13 Schematic representation of the data acquisition during the time-resolved spectroscopy operation of a step-scan FTIR spectrometer. *S* is the settlement time, and *R*, a reference data point.



At the end of the step, the reaction has either returned to its original state, in which the reference point, R , was collected after the settlement time, S , or is returned, that is, by a potential step back. The BioRad FTS 6000 is capable of a time resolution, that is, time between intensity measurements, as high as 200 ns. This is repeated at each step (mirror position), and so the reaction under study *must be reversible*.

In the normal scan, points (retardation, intensity) are collected at a constant mirror velocity, that is along the diagonal of the plot in Fig. 14. In the Time Resolved Spectroscopy (TRS) step-scan mode, the data points at a single time are obtained at each retardation by repeating the number of scans (Fig. 14), to give, when transformed, single beam spectra at each time interval. These are then normalized to the reference spectrum to give the set of time-resolved reflectance spectra.

Clearly, signal averaging would impair the time resolution of the technique; hence, the TRS approach has been limited to operation in conjunction with the SEIRAS effect to ensure sufficient S/N [26]; the (Kretschmann)

ATR configuration necessary for SEIRAS measurements ensures that the electrochemical cell has a sufficiently low RC (time) constant to be able to respond quickly enough to the electrochemical event. Thus, Osawa and coworkers [26] were able to collect TRS spectra during a potential step from -0.2 to -0.55 V with a $100\text{-}\mu\text{s}$ acquisition time, (80 ms repeated at 5 Hz, total time for 1 step-scan interferogram was 10 min), (Fig. 15). The figure shows only the spectra collected every 1 ms, from 6 ms before the step to 24 ms after, for clarity.

The spectra in Fig. 15 are remarkable, not just for the impressive $100\text{-}\mu\text{s}$ time resolution, but also for the fact that they represent single scans with no signal averaging, and using a room temperature tri-glycine sulfate (TGS) detector. The success of the technique was directly attributed by the authors to the significant enhancement in absorption intensities offered by the SEIR effect. This, perhaps, is the only significant drawback of this new approach, that is, that it is limited to studies at thin film electrodes of the coinage metals. In a later paper, Osawa and coworkers [145] reported the

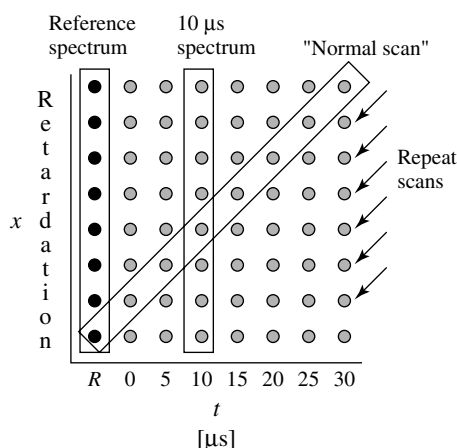


Fig. 14 Schematic representation of the data acquisition during the TRS versus conventional operation of a step-scan FTIR spectrometer.

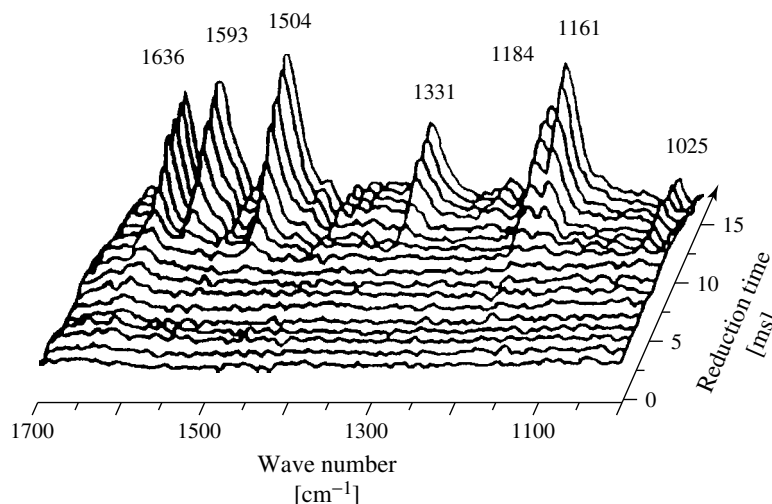


Fig. 15 Time-resolved infrared spectra of the reduction of heptyl viologen, HV^{2+} , at a silver electrode during a potential step from -0.2 to -0.55 V versus Ag/AgCl. The spectra were taken with a $100\text{-}\mu\text{s}$ acquisition time, but only the spectra of every 1-ms interval are shown, for clarity, see text for details. (From the work of Osawa and coworkers, Ref. [26].)

application of 2D-correlation analysis in conjunction with SEIRAS and TRS to study the reduction of HV^{2+} . As well as having noise-rejection capability, the 2D-correlation approach highlights dynamic information obscured in the TRS spectra; that is, bands arising from different transient species are clearly differentiated by their behavior.

3.5.4.2 Thin Layer and Solvent Annulling

An early method of minimizing the thickness of the thin electrolyte layer trapped between the reflective working electrode and the cell window was to employ an elasticized loop [124]. Whilst this approach is still employed [23], higher precision can be attained with more conventional engineered designs employing, for example, a screw and pushrod [29] or micrometer screw [135]. Moreover, elasticized loops do not exert sufficient force to ensure a thin

enough layer of electrolyte is trapped, and this is an important consideration since it has been shown that [146] the maximum absorbance for accurate difference spectrometry is ca. 0.7, or even 0.5 [64].

Some indication of the importance of taking into account the thickness of the electrolyte thin layer when analyzing in situ infrared data may be gleaned from the spectra in Figs. 16(a) and (b). Figure 16(a) shows spectra taken at 1.2 V versus Ag/AgCl from thermal film TiO_2 electrodes under irradiation by light of $\lambda > 300$ nm and immersed in 0.1 M $NaClO_4$ [147]. The spectra were taken at the end of an experiment in which the reference spectra were collected at -0.2 V under irradiation, and the potential stepped up in 100 mV increments, with further spectra being taken at each step. In effect, the spectra simply show the loss of water; however, spectrum (i) shows a markedly higher ratio of the intensities of

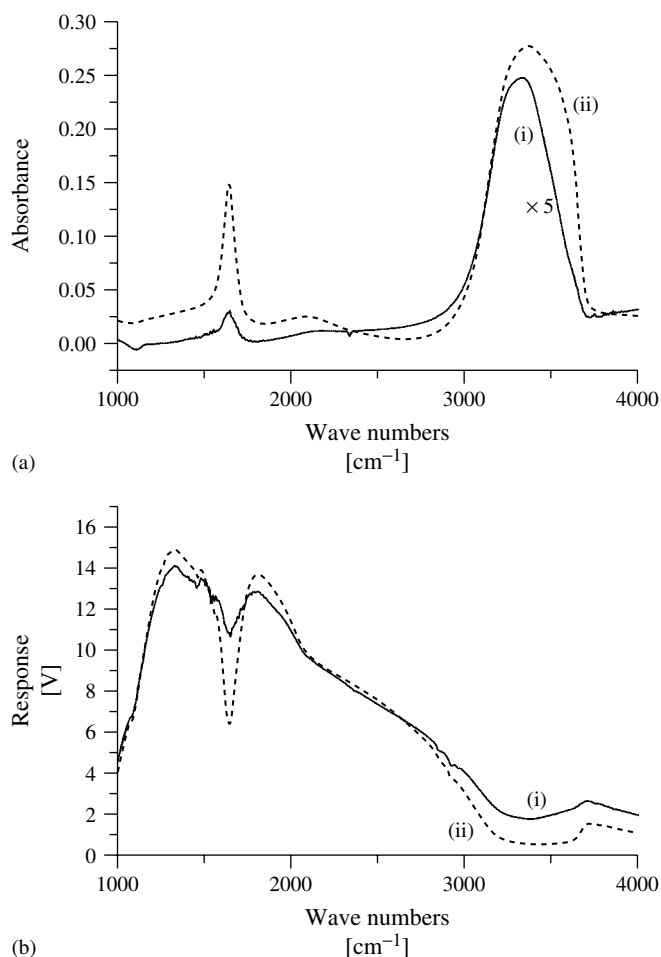


Fig. 16 (a) Spectra taken at 1.2 V versus Ag/AgCl from thermal film TiO₂ electrodes under irradiation by light of $\lambda > 300$ nm and immersed in 0.1 M NaClO₄. The spectra were taken at the end of an experiment in which the reference spectra were collected at -0.2 V versus Ag/AgCl under irradiation, and the potential stepped up in 100-mV increments, with further spectra being taken at each step. The working electrodes were irradiated with UV light (150 W Xe lamp) in situ via a 1 m flexible liquid light guide. The films were produced by heating the Ti “top hat” electrode at (i) 475 °C or (ii) 700 °C for 40 min in air, and the experiments were performed at (i) 10 °C or (ii) 50 °C and (b) The single beam spectra taken at -0.2 V in the experiments in (a).

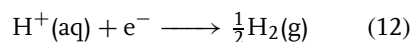
the O–H stretch and O–H scissor modes than would be expected for bulk water. At first sight, it appears that spectrum (i) is anomalous; however, examination of the single beam spectra (Fig. 16(b)), shows that spectrum (ii) in Fig. 16(a) has the lowest throughput in the 3000 to 3500 cm⁻¹ spectral region, with what little throughput there is resulting from reflection from the front face of the (plate) window. Moreover, both McQuillan and coworkers [148] and Tejedor-Tejedor and coworkers [149] have observed such an abnormal ratio of the O–H stretch to O–H scissor at metal oxide surfaces, which were attributed to water present at the TiO₂–aqueous interface, and refractive index effects, respectively.

3.5.5

Specific Examples of In situ Electrochemical Infrared Spectroscopy taken from the Literature, and a Look at the Future

3.5.5.1 The Intermediate in the Hydrogen Evolution Reaction

Along with the identity of the intermediate in the methanol oxidation reaction, the mechanism of the hydrogen evolution reaction, (HER), at Pt group metals has remained relatively ill understood. The key problem lies in reconciling the observed kinetic data with the known coverage of, for example, platinum electrodes by adsorbed hydride at the onset of hydrogen evolution. The HER may be most simply represented by:



that is, the discharge of a hydronium ion. In the simplest terms, the platinum cyclic voltammogram (CV) shows [5] that, at the onset of H₂ evolution in acid electrolyte, the coverage of the electrode surface by adsorbed hydride species is high; however, the current densities for the

HER as a function of overpotential clearly fit models [5, 150] in which the coverage of the *intermediate* is low at potentials above H₂ evolution, and increases only slowly as the potential is moved into the hydrogen evolution region. This led to a search for the intermediate, the identity of which was first directly addressed using in situ FTIR again by Bewick [151] and then more recently, by Kitamura, Tokuda and coworkers [152]. Both groups started from a model in which the HER intermediate was believed to be hydrogen atoms adsorbed on an “on-top” site on Pt, and employed the SNIFTIRS approach, but different data collection times, and obtained somewhat different results.

The HER has been intensively studied, and there is a wealth of data from ultra-high vacuum (UHV) studies; however, studying the reaction in aqueous electrolyte using in situ infrared spectroscopy is complicated by four problems: 1. The evolution of H₂ gas bubbles severely distorts the baseline of in situ infrared spectra. 2. Part of the spectral region within which the postulated intermediate, “on-top” Pt–H, would be expected to absorb (2000–2200 cm⁻¹) is also where the association band of water appears. The association band has been attributed [42] to a combination of a hindered rotation, ($\nu_R \approx 500 \text{ cm}^{-1}$), and the 1640 cm⁻¹ ν_3 band. Any Faradaic current passing as a result of surface oxidation or reduction will result in pH changes and electrolyte movement in the thin layer of an in situ infrared cell; however, the behavior of the association band as a function of pH, electrolyte concentration, adsorption site and so on remains ill understood. Christensen and coworkers [29] have reported spectra showing marked changes in the association band as a function of the experimental conditions; the feature

having a FWHM of ca. 250 cm^{-1} . 3. The thin-layer geometry employed in external reflectance infrared spectroscopy may result in a situation in which the formation of an adsorbed monolayer may substantially, or even completely, denude the electrolyte layer of adsorbed species. Thus, taking 140 mC cm^{-2} as the charge equivalent to monolayer coverage of Pt [153] and an average thin-layer thickness of $2\text{ }\mu\text{m}$ requires a concentration of protons of 6 mM to form a monolayer of Pt-H. If the concentration of protons is insufficient, there will be an increasingly substantial pH swing as the potential is stepped to lower values from the double-layer region, such that the evolution of H_2 will actually involve the reduction of water rather than protons. 4. The reduction of adventitious CO_2 can lead to adsorbed CO species that absorb in the region of interest [152].

Nicholls and Bewick utilized a SNIFTIRS data collection protocol in which a total of 15 000 interferograms were collected at each potential to give the required S/N , the data collection requiring several hours at a potential modulation frequency of 0.025 Hz . In order to maintain a clean electrode surface over such prolonged periods, the potential of the electrode was pulsed for 1 s to $+1.0\text{ V}$ versus SCE between every potential alteration. At a polycrystalline Pt electrode in $1\text{ M H}_2\text{SO}_4$, the authors observed a weak (ca. 10^{-4} a.u.) gain feature with a maximum near 2090 cm^{-1} , which was assigned to hydrogen adsorbed in an “on-top” site on the Pt; the feature appeared at the hydrogen evolution potential, and increased in intensity as the potential was decreased, in agreement with theory. The FWHM of the Pt-H band was ca. 100 cm^{-1} , which increased to ca. 200 cm^{-1} at a Pt(111) electrode, which the authors attributed to more complete ordering at the single crystal surface.

In the more recent paper by Kitamura, Tokuda and coworkers, a total of 320 scans were collected at each potential in the SNIFTIRS experiments. In $0.1\text{ M H}_2\text{SO}_4$, the authors also employed a polycrystalline Pt electrode, and observed a weak gain feature (ca. $10^{-4}\Delta R/R$) with a maximum near 2070 cm^{-1} , which the authors assigned to “on-top” Pt-H; the feature was only observed over a 100 mV potential range immediately prior to the hydrogen evolution potential, with the baseline being distorted at the latter and lower values due to H_2 bubble formation in the thin layer. A more unambiguous assignment was possible in $1\text{ mM H}_2\text{SO}_4 + 99\text{ mM Na}_2\text{SO}_4$ as there was no significant H_2 bubble formation until ca. -0.7 V , where appreciable reduction of H_2O took place, and the Pt-H gain feature was observed over a wider potential range from the onset of H^+ reduction at -0.3 V . However, the system would be somewhat ill-defined as a result of pH swings in the thin layer that were not being properly compensated for (see point (3) above). The authors observed a weak gain feature appeared near ca. 2060 cm^{-1} at potentials $< -0.3\text{ V}$, with a FWHM of ca. $30\text{ to }40\text{ cm}^{-1}$, which could clearly be distinguished from the underlying association band, and which increased in intensity as the potential was stepped down, reaching a maximum at ca. -0.5 V , after which the intensity decreased. The coverage of the on-top hydride intermediate would be expected to depend upon the concentration of protons [154], and this was confirmed by the authors who also observed a decrease in the frequency of the Pt-H band as the coverage of the intermediate decreased.

The work of Nicholls and Bewick, and Nanbu and coworkers, clearly addresses a key problem in electrochemistry, and both groups have shown that their data

are consistent with the intermediate in the HER being hydrogen atoms adsorbed at “on-top” sites on the Pt electrode. However, the differences between the two sets of data and their interpretations, and the severe experimental difficulties associated with this experiment have not yet allowed a definitive assessment to be made.

3.5.5.2 The Interface between Electrochemistry and Biology

The wide-ranging nature of the research currently employing in situ FTIR spectroscopy as an analytical tool was touched upon at the beginning of the chapter. However, a relatively underexploited area is the interface between biological chemistry and electrochemistry. In 1990, Moss and coworkers [38], building upon previous work [155], reported a careful and elegant in situ FTIR study of the oxidation of cytochrome *c* as a means of assessing the potential of the technique to study redox-linked conformational changes in proteins in aqueous solution. The authors obtained high-quality FTIR (difference) spectra using an OTTLE cell employing a gold grid working electrode. The authors acknowledged that a complete interpretation of the in situ FTIR spectra obtained was beyond the scope of the paper; however, by comparing the in situ FTIR spectra of cytochrome *c* obtained from a range of fish, birds, and animals, and by deuteration, assignments were suggested for all but one of the major features observed between 1500 and 1800 cm^{-1} . More recently, Richardson and coworkers [156] employed 2D-correlation FTIR spectroscopy to study chemically induced changes in the secondary structure of β -lactoglobulin in D_2O and H_2O induced by adding varying concentrations of bromoethanol; surely, the combination of in situ FTIR spectroscopy

and 2D-correlation in this particular research area offers exciting possibilities?

3.5.5.3 The Study of Representative Electrodes

Although in situ infrared spectroscopy has been applied widely in terms of the systems studied, the reflective electrodes employed have been predominantly polished metal or graphite, and so an important advance has been the study of electrochemical processes at more representative electrodes such as Pt/Ru on carbon [107, 122, 157], a carbon black/polyethylene composite employed in cathodic protection systems [158] and sol-gel TiO_2 electrodes [159]. Recently, Fan and coworkers [160] took this concept one step further, and reported preliminary in situ FTIR data on the electro-oxidation of humidified methanol vapor at a Pt/Ru particulate electrode deposited directly onto the Nafion membrane of a solid polymer electrolyte fuel cell that was mounted within the sample holder of a diffuse reflectance attachment. As well as features attributable to methanol, a number of bands between 2200 and 1700 cm^{-1} were observed in the spectra, taken under short-circuit conditions, which were attributed to gas phase CO and CO adsorbed in various forms and at various sites. This work represents a significant advance towards the study of electrocatalysis under real operating conditions, the importance of which has already been clearly demonstrated [107].

3.5.5.4 Quantitative In situ FTIR

In addition to the study of electrochemical processes at representative electrodes, in situ FTIR spectroscopy has been slow in evolving as a routine, *quantitative* analytical tool, primarily as a result of the difficulties associated with baseline determination,

particularly with aqueous systems, and the relative paucity of information on extinction coefficients in the infrared, (see Table 1 for some relevant references). However, progress has been made recently in this respect in both aqueous [29] and nonaqueous systems [127, 161], and for adsorbed species [139, 162].

More recently, the work of Lipkowski and coworkers has sought to quantify the application of the SSR in the study of adsorbed species. Lipkowski and coworkers have built up a quantitative treatment of the infrared spectroscopy of adsorbed species based upon the SSR in an elegant series of papers [16, 83, 85, 165, 170, 171] using the combination of SNIFTIRS and conventional electrochemical techniques such as differential capacitance measurements. Thus, Li, Roscoe, and Lipkowski [165] published a study in 1999 on the adsorption of the benzoate anion at

the Au(111) surface in aqueous KClO_4 ; the concentration of potassium benzoate added to the solution was chosen such that the concentration in the thin layer was equivalent to a monolayer when adsorbed at the electrode.

The initial differential capacitance, charge density, and chronoamperometry measurements strongly suggested that the benzoate species were totally desorbed at potentials < -400 mV versus the Ag/AgCl reference electrode, but started to adsorb at higher potentials with adsorption complete by ca. $+500$ mV, and that the adsorbed molecules underwent a potential-dependent reorientation on passing through the potential of zero charge, pzc. These measurements were then employed to determine the choice of base potential, (E_1 ; Fig. 11d), -750 mV, employed in the SNIFTIRS experiments. The values of N and M employed by

Tab. 1 Some useful references

<i>Topic</i>	<i>References</i>
General FTIR spectrometry	64
Extinction coefficients of CO_{ads} and CO_2	162
Extinction coefficients of $\text{Fe}(\text{CN})_6^{3-}$, N_3^- , $^- \text{NCS}$, and $^- \text{OCN}$	139
Extinction coefficients of water as a function of temperature	42
Extinction coefficients of CO_2 , acetonitrile, etc.	127, 161
Refractive indices (n , k) of various organic solvents	163
Refractive indices of acetonitrile, adsorbed acetonitrile, infrared transparent crystals, and Au	164
Intensity stealing by CO_L from CO_H absorptions	114
Quantification of the SSR	19, 165
Molecular orbital view of adsorbed CO and effect on infrared absorptions	166
Phenomena influencing the frequency and intensity of CO_{ads} absorptions	32, 108
Subtraction effects on liquid water spectra in differential FTIR spectroscopy	167
Effect of temperature on FTIR spectrometer response	168
Infrared reviews	1–6, 9, 11, 12
In situ FTIR spectra of water at the gold/aqueous electrolyte interface	169

the authors (Fig. 11d), were 100 and 20, respectively, normalized according to Eq. (6) to give plots of $(\Delta R/R)$ versus $\bar{\nu}/\text{cm}^{-1}$.

A series of SNIFTIRS experiments were carried out by the authors in which E_1 was kept at -750 mV, but E_2 was increased incrementally in sequential experiments up to $+600$ mV, using both s- and p-polarized light. Three absorptions were observed in the spectra: the 1547 cm^{-1} CO_2^- asymmetric stretch, 1595 cm^{-1} C–C stretch, and the CO_2^- symmetric stretch near 1390 cm^{-1} . The isolated benzoate molecule is planar with C_{2v} symmetry, and the 1547 and 1595 cm^{-1} were attributed to b_1 modes, having their transition dipoles perpendicular to the C_{2v} axis in the plane of the molecule, and

the 1390 cm^{-1} absorption to an a_1 mode having its transition dipole parallel to the C_{2v} axis.

In the spectra obtained using both s- and p-polarized light, the b_1 modes were observed as loss features at potentials > -100 mV, whose intensities increased steadily as the limit E_2 was increased (see Fig. 17, which shows a plot of the intensity of the 1547 cm^{-1} loss feature as a function of potential), with no associated gain features. The data were interpreted on the basis of the SSR as follows: if adsorption of the benzoate took place such that the b_1 modes had their transition dipoles parallel to the surface of the electrode (as would be the case if the molecule adsorbed flat, or if it was tilted upwards from such a conformation

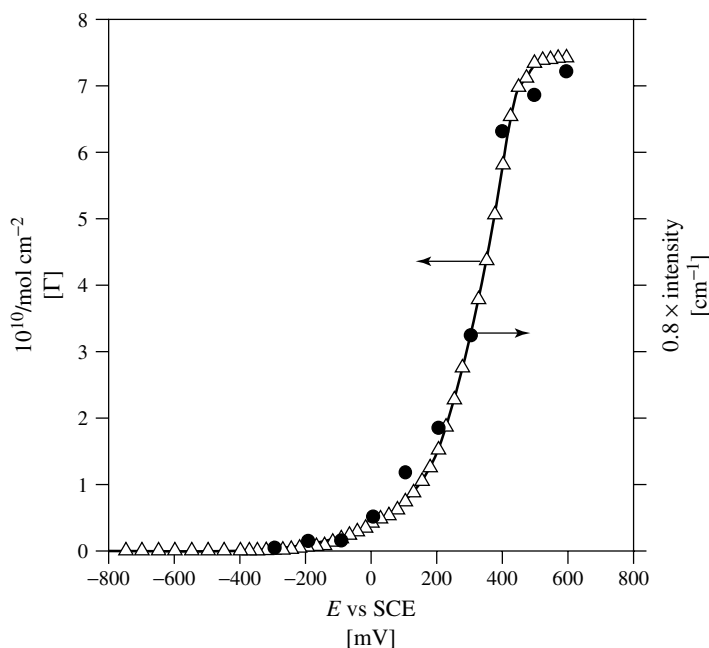


Fig. 17 Comparison of the intensity of the benzoate anion solution loss feature at 1547 cm^{-1} (●) with the surface concentration of the adsorbed benzoate determined from chronocoulometric data. (From the work of Lipkowski and coworkers, Ref. [165].)

without any twisting about the C_{2V} axis), then both these modes of the adsorbed molecule would be inactive towards the absorption of both s- and p-polarized light. Consequently, the corresponding loss features simply represent the loss of the benzoate from solution caused by the adsorption, with the intensities of these features simply correlating with the amount lost from the thin layer, and hence adsorbed.

The authors developed a model to quantify this process, which is formulated as in Eq. (13):

$$\int \left(\frac{\Delta R}{R} \right)_s d\bar{\nu} = \frac{(2.3\Gamma \int \varepsilon(E_1) d\bar{\nu})}{3} \quad (13)$$

where $\int (\Delta R/R)_s d\bar{\nu}$ is the integrated band intensity of a feature observed with s-polarized light, Γ is the surface concentration of adsorbed species, and $\varepsilon(E_1)$ is the molar absorption coefficient of the (solution) species at potential E_1 . As may be expected on the basis of Eq. (13), the integrated band intensity of the 1547 cm^{-1} CO_2^- asymmetric stretch feature tracks exactly the surface concentration of adsorbed benzoate molecules determined from the initial chronoamperometry experiments (Fig. 17).

In contrast to the absorptions of the b_1 modes, the a_1 symmetric CO_2^- absorption near 1390 cm^{-1} shows a marked dependence upon the polarization state of the light (Figs. 18a and b), with the features observed using p-polarized light being bipolar at potentials $> \text{ca. } 0 \text{ V}$, the intensity of the positive lobe increasing with increasing potential. In addition, the positive lobe exhibited a potential-dependent increase in frequency of $\text{ca. } 47 \text{ cm}^{-1} \text{ V}^{-1}$. The spectra obtained using s-polarized light show a steady loss of intensity at potentials $> \text{ca. } -100 \text{ mV}$ (Fig. 18a). The

infrared data were interpreted in terms of the C_{2V} symmetry of the adsorbed benzoate molecule, thus: the 1595 cm^{-1} C–C stretch and 1547 cm^{-1} CO_2^- asymmetric stretch both have transition dipoles perpendicular to the C_{2V} axis in the plane of the molecule, whilst that of the 1390 cm^{-1} CO_2^- symmetric stretch is parallel to the C_{2V} axis; none of the modes therefore have a transition dipole perpendicular to the molecule. On stepping from -750 mV to potentials $> -400 \text{ mV}$, the benzoate species start to adsorb effectively flat on the surface, such that both b_1 modes and the a_1 mode of the surface species are inactive to both s- and p-polarized light; hence, all three bands are observed as loss features, as the benzoate species are removed from the thin layer. Adsorption is complete by $\text{ca. } +500 \text{ mV}$ (Fig. 17). However, at potentials $> \text{ca. } 0 \text{ V}$, the molecules start to lift from the surface, anchored by the CO_2^- group; under these conditions, the b_1 modes (with transition dipoles in the plane of the molecule and parallel to the surface) are still inactive, and so appear in the SNIFTIRS spectra as loss features. In contrast, the a_1 mode shows an increasingly strong component of the transition dipole perpendicular to the surface as the molecule tilts up, and hence interacts increasingly strongly with the p-polarized light (Fig. 18b). The observation of the bipolar band in Fig. 18(b) shows that the adsorption of the benzoate anion through the CO_2^- group causes a potential-dependent shift in the frequency of the symmetric stretch near 1390 cm^{-1} .

The authors developed a model based upon the ratio of the integrated band intensities of an absorption observed with both s- and p-polarized light that allows further information on the orientation of

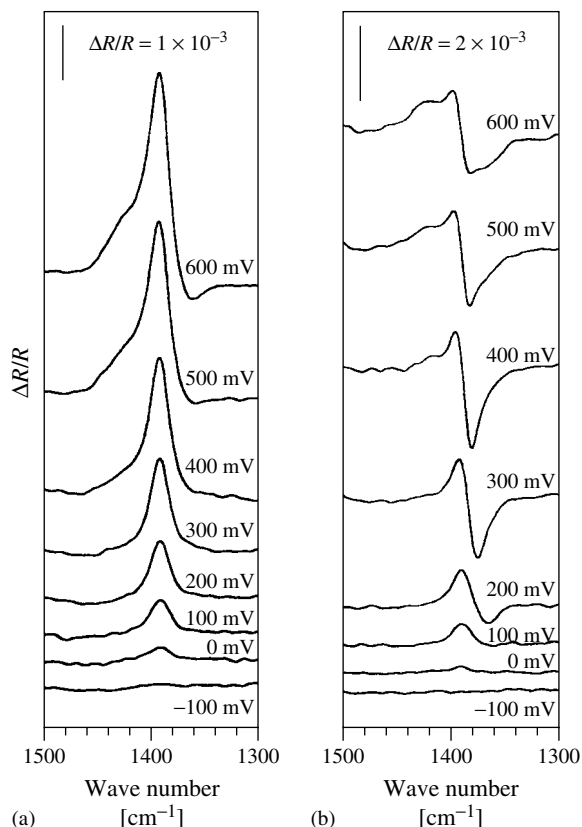


Fig. 18 SNIFTIRS spectra showing the CO_2^- symmetric stretch mode for benzoate adsorbed at an Au(111) electrode from aqueous 0.1 M $\text{KClO}_4 + 9.04 \times 10^{-3}$ M potassium benzoate solution using (a) s- and (b) p-polarized light. The reference potential was -750 mV versus Ag/AgCl and the sample potentials were as shown. (From Ref. [165].)

adsorbed species to be obtained. Thus:

$$\left\{ \frac{\int (\Delta R/R)_P}{\int (\Delta R/R)_S} \right\} d\bar{v} = \left\{ \frac{\langle E_P^2(z) \rangle}{\langle E_S^2(z) \rangle} \right\} - 3 \cos^2 \vartheta \left\{ \frac{\langle E_P^2(z=0) \rangle}{\langle E_S^2 \rangle} \right\} \quad (14)$$

where $\langle E_{P,S}^2(z) \rangle$ is the time- and z -averaged mean square electric field within the thin-layer cell, $\langle E_P^2(z=0) \rangle$ is the time averaged mean square field at the surface and z

varies between 0 and d , in which d is the thickness of the thin layer. ϑ is the angle between the direction of the transition dipole of the relevant vibrational mode of the adsorbed molecule and the direction of the electric field of the p-polarized light at the surface, which is predominantly perpendicular to the surface. Hence, ϑ is effectively a measure of the angle of tilt of the molecule.

The data the authors obtained using Eq. (13), for the intensities of the a_1 loss

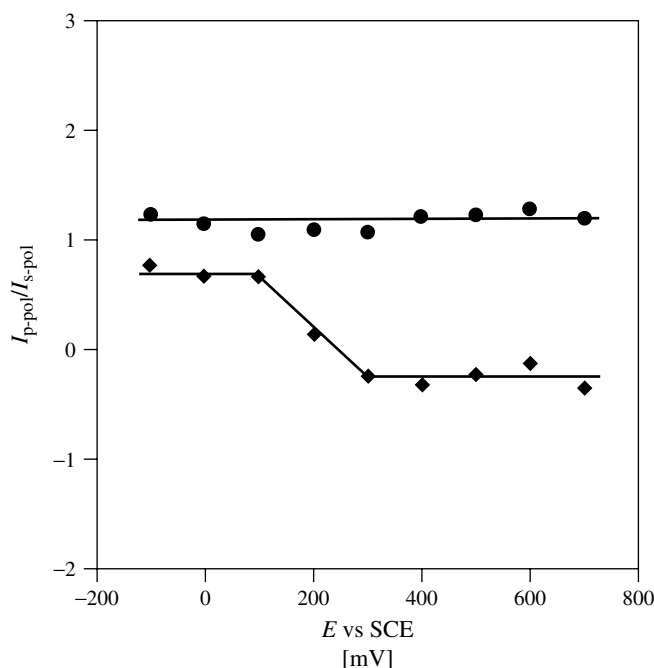


Fig. 19 Ratio of the integrated intensities of (●) (the sum of) the b_1 bands at 1547 and 1595 cm^{-1} and (◆) the a_1 band at 1390 cm^{-1} obtained using s- and p-polarized light during the SNIFTIRS experiments represented by Figs. 17 and 18. (From Ref. [165].)

feature near 1390 cm^{-1} and the sum of the integrated intensities of the two b_1 loss features, are shown in Fig. 19. As expected, the ratio for the b_1 bands does not change with potential (ca. 1.18), indicating that the angle between the transition dipoles of these modes and the direction of the electric field of the p-polarized light is essentially unchanged. The high positive value of the ratio indicates that the direction of the component of the transition dipole parallel to the electric field of the p-polarized photons is small, and the dipole is essentially parallel to the electrode surface. In contrast, the ratio of the integrated intensities of the a_1 mode shows a marked variation with potential. At potentials $< 100\text{ mV}$, the ratio was ca. 0.7, falling to a steady -0.2 at $E > +300\text{ mV}$;

the potential range over which this ratio fell smoothly between these two limits corresponded to that in which the two peaks in the differential capacity measurements occurred, which were attributed to two different orientations of the adsorbed benzoate anion.

In order to calculate the values of the tilt angle corresponding to the data in Fig. 17, the exact thickness of the thin layer is required, which the authors were unable to determine; nevertheless, they were able to obtain further information from the data using their model. Thus, the value of the ratio in Eq. (14) for the a_1 band at potentials $< 100\text{ mV}$ is positive (Fig. 19), but is less than that for the combined b_1 bands; on the basis of their model, the authors interpreted this as

indicating that, even at low potentials, the angle between the surface normal and the transition dipole of the a_1 band is less than 90° , and hence the molecule is not adsorbed perfectly flat at these potentials, but somewhat tilted. At the highest potentials in Fig. 19, the ratio is smaller in magnitude and negative, indicating that the component of the transition dipole normal to the surface is significant, but small, and hence the molecule is not vertical.

Overall, the authors were able to show that the benzoate anion undergoes a change from a “nearly flat” orientation at $E < 200$ mV to a tilted orientation at more positive potentials, with the molecule adsorbed through the CO_2^- group. The transition between these two “extreme” orientations takes place at potentials close to the pzc, with excellent agreement between the in situ FTIR and the electrochemical data.

In addition to the above areas, the future of in situ infrared spectroscopy surely lies in increasing its temporal and spatial resolution, and exploring the temperature domain, in effect mirroring new and emerging trends elsewhere in electrochemistry.

3.5.5.5 High Resolution In situ FTIR

The first paper to report extending the lateral resolution of in situ FTIR spectroscopy was that by Li and Lin [172] in 1995. The authors described a thin-layer microspectroelectrochemical cell based around a conventional FTIR microscope and employing a $200\text{ }\mu\text{m}$ Pt button electrode, which they employed to study the oxidation of aqueous Fe(II)(CN)_6^{4-} and the oxidation of a manganese porphyrin in CH_2Cl_2 . The spectra obtained by the authors showed excellent S/N ratios, although higher reactant concentrations were necessary than for more conventional in situ techniques, with the

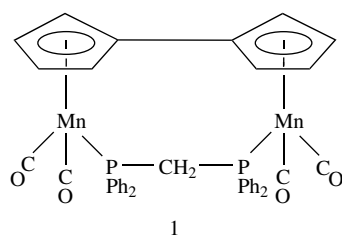
implication that the study of surface adsorbed species was not yet possible. As well as the obvious advantages associated with microelectrodes, such as small iR drop, fast potential response times for kinetic measurements, and the need for very small solution volumes ($<20\text{ }\mu\text{l}$), the approach also offers the potential for spatial studies of electrode activity, as the infrared beam is a spot with a minimum diameter of $10\text{ }\mu\text{m}$.

Melendres and Hahn [173] have extended the vertical spatial resolution of in situ infrared spectroscopy by employing synchrotron radiation in the far-infrared region of the spectrum, (synchrotron far infrared spectroscopy, SFIRS), to study metal–adsorbate bonds. The authors exploited the Kretschmann configuration to improve the sensitivity of the technique, and studied the adsorption of Cl^- and Br^- at the thin Au film working electrode. They observed bands near 263 and 187 cm^{-1} for the Au–Cl and Au–Br stretches, respectively, in good agreement with the SERS data of Gao and Weaver [174].

3.5.5.6 Time-dependent In situ FTIR Spectroscopy

The first report of the exploitation of the fast data collection time of FTIR spectrometers was a paper by Yaniger and Vidrine in 1986 [175], who studied the electropolymerization and electrochemical cycling of several conducting polymers at time resolutions down to ca. 10 ms in an electrochemical ATR cell. The maximum time resolution was that for a single scan, the resolution of which determined the collection time (i.e. 12 ms at 17 cm^{-1}); by selecting strongly absorbing species to study, the need for signal averaging was reduced. More recent developments in increasing the temporal resolution of the technique were discussed above.

Some elegant work related to this area is that reported by Geiger and coworkers [20, 176] who employed a range of in situ spectroscopic techniques including FTIR to study the oxidation of $(\text{fulv})\{\text{Mn}(\text{CO})_2\}_2(\mu\text{-dppm})$, **1**, where $\text{fulv} = \{\text{C}_{10}\text{H}_8\}^{2-}$ and $\text{dppm} = \text{bis}(\text{diphenylphosphino})\text{methane}$ and related homodinuclear complexes.



The authors found that the in situ electrochemical potentiokinetic reactivation (EPR) data obtained for the monocation 1^+ showed that the two Mn centers had identical spin densities, and hence the cation showed delocalized mixed valence; the near-infrared spectrum supported this postulate. If such a delocalized system existed on the infrared timescale, then two bands would be expected in the carbonyl region of the infrared spectrum of 1^+ at frequencies intermediate between those of the $\text{Mn(I)}/\text{Mn(I)}$ neutral complex, (1861 and 1934 cm^{-1}), and those of the fully oxidized $\text{Mn(II)}/\text{Mn(II)}$ species, which were predicted to be ca. 1966 and 2048 cm^{-1} on the basis of the bands observed for $\{\text{CpMn(II)(CO)}_2\text{PPh}_3\}^+$, (Cp = cyclopentadienyl). In contrast, four intense CO absorptions were observed near 1888, 1931, 1952, and 2003 cm^{-1} , which were typical of the trapped valent $\text{Mn(II)}/\text{Mn(I)}$ species. The variation in the response obtained on the EPR timescale, ca. 10^{-8} s , to that observed on the infrared timescale, ca. 10^{-14} s , was taken by the authors as implying a time-dependent localization process.

In addition, the authors were able to analyze the carbonyl infrared spectral shifts for the range of closely related dinuclear systems in terms of a charge distribution parameter, $\Delta\rho$, which was found to correlate linearly with the separation potentials of the successive one-electron oxidations of the dinuclear systems. Overall, the authors clearly showed the power of electrochemistry and in situ spectroelectrochemical techniques with respect to probing site-to-site interactions in homodinuclear complexes. Further studies of inorganic systems are described in Volume 7 of the Encyclopedia.

3.5.5.7 In situ FTIR as a Function of Temperature

The effect of temperature has largely been overlooked in in situ FTIR studies, despite its obvious importance in areas such as electrocatalysis. In 1995, Atwood and coworkers [37], reported work in which they employed an OTTLE cell to study the oxidation of $(\eta^5\text{-C}_5\text{H}_4\text{R})\text{Mn}(\text{CO})_2\text{L}$, $\text{L} = \text{CO}$ or PR_3 , in CH_2Cl_2 at a gold grid electrode at temperatures down to -60°C . In order to retain well-defined isosbestic points, the authors stated that it was necessary to maintain the temperature of the cell to within 2 K [177]. In 1998, Hori and coworkers reported in situ FTIR reflectance spectra of phosphate and CO adsorbed at a Cu(100) electrode at ca. 2°C using a jacketed cell, although no details were given as to how the temperature was monitored and maintained. More recently, Korzeniewski and coworkers [30, 178, 179] have reported the development of a temperature-controlled infrared reflectance cell, as have Christensen and coworkers [29, 31, 123].

Korzeniewski and coworkers employed their cell to study CO and methanol oxidation at polycrystalline Pt electrodes at

temperatures from ambient to $+75^{\circ}\text{C}$, whilst Christensen studied the adsorption of CO at Ru(0001) electrodes and the photoelectrochemical oxidation of methanol at an irradiated TiO_2 electrode at temperatures from 10 to 50°C . The two groups approached the design of the variable temperature cell in completely different ways: Korzeniewski and coworkers employed a heating element and temperature probe in the electrode body (Fig. 20), the cell hence being designed to operate at ambient temperatures and above. In contrast, Christensen and coworkers employed a combination of a jacketed cell and a heated/cooled mounting plate (Fig. 2). The spectroelectrochemical cell, fitted with a hemispherical CaF_2 window, was mounted vertically on the lid of the sample compartment of the spectrometer, and was designed to allow electrolyte exchange under potential control. The cell was jacketed to allow careful control of the temperature of the electrolyte in the body of the cell. To ensure that this control extended to cover the electrolyte in the thin layer, and hence the temperature of the electrode, two modified versions of the plate employed to mount the cell onto the sample compartment of the spectrometer

were produced. For temperatures below ambient, the plate (not shown) consisted of a hollow aluminum block fitted with inlet and outlet ports to allow the circulation of coolant from a Grant cooling/heating unit. For temperatures above ambient, the plate (Fig. 2) consisted of a solid monolith of stainless steel fitted with $4 \times 50\ \Omega$ resistors, 50 W each, the current through which was controlled via homebuilt 30 V power supply and feedback loop, and a commercial temperature controller. The temperature was monitored using a thermocouple; the temperature of the Ru(0001) electrode was also monitored in situ using a second such thermocouple mounted to the rear of the electrode. Careful measurements at the rear of the electrode, and at the electrolyte–window interface confirmed that the temperature of the thin layer of electrolyte trapped between the Ru(0001) electrode and the CaF_2 window agreed to within $\pm 1^{\circ}\text{C}$ of the preset value.

In two papers [31, 32], Christensen and coworkers studied the adsorption and electro-oxidation of CO at the surface of Ru(0001) in aqueous perchloric acid; the first paper concerned room temperature in situ FTIR spectroscopic studies and electrochemical data, and ex situ

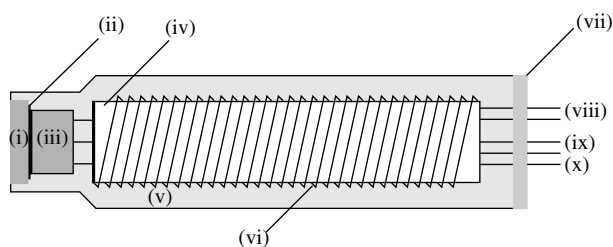


Fig. 20 The variable temperature electrode employed by Korzeniewski (see Ref. [177]). (i) Pt disc; (ii) silver epoxy; (iii) AD590 temperature probe; (iv) ceramic insulator; (v) zinc oxide filled silicone paste; (vi) Nichrome wire; (vii) silicon sealant; (viii) Nichrome wire to temperature controller; (ix) to temperature controller; and (x) working electrode connection to potentiostat. (Redrawn from Ref. [177].)

(emersion) electron diffraction (LEED and RHEED) and Auger spectroscopic data. The emersion studies showed that in both the absence and presence of adsorbed CO, the Ru(0001) electrode undergoes the potential-dependent formation of well-defined and ordered oxygen-containing adlayers, starting with a (2×2) -O phase at low potentials, which is unreactive toward CO oxidation. Increasing the potential results in the formation of (3×1) and (1×1) phases at 410 and 1100 mV versus Ag/AgCl, respectively, with a concomitant increase in the reactivity of the surface towards CO oxidation. Both linear (CO_L) and threefold-hollow (CO_H) binding CO adsorbates (bands at 2000–2040 and 1770–1800 cm^{-1} , respectively) were observed on the Ru(0001) electrode. The in situ FTIR data show that the adsorbed CO species still remain in compact islands as CO oxidation proceeds, suggesting that the oxidation occurs at the boundaries between the CO_ad and the active O_ad domains. At low CO coverages, reversible relaxation (at lower potentials), and compression (at higher potentials), of the CO_L adlayer were observed and rationalized in terms of the reduction and formation of the surface O-adlayers. The data obtained from the Ru(0001) electrode were in marked contrast to those observed at polycrystalline Cu, in which only linear CO is observed.

In the second paper, the authors extended the in situ FTIR studies of the CO/Ru(0001) system to 10 and 50 °C. As was observed at room temperature, both linear (CO_L) and threefold-hollow (CO_H) binding CO adsorbates (bands at 2000–2045 and 1768–1805 cm^{-1} , respectively) were detected on the Ru(0001) electrode at 10 and 50 °C. However, the temperature of the Ru(0001) electrode had a significant effect upon the structure and behavior of the CO adlayer.

At 10 °C, the in situ FTIR data showed that the adsorbed CO species still remain in rather compact islands up to ca. 1100 mV as the CO oxidation reaction proceeds, with oxidation occurring only at the boundaries between the CO_ad and active surface oxide/hydroxide domains. However, the infrared data collected at 50 °C strongly suggest that the adsorbed CO species are present as relatively looser and weaker structures, which are more easily electro-oxidized. The temperature-, potential-, and coverage-dependent relaxation and compression of the CO_L adlayer at low coverages were also discussed.

3.5.5.8 The Application of In situ FTIR with other Analytical Techniques

Section 3.5.3.3 clearly highlights the potential pitfalls of utilizing any analytical approach in isolation, and the benefits of bringing other analytical techniques to bear on a problem in addition to in situ infrared spectroscopy are well attested in the literature. Thus, ellipsometry has proved invaluable in elucidating the complex processes taking place during the growth and electrochemical cycling of conducting polymers [12, 131, 180], whilst STM is frequently employed in conjunction with in situ FTIR spectroscopy [19, 85, 100, 106, 114, 181]. UV–visible and EPR spectroscopies have been employed [125] as has SERS [182] and the electrochemical quartz crystal microbalance (EQCM) [183]. Increasingly, “conventional” analytical techniques such as high performance liquid chromatography (HPLC) [184], liquid chromatography and mass spectroscopy [185] are being employed to supplement in situ FTIR data. Interesting variations of the latter technique are the in situ electrochemical mass spectrometry technique, differential electrochemical mass spectroscopy

(DEMS) [186], and the emersion technique electrochemical thermal desorption mass spectroscopy (ECTDMS) [187]. The combination of UHV analytical techniques such as low energy electron diffraction (LEED), reflection high energy electron diffraction (RHEED), and Auger electron spectroscopy (AES) in emersion studies alongside in situ FTIR spectroscopy has also proved exceptionally powerful in elucidating complex surface processes involving adsorbates such as CO [32, 126].

Acknowledgments

The author would like to thank Prof. A. Hamnett and Dr. W. F. Lin for their helpful suggestions and comments on the manuscript.

References

1. B. Beden, C. Lamy, Infrared reflectance spectroscopy in *Spectroelectrochemistry: Theory and Practice* (Ed.: R. J. Gale), Plenum Press, New York, 1988, p. 189.
2. A. Bewick, B. S. Pons in *Advances in Infrared and Raman Spectroscopy* (Eds.: R. J. H. Clark, R. E. Hester), Wiley-Heyden, London, 1985, Vol. 2.
3. J. K. Foley, C. Korzeniewski, J. J. Daschbach et al. in *Electroanalytical Chemistry, A Series of Advances* (Ed.: A. J. Bard), Marcel Dekker, New York, 1986, pp. 309–440, Vol. 14.
4. P. A. Christensen, A. Hamnett, *Compr. Chem. Kinet.* **1989**, 29, 1.
5. P. A. Christensen, A. Hamnett, *Techniques and Mechanisms in Electrochemistry*, Chapman & Hall, Glasgow, 1994.
6. C. Korzeniewski, *Crit. Rev. Anal. Chem.* **1997**, 27, 81.
7. H. Neugebauer, Z. Ping, *Mikrochim. Acta* **1997**, S14, 125.
8. F. C. Nart, T. Iwasita, *Prog. Surf. Sci.* **1997**, 55, 271.
9. P. A. Christensen, A. Hamnett, *Electrochim. Acta* **2000**, 45, 2443.
10. R. L. Birke, J. R. Lombardi in *Spectroelectrochemistry, Theory and Practice* (Ed.: R. J. Gale), Plenum Press, New York, 1988.
11. M. J. Weaver, D. S. Corrigan, P. Gao et al., *J. Electron Spectrosc. Relat. Phenom.* **1987**, 45, 291.
12. P. A. Christensen, A. Hamnett, S. J. Higgins, *Analyst* **1994**, 119, 735.
13. P. A. Christensen, A. Hamnett, I. Blackham, *J. Electroanal. Chem.* **1991**, 318, 407.
14. V. Climent, A. Rodes, J. M. Orts et al., *J. Electroanal. Chem.* **1999**, 467, 20.
15. Y. Ikezawa, Y. Koda, M. Shibuya et al., *Electrochim. Acta* **2000**, 45, 2075.
16. M. Hoon-Khosla, W. R. Fawcett, J. D. Goddard et al., *Langmuir* **2000**, 16, 2356.
17. N. Nanbu, F. Kitamura, T. Ohsaka et al., *Electrochemistry* **1999**, 67, 1165.
18. P. Talonen, G. Sundholm, S. Floate et al., *Phys. Chem. Chem. Phys.* **1999**, 15, 3661.
19. H. Noda, T. Minoha, L. J. Wan et al., *J. Electroanal. Chem.* **2000**, 481, 62.
20. C. G. Atwood, W. E. Geiger, *J. Am. Chem. Soc.* **2000**, 122, 5477.
21. T. Ito, T. Hamaguchi, H. Nagino, T. Yamaguchi, J. Washington, C. P. Kubiak, *Science* **1997**, 277, 660.
22. T. Yamaguchi, N. Imai, T. Ito et al., *Bull. Chem. Soc. Jpn.* **2000**, 73, 1205.
23. N. S. Marinkovic, J. J. Calvente, A. Kloss et al., *J. Electroanal. Chem.* **1999**, 467, 325.
24. Y. Shingaya, M. Ito, *Surf. Sci.* **1997**, 386, 34.
25. F. Kitamura, N. Nanbu, T. Ohsaka, et al., *J. Electroanal. Chem.* **1998**, 452, 241.
26. M. Osawa, Y. Katsumasa, K. Ataka et al., *Langmuir* **1994**, 10, 640.
27. K. Ataka, G. Nishina, W. B. Cai et al., *Electrochem. Commun.* **2000**, 2, 417.
28. Y. Hori, O. Koga, Y. Watanabe et al., *Electrochim. Acta* **1998**, 44, 1389.
29. P. A. Christensen, J. Eameaim, A. Hamnett, *Phys. Chem. Chem. Phys.* **1999**, 1, 5315.
30. D. Kardash, J. M. Huang, C. Korzeniewski, *Langmuir* **2000**, 16, 2019.
31. W. F. Lin, P. A. Christensen, A. Hamnett, *J. Phys. Chem. B* **2000**, 104, 12 002.
32. W. F. Lin, P. A. Christensen, A. Hamnett, *J. Phys. Chem.* **2000**, 104, 6642.
33. G. N. Ekstrom, A. J. McQuillan, *J. Phys. Chem. B* **1999**, 103, 10 562.
34. J. J. Li, R. Q. Wang, Z. F. Liu, S. M. Cai, X. Y. Xiao, S. G. Sun, *Mol. Cryst. Liq. Cryst.* **1999**, 337, 525.

35. B. H. Ern , F. Ozanam, M. Stchakovsky et al., *J. Phys. Chem. B* **2000**, 104, 5961.
36. S. Z. Zou, R. G mez, M. J. Weaver, *Langmuir* **1997**, 13, 6713.
37. C. G. Atwood, W. E. Geiger, T. E. Bitterwolf, *J. Electroanal. Chem.* **1995**, 397, 279.
38. D. Moss, E. Nabadryk, J. Breton et al., *Eur. J. Biochem.* **1990**, 187, 565.
39. H. B. Mark, B. S. Pons, *Anal. Chem.* **1966**, 38, 119.
40. F. Maroun, F. Ozanam, J. N. Chazalviel, *J. Phys. Chem. B* **1999**, 103, 5280.
41. J. N. Chazalviel, C. DaFonseca, F. Ozanam, *J. Electrochem. Soc.* **1998**, 145, 964.
42. J. J. Fox, A. E. Martin, *Proc. R. Soc. London* **1940**, A174, 234.
43. P. Lange, V. Glaw, H. Neff et al., *Vacuum* **1983**, 33, 763.
44. E. Kretschmann, *Z. Phys.* **1971**, 241, 313.
45. H. Raether, *Phys. Thin Films* **1977**, 7, 145.
46. M. Osawa, K. Yoshii, *Appl. Spectrosc.* **1997**, 51, 512.
47. A. Hatta, Y. Sasaki, W. Su taka, *J. Electroanal. Chem.* **1986**, 215, 93.
48. H. Neff, P. Lange, D. K. Roe et al., *J. Electroanal. Chem.* **1983**, 150, 513.
49. B. Piro, E. A. Bazzouai, M. C. Pham et al., *Electrochim. Acta* **1999**, 44, 1953.
50. M. C. Pham, M. Oulahyane, M. Mostefai et al., *Synth. Met.* **1998**, 93, 89.
51. C. Kvarnstr m, H. Neugebauer, S. Blomquist, H. J. Ahonen, J. Kankare, A. Ivaska, N. S. Saricifici, *Synth. Met.* **1999**, 101, 66.
52. C. Kvarnstr m, H. Neugebauer, G. Matt et al., *Synth. Met.* **1999**, 103, 2430.
53. C. Kvarnstr m, H. Neugebauer, A. Ivaska et al., *J. Mol. Struct.* **2000**, 521, 271.
54. Z. Ping, G. E. Nauer, H. Neugebauer et al., *Electrochim. Acta* **1997**, 42, 1693.
55. M. Osawa, *J. Electroanal. Chem.* **1999**, 460, 188.
56. L. J. Wan, M. Terashima, H. Noda et al., *J. Phys. Chem. B* **2000**, 104, 3563.
57. M. Osawa, *Bull. Chem. Soc. Jpn.* **1997**, 70, 2861.
58. M. Osawa, K. Yoshii, T. Nakano et al., *J. Electroanal. Chem.* **1997**, 426, 11.
59. K. Ataka, Y. Hara, M. Osawa, *J. Electroanal. Chem.* **1999**, 473, 34.
60. H. Noda, K. Ataka, L. J. Wan et al., *Surf. Sci.* **1999**, 428, 190.
61. D. R. Tallant, D. H. Evans, *Anal. Chem.* **1969**, 41, 835.
62. A. Bewick, B. S. Pons, *Surf. Sci.* **1980**, 101, 131.
63. K. Kunimatsu, B. S. Pons, J. W. Russell, *J. Electroanal. Chem.* **1984**, 160, 47.
64. P. R. Griffiths, J. A. deHaseth, Fourier transform infrared spectrometry in *Chemical Analysis* (Eds.: P. J. Elving, J. D. Winefordner, I. M. Kolthoff), John Wiley & Sons, New York, 1986, Vol. 83.
65. A. Bewick, K. Kunimatsu, B. S. Pons et al., *J. Electroanal. Chem.* **1984**, 160, 47.
66. A. Z. Trifonov, I. D. Schopov, *J. Electroanal. Chem.* **1972**, 35, 415.
67. J. S. Mattson, C. A. Smith, *Anal. Chem.* **1975**, 47, 1122.
68. A. H. Reed, E. Yeager, *Electrochim. Acta* **1970**, 15, 1345.
69. A. Hatta, Y. Chiba, W. Suetaka, *Appl. Surf. Sci.* **1986**, 25, 327.
70. A. Bewick, K. Kunimatsu, *Surf. Sci.* **1980**, 101, 131.
71. B. Beden, C. Lamy, A. Bewick et al., *J. Electroanal. Chem.* **1981**, 121, 343.
72. A. Hamnett, Applications of kinetic modelling in *Comprehensive Chemical Kinetics* (Eds.: R. G. Compton, G. Hancock), Elsevier, Amsterdam, 1999, p. 635, Vol. 37.
73. M. W. Breiter in *Modern Aspects of Electrochemistry* (Eds.: J. O. M. Bockris, E. Conway), Plenum Press, New York, p. 161, Vol. 10.
74. J. Sobkowski, A. Wieckowski, *J. Electroanal. Chem.* **1975**, 63, 365.
75. K. Kunimatsu, *J. Electron Spectrosc. Relat. Phenom.* **1983**, 30, 215.
76. S. Juanto, B. Beden, F. Hahn et al., *J. Electroanal. Chem.* **1987**, 237, 119.
77. B. Beden, S. Juanto, J. M. Leger et al., *J. Electroanal. Chem.* **1987**, 238, 323.
78. B. Beden, F. Hahn, C. Lamy, J. M. Leger, N. R. Detacconi, R. O. Lezna, A. J. Aruia, *J. Electroanal. Chem.* **1989**, 261, 401.
79. L. Proen a, M. I. S. Lopes, I. Fonseca et al., *Electrochim. Acta* **1998**, 44, 1423.
80. W. G. Golden, D. S. Dunn, J. Overend, *J. Catal.* **1981**, 71, 395.
81. R. G. Greenler, *J. Chem. Phys.* **1966**, 44, 310.
82. R. G. Greenler, *J. Chem. Phys.* **1968**, 50, 1963.
83. J. F. Richer, A. Chen, J. Lipkowski, *Electrochim. Acta* **1998**, 44, 1037.
84. K. Kunimatsu, H. Seki, W. G. Golden et al., *Surf. Sci.* **1985**, 158, 596.

85. M. Hoon-Khosla, W. R. Fawcett, A. Chen et al., *Electrochim. Acta* **1999**, 45, 611.
86. Y. Ikezawa, H. Saito, H. Matsubayashi et al., *J. Electroanal. Chem.* **1988**, 252, 395.
87. J. W. Russell, J. Overend, K. Scanlon et al., *J. Phys. Chem.* **1982**, 86, 3066.
88. W. G. Golden, K. Kunitatsu, H. Seki, *J. Phys. Chem.* **1984**, 88, 1275.
89. E. I. Saez, R. M. Corn, *Electrochim. Acta* **1993**, 38, 1619.
90. K. A. B. Lee, K. Kunitatsu, J. G. Gordon et al., *J. Electrochem. Soc.* **1987**, 134, 1676.
91. H. Seki, K. Kunitatsu, W. G. Golden, *Appl. Spectrosc.* **1985**, 39, 437.
92. A. Bewick, K. Kunitatsu, B. S. Pons et al., *J. Electroanal. Chem.* **1984**, 160, 47.
93. A. Bewick, *J. Electroanal. Chem.* **1983**, 150, 481.
94. C. Korzeniewski, S. Pons, *J. Vac. Sci. Technol., B* **1985**, 3, 1421.
95. C. Korzeniewski, B. S. Pons, *Langmuir* **1986**, 2, 468.
96. C. Korzeniewski, R. B. Shirts, B. S. Pons, *J. Phys. Chem.* **1985**, 89, 2297.
97. M. Fleischmann, P. J. Hendra, A. J. McQuillan, *Chem. Phys. Lett.* **1974**, 26, 163.
98. P. A. Christensen, A. Hamnett, A. R. Hillman, *J. Electroanal. Chem.* **1988**, 242, 47.
99. G. Q. Lu, S. G. Sun, S. P. Chen et al., *J. Electroanal. Chem.* **1997**, 421, 19.
100. G. Q. Lu, S. G. Sun, L. R. Cai et al., *Langmuir* **2000**, 16, 778.
101. M. Osawa, M. Ikeda, *J. Phys. Chem.* **1991**, 95, 691.
102. N. Matsuda, K. Yoshii, K. Ataka, M. Osawa, T. Matsue, I. Uchida, *Chem. Lett.* **1992**, 1385.
103. M. Osawa, K. Ataka, K. Yoshii et al., *Appl. Spectrosc.* **1993**, 47, 1497.
104. M. Osawa, K. Ataka, K. Yoshii et al., *J. Electron. Spectrosc. Relat. Phenom.* **1993**, 64/65, 371.
105. K. Ataka, M. Osawa, *J. Electroanal. Chem.* **1999**, 460, 188.
106. S. G. Sun, W. B. Cai, L. J. Wan et al., *J. Phys. Chem. B* **1999**, 103, 2460.
107. P. A. Christensen, A. Hamnett, J. Munk et al., *J. Electroanal. Chem.* **1994**, 370, 251.
108. W. F. Lin, T. Iwasita, W. Vielstich, *J. Phys. Chem. B* **1999**, 103, 3250.
109. R. Ortiz, A. Cuesta, O. P. Marquez, J. Marquez, J. A. Mendez, C. Gutiérrez, *J. Electroanal. Chem.* **1999**, 465, 234.
110. A. Hartstein, J. R. Kirtly, J. C. Tsang, *Phys. Rev. Lett.* **1980**, 45, 201.
111. A. Hatta, T. Ohshima, W. Suetaka, *Appl. Phys.* **1982**, A29, 71.
112. A. Hatta, Y. Suzuki, W. Suetaka, *Appl. Phys.* **1984**, A35, 135.
113. A. Hatta, Y. Chiba, W. Suetaka, *Surf. Sci.* **1985**, 158, 616.
114. I. Villegas, M. J. Weaver, *J. Chem. Phys.* **1994**, 101, 1649.
115. B. N. J. Persson, R. Ryberg, *Phys. Rev. B* **1981**, 24, 6954.
116. B. N. J. Persson, A. Lebsch, *Surf. Sci.* **1981**, 110, 356.
117. T. Davison, B. S. Pons, A. Bewick et al., *J. Electroanal. Chem.* **1981**, 125, 237.
118. H. Noda, T. Minoha, L. J. Wan et al., *J. Electroanal. Chem.* **2000**, 481, 62.
119. M. C. Arévalo, C. Gomis-Bas, F. Hahn, *Electrochim. Acta* **1998**, 44, 1369.
120. N. H. Li, S. G. Sun, *J. Electroanal. Chem.* **1998**, 448, 5.
121. D. S. Corrigan, L. W. Leung, M. J. Weaver, *Anal. Chem.* **1987**, 59, 2252.
122. P. A. Christensen, A. Hamnett, G. L. Troughton, *J. Electroanal. Chem.* **1993**, 362, 207.
123. P. A. Christensen, *Port. Electrochim. Acta* **1999**, 17, 91.
124. P. A. Christensen, A. Hamnett, P. R. Trevellick, *J. Electroanal. Chem.* **1988**, 242, 327.
125. M. Vilas-Boas, C. Friere, B. Castro, A. R. Hillman et al., *Inorg. Chem.* **1997**, 36, 4919.
126. W. F. Lin, M. S. Zei, M. Eiswirth, G. Ertl, T. Iwasita, W. Vielstich, *J. Phys. Chem. B* **1999**, 103, 6968.
127. P. A. Christensen, A. Hamnett, S. J. Higgins et al., *J. Electroanal. Chem.* **1995**, 395, 195.
128. P. A. Christensen, A. Hamnett, A. V. G. Muir et al., *J. Chem. Soc., Dalton Trans.* **1992**, 1455.
129. P. A. Christensen, A. Hamnett, A. V. G. Muir et al., *J. Chem. Soc., Faraday Trans.* **1994**, 90, 459.
130. D. A. Chesher, P. A. Christensen, A. Hamnett, *J. Chem. Soc., Faraday Trans.* **1993**, 89, 303.
131. P. A. Christensen, A. Hamnett, *Electrochim. Acta* **1991**, 36, 1263.
132. T. C. Chung, J. H. Kaufman, A. J. Heeger et al., *Phys. Rev. B* **1984**, 30, 702.
133. S. Pons, *J. Electroanal. Chem.* **1983**, 150, 495.

134. S. Pons, T. Davison, A. Bewick, *J. Am. Chem. Soc.* **1983**, 105, 1802.
135. J. G. Love, P. A. Brooksby, A. J. McQuillan, *J. Electroanal. Chem.* **1999**, 464, 93.
136. Y. Ikezawa, R. Sekiguchi, T. Kitazume, *Electrochim. Acta* **1998**, 45, 1089.
137. S. N. Port, S. Cère, D. J. Schiffrin, *J. Electroanal. Chem.* **1997**, 432, 215.
138. A. Kabbabi, R. Faure, R. Durand, B. Beden, F. Hahn, J. M. Leger, C. Lamy, *J. Electroanal. Chem.* **1998**, 444, 41.
139. D. S. Corrigan, M. J. Weaver, *J. Phys. Chem.* **1986**, 90, 5300.
140. S. Zou, R. Gómez, M. J. Weaver, *J. Electroanal. Chem.* **1999**, 474, 155.
141. D. S. Corrigan, M. J. Weaver, *J. Electroanal. Chem.* **1988**, 241, 143.
142. R. Gómez, M. J. Weaver, *J. Electroanal. Chem.* **1997**, 435, 205.
143. L. Proença, M. I. S. Lopes, I. Fonseca, A. Rales, R. Gomez, A. Aldaz, *Electrochim. Acta* **1998**, 44, 735.
144. B. O. Budevska, P. R. Griffiths, *Anal. Chem.* **1993**, 65, 2963.
145. M. Osawa, K. Yoshii, Y. Hibino et al., *J. Electroanal. Chem.* **1997**, 426, 11.
146. R. J. Anderson, P. R. Griffiths, *Anal. Chem.* **1975**, 47, 2339.
147. P. A. Christensen, J. Eameaim, A. Hamnett, *Chem. Phys. Lett.* **2000**, 344, 488.
148. P. A. Connor, K. D. Dobson, A. J. McQuillan, *Langmuir* **1999**, 15, 2402.
149. L. D. Tickanen, M. I. Tejedor-Tejedor, M. A. Anderson, *Langmuir* **1997**, 13, 4829.
150. S. Schuldiner, *J. Electrochem. Soc.* **1959**, 106, 891.
151. R. J. Nicholls, A. Bewick, *J. Electroanal. Chem.* **1988**, 243, 445.
152. N. Nanbu, F. Kitamura, T. Ohsaka et al., *J. Electroanal. Chem.* **2000**, 485, 128.
153. B. E. Conway in *Interfacial Electrochemistry, Theory, Experiment and Applications* (Ed.: A. Wieckowski), Marcel Dekker, New York, 1999, p. 147.
154. B. E. Conway, L. Bai, *J. Electroanal. Chem.* **1986**, 198, 149.
155. W. Mäntele, A. Wollenweber, F. Rashwan, J. Heinze, E. Navedryk, G. Berger, J. Breton, *Photochem. Photobiol.* **1988**, 47, 451.
156. N. L. Sefara, N. P. Magtoto, H. H. Richardson, *Appl. Spectrosc.* **1997**, 51, 536.
157. P. A. Christensen, A. Hamnett, J. Munk et al., *J. Electroanal. Chem.* **1996**, 401, 215.
158. B. E. Eastwood, P. A. Christensen, R. D. Armstrong et al., *J. Solid State Chem.* **1999**, 3, 179.
159. P. A. Christensen, A. Hamnett, R. He et al., *Trace Met. Environ.* **1993**, 3, 765.
160. Q. Fan, C. Pu, K. L. Ley et al., *J. Electrochem. Soc.* **1996**, 143, L21.
161. P. A. Christensen, S. J. Higgins, *J. Electroanal. Chem.* **1995**, 387, 127.
162. L. W. H. Leung, M. J. Weaver, *J. Phys. Chem.* **1988**, 92, 4019.
163. T. G. Goplen, D. G. Cameron, R. N. Jones, *Appl. Spectrosc.* **1980**, 34, 657.
164. P. W. Faguy, W. R. Fawcett, *Appl. Spectrosc.* **1990**, 44, 1309.
165. H. Q. Li, S. G. Roscoe, J. Lipkowski, *J. Electroanal. Chem.* **1999**, 478, 67.
166. K. Rahmelow, W. Hübner, *Appl. Spectrosc.* **1997**, 51, 160.
167. D. M. MacBride, C. G. Malone, J. P. Hebb et al., *Appl. Spectrosc.* **1997**, 51, 43.
168. A. Cuesta, C. Gutiérrez, *J. Electroanal. Chem.* **1995**, 395, 331.
169. F. Kitamura, T. Ohsaka, K. Tokuda, *Electrochim. Acta* **1997**, 42, 1235.
170. A. C. Chen, J. Richer, S. G. Roscoe et al., *Langmuir* **1997**, 13, 4737.
171. A. C. Chen, J. Lipkowski, *J. Phys. Chem. B* **1999**, 103, 682.
172. Z. Li, X. Lin, *J. Electroanal. Chem.* **1995**, 386, 83.
173. C. A. Melendres, F. Hahn, *J. Electroanal. Chem.* **1999**, 463, 258.
174. P. Gao, M. J. Weaver, *J. Phys. Chem.* **1986**, 90, 4057.
175. S. I. Yaniger, D. W. Vidrine, *Appl. Spectrosc.* **1986**, 40, 174.
176. C. G. Atwood, W. E. Geiger, A. L. Rheingold, *J. Am. Chem. Soc.* **1993**, 115, 5310.
177. C. M. Duff, G. A. Heath, *Inorg. Chem.* **1991**, 30, 2528.
178. J. Huang, C. Korzeniewski, *J. Electroanal. Chem.* **1999**, 471, 146.
179. D. Kardash, J. Huang, C. Korzeniewski, *J. Electroanal. Chem.* **1999**, 476, 95.
180. P. A. Christensen, J. Eameaim, A. Hamnett, *Phys. Chem. Chem. Phys.* **1999**, 1, 5147.
181. T. Iwasita, H. Hoster, A. John-Anacker et al., *Langmuir* **2000**, 16, 522.
182. C. Quijada, F. J. Huerta, E. Morallón et al., *Electrochim. Acta* **2000**, 45, 1847.
183. K. Ogura, M. Nakayama, K. Nakaoka, *J. Electroanal. Chem.* **1999**, 474, 101.

184. A. Cherqaoui, D. Takky, K. B. Kokoh, F. Hahn, E. M. Belgsir, J. M. Leger, C. Lamy, *J. Electroanal. Chem.* **1999**, 464, 101.
185. K. Ogura, N. Endo, M. Nakayama, *J. Electrochem. Soc.* **1998**, 145, 3801.
186. V. M. Schmidt, E. Pastor, *J. Electroanal. Chem.* **1996**, 401, 155.
187. W. Vielstich, P. A. Christensen, S. A. Weeks et al., *J. Electroanal. Chem.* **1988**, 242, 327.

3.6**Raman Spectroscopy of Electrode Surfaces**

Zhong-Qun Tian and Bin Ren
Xiamen University, Xiamen, China

3.6.1**Introduction**

Raman spectroscopy, as a vibrational spectroscopy, can record fingerprint spectra from electrodes and provide much insight into a variety of surface and interfacial processes at the molecular level, for example, qualitatively determining surface bonding, conformation, and orientation. Raman spectroscopy invariably uses lasers in the ultraviolet (UV) through to the near infrared (IR). More importantly, the technique can be applied *in situ* to investigate solid–liquid, solid–gas and solid–solid interfaces of both fundamental and practical importance. The technique can be used flexibly to study high-surface-area porous electrode materials, to which many surface techniques are not applicable. Therefore, Raman spectroscopy is among the most promising methods for use in electrochemistry. The major disadvantage of Raman spectroscopy is the very low detection sensitivity. However, surface-enhanced Raman scattering (SERS) can improve the sensitivity significantly by several orders of magnitude for roughened surfaces of many metals including noble and transition metals.

This article first briefly surveys the history of Raman spectroscopy applied to electrochemistry, followed by a brief outline of the basic principles of surface Raman spectroscopy. The SERS phenomena and mechanisms are then introduced. This is followed by a detailed description of Raman instrumentation, and the

experimental setup for electrochemical Raman spectroscopy. The methodology of Raman spectroscopy in the study of a variety of electrode surfaces will be discussed, with an emphasis on the improvement of the detection sensitivity, spectral resolution, temporal resolution, and spatial resolution, as well as combined and hyphenated techniques. Important factors are recognized and prioritized, in order to extend the general utility of surface Raman spectroscopy to *in situ* studies on electrode–solution interfaces under various conditions. A section on troubleshooting is included to deal with some of the problems commonly encountered in Raman studies, for example, low detection sensitivity, poor electrochemical stability and reversibility, surface heating and laser damage, and spectral data analysis. Applications consider areas such as surface adsorption, configuration and reaction, electrocatalysis, corrosion, electrodeposition, batteries, and sensors. Finally, prospects and further developments of this field are given with an emphasis on emerging methodologies.

3.6.1.1 History of Raman Spectroscopy Applied in Electrochemistry

The first *in situ* Raman spectroscopic study on electrochemical systems was reported on thin metal oxide and metal halide film electrodes by Fleischmann et al. in 1973 [1]. The Raman spectroelectrochemical measurements were made on thin films of Hg_2Cl_2 , Hg_2Br_2 , and HgO formed on droplets of mercury electrodeposited onto platinum electrodes. These mercury compounds have exceptionally high Raman scattering cross sections (very good Raman scatterers) so that the spectra of species as little as a few monolayers could be recorded on these high-surface-area electrodes. These experiments proved the viability of Raman spectroscopic measurements of

species at electrode–solution interfaces. Soon after, Van Duyne and coworkers obtained Raman signals from electrochemically generated radical ions, both in the bulk electrolyte and the diffusion layer [2]. As the normal Raman scattering was too weak for measurements in the thin diffusion layer, they used resonance Raman (RR) spectroscopy to increase the detection sensitivity remarkably. Time-resolved studies in the millisecond scale became possible to detect solution species produced by surface reactions.

The most significant breakthrough for electrochemical Raman spectroscopy was the study of adsorbed species with a (sub)monolayer quantity at the electrode–electrolyte interface. The first measurement was reported in 1974 by Fleischmann, Hendra, and McQuillan for pyridine adsorbed at a high surface area silver electrode [3]. Pyridine has a high Raman

scattering cross section and the surface of silver can readily be roughened electrochemically in order to increase the number of adsorbed species. The electrolyte comprised 0.1 mol l^{-1} KCl/ 0.05 mol l^{-1} pyridine and the Raman spectrum was recorded after the application of about 450 potential cycles between $+0.2$ and -0.3 V (vs saturated calomel electrode (SCE)). This Raman spectrum proved to be of very high quality and evidently was due to a surface species, in view of its potential dependence, see Fig. 1. All the major Raman bands changed markedly in intensity as the potential was changed from 0 V to -1.0 V [3]. These authors initially thought that the oxidation–reduction cycle (ORC), significantly increased the surface area of the electrode so that an intense surface Raman signal of pyridine could be obtained. After carefully making the calculations and experimenting, Van Duyne and Jeanmaire

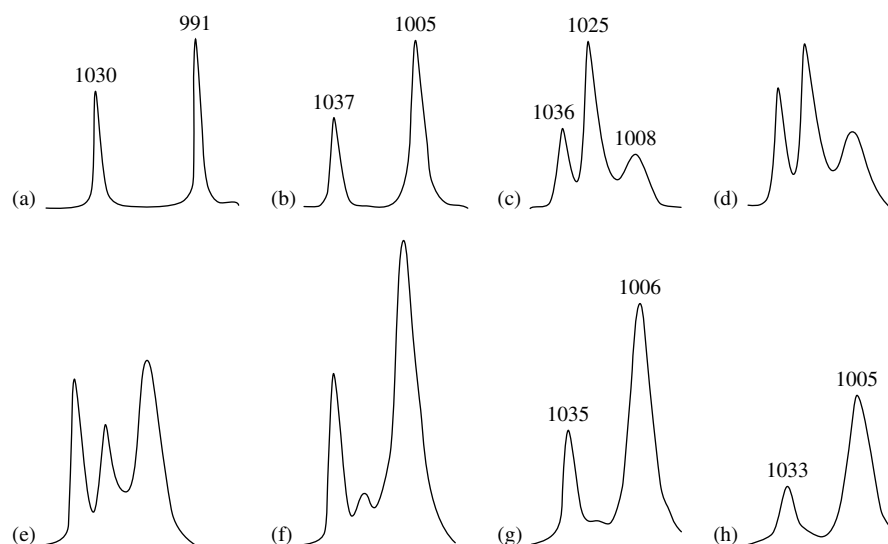


Fig. 1 The first SER spectra obtained from an electrochemically roughened silver electrode in 0.05 mol l^{-1} pyridine and 0.1 mol l^{-1} KCl, compared with normal Raman spectra of a: liquid pyridine and b: 0.05 mol l^{-1} aqueous pyridine. The applied potentials are: c: 0.0 V ; d: -0.2 V ; e: -0.4 V ; f: -0.6 V ; g: -0.8 V ; h: -1.0 V . (Reproduced with permission from Ref. [3]. Copyright 1974, Elsevier Esquida, S.A.)

realized that the major contribution to the intense Raman signal was due to an enhancement of intensity 10^5 to 10^6 times compared to the intensities predicted from the scattering cross section for bulk pyridine. But their paper was subjected to an exhaustive reviewing procedure as people did not believe in surface enhancement. It was eventually published in 1977 [4], and independently Albrecht and Creighton reported a similar result [5]. The effect was later named as SERS [6, 7]. These pioneering works opened up a new scientific field to study the enhanced optical scattering from surfaces and there have been thousands of papers dealing with this phenomenon, either theoretically or experimentally.

In the 1980s it turned out that only a few metals, mainly roughened Ag, Au, and Cu provided great enhancement of the Raman effect, which severely limited the extent of practical applications for SERS. Because of the key importance of transition metals in electrochemistry, catalysis, and materials science, it is of great interest to develop means by which substantial surface Raman enhancements can be imparted to such materials. Several groups have been devising strategies towards this goal. The SERS effect can be extended to transition-metal surfaces by electrodepositing the metal of interest as an ultrathin film on highly SERS-active Ag or Au [8, 9]. There are some excellent reviews concerning electrochemical surface-enhanced Raman spectroscopy during this period [6, 7, 10–14]. Therefore, these efforts have not been well recognized by the communities of Raman spectroscopy and electrochemistry.

However, SERS spectra obtained directly from neat transition metals could either not be repeated or barely detected. Until the late 1990s, the severe limitation

encountered in surface Raman investigations appears to be overcome by the latest advances in Raman instrumentation and surface preparation. Good-quality surface Raman signals have been obtained from bare Pt, Pd, Ru, Rh, Fe, Co, and Ni electrodes, which have been found to exhibit a surface enhancement ranging from one to four orders in magnitude [15, 16]. Nowadays, molecular-level investigations by Raman spectroscopy on diverse adsorbates at various transition-metal electrodes have been realized [15–18]. Furthermore, the effort to extend SERS to the study of single crystal electrodes with truly atom-smooth surfaces in an electrochemical cell, has also proved to be possible in recent years [19]. These advances have provided clear evidence that Raman spectroscopy will be applied as widely as IR spectroscopy (see Chapter 3.5) to surface science and electrochemistry.

3.6.1.2 Normal Raman Scattering and Resonance Raman Scattering

3.6.1.2.1 Normal Raman Effect The Raman effect is an inelastic light-scattering phenomenon [20, 21], which changes the frequency of the incident light illuminating a sample from ν_0 to another frequency ν_1 . The frequency difference, $\nu_0 - \nu_1$ which may be either positive or negative, is generally called the Raman frequency (or Raman shift). The name of this phenomenon comes from the experimental discovery by C. V. Raman, who first observed this effect in the spectrum of liquid benzene in 1928 [22]. In more than 70 years, Raman spectroscopy has been developed to become one of the most powerful techniques for the study of molecular structure.

The Raman effect can be described by an elementary classical theory. When a

light wave of frequency ν_0 with an electric field strength, $E = E_0 \cos 2\pi \nu_0 t$, is incident on a molecule (E_0 is the amplitude and t is the time), the dipole moment, μ , of the molecule is induced by this wave and given by

$$\mu = \alpha E = \alpha E_0 \cos 2\pi \nu_0 t \quad (1)$$

where α is a proportionality constant called the polarizability. If the molecule itself is vibrating at frequency ν corresponding to its normal mode and the nuclear displacement (normal coordinate) is written as $Q = Q_0 \cos 2\pi \nu t$, where Q_0 is the vibrational amplitude, then for small amplitudes of vibration, α is a linear function of Q . Thus

$$\alpha = \alpha_0 + \left(\frac{\partial \alpha}{\partial Q} \right)_0 Q \quad (2)$$

Here α_0 is the polarizability at the equilibrium position, and $(\partial \alpha / \partial Q)_0$ is the rate of change of α with respect to the change in a normal coordinate Q , evaluated at the equilibrium position. The characteristic vibrational frequency, ν , can mix with exciting light, ν_0 , to form sum and difference frequencies in the scattered radiation. By combining the above equations, one can obtain the following equation.

$$\begin{aligned} \mu &= \alpha E_0 \cos 2\pi \nu_0 t \\ &= \alpha_0 E_0 \cos 2\pi \nu_0 t + \left(\frac{\partial \alpha}{\partial Q} \right)_0 \\ &\quad \times Q_0 E_0 \cos 2\pi \nu_0 t \cdot \cos 2\pi \nu t \quad (3) \\ &= \alpha_0 E_0 \cos 2\pi \nu_0 t + \frac{1}{2} \left(\frac{\partial \alpha}{\partial Q} \right)_0 Q_0 E_0 \\ &\quad \times \{ \cos[2\pi(\nu_0 + \nu)t] + \cos[2\pi(\nu_0 - \nu)t] \} \end{aligned}$$

Here, the first term describes an oscillating dipole that radiates light at frequency, ν_0 (Rayleigh scattering or elastic scattering); the second term gives the Raman scattering or inelastic scattering

of frequencies $\nu_0 - \nu$ (Stokes) and $\nu_0 + \nu$ (anti-Stokes). Although weak, these frequencies may be detected as shifts from the Rayleigh frequency. The magnitude of these shifts reflects the characteristic vibrations of the molecule. If $(\partial \alpha / \partial Q)_0$ is zero, the second term vanishes. Thus, the vibration is not Raman active unless the polarizability changes during the vibration.

The schematic representation of the mechanisms involved in different Raman transitions is shown in Fig. 2. The Raman process can be considered as a two-photon process with a timescale of 10^{-12} s. It consists of an excitation initiated by an incident photon with frequency of ν_0 to a “virtual” state between the ground and excited electronic state and a simultaneous emission of the photon as the decay takes place from the virtual state back to the ground electronic state. Transition from ν_m to ν_n leads to the Stokes line and corresponds to the excitation of a particular vibrational mode to its first excited state and resulting in its fundamental absorption, see Fig. 2. While the transition from ν_n to ν_m leads to the anti-Stokes line (see Fig. 2), which has even lower probability, resulting in smaller Raman scattering. For a molecule having a frequency of ν , the Stokes and anti-Stokes spectra correspond to Raman bands at $\nu_0 - \nu$ and $\nu_0 + \nu$. The Raman spectra are usually presented as the intensity of scattered light versus the Raman shift $|\nu_0 - \nu|$, in cm^{-1} . Raman signals are usually very weak because one Raman photon is produced typically by 10^{10} incident photons. Almost all Raman spectra of adsorbed species have therefore relied on enhancement effects (vide infra).

3.6.1.2.2 Resonance Raman Effect When ν_0 is chosen either to be very close or to lie within the range of an electronic absorption of the scattering molecule, see

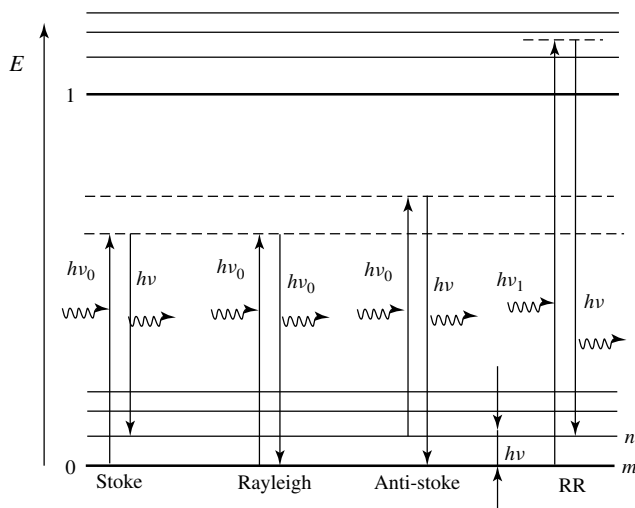


Fig. 2 Idealized model of Stokes, anti-Stokes and RR scattering, and Rayleigh scattering. (0): ground electronic state; (1): first excited electronic state; (*m*): ground vibrational state; and (*n*): first excited vibrational state.

the last process in Fig. 2, the significantly longer resident time at the excited electronic state, compared to that for the virtual state leads to a great enhancement of the probability of the Raman transition. This phenomenon is called the RR effect, and it results in an increase in the Raman scattering cross section by as much as 10^6 for certain vibrational modes. The huge enhancement of RR makes it possible to detect molecules at submonolayer levels. RR spectra are also much simpler than normal Raman spectra, since only the vibration modes coupled to the electronic transition are enhanced.

According to quantum mechanical theory of light scattering, the Raman intensity per unit solid angle of the scattered light arising from a transition between vibrational states *m*(ν_m) and *n*(ν_n) is given by [23],

$$I_{nm} = \frac{27\pi^5}{32c^4} I_L (\nu_0 - \nu_{nm})^4 \sum |(\alpha_{\rho\sigma})_{nm}|^2 \quad (4)$$

where I_L is the power density of the exciting laser light, and $\nu_{nm} = \nu_n - \nu_m$. Recalling Eq. (1), the second-order perturbation theory gives the following expression for the polarizability tensor component:

$$(\alpha_{\rho\sigma})_{nm} = \frac{1}{h} \sum_e \left(\frac{\langle n | \mu_\rho | e \rangle \langle e | \mu_\sigma | m \rangle}{\nu_{em} - \nu_0 + i\Gamma_e} + \frac{\langle n | \mu_\sigma | e \rangle \langle e | \mu_\rho | m \rangle}{\nu_{en} + \nu_0 + i\Gamma_e} \right) \quad (5)$$

where μ_ρ , μ_σ are the electric transition dipole moments, and $\nu_{em} = \nu_e - \nu_m$. The origin of RR scattering can be explained in terms of this equation. As the ν_0 approaches ν_{em} , the first term becomes dominant and is responsible for the resonance effect. Therefore, the intensities are no longer apparently dependent on the ν_0^4 term (see Eq. 4); they are only dependent on the proximity of the incident frequency to an electronic excitation frequency. Furthermore, the polarizability tensors become antisymmetric and analysis of the

symmetry properties of RR lines is complicated.

It should be noted that relatively few molecules have suitable electronic absorption at the laser excitation wavelength employed, particularly in the visible region. Furthermore, RR is not a surface-specific effect, so that solution species may greatly interfere with the surface spectrum. By contrast, SERS is a surface-specific effect, leading to a large increase in the Raman intensity only for surface species.

3.6.1.3 Surface-enhanced Raman Scattering

3.6.1.3.1 Experimental Characteristics of SERS Since the mid-1970s when the first SERS spectrum was obtained from an electrochemical cell, a large number of experimental characteristics of SERS have been discovered, and the key features are summarized as follows [6, 7, 12–14, 24]:

1. The effective increases in the Raman scattering cross sections, or surface enhancement factors (SEF), are typically about 10^6 fold on electrochemically roughened silver, gold, and copper. Few works have been reported on the other “free electron” metals such as alkali metals. Many transition metals have relatively weak surface enhancements. Their SEF values depend on the nature of the metal, for example, $10^3 \sim 10^4$ for Pt, Rh, Ni, Co, and Fe, and 10^1 for Pd.
2. Surface preparation is crucial to produce a strong SERS signal. A variety of morphologies include electrode surfaces roughened by one or more ORC, surfaces roughened by chemical etching in acids, island films deposited on surfaces at elevated temperatures, films deposited by evaporation or sputtering in vacuum onto cold (100 K) substrates or by electrochemical deposition, colloids (especially aggregated colloids) generated by chemical methods or laser ablation, nanoparticle and nanorod arrays prepared by lithographic self-assembly or template techniques.
3. Surface roughness with a scale of $10 \sim 200$ nm is required to produce huge SERS. Rough surfaces with these submicroscopic dimensions are also related inevitably to nanoscopic features, such as surface complexes, ad-atoms, ad-clusters, kinks or vacancies. Those features showing SERS effects are named as SERS-active sites and have proved to contribute to the enhancement in the range of 10 to 10^3 fold.
4. The most important progress recently made in this field is that silver nanoparticles can even generate enormous SERS enhancements up to 10^{14} , making single molecule Raman spectroscopy a reality. It is of particular interest that only silver nanoparticles with a size scale around 90 nm are optimal for obtaining this extremely high SERS effect. It implies that ordered nanostructures with narrow size-distributions compose a very promising class of ultra-active SERS substrates.
5. SERS is an interface-sensitive technique. Molecules adsorbed in the first layer at the surface show the largest enhancements. However, the enhancement also has a long-range aspect with molecules separated from the surface by tens of nanometers showing some enhancement, depending upon the substrate morphology and physical environments.
6. A very large number of molecules adsorbed on or near the surface of metals exhibit SERS, but their SEF values could be very different. For example, the polarizabilities of CO and N₂ are

nearly identical. However, they differ by a factor of 200 in their SERS intensities under the same experimental conditions. It appears that for the 10^6 enhancements for coinage metals in the electrochemical environment, the formation of a chemical bond with that active site is a necessity. In contrast, physisorbed molecules (or ions) show a smaller enhancement.

7. Both vibrational band frequencies and SERS intensities are a function of the applied electrode potential in electrochemical experiments, and the functionality may be different for different sets of vibrational modes. The SERS activity of electrodes can vanish irreversibly by applying a very negative potential and be regenerated by applying a new electrochemical ORC.
8. The Raman bands of SERS activity from rough surfaces are completely depolarized unless single nanoparticles are employed, in contrast to spectra taken from molecules adsorbed on atomically smooth surfaces. Overtone and combination bands are not prevalent. Selection rules are relaxed, resulting in the appearance of normally forbidden Raman modes in the surface spectra. SERS-active surfaces also display a continuum inelastic background scattering and are very effective in quenching fluorescence. The excitation profile (SERS intensity versus exciting frequency) deviates from the fourth-power dependence of normal Raman scattering.

3.6.1.3.2 Electromagnetic Enhancement

A number of SERS mechanisms have been proposed to explain the above experimental characteristics; however, no one mechanism can explain all of the observed evidence. There are at least two major mechanisms that contribute jointly

to the SERS effect [25–29]: (1) an electromagnetic (EM) effect associated with large local fields caused by electromagnetic resonance and (2) a chemical effect (CE) involving a resonance-like Raman process associated with chemical interactions between the molecule and the metal surface. Recalling Eq. (4) describing the Raman intensity contributed from free molecules, the SERS intensity can be expressed in general terms by

$$I_{\text{SERS}} \propto \nu_{\text{sc}}^4 E_{\text{in}}^2 E_{\text{sc}}^2 \sum_{\rho, \sigma} |(\alpha_{\rho\sigma})_{\text{nm}}|^2 \quad (6)$$

where ν_{sc} is the frequency of the Raman scattering light. E_{in} and E_{sc} replace I_{L} as the power density of the exciting laser light in Eq. (4) in order to describe the local electromagnetic (optical electric) fields of the incident and scattering radiation, respectively. Their squares denote the intensities of the incident and scattering light at the surface, resulting in the surface electromagnetic enhanced effect [13]. The summation term of $(\alpha_{\rho\sigma})_{\text{nm}}$ describes the optical response to intramolecular interactions and the interaction between a molecule and the metal surface, resulting in the chemical enhanced effect.

The electromagnetic field enhancement is now considered to come from a geometrically defined localized plasmon resonance within metal nanoparticles such as produced by an ORC pretreatment in an electrochemical system. Electromagnetic effects can be further divided into several enhancement processes. The major contribution is from surface plasmons (SP). The collective excitation of the electron gas of a conductor is termed as a plasmon; if the excitation is confined to the surface region it is called a surface plasmon. The electromagnetic field of the light at the surface can be greatly enhanced under conditions of surface plasmon excitation (collective electron resonance) for the coinage metals

Au, Ag, and Cu. At the plasmon frequency, there is a large field-induced polarization and thus large local fields at the metal surface by the incident radiation. These local fields remarkably increase the Raman scattering intensity of surface species, which is proportional to the square of the applied field. The rough surface not only enhances the incident laser field but also the Raman scattered field; therefore, the overall enhancement of the Raman intensity scales roughly with the fourth power of the field.

EM enhancement mechanisms are characterized by the following features: (1) The effects are long range in nature, since the dipole fields induced in polarizable metal particles vary as the inverse cube of the distance to the center of the particle. (2) EM effects are generally independent of the adsorbed molecule. (3) The enhancements depend on the electronic structure of the substrate and the roughness of the surface, since the frequency of the surface plasmon resonance depends on these factors.

There have been many versions of EM theory treating the physical problem at different levels [25–29]. Various models to simulate the SERS-active surface and colloids have been used, including spheres, ellipsoids, gratings, hemispherical and hemispheroidal bumps on flat surfaces, random rough surfaces, and highly irregular fractals. For isolated regular particles, such as spheres and ellipsoids, the exact classical solutions of the scattering effect can be solved by the Maxwell equation. On the basis of the solution of the Maxwell equation, the Mie scattering theory is well established for studying spherical particles with different sizes, using various excitation wavelengths. It indicates that the surface plasmon can be excited and mainly contributes to the SERS effect. For

isolated spheroidal particles, including the prolate and oblate shapes, a theoretical method using the spheroidal coordinate was proposed. The aspect ratio of the particle is an important parameter influencing the surface enhancement factor. Surface plasmon resonance and the lightning rod effect all contribute to the SERS effect. For irregular isolated particles, numerical methods can be used to calculate the scattering efficiency. However, the SERS effect generally involves complex morphological substrates, such as electrochemically roughened surfaces. In this case, collective effects between the particles play an important role in the SERS process, and the single particle models alluded to above are not very appropriate to simulate the scattering effect.

The effective medium theory has been applied to the composite system with many particles, by which the detailed geometric configuration need generally not be considered. On the basis of the model, the SERS effect has been predicted for Cu, Ag, and Au particles doped in an Al_2O_3 medium. Recently, the discrete dipole approximation has been applied to truncated tetrahedron Ag particles and aggregation clusters on mica substrates, as well as fractal structures consisting of Ag particles [30]. However, the application of this method is limited to metals with the refractive index smaller than 2. For transition-metal particles (clusters) and rough surfaces, the refractive index is larger, and it has therefore been an open question to estimate the EM contribution to the SERS effect for these systems. It should be noted that the surface plasmon is not the only source of enhanced local electromagnetic fields. Other types of electromagnetic fields, such as the dipole image field effect and the “lightning rod” effect, occur at near high-curvature points existing on the

rough surface. The latter may be an important contribution to the enhancement for transition metals.

3.6.1.3.3 Chemical Enhancement Compared to electromagnetic enhancement, aspects of the contribution of chemical enhancement [27–29], are less known. Chemical enhancement has other synonyms such as charge transfer (CT) and the short-range effect. It is associated with the electronic structure (state) of the metal and the adsorbate, which can be explained by a resonance-like Raman mechanism (*vide infra*). As most of the electrochemical SERS systems involve the formation of strong or weak chemical bonds for the adsorbate with the electrode surface, it is

necessary to discuss the chemical enhancement in more detail.

Figure 3(a) depicts the operative CT mechanism for a molecule adsorbed at an electrode. In spite of the perturbed redistribution of the energy level for a molecule adsorbed on a rough surface, the RR process is still very unlikely because of the large energy gap between the highest occupied molecular orbitals (HOMO) and the lowest unoccupied molecular orbitals (LUMO). However, RR scattering can occur through photon-driven charge-transfer processes between the metal and adsorbate. It is assumed that transitions from states near the Fermi level are preferred because of favorable matrix elements involving wave function overlap or because of a localized electron density of states. For Step 1, an electron-hole pair of the metal is created by the incident photon, and the electron is excited as a “hot electron”. It then tunnels into the accessible vacant levels, such as the LUMO, of the adsorbate, generating a charge-transfer excited state, Step 2. This results in a negative ion (adsorbate molecule-electron) having equilibrium geometry differing from that of the original adsorbate molecule. Therefore, the charge-transfer process induces a nuclear relaxation in the adsorbate molecule which, after the return of the electron to the metal (Step 3), and recombination of the electron-hole pair, leads to a vibrationally excited neutral molecule and to emission of a Raman-shifted photon, see Step 4.

It should be emphasized that the SERS-active sites include various microscopic

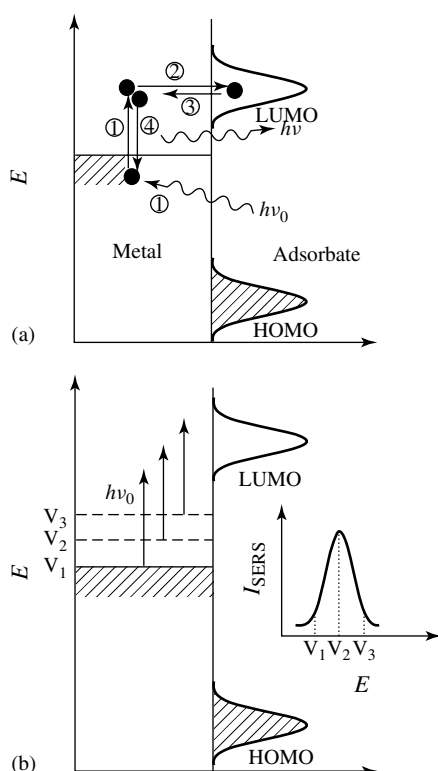


Fig. 3 Schematic diagrams of (a) the four-step process of the photon-driven CT model for a molecule adsorbed at an electrode and (b) the SERS intensity-potential profile obtained by tuning the potential to the RR process (see text).

surface structures interacting with adsorbates. They can have energy levels that do not exist in either the bulk metal or in the free molecule. More importantly, they can have transition matrix elements that are not allowed in the bulk metal because the spatial localization of the metallic ad-clusters relaxes the momentum selection rules. Therefore, the SERS-active sites could facilitate significantly the CT between the surface and adsorbate, and electron–phonon couplings are also increased greatly by these microscopic surface roughness features.

To probe the presence of the charge-transfer RR process, one can design a simple experiment to quantitatively evaluate the energy position and width of the CT band, as shown in Fig. 3(b). Taking pyridine adsorbed on an electrode as an example, with a fixed photon energy, one can tune the CT excitation into and out of resonance by simply controlling the applied electrode potential, that is, the metal energy state (Fermi level). As the potential is moved from V_1 to V_3 , the SERS intensity reaches the maximum value at V_2 , as the CT excitation energy is equal to the excitation energy of the incident photon. It indicates that the enhancement is partially induced by efficient photon stimulated transitions involving CT between the Fermi level and the molecular levels. As the photon energy is changed, with all other experimental factors remaining constant, the shift in the optimum voltage must be interpreted as being caused by CT.

In general, chemical effects contribute to SERS in a short range, on the molecular scale. This mechanism depends on the adsorption site, the geometry of bonding, and the energy levels of the adsorbate molecule. Although the CT is not a general mechanism, and is restricted by its

chemical specificity, it can provide useful information uniquely on chemisorptive interactions between metal and adsorbate. The total enhancement can mainly be attributed to both an electromagnetic enhancement, which does not require a surface bond, and a chemical enhancement, most likely a CT RR enhancement, which requires the surface and molecule interaction. Because of the heterogeneous nature of SERS-active surfaces, it is a very difficult task to determine how their contributions change when the experimental conditions, such as adsorbate, metal, and electrolyte, are changed. A quantitative understanding of the relative contributions of these mechanisms is still insufficient.

For readers interested in a comprehensive review of SERS, several excellent review articles with more detail on various aspects of the subject are recommended [13, 14, 25–29]. For recent progress in SERS, readers may refer to a special issue on SERS in the *Journal of Raman Spectroscopy* [31] and symposium proceedings on surface Raman spectroscopy [24].

3.6.1.4 Vibrational Properties of Electrode Surface Species

The vibrational properties of surface species are significantly different from those of the same species in bulk phases. The individual molecules may be distorted and their symmetry altered as compared to the free molecules, thus leading to modifications of their vibrational behaviors. There are various processes contributing to the bandwidths, intensities and positions, including change of molecular symmetry, dipole coupling, inhomogeneous broadening, intramolecular vibrational relaxation, dephasing, electron-hole pair creation, and phonon coupling. It is necessary to briefly describe some key features of a molecule interacting (or

adsorbing) with a surface and/or with the same or other surface species, in terms of molecular symmetry [32], dipole coupling interactions [33], and the electrochemical Stark effect [34–36].

A systematic and good illustration requires a model molecule as an adsorbate interacting with a surface. There are several important reasons for using carbon monoxide as the adsorbate. CO possesses a minimum of internal vibrational modes and can easily be isotopically labeled at either end. Besides, the ν_{CO} band position and shape are sensitive to the chemical and electrostatic environment, as well as to the mode of surface bonding. The strong chemisorption found on transition metals enables adsorbed CO to be examined over a wide range of coverage, under ambient conditions, and at higher temperatures. Moreover, a rich base of knowledge about CO adsorption at well-defined metal surfaces in ultrahigh vacuum (UHV) can be used to probe the additional complexities of catalyst surfaces and electrochemical interfaces.

3.6.1.4.1 Molecular Symmetry of Surface Species

It is well known that the number of dipole active vibrations of a molecule is determined by the degrees of vibrational freedom and symmetry [32]. The freedom of the molecule depends on its physical state. A free molecule with N atoms has $3N$ degrees of freedom, with $3N-6$ ($3N-5$ for a linear molecule) degrees of vibrational freedom. When a molecule becomes attached to the surface, the translational motion and rotational motion are restricted and the degree of vibrational freedom equals $3N$. That means, an adsorbed molecule has an excess of 6 (or 5) modes of vibrational freedom. To illustrate what can happen when a gaseous species adsorbs on a surface, let us consider CO adsorbed on a single crystal (100) surface. CO can adsorb either linearly or by a bridge mode, see Fig. 4. Linearly adsorbed species belong to the C_{4v} point group with two totally symmetric vibrational modes belonging to the A_1 representation. One of these corresponds to the stretching mode of the free CO molecule; another comes from the restricted translational motion

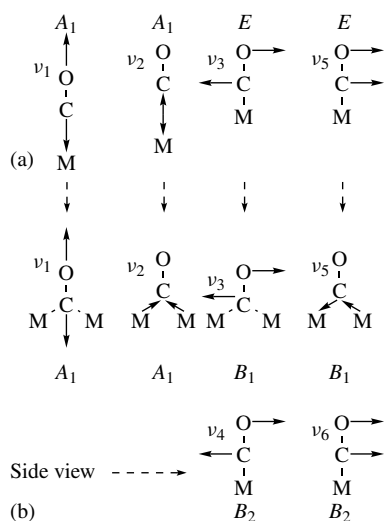


Fig. 4 Possible structural features (vibrational modes) of CO on a metal surface: (a) on-top site and (b) bridge site.

of the whole CO molecule relative to the surface, that is, the stretching mode of the surface atom with the C atom. The other four modes are twisted vibrations parallel to the surface and belong to the degenerate E representation. The freedom for these vibrations comes from restricted molecular translation and rotation. Bridge-bonded species have C_{2v} symmetry, with two A_1 stretching modes perpendicular to the surface. The degeneration of the parallel mode leaves two B_1 modes parallel to the bridged plane and two B_2 modes normal to the bridged plane (molecular models for the B_2 vibrations are given as a side view in Fig. 4).

3.6.1.4.2 Dipole Coupling In adsorbed layers at surfaces, electrostatic interactions between the dipoles induced in neighboring molecules serve to couple together the vibrational motion. The effects of such dipole coupling interactions [33] have been investigated in considerable detail on single crystal surfaces. Briefly, coupling has two important consequences: (1) Coupling between identical molecules gives rise to a vibrational frequency somewhat higher than that of the isolated single molecule. (2) Coupling between two species with different frequencies yields two active modes. Each of these has a vibrational frequency close to that of the original species, so there are no significant shifts in the positions of the absorption bands. There is, however, a characteristic transfer of intensity from the low frequency mode to its higher frequency counterpart.

3.6.1.4.3 Electrochemical Stark Effect and the Influence of a Solvent Surface vibrational spectra of adsorbed species on an electrode are often characterized by

changes in their vibrational frequencies with applied potential. This is frequently termed the electrochemical Stark tuning effect [34–36]. Taking chemisorbed CO at Pt group metals as an example, the potential dependent metal-carbon and intramolecular band frequencies for CO can be plotted almost linearly in a wide potential range. The slope $d\nu_{CO}/dE$ values are positive from ca. 30 to 60 $\text{cm}^{-1} \text{V}^{-1}$, contrasting the negative $d\nu_{M-C}/dE$ values, ca. –10 to –20 $\text{cm}^{-1} \text{V}^{-1}$ [35]. These frequency-potential dependencies originate from potential dependent metal-adsorbate bonding and from the influence of the variable electronic field exerted across the adsorbed layer. Accordingly, two mechanisms have been proposed to explain this general behavior.

The first mechanism involves surface charge-induced changes in the CO intermolecular bond and the metal-CO bond. The molecular orbital picture involves electron donation from filled adsorbate orbitals of correct symmetry to empty metal orbitals through σ overlap. The metal can then back-donate electrons from filled d orbitals to empty π^* adsorbate antibonding orbitals. Because the π -bonding interaction is dominant, the frequency of an adsorbed CO (with respect to solution species) will decrease. When the electrode potential is made more negative, the $(d\pi - 2\pi^*)$ back donation is more favorable, leading to further decrease of the CO bond strength and the intramolecular stretching frequency. The negative $d\nu_{M-C}/dE$ values observed can be explained by a progressive shortening of the M–CO bond length; thus the frequency shifts to higher wave numbers, which is induced by an increased extent of back donation at more negative potentials.

The second mechanism involves coupling of highly polarizable electrons of the adsorbate with the strong electrostatic field across the adsorbed layer, that is, a vibrational Stark effect [36]. If the electrolyte concentration is high enough (about 1 mol l^{-1}), most of the potential drop in the electrochemical double layer will be approximately linear with distance and will occur within a few angstroms of the interface. An adsorbed species can act as a dielectric across which the largest portion of the potential drop will occur. Very high electric fields (on the order of 10^7 V cm^{-1}) are predicted to exist in the double layer. Interaction of this interfacial electric field with the dipole moment of an adsorbed molecule can lead to changes in the molecular vibrational frequency.

3.6.1.5 Surface Selection Rules

As the vibrational properties of surface species are so different from those of the same species in the bulk phase, surface selection rules [37, 38] are extremely important for analyzing surface Raman spectra correctly. These rules can be the basis for determining molecular orientation and conformation on surfaces. Let us consider a molecule placed on a flat surface. The molecule illuminated by the incident light at a certain angle can be thought to be illuminated by two beams, a direct beam and a reflected beam at the surface, which superimpose coherently at the molecule. Thus, it is known that the molecule is polarized by the local electric field on a flat surface and the induced dipole of the molecule radiates the scattering light. The relationships between the local electric field caused by the incident and reflected light and the scattering one, can be described by a polarizability tensor, which contains nine

components, i.e. α_{xx} , α_{yy} , α_{zz} , α_{xy} , α_{yx} , α_{xz} , α_{zx} , α_{yz} , and α_{zy} . The polarizability tensor is written by the matrix representation,

$$\alpha = \begin{bmatrix} \alpha_{xx} & \alpha_{xy} & \alpha_{xz} \\ \alpha_{yx} & \alpha_{yy} & \alpha_{yz} \\ \alpha_{zx} & \alpha_{zy} & \alpha_{zz} \end{bmatrix} \quad (7)$$

Since $\alpha_{xy} = \alpha_{yx}$, $\alpha_{xz} = \alpha_{zx}$, $\alpha_{yz} = \alpha_{zy}$, there are only six independent tensor elements. The intensity of the Raman scattering light on the surface is directly related to the derivative of the polarizability tensor, with respect to the given normal coordinates. In order to determine these tensor elements, it is necessary to consider the system, including the molecule and surface atoms, and to define the Cartesian coordinate axis, z , along the surface normal and others along the surface parallel.

Then, one is able to determine the symmetry point group of the molecule adsorbed on the surface. For a chemisorbed molecule, there is likely to be lower symmetry compared to the molecule in the bulk phase. In particular, for a strongly chemisorbed molecule, its geometry may be changed significantly by the interaction with the surface.

After obtaining the symmetry point group of the metal-adsorbate system, one can determine which symmetry representations of the vibrations of the molecule will be Raman active using group character tables for the given point group. Raman-active modes are those that possess nonzero components of the Raman polarizability tensor.

Surface Raman spectra can be significantly different from ordinary Raman spectra. It is reasonable that the tangential component of the surface electric field is nearly zero, due to the superimposition of

the incident field with an out-of-phase reflected field, while the normal component of the incident field is reinforced by the reflected field. So, the field component normal to the surface has an important contribution to totally symmetric vibration modes. Accordingly, it is possible to design Raman experiments so that the directions of the incident and scattering light, and their polarization directions, enable the determination of the particular polarizability tensor elements from the observed Raman intensities. This is related directly to the surface orientation of the molecule. In addition to metals, the surface selection rules should apply to insulators at frequencies in which they have metallic reflectance.

On the basis of the EM mechanism one can approximately predict the relative enhancements of the different vibrational modes for surface species. Since the component of the enhanced local electric field perpendicular to the surface has the largest enhancement, the vibrational modes with the totally symmetric polarizability tensor component (α_{zz}) have the strongest enhancement. The vibrational modes with the nontotally symmetric polarizability tensor elements (α_{xz} or α_{yz}) are less enhanced. Vibrational modes with the polarizability tensor

along the xy plane show the weakest enhanced effect.

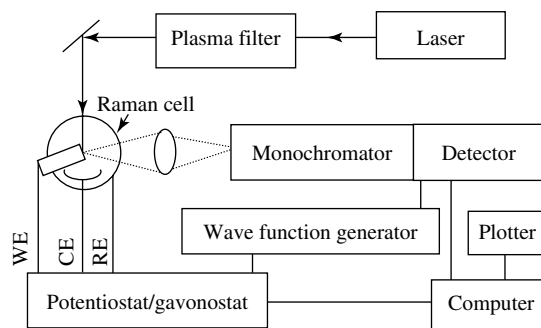
3.6.1.6 Comparison of Raman Spectroscopy with Infrared (IR) Spectroscopy and their Applications in Electrochemistry

The preceding chapter considered IR spectroscopy in electrochemistry and to conclude this section, it is useful to compare both the techniques (Table 1).

3.6.2 Experimental Details

Figure 5 presents the experimental setup of in situ electrochemical Raman spectroscopy. The instrument for in situ Raman spectroscopic studies of electrochemical systems includes a laser as the excitation source, a Raman spectrometer, a personal computer for control of the Raman spectrometer, data acquisition and manipulation, as well as a plotter or printer for data output, a potentiostat/galvanostat and possibly a wave function generator for generation of various kinds of potential/current control over the electrode, and the spectroelectrochemical cell. Details of electrochemical instrumentation were given in Chapter 1.2; see this chapter for various definitions, including WE

Fig. 5 Block diagram of the experimental setup of in situ electrochemical Raman spectroscopy.



Tab. 1 Comparison of the similarities and differences of Raman and IR spectroscopy

	<i>Raman</i>	<i>Infrared</i>
Optical phenomenon	Scattering	Absorption
Photon process	Two photon	One photon
Sensitivity (cross section/cm ²)	Low ($\sim 10^{-29}$) ^a	High ($\sim 10^{-20}$)
Spectral windows (cm ⁻¹)	Normally 30 ~ 4000	Normally 900 ~ 4000 ^b
Band shape	Sharp	Broad
Intensity-concentration	Linear	Exponential
Spatial resolution	$\sim 1 \mu\text{m}$	$\sim 30 \mu\text{m}$
Surface enhancement	Yes	Yes
SEF for coinage metals	$\sim 10^{6c}$	~ 80
SEF for transition metals	$\sim 10^2 - 10^4$	$\sim 20 - 50$
Surface selection rules	Relaxed, complex	Strict, simple
Determination of molecular orientation at surface	Difficult and complex (especially for SERS)	Simple and clear
Typical sampling methods	180 degree backscattering and 90 degree scattering collection	70 degree external reflection Attenuated total reflection ATR
Interference from ambient environment	No	Strong interference from water and CO ₂
Typical spectroelectrochemical measurement and spectrum	No specific requirement (absolute spectrum)	Electrode potential modulation (potential difference spectrum)
Cell configuration	No specific requirement	Thin solution layer with ca 10 μm (for the external reflection)
Most used surface morphology	Rough ^d	Mirror finish
Typical light source	Laser	Silicon carbide or "Nernst Filament"
Possible surface destruction	Laser heating or annealing	Nondestructive

^aThe probability of a molecule producing Raman scattering is much less than the probability of IR absorption. However, advances in Raman instrumentation and lasers have narrowed the gap considerably, in some optimal cases, the sensitivity of normal Raman scattering compares favorably with IR absorption. In addition, the Raman scattering efficiency can be greatly increased by use of the surface enhanced and/or RR effects.

^bA current limitation is that the IR technique becomes difficult to apply at wave numbers below about 800 cm⁻¹ because of the low intensity of thermal infrared sources in this region. This difficulty can be overcome by the use of a synchrotron radiation source.

^cFor specific silver and gold nanoparticles with adequate size of about 90 nm and 60 nm, SEF values up to 10^{14} can be achieved.

^dTo prepare highly SERS-active substrates, proper surface roughening procedures are necessary.

(working electrode), CE (counter electrode) and RE (reference electrode). It is necessary to have general knowledge about every part of the Raman instrumentation in order to apply Raman spectroscopy appropriately.

3.6.2.1 Instrumentation for Raman Spectroscopy

The basic Raman instrument [20, 21, 39–42] mainly consists of the excitation source, collection optics, monochromator, and detection and recording system.

The laser has to be filtered by a plasma filter to remove the plasma lines, in order to make it truly monochromatic. The collection optics can either be a normal camera lens for macro sample studies or a microscope (conventional or confocal). There are several types of incident and collection configurations for Raman studies on the electrode surface (vide infra). The monochromator normally disperses the Raman light and separates the Rayleigh scattering light (or even the reflected laser) from the Raman signal. Depending on the system, the monochromator may be a double or triple monochromator, or a combination of one or two notch filter(s) with a single monochromator. There are various types of detectors, such as PMT (photomultiplier tube), PDA (Photodiode arrays), and CCD (charge-coupled device). Systems can either be assembled by a researcher for specific investigations or purchased commercially for general-purpose applications. However, each kind of setup has its advantages and disadvantages. Therefore, a concise description of the different types of Raman instrument is given below.

3.6.2.1.1 Lasers As mentioned in Sect. 3.6.1.2.1, the Raman signal is the frequency shift from the excitation line. The wavelength of the excitation sources applied in Raman instrumentation can vary from UV to the near-infrared region. There are two types of lasers [43]: continuous wave (CW) and pulsed lasers. CW lasers give a continuous supply of photons and are by far, currently, the most widely used lasers. On the whole, the argon (Ar^+) laser is of most value for studies requiring blue (488.0 nm) or green excitation (514.5 nm), the helium/neon laser is of greatest value in the red (632.8 nm) region and the krypton laser in the red (647.1 nm) and yellow (568.2 nm) regions of the spectrum. Of

the three, provided that there is no specific wavelength requirement, the argon laser is probably the better option. This is because it can be obtained in much higher power output (5 W to 5 mW) than the He/Ne laser (30 mW to 3 mW) and will give a wide range of lines without the need for changing the laser optics. It is also better than the krypton laser in terms of the output stability and is easier for the non-expert to use. The most easily used laser is the He/Ne laser, since it is robust and relatively low priced.

Several lines in the UV region are available for the He-Cd laser (325 nm) or by doubling the wavelength of the argon laser to 244 nm and 257 nm. However, their use to give UV output needs very careful handling because of the obvious dangers associated with high power outputs of high-energy photons where the beams cannot be observed by eye. If the sample to be analyzed exhibits significant fluorescence that may totally obscure the Raman signal, it can often be reduced considerably by using far-red excitation, and for this purpose the 758 nm line available from the semiconductor laser is useful. The CW Yttrium Aluminum Garnet (YAG) laser can work for this purpose very effectively. It gives an output at 1.064 μm , well beyond the operating range of conventional monochromator/detector systems. However, it finds application in the area of Fourier Transform Raman spectroscopy (vide infra). The CW YAG laser has a high power output, being robust, air-cooled, reliable, and inexpensive to maintain.

The use of pulsed lasers for Raman spectroscopy has, because of the very high powers involved, been largely in the area of nonlinear studies, and it is only recently that their value in the Raman work has been appreciated. The most commonly

used system is based on the pulsed YAG laser with the fundamental output at 1.064 μm and its frequency-doubled wavelength, 532 nm. The predecessor of the YAG system, based on the pulsed nitrogen laser, is now scarcely used for this type of work because of the much greater versatility of the former system. The great advantage of YAG and excimer lasers is the very high degree of tunability, which can be continuously varied from about 190 nm to 4 μm . This is achieved by means of either Ti:Sapphire or dye laser outputs and fundamentals that are frequency doubled, tripled and mixed. A capability of this type opens up the possibility of extending RR and SERS to the study of a much wider range of compounds than is possible with CW lasers and also offers considerable potential for fluorescence suppression.

Apart from the high degree of tunability, pulsed laser systems provide very high power output, often of the order of megawatts, but their main drawback lies in their very low pulse rate and the short duration of the pulse. The repetition rate for a YAG-based system is typically 10 to 40 Hz and for an excimer about 50 to 300 Hz, and in each case the duration of the pulse is approximately 10 ns. This means that the detector is only exposed to the Raman signal for a maximum of 3 μs in every second, but in the rest of the time it is still building a noise signal. The detector thus needs to be gated so that it only operates during the duration of the laser pulse. Both the YAG and the excimer systems are extremely expensive to purchase. Both are intrinsically much more hazardous than the CW laser because of their very high peak powers, and they also require appreciably more operator skill. Such systems are only of value, therefore, for highly specific applications.

3.6.2.1.2 Monochannel Instruments The conventional Raman system can be classified into two types: scanning monochannel instruments [39] and multichannel instruments. In a single spectrometer, a collimating mirror collects the Raman scattered light from the entrance slit and spreads the light uniformly over a plane grating. Light diffracted by the grating is collected by a second mirror, which focuses it onto the exit plane. In a monochromator, a single wavelength, altered by changing the position of the grating, passes through an exit slit to a detector. The performance of a spectrometer depends on a variety of parameters and can be adjusted for the problem at hand after several trade-offs between the spectral resolution attainable and the signal passing through to the detector. The latter, in turn, depends on the dispersion and the throughput.

PMTs used most often in the scanning monochannel instruments are high-gain devices of generalized use for light detection. For detection of low-light levels, the figures of merit are the quantum efficiency and the dark current. For low-light-level spectroscopies, where large acquisition times are often employed, dark current becomes the limiting factor of the maximum acquisition time before saturation of the photon counter occurs.

3.6.2.1.3 Multichannel Instruments Multichannel spectral acquisition was introduced in Raman spectroscopy in the 1980s. A multichannel spectrometer [39] allows the recording of a substantial segment of the Raman spectrum (ideally, the entire region of interest) simultaneously, without scanning the spectrometer wavelength. This results in a large improvement in sensitivity over that of the scanning instrument of the preceding section. Therefore, the multichannel instrument has gradually

become dominant in Raman spectroscopy laboratories. The two basic components of the multichannel instrument are the spectrograph and the multichannel detector itself.

In a spectrograph, the spectral region of interest is dispersed across a focus field. The matching of this field with the sensitive area of the multichannel detector must be the best possible. By combining the selection of the pixel (light-sensitive element) number and size with gratings of different grooves, the spectral resolution can be varied to achieve this.

There are two practical choices for a multichannel detector, namely, PDAs and CCDs. Different detectors use different methods to transfer the photon signals into the detectable current. The CCD detector has a relatively low dark current and high quantum efficiency, especially for the intensified CCD (ICCD).

The combination of a spectrograph with a multichannel detector provides advantages in terms of detection sensitivity and temporal resolution. Since a large number of pixels are illuminated simultaneously with dispersed light during the entire measurement, the signal level in each resolution element is much higher than that obtained with a monochannel instrument for the same total acquisition time. The improved sensitivity of the multichannel instrument, called the multiplex advantage, results in a saving of time for the acquisition of a spectrum, with a given signal-to-noise ratio (S/N) over that of the scanning instrument.

3.6.2.1.4 Fourier Transform Raman (FT-Raman) Spectrometer In the mid-1980s, another type of multichannel Raman system was introduced. By exciting with a near-IR laser, good-quality Raman spectra can be recorded with a near-IR

interferometer. The most frequently used laser source for the FT-Raman spectroscopy [40] is the 1064 nm laser line provided by a Nd-YAG laser or the tunable Ti:Sapphire laser, covering a wavelength range from 843.2 to 1064 nm. A GaAs laser can also be used to provide the excitation line. After collection of the Raman scattered light, a set of filters should be properly designed to eliminate or block the source radiation and stray scattered light. The filters directly influence the detection sensitivity of the system, because there is no monochromator before the detector for the FT-Raman system. The commercialized FT-Raman system can now work to a frequency region as low as 100 cm^{-1} . After the filter, the scattered light goes directly into the Michelson interferometer. Half of the light is reflected to a fixed mirror, and the other light transmits to a moving mirror. The two beams are then mixed at the detector after transmittance and reflection by the beam splitter, resulting in the interference pattern on the detector. The most popular detectors in the FT-Raman system are the extended Ge detector operated at -190°C and the InGaAs detector, which works at room temperature, or with slightly better performance at cryogenic temperatures. The detected signals are Fourier-transformed to obtain FT-Raman spectra.

Since in the FT-Raman system, there is no need to use slits, optical alignment becomes easier, and the laser does not need to be focused. Thus, the throughput of the system is mainly limited by the size of the mirrors in the interferometer. With the same spectral resolution, the throughput of the FT-Raman spectrometer is higher than the conventional Raman system. However, on the basis of Eq. (4), the intensity of a conventional system is proportional to the excitation

frequency, ν_0 , and the detection efficiency of the detector. In contrast, the FT-Raman instrument uses near-IR lasers and the detector works in the near-IR region, with high noise and low quantum efficiency. Therefore, the overall sensitivity of the FT-Raman instrument is quite low compared with the conventional Raman system, and remarkably lower than that of the confocal Raman microscope. Moreover, the strong absorption of light by water in the near-IR makes it difficult to use the FT-Raman spectroscopy to investigate the electrode–aqueous solution interface. However, since the photon energy in the near IR is usually not sufficient to cause transitions between the electronic states that give rise to fluorescence, the FT-Raman spectroscopy has the unique advantage in the discrimination of fluorescence. This is especially ideal for some film electrodes having fluorescence, including polymer and biological film electrodes.

3.6.2.1.5 Raman Microscope Raman microscopy [41, 42] is a hybrid of optical microscopy and Raman spectroscopy and, in consequence, has all the concomitant advantages of both techniques. The main purpose of the microscope is to excite, collect, and couple the Raman radiation very efficiently from the sample to the Raman spectrometer, and to provide a means for sample positioning and viewing at high magnification. The Raman microscope can analyze the vibrational frequency shift at different points of a surface, so as to resolve areas with different chemical composition, which is referred to as chemical imaging.

To increase the spatial resolution and detection sensitivity in surface analysis, two important characteristics of a microscope lens [magnification and numerical aperture (NA)] should be considered.

Magnification is simply the ratio of the image size to the object size. It is important only to the visual operation of the microscope, since it does not affect the energy throughput. The intensity of Raman scattering is proportional to the irradiance (power/area of cross section) of the exciting beam, thus what really affects the Raman intensity is the laser power, not the power density. As a consequence, although the amount of sample decreases, the intensity does not decrease. However, the Raman intensity also depends critically on the solid angle, Ω over which the scattered light is collected. Ω is directly related to the NA, which is given by $NA = n \sin \theta$. The NA is directly proportional to the energy throughput and so should be as high as practically possible. Typical NAs of Raman microscopic lenses are 0.5 to 1.2. For in situ studies, in which immersion of the objective in the electrolyte is to be avoided, a long working distance (3–8 mm) microscopic objective with $NA = 0.5$ is used, at the expense of the lowering of the collection efficiency. Moreover, the ratio of the collection lens radius to the distance between the lens and the entrance slit should be equal to the ratio of the radius of the first optical element in the monochromator to its distance to the entrance slit. This condition will ensure that the scattered light will fill the spectrometer optics, giving optimum sensitivity and resolving power.

The Raman scattered radiation is collected at 180° to the incident excitation by the same objective and transmitted back through the beam splitter. Recently, most Raman microscopes have employed holographic notch filters as the beam splitter. The filter reflects the excitation wavelength with very high efficiency and transmits the Raman scattered radiation with an efficiency of more than 85%, by which a very high Rayleigh rejection is

achieved (10^{-5} – 10^{-6}). This achievement allows the use of a single short focal length monochromator ($0.25 \sim 0.35$ m). However, to obtain information on extremely low wave number shifts (i.e., 5 to 20 cm^{-1} shift), a double monochromator may be required. The overall benefit is that the size and cost of Raman microprobes have been reduced considerably and the surface sensitivity has increased remarkably.

3.6.2.1.6 Confocal Raman Microscope

There has recently been an important development over the conventional Raman microscope, namely the confocal Raman microscope [41, 42]. The term “confocal” is used to describe optical systems that limit the light collection to a small volume. This configuration accounts for the ability of the system to provide optical sectioning normal to the surface.

Two different approaches to confocal Raman microscopy have been made. The first

approach uses the optical configuration with a pinhole as the working principle, as illustrated in Fig. 6. The laser excitation beam is first filtered by an illumination pinhole, H1. This initial spatial filter removes the appearance of diffraction rings and speckle noise around the focus spot and results in a clean point source waist that is imaged onto the sample. The scattered Raman radiation is collected by a wide-aperture microscope objective. A notch filter ensures coaxial illumination and light collection by the same objective in the back-scattering configuration. The image of the sample is focused at H2. The exact optical conjugation of H2 with the point source on the sample surface ensures that only the light originating from the sample region, which coincides exactly with the illumination spot, is transmitted to the spectral analyzer and detector. The two effects of spatial filtering, both for illumination and collection, multiply and increase the spatial resolution by

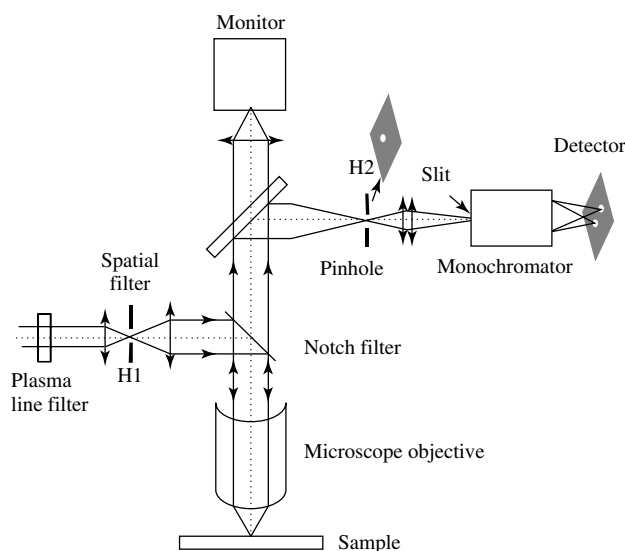


Fig. 6 Schematic diagram of the working principle of confocal microscopy making use of a real pinhole.

eliminating stray light coming from the out-of-focus regions of the sample.

Another approach uses a “virtual” pinhole, which shifts the designed emphasis from the pinhole to the detector and software. This so-called “easy confocal” is illustrated schematically in Fig. 7. In the illumination optics, this system also uses an aperture as in the case of the normal microscopic system. However, in order to realize the confocal effect, the mechanical adjustment of the width of the slit and the aperture are software controlled. This avoids the problems of the pinhole approach, that is, difficult alignment and mechanical drift. Easy alignment and long term stability are the main factors needed for high spatial resolution mapping using motorized stages.

3.6.2.1.7 Comparison of Different Raman Systems The Raman microprobe system has a very high collection efficiency compared with the conventional Raman spectrometer. However, since the laser spot is highly focused, it is very difficult to avoid

damage of the sample by the high-power density of the laser (even in the order of several milliwatts power from the laser), especially for some biosamples or unstable samples. Considering the laser rejection system, a notch filter can only exclude one laser line, thus it is costly to own many notch filters to cover all laser lines. It is therefore unsuitable for Raman studies that use several laser excitation lines. However, the high throughput of this device is so significant in improving the sensitivity that it is widely used in modern Raman systems. The holographic grating can reject different laser lines, by changing its angle easily; thus it can reject all the laser lines in the visible region, possibly extended to UV and near-IR regions. Unfortunately, the low throughput of this device is an obvious shortcoming. The CCD, as the most commonly used detector, may have a high quantum efficiency, for example, of up to 80% in the visible region and about 35% in the UV region. Most importantly, it has a very low noise level. This is a decisive experimental factor for weak signal detection, where a long time is needed to

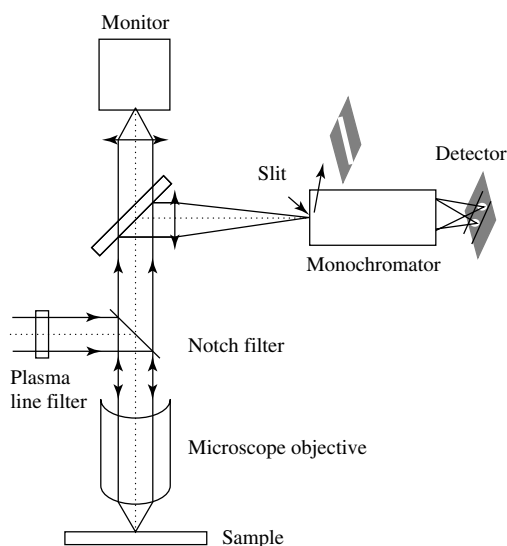


Fig. 7 Schematic diagram of the working principle of “easy confocal” microscopy using a virtual pinhole, by controlling the slit width and the acquisition pixel of the CCD detector.

record a satisfactory spectrum. However, because of its low read out speed, it is very difficult to use for time-resolved studies. The PMT has a very high sensitivity, however, the high noise accompanying it makes it difficult to use for weak signal detection. Furthermore, since it is a single channel detector, it takes time to acquire a full spectrum. The PDA is a multichannel detector and suitable for time-resolved studies, for example, on the millisecond scale. Further higher time-resolved values need electronics or a photoshutter. However, a key problem is also the high dark current noise. This discussion highlights the importance of experimentalists selecting a particular kind of Raman instrument based on the purpose of the study.

3.6.2.2 Experimental Setup for Electrochemical Raman Spectroscopy

In order to perform an in situ Raman spectroscopic study on an electrochemical system, the coupling of the Raman instrument with the electrochemical apparatus is important. A potentiostat should be used

to control the electrode potential, and in some cases, a wave function generator may be needed for more flexible or complicated electrochemical control. On the basis of the characteristics of the electrochemical cell and instrument, several optical operation modes have been used in the various experimental setups.

3.6.2.2.1 Optical Operation Modes Fig. 8 illustrates five types of light incident and collection configurations for the Raman study of an electrode surface. They can be classified into three general kinds of operation modes: front incident and collection mode; back-scattering mode; and the attenuated total reflection (ATR) mode. The front incident and collection mode is employed most extensively in the conventional Raman instrument, especially the macro-Raman instrument. The incident laser is illuminated on the electrode surface in the optical plane of the Raman system with an angle of θ to the normal of the electrode surface, and the scattering light is collected in the direction normal to

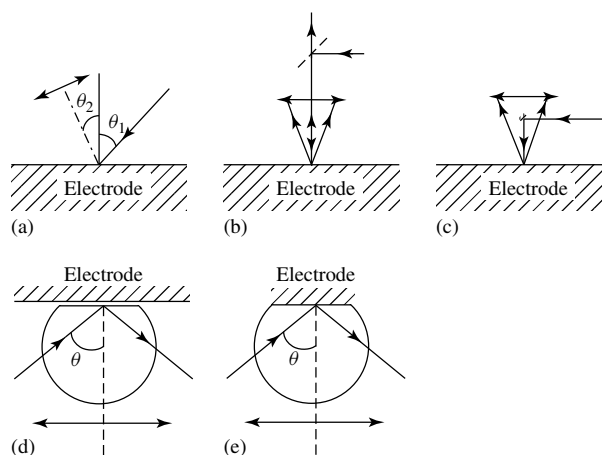


Fig. 8 Five optical collection modes in electrochemical Raman spectroscopy. (a) Front collection mode; (b) and (c) back-scattering mode; (d) and (e) internal and external ATR mode.

the surface. With proper selection of the incident angle at around 60° , the Raman scattered light can be collected efficiently without the collection of the reflected laser excitation light.

The back-scattering geometry is the most efficient way to collect the Raman scattered light. In general, there are two configurations: one is used in Raman microscopy, where the laser light is delivered by a beamsplitter and focused by a microscopic objective vertically on the sample surface. The scattered signals are collected by the same objective, transmitted by the beamsplitter, then introduced into the Raman spectrometer, see Fig. 8(b). In this configuration the reflected laser light goes directly into the Raman instrument. Thus, a good laser line rejection efficiency should be considered with this kind of operation mode. Mode (c) shows another back-scattering configuration to introduce the laser light onto the sample surface. Light is vertically reflected by a tiny mirror and the Raman scattered light is collected by a large lens behind the mirror. The reflected laser line does not enter the spectrometer, since it is blocked by the tiny mirror.

Besides the above two most frequently used back-scattering modes, another kind of configuration is specially designed for higher collection efficiencies [14], see Fig. 9. It consists of an elliptical mirror with a higher eccentricity, to which an electrochemical cell is attached from the back. The cell has a half-spherical window

and the electrode surface is placed into the half sphere's center and right at the first focal point of the elliptic mirror. The mirror itself serves to focus the laser beam at the sample and simultaneously to collect a great part of the scattered light, which will be focused at the second focal point. This increases the collection efficiency dramatically, so as to detect some very weak surface Raman signals from smooth Ag electrodes [14]. However, this configuration is relatively complicated in design and difficult to align.

The application of the ATR method in Raman spectroscopy provides a unique way to study essentially mirrorlike polished metals, in particular single crystalline surfaces. The ATR method is used to excite surface plasmon polaritons (SPPs) effectively at the smooth metal surface, to improve the sensitivity in Raman spectroscopy by electromagnetic field enhancement [19]. The enhancement of the ATR configuration, as shown in Figs. 8(d and e), with respect to the normal external reflection geometry spans one to three orders, depending on the electrodes and their crystallographic orientations.

3.6.2.2 Spectroelectrochemical Cells

The spectroelectrochemical cell is a core component of the experimental setup, which consists of a working electrode (WE), an inert counter electrode (CE), and a reference electrode (RE). There are several important factors, such as the cell configuration and electrode preparation, which

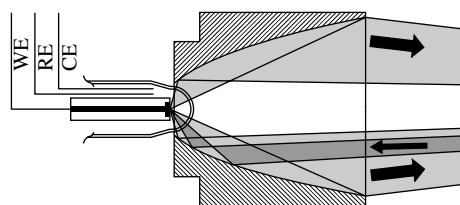


Fig. 9 Diagram of specially designed collecting optics and cell. An elliptic mirror attached to an electrochemical cell having a half-spherical window. (Reproduced with permission from Ref. [14]. Copyright 1992.)

affect decisively the successful coupling of the Raman and the electrochemical measurements. For example, the three electrodes should be assembled in a good relative geometric position to allow both Raman and electrochemical measurements. Depending on the purpose, the cell is designed to different configurations and contains different kind of accessories, such as optical windows, together with inlets and outlets for the exchange of the solutions and gases. Detailed designs for different systems are described in the following sections.

Aqueous systems and nonaqueous systems

The Raman cell for the study of electrodes in an aqueous electrolyte is relatively simple and more flexible in design compared with the nonaqueous system. Figure 10 shows the two most commonly used cells. Cell (a) is suitable for the front collection mode with different incident angle and the back-scattering mode in the macro-Raman system. Cell (b) is for the micro-Raman system. An optically transparent quartz or glass window may be used, especially to avoid contamination from the ambient atmosphere. Usually, it is not necessary to

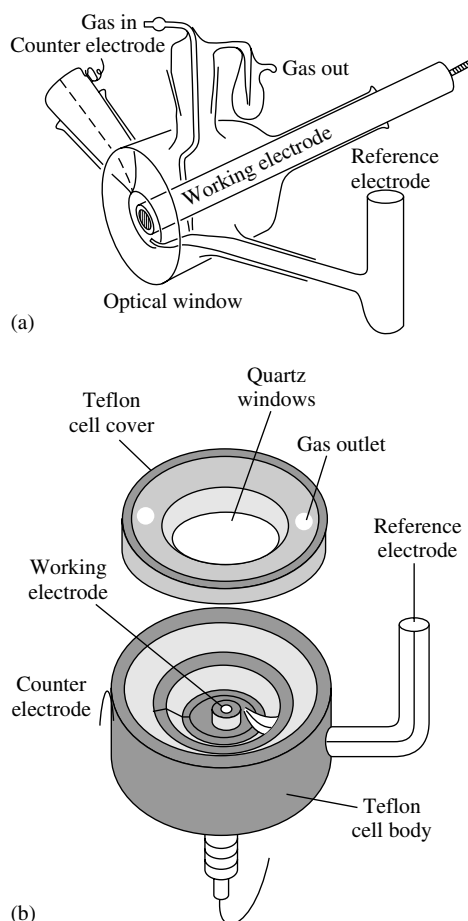


Fig. 10 The two most common electrochemical Raman cells used in aqueous solutions: (a) is suitable for the front collection mode of different incident angle and the back-scattering mode in the macro-Raman system and (b) is for the micro-Raman system with a microscope.

separate the working electrode from the counter and reference electrodes. However, if a deleterious species is produced at the counterelectrode or the reference electrode introduces impurities, a two- or three-compartment cell separated by a ground glass frit separator might be a good precaution.

The main difference between the non-aqueous system and the aqueous system is to isolate the exchange of the solvent with moisture and gases of the ambient environment. Thus, the main points for the design are to be water tight and gas tight [44]. Two difficulties encountered are the design of the reference electrode and the seals of the optical windows and the working electrode. Most cells use a rubber O-ring (fluorized) to realize watertight and gastight seals. In some cases, a silicone rubber ring can also serve as the sealing material. To simplify the cell construction with one compartment, a metal wire can be used as a quasi reference electrode. Fig. 11 gives a typical design of a nonaqueous Raman cell [45].

Flow cells In some cases, especially when a system undergoes vigorous reaction, the consumption of the solution species is very fast in the confined volume between the

working electrode surface and the optical window. Meanwhile, the products of the surface reaction have to be removed from this volume, since they may have a negative influence on the reaction occurring on the surface. In order to investigate surface reactions free from the interference of products, a spectroelectrochemical cell is needed that is capable of solution exchange during the measurement. Moreover, to characterize surface species unambiguously, the solution composition can be changed to detect the possible spectral change without changing the applied potential. This kind of cell is called a flow cell [46, 47]. The key point for the cell design is to allow the fast and thorough exchange of the solution confined between the electrode surface and the optical window, not just outside this volume. Fig. 12 gives a good design for a flow cell system.

Movable cells Since the laser power density during a Raman microscopic study is quite high, it is possible that some active or unstable species may decompose on the surface under laser irradiation, especially if biomolecules are studied. Therefore, a movable cell [48] is needed to reduce the laser irradiation time on the surface. An example of a movable Raman cell is shown

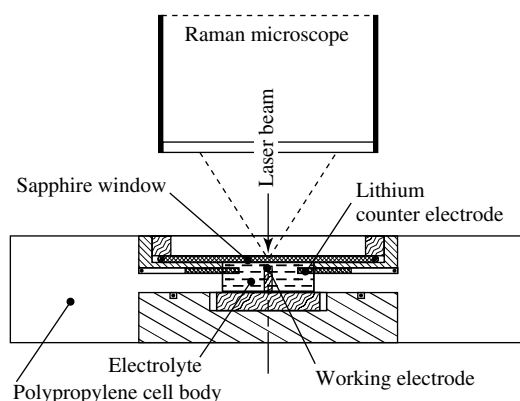


Fig. 11 An electrochemical Raman cell for nonaqueous systems. (Reproduced with permission from Ref. [44]. Copyright 1986.)

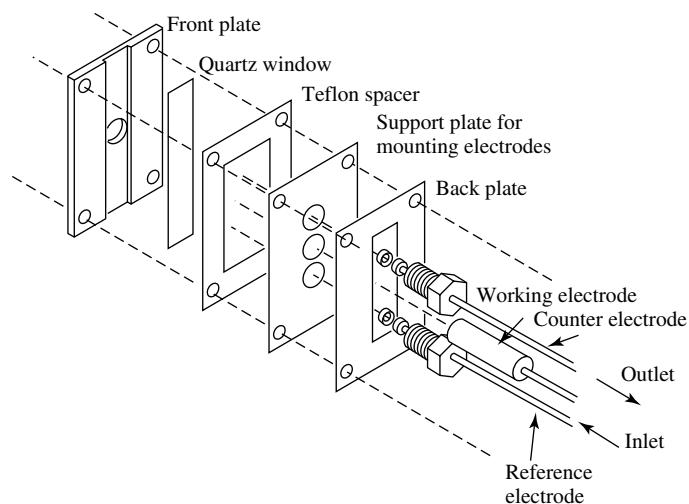


Fig. 12 A flow cell for in situ electrochemical Raman spectroscopy. (Reproduced with permission from Ref. [46, 47]. Copyright 1986.)

in Fig. 13. Different cell geometries are possible, although the example shown is cylindrical. The cell is connected to a cell holder consisting of a two-axis manual stage. The movement of the cell holder and the cell is implemented by the rotation of the disk, which pushes against the wall of the manual stage.

High temperature and pressure cells In the study of corrosion and catalytic processes, especially when using molten salts as the medium, a spectroelectrochemical

cell capable of working at high temperatures and pressures [49] is needed. Fig. 14 shows a cell that works from 25 to 290 °C at 100 bar pressure. The design contains all the essential features for this type of work and could be adapted to suit most instrument arrangements. The electrolyte solution is preheated and continuously pumped through the cell entering at port D and leaving at port C. The counter electrode is inserted through E and the cell is heated by cartridges H, embedded in the cell body. A shaft seal G allows positioning

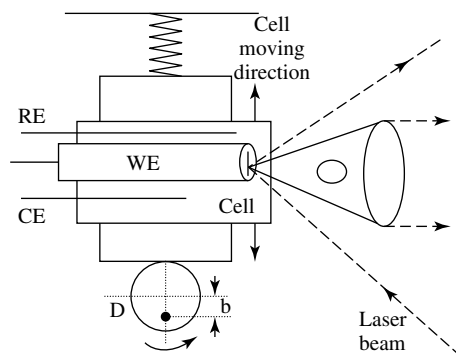
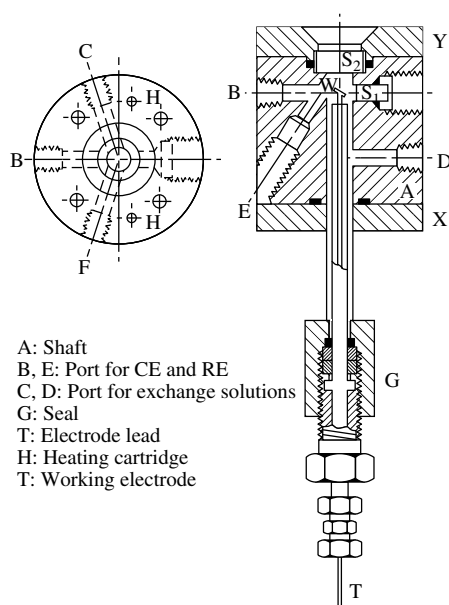


Fig. 13 A movable cell for in situ electrochemical Raman spectroscopy. (Reproduced with permission from Ref. [48]. Copyright 1997.)



of the electrode, and the electrode leads are brought out at T. Actually, the sample configuration can be slightly modified for different Raman systems. In a macro-Raman system, the laser incidence can be horizontal and the scattered light is collected vertically. While for the micro-Raman system, a back-scattering configuration can be used.

Attenuated total reflection (ATR) cells

Fig. 15 shows a cell of ATR configuration [19] under electrochemical working conditions. The Weierstrass prism made of ZnSe (radius $r = 5$ mm, refractive index $n = 2.6$ at 647.1 nm excitation), which is longer by r/n than a hemispherical prism, is mounted in the bottom of the electrochemical cell. The experimental procedure is much more difficult than that of a normal SERS measurement. The single crystal electrode is carefully pressed against the prism with a micrometer and a spring, so that the optimum gap size d

Fig. 14 A spectroelectrochemical cell capable of working at high temperatures and pressures. (Reproduced with permission from Ref. [49]. Copyright 1986.)

for the SPP excitation (about half a wavelength) can be adjusted. By moving the p -polarized laser beam with a small prism perpendicular to the optical axis, the angle of incidence α with respect to the surface normal, and therefore the momentum of the incident photon, can be controlled. The laser beam is reflected at the prism base and the intensity of the reflected beam can be measured by a diode. When the angle of incidence and the gap size are close to the optimum conditions for SPP excitation, a bright cone of scattered light is emitted and appears as a sharp ring behind the 1 : 1 collection objective. The intensity of the reflected light goes to zero and the Raman intensity has a maximum under optimum conditions, so that a fine adjustment of the experimental parameters is possible.

Since the ATR configuration is very different from that of the conventional cells, it is necessary to describe it in more detail. The optimum condition for SPP excitation at $\lambda = 647$ nm has been found to be at $\alpha = 34^\circ$. The scattered light is collected by an additional objective that provides a good matching to the monochromator. With the extra enhancement given by the ATR method, it is possible to study the Raman signal of adsorbates at electropolished single crystal electrodes, including Ag, Cu, Pt, and Ni, as a function of the electrode potential. However, obviously, the sample volume between the electrode and optical window is really small. This may cause a distortion of the electrochemical reaction and potential control. Fig. 8(e) shows another ATR configuration. A very thin metal film is deposited directly on the surface of the lens, so that there is no limitation

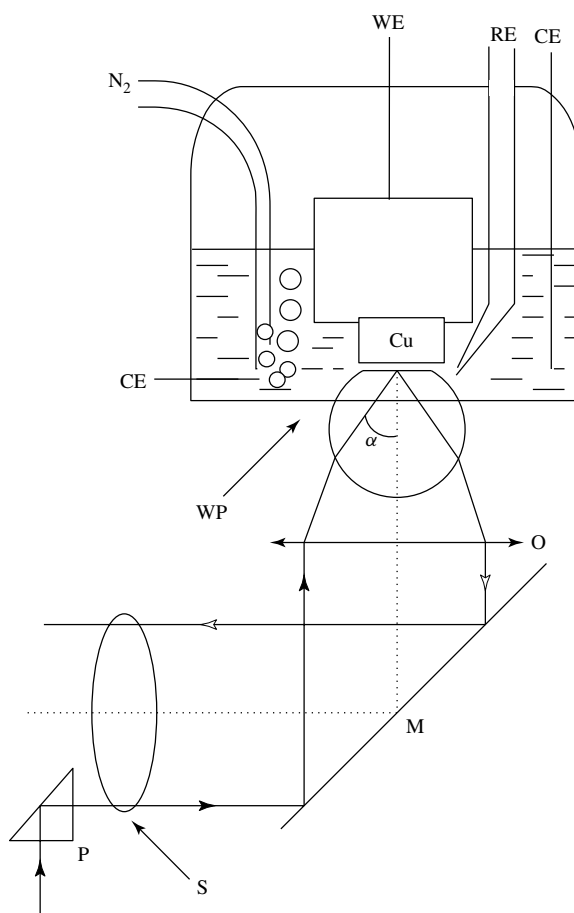


Fig. 15 A Raman cell of ATR configuration for working under electrochemical conditions. (Reproduced with permission from Ref. [19]. Copyright 1998.)

on the sample volume, which could provide the ideal electrochemical control of the surface process. However, a more serious problem arises mainly concerning the preparation of the ultrathin film electrode, especially if a single crystal surface is required.

3.6.2.3 Electrode Preparation

An advantage of laser Raman spectroscopy over other spectroscopic techniques is that the sample does not require special

preparation and it can be flat, porous or a powder. This applies to the electrochemical Raman technique that covers bulk electrode materials such as polymers, carbon, silicon, and semiconductor electrodes. However, for studying electrode surfaces and electrochemical interfaces, special concern must be given to the pretreatment of the electrode surface, since there are only monolayer or submonolayer amounts of species of interest on the surface. Therefore, this

section will focus on how to prepare various electrode surfaces exhibiting high SERS activity, followed by brief discussion on non-SERS active surfaces.

3.6.2.3.1 SERS-active Electrode Surfaces

It is well known that to obtain good-quality SERS spectra, the electrode surface must be pretreated properly. Fig. 16 illustrates the distinct effect of the surface roughening procedure on the Raman intensity of pyridine adsorbed on iron electrode surfaces that only have weak-SERS activity. The surface signal is barely detectable from the mirrorlike surface after mechanical polishing with fine grades of alumina powdered down to 0.05 μm . Even the strongest band intensity for adsorbed pyridine is extremely weak, only about 0.5 count per second, see Fig. 16(a). The spectrum is certainly too weak to be investigated with detail. The signal-to-noise ratio (SNR) was improved after the electrode was chemically etched in a 1.0 mol l^{-1} solution of HNO_3 . The signal intensity doubled if the electrode was further treated in a

0.1 mol l^{-1} solution of KCl by a double-step ORC. An even more intense signal was obtained when an additional ORC was performed in situ in the spectroelectrochemical cell just before the measurement. This set of spectra show that an appropriate surface roughening procedure is key to obtaining reasonably good spectra and that there are several ways to roughen the electrode surface. Electrochemical roughening has been used most extensively for the SERS activation of the electrode surface, and is described in the following section.

Electrochemically roughened electrodes In general, the electrode is made by a metal (or carbon, silicon or other semiconductor) wire, rod or disc sealed into an inert holder (glass, Kel-F or Teflon). The size and shape of the electrode do not have specific requirements, as a microelectrode with diameter down to 1 micron in diameter can still be studied using Raman microscopy. Before the SERS activation procedure, performed with electrochemical roughening,

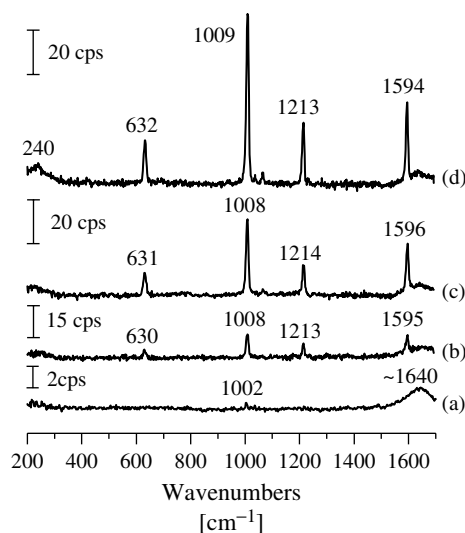


Fig. 16 Raman spectra of pyridine adsorbed on iron electrode surfaces with different roughening procedure in a solution of 0.01 mol l^{-1} pyridine and 0.1 mol l^{-1} KCl: (a) mechanical polishing; (b) chemical etching in 2 mol l^{-1} H_2SO_4 ; (c) ex situ ORC in 0.5 mol l^{-1} H_2SO_4 by a double-step ORC from -0.7 V to -0.35 V, where the potential was held for 15 s and then returned to -0.7 V; and (d) in situ ORC in 0.01 mol l^{-1} Py and 0.1 mol l^{-1} KCl in the spectroelectrochemical cell prior to the measurement. The excitation line was 632.8 nm.

the electrode surface is usually first polished mechanically using decreasing sizes of alumina powders (normally down to $0.3\ \mu\text{m}$ or $0.05\ \mu\text{m}$), cleaned with highly pure water, and ultrasonicated to remove any adhering alumina. In some cases, the electrode is further treated by a chemical polishing procedure to further smoothen the surface, and/or by an electrochemical cleaning procedure by controlling the electrode potential negative of $-1.8\ \text{V}$ versus SCE to promote hydrogen evolution. There are more than five methods to prepare SERS-active electrode surfaces. The application of an electrochemical oxidation-reduction cycle and overlayer techniques are the two most important methods, and will be discussed in more detail. Table 2 is a summary of the typical experimental variables for various metal electrodes (vide infra).

ORC-roughened electrodes The electrochemical ORC [10, 11, 50, 51] has been widely applied to surfaces for effective SERS activation. The ORC process produces sites of large-scale roughness (e.g., 10 to 500 nm in diameter) and atomic-scale roughness (ad-atoms and ad-clusters) [52]. The large-scale features are associated with the electromagnetic enhancement mechanism and the atomic-scale roughness with the chemical enhancement mechanism [11, 25–28]. Experimental variables in the ORC include the oxidation and reduction potentials, the type of potential-time function utilized (triangular-wave potential sweep or double potential steps), the amount of charge passed for each oxidation step or sweep, the number of cycles, and the composition of the electrolyte. As silver and gold are the most extensively used SERS substrates, it is reasonable to first take them as examples to illustrate the ORC procedure in detail.

The initial electrode potential is set negative to the onset of Ag oxidation, and the potential is either stepped or swept to a potential in which Ag oxidation occurs. In a halide-containing electrolyte, typically a KCl solution, silver is oxidized to insoluble silver chloride as a discontinuous film on the electrode, which is then reduced back to metal upon either reversing the potential sweep or stepping back to the initial potential. The applied potential, especially the oxidation potential, is dictated by the electrolyte used. In a $1.0\ \text{M}$ KCl electrolyte, the potential is stepped from $-0.25\ \text{V}$ to $+0.18\ \text{V}$ versus SCE with a dwell time of about 7 s, then swept back to $-0.25\ \text{V}$ versus SCE with the rate of $0.10\ \text{Vs}^{-1}$. The optimum SERS signals are obtained following the charge passage of 20 to $50\ \text{mC cm}^{-2}$, equivalent to ca. 100 to 200 monolayers of Ag atoms. It should be emphasized that the experimental parameters for the ORC have to be mildly modified for each Ag electrode, depending on the crystallinity and purity.

One oxidation–reduction cycle produces an Ag surface that usually yields intense SERS spectra. While for an Au electrode in a $0.1\ \text{M}$ KCl, a succession of triangular potential sweeps (20–25) is necessary to yield intense and stable SERS spectra [51]. The potential is swept from $-0.3\ \text{V}$ to $1.25\ \text{V}$ versus SCE with a sweep rate of $1.0\ \text{V s}^{-1}$, and back to $-0.3\ \text{V}$ with $0.5\ \text{V s}^{-1}$. It is essential to hold the potential for 1 to 1.5 s at the positive limit during each cycle. The SERS intensity progressively increases after each cycle when $5\ \text{mC cm}^{-2}$ of cathodic charge is passed during a cycle.

Since transition metals only exhibit a weak-SERS effect, it is essentially important to develop different kinds of ORC procedures for optimizing the SERS

Tab. 2 Electrochemical roughening procedures for various metal electrodes

Unit: $E(V)$, $t(s)$, $I(A\ cm^{-2})$, $v(V\ s^{-1})$, $f(kHz)$

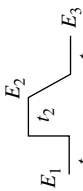
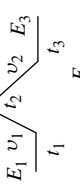
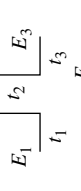
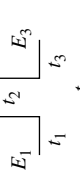
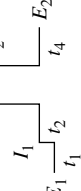
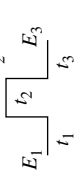

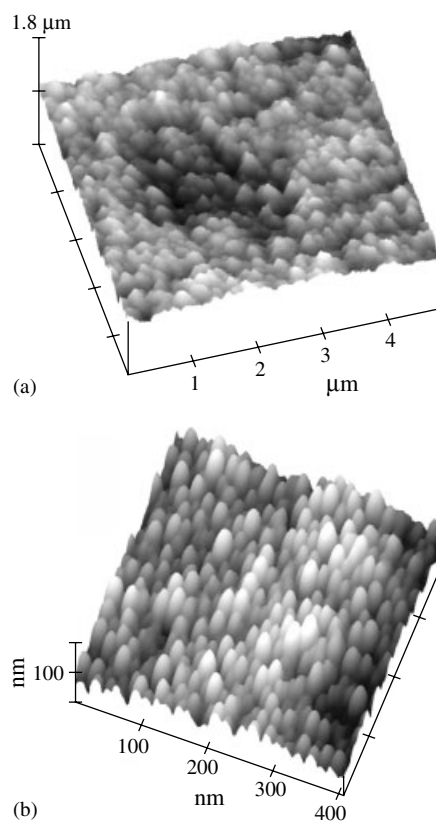
Pretreatment	Electrolyte	Potential waveform	Parameters	Cycles	Surface appear
Ag Chemical etching (optional)	0.1 M KCl		$E_1 = E_3 = -0.25$, $E_2 = 0.25$ $t_1 = 15$, $t_2 = 8$, $t_3 = 60$	1	Milky yellow
Au Electrochemical cleaning (optional)	0.1 M KCl		$E_1 = E_3 = -0.3$, $E_2 = 1.2$ $t_1 = t_3 = 30$, $t_2 = 1.2$ $v_1 = 1$, $v_2 = 0.5$	25	Dark brown
Cu Electrochemical cleaning (optional)	0.1 M KCl		$E_1 = E_3 = -0.4$, $E_2 = 0.4$ $t_1 = 15$, $t_2 = 3 - 5$, $t_3 = 60$	1–5	Dark brown
Pt Electrochemical cleaning	0.5 M H ₂ SO ₄		$E_1 = E_3 = -0.2$, $E_2 = 2.4$ $F = 1.5(t_1 + t_2 = 1/f)$	30–900	Gray to dark yellow
Pt, Rh Electrochemical cleaning	0.5 M H ₂ SO ₄		Pt, $I_1 = -I_2 = 1.6$, $f = 0.5$ Rh, $I_1 = -0.1$, $I_2 = 0.13$, $f = 0.2$ ($f = t_2 + t_3$) $E_1 = E_2 = -0.2$	10–600	Misty gray to dark brown
Fe Chemical etching (optional)	0.5 M H ₂ SO ₄		$E_1 = E_3 = -0.7$, $E_2 = 0.35$ $t_1 = t_3 = 60$, $t_2 = 15$	1	Gray
Co Chemical etching (optional)	0.5 M NaClO ₄		$E_1 = -1.0$, $E_2 = -1.4$, $E_3 = -1.2$, $E_4 = 1.0$, $E_5 = -1.25$, $t_1 = t_3 = 20$, $t_2 = 15$, $t_4 = 60$, $v_1 = 0.2$, $v_2 = 0.1$	1	Dark

Fig. 17 (a) STM image of a roughened Pt electrode and (b) atomic force microscopy (AFM) image of ordered Ni nanowire array.

activity. For some very stable metals, such as Pt and Rh, it is very difficult to roughen only by the dissolution and deposition of the surface atoms. These metals tend to form a compact surface oxide layer that prevents further oxidation of the surface. An alternative way to roughen the surface can be realized by applying a high frequency alternating potential with high oxidation potential and mild reduction potential to allow severe oxidation of the surface, see Table 2. The high frequency potential applied enables the exchange of the surface oxygen with the bulk metal atoms leading to the further oxidation of the inner layers of the surface. The surface roughness factor ranges from 30 to 500 for the Pt surface, and can be controlled by varying the roughening time and the applied potential and the frequency. The surfaces present darker color than that obtained by an ordinary ORC procedure. Figure 17(a) shows a scanning tunneling microscopy (STM) image of a roughened Pt electrode that exhibits high SERS activity.

The Rh electrode is more difficult to roughen, even by applying the square-wave potential procedure described for Pt. It is of special interest that Rh is very easily roughened by applying a square-wave current. This method is also very effective for producing a Pt electrode of low surface area, for example, with a surface roughness factor down to 3 to 5, but with high SERS activity, however, the selection of the current and frequency are very different from those for Rh.



Chemically etched electrodes In comparison with the ORC, a very simple tactic to roughen an electrode surface is chemical etching, which partially dissolves surface atoms by a chemical reaction with the solution [53]. This approach requires experimental skill to optimize the SERS activity for different metal samples. The following section highlights procedures that may be useful to several metals. Copper foils were immersed into a $2 \text{ mol l}^{-1} \text{ HNO}_3$ solution at 303 K, after about 10 s bubbles were formed near the copper surface. Vigorous agitation was then applied. After 2 min, a sponge-type surface with substantial roughness was created. In the case of Ag foils, a $5 \text{ to } 6 \text{ mol l}^{-1} \text{ HNO}_3$ solution was used and the etching time was prolonged to

5 to 10 min until the surface became milky. For a Ni surface, a dilute solution of HNO_3 with concentration of about 1 mol l^{-1} was used, and the etching time was about 5 to 7 min. While for a Fe surface, the best result was obtained by etching in an ultrasonic bath of a 2 mol l^{-1} H_2SO_4 solution for 5 min. The surface should be gray. After etching, the metal foils or surfaces should be thoroughly rinsed with water and maintained wet in order to protect the fresh electrode and to prevent contamination from the atmosphere.

It should be pointed out that, for some electrodes, chemical etching is not sufficient to obtain the optimal surface roughness for SERS, as shown in Fig. 16. One may consider further SERS activation to chemically etched electrodes by ORC, either in the chemical etching solution (*ex situ*) or in the measured solution (*in situ*). However, the electrode treated by the *in situ* ORC, in general, has the higher activity, but poorer stability, as the intensity decreases with time irreversibly. A detailed discussion of how to deal with this problem will be given in the Sect. 3.6.3.7.4 on Troubleshooting.

Film electrodes In contrast to the chemical etching methods, the film deposition method adds atoms at the substrate to form a rough film and/or discontinuous islands. This technique is commonly adapted from prior work in surface science and often realized in UHV chambers. However, the deposited film electrode is unlikely to have the same crystalline structure as the bulk metal phase formed by metallurgy that is usually used in electrochemistry. Moreover, film electrodes exhibit relatively poor surface stability and electrochemical reversibility, particularly if the experiment is conducted over a wide potential region.

This SERS activation method can be realized by vacuum depositing or sputter depositing a metal on various substrates, including silica slides, graphite or glass. The deposited metal forms hemispherical nanoparticles or small islands when the layer deposited is thin enough (ca. 5 nm). The SERS activity depends on the deposition rate and temperature, as well as the film thickness. A more rapid, simple, and reproducible method for preparing silver island films on various substrates is to use Tollens' reagent. A rough film can also be prepared by electrochemical deposition of a metal onto a smooth electrode surface from a solution containing the metal ions. By carefully controlling the potential, reasonably good SERS signals from thick films of transition metals, such as Ru, Rh, Pd, Ni, Co, and Fe, exhibiting a weak-SERS effect have been achieved [54].

Overlayer electrodes The idea of developing overlayer techniques is totally different from the film electrode approach, although they can use the same deposition process. Two important approaches related to the overlayer technique have been developed in order to utilize the SERS effect for many metals and even semiconductors that only have non- or weak-SERS activity. The first one is to coat SERS-active Ag or Au substrates with ultrathin films of metals or semiconductors of interest by deposition [8, 9, 17, 18], as shown in Fig. 18(a). With the aid of the long-range effect of the electromagnetic enhancement, created by the high SERS-active substrate underneath, good-quality SERS spectra of adsorbates on these non- or weak-SERS active films can be obtained. It has been found that the signal intensity is one to two orders higher than that from bare transition metals, which allows satisfactory

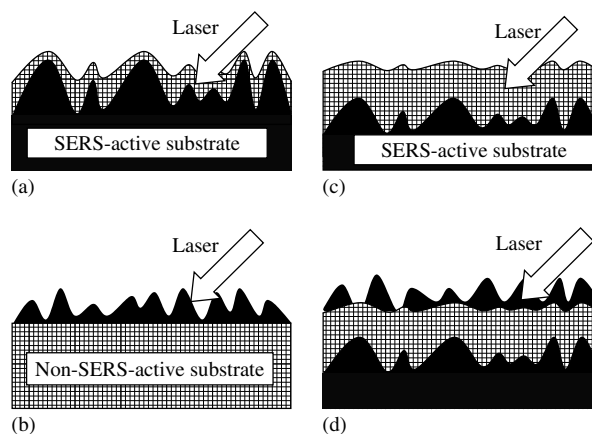


Fig. 18 (a) Schematic diagram showing the overlayer technique utilizing the SERS effect for non- or weak-SERS-active materials. (a) Coating SERS-active Ag or Au substrates with ultrathin films of non-SERS-active materials; (b) coating SERS-active metal islands on non-SERS materials; (c) deposition of a thick layer of non-SERS-active materials; (d) to use method (b) on (c) (see text).

spectra to be obtained for detailed analysis [55]. This method provides a unique way to study a variety of materials, and offers enormous potential for SERS [17, 18].

In order to benefit from the SERS effect due to the SERS-active substrate underneath, generally the deposited overlayer is ultrathin, comprising less than ten monolayers. In comparison with the above mentioned film electrodes, with several micron thickness, the overlayer (ultrathin film) electrode, with good uniformity on the rough surface, is difficult to prepare. The second approach is to use the reverse geometry of the overlayer technique in those islands of the SERS-active metal (e.g., Ag and Au) that are deposited electrochemically or chemically onto non-SERS active substrates including semiconductors, metal oxides or polymers [56]. By taking advantage of the long-range effect of SERS, one can investigate the structures and properties of these substrates that are themselves of non-SERS activity,

see Fig. 18(b). It should be noted that this approach is not suitable for the study of surface adsorption and reactions unless the surface species can selectively adsorb at the non-SERS active substrate. Otherwise, one cannot eliminate the possibility that the adsorbate is located at the boundary of the SERS-active islands and the non-SERS-active substrate.

In some special cases, the two approaches can be combined with the normal Raman or resonance Raman spectroscopy to comprehensively study a film electrode. For example, a thin film of polymer, oxide, semiconductor, or Langmuir–Blodgett (LB) film is coated in different ways onto the SERS-active substrate, such as Fig. 18(a). The SERS spectrum recorded at this stage can provide the bottom layer structure of the film. The film can then be deposited as a thicker layer, which enables the Raman signal from the bulk phase to be sufficiently strong and detected by normal Raman

or resonance Raman spectroscopy, see Fig. 18(c). After that, discontinuous SERS-active metal islands are deposited over the film to enhance the Raman signal from the top layer of the film, as shown in Fig. 18(d). Thus, with the combination of both overlayer techniques, one can investigate in sequence the bottom layer, the bulk phase, and the top layer structure of the film of interest. It provides some meaningful information of various interfacial and bulk structures that are difficult to obtain by other means.

3.6.2.3.2 Non-SERS-active Electrodes The above description on the preparation of electrode surfaces for Raman studies is mainly concentrated on making use of the giant or weak-SERS effect. However, for the wider application of Raman spectroscopy to electrochemistry, it is essential to extend surface Raman studies to electrochemical systems without surface enhancement. Unfortunately, at present, *in situ* electrochemical Raman spectroscopy seems not to be able to gain a sufficiently high surface Raman signal from an adsorbate of one monolayer unless this molecule has an exceptionally large Raman cross section. However, if only the surface species forms a single monolayer, such as in the study of adsorption on smooth or even single crystal surfaces, the ATR method will be helpful for detecting these signals. On the other hand, if one can select properly the excitation laser frequency, it is possible to make use of the RR effect to enhance the surface Raman signal. Nevertheless, many electrochemical systems intrinsically have thicker surface layers, such as polymer films or biological membrane electrodes. Sufficient bulk intensity from a surface layer comprising 10 to 100 monolayers can be achieved depending on the material to

be studied and the Raman microscope to be used. Generally, the thicker the layer, the stronger the signal. However, as the penetration depth for the laser ranges from a scale of nanometers to micrometers, depending on the materials studied and the laser wavelength, it is also unnecessary to prepare very thick layers. The following section will provide a very brief introduction on how to prepare non-SERS active surfaces, such as single crystal surfaces, polymers electrodes, metal oxide electrodes, and biologically relevant electrodes.

Single crystal electrodes So far, only a few surface Raman studies have been reported on single crystal surfaces due to its inherently low sensitivity. Early Raman studies were restricted to vacuum–solid and air–solid interfaces. For electrochemical interfaces, the studies were mainly carried out on single crystal surfaces after mild oxidation and reduction cycles or mechanical polishing [14]. Although such kinds of mild-ORC treated surfaces present essentially the same voltammogram as a typical single crystal surface, it should be noted that only a small amount of ad-atoms or ad-clusters, as SERS-active sites, is sufficient for creating SERS. Only recently, the *in situ* SERS study of true atomically smooth surfaces of single crystal electrodes has been accomplished with aid of the ATR configuration (*vide infra*) [19]. Single crystal surfaces can be pretreated by applying cycles of sputtering and annealing to the sample in an UHV chamber. However, electrochemists have developed a simpler flame annealing method, (Clavilier and his coworkers) [57], applicable to various types of electrodes. It should be noted, the flame melting method can only prepare small-size beads, presenting a very small area

of crystal facets, but sufficient for the Raman study. To obtain a larger facet, the bead needs to be orientated, cut, and polished and then flame-annealed. For the ATR method, a larger facet of bead or disk single crystal surface is helpful for optical alignment.

For some active metals, the flame annealing method cannot be used, and the electrochemical polishing method comes to the fore. For example, a good single crystal copper surface can be obtained by electrochemical polishing for 20 s in a solution of 60% H_3PO_4 in water, at 2.0 V. For most crystal surfaces, in order to help preserve the perfectness of the surface, the electrode is normally immersed into a solution with potential control.

Semiconductor and carbon electrodes A single crystal semiconductor wafer can be cut into the desired size and shape. For example, an In/Ga alloy can be applied to the back of the wafer to form ohmic contact. Then a copper foil is attached to the alloy surface to form electric contact. After that, the electrode can be used directly for an in situ study or sealed into a Teflon sheath with epoxy resin for further electrochemical or chemical treatment. The preparation of glassy carbon electrodes is similar to that of a metallic electrode. However, for highly oriented pyrolytic graphite (HOPG) surfaces, the design of the electrode should allow easy cleavage of the surface layer for exposure of a fresh surface.

Polymer electrodes Polymer electrodes can be obtained routinely by electropolymerization of monomer to form a polymer film on a smooth conducting substrate, such as a Pt, C or Au surface, by controlling the electrode potential or current density.

These electrodes can also be obtained by casting methods, in which the polymer is first dissolved into a certain organic solvent, and then the solution is dropped on an electrode surface. In order to form a fairly uniform surface, the electrode may be spin coated. After the evaporation of the solvent, the polymer film surface is formed.

Metal oxide electrodes To obtain a thin layer, the oxide film can simply be formed by applying an anodic overpotential (current) to the surface. To form a thicker layer, a square-wave potential (current) may be helpful. Metal oxide electrodes can also be produced by chemical vapor deposition on a substrate, allowing greater control of the thickness.

Chemically modified electrodes Chemically modified electrodes, such as self-assembled membranes (SAM), LB films, and biological-layer electrodes, need to utilize the RR effect to enhance the Raman scattering from the layer, unless the film or membrane is relatively thick, for example, more than ten monolayers. Special care has to be taken on the preparation of electrodes of biological interest, obtained by a casting or a dipping-adsorption method. In order to eliminate deactivation effects of the metal substrate on the biological molecules, a mediating layer such as a LB film or SAM film is deposited before the adsorption or casting of the biomolecule layer.

3.6.3

Electrochemical Raman Measurements

3.6.3.1 Measurement Procedures

A layout of the measurement procedure for an electrochemical (EC) Raman study is

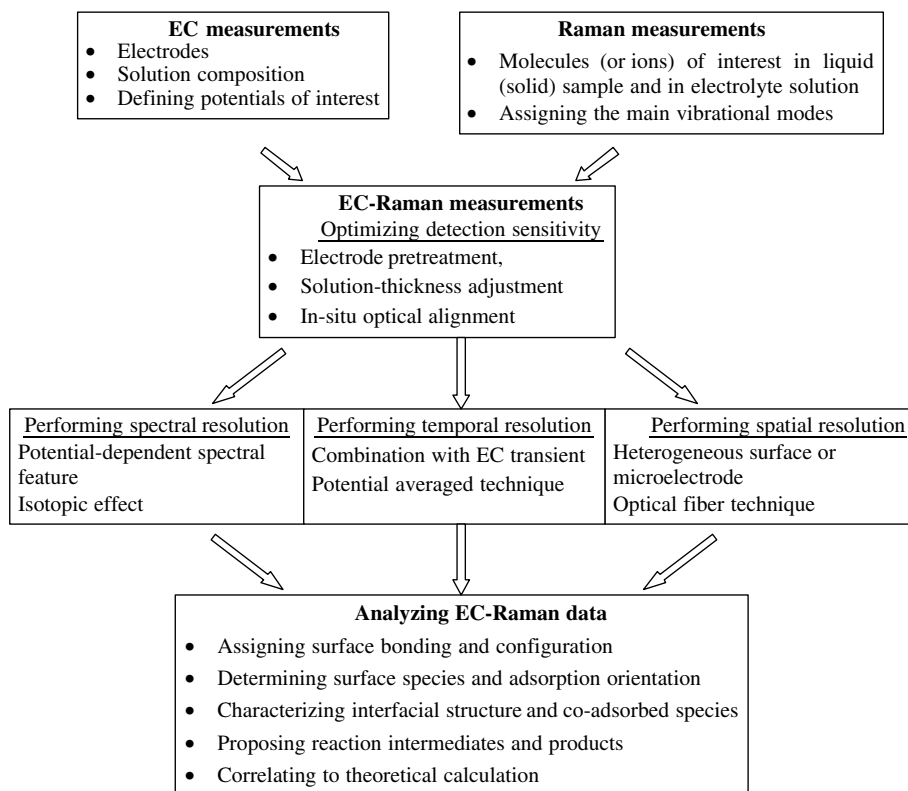


Fig. 19 Layout of the procedures for performing electrochemical Raman spectroscopic measurements.

illustrated schematically in Fig. 19. Before any study, it is necessary to calibrate the Raman and the electrochemical instrument. Since many optical components are very sensitive to environment, such as temperature and humidity, it is very important to calibrate the sensitivity of the instrument and the accuracy of the frequency. Normally, for a conventional macro-Raman system, a room fluorescent light or a mercury-argon lamp can be used simply as the calibration standard. The 546.073 nm line is suitable as the standard for the 514.5 nm laser excitation line. For the new generation micro-Raman systems of high sensitivity, a piece of single crystal Si wafer

[preferably the Si(111) surface] can be used most conveniently. It has a very sharp and intense vibrational peak at 520.6 cm^{-1} as both the intensity and frequency standard. If the excitation line shifts to the UV region because of the absorption by Si of the UV light, the band intensity decreases dramatically. Thus, a piece of diamond with vibrational frequency at 1333.2 cm^{-1} is used as the calibration standard. The calibration of both the frequency and intensity is especially important for an electrochemical study, since both these may vary with the change of the electrode potential, which are the criteria for determining the orientation and coverage of species at the surface.

Before starting a new EC-Raman study, it is important to first obtain the normal Raman spectrum of the species in its original form, such as pure liquid, solid, or even some standard samples for the expected reaction product; then to obtain the Raman spectra in the solution to be measured during the in situ study. These good-quality spectra will serve as the reference to compare with the surface Raman spectra. If the spectrum is too complex, an isotopic study will be very helpful for identifying the vibrational modes.

For some systems, there is no RR or SERS effect to be utilized, and sensitivity becomes the main problem. In this case, a potential difference method will be of great help [14]. One can acquire a spectrum at a desired potential to be subtracted by the spectrum acquired at potentials where possibly no, or weak, surface signal is present. Concerning spectral resolved studies, one may consider a change in the composition of the electrolyte or an isotopic labeling experiment to identify the surface species and verify its orientation and structure. For temporally resolved studies, electrochemical transient techniques are helpful to understand the surface dynamics and the restructuring processes of surface species. For nonuniform surfaces, spatially resolved measurements provide more reliable and complete information on the surface. This is also useful for electrode surfaces that change either chemically or topographically in a microzone upon the variation of the potential. For some complex systems, combined studies with infrared spectroscopy or with scanning probe microscopy (SPM) are essential, and the use of hyphenated techniques for simultaneous measurement may be necessary, as discussed later. Several SPM techniques were discussed earlier in this volume (Chapters 3.1, 3.2 and 3.3).

3.6.3.2 Sensitivity

Recalling Eq. (4) that gives the Raman intensity expression for a molecule based on Placzek's polarizability theory, the following gives a more complete expression with regard to the instrumental and surface factors:

$$I_{mn} = \frac{2^7 \pi^5}{3^2 c^4} I_0 (\nu_0 - \nu_{mn})^4 \sum_{\rho\sigma} |(\alpha_{\rho\sigma})_{mn}|^2 \times N A \Omega Q T_0 T_m \quad (8)$$

where N is the number density of the adsorbate (molecules cm^{-2}), A is the surface area illuminated by the laser beam (cm^2), Ω is solid angle of the collection optics (steradian, sr), $Q T_m T_0$ is the product of the detector efficiency, the throughput of the dispersion system and the transmittance of the collection optics.

Although the surface Raman scattering intensity scales with the incident laser power and energy, the ultimate sensitivity is limited by the surface damage threshold of the substrate with respect to I_0 . An alternative way to increase the intensity can be achieved by increasing the sample concentration. This approach is effective for studying the bulk signal from a liquid phase and transparent sample, but fails for the study of electrode surface adsorption, in which normally only one monolayer can be obtained, and the signal for most species at this level is well below the detection limit. Thus, without the aid of SERS and/or the RR effect, this approach suffers many constraints for the study of surface species.

The Raman signal can be increased by increasing the Raman scattering cross section, α , and electromagnetic enhancement factor, L [13]. The α value can be increased by introducing the RR effect or surface enhancement Raman effect (the chemical effect), as already discussed. L

can be increased by selectively roughening a certain substrate and employing a suitable excitation wavelength. However, these two approaches have their own restrictions. Only certain chromophores can take the advantage of the RR effect to be excited in the visible region. The same situation occurs in the surface-enhanced Raman effect, in that only few surfaces (Ag, Cu, and Au) can give giant electromagnetic enhancement [10–14]. By properly choosing the roughening procedures, we have successfully obtained surfaces with mild-SERS activity for Pt, Rh, Ni, Co, and Fe surfaces [15, 16, 24].

In many cases, including the mild-SERS active surfaces, it is essential to increase the detection sensitivity of the Raman instrument through the improvement on $\Omega QT_m T_0$: using a microscopic setup equipped with a wide NA microscope objective to increase the solid angle (Ω) of the collection system; utilizing the confocal configuration to eliminate stray light; employing a CCD detector of very low dark current and high quantum efficiency (Q) to increase the detection of weak signals; and using a holographic notch filter to decrease the number of optics so as to increase the throughput ($T_m T_0$) of the spectrometer. However, commercial systems are not built for special investigations on electrode surfaces, hence proper configuration of the system and the appropriate selection of optic components are quite important to utilize the full potential of the Raman instrument.

Since Raman spectrometers use some form of electronic amplification to magnify the signal produced by the detector, every recorded spectrum has a background of random fluctuations caused by spurious electronic signals produced by the detector, or generated in the amplifying equipment. These fluctuations are usually referred to

as “noise”. In order that a real spectral peak should show itself as such and be sufficiently distinguished from the noise, it must have an intensity of about three times that of the noise fluctuations (a SNR of three). This requirement places a lower limit on the intensity of observable signals.

Although the use of longer spectral acquisition time can improve the SNR, special attention has to be paid to saturation of the PMT and PDA detectors. Thus, when taking the spectrum, one should first try shorter times, lower laser power and narrower slit width to first check the intensity. For the sake of the spectral resolution, the same consideration should also be taken with regard to the CCD detector. With knowledge of the intensity of the signal, the total acquisition time and accumulation time is set to obtain a Raman spectrum of reasonably good SNR. The potential difference method can improve the quality of surface Raman spectra and enable the detection of the weak signals. For example, SERS seems to be a powerful tool for investigating the interfacial structure of water because it can greatly enhance the Raman signal of interfacial (surface) water molecules. However, tremendous interference of bulk water (about 55 M) still overwhelms the SERS signal from the interface. Using the potential difference method, the SERS signal of surface water has been obtained [58].

3.6.3.3 Spectral Resolution

Only after optimizing the sensitivity, can one take full advantage of Raman spectroscopy with very high energetic resolution, which refers to high spectral resolution. The width of the slit and the length of the optical path of the dispersion elements (gratings) play the determining role in the spectral resolution

of instruments. For example, two spectral bands are close together, as illustrated in Fig. 20. The dotted curve represents each band separately and the full line is their combined band shape. Consider first the case where the exit slit width is taken to be larger than the separation between the bands. Scanning the spectrum involves moving the twin peaks steadily to the left so that they pass across the exit slit and into the detector. The recording at successive stages is shown in (b, c, and d) of Fig. 20, the shaded area showing the portion of the band to be detected. The total band shape is plotted against frequency and the separation between the two bands has disappeared. It is evident that the use of a much narrower slit results in higher spectral resolution, as the right column of Fig. 20. However, a narrower slit allows less Raman photons to reach the

detector and consequently the intrinsic signal intensity will decrease. Weak signals may become indistinguishable from the background noise. Thus, it is crucial to find the minimum slit width consistent with acceptable signal-to-noise values.

In the old generation Raman instrument, where over 1 m dispersion length is available, a resolution as high as 0.2 cm^{-1} is attainable in the visible region [20, 21, 39]. In recent compact Raman instruments, because of the limitation of the size of the instrument, it is impossible to have a long dispersion space. Thus, in order to meet the requirement of different spectral resolution, the instrument is installed with gratings of different resolutions ($300 \text{ grooves mm}^{-1}$, $1800 \text{ grooves mm}^{-1}$, or even $3600 \text{ grooves mm}^{-1}$). The resolution for the compact Raman instrument normally is about $1 \text{ to } 6 \text{ cm}^{-1}$ depending on the grating and the wavelength of

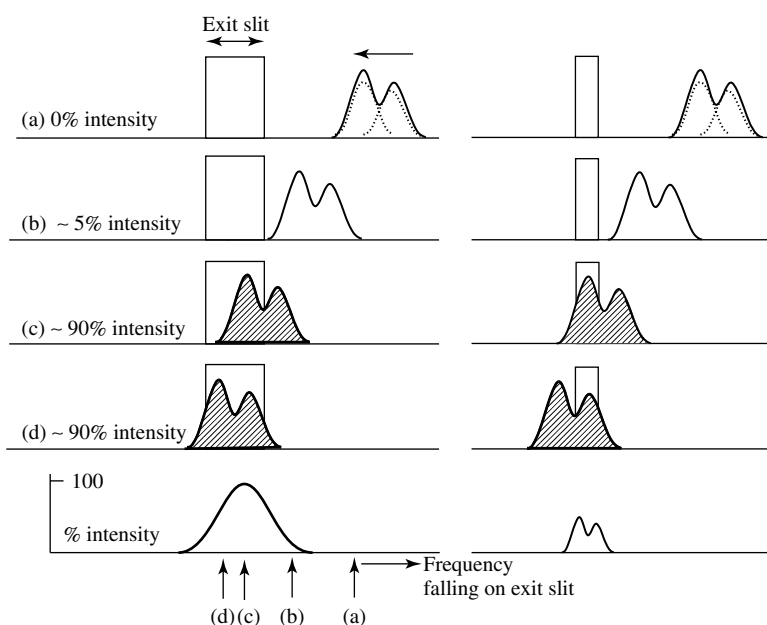


Fig. 20 Schematic diagram showing the effect of the slit width in determining the spectral resolution of a Raman spectrum.

the excitation line. However, in surface electrochemistry, the requirement on the spectral resolution of the instrument is not as high as in other areas, as the Raman bands are broadened for the surface species. Normally a spectral resolution in the range from 1 cm^{-1} to 3 cm^{-1} is sufficient for the Raman study of electrode surfaces.

Raman spectroscopy has been widely used to record fingerprint spectra for detailed chemical characterization. It can identify unambiguously the same molecule in the bulk solution or at the surface, as some vibrational modes will change in frequency, depending on the interaction between the molecule and surface. Even different surface configurations (and adsorption orientations) of the same molecule can be distinguished quite sensitively. Given the extremely high sensitivity and spectral resolution of SERS, mild changes in both frequency and intensity of the surface species can

be detected. This has proven very useful for investigating some complicated electrode surface processes such as coadsorption.

A typical example of a complicated coadsorption process is that electrolyte ions such as ClO_4^- or SO_4^{2-} can be induced to adsorb to a surface by organic molecules, such as thiourea (TU), as shown in Fig. 21. The strong SERS signal from ClO_4^- can only be detected when TU is added to the solution. Unlike most electrochemical adsorbates, the band frequency of ClO_4^- at 933 cm^{-1} is entirely independent of the applied potential, but identical to that of free anions in the electrolyte. This phenomenon indicates that the anion is induced by the organic molecule to coadsorb at the electrode surface but it only interacts indirectly with the surface. In order to analyze the coadsorption configuration, some SO_4^{2-} was added to the spectroelectrochemical cell in situ. New SERS bands, for example, at 986 cm^{-1} , from SO_4^{2-} replaced those of ClO_4^- completely, and meanwhile the band frequency of the amino group of TU changed from 3345 and 3212 cm^{-1} to 3317 and 3186 cm^{-1} , while the other bands of TU remained unchanged. The detection of this mild but meaningful change reveals that the coadsorption of TU with electrolyte anions is through the NH_3^+ group of TU, see Fig. 21. The systematic study on the frequency-potential and intensity-potential profiles for different electrolyte anions has been classified for different types of induced coadsorption [59].

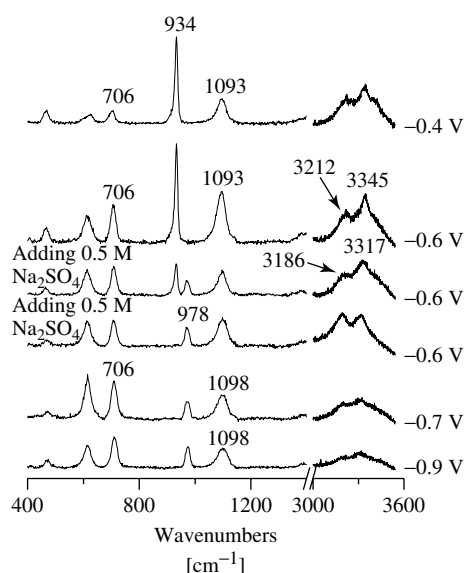


Fig. 21 SERS from an Ag surface for the coadsorption process of thiourea with SO_4^{2-} and ClO_4^- , as a function of the electrode potential. Excitation line: 632.8 nm .

3.6.3.4 Temporal Resolution

Raman spectroscopy is, in principle, amenable to dynamic studies, which affords additional information about electrochemical interfaces. The conceptually most straightforward extensions into this field are time-resolved investigations. Here, changes in the molecular structure and interaction at the surface, initiated by some external activation at a given time, are monitored.

During the last 15 years, several technical developments in the light source and detector made time-resolved Raman spectroscopy an important branch of time-resolved surface spectroscopy [60]. It should be emphasized that there are two kinds of time-resolved studies. The first kind of measurement is triggered by a certain surface process (reaction) named as a single shot experiment and the second one is a pump and probe technique.

3.6.3.4.1 Single Shot Measurement By applying a potential step or ramp, as a single shot, to the electrode, one can monitor the whole dynamic process, covering both spectral and temporal aspects using a CW laser, where the time resolution depends on the detector [60]. Depending on the detector used in the Raman system, the setup and operation for the time-resolved study will be different.

The most frequently used multichannel detectors for time-resolved measurements are the CCD and PDA detectors. During the measurement, a trigger generator is used to trigger the potential pulse or ramp (see Fig. 22a and b) on the electrode through the potentiostat or a waveform generator, simultaneously with the electronic shutter of the detector and the data acquisition and analyzing system, Fig. 22(c). With the preset acquisition time

delay and dwell time of the detector (see Fig. 22e), one can obtain a series of time-dependent spectra in t_2 . For the potential pulse experiment, the surface change after the potential step at $t = 0$ in Fig. 22(a) was monitored every $t_1 + t_2$, where t_2 is the acquisition time. On the other hand, in a potential ramp experiment, the spectra are acquired in the same mode while the potential is ramped. The laser is illuminated on the surface during the whole acquisition process (see Fig. 22d). Without a gating device on the detector, the detector has to work at the CW mode, and the time-resolved value will be limited by the response rate of the electronic shutter, together with the delay and dwell time of the detector. The best time resolution provided by this method is only about 10 milliseconds. However, with the use of a gating system, the time resolution can be as high as 100 ns and the response of the electrochemical system becomes limiting even if a microelectrode is used.

In a single channel detection system, a PMT is used as the detector. Thus, the time-resolved Raman investigation can only be done with the grating set at the desired peak position (frequency). The spectral band of surface species is in general quite broad, and the entrance and exit slits are tuned at a wider width to detect the signal of the whole band. The signal is then collected after the external signal pulse is in a standstill mode (also called intensity-time curve). Provided there is sufficient signal intensity, the time resolution depends on the response rate of the PMT detector.

3.6.3.4.2 Pump-probe Measurement The second type of measurement is performed at a steady state of the surface process that can be disturbed by a pump pulse

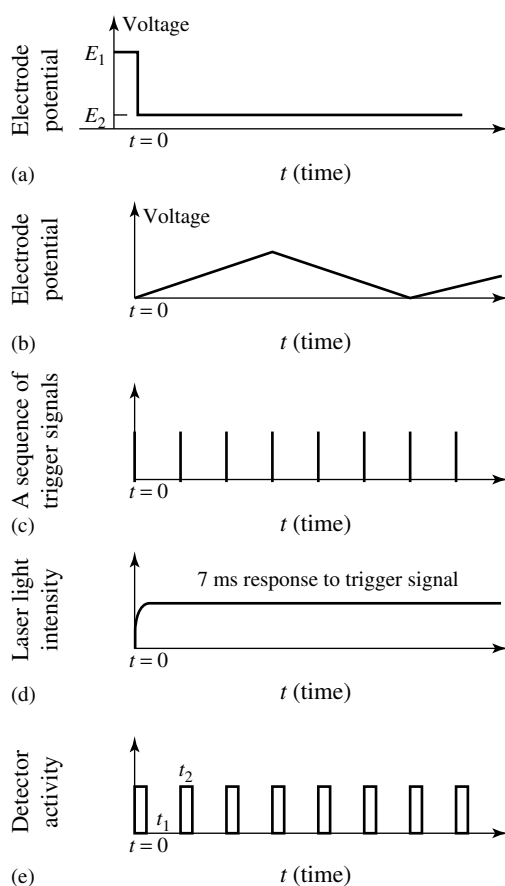


Fig. 22 Timing sequence for Time-resolved SERS (TRSERS) measurements with a voltage ramp. (a), (b) Potential pulse or triangular voltage ramp applied to the working electrode. (c) Sequence of Transistor–Transistor Logic (TTL) pulses from the trigger generator. (d) Schematic of the rise time of the electronic shutter that controls the rise time of the light on the working electrode. (e) Control of the diode array detector activity by the Optical Multichannel Analyzer (OMA). The delay time between acquisition of each spectrum is t_1 and the time the detector is active (dwell time) is t_2 . (Reproduced with permission from Ref. [60]. Copyright 1994, Kluwer Academic Publishers.)

laser and probed by another CW laser, which is suitable to probe the surface CT processes and characterize vibrational energy transfer rates for surface species. The probe laser is illuminated on the sample during the whole measurement (Fig. 23a). The pulse laser is split into two beams: one delivered onto the sample to initiate surface changes (Fig. 23b) and another used to trigger a computer-controlled pulse gating generator (Fig. 23c), the output of which triggers the activity of the detector (Fig. 23d). The delay time and dwell time of the detector (Fig. 23e) is controlled by this signal. In order to obtain different time resolutions, one can

change t_1 and t_2 . Normally, repeated acquisition of spectra is anticipated, in order to provide sufficient intensity, even with the aid of the SERS effect or RR effect. The higher the time resolution required, the stronger the Raman signal should be. Thus, in nanosecond resolved Raman studies, a molecule with very strong resonance and/or surface-enhanced Raman effect is adopted in order to provide a strong enough signal. Fig. 24 gives a nanosecond time-resolved Raman study on the photochemical process of flavin mononucleotide [61].

As a common strategy, in time-resolved studies, repeated acquisition is normally

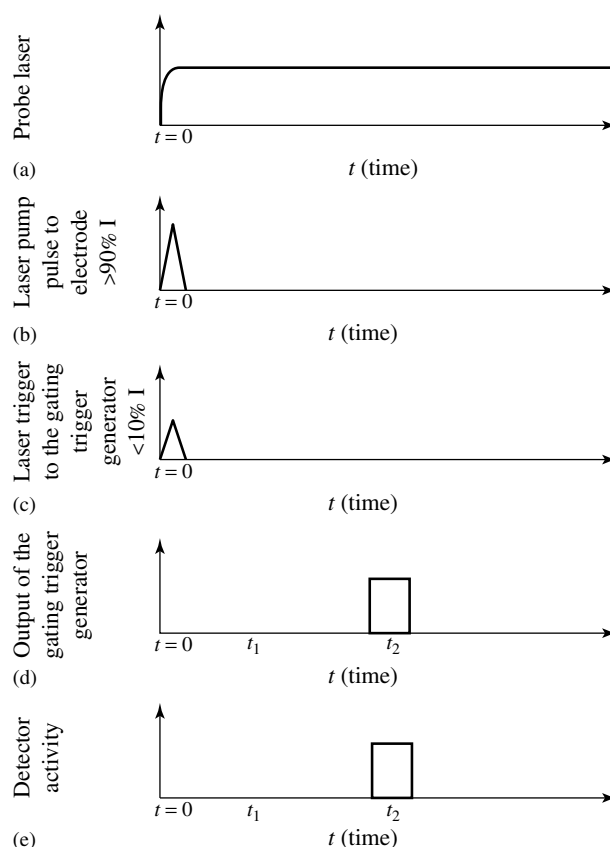


Fig. 23 Timing sequence for the pump-probe experiment. (a) The CW probe laser output in this experiment is always applied to the working electrode. (b) Major part of the pump pulse is reflected off the dichroic mirror and directed towards the working electrode. (c) Small part of the pump pulse passes through the optical adaptor and triggers the gating trigger generator. (d) Output of the gating trigger generator for control of the gated detector. The delay time, t_1 , and the gate width, t_2 , were controlled. (e) Delay time and dwell time of the detector. The correct setting of the detector allows many repetitions of this timing sequence at fixed delay time, t_1 , for ensemble averaging. Variation of t_1 then allows a series of TRSERS spectra to be recorded as a function of time. True time resolution occurs when t_2 is much shorter than t_1 . (Reproduced with permission from Ref. [60]. Copyright 1994, Kluwer Academic Publishers.)

adopted in order to increase the signal-to-noise ratio. However, this can only be applied to those surface changes possessing good reversibility.

3.6.3.4.3 Potential Averaged Raman Spectroscopy (PARS) Because the time resolution is generally limited by the detector, it has to be equipped with the costly gatatable

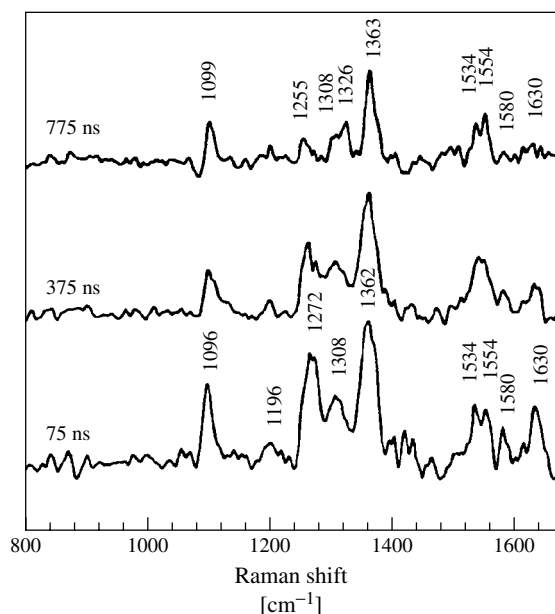
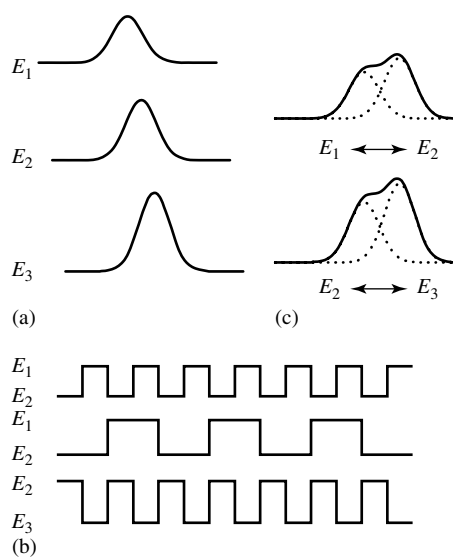


Fig. 24 Time-resolved SERS spectra of flavin mononucleotide excited with 337 nm light and probed with 488 nm laser light. Acquisition time: 200 ns. The delay time is shown in the figures. (Reproduced by permission from Ref. [61]. Copyright 1995, The American Chemical Society.)

ICCD in the present CCD Raman system. For those who do not have pulse lasers and fast response rate detectors, a unique method named PARS [62] is applicable in spectroelectrochemical studies.



The schematic layout of the technique is shown in Fig. 25. The PARS method is based on the application of a CW potential modulation to the electrode during the spectral acquisition period. A PARS spectrum is recorded while the two electrode potentials of interest are being rapidly modulated, and the spectrum contains the sum information of surface species at the two modulated potentials. Later, each spectrum at individual potentials can be extracted by deconvolution. By properly choosing a series of modulating frequencies in sequence (e.g., ranging from 100 K to 1 Hz), one can obtain a

Fig. 25 (a) The intensity and frequency of a Raman band varying with applied electrode potential. (b) Different potential pulse frequencies and amplitude can be used in PARS. (c) PARS spectra at different modulating potentials. (Reproduced with permission from Ref. [62]. Copyright 1996, Society for Applied Spectroscopy.)

set of time-resolved (ranging from $5\ \mu\text{s}$ to $0.5\ \text{s}$) spectra of surface species at the two electrode potentials. A typical example is given in Fig. 26. The time resolution no longer depends on the detector, but only on the electrochemical experimental parameters. To reduce the charging time of the capacitance of the electrochemical double layer, ultramicroelectrodes (see Chapter 2.5) are required to achieve sub-microsecond resolution with a simple nongatable CCD detector. Therefore, taking advantage of easy switching of the electrode potential, it is feasible to use PARS to achieve electrochemical dynamic information on a microsecond scale with a prolonged acquisition time (e.g., $60\ \text{s}$), to obtain time-resolved spectra of better SNR. This technique is not suitable for use in the study of surface processes with

an irreversible change between the two modulated electrode potentials.

3.6.3.5 Spatial Resolution

Conventional Raman spectroscopy has a poor spatial resolution as the laser spot is normally ca. $0.5\ \text{mm}$. However, with the introduction of a Raman microscope, a spatial resolution as high as the diffraction limit is attainable [41, 42]. Recently, with the further development of the Raman microscope into the confocal microprobe Raman instrument, three-dimensional resolution is achievable. The quite high vertical spatial resolution ensures elimination of the signal from the bulk solution. This is certainly a great help for detecting relatively weak surface Raman signals from weak-SERS or non-SERS active electrodes. It should be pointed out that the spatial

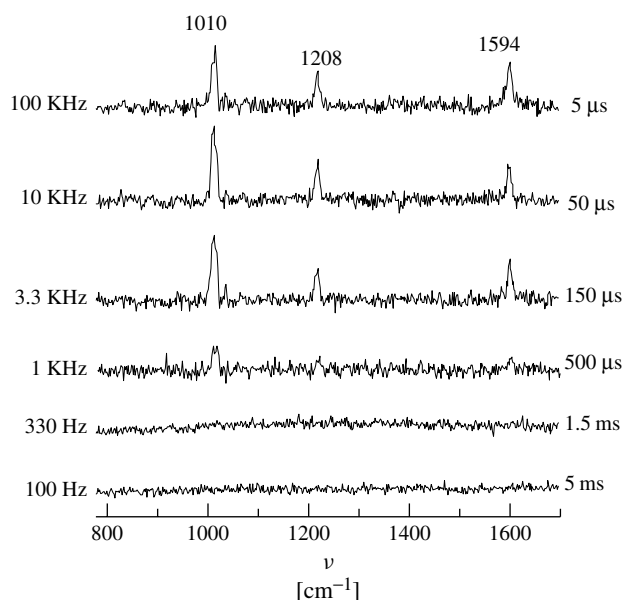


Fig. 26 Potential-averaged SER spectra of pyridine at a silver microelectrode (diameter: $100\ \mu\text{m}$) in $0.01\ \text{mol l}^{-1}$ pyridine and $0.1\ \text{mol l}^{-1}$ KCl solutions with the $632.8\ \text{nm}$ excitation line. The electrode potentials were modulated between $-0.5\ \text{V}$ and $-1.4\ \text{V}$ by a symmetric square wave.

resolution of the Raman microscopy is directly related to the magnification of the objective and the microscopy. A higher magnification provides a higher lateral resolution. However, as has been mentioned above, a very high magnification is not feasible because of the requirement on the working distance between the lens and the electrode surface.

3.6.3.5.1 Lateral Resolution Confocal Raman microscopy can provide relatively high lateral resolution, determined by the size of the laser spot and the stepping resolution of the X–Y scanning stage. A resolution of ca. $1 \sim 2 \mu\text{m}$ is sufficient to study a microelectrode system and helpful in analyzing nonuniform electrode surfaces. It is necessary to point out that nonuniform surfaces can be classified into two types: (1) where the surface only has few small specific areas that are different from the major uniform area in terms of

chemical composition; (2) where the whole surface is nonuniform and is composed of several different chemical structures. In the first case, one can just use the micropositioning X–Y stage to move a specific area of interest to the focused laser spot, then take the spectrum. This method has been used often for studying corrosion pits at the electrode surface. Fig. 27 gives a good demonstration of the method. The experiment was carried out by focusing the laser into different regions of a corrosion pit, the black center (a) and the colored ring zone (b) of the pit. The Raman spectra were recorded accordingly. The spectra (a) and (b) presents the characteristic of MoO_4 and MoO_3 iron compounds, respectively. This is certainly very helpful in identifying corrosion products and understanding the corrosion process [63]. Although this technique yields information about the local composition of the surface, some electrode surfaces are heterogeneous specimens,

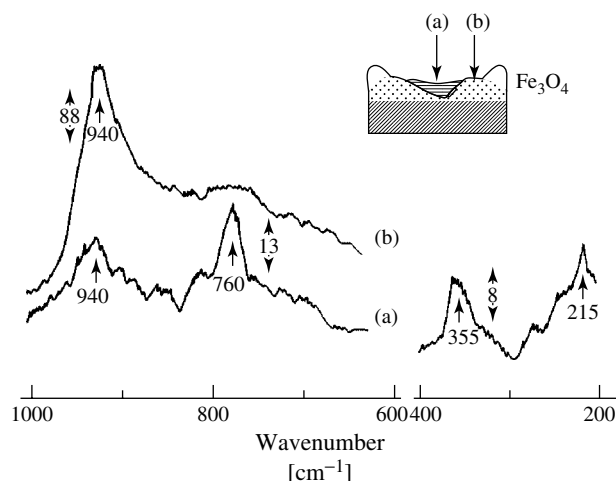


Fig. 27 Raman spectra obtained ex situ in a pit area at an iron surface polarized for 5 min at 100 mV vs. SCE in 0.03 mol l^{-1} NaCl and 0.01 mol l^{-1} Na_2MoO_4 solutions: (a) inside the pit and (b) colored area around the pit. Intensity scale given by the arrows. Inset: interface section. (Reproduced with permission from Ref. [63]. Copyright 1993, The Royal Society of Chemistry.)

which require the techniques described in the following sections.

Raman mapping technique If the surface is arranged spatially with various molecular species or chemical composites, the whole surface area needs to be analyzed and a set of Raman images corresponding to various characteristic Raman bands can be obtained, as shown in Fig. 28. Therefore, Raman imaging is also called chemical imaging. Basically, Raman imaging methods can be classified in two categories, referred to as point-by-point mapping and global imaging. The mapping technique is also named series imaging. It uses a computer-controlled stepping-motor-driven sample stage on the microscope, relative to the stationary focused laser beam, to record a set of spectra point by point. In this computer-programmed

procedure, the spectra are detected at several hundred positions on a sample surface in a raster pattern. In this way, two-dimensional maps of the different species present on the surface are built up.

Another optical arrangement for Raman mapping has proved to be convenient for a variety of cumbersome surface samples and holders, such as variable temperature or pressure cells. The focused laser spot is scanned over the stationary sample and the spectra recorded in sequence. This method is achieved by a new kind of transfer optics placed between the microscope and the spectrometer, which enables an optimized coupling. The coupling optics consist of a pair of lenses. One lens, optically coupled to the back aperture of the objective, can be moved in two orthogonal directions perpendicular to the laser beam. Thus, this lens can focus the light beam on any point

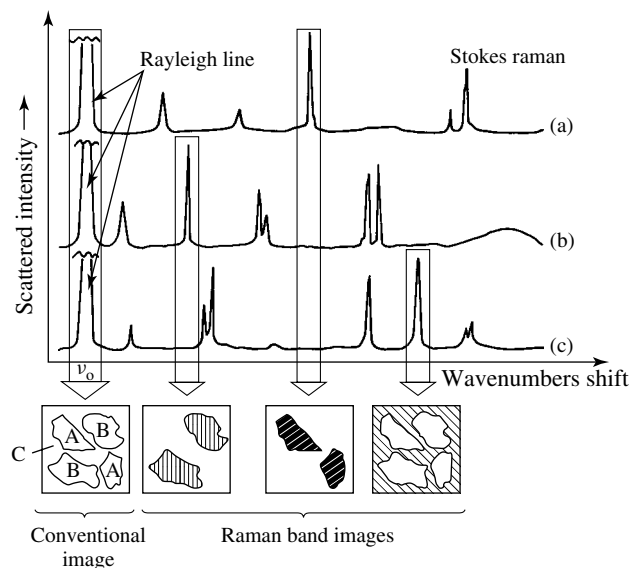


Fig. 28 Illustration of the principle of selective imaging by use of specific spectral bands of Raman scattered radiation. (Reproduced with permission from G. J. Rosasco, *Raman Microscope Spectroscopy*, in: *Advances in Infrared and Raman Spectroscopy*, Vol. 7. Copyright 1980, Heyden & Son Ltd.)

in the microscope field and therefore on any point of the sample. The second lens is mechanically coupled to the first and placed in the scattered beam, to balance any shift in the image probed area, and focus the scattered beam on the entrance slit of the spectrometer.

It should be noted that the mapping method is time consuming with several hours needed to obtain a full image of the surface. Thus, it is not suitable for unstable surfaces. To cope with this problem, a one-dimensional mapping line profile is sometimes used if the results are representative of the two-dimensional surface.

Raman imaging technique One of the most promising Raman imaging techniques nowadays is the global imaging technique [64, 65]. It requires the laser beam to be expanded to fill (or overfill) the field of view of the microscope objective, which is realized by the use of a normal beam expander, an optical fiber. The detector is a two-dimensional low-light-level CCD detector. The working principle involved is that the sample is placed under the microscope and the light beam illuminates the whole field of view of the microscope. Thus, the sample is uniformly irradiated with monochromatic radiation. The microscope then transfers the image of the sample to a monochromator that selects the desired wavelength to be imaged onto the CCD, placed at the exit focal plane. If the wavelength selected corresponds to a Raman band frequency of a component of the surface, the micrographic image indicates the distribution of the component throughout the illuminated area. The spatial resolution of the system can reach about 1 micron. It works well with surfaces that are good Raman scatterers, but tends not to work with poor

Raman scatterers because it is difficult to discriminate Raman features from fluorescent backgrounds. Thus, a sample with a SERS or RR effect is helpful to obtain good images. The major advantage of global imaging is that the detector (CCD detector) observes the entire field, so that the image of the whole area can be recorded simultaneously in a short time.

3.6.3.5.2 Vertical Resolution Besides all the features (high lateral resolution) of a normal Raman microscope, confocal Raman microscopy also has the capability of vertical spatial resolution. This feature ensures the elimination of the signal of interest from the bulk solution. This is certainly of great help in detecting a relatively weak surface Raman signal from weak SERS or non-SERS active electrodes. Moreover, this optical sectioning method can analyze concentration changes of solution species in the solution layer near to the surface during the electrochemical oxidation or reduction processes. When a laser spot is focused upon the electrode surface, the Raman signal is mainly contributed by the adsorbed species. However, when the position of the focus is above the surface, the Raman signal mainly comes from the bulk species. Thus by adjusting the focal point at different heights above the electrode surface, one can get a concentration gradient of different solution species based on their spectral signals. A good example is the *in situ* monitoring of the electrochemical oxidation process of methanol on a roughened Pt surface in sulfuric acid. During the oxidation process, the focus was moved step-by-step away normal to the electrode surface, thus allowing the increase of the methanol concentration to be seen. At the same time the relative band intensity of SO_4^{2-} with respect to HSO_4^- increases, which clearly

reflects the increase of the solution pH near the electrode surface as a result of the methanol oxidation. According to the ratio of the relative intensity of these two species, one is able to estimate the solution pH profile normal to the electrode surface during the electrochemical reaction [65].

3.6.3.6 Calculation of the Surface Enhancement Factor (SEF)

The calculation of the SEF [66] is important for SERS applications on electrode surfaces. It is calculated generally by comparing the integrated Raman intensity obtained from the surface with that from the solution phase. Thus, the SEF can be defined as

$$G = \frac{I_{\text{surf}}/N_{\text{surf}}}{I_{\text{bulk}}/N_{\text{bulk}}} \quad (9)$$

where I_{surf} and I_{bulk} denote the integrated intensities for the strongest band of the surface and solution species respectively, which can be obtained directly from the Raman measurement, as shown in Fig. 29(a) and N_{surf} and N_{bulk} represent the number of the corresponding surface and solution molecules effectively excited by a laser beam.

N_{surf} can be calculated by the following approximation, after considering the contribution of the surface roughness:

$$N_{\text{surf}} = \frac{RA}{\sigma} \quad (10)$$

where R is the roughness factor of an electrode, A is the area of the focal spot of the laser; σ is the surface area occupied by an adsorbed molecule, which is obtainable for a model molecule through other techniques.

The calculation of N_{bulk} is complex and should be considered very carefully to obtain the correct value. Because confocal Raman microscopy is becoming more popular, the calculation of SEF based on a confocal system is given here [61]. Fig. 29(b) shows the waist profile of a focused laser beam in an aqueous solution. In principle, all molecules within the illuminated volume of the solution contribute to N_{bulk} . However, the collection efficiency of scattered photons from molecules in each plane of the solution varies with confocal depth, that is, the distance deviated from the ideally focal plane, where z equals zero and molecules therein contribute the most to the overall intensity, the integrated intensity of which is defined to be I_{max} . Experimentally, a single crystal silicon wafer immersed in a solution can be used to provide the confocal depth profile. The integrated intensity of the strongest band for Si at 520.6 cm^{-1} was measured as the Si wafer plane was moved up and down vertically, while the confocal position was kept stationary. Fig. 29(c) presents the intensity-distance profile that simulated the confocal depth profile, see the solid line. It shows an abrupt decrease at both sides of the ideally focused plane. For the illuminated volume of the solution, a plane of solution can be imagined to move up and down vertically, just like the realistically moveable Si wafer. It can be seen that the contribution from molecules, outside the region of $|z| > 75 \mu\text{m}$, is negligible to N_{bulk} . Now, assume an ultrathin layer of solution with a thickness of h , and volume hA in the vicinity of the ideally focused plane, in which all the molecules have the same contribution to the overall signal as that in the ideal focal plane. The overall signal can be obtained by integrating the signal over the intensity-depth profile. Thus, the thickness h can be

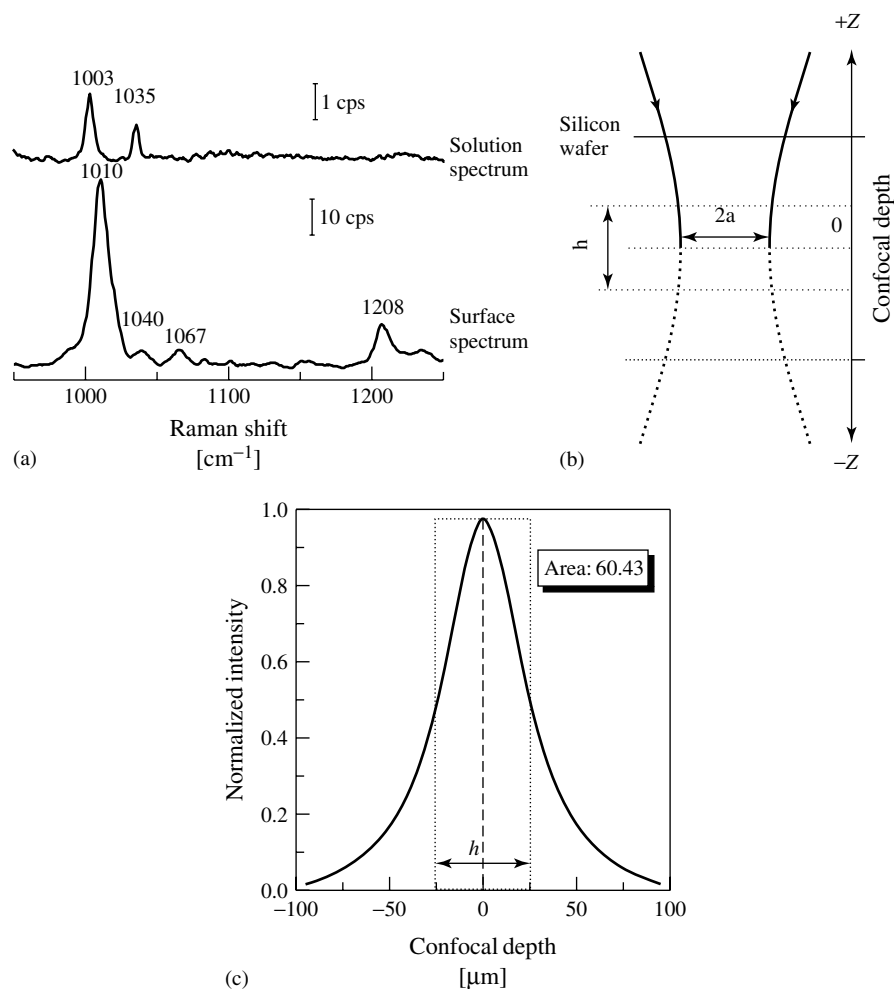


Fig. 29 (a) Solution normal Raman spectra and SER spectra obtained from a rough platinum surface. (b) Waist profile of the laser beam of Raman microscopy and the integrated intensity-depth (I - Z) profile of solution species along the laser waist. (c) The simulated distribution and the integrated intensity-depth (I - Z) profile of solution species along the laser waist. The pinhole was set at 600 μm .

calculated by

$$h = \frac{\int_{-\infty}^{\infty} I(z) dz}{I_{\max}} \quad (11)$$

The h value (in units of μm) depends on the pinhole size and the objective lens of the Raman microscope. This value can be

considered as the key parameter of the confocal characteristic. After systematic study of the water overlayer effect on the spatial resolution for the solid-liquid interface, we found that the spatial resolution for the confocal system at the same pinhole size and slit width, using the same microscopy objective, is quite different with

and without the water overlayer. The effectively illuminated number of molecules in the aqueous solution, N_{bulk} , can be written as

$$N_{\text{bulk}} = AhcN_A \quad (12)$$

where c is the concentration of adsorbate, and N_A the Avogadro constant. With Eqs. (7 and 9), Eq. (6) can be rearranged as

$$G = \frac{cN_A\sigma hI_{\text{surf}}}{RI_{\text{bulk}}} \quad (13)$$

G can be obtained after substituting all the known data and constants into the above equation.

3.6.3.7 Combined and Hyphenated Techniques

For some special studies, combined techniques should be considered and hyphenated techniques developed, as described in the following section.

3.6.3.7.1 Optical Fiber Raman Spectroscopy With the expansion of surface Raman spectroscopy, there is an increasing requirement on the measurement of systems in some very special environments, such as high temperature reactions, explosive, irradiative and combustible systems, or live animals. For the protection of the experimentalist and the instrument, an optical fiber technique is combined with Raman spectroscopy. Optical fibers can be employed to deliver the laser excitation source and collect the Raman signal with greater flexibility. As Raman is intrinsically a weak process, the major consideration of the optical fiber Raman system is to increase the collection efficiency. Typical systems consist of the laser, premonochromator, incident optical fiber, collection optical fiber, and the spectrograph. Additional adaptors are needed to

couple the laser and the Raman signal into the incident and collection optical fibers and to couple the light signal from optical fibers into the spectrometer. Minimizing the loss of the signal in the coupling optics is very important to optical Raman spectroscopy. Normally there is only one incident optical fiber and several collection optical fibers in order to increase the collection efficiency. There is also a very unique design in which only one optical fiber is employed to irradiate and collect the Raman signal, which is coupled by a microscopic objective to the Raman spectrometer [67]. The sampling end of the optical fiber was coated with rough silver, and the sample adsorbed on the unique tiny silver surface. This configuration ensures the maximum collection efficiency. However, the interference from the optical fiber itself, when the sample signal is weak, should be considered.

Recently, with the development of the compact Raman system and maturation of the notch filter technique, a novel design of an optical fiber Raman spectrometer was commercialized. Fig. 30 gives a schematic diagram of such a design. The laser is introduced by an optical fiber into the head, then monochromated by a plasma line filter. The laser beam was then reflected by a small mirror and focused on the sample by a camera lens. The Raman signal was collected by the lens and the Rayleigh and stray light were rejected by the notch filter and coupled into the collection optical fiber. This use of a monochromator after the incident optical fiber ensures no interference from the incident fiber. The use of a notch filter before the collection fiber ensures no excitation of the Raman signal of the optical fiber by the laser. Thus, the interference of the signal by the optical fiber is reduced to a minimum. Further development of this technique

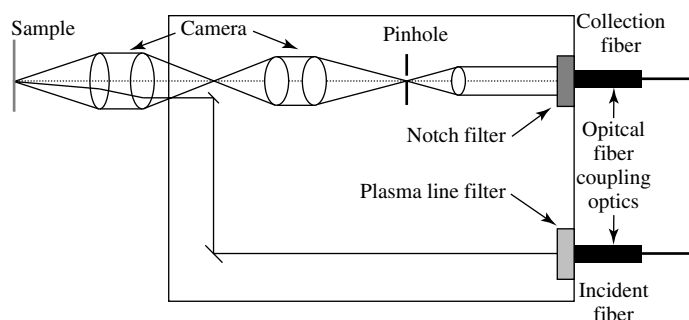


Fig. 30 Schematic diagram of a collection head of an optical fiber Raman system.

seeks to increase the collection efficiency, as well as reduce interference from the fiber itself.

3.6.3.7.2 Hyphenated Techniques of Raman Spectroscopy with SPM The spatial resolution of Raman spectroscopy, which provides chemical identification, only falls into the micrometer scale, while STM (Chapter 3.1) has an extremely high spatial resolution, up to the atomic scale, but generally without chemical identification. It is increasingly desirable to couple vibrational data with corresponding information on the surface morphology at the microscopic level, to probe electrode surface adsorption and reaction sites. These two techniques are obviously complementary to each other for probing interfaces. Several studies have been directed to investigate Ag films at higher resolution by combining SERS with STM or by AFM (Chapter 3.2) separately [68, 69].

There is no doubt that much useful and reliable information can be obtained if one makes use of the advantages from these two techniques simultaneously to study the interface. Fig. 31 is a schematic diagram of the hyphenated Raman-STM [70]. Remote operation of the optical fiber

technique is used, so that simultaneous measurements on one electrochemical cell can be carried out using two instruments set in two rooms. The STM head is specially designed so that the limited spaces surrounding the STM tip can be fully used to introduce the fibers. Five collection fibers and one excitation fiber are mounted in a fiber fixer, consisting of a hemisphere cap through which the fibers can be positioned closely surrounding the STM tip, above the sample and close to the tip without any mechanical contact. Furthermore, a graded refractive index lens is fixed at the head of each fiber to ensure larger relative aperture. The scattered light is collected and transmitted through five fibers and then coupled into the Raman spectrometer. Using an optical multichannel analyzer, to record the Raman signal, the signal acquisition time can be reduced to 0.1 to 5 s. Therefore, the laser illumination time can be shortened, to minimize thermal interference. It has been found that STM images are essentially reproducible with a drift of less than 10% before, during, and after the Raman measurement. Further tests of simultaneous STM and Raman measurements were carried out on the electrodeposition of silver on HOPG electrodes, in the presence of

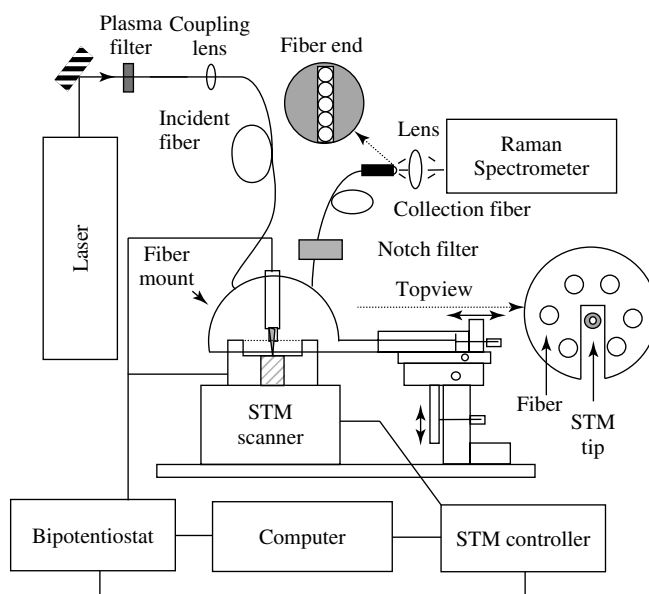


Fig. 31 A block diagram of a hyphenated STM and Raman base.

thiourea as an organic additive, to correlate the SERS activity and surface morphology [70].

3.6.3.8 Troubleshooting

The major problems associated with Raman spectroscopy have already been mentioned. In EC-Raman measurements, additional problems related to the cell occur. Since in most electrochemical systems, there is a solution layer and an optical window between the collection lens and the electrode surface, special attention has to be paid to alignment. The measurement may be compromised by the signal from solution species and/or bubbles generated during the electrochemical reaction. Some electrodes may suffer severe heating damage effects or fluorescence by the laser irradiation when Raman microscopy is applied. In the following sections, solutions to the problems mentioned earlier will be given.

3.6.3.8.1 Optical Alignment The most serious problem, especially for studying the electrochemical interface of two condensed phases, is detection sensitivity. Many problems are caused by the optical alignment related to the spectroelectrochemical cell and sample. Since the confocal microprobe Raman system has much higher sensitivity than other Raman systems, it is used most frequently for spectroelectrochemical studies. This will be taken as an example for the detailed discussion that follows.

Without making careful and correct optical alignment of the electrochemical cell, it is not possible to take advantage of the confocal microscope and the surface Raman signal may even not be detectable. For example, the solution layer of the electrochemical system could dramatically affect the collection efficiency of the microscope and hence the detection sensitivity. An investigation of the effect of the thickness

of the solution layer on the Raman signal detected revealed that with a decrease of the thickness of the solution layer from about 2 mm, 1 mm, 0.5 mm to 0.2 mm, the Raman intensity increases from 35%, 52%, 71%, and 89% of the maximum intensity obtained on a silicon wafer without the water overlayer [16]. At the thickness of 0.2 mm, the Raman intensity suffers only about 10% loss and a solution layer of this thickness does not have much effect on the electrochemical process. This thickness is often used as the optimized condition after considering both the Raman intensity and the electrochemical processes.

Furthermore, in the electrochemical system, most of the electrolytes are corrosive, and to protect the objective, a cover glass or quartz window has to be employed between the electrolyte and the objective, this results in 50% loss of the signal. An alternative way to protect the objective is to wrap it with a very thin and highly transparent polyvinyl chloride (PVC) film. A benefit of the confocal setup is that there is no signal from PVC in this configuration. By this approach, the Raman signal only suffers 20% loss. The disadvantage of this approach is that without the quartz window, the solution has to be exposed to the air, and impurities in the air will contaminate the solution. For systems that are very sensitive to any contamination, a thin quartz window, with thickness of 0.2 to 0.5 mm, has to be employed at the cost of the intensity.

The thickness of the water layer over the electrode surface can also affect the vertical spatial resolution of the confocal system. For example, with smaller pinhole size (300 μm), the spatial resolution is about 17 μm and 19 μm , without and with the solution layer, while when the size is about 600 μm , the spatial resolution amounts to 21 and 53 μm for the surface without

and with a solution layer, respectively. This indicates that in an experiment in which high spatial resolution is required, decreasing the pinhole size is a very effective way to eliminate distortion due to the solution layer.

3.6.3.8.2 Interference of Solution Species

In some cases, in which the concentration of the molecule in the electrolyte is quite high, the solution signal will also contribute to the final signal detected. This is especially serious in a conventional macro-Raman system. One way to eliminate the interference from solution species is to reduce the distance between the electrode surface and the optical window, that is, the thickness of the solution layer, as already discussed. Another method is to use a confocal microscope to reduce the collection volume around the laser spot (vide supra).

However, there are cases in which the above methods cannot work effectively, and the method described earlier, based on the potential subtractive tactic can be used, which is also routinely applied in electrochemical IR spectroscopy (see Chapter 3.5). It works by subtracting the spectrum acquired at a potential with weak or no surface signal, such as the desorption potential, and that acquired at another potential, in favor of the surface adsorption to manifest the surface signal. Usually the solution signal is independent of the potential, thus the strong solution signal can be subtracted completely. It should be noted that, for some solution species, when the electrode surface charge is changed, it is possible that the concentration in the interface will increase due to electrostatic attraction, which results in an increase of the intensity of the detected spectrum. There are still two ways to distinguish the spectral bands of surface species from the solution

species, in terms of the band intensity and frequency. The first way is to change the solution concentration. If the signal is from the solution species, there will be no signal saturation upon increasing the concentration of the bulk species. If the signal is from the surface species, normally there will be a saturation of the signal upon the increase of the solution concentration as the surface concentration will be saturated. The second way involves recording a set of spectra at different potentials, to see if the bands are potential dependent or not.

3.6.3.8.3 Interference of Gas Evolution during In situ Measurements

To carry out spectroelectrochemical measurements in the potential region of severe gas evolution, such as hydrogen or oxygen evolution, is always a big problem for any optical spectroscopy technique. Vigorous gas evolution from the surface with discontinuous large bubbles can alter either the incident or the scattering (or reflecting) light intensities seriously. There may be three ways to surmount, at least to some extent, the disturbance due to strong gas bubbling. (1) To use the optical internal reflection spectroscopic configuration. A special metal (or oxide) thin film coated onto a transparent substrate serves as the electrode. In this configuration, the probing light beam does not pass through the solution phase, but it enters the substrate from the back so that bubbles will not block the probing beam. (2) To press the electrode against the cell window. With the help of such a thin-layer cell configuration, the strong gas is dispersed and evolves with very fine bubbles, so that neither the incident nor the scattering (or reflecting) light intensities are altered seriously. However, ohmic drop in the thin layer should be taken

into account. (3) To utilize the surface enhancement effect, which can be up to 10^6 , as already discussed.

The first method employing internal reflection requires special cell and electrode configurations. The very thin metal (or oxide) film electrode needs to be evaporated on an optical material such as a quartz prism. It makes routine surface pretreatment and measurement very difficult, and indeed, this method has not been adapted commonly in spectroelectrochemistry. The best way to carry out measurements with severe gas evolution is a combination of (2) and (3), although they have their own drawbacks.

3.6.3.8.4 Electrode Stability and Potential Reversibility

At most SERS substrates, such as Ag, Cu, Ni, and Fe, after being electrochemically roughened for creating SERS activity, the SERS stability and reversibility should be monitored critically. Fig. 32 shows a very typical curve manifesting the change of SERS intensities upon the change of the electrode potential. It can be found in the figure that SERS intensities reduce markedly upon setting the potential in the very negative region. Even without moving to very negative potentials, the SERS intensity may decrease with time at a steady potential. These phenomena have been interpreted as the decomposition, then irreversible loss, of the unstable SERS-active sites [71]. Thus, a surface coverage decrease, or the tuning out of the CT band, are not the only reasons for the intensity change.

In order to reduce the chance for the misinterpretation of a SERS result, it is important to prepare the electrode surface properly. For example, after roughening the surface, one may conduct an electrochemical cleaning procedure to remove

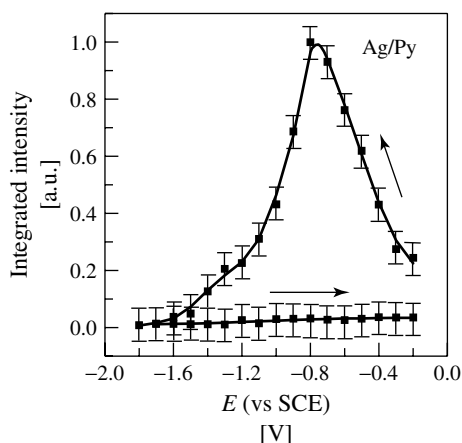


Fig. 32 The profile of the intensity of the pyridine ν_1 mode with the electrode potential, demonstrating the irreversibility of a SERS-active silver electrode.

those unstable sites. A simple way is to make potential cycles in the potential region to be studied. A specific method called diminished SERS (DSERS) has been proposed for more extensive surface cleaning [8]. DSERS can be achieved by underpotential deposition of foreign metals of submonolayer amounts onto SERS-active substrates or by applying a cathodic polarization to hydrogen evolution to quench a certain SERS activity irreversibly, by removing those SERS-active sites. After such kinds of pretreatment, the electrode surface shows much better stability and reversibility at the expense of the SERS intensity. However, this is necessary, and crucially important, for some EC-SERS studies in order to correlate the SERS intensity with the surface coverage.

A unique method to overcome the problem of gradual change in the SERS activity during the measurement is to use the PARS method, which has been described in detail earlier. The essentials of the tactics are (1) to shorten the time for the electrode at potentials that are unfavorable for the SERS-active site and (2) to ensure the SERS activities at the two potentials are exactly the same.

3.6.3.8.5 Surface Heating and Damage

Laser-induced sample damage is another cause of unsuccessful sample analysis in surface Raman spectroscopy. Most SERS-active substrates have to be roughened to create SERS activity. After being roughened, the surface changes from optically smooth to dark or milky color, because of the rough surface. Absorption by the surface of the excitation line will increase. This leads to more severe heating or damage effects of the substrate by the laser irradiation, especially in microscope Raman systems. A common strategy, in order to obtain a stronger signal, is to raise the laser power. However, for a conventional Raman spectroscopic measurement, involving a 100 mW laser beam with a cross-sectional area of 0.785 mm^2 (diameter 1 mm) the power per unit area is 127 mW mm^{-2} , while for a Raman microscope, the objective characteristically yields a $1\text{-}\mu\text{m}$ diameter beam waist at the sample focus. The power density at the focus is then of the order of $127 \times 10^6 \text{ mW mm}^{-2}$. This power confinement represents a millionfold increase in the power per unit area. Furthermore, when the wavelength of the laser line moves towards the UV region, the energy becomes higher and

the radius of the focal point becomes smaller, thus both the energy and the power density of the UV laser are higher than that of near-infrared lasers, so that sample heating or even damage effects may be more severe. The extent of these problems can range from subtle color or crystalline changes in the materials, to the complete ablation of the sample beneath the microscope objective. The situation is particularly troublesome for solid substrates, where a longtime exposure to the laser source may lead to destruction of the substrate and the decomposition of the surface species. Even for conventional Raman measurements, heating may cause corresponding spectral changes, including subtle shifts in Raman transitions, the appearance of new transitions, or complete loss of signals. In order to prevent these possibilities from occurring, a plan of action is suggested as described next.

Prior to the collection of a spectrum, a photograph or mental note of the appearance of the electrode surface should be made. This photograph or note can then be compared to the appearance of the surface, after a spectrum has been collected. More subtle heating effects are best detected by collecting several spectra at different power levels. If these spectra are not reproducible, the sample may be changing as a result of the irradiation. If care is not taken during the analysis, results can easily be misinterpreted. On some Raman microprobe systems, it is possible to view the sample while it is being illuminated with the laser. For these systems, one can view the laser focus and determine whether it changes as a function of time. Should material be ablated from the sample, the size of the focused laser will appear large, since the remaining sample surface is below the focus of the microscope. Because of the fact that the

objective is directly above the sample and in close proximity to the sample, any material that is vaporized will condense on the cell window or the microscope objective. This material must be removed, since it will affect the focal characteristics of the laser and could yield a parasitic background in the Raman spectrum.

In the event that the sample undergoes degradation, even at the lowest power levels, one of the more obvious solutions is to reduce the laser power still further. This solution can be implemented by defocusing the laser beam. This is usually accomplished by adjusting the beam expander in the prefiltering optics of the system so that the aperture of the objective is underfilled, by which a large beam waist is obtained at the objective's focus. If lowering the power of the laser does not decrease the sensitivity too much, an alternative method is to make a cell that can be moved horizontally or vertically, using mechanical or pneumatic apparatus, thereby minimizing thermal effects and damage very efficiently.

3.6.3.8.6 Fluorescence Elimination One of the major problems that has to be overcome with surface Raman spectroscopy is parasitic fluorescence. It is obvious that the Raman process and the fluorescence process are competing processes in the emission of the absorbed photons, as has been mentioned in the introduction section. The dramatic increase of the Raman process by the SERS effect will inevitably suppress the fluorescence process. Furthermore, because of the interaction of heavy metal atoms with the adsorbed molecules, the energy levels of the molecules will possibly be redistributed, which may result in an effective quenching of fluorescence. However, if the surface Raman study concerns

non-SERS systems, such as organic, polymer, and biological-layer (film) electrodes, other methods have to be used. Raman is a scatter-based phenomenon, inherently a two-photon effect. Fluorescence, on the other hand, consists of two sequential photon-induced transitions, an absorption followed by spontaneous emission. The timescale of scattering is of the order of 10^{-12} s, while fluorescence lifetimes are typically of the order of 10^{-8} s. Thus, the problem can be tackled using temporal fluorescence rejection techniques with fast response rate detectors. Fluorescence quenching is also a technique in which the sample is irradiated for a long period of time. After that, the fluorescence signal may be eliminated or reduced to a tolerable level. The use of an aperture at a remote image plane (confocal microscopy) can also be employed in the elimination of fluorescence from neighboring locations.

To change the excitation line from visible to near infrared, or even UV, is another effective way to avoid strong fluorescence. Although FT-Raman spectroscopy has relatively low sensitivity, it allows spectra of many samples that fluoresce in the visible region, to be recorded. This is because the samples are excited using near-IR excitation that does not induce sample fluorescence. Moreover, UV-Raman spectroscopy has been used in some situations very efficiently.

3.6.4

Applications

Raman spectroscopy, because of its high surface specificity and sensitivity, especially with the help of the SERS effect, has been widely used in electrochemistry, which can be classified into two broad categories: (1) of fundamental interest are

the surface bonding, configuration of adlayers, interfacial structure, and surface reaction and (2) of practical importance are batteries, electroplating, corrosion, surface processing, and new materials. Since the discovery of the SERS effect, thousands of papers have been published on the above fields and it is only possible for this article to give a brief introduction to SERS applications in electrochemistry. For a more specific and detailed overview, readers are recommended to the following reviews: early works by Van Duyne [6] and Fleischmann and Hill [10], electrochemical adsorption and interfacial structure by Pettinger [14], Weaver et al [72, 73], Fleischmann and Hill [10] and Chang et al [11], electrode surface processes and reactions by Birke et al [13] and Weaver [72, 73], biomolecule modified electrodes by Cotton [74], carbon electrodes by McCreery [75, 76], nonaqueous systems by Irish et al [77], corrosion and metal oxides by Melendres [78, 79], electroplating by Pleith [80].

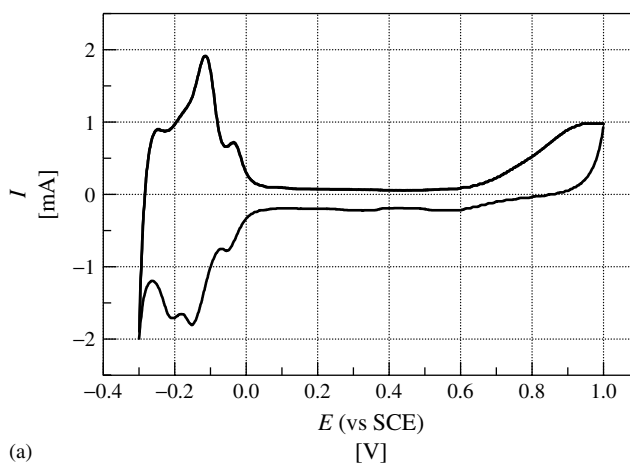
3.6.4.1 Surface Bonding

3.6.4.1.1 Identification of Different Surface Species

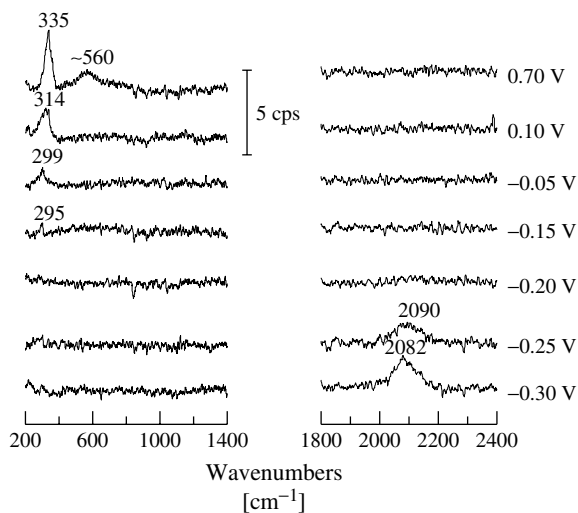
The most outstanding feature of Raman spectroscopy is its ability to identify the surface bonding between an adsorbate and the metal surface, thus it readily provides a wider span of adsorbates than IR. The Raman investigation on a roughened platinum electrode in an HCl solution can be used to demonstrate this feature. The cyclic voltammogram (CV) of a roughened Pt electrode in a 1 mol.l^{-1} HCl solution is given in Fig. 33(a). Two desorption and three adsorption peaks can be found in the negative potential region, which represents the adsorption and desorption of hydrogen and chloride. Hydrogen evolution starts at -0.25 V versus SCE, and becomes significant at -0.3 V . The

adsorption of oxygen is evident at 0.7 V. Fig. 33(b) gives the corresponding surface Raman spectra from the Pt electrode when the potential is moved to positive values stepwise. A broad band at 2082 cm^{-1} can be found in the potential region of hydrogen evolution (-0.30 to -0.25 V). With further positive movement of the potential into the hydrogen

underpotential deposition region, no band related to the underpotential deposited hydrogen can be found. This reveals that the nature of hydrogen bonding in these two potential regions is substantially different [81, 82]. When the potential was moved into the strongly bound hydrogen adsorption region, a band at 295 cm^{-1} emerges, whose frequency blue shifts with



(a)



(b)

Fig. 33 (a) Cyclic voltammogram of a roughened Pt electrode in 1 mol l^{-1} HCl. Scanning rate: 50 mV s^{-1} . (b) Potential-dependent Raman spectra of the Pt electrode in the same solution. Excitation line: 514.5 nm .

the positive going of the electrode potential. It can readily be assigned to be from the Pt-Cl vibration, based on previous data obtained on platinate chloride compounds. This band shifts quite dramatically with the positive movement of the potential, with a Stark effect value $d\nu/dE$ of about $65 \text{ cm}^{-1}\text{V}^{-1}$. Interestingly, at 0.70 V, where in the CV the oxygen adsorption commences, a new broad band at ca. 560 cm^{-1} can be found, which has been assigned to the oxygen-containing species formed at the Pt surface.

The ability to detect three distinctly different Raman signals originating from different species adsorbed at the electrode surface convincingly demonstrates the merit of Raman spectroscopy. From the result, we could characterize the interaction of different species on the surface. It is evident that both hydrogen and chloride interact strongly with the platinum surface. However, the existence of hydrogen inhibits Cl^- adsorption. Cl^- and oxygen can also interact strongly with Pt, but they can coexist at the electrode surface in a certain potential range. This latter behavior has been interpreted as the characteristic of parallel coadsorption. Raman spectroscopy, in itself, not only presents its advantage in analyzing the adsorbate and substrate interaction in the rather low frequency region that is difficult for sum frequency generation (SFG) and IR, but also behaves as a powerful tool to identify the behavior for species adsorbed at the surface.

3.6.4.1.2 Determination of the Surface Adsorption Sites Raman spectroscopy cannot only identify different species at a surface, but also the same species adsorbed on different surface sites, with and without a change of the electrode potential. The adsorption of carbon monoxide

(CO) on metal surfaces is a very typical case.

It has been found that the intramolecular C–O(ν_{CO}) and Metal–CO ($\nu_{\text{M–CO}}$) stretching vibration frequencies are very sensitive to the surface chemical and physical properties, and that the adsorption geometry depends greatly on the surface. In order to demonstrate this, the result of a SERS study of CO adsorption on a roughened Pt surface (roughness factor = 200) is given in Fig. 34. CO was preadsorbed by dipping the electrode in a 0.1 M H_2SO_4 solution saturated with CO at -0.2 V for 5 min. It can be seen that one cannot detect not only the strong band at 2071 cm^{-1} and 489 cm^{-1} attributable to the ν_{CO} and $\nu_{\text{M–CO}}$ of atop-adsorbed CO according to IR and electron energy loss spectroscopy (EELS) results, but also a weak feature on the low frequency side of the two peaks at 1840 and 413 cm^{-1} , respectively. There is a correlation between them in intensities. They were tentatively assigned to the ν_{CO} and $\nu_{\text{M–CO}}$ of the bridging CO. The intensity of this band increases with a decrease of atop CO, especially at the potential just before the oxidation of CO. It indicates that CO cannot only adsorb on the atop site, but also on the bridge site of the surface, and the proportion of CO on these two sites depends on the electrode potential. The most valuable information derived from this study is that the M–CO vibration gives higher intensity than the C–O vibration, which illustrates the advantage of Raman spectroscopy in identifying substrate–adsorbate interactions.

3.6.4.1.3 Distinguishing Different Interactions of the Adsorbate with Substrates When the identify of the metal substrate is changed, the Raman spectra will show a dramatic difference for adsorbed CO.

Fig. 34 SER spectra of CO adsorption on a roughened Pt surface in $0.1 \text{ mol l}^{-1} \text{ H}_2\text{SO}_4$ (roughness factor = 200). CO was preadsorbed by dipping the electrode in $0.1 \text{ mol l}^{-1} \text{ H}_2\text{SO}_4$ saturated with CO at -0.2 V for 5 min. Excitation line: 632.8 nm .

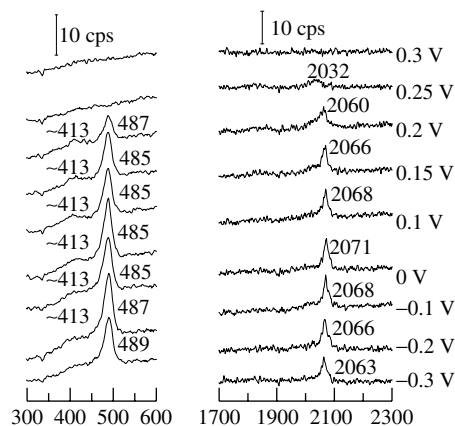


Fig. 35 shows examples of Raman spectra for saturated CO adlayers on various transition-metal surfaces of interest, and it is obvious that ν_{CO} and $\nu_{\text{M-CO}}$ are very sensitive to the identity of the transition metal [83]. The frequencies and relative intensities of the ν_{CO} ($2040\text{--}2080 \text{ cm}^{-1}$) attributed to atop CO and bridging CO ($1870\text{--}1960 \text{ cm}^{-1}$) vary substantially with the metal in a similar fashion. For example, on the Ir surface, the adsorbed CO is dominated by the linearly adsorbed CO, and on the Pd surface, the bridging CO dominates. While for Pt and Rh surfaces, both bridged and linearly bound CO exist. The vibrational frequencies for different metals with adsorbed CO in the same adsorption geometry are also different. For example, for the atop-adsorbed CO, ν_{CO} follows the order $\text{Pt} > \text{Ir} > \text{Pd} > \text{Rh}$, while $\nu_{\text{M-CO}}$ follows the order $\text{Ir} > \text{Pt} > \text{Rh} > \text{Pd}$. On the basis of the band positions, and relative intensities of the bridging and linearly bound CO, it is possible to identify different metals by the adsorbed CO via Raman spectroscopy.

3.6.4.2 Surface Configuration

Raman spectroscopy can also be used to obtain information about the surface

configuration (structure and orientation) of adsorbed species.

3.6.4.2.1 Adsorption Orientation

Pyridine adsorption on a silver electrode

As a first example for illustrating the application of Raman spectroscopy in characterizing the orientation of surface species, we consider pyridine adsorption on an Ag surface [84], for several reasons. The first SERS experiment was carried out using pyridine as the adsorbed species. Secondly, pyridine has a large Raman cross section, relatively simple molecular structure, and a good assignment of bands appearing in its normal Raman spectrum and SER spectrum. Thirdly, pyridine is an excellent model molecule for surface coordination studies. Fourthly, interactions of the pyridine molecule with the metal surface involve both the π and lone-pair electrons.

Furthermore, because of its high solubility in water and the large Raman cross sections, it is easy to obtain signals of the solution species. The SEF of the surface species, in comparison with the surface adsorbed species is thus readily calculated, and when a new substrate or a new Raman

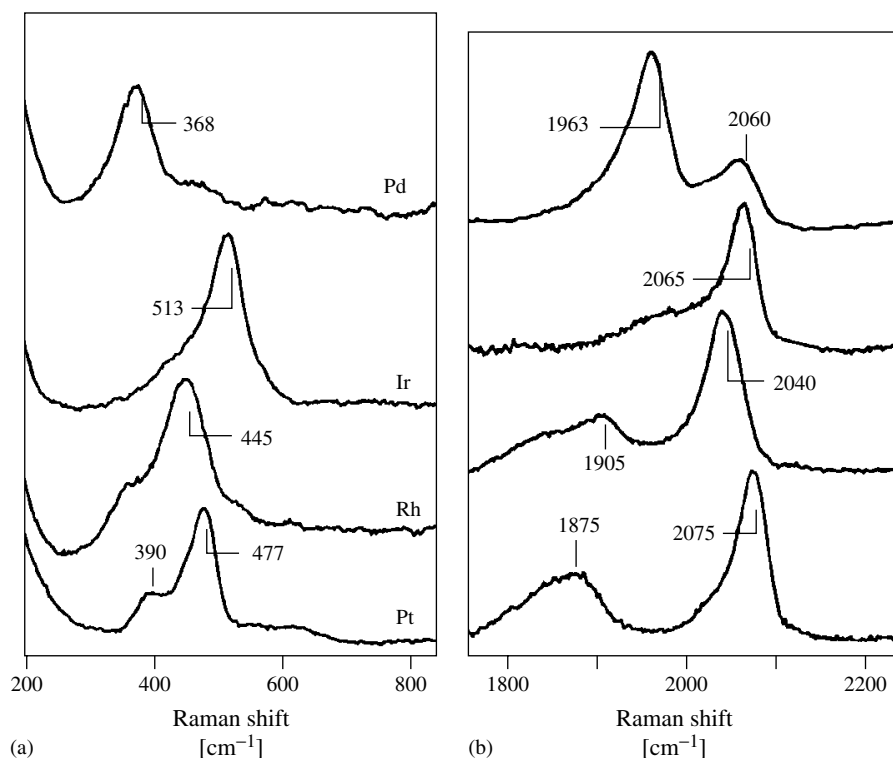


Fig. 35 SERS spectra of CO adlayers formed on various transition-metal overlayer films (thickness 3–5 ML) in 0.1 mol l⁻¹ HClO₄ with the metal–carbon and the C–O stretching bands in the low and high frequency region. Excitation line: 647.1 nm. (Reproduced with permission from Ref. [83]. Copyright 1998, American Chemical Society.)

technique is proposed, pyridine is usually chosen as the model molecule to check the validity and sensitivity of the method.

Orientation studies by SERS for pyridine at Ag electrodes show that both flat and vertical orientations are possible, depending on the electrode potential, see Fig. 36. The determination of the surface orientation is made by analyzing the molecule geometry and measuring the ratio of the band intensities for vibrational modes with a_2 and b_2 symmetry to those for modes with b_1 symmetry with the change of the excitation frequency at certain potential, see Fig. 36. The a_2/b_1 ratio will increase with decreasing excitation

frequency if the molecule is standing up, while keeps constant with lying down geometry. However, the b_2/b_1 ratio will keep constant with standing up geometry while increase with decreasing excitation frequency with the lying down geometry. The bands compared and assignments used were 388 cm⁻¹(a_2):414 cm⁻¹(b_1) and 1155 cm⁻¹(b_2):944 cm⁻¹(b_1). It was found that the former ratio was around 1 and the latter was about 1.60 when the potential was -0.6 V, which indicates that pyridine is flat on the rough surface at the potential, see Fig. 37(a). On the other hand, when the potential was moved to -0.9 V, the ratios changed. The former

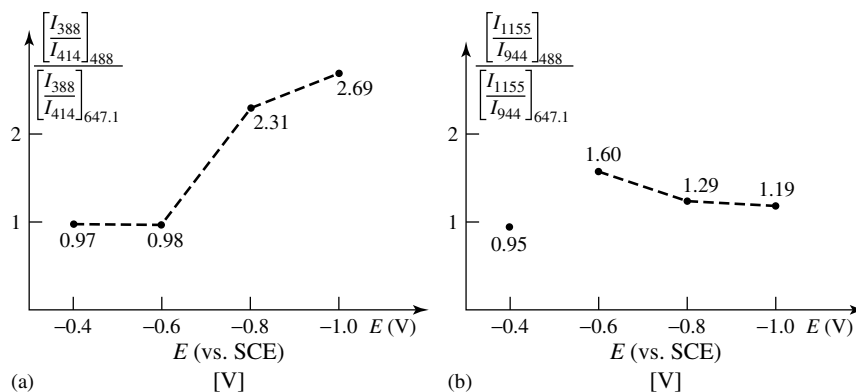


Fig. 36 Potential dependence of intensity ratios of pyridine on the silver surface: (a) a_2/b_1 intensity ratio; (b) b_2/b_1 intensity ratio. (Personal communication with R. L. Birke.)

was about 2.8 and the latter 1.3, indicating that pyridine adsorbs on the surface standing up. It should be noted that at -0.4 V versus SCE, both ratios are close to unity, showing that the preferred orientation is inclined to the surface and possibly rotated about the C_{2v} axis, see Fig. 37(b) [84].

Pyrazine adsorption on a Ni electrode It is well known that pyrazine has a centrosymmetric (D_{2h}), nonpolar structure that results in the separation of its Raman and infrared active modes due to the so-called “exclusion principle”. The modes assigned to the g -class are Raman active and the vibrational modes antisymmetrical to the inversion center (u -type) are Raman inactive. In the normal Raman spectrum of the aqueous solution (Fig. 38a), the fundamental vibrations of A_g symmetry at

1021 , 1237 , and 1591 cm^{-1} are attributed to the totally symmetric ring breathing (ν_1), the C–H in plane deformation (ν_{9a}) and the ring stretching (ν_{8a}) modes, respectively. The spectrum also exhibits 703 cm^{-1} (ν_4 , B_{2g}) and 1528 cm^{-1} (ν_{8b} , B_{3g}) peaks.

Although the spectrum is explicable within the exclusion principle, the situation changes dramatically upon the adsorption of pyrazine. Potential-dependent surface Raman spectra of pyrazine adsorbed at Ni electrodes [85] are shown in Fig. 38. The spectra were recorded from positive to negative potentials, starting at -0.6 V, where only one band is detected at 933 cm^{-1} , assigned to the totally symmetric stretching of the ClO_4^- anion from the solution. A weak surface signal from the adsorbed pyrazine was observed at -0.7 V, indicating the adsorption of

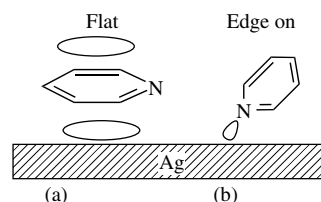


Fig. 37 Possible orientations of pyridine on a metal surface.

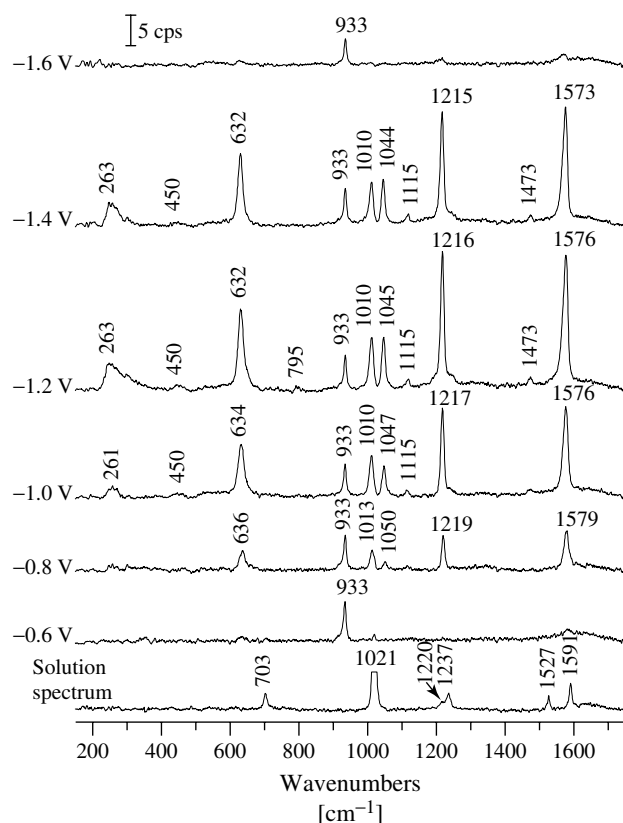


Fig. 38 The solution spectrum of 0.1 mol l^{-1} pyrazine and $0.1 \text{ mol l}^{-1} \text{ NaClO}_4$, and the SER spectra of pyrazine adsorbed on bare nickel electrodes at various potentials in solutions of 0.01 mol l^{-1} pyrazine and $0.1 \text{ mol l}^{-1} \text{ NaClO}_4$. Excitation line: 632.8 nm .

pyrazine at this potential. All the bands reach their maximum intensities at -1.1 V then disappear completely at -1.6 V . Besides the drastic change of the peak positions and the relative intensities for the peaks at 632 , 703 , 1021 , and 1591 cm^{-1} , respectively, upon adsorption, several new bands located at near 450 , 795 , 1045 , and 1473 cm^{-1} and assigned to Raman “forbidden” bands (u -class modes) appear in the surface spectra. These “abnormal” features can easily be understood once one accepts that owing to the gross interaction of

the Ni with the N atom of pyrazine (which is evident by the broad band at 263 cm^{-1}), the point group of the pyrazine will be lowered from D_{2h} to C_{2v} , by the removal of the inversion element. This changes the Raman-forbidden modes of the isolated molecule into Raman-active modes of the total system, because all modes are Raman active under C_{2v} symmetry. Thus, by analyzing the spectra, one is able to understand the adsorption behavior of pyrazine on the Ni electrode. This study clearly shows that Raman spectroscopy can have

more relaxed selection rules and that in some cases, Raman-inactive modes can be observed, which is helpful in determining the adsorption behavior.

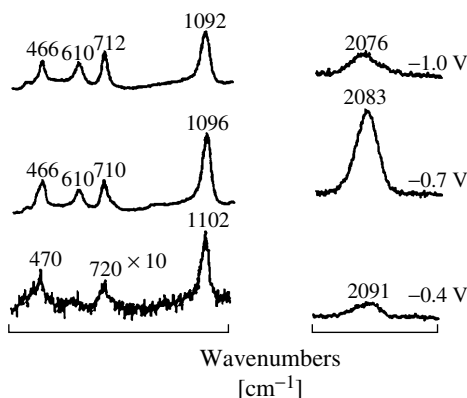
3.6.4.2.2 Coadsorption of Thiourea and Thiocyanide

Raman spectroscopy, not only identifies the orientation of a single species bonding to the electrode, but also reflects the interaction of the different adsorbed species at the electrode; the coadsorption behavior. By carefully analyzing the potential-dependent band features including frequency, intensity, width, and shapes, one can classify the electrochemical coadsorption into two types: parallel (competitive) and induced coadsorption. Furthermore, with precise control of the experimental conditions, one is able to see the transition of the type of coadsorption.

The coadsorption of SCN^- and thiourea at Ag electrodes [59] serves as an example, illustrating the transition. The SERS spectra are given in Fig. 39. Under relatively positive potentials, two coadsorbates interact strongly, not only to the Ag electrode surface but also to each other through the NH_3^+ group of thiourea and the nitrogen of SCN^- . This is reflected by

the intensity and frequency difference of the coadsorbed SCN^- from those of the free anion in electrolyte or the individually adsorbed anion. This is the behavior of parallel adsorption. At the negatively charged surface, because of the diminishing electronic CT from SCN^- ions to the Ag electrode surface, the adsorption of SCN^- ions is weakened. As a result, the desorption of SCN^- is preferred while thiourea can still interact with the surface strongly through its sulfur atom. Finally, the desorption of SCN^- ions is preferential as the potential reaches a critical value, in the absence of thiourea. However, as the strongly adsorbed thiourea can still remain at the negatively charged Ag electrode surface and interact strongly with SCN^- , it can induce SCN^- to be coadsorbed at the electrode surface, mainly because of a strong mutual interaction through the NH_3^+ group of thiourea and the nitrogen atom of SCN^- . Now, the coadsorption of SCN^- and thiourea at the Ag electrode changes from parallel coadsorption to induced coadsorption. The results illustrate that complicated potential-dependent coadsorption phenomena can be understood at the molecular level by analyzing SERS spectra.

Fig. 39 SERS spectra of CN stretching vibration band of SCN^- coadsorbed with TU on an Ag electrode in solutions of $0.1 \text{ mol l}^{-1} \text{ NaSCN}$, $0.1 \text{ mol l}^{-1} \text{ TU}$, and $0.01 \text{ mol l}^{-1} \text{ HClO}_4$ at various potentials. Excitation line: 514.5 nm.



3.6.4.3 Surface Water

3.6.4.3.1 Water Adsorption in Aqueous Systems

Water within the electrochemical “double layer” near a metal electrode differs significantly from bulk water. A detailed molecular-level description of the structure and dynamics of these water molecules is of fundamental importance for understanding electron transfer, electrocatalysis, and corrosion. However, there is no consensus on the detailed structure and behavior. In the classical model of the electrochemical interface, water molecules at the surface are thought to be oriented by solvent dipole-electric field interactions (see Volume 1). Thus, water molecules reorient as the applied potential passes through the potential of zero charge (pzc). At potentials positive of the pzc, the water dipoles are oriented towards the metal surface. At potentials negative of the pzc, the water dipoles flip and are oriented away from the surface. Thus, the interaction between the water molecules and the surface is through the oxygen atom at potentials more positive than the pzc and through the hydrogen atoms at potentials more negative than the pzc [86].

Experimental observation is more complex than what is expected from the classical model. Fig. 40 gives a typical SERS spectrum of water on Cu, which is dramatically different from the normal spectrum of bulk water. In bulk water, the peak intensity of the bending mode is about twenty times lower than that of the stretching mode, while the vibrational band is extremely weak and hardly detectable. However, on the surface, the intensities of the bending mode and the vibration mode are abnormally enhanced. This phenomenon can only be observed at potentials negative of -1.00 V. More interestingly, the SERS intensity has been found to be critically dependent on the current density of the hydrogen evolution reaction, rather than the applied potential. It is thus possible that the abnormal SERS feature of water is related to hydrogen evolution. It is well known that hydrogen evolution can occur in two ways: the discharge of protonated water in a more acidic solution and the dissociation of the water molecule in neutral and basic solutions. By changing the solution pH, it was found that the former does not contribute to the SERS of water, although the hydrogen evolution reaction is quite vigorous. So it is

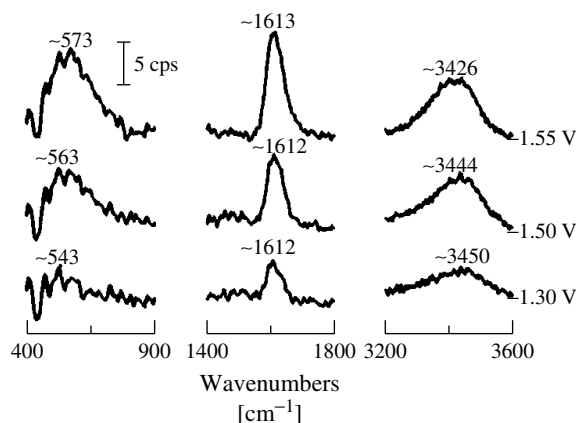


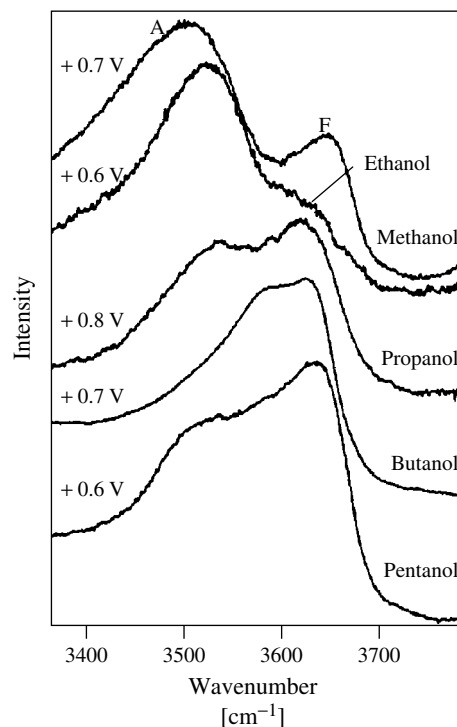
Fig. 40 SERS of water from a Cu electrode in a solution of $1.0 \text{ mol l}^{-1} \text{ Na}_2\text{SO}_4$. Excitation line: 632.8 nm .

Fig. 41 SERS spectra from Ag electrodes in the $\nu(\text{O-H})$ region for methanol, ethanol, propanol, butanol, and pentanol containing a 0.4 mol l^{-1} LiBr solution at positive potentials. Excitation line: 514.5 nm. (Reproduced with permission from Ref. [87].)

possible that it is the dissociation of water, which makes the major contribution. The relatively ordered interfacial structure of water molecules, favorable for deprotonation and H^+ transfer, is attributed to the observation of the strong intensity of the vibration and bending modes. The correlation of SERS intensity and hydrogen evolution current density, strongly suggests that the CT involved in the water dissociation reaction contributes significantly to the enhancement of the Raman scattering. It also reveals that the structure of the interfacial water is more complicated than expected, especially when undergoing surface reaction processes.

3.6.4.3.2 Water Adsorption in Nonaqueous Systems In nonaqueous systems [87], the amount of water is very limited, coming from trace water that remains after purification of these solvents or from water intentionally added to the solvent. The extensive hydrogen bonding of bulk water is broken, resulting in $\nu_{\text{O-H}}$ bands of greater resolution than observed in aqueous media. Fig. 41 gives selected SERS spectra of water in different solvents using LiBr as the electrolyte.

The spectra were obtained at the most positive potential achievable in which the 3500 cm^{-1} bands are at their maximum intensity. The bands at around 3650 cm^{-1} arise from the free interfacial water. The frequency of this band decreases with an increase of the alcohol chain length in the solvent, since the alcohols solvate



specifically adsorbed Br^- less, promoting greater hydrogen bonding between the free water and Br^- , leading to a systematic decrease in the frequency for free water species.

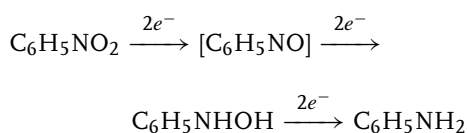
The 3500 cm^{-1} band is thought to be from the adsorbed water molecules, through the oxygen atoms directly contacting the positively charged surface. The hydrogen atoms of the water are engaged in lateral hydrogen bonding with specifically adsorbed Br^- . The peak frequency at a given potential increases with chain length in going from methanol to butanol. This is because of the ion pairing of the specifically adsorbed Br^- with Li^+ , which decreases the hydrogen bonding of the adsorbed water with the specifically adsorbed Br^- . However, the hydrogen bonding between the adsorbed water and solvent decreases with increasing chain length,

promoting the interaction between water and Br^- . The reversal in peak frequency between butanol and pentanol is because of the former effect becoming less important and the latter effect dominating. These studies demonstrate the high interfacial sensitivity of Raman spectroscopy. The ease of obtaining a surface Raman signal of adsorbed water shows the advantage of Raman spectroscopy over other vibrational spectroscopies in investigating electrochemical interfacial structures.

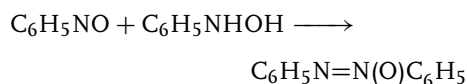
3.6.4.4 Surface Reactions

SERS can detect not only adsorption/desorption behavior, but also redox processes of surface species [88] since the method can provide direct identification of adsorbed intermediates and/or products formed in multistep processes. Thus, when combined with conventional electrochemical measurements, Raman spectroscopy can identify the intermediates and evaluate the reaction pathways of electrochemical reactions.

With the intense SERS signal provided by an Au substrate and a fast optical multichannel analyzer (such as, PDA or CCD), it is possible to obtain SERS of a surface reaction during the potential ramp, which is extremely important when irreversible processes occur. A good example is the combined SERS and cyclic voltammetric study of nitrobenzene surface reaction on a SERS-active Au surface. It is known that nitrobenzene can be reduced by three two-electron steps to form nitrosobenzene, phenylhydroxylamine and aniline:



Nitrosobenzene was not detected by analytical methods, and it is possible that it is consumed by a chemical coupling reaction following the electrochemical reaction:



From the cyclic voltammograms of nitrobenzene in sulfuric acid solution in Fig. 42(a), one can find a pair of peaks at -0.11 and -0.27 V of the reduction of nitrobenzene. The anodic peak at 0.33 V has been assigned to the formation of nitrosobenzene, and the cathodic peak at 0.30 V is from the reduction of nitrosobenzene to phenylhydroxylamine. The 30 mV separation, independent of the scan rate, indicates that the above pair of reactions represent a reversible process. The SERS spectra were acquired during the potential sweep for the reduction of nitrobenzene at a gold electrode, see Fig. 42(b). It can be seen during the positive movement of the electrode potential, the band at 1330 cm^{-1} , corresponding to nitrobenzene, decreases. Meanwhile, new bands located at 1146 , 1388 , and 1588 cm^{-1} , respectively, appear when the potential is negative of -0.11 V. Compared with the normal Raman and SERS spectra of possible reaction products, these new peaks are essentially the feature of nitrosobenzene. Correlating the voltammetric and SERS results, the peak at -0.11 V in the CV can be assigned to the reduction of nitrobenzene to nitrosobenzene. This study provides a good example of the combination of electrochemical methods and SERS to investigate the pathways and intermediates of electrochemical reactions.

3.6.4.5 Surface Adlayers

The main purpose of surface Raman spectroscopy, applied to chemically modified

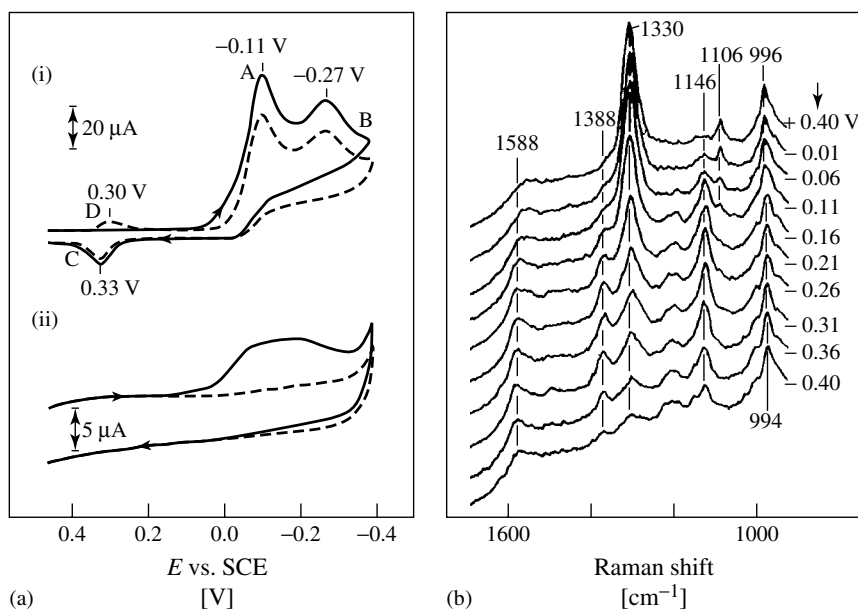


Fig. 42 (a) Cathodic-anodic cyclic voltammogram (i) at 100 mV s⁻¹ for 1 mM nitrobenzene in 0.1 mol l⁻¹ H₂SO₄ at a 0.125 cm² area gold electrode. Solid and dashed traces refer to the first and second consecutive cycles, respectively. Cyclic voltammogram (ii) for irreversibly adsorbed nitrobenzene in 0.1 mol l⁻¹ H₂SO₄. (b) Sequence of surface-enhanced Raman spectra obtained during linear sweep voltammetric reduction of nitrobenzene at a gold electrode. The potential sweep rate was 5 mV s⁻¹, negative-going from 0.4 V vs. SCE. The solution was 3 × 10⁻³ mol l⁻¹ nitrobenzene in 0.1 mol l⁻¹ H₂SO₄. Potentials indicated beside each spectrum are average values during the 5-s detector integration time. Excitation line: 647.1 nm. (Reproduced with permission from Ref. [88]. Copyright 1988, American Chemical Society.)

electrodes, is to utilize the unique SERS effect with dramatically high sensitivity and molecular (or even chemical bond) selectivity, as a powerful analytical tool. Here, biological membrane-modified electrodes are used as an example. Applications on this aspect are classified into two major classes: SERS and surface-enhanced resonance Raman spectroscopic (SERRS) studies [74]. In the first group, deoxyribonucleic acid and constituents, protein and constituents, lipid and related materials as well as some small molecules, such as citric acids, aromatic carboxylic acids, and nicotinamide adenine dinucleotide

(NAD), which are adsorbed or form adlayers at the surface, have been extensively studied. Information concerning both the structure of the molecule itself, the orientation of molecules on the surface and the potential-dependent behavior has been provided. In the second group, molecules such as heme proteins and protoporphyrin IX, photosynthetic membranes and components, porphyrins, flavoenzymes and flavin derivatives, are used. The enhancement factor for these molecules on SERS substrates can reach up to 10⁹. Thus, the detection limit for these molecules can be nanomolar to picomolar, and this also

provides a considerable increase in sensitivity for SERRS over SERS.

The adsorption of NAD^+ on a gold electrode served as an example of the application of Raman spectroscopy to biological molecules [89]. The SERS spectra, varying with the electrode potential, as well as the normal solution Raman spectra are given in Fig. 43(a). The 745 and 1335 cm^{-1} bands are from adenine, 1035 cm^{-1} is the characteristic band from the pyridine ring of nicotinamide. With the electrode potential changing negatively, several significant changes can be observed: at potentials negative of -0.25 V, the signal at about 1335 cm^{-1} becomes weaker, while that at 1035 cm^{-1} is enhanced. The adenine band shifts suddenly from 735 cm^{-1} to 745 cm^{-1} when the potential moves across -0.25 V. Thus it is reasonable to assume, as depicted in Fig. 43(b), that at potentials positive of -0.25 V, the adenine moiety of NAD^+ adsorbs through the N_1

atom and the amino group, where as the pyrimidine right of the adenine moiety is in direct contact with the electrode (reflected by the significant increase of the adenine band frequency from 735 cm^{-1} to 745 cm^{-1}). This configuration results in a closer distance of the nicotinamide moiety to the electrode surface in a vertical conformation, giving a clear band at 1035 cm^{-1} . At potentials negative of -0.25 V, the increase in the intensity of the 1335 cm^{-1} band, because of the vibration of $\text{N}_7\text{--C}_5$ atoms, indicates that the orientation changes from the $\text{N}_1\text{--N}_7$ to the adsorption of N_7 atom, with the $\text{N}_7\text{--C}_5$ bond normal to the electrode surface. This change, in turn, increases the distance of the nicotinamide to the surface, resulting in a decrease of the intensity of the 1335 cm^{-1} band. However, at potentials negative of -1.0 V, the SERS signal disappears as a result of the desorption of the NAD^+ from the Au

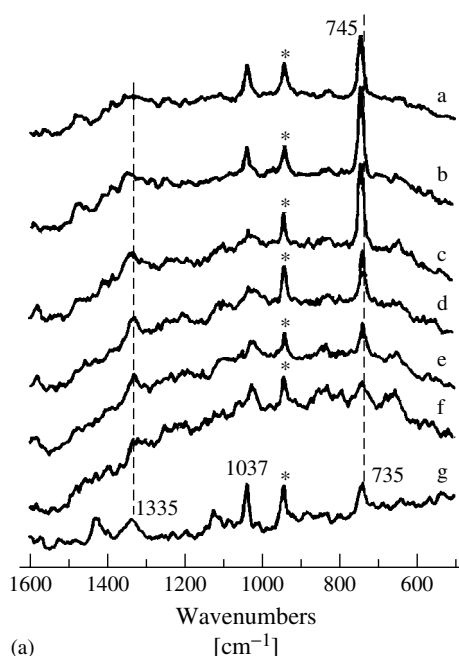


Fig. 43 SERS spectra of a gold electrode in the presence of $2 \times 10^{-3} \text{ mol l}^{-1} \text{ NAD}^+$ in a phosphate buffer solution with $0.1 \text{ mol l}^{-1} \text{ NaClO}_4$ ($\text{pH} = 7$) at (a) 0.25; (b) 0; (c) -0.25 ; (d) -0.5 ; (e) -0.75 ; and (f) -1.0 V vs SCE, together with the Raman spectrum of $100 \times 10^{-3} \text{ mol l}^{-1} \text{ NAD}^+$ in the solution. The signal labeled with an asterisk is from $0.1 \text{ mol l}^{-1} \text{ ClO}_4^-$ in the solution. (b) The molecular structure and the proposed model of NAD^+ adsorption at an Au surface at various potentials. (Reproduced with permission from Ref. [89]. Copyright 1986, Elsevier Sequoia S.A., Lausanne.)

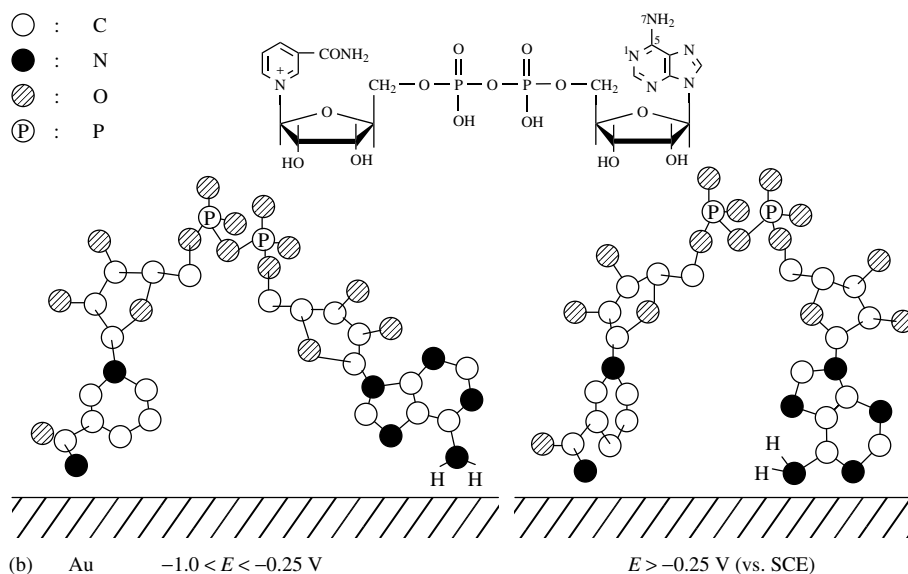


Fig. 43 (Continued)

surface, which is supported by reflectivity measurements.

3.6.4.6 Batteries and Fuel Cells

3.6.4.6.1 Lithium Ion Batteries With the rapid development of Raman instrumentation, it is feasible to investigate the structure of electrode materials that have no SERS activity. For the lithium ion battery, it is possible to provide information about changes of the anode and cathode material, the solution composition and products during cycling. As a consequence, the in situ Raman investigation of reactions and dynamics during the charge and discharge process has boomed in recent years. Since the lithium ion battery uses nonaqueous solvent, it needs a cell that is water tight and air tight. The electrochemical and spectroscopic investigation of Li^+ batteries has mainly concentrated on the insertion/extraction processes of Li^+ in the cathode and anode

of the batteries. The following examples consider this aspect further.

The insertion mechanism of the lithium ion into various kinds of carbons, when used as an anode in Li ion batteries has been extensively studied both experimentally and theoretically. However, the electrochemical insertion process is not yet fully understood. Polyparaphenylene (PPP)-based disordered carbon has a superior lithium storage capacity when used as an anode in the Li ion battery, and thus attracts much attention. In order to investigate the insertion mechanism of lithium into this material, the uptake and release processes of lithium were monitored by in situ Raman spectroscopy [90]. It was found that the band intensities of the characteristic peaks of disordered carbon decrease upon the discharging process and increase with the charging process, with quite good reversibility. Moreover, the frequency of the band related to the intraring C–C stretching mode of PPP at 1605 cm^{-1} also

changes with the voltage. The frequency is plotted versus electrode voltage and shown in Fig. 44. It can be seen that there is slight irreversibility of the peak position change of the band during the charging process, which may reflect directly the irreversible discharge/charge capacity of the electrode. Li insertion in PPP was identified from the in situ Raman spectrum as a change in band shape and in the band position. Li^+ is taken up at a preferred binding site in PPP and this occurs in the high voltage range $2.8 \text{ V} - 1.0 \text{ V}$ as denoted by Zone I, while Li^+ doping and undoping in PPP, which is accompanied by a shift of the peak position, occurs in the lower voltage range $1-0.04 \text{ V}$, as denoted by Zone II. The behavior in Zone II has some similarity to the staging phase transition associated with the charge-transfer effect that is observed in graphite intercalation compounds, and

provides evidence for CT even in PPP-based disordered carbons. The intensity changes of the Raman bands, observed in PPP, are correlated with the electrical conductivity associated with lithium insertion and release. The large Li storage capacity of the PPP electrode could be largely due to the formation of very small flat pregraphitic clusters coexisting with polymer-like quinoid-like segments. This is a persuasive example that in situ Raman spectroscopy is a very powerful tool for analyzing Li insertion into PPP disordered carbon [90].

Spinel-type magnesium oxide with its low cost, relatively low toxicity, and abundance has become a very promising cathode material for the lithium ion battery. However, the capacity and stability of magnesium oxide have to be improved. Thus, it is most important to study the

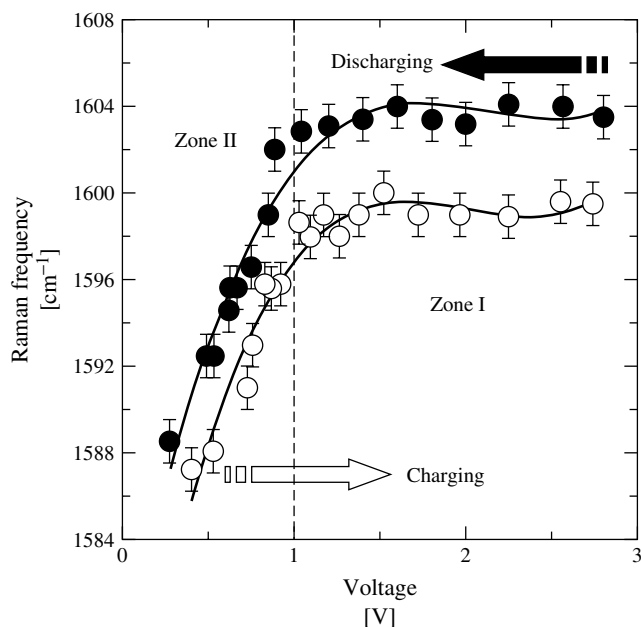
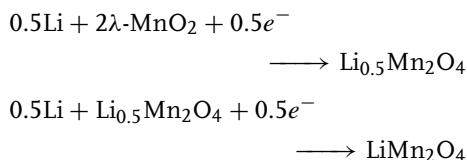


Fig. 44 The voltage dependence for the high frequency Raman modes of a PPP-700 electrode obtained by fits to a Lorentzian line shape. (Ref. [90].)

structure of the material at the molecular level. Upon the cathodic insertion of Li into the oxide bulk, two steps occur:



These are topotactic reactions, and $\text{Li}_x\text{Mn}_2\text{O}_4$ ($0 \leq x \leq 1$) spinels possess MnO_6 units, irrespective of x . It is documented that the insertion of Li into the lattice will change the lattice constant. In situ Raman measurements of Li^+ electroinsertion into a Pt/ $\lambda\text{-MnO}_2$ electrode in an aqueous solution showed spectra with a broad band at about 600 cm^{-1} , containing two components, 593 and 628 cm^{-1} that are characteristics in the spectra of $\lambda\text{-MnO}_2$ and LiMn_2O_4 [91]. Although the Raman intensity of $\lambda\text{-MnO}_2$ is generally much greater

than that of LiMn_2O_4 , the logarithm of the ratio of the intensity at 593 cm^{-1} to that at 628 cm^{-1} , $\log(I_{593}/I_{628})$ has been found to be a good measure of the change of the lithium content, x , in $\text{Li}_x\text{Mn}_2\text{O}_4$. Thus, when $\log(I_{593}/I_{628})$ is plotted with the potential, the curve correlates well with two pairs of cathodic and anodic peaks in the cyclic voltammogram, see Fig. 45.

3.6.4.6.2 Methanol Fuel Cells The electrooxidation and dissociation of small organic molecules such as methanol on Pt-based electrodes is one of the most extensively studied systems in terms of both fundamental and applied research in surface (interfacial) electrochemistry (see also Chapter 3.5). It involves a very complex reaction occurring in many steps and various kinds of surface (interfacial) species, including reactants, intermediates, poisons, supporting electrolytes and even solvent

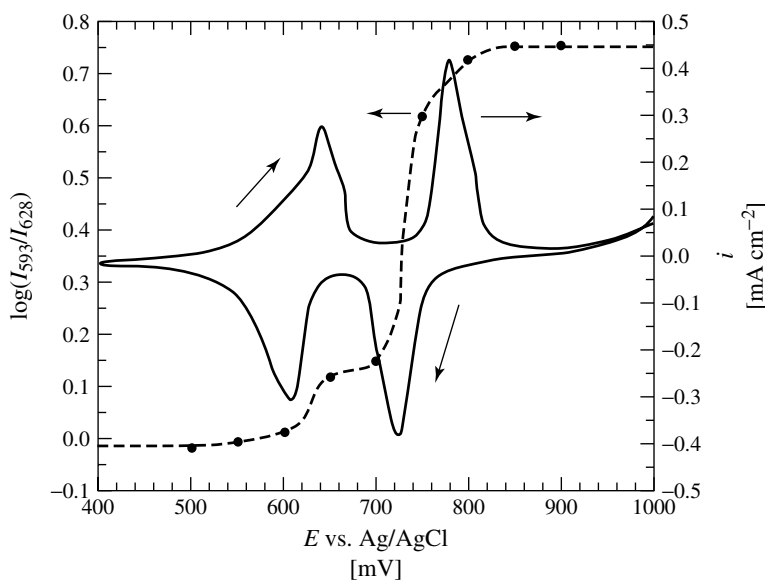


Fig. 45 A plot of $\log(I_{593}/I_{628})$ vs. E (--- • ---) and cyclic voltammogram (---) of a Pt/ $\text{Li}_x\text{Mn}_2\text{O}_4$ electrode in a 0.1 M LiCl and 0.05 M borate buffer solution (pH 7.5). (Reproduced with permission from Ref. [91].)

molecules. Although great efforts have been made, an understanding of the mechanism of methanol electrooxidation at the molecular level remains elusive. Some important issues, such as the reaction path, the nature of the surface oxidant and intermediates, the influence of the surface morphology, the surface roughness, and the effect of foreign metals on the reaction process, are still controversial issues. With the above-mentioned development of Raman spectroscopy, the investigation of real catalysts and electrodes of high surface roughness, for practical application, becomes possible [92]. Furthermore, with the correct design of the electrochemical setup, it is possible to study systems under rigorous reaction conditions.

Fig. 46 shows surface Raman spectra obtained from a rough Pt electrode in contact with solutions containing various small organic molecules. The Raman spectra show very characteristic bands located at about 400 to 430, 480 to 520, 1750 to 1810, 1990 to 2070 cm^{-1} , which are for ν_{CO} and $\nu_{\text{Pt-CO}}$ vibrations. They

are from the adsorbed CO produced during the dissociative adsorption of small organic molecules on the platinum surface. With the consideration that the CO frequency blue shifts with the positive movement of the electrode potential before the oxidation of CO, it is very difficult to interpret the difference in frequency only by the potential effect. At least two more effects influence the frequency of the adsorbed CO: first, the coverage effect. If the CO is adsorbed by immersing the electrode in CO saturated solution, it is possible to form a saturated monolayer (fractional surface coverage, $\theta \approx 0.67$). As a result, the interaction (dipole–dipole coupling) among the neighboring CO molecules could be strong, which leads to the blue shift of the vibrational frequency of CO. However, for those CO adsorbed by dissociation, more than one Pt atom is needed for dissociation. Thus, the coverage will be lower than the above value, weakening the dipole–dipole coupling of the neighboring CO, resulting in a lower frequency. The second possible effect

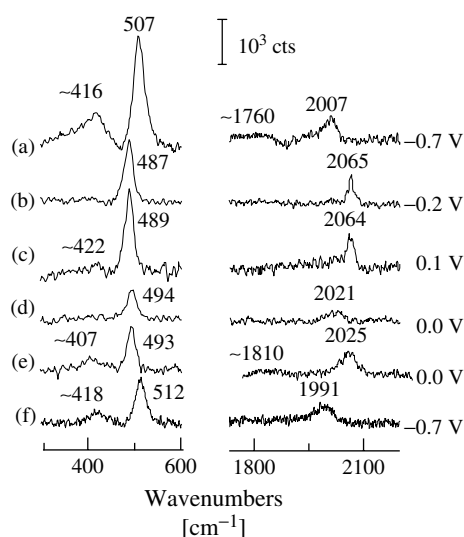


Fig. 46 SERS spectra of the adsorption and dissociative adsorption of CO and various organic molecules on platinum surfaces. Solution: (a) CO saturated 0.1 mol l^{-1} NaOH; (b) CO saturated 0.1 mol l^{-1} H_2SO_4 ; (c) 0.5 mol l^{-1} HCOOH and 0.1 mol l^{-1} NaOH; (d) 0.1 mol l^{-1} $\text{CH}_3\text{CH}_2\text{CH}_2\text{OH}$ and 0.1 mol l^{-1} H_2SO_4 ; (e) 0.1 mol l^{-1} CH_3OH and 0.1 mol l^{-1} H_2SO_4 ; and (f) 0.1 mol l^{-1} CH_3OH and 0.1 mol l^{-1} NaOH.

comes from coadsorbed species, which may change the electronic negativity of the electrode surface and further change interaction between CO and the electrode surface, resulting in a change of the frequency of the adsorbed CO.

Electrochemical Raman spectroscopy can provide information on the adsorbed species both under static conditions, and also in rigorous reaction situations. Fig. 47 gives the dependence of the steady state current and the band intensity of $\text{C}\equiv\text{O}$ stretching vibration of linearly adsorbed CO on the electrode potential in 1.0 M CH_3OH and 1.0 M H_2SO_4 . The oxidation current of methanol was found to increase rapidly, with the oxidation of CO at around 0.3 V, and reached its maximum at around 0.5 V, while the band intensity of CO still remained 30% of the maximum at the peak current potential. Thus the severe oxidation of methanol oxidation can still occur in the presence of CO on the rough surface.

Another study is the investigation of the electrooxidation of formic acid on Rh [93]. A substantial amount of CO was observed on the Rh surface at potentials below and close to the onset of formic acid electrooxidation. However, the frequency was lower by 50 cm^{-1} than that of CO adsorbed from CO saturated solutions, and the oxidation potential is negative by 0.3 V than the latter. This great difference was attributed to the different surface coverage and the more ready availability of adjacent adsorption sites. In order to understand the mechanism, isotopic ($^{12}\text{C}/^{13}\text{C}$) experiments were carried out. At electrode potentials for the onset of formic acid electrooxidation, only slow $^{13}\text{CO}/^{12}\text{CO}$ isotopic exchange was observed. The kinetics were markedly slower than those observed when using solution CO rather than formic acid. Altering the potential beyond the onset of formic acid electrooxidation yielded relatively rapid, albeit incomplete, isotopic exchange. The

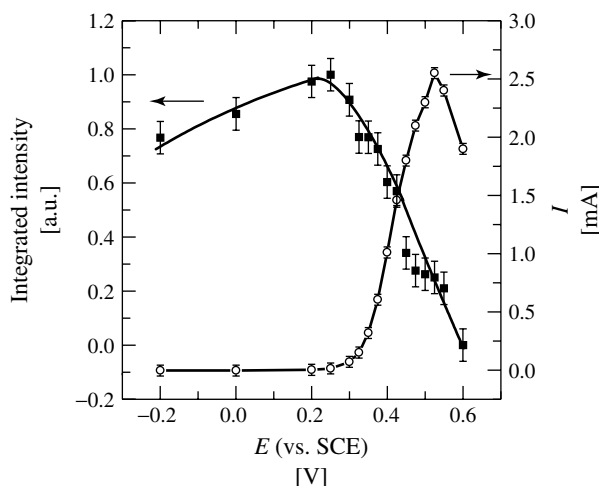


Fig. 47 Dependence of static state current (I) and the integrated intensity of the Raman band on the electrode potential in $1.0\text{ mol l}^{-1}\text{ CH}_3\text{OH}$ and $1.0\text{ mol l}^{-1}\text{ H}_2\text{SO}_4$ during the electrooxidation of methanol on a rough platinum surface (roughness factor 200).

sharply potential-dependent emergence of electrocatalytic oxidation currents correlated well with the onset of $^{13}\text{CO}/^{12}\text{CO}$ exchange, and by calculating the “turn-over frequency” of formic acid to CO_2 , by the way of CO, the adsorbed CO was proposed to act as a reaction intermediate, especially under facile reaction conditions.

3.6.4.7 Corrosion

3.6.4.7.1 Passive Films The reaction of oxide-covered metal surfaces with the environment is the initial process of corrosion (see Volume 4). The most systematic work has been carried out by Melendres [78, 79], who developed laser Raman spectroscopy for investigating

processes occurring during corrosion and at high temperature and pressure. The systems investigated involved anodic corrosion and passive film formation on various noble and transition-metal surfaces, including Ag, Cu, Pd, Fe, Ni, Cr, Al, and alloys.

Interesting Raman studies of the corrosion process, have utilized Ag or Au overlayers or sublayers to investigate the passive film [94]. It was found that the SERS of the passive film on iron has two characteristic, high intensity peaks at approximately 550 and 670 cm^{-1} . SERS spectra were acquired during reduction of preformed passive films at different potentials, see Fig. 48. In order to obtain an observable signal, Au particles were deposited onto the surface to produce a surface-enhanced

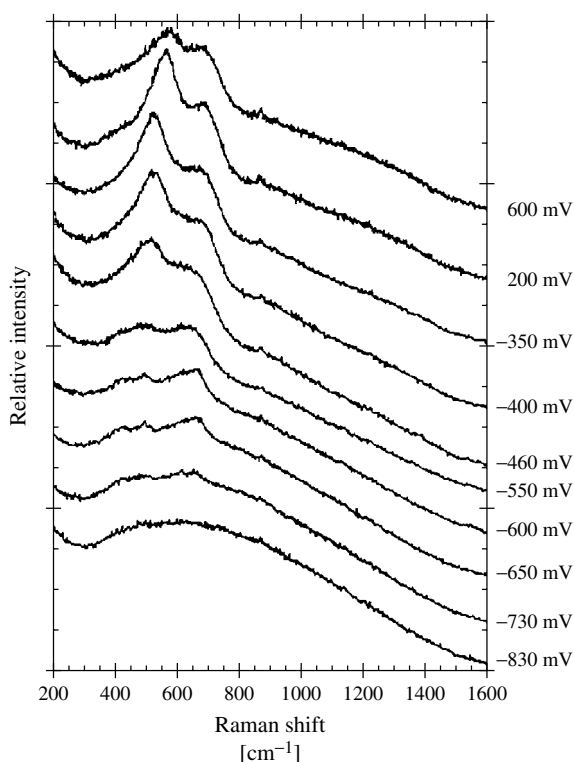


Fig. 48 SERS spectra of iron/Au acquired during galvanostatic cathodic polarization ($10\text{ }\mu\text{A}/\text{cm}^2$), which followed potentiostatic polarization at $+600\text{ mV}$ for 1 min. (Reproduced with permission from Ref. [94]. Copyright 1999, The Electrochemical Society.)

signal. The deposited Au did not influence the behavior of the substrate studied. The band, at around 550 cm^{-1} , was assigned to ferric oxide or hydroxide, while the band at 680 cm^{-1} was assigned to Fe_3O_4 or defective $\gamma\text{-Fe}_2\text{O}_3$. Since the band at around 550 cm^{-1} decreased at more positive potentials and the 680 cm^{-1} band existed at more negative potentials, it was proposed that the film consisted of at least two, and possibly three, components arranged in a quasi-layered structure. The inner layer resembled Fe_3O_4 or $\gamma\text{-Fe}_2\text{O}_3$ defected with Fe^{2+} . The outer layer was a mixture of a small amount of a phase that resembled Fe_3O_4 or $\gamma\text{-Fe}_2\text{O}_3$ and an unknown ferric oxide, hydroxide or oxyhydroxide.

Raman microscopy makes possible the investigation of the corrosion process on pure transition-metal surfaces [95]. The corroding pits in aluminum alloy used

for aerospace applications serves as an example. Raman spectra were acquired across the light area and dark area of the video micrograph, as shown in Fig. 49. The main band measured is at 847 cm^{-1} from adsorbed CrO_4^{2-} , which greatly reduces the corrosion of the alloy. The inhibition effect results from Cr(VI) that could cause migration or diffusion into corrosion pits, where it adsorbs to $\text{Al}(\text{OH})_x$ to form a surface mixed oxide product.

3.6.4.7.2 Corrosion Inhibitors The corrosion process and the mechanism of inhibitors is an important research direction for electrochemistry. Raman spectroscopy is advantageous in the investigation of adsorption-mediated corrosion inhibition, because it is readily applicable to the in situ observation of the behavior of inhibitors

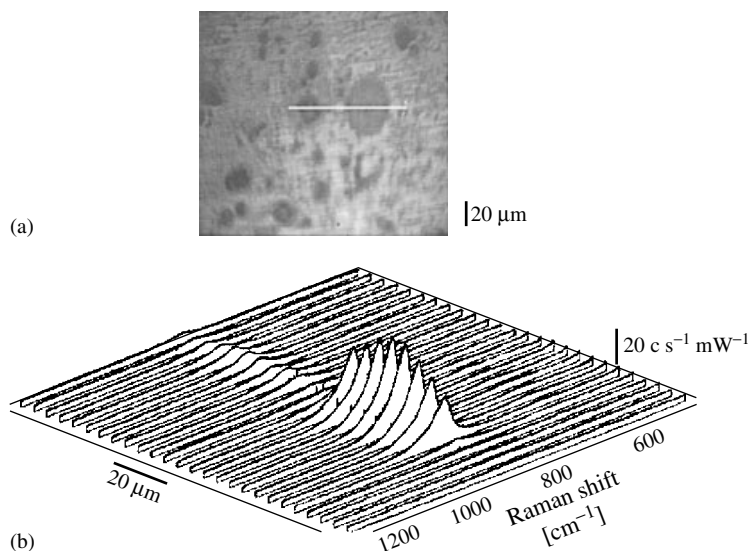


Fig. 49 (a) Video micrograph of a AA 2024-T3 surface after 24h of exposure to $1.6 \times 10^{-3}\text{ mol l}^{-1}$ Cr(VI) solution, bulk pH 4.7. (b) 26 Raman spectra obtained at equally spaced intervals along the line in the micrograph, which crosses both a dark and a light pit. Z-axis is Raman intensity; intensity spikes are due to random interference from background hard radiation. (Reproduced with permission from Ref. [95]. Copyright 1999, The Electrochemical Society.)

on metal surfaces in corrosive media, and readily provides bonding information of the inhibitor with the substrate. It is able to identify the anticorrosion effect of coatings on different substrates, and study and compare the effect of corrosion inhibitors. In the study of the inhibition effect of inhibitors, the most widely studied SERS system is benzotriazole (BTAH) and its derivatives at the copper surface. Combined with the electrochemical investigation, it was found that BTAH can occur in various forms on the electrode surface: the deprotonated form 1H-benzotriazole (BTA^-), neutral form (BTAH) and protonated form (BTAH_2^+) in

solutions of different pH, Fig. 50(a), which is supported by the broadening of the peak at around 1380 cm^{-1} and the decrease and increase of the peak at 1190 cm^{-1} and at 1140 and 1125 cm^{-1} [96]. The assignment of the complex Raman bands was made with the help of a deuterium substituted BTA molecule. The adsorption geometry was obtained by examining the adsorption-induced alterations in frequency, bandwidth, and relative intensity of various BTA ring modes. BTAH and BTA^- are thought to bind to the surface with a tilted (or vertical) orientation via a pair of triazole nitrogens, which is reflected by the change of the SERS band

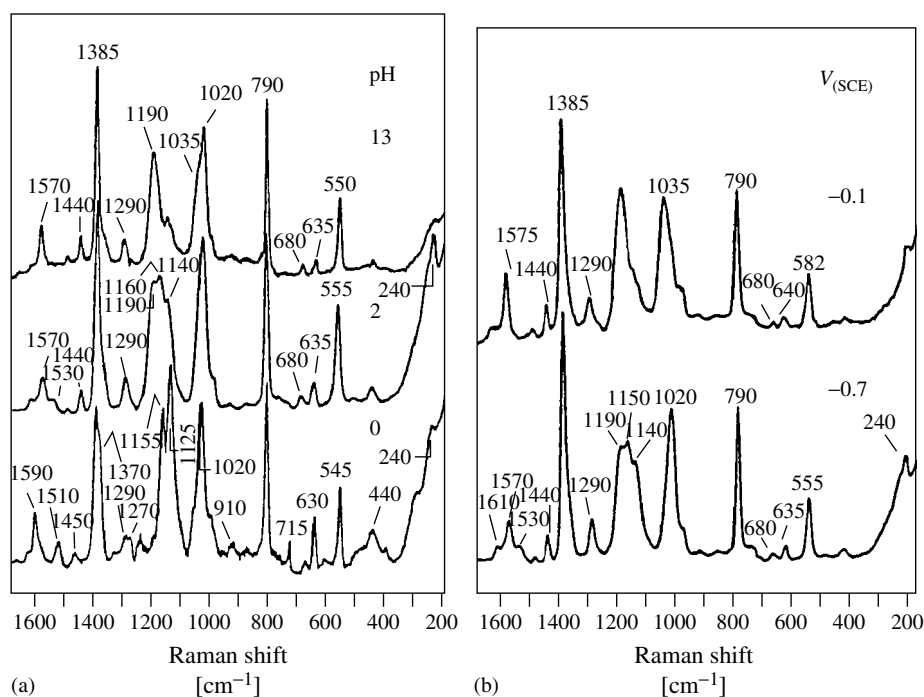


Fig. 50 (a) SERS spectra obtained on copper in electrolytes with indicated pH. Key: pH ca. $0.2\text{ mol l}^{-1}\text{ H}_2\text{SO}_4$; pH 2, $0.1\text{ mol l}^{-1}\text{ Na}_2\text{SO}_4$ and $0.01\text{ mol l}^{-1}\text{ H}_2\text{SO}_4$; pH 13, $0.1\text{ mol l}^{-1}\text{ NaOH}$; each containing $0.01\text{ mol l}^{-1}\text{ BTAH}$. Electrode potentials were -0.7 V for pH 0

and 2 and -1.0 V for pH 13. (b) Comparison of SERS spectra on copper at -0.7 and -0.1 V , as indicated, in $0.01\text{ mol l}^{-1}\text{ BTAH}$, $0.1\text{ mol l}^{-1}\text{ Na}_2\text{SO}_4$ and $5 \times 10^{-3}\text{ mol l}^{-1}\text{ H}_2\text{SO}_4$ (pH 2). (Reproduced with permission from Ref. [96]. Copyright 1999, The Electrochemical Society.)

at ~ 550 , 630 and 1020 cm^{-1} , related to the triazole ring. However, BTAH_2^+ is adsorbed via a single nitrogen, which agrees with the unchanged SERS feature compared to the bulk phase signal. Fig. 50(b) reveals that at the relatively positive potential, -0.1 V , the SERS data presents the features of Cu(I)BTA complex, which has a kind of polymeric structure. The polymeric film is assumed to be the reason for the good inhibition effect of BTAH on the anodic dissolution of Cu. An accompanying effect of the film is to further prevent hydrogen evolution on the copper surface, which in turn reduces the break down of the inhibiting layer. Investigation of the inhibition effect of various inhibitors, such as thiourea (TU) and BTA on pure Fe, Ni, and Co surfaces, has also been carried out. Reasonably good signals were obtained with the help of proper surface pretreatment procedures. It was found that the inhibition process of BTAH involves the formation of surface complexes and a compact polymer film in two different potential regions. On the other hand, thiourea formed an adsorbed layer. The difference in the adsorption of the two species on the Fe surface accounts for the different inhibition efficiency [97].

3.6.4.8 Electrodeposition and Surface Processing

3.6.4.8.1 Electrodeposition In order to obtain a compact and bright deposited layer, additives are usually added in electroplating solutions, which can also increase or decrease the stress in the deposited layer and the embrittlement of the layer [80]. The effect of the additives in the electroplating process is directly related to their adsorption behavior on the surface [98]. For example, the electrochemical

and SERS study of TU adsorption on an Ag surface showed that TU adsorption takes place over the whole potential region and that crystal growth takes place through this strongly adsorbed layer, which is probably the cause of the formation of smooth deposits. On the other hand, silver deposition from Ag(CN)_2^- , takes place by the removal of the central atom of the coordinated complex. To unravel the mechanism, SERS spectra were obtained during the deposition process, Fig. 51. The SERS signal develops with time, reflecting the growth of the crystalline structure of the silver layer on the metal surface. By considering the same trends in the increase in the double-layer capacity and the Raman intensity, the change in the SERS intensity could be explained by an attribute in the real area of the surface.

3.6.4.8.2 Semiconductor Processing Raman spectroscopy can be used to obtain information during semiconductor surface processing. Taking silicon, the most important material in the semiconductor industry, for example, the surface-bonding configuration of a silicon surface critically affects the properties of the material in the surface etching process. There are several possible configurations for the surface in an HF solution, such as Si-H_x , Si-OH and Si-F , and so forth. Usually these Raman bands are too weak to be detected from smooth Si surfaces. Thus silicon surfaces have been roughened either by chemical or electrochemical methods. After this pretreatment, a surface Raman signal with good SNR from a silicon surface can be obtained [99]. The influence of pH on the initial oxidation of an H-terminated silicon surface in a NaF solution was studied by in situ Raman spectroscopy and the

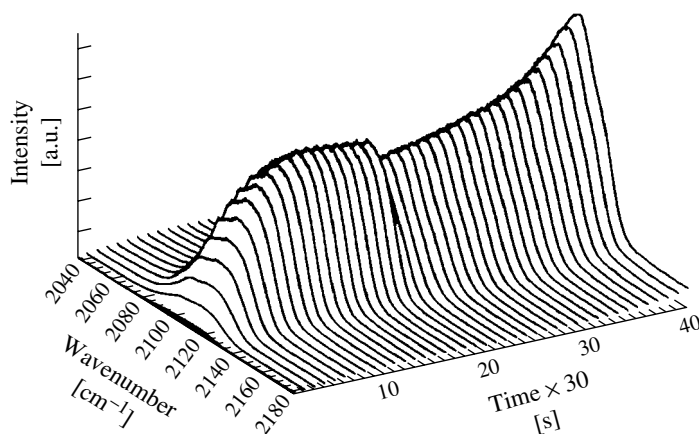


Fig. 51 Development of the SERS signal of the CN stretch vibration during deposition on platinum in 0.027 mol l^{-1} KCN, 0.003 mol l^{-1} AgNO₃ and 0.36 mol l^{-1} KNO₃. Excitation line: 514.5 nm. (Reproduced with permission from Ref. [80].)

spectra are given in Fig. 52. The intensity of the 629 cm^{-1} band decreases with increasing solution pH. It is an overlapped band of the silicon hydride and the multiphonon structure of silicon bulk. A new peak arose at 662 cm^{-1} when the pH was in the range of 7 to 9, which was assigned to SiF_6^{2-} . When the solution pH was higher than 9, hydrolysis to $\text{SiF}_4\text{OH}_2^{2-}$ occurred, hence the band at 662 cm^{-1} disappeared.

On the high frequency side, the band centered at 2100 cm^{-1} decreases remarkably with increasing pH leaving the bands of the mono- and trihydride, at about 2086 cm^{-1} . When the pH is higher than 7, another band centered at 2257 cm^{-1} , assigned to the Si-H stretching vibration in $-\text{O}_3\text{SiH}$ appeared. On the basis of the above finding, a mechanism for removal of hydride on the silicon surface in a F^- containing solution was proposed: an

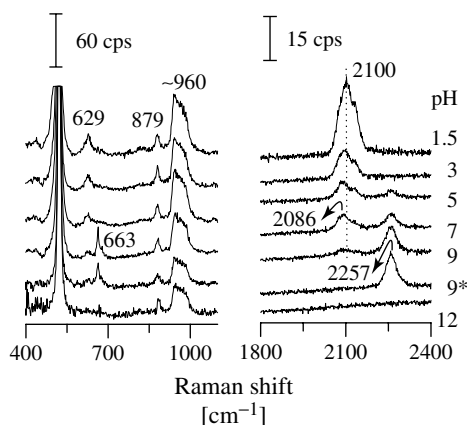


Fig. 52 In situ Raman spectra from a hydrogenated Si electrode in a solution of 0.1 mol l^{-1} NaF and a 20 % $\text{C}_2\text{H}_5\text{OH}$ solution with different pH, respectively. *20 min after detection, in solution of pH = 9. Excitation line: 632.8 nm.

intermediate containing both OH and F atoms might form during the oxidation processes. In this case, the oxygen atom in the Si-OH would easily transfer and attack the silicon backbond (Si-Si), assisted by the strong polarization of the F atom, leading to the removal of surface hydride and the formation of oxygen-containing species.

3.6.5

Prospective and Future Developments

Along with significant developments in laser technology, Raman instrumentation, and nanotechnology, many opportunities will be provided for progress in electrochemical Raman spectroscopy to further enhance our understanding of electrode surfaces. The future prospects will be given briefly and are divided into two parts, involving new surfaces and methods.

3.6.5.1 New Surfaces

3.6.5.1.1 Ordered Nanostructured Surfaces A recent breakthrough in the SERS field was the enormous enhancements, with SEF up to 10^{14} , for molecules of very large Raman cross section. This made it possible to obtain Raman signals from a single molecule [100–103]. High-quality SERS or (SERRS) spectra from a single molecule adsorbed on the surface of a single silver particle or aggregated silver colloids could be obtained. It is of particular interest that only substrates with particle sizes of 80 to 100 nm could have the highest enhancement effect for Ag. Compared with the normal surface enhancement factor of 10^6 , this phenomenon indicates SERS substrates with much higher activity can be prepared, in particular with the aid of rapid development of nanofabrication technology (vide

infra). There is no doubt that by using well controlled surface nanostructuring techniques, nanostructured electrodes, with the optimized particle size and shape and very narrow size distribution, will be prepared. Many electrode substrates with extremely high SERS activity can be made and the detection sensitivity of SERS for a variety of electrode materials will further improve. This strategy will be very helpful for obtaining deeper insight into the complicated enhancement mechanism of SERS.

Lithography Highly ordered periodic arrays of nanodots or nanorods can be prepared by lithography. One can use metal film or particle deposition over periodic arrays of polymer nanospheres or silica posts, which are generated by electron-beam lithography [104, 105]. The possibility of generating 2-dimensional ordered arrays with SERS-active structures of different structural parameters on one substrate, in a single production cycle, further increases the usefulness of the e-beam method in the fast development of optimum SERS substrates. By evaporating the metal at a different angle, along a direction in which the posts shadow each other, isolated metal particles are obtained on top of each post, with different shapes. However, in order to make the substrate applicable to the electrochemical system, one has to make it electrochemically conductive.

Template synthesis Ordered nanostructured surfaces can be prepared by the template synthesis technique [106, 107]. The metal can be evaporated into a template of ordered nanopores, which is then removed, leaving behind metal rod or wire arrays formed in the interstices. This approach of making ordered nanorod arrays

has been realized in the authors' laboratory as high SERS-active substrates, especially for transition metals (e.g. Ni, Co, and Fe) [108], see Fig. 17(b) for an example of ordered surface structure. The arrays are fabricated by electrodepositing metals into the ordered and parallel nanoholes of the alumina film as the template. The SERS intensities depend critically on the length of the rods emerging from the surface. The reasonable reproducibility of the regularly structured SERS substrates on the nanometer scale improves the applicability of the technique in electrochemistry, quantitative chemical analysis, and even electrochemical or optical sensors.

3.6.5.1.2 Well-defined Single Crystal Surfaces

The SERS study using an ATR Raman cell with Otto configuration on true smooth single crystal surfaces, under electrochemical conditions, has been accomplished recently [19]. The enhancement factor assisted by the surface plasma enhancement for single crystal Cu surfaces is estimated to be around 1 to 2 orders. Another type of ATR Raman cell, with Kretschmann configuration, has been used to obtain SERS from the Ag(111) surface, as well as Pt and Ni surfaces, without applying an electrode potential. It should be noted that, at present, there are only a very limited number of molecules with large Raman cross sections that can be used for these difficult investigations. One of the major challenges to the further application of surface Raman spectroscopy is to improve the Raman instrumentation and method to extend the study to a variety of molecules. A detailed comparison of the signal from well-defined monocrystalline surfaces and rough surfaces will surely lead to a better level of understanding of SERS mechanisms as well as surface (interfacial) electrochemistry.

3.6.5.2 New Methods

3.6.5.2.1 Tip-enhanced Raman Spectroscopy

In addition to ATR SERS, there is a new approach to study smooth metal surfaces, which is named tip surface-enhanced Raman spectroscopy [109]. It combines Raman spectroscopy at smooth metal surfaces with an STM tip used as an amplifier of the electromagnetic field. This approach is generally applicable, to metal–vacuum, metal–gas phase or metal–electrolyte interfaces. As shown in Fig. 53, a homogeneous and smooth gold film of 12 nm thickness was used, evaporated on a 1 mm thick glass support. This allowed light to pass from the backside to the metal-adsorbate–solution interface and to the collection of the Raman scattering from the adsorbate in the back-scattering mode. The size of the focal area was about 2 μm in diameter. An electrochemically etched Ag wire is used as an STM tip.

Fig. 53(b) shows two Raman spectra obtained with the STM tip retracted and in tunneling mode. If the tip is retracted, only very weak Raman scattering occurs. However, if the tip is in tunneling position (with the tip-surface distance around 1 nm), the total Raman intensity increases by a factor of 15. Many bands, which were previously obscured by noise, are now clearly discernible. The field enhancement by the tunneling tip is due to the excitation of localized SP, which is also effective at the substrate areas in close proximity to the tip apex. Thus, the illuminated tip in tunneling mode can induce SERS from the smooth surface. Although this new technique has not yet been applied to electrode surfaces, it shows great promise for two reasons: it can be used to study atomically flat surfaces and it has a very high spatial resolution.

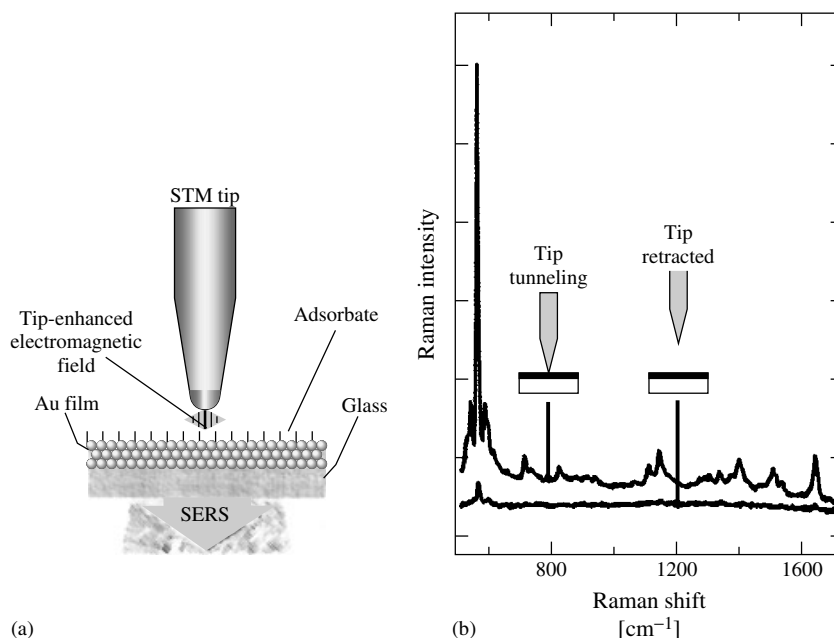


Fig. 53 (a) Scheme of tip enhancement of Raman scattering. (b) Comparison of a RR spectrum with the tip-enhanced Raman spectrum for brilliant cresyl blue at a smooth gold film. Coverage: 0.5 ML. Tunneling distance 1 nm, retracted distance: 1000 nm. Laser source: 633 nm, 0.05 mW. (Reproduced with permission from Ref. [109].)

3.6.5.2.2 Near-field Raman Spectroscopy

Another important approach is to develop scanning near-field optical microscopy (SNOM), also called near-field scanning optical microscopy (NSOM), which allows the optical imaging with a spatial resolution (~ 20 nm) well beyond the diffraction limit. Near-field Raman spectroscopy [110] is a combination of SNOM with Raman spectroscopy, which will provide a powerful tool to obtain chemical information on surfaces (interfaces) with nanoscale spatial resolution. The cross sections of Raman scattering are usually extraordinarily small, however, the combination of SNOM and Raman spectroscopy can be facilitated by the use of RR scattering and SERS. A high spatial resolution SNOM apparatus has been developed by using high efficiency optical

fiber probes, to obtain Raman spectra of copper phthalocyanine film with a thickness at about 50 nm on a prism. However, it should be noted that the sensitivity of this technique is still quite low compared to the conventional Raman system, because of the extremely low output of laser power. Therefore, the ATR configuration is combined with SNOM to gain a field enhancement because of the excitation of localized SP [111], which will be feasible for application to electrode surfaces in the future.

3.6.5.2.3 Surface Enhanced Hyper-Raman Spectroscopy (SEHRS)

Hyper-Raman scattering is a nonlinear three-photon energy conversion process, that offers complementary information to Raman spectroscopy and has some advantages

because of relaxed selection rules. In principle, the hyper-Raman-active vibrational modes of a centrosymmetric molecule are complementary to its Raman-active vibrational modes. However, the low scattering efficiency has single-handedly impeded the development of hyper Raman as a prominent analytical technique. Especially for surface species, one has to use surface enhancement to circumvent the low intensity problem. Surface-enhanced hyper-Raman scattering [112] can greatly increase the surface detection sensitivity with an enhancement factor of up to 10^{10} . As a result, compared with SERS, the surface-enhanced hyper-Raman scattering (SEHRS) for a centrosymmetric molecule shows some new vibrational bands and significant relative intensity changes. By contrast, the SEHRS spectrum for a noncentrosymmetric molecule resembles SERS, showing the absence of new vibrational bands. It is possible to obtain rich vibrational information and observe both IR and Raman-inactive vibrational modes. At present, SEHRS can only obtain signals from adsorbates with large Raman cross sections (such as pyrazine) and dye-samples on electrode surfaces. The approach to find stable SEHRS substrates with very high activity is a key aim.

Acknowledgments

This work has been possible by the financial support of the Natural Science Foundation of China and the Ministry of Education of China under the contracts Nos. 29625306, 29833060, 29903009, 2020012 and 99177. We are most grateful to the editor of this volume, P. Unwin, for extensively editing the English with some valuable suggestions. We are also very grateful to D. Y. Wu, Z. F. Huang, K. Q. Huang, F. M. Liu, B. W. Mao

and G. K. Liu who have provided much help and assistance in editing and typing the article. Whenever the work from the authors' group is mentioned in the article, it is the contribution of the self-motivated and hard working students and all other group members.

References

1. M. Fleischmann, P. J. Hendra, A. J. McQuillan, *J. Chem. Soc., Chem. Commun.* **1973**, 80–81.
2. D. L. Jeanmaire, M. R. Suchanski, R. P. Van Duyne, *J. Am. Chem. Soc.* **1975**, 97, 1699–1707.
3. M. Fleischmann, P. J. Hendra, A. J. McQuillan, *Chem. Phys. Lett.* **1974**, 26, 163–166.
4. D. L. Jeanmaire, R. P. Van Duyne, *J. Electroanal. Chem.* **1977**, 84, 1–20.
5. M. G. Albrecht, J. A. Creighton, *J. Am. Chem. Soc.* **1977**, 99, 5215–5217.
6. R. P. Van Duyne in *Chemical and Biochemical Applications of Lasers* (Ed.: C. B. Moore), Academic Press, New York, 1979, pp. 101–185, Vol. 4.
7. R. K. Chang, T. E. Furtak, *Surface Enhanced Raman Scattering*, Plenum Press, New York, 1982.
8. M. Fleischmann, Z. Q. Tian, L. J. Li, *J. Electroanal. Chem.* **1987**, 217, 397–410.
9. L. W. Leung, M. J. Weaver, *J. Am. Chem. Soc.* **1987**, 109, 5113–5119.
10. M. Fleischmann, I. R. Hill in *Comprehensive Treatise of Electrochemistry* (Eds.: R. E. White, J. O'M. Bockris, B. E. Conway et al.), Plenum Press, New York, 1984, pp. 373–432, Vol. 8.
11. M. J. Weaver, P. Gao, D. Gosztola et al. in *Excited States and Reactive Intermediates* (Ed.: A. B. P. Lever), ACS Symposium Series, Washington, 1986, pp. 135–149, Vol. 307.
12. J. E. Pemberton in *In situ Studies of Electrochemical Interfaces: A Prospectus* (Ed.: H. D. Abruna), VCH Verlag Chemie, Berlin, Germany, 1991, pp. 328–352.
13. R. L. Birke, T. Lu, J. R. Lombardi in *Techniques for Characterization of Electrodes and Electrochemical Processes* (Eds.: R. Varma, J. R. Selman), John Wiley & Sons, New York, 1991, pp. 211–277.

14. B. Pettinger in *Adsorption at Electrode Surface* (Eds.: J. Lipkowski, P. N. Ross), VCH Publishers, New York, 1992, pp. 285–345.
15. Z. Q. Tian, J. S. Gao, X. Q. Li et al., *J. Raman Spectrosc.* **1998**, 29, 703–711.
16. Z. Q. Tian, B. Ren, D. Y. Wu, *J. Phys. Chem. B* **2002**, 106, 9463–9483.
17. S. Z. Zou, C. T. Williams, E. K. Y. Chen et al., *J. Am. Chem. Soc.* **1998**, 120, 3811–3812.
18. M. J. Weaver, S. Z. Zou, H. Y. H. Chan, *Anal. Chem.* **2000**, 72, 38A–47A.
19. A. Bruckbauer, A. Otto, *J. Raman Spectrosc.* **1998**, 29, 665–672.
20. G. W. Chantry in *The Raman Effect* (Ed.: A. Anderson), Marcel Dekker, New York, 1971, pp. 49–93.
21. D. A. Long, *The Raman Effect*, John Wiley & Sons, New York, 2002.
22. C. V. Raman, K. S. Krishnan, *Nature* **1928**, 121, 169.
23. J. Behringer, J. Brandmuller, *Z. Elektrochem.* **1956**, 60, 643–673.
24. Z. Q. Tian, B. Ren, *Progress in Surface Raman Spectroscopy*, Xiamen University Press, Xiamen, 2000.
25. M. Moskovits, *Rev. Mod. Phys.* **1985**, 57, 783–826.
26. M. Moskovits, L. L. Tay, J. Yang et al., *Top. Appl. Phys.* **2002**, 82, 215–226.
27. A. Otto in *Light Scattering in Solid* (Eds.: M. Cardona, G. Guntherodt), Springer-Verlag, Berlin, Germany, 1984, pp. 289–418, Vol. IV.
28. A. Otto, I. Mrozek, H. Grabhorn et al., *J. Phys. Condens. Matter* **1992**, 4, 1143–1176.
29. A. Campion, P. Kambhampati, *Chem. Soc. Rev.* **1998**, 27, 241–249.
30. B. T. Draine, P. J. Flatau, *J. Opt. Soc. Am. A* **1994**, 11, 1491–1499.
31. J. Corset, J. Aubard, *J. Raman Spectrosc.* **1999**, 29(8).
32. M. K. Urban, *Vibrational Spectroscopy of Molecules and Macromolecules on Surfaces*, John Wiley & Sons, New York, 1993.
33. P. Hollins, J. Pritchard, *Prog. Surf. Sci.* **1985**, 19, 275–350.
34. A. Bewick, S. Pons in *Advances in Infrared and Raman Spectroscopy* (Eds.: R. J. H. Clark, R. E. Hester), Hayden, Chichester, UK, 1985, pp. 1–63, Vol. 12.
35. M. J. Weaver, S. Zou in *Spectroscopy for Surface Science* (Eds.: R. J. H. Clark, R. E. Hester), John Wiley & Sons, New York, 1998, pp. 219–272, Vol. 26.
36. D. K. Lambert, *Electrochim. Acta* **1996**, 41, 623–630.
37. M. Moskovits, *J. Chem. Phys.* **1982**, 77, 4408–4416.
38. J. A. Creighton in *Spectroscopy of Surface* (Eds.: R. J. H. Clark, R. E. Hester), John Wiley & Sons, New York, 1988, pp. 37–88.
39. H. Baranska, A. Labudzinska, J. Terpinski, *Laser Raman Spectroscopy – Analytical Applications*, Ellis Horwood, Chichester, UK, 1987.
40. D. B. Chase, J. F. Rabolt, *Fourier Transform Raman Spectroscopy – from Concept to Experiment*, Academic Press, San Diego, Calif., 1994.
41. G. Turrell, J. Corset, *Raman Microscopy*, Academic Press, San Diego, Calif., 1996.
42. R. L. McCreery, *Raman Spectroscopy for Chemical Analysis*, John Wiley & Sons, New York, 2000.
43. D. J. Gardiner, P. R. Graves, *Practical Raman Spectroscopy*, Springer-Verlag, Berlin, Germany, 1988.
44. P. Novak, J.-C. Panitz, F. Joho et al., *J. Power Sources* **2000**, 90, 52–58.
45. A. M. Stacy, R. P. Van Duyne, *Chem. Phys. Lett.* **1983**, 102, 365–370.
46. M. Datta, R. E. Jansson, J. J. Ereeman, *Appl. Spectrosc.* **1986**, 40, 251–258.
47. H. Luo, M. J. Weaver, *J. Electroanal. Chem.* **2001**, 501, 141–150.
48. G. Niaura, A. K. Gaigalas, V. L. Vilker, *J. Raman Spectrosc.* **1997**, 28, 1009–1011.
49. C. A. Melendres, J. McMahon, W. Ruther, *J. Electroanal. Chem.* **1986**, 202, 175–178.
50. J. E. Pemberton, R. P. Buck, *J. Phys. Chem.* **1981**, 85, 248–262.
51. P. Gao, D. Gosztola, L. W. H. Leung et al., *J. Electroanal. Chem.* **1987**, 233, 211–222.
52. T. E. Furtak, D. Roy, *Surf. Sci.* **1985**, 158, 126–146.
53. K. T. Carron, G. Xue, M. L. Lewis, *Langmuir* **1991**, 7, 2–4.
54. J. S. Gao, Z. Q. Tian, *Spectrochim. Acta, Part A* **1997**, 53, 1595–1600.
55. S. Z. Zou, M. J. Weaver, X. Q. Li et al., *J. Phys. Chem. B* **1999**, 103, 4218–4222.
56. R. P. Van Duyne, J. P. Haushalter, *J. Phys. Chem.* **1983**, 87, 2999–3003.
57. J. Clavilier in *Interfacial Electrochemistry* (Ed.: A. Wieckowski), Marcel Dekker, New York, 1999, pp. 231–248.

58. Z. Q. Tian, Y. X. Chen, B. Ren et al., *J. Chem. Soc., Faraday Trans.* **1996**, 96, 3829–3838.
59. Z. Q. Tian, W. H. Li, Z. H. Qiao et al., *Russ. J. Electrochem.* **1995**, 31, 935–940.
60. R. L. Birke, J. R. Lombardi, *Mol. Eng.* **1994**, 4, 277–310.
61. W. Zhang, A. Vivoni, R. L. Birke et al., *J. Phys. Chem.* **1995**, 99, 12846–12857.
62. Z. Q. Tian, W. H. Li, B. W. Mao et al., *Appl. Spectrosc.* **1996**, 50, 1569–1577.
63. N. Boucherit, A. Hugot-Le Goff, *Faraday Discuss.* **1992**, 94, 137–147.
64. T. Ozeki, D. E. Irish, *J. Electroanal. Chem.* **1990**, 280, 451–455.
65. C. Amatore, F. Bonhomme, J. L. Bruneel et al., *Electrochem. Commun.* **2000**, 2, 235–239.
66. W. B. Cai, B. Ren, X. Q. Li et al., *Surf. Sci.* **1998**, 406, 9–22.
67. W. Hill, V. Fallourd, D. Klockow, *J. Phys. Chem. B* **1999**, 103, 4707–4713.
68. R. P. Van Duyne, J. C. Hulteen, D. A. Treichel, *J. Chem. Phys.* **1993**, 99, 2101–2115.
69. G. Aloisi, A. M. Funtikov, R. Guidelli, *Surf. Sci.* **1993**, 296, 291–298.
70. Z. Q. Tian, W. H. Li, B. Ren et al., *J. Electroanal. Chem.* **1996**, 401, 247–251.
71. M. Fleischmann, P. R. Graves, I. R. Hill, *Chem. Phys. Lett.* **1983**, 98, 503–506.
72. M. J. Weaver, S. Zou in *Interfacial Electrochemistry: Theory, Experiment and Applications* (Eds.: A. Wieckowski), Marcel Dekker, New York, 1999, pp. 301–316.
73. M. J. Weaver, *J. Raman. Spectrosc.* **2002**, 33, 309–317.
74. T. M. Cotton in *Spectroscopy of Surface* (Eds.: R. J. H. Clark, R. E. Hester), John Wiley & Sons, New York, 1988, pp. 89–153.
75. Y. C. Liu, R. L. McCreedy, *Anal. Chem.* **1997**, 69, 2091–2097.
76. K. Ray, R. L. McCreedy, *Anal. Chem.* **1997**, 69, 4680–4687.
77. A. G. Brolo, D. E. Irish, B. D. Smith, *J. Mol. Struct.* **1997**, 405, 29–44.
78. C. A. Melendres in *Spectroscopic and Diffraction Techniques in interfacial Electrochemistry* (Eds.: C. Gutierrez, C. Melendres), Kluwer Academic Publishers, Dordrecht, The Netherlands, 1990, pp. 181–222.
79. C. A. Melendres in *Electrochemical and Optical Techniques for the Study and Monitoring of Metallic Corrosion* (Eds.: M. G. S. Ferreira, C. A. Melendres), NATO-ASI Series 203, Kluwer Academic Publishers, Dordrecht, The Netherlands, 1991, pp. 355–388.
80. W. Plieth, *Z. Phys. Chem.* **1999**, 208, 211–223.
81. X. Xu, B. Ren, D. Y. Wu et al., *Surf. Interface Anal.* **1999**, 28, 111–114.
82. S. A. Wasileski, M. J. Weaver, *Faraday Discuss.* **2002**, 121, 285–300.
83. S. Z. Zou, M. J. Weaver, *Anal. Chem.* **1998**, 70, 2387–2395.
84. J. Xu, R. L. Birke, J. R. Lombardi, *J. Am. Chem. Soc.* **1987**, 109, 5645–5649.
85. Q. J. Huang, J. L. Yao, R. A. Gu et al., *Chem. Phys. Lett.* **1997**, 271, 101–106.
86. Y. X. Chen, S. Z. Zou, K. Q. Huang et al., *J. Raman Spectrosc.* **1998**, 29, 749–756.
87. A. Shen, J. E. Pemberton, *Phys. Chem. Chem. Phys.* **1999**, 1, 5677–5684.
88. P. Gao, D. Gosztola, M. J. Weaver, *J. Phys. Chem.* **1988**, 92, 7122–7130.
89. I. Taniguchi, K. Umekita, K. Yasukouchi, *J. Electroanal. Chem.* **1986**, 202, 315–322.
90. M. Endo, C. Kim, T. Karaki et al., *Synth. Met.* **1998**, 98, 17–24.
91. H. Kanoh, W. P. Tang, K. Ooi, *Electrochem. Solid State Lett.* **1998**, 1, 17–19.
92. B. Ren, X. Q. Li, C. X. She et al., *Electrochim. Acta* **2000**, 46, 193–205.
93. M. F. Mrozek, H. Luo, M. J. Weaver, *Langmuir* **2000**, 16, 8463–8469.
94. V. Schroeder, T. M. Devine, *J. Electrochem. Soc.* **1999**, 146, 4061–4070.
95. J. D. Ramsey, R. L. McCreedy, *J. Electrochem. Soc.* **1999**, 146, 4076–4081.
96. H. Y. H. Chan, M. J. Weaver, *Langmuir* **1999**, 15, 3348–3355.
97. J. L. Yao, H. C. Liu, P. G. Cao et al. in *Electrochemical Approach to Selected Corrosion and Corrosion Control Studies* (Eds.: P. L. Bonora, F. Deflorian), European Federation of Corrosion Publications No. 28, IOM Communications Ltd, London, 2000, pp. 37–46.
98. G. Lacconi, B. Reents, W. Plieth, *J. Electroanal. Chem.* **1992**, 325, 207–217.
99. B. Ren, F. M. Liu, J. Xie et al., *Appl. Phys. Lett.* **1998**, 72, 933–935.
100. S. Nie, S. R. Emory, *Science* **1997**, 275, 1102–1106.
101. S. R. Emory, S. Nie, *J. Phys. Chem. B* **1998**, 102, 493–497.
102. K. Kneipp, Y. Wang, H. Kneipp et al., *Phys. Rev. Lett.* **1997**, 78, 1667–1670.

103. K. Kneipp, H. Kneipp, I. Itzkan et al., *Chem. Rev.* **1999**, 99, 2957–2978.
104. L. A. Dick, A. D. McFarland, C. L. Haynes et al., *J. Phys. Chem. B* **2002**, 106, 853–860.
105. S. Baldelli, A. S. Eppler, E. Anderson et al., *J. Chem. Phys.* **2000**, 113, 5432–5438.
106. C. R. Martin, *Science* **1994**, 266, 1961–1966.
107. H. Masuda, K. Fukuda, *Science* **1995**, 268, 1466–1468.
108. J. L. Yao, G. P. Pan, K. H. Xue et al., *Pure Appl. Chem.* **2000**, 72, 221–228.
109. B. Pettinger, G. Picardi, R. Schuster et al., *Electrochemistry* **2000**, 68, 942–949.
110. J. Rausem, B. Humbert, M. Spajer et al., *J. Raman Spectrosc.* **1999**, 30, 833–840.
111. M. Futamata, A. Bruckbauer, *Chem. Phys. Lett.* **2001**, 341, 425–430.
112. W. H. Li, X. Y. Li, N. T. Yu, *Chem. Phys. Lett.* **2000**, 327, 153–161.

